PHARMACOGNOSTIC CHARACTERIZATION, PHYTOCHEMICAL PROFILING AND BIOLOGICAL ACTIVITIES OF SELECTED SPECIES OF *SYZYGIUM* GAERTNER (MYRTACEAE) ENDEMIC TO WESTERN GHATS

Part I

Thesis
submitted to the University of Calicut
for the award of the Degree of

DOCTOR OF PHILOSOPHY IN BOTANY

By

SNEHALATHA V R

Under the guidance of

Prof. (Dr.) RASMI A R

PG AND RESEARCH DEPARTMENT OF BOTANY
GOVT. VICTORIA COLLEGE, PALAKKAD, KERALA-678001, INDIA
AFFILIATED TO THE UNIVERSITY OF CALICUT
SEPTEMBER 2025

PHARMACOGNOSTIC CHARACTERIZATION, PHYTOCHEMICAL PROFILING AND BIOLOGICAL ACTIVITIES OF SELECTED SPECIES OF *SYZYGIUM* GAERTNER (MYRTACEAE) ENDEMIC TO WESTERN GHATS

Part II

Thesis
submitted to the University of Calicut
for the award of the Degree of

DOCTOR OF PHILOSOPHY IN BOTANY

By

SNEHALATHA V R

Under the guidance of

Prof. (Dr.) RASMI A R

PG AND RESEARCH DEPARTMENT OF BOTANY
GOVT. VICTORIA COLLEGE, PALAKKAD, KERALA-678001, INDIA
AFFILIATED TO THE UNIVERSITY OF CALICUT
SEPTEMBER 2025

POSTGRADUATE AND RESEARCH DEPARTMENT OF BOTANY
GOVERNMENT VICTORIA COLLEGE
PALAKKAD, KERALA, INDIA–678001
Phone (Off.) – 04912576773; Website: www.victoriacollege.ac.in

Dr. Rasmi A R
Professor & Head
PG and Research Department of Botany

CERTIFICATE

This is to certify that the thesis entitled **"PHARMACOGNOSTIC CHARACTERIZATION, PHYTOCHEMICAL PROFILING AND BIOLOGICAL ACTIVITIES OF SELECTED SPECIES OF *SYZYGIUM* GAERTNER (MYRTACEAE) ENDEMIC TO WESTERN GHATS"** submitted to the University of Calicut by **Ms. Snehalatha V R** in partial fulfillment for the award of the Degree of Doctor of Philosophy in Botany is a bonafide record of the research work carried out by her under the guidance and supervision at research Department of Botany, Govt. Victoria College, Palakkad.

Palakkad
09/09/2025

Dr. Rasmi A R
(Professor of Botany)

Govt. VICTORIA COLLEGE
DEPT. OF BOTANY
Date :.....
Palakkad, Kerala- 678 001

Prof. (Dr.) RASMI A.R Msc., BEd., Phd
PEN : 596335
Professor & Head
Department of Botany
Govt. Victoria College, Palakkad-678001
rasmibotany@gmail.com

GOVERNMENT VICTORIA COLLEGE, PALAKKAD

Kerala, India, PIN 678001

Affiliated to the University of Calicut

NAAC Accreditation - A Grade (3.2, Fourth Cycle)

Mobile: +91 8281716773 | Email: victoriapkd@gmail.com | Web: www.gvc.ac.in

No.GVCPKD/192/2025-A3

Dated. 09/09/2025

CERTIFICATE FROM THE HEAD OF THE INSTITUTION

This is to certify that the thesis entitled **"PHARMACOGNOSTIC CHARACTERIZATION, PHYTOCHEMICAL PROFILING AND BIOLOGICAL ACTIVITIES OF SELECTED SPECIES OF *SYZYGIUM* GAERTNER (MYRTACEAE) ENDEMIC TO WESTERN GHATS"** submitted to the University of Calicut by **Ms. Snehalatha V.R.**, in partial fulfillment for the Degree of Doctor of Philosophy in Botany. This thesis is hereby acknowledged as a bonafide record of the research work conducted by the candidate under the guidance of Prof.(Dr.) Rasmi A.R., Research guide, PG and Research Department of Botany, Govt. Victoria College, Palakkad. I affirm that this thesis represents the independent work of the candidate under her supervision, and no part of it has been submitted previously for the award of any other degree, or diploma in any other university.

GOVERNMENT VICTORIA COLLEGE * PALAKKAD - 678 001 * Date .....

9/9/25

Principal

PRINCIPAL

GOVT. VICTORIA COLLEGE

PALAKKAD

DECLARATION

I hereby declare that the work presented in the thesis entitled **"PHARMACOGNOSTIC CHARACTERIZATION, PHYTOCHEMICAL PROFILING AND BIOLOGICAL ACTIVITIES OF SELECTED SPECIES OF *SYZYGIUM* GAERTNER (MYRTACEAE) ENDEMIC TO WESTERN GHATS"** is based on the original work done by me under the guidance of **Prof. (Dr.) Rasmi A R** at PG and Research Department of Botany, Govt. Victoria College, Palakkad, Kerala, has not been included in any other thesis submitted previously for the award of any degree. The contents of the thesis have undergone a plagiarism check using iThenticate software at C.H.M.K. Library, University of Calicut, and the similarity index found within the permissible limit. I also declare that the thesis is free from AI-generated contents

Ms. Snehalatha V R

Palakkad
09/09/2025

Prof. (Dr.) Rasmi A R
PG and Research Department of Botany
Govt. Victoria College, Palakkad, Kerala,

Govt. VICTORIA COLLEGE
DEPT. OF BOTANY
Date :.....
Palakkad, Kerala- 678 001

Prof. (Dr.) RASMI A.R Msc., BEd., Phd
PEN : 596335
Professor & Head
Department of Botany
Govt. Victoria College, Palakkad-678001
rasmibotany@gmail.com

ACKNOWLEDGEMENT

"For the Mighty One Has Done Great Things for Me-
Holy is His Name" (Luke 1:49).

First and foremost, I offer my deepest gratitude, praise, and heartfelt reverence to my Lord Jesus Christ. I am sincerely thankful to the Holy Family- St. Joseph, St. Mary, and all the saints, especially St. Antony, whose blessings have guided and strengthened me throughout my research journey, enabling the successful completion of this work. Thank you, Jesus.

I am profoundly grateful for the unwavering love, encouragement, and support of my parents, Joseph and Mary. Their constant faith in me has been my foundation and source of strength.

I express my sincere appreciation to my research guide, Prof. (Dr.) Rasmi A R, for her invaluable supervision, expert guidance, and constant encouragement throughout this study. Her mentorship has been instrumental in shaping this research.

I extend my heartfelt thanks to the principal for providing excellent laboratory facilities and continuous support. I also thank all the faculty members of the Department of Botany, including Dr. Suresh, Dr. Sojan Jose, Dr. Reethu, Dr. Sajitha Menon, Ms. Alen Alex, Dr. Leeja, and the entire teaching and non-teaching staff for their cooperation and assistance.

Special gratitude is due to Dr. Sujanapal (KFRI) and Dr. Pradeep (University of Calicut) for their expert assistance in plant identification, and to Dr. Dantus and Sumod for their help with plant collection.

I am thankful to Mr. Shajihan and Ms. Seema, librarians at Government Victoria College, Palakkad, and Calicut University, respectively, as well as all DOR members and staff of the University of Calicut.

My sincere thanks to Dr. Leena, Dr. Maya C. Nair, Dr. K. M. Jayaram, Dr. Jose T. Puthur, Anandvalli Teacher, and all my teachers for their continuous encouragement.

I gratefully acknowledge the support and cooperation of the Forest and Wildlife Department, Trivandrum; Amala Cancer Research Centre's Dr. Babu T. D., Dr. Achuthan, and my friends Dr. Silpa, Dr. Pareeth, Dr. Soumya, Dr. Sangeetha, and Meera.

I also thank Dr. Rajesh, Dr. Leeba Balan, Austin, Dr. Anand Sebastiane, Dr. Asish, Harinarayanan, Dr. Nimmi Haridas, Dr. Haridas, Civil Service Academy, Shilpa Arora, Susha, and many others who have provided valuable support.

I am deeply thankful to my friends Ashfaq, Karthika, Ummu Habbeba, Muhsina, Jayalakshmi, Reshma, Dr. Aswani, Dr. Maya, Dr. Jisha, Dr. Jabeena, Dr. Rekha, Kanakambika, Athira, Remya, and all others who have supported me both academically and personally.

I gratefully acknowledge my Palakkad Diocese, Bishop, St. Joseph Parish, and St. Thomas Convent for their spiritual support. Special thanks to Fr. Jose Kochuparambil, Fr. Sebin, Fr. Sebastian Thamarassery, Fr. Jose Kulambil, and Fr. Jose Angeeveetil. Special thanks also to Fr. Reni and the Dhoni Retreat Centre community, and all my brothers and sisters in faith. Thanks to Fr. Jain, Fr. Franco, Fr. Raphy, Fr. Bitto, Fr. Joby, Fr. Nickson, Fr. Issac, and all members of the Sinai Retreat Centre.

I extend gratitude to Fr. Dr. Arun (STARS), Fr. Biju, Fr. Jose Kannampuzha, Fr. Robin, Fr. Varkey, Fr. Joseph Arakkal, Fr. Dibin, Fr. Martin, Fr. Togy, Fe. Freejo, Mr. Subin, Pravachaka Sabdham team, Mr. Ramesh, Mrs. Khesia Ramesh, Sr. Rose, Sr. Jesmy, Sr. Lisieux, Sr. Lilly, Sr. Leena Jose, Sr. Teena, Sr. Shanti, Sr. Jancy, Sr. Gracy, Sr. Linda, Sr. Lincy, Sr. Rosmy, Sr. Rose James, and Sr. Lincy.My thanks also go to the Jesus Youth movement, Kids Ministry, Catechism Department, and KCYM.

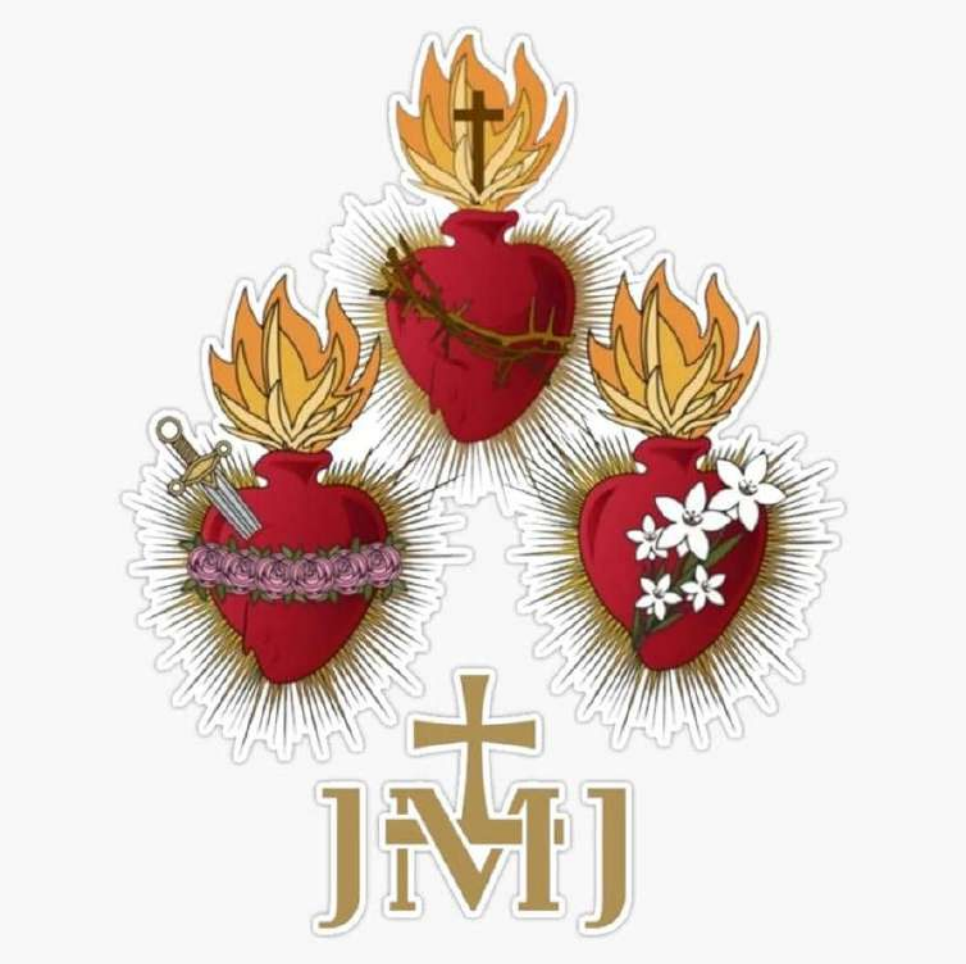
I am thankful for the constant prayers and support of Br. Sebastian and family, Fr. John MSFS, and all prayer and supporting team members, including Varkey Shaju, Manesh, George, Gracy, Oommen, James Chetan, Sr. Teena msbs, Sr. Phonsy, the St. Seraphic Provincial House, Sr. Linsa, Vimal Rani Provincial House, Jerry Nirmal, Sr. Anjalin, Sr. Beena, Reji, Beena Laly, George Cyriac, Lissy, Jessy, Jessy George, Joseph George, Aji Davis, Shaju, Ammini, Jayakrishan, Cyril Joseph, Missy, Jose, St. Thomas and St. Paul unit.

Thanks to Prasad, Rafeeq, and Bina Rajesh for their help with editing and binding. I sincerely thank my students and staff of St. Mary's College for their ongoing encouragement and support, especially Dr. Regi Raphael K and Sr. Dr. Santra.

Lastly, my heartfelt appreciation goes to my mother's family members- Siva cheriachan, Kamala mema, Amrutha mema, Ajitha chechi, Anikuttan, Sangeetha chechi, Santhosh chechi, Rajalakshmi aunty, Devan uncle, Sankunthala aunty, Chandran uncle, Baby chechi, Ashoketan, and all my mother's relatives- for their unconditional love and steadfast support.

It is impossible to thank individually all those who have contributed to this achievement, as it is built upon the support and efforts of many yesterdays. I am personally grateful to all those, both known and unknown, who have directly or indirectly helped me throughout the journey of this thesis dissertation.

Snehalatha V R



Dedicated to

The Sacred Heart of Jesus
Through
The Chaste Heart of Saint Joseph
and
The Immaculate Heart of Mother Mary

ABSTRACT

The genus *Syzygium*, known for its diverse medicinal applications, is represented by numerous endemic species in the Western Ghats. This study focused on the morpho-anatomical, pharmacognostic, and bioactive profiling of three such endemic species: *S. laetum*, *S. occidentale*, and *S. palghatense*. Detailed macroscopic examination revealed distinctive morphological features, including leaf shape, venation, and flower structure, that aid in species differentiation. Microscopically, variations in stomatal type, secretory structures, and crystal deposition were observed, reflecting their adaptation to the humid evergreen forest ecosystem. Histochemical studies demonstrated the presence of pharmacologically significant compounds such as tannins and oils, while powder microscopy and fluorescence analysis provided unique diagnostic markers for quality control.

Physicochemical analyses showed significant nutritional and chemical differences across species, with *S. laetum* leaves rich in phenolics and vitamin C, *S. occidentale* bark high in fibre and minerals, and *S. palghatense* bark showing elevated extractive values and mineral content. A novel aspect of this study was the green synthesis of silver nanoparticles (AgNPs) using methanol extracts of *S. palghatense* bark. Comprehensive bioactivity assays revealed that these AgNPs exhibit potent antioxidant, antimicrobial, anti-inflammatory, anthelmintic, and anticancer activities. The antioxidant capacity of the AgNPs surpassed standard antioxidants in free radical scavenging assays, while antimicrobial tests demonstrated broad-spectrum efficacy, including disruption of biofilms by pathogenic bacteria. Anti-inflammatory assays showed multi-target enzyme inhibition comparable or superior to conventional drugs. The anthelmintic effect on *Lumbricus terrestris* was rapid and potent, and cytotoxicity assays on cancer cell lines indicated significant induction of apoptosis.

The biological activity studies revealed that silver nanoparticles (AgNPs) synthesized from the methanol extract of *S. palghatense* bark exhibited significantly higher activity than both the isolated compound and the crude methanol extract alone. The enhanced efficacy of AgNPs is due to their nanoscale size, which improves bioavailability and interaction with biological targets. Among tested activities, AgNPs showed superior antioxidant, antimicrobial, anti-inflammatory, anthelmintic, and

anticancer effects, followed by the isolated compound and lastly the crude extract. This demonstrates the promising potential of green-synthesized nanoparticles to amplify the therapeutic effects of natural plant compounds.

Complementing experimental work, molecular docking and dynamic simulations provided mechanistic insights into the interaction of key phytochemicals and isolated compounds with protein targets, advancing the potential for drug discovery. The compound 2-Phenyl-4H-chromen-4-one, isolated from *S. palghatense*, consistently exhibited strong bioactivities across assays. This study not only clarifies taxonomic ambiguities through integrated morpho-anatomical and pharmacognostic data but also highlights the high medicinal potential and ecological importance of these Western Ghats endemics. Ultimately, the research supports their sustainable utilization in developing novel phytomedicines and nanomedicines, fostering conservation and validating traditional medicinal claims.

Keywords: *Syzygium laetum*, *Syzygium occidentale*, *Syzygium palghatense*, Pharmacology, Phytochemical profiling, Silver nanoparticles, 2-Phenyl-4H-chromen-4-one, Molecular docking and dynamics, Network pharmacology

സംഗ്രഹം

വൈവിധ്യമാർന്ന ഔഷധ പ്രയോഗങ്ങൾക്ക് പേരുകേട്ട സിസിജിയം ജനുസ്സിനെ പശ്ചിമഘട്ടത്തിലെ നിരവധി തദ്ദേശീയ സ്പീഷീസുകൾ പ്രതിനിധീകരിക്കുന്നു. സിസിജിയം ലേറ്റം, സിസിജിയം ഓക്സിഡന്റേൽ, സിസിജിയം പാൽഗാറ്റെൻസ് എന്നീ മൂന്ന് തദ്ദേശീയ സ്പീഷീസുകളുടെ രൂപാന്തര-ശരീരഘടന, ഫാർമക്കോഗ്നോസ്റ്റിക്, ബയോആക്ടീവ് പ്രൊഫൈലിംഗിലാണ് ഈ പഠനം ശ്രദ്ധ കേന്ദ്രീകരിച്ചത്. വിശദമായ മാക്രോസ്കോപ്പിക് പരിശോധനയിൽ ഇലയുടെ ആകൃതി, വെനേഷൻ, പൂവിന്റെ ഘടന എന്നിവയുൾപ്പെടെയുള്ള വ്യതിരിക്തമായ രൂപഘടന സവിശേഷതകൾ വെളിപ്പെടുത്തി, അവ സ്പീഷീസ് വ്യത്യാസത്തിന് സഹായിക്കുന്നു. സൂക്ഷ്മദർശിനിയിൽ, സ്റ്റോമറ്റൽ തരം, സ്രവ ഘടനകൾ, ക്രിസ്റ്റൽ നിക്ഷേപം എന്നിവയിലെ വ്യതിയാനങ്ങൾ നിരീക്ഷിക്കപ്പെട്ടു, ഇത് ഈർപ്പമുള്ള നിത്യഹരിത വന ആവാസവ്യവസ്ഥയുമായുള്ള അവയുടെ പൊരുത്തപ്പെടുത്തലിനെ പ്രതിഫലിപ്പിക്കുന്നു. ടാനിനുകൾ, എണ്ണകൾ തുടങ്ങിയ ഔഷധശാസ്ത്രപരമായി പ്രാധാന്യമുള്ള സംയുക്തങ്ങളുടെ സാന്നിധ്യം ഹിസ്റ്റോകെമിക്കൽ പഠനങ്ങൾ തെളിയിച്ചു, അതേസമയം പൗഡർ മൈക്രോസ്കോപ്പിയും ഫ്ലൂറസെൻസ് വിശകലനവും ഗുണനിലവാര നിയന്ത്രണത്തിന് സവിശേഷമായ ഡയഗ്നോസ്റ്റിക് മാർക്കറുകൾ നൽകി.

ഭൗതിക രാസ വിശകലനങ്ങൾ സ്പീഷീസുകളിലുടനീളം ഗണ്യമായ പോഷക, രാസ വ്യത്യാസങ്ങൾ കാണിച്ചു, സിസിജിയം ലേറ്റം ഇലകൾ ഫിനോളിക്സും വിറ്റാമിൻ സിയും കൊണ്ട് സമ്പന്നമാണ്, സിസിജിയം ഓക്സിഡന്റേൽ പുറംതൊലിയിൽ നാരുകളും ധാതുക്കളും കൂടുതലാണ്, സിസിജിയം പാൽഗാറ്റെൻസ് പുറംതൊലി ഉയർന്ന എക്സ്ട്രാക്റ്റീവ് മൂല്യങ്ങളും ധാതു ഉള്ളടക്കവും കാണിക്കുന്നു. സിസിജിയം പാൽഘാറ്റൻസ് പുറംതൊലിയിലെ മെഥനോൾ സത്ത് ഉപയോഗിച്ച് സിൽവർ നാനോപാർട്ടിക്കിളുകളുടെ (AgNPs) പച്ച സിന്തസിസ് നടത്തിയതാണ് ഈ പഠനത്തിന്റെ ഒരു പുതിയ വശം. ഈ AgNP-കൾ ശക്തമായ ആന്റിഓക്സിഡന്റ്, ആന്റിമൈക്രോബയൽ, ആന്റി-ഇൻഫ്ലമേറ്ററി, ആന്തെൽമിന്റിക്, കാൻസർ വിരുദ്ധ പ്രവർത്തനങ്ങൾ പ്രകടിപ്പിക്കുന്നതായി സമഗ്രമായ ബയോ ആക്ടിവിറ്റി പരിശോധനകൾ വെളിപ്പെടുത്തി. ഫ്രീ റാഡിക്കൽ സ്കാവെഞ്ചിംഗ് അസ്സേകളിൽ AgNP-കളുടെ ആന്റിഓക്സിഡന്റ് ശേഷി സ്റ്റാൻഡേർഡ് ആന്റിഓക്സിഡന്റുകളെ മറികടന്നു, അതേസമയം ആന്റിമൈക്രോബയൽ പരിശോധനകൾ രോഗകാരികളായ ബാക്ടീരിയകൾ ബയോഫിലിമുകളെ തടസ്സപ്പെടുത്തുന്നത് ഉൾപ്പെടെ വിശാലമായ സ്പെക്ട്രം ഫലപ്രാപ്തി പ്രകടമാക്കി. പരമ്പരാഗത മരുന്നുകളേക്കാൾ താരതമ്യപ്പെടുത്താവുന്നതോ മികച്ചതോ ആയ മൾട്ടി-ടാർഗെറ്റ് എൻസൈം ഇൻഹിബിഷൻ ആന്റി-ഇൻഫ്ലമേറ്ററി പരിശോധനകൾ കാണിച്ചു. ലംബ്രിക്കസ് ടെറസ്ട്രിസിലെ ആന്തെൽമിന്റിക് പ്രഭാവം വേഗത്തിലും ശക്തവുമായിരുന്നു, കൂടാതെ കാൻസർ സെൽ ലൈനുകളിലെ സൈറ്റോടോക്സിസിറ്റി അസ്സേകൾ അപ്പോപ്ടോസിസിന്റെ ഗണ്യമായ ഇൻഡക്ഷനെ സൂചിപ്പിക്കുന്നു.

സിസിജിയം പാൽഘാറ്റൻസ് പുറംതൊലിയിലെ മെഥനോൾ സത്തിൽ നിന്ന് സമന്വയിപ്പിച്ച സിൽവർ നാനോപാർട്ടിക്കിളുകൾ (AgNPs) ഒറ്റപ്പെട്ട സംയുക്തത്തേക്കാളും അസംസ്കൃത മെഥനോൾ സത്തിൽ നിന്നുമാത്രമുള്ളതിനേക്കാൾ ഗണ്യമായി ഉയർന്ന പ്രവർത്തനം പ്രകടിപ്പിച്ചതായി ജൈവ പ്രവർത്തന പഠനങ്ങൾ വെളിപ്പെടുത്തി. AgNP-കളുടെ

മെച്ചപ്പെട്ട ഫലപ്രാപ്തി അവയുടെ നാനോസ്കെയിൽ വലുപ്പം മൂലമാണ്, ഇത് ജൈവ ലഭ്യതയും ജൈവ ലക്ഷ്യങ്ങളുമായുള്ള ഇടപെടലും മെച്ചപ്പെടുത്തുന്നു. പരീക്ഷിച്ച പ്രവർത്തനങ്ങളിൽ, AgNP-കൾ മികച്ച ആന്റിഓക്സിഡന്റ്, ആന്റിമൈക്രോബയൽ, ആന്റി-ഇൻഫ്ലമേറ്ററി, ആന്തെൽമിന്റിക്, കാൻസർ വിരുദ്ധ ഫലങ്ങൾ കാണിച്ചു, തുടർന്ന് ഒറ്റപ്പെട്ട സംയുക്തവും ഒടുവിൽ അസംസ്കൃത സത്തും. പ്രകൃതിദത്ത സസ്യ സംയുക്തങ്ങളുടെ ചികിത്സാ ഫലങ്ങൾ വർദ്ധിപ്പിക്കുന്നതിന് ഗ്രീൻ-സിന്തസൈസ് ചെയ്ത നാനോപാർട്ടിക്കിളുകളുടെ വാഗ്ദാനമായ സാധ്യത ഇത് പ്രകടമാക്കുന്നു.

പരീക്ഷണ പ്രവർത്തനങ്ങൾക്ക് പൂരകമായി, മോളിക്യുലാർ ഡോക്കിംഗ്, ഡൈനാമിക് സിമുലേഷനുകൾ എന്നിവ പ്രധാന ഫൈറ്റോകെമിക്കലുകളുടെയും ഒറ്റപ്പെട്ട സംയുക്തങ്ങളുടെയും പ്രോട്ടീൻ ലക്ഷ്യങ്ങളുമായുള്ള പ്രതിപ്രവർത്തനത്തെക്കുറിച്ചുള്ള യാന്ത്രിക ഉൾക്കാഴ്ചകൾ നൽകി, മരുന്ന് കണ്ടെത്തലിനുള്ള സാധ്യതകൾ മെച്ചപ്പെടുത്തി. സിസിജിയം പാൽഗാറ്റെൻസിൽ നിന്ന് വേർതിരിച്ചെടുത്ത 2-ഫീനൈൽ-4H-ക്രോമെൻ-4-വൺ സംയുക്തം, പരിശോധനകളിലുടനീളം ശക്തമായ ജൈവപ്രവർത്തനങ്ങൾ സ്ഥിരമായി പ്രദർശിപ്പിച്ചു. സംയോജിത മോർഫോ-അനാട്ടമിക്കൽ, ഫാർമക്കോഗ്നോസ്റ്റിക് ഡാറ്റയിലൂടെ ഈ പഠനം വർഗ്ഗീകരണ അവ്യക്തതകൾ വ്യക്തമാക്കുക മാത്രമല്ല, ഈ പശ്ചിമഘട്ടത്തിലെ തദ്ദേശീയ ജീവികളുടെ ഉയർന്ന ഔഷധ സാധ്യതയും പാരിസ്ഥിതിക പ്രാധാന്യവും എടുത്തുകാണിക്കുകയും ചെയ്യുന്നു. ആത്യന്തികമായി, നൂതനമായ ഫൈറ്റോമെഡിസിനുകളും നാനോമെഡിസിനുകളും വികസിപ്പിക്കുന്നതിലും സംരക്ഷണം വളർത്തുന്നതിലും പരമ്പരാഗത ഔഷധ അവകാശവാദങ്ങൾ സാധൂകരിക്കുന്നതിലും അവയുടെ സുസ്ഥിര ഉപയോഗത്തെ ഗവേഷണം പിന്തുണയ്ക്കുന്നു.

സൂചകപദങ്ങൾ: സിസിജിയം ലേറ്റം, സിസിജിയം ഓക്സിഡന്റേൽ, സിസിജിയം പാൽഗാറ്റൻസ്, ഫാർമക്കോളജി, ഫൈറ്റോകെമിക്കൽ പ്രൊഫൈലിംഗ്, സിൽവർ നാനോകണങ്ങൾ, 2-ഫീനൈൽ-4-എച്ച്-ക്രോമെൻ-4-വൺ, മോളിക്യുലാർ ഡോക്കിംഗും ഡൈനാമിക്സും, നെറ്റ്വർക്ക് ഫാർമക്കോളജി

CONTENTS

	Page No.
1. GENERAL INTRODUCTION	**1-6**
1.1. *Syzygium* endemics in the Western Ghats	1
1.2. Role of *Syzygium* in traditional and modern medicine	2
1.3. Biological potentials of *Syzygium*	3
1.3.1. Antioxidant property	3
1.3.2. Antimicrobial activity	3
1.3.3. Anthelmintic effect	3
1.3.4. Anti-inflammatory action	3
1.3.5. Antidiabetic potential	4
1.3.6. Anticancer properties	4
1.4. Importance of the present study	4
1.5. Objectives of the study	5
2. REVIEW OF LITERATURE	**7-50**
2.1. Historical perspectives and taxonomic evolution of the genus *Syzygium*	8
2.2. Traditional and modern uses of *Syzygium*: A multifaceted approach	11
2.3. Recent discoveries and taxonomic advances in *Syzygium*	13
2.4. IUCN status and conservation of Western Ghats *Syzygium* endemics	16
2.5. Morpho-anatomical studies in *Syzygium*	17
2.6. Pharmacognostic studies	22
2.7. Phytochemical diversity and pharmacological potential of *Syzygium*	24
2.8. Biological activities of *Syzygium*	26
2.8.1. Antioxidant properties	28
2.8.2. Antimicrobial properties	30
2.8.3. Anthelmintic properties	33
2.8.4. Anti-inflammatory properties	35
2.8.5. Antidiabetic properties	37
2.8.6. Anticancer properties	40
2.9. Green synthesis of silver nanoparticles in *Syzygium*	43
2.10. Isolation of compounds in *Syzygium*	46
2.11. Molecular docking and dynamics	47

2.12. Network pharmacology in computational drug discovery and target interaction studies in *Syzygium* 48
CHAPTER 3 **51-88**
MORPHO-ANATOMICAL CHARACTERIZATION
3.1. Introduction 51
3.2. Materials and methods 56
3.2.1. Plant collection and authentication 56
3.2.2. Preparation of voucher herbarium specimen 56
3.2.3. Morpho-anatomical studies 56
3.2.4. Histochemical studies 57
3.3. Results 58
3.3.1. Macroscopic studies 58
3.3.2. Microscopic studies 60
3.3.3. Histochemical analysis 81
3.4. Discussion 83
3.5. Conclusion 87
CHAPTER 4 **89-116**
PHARMACOGNOSTIC CHARACTERIZATION
4.1. Introduction 89
4.2. Materials and methods 94
4.2.1. Powder analysis 94
4.2.2. Fluorescence analysis 95
4.2.3. Physicochemical evaluation 95
4.2.4. Statistical analysis 103
4.3. Results 105
4.3.1. Powder characteristics of leaves and bark of *Syzygium* endemics 105
4.3.2. Fluorescence analysis 106
4.3.3. Physicochemical and nutritional evaluation 107
4.4. Discussion 111
4.5. Conclusion 116
CHAPTER 5 **117-156**
PHYTOCHEMICAL PROFILING
5.1. Introduction 117
5.2. Materials and methods 122
5.2.1. Extraction of plant samples 122
5.2.2. Qualitative phytochemical analysis 123

5.2.3. Quantitative phytochemical analysis 128
5.2.4. Gas Chromatography-Mass Spectrometry (GC-MS) analysis 132
5.2.5. Liquid Chromatography-Mass Spectrometry Quadrupole Time of Flight (LC-MS QTOF) analysis 133
5.2.6. Statistical analysis 134
5.3. Results 135
5.3.1. The percentage of yield 135
5.3.2. Qualitative phytochemical analysis 135
5.3.3. Quantitative phytochemical analysis 136
5.3.4 Gas Chromatography-Mass Spectrometry (GC-MS) analysis 144
5.3.5. Liquid Chromatography-Mass Spectrometry Quadrupole Time of Flight (LC-MS QTOF) analysis 148
5.4. Discussion 151
5.5. Conclusion 156
CHAPTER 6 **157-186**
BIOLOGICAL ACTIVITIES
6.1. Introduction 157
6.2. Materials and Methods 162
6.2.1. Antioxidant activities 162
6.2.2. Antimicrobial activities 166
6.2.3. Anthelmintic activities 169
6.2.4. Anti-inflammatory activities 170
6.2.5. Anti-diabetic activity 172
6.2.6. Anticancer study 172
6.2.7. Statistical analysis 173
6.3. Results 174
6.3.1. Antioxidant studies 174
6.3.2. Antimicrobial studies 174
6.3.3. Anthelmintic activities 177
6.3.4. Anti-inflammatory activities 178
6.3.5. Antidiabetic studies 180
6.3.6. Anticancer study 181
6.4. Discussion 182
6.5. Conclusion 186

CHAPTER 7 **187-285**

GREEN SYNTHESIS, CHARACTERIZATION, AND BIOACTIVE EFFICACY OF SILVER NANOPARTICLES

7.1. Introduction 187

7.2. Materials and methods 191

7.2.1. Precursor preparation 191

7.2.2. Biosynthesis of Silver Nanoparticles 191

7.2.3. UV-Visible Absorbance Spectroscopy (UV-Vis) 191

7.2.4. Fourier Transforms Infrared Spectroscopy (FTIR) 192

7.2.5. Scanning Electron microscopy (SEM) Analysis 192

7.2.6. Transmission Electron Microscopy (TEM) Analysis 192

7.2.7. Atomic Force Microscopy (AFM) 193

7.2.8. X-Ray Diffraction (XRD) Analysis 193

7.2.9. Bioactivity screening of *S. palghatense* silver nanoparticles (AgNPs) 193

7.2.10. Statistical analysis 241

7.3. Results 242

7.3.1. UV-Visible analysis 242

7.3.2. FT-IR analysis 243

7.3.3. SEM analysis 243

7.3.4. TEM analysis 244

7.3.5. AFM analysis 244

7.3.6. XRD analysis 245

7.3.7. Antioxidant properties 245

7.3.8. Antimicrobial properties 247

7.3.9. Anthelmintic properties 256

7.3.10. Anti-inflammatory properties 256

7.3.11. Histopathology and wound healing studies 263

7.3.12. Antidiabetic properties 264

7.3.13. Anticancer properties 269

7.3.14. Formulation of a cream from the methanol extract of *S. palghatense* bark silver nanoparticles (AgNPs) 276

7.4. Discussion 278

7.5. Conclusions 285

CHAPTER 8 **287-326**

ISOLATION AND BIOACTIVITY VALIDATION OF PHYTOCOMPOUNDS

8.1. Introduction 287

8.2. Materials and methods 293

8.2.1. Isolation of and characterization of bioactive phytocompounds from the methanol extract of *S. palghatense* bark 293

8.2.2. Validation of the biological activities of an isolated compound 296

8.2.3. Statistical analysis 300

8.3. Results 302

8.3.1. Soxhlet extraction of *S. palghatense* bark 302

8.3.2. Isolation of bioactive compounds from *S. palghatense* bark 302

8.3.3. Characterization of compound 303

8.3.4. Biological activities of isolated compounds 309

8.4. Discussion 320

8.5. Conclusion 326

CHAPTER 9 **327-520**

MOLECULAR DOCKING AND DYNAMICS OF PHYTOCOMPOUNDS AGAINST KEY TARGETS

9.1. Introduction 337

9.2. Materials and Methods 337

9.2.1. Selection and preparation of target proteins 337

9.2.2. Physicochemical property prediction using ProtParam 338

9.2.3. Secondary structure prediction using Prosite 339

9.2.4. Ramachandran plot analysis using PROCHECK 340

9.2.5. Retrieval of bark phytocompounds 341

9.2.6. Docking with PyRx 342

9.2.7. Visualization 343

9.2.8. Post-docking analysis 343

9.2.9. Pharmacokinetic profiling of top–hit ligands 344

9.2.10. Toxicity profiling 345

9.2.11. Docking with a marketed drug 346

9.2.12. Trajectory–based structural analysis 346

9.2.13. Conformational sampling and landscape analysis 347

9.2.14. Binding free energy analysis 348

9.2.15. Normal mode analysis 348
9.2.16. Density Functional Theory (DFT) studies 349
9.3. Results 350
9.3.1. Selection and preparation of target proteins 350
9.3.2. Physicochemical properties of target proteins 350
9.3.3. Secondary structural analysis of target proteins 372
9.3.4. Ramachandran plot analysis of target proteins 386
9.3.5. Docking with PyRx 399
9.3.6. Visualization 403
9.3.7. Post-docking analysis 438
9.3.8. Pharmacokinetic profiling of top-hit ligands 453
9.3.9. Physicochemical properties 454
9.3.10. Drug-likeness 454
9.3.11. Medicinal chemistry 454
9.3.12. Metabolism 455
9.3.13. Toxicity 455
9.3.14. Docking with a marketed drug 456
9.3.15. Docking with an antioxidant market drug 457
9.3.16. Overall conclusion- Antioxidant activity from Molecular dynamics (MDS) analysis 462
9.3.17. Binding Free Energy (MM/PBSA) 463
9.3.18. Normal Mode Analysis (NMA) for antioxidant target (KEAP1) 464
9.3.19. Docking with a marketed antimicrobial drug 466
9.2.20. Docking with a marketed anthelmintic drug 476
9.3.21. Docking with a marketed anti-inflammatory drug 485
9.3.22. Docking with a marketed antidiabetic drug 495
9.3.23. Docking with an anticancer marketed drug 504
9.4. Discussion 513
9.5. Conclusion 520
CHAPTER 10 **521-564**
NETWORK PHARMACOLOGY AND FUNCTIONAL ANALYSIS OF ISOLATED COMPOUND
10.1. Introduction 521
10.2. Materials and methods 526
10.2.1. Compound retrieval and structure preparation 526
10.2.2. Pharmacokinetic profiling 526

10.2.3. Target prediction using the similarity ensemble approach 527
10.2.4. SwissTargetPrediction-Based Target Prediction 527
10.2.5. Construction of 2-Phenyl-4H-chromen-4-one target library 528
10.2.6. Construction of Protein–Protein Interaction (PPI) network 528
10.2.7. Functional enrichment analysis 529
10.2.8. Pathway enrichment analysis 530
10.2.9. Disease association analysis 530
10.2.10. Identification of Hub genes 531
10.2.11. Molecular Docking with the EGFR 531
10.2.12. Molecular dynamics simulation 532
10.2.13.Conformational sampling and landscape analysis 533
10.2.14. Binding free energy analysis 533
10.2.15. DFT studies for 2-Phenyl-4H-chromen-4-one 533
10.3. Results 535
10.3.1. Compound retrieval and structure preparation 535
10.3.2. Pharmacokinetic profiling 535
10.3.3. Target prediction using the Similarity Ensemble Approach (SEA) 538
10.3.4. SwissTargetPrediction-based target prediction 539
10.3.5. Construction of 2-Phenyl-4H-chromen-4-one target library 540
10.3.6. Construction of Protein–Protein Interaction (PPI) network 540
10.3.7. Functional Enrichment Analysis 541
10.3.8. Pathway enrichment analysis 543
10.3.9. Disease association analysis 547
10.3.10. Identification of Hub genes 547
10.3.11. Molecular docking with the EGFR 548
10.3.12. Molecular Dynamics Simulation 548
10.3.13. Conformational sampling and landscape analysis 552
10.3.14. Binding Free Energy analysis 553
10.3.15. DFT Studies for 2-Phenyl-4H-chromen-4-one 555
10.4. Discussion 558
10.5. Conclusion 564
CHAPTER 11 **565-573**
SUMMARY AND GENERAL CONCLUSION
CHAPTER 12 **575-577**
RECOMMENDATIONS

REFERENCES **579-633**
APPENDICES **635-640**
LIST OF PUBLICATIONS **641-646**
INDEX **647-651**

LIST OF ABBREVIATIONS

%	:	Percentage
°C	:	Degree Celsius
µg/mL	:	Micrograms per milliliter
µl	:	Microliter
µm	:	Micrometer
2D	:	Two-Dimensional
3D	:	Three-Dimensional
6-31G (d,p)	:	Basis set used in quantum chemistry
Å	:	Angstroms (unit of length)
a.u.	:	Atomic Units (unit for electrostatic potential)
AAS	:	Atomic absorption spectrometer
ABC	:	ATP-Binding Cassette (Transporter family)
ABTS	:	2,2'-Azino-bis (3-ethylbenzothiazoline-6-
Ac	:	Absorbance of control
AC	:	Adenylate Cyclase
ADME	:	Absorption, Distribution, Metabolism, and Excretion
ADMET	:	Absorption, Distribution, Metabolism, Excretion, Toxicity
AFM	:	Atomic Force Microscopy
$AgNO_3$	:	Silver Nitrate
AgNPs	:	Silver Nanoparticles
Ag-TiO_2	:	Silver-doped titanium dioxide
AMR	:	Antimicrobial resistance
AO	:	Acridine Orange
API	:	Active Pharmaceutical Ingredient
APIs	:	Active Pharmaceutical Ingredients
As	:	Absorbance of sample
ATCC	:	American Type Culture Collection
ATP	:	Adenosine Triphosphate

AYUSH	:	Ayurveda, Yoga and Naturopathy, Unani, Siddha and Homeopathy
B3LYP	:	Becke, 3-parameter, Lee–Yang–Parr hybrid functional
BBB	:	Blood–Brain Barrier
B-factor	:	Temperature Factor (atomic displacement parameter)
BHIB	:	Brain Heart Infusion Broth
BMP/TGF-β	:	Bone Morphogenetic Protein / Transforming Growth Factor Beta
BP	:	Biological Process
BW	:	Body Weight
℃	:	Degree Celsius
C.S.	:	Cross Section
CALI	:	Calicut University Herbarium
Carcino	:	Carcinogenicity
Cardio	:	Cardiotoxicity
CAT	:	Catalase
CC	:	Cellular Component
CDK-2	:	Cyclin-Dependent Kinase 2 (cancer-related protein)
CDs	:	Carbon dots
CFU/ml	:	Colony Forming Units per milliliter
CGenFF	:	CHARMM General Force Field
CHARMM	:	Chemistry at HARvard Macromolecular Mechanics
CHL	:	Chlorogenic Acid
CLSI	:	Clinical and Laboratory Standards Institute
cm	:	centimetre
COX	:	Cyclooxygenase enzyme
COX_2	:	Cyclooxygenase-2
CRA	:	Congo Red Agar
Csp3	:	Carbon sp^3 hybridization fraction
Cu	:	Copper
CYP	:	Cytochrome P450
CYP1A2	:	Cytochrome P450 Family 1 Subfamily A Member 2
CYP2C19	:	Cytochrome P450 Family 2 Subfamily C Member 19

CYP2C9	:	Cytochrome P450 Family 2 Subfamily C Member 9
CYP2D6	:	Cytochrome P450 Family 2 Subfamily D Member 6
CYP3A4	:	Cytochrome P450 Family 3 Subfamily A Member 4
CYP450	:	Cytochrome P450 enzyme family
Cyto	:	Cytotoxicity
DAPI	:	4',6-diamidino-2-phenylindole (DNA stain for apoptosis detection)
DDLA	:	D-Alanine–D-Alanine Ligase
DFT	:	Density Functional Theory
DL	:	Low-Density Lipoprotein
DLA	:	Dalton's Lymphoma Ascites
DMEM	:	Dulbecco's Modified Eagle's Medium
DMF	:	Dimethyl Fumarate
DMSO	:	Dimethyl Sulfoxide (solvent)
DNS	:	3,5-dinitrosalicylic acid (enzyme assay reagent)
DOID	:	Disease Ontology Identifier
DPIs	:	Dry Powder Inhalers
DPP4	:	Dipeptidyl Peptidase-4
DPPH	:	2,2-diphenyl-1-picrylhydrazyl (a free radical used in antioxidant assays)
DPPH-H	:	Reduced form of DPPH radical
EC	:	Enzyme Commission (numbering for enzymes)
EDTA	:	Ethylenediaminetetraacetic acid (a chelating agent)
EGFR	:	Epidermal Growth Factor Receptor
ELISA	:	Enzyme-Linked Immunosorbent Assay
EO	:	Essential Oil
EPOX	:	Epoxygenase
EPS	:	Extracellular Polymeric Substances
ERK	:	Extracellular Signal-Regulated Kinase
ESI-MS	:	Electrospray Ionization Mass Spectrometry
FAA	:	Formalin-Aceto-Alcohol
FACS	:	Fluorescence-Activated Cell Sorting
FBS	:	Fetal Bovine Serum

FDR	:	False Discovery Rate
Fe (II)	:	Ferrous ion
Fe (III)-TPTZ	:	Ferric tripyridyl triazine complex
FEL	:	Free Energy Landscape
FMO	:	Frontier Molecular Orbital
FRAP	:	Ferric Reducing Antioxidant Power (assay)
FSHR	:	Follicle-Stimulating Hormone Receptor
FTIR	:	Fourier Transform Infrared Spectroscopy
g	:	gram
GAE	:	Gallic Acid Equivalent
GC	:	Gas Chromatography
GC-MS	:	Gas Chromatography–Mass Spectrometry
GDP	:	Guanosine Diphosphate
GI absorption	:	Gastrointestinal Absorption
GLUT4	:	Glucose Transporter Type 4
GnRH	:	Gonadotropin-Releasing Hormone
GO	:	Gene Ontology
GPCR	:	G Protein-Coupled Receptor
GPx1	:	Glutathione Peroxidase 1
GTP	:	Guanosine Triphosphate
H&E	:	Haematoxylin and Eosin (staining)
H_2O_2	:	Hydrogen peroxide
H_2SO_4	:	Sulphuric acid
HAI	:	Hospital-Acquired Infections
H-bond	:	Hydrogen Bond
HCl	:	Hydrochloric acid
HDL	:	High-Density Lipoprotein
Hepato	:	Hepatotoxicity
HepG2	:	Human hepatocellular carcinoma cell line
HNO_3	:	Nitric acid
HOMA B	:	Homeostatic Model Assessment of Beta-cell function
HOMA IR	:	Homeostatic Model Assessment of Insulin Resistance
HOMO	:	Highest Occupied Molecular Orbital

HPLC	:	High-Performance Liquid Chromatography
HPTLC	:	High-Pressure Thin Layer Chromatography
HRBC	:	Human Red Blood Cell
HRMS	:	High-Resolution Mass Spectroscopy
HSD	:	Hydroxysteroid Dehydrogenase
HSP70	:	Heat Shock Protein 70
IAWA	:	International Association of Wood Anatomists
IC_{50}	:	Half-maximal Inhibitory Concentration
ICMR	:	Indian Council of Medical Research
IGF-1	:	Insulin-like Growth Factor 1
Immuno	:	Immunogenicity
IMTECH	:	Institute of Microbial Technology
In vitro	:	outside the living organism
In vivo	:	within the living organism
iNOS	:	Inducible Nitric Oxide Synthase
IPNI	:	International Plant Name Index
IR	:	Infrared
IUCN	:	International Union for Conservation of Nature
kcal/mol	:	Kilocalories per mole (energy unit)
KEAP1	:	Kelch-like ECH-associated protein 1
KEGG	:	Kyoto Encyclopedia of Genes and Genomes
kJ/mol	:	Kilojoules per mole (energy unit used in MD/MMPBSA)
KOH	:	Potassium hydroxide
KRAS	:	Kirsten Rat Sarcoma Viral Oncogene Homolog
L.S. view	:	Longitudinal Section view
LasR	:	(Implied protein target in figure, often a quorum-sensing regulator)
LB	:	Luria-Bertani
Lbs	:	Pounds
LC-MS-QTOF	:	Liquid Chromatography–Mass Spectrometry Quadrupole Time-Of-Flight
LD50	:	Lethal Dose 50%
LDLR	:	Low-Density Lipoprotein Receptor

LHCG	:	Luteinizing Hormone/Chorionic Gonadotropin
LHR	:	Luteinizing Hormone Receptor
LINCS	:	Linear Constraint Solver
LM	:	Light microscopy
LMA	:	Leaf Mass per Area
logP	:	Partition coefficient
logS	:	Solubility coefficient
LOX	:	Lipoxygenase
LPS	:	Lipopolysaccharide
LUMO	:	Lowest Unoccupied Molecular Orbital
M	:	Molar (Molarity)
m	:	Meter
M	:	meter (used in tree height description)
M	:	Molar
M	:	Molar (concentration unit)
MAPK1	:	Mitogen-Activated Protein Kinase 1
Maslinic Acid / MSA	:	A pentacyclic triterpenoid phytochemical
MBC	:	Minimum Bactericidal Concentration (lowest concentration killing bacteria)
MCF-7	:	Human breast cancer cell line
MD or MDS	:	Molecular Dynamics Simulation
MD	:	Molecular Dynamics
MDR	:	Multidrug-resistant
Mean ± SD	:	Mean plus or minus Standard Deviation
Mean ± SE	:	Mean plus or minus Standard Error
MEP	:	Molecular Electrostatic Potential
MEPS	:	Molecular Electrostatic Potential Surface
MF	:	Molecular Function
MFC	:	Minimum Fungicidal Concentration
mg/kg	:	Milligrams per kilogram (dose unit)
mg/mL	:	Milligrams per milliliter
MHA	:	Mueller Hinton Agar
MHB	:	Mueller Hinton Broth

MIC	:	Minimum Inhibitory Concentration (lowest concentration preventing microbial growth)
mL	:	Milliliter
mm	:	Millimeter
MM/PBSA	:	Molecular Mechanics/Poisson–Boltzmann Surface Area
mm	:	millimetre
mM	:	Millimolar
MMP	:	Mitochondrial Membrane Potential
MMPBSA	:	Molecular Mechanics Poisson–Boltzmann Surface Area
Mn	:	Manganese
MPO	:	Myeloperoxidase enzyme
MR	:	Molar Refractivity
MS	:	Mass Spectrometry
MTCC	:	Microbial Type Culture Collection
MTT	:	3-(4,5-dimethylthiazol-2-yl)-2,5-diphenyltetrazolium bromide
Mutagen	:	Mutagenicity
MW	:	Molecular Weight
N	:	Normal (Normality)
Na_2HPO_4	:	Disodium hydrogen phosphate
$Na_2S_2O_3$	:	Sodium thiosulphate
NaCN	:	Sodium cyanide
NaH_2PO_4	:	Sodium dihydrogen phosphate
NaOH	:	Sodium hydroxide
NBT	:	Nitro Blue Tetrazolium (dye for superoxide detection)
Nephro	:	Nephrotoxicity
Neuro	:	Neurotoxicity
NF-κB	:	Nuclear Factor kappa-light-chain-enhancer of activated B cells
nm	:	Nano metre
NM	:	Nuclear Magnetic
NMA	:	Normal Mode Analysis
NMR	:	Nuclear Magnetic Resonance

NO	:	Nitric Oxide (assay/biomarker)
NPN	:	Nitrophenol (4-Nitrophenol reduction assay substrate)
NPT	:	Constant Number, Pressure, Temperature (ensemble)
NRF2	:	Nuclear Factor Erythroid 2–Related Factor 2
ns	:	Nanoseconds
NSAID	:	Non-Steroidal Anti-Inflammatory Drug
NVT	:	Constant Number, Volume, Temperature (ensemble)
OD	:	Optical Density
OM	:	Optical Microscopy
OMIM	:	Online Mendelian Inheritance in Man
PAINS alerts	:	Pan-Assay Interference Compounds Alerts
PBP3	:	Penicillin-Binding Protein 3
PBS	:	Phosphate Buffered Saline
PBS-Tween	:	Phosphate Buffered Saline with Tween (detergent)
PC1 / PC2	:	Principal Component 1 / Principal Component 2
PCA	:	Principal Component Analysis
PCR	:	Polymerase Chain Reaction
PDA	:	Potato Dextrose Agar
PDB ID	:	Protein Data Bank Identifier
PDB	:	Protein Data Bank
Pgp substrate	:	P-glycoprotein Substrate
Pgp	:	P-glycoprotein
pH	:	Measure of acidity/basicity
PHE	:	2-Phenyl-4H-chromen-4-one (short form in simulation)
Phloem	:	Type of vascular tissue in plants
PI	:	Propidium Iodide (fluorescent DNA stain)
PI3K	:	Phosphoinositide 3-Kinase
PKA	:	Protein Kinase A
PLA2	:	Phospholipase A2
PME	:	Particle Mesh Ewald
PMS	:	Phenazine Methosulfate
p-NPG	:	p-nitrophenyl-α-D-glucopyranoside
PPA	:	Pancreatic Alpha Amylase

PPARG	:	Peroxisome Proliferator-Activated Receptor Gamma
PPI	:	Protein–Protein Interaction
ppm	:	Parts per million
PqsR	:	Pseudomonas Quinolone Signal Regulator
PSI	:	Pounds per Square Inch
PTLC	:	Preparative Thin Layer Chromatography
PTP1B	:	Protein Tyrosine Phosphatase 1B
QbD	:	Quality By Design
qPCR	:	Quantitative Polymerase Chain Reaction
QSAR	:	Quantitative Structure–Activity Relationship
R. L. S.	:	Radial Longitudinal Section
RAW 264.7	:	Murine macrophage cell line
RCSB	:	Research Collaboratory for Structural Bioinformatics
Respi	:	Respiratory Toxicity
Rf	:	Retention factor
Rg	:	Radius of Gyration
RhlR	:	Quorum Sensing Regulator Protein RhlR
RMSD	:	Root Mean Square Deviation
RMSF	:	Root Mean Square Fluctuation
ROL	:	Radial Oxygen Loss
ROS	:	Reactive Oxygen Species
rpm	:	Revolutions per minute
S. cumini	:	*Syzygium cumini*
S. laetum	:	*Syzygium laetum*
S. occidentale	:	*Syzygium occidentale*
S. palghatense	:	*Syzygium palghatense*
SA Score	:	Synthetic Accessibility Score
SAR	:	Structure–Activity Relationship
SASA	:	Solvent Accessible Surface Area
SAV	:	Surface Area–Volume
SBDD	:	Structure-Based Drug Design
SDA	:	Sabouraud Dextrose Agar (fungal culture medium)
SDS	:	Sodium Dodecyl Sulfate

SEA	:	Similarity Ensemble Approach
SEM	:	Scanning Electron Microscopy
Silicos-IT class	:	SwissADME's Silicos-IT Classification for Druglikeness
SMILES	:	Simplified Molecular Input Line Entry System
SOD	:	Superoxide dismutase (antioxidant enzyme)
SOD1	:	Superoxide Dismutase 1
SOT	:	Sotorasib
SPR	:	Surface Plasmon Resonance
SR-B1	:	Scavenger Receptor Class B Type 1
StAR	:	Steroidogenic Acute Regulatory Protein
STRING	:	Search Tool for the Retrieval of Interacting Genes/Proteins
		sulfonic acid) (antioxidant assay reagent)
		sulfonic acid) (antioxidant assay)
SYTO 9	:	A green fluorescent nucleic acid stain used in cell viability assays
T.L.S.	:	Tangential Longitudinal Section
T.S.	:	Transverse Section
TAE	:	Tris-Acetate-EDTA buffer
TBA	:	Thiobarbituric Acid
TBARs	:	Thiobarbituric Acid Reactive Substances
TEM	:	Transmission Electron Microscopy
TFC	:	Total Flavonoid Content
TIP3P	:	Transferable Intermolecular Potential 3-Point (water model)
TKI	:	Tyrosine Kinase Inhibitor
TLC	:	Thin Layer Chromatography
Tm	:	Melting Temperature (for primers)
TME	:	Tumor Microenvironment
TNF-α	:	Tumor Necrosis Factor-alpha
TP53	:	Tumor Protein p53
TPC	:	Total Phenolic Content
TPL	:	The Plant List
TPSA	:	Topological Polar Surface Area
TRX	:	Thioredoxin

TXNIP	:	Thioredoxin-Interacting Protein
UFF	:	Universal Force Field
UNESCO	:	United Nations Educational, Scientific and Cultural Organization
UPLC	:	Ultra-Pressure Liquid Chromatography
UV light	:	Ultraviolet light
UV	:	Ultraviolet
UV-Vis	:	Ultraviolet-Visible Spectroscopy
v/v	:	Volume/volume ratio
vdW	:	van der Waals
VEGFR-2	:	Vascular Endothelial Growth Factor Receptor 2 (cancer marker)
w/v	:	Weight/volume ratio
W/W	:	Weight per Weight
WCA	:	Water Contact Area
WGD	:	Whole-Genome Duplication
WHO	:	World Health Organization
XRD	:	X-Ray Diffraction
XTT	:	2,3-Bis-(2-Methoxy-4-Nitro-5-Sulfophenyl)-2H-Tetrazolium-5-Carboxanilide
Zn	:	Zinc
ZnO NPs	:	Zinc Oxide Nanoparticles
α-glucosidase	:	Alpha-glucosidase enzyme
ΔG_bind	:	Binding Free Energy
π-stacking	:	Pi–Pi Interaction

PREFACE

This study emerged from a profound dedication and sustained interest in the botanical and pharmacological study of the genus *Syzygium*, a litmus of ecological diversity and medicinal potential. The motivation guiding this study was grounded in the recognition of this genus's immense ecological and ethnopharmacological significance, especially focusing on the three endemic species of the Western Ghats- *S. laetum*, *S. occidentale*, and *S. palghatense*-whose biological and medicinal characteristics remain inadequately documented despite the genus itself encompassing over 1200 species worldwide. The Western Ghats, rightly designated as a UNESCO World Heritage Site, provide a unique and sensitive ecological niche where these species thrive, yet face threats from habitat degradation and overexploitation. Recognizing the gap in extant scientific literature regarding these particular species, this research endeavoured to conduct a comprehensive exploration encompassing morpho-anatomical, phytochemical, pharmacognostic, biological activities, green synthesis, isolation of compounds, molecular docking and dynamics, and network pharmacology, thereby laying a foundational framework for their sustainable utilization and conservation.

The inquiry began with detailed morphological and anatomical studies of leaves, flowers, stems, and bark, establishing characteristic markers essential for taxonomic differentiation and botanical understanding. Further, phytochemical profiling was meticulously conducted to identify secondary metabolites contributing to their medicinal properties. These analyses formed the bedrock for subsequent bioactivity assays, where antioxidant, antimicrobial, anthelmintic, anti-inflammatory, and anticancer potentials were systematically evaluated. In parallel, this research integrated contemporary nanotechnological methodologies through the environmentally benign synthesis of silver nanoparticles using plant extracts- a novel approach aimed at enhancing therapeutic delivery and efficacy. Molecular docking and network pharmacology analyses complementarily elucidated the molecular targets and possible mechanisms underpinning the pharmacological effects observed, thus bridging traditional knowledge with modern scientific validation. Beyond expanding scientific understanding, this thesis aspires to advocate for ecological stewardship and the integration of traditional medicinal knowledge with cutting-edge

research, ultimately fostering novel drug discovery pathways and conservation strategies.

In this study, each objective is systematically addressed in individual chapters. Chapter 1 provides the introduction, setting the context, and outlining the research questions. Chapter 2 presents a comprehensive review of related literature. Chapter 3 focuses on the morpho-anatomical characterization of the study plants. Chapter 4 details the pharmacognostic characterization. Chapter 5 covers the phytochemical profiling. Chapter 6 discusses the biological activities assessed during the research. Chapter 7 describes the green synthesis, characterization, and bioactive efficacy of silver nanoparticles. Chapter 8 is dedicated to the isolation and bioactivity validation of phytocompounds. In Chapter 9, molecular docking and dynamics studies of the phytocompounds against key biological targets are presented. Chapter 10 explores network pharmacology and functional analyses of the isolated compounds. Finally, Chapter 11 summarizes the main findings and provides general conclusions, while Chapter 12 offers recommendations based on the research outcomes. The thesis concludes with references, an appendix, and an index.

This doctoral thesis is organized into two principal parts to systematically present the research work. Part I comprises Chapters 1 to 7, encompassing the introduction, literature review, methodology, and core research findings of each chapter that establish the foundational framework of the study. Part II includes Chapters 8 to 12, which focus on advanced analyses followed by the references, appendices, and the index. This structured division enables a coherent progression from fundamental concepts to complex insights, facilitating clear navigation and comprehensive understanding for the reader.

The intended audience for this dissertation includes academic researchers in pharmacognosy, plant sciences, ethnobotany, phytochemistry, bioinformatics, and ecology, as well as practitioners in traditional medicine and conservation biology. It aims to inspire further scientific inquiries into the rich biodiversity of the Western Ghats and facilitate cross-disciplinary dialogues to promote holistic approaches towards health and the environment. It is anticipated that the insights yielded herein will catalyse more extensive exploration and sustainable exploitation of *Syzygium* species, enriching both scientific literature and practical applications.

In conclusion, this study represents a pioneering effort to document, analyse, and valorise three endemic *Syzygium* species in an integrated scientific context. By interweaving botanical, pharmacological, ecological, and technological perspectives, this work not only contributes novel knowledge but also offers a robust platform for continued research and sustainable development. It is with a sense of humility and accomplishment that this thesis is submitted, hopeful that it will serve both as a scholarly resource and a beacon for future explorations in the vast domain of plant sciences.



1

GENERAL INTRODUCTION

CHAPTER 1
GENERAL INTRODUCTION

The plant kingdom has always been the storehouse of natural remedies, nutritional supplements, and new compounds of therapeutic value. Our ancestors, since time immemorial, have also turned to plants to extract medicine in addition to using them as sources of food and even shelter (Fernandes et al., 2022). The traditional ethnobotanical expertise, which is the result of generations and generations of experience and practice, still forms one of the foundations of the contemporary pharmacological field. Specifically, the Myrtaceae family of plants has also received a significant amount of scientific interest because of their abundance of bioactive secondary metabolites and also their wide varying ethnomedicinal applications. Of these, though, the genus *Syzygium* is undoubtedly of exemplary diversity, ecologically and medicinally important, and widely used in various spheres of traditional and modern medicine (Mostafa et al., 2023).

The *Syzygium* genus, with over 1,200 species, is spread largely in tropical and subtropical parts of Asia, Africa, and Oceania (Fernandes et al., 2022). There are a few which are cultivated or harvested, either as fruits or spices or source of essential oils or medicines. Indian sub-continent and particularly the Western Ghats have been considered a biodiversity hotspot and several species of *Syzygium* are endemic. It is a region which has distinct ecological niches that can give rise to a number of distinct morpho-anatomical and phytochemical characters in plant species, thus providing fertile ammunition to the area of pharmacognosy. *Syzygium* species play a vital role in healthcare practices of the local population whereas the culture is tenured in traditional knowledge systems, which are sustained via the Western Ghats thus bearing vital ecological services (Rashid et al., 2022).

1.1. *Syzygium* endemics in the Western Ghats

Western Ghats are a UNESCO World Heritage site. It forms the western coastal line of India, characterised by dense trees with high rainfall and vary altitude (Fernandes et al., 2022). All these conditions helps in building the microhabitat, this

further helps in the survival of various indigenous species. Species of the genus *Syzygium* also show a high degree of endemism, as some of them are confined to certain heights. The biogeographic occurrence shows the ecological preference of this genus. As this is an important medicinal species and is confined to a specific area, the conservation of this species is of major concern (Mostafa et al., 2023).

In ethnomedicinal practices, some species of *Syzygium* have been employed in the treatment of digestive complaints and skin disorders, metabolic diseases, and inflammatory processes (Tambe et al., 2021). These are applications which have been shared intergenerationally, spawning contemporary scientific interest in their phytochemistry, and pharmacology. The total of the pharmacognostic information in *Syzygium* is scarce in the Western Ghats, although numerous species are available. *Syzygium gartnerianum* (hereafter referred to as *Syzygium* Gartner) is one of those less studied species, and therefore, integrative studies comprising traditional knowledge, morphology, phytochemical profiling, and extreme drug testing will help to open this underexplored species ahead of the curve (Rashid et al., 2022).

1.2. Role of *Syzygium* in traditional and modern medicine

Syzygium is embedded with a therapeutic reputation in Ayurveda, Siddha, and Unani systems of medicine. The most popular species, *S. cumini* (known as Jamun or Indian blackberry) has long been used as an antidiabetic medication, and both seeds and bark, and leaves possess hypoglycaemic and antioxidant properties (Tambe et al., 2021). Other plants like *S. aromaticum* (clove) have been identified as catering to botanical foods and medicine whose products include antimicrobial, analgesic, and anti-hematoglobin effects. These conventional applications have been translated into pharmacological properties that were recognized by the scientific community, which makes the genus a possible mediator between traditional medicine and evidence-based medicine (Mostafa et al., 2023).

Flavonoids, tannins, terpenoids, alkaloids, and phenolic acids are bioactive compounds isolated in *Syzygium* and impart a variety of biological effects (Tambe et al., 2021). These constituents are linked with antioxidant property, antimicrobial activity, anthelmintic activity, anti-inflammatory activity, antidiabetic effects, and

even anticancerous properties. All these pharmacological properties are complex and sufficient to support the application of *Syzygium* as an ethnomedicine and as a potential source of drug discovery and development (Rashid et al., 2022).

1.3. Biological potentials of *Syzygium*

1.3.1. Antioxidant property

Reactive oxygen species (ROS) and oxidative stress have been considered as contributors to chronic diseases, including diabetes, cancer, and cardiovascular diseases. *Syzygium* species contain highly active polyphenolic compounds with the potential to scavenge free radicals, hence cellular protection (Qamar et al., 2022).

1.3.2. Antimicrobial activity

Syzygium species extracts and essential oils exhibit inhibitory effects against a wide variety of bacteria, fungi, and viruses. For this reason they can used in various infections. There this feature help to tackle antimicrobial resistance (Ochieng et al., 2022).

1.3.3. Anthelmintic effect

Helminthic diseases are an important problem for population. Mainly in the tropical region. There are various active compound present in the different species of *Syzygium*, which effect the survival of parasites. So, these shows potential against parasites (Qamar et al., 2022).

1.3.4. Anti-inflammatory action

Inflammation is considered as one of the first sign of various health problems. These problems includes arthritis, metabolic syndrome, and neurodegeneration. Favonoids and terpenoids compounds that are present in *Syzygium* can affect the functioning of the inflammatory mediators and cytokines (Ochieng et al., 2022).

1.3.5. Antidiabetic potential

The hypoglycemic effect of *Syzygium* seeds and leaves has been well documented. Active ingredients boost insulin release, glucose metabolism, and cut oxidative stress, which makes them an effective way to treat diabetes mellitus (Qamar et al., 2022).

1.3.6. Anticancer properties

Recent research have shown cytotoxic effect of *Syzygium* extracts against cancer cell lines. Mechanistic considerations indicate the inhibition of apoptotic channels, blocking angiogenesis, and providing antioxidant assistance (Ochieng et al., 2022).

This pharmacological discussion can support the systematic pharmacognostic investigation of less studied *Syzygium* species (Uddin et al., 2022).

1.4. Importance of the present study

Although the medicinal use of *Syzygium* species is well acknowledged, studies have largely concentrated on a small number of recognizable species, and much remains unknown about the local and endemic species (Rashid et al., 2022). Many *Syzygium* species are endemic to the Western Ghats, which is poorly described with regard to morphology, pharmacology, phytochemistry, biological activities, silver nanoparticle studies, isolation of compounds, molecular docking, molecular dynamics, and network pharmacology. Since there is a worldwide concern of exploring natural products and due to the demand for safe and new, unexplored therapeutic agents, there is a necessity to explore this species in a more detailed manner (Mostafa et al., 2023).

The Western Ghats endemic species, *S. laetum* (Buch.-Ham.) Gandhi, *S. occidentale* (Bourd.) D.N. Gandhi and *S. palghatense* Gamble were selected for the study. The current research then fills this gap by combining conventional pharmacognostic methods with contemporary methods of analysis (Rashid et al., 2022). Documentation and photography will provide opportunities for more advanced

future study. Morphological and anatomical characterization would assist in defining diagnostic aspects, which are critical in identification to avoid adulteration of herbal medicine. Phytochemical profiling will determine the range of secondary metabolites, whereas pharmacological and biological assays will confirm these biological activities advocated by ethnomedicinal practices. Characterization of compounds and various pharmacognostic efficacy of the plant will uplift the status of herbal medicines (Uddin et al., 2022).

Moreover, the research will use updated technologies like the synthesis of silver nanoparticles, formulation studies, compound extraction, molecular docking, molecular dynamics, and network pharmacology (Fernandes et al., 2022). There is an impending increase in the use of nanoparticle-mediated drug delivery in terms of enhancing the bioavailability of plant-derived compounds as well as their therapeutic efficacy. Docking and network pharmacology will offer mechanistic insights by the prediction of the molecular targets and pathway, thereby filling the gap between traditional and the systems level of understanding of the drug effects (Mostafa et al., 2023).

This doctoral thesis is organized into two parts, with each research objective developed and presented in a separate chapter to ensure clarity and coherence in addressing the specific aims of the study.

1.5. Objectives of the study

- ❖ Collection and authentication of plant materials
- ❖ Morpho-anatomical characterization
- ❖ Characterization of pharmacognostic features
- ❖ Phytochemical profiling
- ❖ Characterization of biological activities
- ❖ Synthesis of nanoparticles using plant extract, and their characterization and biological activities

- ❖ Isolation of compound, and bioactivity validation
- ❖ Molecular docking and dynamics studies of phytochemicals and target proteins
- ❖ Network pharmacology



2

REVIEW OF LITERATURE

CHAPTER 2
REVIEW OF LITERATURE

Syzygium Gaertner (Myrtaceae) is one of the largest and most diverse genera of evergreen trees and shrubs, with approximately 1,200 species distributed throughout tropical and subtropical regions; from Africa and Madagascar, south Asia and extending eastwards to the Pacific Islands (Dewijanti et al., 2020; Govaerts et al., 2008; Parnell et al., 2007). The Indo-Malaysia region is thought to be the primary centre of speciation for the genus where the greatest species diversity is concentrated. The genus is a morphologically highly diverse one, and the species display a wide range of size, habit, leaf form and type of fruit. Leaves are small (a few cm long) to large (more than 1 m long in some species.), and typically their fruits are called "rose apples". They are also edible and have high economic as well as nutritional and medical value. A number of species are grown for their decorative foliage, or as urban shade trees (Cock & Cheesman, 2019).

Syzygium is the largest genus of Myrtaceae and represents an economically and medicinally significant group of plants with a wide number of species and a rich history in ethnomedicinal applications. The fruits, leaves and barks of these plants are generally practiced in traditional medicine, food packaging and industry (El-Saber Batiha et al., 2020; Yuniarni et al., 2021). The most widely known species is clove (*S. aromaticum*), the unopened flower buds of which are used commercially as a widely used spice. The oil from these buds, commonly known as clove oil, is used in dentistry, aromatherapy, the flavouring of food, and the preservation of food items, owing to its antimicrobial and antioxidant properties. Besides involvement in spice industry, members of *Syzygium* are used for their edible fruits and one of the species, *S. cumini* (Java plum or jamun) is a source of fresh or processed fruits (jams, jellies), highly appreciated for its antioxidant and anthocyanin compounds. Several *Syzygium* species are used in traditional medicine to treat diabetes, inflammation, gastrointestinal disorders, and as a tonic. Ecologically, it is essential to maintain the tropical forest ecosystem and will protect species diversity and provide food plants

for frugivores and mediate the structure and function of the environment (El-Saber Batiha et al., 2020). *Syzygium* is a large and species-rich genus of angiosperms, yet it has received limited attention compared to other genera. *Syzygium* is a flagship taxon of India's endemic flora and yet to become the focus from the taxonomic, phytogeographic and conservation perspective (Sujanapal & Kunhikannan, 2017).

2.1. Historical perspectives and taxonomic evolution of the genus *Syzygium*

In Hooker's Flora of British India, Duthie (1878–1879) treated Indian representatives of the *Syzygium* complex under *Eugenia*, comprising 131 species in three sections, including *Jambosa*, *Syzygium*, and *Eugenia*. Wight (1842; 1846), Beddome (1872, 1874), and Duthie described 21 species from South India. Thereafter, Gamble (1919) reclassified the south Indian specimens to three different genera, *Eugenia*, *Jambosa* DC., and *Syzygium*, describing ten new species additionally.

Biffin et al. (2006) highlight that taxonomically, the genus *Syzygium* has been tangled with the morphologically similar genus *Eugenia* due to their striking similarity. Most species currently recognised as *Syzygium* were previously placed in *Eugenia* or, sometimes, even in the now-synonymous genus *Jambosa*. *Syzygium* was first formally recognised as a distinct genus by Joseph Gaertner in the late 18th century in his influential work. The difference between *Syzygium* and *Eugenia* is becoming clearer over time, mainly due to advances in knowledge of several morphological, anatomical, and biogeographical features. Importantly, diversity in *Eugenia* reaches its highest species richness in the Neotropics (the tropical Americas), while diversity in *Syzygium* is largely centred in the Old-World tropics, particularly from Malaysia through Southeast Asia to Australia and the Pacific. Recent studies have concentrated on self-correction of these taxonomic barriers by concerted regional revisions and molecular analyses, which in part has established the predictive phylogenetic setting for the genus. The genus has also undergone significant taxonomic restructuring based on pivotal research, with other taxa, such as *Acmena* and *Cleistocalyx*, being reclassified into *Syzygium*, thereby verifying the complex phylogenetic history of this group.

Syzygium highlighting major shifts based on both classical morphological studies and modern molecular phylogenetic analysis. Initially, prior to the 1970s, *Syzygium* and several morphologically similar genera, *Eugenia*, *Jambosa*, *Acmena*, and *Cleistocalyx* were recognized as distinct. This separation was largely maintained due to differences in fruit and flower morphology, leaf arrangement, and other anatomical features. From the 1970s through the early 2000s, rigorous taxonomic studies and revisions re-examined the relationships among these genera, drawing attention to ambiguous boundaries and overlapping characteristics. As Figure 2.1 illustrates, these systematic revisions led to a movement toward consolidating generic concepts (Henderson, 1949; Merrill & Perry, 1939; Schmid, 1972; Parnell et al., 2007).

Abdulrahman & Hama (2023) later observed how the knowledge of systematic limits within *Syzygium* and allied genera has been substantially improved by way of integration of geography with molecular data thus helping to resolve longstanding taxonomic ambiguities. Uddin et al. (2022) also affirmed that molecular phylogenetic work has become indispensable for the stabilization and redefinition of genera geographically. Li et al. (2021) emphasized the indicated fossil information which is very few but important evidence to affirm the ancient *Syzygium* in eastern Asia. The results substantiate the hypothesized Miocene migration of ancestors of the *Syzygium* lineages from Australia to eastern Asia during this time through islands confronted by geological events, and similarly fit to most conclusions drawn in earlier studies. This is supported by the discovery of fossilised wood from the Miocene, estimated to be about 11.4 million years old and currently represented in the fossil record as the earliest proven occurrence for the genus.

Chantaranothai (2024) described that in *Syzygium*, the traditional taxonomic keys are based on vegetative and floral characters, including leaf arrangements, fruit type (capsular vs. fleshy), and flower morphology. Nonetheless, the taxonomic complexity of the genus, which is not separated from two close genera, *Acmena* and *Cleistocalyx* by specific boundaries, often results in competing opinions and different taxonomic concepts (Table 2.1).

Table 2.1: Diagnostic morphological traits distinguishing *Syzygium* from closely related genera

Morphological trait	*Syzygium*	*Eugenia*	*Acmena/Cleistocalyx*	Distinguishing features
Leaf surface	Mostly glabrous (Schmid, 1972; Craven, 2001)	Predominantly pubescent (Schmid, 1972; Craven, 2001)	Usually glabrous (Craven, 2001)	Vegetative hairiness often distinguishes Eugenia from *Syzygium*
Bracteoles	Inconspicuous, very fugacious (deciduous early) (Schmid, 1972)	Conspicuous, often persistent (Schmid, 1972)	Similar to *Syzygium*, generally deciduous (Schmid, 1972)	Bracteole persistence is a key differential character
Flower pedicel	Pedicellate, articulation between pedicel and flower present (Schmid, 1972)	Usually pedicellate, articulation absent (Schmid, 1972)	Similar to *Syzygium*	Articulation more distinct in *Syzygium*
Perianth parts	Mostly tetramerous, often calyptrate (fused sepals forming a cap) (Schmid, 1972; Chantaranothai et al., 2024)	Mostly tetramerous, free sepals and petals, never calyptrate (Schmid, 1972)	Calyptrate common (Craven, 2001)	Calyptrate flowers are absent in *Eugenia*
Stamens	Numerous; often associated with staminal disc; anthers with terminal gland (Schmid, 1972; Craven, 2001)	Numerous, free; anther morphology varies, lacking terminal secretory cavity (Schmid, 1972)	Similar to *Syzygium*	Anther structure is an important taxonomic marker
Ovary structure	Axile placentation (Schmid, 1972)	Often transeptal placentation (Schmid, 1972)	Axile placentation (Schmid, 1972)	Ovule arrangement helps separate *Eugenia* from *Syzygium*
Fruit type and seed	Berry or capsular; thick pericarp; embryo with two distinct cotyledons loosely attached (Merrill & Perry, 1939; Wilson, 1957)	Berry; thinner pericarp; cotyledons fused or pseudo monocotyledonous (Merrill & Perry, 1939; Wilson, 1957)	Similar to *Syzygium*	Seed morphology is diagnostic
Cotyledons	Usually bifid (two distinct cotyledons) (Merrill & Perry, 1939)	Usually fused (Merrill & Perry, 1939)	Variable, generally like *Syzygium*	Distinct cotyledons, *Syzygium* trait

Inflorescence type	Mostly paniculate, often terminal; bracts leafless, bracteoles deciduous (Craven, 2001)	Often racemose, axillary or terminal; bracteoles persistent (Craven, 2001)	Similar to *Syzygium*	Inflorescence architecture contributes to separation
Vegetative pubescence	Generally glabrous (Schmid, 1972; Craven, 2001)	Often pubescent (Schmid, 1972)	Usually, glabrous	Pubescence is a quick field character
Hypanthium	Floral tube often prolonged; calyptrate forms possible (Schmid, 1972)	Floral tube short; never calyptrate (Schmid, 1972)	Similar to *Syzygium*	Length and morphology of the floral tube differentiate taxa

Recent advances in molecular phylogeny have transformed our understanding of *Syzygium*. Genomic analyses confirm an origin in the Australia-New Guinea region and subsequent radiation eastward and westward in several waves, facilitated by geographic isolation and environmental adaptation. Uddin et al. (2022) have demonstrated, through phylogenomic studies, that *Syzygium* underwent an ancient whole-genome duplication (WGD) event referred to as the "pan-Myrtales" WGD, shared with other members of the order Myrtales, which has favoured diversification. However, to this date, there is no clear indication of recent whole-genome duplication events within *Syzygium* itself.

Craven (2001) demonstrated through detailed morphological and molecular analyses that the former genera *Acmena* and *Cleistocalyx* are phylogenetically embedded within *Syzygium*, justifying their merger into an expanded *Syzygium* genus. Subsequent molecular phylogenetic studies by Sun et al. (2024) and Wei et al. (2022), utilizing chloroplast genome sequences, have confirmed the robust monophyly of *Syzygium*, clarified species-level relationships, and reinforced its separation from *Eugenia* as a distinct lineage in the Myrtaceae family (Figure 2.2).

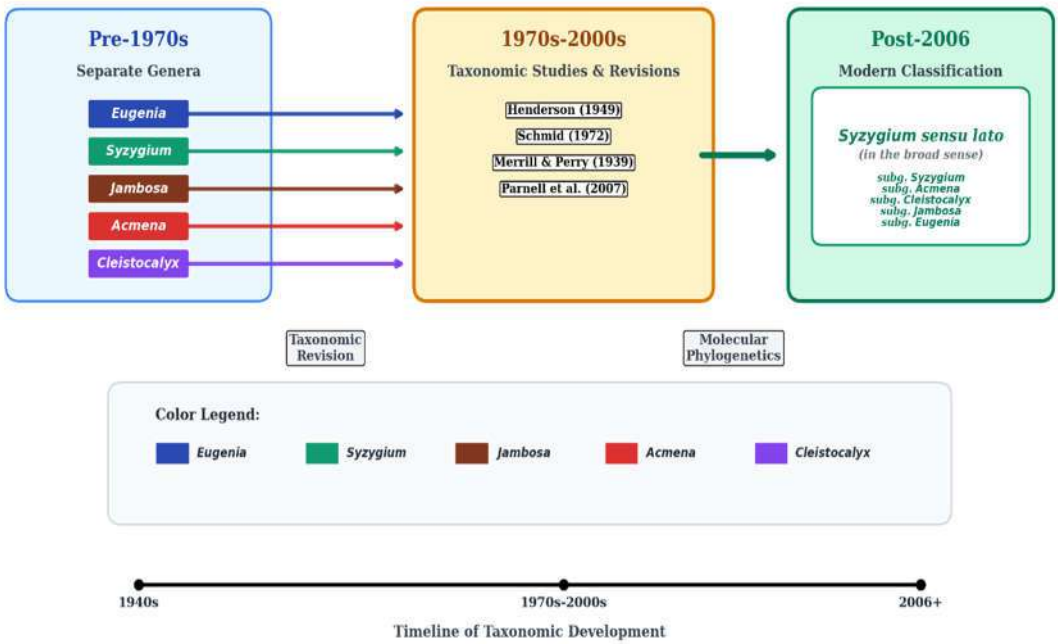


Figure 2.1: Historical and Molecular Taxonomy of *Syzygium*- An Illustrated Overview

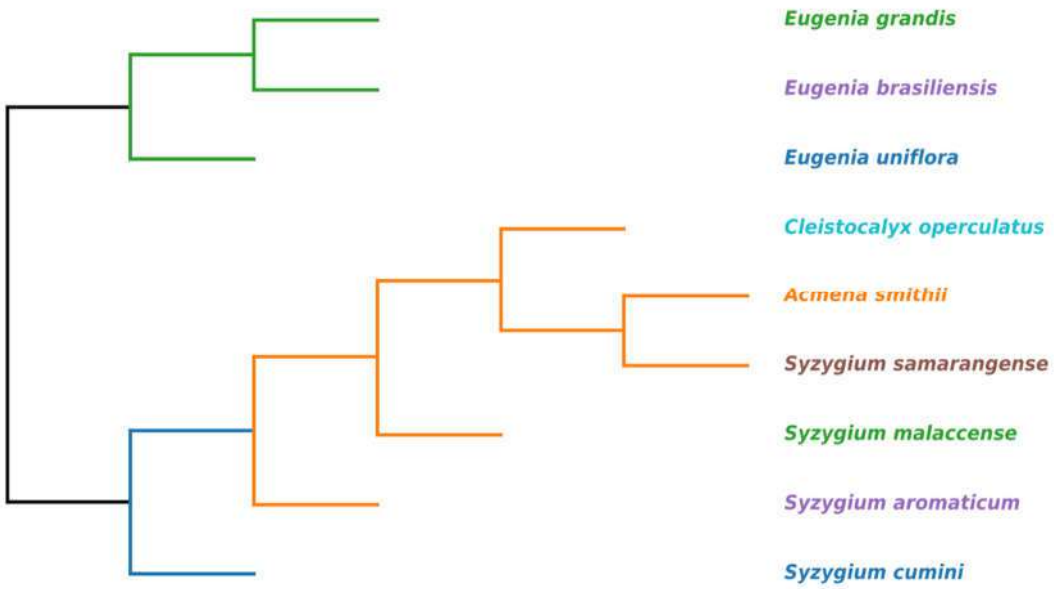


Figure 2.2: Phylogenetic relationships and recent reclassifications of *Syzygium*, *Eugenia*, *Acmena*, and *Cleistocalyx*

2.2. Traditional and modern uses of *Syzygium*: A multifaceted approach

Syzygium is one of the largest generic groupings of Myrtaceae, with an estimated 1,200 species in the world (Govaerts et al., 2008; Parnell et al., 2007). Frodin (2004) reported that *Syzygium* is an effective traditional medicine, ranked 16th among the 57 largest genera of flowering plants.

Syzygium is a unique genus with various medicinal, economic, and ecological aspects. *S. cumini*, *S. caryophyllatum,* and *S. cordatum* are employed in traditional medicine systems, Ayurveda, and Unani for the treatment of diverse diseases (diarrhea, ulcers, diabetes, and neurodegenerative disorders like Alzheimer's disease) (Cho, 2023; Gaikwad et al., 2024; Nigam et al., 2012; Pemmereddy et al., 2022; Amir Rawa et al., 2022). It shows various pharmacological properties. The compounds that are responsible for it includes flavonoids, polyphenols, and anthocyanins (Abbas et al., 2024; Anjali et al., 2017; Gaikwad et al., 2024).

In countries like Bangladesh, China, and India the species of *Syzygium* genus is believed to cure problems with memory, inflammation and glycemia (Amir Rawa

et al., 2022; Uddin et al., 2022). *S. cumini* contains various compounds like flavonoids, tannins, and phenols. These compounds helps in providing it various medicinal role like in anti-inflammatory, antidiabetic, and antioxidant properties (Srivastava & Chandra, 2013; Sharma et al., 2020). *S. aromaticum* are high in eugenol, which provides it antimicrobial and analgesic qualities (Xue et al., 2022). In the ancient times, *Syzygium* was considered to have roles in diabetes, inflammation and memory disease like Alzheimer's disease (Amir Rawa et al., 2022).

Syzygium species were described as ecologically important, and their role in bioremediation through natural agents towards the toxicity of heavy metals and industrial waste. In addition, these species were reported to act as biopesticides and herbicides under agricultural practices (Pemmereddy et al., 2022; Amir Rawa et al., 2022). *Syzygium* species are known to possess a diverse array of bioactive properties, which is a result of the presence of various phytochemicals, including terpenoids, carotenoids and essential oils hence these plants can be considered as future source materials for medicinal and ecological needs (Pemmereddy et al., 2022; Sujana & Wijayanti, 2022). There is evidence of many species that do have these traits, yet more study must be conducted to find new values and new species of the same, in order for them collectively to wield any greater use (Amir Rawa et al., 2022).

Amir Rawa et al. (2022) reported that currently, many *Syzygium* species are being investigated for their neuroprotective potential in particular of Alzheimer disease through anti-cholinesterase action and the oxidative stress reduction. Apart from the medicines, Mudaningrat et al. (2023) underlined the importance of *Syzygium* in agriculture due to its broad spectrum of natural pesticides and environmental regulation as a bioremediation factor for degraded areas. According to Maroyi (2018), virtually, *S. cordatum* is used throughout East and Southern Africa for a number of diseases such as gastrointestinal disorders and respiratory complaints with scientific evidences demonstrating its antibacterial and antifungal properties. Furthermore, Xue et al. (2022) reported that several nutritional and bioactive elements from *Syzygium* species, primarily from *S. aromaticum*, have human applications, which have had a considerable economic impact on the food and cosmetic industries. However, Uddin

et al. (2022) highlighted the need for expanded research to define and classify the phytochemical compounds in some of the least studied *Syzygium* species and to expand their potential applicability. The medicinal applications and targeted ailments of selected *Syzygium* species were listed in Table 2.2 and Figure 2.3.

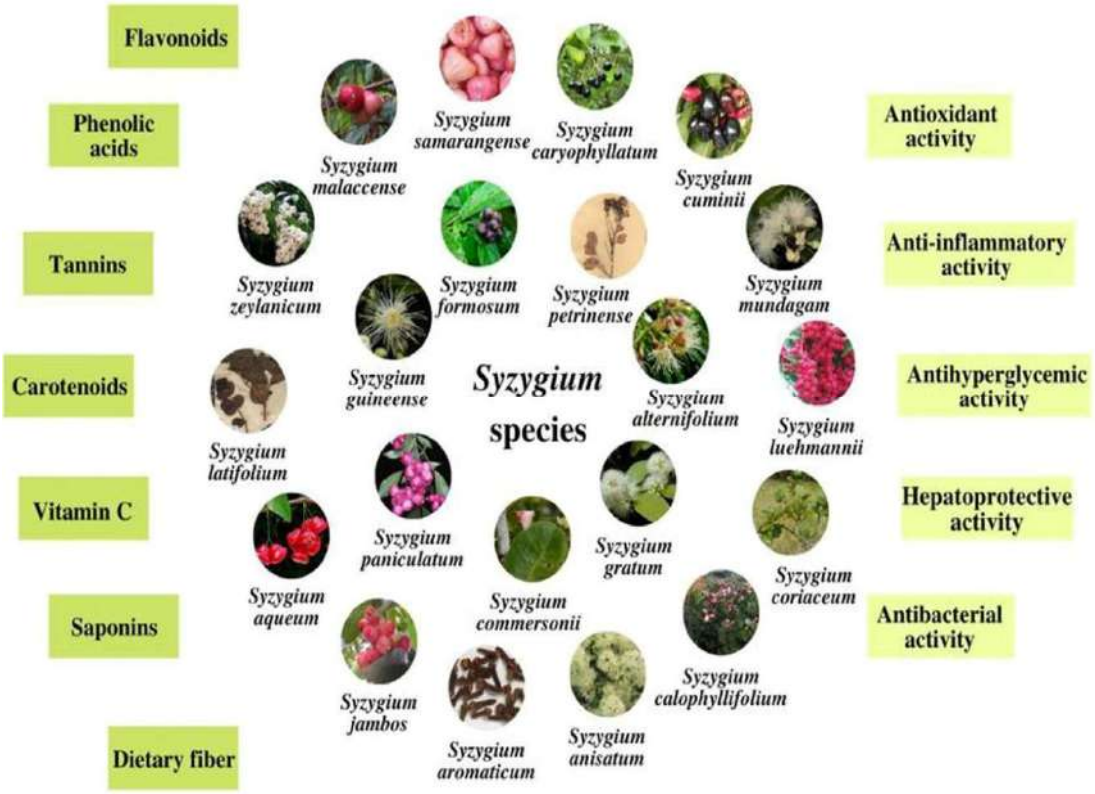


Figure 2.3. Bioactive compounds and therapeutic potentials of *Syzygium* species (Source: Bijauliya et al., 2017)

2.3. Recent discoveries and taxonomic advances in *Syzygium*

The Western Ghats is one of the megadiverse centres in India and is also a biodiversity hotspot. *Syzygium* forms the single largest genus, with 48 taxa, of which 27 are endemic to the region. The plant has high species richness, and new species were described recently from various parts of the Western Ghats. It includes *S. parameswaranii* Mohanan & Henry and *S. travancoricum* are the species only found in Travancore. On the other hand, *S. bourdillonii* was a species that was only found in Kollam, (Mohanan & Henry, 1987); *S. periyarensis* Jomy & Sasidharan

Table 2.2: Traditional medicinal applications and targeted ailments of selected *Syzygium* species

Syzygium species	Traditional medicinal applications	Targeted ailments / conditions	References
S. aromaticum	Antimicrobial, anti-inflammatory, dental pain relief, digestive aid	Microbial infections, inflammation, dental pain, digestive disorders	El-Saber Batiha et al., 2020; Jimoh et al., 2017
S. cumini	Blood sugar control, anti-diarrheal, wound healing	Diabetes mellitus, gastrointestinal infections, wounds, inflammation	Nigam et al., 2012; Ayyanar & Subash-Babu, 2012
S. malaccense	Skin treatment, fever reduction	Skin infections, fever, inflammation	Raina et al., 2022; Sobeh et al., 2024
S. jambos	Anti-inflammatory, skin healing, antimicrobial	Skin ailments, inflammation, microbial infections	Sobeh et al., 2018; Ochieng et al., 2022
S. grande	Gastrointestinal relief, fever remedy	Gastrointestinal disorders, fever	Nigam et al., 2012
S. samarangense	Pain relief, anti-inflammatory, antimicrobial	Pain, inflammation, microbial infections	Tarigan et al., 2021; Jimoh et al., 2017
S. polypetalum	Digestive aid, antimicrobial	Gastrointestinal disorders, infections	Dey et al., 2022
S. travancoricum	Leaf decoctions for fever and wound care (local folk use)	Fever, wounds	Ramachandra et al., 2017
S. munroi	Anti-inflammatory, antimicrobial	Inflammation, infections	Cock & Cheesman, 2019
S. kurzii	Fever remedy, antimicrobial	Fever, microbial infections	Nigam et al., 2012
S. lanceolatum	Skin disease treatment, digestive disorders	Skin diseases, gastrointestinal problems	Nigam et al., 2012
S. microphyllum	Anti-inflammatory, antimicrobial	Inflammation, microbial infections	Nigam et al., 2012
S. campanulatum	Skin ailments, anti-inflammatory	Dermatitis, inflammation	Kumar et al., 2020
S. beddomei	Inflammation relief, antimicrobial	Inflammation, infections	Nigam et al., 2012
S. densiflorum	Fever reduction, antimicrobial	Fever, microbial infections	Nigam et al., 2012
S. firmum	Anti-inflammatory, antibacterial	Inflammation, infections	Nigam et al., 2012
S. francisii	Leaf preparations for inflammation	Inflammation	Nigam et al., 2012

S. jambolanum	Anti-diabetic, anti-inflammatory, antimicrobial	Diabetes, inflammation, microbial infections	Nigam et al., 2012
S. wightianum	Folk use for skin issues, infection control	Skin infections, inflammation	Nigam et al., 2012
S. ampliflorum	Anti-inflammatory, antimicrobial	Inflammation, microbial infections	IUCN, 2024
S. setosum	Anti-infective, anti-inflammatory	Microbial infections, inflammation	Low et al., 2022
S. parameswaranii	Gastrointestinal ailments, inflammation relief	Gastrointestinal disorders, inflammation	Anselmella et al., 2023
S. kuranda	Anti-inflammatory, digestive remedies	Inflammation, digestive problems	Nigam et al., 2012
S. alternifolium	Diabetes control, digestive aid	Diabetes mellitus, gastrointestinal ailments	Raju, 2014
S. paniculatum	Wound healing, anti-inflammatory	Wounds, inflammation	NSW Government, 2024

(Sasidharan & Jomy, 1999); *S. agastyamalayanum* M.B. Viswan. & Manik. (Viswanathan & Manikandan, 2008); *S. claviflorum* (Shareef et al., 2010); *S. palodense* Shareef, E.S.S. Kumar & Shaju (Shareef et al., 2012); *S. chemunjianum* Shareef, E.S.S. Kumar & Roy (Shareef et al., 2013a); *S. munnarensis* Shareef, Roy & Krishnaraj (Shareef et al.,2013b); *S. sasidharanii* Sujanapal (Sujanapal et al., 2013); *S. dhaneshiana* Ratheesh, Shareef and Nandakumar (Ratheesh Narayanan et al., 2014); *S. sahyadricum* Sujanapal (Sujanapal et al., 2014) etc.Among the 27 endemic species of *Syzygium*, some of the species including *S. laetum* (Buch.-Ham.) Gandhi, *S. munronii* (Wight) N.P. Balakr., *S. occidentale* (Bourd.) D.N. Gandhi, *S. palghatense* Gamble (only found in Palakkad district), and *S. stocksii* (Duthie) Gamble are less explored, and no phytochemical, pharmacognostic, or molecular studies have been carried out on these *Syzygium* species till date.

The discovery of novel *Syzygium* species has significantly widened the botanical and pharmacological insight into this versatile genus with known broad-spectrum biological activities. Research in the last few decades revealed additional species with characteristics and possibilities of use unique to their geographical distribution. In recent studies, scientists have discovered new species in diverse locations, all contributing to the overall gene pool of various characteristics and potential uses. *S. lampeapiense* and *S. wawoniense*, discovered on Wawonii Island in Indonesia, resemble *S. comosum* and *S. ketambense*, respectively. These species are fully described, including their conservation status, and this study marks the ecological role of protection for private species (Sunarti & Rugayah, 2024). Likewise, *S. bharathii* from the Megamalai Wildlife Sanctuary of Tamil Nadu, India, has unique morphological characteristics, such as a cylindrical stem with red young shoot lets and large-sized flowers, which help distinguish it from its close relatives, *S. benthamianum* and *S. agastyamalayanum* (Raju et al., 2018). *S. kampotense* is recognized as a new species, but a few new records of *S. cerasiforme*, *S. foxworthianum*, and other regional species are newly recorded in Cambodia (Chantaranothai, 2024).

Venkat Ramana et al. (2014) described *S. hookeri* and *S. sanjappaiana* from Saddle Peak National Park, North Andaman Islands, presenting comparisons of these new species with related taxa from Myanmar and Sri Lanka, and emphasizing critical biogeographic connections in this part of the world. In Vietnam, Lê et al. (2024) treated *S. ngheanense* as a separate species, with closes affinity to *S. vestitum* and *S. scarbum*; distinguished from these in having glabrous bracts and bracteoles, sparsely scabrid flower buds and hypanthia, sepals on shorter pedicels and petals larger or nearly same size of sepals, with longer reproductive parts which distinguish the new taxon from all other taxa within this genus.

Mustaqim et al. (2020) described a new species from Bird's Head Peninsula in New Guinea*, S. oransbariense* which exhibited specific morphological characters differentiating it from *S. longipes* and broadening the diversity of the genus in the Pacific region. Recently, Widodo and Lucas (2018) have described two new species as *S. namosialangense* and *S. padangense* in Sumatra extending the *Syzygium* diversity in Indonesian archipelago.

Two new species from the southern Western Ghats have been described by Ravikumar (1999): *S. sriganesanii* K. Ravik. & V. Lakshm. And *S. zeylanicum* var. *megamalayanum*. It also is closely related to *S. lanceolatum* and most likely to *S. sriganesanii*, which were also described having quadrangular branchlets, sessile leaves in oblong-elliptic form and the presence of obconical fruits.

Four new species of *Syzygium* from Queensland, Australia, are described by Craven (2003), including *S. fratris*, *S. glenum*, *S. monimioides*, and *S. monospermum*. The findings not only describe and compare these species but also reveal their phylogenetic affinities within the larger *Syzygium* complex, illuminating some of the biological contexts in which they are relevant. The study's findings further indicate challenges in the delimitation of genera, such as the *Syzygium* complex. To facilitate a better understanding and to harmonize the present classifications with available molecular data, the author recommends treating *Syzygium* as a large genus, including all related taxa. The results of this study provide valuable insights into the diversity and complexity of the *Syzygium* genus in Australia from perspectives relating to both

nomenclature (taxonomy) and ecological knowledge. The accounts of these new species not only stress the importance of comprehensive morphological and ecological study for resolving taxonomic confusion but further underscore the need to reconnect ongoing research with conservation programs to secure Australia's unique rainforest biodiversity.

2.4. IUCN status and conservation of Western Ghats *Syzygium* endemics

The Western Ghats is a world heritage centre, an area of high endemism, and is one of the biodiversity hotspots in the world, displaying several species of *Syzygium*. They are biologically sensitive with habitat specificity and experience multiple anthropogenic pressures, thus have been classified as critically endangered and need conservation urgency. Even *S. gambleanum* has been listed as a rediscovered species after 120 years (Irwin et al., 2024).

In the Western Ghats, 27 species of *Syzygium* are endemic, including *S. laetum* (Buch.-Ham.) Gandhi, *S. munronii* (Wight) N.P. Balakr., *S. occidentale* (Bourd.) D.N. Gandhi, *S. palghatense* Gamble, *S. stocksii* (Duthie) Gamble. Most of these species are narrowly distributed in certain forest patches of Agasthyamala, Anamalai, and Nilgiris in the Southern Western Ghats (Sujanapal & Kunhikannan, 2017).

Among the known 645 tree species in the Western Ghats (Nayar et al., 2014), *Syzygium* forms the single largest genus, with 48 taxa, of which 27 are endemic to the region. Nayar et al. (2006) and Sasidharan (2013) reported that 39 taxa occur in the Kerala part of the Western Ghats, with 19 endemic species. Viswanathan & Manikandan (2008) recorded 33 species and four varieties of the genus in Tamil Nadu.

The IUCN Red List includes species lists with statuses (categories) of Critically Endangered, Endangered, and Vulnerable, and is a cornerstone in evaluations that inform conservation practices (Cardoso et al., 2016). At least 352 tree species are endemic to the Western Ghats, of which 325 are threatened globally (including 51 that are Critically Endangered), thus highlighting its conservation priority status at a global level (Warrier et al., 2020). The IUCN has assessed *S. densiflorum* as Vulnerable due to threats including habitat alteration, overexploitation,

and invasive species. Conservation strategies are being developed to micropropagate it for proliferation, and that too in a sustainable manner (Raju et al., 2020). The tree has similar ecological requirements with another critically endangered species, *S. travancoricum,* which has low seedling survival due to habitat destruction and warranting ex-situ conservation through air layering. The Northern Western Ghats are the hotspots of biodiversity for the endemic species. But still it remains poorly presented in the global IUCN assessment (Shigwan et al., 2020).

Habitat transformation (land transformation into living or agricultural land) is one of the important factors responsible for the decline in biodiversity (Warrier et al., 2020). Conservation strategies should be implemented so that it maintains a balance between the livelihood and ecology (Kumar et al., 2020). Genus *Syzygium* is highly diverse in the Western Ghats. There is a need of conservation approaches that can conserve this endemic species for future generations (Kumar et al., 2020; Warrier et al., 2020).

To predict the adaptability of *Syzygium* species in the changing environment, it is essential to get an idea of the ecological habits like its distribution patterns, and altitude preference (Dubey & Dubey, 2011; Uddin et al., 2022). The growing demand for these medicinal plants, especially *Syzygium* species, has increased the pressure on wild populations, and this necessitates urgent actions in biodiversity conservation strategies to maximize sustainable utilization. The ecological distribution with its cultural, economic, and medicinal significance of *Syzygium* is tabulated in Table 2.3.

2.5. Morpho-anatomical studies in *Syzygium*

Morpho-anatomical studies of plants are of great importance in *Syzygium*. Due to the large number of species in the genus with several closely related morphological species, detailed morphoanatomical studies are necessary for species delimitation and identification (Aung et al., 2020; Bhatt et al., 2021). *Syzygium* is a diverse genus of evergreen trees and shrubs, with remarkable variations in the vegetative form and habitat specificity among its members. They occupy the tropical and subtropical humid lowlands and the mountains. The size ranges from small shrubby understorey plants to large canopy trees of over 30 m. They occur in rainforest habitats, with bark

Table 2.3: Distribution, uses, and conservation status of selected *Syzygium* species

Scientific names	Common names	Distribution	Economic uses	Medicinal uses	Conservation status	References
S. aromaticum	Clove	Indonesia (Maluku Islands), tropics	Spice, clove oil (dentistry, aromatherapy)	Antimicrobial, antioxidant, analgesic	Not threatened	El-Saber Batiha et al., 2020
S. cumini	Jamun, Java plum, Black plum	South Asia, India, Southeast Asia, tropics	Edible fruit, jams, jellies	Antidiabetic, anti-inflammatory, antioxidant	Not threatened	Nigam et al., 2012
S. malaccense	Malay apple, Mountain apple	Malaysia, Indonesia, Pacific Islands	Edible fruit	Traditional uses	Data Deficient	Cock & Cheesman, 2019
S. jambos	Rose apple, Water apple	Southeast Asia, pantropics	Edible fruit, ornamental	Anti-inflammatory, antimicrobial	Not threatened	Ochieng et al., 2022
S. grande	Sea apple	India, SE Asia, Malaysia	Ornamental, edible	Traditional uses	Not assessed	Nigam et al., 2012
S. samarangense	Wax apple, Java apple	Malaysia, Indonesia	Edible fruit, ornamental	Antioxidant, anti-inflammatory	Not assessed	Ochieng et al., 2022
S. polypetalum	Chasmophytic *Jambolan*	NE India, Bangladesh, Myanmar	Limited	Traditional uses	Not assessed	Dey et al., 2022
S. travancoricum		Western Ghats, India (endemic)			Critically Endangered	Ramachandra et al., 2017
S. munroi		Kerala (India), Sri Lanka			Not assessed	Cock & Cheesman, 2019
S. kurzii		Andaman & Nicobar Isl., NE India, SE Asia			Not assessed	Nigam et al., 2012
S. lanceolatum		Kerala, Tamil Nadu (India)			Not assessed	Nigam et al., 2012
S. microphyllum		Kerala, Tamil Nadu (India)			Not assessed	Nigam et al., 2012

S. campanulatum	Malabar rose apple	Western Ghats (India), Sri Lanka	Ornamental	Traditional uses	Not assessed	Kumar et al., 2020
S. beddomei		India			Not assessed	Nigam et al., 2012
S. densiflorum		Western Ghats (India)			Not assessed	Nigam et al., 2012
S. firmum		Western Ghats (India)			Not assessed	Nigam et al., 2012
S. francisii	Giant water gum	Australia	Ornamental		Not assessed	Nigam et al., 2012
S. jambolanum	*Jambolan* plum	India & tropics	Edible fruit	Antidiabetic, antioxidant	Not assessed	Nigam et al., 2012
S. wightianum		India, Sri Lanka			Not assessed	Nigam et al., 2012
S. ampliflorum		Indonesia (Java, endemic)			Critically Endangered	IUCN, 2024
S. setosum		Peninsular Malaysia, Sumatra			Endangered	Low et al., 2022
S. parameswaranii		Western Ghats, India (endemic)			Endangered	Anselmella et al., 2023
S. kuranda		Australia, New Guinea			Not assessed	Nigam et al., 2012
S. alternifolium		S. & Central India	Edible fruit	Digestive, diuretic, antidiabetic	Endangered	Raju, 2014
S. paniculatum	Magenta lilly pilly, brush cherry	Coastal E Australia (NSW)	Ornamental, edible fruit	Antioxidant, traditional uses	Vulnerable (NSW, Australia)	NSW Government, 2024
S. aqueum	Water apple	SE Asia, Indo-Pacific	Edible fruit, cultivated	Antioxidant, anti-inflammatory	Not assessed	Aung et al., 2023

varies from smooth, green or grey, to thick, corky or even flaky on mature trees. The branching in *Syzygium* is generally opposite or subopposite as in Myrtaceae (Chantaranothai, 2024; Wangkhem et al., 2020).

The study conducted by Soh & Parnell (2011) reported that, among other characteristics, the leaf anatomical traits recorded in *Syzygium* are homoplasic since they are not likely to represent plesiomorphic states, which are a result of independent evolution owing their origin to different genetic origins. Furthermore, leaf anatomy cannot be used as an autapomorphy to phylogenetically classify taxa within this genus accurately because traits are not homoplasy.

Hao & Xiao (2020) emphasized that morphoanatomical methodologies are indispensable for precisely differentiating taxa in *Syzygium* due to overlapping and non-consistently discriminating morphological characters with related genera, like *Eugenia*. They stressed the necessity of establishing morphoanatomical markers to achieve clarity in systematics. Leaf characters also play a role in determining the ecological distribution and physiology of *Syzygium*. It includes characters like leaf thickness, type of stomata it possess, and its distribution, and the presence of oil glands.

Leaf form and distribution are critical for the delineation of species of *Syzygium*. Mostly leaves are simple and opposite. But shape of leaf blade is different even in closely related species. *S. aromaticum* possess elliptic leaves (6-13 × 3-6 cm), while *S. cumini* exhibit oblong leaves (6-15 × 3-7 cm) (Van der Walt et al., 2021). Morphological and anatomical studies are important for the identification, phylogenetic analysis and finding the ecology of the *Syzygium* species. *Syzygium* exhibits numerous variations in vegetative as well as reproductive characteristics like different leaf types and size (as few mentioned above), different flower colours and fruit types (Aung et al., 2020; Itam et al., 2021).

A thorough examination of morphological (leaf morphology and venation) as well as anatomical characters of the species of the family Myrtaceae was conducted by Mohamed et al. (2023). The study involved 26 species belonging to 15 genera and included macromorphological aspects such as leaf arrangement, shape, apex, base,

and venation types, which varied considerably among the studied taxa. Most taxa exhibited simple leaves with entire margins, pinnate, and brochidodromous venation. Within the Leptospermoideae, several species exhibited cladodromous, eucamptodromous, and craspedodromous venation. The leaves were alternate in eight studied taxa (all Leptospermoideae), opposite in the remaining 17 (Myrtoideae and Leptospermoideae). Lamina form obovate sizes in *Pimenta racemosa*, oblong in *S. paniculatum* and *S. samarangense*, and oblanceolate in *S. malaccense* and *Xanthostemon fruticosus*, this observation is consistent with Defaveri et al. (2011), Khan et al. (2016), and Oliveira et al. (2017). According to them, the leaves of the *Eugenia rotundifolia*, *Myrtus communis,* and *Psidium* species are opposite in arrangement. The leaf attachment was sessile in seven of the studied taxa (all of which belong to Leptospermoideae) and petiolate in nineteen taxa. Oliveira et al. (2017) referred to the occurrence of petioles in some taxa of Myrtaceae.

Morpho-anatomical studies of *S. polyanthum* demonstrate that the palisade mesophyll is dense, and abundant oil glands and anisocytic stomata are documented, with an abaxial surface and visible trichomes. The midrib has a single series (open) vascular system in its mostly circular arrangement. It has a circular pattern of vascular tissue surrounded by sclerenchyma cells, and parenchymal tissue also assists in taxonomic identification. These characteristics offers an important criteria for the identification and taxonomy of the species and also play a role in the plants ability to grow in the tropical conditions (Abdulrahman, 2022). A proper description on the morpho-anatomical features of *S. polyanthum* is important for the classification in the Myrtaceae family. Leaf characteristics (stomata types, mesophyll) also play role in the distinction of the species from other ones in a genus. Oil gland (arrangement and direction) in leaf and petiole are also important characters for distinction. All these modifications helps in the survival of the species into the tropical conditions. These also have medicinal importance as it provides therapeutic properties to the plant.

Briggs and Johnson (1979) worked on Myrtaceae family and observed that inflorescence varies in different genera. The primitive condition is a flexible, opposite-decussate inflorescence, where the apical buds may be vegetative or contain

flowers. This might indicate an origin from different inflorescences that have evolved across the family. The differences in inflorescence distinguish species and provide knowledge about the evolution of these features within the family. Inflorescence helps in determining the evolutionary relationships. Because of the inflorescence *Syzygium* was placed in *Acmena* alliance (Briggs & Johnson, 1979). This shows advances in Myrtaceae classification by providing a flexible and more accurate context.

Wilson et al. (2001) study offers detailed information on the Myrtaceae family. With about 133 genera and over 3800 species, mostly found in Australia, Southeast Asia, and the America. It is one of the most important families of lignified dicotyledons. The analysis comprised 45 morphological and anatomical characters that were modified from previous studies and derived from the literature (Johnson & Briggs, 1984). The Myrtoideae, (have fleshy fruits), and the Leptospermoideae, (have capsular fruits), are the two traditional divisions of the family. Cladistic analyses later led to the revocation of this classification. One of the more substantial taxonomic implications is the refutation of these typical sub familial division. By using both morphological and molecular analysis these groups were identified. Instead, this suggests that the conventional dichotomy is a poor fit for the family's evolutionary history and should be abandoned in favour of a more cladistic classification.

Wilson et al. (2001) stated that among Myrtaceae, the indumentum varies markedly at the generic level from glabrous to multicellular and unicellular trichomes. Normal hairs are usually unicellular and have a thick wall and an acute apex. In contrast, multicellular hairs occur in some genera (*Angophora*), which is recognized as a unique character for the phylogenetic diversification within the eucalypt group.

Groom & Lamont (1999) demonstrated how plant groups adapt to environmental stresses through modifications in leaf structure, particularly sclerophylly. Sclerophylly is a necessary adaptation that enables plants to survive in stressful environments like limited water and nutrient resources with tough, thick, leathery leaves. The various researchers focus on the ecological importance of these adaptations, especially in arid environments where water and nutrient availability are low. Groom & Lamont (1999) also considered that Leaf Mass per Area (LMA) was

related to both increased leaf thickness and internal structural elements, such as dense palisade layers or thickened layers of epidermal cells, which directly followed the results obtained from various studies on different *Syzygium* leaves. The *Syzygium* species and the leaves described by Groom & Lamont (1999) revealed evidence of sclerophylly, characterized by increased thickness and cell density. The thick cuticle and densely packed mesophyll of the *Syzygium* leaves reflect these sclerophylly traits. The adaptation of thick leaves hints at a reaction to environmental forces that prevail upon water shortage and nutrient-poor soils. The strong leaf structures limit the dissipation of moisture, thereby improving survival.

No diagnostic differences in leaf anatomy were detected among the subgenera *Acmena*, *Perikion*, *Sequestratum,* and *Syzygium* studied by Soh & Parnell (2011). But they uses different combinations of non-unique characters. These includes stomata types, types of crystal and the frequency of midrib vascular system like whether the partition in adaxial phloem is present or not. These underscore difficulties using leaf anatomy alone to discriminate among taxa in the genus. An improved phylogenetic analysis of these relationships was aided by adding morphological characters (leaf anatomy and, to a lesser extent, macromorphology) and DNA data, yielding superior support for clades. In particular, strong support for the subgenera *Perikion*, *Sequestratum*, and *Syzygium* was obtained, whereas *Acmena* received moderate support in Bayesian but weak support in parsimony analysis. This is important because leaf anatomical characters are homoplasic. They do not undergo evolutionary constraint or selection pressure and have finite diversity, but remain informative when integrated with molecular evidence. Many authors emphasized morpho-anatomical studies for identifying species. The morphological variations in the shape of the vascular strand in the midrib and petiole are described as diagnostic characteristics in *Eugenia* by Hussin et al. (1992). They reported that U-shaped or crescentic bundles are seen among some species of *Eugenia.*

Anatomical and histochemical features of *S. travancoricum* (an endangered and endemic species of Western Ghats of India) were studied by Smitha and Anto (2023). Microscopic study was used to observe anatomical characters. Histochemical studies included paracytic stomata associated with a single adaxial palisade layer and the occurrence of druses and oil glands. These characters act as a basis for the

distinction of *S. travancoricum* from related species and important for the species delimitation.

Syzygium species shows a wide variety of leaf morphologies (vein structure, stomatal traits, and laminar shape) (Chatri et al., 2020; Zahro et al., 2024). Anatomical studies of *S. cumini* wood infected with the white-rot fungus provide a comprehensive understanding of the wood decay process. These investigations showed a number of noteworthy structural alterations, including the lignin and cellulose degradation (Padhiar & Albert, 2011).

Species of *Syzygium* from Manipur, India, demonstrated simple perforation plates and vestured inter-vessel pits are prevalent in many species, and that some differences in vessel form and fiber properties aid in the classification of taxa (Wangkhem et al., 2020). Research on anatomy and histochemistry of *S. aromaticum* showed that it has secretory structures that produce aroma, responsible for its properties (Zaman et al., 2018). Table 2.4 represents recent taxonomic and molecular studies of *Syzygium*.

2.6. Pharmacognostic studies

A pharmacognostic analysis using powder microscopy is a valuable tool for identifying and quantifying the quality of plant materials, which is especially applicable to traditional medicine (Robbers et al., 1996). Plant materials can be standardized by way of elaborate microscopic evaluations. Pharmacognostic standardization of plant materials primarily involves morphological, anatomical and biochemical characteristics. They are also used as attractive taxonomic markers for the identification of plants in modern taxonomy based on powder microscopy (Bijeshmon & George, 2014).

Freeman (2010) highlights that powder characterization is crucial in pharmaceuticals, as most active pharmaceutical ingredients (APIs) are administered in powder form across various dosage formulations. Taking into account powder behaviour accelerates formulation development, manufacturing, and quality control processes more efficiently. Under the principles of Quality by Design (QbD), it is essential to produce consistently high-quality products, and thorough powder characterization aids in designing robust manufacturing processes.

Table 2.4: Summary of recent molecular and taxonomic research on *Syzygium*

Authors	Methods	Major findings
Wei et al. (2022)	Complete chloroplast genome sequencing; ML (Maximum Likelihood) phylogenetic analysis	Clarified phylogenetic clades; resolved relationships including *Syzygium zeylanicum* and *S. acuminatissimum*; high-resolution chloroplast genome data
Nguyen et al. (2023)	Chloroplast genome assembly; ML (Maximum Likelihood) phylogenetic analysis	Supported genus monophyly; detailed evolutionary history and biogeographic patterns
Liu et al. (2024)	Comparative chloroplast genomics: genome annotation	Demonstrated taxonomic clarifications and diversity hotspots; enhanced molecular taxonomy
Cheong & Ranghoo-Sanmukhiya (2013)	Chloroplast DNA sequencing; ML (Maximum Likelihood) and BI (Bayesian Inference) phylogenetic analyses	Resolved controversy regarding *Syzygium* and *Eugenia* boundaries; detailed species placement
Sun et al. (2024)	High-throughput chloroplast genome sequencing; BI (Bayesian Inference) and ML phylogeny	Clarified evolutionary relationships; noted incongruent nuclear vs plastid phylogenies
Biffin et al. (2022)	Chromosome-level genome assembly; comparative genomics; synteny analysis	Confirmed whole-genome duplication event in Myrtales, including *Syzygium*; origin in Australasia with dispersals
Ran et al. (2022)	Genome synteny and comparative genomic analysis	Supported evolutionary hypotheses of origin and diversification across Myrtaceae
Ramachandra et al. (2017)	Morphological taxonomy; distribution mapping; molecular markers	Refined taxonomy of Indian endemics; identified new species records
Low et al. (2022)	Nuclear SNP genotyping; phylogenomic analyses	Revealed stepwise speciation driven by geography; documented genetic clines and discordance between datasets
Shareef (2020)	Morphological and molecular characterization; barcoding	Assessed Indian *Syzygium* diversity; clarified cryptic species; updated species identification

According to Modi et al. (2010), powder microscopy of *S. cumini* seeds emphasizes the parenchymatous cells, starch grains, and testa, providing unique identifiers for quality assurance and authentication. Suma et al. (2020) examination of *Eugenia jambolana* (Jambu) (smooth epidermis with cluster crystals of calcium oxalate) and *S. caryophyllatum* (Kshudra Jambu) (has a beaded epidermis and rosette crystals) outlines some particular diagnostic traits based on powder microscopy between these two species. Both species are forms of calcium oxalate, but they differ structurally, making it easy to distinguish between them. *E. jambolana* also has storage parenchyma, in contrast to *S. caryophyllatum*, which exhibits palisade parenchyma, a feature of photosynthesis, and vascular strands with chlorophyll in the lamina. Because of these microscopic features, authenticity is essential in Ayurvedic medicines for their purity and actions.

The study by More et al. (2024) on *S. cumini* reported that the presence of polygonal cork cells, spiral vessels, tracheids, starch grains, and lignified fibers are some important anatomical features of *S. cumini* that facilitate its differentiation from other species. Powder microscopic studies show that the stomata on the adaxial side of the leaves are anisocytic type. Stomata number (between 13-18) and index (average 16%) helps in the identification of structure of leaf and its adaptation. The powder from different parts of *S. cumini* shows different characteristics. Leaf powder is dark green in colour and uniform, stem powder is grey in colour and crumbly, while fruit have sweet and pale purple colour powder.

Characterisation of the structure of the medicinal product of *Syzygium* species are important in quality control and differentiation of the species (Prasad et al., 2021). While related species differed in fiber structure, colour, and grinding amenability, *S. cumini* possessed traits like crystal sheaths, multilayered palisade and spongy cells, and undulating epidermis cells.

Chitnis et al. (2012) found that the powder from the seeds of *S cumini* showed distinct characters in microscopic and organoleptic analysis. The phytocompounds of *S. calophyllifolium* was identified using daylight and the UV florescence. This provide information on the chemical composition of the leaf (Nagulan & Kumar, 2016). To determine the medicinal application of phytocompounds, analysis on phytochemicals as well as physicochemical analysis is important. Secondary metabolites like

alkaloids, flavonoids, and phenols can be identified by these qualitative tests. This can be done by using the different solvents like water. methanol etc. Nagulan & Kumar (2016).

Fruits of *S. caryophyllatum* and *S. zeylanicum* have good nutritional as well as medicinal importance as per reports by Shilpa et al. (2015). *S. paniculatum* fruits' suitability for human intake was confirmed by physicochemical analysis, particularly in light of the reproductive organs' high minerals and phenolic compounds (Pérez & Mojica, 2018). Anthocyanins and flavonoids, two phytochemicals abundant in *S. cumini*, provide it with the antidiabetic and antioxidant qualities necessary for its conventional medical applications. (Bijauliya et al., 2017).

2.7. Phytochemical diversity and pharmacological potential of *Syzygium*

The leaf and bark of *Syzygium* are the reservoirs of important bioactive compounds responsible for the pharmaceutical properties of the species (Table 2.5). Some of the identified phytochemicals include high tannin content like methyl gallate and 3-methoxy ellagic acid from *S. samarangense* bark using acetone extract which have been further established with spectral techniques (Bhanu et al., 2020). The bark of *S. guineense* is exhibit the substantial content of total phenolic and flavonoid in the ethanol extracts, furthermore equipped with strong antioxidant properties as other plants which gave the high total phenolic content, TPC (37.80 ± 3.70 mgGAE/g) and total flavonoid content (TFC) (19.22 ± 1.44 mgQE/g) (Dessalegn et al., 2025).

The bark of *S. cumini* is known to have the bioactive compounds that may have different pharmacological activities like alkaloids, flavonoids, terpenoids and steroids (Srivastava & Chandra, 2013; Viswambharan, 2015). S. cumini bark extracts also worked well in a variety of assay techniques, including the DPPH, NO, and H2O2 assays (Rajeshkumar & Naik, 2013). Various compounds (phenolic and flavonoid) in bark of *S. cymosum* are responsible of cytotoxic and antioxidant properties (Dhar et al., 2016).

The phenolic substances found in *S. zeylanicum* bark have antihyperglycemic properties and have been described as agents for managing hyperglycemia (Nguyen et al., 2023). The bark of *S. cumini* has exceptional antioxidant property, in

Table 2.5: Phytochemical profiles and biological activities of selected *Syzygium* species

Syzygium species	Major phytochemical compounds	Reported biological activities	References
S. aromaticum	Eugenol, eugenyl acetate, β-caryophyllene, quercetin, ursolic acid, gallic acid, tannins, flavonoids, alkaloids, terpenoids	Antimicrobial, antioxidant, analgesic, anti-inflammatory, anticancer, antidiabetic	El-Saber Batiha et al. (2020); Jimoh et al. (2017); Qamar et al. (2022)
S. cumini	Anthocyanins, gallic acid, ellagic acid, quercetin, myricetin, β-sitosterol, tannins, flavonoids	Antidiabetic, antioxidant, anti-inflammatory, antimicrobial, hepatoprotective	Nigam et al. (2012); Ayyanar & Subash-Babu (2012); Qamar et al. (2022)
S. malaccense	Alkyl-salicylic acids (anacardic acids), phenolics, tannins	Antimicrobial, anti-inflammatory	Raina et al. (2022); Sobeh et al. (2024)
S. jambos	Phenolic acids, flavonoids (myricetin, quercetin), ellagitannins, organic acids	Antioxidant, anti-inflammatory, antimicrobial, dermatological, anti-aging	Sobeh et al. (2024); Ochieng et al. (2022); Sobeh et al. (2018)
S. grande	Flavonoids, phenolic compounds	Antioxidant, antimicrobial	Nigam et al. (2012)
S. samarangense	Alkaloids, flavonoids, phenols, saponins, tannins, terpenoids	Antioxidant, antimicrobial, anti-HIV, analgesic	Tarigan et al. (2021); Jimoh et al. (2017)
S. polypetalum	Phenols (syringic acid, ellagic acid), flavonoids, tannins	Antioxidant, antimicrobial	Jimoh et al. (2017); Herbmed Pharmacol (2020)
S. aqueum	Flavonoids, phenolic acids, anthocyanins, terpenoids	Antioxidant, anti-inflammatory, antimicrobial	Sobeh et al. (2018); Aung et al. (2023)
S. jambolanum	Anthocyanins, flavonoids, tannins, phenolic acids	Antidiabetic, antioxidant, anti-inflammatory	Nigam et al. (2012)
S. wightianum	Phenolic compounds, flavonoids	Antioxidant, antimicrobial	Nigam et al. (2012)
S. campanulatum	Flavonoids, phenols	Antioxidant, antimicrobial	Kumar et al. (2020)
S. lanceolatum	Tannins, flavonoids	Antioxidant, antimicrobial	Nigam et al. (2012)
S. microphyllum	Phenolic compounds, flavonoids	Antioxidant	Nigam et al. (2012)

S. kurzii	Flavonoids, tannins	Antioxidant, antimicrobial	Nigam et al. (2012)
S. densiflorum	Phenolic acids, flavonoids	Antioxidant, antimicrobial	Nigam et al. (2012)
S. firmum	Flavonoids, tannins	Antioxidant	Nigam et al. (2012)
S. francisii	Phenolic compounds, flavonoids	Antioxidant	Nigam et al. (2012)
S. munroi	Flavonoids, phenols	Antioxidant, antimicrobial	Cock & Cheesman (2019)
S. beddomei	Flavonoids	Antioxidant	Nigam et al. (2012)
S. ampliflorum	Phenolic compounds	Antioxidant	IUCN (2024)
S. setosum	Flavonoids, phenolic compounds	Antioxidant	Low et al. (2022)
S. parameswaranii	Flavonoids, phenolic compounds	Antioxidant	Anselmella et al. (2023)
S. kuranda	Flavonoids, tannins	Antioxidant	Nigam et al. (2012)
S. alternifolium	Flavonoids, phenolic compounds	Antioxidant, antidiabetic	Raju (2014)
S. paniculatum	Anthocyanins, phenolic acids	Antioxidant, anti-inflammatory	NSW Government (2024)

comparison to its leaves. This is because the bark contain high phenolic content (Dulay & Castro, 2016). Derivatives of myricetin are important class of compounds found in family Myrtaceae. It is also abundant in flavonols and tannins (Amaral et al., 2001).

The bark of *S. cumini* bark shows rich presence of hydrocarbons and esters as determined by GC-MS. Tiwari, (2024) identified a total 39 phytocompounds in its bark. Some of these are having different applications in flavouring, medicines and perfumes. While rich range of chemical are found in leaves of *S. dhaneshiana.* These includes carbohydrates, proteins, amino acids, alkaloids and phenols. 17 compounds in ethanol extract and 19 compounds in the chloroform extract were identified by Krishna et al. (2017). The medicinal importance of the *Syzygium* species is given in Figure 2.4.

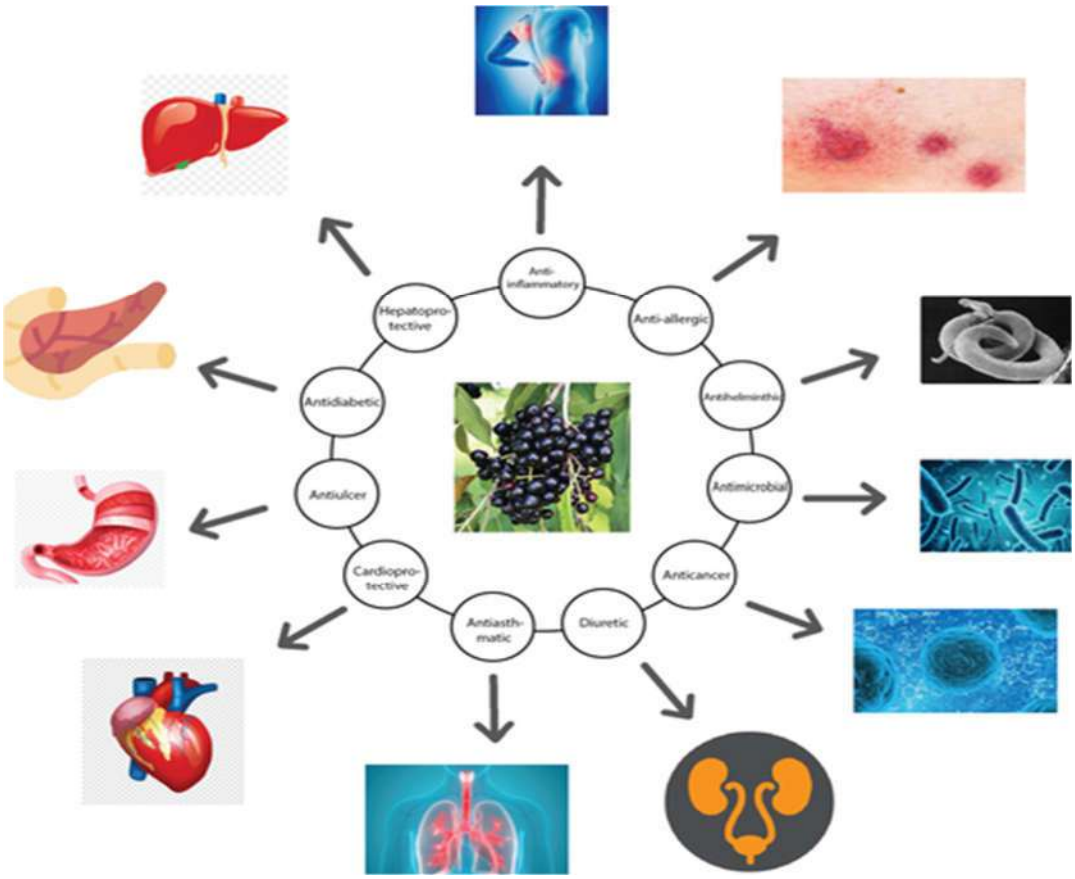


Figure 2.4: Pharmacological potential of *Syzygium* (Uddin et al., 2022)

The antibacterial activity is strong in the leaves of *S. cumini* when compared to bark. It helps in inhibition of various foodborne pathogens, so are natural source of antibacterial agent. Antioxidant activity also possessed by its leaves. Because its aqueous fraction exhibits largest phenolic content, that helps in scavenging free radical (Mathialagan et al., 2024). Leaves of *S. jambos* also possess higher activity for bacteria. Its leaf extract also work against resistant bacterial strains which gives a proof of its activity and potency (Tchana et al., 2018). Bark extract of *S. afromontanum* shows the presence of Sesquiterpene hydrocarbons and oxygenated monoterpenoids. These also have medicinal importance (Ajetunmobi et al., 2024).

From HPTLC and FT-IR analysis of *S. stocksii*, a species that is critically endangered, it was found that it contains contains alkaloids, phenolics, flavonoids, tannins, and terpenoids. Which helps in providing the medicinal properties to it (Johns & Radhamany, 2024). *S. cumini* has been identified to have many medicinal properties as it bark, stem, fruit contains various phytocompounds. The presence of these compounds showed it historical importance as an antioxidant as well as in the treatment of the skin diseases and diabetes (Aziz and Banerjee 2018).

Triterpenes (Djoukeng et al., 2005; Kuiate et al., 2007), chromone derivatives (Tanaka et al.,1993), tannins, flavonoids (Vaishnava et al., 1992; Kuo etal., 2004), phenylpropanoids and phloroglucinol derivatives (Miyazawa & Hisama, 2003; Tanakaet al.,1993) have also been isolated from the genus *Syzygium*. Miyazawa & Hisama (2003) worked to identify the chemotaxonomic significance of monolignans in *S. grijsii* and identified a close relation with *S. aromaticum*.

This indicates that the bark might have more to offer in medicinal terms as compared to the leaves, although the precise phytochemical profile may very well differ from species to species and between extractions.

2.8. Biological activities of *Syzygium*

S. aromaticum (clove), *S. cumini* (Java plum), and *S. samarangense* (Java apple) are associated with various pharmacological effects, including antioxidant, antimicrobial, anti-inflammatory, anthelmintic, antidiabetic, and anticancer activities.

This action is due to the large number of phyto-balances (flavonoids, terpenoids, tannins) found in the plants and also other compounds include glycosides and phenolics (Aung et al., 2020; Nair & Sathianarayanan, 2020). Especially *S. aromaticum* is known for its content of eugenol, which plays a substantial role in the antioxidant and antimicrobial activity of clove oil that allows it to kill a wide range of bacteria as well as fungi including *E. coli* and *Candida albicans* (De Lavor et al., 2024).

S. cumini seeds manifested significant antioxidant and anti-inflammatory actions and can be used in the pharmaceuticals and food industries (Ayyanar & Subash-Babu, 2012). The edible portion of the *S. cumini* fruit contains anthocyanins, tannins, gallic acid, vitamin C, cyanidin, malvidinglucoside, petunidin, malvidinglucoside, and other substances, while its seeds possess anti-diarrheal, psychopharmacological, anti-inflammatory, antibacterial, anti-diabetic, and antipyretic properties Aziz & Banerjee (2018). Astringent, antidiabetic, and cytotoxic properties has been found in *S. samarangense* (Nair & Sathianarayanan, 2020). Nguyen (2023) presents a more thorough understanding of the phenolic contents and possible health-promoting qualities of *S. nervosum*, which is essential for generating natural agents for the prevention and treatment of diseases (Figure 2.5).

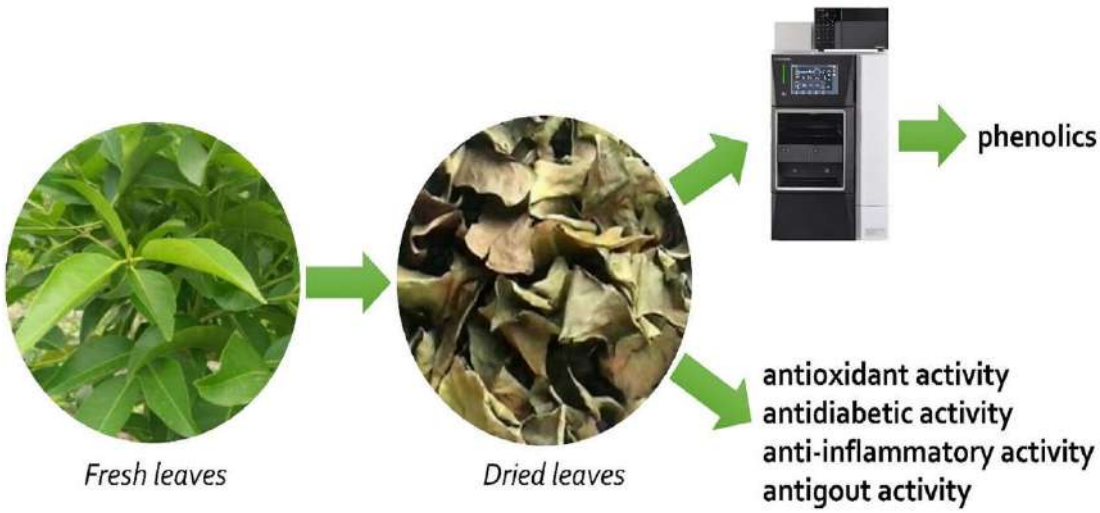


Figure 2.5: Biological properties of *Syzygium* (Nguyen, 2023)

2.8.1. Antioxidant properties

S. cumini (Jamun) has antioxidant properties. Phenolica and flavonoids are identified in its fruit pulp, seed coat, and kernels. Higher radical scavenging activity reported in kernel than Trolox or catechin as standard antioxidants (Benherlal & Arumughan, 2007).

S. jambos fruit and seed possess high antioxidant properties, with higher content of phenolic and flavonoid present in the seed, making them very effective against oxidative stress-induced diseases (Dutta et al., 2021). Jayamohan et al. (2013) reported that the bark of *S. cumini* contains potential antioxidant activity due to its total phenolic content. Kamsala et al. (2014) reported antioxidant and antimicrobial benefits of leaf extracts of *S. alternifolium* and stated that ethanol as well as aqueous extracts of the leaves were rich antioxidants with moderate antibacterial proprieties against various bacterial strains including some fungal species (Kamsala et al., 2014; Kamsala & Raju (2015). Phenolic compounds and flavonoids are responsible for effective antioxidant properties, are found concentrated in the leaves of *S. aqueum* (Priyanka & Rajalakshmi, 2020).

The leaves of *S. antisepticum* is the native vegetable. It has the potential for health improvement and combat oxidative stress. Triterpenoids and polyphenolic chemicals are the bioactive chemical in its leaves. Flavonoids helps in oxidative stress and intracellular ROS generation therefore important in antioxidant activity. By increasing the production of catalase and Glutathione Peroxidase 1 (GPx-1) in human embryonic kidney-derived 293 (HEK-293) cells, myricitrin and quercitrin, which are present in *S. antisepticum* leaves (Figure 2.6), demonstrated a cellular antioxidant defense mechanism (Mangmool et al., 2021).

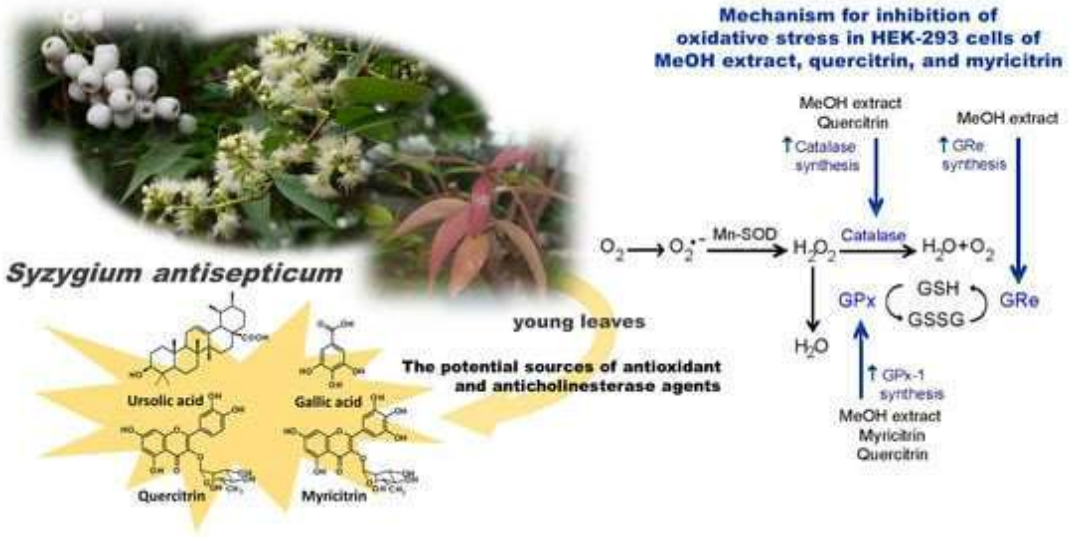


Figure 2.6: Antioxidant mechanism of *Syzygium antisepticum* (Mangmool et al., 2021)

Sabandar et al. (2022) evaluated the stem and root bark of *S. polyanthum,* discovering it is rich with phenolics and flavonoids that supported very strong DPPH scavenging and FRAP activities due to the high content of phenolics and flavonoids. *S. zollingerianum* presented as a more neglected plant, however leaf extracts of this *S. zollingerianum* which is a traditionally Indonesian species shows potent antioxidant activity while mild cytotoxic, this would permit strongly to study it as one of the natural antioxidants with rare sources available (Sujana & Wijayanti, 2022).

Several investigations have described the antioxidant activity of various *Syzygium* species due to their high content of phytochemicals and bioactive compounds. The significant antioxidant properties in the bark, particularly high polyphenolic, flavonoids and tannins have been demonstrated by *S. caryophylatum* and were not only proved with their good scavenging activities in DPPH, ABTS, and Nitric oxide assays but also suggested for its use in formulations against oxidative stress ailments (Chandra et al., 2020).

According to the spectrophotometric test findings, the ethanolic extract of *S. zollingeranum* leaves included tannins, alkaloids, flavonoids, and phenolic compounds. The antioxidant activity index demonstrated a considerable ability to block free radicals (Sujana & Wijayanti, 2022). The findings of Dahiru et al. (2022)

demonstrated that the three distinct clove (*S. aromaticum*) extracts (hydromethanolic, hydroethanolic, and aqueous extracts) had detectable effectiveness in neutralizing the free radicals and other harmful compounds in human bodies because of its capacity to neutralize free radicals, hydrogen peroxide, and the conversion of Fe3+ to Fe2+. The 70% ethanolic extract of *S. polycephalum* leaves exhibited exceptional antioxidant qualities (Frediansyah et al., 2023).

The high total phenolic content and antioxidant activities have been observed for *S. aromaticum* and *S. polycephalum*. *S. aromaticum* shows potential cytoprotective and genoprotective effects (Tukiran et al., 2019; Yasir et al., 2024). These studies provided evidence on the therapeutic potentials of *Syzygium* species as nutraceuticals to prevent or treat oxidative stress, and health disorders related with it. The leaves of *S. eticulatum* have been discovered for various medicinal properties like antioxidant, cytotoxic, analgesic, and anti-diarrheal potential, which show great potential of methanol extracts over hexane extracts (Das et al., 2024). *S. aromaticum* is usually used for its essential oil, which presents relevant antioxidant and antistaphylococcal activities, a feature that can be mainly attributed to the high level of eugenol present in this plant (Ghallab et al., 2020; Boughroud et al., 2024).

2.8.2. Antimicrobial properties

Various publications reported antimicrobial properties in *Syzygium* species Djipa (2000) and Djipa et al. (2002) reported that *S. jambos* exhibits antimicrobial activity against *Staphylococcus aureus*, *Yersinia enterocolitica*, and coagulase-negative *staphylococci* may be related to the tannin content. In general, the *Syzygium* genus is very valuable in terms of their various medicinal properties as they consider a potential source for phytochemicals leading to diverse therapeutic effects; hence further investigation and conservation practices are needed (Aung et al., 2020).

The study conducted by Mericli et al. (2020) , Elisha et al. (2022), and Sukohar et al. (2022) reported that *S. aromaticum* have antimicrobial activity against a wide range of bacteria also including multi-drug-resistant strains such as *Salmonella typhi*. Its eugenol-containing essential oils have reportedly potent antimicrobial activities

against *Candida albicans* and *Streptococcus mutans*, with inhibition zones similar to or higher than those of antibiotics.

The methanolic extract of medicinal plant *S. jambos* is widely used in the traditional medicine system of India and showed to have antibacterial effect on several species like *P*. aeruginosa. The acetone extract of its bark was most effective because it had more tannins than the aqueous extracts and even showed equal effectiveness as standard antibiotics ampicillin and streptomycin (Murugan et al., 2011). Similarly, *S. aromaticum* (clove) was found to be highly effective against *Pseudomonas aeruginosa*. It was observed that ethanolic extracts of clove showed maximum inhibition zone (23 mm) and was active against multi drug-resistant strains, which indicated that cloves might be a hope in alternative treatment of infections specifically urinary tract infection by *P. aeruginosa* (Ahmed et al., 2021; Jabeen et al., 2014).

Clove essential oil with high percentage of eugenol efficiently inhibited multidrug-resistant isolates of *P. aeruginosa* from canine otitis; the minimum inhibitory concentrations (MIC) ranged from 3.26 to 6.53 mg/mL, displaying a good potential for use as economically accessible antimicrobial agent (Costa et al, 2022). Moreover, clove also exhibited antibacterial activity against the foodborne pathogen, *P. aeruginosa* when tested using aqueous and ethanolic extracts. The highest sensitivity detected in the ethanolic extract by disc diffusion assays (Mostaqim et al., 2019). According to Sidney et al., 2015) the pulp extract of *S. cordatum* showed the lowest minimum inhibitory concentration (MIC) value (3.13 mg/ml), when tested against several gram-positive and gram-negative bacteria. As reported by (Fatima et al., 2023) the methanolic extract of *S. aromaticum* was shown to have the greatest antibacterial, anti-biofilm, and antioxidant activity, its secondary metabolites are inexpensive alternatives that might aid in the current antibiotic development process.

Biofilm is a microorganism's community in an extracellular polymeric substance (EPS) and display greater resilience to unfavorable environmental stressors (Meliani & Bensoltane, 2016). *Pseudomonas aeruginosa* is a gram-negative microbe that produces biofilm, which proves crucial for both acute and chronic infections (Gunardi et al., 2016). Because *P. aeruginosa* may build thick and persistent biofilms,

antimicrobial therapies for *P. aeruginosa* infections remain difficult. Polysaccharides (Pel, Psl, and alginate) and extracellular DNA make up *P. aeruginosa* biofilms, and are essential for shielding bacterial colonies from external stressors imposed through antibiotics. Its remarkable capacity to produce biofilms is supported by a complex hierarchical cell communication system known as quorum sensing, which is actively induced by an increase in cell density or by food restriction (Thi et al., 2020). Type IV pili also play an important role in biofilm formation and surface colonization by enabling other motility mechanisms, such as twitching and swarming (Otton et al., 2017).

The essential oils obtained from *S. samarangense* and *S. malaccense* showed a broad spectrum of antimicrobial activity against oral pathogens due to they were significantly more powerful than the others, and the hydro distillation method was demonstrated as an effective extract preparation. It was reported that these oils effectively can inhibit of *Escherichia coli* and *Candida albicans* biofilm formation which could be used as adjuvant in the control of oral infections (Salem et al., 2023). The essential oil of *S. oblatum* and S. *abortivum*, which have (E)-caryophyllene type, known to bind hydrophobically to proteins in microorganisms is proven with antimicrobial effect as useful as that of conventional standard drugs against *Bacillus cereus*, *Enterococcus faecalis*, and *Candida albicans* (Đài et al., 2024).

Meliani & Bensoltane (2016) emphasized that *Pseudomonas* biofilms have also been found to exhibit increased abilities in heavy metal uptake and recently have shown potential in bioremediation due to their tradition of tolerant heavy metals toxicity and environmental stress. This ability helps to demonstrate itself the environmental importance of biofilms in creating haven for microbial colonization under adverse conditions. The formation of biofilms by these bacteria depends on nutrients possessing specific media components portraying their adaptability in an array of environments (Ueda & Saneoka, 2015).

According to Ahmad et al. (2022) study on *S. myrtifolium'*s antimicrobial activity against human pathological bacteria and yeasts, its antibacterial and antifungal properties are probably caused by alkaloids, terpenoids (saponins and

triterpenoids), and polyphenols (phenolics, anthraquinones, flavonoids, and tannins) found in its leaves. Superior antibacterial activity against the two bacterial pathogens (*Burkholderia* species and *Serratia marcescens*) was demonstrated by the methanolic extract of *S. polycephalum* (Frediansyah et al., 2023).

A distinct combination of volatile components with broad-spectrum antibacterial action was present in the essential oils (EOs) that were extracted using the leaves of *S. samarangense* and *S. malaccense* by various techniques. In order to prevent mouth infections, they were advertised as bioactive impacts (Salem et al., 2023).

The disc diffusion technique, with minor modifications, was used by Yahayaa et al. (2024) to assess the antibacterial activity of *S. samarangense* leaf extract. Four pathogenic bacterial species (*Klebsiella pneumoniae*, *Salmonella paratyphi* A, *Escherichia coli*, and *Pseudomonas aeruginosa*) were evaluated against the crude extracts of *S. amarangense* (ethanol, hexane, and aqueous), using Ciprofloxacin as a control. The findings suggest that *S. samarangense* leaf crude extracts may function as organic antibacterial agents to combat harmful microorganisms.

Maggini et al. (2024) reported that *S. aromaticum* has shown to be a potent inhibitor of biofilm formation by *Pseudomonas aeruginosa*. Some phytochemicals of *S. aromaticum* showed an excellent antibiofilm activity, such as eugenol. These natural antimicrobials can affect biofilm architecture and decrease bacterial viability; they might have the possibility of becoming an alternative treatment for biofilm-associated infections.

2.8.3. Anthelmintic properties

Anthelmintic activity was associated with volatile phenolics as well as tannins and other polyphenolic components. Hoste et al. (2006) and Athanasiadou et al. (2001) reported that the predominant phytochemicals, eugenol in clove essential oil disrupt membranes of helminth surrogates, leading to rapid-onset paralysis and death as a result of immobility and destruction which are observed microscopically following exposure to EO-rich fractions (Chaieb et al., 2007). The condensed tannins

and other phenolic compounds present in the *Syzygium* extracts are capable of binding to cuticular and gut proteins of worms, inhibiting key digestive and metabolic enzymes, which impairs nutrient uptake, resulting ultimately in longer-term reductions in viability and fecundity that accompany the acute actions of terpenoids.

Lumbricus terrestris are commonly used as practical surrogates for primary anthelmintic assay. They offer clear motility and paralysis endpoints that can be seen with the naked eye and are permissive of measurements in the neuromuscular physiology including agents that interfere with neurotransmission, ion channels and energy metabolism, which are among classic targets of anthelmintics. Typically, studies assess time to paralysis or mortality after exposure of extracts or pure compounds from plants that provide an initial, inexpensive indicator of potential anthelmintic efficacy. While extrapolation to parasitic nematodes or platyhelminths requires caution, earthworm assays remain an accepted early-stage screening tool in pharmacognosy and parasitology research (Taylor et al., 2016).

The first study to report on the anthelmintic properties of aqueous and methanolic extracts of *S. cumini* bark was conducted by Kavitha et al. (2011). They reported that the methanolic extract of *S. cumini* bark has the potential to be effective as an anthelmintic, whereas the aqueous extract has modest anthelmintic activity.

Significant concentration- and time-dependent endpoints in experimental earthworm assays, typically reduced motility, paralysis and mortality can be compared to standard anthelmintics for primary quantitation of potency and safety. It is useful as screening models due to their often-simple mechanisms of action. These predictors need subsequent validation against target parasitic helminths or *in vivo* systems (Taylor et al., 2016).

Azam et al. (2020) emphasized that the common medication albendazole proved less efficient than the methanolic extract of *S. cumini* (Jamun) leaves in paralyzing and killing tape worms, earth worms, and red worms, even at lower dosages. They concluded that the anthelmintic action of *S. cumini* leaves is due to active constituents found in the methanolic extract of those leaves. According to Anggrahini et al. (2021), there are several active substances in clove-leaf ethanol

extract (CLE) that can kill *Ascaridia galli* and alter their ultrastructure. Clove (*S. aromaticum)* leaves may therefore be anthelmintic.

Nawaz et al. (2022) examined the methanolic extract made from the leaves of *S. cumini, Ziziphus jujube,* and *Calotropis procera* for its antitick and anthelmintic properties. Moderate antiparasitic activity was demonstrated by this extract.

2.8.4. Anti-inflammatory properties

S. zeylanicum showed high *in vitro* anti-inflammatory activity by significant inhibition of cyclooxygenase and 5-lipoxygenase enzyme activities and protein denaturation. The ethyl acetate extracts found to be more potent probably due to its phenolic content (Anoop & Bindu, 2015).

The leaves of *S. formosum* are highly enriched with flavonoids and triterpenoids that have been implicated in antibacterial and anti-inflammatory activities (Hoang et al., 2021), important for cosmetic and pharmaceutical applications.

The study conducted by Lee et al. (2023) pointed out that *S. polyanthum* has anti-inflammatory and antioxidant properties. The methanolic stem extract and methanolic root bark extracts of *S. polyanthum* showed good inhibitory effect on prostaglandin E2 production. High phenolic and flavonoid compounds in the species claiming it is a candidate as a therapeutic agent.

Seed and leaf extracts of *S. cumini* were investigated for anti-inflammatory activity in aqueous and methanolic extract through carrageenan-induced paw edema models of rats. Both of the extracts showed highly significant anti-inflammatory activities with more pronounced effects in the aqueous extract (Jain et al., 2010; Kumar et al., 2008; Modi et al., 2010).

The effective dosage of *S. myrtifolium* (Pucuk Merah) ethanol extract as an anti-inflammatory in Wistar strain white rats was determined by Nursyafni et al. (2023). Rats in with 125 mg/kgBW of *S. myrtifolium* had the most anti-inflammatory impact, with a 97% anti-inflammatory potential when compared to diclofenac sodium.

Anti-inflammatory and analgesic effects of methanol extract from bark of *S. mundagam* has been significant in various models, which makes it a potential candidate for modulation of current therapeutic strategies (Chandran et al., 2020). The aqueous root extract of *S. caryophyllatum* has displayed high *in vitro* potency for anti-inflammatory activity relative to diclofenac sodium, along with the potential of other *Syzygium* species (Heendeniya et al., 2018). According to Qamar et al. (2021), fruit extracts from *S. cumini* are a strong source of bioactive substances that attract more research as potential candidates for anti-inflammatory medication development.

S. jambos was used to extract two glycosylated flavonoids, myricetin-3-O-β-D-xylofuranosyl-(1→2)-α-L-rhamnopyranoside and quercetin-3-O-β-D-xylofuranosyl-(1→2)-α-L-rhamnopyranoside. The results indicate this particular plant possesses an anti-inflammatory impact on acute experimental arthritis. The anti-inflammatory and anti-arthritic activities have been evaluated by assessing inflammatory parameters in mouse models. These also exhibit a strong suppression of pro-inflammatory reactions (Figure 2.7), making them a viable therapy option for inflammatory illnesses (Apaza Ticona et al., 2021).

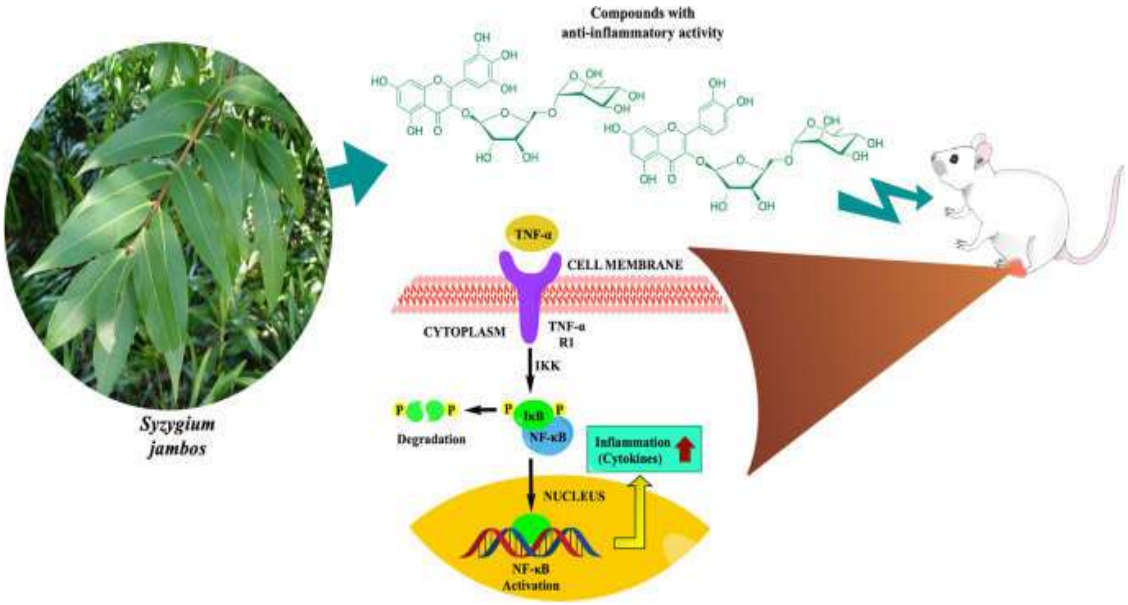


Figure 2.7: Anti-inflammatory property of *Syzygium jambos* (Apaza Ticona et al., 2021)

Zawawi & Sahidin (2022) evaluated the anti-inflammatory activity based on the inhibition of prostaglandin E_2 production in the LPS-induced human whole blood by using the radioimmunoassay technique, estimated the total phenolic and total flavonoid in the methanol extracts and fractions of stem bark and root bark, isolated and clarified the structure of chemical compounds, and assessed the antioxidant activity based on assays using the free radical scavenging DPPH and FRAP. The results indicated that both regions *S. polyanthum* have significant levels of flavonoids and phenolics. Concluded that *S. polyanthum* might be a source of medicinal substances having antioxidant and anti-inflammatory properties.

Many disorders may be influenced by the overproduction of free radicals by activated inflammatory leukocytes, particularly in chronic inflammatory situations. There have been numerous studies indicating that polyphenols may help treat inflammatory disorders (Qamar et al., 2022).

Dharini et al. (2024) found that mouthwash made from the edible portion of *Persea americana* and *S. aromaticum* had excellent anti-inflammatory qualities. The maximum activity was shown at a 50 µL concentration. Consequently, the created mixture may be employed to treat mild inflammatory diseases.

Yadav et al. (2025) employed Enzyme-Linked Immunosorbent Assay (ELISA) assays to quantify cytokines, insulin, and oxidative stress markers modulated by treatment with *Syzygium*. These findings demonstrate the anti-inflammatory and metabolic regulatory effects, further validating its therapeutic potential.

2.8.5. Antidiabetic properties

The secondary metabolite content of *S. polyanthum* has been linked to its application as a medication. As an ingredient in traditional medicine *S. polyanthum* is used to treat diabetes mellitus, stomach issues, skin conditions, hypertension, diarrhea, cholesterol, and hemorrhoids. It has been shown to have antibacterial, antidiabetic, antioxidant, and anti-cholesterol properties (Silalahi, 2017). *Syzygium* species also contribute to neuroprotection by inhibiting AChE to regulate cholinergic transmission, restoring brain ion homeostasis; suppressing pro-inflammatory

mediators, oxidative stress markers, and ROS production; increasing antioxidant enzymes; inhibiting microglial invasion; regulating ß-cell insulin release; and enhancing lipid accumulation, glucose uptake, and adiponectin secretion through the activation of the insulin signaling pathway (Amir Rawa et al., 2022).

Antidiabetic action of different *Syzygium* was evaluated by Shilpa et al. (2023) and suggest that it is has potential Antidiabetic. Methanol extracts of *S. caryophyllatum* and *S. zeylanicum* possess good antidiabetic activity in alloxan and streptozotocin-induced diabetic rats.

Methanol and water extracts of the bark and leaf were tested *in vitro* using the alpha-glucosidase- and alpha-amylase-inhibitory tests to determine their antidiabetic effectiveness. Rats given extract revealed enhanced liver architecture, glomerular regeneration without fat deposition, and revitalized islets and increased beta-cell density in the pancreas. Compared to the leaf extracts, the bark extracts exhibited the highest alpha-glucosidase and alpha-amylase inhibitory action. There is a considerable correlation between antioxidants, phytoconstituents, and antidiabetic effect, as well as protection against damage from free radicals Sushmitha & Krishnakumar (2023).

S. cumini hydro-ethanolic seed extract (SCE) can provide a dose-dependent, significant decrease in fasting blood glucose, serum lipid levels, and HOMA IR (Homeostatic Model Assessment of Insulin Resistance) while simultaneously raising serum insulin and HOMA B (Homeostatic Model Assessment of Beta-cell function) levels. By enhancing pancreatic beta cell function and decreasing insulin resistance, Wistar rats given SCE doses of 100 and 200 mg/kg body weight showed statistically significant anti-diabetic action (Asanaliyar et al., 2021; Hertiani et al., 2023). The antidiabetic properties of *S. cumini* seed kernels and their separated extracted substance (Mycaminose) were demonstrated by Kumar et al. (2008).

Pujiastuti et al. (2023) observed that *Syzygium* bioactives reduce endogenous glucose production through downregulation of gluconeogenic enzymes in hepatocyte models. This mechanism plays an important role in the anti-diabetic effect of *Syzygium* by its capacity to decrease hepatic glucose production

Saiprasanna et al. (2019) demonstrated that the ethanolic bud extract of *S. aromaticum* leaves had an antidiabetic effect in streptozotocin-induced diabetic rats. The strongest hypoglycemic result was achieved at the highest dose. The trunk bark from *S. zeylanicum* has been identified as a good source of polyphenols and exhibits antioxidant and antihyperglycemic activities, the compounds for which gallic acid, and quercetin are the major contributors (Nguyen et al., 2023). These results indicated that *Syzygium* can natural alternative for the treatment of diabetes with fewer side-effects (Santos et al., 2023; Zulcafli et al., 2020).

Rashid et al. (2022) identified two potent phytochemicals from *S. cumini* seeds that act as α-glucosidase inhibitors. Among the bioactive compounds tested, gallic acid exhibited higher inhibitory activity compared to kaempferol and acarbose. Therefore, *S. cumini* seeds can be considered a valuable source for managing hyperglycemia in diabetic patients.

Yadav et al. (2025) observed increased uptake of glucose in *S. cumini* phytochemical-treated cells. The study claimed that the bioactive constituents could increase Glucose Transporter Type 4 (GLUT4) translocation, enhance insulin sensitivity, and be beneficial in glycemic control, thereby validating the anti-diabetic potential of *Syzygium*.

The phytochemicals of *S. cumini* shown effective anti-diabetic activities. According to Pujiastuti et al. (2023), bioactive components sources such as flavonoids (myricetin, quercetin and D-(+)-Catechin), phenolics (ellagic acid, gallic acid, tannin), alkaloids and saponins are found to be more responsible for antidiabetic effects. This class of compounds act as anti-diabetic potential by increasing insulin secretion, insulin sensitivity, glucose absorption in tissues, and also by establishing the inhibition of the carbohydrate digesting enzymes including α-glucosidase. Molecular docking have revealed that a few flavonoids, such as D-(+)-Catechin, are good inhibitors of α-glucosidase, implying selectively and low toxicity as drug candidate. In general, the phytochemicals from *S. cumini* could alleviate hyperglycemia and control diabetic complications, which in turn validate their traditional uses and

indicate the requirement for preclinical and clinical validations to manage diabetes (Figure 2.8).

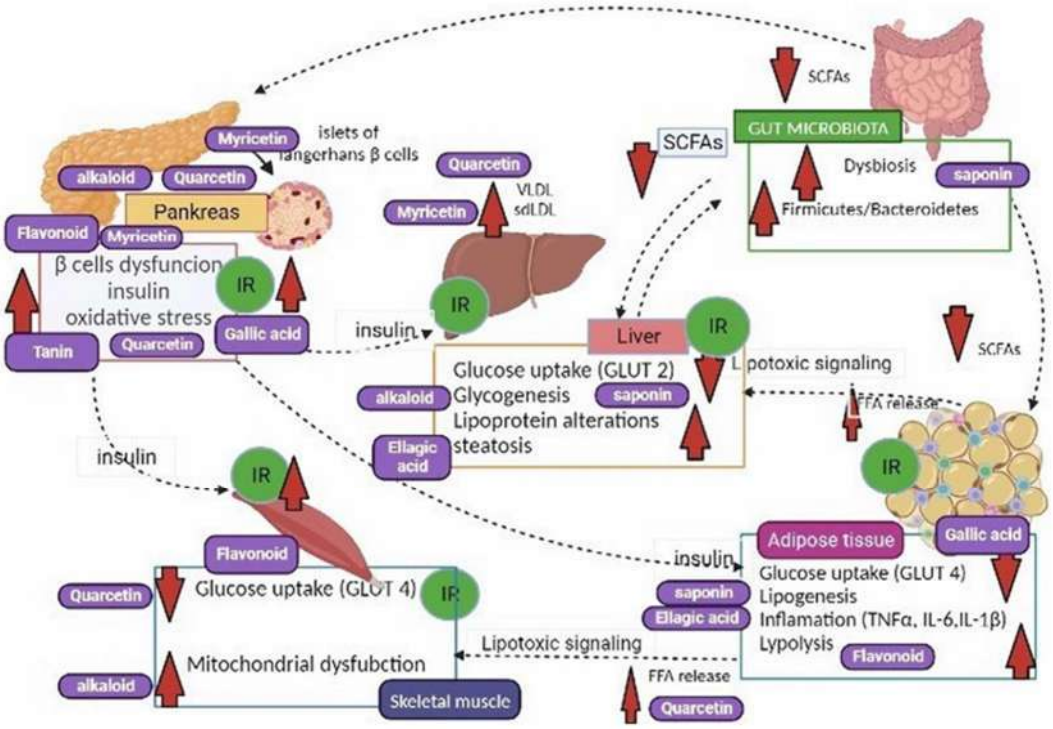


Figure 2.8: Anti-diabetic action of the phytochemical compound of *Syzygium cumini* (Pujiastuti et al., 2023)

2.8.6. Anticancer properties

Research on anticancer properties of the plant genus *Syzygium* have demonstrated positive results from multiple studies, and efficacy across different cancer cell lines. *S. cumini* is more studied for their anticancer effects. Results of cytotoxicity studies against MDA-MB-231 human breast cancer cell line showed that the ethanol and hexane extracts of *S. cumini* seeds are promising with IC_{50} values equal to 142 µg/ml and 195 µg/ml respectively. These extracts also exhibited induction of apoptosis, DNA fragmentation and mitochondrial membrane potential (MMP) suggesting the potential nature of these extracts as novel anticancer agents (Salomi & Parimala, 2023). *S. cumini* fruit extracts exhibited strong antioxidant and anti-leukemia activities, with phenolic compounds like Kaempferol 7-O-methylether and γ-Sitosterol being identified as active components (Afify et al., 2011).

Abdulrahman & Hama (2023) emphasized that *S. cumini* and *S. aromaticum* possess powerful anticancer effects due to the high amounts of phytochemicals such as flavonoids, phenolics, and eugenol. These compounds block cell proliferation and induce apoptosis, as well as inhibit inflammation and metastasis in diverse cancers. Expression of pro-apoptotic markers is upregulated by *Syzygium* extracts, and expression of anti-apoptotic signals is downregulated by *Syzygium* extracts. Their antioxidant effects protect against carcinogen-induced cellular damage. These results emphasise the potential of *Syzygium* as a natural anticancer drug resource and the requirement for more studies and clinical trials specific to this aspect (Figure 2.9).

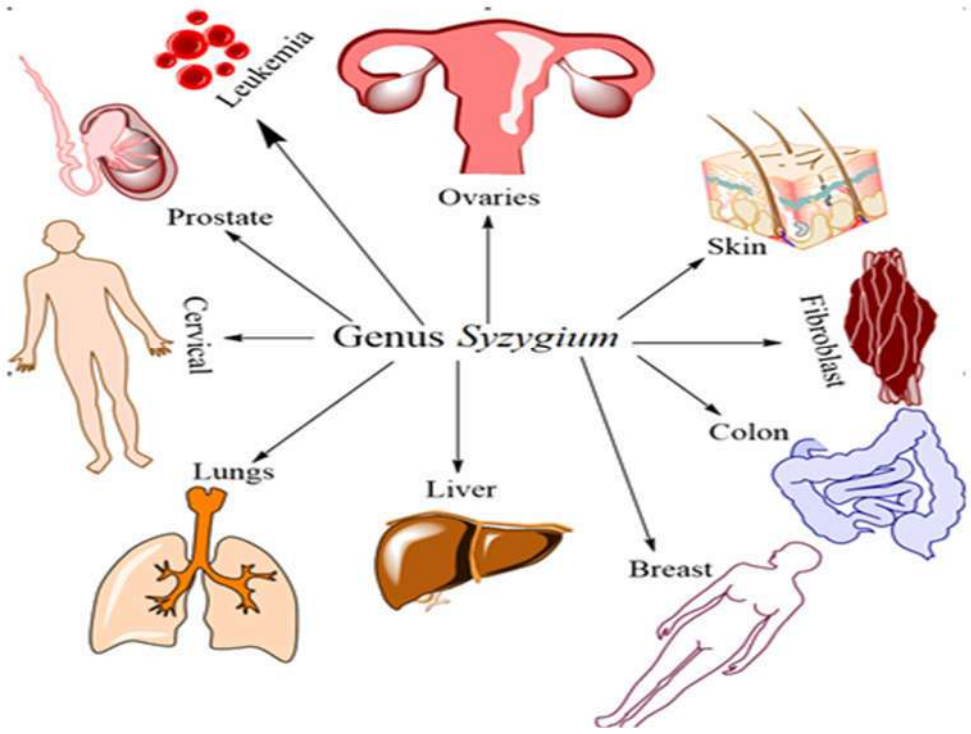


Figure 2.9: Anticancer properties of *Syzygium* on different organs (Abdulrahman & Hama, 2023)

Dwivedi et al., (2011) compared the *in vitro* anticancer properties of the three distinct extracts of Clove (*S. aromaticum*) using five cancer cell lines (MCF-7 (ER + ve) and MDA-MB-231 (ER – ve) breast cancer, HeLa cervical cancer, DU-145 prostate cancer, and TE-13 esophageal cancer cell lines). They found that the extracts displayed various patterns of cell growth inhibition activity, with the oil extract exhibiting the highest cytotoxic activity. According to morphological examination

and DAPI staining, cytotoxicity results from cell disintegration followed by membrane rupture. In contrast to DU-145 cells, which displayed low cell death, TE-13 cells exhibited maximum cell death and apoptotic cell demise after 24 hours when exposed to 300µl/ml of clove oil. The anticancer effects of *S. aromaticum* have been studied in various cell lines, such as breast cancer cells MCF-7 and MDA-MB-231, by Kumar et al. (2014). Cytotoxic effect of Clove essential oil extracts was highest with IC_{50} 36.43 µg/ml and 17.6 µg/ml values respectively in MTT assay (Abdulrahman & Hama, 2023; Chua et al., 2019).

Abdulrahman and Hama (2023) employed Polymerase Chain Reaction (PCR) methods to assess the expression of apoptosis, glucose metabolism, and inflammation of genes following the treatment with *Syzygium*. Modifications in these molecular markers indicated that they were regulated by *Syzygium* phytochemicals, reflecting the effects of those chemicals on cell death, metabolism, and the inflammation response.

Edis et al. (2025) provided evidence that compounds from *Syzygium* species lead to apoptotic cell death of carcinoma cells as revealed by increased early and late apoptotic populations by Fluorescence-Activated Cell Sorting (FACS) analysis. This apoptotic induction is a major cause of the synergistic anticancer activity of *Syzygium*.

Abdulrahman and Hama (2023) reported that *Syzygium* extracts suppress cell proliferation and induce cell cycle arrest at the G0/G1 arrest or G2/M arrest of several cancer cell lines. These cell cycle alterations are essential to *Syzygium* anticancer effects.

Anti-cancer activity of *S. cumini* and *S. jambolanum* against MCF-7 cells showed significant cytotoxic activity; the seed extract of *S. cumini* showed an IC_{50} value 45 µg/ml (Suhail et al., 2025). The study conducted by Madhuri & Reddy (2022) on *S. alternifolium* reported that the methanolic extracts of the bark displayed cytotoxic activity against HepG2 liver cancer cells in a selective manner (IC_{50} = 185.585 µg/ml), but not against normal cells. Certain phytoconstituents were predicted to be inhibitors of several cancer proteins which conferred a mechanism based on inhibition of topoisomerase-II and CDK-2 proteins through molecular

docking studies. Bark of *S. alternifolium* showed substantial anticancer activity, with stigmasterol and squalene compounds showing high binding affinities with Bcl-2 and VEGFR-2 cancer-related proteins hence supporting its use in therapeutic purposes (Madhuri et al., 2024).

According to Pujiastuti et al. (2023), XTT (2,3-Bis-(2-Methoxy-4-Nitro-5-Sulfophenyl)-2H-Tetrazolium-5-Carboxanilide) and MTT (3-(4,5-dimethylthiazol-2-yl)-2,5-diphenyltetrazolium bromide) assay, performed with *Syzygium* extracts and nanoparticles, show that they block cell proliferation dose dependently in cancer cell and diabetic cell models, which could be indicative of their therapeutic effect.

2.9. Green synthesis of silver nanoparticles in *Syzygium*

Because of its unique properties, the ability to create silver nanoparticles (AgNPs) using a number of *Syzygium* species has been thoroughly studied and has tremendous potential for a range of applications. Among them, due to its environmental friendliness and efficiency, green synthesis approach is highlighted mainly using plant extracts as reducing agent. *S. samarangense* pollen flower bud-derived 20–35 nm sized AgNPs. It was synthesized at room temperature with the optimized conditions of 5 mM concentration of AgNO3 and at a reaction temperature of 70 °C and these NPs were reported to exhibit higher yield and stability as confirmed by spectroscopy and X-ray diffraction technique (Doan et al., 2023).

The silver nanoparticles prepared from *S. aromaticum* possess significant antibacterial and photocatalytic activities, successful decolourization of malachite green dye, and bacteriostatic function, making them one of the best choices for environmental and bio-medical applications (Sikdar & Sikdar, 2023).

Bhavi et al. (2024) reported that *S. cumini* leaf extract has been employed for the green synthesis of silver nanoparticles (AgNPs), which exhibited potent antidiabetic and wound-healing activities, demonstrating highly effective glucose uptake and α-amylase inhibition along with good biocompatibility. Bhavi et al. (2024) further utilized *S. caryophyllatum* for the synthesis of AgNPs, which showed enhanced antidiabetic, antioxidant, and antibacterial properties compared to the crude

plant extract. The integration of these nanoparticles with antibiotics, as seen with clarithromycin, further enhances their antimicrobial efficacy, suggesting a promising avenue for combating resistant microbial strains (Edis et al., 2025).

Maciel et al. (2019) provides an ecologically safe substitute for the hazardous chemical reducing agents in the green production of silver nanoparticles (AgNPs) by employing essential oils of clove (*S. aromaticum)*. According to UV-Vis spectrophotometry, the greatest results for the synthesis of AgNPs were obtained when clove essential oil was used, with eugenol (80%) being the main constituent. Their method produced stable nanoparticles sized between 27 and 94 nm, which exhibited potent antibacterial activity against *Escherichia coli* and *Staphylococcus aureus*, with minimum inhibitory concentrations ranging from 60 to 100 µL/mL. Similarly, Yugandhar and Savithramma (2015) synthesized AgNPs using the leaf extract of *S. alternifolium*, where phenols and proteins acted as capping and stabilizing agents. The resulting nanoparticles, with sizes ranging from 7 to 44 nm, displayed high toxicity toward various bacterial and fungal strains, indicating strong antimicrobial potential.

Chakravarty et al. (2022) prepared AgNPs from *S. cumini* fruit extracts that exhibited antibacterial, antioxidant, and anti-inflammatory activities, supporting their use as eco-friendly therapeutic agents. In addition, *S. cumini-mediated* synthesis has been optimized for catalytic applications, including the reduction of 4-nitrophenol, demonstrating the nanoparticles' versatility in medical and industrial contexts (Waghmode et al., 2021). Kumar et al. (2015) further reported the use of *S. cumini* flowering extract to synthesize AgNPs with significant antibacterial and moderate antifungal activity.

The characterization data of *S. cumini* reported by Maciel et al. (2019), Yugandhar and Savithramma (2015), Chakravarty et al. (2022), Kumar et al. (2015), and Bhavi et al. (2024) using UV-VIS spectroscopy, FTIR, XRD, SEM, and TEM confirmed the crystalline nature and effective size distribution of the nanoparticles, which are critical for stability and bioactivity. Collectively, these studies establish green synthesis of AgNPs using *Syzygium* species as a sustainable and versatile

strategy with wide-ranging applications in medicine, catalysis, and environmental remediation.

S. cumini leaf extract was used by Yadav et al. (2025) to create Zinc oxide nanoparticles (ZnO NPs). In a 1.0 M H_2SO_4 solution, ZnO NPs demonstrated a remarkable 90% inhibitory efficacy at 100 ppm concentration, along with paramagnetic characteristics and good anti-corrosive qualities.

Edis et al. (2025) reported significant progress in method development for formulation studies with AgNPs, green-synthesized with an extract of *S. aromaticum* (clove). They stated that green synthesis of silver nanoparticles using clove extract has been accomplished through an environmentally benign method, and clove nanoparticles not only have therapeutic potential of its own, but also is due to the co-existence of the antioxidant eugenol and the bioactive phytochemicals. In their research, AgNPs were synthesized with the presence and absence of the antibiotic clarithromycin as a comparison, which demonstrates that AgNPs prepared with solely *Syzygium* extract have smaller particles and enhanced antimicrobial activity. This interaction between phytochemicals and nanoparticles enhances stability, bioavailability, and biological potential of metal nanoparticles. These functionalized nanoparticles possess specific release behaviour and a higher cellular uptake, thus, they are conducive for successful therapeutic applications. In general, formulation issues related to *Syzygium*-based AgNPs are indeed a promising area in the field of nanomedicine that unites the medicinal properties of plants and metallic characteristics to serve as multi-action drug candidates (Edis et al., 2025)

Edis et al. (2025) also reported the potential for both using and not using the antibiotic clarithromycin to mediate silver nanoparticle (AgNP) production using clove (*S. aromaticum*) extract. Synthesis of nanoparticles from clove extract is a potential technique for integrating metals and medicines at the nanoscale (Figure 2.10).

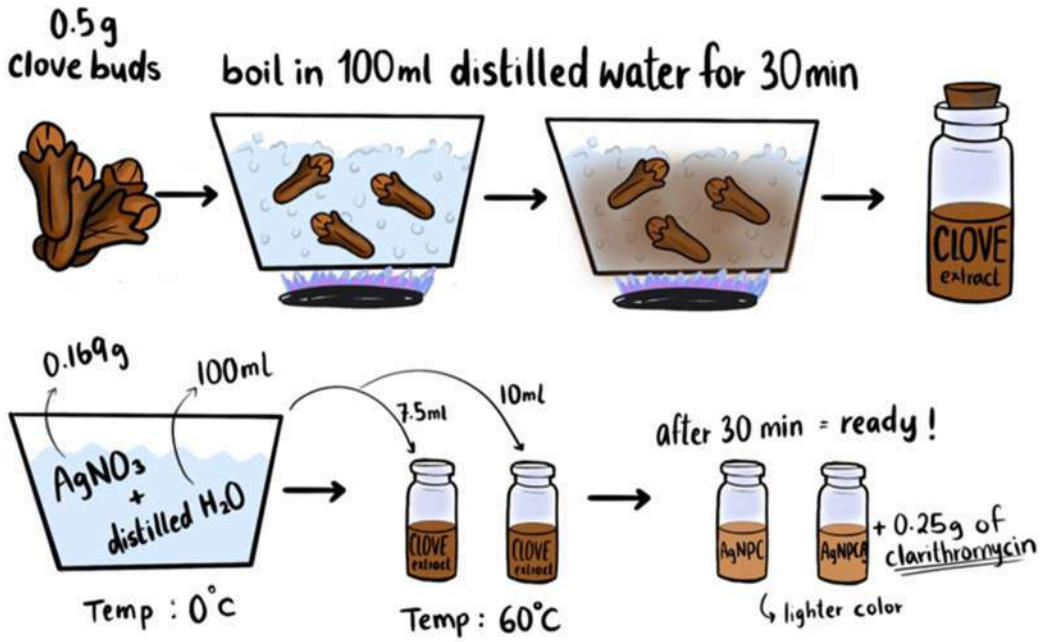


Figure 2.10: Silver nanoparticle biogenesis based on clove extract (Edis et al., 2025)

2.10. Isolation of compounds in *Syzygium*

Sara et al. (2018) reported that the isolation process typically involves methanol extraction of dried flower buds, followed by fractionation and chromatographic techniques to yield bioactive compounds such as asiatic acid and arjunolic acid. These compounds were subsequently identified using advanced spectroscopic methods, including nuclear magnetic resonance (NMR) and mass spectrometry (MS). Similarly, Kristanti et al. (2022) explored the phytochemistry of the stem bark of *S. aqueum*, and the chemicals that were recovered were identified to be arjunolic acid and alphitolic acid. And results showed that both substances inhibited the growth of cancer cell lines.

Gopinath et al. (2020) carried out research to separate the main phytoconstituents from the fruits of *S. densiflorum* and to compute the compounds' chemical and biological reactivity. HPLC was used to purify two distinct chemicals that were separated from the ethanolic extract of S. densiflorum fruits. The compounds' inhibition of β-glucosidase, β-galactosidase, α-glucosidase, and β-amylase had been predicted based on their structure-activity relationship. These results showed have *S. densiflorum* exhibit potential in diabetic management. Haque

et al. (2015) demonstrated that *S. jambos* produces secondary metabolites such as pentacyclic triterpenes and sitosterol, which possess cytotoxic properties as evidenced by brine shrimp lethality assays. Kaisar et al. (2012) and Naz et al. (2023) found that *S. cumini* contains compounds including 7-hydroxycalamenene and oleanolic acid, which show significant biological activities such as antibacterial and antioxidant effects.

2.11. Molecular docking and dynamics

Molecular docking has become a vital tool in recent years, providing rational insight into the binding interactions of phytochemicals with various biological targets, which validates their pharmacological activities. Pujiastuti et al. (2023) mentioned the implication of molecular docking in elucidating the anti-diabetic activities of *S. cumini* compounds, particularly flavonoids such as D-(+)-Catechin, myricetin, and quercetin. These in silico investigations revealed high binding affinities of these phytochemicals with enzymes (α-glucosidase and α-amylase) that are very important for carbohydrate metabolism. These findings support the known effects of the compounds at the molecular level, inhibiting glucose absorption and insulin regulation.

Madhuri and Reddy (2022) examined the anticancer effects of a methanolic extract of *S. alternifolium* bark on a human hepatocyte carcinoma (HepG2) cell line in comparison to the conventional medication doxorubicin. According to cytotoxicity studies, phytoconstituents from *S. alternifolium* can specifically target cancer cells (IC_{50} = 185.585 µg/ml) with negligible to no harmful effects on healthy cells. Molecular docking and dymanic tests were conducted against the human Topoisomerase-2 and CDK-2 proteins (Protein Data Bank-ID: 1ZXM and 1DI8, respectively) using Mcule docking software. Based on *in silico* investigations, seven of the bioactives that were identified are regarded as safe inhibitors. This shows a notable amount of its anticancer therapeutic drug potentials using *in vitro* and *in silico* methods, paving the way for a deeper comprehension of how combining molecular docking and *in vitro* investigations might enhance the discovery of cancer medications. Similarly, Madhuri et al. (2024) found that compounds such as

stigmasterol and squalene from the bark exhibited strong binding affinities toward Bcl-2 and VEGFR-2 proteins, further supporting their anticancer activity.

In diabetes research, *S. aromaticum* demonstrated the ability to inhibit alpha-amylase and alpha-glucosidase enzymes, with stigmasterol showing notable binding free energy, indicating its promise as an antidiabetic agent (Manurung et al., 2024). *S. cumini* phenolic compounds like rutin and catechin showed strong binding to multiple diabetes-related targets, highlighting their multifunctional antidiabetic drug potential (Grewal et al., 2018).

2.12. Network pharmacology in computational drug discovery and target interaction studies in *Syzygium*

According to Cichonska et al. (2015), these network pharmacology approaches may identify entirely unexpected and novel investigational probes for drug development, even though they are currently primarily utilized to supplement the experimentally mapped compound–target networks for drug repurposing applications, such as expanding the target space of already approved drugs. Tang and Aittokallio (2014) demonstrate how, in the context of system-level network approaches to polypharmacology designs in anticancer drug development, network-centric modeling may offer systematic ways for comprehending and even predicting the phenotypic responses to multi-target therapy.

Nair (2018) described network pharmacology as a transformative approach in computational drug discovery that integrates systems biology and computational biology to study drug interactions with multiple targets. This marks a shift from the traditional "one drug, one target" model to a holistic "multi-target, multi-component" strategy. Yong-xiang (2012) emphasizes the potential of network pharmacology in addressing complex diseases such as cancer by capturing the intricate interactions of drugs within biological systems.

Zhang and Zhao (2021) discussed how network pharmacology relies on constructing drug-target interaction networks derived from public databases, high-throughput screening, and omics studies. These data sources provide insights into

systemic drug mechanisms and biological pathways involved in disease progression. Iorio et al. (2013) and Zhi-yon (2014) framed network pharmacology as a paradigm shift in drug discovery, offering a comprehensive systems-level framework to understand drug actions and interactions, thereby accelerating the development of innovative therapeutic strategies. Molecular and drug networks are effective integrated computational and experimental methods that, when completely included into the academic and industrial drug discovery pipeline, are expected to accelerate and enhance the drug discovery process.

According to Noor et al. (2023), the integration of network pharmacology with sophisticated machine learning algorithms may represent a promising advancement in multi-target drug development. Network pharmacology's prediction capabilities, however, require improvement. With the recent accomplishments of machine/deep learning (ML/DL) technologies in drug discovery, network pharmacology's shortcomings may be resolved.

Amanah et al. (2023) identified active compounds in *Syzygium myrtifolium* which inhibit leukotriene A4 hydrolase, a protein with anticancer properties. And demonstrate that the four active compounds found in *S. myrtifolium* leaves (bis (2-ethylhexyl) hexanedioate, 3-octadecyne, 1-octadecene, and (2E,6E)-farnesol) have a lower docking score than bestatin. As a result, these compounds may be able to block leukotriene A4 hydrolase receptors and potentially serve as colorectal anticancer drugs. *S. cumini* compounds such as Beta-Glucogallin and Dihydro Dehydro Coniferyl alcohol showed stable interactions with AMR *Staphylococcus aureus* targets in molecular dynamics simulations (Shravani et al., 2024).

Pemmereddy et al. (2025) applied network pharmacology to the traditional medicinal plant *Syzygium caryophyllatum*, elucidating its potential mechanisms against colon cancer. Their study identified key compounds and targets, including Estrogen Receptor Alpha and Epidermal Growth Factor Receptor, using computational tools such as Cytoscape and the Schrödinger suite. They demonstrated significant *in vitro* cytotoxic activity, exemplifying the hallmark multi-target, multi-pathway approach characteristic of network pharmacology.

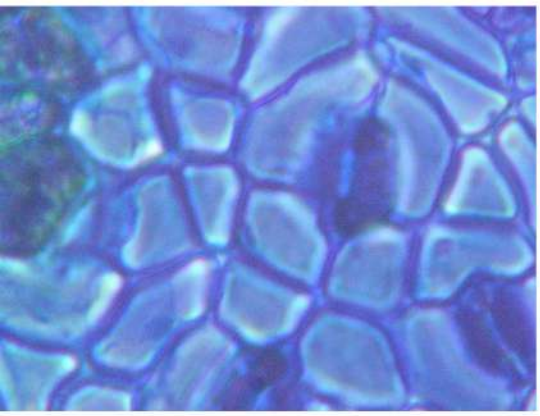
Altogether these studies showed that *Syzygium* has various medicinal properties because of several bioactive molecules, thereby suggesting their potential as novel candidates for combating infectious diseases. The various bioactivities of the genus *Syzygium* emphasize its potential as a treasure-trove of natural therapeutic agents for different health conditions (Lakshmi & Manasa, 2021; Pemmereddy et al., 2022). The key research gaps and future directions in *Syzygium* studies are listed in Table 2.6.

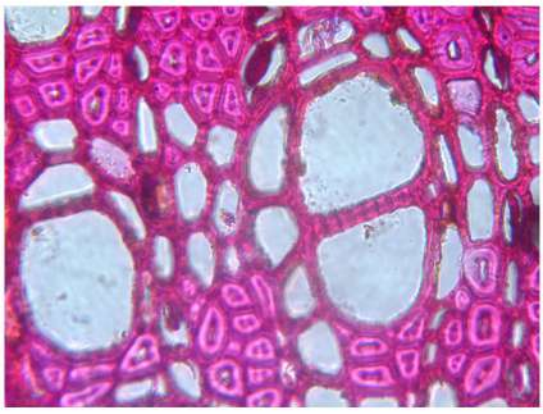
Table 2.6: Key research gaps and future directions in *Syzygium* studies

Number	Research gap / future direction	Details	Citation
1	Comparative metabolite profiling	Lack of systematic metabolomic comparisons across multiple *Syzygium* species linking phytochemical diversity to bioactivity	Youssef, 2025
2	Limited *in vivo* and clinical validation	Few *in vivo* studies and almost no clinical trials to confirm the safety and efficacy of extracts or compounds	Rawa, 2022
3	Isolation and structural characterization of active compounds	Need for isolation and characterization of pure bioactives beyond crude extracts using advanced analytical methods	Rawa, 2022
4	Understudied regional and endemic species	Research bias toward economically important species; endemics from Australia, the Pacific Islands, and Africa are understudied	Rawa, 2022
5	Integration of multi-omics approaches	Rare combination of genomics, transcriptomics, metabolomics, and proteomics for linking genotype to bioactivity	Youssef, 2025; Rawa, 2022
6	Bioavailability and pharmacokinetic data (ADME) scarcity	Limited studies on the absorption, distribution, metabolism, and excretion profiles of major phytochemicals	Abdulrahman et al., 2023
7	Molecular taxonomy inconsistencies	Incongruences between nuclear vs. chloroplast phylogenies; need for stronger molecular markers	Low et al., 2022
8	Mechanistic studies insufficient	Molecular pathways behind medicinal effects like anti-inflammatory or antidiabetic remain underexplored	Rawa, 2022
9	Environmental influence on phytochemistry	Climate, soil, and cultivation conditions impacting phytochemical yield are rarely studied systematically	Salem et al., 2023
10	Standardization of extraction and quality control	Need for consistent extraction, formulation, and quality protocols for herbal products	Jimoh et al., 2017

3

MORPHO-ANATOMICAL CHARACTERIZATIONS







CHAPTER 3

MORPHO-ANATOMICAL CHARACTERIZATION

3.1. Introduction

The morpho-anatomical study of a plant species examines its external and internal features, particularly structure, orientation, growth, and development. Such characters assist in distinguishing closely related species, provide information on evolutionary relationships between species, and aid in the taxonomic identification of economically, therapeutically, or pharmacologically significant taxa (Maheshwari & Joshi, 2018).

This work presents a study on the morpho-anatomical characterization of three species, *S. laetum*, *S. occidentale,* and *S. palghatense,* emphasizing their Western Ghats endemicity. The research not only adds to the existing botanical knowledge about these species but also provides practical conservation strategies for the sustainable utilization of these essential plant resources, highlighting the direct relevance of this study to our work.

Syzygium, one of the largest genera in the Myrtaceae family, comprises a wide range of tropical tree and shrub species representing diverse ecological groups. *Syzygium* includes more than 1,200 species in many tropical and subtropical regions, with a remarkable presence in Southeast Asia (Govaerts et al., 2008; Parnell et al., 2007). These species support the ecological status of forest ecosystems by providing food and shelter for a wide range of other organisms, including birds, bats, and insects, amongst many others (Calle-Rendón et al., 2016).

Syzygium species are usually considered evergreen trees or shrubs with simple paired leaves with a glossy appearance, often strongly scented of essential oils (Parnell et al., 2007). The taxonomic categorization of *Syzygium*, along with other genera of Myrtaceae, remains a significant challenge for plant taxonomists today due to the high diversity and morphological similarity among species (Abdulrahman et al., 2018).

Many authors have extensively discussed the phylogenetic basis and taxonomic problems of this group, highlighting the need for detailed morpho-anatomical studies (Cardoso et al., 2009; Craven, 2001; Hussin et al., 1992; Schmid, 1972; Soh & Parnell, 2011; Wilson et al., 2001).

The unique leaf shape, size, and venation patterns are vital morphological features that distinguish *Syzygium* species. The lanceolate to ovate leaves, smooth edges, and pronounced midrib are characteristic of these species, adding to the fascination of studying them. The ovate-oblong leaves of *S. cumini*, with a well-marked midrib and reticulate venation, are not unique to this species but are also found in several others within the same genus. This contrasts with all other families in the order, as Chattaway (1959) recognized that the secondary venation of Myrtaceae is closely spaced and parallel. The smooth bark of *Syzygium*, often easily peeled in thin strips, is a common feature, particularly in species such as *S. cumini* (Niedenzu, 1893). Most *Syzygium* flowers are actinomorphic and hermaphroditic, forming small clusters at the tips of branches or above leaf bases to create terminal or axillary inflorescences.

The flowers of *Syzygium* species are mostly white or pale pink, with many long, conspicuous, and delicate stamens, a characteristic of this species. Apart from colour, another notable feature is a well-developed hypanthium, most often fused to the ovary. These morphological traits not only support pollination but also help protect reproductive organs from herbivores and environmental stress. The morphological variation among *Syzygium* species enables them to occupy various ecological niches, from wet tropical forests to dry deciduous forests. The fruit of *Syzygium* is typically a berry containing multiple seeds in an edible pulp (compound fruit or drupe). Most fruits are handled by specialized dispersal agents (birds and mammals), so *Syzygium* had to evolve alternate strategies to survive. Fruits have been modified for dispersal by frugivores, and the overall composition is that of an edible juicy pericarp that surrounds a seed coat to protect it. This adaptation reinforces seed dispersal and their ability to endure poor conditions, facilitating resilience and a broad reach (Govaerts et al., 2008; Lughadha & Proença, 1996; Raju et al., 2014).

There was a significant advancement in the field of micromorphology study when macromorphological characteristics could not assist in classifying Myrtaceae into generic or suprageneric groupings. A typical example is the taxonomic misunderstanding between *Eugenia* in the Ancient World and *Syzygium in* the Modern World. Floral anatomy studies showed that the ovule vascular system of supply, transeptal in *Eugenia* and axile in *Syzygium*, is an excellent way to tell them apart. Many scientists can distinguish between the two species by using data on the anatomy of wood and flowers (Schmid, 1972; Soh & Parnell, 2011).

Anatomical studies take a closer look at the tiny building blocks of plant tissues. This includes the epidermis, mesophyll, vascular bundles, and secondary xylem. *Syzygium* species have some unique traits. One neat feature is the glandular trichomes spotted on the leaf surface. These structures help to protect against hungry herbivores and sneaky pathogens (Cardoso et al., 2009). The secondary xylem shows diffuse-porous wood with vessels of different sizes. This variation is essential for transporting water and supporting the plant (Schmid, 1972). The xylem rays found in *Syzygium* species usually have homocellular structures. They mainly consist of procumbent cells. These rays are vital in moving water and nutrients from one part of the plant to another (Chattaway, 1959; Keating, 1984).

These anatomical adaptations of *Syzygium* allow variability in a vast range of tropical habitats. The leaves of *Syzygium* species are characteristically hypostomatic and have highly developed cuticles and a multiseriate epidermis without stomatal depressions or crypts, features that may partially explain the reduced water loss by transpiration found in this study (Solereder, 1908). This species has the characteristic of glandular spots, or pellucid glands on the leaves, which shine under light. The oil glands present in the leaves are more advantageous in attracting pollinators and deterring herbivores from eating plants (Metcalfe & Chalk, 1950). In *Syzygium*, the vascular organization is well-ordered with a distinct pattern of xylem and phloem elements. Large, well-spaced xylem vessels are common and valuable for efficient water transport; they are essential for species that live in dry or seasonally arid

environments (Dahlgren & Thorne, 1984; Evert, 2006). The phloem tissue is usually well-developed, and nutrients can quickly move throughout the plant.

The morphological and anatomical characteristics of *Syzygium* are essential for their survival, as well as their ecological and economic importance. *Syzygium* species provide essential ecosystem services, which may include habitat support and food resources and being involved in nutrient cycling. Further, a more significant part of the species also holds levels of primordial economic importance, such as fruits of java plum (*S. cumini*) are farmed for their nutritional and pharmaceutical properties known to man since ancient times, underscoring the long-standing tradition of studying these plants (Abdulrahman et al., 2018; Soh & Parnell, 2011).

The morphological and anatomical studies are primarily for taxonomic distinction (Kantachot et al., 2007; Pacheco-Silva & Donato, 2016). The safety and quality of modern medicine require authentication and standardization of modern drugs, which can be possible only by documenting the complete macroscopic and microscopic study of medicinal plants (Abdulrahman et al., 2018). Micromorphological and anatomical characteristics are proved to be taxonomic significance in circumscribing and distinguishing the *Syzygium* family. Several other authors also discussed this review in detail at the species and general level based on an evolutionary basis and for taxonomic classification challenges (Abdulrahman et al., 2018). However, only a few species have been studied thus far. Here, we provide an extensive morpho-anatomical representation of the three *Syzygium* endemics studied in the current study. So, the study will supply details of interesting taxonomic data additions that are valuable in developing natural products.

This investigation pertains to the meticulous examination of the morphological characteristics of three endemic plants chosen for the investigation. The data collected from the research will be sufficient to eliminate any ambiguity and distinguish these species. Appreciating the morpho-anatomical characteristics has profound implications for the taxonomic classification and ecological conservation strategies of *Syzygium*. Those characteristics are fundamental to the genus and demonstrate its importance in conserving biodiversity and functioning in tropical

ecosystems. The micromorphological examination increases the clarity of macroscopic studies, thereby facilitating the accurate identification, classification, and determination of the pharmacological relevance of these Western Ghats. In summary, the study makes a complex but exciting list of the features on which this thesis attempts to provide insights that support their biological reality and ecological significance while contributing to taxonomic alignment within *Syzygium*.

❖ **Objectives**

- Plant collection and verification.
- Herbarium preparation and deposition.
- Drying and powdering of the collected plant samples for further study.
- Morphological and anatomical studies of the selected three species.
- Histochemical studies.

3.2. Materials and methods

3.2.1. Plant collection and authentication

Syzygium laetum (Buch.-Ham.) Gandhi and *Syzygium palghatense* Gamble were gathered from the Nelliyampathy hills in the Nemmara forest division, Palakkad, Kerala, India. *Syzygium occidentale* (Bourd.) D.N. Gandhi was obtained from the Athirappilly-Vazhachal section of the Vazhachal forest division, Thrissur, Kerala, India.

Dr. P. Sujanapal, Principal Scientist in the Department of Silviculture, Sustainable Forest Management Division, Kerala Forest Research Institute, Peechi, Thrissur, and Dr. A.K. Pradeep (Retired), Assistant Professor in the Department of Botany, University of Calicut, recognized and verified the plant materials. The plant names were verified using The Plant List (TPL: http://www.theplantlist.org/) and the International Plant Name Index (IPNI: http://www.ipni.org/).

3.2.2. Preparation of voucher herbarium specimen

The voucher specimens of *S. laetum*, *S. occidentale,* and *S. palghatense* were prepared using the standard herbarium procedure. The completed herbarium was submitted to the Calicut University Herbarium (CALI), Department of Botany, University of Calicut. The accession numbers 7054,7055, and 7056, respectively, were allocated to the specimens in the catalogue.

Table 3.1 tabulates the details of the plants collected for the entire investigation. Figures 3.1 to 3.3 describe the location map of the plant collection regions. Plates 3.1 and 3.2 represent the habit and voucher specimens of the selected *Syzygium* species of the present investigation.

3.2.3. Morpho-anatomical studies

The morphological features of *S. laetum*, *S. occidentale,* and *S. palghatense* were observed and meticulously documented using the naked eye or a magnifying lens. The stomatal morphology was studied using epidermal peeling and leaf maceration techniques. The paraffin-fixed leaf, stem, flower, and bark samples were

Table 3.1: Plant data record

Plant name	Latitude	Longitude	Altitude (m)	Habit	Habitat	Status	Reproductive phenology	Distribution	Localities	Local names	Voucher specimen number
***Syzygium laetum* (Buch.-Ham.) Gandhi**	10°32'14 N	76°43'01 E	1290	Tree	Evergreen forests	NE**	December-July	Endemic to Southern Western Ghats	Kasargode Kannur Wayand Kozhikkode Malappuram Palakkad Thrissur Ernakulam Idukki Pathanamthitta Kollam Trivandrum	Kollinjaval Kattuchamba Manjachamba	CALI 7055
***Syzygium occidentale* (Bourd.) D.N. Gandhi**	10°18'09 N	76°36'29 E	212	Shrub	Evergreen forests along banks of rivers	EN***	March-April	Endemic to Southern Western Ghats	Palakkad Thrissur Idukki Pathanamthitta Kollam Trivandrum	Attuchamba Karinjara	CALI 7056
***Syzygium palghatense* Gamble**	10°32'14 N	76°43'01 E	1290	Tree	Evergreen forests	CR*	Tree	Evergreen forests	Palakkad	Sevappunjaval	CALI 7054

* Critically Endangered; ** Not Evaluated; *** Endangered

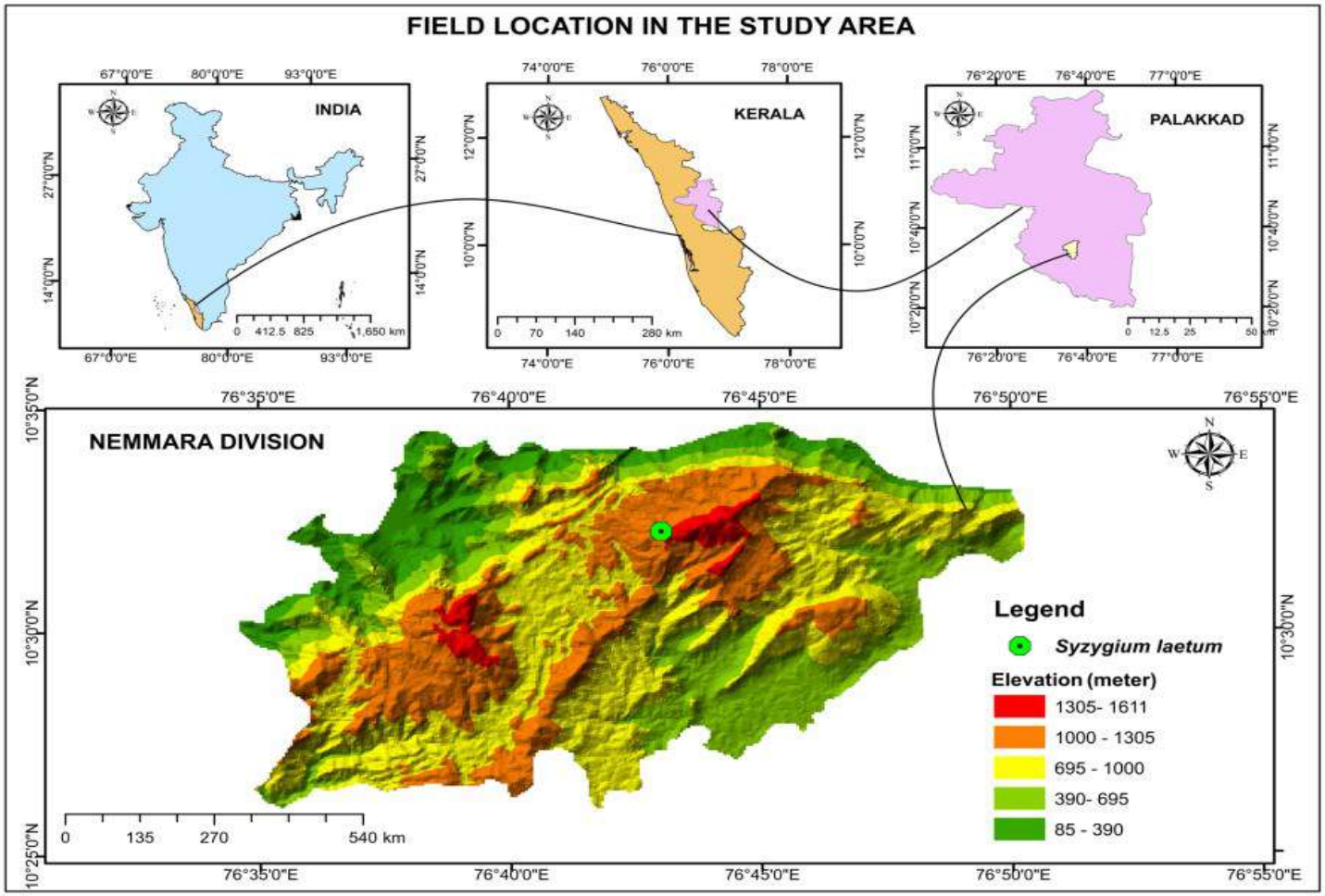


Figure 3.1: Digital Elevation Model (DEM) of the study area for *Syzygium laetum* in the Western Ghats

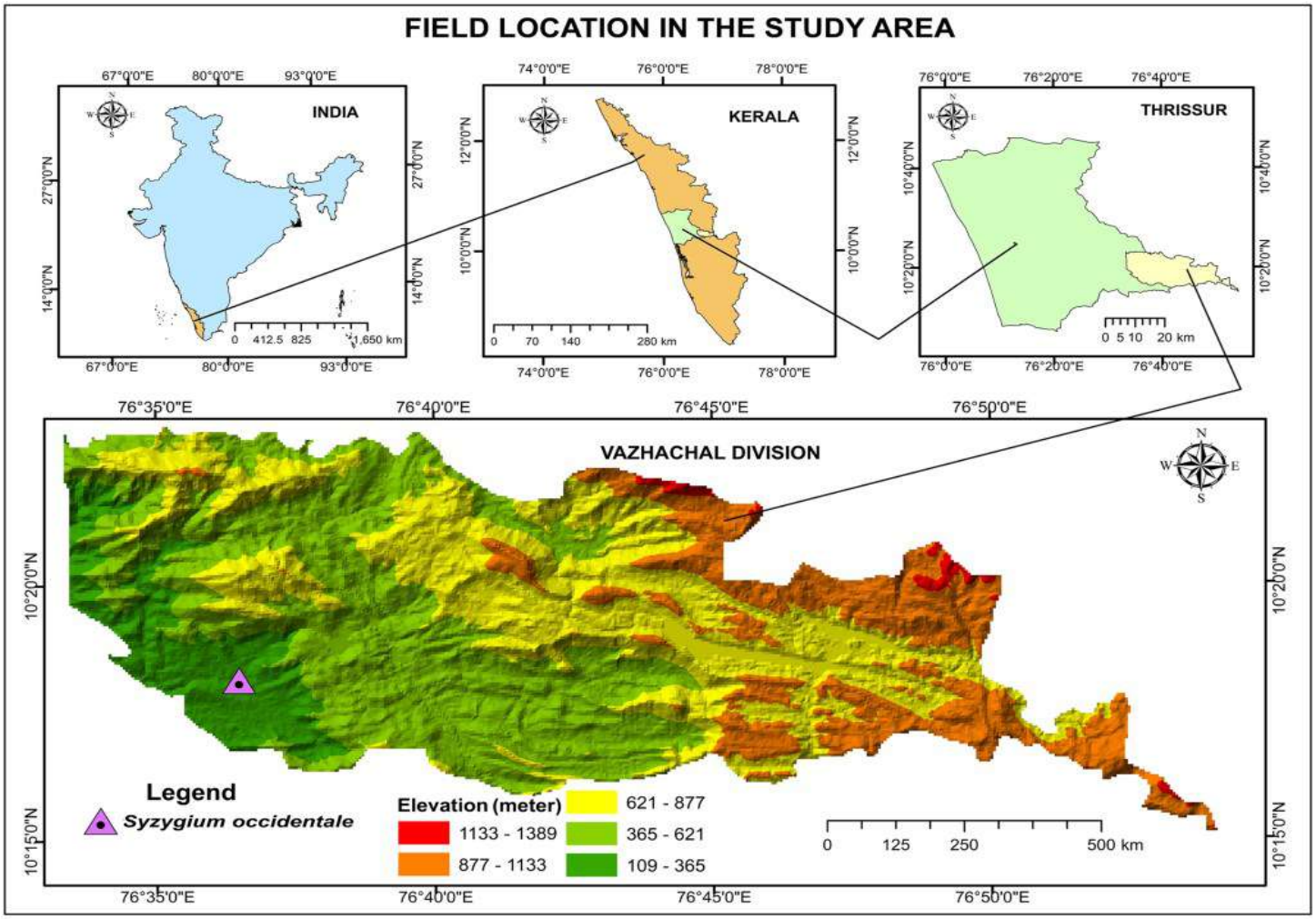


Figure 3.2: Digital Elevation Model (DEM) of the study area for *Syzygium occidentale* in the Western Ghats

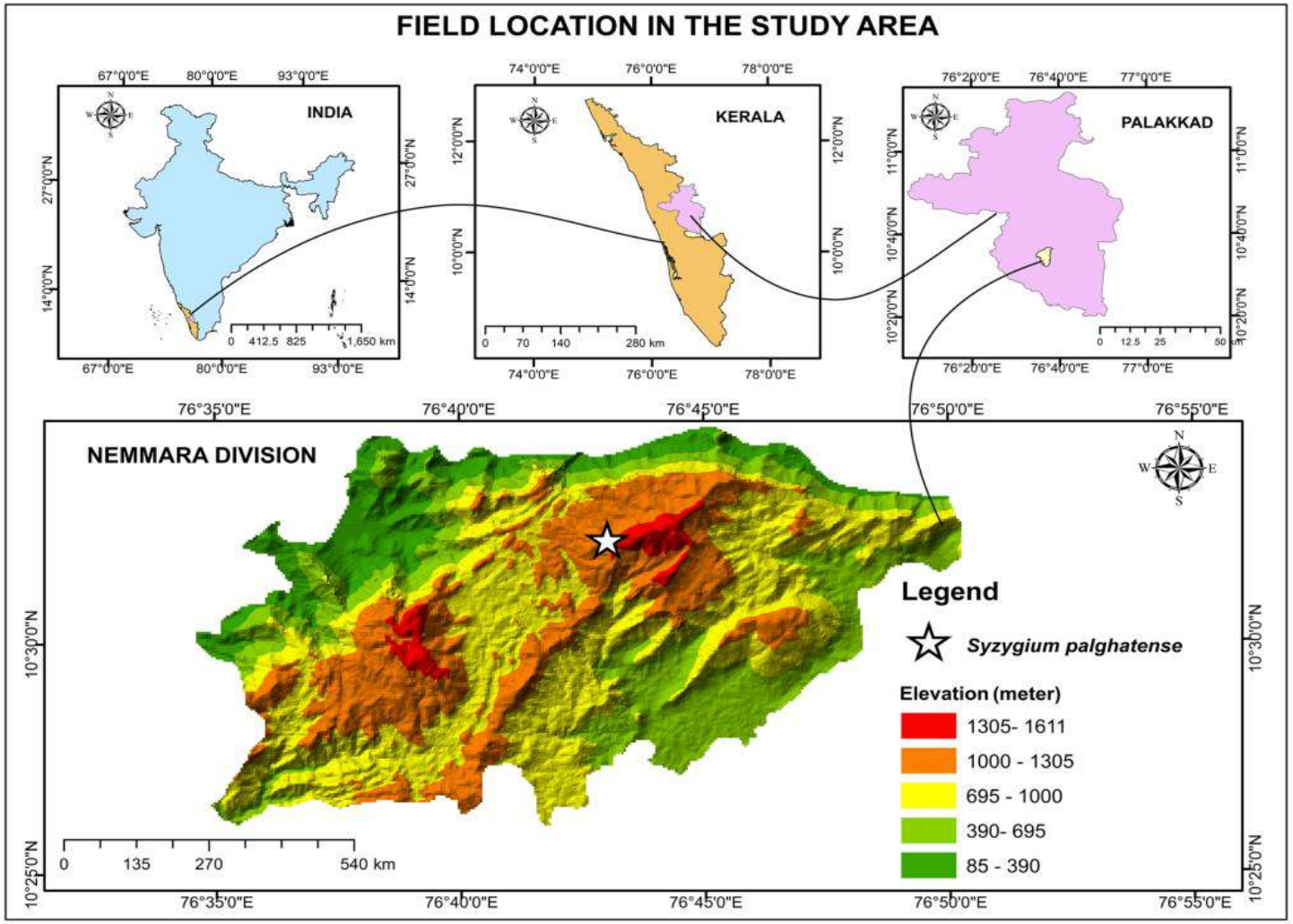


Figure 3.3: Digital Elevation Model (DEM) of the study area for *Syzygium palghatense* in the Western Ghats







Plate 3.1: Habit of *Syzygium* species (a) *Syzygium laetum* (b) *Syzygium occidentale* (c) *Syzygium Palghatense*

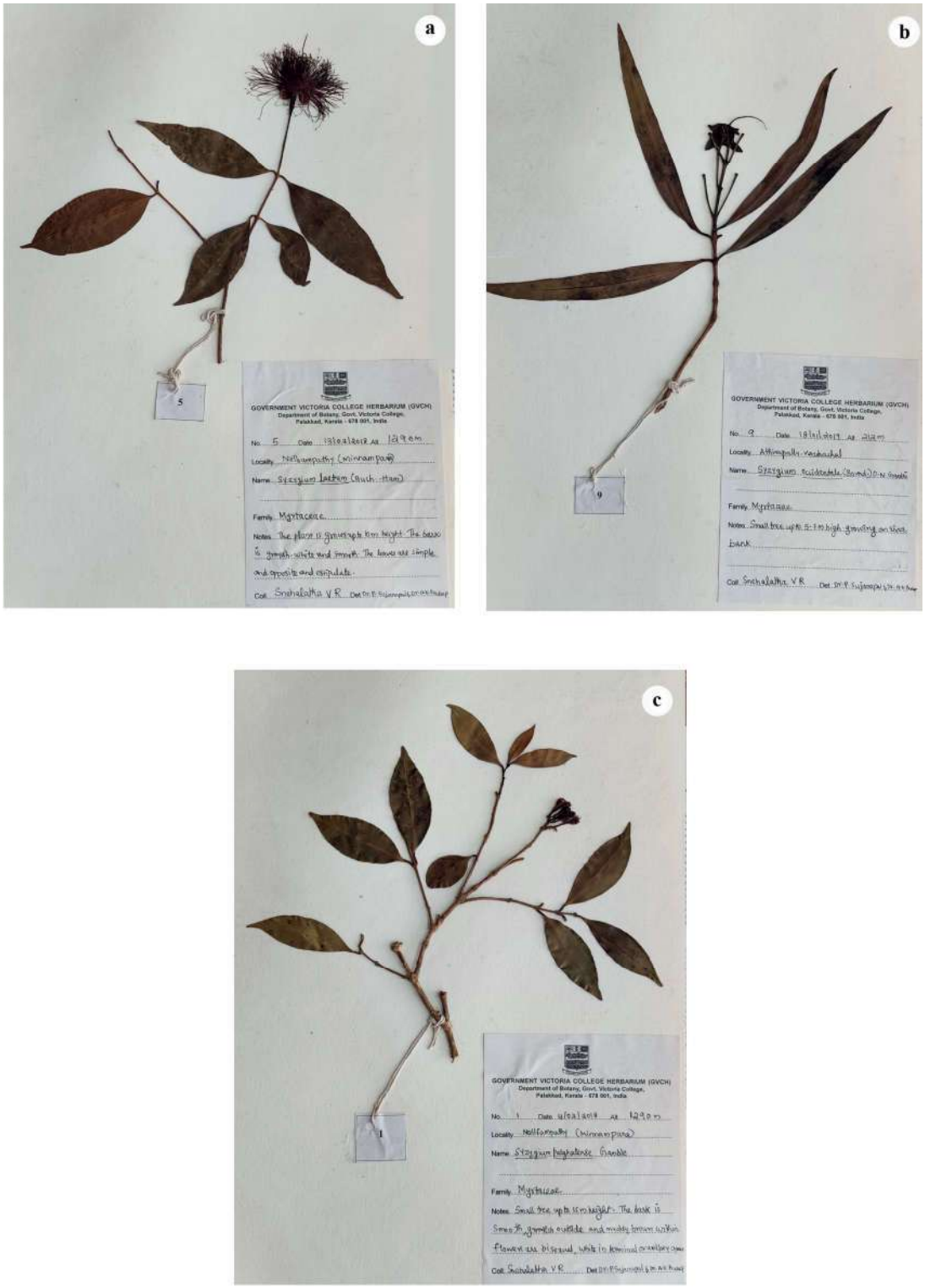


Plate 3.2: Voucher specimens of *Syzygium* species (a) *Syzygium laetum* CALI 7055 (b) *Syzygium occidentale* CALI 7056 (c) *Syzygium palghatense* CALI 7054

sectioned with a rotary microtome (Leica RM2235) to a 10-12 µm thickness. This experiment used toluidine blue to stain the plant sections (Sass, 1940). The images were taken with a Leica DM 750 HD digital microscope.

3.2.4. Histochemical studies

Fresh plant materials of *S. laetum*, *S. occidentale*, and *S. palghatense* leaves, petiole, stem, bark, and wood were collected, washed thoroughly with distilled water, and thin sections were prepared using a Leica RM2235 plant microtome for thicker tissues. These sections were subjected to histochemical staining to detect specific cell components. Lignified cells were identified by treating the sections with phloroglucinol followed by hydrochloric acid, which stained the tissues pink to red. Fixed oils were detected by staining with Sudan Red, resulting in orange to reddish-pink colouration of oil droplets. Starch and aleurone grains were visualized using iodine-potassium iodide solution, which stained them blue. The presence of tannins was confirmed by staining with ferric chloride, which produced a bluish or greyish-black colour. Microscopic observations were recorded using a Leica DM 750 HD digital microscope (Tandon & Sharma, 2018).

3.3. Results

3.3.1. Macroscopic studies

The morphological features of three *Syzygium* endemics in the current study were evaluated for their macroscopic features by observing their habit, habitat, vegetative, and reproductive characteristics. Table 3.2 tabulates the main characteristics of the comparative examination of the morphological attributes of *S. laetum, S. occidentale,* and *S. palghatense*.

3.3.1.1. Description of the collected plant samples

Plates 3.3 to 3.5 depict the morphological details of the *S. laetum, S. occidentale,* and *S. palghatense*.

❖ ***Syzygium laetum* (Buch.-Ham.) Gandhi**

Trees grow up to 10 m high. The bark is smooth and greyish-white. The branchlets are terete and slender. The leaves are oppositely arranged and simple with elliptic, ovate, elliptic-lanceolate, elliptic-ovate, elliptic-oblong shape. The apex of the leaf is acuminate or obtusely acuminate. The leaf is glabrous, estipulate, chartaceous, and the margin entire. The petiole is 5-10 mm long. The venation of the leaf is intercostae reticulate. The bisexual flowers grow alone or in groups of 2-5 in inflorescences arranged in the axils or at the ends of branches in a cymose pattern. The flower colour is crimson or lemon yellow. *S. laetum* is distinguished from other *Syzygium* species by its crimson red stamens that protrude above the blossom. A persistent pedicel that is 2-5 cm long adorns the flower. The calyx tube is 1.5-2 cm long and is subcylindrical. The glandular, orbicular, and punctuate petals have distinct veins. The stamens occur in numerous, and each is 2-3 cm, yellow, crimson, pinkish, and curved to the centre of the sprout. The flower has a 2-celled inferior ovary with many ovules. In this species, the persistent style is long, and the stigma is acute. The tree has ovoid berry fruit with reflexed calyx lobes forming a crown (Sasidharan, 2011).

Table 3.2: Comparative analysis of morphological features of *Syzygium laetum*, *S. occidentale,* and *S. palghatense*

Morphological features	***S. laetum***	***S. occidentale***	***S. palghatense***
Height	Medium-sized tree, 10 m	Small tree, 5-7 m	Large tree, 15 m
Branchlets	Terete, slender	Slender, quadrangular to terete, slightly pubescent	Subtetragonous, brownish
Bark	Smooth, greyish-white	Smooth, thin, pale grey to light brown.	Smooth, greyish outside, muddy brown inside
Leaves	Opposite, elliptic to lanceolate, entire margin	Linear-lanceolate, acuminate ends	Opposite or subopposite, elliptic, glandular
Petiole	5-10 mm, slender	Slender, 1 cm long	3-5 mm, slender, glabrous
Lamina	Elliptic, ovate, lanceolate	Linear-lanceolate, chartaceous	Glabrous, elliptic, cuneate base
Venation	Intercostae reticulate	Reticulate venation	Intercostae reticulate
Flowers	Bisexual, crimson or lemon yellow	White or pinkish tinge	Bisexual, white, terminal or axillary cymes
Inflorescence	Axillary or terminal cymes, single or in groups	Terminal cymes, 10 cm broad, divaricate	Terminal or axillary cymes, 2-4 cm
Calyx Tube	Subcylindric, 1.5-2 cm long	Funnel-shaped, 15 mm	Funnel-shaped
Petals	Glandular, orbicular, distinct veins	Creamy white, orbicular, shortly clawed	Creamy white, calyptrate, caducous
Stamens	Numerous, 2-3 cm, crimson, pinkish, curved	Numerous, 25 mm long, bent inward in buds	Numerous, 8 mm long, bent inward in buds
Ovary	Inferior, two-celled, many ovules	Inferior, two-celled, bilocular	Inferior, two-celled, many ovules
Style	Long persistent	4-5 cm style	Simple
Stigma	Acute	Simple thin-tipped	Simple
Fruit	Ovoid berry with reflexed calyx lobes	Berry-like, obovoid to globose, pinkish-green	Berry
References: Sasidharan, 2011; Murthy & Nair, 2016; Varghese & Sreekala, 2017			

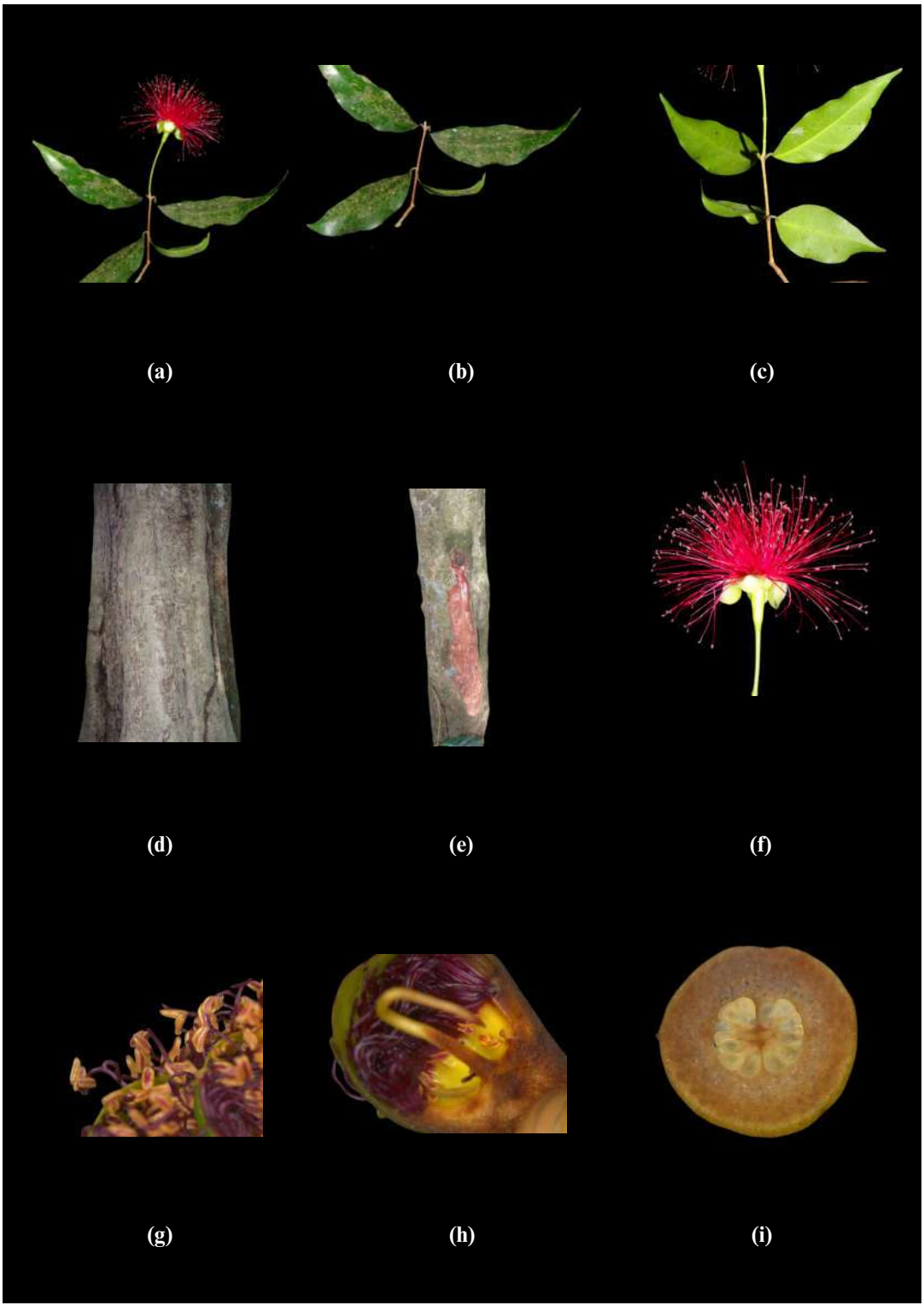


Plate 3.3: Vegetative and reproductive structures of *Syzygium laetum*: (a) Flowering twig (b) Adaxial leaf surface (c) Abaxial leaf surface (d) Wood (e) Blaze (f) Flowers (g) Androecium (h) Gynoecium (i) Ovary

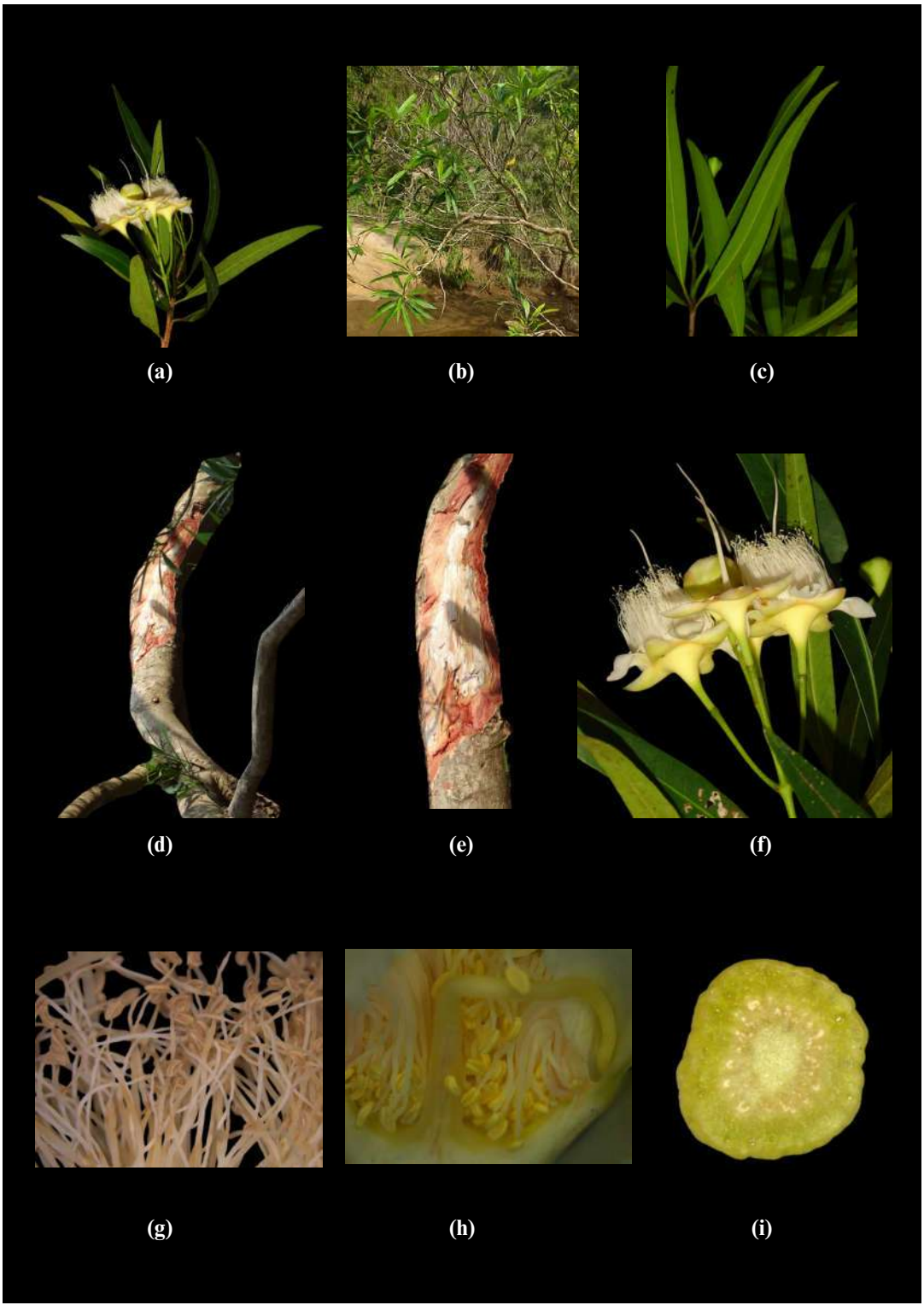


Plate 3.4: Vegetative and reproductive structures of *Syzygium occidentale*: (a) Flowering twig (b) Adaxial leaf surface (c) Abaxial leaf surface (d) Wood (e) Blaze (f) Flowers (g) Androecium (h) Gynoecium (i) Ovary

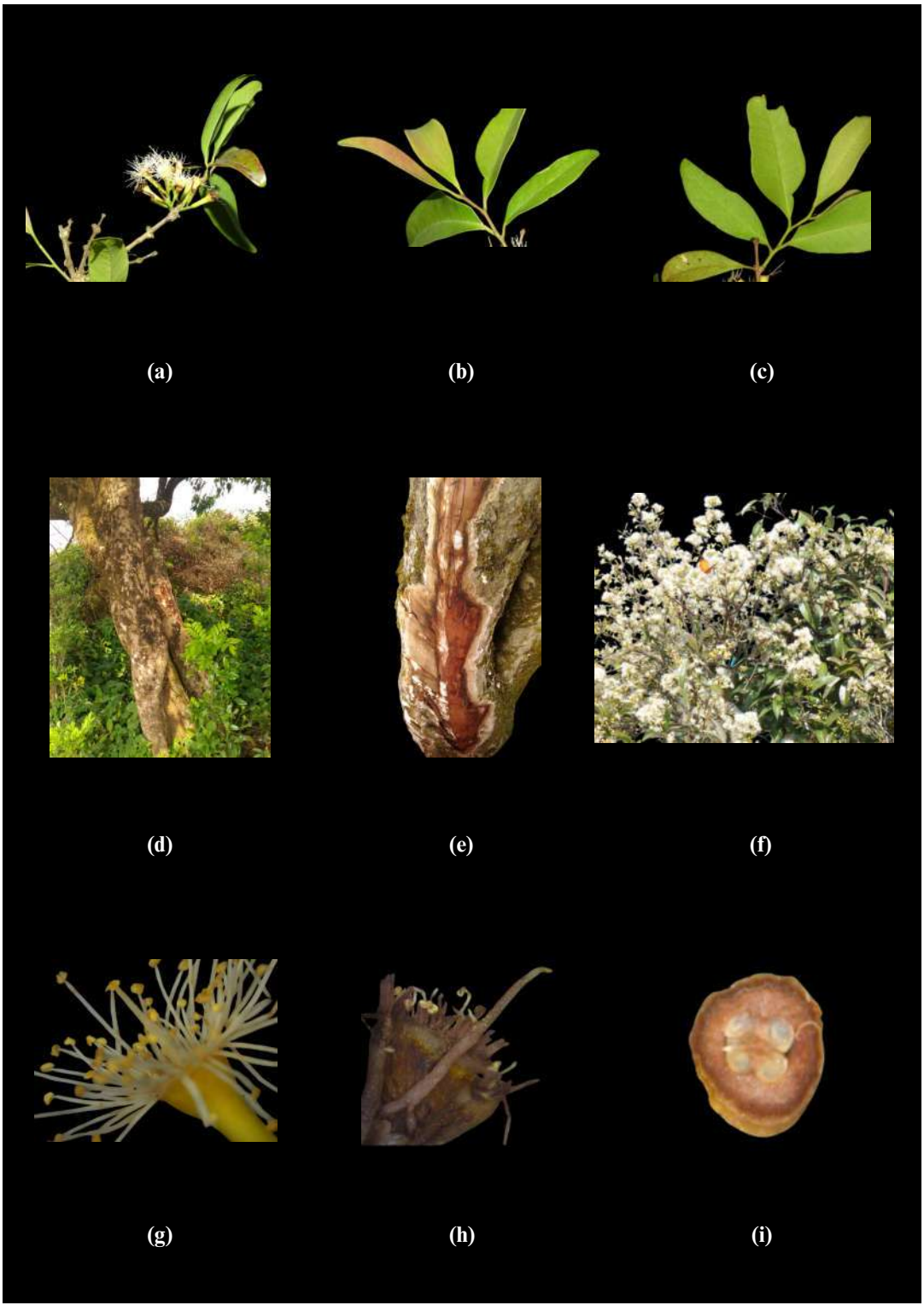


Plate 3.5: Vegetative and reproductive structures of *Syzygium palghatense*: (a) Flowering twig (b) Adaxial leaf surface (c) Abaxial leaf surface (d) Wood (e) Blaze (f) Flowers (g) Androecium (h) Gynoecium (i) Ovary

❖ ***Syzygium occidentale* (Bourd.) D.N. Gandhi**

Small trees 5-7 m high and growing along river banks of evergreen forests. The leaves are 14 x 2.5 cm long, linear-lanceolate in shape, acuminate at both ends and chartaceous. The petiole is 1 cm in length. The inflorescence is cymes 10 cm broad, terminal, and dichotomously divaricate. The flowers are white or pinkish tinge. The calyx tube of the flower is 15 mm long and funnel-shaped. The petals are creamy white, shortly clawed, broad, and orbicular. The filaments are 25 mm long and yellow. In the bud phase, filaments bend inwards and straighten during the anthesis. The anthers are medifixed and oblong. The ovules are placed in the axile of the ovary, which is a syncarpous, inferior, two-celled, and bilocular. The style is between 4 and 5 cm long. The tree has a simple, thin-tipped stigma. The fruit is berry-like, obovoid to globose in shape, and pink or greenish-pink in colour (Sasidharan, 2011; Varghese &Sreekala, 2017).

❖ ***Syzygium palghatense* Gamble**

Large tree reaching a height of 15 m. The branchlets are subtetragonous and brownish. The bark is muddy brown on the inside and smooth, greyish outside. The tree leaves are glandular, recurved at margins, subsessile, obovate, cuneate at the base, coriaceous, estipulate and opposite, or subopposite in arrangement. The slender petiole is 3-5 mm in length and glabrous. Lamina is glabrous and elliptic, the base is cuneate or acute, and the apex is obtusely accuminate or acute. The lower surface of the lamina is sparsely gland-dotted. The leaf has intercostae reticulate venation. The flowers of the plant are bisexual and white. The plant has inflorescences consisting of terminal or axillary cymes 2-4 cm long, characterized by a funnel-shaped calyx tube. The petals are creamy white, calyptrate, and caducous. The stamens are 8 mm long and found in large numbers. In the bud, stamens are bent inwards in the middle. The inferior ovary is two-celled with many ovules. The style is one and has a simple stigma. The fruit of the *S. palghatense* is berry (Murthy & Nair, 2016; Sasidharan, 2011).

3.3.2. Microscopic studies

The anatomical features of the endemic species of three selected *Syzygium* species of the current research were analyzed for their microscopical characteristics by taking microtome sectioning of their stem, leaves, bark, and flowers. Table 3.3 portrays the main characteristics of the comparative examination of the anatomical traits of *S. laetum, S. occidentale,* and *S. palghatense*.

3.3.2.1. Anatomical features of *S. laetum*

Plates 3.6 to 3.11 represent anatomical features of the *S. laetum*

3.3.2.1.1. Leaves

The leaf has a prominent, plano-convex midrib and thick, smooth lamina. The midrib is 750 μm thick (in a vertical plane) and 1 mm wide (horizontal plane). The epidermis of the midrib on both adaxial and abaxial sides has small, squarish, thick-walled cells. The ground tissue includes large, squarish, thin-walled, and compact parenchyma cells. Some ground parenchyma cells are dilated into wide circular secretory cavities in dark brown spherical chemical compounds.

The midrib has a broad bowl-shaped vascular system loosened in the median part. The loosened segments are thick and slanting in position. The segments are 300 μm thick and 500 μm long. The vascular segments are bi-collateral, having phloem layers on the xylem's upper and lower areas. The xylem elements are short and compact, with several vertical lines. The elements are squarish, thick-walled, and wide-lumened.

- **Lamina**

The lamina is 370 μm thick. It is dorsoventrally differentiated, comprising two adaxial layers of vertically elongated palisade parenchyma cells and an abaxial wide zone of about eight layers of large, circular, fairly thick-walled, less compact spongy mesophyll cells. The adaxial epidermal cells are squarish or rectangular with thick cuticles. The abaxial epidermal cells are more minor, squarish, and thick-walled. Small circular vascular bundles are embedded in the median part of the lamina.

- **Paradermal layer**

The lamina has abundant wide circular secretory cavities. The cavities are occupied by wide, more, or less circular solid tannin content. Only one tannin body is found in a cavity. The mesophyll cells of the leaf form a radiating circle of cells around the cavity. The cavities are 100 mm in diameter.

- **Epidermal tissue**

The epidermal peelings of the leaf provided the epidermal tissue for the study. The adaxial epidermal layer consists of highly wavy, thick-walled cells. The cells have an amoeboid appearance. The epidermis is apostomatic. The abaxial epidermal cells are also thick-walled and amoeboid in appearance. The epidermis is densely stomatiferous. The stomata are paracytic. The guard cells are encircled by one or two pairs of subsidiary cells. The stomata are paracytic. The guard cells are 30 μm long, 20 μm broad, thick, and elliptical with narrow slit-like stomatal pores.

➢ **Leaf margin**

The leaf margin is thick and conical. The epidermal cells along the marginal part have a very thick cuticle. The palisade mesophyll extends up to the extreme marginal part. However, the cells become reduced into short vertical rectangular cells. The spongy mesophyll tissue remains unchanged. Small circular vascular strands are distributed along the leaf margin's median part.

➢ **Leaf venation**

The venation pattern of the lamina is densely reticulate. It consists of a significant mid-vein from which several lateral veins emerge. The primary lateral vein again branches, forming secondary lateral veins and forming closed areas with veins enclosing vein islets.

The vein termination arises from the inner part of the veins of the vein islets and extends freely without any connection with their ends to the veinlets. These free-

floating vein terminations are either simple without further branching or branch once or more times, forming tree-like outlines.

- **Petiole**

The petiole is 12 mm thick, 15 mm wide, and semicircular in outline with flat adaxial and convex abaxial sides. The petiole consists of small epidermal cells with a highly lignified cell wall. The ground tissue consists of angular, thick-walled, compact parenchyma cells. A few irregular, fairly wide air chambers exist in the adaxial zone. Wide circular secretory cavities are frequently seen in the ground tissue. The vascular strand is wide, bicollateral, and arc-shaped. The strand comprises a thick arc of numerous vertical rows of small angular thick-walled xylem elements. The phloem components are thick cylinders on both the adaxial and abaxial sides. The ground parenchyma and phloem elements exhibit an extensive distribution of calcium oxalate druces.

The petiole, midrib, and lamina have frequent circular-wide secretory cavities lined by one or two rectangular thick-walled cells. These cavities are idioblasts, which possess a large spherical brown-coloured resinous substance. The lamina has highly dilated circular hypodermal cells that function as idioblasts. A single large druce type of calcium oxalate crystal occurs within the idioblast.

3.3.2.1.2. Stem

The stem consists of a roughly broken periderm, wide cortex, and hollow cylinder of secondary vascular tissues. The periderm includes a phellogen layer, 4 or 5 outer phellem, and a poorly developed phelloderm. Some of the phellem cells are thick-walled and lignified. These lignified phellem cells are called phelloid cells. Inner to the periderm occurs a wide cortical zone where thick masses of sclerenchyma cells are distributed among parenchymatous ground tissue. The vascular cylinder consists of an outer thick, continuous layer of secondary phloem. The secondary phloem includes dense radial rows of angular, thick-walled phloem elements and phloem parenchyma cells. The phloem parenchyma cells include prominent calcium oxalate crystals.

The secondary xylem cylinder measures 200 μm thick. It consists of diffusely distributed vessel elements that are wide, angular, and thick-walled. Some of the vessels are in radial multiples, and others are solitary. The ground tissue of the secondary xylem includes tiny, angular, highly thick-walled fibres with a narrow lumen. Several circular, thin cylinders of tangentially oblong thick-walled fibres are distributed in the secondary xylem. In the centre of the stem occurs a broad circular pith. A phloem layer is found on the periphery and within the xylem cylinder. Thin blocks of sclerenchyma cells ensheathe this medullary phloem. Calcium oxalate druces are abundant in the parenchyma cells of the outer secondary phloem cylinder.

3.3.2.1.3. Flower

In the transectional view, the perianth lobes appear folded in a radial position. Each lobe consists of a midrib, and the lateral veins are folded radially and occur parallel to adjacent perianth lobes. The perianth lobes are deeply ridged, furrowed on the outer part, and relatively smooth on the lower part. The lobe includes the outer epidermis of small rectangular, thin-walled cells. The inner epidermal cells are small and squarish.

The mesophyll tissue of the perianth lobe is differentiated into the outer palisade layer and inner spongy parenchyma. The palisade cells are thin, columnar, and loosely arranged. The spongy parenchyma cells are small lobes and have wide air chambers. There are small circular vascular bundles of the veins and the perianth lobes. The midrib is bulged on the outside and has larger, thin-walled, radially oblong epidermal cells. The midrib has a small vascular bundle comprising inner xylem and outer phloem elements.

In the centre of the perianth is a small circular sectional view of the style. The style comprises a thin epidermal layer and thick ground tissue of circular, less compact parenchyma cells. There is a central thick mass of the phloem and collateral segment of the xylem. Along the periphery of the central cylinder, small circular vascular strands occur. These strands have a central core of the xylem ensheathed by the phloem.

3.3.2.1.4. Bark

The bark has a very thick periderm, measuring more than 650 μm in a vertical plane. The periderm cells are unique in structure and organization. It consists of small, horizontally oblong rectangular, thick-walled cells. The cells are in regular vertical straight lines. The cells in the vertical lines are of two types: wide, squarish, and narrow rectangular. The wide, squarish, narrow rectangular cells alternate, one below the other. Alternating these squarish and rectangular cell rows, these are vertically oblong, fairly wide cells that appear darker due to some cell inclusions. The squarish cell rectangular rows and darker wide cell rows appear in regular alternate characteristic layers. The row possessing vertically oblong and small rectangular cells regularly alternates with darker squarish cells.

Inner to the periderm zone occurs the cortical zone. The cortical cells are angular, compact, and possess dense tannin. The secondary phloem follows the cortical zone. The outer part of the secondary phloem includes dilated rays and collapsed phloem elements. The phloem ray cells are horizontally rectangular and possess dense tannin contents. The collapsed phloem elements are seen in between broad rays. The collapsed sieve elements are crushed and obliterated. The inner part of the secondary phloem has narrow, dark phloem rays. In between the rays, intact, non-collapsed sieve elements are found. The sieve elements are angular, thick-walled, and compact. The companion cells and the corners are tiny and attached to the sieve elements.

- **Tangential Longitudinal Section (T.L.S.)**

In T.L.S. view, the phloem rays appear in the spindle-shaped vertical plane. The rays appear dark due to the presence of dense tannin. The cells in the ray are vertically elongated, and the rays are heterocellular. The sieve elements and phloem parenchyma cells are located in between the rays. The sieve elements are wide, angular, and thin-walled.

- **Radial Longitudinal Section (R.L.S.)**

In R.L.S. view, the ray shows the rays in flat, tangential, ribbon-shaped layers resembling bricks in the wall. The ray cells are thin-walled and consist of two types of cells. The cells in the middle portion of the ray consist of horizontally elongated rectangular cells. These cells are called procumbent cells. The cells at a ray's upper and lower ends are vertically erect and wide. These cells are called upright cells. The rays having upright and procumbent cells are known as heterocellular rays.

- **Crystal distribution**

Calcium oxalate crystals of raphides occur frequently in the phloem parenchyma cells. The raphides are thick cylindrical bundles of compact, thin, pointed needles. The raphide bundles occur singly in elongated cells.

3.3.2.1.5. Wood

The wood is diffuse-porous because there is no growth. The wood consists of vessels, fibres, parenchyma, and rays. The vessels are angular and thin-walled. Some of them are short radial multiples, and others are solitary. The axial parenchyma of the wood forms a paratracheal banded type. The parenchyma cells occur in thin, continuous, wavy tangential bands. The bands pass across, enclosing the vessels. The xylem rays are thin and straight. Xylem fibres are highly thick-walled and lignified. The vessels are 80 μm in diameter.

- **Transverse Section (T.S.) of wood**

In the T.S. view, the wood shows solitary or radial multiples of vessels. The vessels are elliptical, circular, or angular in cross-sectional outline. The vessels are thick-walled. The diameter of the vessel is 70 μm. The wood consists of xylem fibres that are highly thick-walled and lignified.

- **Xylem parenchyma**

Xylem parenchyma occurs in thick, tangential, wavy lines. The parenchyma lines cross the vessels by surrounding them. This type of parenchyma, tangential continuous lines crossing the vessel, is called paratracheal banded parenchyma.

- **Xylem rays**

The abundant xylem rays are composed of parenchyma cells and contribute to the overall radial stability of the wood. The rays consist of upright, procumbent, and square-shaped cells. Typically, they consist of a single row of cells, but sometimes, they might consist of two rows of cells. The height of the ray cells is varied, enabling efficient radial conduction and storage. Taller rays span multiple growth rings and facilitate long-term storage and transportation.

➢ **Tangential Longitudinal Section (T.L.S.) of the wood**

The vessel lines are seen with their lateral wall pits in the T.L.S. view. The lines consist of narrow, thin vessels; the end walls of the vessel elements are oblique. The vessel elements are 400-450 μm long and 45-50 μm wide. The wide, polygonal, multiseriate alternate-bordered pits are found on the lateral walls. The T.L.S. view shows xylem fibres in a compact vertical row. The fibres have thick lignified walls and narrow cell lumen. There are also xylem parenchyma cells that occur in vertical lines. The parenchyma cells are also thick-walled with a wide cell lumen.

In T.L.S. view, xylem rays appear in vertically elongated spindle-shaped bodies. The rays are thick, many-celled in the middle, and tapering at the ends. The rays are non-storied and at different height levels. Some of the rays are biseriate or uniseriate. Xylem parenchyma cells are in many vertical lines. The parenchyma cells are wide and thick-walled. The xylem fibres are in thick, compact vertical bundles. The fibres are thick-walled and lignified.

Table 3.3: Comparative analysis of anatomical features of *Syzygium laetum*, *S. occidentale*, and *S. palghatense*

Anatomical features	*S. laetum*	*S. occidentale*	*S. palghatense*
Leaves	Prominent plano-convex midrib, smooth lamina; dense venation	Thick dorsiventral lamina, thick-walled epidermal cells	Plano-convex midrib, smooth lamina; abaxial stomatiferous epidermis
Midrib	Broad bicollateral vascular system	Shallow arc-shaped vascular strand	Wide bowl-shaped vascular strand
Lamina	Vertically elongated palisade cells	Thick, xeromorphic; palisade and spongy parenchyma	Dorsiventral with smooth surfaces; thick palisade and spongy parenchyma, cicatrix
Petiole	Semicircular	Semicircular, arc-shaped vascular strand	Circular, bowl-shaped vascular strand
Stem	Roughly broken periderm, wide cortex, and hollow vascular cylinder	Circular, smooth, with distinct growth rings; wide vascular cylinder	Circular, deeply fissured periderm; sclerenchymatous cortex
Flowers	Perianth lobes radial, outer palisade, and inner spongy parenchyma	Five corollas, dithecous anthers, thick petals	Cylindrical ovary, calyx tubes; thick style with stylar canal
Bark	Very thick periderm with alternating cell rows; dense tannin in cortical zone	Thick periderm; dense sclereids and tannin in phloem rays	Wide, rough, fissured surface; thick periderm
Wood	Diffuse-porous, thick-walled vessels, tangential wavy parenchyma bands	Porous, radial multiples of vessels, thick lignified walls	Dense hardwood, diffuse-porous vessels, libriform fibres

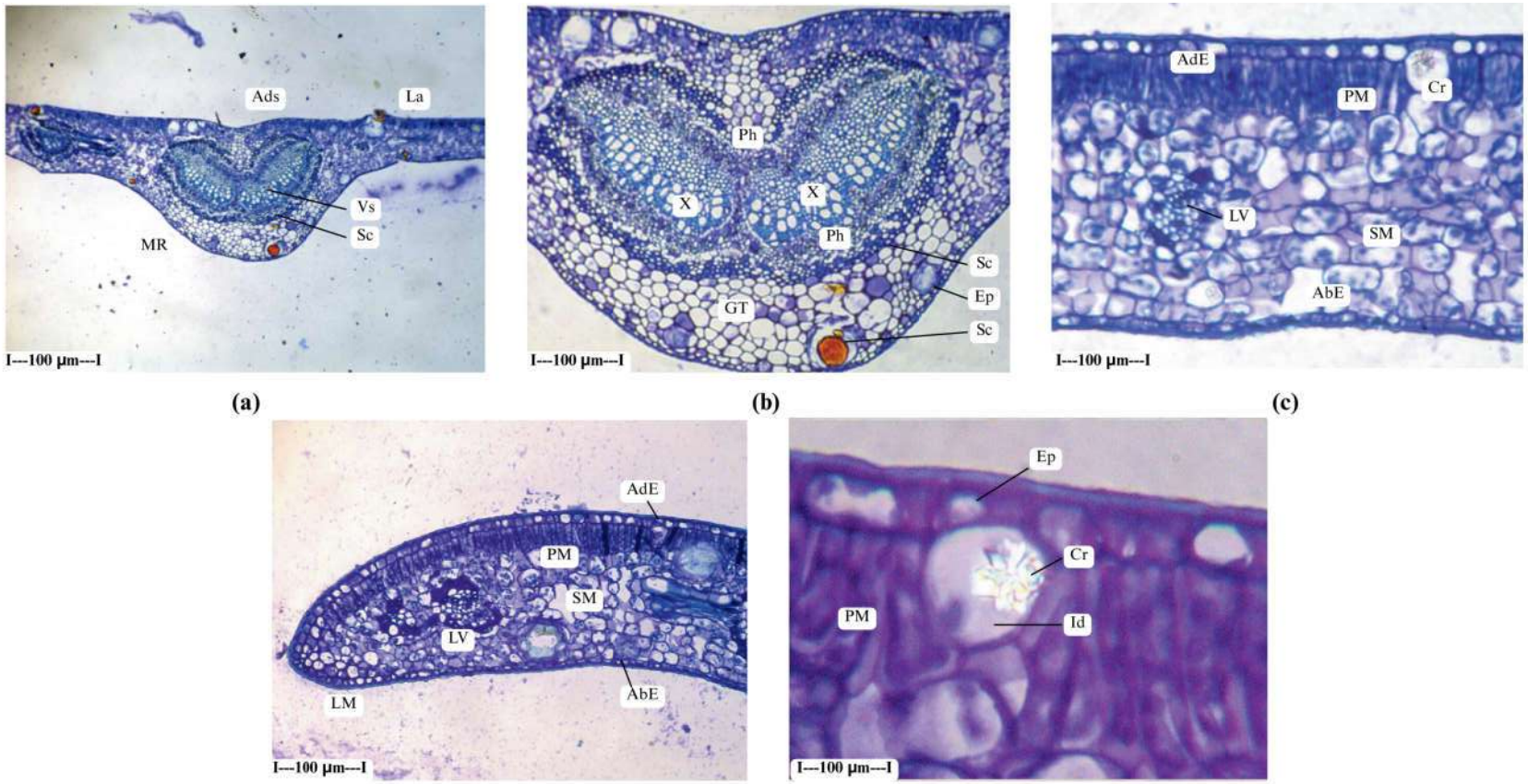


Plate 3.6: Anatomical features of *Syzygium laetum* leaves: (a) T.S. of leaf passing through the midrib (b) Vascular strands of the midrib enlarged (c) T.S. of lamina (d) T.S. of leaf margin (e) Druce type of crystal in the idioblast of the leaf
(T.S.: Transverse section; Ads: Adaxial side; La: Lamina; MR: Midrib; Vs: Vascular strand; Sc: Sclerenchyma; Ph: Phloem; X: Xylem; GT: Ground tissue; Ep: Epidermis; AdE: Adaxial epidermis; PM: Palisade mesophyll; Cr: Crystal; LV: Lateral vein; SM: Spongy mesophyll; AbE: Abaxial epidermis; LM: Leaf margin; Id: Idioblast)

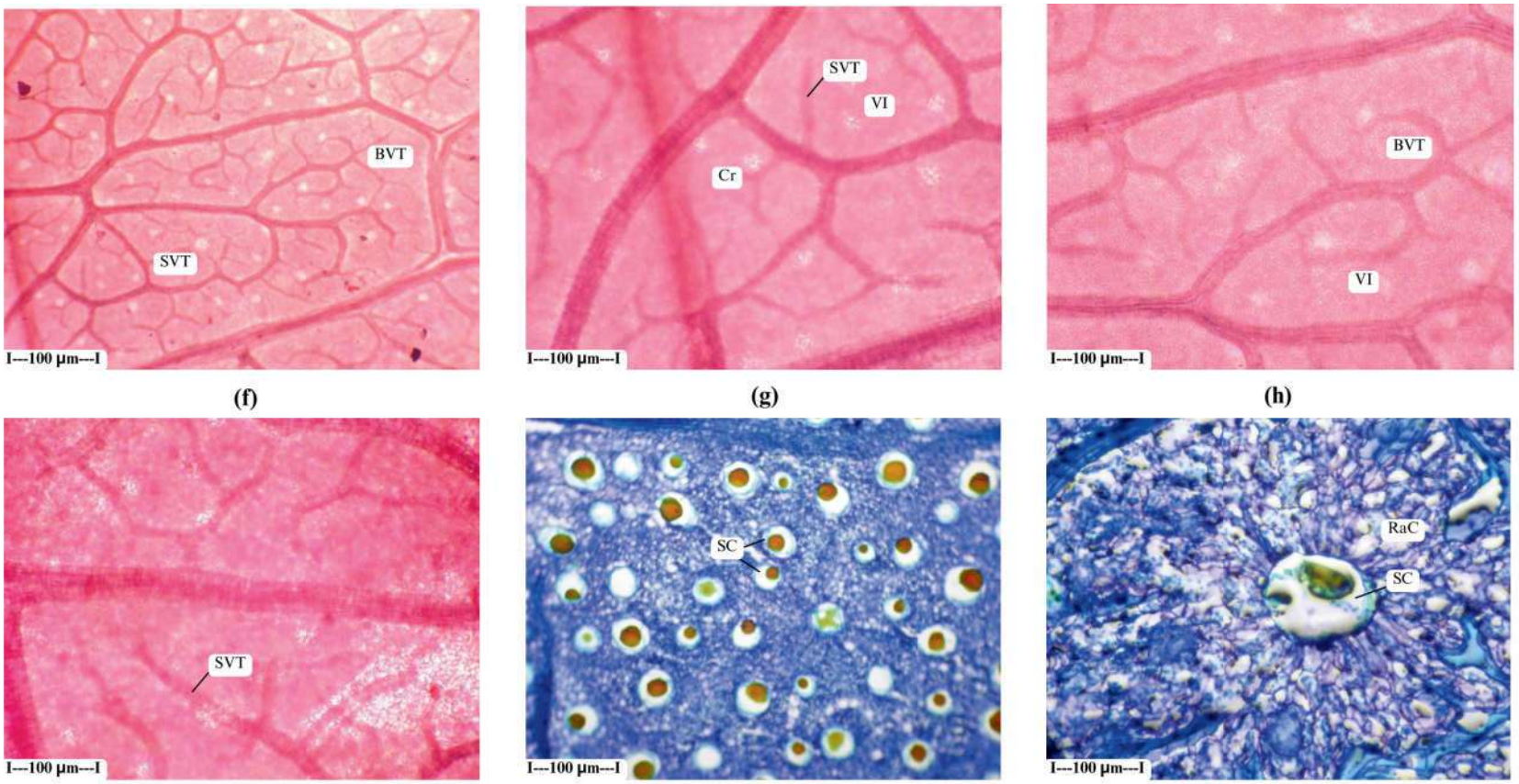
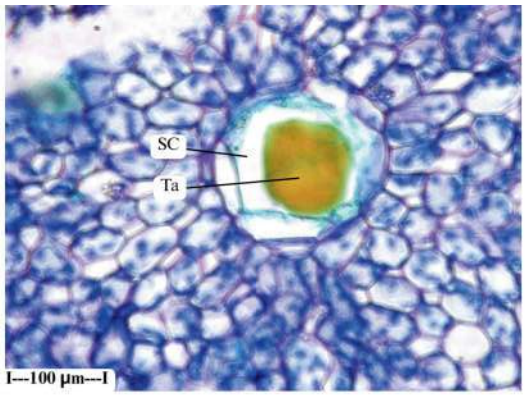


Plate 3.6: Anatomical features of *Syzygium laetum* leaves: (f) Venation pattern of the lamina showing vein islets, simple and branched vein terminations (g) Vein islets with simple vein termination (h) Vein islets with branched dendroid vein terminations (i) Simple vein termination (j) Surface vein of the lamina showing numerous crowded circular secretory cavities with darkly stained secretory bodies (k) Secretary cavities with secretary body (tannin) enlarged



(l)

Plate 3.6: Anatomical features of *Syzygium laetum* leaves: (l) Secretary cavities with secretary body (tannin) enlarged
(BVT: Branched vein termination; SVT: Simple vein termination; VI: Vein islet; Cr: Crystal; SC: secretory cavity; RaC: Radiating cells; Ta: Tannin)

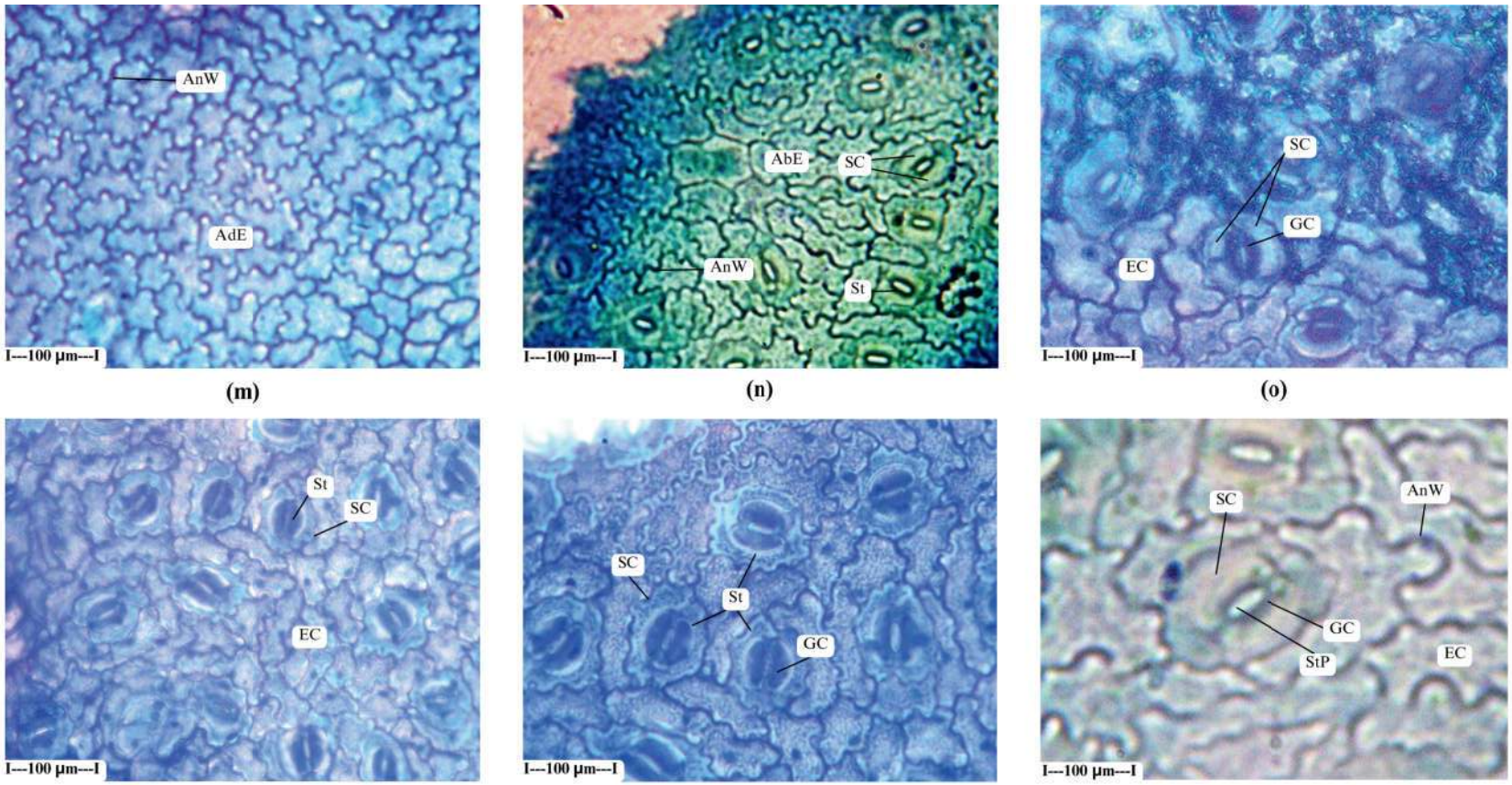


Plate 3.6: Anatomical features of *Syzygium laetum* leaves: (m) Paradermal section of the lamina showing adaxial epidermal cells (n) Paradermal section of abaxial epidermis with stomata (o–p) Abaxial epidermis showing paracytic stomata (q) Abaxial epidermis with paracytic stomata (r) Single stomata enlarged

(AnW: Anticlinal wall; AdE: Adaxial epidermis; AbE: Abaxial epidermis; SC: Subsidiary cells; St: Stomata; GC: Guard cells; EC: Epidermal cells; StP: Stomatal pore)

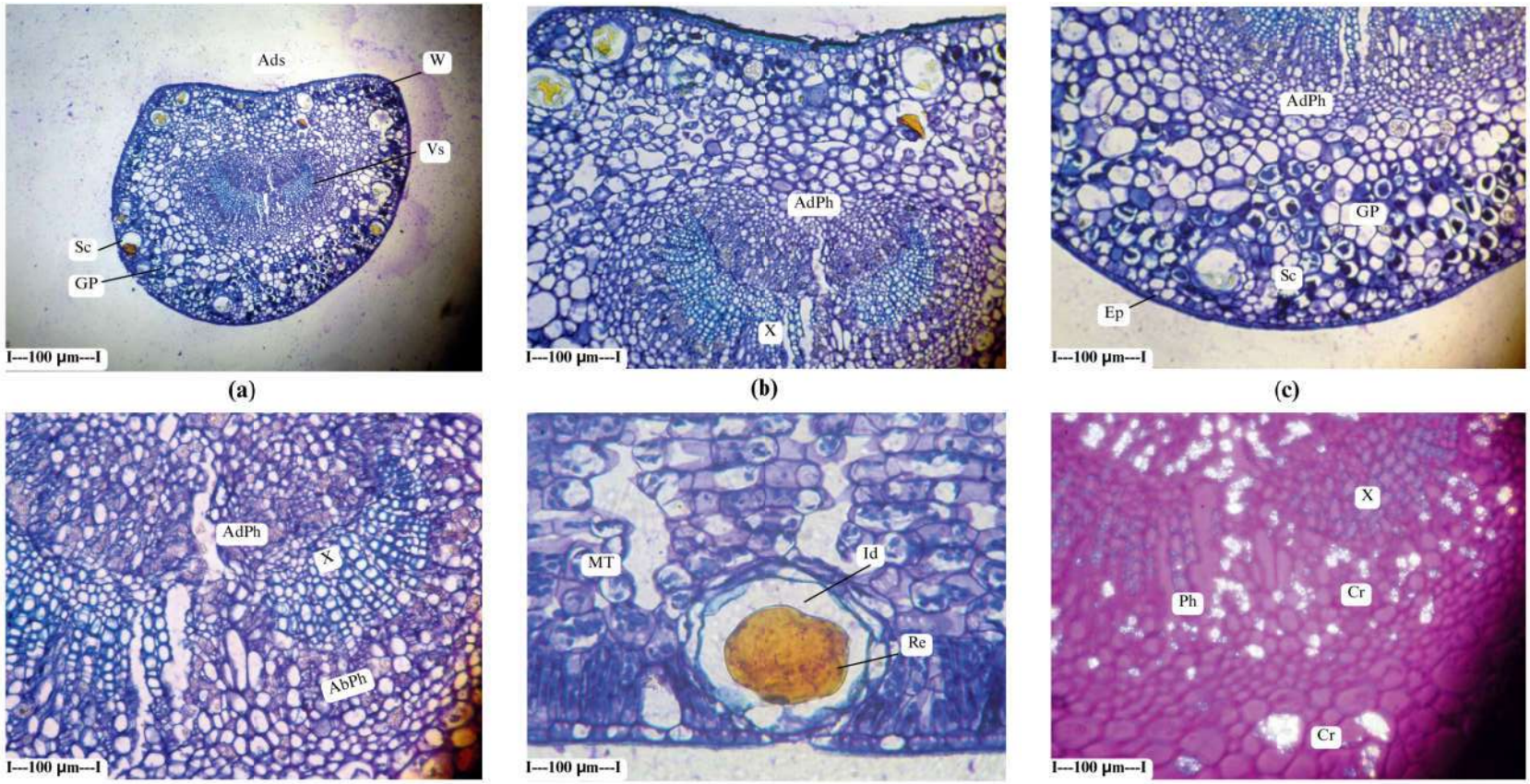


Plate 3.7: Anatomical features of *Syzygium laetum* petiole: (a) T.S. of petiole, entire view (b-c) T.S. of petiole enlarged (d) T.S. of petiole showing xylem and phloem strands (e) T.S. of leaf showing resin-containing idioblast (f) T.S. of petiole showing crystal distribution

(T.S.: Transverse section; Ads: Adaxial side; W: Wing; Vs: Vascular strand; Sc: Sclerenchyma; GP: Ground parenchyma; AdPh: Adaxial phloem; X: Xylem; Ep: Epidermis; AbPh: Abaxial phloem; MT: Mesophyll tissue; Re: Resin; Id: Idioblast; Ph: Phloem; Cr: Crystal)

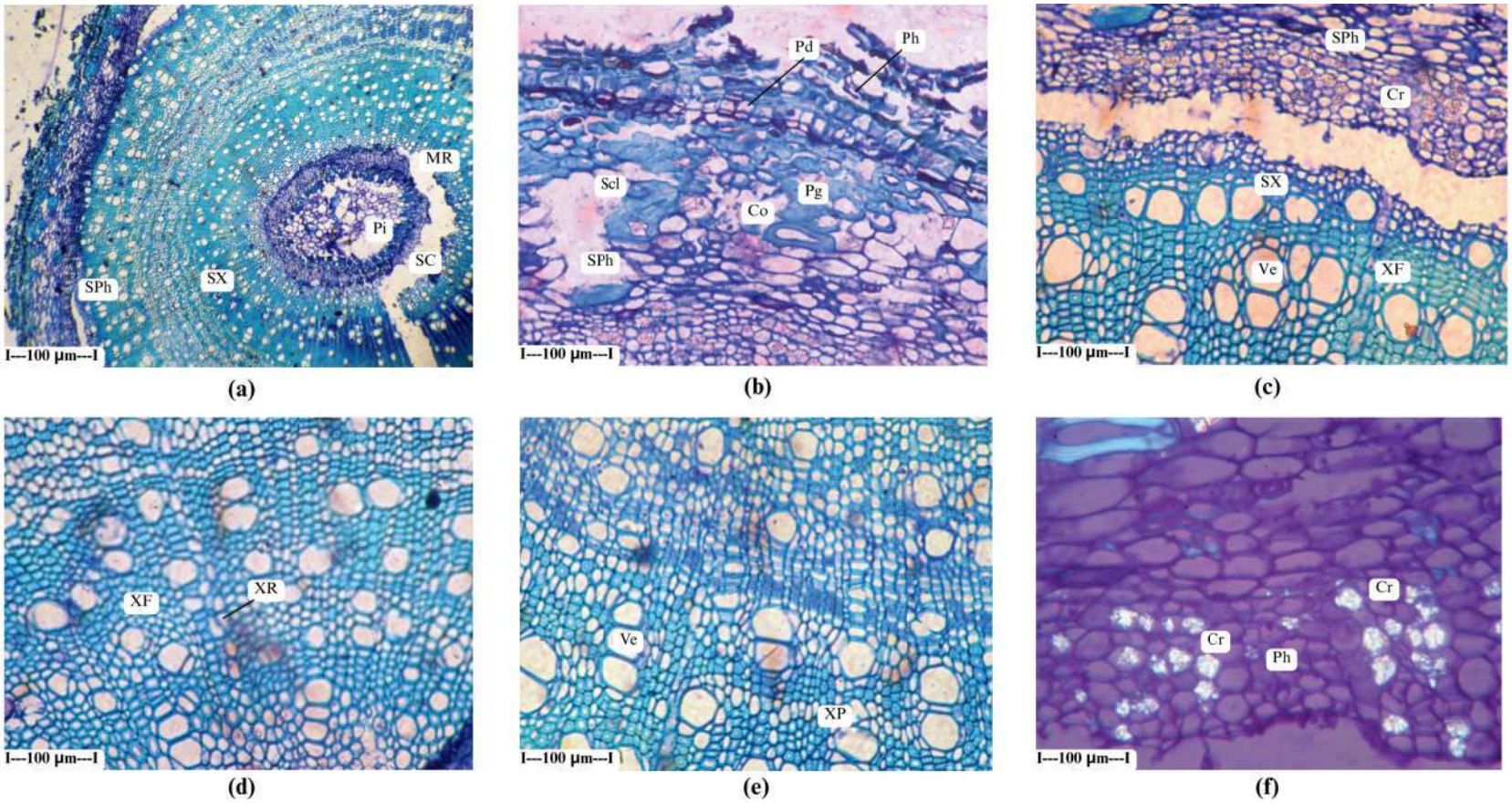


Plate 3.8: Anatomical features of *Syzygium laetum* stem: (a) T.S. of stem under low magnification (b–c) T.S. of stem- a sector of cortex, secondary phloem, and secondary xylem (d–e) T.S. of stem showing secondary xylem (f) Secondary phloem of the stem showing crystals (T.S.: Transverse section; Pe: Periderm; MR: Midrib; SPh: Secondary phloem; SX: Secondary xylem; Pi: Pith; Sc: Sclerenchyma; Pd: Phelloderm; Ph: Phloem; Scl: Sclerenchyma; Pg: Phellogen: Co: Cortex; Cr: Crystal; Ve: Vessel; XF: Xylem fibre; XR: Xylem rays; XP: Xylem parenchyma; Cr: Crystal; Ph: Phloem)

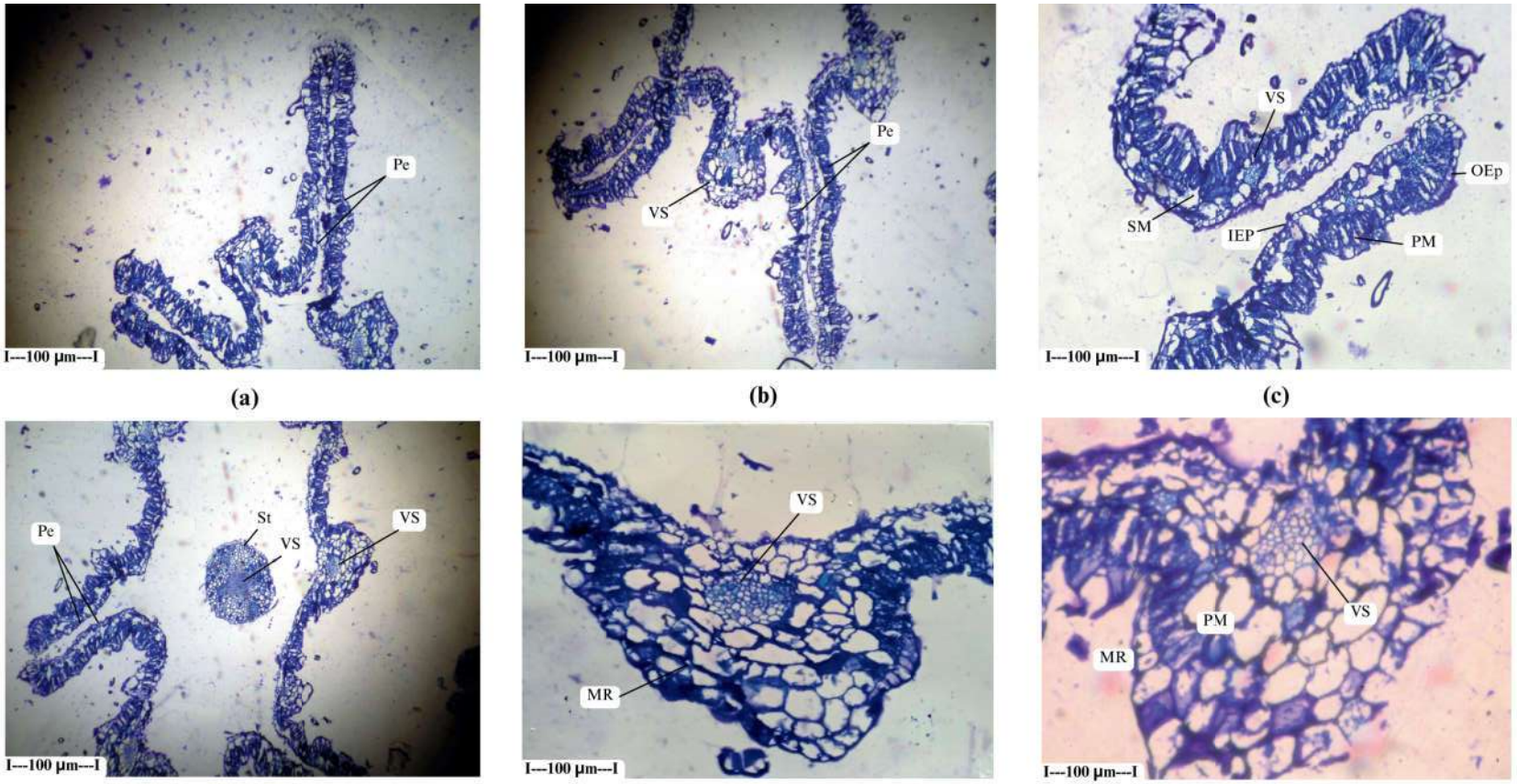
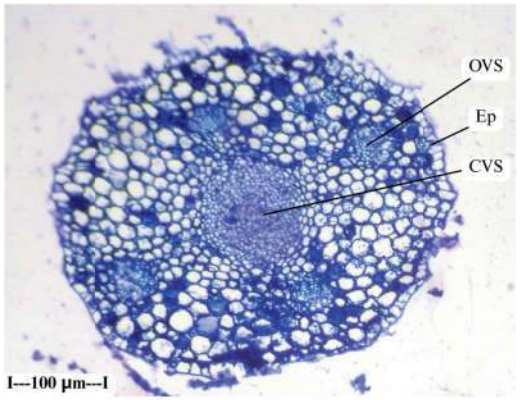
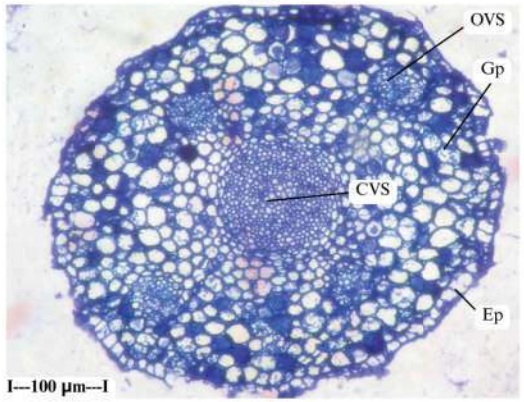


Plate 3.9: Anatomical features of *Syzygium laetum* flower: (a–b) T.S. of flower showing folded petal lobes (c) T.S. of margins of two petals (d) T.S. of petal enclosing the style (e) T.S. of style and midrib of the petal (f) Vascular strand of the midrib of the petal



(g)



(h)

Plate 3.9: Anatomical features of *Syzygium laetum* flower: (g–h) T.S. of style enlarged
(T.S.: Transverse section; Pe: Petal; Vs: Vascular strand; SM: Spongy mesophyll; IEP: Inner epidermis; PM: Palisade mesophyll; OEp: Outer epidermis; St: Style; MR: Midrib; OVS: Outer vascular strand; EP: Epidermis; CVS: Central vascular strand; GP: Ground parenchyma)

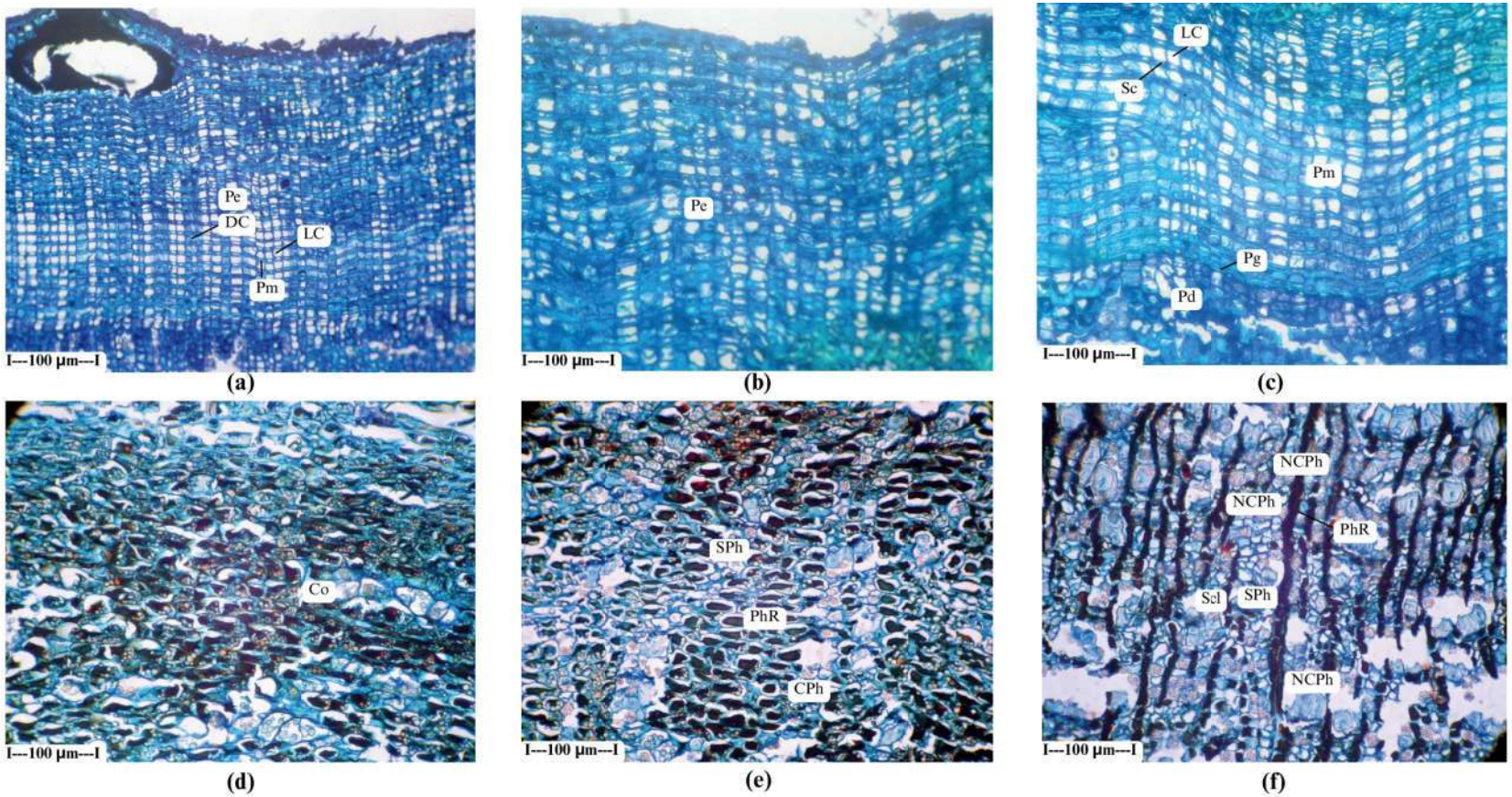


Plate 3.10: Anatomical features of *Syzygium laetum* bark: (a) T.S. of periderm (b–c) Phellem, phellogen, and phelloderm region of the periderm (d) T.S. of bark cortical zone (e) Collapsed phloem zone (f) Non-collapsed phloem zone

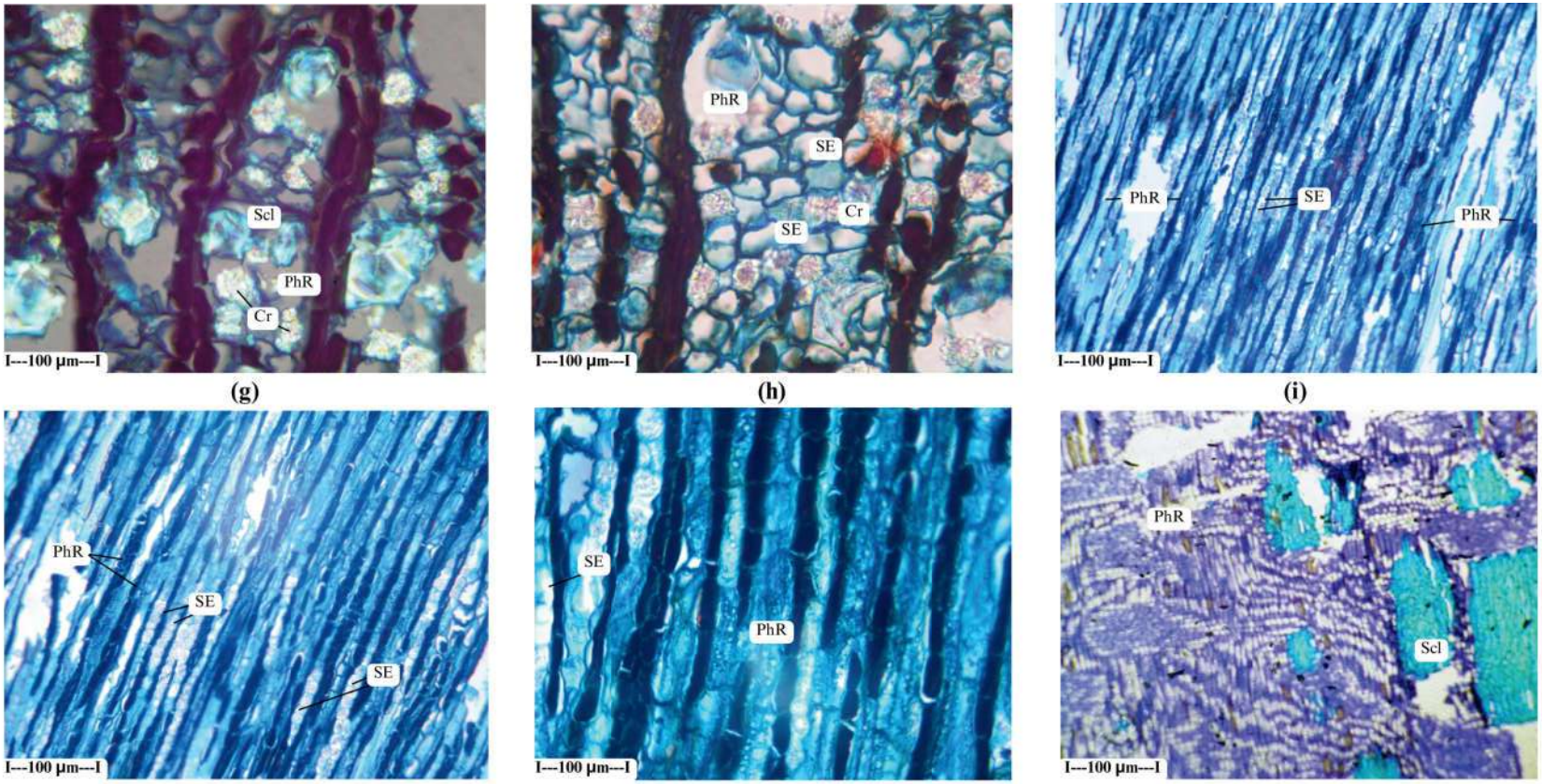


Plate 3.10: Anatomical features of *Syzygium laetum* bark: (g) T.S. of phloem showing dark parallel rays (h) T.S. of phloem showing sieve elements (i-j) T.L.S. of phloem showing phloem rays and phloem fibres (k) T.L.S. of phloem enlarged rays (l) Phloem R.L.S. view

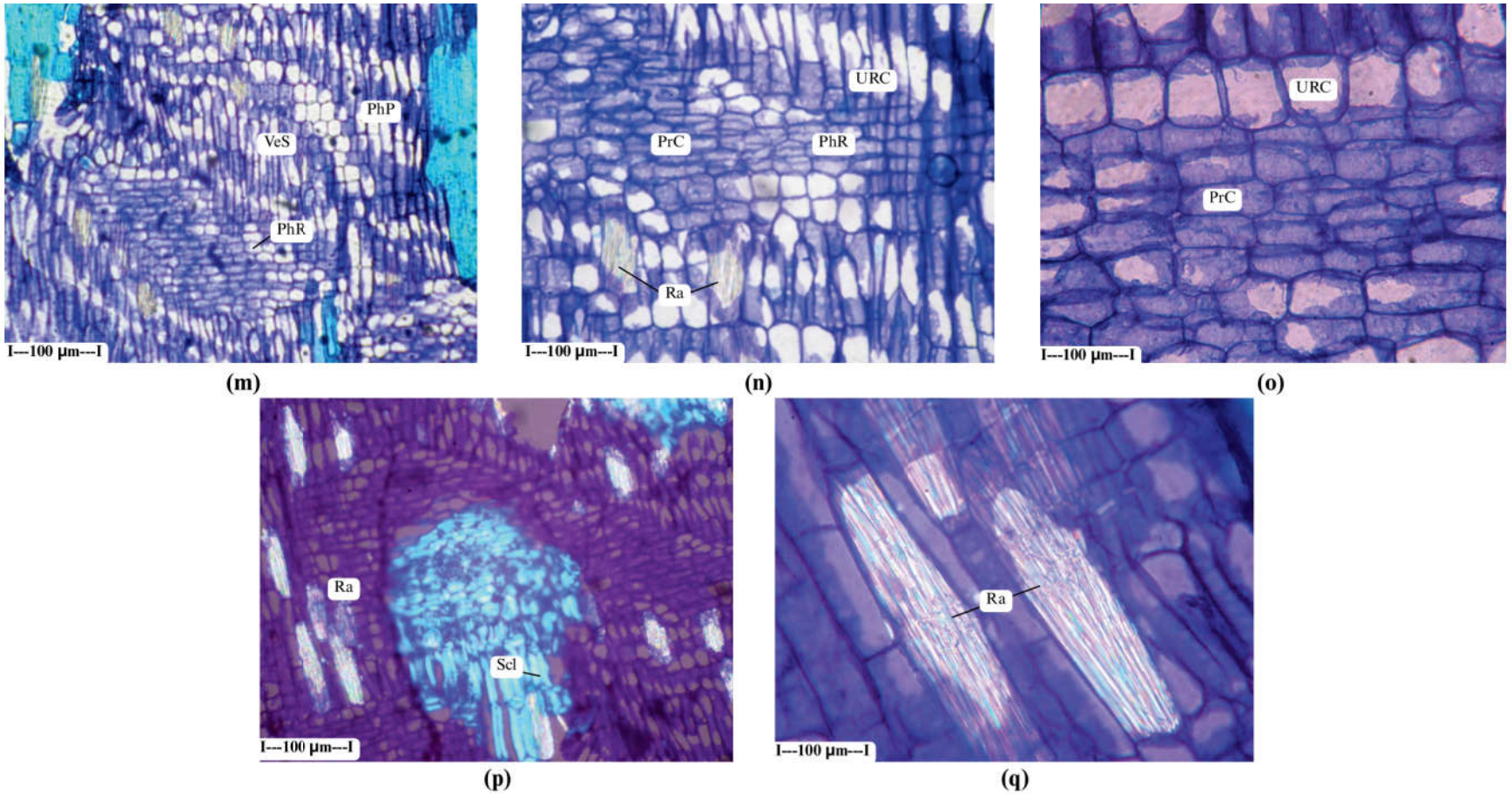


Plate 3.10: Anatomical features of *Syzygium laetum* bark: (m) Phloem R.L.S. view (n) Phloem ray cells enlarged (o) Phloem R.L.S. showing procumbent and upright cells (p) R.L.S. of phloem showing raphide distribution (q) R.L.S. of phloem showing raphide bundles (T.S.: Transverse section; T.L.S.: Tangential longitudinal section; R.L.S.: Radial longitudinal section; Pe: Periderm; DC: Dark cells; LC:Large Phloem cell; Pm: Phellem; Sc: Sclerotic phelloid cells; Pg: Phellogen; Pd: Phelloderm; Co: Cortex; SPh: Secondary phloem; PhR:Phloem ray; CPh: Collapsed phloem; NCPh: Non-collapsed phloem; Scl: Sclereids; Cr: Crystal; SE: Sieve elements; PhP: Phloem parenchyma; VeS: Vertical system of parenchyma cells; URC: Upright cells; PrC: Procumbent cell; Ra: Raphide)

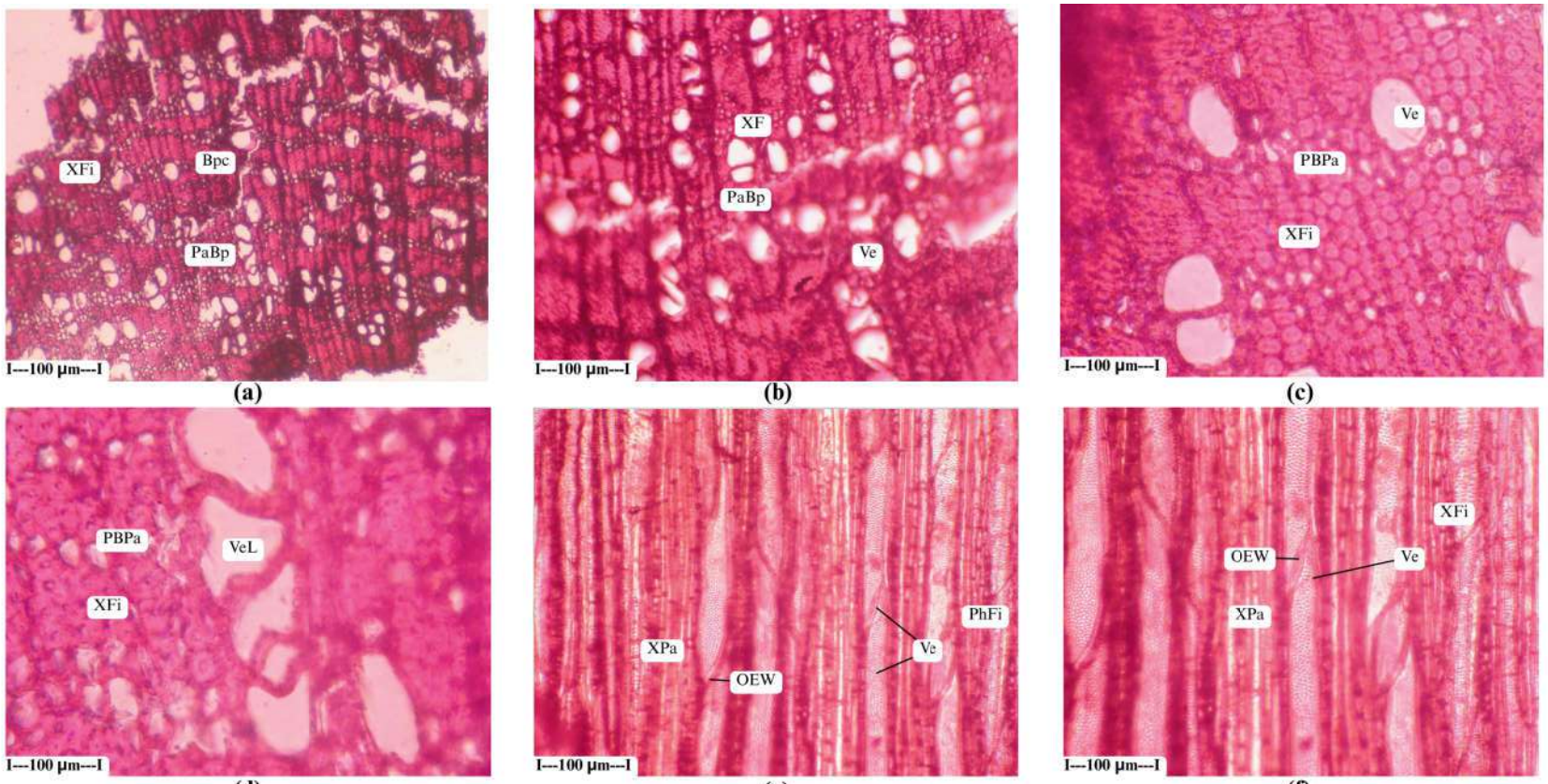


Plate 3.11: Anatomical features of *Syzygium laetum* wood: (a) T.S. of wood under low magnification (b) T.S. of wood enlarged showing vessel distribution and axial parenchyma type (c) T.S. of wood showing vessels and paratracheal banded parenchyma (d) Vessel multiples and axial parenchyma (e) – (f) T.L.S. view of the wood

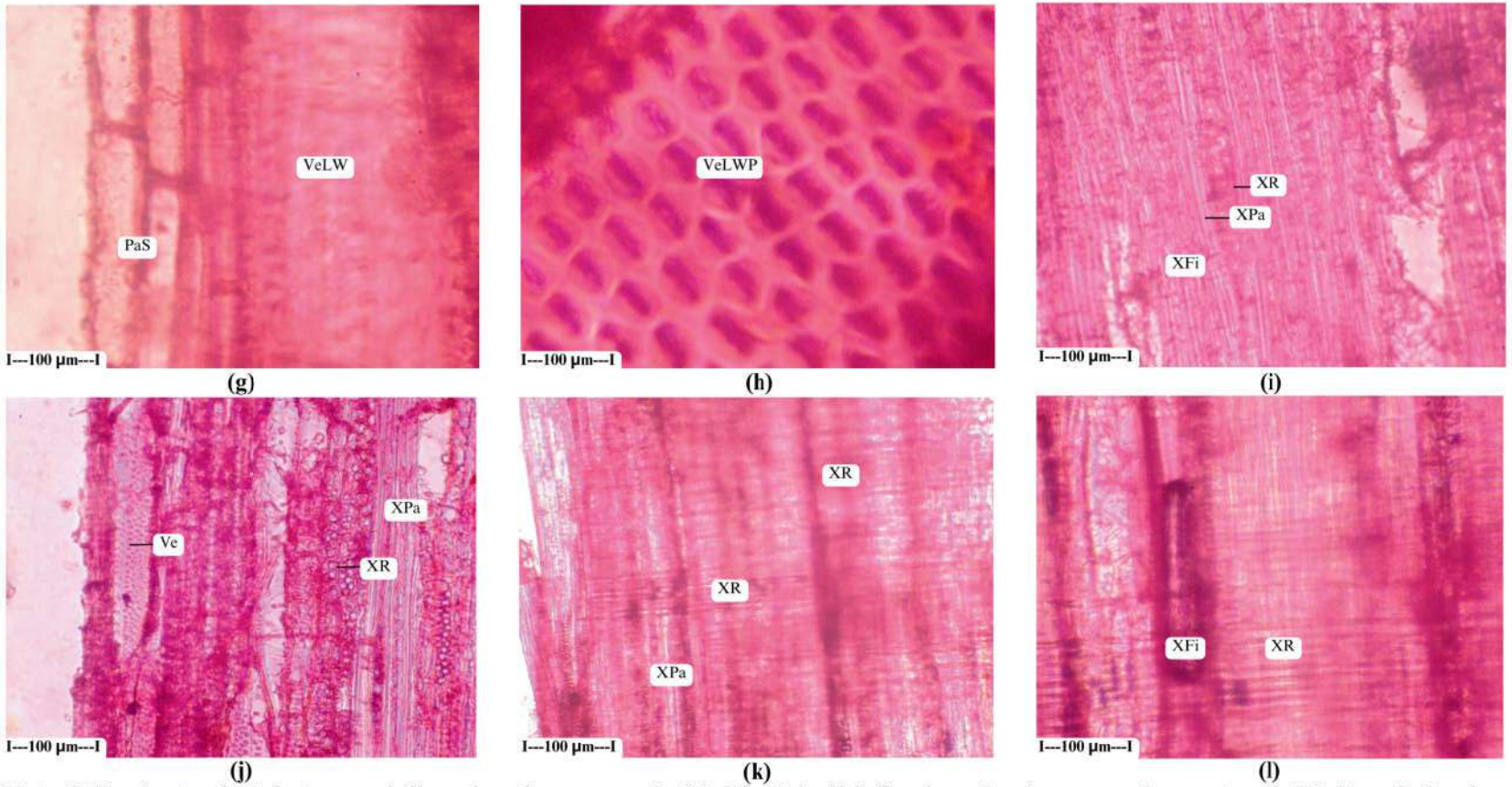


Plate 3.11: Anatomical features of *Syzygium laetum* wood: (g) Wood in T.L.S. view showing parenchyma strand (h) Vessel showing lateral wall angular wide bordered pits (i) T.L.S. of wood showing ray, parenchyma and fibres (j) T.L.S. of wood showing xylem ray, xylem parenchyma and vessels (k) R.L.S. of xylem showing horizontal ribbon shaped xylem rays and xylem fibres (l) R.L.S. of xylem, xylem rays and xylem fibres

(T.S.: Transverse section; T.L.S: Tangential longitudinal section; R.L.S: Radial longitudinal section; XFi: Xylem fibres; Bpc: Banded parenchyma; PaBp: Paratracheal banded parenchyma; XF: Xylem fibres; Ve: Vessel; VeL: Vessels in radial line; XPa: Xylem parenchyma; OEW: Vessel with oblique end wall; PhFi: Phloem fibres; PaS: Parenchyma strand; VelW: Vessel lateral wall; VeLWP: Vessel with lateral wall bordered pits; XR: Xylem rays)

- **Radial Longitudinal Section (R.L.S.) of the wood**

In R.L.S. View, the rays are plain horizontal, and the ray cells are small and rectangular. The ray cells occur in several vertical and horizontal lines. The xylem fibre and parenchyma cells are oriented vertically at the right angle to the ray. The xylem fibres are narrow, thick-walled, and compact. The parenchyma cells are narrow and occur in vertical strands.

3.3.2.2. Anatomical features of *S. occidentale*

Plates 3.12 to 3.17 represent anatomical features of the *S. occidentale*

3.3.2.2.1. Leaves

The leaf in cross-sectional view exhibits a thick abaxial midrib and thick dorsiventral lamina, with smooth upper and lower surfaces. The midrib is convex on the abaxial side and slightly concave on the adaxial side. It is 530 μm in a vertical plane and 650 μm in a horizontal plane.

The adaxial epidermis comprises wide, squarish, thick-walled cells with thick cuticles. The abaxial epidermal layer also has a similar type of small squarish cells and a thick cuticle. The ground tissue of the midrib comprises angular, thick-walled, compact parenchyma cells with small air chambers within the parenchyma tissue. The vascular strand is thick and shallow arc-shaped. It is bicollateral, having a phloem on both the adaxial and abaxial sides. The xylem elements of the vascular strand are numerous in vertical parallel lines. The protoxylem elements are directed towards the adaxial side of the midrib. The xylem elements are polygonal in outline, and their walls are thick and liquified. A thick, continuous phloem cylinder occurs along with the lower parts of the xylem arc. Apart from the abaxial phloem, an adaxial layer of the phloem lies along the concave side of the xylem strands. The phloem elements are small, darkly stained, and are in vertical lines. The vascular arc is ensheathed by a thick sclerenchyma cell.

➢ **Lamina**

The lamina is bifacial and xeromorphic. The epidermal layers consist of small, angular, thick-walled cells. The cuticle is thick and smooth. The mesophyll tissue is differentiated into two layers of palisade cells, which are vertically oriented and compact cylindrical cells. The remaining mesophyll tissue is spongy parenchyma. The lamina is 250 μm thick.

● **Paradermal layer**

The adaxial epidermis of the lamina is apostomatic. The epidermis cells are small in size, polygonal, and highly thick-walled. The anticlinal walls are straight and smooth. The abaxial epidermis is densely stomatiferous. The abaxial epidermal cell is also tiny, with thick, straight anticlinal walls. The stomata are random in distribution. The guard cell of the stomata is oriented in different directions. The guard cells are elliptical with a narrow, long stomatal pore. The guard cells are 8 μm long and 5 μm thick. The stomata are surrounded by five rectangular subsidiary cells in the guard cell, with a thick layer of calcium oxalate crystals. The crystals are tiny and spindle-shaped and radiate from the guard cell. The stomata are cyclocytic, surrounded by 4 or 5 spindle-shaped subsidiary cells.

➢ **Leaf margin**

The leaf margin is more or less as thick as the lamina; the marginal part is slightly bent down. The leaf margin has small, thick-walled epidermal cells with cuticle. The mesophyll tissue differentiated into two adaxial layers of palisade cells and many abaxial layers of spongy parenchyma. The submarginal part has a mass of compact, thick-walled cells. There is a circular, wide vascular bundle in the middle part of the mesophyll tissue.

Calcium oxalate crystals of druses are common in the mesophyll tissue of lamina. Druses are spherical bodies with surfaces covered with sharp, short spines. The crystals have birefringent properties, making them appear bright white and shining under polarized light. The druses are 30 μm in diameter.

Wide circular secretory cavities are often seen in the mesophyll tissue. They are encircled by cylindrical cells radiating from the cavity's outer surface. When stained with toluidine blue, the cavities are filled with dense dark green liquid. They are 90 μm in diameter.

- **Leaf venation**

The lamina consists of a thin reticulate venation pattern. There are thick lateral veins from which thin lateral veins are formed. The thin lateral veins again divide and form very thin veinlets. The veinlets form several wide, angular, closed vein islets within the vein islets. Thin and narrow veins are formed from the lateral part of vein islets. The thin vein islets arising from the inner part of the vein islet spread inside the vein islets. These veinlets are mainly simple and unbranched or branched repeatedly in the islets.

- **Petiole**

The petiole is semicircular and plano-convex in sectional view. It measures 1.9 mm in diameter. The epidermal layer comprises small, rectangular, highly thick-walled cells with prominent cuticles. The ground tissue consists of angular, thin-walled, compact parenchyma cells. Tannin accumulates in most of the ground parenchyma cells. The vascular strand is deep arc-shaped. It comprises numerous vertical lines of xylem elements. The xylem elements are narrow, circular, and thick-walled with liquified secondary walls. The phloem occurs in a thick layer along the xylem arc. Calcium oxalate druses occur in a deep arc along with phloem cells. The crystals are also seen scattered in ground parenchyma cells.

- **3.3.2.2.2. Stem**

The stem has a circular transectional outline and a smooth, even surface. The stem is 3.7 cm in diameter. The stem consists of a thin epidermal layer. The epidermal cells are radially oblong and thick-walled. The inner surface of a mature stem ceases when the epidermal cell breaks and peels off. The cortical zone is wide and parenchymatous. The vascular cylinder is also vast, measuring 2.4 cm in diameter.

The outer part of the vascular cylinder is circular. The xylem cylinder has distinct growth rings. A uniformly thick phloem cylinder surrounds the xylem cylinder. The pith features ridges and furrows that follow the shape of the xylem cylinder. In the pith portion, a secretory canal is present.

The periderm originated beneath a broken epidermis and consisted of a few layers of phellem and 2 or 3 layers of phelloderm. In a mature stem, the phellem is several layers in thickness, followed by an equal thickness of phelloderm. The phelloderm cells are thin-walled and possess dense tannin content. The cortical cells are angular, comprehensive, and compact. They are composed of calcium oxalate crystals and a circular secretary canal. The secondary phloem has compact radial lines of sieve elements and phloem parenchyma cells. The phloem also consists of small, circular, solitary sclereids.

The phloem elements are regular long radial lines in the medullary portion. Additionally, there is a prominent cylinder of medullary or pith phloem. The medullary phloem also features sclereids. The secondary xylem cylinder is wavy in outline. It consists of 2 or 3 distinct growth rings. The vessels are equal in diameter in the initial region of the growth rings.

The vessels at the end of the growth ring have a larger diameter. This type of vessel distribution pattern is called diffused porus. The wood comprises angular, thick-walled solitary vessels or radial multiples of 2 or 3 vessels. The vessel wall is thick and lignified. The xylem rays are thin and straight, with one cell in thickness. Horizontal lines distribute the xylem parenchyma cells, each with a single cell thickness.

- **3.3.2.2.3. Flower**

The flower in the cross section displays five gamopetalous corollas. The petals are imbricate in aestivation. The petals are thick in the middle and gradually become thin and linear towards the margin. There are wide circular secretory cavities in the petals. The cavities hold a greenish liquid. The petals are 400 µm thick in the middle, and at the extreme margins, they are 10 µm thick. The petals consist of thin,

rectangular epidermal cells. The mesophyll tissue is enclosed by small, loosely arranged spherical cells in the outer part and angular, compact cells in the inner part. The anthers are dithecous and four-chambered. The anther wall consists of a thin layer of anticlinal and radially elongated wide radial walls. The anther chamber encloses numerous pollen grains. The pollen grains are 4-angled with a thick, smooth exine cell layer. The pollen grains are 10 µm in diameter.

The fruit is a thick berry. It consists of the thin layer of epicarp and thick parenchymatous loosely arranged mesocarp cells. There are two ovules, and the ovary has two chambers. The ovules are attached to the median transverse partition septum. The mesocarp of the fruit consists of circular compact parenchyma cells in the outer region. There are also circular secretory cavities in the outer parenchymatous region. In the inner zone of the mesocarp, prominent vascular strands are distributed randomly. The vascular strands are circular, with several central polygonal xylem elements surrounded by discontinuous masses of phloem elements. The inner part of the mesocarp has small, lobbed parenchyma cells, which form a vast and irregular air chamber. The innermost part of the mesocarp has 2 or 3 thick-walled compact layers of cells. The fruit consists of a central partition with one seed in each chamber. In the transcetional view, the seeds appear semi-circular with highly stained parenchyma cells.

- **3.3.2.2.4. Bark**

The periderm is thick, measuring 300 µm thick. The phellem cells are rectangular and occur in compact radial lines. Some of the radial cells are wider than neighbouring cells. The phellem cells are thick, suberised walls. Phelloderm is very narrow and consists of a few phelloderm cells derived from the phellogen layer of the periderm. The periderm cells are in compact radial rows. The tangential wall of the phellem is thicker than the radial walls. The phelloderm cells have semi-circular, thickening on the inner tangential wall. The phelloderm cells are very few and have the characteristic tangential wall thickening.

The secondary phloem, located inner to the periderm, comprises darkly stained and dilated phloem rays, scattered circular masses of sclereids, and sieve elements. The phloem rays are dark and somewhat wavy. Sclereids and sieve elements are present in between the rays. The phloem parenchyma cells possess large, prominent calcium oxalate druses. The druses containing parenchyma cells are seen in regular lines. The dilated ray cells also contain druses. The sieve elements are rectangular and thick-walled. They occur in compact layers. The companion cells are small and occur at the corner of the sieve elements.

- **Tangential Longitudinal Section (T.L.S.)**

The phloem rays appear as long, thin, straight, elliptical lines in T.L.S. views. The middle part of the ray is dilated, and the ends of the ray are tapered into thin and pointed ends. The rays are very dark due to the accumulation of tannin. The phloem parenchyma cells occur in vertical strands parallel to phloem rays. The parenchyma cells are wide and barrel-shaped. Some of the parenchyma cells possess large druses. Each parenchyma cell contains only one druse. The druses also occur in the phloem rays. The druses are in compact vertical rows in the ray cell.

- **Radial Longitudinal Section (R.L.S.)**

In the R.L.S. view, the rays are seen in horizontal ribbon-shaped layers. The ray cells are densely tanniferous. The ray cells are thin-walled and may be squarish or rectangular. Some of the ray cells in the middle part of the ray are tangentially elongated and rectangular. These cells are called procumbent cells. The cells at the upper and lower ends of the ray are vertically elongated and rectangular. These cells are called upright cells. Because of the presence of two types of cells, the rays are called heterocellular.

- **3.3.2.2.5. Wood**

The wood is porous (vessels). Pores are circular, elliptical, and in radial multiples of 2 or 3 vessels. Growth rings are not evident. The wood is diffuse in distribution. The vessels have thick lignified walls. The diameter of the vessels varies

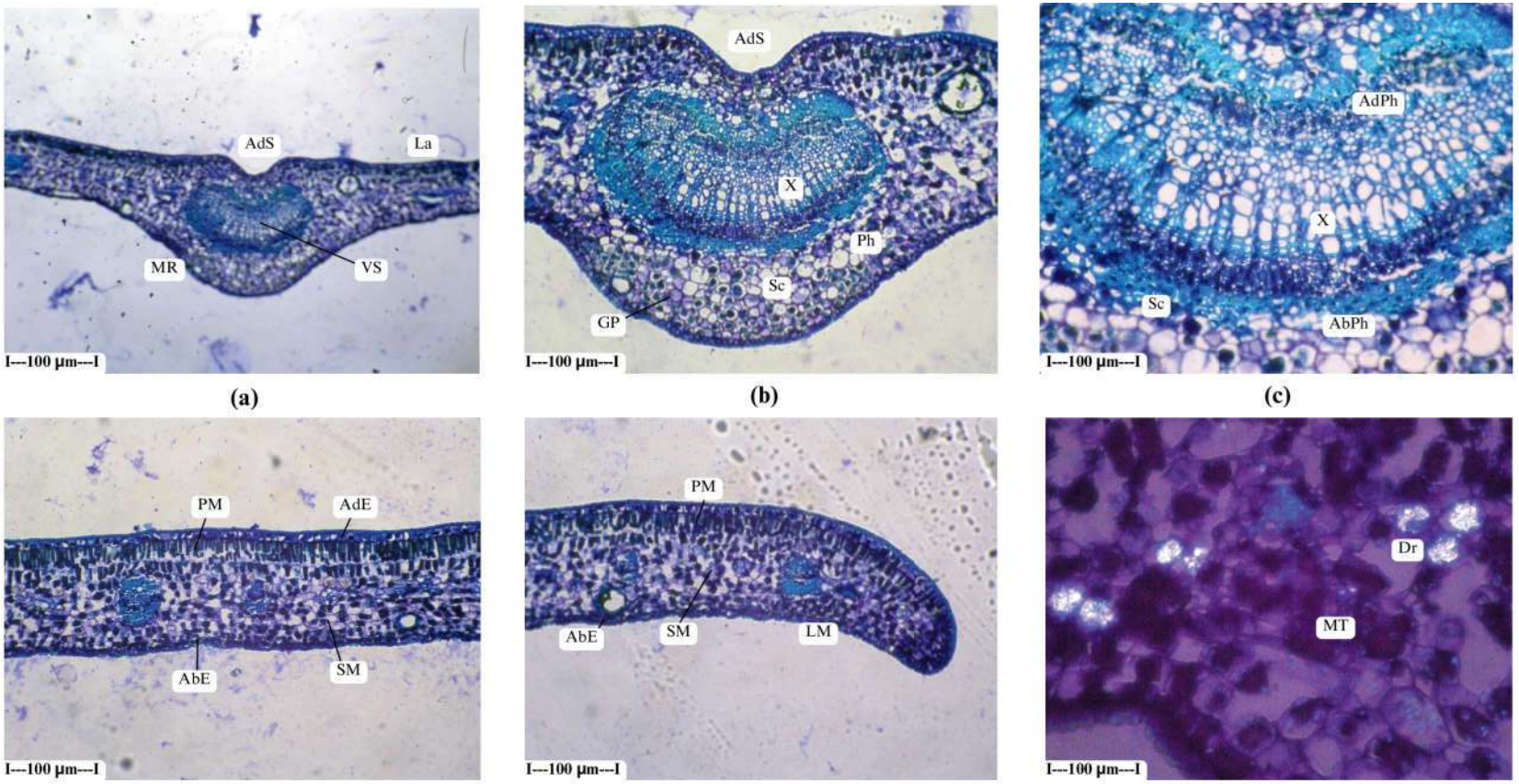


Plate 3.12: Anatomical features of *Syzygium occidentale* leaves: (a) T.S. of leaf through midrib (b) T.S. of midrib enlarged (c) Vascular system of the midrib enlarged (d) T.S. of lamina (e) T.S. of leaf margin (f) Mesophyll tissue of the leaf showing the presence of a crystal druse

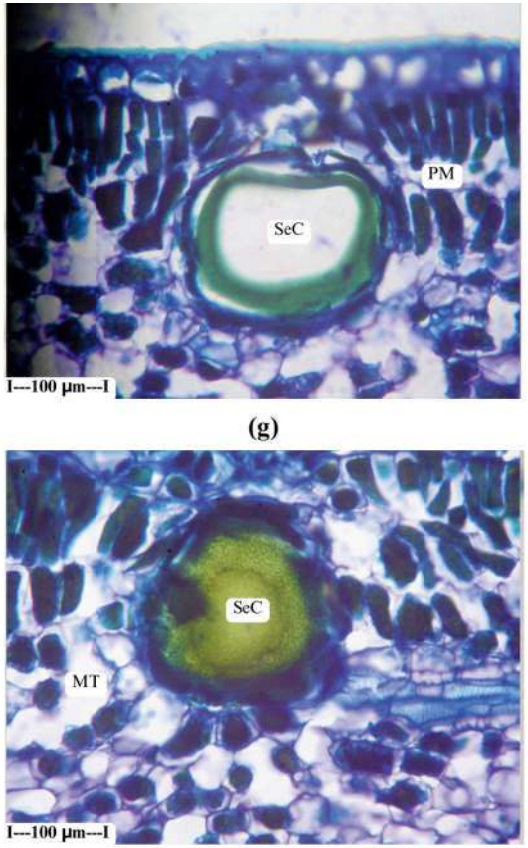


Plate 3.12: Anatomical features of *Syzygium occidentale* leaves: (g–h) T.S. of leaf showing a wide circular secretory cavity (T.S.: Transverse section; AdS: Adaxial side; La: lamina; VS: Vascular strand; MR: Midrib; X: Xylem; Ph: Phloem; Sc: Sclerenchyma; GP: Ground parenchyma; AdPh: Adaxial phloem; AbPh: Abaxial phloem; PM: Palisade mesophyll; AdE: Adaxial epidermis; AbE: Abaxial epidermis; SM: Spongy parenchyma; LM: Leaf margin; Dr: druses; MT: mesophyll tissue; SeC: Secretory cavity)

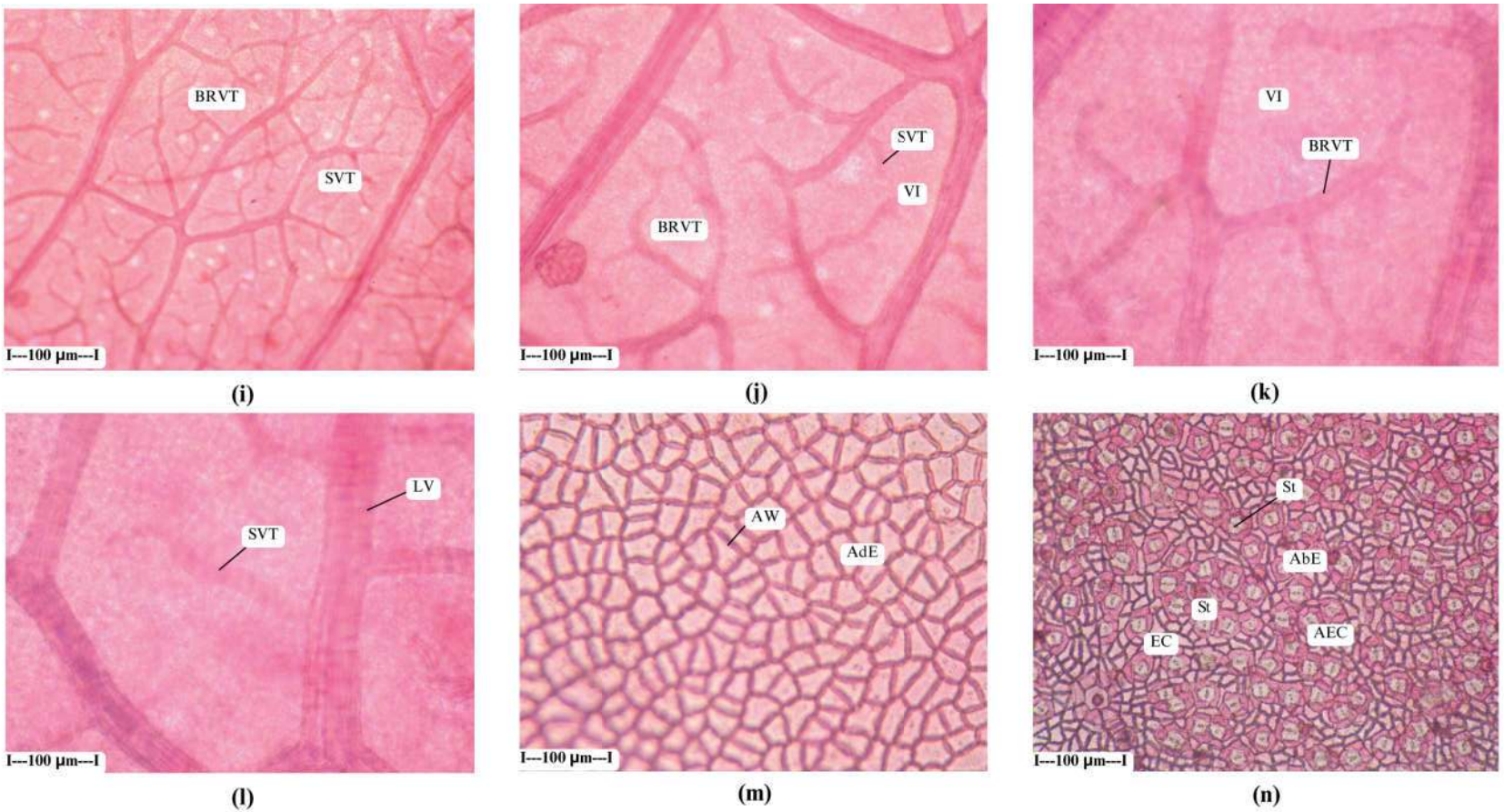


Plate 3.12: Anatomical features of *Syzygium occidentale* leaves: (i) Venation pattern of the lamina (j) Venation sharing vein islets, simple and branched vein termination (k-l) Venation showing branched and simple vein termination (m) adaxial epidermis in surface view (n) Abaxial epidermis showing stomata

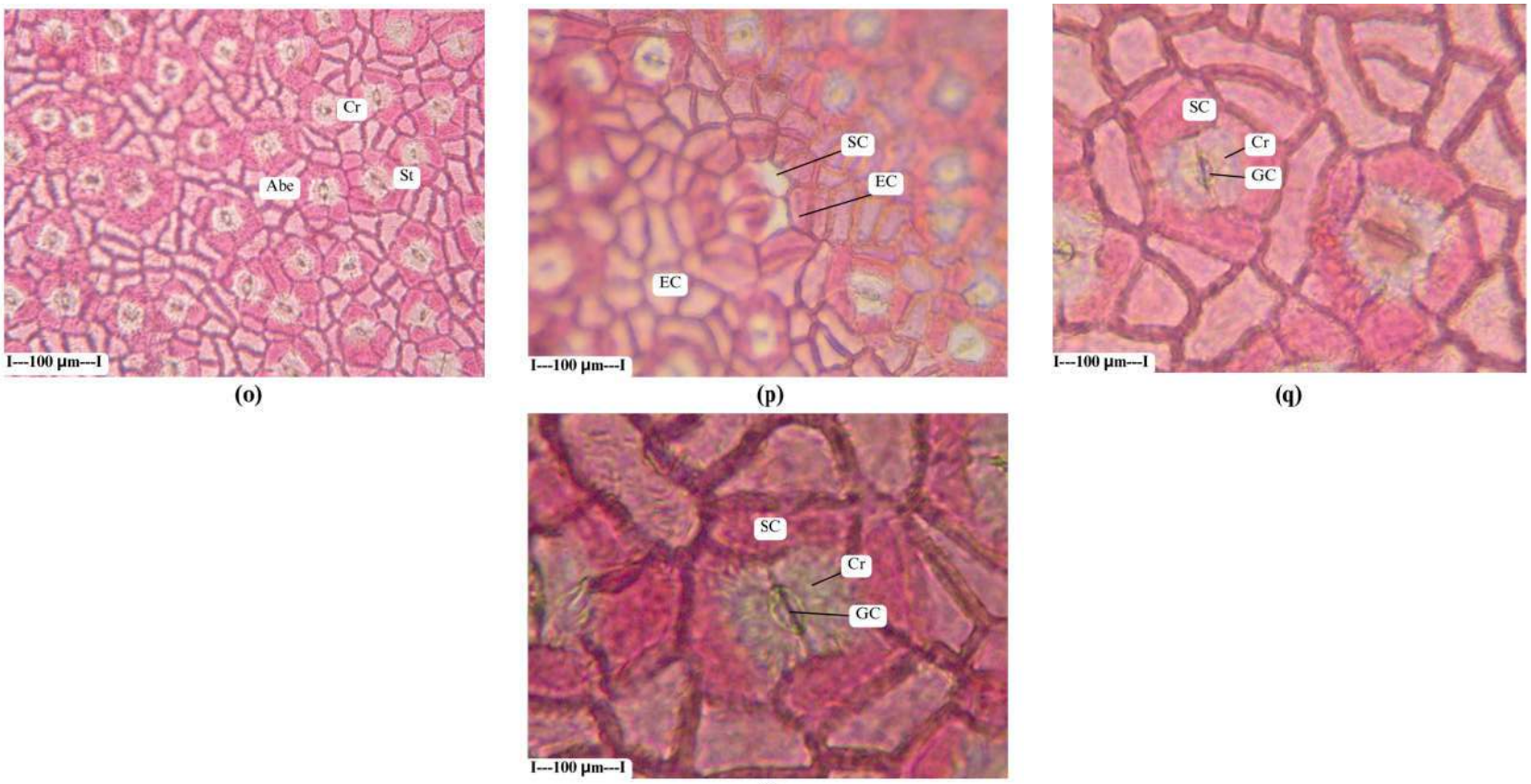


Plate 3.12: Anatomical features of *Syzygium occidentale* leaves: (o) Abaxial epidermis showing enlarged stomata (p) Abaxial epidermis showing a surface view of a cicatrix (q) Two stomata enlarged to show the guard cell and subsidiary cells (r) A single stoma enlarged showing guard cels, radiating calcium oxalate crystal from the guard cells

(BRVT: Branched vein termination; SVT: Simple vein termination; VI: Vein islet; LV: Lateral vein; AW: Anticlinal wall; AdE: Adaxial epidermis; St: Stomata; AbE: Abaxial epidermis; AEC: Abaxial epidermal cells; EC: Epidermal cells; Cr: crystal; SC: Subsidiary cells; GC: Guard cell)

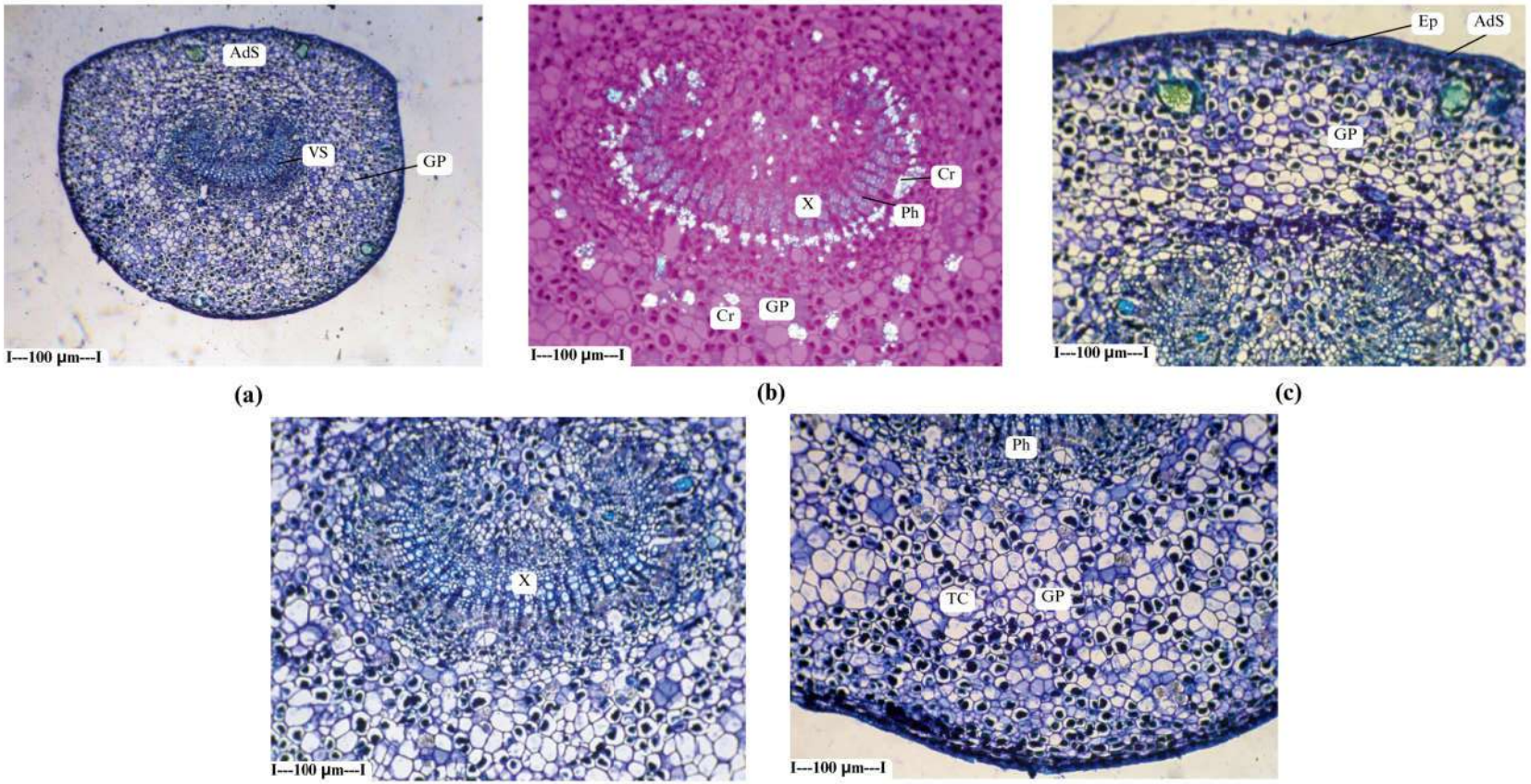


Plate 3.13: Anatomical features of *Syzygium occidentale* petiole: (a) T.S. of petiole, entire view (b) T.S. of petiole showing calcium oxalate crystal distribution as seen under polarized light (c-e) T.S. of petiole, enlarged, showing the vascular and ground tissue (T.S.: Transverse section; AdS: Adaxial side; VS: Vascular strand; GP: Ground parenchyma; Cr: Crystals; Ph: Phloem; X: Xylem; Ep: Epidermis; TC: Tannin cell)

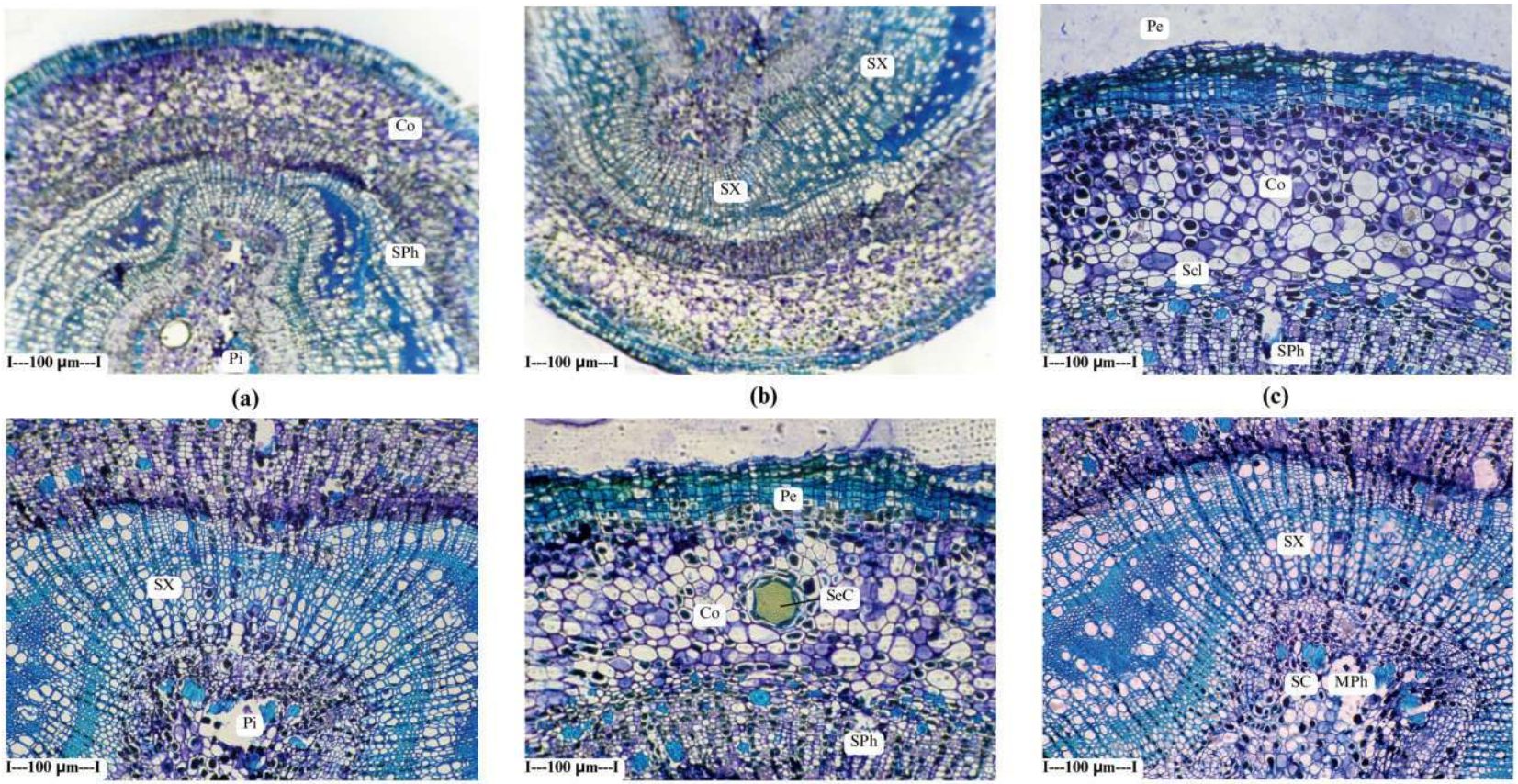
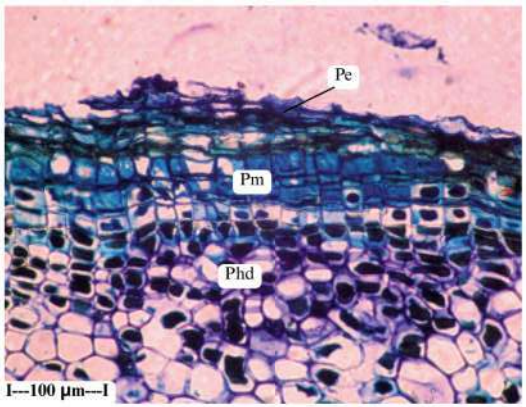
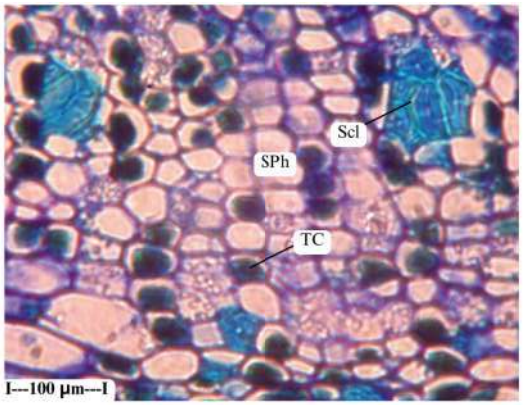


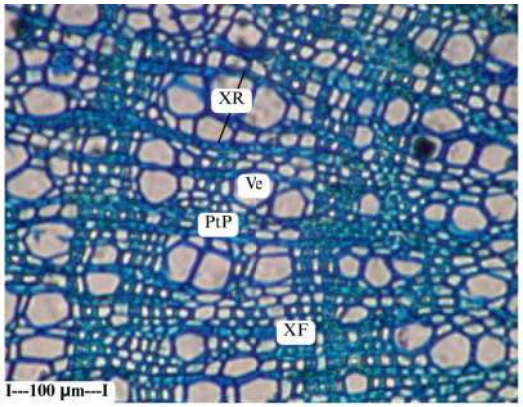
Plate 3.14: Anatomical features of *Syzygium occidentale* stem: (a–b) T.S. of stem, entire view (c–d) T.S. of stem, a sector enlarged (e-f) T.S. of stem, a sector further enlarged



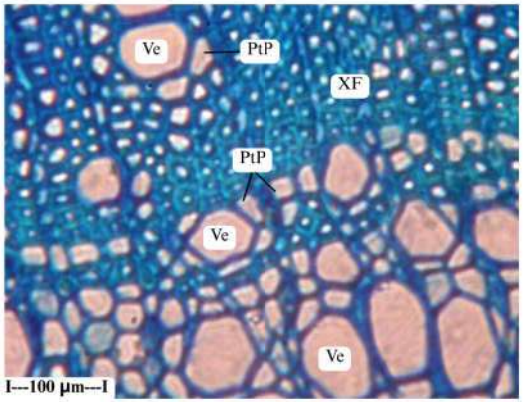
(g)



(h)



(i)



(j)

Plate 3.14: Anatomical features of *Syzygium occidentale* stem: (g-h) T.S. of stem showing the periderm and secondary phloem (i) Secondary xylem showing a growth ring (j) Vessels and fibres of the growth ring enlarged
(T.S.: Transverse section; Co: Cortex; SPh: Secondary phloem; Pi: Pith; SX: Secondary xylem; Pe: Periderm; Scl: Sclereids; SeC: Secretory cavity; SC: Sclereids; MPh: Medullary phloem; Pm: Phellem; Phd: Phelloderm; TC: Tannin content; XR: xylem ray: Ve: Vessel; PtP: Paratracheal parenchyma; XF: Xylem fibre)

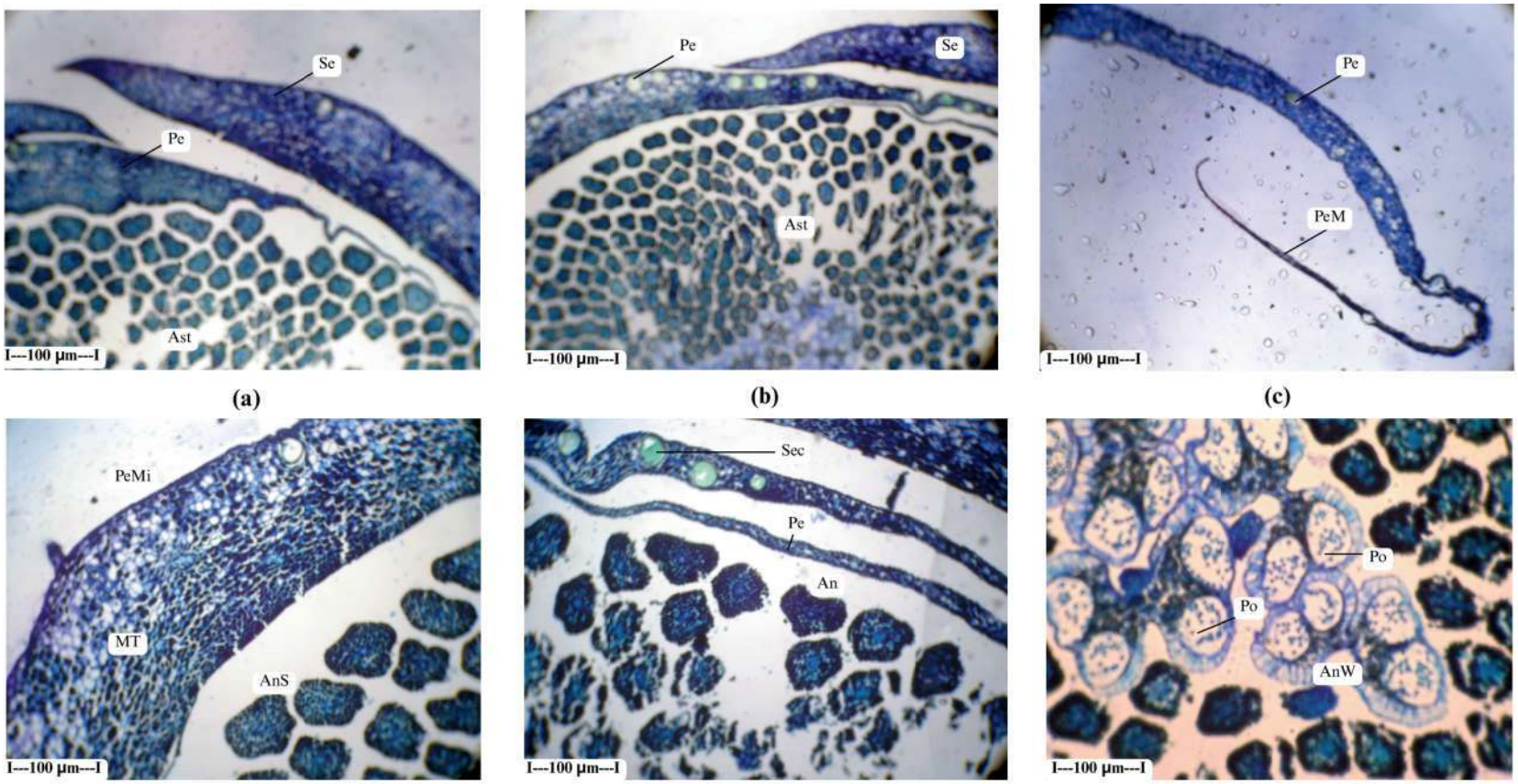
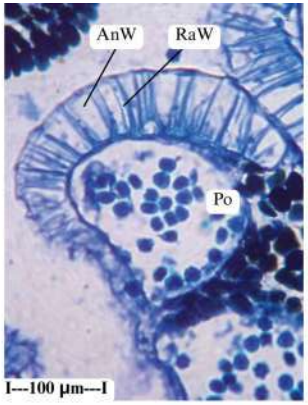
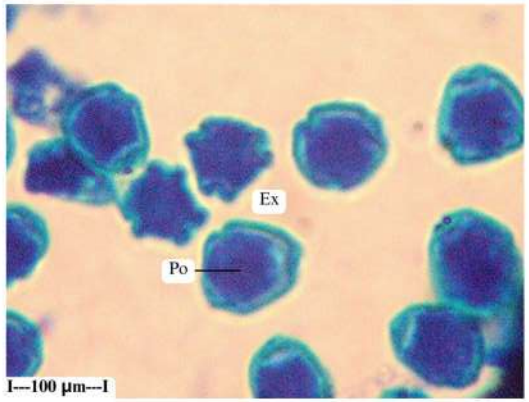


Plate 3.15: Anatomical features of *Syzygium occidentale* flower: (a-b) T.S. of flower showing outer sepal, inner petal, and filaments of the anther (c) A petal with middle part and thin marginal part (d) Middle part of the petal enlarged (e) Marginal tapering part of the petal enlarged (f) T.S. of anther showing pollen chamber and pollen



(g)



(h)

Plate 3.15: Anatomical features of *Syzygium occidentale* flower: (g) A pollen chamber with pollen enlarged (h) Pollen grains enlarged (T.S.: Transverse section; Se: Sepal; Pe: petal; Ast: Anther of stamen; PeM: Petal margin; PeMi: Petal middle part; MT: Mesophyll tissue; AnS: Anther of the stamen; Sec: Secretory cavity; An: Anther; Po: Pollen; AnW: Anther wall; RaW: Radial wall; Ex: Exine)

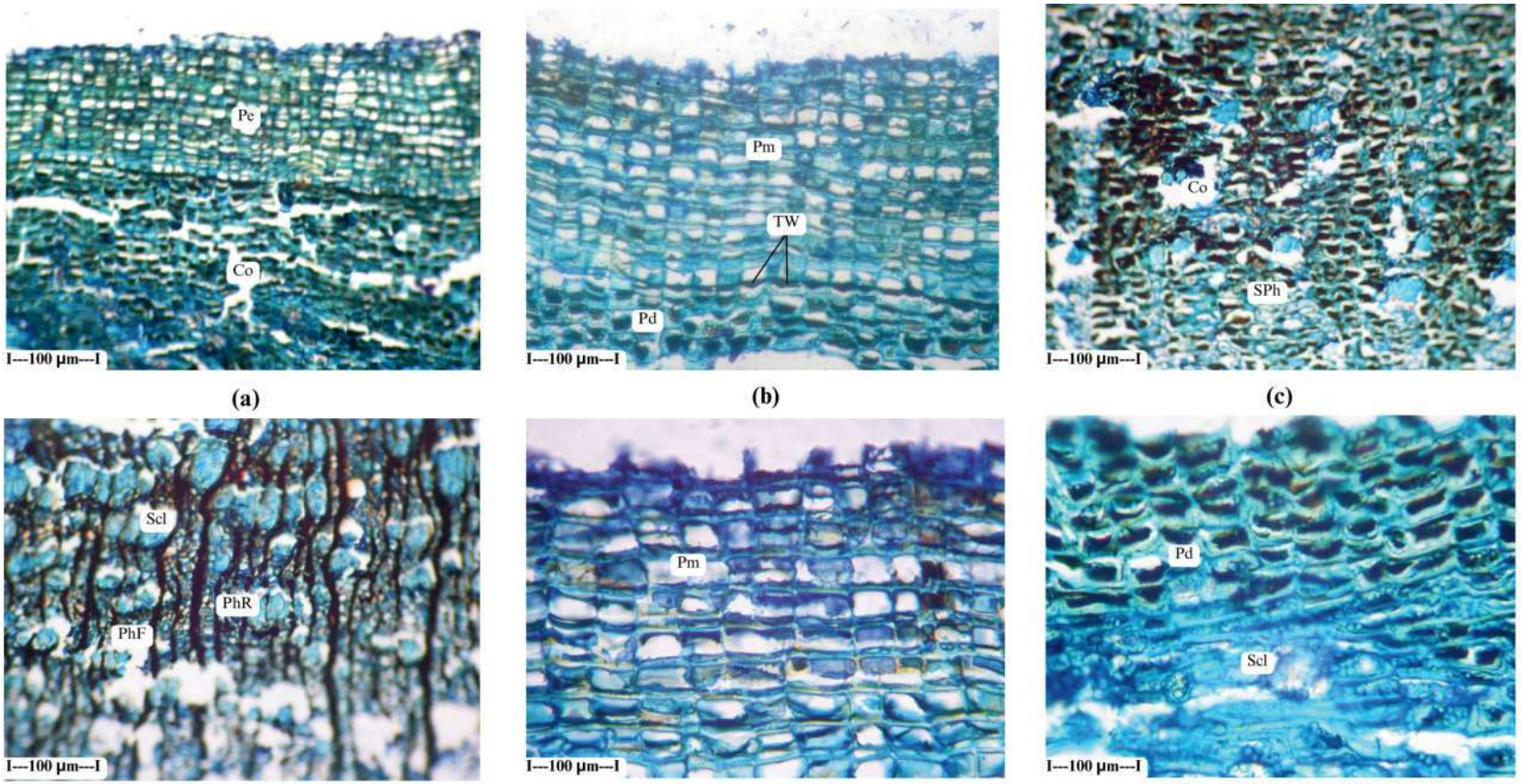


Plate 3.16: Anatomical features of *Syzygium occidentale* bark: (a) T.S. of bark showing phellem, periderm, and cortex (b) Horizontal lines of phloem ray enlarged (c) T.S. of bark showing cortical zone and secondary phloem (d) T.S. of secondary phloem showing darkly stained rays, isolated scattered group of sclereids, and phloem elements (e) T.S. of bark showing outer phellem cells (f) T.S. of bark showing inner phelloderm cells

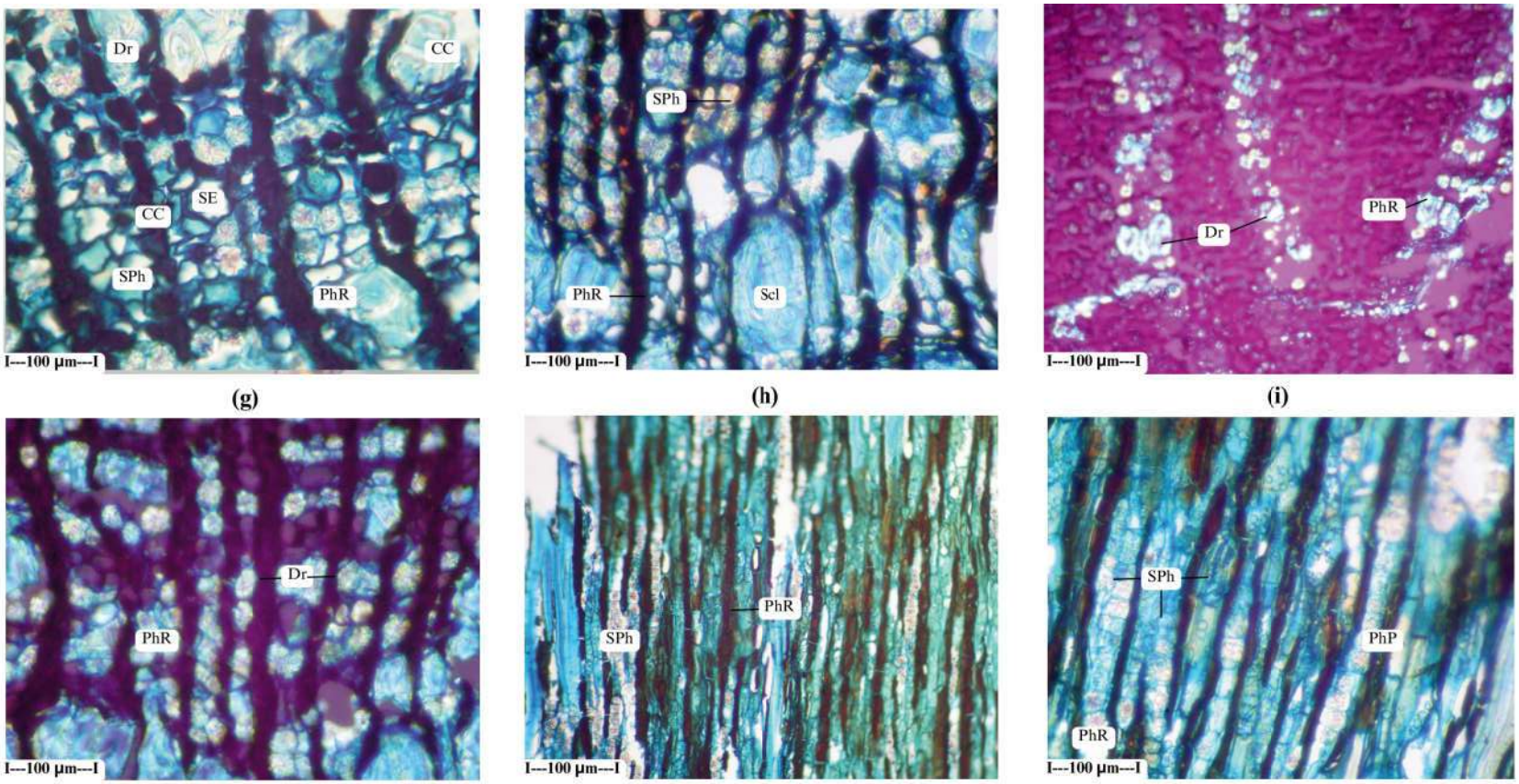


Plate 3.16: Anatomical features of *Syzygium occidentale* bark: (g) T.S. of secondary phloem showing darkly stained sieve elements and druses on the phloem parenchyma (h) T.S. of secondary phloem showing brachy sclereids, sieve elements and parenchyma showing druses (i) Dialted phloem rays possessing calcium oxalate druses as seen under polarized light (j) Secondary xylem showing dark thin rays and phloem parenchyma cells possessing druses as seen under polarized light (k-l) T.L.S. of phloem showing uniseriate and multiseriate phloem rays running parallel to each other

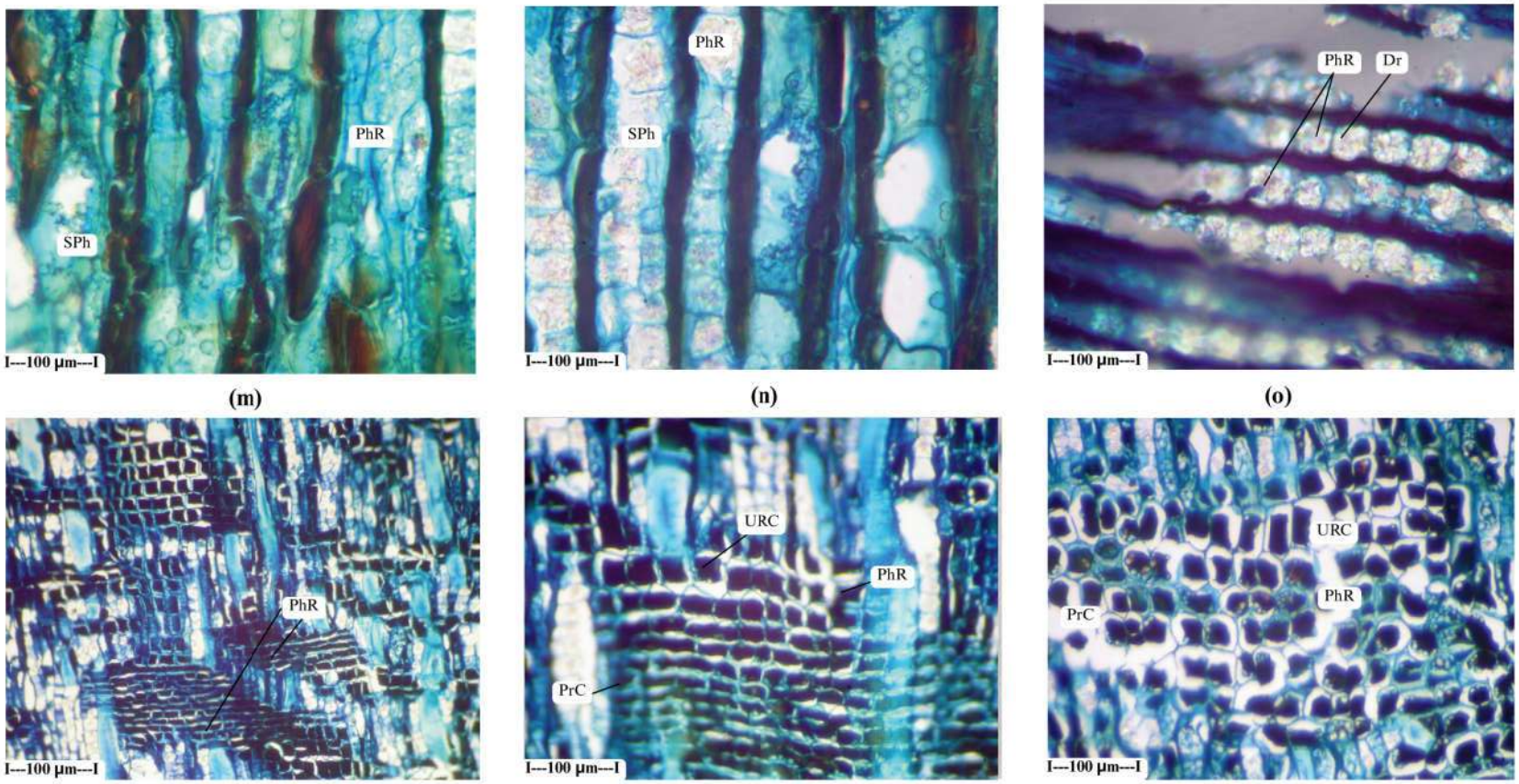
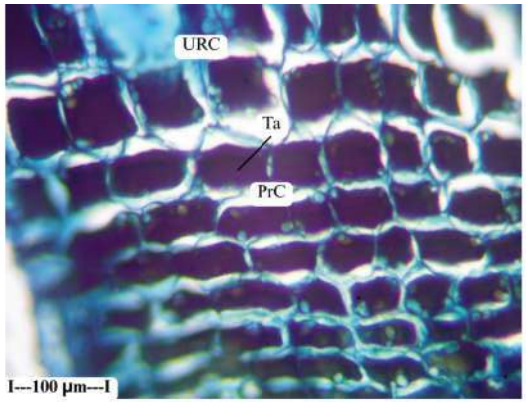


Plate 3.16: Anatomical features of *Syzygium occidentale* bark: (m) Phloem rays and phloem parenchyma (n) Phloem rays and phloem parenchyma with large druses (o) Phloem rays with vertical continuous distribution of calcium oxalate druses (p) R.L.S. of phloem showing horizontal ribbon shaped phloem rays (q) A phloem rays enlarged showing procumbent and upright cell (r) R.L.S. of ray showing procumbent and upright cell



(s)

Plate 3.16: Anatomical features of *Syzygium occidentale* bark: (s) Procumbent cell and upright cell of the enlarged
(T.S.: Transverse section; T.L.S.: Tangential longitudinal section; R.L.S.:Radial longitudinal section; Pe: Periderm; Co: Cortex; Pm: Phellem; TW: Tannin wall; Pd: Phelloderm; SPh: Secondary phloem; Scl: Sclereids; PhR: Phloem ray; PhF: Phloem fibre; Dr: Druses; SE: Sieve elements; CC: Companion cells; SPh: Secondary phloem; PhP: Phloem parenchyma; URC: Upright cells; PrC: Procumbent cells; Ta: Tannin)

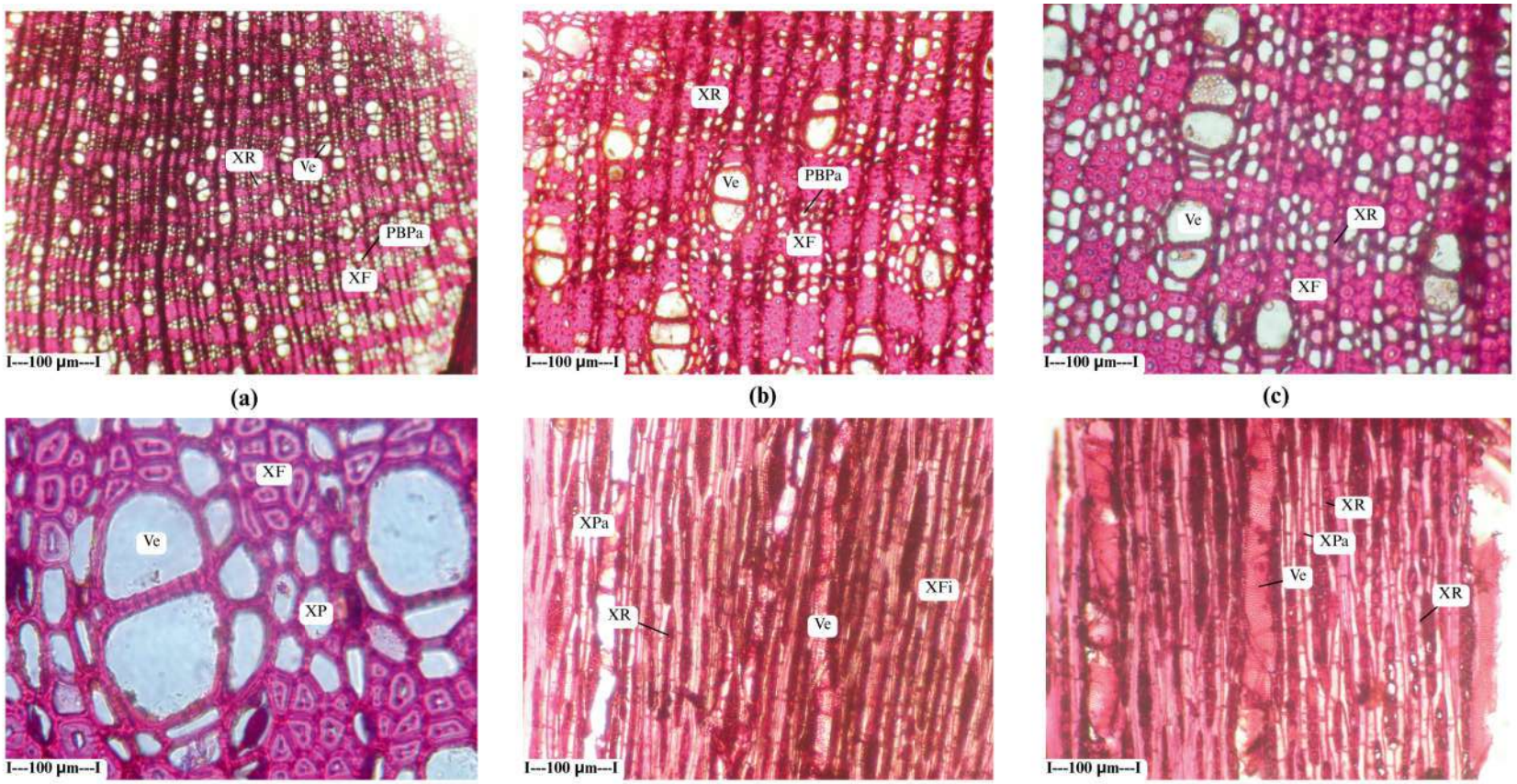


Plate 3.17: Anatomical features of *Syzygium occidentale* wood: (a) T.S. of wood under low magnification (b) A portion of the secondary xylem showing vessel distribution and parenchyma pattern (c) T.S. of wood showing vessel paratracheal parenchyma and banded fibres (d) T.S. of secondary xylem showing vessels and sclerenchyma (e) T.L.S. of xylem showing xylem rays under low magnification (f) T.L.S. of xylem showing xylem rays and vessel line

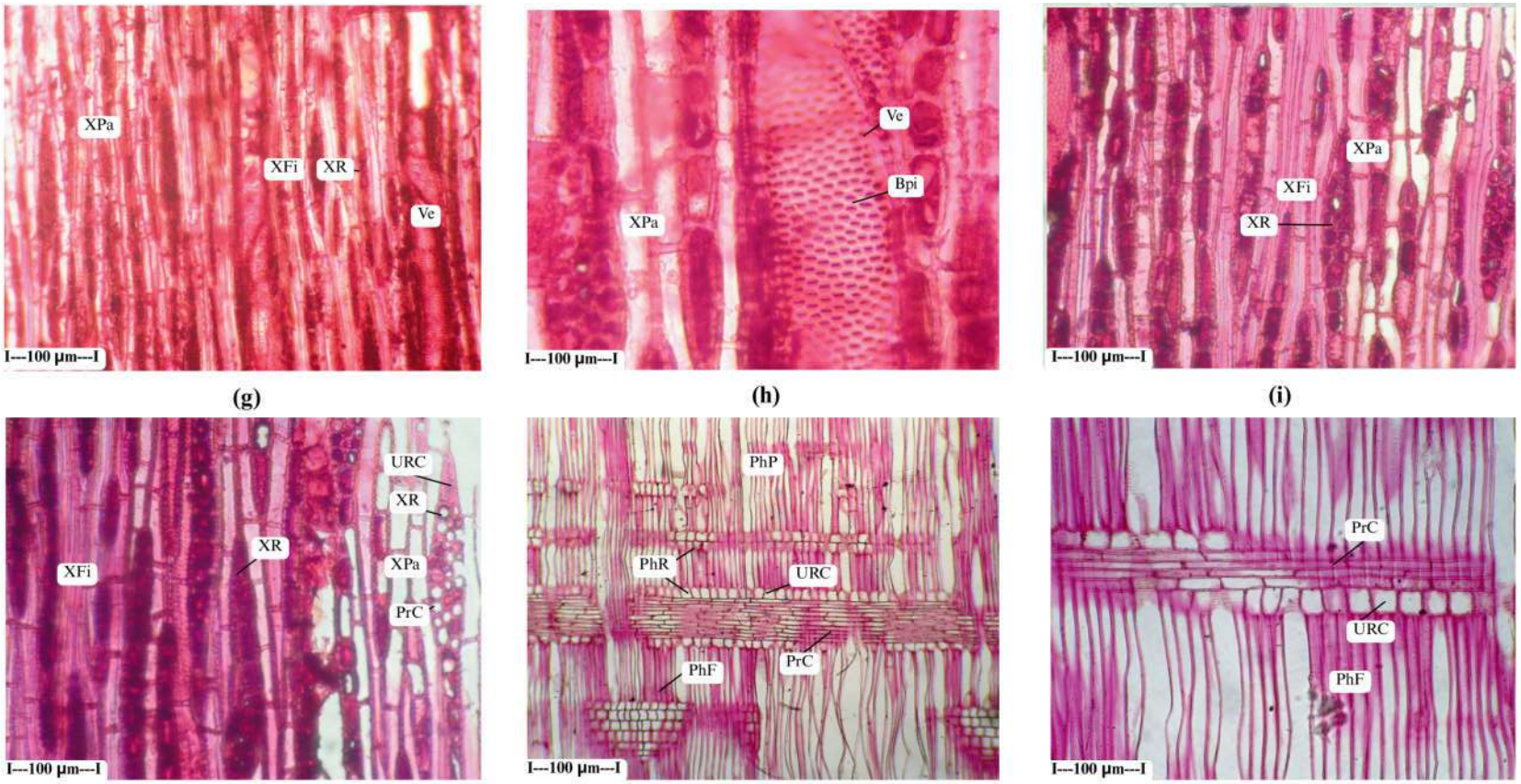
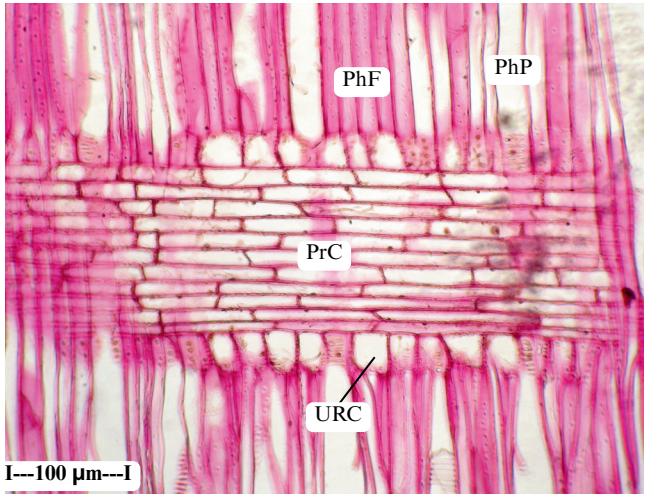
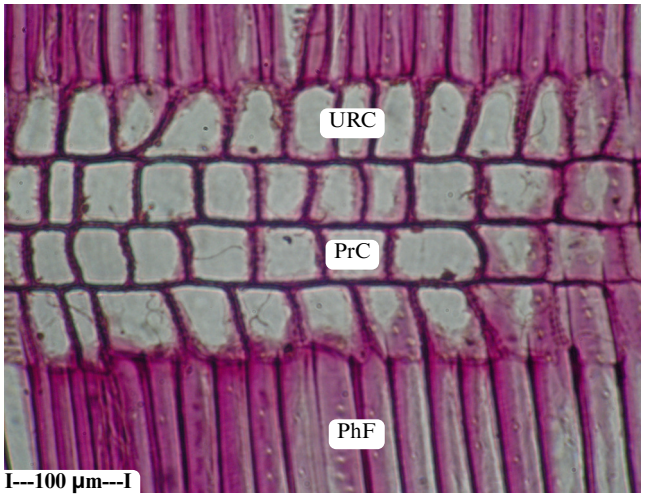


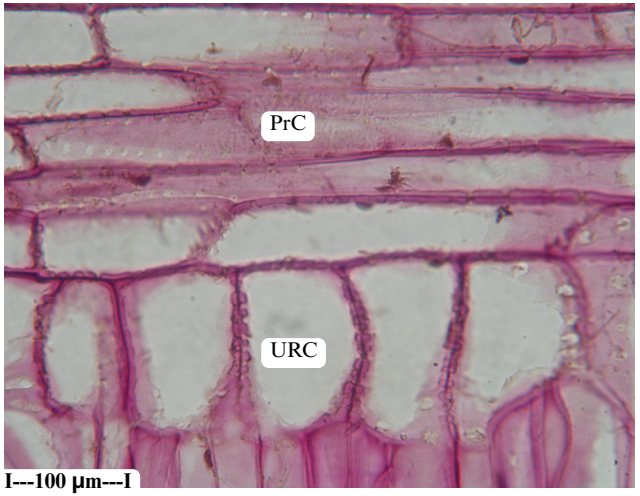
Plate 3.17: Anatomical features of *Syzygium occidentale* wood: (g) T.L.S. of xylem showing xylem ray, vessels, xylem fibres, and xylem parenchyma (h) T.L.S. of xylem showing xylem parenchyma and lateral wall pits of a vessel (i) T.L.S. of xylem showing xylem parenchyma, xylem fibres and xylem rays (j) T.L.S. of xylem showing heterocellular ray, xylem ray and xylem fibres (k-l) R.L.S. of phloem showing horizontal ribbon shaped ray with procumbent and upright cell



(m)



(n)



(o)

Plate 3.17: Anatomical features of *Syzygium occidentale* wood: (m) A radial ray enlarged showing procumbent cells, phloem parenchyma, phloem fibre and upright cells (n) T.S. of wood showing phellem, periderm, and cortex (o) Horizontal lines of phloem rays enlarged (T.S: Transverse section; XR: Xylem ray; Ve: Vessel; PbPa: Paratracheal branded parenchyma; XF: Xylem fibres; XP: Xylem parenchyma; XPa: Xylem parenchyma; XFi: Xylem fibres; BPi: Bordered pits; URC: Upright cells; PrC: Procumbent cells; PhP: Phloem parenchyma; PhR: Phloem rays; PhF: Phloem fibres)

from 40 to 100 μm in diameter. The xylem parenchyma is abundant, and the cells are broad. They are radially elliptical in outline and are thick-walled. The distribution of parenchyma is paratracheal banded. Thick tangential bands of parenchyma cells occur while crossing the wood. The vessels are enclosed by the parenchyma cells. The wood fibres are thick tangential bands alternating with parenchyma bands. The fibres have thick, lignified walls. Xylem rays are thin and travel in straight radial lines. The rays are also thick-walled.

➢ **Tangential Longitudinal Section (T.L.S.)**

In the T.L.S. view, the length and breadth of the xylem rays, vertical elements like xylem parenchyma, and xylem vessels are visible. These xylem rays are uni or multiseriate, spindle-shaped, and vertically elongated. The ray cells are thick-walled and lignified. The rays are non-storied at different levels. The ray consists of two types of cells. The cells in the middle of the ray are circular and horizontally rectangular. These cells are called procumbent cells. The cells on the upper and lower ends of the ray are vertically elongated and are called upright cells. The rays comprising two types of cells are called heterocellular rays.

- **Xylem parenchyma**

The parenchyma cells are in vertical strands. They are vertically elongated, thick-walled cells arranged one below the other. The parenchyma cell wall has dense, simple pits on the lateral walls, which appear bent.

- **Xylem fibres**

They are vertical elements running parallel to the rays and parenchyma cells. These cells are very thick and lignified. The fibre has a cross-septa, which is called septate fibre. The lateral walls of the vessels have dense multiseriate compact pentagonal-bordered pits. The vessels are 100 μm in length.

- **Radial Longitudinal Section (R.L.S.)**

The xylem rays appear in a horizontal ribbon-like structure in the R.L.S. view. The rays consist of tangential elongated compact narrow cells in the middle of the ray. On the upper and lower ends of the ray, there are vertically oblong rectangular erect cells called upright cells. The central horizontal, rectangular cells are called procumbent cells. The ray consists of two types of cells, mainly procumbent and upright cells, called heterocellular rays. The phloem parenchyma and phloem fibres occur in vertical lines at right angles to the rays. The parenchyma cells are wide and thin-walled. The fibres are narrow and thick-walled.

3.3.2.3. Anatomical features of *S. palghatense*

Plates 3.18 to 3.23 represent anatomical features of the *S. palghatense*

3.3.2.3.1. Leaves

The leaves of *S. palghatense* have plano-convex midrib and smooth lamina. The midrib is 600 µm on the vertical planar and 900 µm on the horizontal plane. The epidermal layer of the midrib has pyramid-shaped cells with prominent cuticles and undulate epidermis. Beneath the epidermal layer has four layers of small elliptical parenchymatous cells. 6-8 angular small compact cells present in the abaxial ground tissue. The vascular system occupies the major central zone of the midrib. It is a wide, shallow, bowl-shaped structure. The vascular strand consists of an arc of collateral xylem-phloem tissues, and the two margins of the arc curve towards the inner side. The xylem consists of wide, elliptical, thick-walled, lignified cells. Phloem occurs in continuous cylinders along with the lower parts of the xylem arch. The phloem elements have small, thick-walled, darkly stained phloem elements. A thick, continuous sheath of fibres covers the entire vascular system.

- **Lamina**

The lamina is dorsiventral with smooth, even surfaces and 450 µm in thickness. The adaxial epidermal layer is 50 µm thick. The cells are vertically oblong with a prominent cuticle. The abaxial epidermal cells are small, squarish, and the only

cuticularized. There is a subepidermal layer of cells similar to the adaxial epidermis. Beneath the adaxial epidermal layer is a single layer of short, thin, compact palisade cells. The spongy mesophyll tissue has several layers with different types of cells. The cells are loosely arranged to form wide air chambers. Wide, circular secretory cavities are sometimes seen in the mesophyll. The cavity is 100 µm in diameter and has small epithelial cells.

- **Epidermal tissue of the lamina**

The adaxial epidermal cells are polygonous in outline. Their anticlinal walls are thick and straight. The epidermis is apostomatic. The abaxial epidermis has polyhedral cells, and the cell walls are straight. The epidermis is stomatiferous. The stomata are random in distribution and orientation. The stomata are oblong, 20 x 10 µm in size. The stomata are tetracyclic/pentacyclic (cyclocytic). A stoma is ensheathed by 4/5 elongated, rectangular subsidiary cells. Some epidermal cells are modified into wide, circular, thick-walled cells. These cells are the basal cells bearing the epidermal trichomes. The epidermal cells are surrounded by several radiating rectangular cells called rosette cells. The entire structure is called a cicatrix. Calcium oxalate crystals are seen deposited all along veins. The crystals are columnar and usually have more than one flat face, giving them the appearance of a prism called prismatic type crystals. The individual prismatic crystals are located in each cell, and they are in a vertical row.

- **Leaf margin**

The marginal parts of the leaf become gradually thin, terminating into a semicircular tip. The marginal part is 200 µm thick. The epidermal cells of the marginal portions are slightly enlarged and become thick-walled. The cuticular layer is also thicker. There is no differentiation of mesophyll tissue into palisade and spongy parenchyma. The submarginal part of the lamina consists of a compact mass of small, squarish, thick-walled cells. Small vascular strands are seen in the marginal parts.

- **Leaf venation**

The venation of the leaf was dense and reticulate, with repeated branching of the veins. The branching veins form wide closed spaces called vein islets. The vein islets vary in shape and size. Within the islets, small ultimate veins are called vein terminations. The vein terminations are either simple or unbranched. The simple vein terminations arise from the inner part of the vein islets and remain straight or curved. The vein termination may also be branched twice or more times, appearing in dendroid outlines, and is seen within the islets without connection with the walls of vein islets. The branched vein terminations occupy the inner space of the vein islets.

- **Petiole**

The petiole was circular in C.S. view with shallow concavity on the adaxial side and short, thick lateral wings. The petiole is 1.4 mm in diameter. Epidermal cells of the petiole are small and semicircular with a smooth, thick cuticle. Ground tissue includes small radially arranged parenchyma cells; the cells farther inside are polygonal layers and compact. The vascular system is profoundly curved and bowl-shaped, and concavity is directed upward. The xylem arc consists of numerous fairly long lines of vessels with narrow intervals in between. The cells surrounding the vessel's lines are narrow, thick-walled, and lignified fibres. Phloem elements are small, thick-walled, and darkly stained. A discontinuous layer of thick-walled lignified fibres surrounds the entire vascular system. Wide circular cavities are seen in the ground tissue. The cavity is lined internally by a thin layer of epithelial cells. Calcium oxalate crystals and starch grains are abundant in the phloem tissue of the petiole. The crystals are rhomboidal/cuboidal/rectangular type. The second type of crystals seems to be spherical masses of prismatic crystals. Sometimes, large prismatic crystals are seen enclosed with small crystal masses. When viewed under polarized light, the starch grains are circular in different sizes with an X-shaped polarimark.

3.3.2.3.2. Stem

The stem is circular with deeply and irregularly fissured periderm. Inner to the heterogeneous periderm, the sclerenchymatous cortex is followed by the secondary

phloem and secondary xylem cylinder. The periderm is heterocellular, comprising alternating layers of suberized phellem cells and non-suberised thin-walled phelloid cells. Inner to the phelloid layer is the phelloderm zone, which consists of 3-7 layered and undulated cylinders. The phelloderm cells are small, thick-walled, and are in regular vertical lines. The cortical zone is vast, and it includes sclerenchymatous cells. The cells are small, angular, thick-walled, and comprehensive. Calcium oxalate prismatic crystals are seen inside the sclerenchymatous cells. The secondary phloem is a vast, continuous cylinder consisting of sieve elements, companion cells, and phloem parenchyma cells. The sclerenchyma cells are seen sparsely in the phloem. The secondary xylem is thick, comprising vessels, fibres, xylem rays, and xylem parenchyma. The parenchyma cells are characteristic of arrangements and occur in continuous successive cylinders. The parenchyma cylinder is arranged across the vessels. This type of arrangement is called paratracheal banded parenchyma. The vessels are primarily radial multi-cells of long or short rows or solitary. Xylem rays are thick, straight, rectangular, circular, small, and thick-walled. Xylem fibres are rectangular in sectioned view, the lumen is narrow, and the cells are lignified. The pit cells are circular, wide, and compact. Calcium oxalate crystals of prismatic type are sparsely seen in the pit cells. The crystals are folded, cuboidal/rhomboidal.

3.3.2.3.3. Flowers

L.S. shows a cylindrical ovary with a thick, long style. Ovules hang from the top of the ovary wall. C.S. through the upper region shows calyx tubes that enclose the style. The style is thick and circular. The sepal is thick with several layers of homogenous, angular, polyhedral, thin-walled, and compact parenchyma cells. Small, circular secretory cavities are distributed along the peripheral part of the sepal and style. The sepal and style epidermal cells have the outer median part of the cell wall to form a small dome with thick cuticles. The sepal consists of the outer epidermis, outer zone of cortical parenchymatous, middle zone aerenchyma of air chambers, partition filaments, and inner zone parenchyma with inner epidermis. Discrete bundles of fibres are arranged all around the inner boundary of the outer parenchyma of the sepal. The style is thick and circular with the central stylar canal. The cells of the style

are regularly arranged in compact radial lines. Around the stylar canal, about nine small vascular strands occur with narrow intervals between the strands.

3.3.2.3.4. Bark

The bark is broad with a rough and fissured surface: thick periderm, well-developed cortex, and wide secretory phloem. The periderm is 1200 µm thick. The phellem zone is 1050 µm thick, while the phelloderm region is 150 µm thick. The phellem zone is heterocellular in composition, and its primary type of cells are suberised and dead cells. The phellem region has about eight thin and thick layers of small cells with lignified walls. These lignified walls are called phelloid layers. Thus, the phellem region is a dead portion of the periderm and functions as a protective barrier against the invasion of microorganisms into the inner part of the bark. The inner zone of the periderm is the phelloderm. The phelloderm cells are the continuation of the radial seriation of phellem cells. However, phelloderm cells are non-suberised and non-liquified. They have cellulose walls, are living cells, and store ergastic substances. The cortical region follows the periderm. The cells of the cortex have branchy sclereids. The branchy sclereids are circular (spherical) cells with thick, liquified walls. These are wide, simple, or branched canal-like pits in the cell walls of these sclereids. The cell lumen of the sclereids is wide.

The secondary phloem is a significant component of the bark. It consists of sieve elements, phloem rays, phloem parenchyma, and phloem sclerenchyma. The sieve elements are wide and circular with thick primary walls. The sieve elements are 12 µm in diameter. The companion cells are wide and prominent. Usually, there will be only one companion cell for each sieve element. Occasionally, this may be two companion cells for a single sieve element. The secondary phloem is differentiated into two different zones, namely collapsed phloem and non-collapsed phloem. The collapsed phloem consists of crushed and collapsed sieve elements, seen as dark irregular spots. The phloem rays and phloem parenchyma cells are highly dilated, causing the sieve elements to be crushed and collapse. The parenchyma cells and phloem rays are not dilated in the non-collapsed phloem zone and remain normal.

- **Tangential longitudinal section (T.L.S.)**

In the T.L.S. view, the phloem rays are spindle-shaped, multiseriate, and long. These are uniseriate rays. The rays are 400 µm long and 100 µm wide. The cells in the middle part of the rays are circular or squarish in shape. These cells are called procumbent cells. The cells at the upper and lower ends of the rays are vertically elongated, called upright cells. Since the rays consist of two types of cells, they are heterocellular.

- **Radial longitudinal section (R.L.S.)**

In the R.L.S. view, the phloem rays are in a horizontal, flat, ribbon-shaped structure. The cells are thick-walled. Those cells in the middle of the rays are procumbent, and those along the upper and lower margins are upright cells.

- **Crystal distribution**

Calcium oxalate crystals are abundant in the phloem cells. They are prismatic and mostly cuboidal in shape. They occur in ray parenchyma cells, phelloderm cells, and marginal cells of the ray cells. The crystals are birefringent, and when viewed under polarised light, they appear bright against a dark background.

3.3.2.3.5. Wood

The *S. palghatense* wood has a fine to medium texture and smooth finish. It is a dense hardwood with decay-resistant and long-lasting properties. This wood does not distinguish between its early and late phases. The wood evenly distributes the diffused porous vessels. In the vessel elements, typical hardwoods have simple perforation plates. The libriform fibres, which provide structural support to the wood, are long and have thin walls. The moderate-thickness fibre wall gives density and hardness to the wood. The growth rings are indistinct.

- **Transverse Section (T.S.) of the wood**

In transverse sections, the wood exhibits different features of vessels, such as axial (vertical) parenchyma, fibres, and xylem rays. The vessels are circular or angular

in cross-section. There are both narrow and wide vessels. The narrow vessels are 40 μm in diameter, and the wide vessels are 90 μm in diameter. The distribution and arrangement of the vessels exhibit distinct characteristics. The majority of the vessels are seen in radial multiples ranging from 2 to 7 vessels. Short radial multiples are also common.

- **Xylem parenchyma**

Xylem (axial) parenchyma cells are abundant in the wood. The parenchyma cells are distributed in thick to wavy horizontal bands. This type of arrangement is called banded parenchyma. The parenchyma bands are profusely branched; as they pass in horizontal bands, they cross the vessels and get surrounded by the parenchyma cells. Such enclosing cells around the vessels are called paratracheal banded parenchyma.

- **Xylem rays**

The xylem rays are arranged in radial lines. They are one cell in thickness. The ray parenchyma cells are also lignified and thick-walled. The xylem fibres are in thick continuous cylinders. They are frequently traversed by xylem rays, breaking the fibre cylinders into large masses.

➢ **Tangential Longitudinal Sections (T.L.S.) of the Wood**

In the T.L.S. view, the xylem rays appear to uniseriate or partly multiseriate in the middle and uniseriate at the ends. The rays are spindle-shaped with uniseriate tails. Some of the rays are uniseriate from the upper and to the lower end. The ray cells are angular, compact, and thick-walled. The cells are upright, short, angular, procumbent, and in the ray's centre. The cells are of two different types and are known as heterocellular. The xylem parenchyma cells are vertically elongated cells arranged with parenchyma strands.

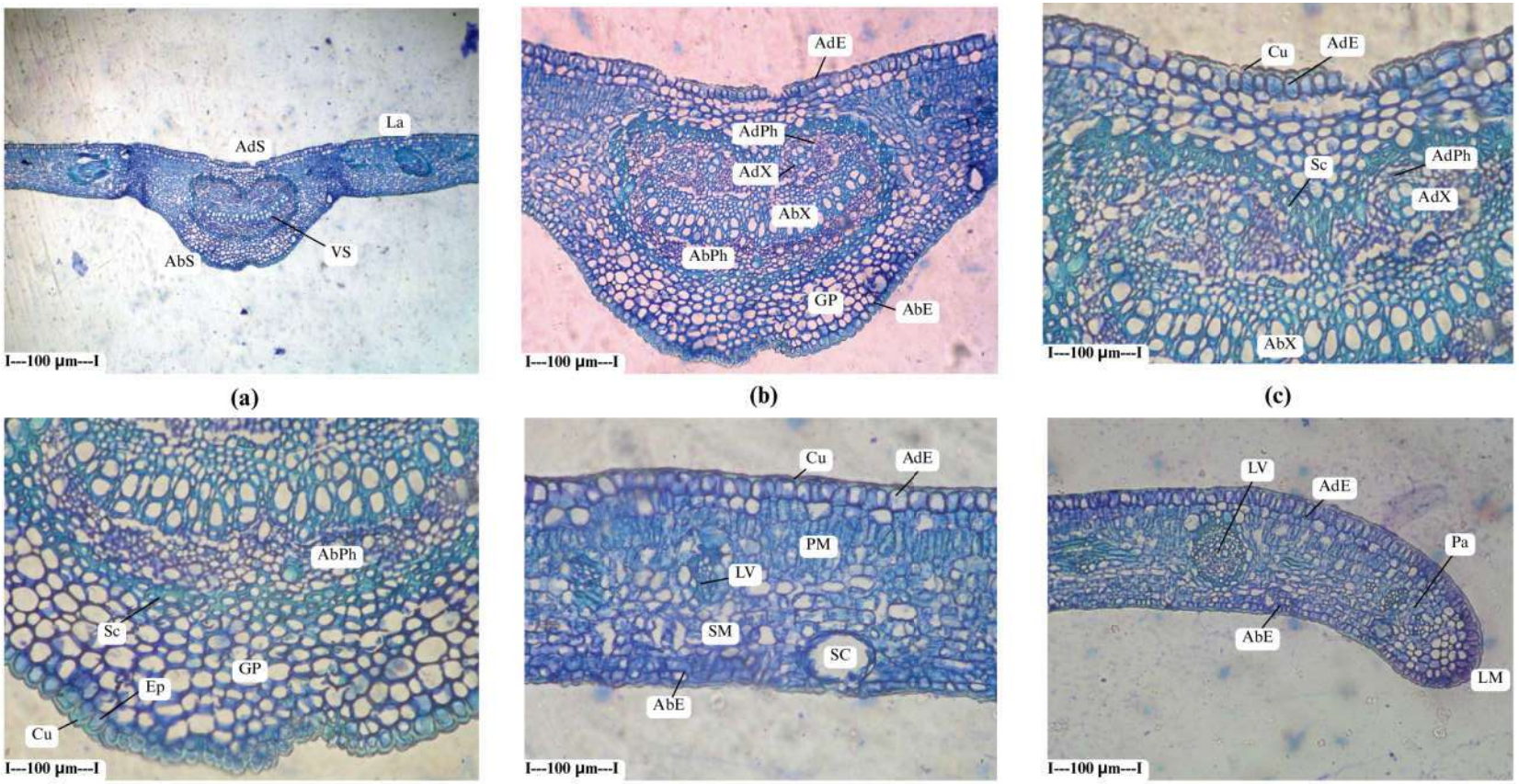


Plate 3.18: Anatomical features of *Syzygium palghatense* leaves: (a) T.S. of leaf through midrib (b) T.S. of midrib enlarged (c-d) Vascular bundle of the midrib enlarged (e) T.S. of lamina (f) T.S. of leaf margin

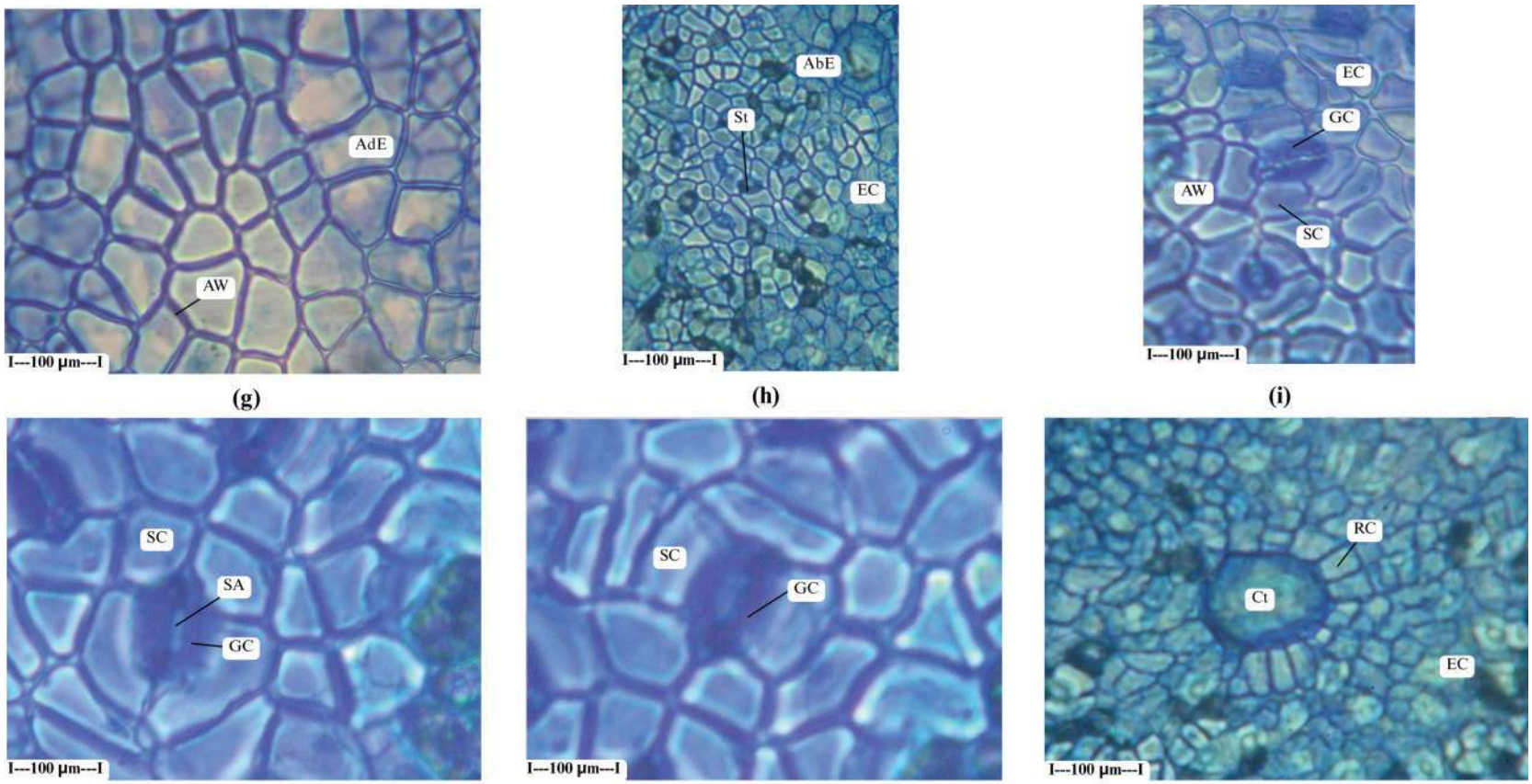
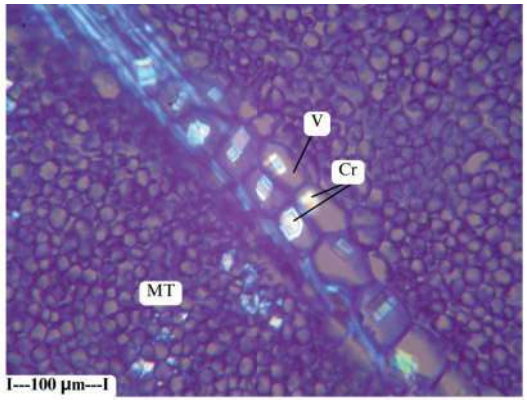


Plate 3.18: Anatomical features of *Syzygium palghatense* leaves: (g) Adaxial epidermis in surface view (h) Abaxial epidermis with stomata (i) Paradermal section of the leaf showing epidermal cells, subsidiary cells, and stomata (j-k) Single stoma enlarged (l) Epidermal tissue with cicatrix



(m)

Plate 3.18: Anatomical features of *Syzygium palghatense* leaves: (m) Calcium oxalate crystals in the cells of the vein in the lamina (T.S.: Transverse section; AdS: Adaxial side; La: Lamina; AbS: Abaxial side; VS: Vascular strand; AdE: Adaxial epidermis; AdPh: Adaxial phloem; AdX: Adaxial xylem; AbX: Abaxial xylem; AbE: Abaxial epidermis; Scl: Sclerenchyma; GP: Ground parenchyma; Cu: Cuticle; Ep: Epidermis; PM: Palisade mesophyll; LV: Lateral vein; SM: Spongy mesophyll; SC: Secretory cavity; Pa: Palisade mesophyll; LM: Leaf margin; AW: Anticlinal wall; St: Stomata; EC: Epidermal cells; GC: Guard cells; Sbc: Subsidiary cells; SA: Stomatal aperture; Ct: Cicatrix; RC: Rosette cells; V: Vein; Cr: Crystal; MT: Mesophyll tissue)

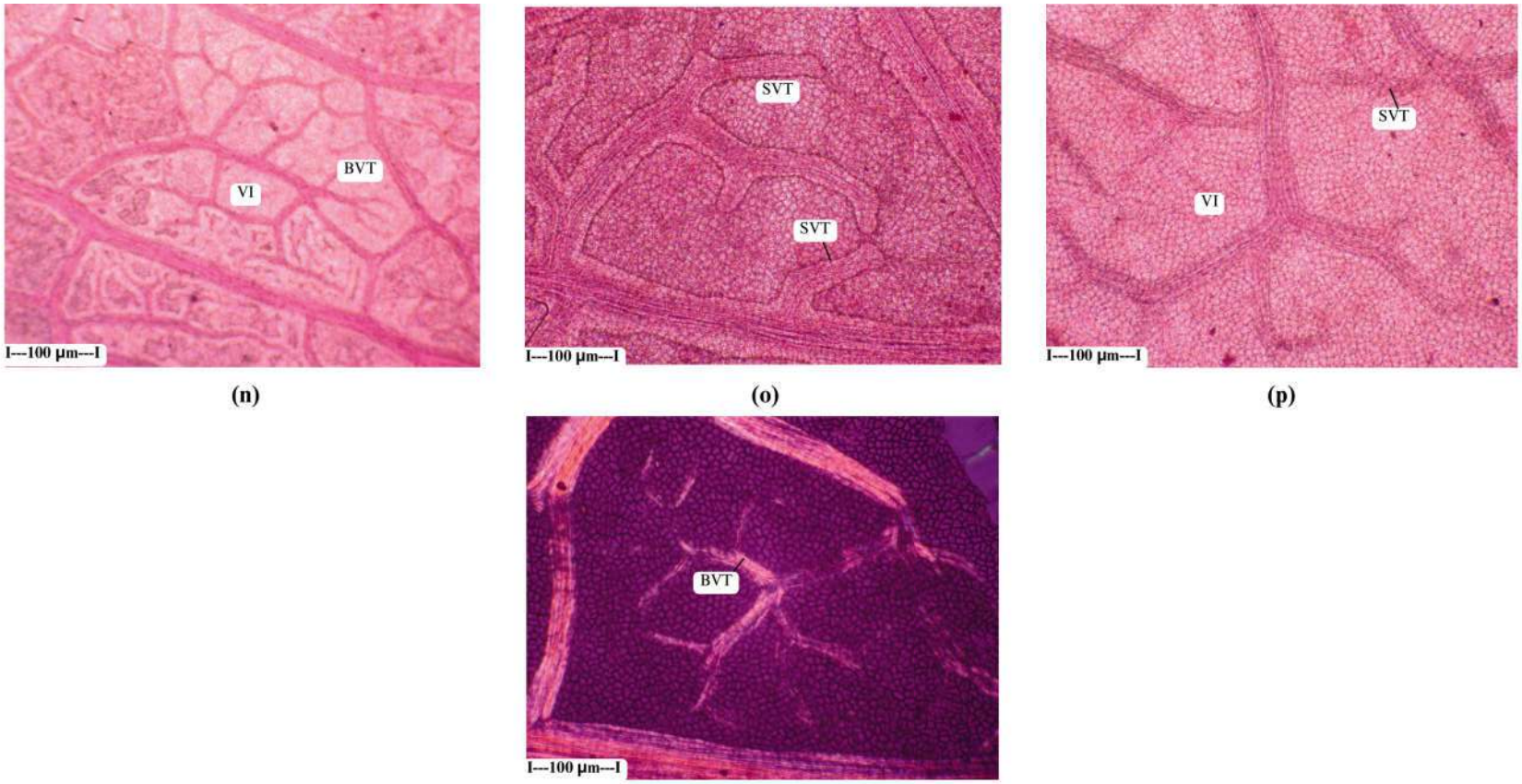


Plate 3.18: Anatomical features of *Syzygium palghatense* leaves: (n) Leaf clearing showing reticulate venation system with vein islets and branched vein termination (o) Leaf showing simple vein termination (p) Lamina showing vein islet and simple vein termination (q) Vein islet with branched vein termination as seen under polarized light
(VI: Vein islet; BVT: Branched vein termination; SVT: Simple vein termination)

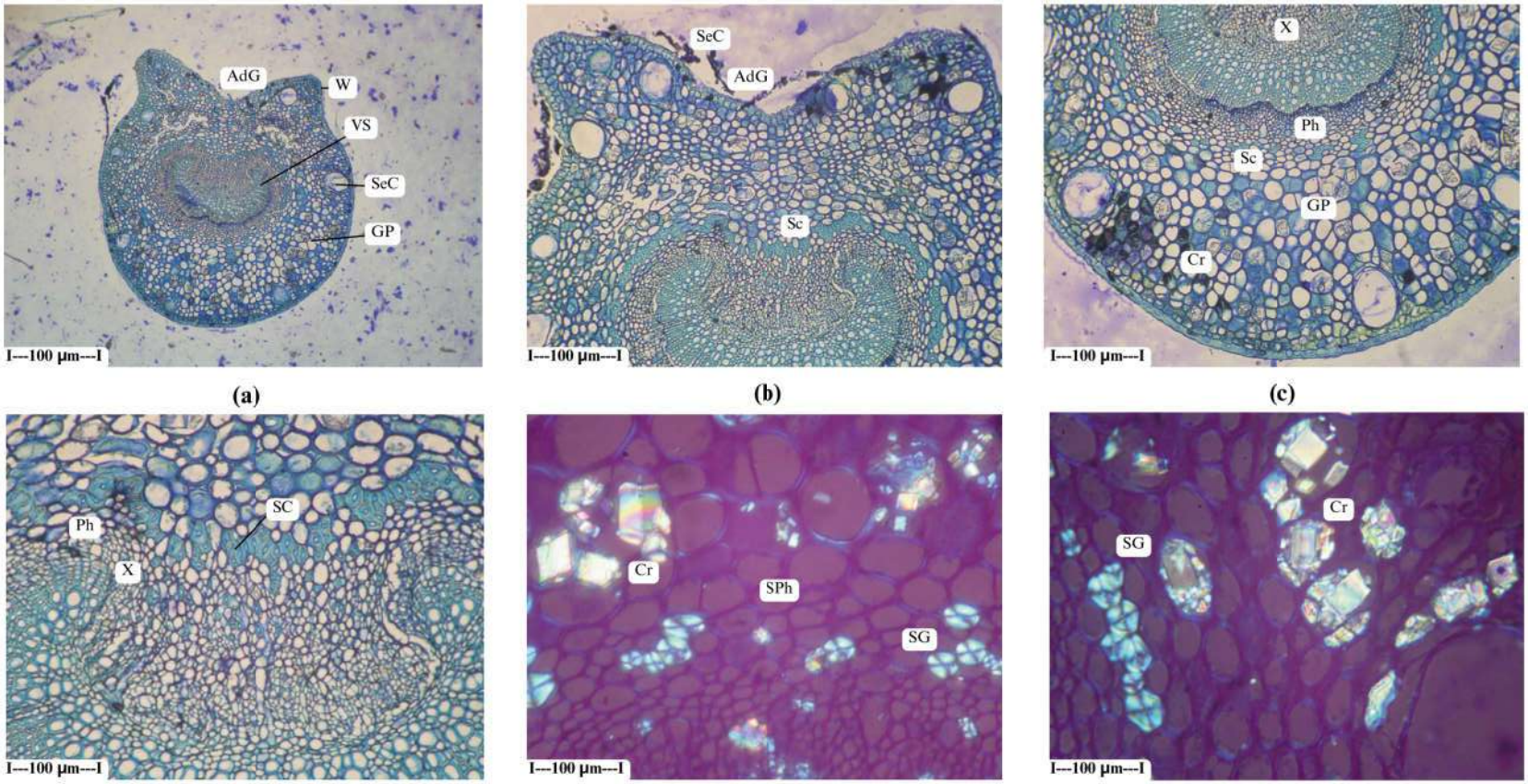


Plate 3.19: Anatomical features of *Syzygium palghatense* petiole: (a) T.S. of petiole, entire view (b-c) T.S. of petiole, enlarged (d) Adaxial part of the petiole showing vascular arc (e) Starch grain in crystals in the phloem parenchyma (f) Starch grain and crystal in the ground parenchyma of the petiole

(T.S.: Transverse section; AdG: Adaxial groove; W: Wing; VS: Vascular strand; SeC: Secretory cavity; GP: Ground parenchyma; X: Xylem; Ph: Phloem; Sc: Sclerenchyma; GP: Ground parenchyma; Cr: Crystal; EP: Epidermis; SPh: Secondary phloem; SG: Starch grain)

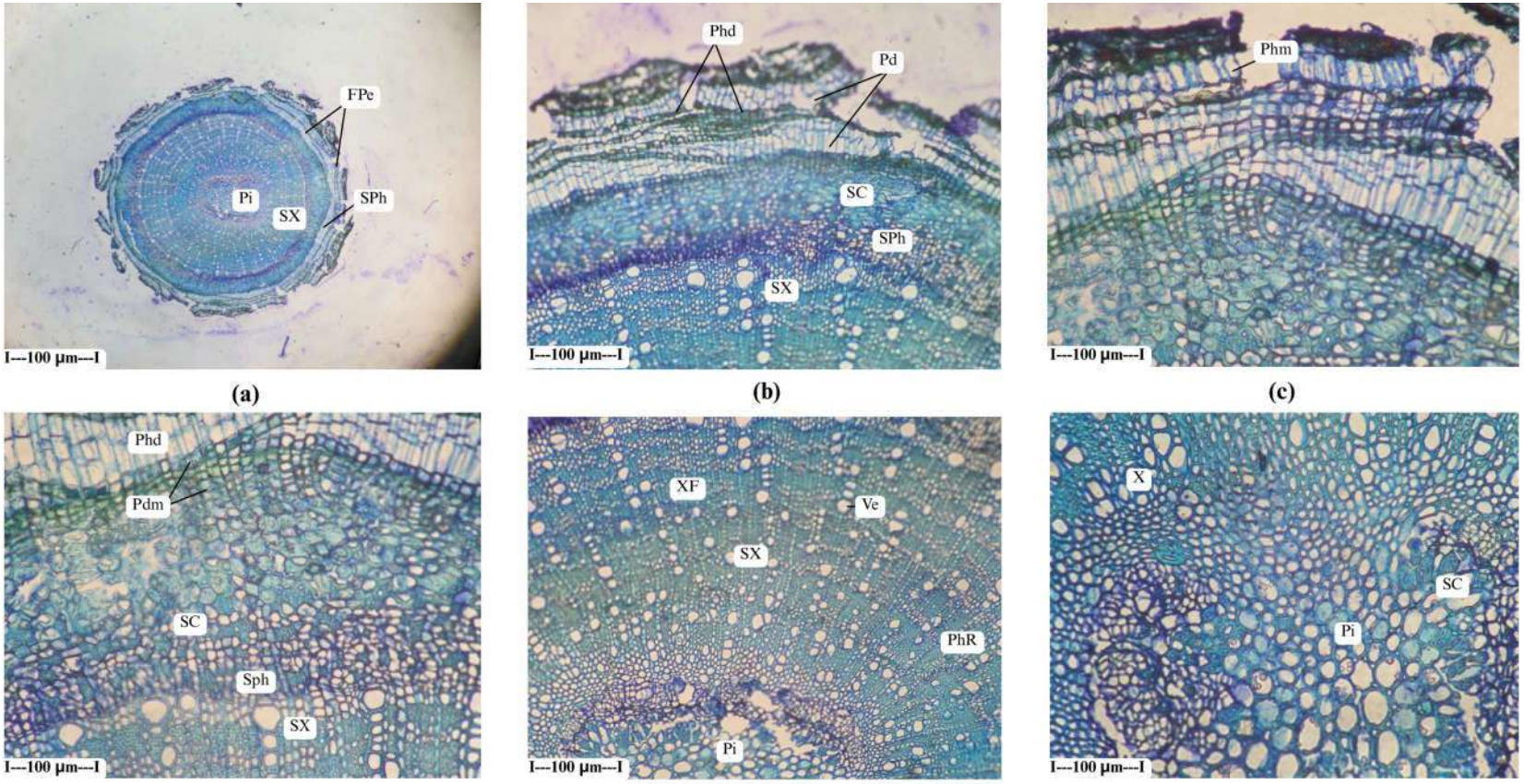
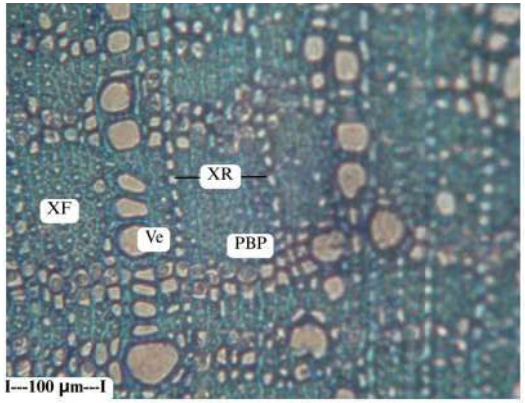
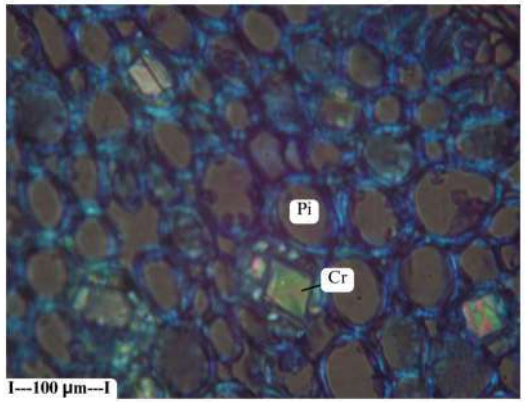


Plate 3.20: Anatomical features of *Syzygium palghatense* stem: (a) T.S. of stem, entire view (b) T.S. of stem showing periderm, sclerenchyma, and vascular tissue (c–d) T.S. of stem bark showing different zones of phelloderm, fibres, secondary phloem, and xylem (e) T.S. of stem showing secondary xylem and pith (f) T.S. of stem showing secondary xylem and pith



(g)



(h)

Plate 3.20: Anatomical features of *Syzygium palghatense* stem: (g) T.S. of stem showing paratracheal banded parenchyma (h) Pith tissue of the stem with crystals

(T.S.: Transvers section; FPe: Fissured periderm; Pi: Pith; SX: Secondary xylem; SPh: Secondary phloem; Phd: Phelloid; Pd: Phelloderm; SC: Sclerenchyma; Phm: Phellem; SX: Secondary xylem; XF: Xylem fibre; Ve: Vessel; PhR: Phloem ray: Pi: Pith; XR: Xylem rays; PBP: Paratracheal banded parenchyma; Cr: Crystals)

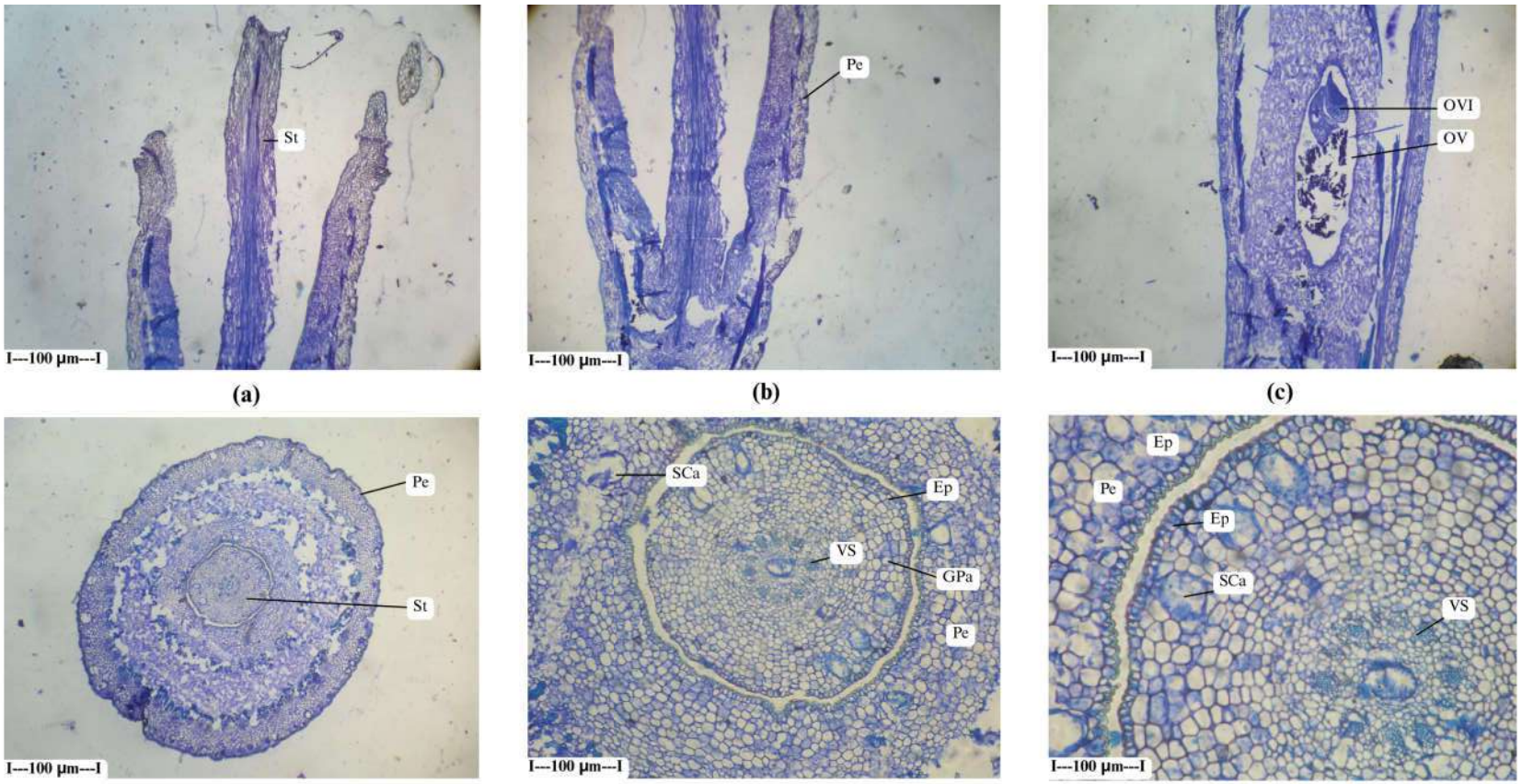
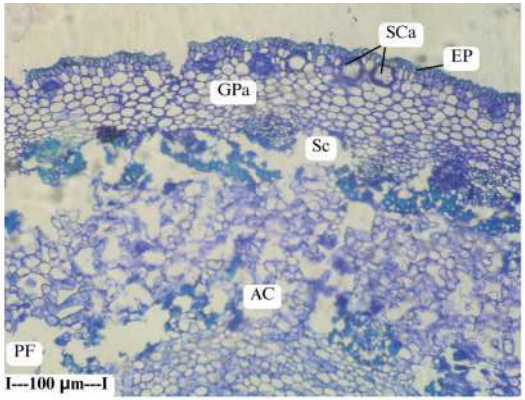


Plate 3.21: Anatomical features of *Syzygium palghatense* flower: (a-c) L.S. of flower showing ovary, ovule, petal, and style (d) T.S. of flower bud showing petal enclosing style (e) T.S. of flower bud showing style enclosed by corolla tube (f) T.S. of flower bud showing vascular strands



(g)

Plate 3.21: Anatomical features of *Syzygium palghatense* flower: (g) T.S. of petal showing outer and inner parenchyma tissue and middle aerench
(L.S.: Longitudinal section; T.S.: Transverse section; St: Style; Pe: Petal: OVI: Ovule; OV: Ovary; SCa: Secretory cavity; VS: Vascular strand; EP: Epidermis; Sc: Sclerenchyma; Gpa: Ground parenchyma; AC: air chambers; PF: Partition filament)

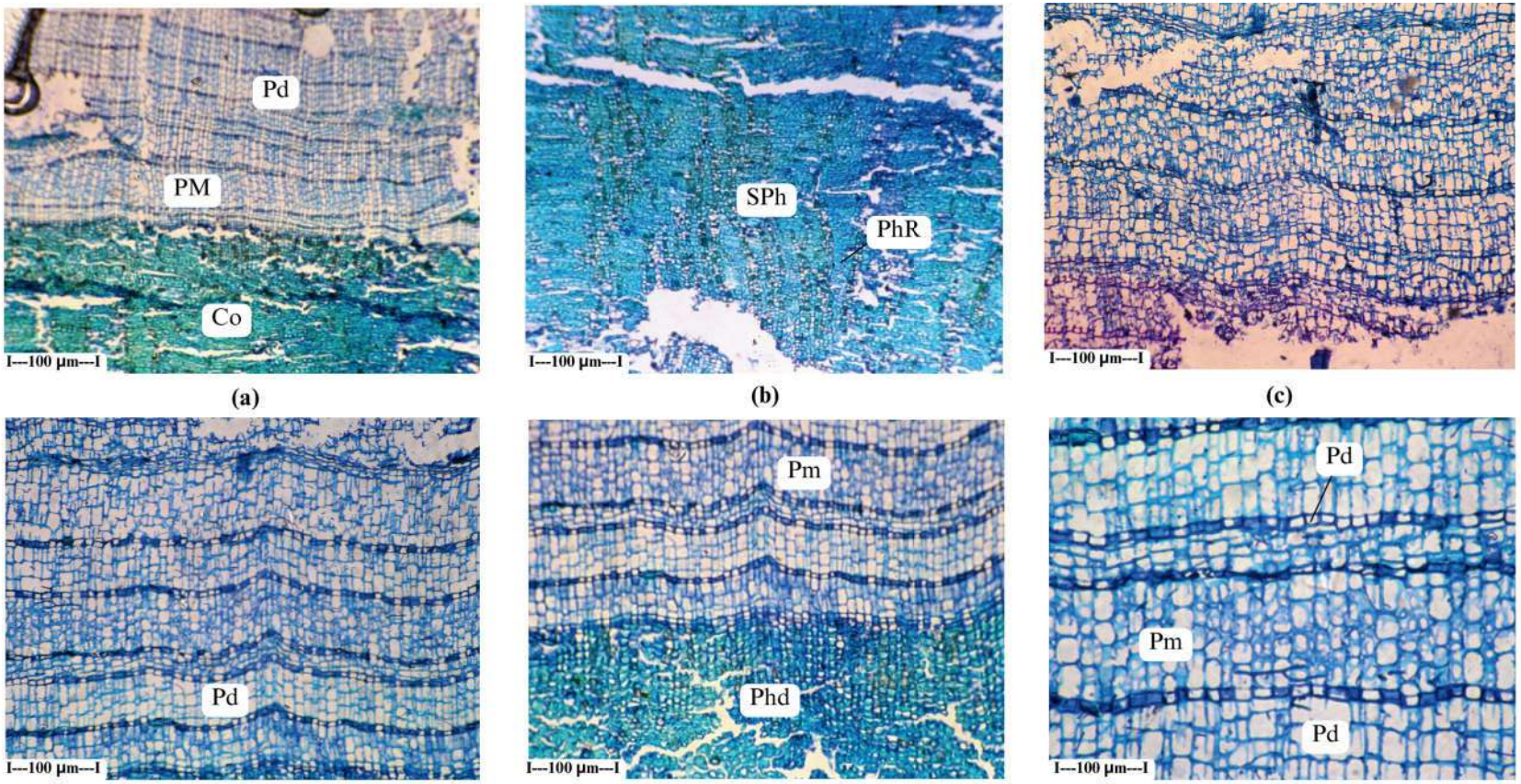


Plate 3.22: Anatomical features of *Syzygium palghatense* bark: (a) T.S. of periderm showing phellem cylinders and thin phelloid cylinders (b) Secondary phloem showing highly dilated rays and collapsed phloem tissue (c-e) T.S. of periderm showingsuberized phellem and lignified phelloid layers (f) T.S. of periderm, enlarged view of phellem, phelloid, and phelloderm

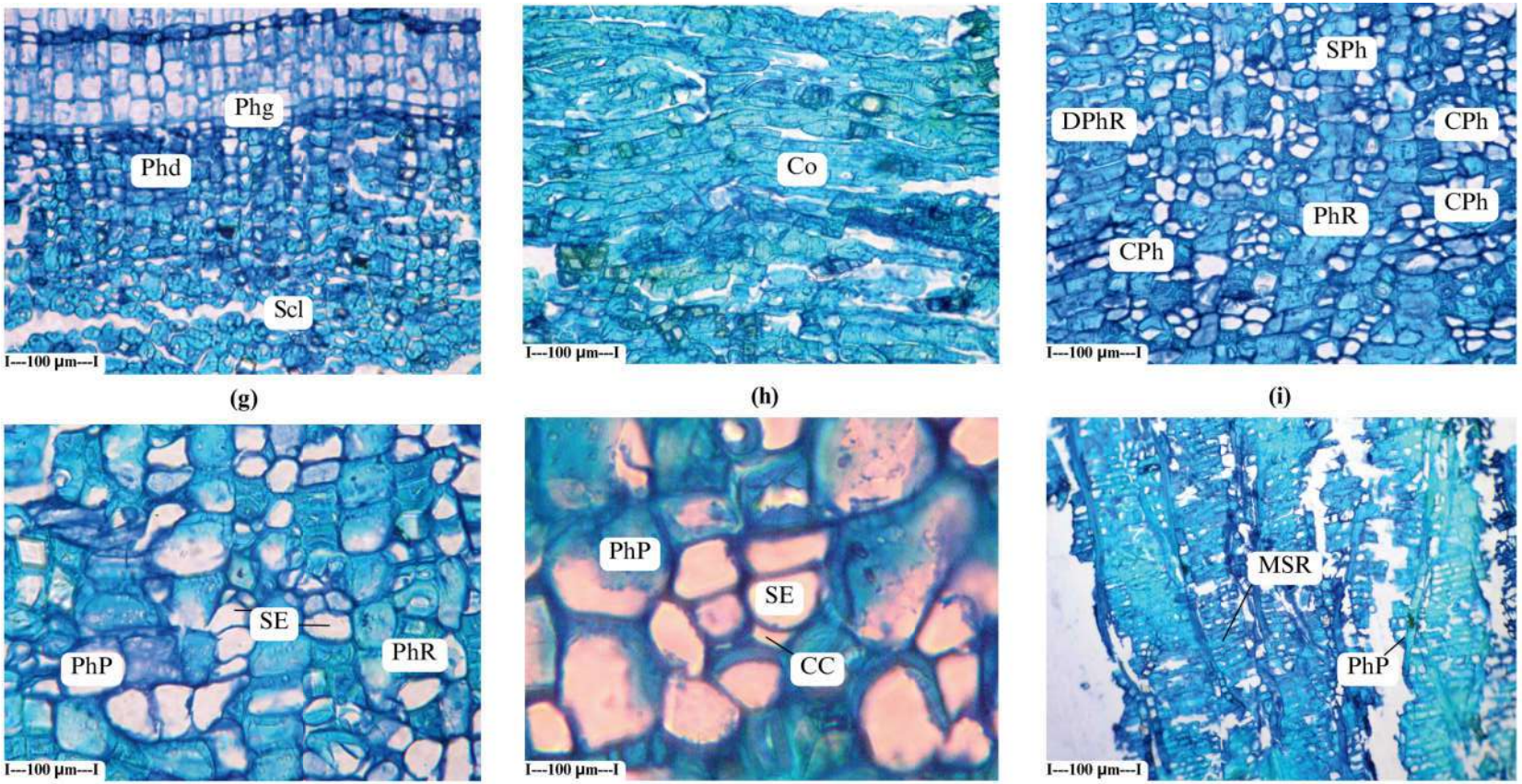


Plate 3.22: Anatomical features of *Syzygium palghatense* bark: (g) T.S. of periderm, enlarged view of phellem, phelloid, and phelloderm (h) T.S. of bark showing horizontally elongated cortical cells (i) T.S. of collapsed phloem zone with dilated phloem rays and crushed collapsed sieve elements (j) T.S. of phloem showing non-collapsed sieve elements (k) Sieve elements with companion cells (l) T.L.S. of phloem showing multiseriate rays, phloem, parenchyma and uniseriate rays

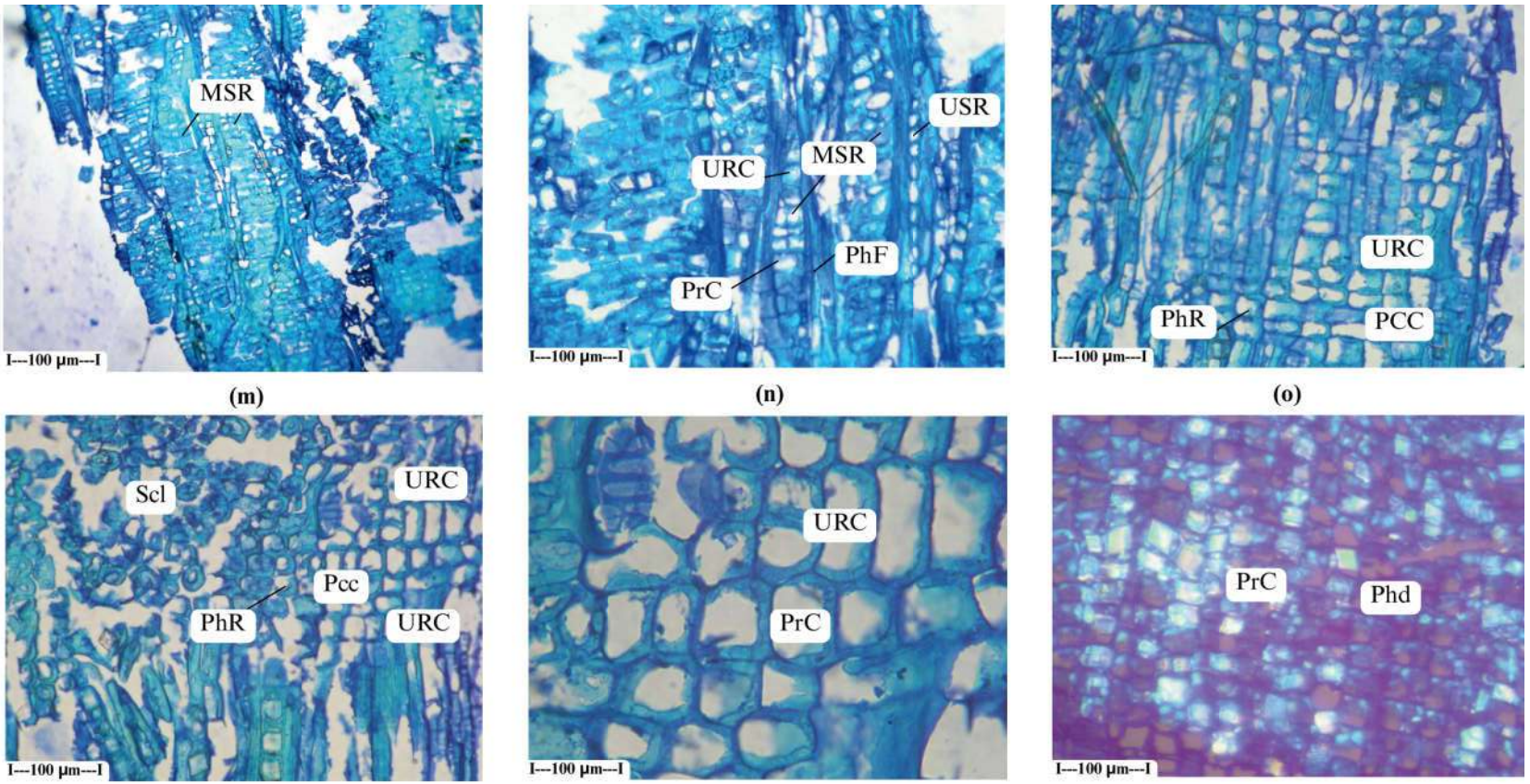
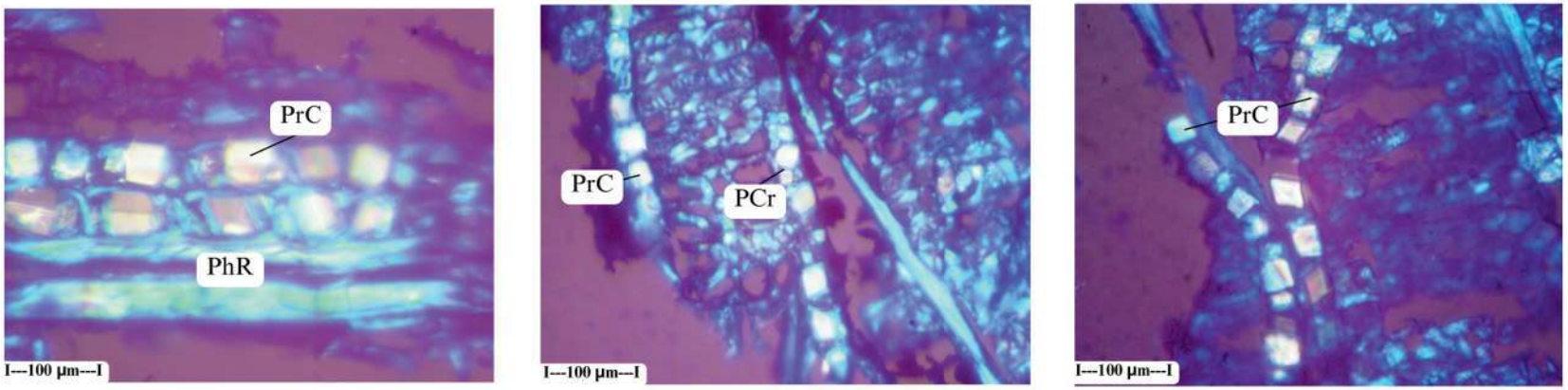


Plate 3.22: Anatomical features of *Syzygium palghatense* bark: (m-n) T.L.S. of phloem showing multiseriate rays, phloem, parenchyma and uniseriate rays (o) R.L.S. of the phloem showing horizontal ribbon of phloem rays (p) Phloem ray enlarged showing upright cells and procumbent cells (q) Phloem ray with enlarged upright and procumbent cells (r) Phelloderm cells with prismatic crystals as seen as polarized light



(s) (t) (u)

Plate 3.22: Anatomical features of *Syzygium palghatense* bark: (s) Prismatic crystals in the ray enlarged (t-u) Prismatic crystals in the vertical parenchyma cells
(T.S.: Transverse section; T.L.S.: Tangential longitudinal section; R.L.S.: Radial longitudinal section; Pd: Phelloderm; Pm: Phellem; Co: Cortex; SPh: Secondary phloem; PhR: Phloem ray: Phd: Phelloderm; Phg: Phellogen; Scl: Sclerenchyma; CPh: collapsed phloem; DphR: Dialted phloem ray; PhP: Phloem parenchyma; PhR: Phloem ray; SE: Sieve element; CC: Companion cell; MSR: Multiseriate ray; URC: Upright cell; USR: Uniseriate ray; PhF: Phloem fibre; PrC: Procumbent cell; PCC: Procumbent cell; PCr: Prismatic crystal)

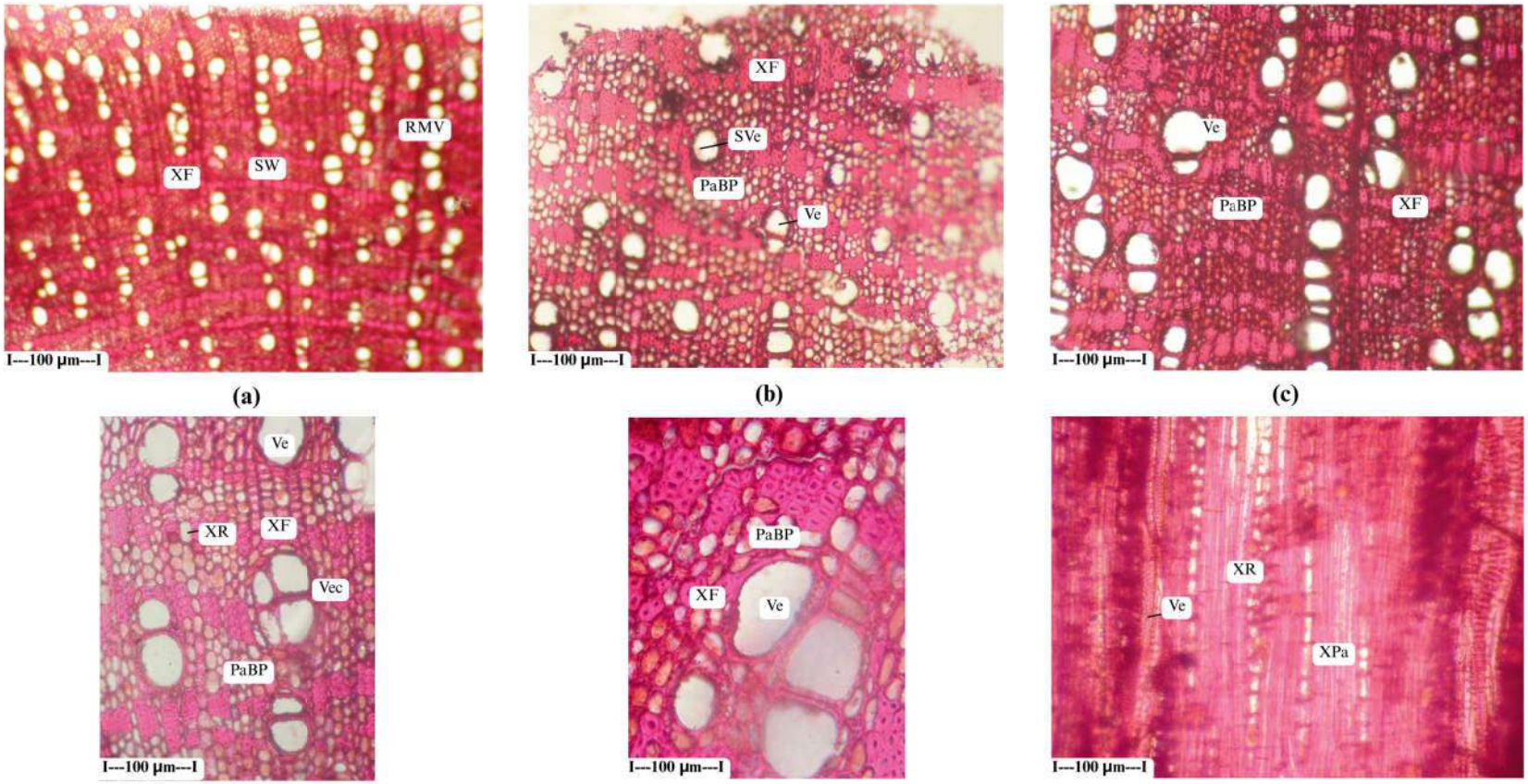
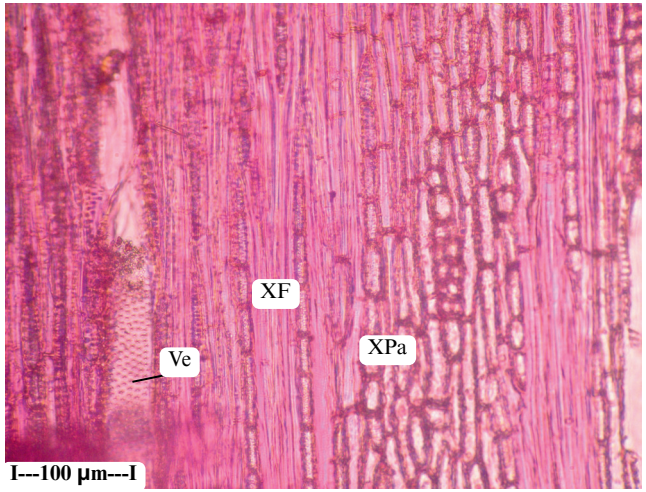
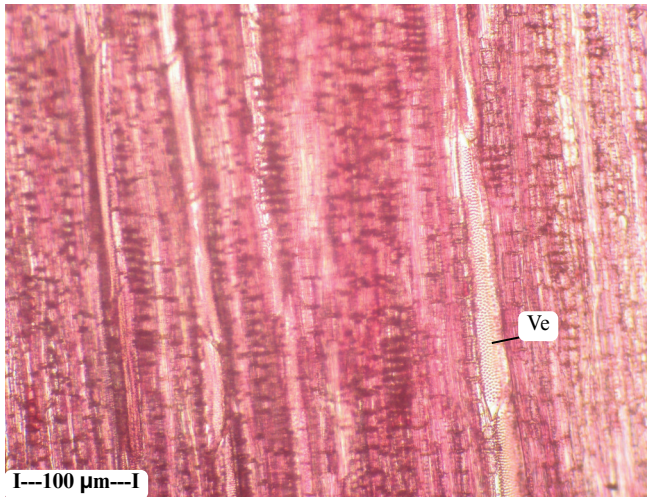


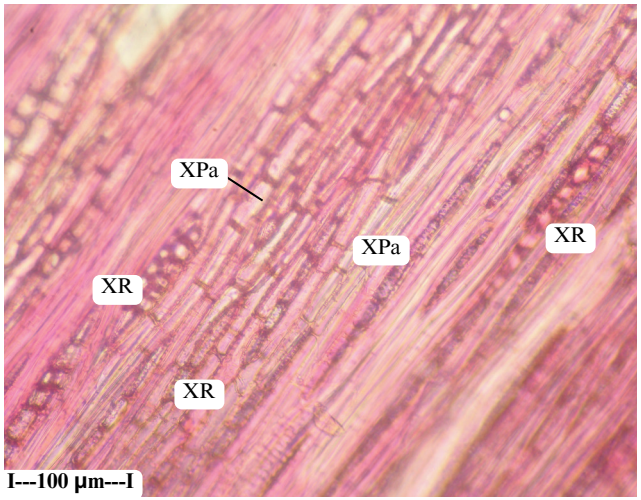
Plate 3.23: Anatomical features of *Syzygium palghatense* wood: (a) T.S. of woof showing pattern of vessel distribution (b) T.S. of wood showing solitary vessel and tangential lines of paratracheal banded parenchyma (c) T.S. of wood showing paratracheal banded parenchyma, solitary and radial multiple vessels (d) T.S. of wood showing vessel clusters and paratracheal banded parenchyma (e) Wood showing vessels (f) T.L.S. of wood showing xylem rays, parenchyma strands and vessels



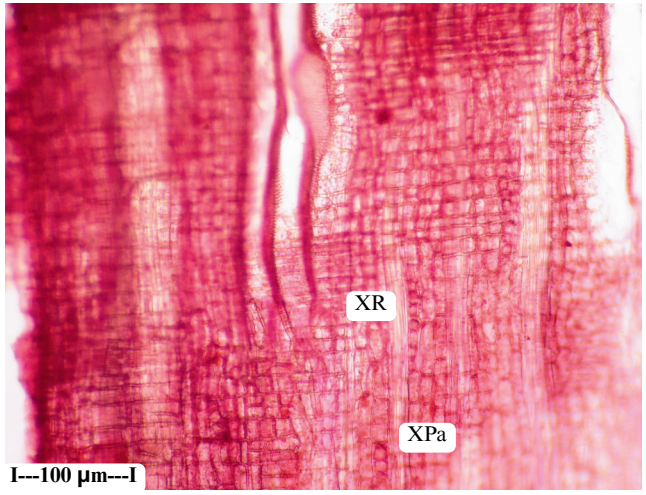
(g)



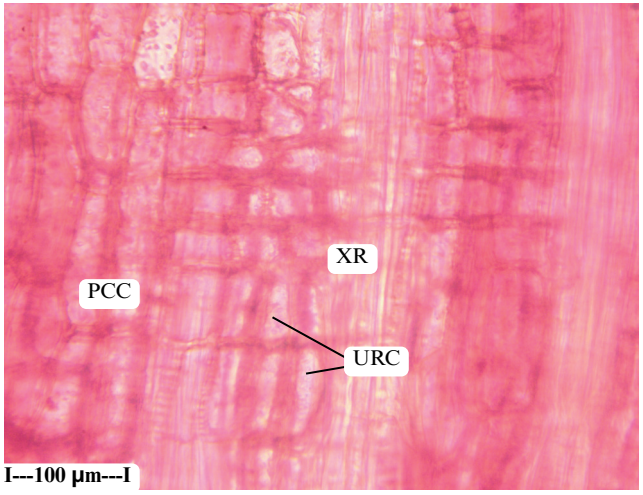
(h)



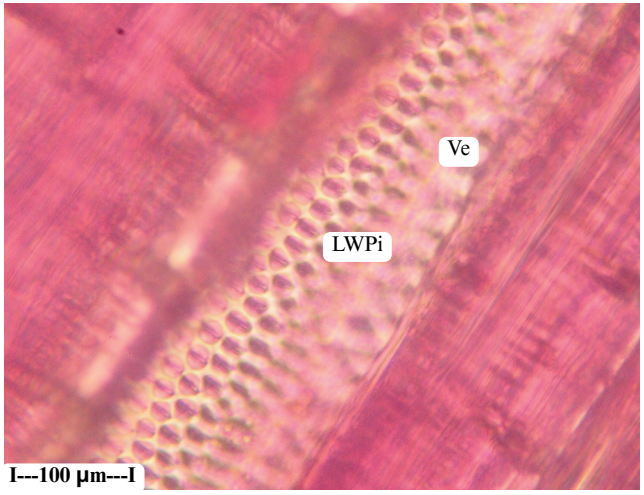
(i)



(j)



(k)



(l)

Plate 3.23: Anatomical features of *Syzygium palghatense* wood: (g) T.L.S. of wood showing lateral wall pits of vessels, xylem parenchyma and biseriate rays (h) T.L.S. of wood showing vessels and fibres (i) T.L.S. of wood showing xylem rays and xylem parenchyma (j-k) R.L.S. of wood showing horizontal layers of rays (l) R.L.S. of wood showing lateral wall and bordered pits of vessels (T.S.: Transverse section; T.L.S.:Tangential longitudinal section; R.L.S.: Radial longitudinal section;RMW: Radial multiple vessel; SW:Secondary wood; XF: Xylem fibres; SVe: Solitary vessel; PaBP: Paratracheal banded parenchyma; Ve: Vessel; XR: Xylem rays; Vec:Vessel clusters; XPa: Xylem parenchyma; PCC: Procumbent cell; URC: Upright cell; LWPi: Lateral wall pith)

- **Radial Longitudinal Section (R.L.S.)**

In the R.L.S. view, the xylem rays occur in a horizontal, flat, ribbon-shaped structure. The vertical system of cells, fibre, and parenchyma is vertically oriented at the right angle to the ray. The central horizontally elongated procumbent and marginal upright cells are thick-walled, making the ray heterocellular. The vessels appear in a vertical orientation, showing lateral walls. On the lateral walls, there are multiseriate compact angular-bordered pits. The pits are 40 μm in diameter.

3.3.3. Histochemical analysis

The histochemical analysis of *S. laetum*, *S. occidentale*, and *S. palghatense* revealed the presence of important secondary metabolites relevant to their pharmacological activities. Lignified tissues were well-developed in stems, bark, and wood, showing strong positive staining with phloroglucinol-HCl, confirming extensive lignin deposition in vascular elements and fibers. Fixed oil droplets were localized successfully with Sudan Red staining, particularly abundant in seeds and certain parenchymatous cells, indicating significant lipid content. Starch grains were observed mostly in the leaf parenchyma and cortex, staining blue with iodine solution, consistent with energy storage. Tannins were detected in the bark and leaf tissues, producing bluish-black colouration upon ferric chloride treatment, supporting their role as defense compounds. These results align with previous reports on the genus *Syzygium*, which emphasize the richness of flavonoids, phenolics, tannins, and essential oils contributing to the species antioxidant and antimicrobial properties (Tandon & Sharma, 2018).

The comprehensive histochemical analyses presented in Plates 3.24-3.43 reveal the distribution and presence of key biochemical compounds—lignin, oils, starch, and tannins—across various anatomical parts of three *Syzygium* species: *S. laetum*, *S. occidentale*, and *S. palghatense*. Plates 3.24 to 3.28 demonstrate the localization of lignin in leaves, petioles, stems, bark, and wood, where the characteristic red staining confirms its abundant presence, particularly in vascular tissues such as xylem and sclerenchyma, indicating its vital role in structural support and water conduction. Plates 3.29 to 3.33 highlight the variable distribution of oils

within these same tissues, underscoring their protective functions against herbivory and pathogens as well as their potential roles in allelopathic interactions. Meanwhile, Plates 3.34 to 3.38 show widespread starch granules in leaves, petioles, and stems, evidenced by the blue-black colouration typical of starch staining, which suggests a significant role of starch as an energy reserve supporting metabolic processes and growth. Oils are absent in wood and bark. Starch is also absent in bark. Plates 3.39 to 3.43 reveal the presence of tannins- polyphenolic compounds implicated in defense mechanisms- across the same tissues, with dark brown staining confirming their accumulation and highlighting their importance in protection and medicinal potential. Collectively, these histochemical findings offer a detailed depiction of the biochemical composition and functional anatomy of *Syzygium* species, emphasizing their ecological adaptations and phytochemical richness with implications for pharmacological applications.



(a) **(b)** **(c)**

Plate 3.24: Histochemical studies showing the presence of lignin in the leaves of (a) *Syzygium laetum*, (b) *S. occidentale*, and (c) *S. palghatense*



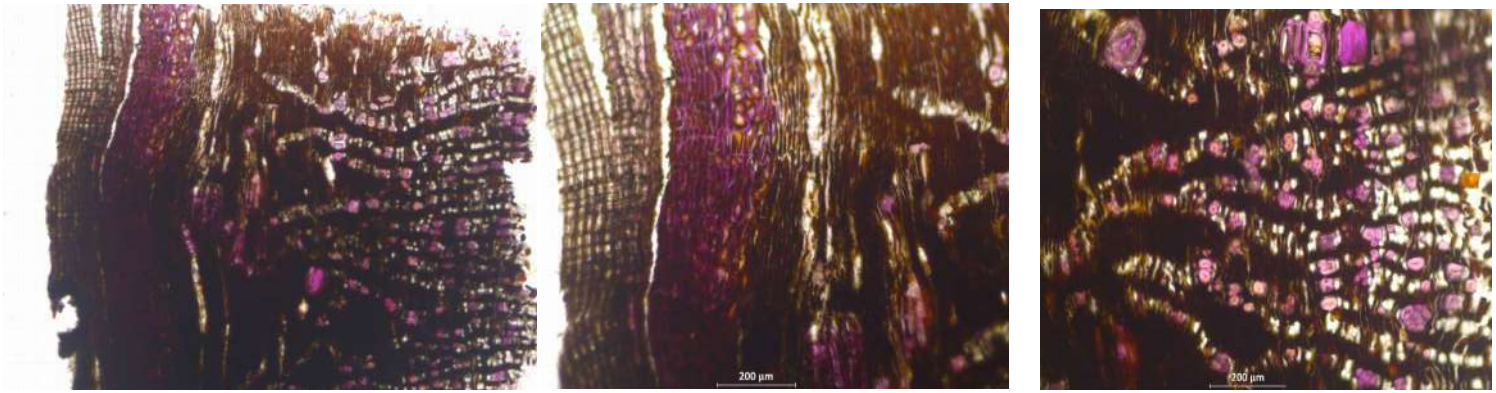
(a) **(b)** **(c)**

Plate 3.25: Histochemical studies showing the presence of lignin in the petiole of (a) *Syzygium laetum*, (b) *S. occidentale*, and (c) *S. palghatense*



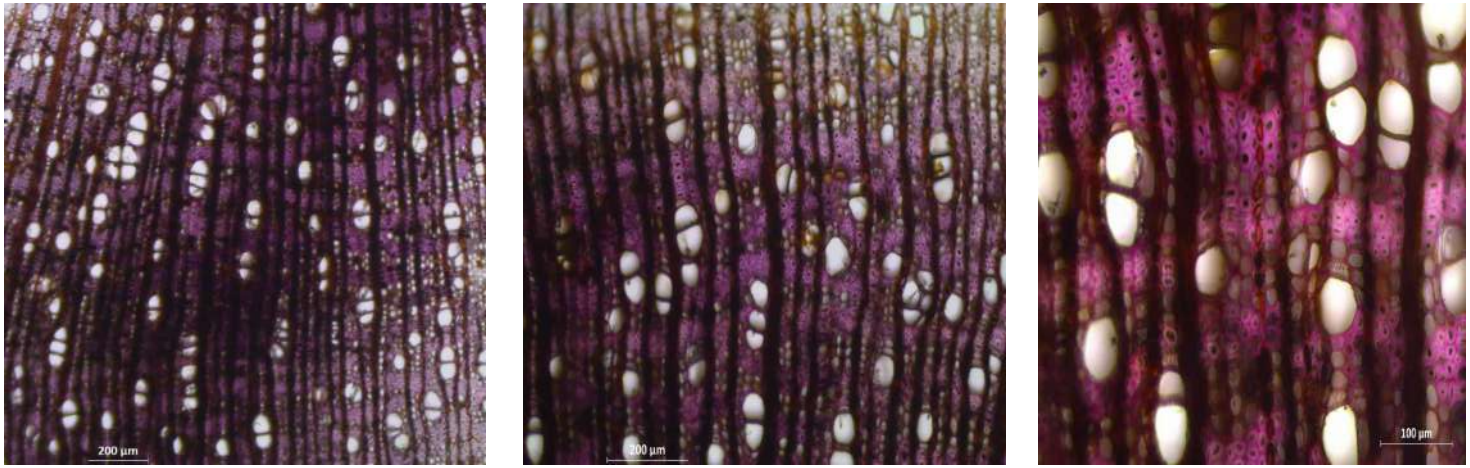
(a) **(b)** **(c)**

Plate 3.26: Histochemical studies showing the presence of lignin in the stem of (a) *Syzygium laetum*, (b) *S. occidentale*, and (c) *S. palghatense*



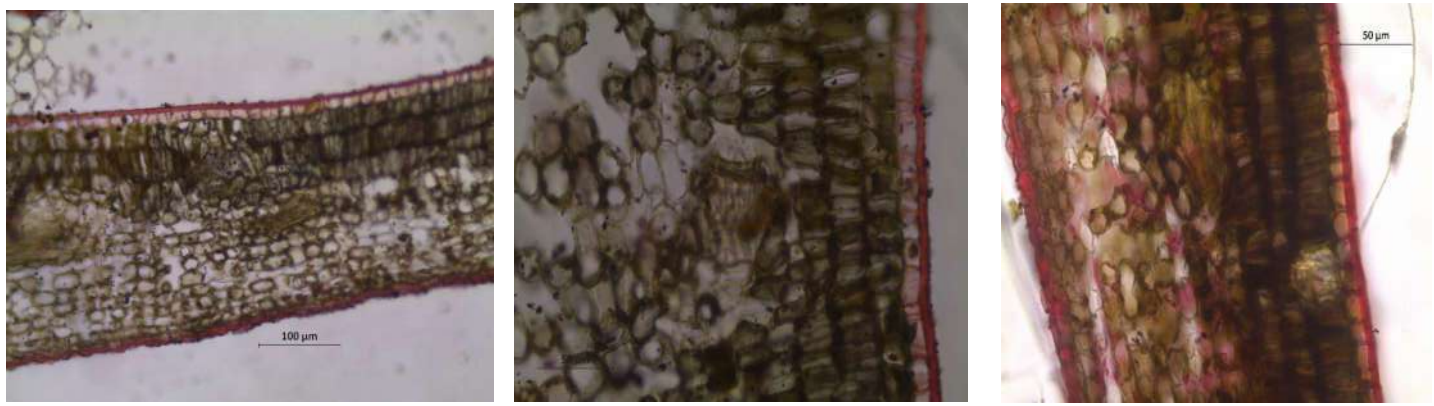
(a) **(b)** **(c)**

Plate 3.27: Histochemical studies showing the presence of lignin in the bark of (a) *Syzygium laetum*, (b) *S. occidentale*, and (c) *S. palghatense*



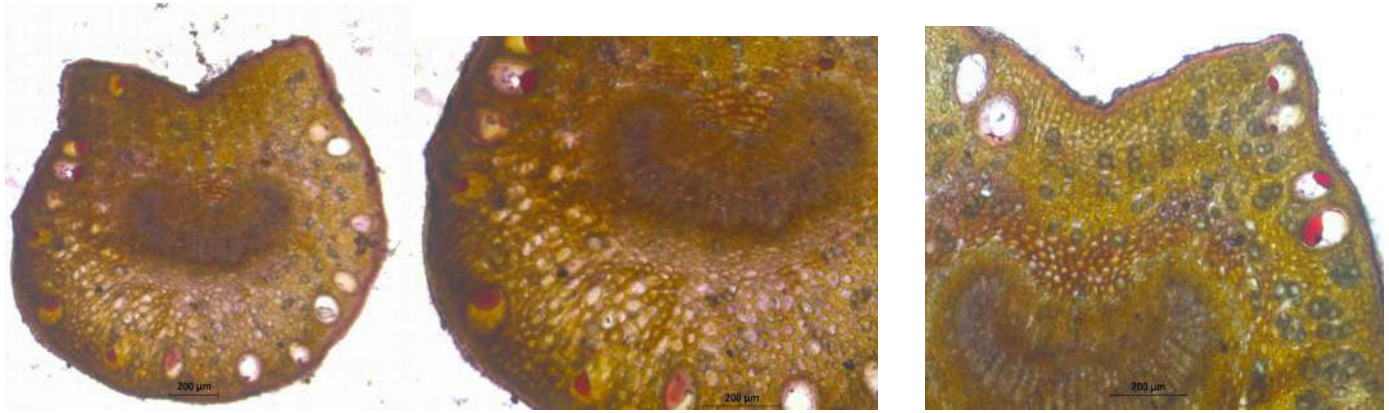
(a) **(b)** **(c)**

Plate 3.28: Histochemical studies showing the presence of lignin in the wood of (a) *Syzygium laetum*, (b) *S. occidentale*, and (c) *S. palghatense*



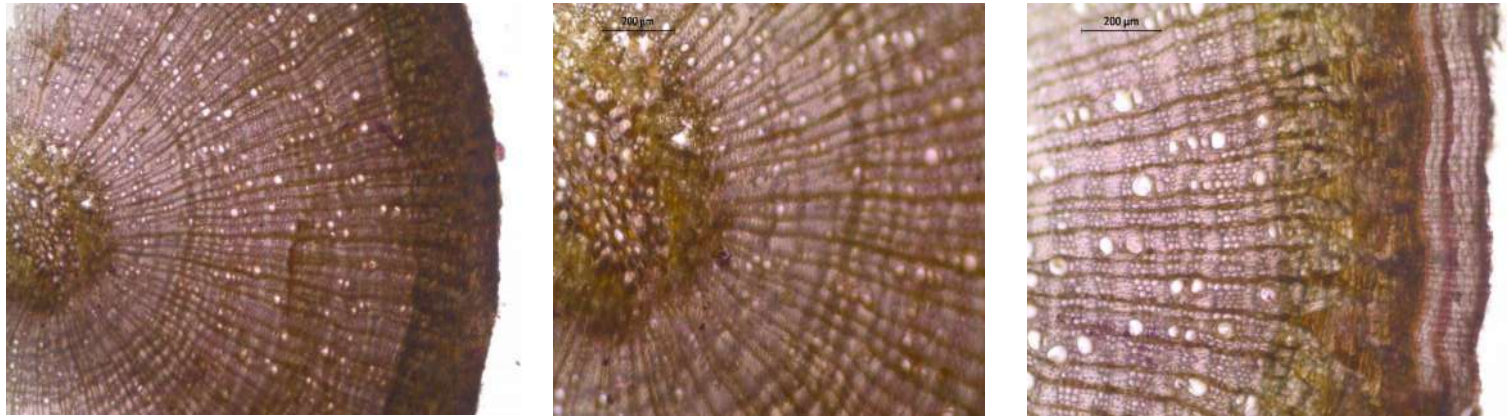
(a) **(b)** **(c)**

Plate 3.29: Histochemical studies showing the presence of oil in the leaves of (a) *Syzygium laetum*, (b) *S. occidentale*, and (c) *S. palghatense*



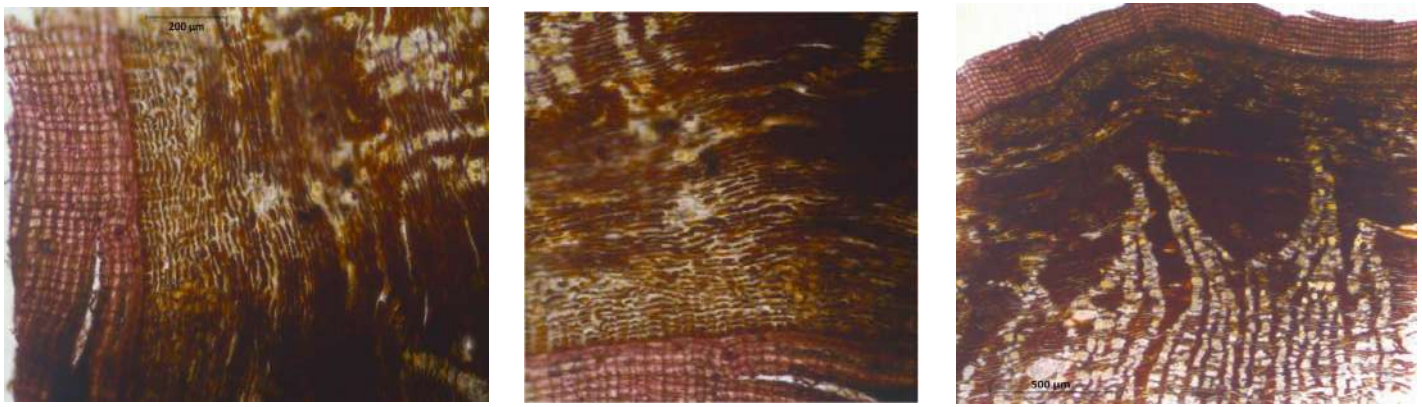
(a) **(b)** **(c)**

Plate 3.30: Histochemical studies showing the presence of oil in the petiole of (a) *Syzygium laetum*, (b) *S. occidentale*, and (c) *S. palghatense*



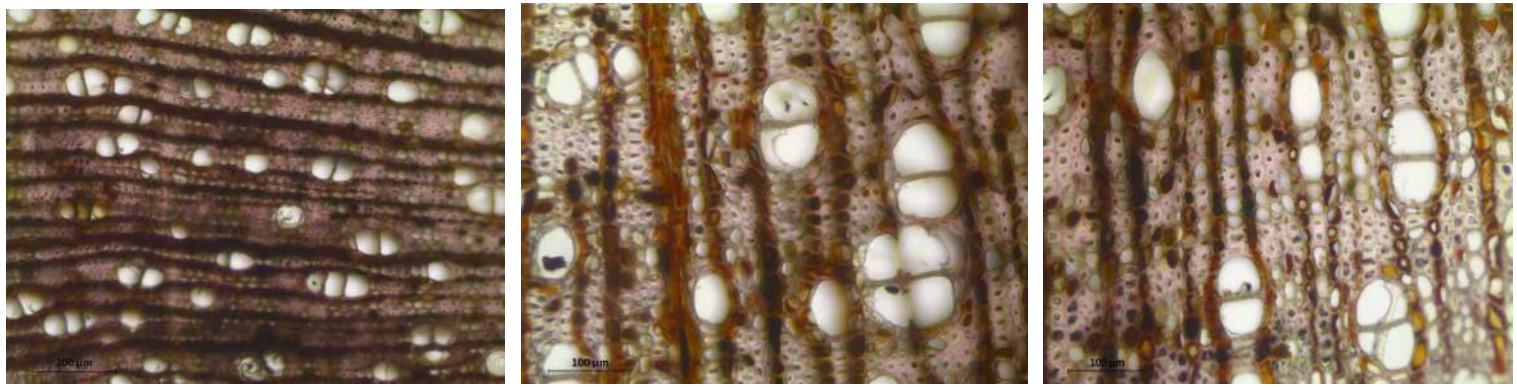
(a) **(b)** **(c)**

Plate 3.31: Histochemical studies showing the presence of oil in the stem of (a) *Syzygium laetum*, (b) *S. occidentale*, and (c) *S. palghatense*



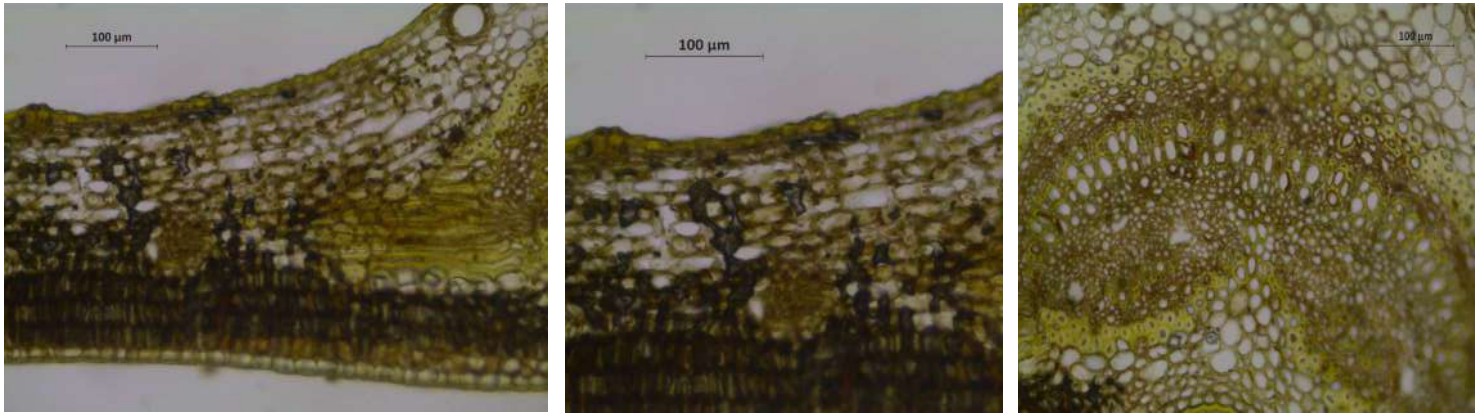
(a) **(b)** **(c)**

Plate 3.32: Histochemical studies showing the oil test in the bark of (a) *Syzygium laetum*, (b) *S. occidentale*, and (c) *S. palghatense*



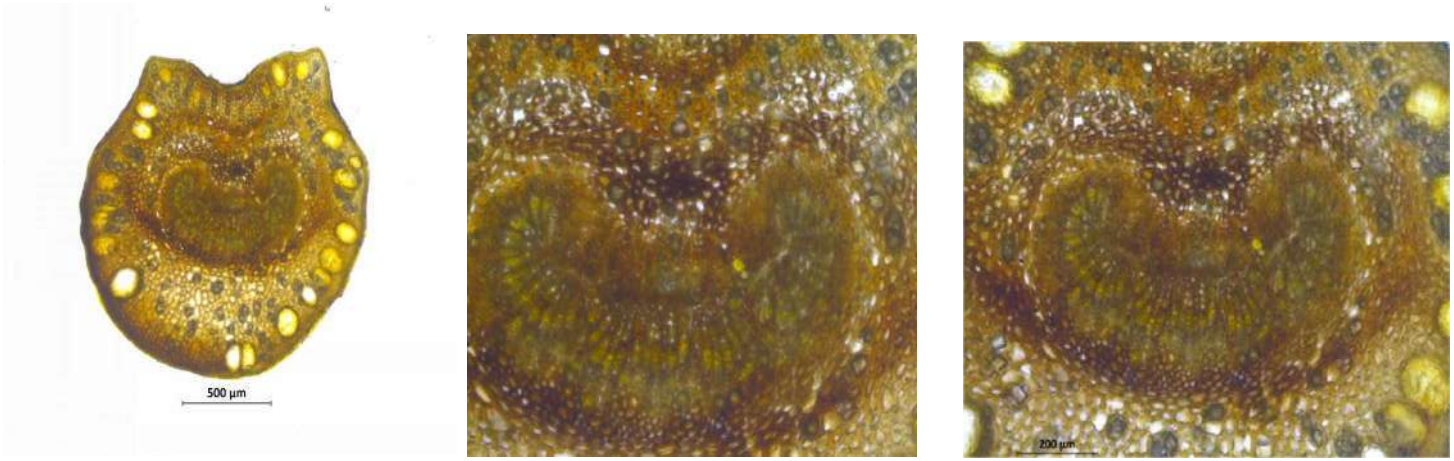
(a) **(b)** **(c)**

Plate 3.33: Histochemical studies showing the oil test in the wood of (a) *Syzygium laetum*, (b) *S. occidentale*, and (c) *S. palghatense*



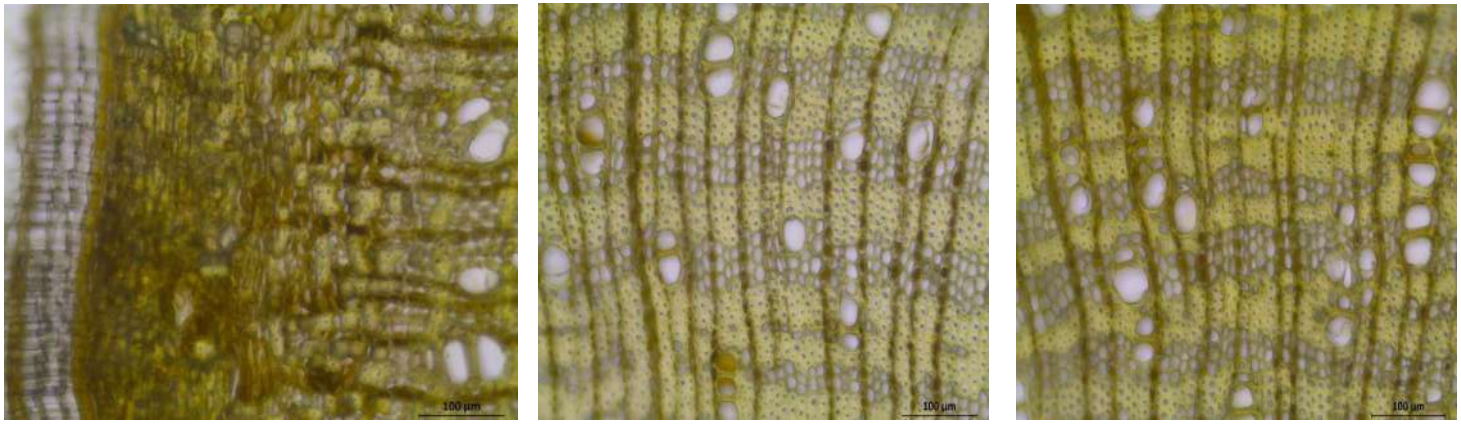
(a) **(b)** **(c)**

Plate 3.34: Histochemical studies showing the presence of starch in the leaves of (a) *Syzygium laetum*, (b) *S. occidentale*, and (c) *S. palghatense*



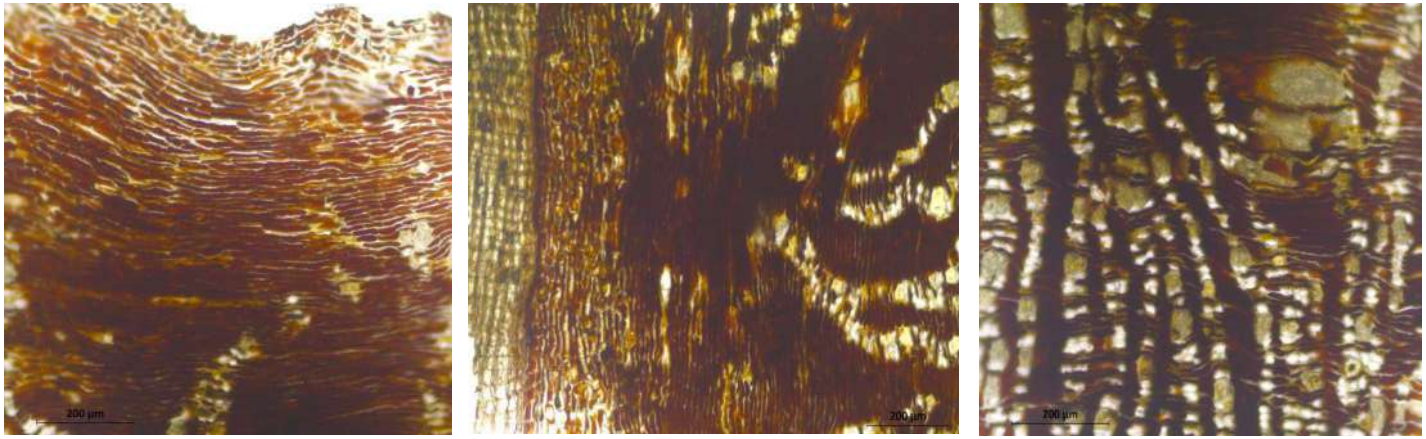
(a) **(b)** **(c)**

Plate 3.35: Histochemical studies showing the presence of starch in the petiole of (a) *Syzygium laetum*, (b) *S. occidentale*, and (c) *S. palghatense*



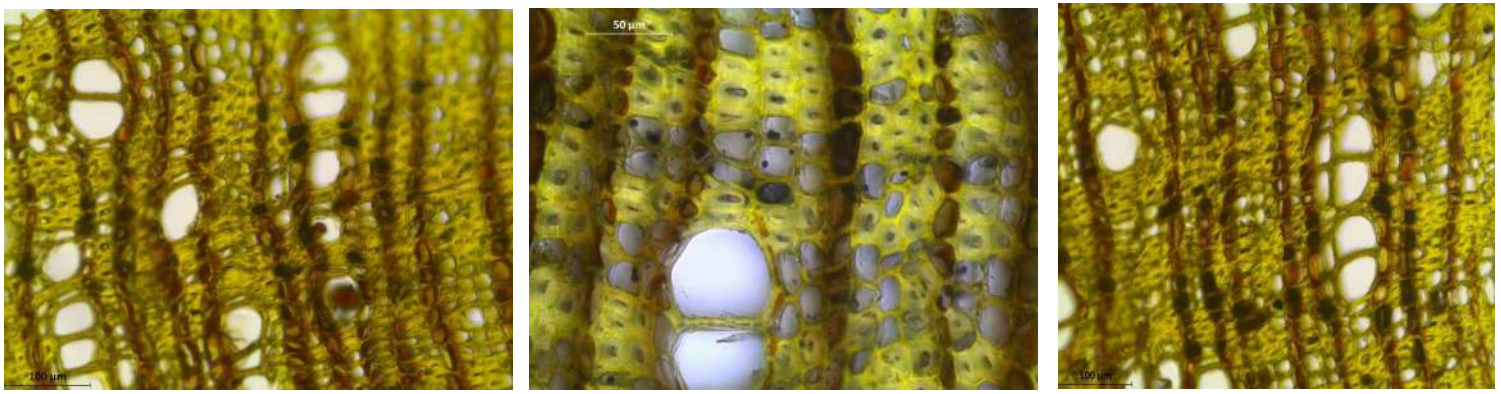
(a) **(b)** **(c)**

Plate 3.36: Histochemical studies showing the presence of starch in the stem of (a) *Syzygium laetum*, (b) *S. occidentale*, and (c) *S. palghatense*



(a) **(b)** **(c)**

Plate 3.37: Histochemical studies showing the starch test in the bark of (a) *Syzygium laetum*, (b) *S. occidentale*, and (c) *S. palghatense*



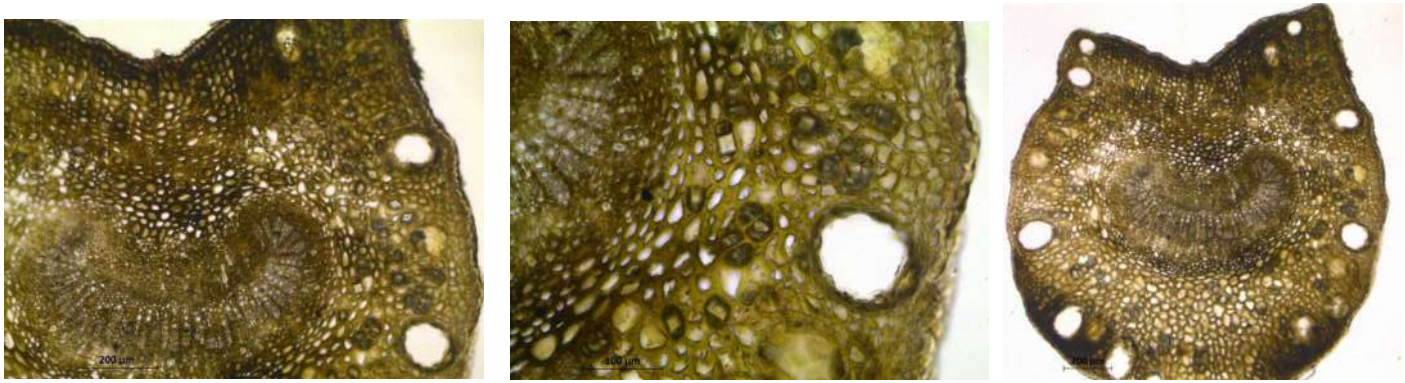
(a) **(b)** **(c)**

Plate 3.38: Histochemical studies showing the presence of starch in the wood of (a) *Syzygium laetum*, (b) *S. occidentale*, and (c) *S. palghatense*



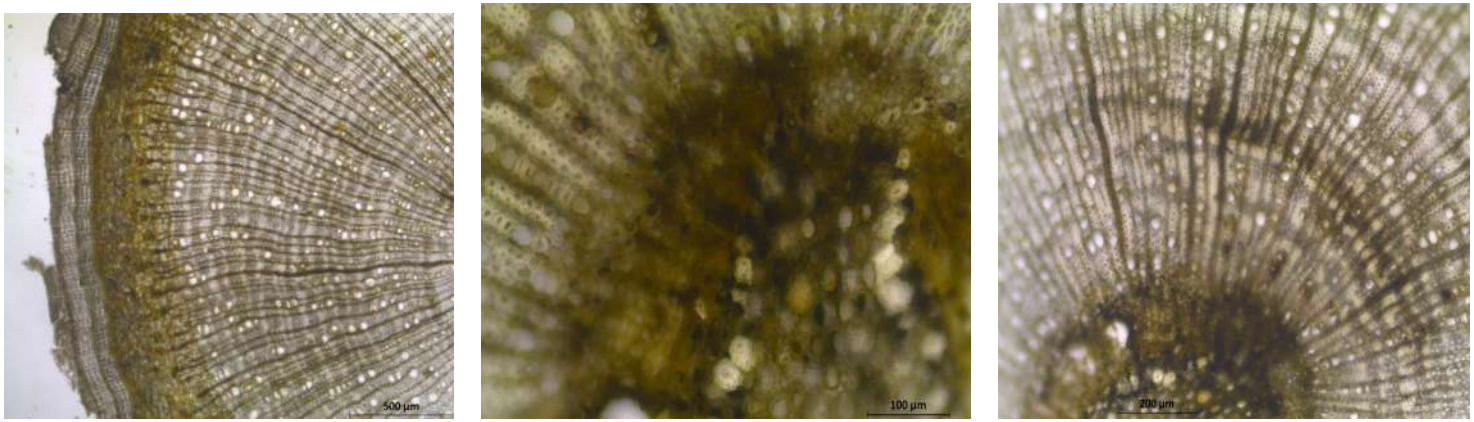
(a) **(b)** **(c)**

Plate 3.39: Histochemical studies showing the presence of tannin in the leaves of (a) *Syzygium laetum*, (b) *S. occidentale*, and (c) *S. palghatense*



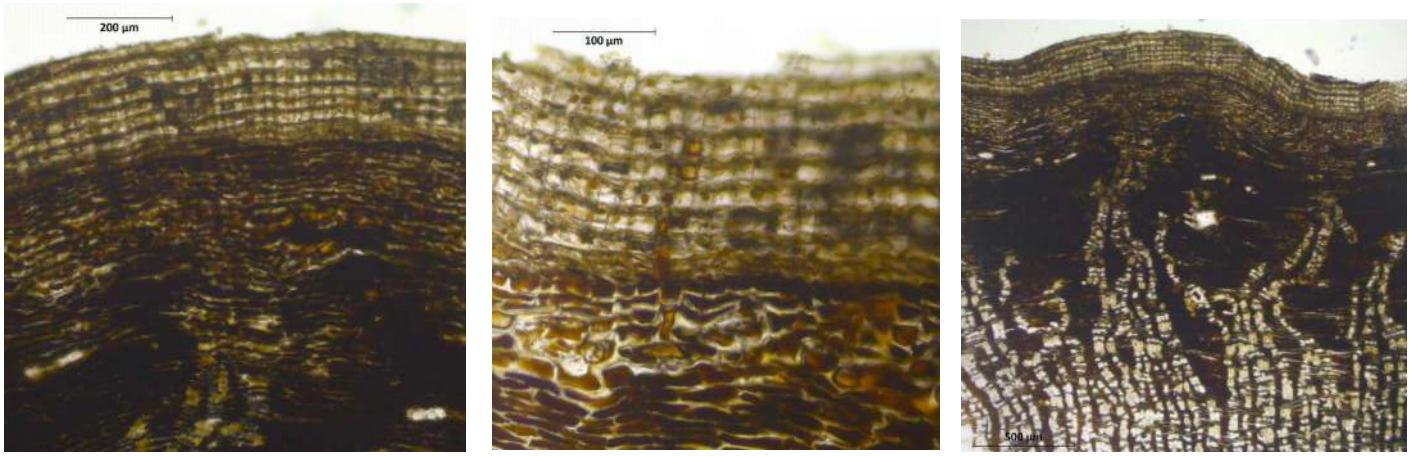
(a) **(b)** **(c)**

Plate 3.40: Histochemical studies showing the presence of tannin in the petiole of (a) *Syzygium laetum*, (b) *S. occidentale*, and (c) *S. palghatense*



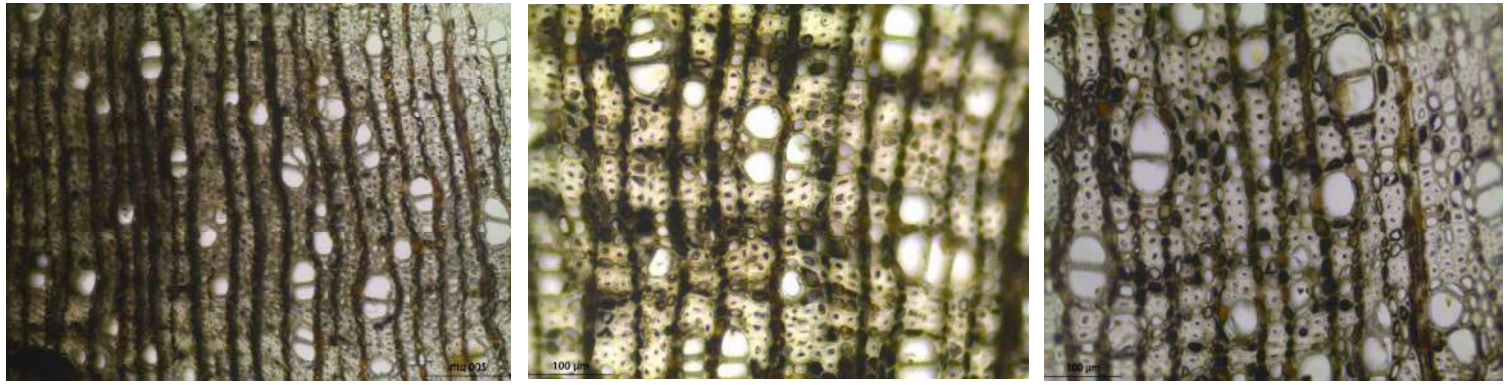
(a) **(b)** **(c)**

Plate 3.41: Histochemical studies showing the presence of tannin in the stem of (a) *Syzygium laetum*, (b) *S. occidentale*, and (c) *S. palghatense*



(a) **(b)** **(c)**

Plate 3.42: Histochemical studies showing the presence of tannin in the bark of (a) *Syzygium laetum*, (b) *S. occidentale*, and (c) *S. palghatense*



(a) **(b)** **(c)**

Plate 3.43: Histochemical studies showing the presence of tannin in the wood of (a) *Syzygium laetum*, (b) *S. occidentale*, and (c) *S. palghatense*

3.4. Discussion

The present investigation on *S. laetum*, *S. occidentale*, and *S. palghatense* provides a comprehensive morpho-anatomical and histochemical characterization of three endemic species from the Western Ghats. These findings hold significance not only for their taxonomic placement but also for their ecological and pharmacological relevance. The genus *Syzygium*, belonging to the family Myrtaceae, is one of the largest tropical woody genera, comprising over 1200 species distributed across Asia, Africa, and Australia (Parnell et al., 2007; Govaerts et al., 2008). The close morphological similarity among species often complicates their identification, making detailed anatomical and micromorphological studies indispensable (Abdulrahman et al., 2018). The current study attempts to resolve such ambiguities by documenting a detailed account of macroscopic, microscopic, and histochemical attributes of three lesser-studied taxa endemic to peninsular India.

The macromorphological features observed in the three species demonstrated clear distinguishing traits that support their separation at the species level. *S. laetum* is recognized by its elliptic to ovate-oblong leaves, crimson red stamens, and ovoid berries with reflexed calyx lobes, in agreement with the description of Sasidharan (2011). The distinguishing floral feature of persistent crimson stamens is an important diagnostic character, as stamen morphology has been consistently emphasized in Myrtaceae taxonomy (Craven, 2001). *S. occidentale*, on the other hand, exhibited linear-lanceolate leaves and terminal cymose inflorescences with white to pinkish flowers, closely matching the descriptions provided by Varghese and Sreekala (2017). *S. palghatense* differed by its large obovate leaves with recurved margins and coriaceous texture, and by its characteristic calyptrate, caducous petals, consistent with earlier reports by Murthy and Nair (2016).

Leaf venation patterns, often considered diagnostic in Myrtaceae, were densely reticulate across all three species, but subtle differences in vein islet and termination patterns were noted. The presence of reflexed calyx lobes in *S. laetum*, linear leaves in *S. occidentale*, and caducous petals in *S. palghatense* further confirms their morphological separation. Such variations underline the importance of detailed

morphological documentation in resolving taxonomic challenges within *Syzygium*, which often suffers from overlapping vegetative characters (Soh & Parnell, 2011; Wilson et al., 2001).

Microscopic examination of leaves revealed dorsiventral lamina structures in all species, a characteristic feature of Myrtaceae (Metcalfe & Chalk, 1950). In *S. laetum*, the presence of secretory cavities filled with tannin-like compounds and paracytic stomata suggests structural adaptations for herbivore deterrence and water-use efficiency. Similar findings have been reported in *S. cumini*, where the presence of tannins and oil glands plays a dual role in defense and ecological interactions (Gogoi et al., 2016). *S. occidentale* exhibited cyclocytic stomata with calcium oxalate crystal deposits around the guard cells, a trait that has been associated with xeromorphic adaptations (Keating, 1984). The druse-type crystals observed in the mesophyll of *S. occidentale* are consistent with previous studies on *S. jambos* and other Myrtaceae members (Pacheco-Silva & Donato, 2016).

In *S. palghatense*, the presence of cicatrix structures associated with epidermal trichomes, and abundant prismatic crystals highlights its adaptive strategies against herbivory. Furthermore, the dense reticulate venation pattern observed in *S. palghatense* strengthens mechanical support while maintaining efficient hydraulic conductivity, an adaptation crucial for species occupying evergreen forests (Dahlgren & Thorne, 1984). Collectively, the anatomical attributes of these species reflect their ecological niches- *S. occidentale* along river banks, *S. palghatense* in dense forests, and *S. laetum* in hill slopes- indicating strong environment-driven anatomical differentiation.

The stem anatomy of all three species exhibited features characteristic of diffuse-porous wood, in accordance with descriptions of other *Syzygium* taxa (Schmid, 1972). *S. laetum* showed well-developed bicollateral vascular bundles and medullary phloem, while *S. occidentale* exhibited distinct growth rings and a thick phelloderm with abundant sclereids. In contrast, *S. palghatense* was characterized by heterocellular phellem and abundant prismatic crystals, features that may represent adaptive responses to mechanical and environmental stress.

The bark of *S. palghatense* was notably thicker (up to 1200 µm) compared to the other two species, with prominent sclereids and calcium oxalate deposition. Bark anatomy in Myrtaceae is considered taxonomically informative, especially in distinguishing species that are otherwise morphologically similar (Abdulrahman et al., 2018; Keating, 1984). The presence of heterocellular rays in bark and wood, observed across all species, supports earlier findings that ray composition is highly consistent within Myrtaceae and thus of limited diagnostic value above the generic level. However, the occurrence of paratracheal banded parenchyma in wood, particularly in *S. occidentale* and *S. palghatense*, reflects an adaptation to efficient storage and conduction, as previously reported in *S. cumini* and *S. jambos* (Rao et al., 2011).

Floral anatomical observations provided insights into reproductive adaptations. *S. laetum* showed actinomorphic flowers with bicollateral vascularization, supporting efficient nutrient transport to reproductive tissues. The pollen morphology observed in *S. occidentale* (four-angled grains with smooth exine) corroborates earlier palynological studies where *Syzygium* pollen is generally characterized by tricolporate grains with thick exine (Punt et al., 2007). The caducous petals of *S. palghatense* reflect a strategy to expose stamens rapidly during anthesis, thereby facilitating cross-pollination by insects, as also reported in *S. cumini* and *S. malaccense* (Raju et al., 2014).

Histochemical studies revealed the abundant presence of tannins, secretory cavities, oil glands, and calcium oxalate crystals across all three species. Such ergastic substances are of immense taxonomic and pharmacological significance. Secretory cavities containing resinous or tannin-like compounds, frequently observed in the leaves and bark of Myrtaceae, play roles in herbivore deterrence and antimicrobial defense (Metcalfe & Chalk, 1950; Solereder, 1908). The presence of tannin-rich idioblasts aligns with phytochemical reports that *Syzygium* species are rich in polyphenols and flavonoids, compounds associated with antioxidant and antidiabetic properties (Baliga et al., 2011).

Calcium oxalate crystals, both druse and prismatic, were widespread in mesophyll, phloem, and phelloderm tissues. Their role in structural support, regulation of calcium levels, and herbivore defense has been well documented

(Franceschi & Nakata, 2005). In *S. occidentale*, the localization of druses around guard cells may represent a unique adaptation, as such crystal-stomatal associations have been reported in relatively few angiosperms (Prychid & Rudall, 1999). The starch grains observed in *S. palghatense* petiole tissue, with distinct X-shaped polarimark under polarized light, suggest high metabolic activity and storage, supporting seasonal growth and reproduction. These histochemical features strongly support the pharmacognostic potential of these taxa, providing microscopic markers for the authentication of crude drugs derived from *Syzygium*.

The anatomical and histochemical features of the three species also reveal important ecological adaptations. The presence of thick cuticles, sclerenchymatous support tissues, and secretory cavities suggests resilience to herbivory and environmental stress. The specialized distribution of calcium oxalate crystals and tannins indicates defensive adaptations crucial for survival in the competitive habitats of the Western Ghats, one of the eight "hottest hotspots" of biodiversity (Myers et al., 2000). Since *S. laetum*, *S. occidentale*, and *S. palghatense* are narrow endemics, detailed morphological and anatomical characterization supports their accurate identification, which is essential for conservation planning. Furthermore, such studies provide baseline data for the sustainable utilization of *Syzygium* species, many of which are economically significant as fruit, timber, or medicinal resources (Parnell et al., 2007).

The present findings reaffirm the taxonomic complexity of *Syzygium* and the critical role of morpho-anatomical studies in its systematics. The combination of macromorphological features (leaf shape, flower structure, fruit morphology) with micromorphological and histochemical characters (crystals, idioblasts, secretory cavities) provides a holistic framework for distinguishing closely allied species. This approach has been advocated by several researchers, who emphasized the integration of morphological, anatomical, and molecular datasets in Myrtaceae taxonomy (Abdulrahman et al., 2018; Craven, 2001). The present study contributes valuable data towards resolving the identity of these lesser-known endemics and enhances the reference base for future taxonomic revisions.

3.5. Conclusion

The present investigation provides a comprehensive morpho-anatomical and histochemical account of three endemic species of *Syzygium*- *S. laetum*, *S. occidentale*, and *S. palghatense*- from the Western Ghats. Detailed observations of macroscopic characters such as leaf morphology, venation patterns, floral traits, and fruit structures, along with microscopic features of leaf, stem, bark, and wood, have revealed a set of distinguishing characteristics that are taxonomically and diagnostically significant.

Leaf anatomy exhibited dorsiventral lamina, varied stomatal types, distinct venation patterns, and the presence of ergastic substances such as tannins, oil glands, calcium oxalate crystals, and starch grains. Stem and bark anatomy demonstrated variations in phellem structure, sclereid distribution, and crystal deposition, while wood anatomy confirmed diffuse-porous characteristics with species-specific patterns of parenchyma and ray composition. Floral anatomical traits, particularly the persistence or caducous nature of petals and vascular supply to reproductive organs, further contributed to distinguishing these taxa.

Histochemical studies confirmed the presence of tannins, druse and prismatic crystals, and secretory cavities, all of which not only serve as diagnostic markers but also underline the pharmacognostic and ecological significance of these species. These features provide adaptive advantages such as herbivore deterrence, structural reinforcement, and ecological resilience.

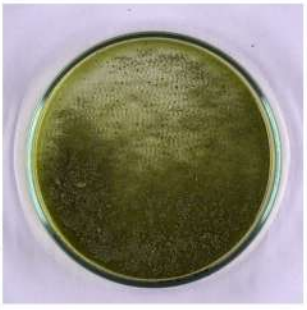
Altogether, the integration of morphological, anatomical, and histochemical data has proved effective in delineating closely allied species within *Syzygium*, a genus often plagued by taxonomic complexity due to overlapping vegetative features. The present findings enrich the existing knowledge of Western Ghats endemics, offering baseline data for their accurate identification, sustainable utilization, and conservation. Moreover, the pharmacognostic markers identified herein hold promise for future studies on the medicinal and economic potential of these species.

Thus, the study highlights that morpho-anatomical and histochemical investigations, when employed together, provide a reliable framework for species delimitation in *Syzygium* and contribute meaningfully to taxonomy, pharmacognosy, and conservation biology.

4

PHARMACOGNOSTIC CHARACTERIZATION









CHAPTER 4

PHARMACOGNOSTIC CHARACTERIZATION

4.1. Introduction

Pharmacognosy, the branch of pharmacology that identifies and quantifies naturally derived plant compounds, plays a crucial role in standardizing traditional remedies. Its importance for the pharmacy community and its ability to attract the general public are due to the secondary metabolites available in bioactive chemicals that could be employed for therapeutic activities. Pharmacognosy research reveals plants' physical, chemical, and biological features, which helps to inform people about their medicinal utility. It is an essential science from the perspective of herbal medicine, new drug discovery, and standardization of traditional remedies (Fabricant & Farnsworth, 2001).

Pharmacognosy is of Greek origin, meaning “pharmakon” (drug) and “gnosis” (knowledge). Pharmacognosy is the science of drugs derived from natural sources. Previously, only the external morphological characters were used for drug identification. In the initial phases, pharmacognosy developed primarily regarding botanical aspects, particularly describing and identifying drugs in whole and powder form. Modern elements of pharmacognosy not only study crude drugs but also their natural constituents (micro and macro) and their derivatives (Das, 2019; Mukherjee, 2002; Raghunathan & Mitra, 1985; Trease & Evans, 2002).

The term 'pharmacognosy' was first used by the Austrian physician Schmidt in 1811 and later coined by Anotheus Seydler in his dissertation, ‘Analecta pharmacognostic,’ In 1815. Pharmacognosy, closely allied to medicine, developed during the early century as part of Materia Medica and applied biology. It forms a bridge between pharmaceutics, traditional Ayurvedic knowledge, basic sciences associated with plant science, and modern allopathic medicine, showcasing its interdisciplinary nature. In general, it provides information for extracting and

identifying active substances from crude drugs used in dispensing, formulating, and manufacturing dosage forms. Pharmacognosy assists industries, acts as a research instrument, and develops new drug delivery systems, thus universally improving healthcare facilities in all pharmaceutical sectors (Das, 2019).

Pharmacognosy is an easy, reliable tool for obtaining complete information about a crude drug (Modi et al., 2010). Plants from natural sources are used for human benefit. Pharmacognostic characterization provides the fundamental requirement to distinguish between similar plant species and identify active bioactive agents with therapeutic potential. Herbal medicines are good alternatives to modern synthetic drugs. They have zero or few side effects and are considered safe. Most herbal formulations consist of fresh or dried parts, usually extracted first, to enhance healing effects.

Pharmacognosy deals with correctly identifying, collecting, and storing medicinal plant products or crude drugs to contain those in pure, genuine form related to herbal/ayurvedic drug preparations. The pharmacognostic study of crude drugs is a more accessible and more reliable tool that helps to provide exhaustive information. In pharmacognosy, plant specimens are assessed for their authentication. In this process, pharmacognostic profiling is an excellent technique that allows the differentiation of varieties of plants with diverse compounds (Mukherjee, 2002).

The evolution of modern pharmacognosy began between the 1930's and 1960's when it was expanded into different biological and socio-scientific disciplines (Das, 2019; Dhami, 2013). The present-day trends in pharmacognostic research are more favourable towards the herbal drugs' standardization and the quality control. Due to the surge in demand for plant-based medicines, each step involved in the pharmacognostic study must be carried out meticulously before such plants are identified with certainty, including free from contaminants. The crude extracts or their pure constituents need to be subjected to further investigation regarding the detailing of organoleptic properties, physicochemical parameters, and phytochemistry to determine their pharmacological activities and favour the establishment of evidence-based therapies (Pandey & Rawat, 2017). This includes the use of sophisticated

analytical methods like high-pressure thin layer chromatography (HPTLC), high-performance liquid chromatography (HPLC), ultra-pressure liquid chromatography (UPLC), gas chromatography-mass spectrometry (GC-MS), liquid chromatography combined with mass spectroscopy (LC/MS), high-resolution mass spectroscopy (HRMS), gas chromatography (GC), and paper-thin layer chromatography (TLC) for the separation and quantification of active phytochemicals having pharmacological significance (Das, 2019; Tripathi & Kohli, 2014).

Present trends of pharmacognostic research underscore the standardization and quality control of herbal drugs. Pharmacognostic studies are critical due to the increasing demand for herbal medicine, and these help in the proper identification/authentification and are also accessible from impurities. *Syzygium* species possess a variety of therapeutic properties like antioxidant, anticancer as well as antidiabetic activity, and to justify their use scientifically and promote them for the development of evidence-based therapies, it is essential to carry out an organoleptic evaluation based on phytochemical composition and physicochemical parameters, (Pandey & Rawat, 2017). This includes the identification and quantification of pharmacologically active compounds through sophisticated analytical methods like high-performance liquid chromatography (HPLC) and gas chromatography-mass spectrometry (GC-MS) (Tripathi & Kohli, 2014).

Pharmacognosy plays a vital role in the quality of herbal medicines, their safety and efficacy, and biomedical research. It is paramount that pharmacognostic studies are used to identify and prevent adulteration by using them taxonomically, which also acts as a standard set according to regulatory frameworks, such as in quality control (Pandey & Rawat, 2017). These assays facilitated the determination of macroscopical, microscopical as well as physicochemical properties or quality parameters, which are fundamental to assessing genuineness and purity range based on standard norms for preparing herbal drugs (Pandey & Rawat, 2017; Tripathi & Kohli, 2014).

Pharmacognostic studies are paramount in drug development to understand bioactive compounds in medicinal plants and delineate and debar adulteration. The

phytochemical profiling can help isolate new drugs for treating various diseases, including diabetes, infections, and inflammation. A few researches on *S. cumini* reported secondary metabolites like flavonoids, alkaloids, and phenolic compounds. The plant showed antidiabetic and antioxidant effects with these metabolites (Biswas & Sen, 2018). To establish new therapeutics using plant sources leading with the significance of the pharmacognostic research in modern pharmaceutical science (Lakshmi et al., 2021).

Systematic pharmacological characterization is critical in identifying bioactive molecules from plant metabolites, and this helps to provide a rational base for designing clinical trials and testing their use as therapeutic potential. The most important task of this process is to validate the traditional claims regarding these plants scientifically. The genus *Syzygium* includes numerous species widely distributed throughout the tropics and subtropics. It has been used as medicine for a long time. *S. cumini* (L.) Skeels are commonly known as jamun and are used in Ayurveda for their anti-diabetic properties, while *S. aromaticum* (L.) Merrill & Perry, also called clove, has been reported to show analgesic and antimicrobial activities, respectively. Various species under the genus *Syzygium* have been described to possess significant ethnomedical/pharmacological importance (Tripathi & Kohli, 2014). Lakshmi et al. (2021) reported that *S. cumini*, *S. aromaticum,* and *S. caryophyllatum* were used for their medicinal benefits for centuries to cure several disorders, including diabetes, inflammation, and microbial infections. Newer research has strengthened the drug-like properties of the targeted genus; indeed, when validated for efficacy, such plants are likely to be safer during their use in modern drug discovery.

They are also convenient in natural resource conservation. Pharmacognostic studies provide an innovative means of recognizing sustainable medicinal plant sources; this helps encourage the stakeholders to participate in the responsible utilization and conservation of biodiversity. Pharmacognostic research helps check overexploitation and conserves medicinal plant resources, sustainably providing them for other generations. This point is especially relevant due to the growing international

market for herbal medicines, which causes a strain on natural systems and calls for sustainable sourcing methods (Pandey & Rawat, 2017).

Pharmacognostic characterization was carried out in this investigation using different techniques. The pharmacognostic status of the three plant species was determined by performing powder microscopy, fluorescence analysis, and physicochemical evaluation. *S. laetum* and *S. palghatense* were gathered from Nelliyampathy, Palakkad, Kerala, while the *S. occidentale* was obtained from the Athirapilly-Vazhachal forest, Thrissur, Kerala. The collected leaves, stems, and bark of these endemic plants were dried separately under the shade. The dried samples were chopped into small pieces and separately powdered using a blender. These pharmacognostic studies together lay down the groundwork for further study of the therapeutic potential of these *Syzygium* species and will ensure their safe use in herbal formulations. For further studies, each dried powdered plant sample was tightly capped with airtight sterile containers.

This comprehensive pharmacognostic study will help in accurate botanical identification and quantitatively determine the primary biochemical entities, eventually benefiting genuine traditional utilization and drug standardization. These analyses were thought to be helpful for the development of investigative pharmacologic and therapeutic strategies.

- **Objectives**
    - The leaves and bark powders of *S. laetum*, *S. occidentale,* and *S. palghatense* were subjected to powder microscopic study.
    - Fluorescence analysis of powder samples of the selected samples.
    - Physicochemical evaluation of the leaf and bark powders of the selected samples.
    - Assessment of the nutritional potential of the selected endemic plants.

4.2. Materials and methods

The leaf and bark powders of selected species, *S. laetum*, *S. occidentale*, and *S. palghatense*, were subjected to pharmacognostic evaluation involving powder microscopy studies, physicochemical, and fluorescence analysis. These techniques will provide unique information on plant materials' structural, chemical, and physical properties. Powder microscopy is utilized to distinguish and authenticate cellular characteristics like fibres, trichomes, and parenchyma cells so that the samples meet quality standards.

The fluorescence analysis justifies the presence of specific phytochemicals to discern colour variations under visible (254 nm) and UV light (366 nm), which demarcates characteristic bioactive compounds wherein each species is distinctive. Physicochemical evaluation deals with mandatory parameters, including ash value, crude fibre, vitamins, and extractive values, that assist in quality control and standardization. These concordant results from the pharmacognostic studies will provide a base for the therapeutic use of these *Syzygium* species, which could improve safety and efficacy in herbal formulations.

4.2.1. Powder microscopy

Microscopical studies are essential for identifying and analyzing anatomical structures of plant materials based on pharmacognostic parameters. Plant powders of selected samples were shade dried and finely ground using a mortar and pestle, then passed through a 40-mesh sieve to achieve uniform particle size, facilitating accurate microscopic observation. The powder samples were soaked overnight in 4% potassium hydroxide (KOH) solution to soften the tissues. Following softening, the samples were stained with safranin, a histological dye that colours lignified and other structures red, aiding in differentiating tissues such as xylem fibers and parenchyma cells. The stained powders were mounted on clean glass slides using glycerine, which preserves tissue clarity and prevents dehydration, providing a consistent refractive index for microscopy. Microscopic observations were performed using a Nikon ECLIPSE E200 trinocular microscope equipped with a Zeiss AxioCam ERc 5s digital camera. Photomicrographs were captured at various magnifications to document the

characteristic microscopic features critical for pharmacognostic evaluation. This method follows established pharmacognostic protocols (Anonymous, 2008; Jagtap & Koche, 2023; Singh et al., 2018; Tandon & Sharma, 2017).

4.2.2. Fluorescence analysis

Pharmacognostic research includes a preliminary study of plant powders treated with different reagents. The leaf and bark powders of selected plant samples were exposed to solvent treatments (acetone, acetonitrile, methanol, and distilled water) to understand any biochemical reaction that caused a colour change. Otherwise, these interactions may reflect the presence of some phytochemicals or bioactive compounds in plant material. The difference in chemical constituents is detected by fluorescence analysis of these solvents and the sample after treatment with visible light (254 nm) and UV (366 nm). Such changes in colour and fluorescence give qualitative information, which is also crucial for the barcoding of plant materials. When adequately excited with ultraviolet light, all phytochemicals will fluoresce. This, therefore, revealed an essential pharmacognostic pathway in distinguishing secondary metabolites. Such types of studies will also help to provide additional support for the identification and assessment concerning chemical composition profiling towards quality standardizations depicting critical concentrations that can bring about medicinal applications (Gupta et al., 2006; Jagtap & Koche, 2023; Tandon & Sharma, 2017).

4.2.3. Physicochemical evaluation

The powdered leaves and bark samples of the selected plants were evaluated for the following physicochemical investigations using well-established procedures (Anonymous, 1996; Bekele & Geleta, 2015; Bhattacharya & Zaman, 2009; Bigoniya et al., 2012; Kumar et al., 2012; Mulla & Paramjyothi, 2010; Pandey & Rawat, 2017; Rutkowski & Grzegorczyk, 2007; Sasmal et al., 2012; Sharma et al., 2013; Tandon & Sharma, 2017).

4.2.3.1. Determination of extractive values

The extractive value of any plant material is a vital parameter in pharmacognostic studies as it specifies the active constituents dissolved per unit weight of the solvent drug. The extractive value could be utilized to examine the effectiveness and efficiency of acquiring chemical elements from the crude drug. One such value is indicative of the type of mixtures present in the plant material, and it may provide helpful information if determined by extraction with solvents.

Solvent selection facilitates extracting bioactive principles and is an essential aid in the quality assurance of herbal products since they express identity and quantity (Pandey & Rawat, 2017). Hence, the in-depth assessment of extractive values is necessary for pharmaceutical applications to maintain standardization and efficacy in plant-derived formulations concerning traditional and modern medicine.

4.2.3.1.1. Water-soluble extractive

An air-dried granulate (5.0 g) was introduced into a stoppered flask; 100 mL deionized water was added, and the mixture allowed to soak over ≈24 h, then stirred for an additional ≈6 h. The suspension was passed through a paper filter while minimizing solvent loss. A 25 mL portion of the aqueous extract was transferred to a pre-tared, shallow flat-bottom dish, evaporated to a dry residue, oven-dried (105 °C), and weighed.

A higher extractive value indicates that more bioactive compounds increase medicinal and other uses of plants. This standardization process is indispensable because it guarantees that the raw material employed in herbal medicine corresponds to drug quality standards established for therapeutic effects.

4.2.3.1.2. Alcohol-soluble extractive

Approximately 5g the granular sample was dried using air with 100 mL of alcohol (95 % ethanol) in a stopper flask kept for 24 hours. The content was shaking frequently for six hours. It was filtered through filter paper taking precautions against excessive loss of alcohol. 25 mL of alcohol-soluble extract was evapourated to

dryness in a tarred flat-bottomed shallow dish. It was dried at 105°C and weighed. The percentage of alcohol soluble extractive value was determined with special standard reference to the air-dried drug.

More alcohol extractive value indicates more ethanolic soluble portion and, ultimately, more significant therapeutic potential. Such analysis is essential to controlling the quality, efficacy, and safety of herbal products by setting standards in terms of plant material. The quality of tinctures, extracts, and other ethanol-based preparations is crucial for traditional herbal medicine and modern science.

4.2.3.1.3. Petroleum ether extractive

The petroleum ether extractive value is one of the index values in pharmacognostic research, and it can be used to evaluate materials with high concentration levels of non-polar compound constituents (i.e., essential oils) or plant-active substances containing fats, resins, and lipophilic compounds. Here, refluxing 5 g of air-dried and powdered plant sample with 100 mL petroleum ether overnight (24 hours) has been used to extract the non-polar bioactive compounds. Reflux prevents the solvent from evaporating and ensures continuous contact with the plant material because it keeps the solution at a constant temperature during extraction, enhancing the efficient extraction rate. The mixture is refluxed for 24 hours and filtered through Whatman No. 1 filter paper to afford the solid residue and petroleum ether extractable component in filtrate collection as separations complete of costly time wasted clinging via solvent management. To determine these compounds, 10 mL of that extract is transferred into a container with known weight, where this diluted filtrate will be evaporated and measured to obtain the final value for both extracts after evaporation.

The filtrate was concentrated to dryness at 105°C until no solvent traces were present, leaving the solid petroleum ether-soluble residue. When dry, the dish is reweighed to measure how much petroleum ether-soluble material was in that sample. The petroleum ether-soluble extractive value is expressed as a percentage of the weight of the dried residue to that of the drug used initially. This value assists in assessing their quality and therapeutic utility, mainly for drugs with non-polar constituents (e.g., essential oils or resins). This method ensures standardization,

quantifies the petroleum ether-soluble fraction in plant material, and maintains quality control.

4.2.3.1.4. Ethyl acetate soluble extractive

An accurately weighed 5 g portion of powdered, air-dried plant material was subjected to reflux with 100 mL of ethyl acetate for 24 h to extract solvent-soluble constituents. Continuous refluxing maintained direct solvent–sample contact, promoting complete dissolution of target compounds. The hot mixture was passed through Whatman filter paper to remove undissolved residues. From the clear filtrate, a 10 mL portion was transferred into a pre-tared dish. The solution was again clarified, if necessary, then evaporated to dryness in an oven at 105 °C, leaving only the solid extract.

Dried residue was weighed and the weight of dried residuum, calculated as percentage concerning original plant sample represents ethyl acetate soluble extract value. This technique also provides identification and quantification of non-polar or moderate polar constituents, which is beneficial for the standardization and quality control of herbal medicines.

4.2.3.2. Crude fibre

A finely ground crude sample (34 g) was weighed accurately and defatted at room temperature with petroleum ether to remove lipids and other non-polar substances. After drying, 2 g of the material was boiled in 200 mL of 1.25% H_2SO_4 for ~30 min to hydrolyze water-soluble carbohydrates and related impurities. The hot mixture was passed through muslin cloth, and the residue was rinsed thoroughly with boiling water to eliminate excess acid. The recovered solid was then treated with 200 mL NaOH (aqueous) and boiled for 30 min to solubilize alkali-extractable components, including proteins. After this step, the residue was again filtered through a cloth made from the muslin fabric, adequately washed using 25 mL of 1.2 percent sulphuric acid, and subsequently rinsed twice each with distilled water (50 mL) and ethanol (25 mL). The cleaned residue was transferred to a pre-weighed silica crucible for further analysis.

The crucible that contained the residue was then dried at 130°C for two to three hours, left in a desiccator to cool down, and weighed. The residue was incinerated at 600°C for 30 minutes to remove any organic matter, and the ash content was used as a measure of fibre fraction in the final material. The crucible was made to cool again inside the desiccator and weighed to get the final reading. Crude fibre in the sample was expressed as percent by comparing it with weight of dried and incinerated residue. This process provides a good approximation of the crude fibre content; hence, it gives insights into what structural carbohydrates are present in that plant material.

4.2.3.3. Vitamin A

A regulated, well-ordered procedure was adapted for the analysis of Vitamin A from plant samples whereby extraction and quantification were executed ensuring accurate results with maximum reliability. A 10 g of homogenized sample powder was mixed with pyrogallic acid (1 g), ethanol (70 mL), and a 50 % potassium hydroxide (30 mL) solution. The mixture was subjected to refluxing inside the water bath at a temperature of fifty degree Celsius for forty minutes to support continuous drug interaction and extraction of vitamin A efficiently. To be comprehensive, the extraction was performed 3 times with ether.

The extract derived was neutralized with double-distilled water to eliminate excess alkalinity. The anhydrous sodium sulphate powder was added to check the intactness of the moisture, and the residue was removed. Subsequently, the extract was evaporated to dryness by a solvent at 50°C in a water bath. In 10 mL of methanol, the crude extract was dissolved and filtered by a 0.45 µm membrane filter to prepare further testing methods with an effective, clean extraction.

Vitamin A content was determined by spectrophotometry. An aliquot of 2.0 mL of the extract was transferred into a stoppered tube (Tube I). To this, 1.0 mL of KOH solution (1 M, prepared in 90% ethanol) was added, and the mixture was vortexed for ~1 min. The tube was then placed in a 60 °C water bath for 20 min, followed by rapid cooling in ice water. After cooling, 2.0 mL of xylene was added, and the tube was shaken for 1 min to allow phase separation. For raw samples, 2.0 mL

was measured into a tightly capped tube and combined with 1.0 mL of 1 M ethanolic KOH. The mixture was vortexed again for 1 min, then heated inside a 60℃ bath for about twenty minutes to complete saponification of esterified vitamin A. The solution was cooled by immersion in cold water, and 2.0 mL of xylene was introduced and shaken vigorously to transfer vitamin A into the organic layer.

This was followed by centrifuging the mixture for 10 minutes at 1500 rpm. The supernatant was then collected into another test tube (II). Extracts were tested for absorbance at 335 nm against xylene, and the extract was named AI. After 30 minutes, the extract in test tube II was exposed to UV light, and the absorbance was measured and labelled A2. The maximum absorption wavelength was evaluated.

4.2.3.4. Vitamin C

Vitamin C was extracted by homogenizing 10 g of powdered sample in an extraction solution that contained exactly 1.4 M acetic acid and 0.3 M metaphosphoric acid. The mix, after that, was put into a conical flask for 15 minutes with agitation at 10,000 rpm, ensuring complete extraction. Extraction was carried out in triplicate to validate the robustness and reproducibility of the method.

Determination of ascorbic acid (vitamin C) was done by the iodometric titration. It has used 0.05 M sodium thiosulphate ($Na_2S_2O_3$) solution and starch indicator for endpoint determination. The titration was performed by adding 0.05 M sodium thiosulphate solution dropwise from a burette to the mixture of 10 mL extract, 10 mL iodine solution, and three drops starch indicator. Iodine titration continued until the solution turned blue-black to colourless, signifying that all iodine had reacted with ascorbic acid.

To ensure accuracy, a blank calibration was performed by repeating the titration using distilled water, iodine solution, and starch indicator, in order to establish the baseline iodine level. The volume of sodium thiosulphate necessary to produce the discolouration in the test solution was recorded. From the volume of sodium thiosulphate consumed for titration, the concentration/amount of ascorbic acid was determined in stoichiometric calculations. That ensures a complete reaction of

iodine and ascorbic acid, accounting for the accurate measurement of vitamin C in the sample.

4.2.3.5. Minerals

Approximately 5.0 g of the powdered, air-dried material was placed on an electric hot plate to remove organic matter, then ignited in a muffle furnace ramped to 525 °C until a white ash was obtained. The mineral ash was treated with 15 mL of dilute HNO_3 to dissolve mineral components, and the solution was filtered through acid-resistant quantitative paper. To maximize recovery, the residue was rinsed several times with distilled water, and the combined filtrates were adjusted to a final volume of 100 mL in a volumetric flask.

Calibration standards were prepared in the ranges of 10–100 ppm (Na and K) and 15–100 ppm (Ca). These were used to generate calibration curves for quantifying sodium, potassium, and calcium by absorbance measurements. Mineral concentrations were reported on a moisture-free basis, providing accurate values for each element in the plant sample. This approach is essential for standardization and for assessing the nutritional and pharmacological properties of *Syzygium* species.

4.2.3.6. Heavy metals

The contents of heavy metals (copper, Cu; manganese, Mn; zinc, Zn; lead, Pb; arsenic, As; cadmium, Cd; mercury, Hg) were established by an atomic absorption spectrometer (AAS). Calibration was carried out by preparation of a series of working standards from the stock solutions of each metal. 0.2-0.5 g of plant material was transferred to a digestion tube for sample preparation, followed by the digestion of samples with 5 mL of nitric acid (HNO_3), 0.5 mL of hydrochloric acid (HCl), and 1 mL of hydrogen peroxide (H_2O_2). After this, the mixture was self-digested for 15 minutes to degrade any organic matrix and liberate metals.

Then, after digestion, the mixture was transferred into a 50 mL glass volumetric tube and the volume was modified to 50 mL with the help of ultra-pure water. After this process, absorbance of the known metal concentrations working standards was recorded to prepare a calibration curve. The absorbance of the sample solutions was

measured against a calibration curve to determine concentrations of copper, manganese, and zinc in the studied samples. The results were finally represented as the percentage of each metal present in the sample, accurately estimating the heavy metals.

4.2.3.7. Total ash

The total ash value was estimated using 2–3 g of accurately weighed, air-dried powdered sample placed in a pre-tared platinum or silica crucible. To prevent loss of mineral constituents, the temperature during ignition was maintained below 800 °C, with gradual heating to minimize carbonization. After ignition, the crucible was cooled in a desiccator and weighed.

The partially charred residue was rinsed with hot water to remove any carbon present, and the insoluble fraction was collected on ashless filter paper. Both the filter paper and retained residue were incinerated together in the original crucible until a white or nearly white ash was obtained. The washed and charred fraction was returned to the crucible, evaporated to dryness, and ignited again to ensure complete removal of organic matter.

Finally, the crucible was cooled, weighed, and the ash percentage calculated relative to the original dry sample weight. This method provides accurate determination of inorganic matter, contributing to standardization and quality evaluation of plant material.

4.2.3.8. Acid-insoluble ash

The total ash was treated with 25 mL of 2 M HCl and gently boiled for about 5 minutes. The insoluble fraction was collected on ashless filter paper or in a Gooch crucible, rinsed thoroughly with hot water, ignited to a constant weight, cooled in a desiccator, and weighed. If traces of organic matter remained, the residue was re-ignited until completely free of carbon, then cooled again in the desiccator and reweighed. The percentage of acid-insoluble ash was then calculated for each sample, and the results were applied in the standardization and quality evaluation of the botanical material.

4.2.3.9. Water-soluble ash

The ash obtained from the previous step was treated with 25 mL of distilled water and heated for ~5 minutes to dissolve water-soluble components. The undissolved fraction was collected either on ashless filter paper or in a Gooch crucible, then thoroughly rinsed with hot water to remove any remaining soluble matter. The dried residue was ignited at 800 °C for about 15 minutes under airflow to ensure complete combustion of organic content, cooled, and weighed. The mass of this insoluble fraction was subtracted from the total ash to calculate the water-soluble ash. The final value was expressed on a dry-weight basis and reported as percentage yield.

4.2.3.10. Sulphated ash

Sulphated ash was determined by igniting 2 g of airdried and powdered sample with nickel crucibles pre-moistened within sulphuric acid to promote oxidation of organic matter. The sample was then ignited gently to start the decomposition process. The residue was again moistened with concentrated sulphuric acid till complete oxidation and reignition.

The crucible was transferred to a desiccator at room temperature for cooling, and then the weight of the residue was calculated. The results are expressed as a percent of the weight of the air-dry sample and should give a rough idea of the number of inorganic constituents present, usually known as sulphate ash content. Following organic removal, determining mineral residues provides a measure to establish reproducibility and quality control for standardization.

4.2.4. Statistical analysis

One-way ANOVA was carried out to test the differences among group means for various parameters. The data were analyzed by computing the sum of squares between groups and within groups to obtain mean squares. The F-statistic was calculated as the ratio of mean square between groups to mean square within groups. A p-value less than 0.05 indicated significant differences between the groups. Following significant ANOVA results, post-hoc analysis was performed using the

least significant difference (LSD) or critical difference (CD) method to identify which specific groups differed significantly (Salkind, 2017).

Cluster analysis was performed using hierarchical clustering based on Euclidean distance and the average linkage method. This agglomerative method began with each object as its own cluster and progressively merged clusters based on similarity until the final clusters were formed. The results were visualized using a dendrogram to interpret grouping patterns. These methods follow standard statistical procedures for analyzing group differences and patterns without prior assumptions of cluster membership (Salkind, 2017).

Principal component analysis (PCA) was performed to reduce data dimensionality and visualize patterns among variables. The analysis was based on the correlation matrix, and components with eigenvalues greater than one were retained. A biplot was constructed to display the distribution of variables and samples on the first two principal components, enabling interpretation of associations and groupings (Jolliffe & Cadima, 2016).

4.3. Results

4.3.1. Powder characteristics of leaves and bark of *Syzygium* endemics

The visible macroscopic features of the plants in whole and powdered forms were documented through the natural senses. The organoleptic features of the plants (powdering behaviour, particle size, texture, colour, feel, odour, and taste) in fresh and dried forms were systematically observed and documented. The organoleptic features of the powdered drugs are documented in Table 4.1, Plate 4.1, and Plate 4.2. Before conducting other tests, the identity and purity of the medicinal plant materials can be established through organoleptic evaluation. Organoleptic characters are a very simple and quicker way to judge the quality and purity of a particular crude drug. Powder microscopic studies of the leaves and bark of *S. laetum*, S. *occidentale,* and *S. palghatense* revealed distinct anatomical characteristics, which are documented in Plates 4.3 to 4.8.

Distinct characteristics were observed upon macroscopic analysis of leaf and bark powders from *S. laetum*, *S. occidentale,* and *S. palghatense*. The grinding nature of the leaf powders was varied, with *S. laetum* and *S. palghatense* readily ground as opposed to *S. occidentale*, which required moderate grinding effort. All the species had similar particle distribution for leaf powders, which had moderately coarse (*S. laetum*) to fine and smooth (*S. palghatense*) textures. The different coloured variants included dark green (*S. laetum*), light green (*S. occidentale*), and pale green (*S. palghatense*). Aromatic properties were identified in all the leaf powders, and the characteristic smell was found in the bark powders while conducting organoleptic evaluation. *S. laetum* and *S. occidentale* exhibited astringent leaf powders and bitterly pungent bark powders, while *S. palghatense* exhibited bitterly pungent leaf and bark powders. Bark powders maintained gritty, fibrous textures with greater astringency than other powders, likely attributed to tannins. Such unique properties provide good taxonomic markers for species identification and even quality assessment.

Each *Syzygium* species in the current study provided unique distinguishing characteristics, as revealed by the powder microscopic study. The sectional and surface from the petiole and midrib show stomata and crystals of *S. laetum* leaf

powder. They also contained parenchymatous cells, collenchymatous cells, mesophyll fragments, vessels, fibers, starch grains, stone cells, and oil droplets. The bark powder contained cork, cortical cells and different types of crystals, crystal fibers, septate fibers with peculiar outgrowths or projections, parenchyma cells with reddish-brown content, sclereids, and stone cells. The powder microscopic examination of *S. occidentale* leaf powder revealed typical epidermal features, both adaxial and abaxial surfaces, stomata type, palisade cells, vascular strands, and the presence of three forms of calcium oxalate crystals (rosette, prismatic, and rod). The bark powder comprised cork cells in different orientations, pitted parenchyma cells, fibre fragments, sclereids, pigment cells, starch grains, and calcium oxalate crystals. *S. palghatense* leaf powder revealed stomata, sclereids, fibres, vessels, starch grains, and crystals. The bark powder showed cork cells, thick-walled parenchyma cells with reddish-brown content, medullary ray cells, crystal fibres, and stone cells commonly associated with starch grains. Overlapping powder microscopic attributes are consistent taxonomic markers for identifying and authenticating species.

4.3.2. Fluorescence analysis

Fluorescence study seems to be a necessary parameter for the initial crude drug standardization. In fluorescence, the fluorescent light will always have a longer wavelength than the exciting light. Short-wave light is very active in causing fluorescence, and for this reason, especially UV light leads to a phenomenon (known as fluorescence) found in several substances that do not visibly fluoresce under daylight.

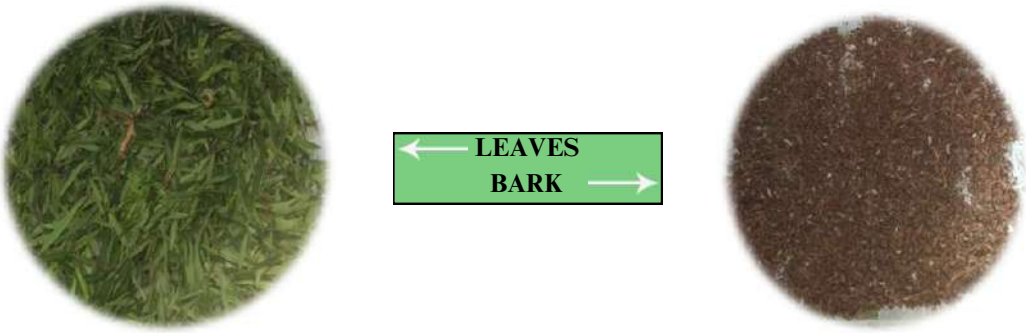
The dry powders and extracts of *S. laetum*, *S. occidentale*, and *S. palghatense* fluoresce differently (Tables 4.2 to 4.7). The three species give a broad range of fluorescence colours when the solvent or reagent is varied. *S. laetum* directs colours such as verdant green and olive using reagents like acetone and benzene, and *S. occidentale* uses pigments such as verdant green and olive with identical treatment. With other solvents, *S. palghatense* also shows colours like light green and pale brown. Regarding extracts, *S. laetum* and *S. occidentale* yield fluorescent colours, including green, brown, and olive green under petroleum ether and chloroform

Table 4.1: Organoleptic features of the powdered drugs: *Syzygium laetum*, *Syzygium occidentale,* and *Syzygium palghatense*

Macroscopic Characters	*Syzygium laetum*		*Syzygium occidentale*		*Syzygium palghatense*	
	Leaf powder	**Bark powder**	**Leaf powder**	**Bark powder**	**Leaf powder**	**Bark powder**
Powdering behaviour	Easy to grind	Moderately difficult to grind	Moderately easy to grind	Difficult to grind	Easy to grind	Moderate to difficult to grind
Particle size	Uniform	Uneven with larger fragments.	Uniform	Uneven with larger fragments	Uniform	Uneven with larger fragments
Texture	Moderately coarse with visible fragments	Coarser and fibrous	Slightly coarse and fibrous	Highly fibrous	Fine and smooth	Granular and fibrous
Colour	Green to dark green	Light to dark brown	Light green	Light brown	Pale green	Light to dark brown
Feel	Light and flaky, not very dense	Rough and gritty due to the fibrous structure.	Soft and slightly granular	Rough and gritty, with noticeable fibers.	Light, fine, and smooth	Rough and granular
Odour	No distinctive odour	No noticeable odour or characteristic smell	No noticeable odour	No noticeable odour	No noticeable odour	No noticeable odour
Taste	Neutral or mildly bitter without any strong characteristic taste	Slightly astringent taste due to tannin content, which is common in bark samples	No characteristic taste	Slightly astringent	Slightly bitter	Moderately astringent



(a)



(b)



(c)

Plate 4.1: Comparative morphological display of shade-dried leaves and bark of (a) *Syzygium laetum* (b) *Syzygium occidentale* (c) *Syzygium palghatense*

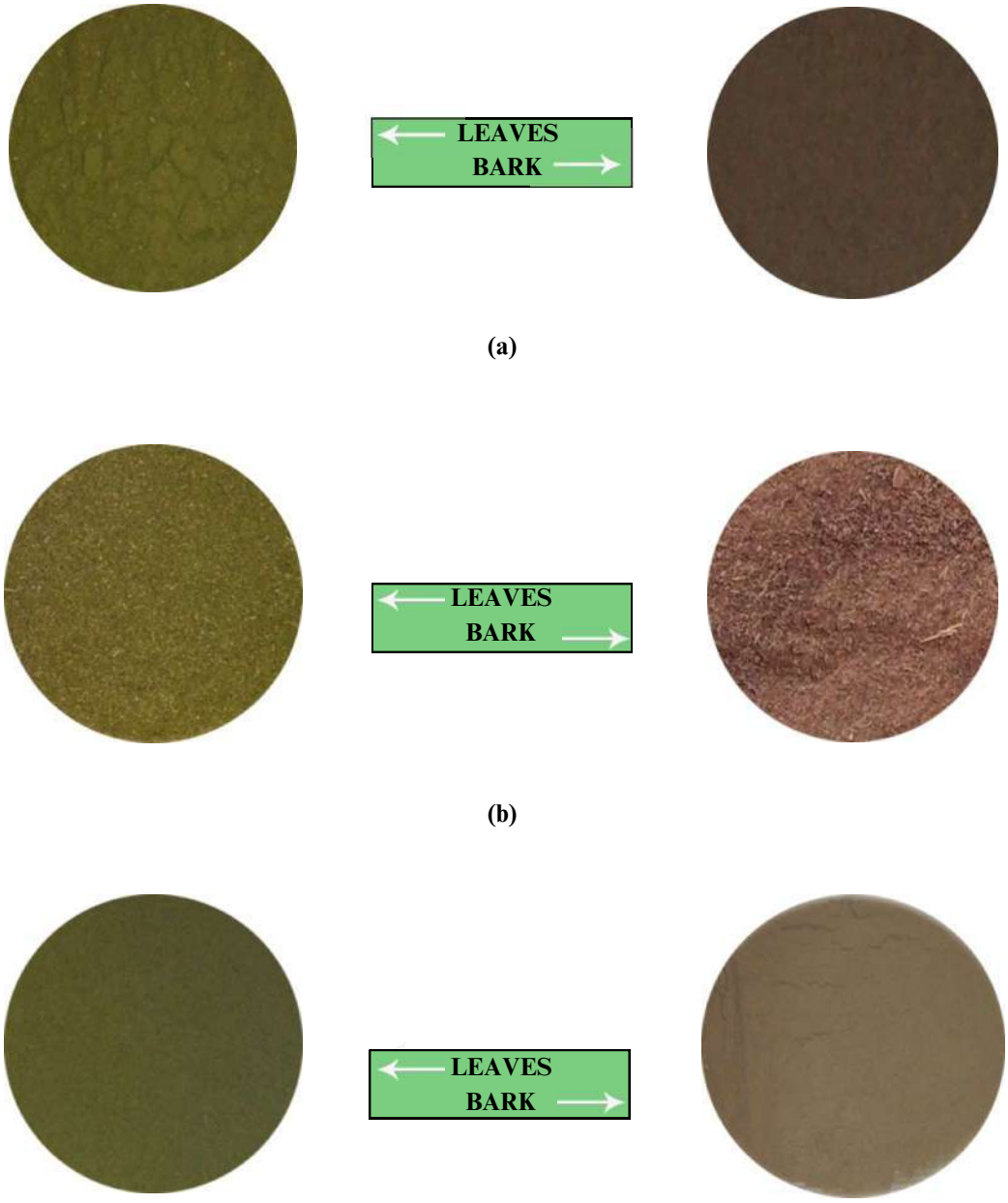
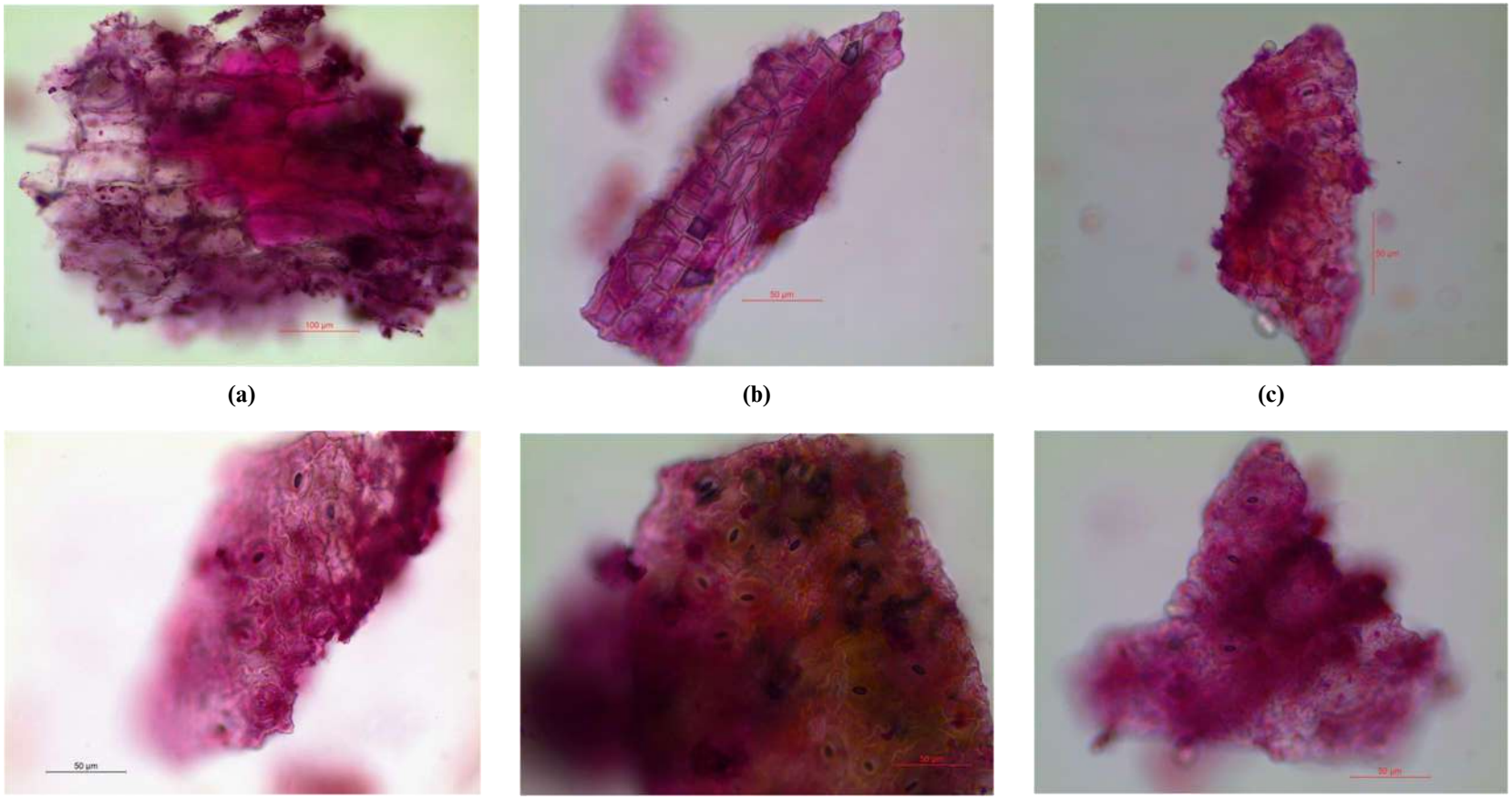


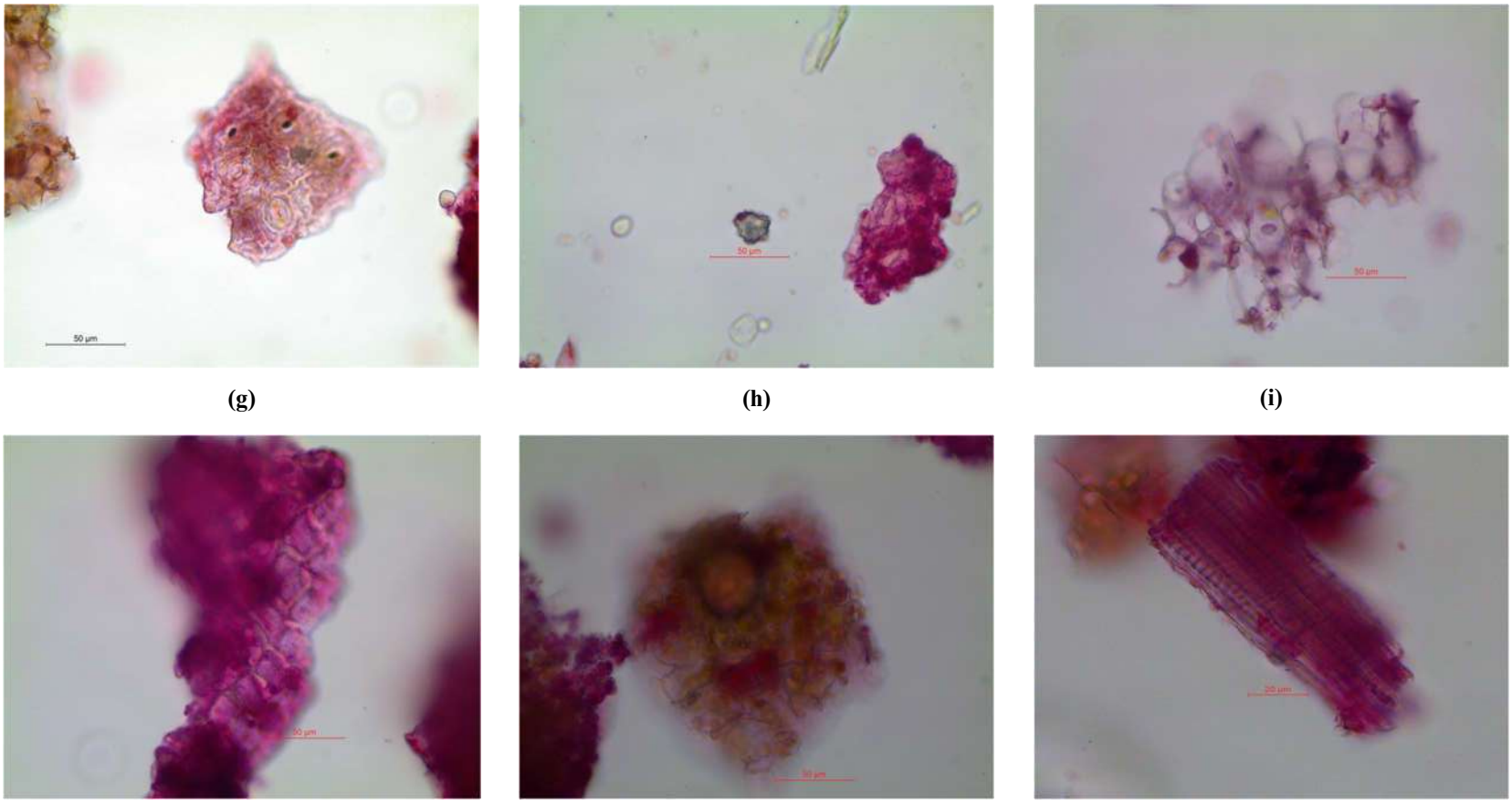
Plate 4.2: Comparative morphological display of powdered leaves and bark of (a) *Syzygium laetum* (b) *Syzygium occidentale* (c) *Syzygium palghatense*



(a) **(b)** **(c)**

(d) **(e)** **(f)**

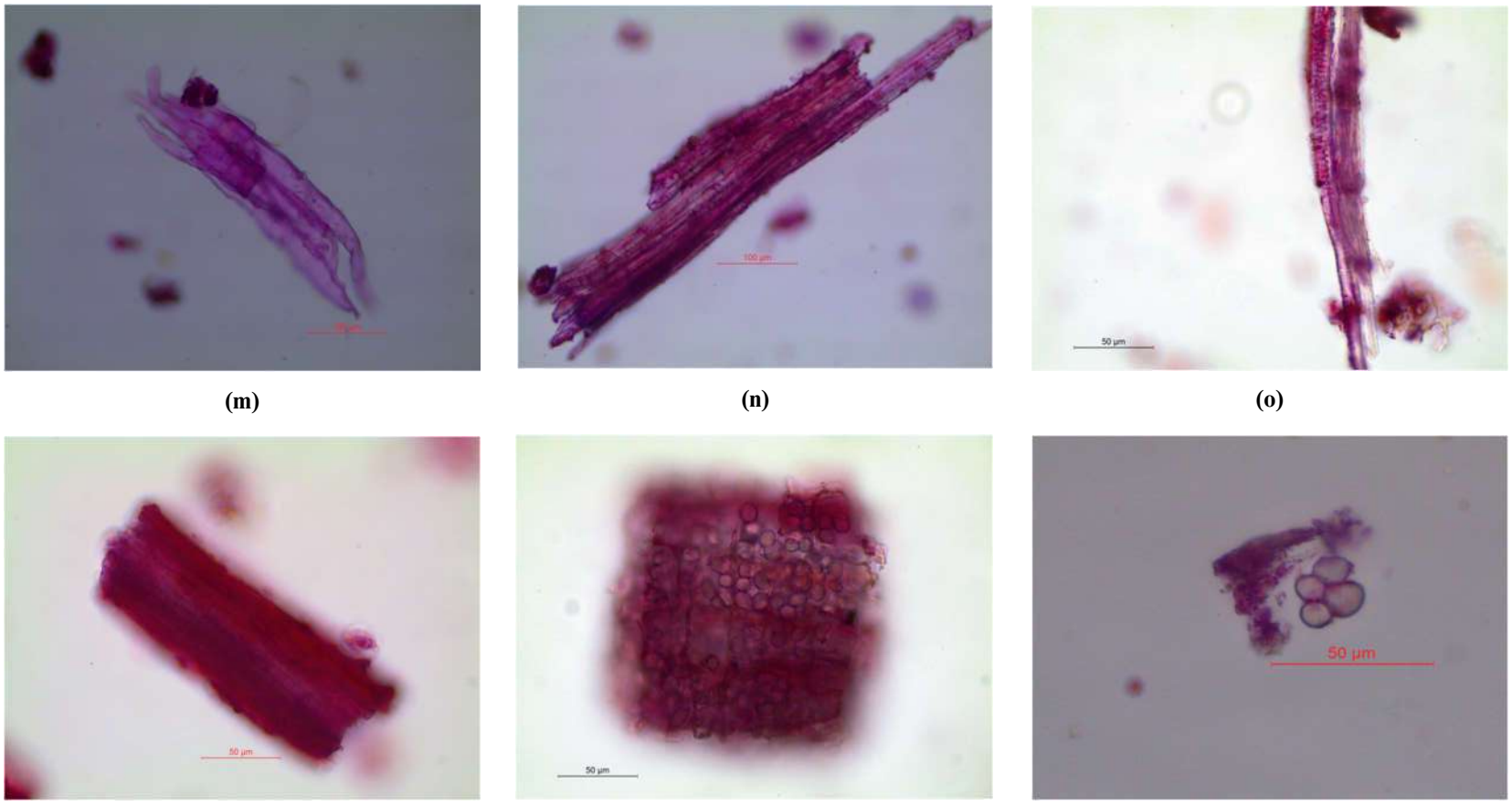
Plate 4.3: Powder microscopic studies of *Syzygium laetum* leaves- (a) Epidermis in sectional view from the petiole (b) Epidermis in surface view from the midrib (c) Epidermis showing stomata and crystals (d) & (e) Surface view of the epidermis with stomata (f) Lower epidermis with stomata



(g) **(h)** **(i)**

(j) **(k)** **(l)**

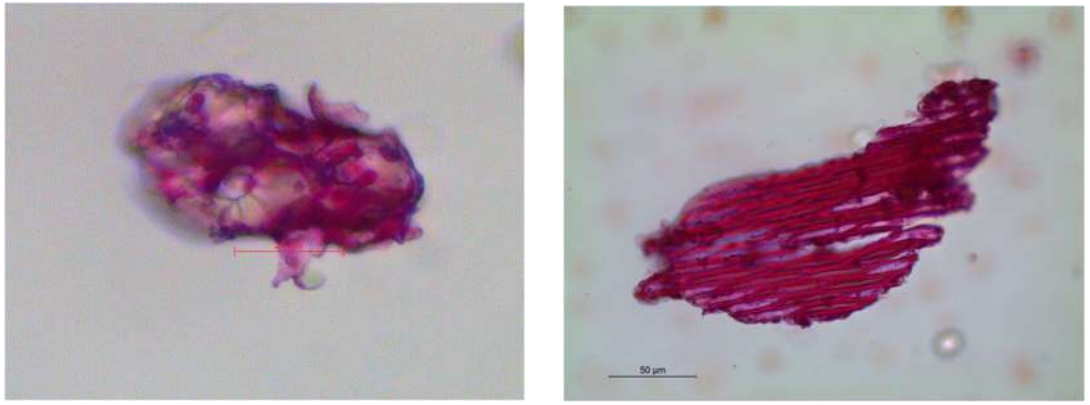
Plate 4.3: Powder microscopic studies of *Syzygium laetum* leaves- (g) Stomata (h) Calcium oxalate crystals (i) Fragments of parenchymatous cells (j) Collenchymatous cells in surface view (k) Fragments of mesophyll cells (l) Vessels and fibres



(m) **(n)** **(o)**

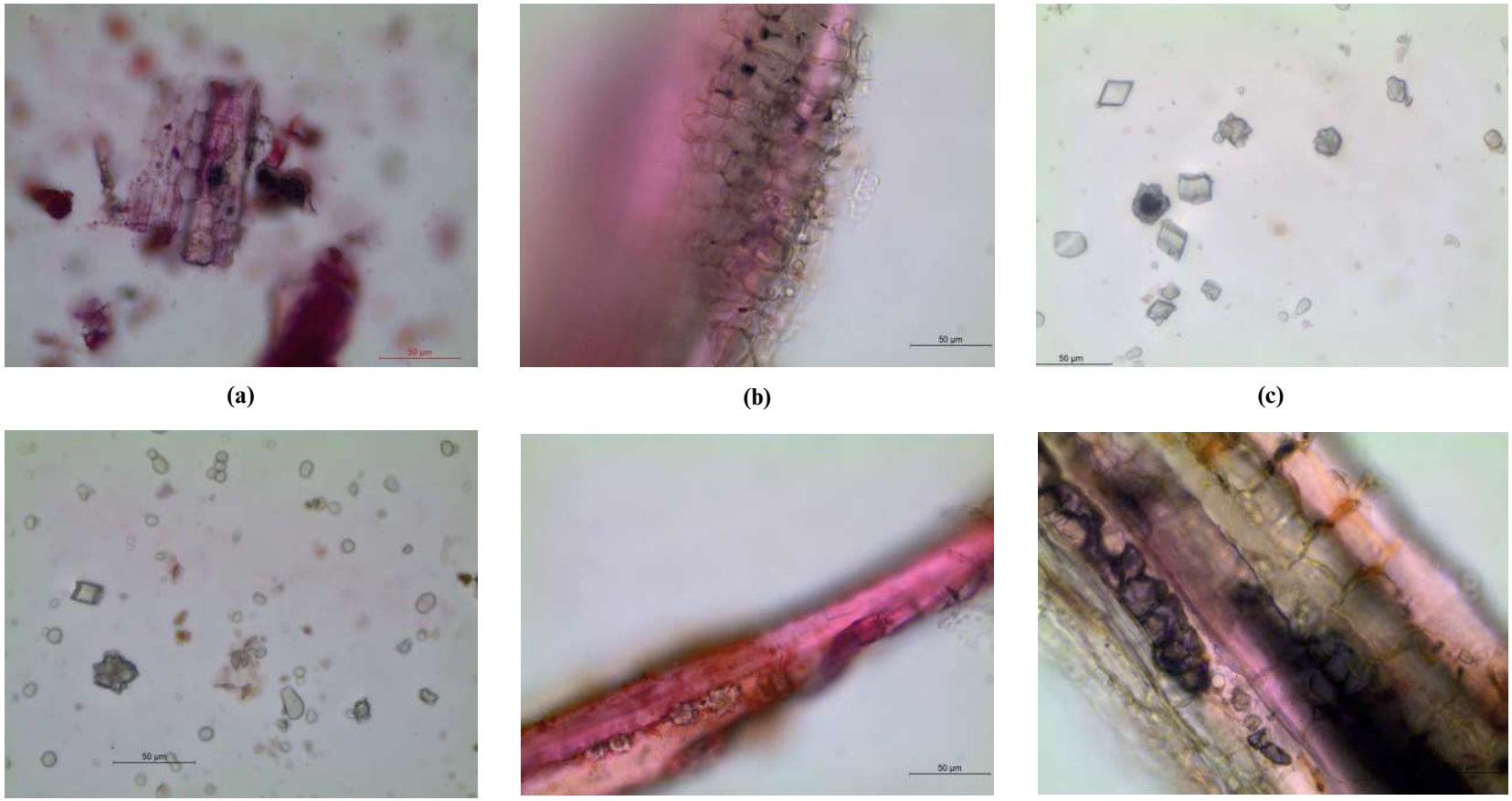
(p) **(q)** **(r)**

Plate 4.3: Powder microscopic studies of *Syzygium laetum* leaves- (m) Vessels and fibres (n)-(o) Fibres (p) Fragments of fibres (q) & (r) Starch grains



(s) **(t)**

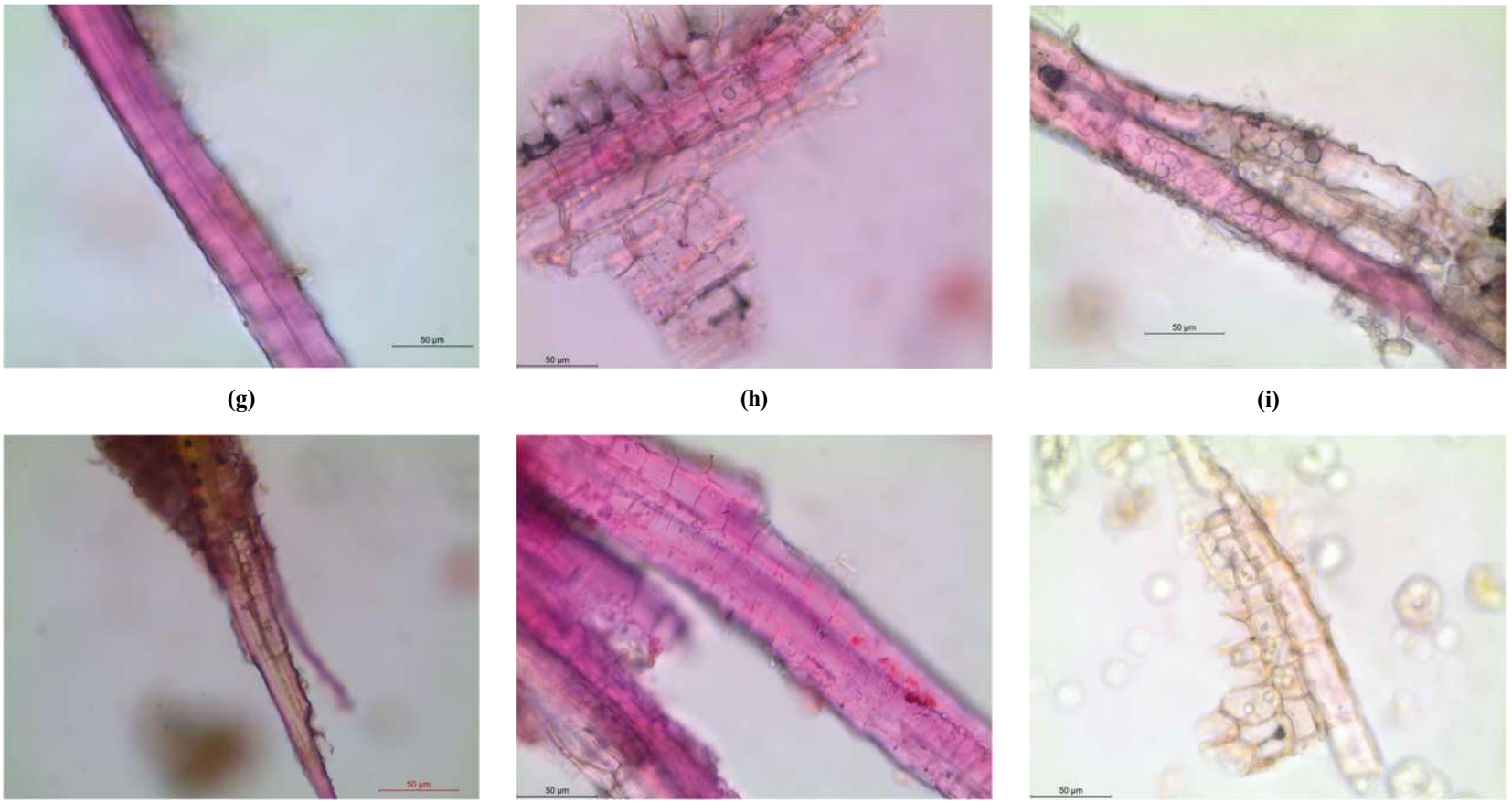
Plate 4.3: Powder microscopic studies of *Syzygium laetum* leaves- (s) Stone cells from the petiole (t) Disrupted cells with oil droplets released after milling



(a) **(b)** **(c)**

(d) **(e)** **(f)**

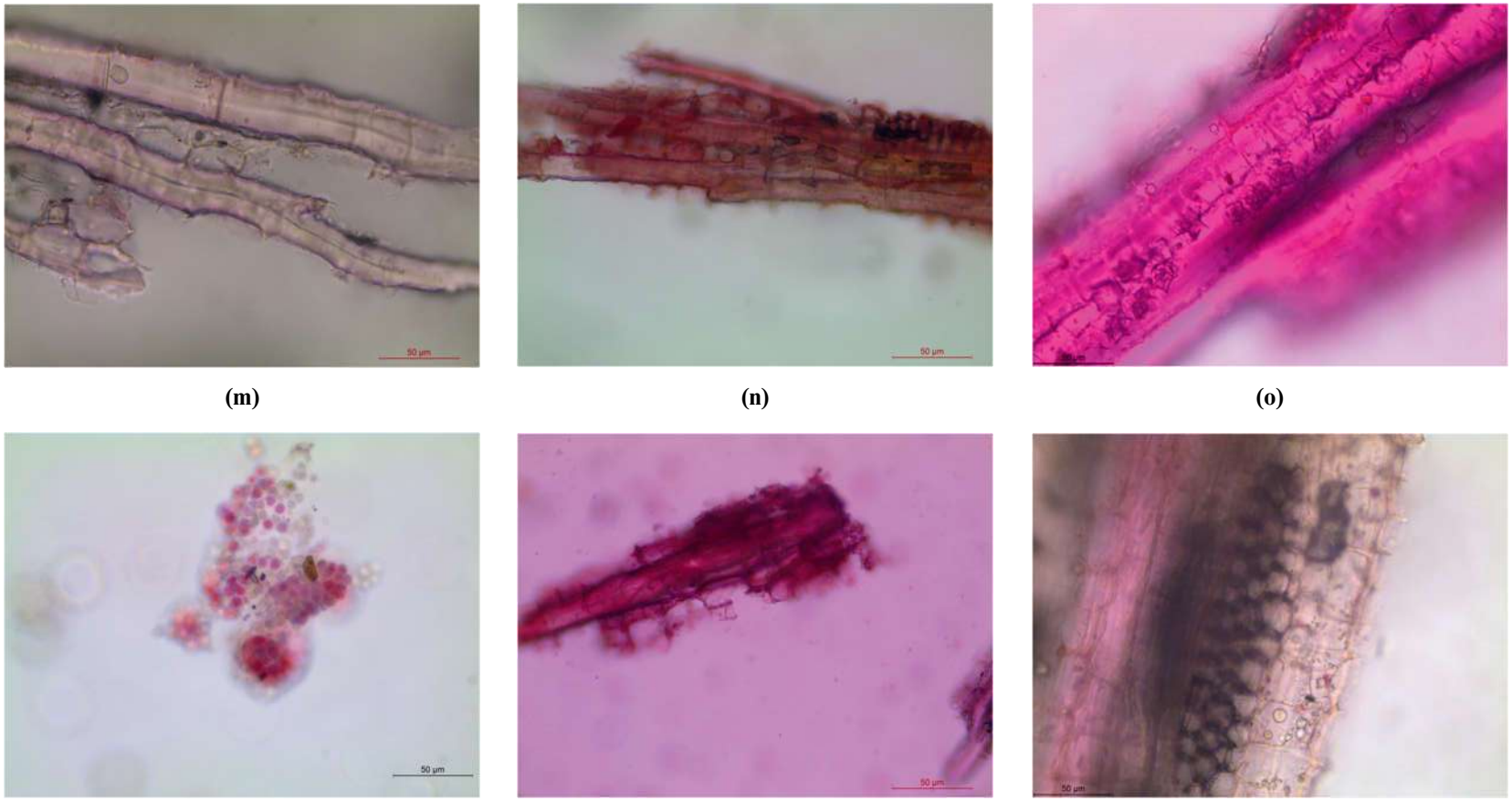
Plate 4.4: Powder microscopic studies of *Syzygium laetum* bark- (a) Cork (b) Cortical cells (c) Crystals (d) Crystals and starch grains (e) & (f) Crystal fibres



(g) **(h)** **(i)**

(j) **(k)** **(l)**

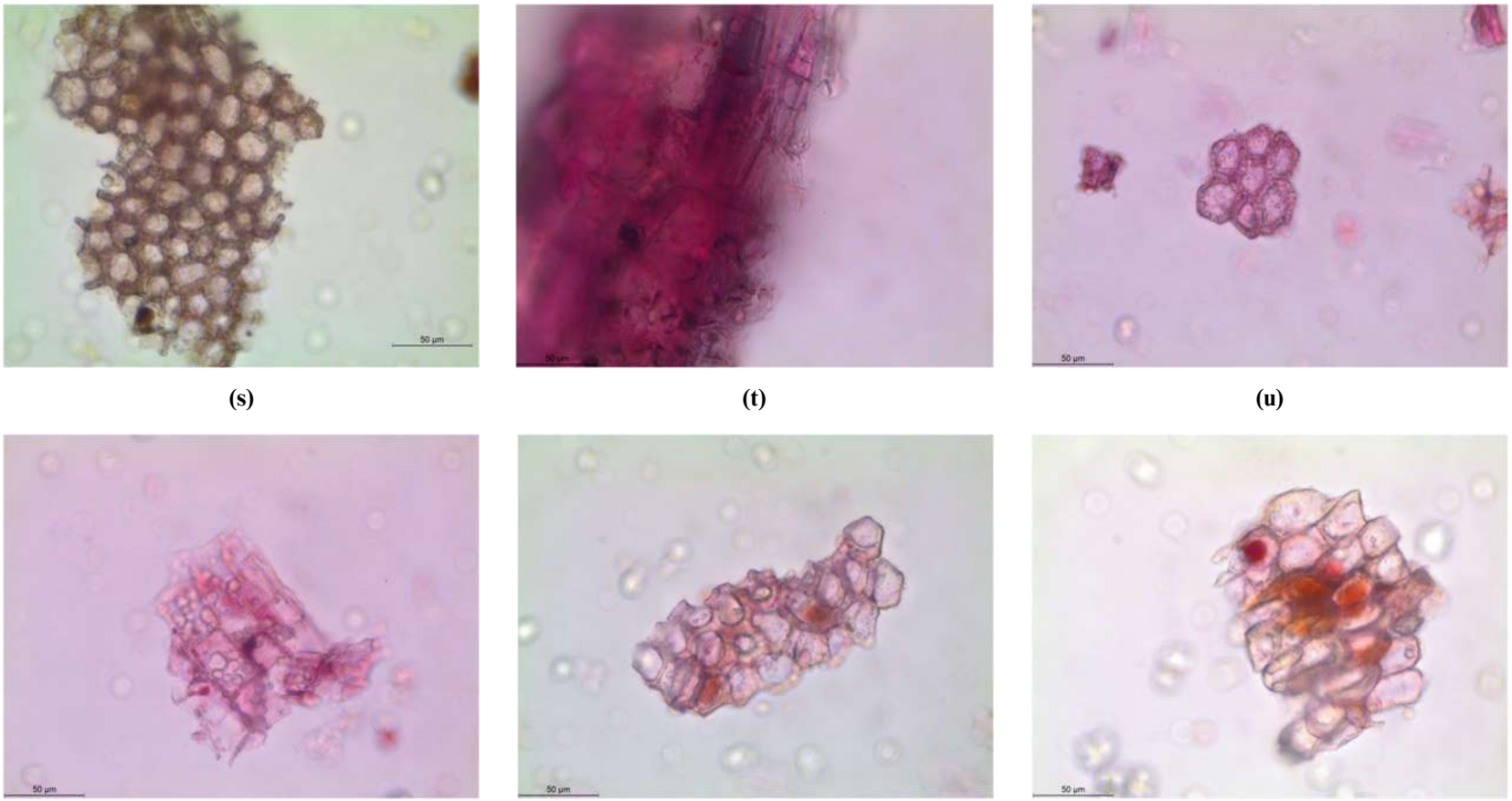
Plate 4.4: Powder microscopic studies of *Syzygium laetum* bark- (g) Fibres (h) Fibre associated with parenchyma cells (i) Fibre with starch grains (j) Fibre tracheids with starch grains (k) & (l) Septate fibres



(m) **(n)** **(o)**

(p) **(q)** **(r)**

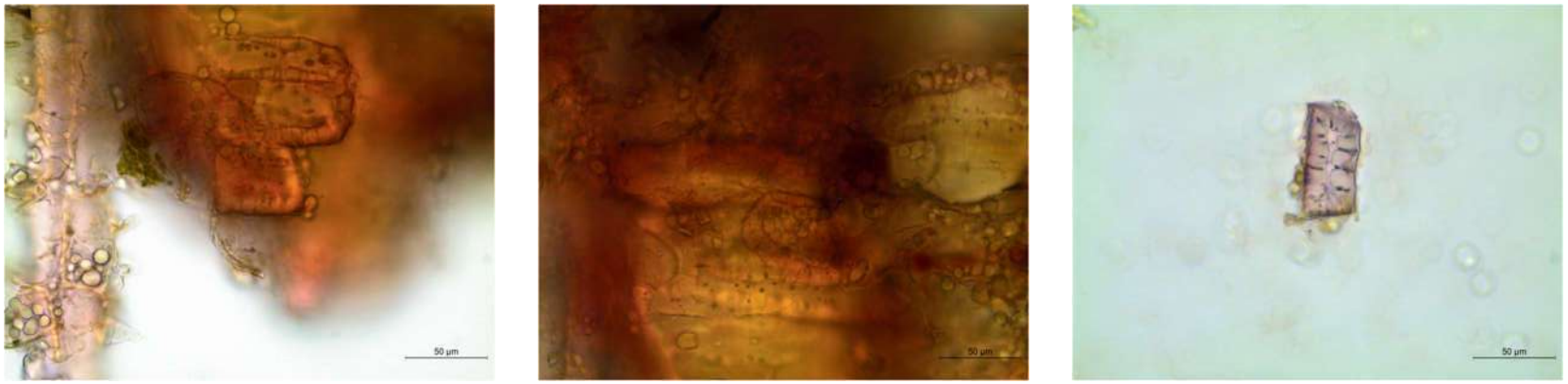
Plate 4.4: Powder microscopic studies of *Syzygium laetum* bark- (m) Septate fibres (n) Septate fibres with projections on the outer wall (o) Septate fibre with crystals (p) Parenchyma cells with reddish brown content and starch grains (q) Sclereids with parenchyma cells of cortex (r) Medullary ray cell fibers and parenchyma cells



(s) **(t)** **(u)**

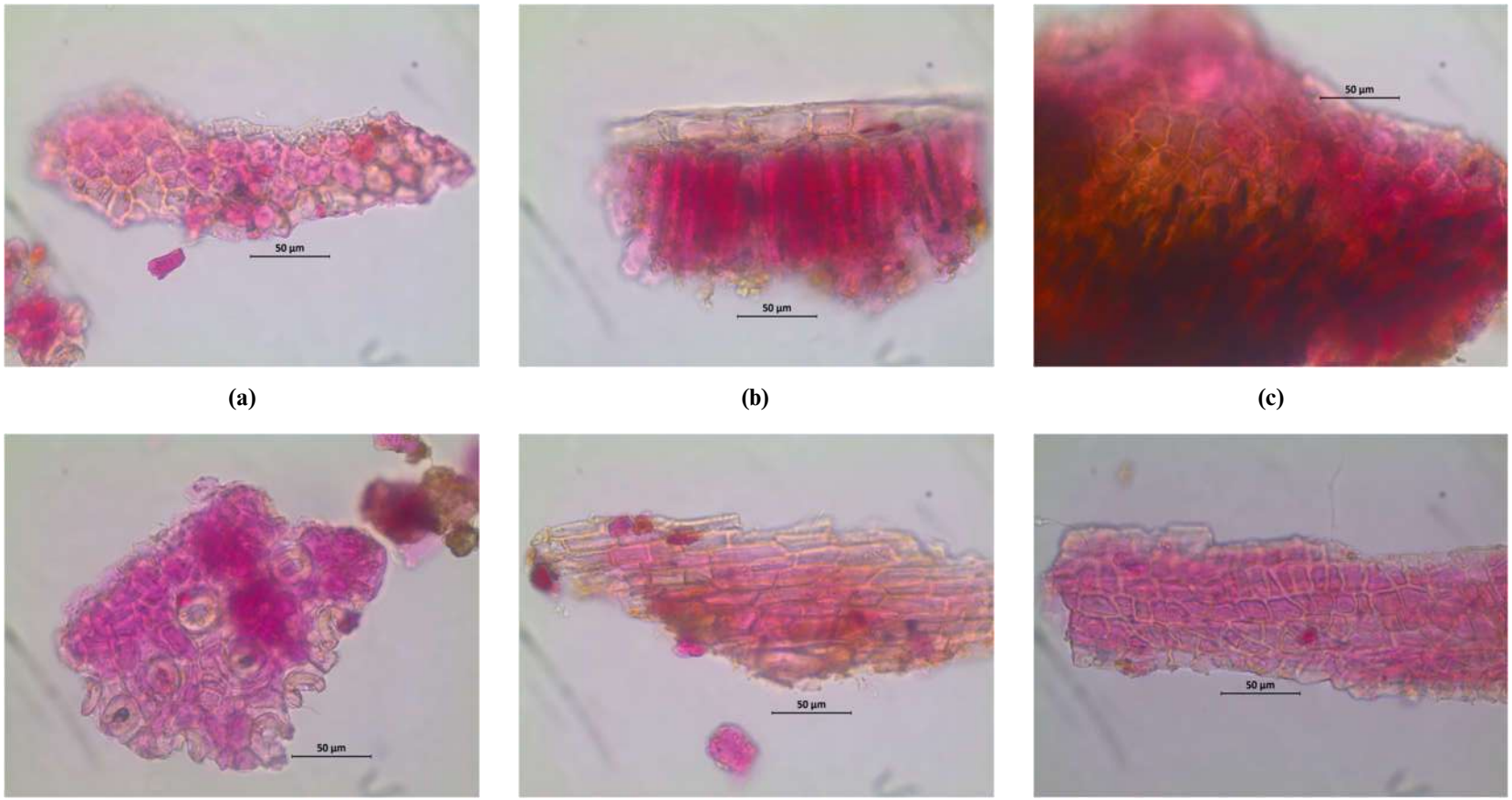
(v) **(w)** **(x)**

Plate 4.4: Powder microscopic studies of *Syzygium laetum* bark- (s) Pitted parenchyma cells (t)-(v) Stone cells (w) & (x) Group of stone cells



(y) (z) (aa)

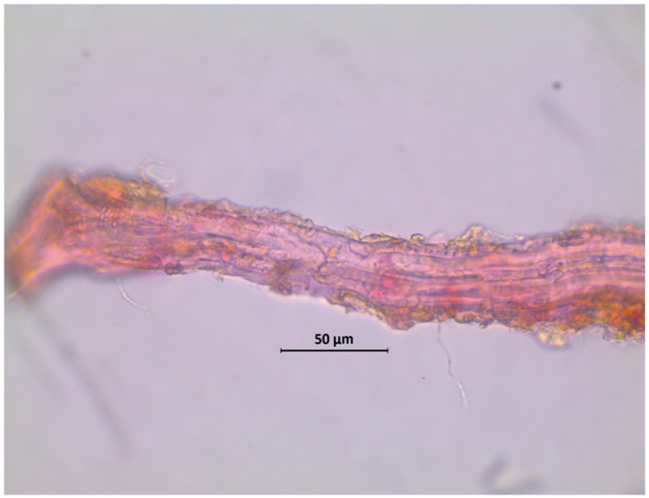
Plate 4.4: Powder microscopic studies of *Syzygium laetum* bark- (y)-(aa) Stone cells with starch grains



(a) **(b)** **(c)**

(d) **(e)** **(f)**

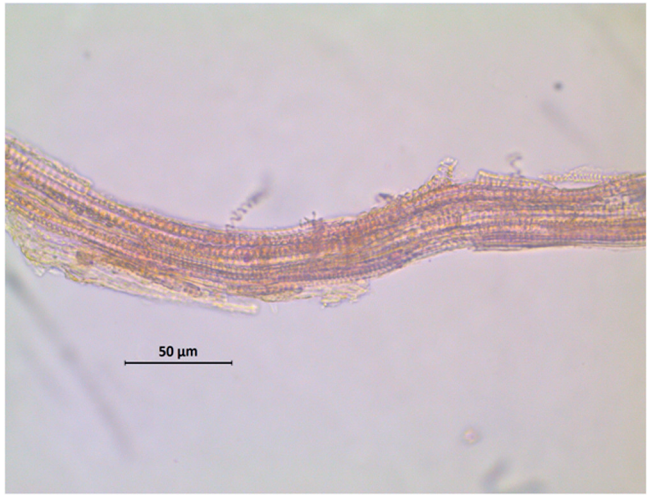
Plate 4.5: Powder microscopic studies of *Syzygium occidentale* leaves- (a) Surface view of the epidermal cells (b) Epidermis in sectional view with underlying palisade cells (c) Fragments of the upper epidermis in surface view with underlying palisade cells (d) Fragments of the lower epidermis with stomata (e) Fragments of the epidermal cells of the petiole (f) Fragments of the epidermal cells of the midrib region in surface view



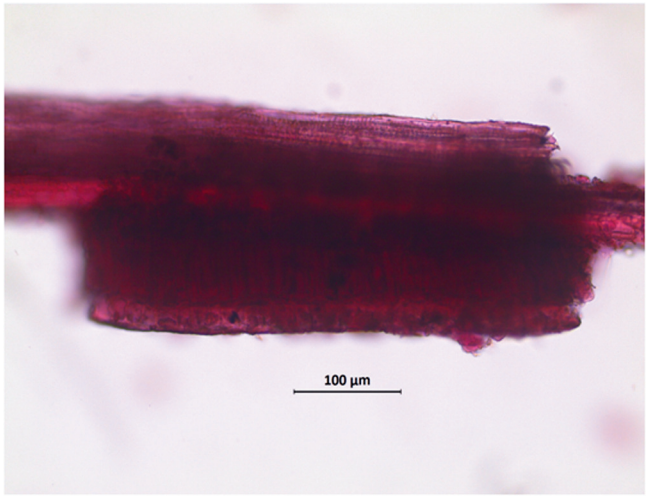
(g)



(h)



(i)



(j)



(k)



(l)

Plate 4.5: Powder microscopic studies of *Syzygium occidentale* leaves- (g) Fragments of the vascular strands (h) Fragments of the fibre (i)Fragments of the spiral vessels (j) & (k) Fragments of the fibres and vessels (l) Starch grains



(m)

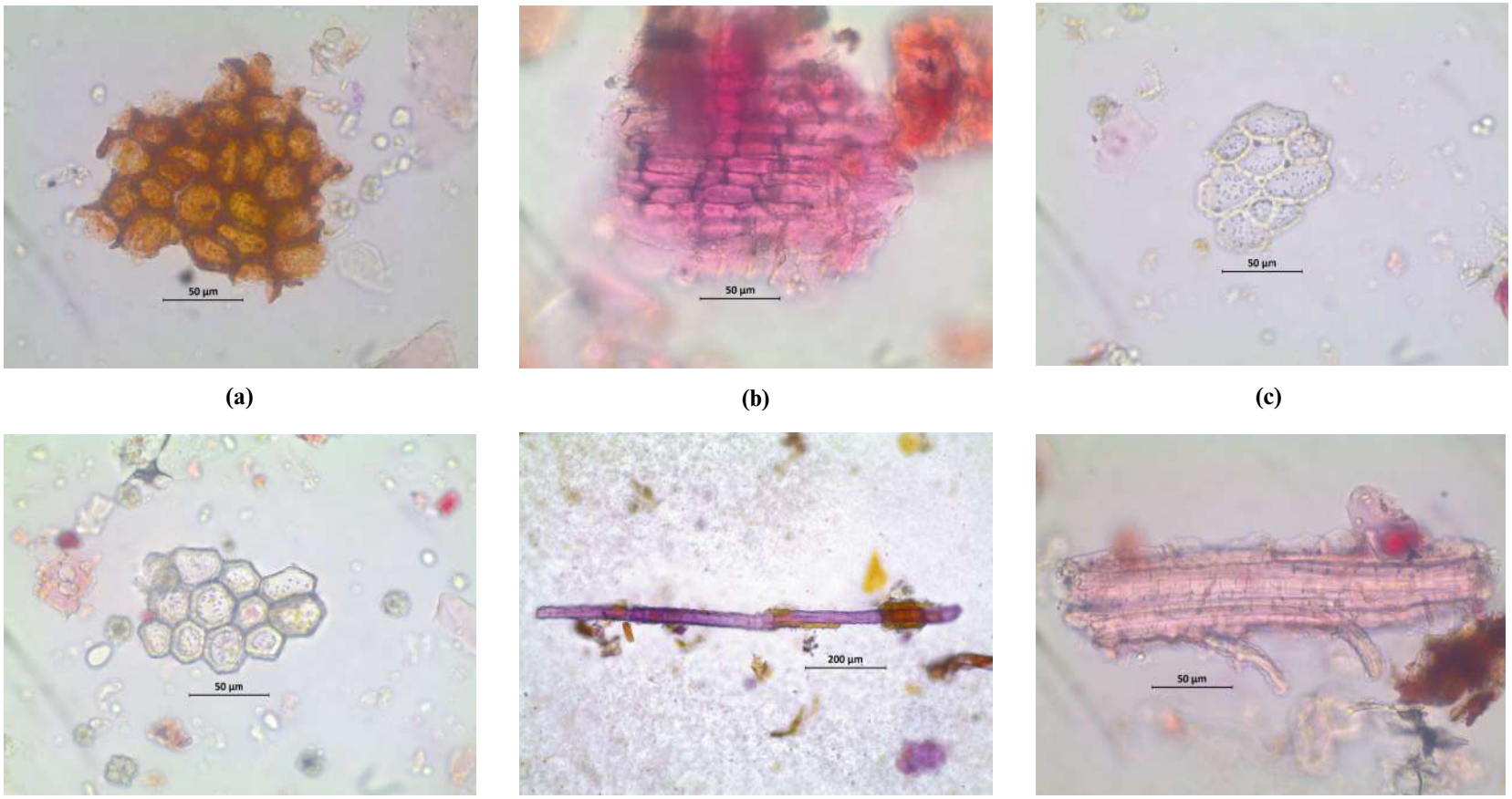


(n)



(o)

Plate 4.5: Powder microscopic studies of *Syzygium occidentale* leaves- (m) Rosette crystals of calcium oxalate (n) Prismatic crystals of calcium oxalate (o) Rod-shaped crystals of calcium oxalate



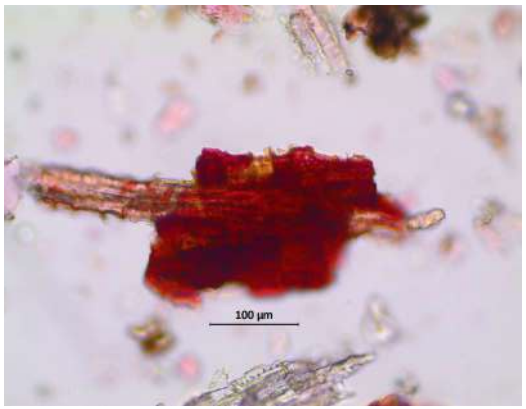
(a) **(b)** **(c)**

(d) **(e)** **(f)**

Plate 4.6: Powder microscopic studies of *Syzygium occidentale* bark- (a) Cork cells in surface view (b) Cork cells in sectional view (c) & (d) Pitted parenchyma cells (e) & (f) Fibre fragments



(g)



(h)



(i)



(j)

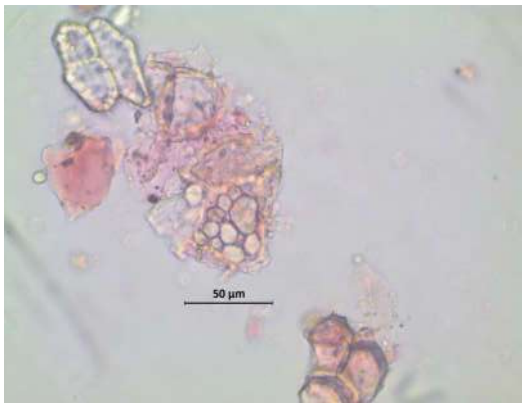


(k)



(l)

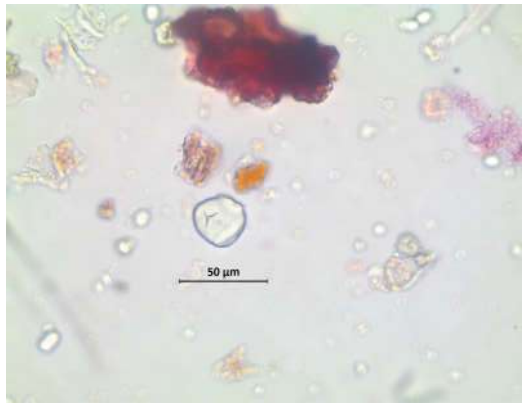
Plate 4.6: Powder microscopic studies of *Syzygium occidentale* bark- (g) Fibre and associated parenchyma cells (h) Fragment of fibre with parenchyma cells containing reddish-brown content and starch grains (i) Sclereids (j) Cells containing pigment cells (k) Cells containing starch grains (l) Starch grains



(m)



(n)



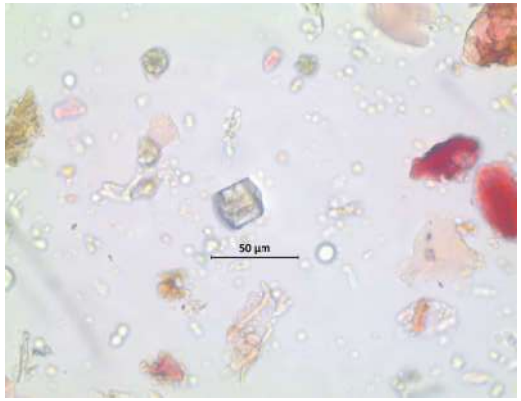
(o)



(p)



(q)



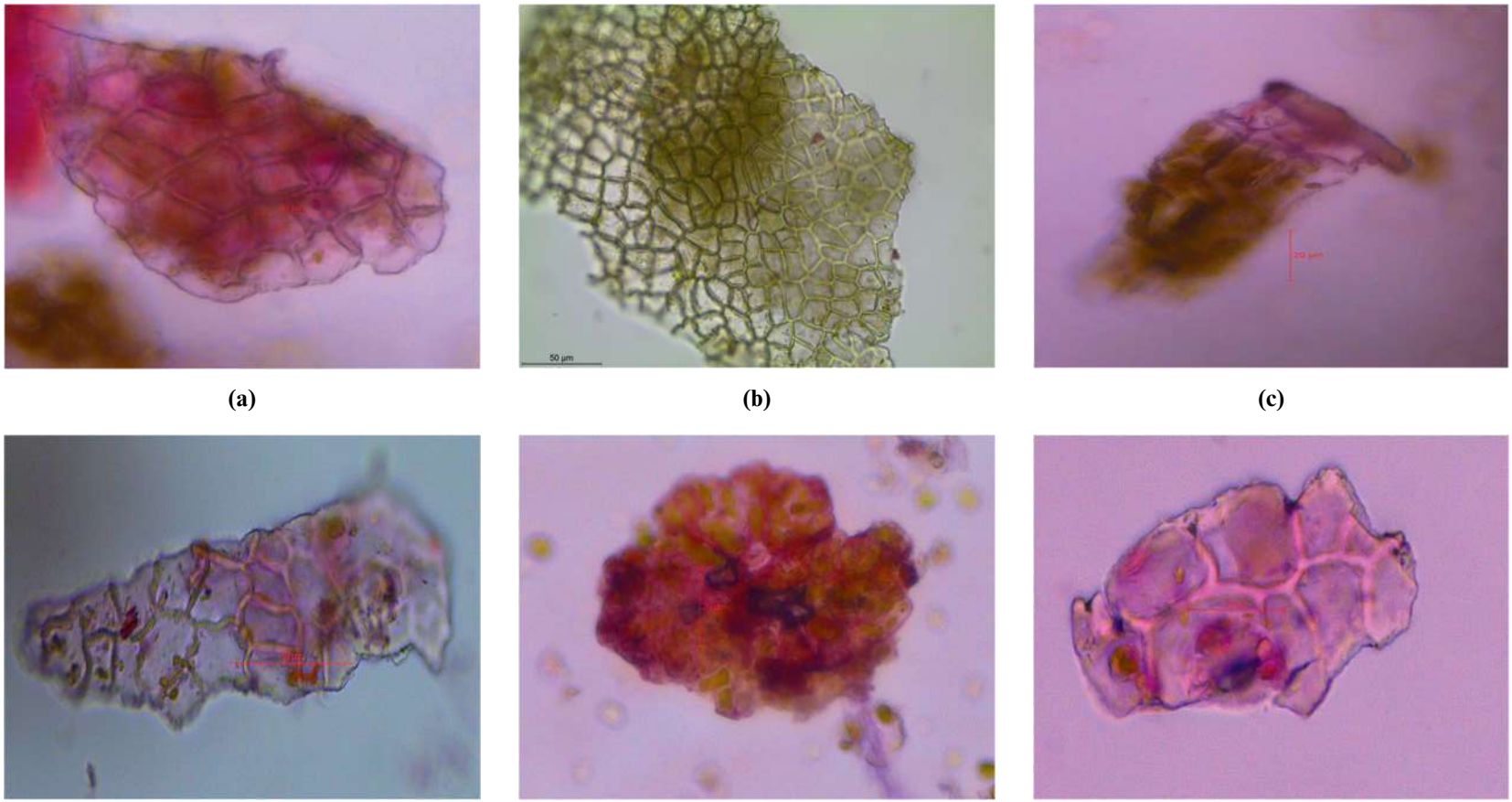
(r)

Plate 4.6: Powder microscopic studies of *Syzygium occidentale* bark- (m)-(o) Starch grains (p) Group of starch grains(q) Group of stone cells (r) Prismatic crystals



(s) **(t)** **(u)**

Plate 4.6: Powder microscopic studies of *Syzygium occidentale* bark- (s) Prismatic crystals (t) Prismatic crystal of calcium oxalate (u) Rosette crystals of calcium oxalate



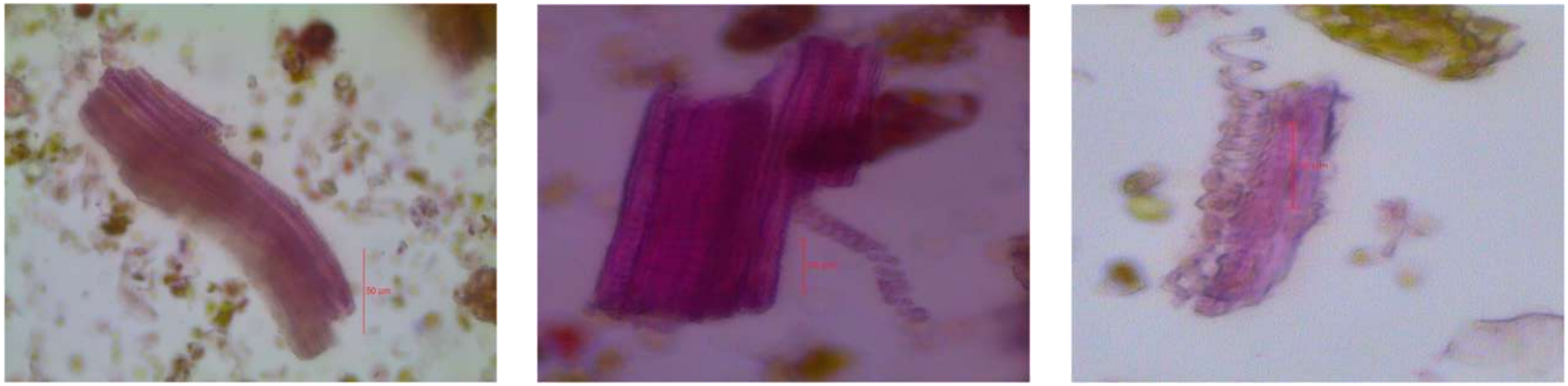
(a) **(b)** **(c)**

(d) **(e)** **(f)**

Plate 4.7: Powder microscopic studies of *Syzygium palghatense* leaves- (a) & (b) Epidermal cells in surface view (c) Epidermis with underlying palisade cells (d) Upper epidermis (e) Epidermis with stomata (f) Epidermal cells of the midrib



(g) (h) (i)

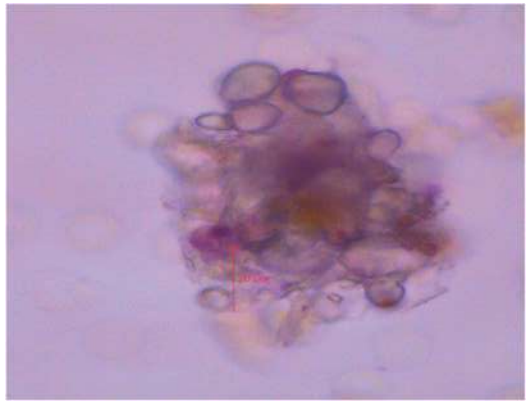


(j) (k) (l)

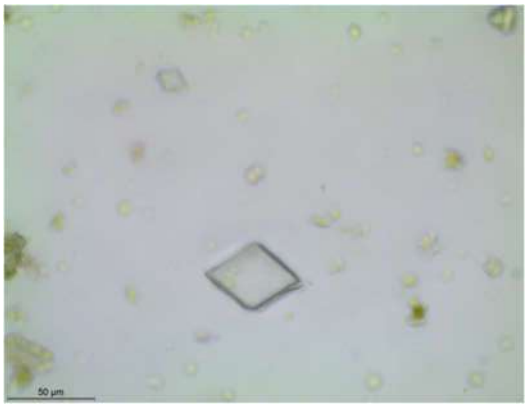
Plate 4.7: Powder microscopic studies of *Syzygium palghatense* leaves- (g) Sclereids (h) Fibre fragments (i) Fibres (j) Fibres and vessels (k) & (l) Vessels



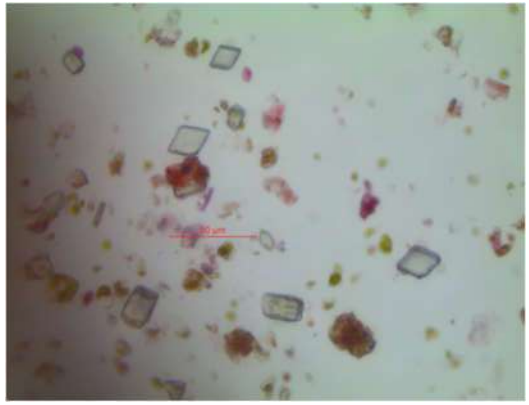
(m)



(n)

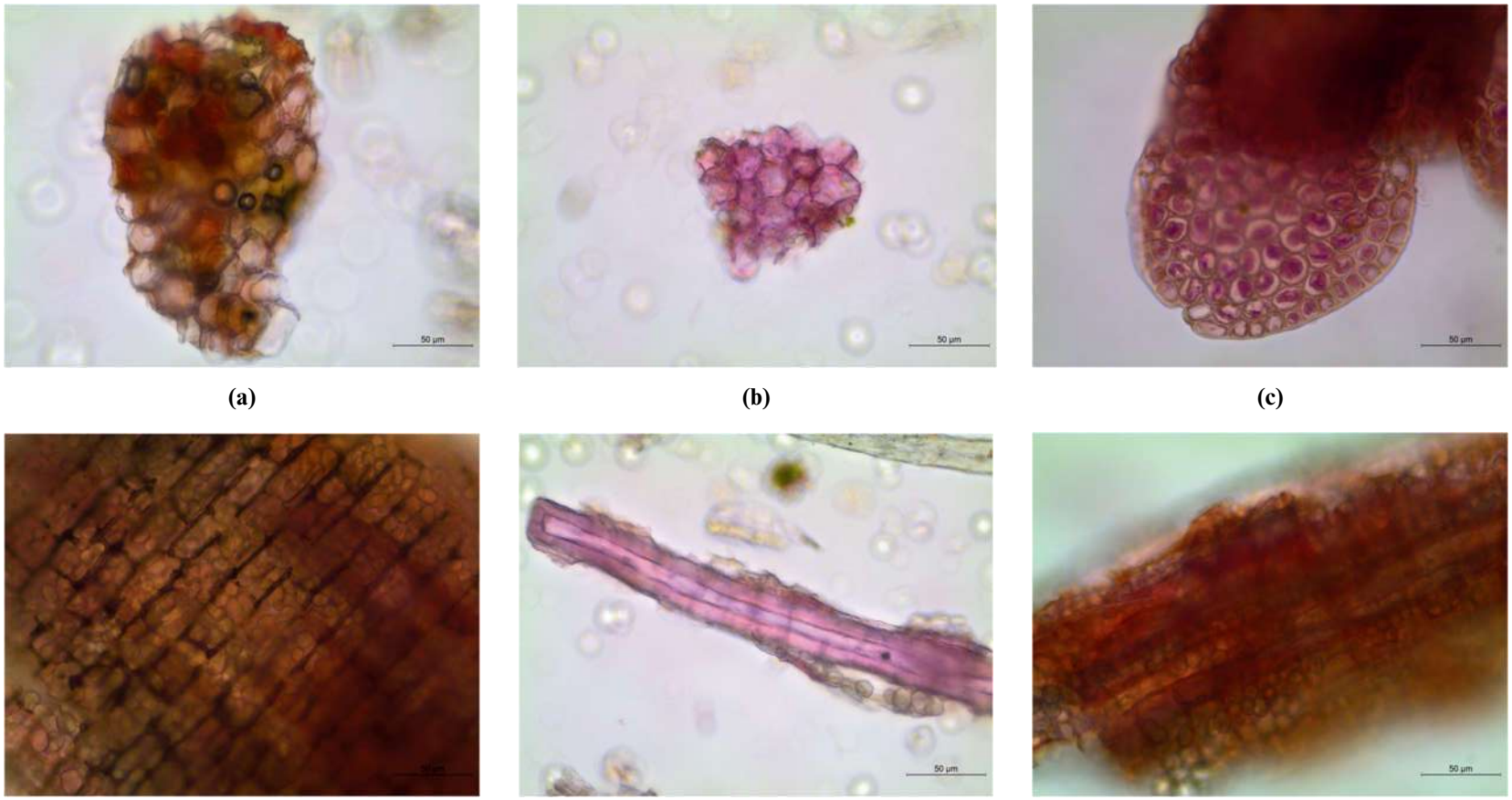


(o)



(p)

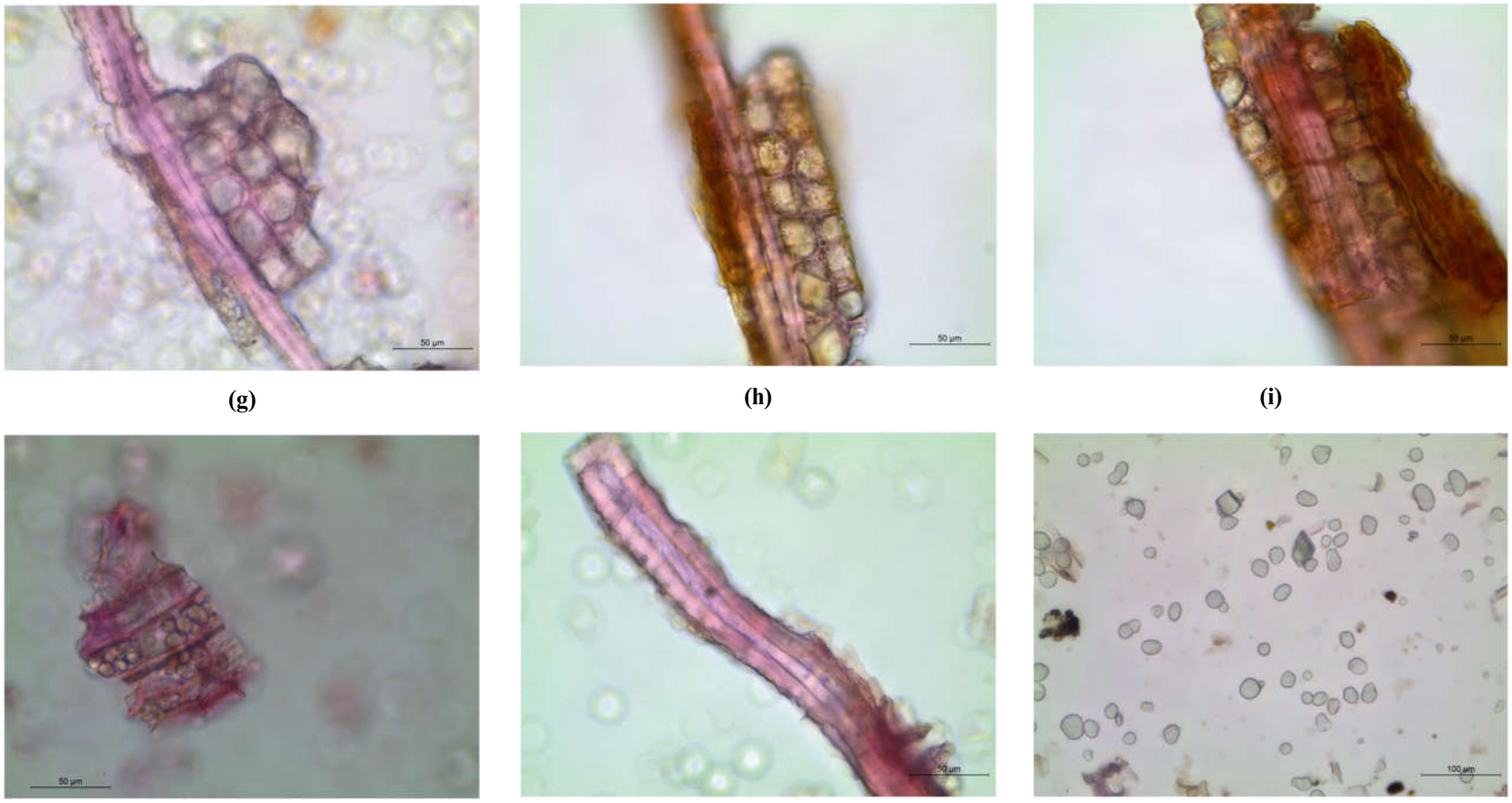
Plate 4.7: Powder microscopic studies of *Syzygium palghatense* leaves- (m) Vessels (n) Starch grains (o) & (p) Crystals



(a) **(b)** **(c)**

(d) **(e)** **(f)**

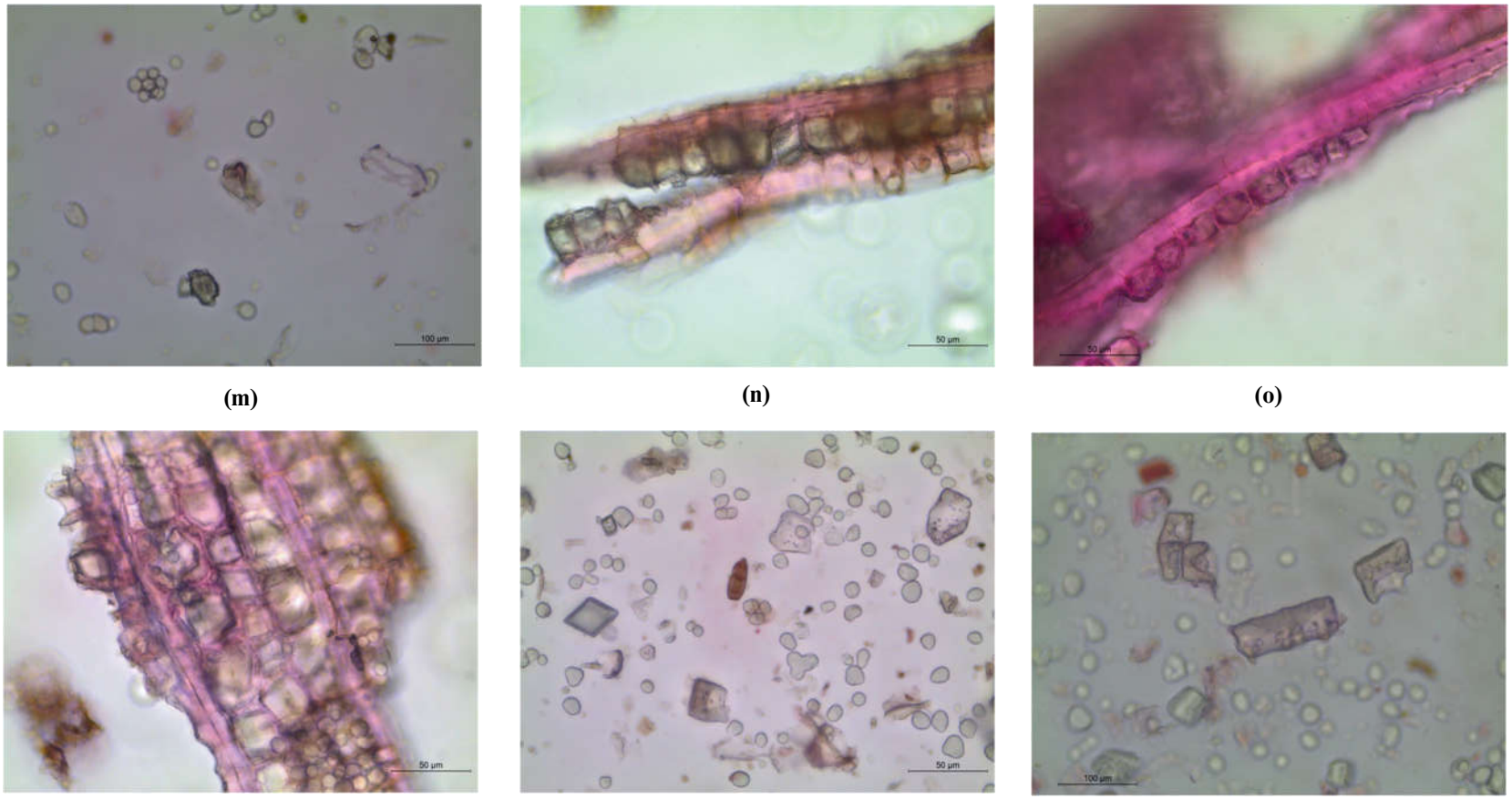
Plate 4.8: Powder microscopic studies of *Syzygium palghatense* bark- (a) & (b) Cork cells in surface view (c) Thick-walled parenchyma cells with reddish-brown content and starch grains (d) Medullary ray cells in sectional view with starch grains (e) Fibre sclereids (f) Fiber with starch grains



(g) **(h)** **(i)**

(j) **(k)** **(l)**

Plate 4.8: Powder microscopic studies of *Syzygium palghatense* bark- (g) Fibre associated with thick-walled cells (h) & (i) Fiber associated with crystals (j) Septate fibre with starch grains (k) Sclereids (l) Crystals



(m) **(n)** **(o)**

(p) **(q)** **(r)**

Plate 4.8: Powder microscopic studies of *Syzygium palghatense* bark- (m) Crystals (n) & (o) Crystal fibres (p) Crystal fibre associated with starch grains (q) Starch grains (r) Stone cells

Table 4.2: Fluorescence analysis of leaf and bark dry powders of *Syzygium laetum*

Syzygium laetum dry powder with reagents	Visible light		254 nm UV light		366 nm UV light	
	Leaves	Bark	Leaves	Bark	Leaves	Bark
Powder alone	Verdant green	Earthy brown	Olive	Dark brown	Olive green	Ebony brown
Powder + Ethanol	Brown	Dark brown	Bluish black	Fuscous black	Bluish black	Black
Powder + Acetone	Verdant green	Earthy brown	Olive green	Dark brown	Greenish black	Dark brown
Powder + Acetonitrile	Green	Earthy brown	Olive green	Dark brown	Dark blue	Dark Brownish blue
Powder + Glacial Acetic acid	Light green	Pale brown	Pale green	Pale brown	Blackish green	Dark brown
Powder + Picric acid	Yellow	Dark brown	Pale yellow	Dark brown	Pale yellow	Black
Powder + Formic acid	Green	Brown	Greenish brown	Brown	Dark green	Dark brown
Powder + Benzene	Verdant green	Earthy brown	Olive	Dark brown	Greenish black	Fuscous black
Powder + Butanol	Green	Brown	Dark green	Dark brown	Greenish black	Blackish blue
Powder + Iodine	Light green	Earthy brown	Light sky blue	Bluish brown	Bluish-green	Dark brown
Powder + Aniline	Reddish green	Reddish brown	Olive green	Dark brown	Blackish red	Reddish brown
Powder + Ammonia	Light green	Light brown	Verdant green	Earthy brown	Olive green	Earthy brown
Powder + n-Hexane	Dark green	Dark brown	Greenish black	Dark brown	Greenish black	Reddish brown
Powder + Diethyl ether	Green	Brown	Green	Brown	Brownish green	Dark brown
Powder + Isopropyl alcohol (2-Propanol)	Brownish green	Fuscous black	Fuscous black	Dark brown	Brownish green	Dark brown
Powder + NaOH	Greenish orange	Fuscous black	Greenish yellow	Fuscous black	Brownish green	Black
Powder + KOH	Olive green	Dark brown	Blackish green	Fuscous black	Black	Black
Powder + HCl	Dull yellow	Yellowish brown	Dark yellow	Brownish-yellow	Yellowish brown	Brownish-yellow
Powder + $AgNO_3$	Bluish-green	Brownish black	Yellowish green	Dark brown	Pale green	Blackish brown
Powder + HNO_3	Greenish black	Earthy brown	Olive green	Fuscous black	Greenish blue	Dark brown
Powder + H_2SO_4	Greenish yellow	Brownish-yellow	Greenish yellow	Yellowish black	Yellowish green	Dark brown
Powder + $CaCl_2$	Pale green	Pale brown	Bluish yellow	Mint green	Dark green	Blackish brown
Powder + $FeCl_3$	Olive green	Brownish-yellow	Greenish yellow	Dark brown	Dark yellow	Dark brown
Powder + Liquid NH_3	Light green	Pale brown	Light green	Pale brown	Olive green	Ebony brown
Powder + Potassium dichromate solution	Forest green	Reddish brown	Forest green	Yellowish brown	Olive green	Black

Table 4.3: Fluorescence analysis of leaf and bark extracts of *Syzygium laetum*

Syzygium laetum extracts	Visible light		254 nm UV light		366 nm UV light	
	Leaves	Bark	Leaves	Bark	Leaves	Bark
Petroleum ether extract	Green	Brown	Olive green	Dark brown	Olive green	Blackish brown
Chloroform extract	Pastel green	Sandy brown	Pear green	Greenish black	Pear green	Brownish black
Ethyl acetate extract	Mint green	Light brown	Mint green	Light brown	Dark moss green	Sandy brown
Methanol extract	Dark green	Mocha brown	Greenish black	Brownish black	Greenish black	Brownish black
Distilled water extract	Dark green	Brown	Olive green	Dark brown	Olive green	Dark brown

Table 4.4: Fluorescence analysis of leaf and bark dry powders of *Syzygium occidentale*

Syzygium occidentale dry powder with reagents	Visible light		254 nm UV light		366 nm UV light	
	Leaves	Bark	Leaves	Bark	Leaves	Bark
Powder alone	Mint green	Light brown	Olive	Dark brown	Olive green	Dark brown
Powder + Ethanol	Reddish brown	Dark brown	Bluish-green	Fuscous black	Bluish black	Black
Powder + Acetone	Pine green	Dark brown	Forest green	Brownish black	Greenish blue	Dark brown
Powder + Acetonitrile	Olive green	Earthy brown	Olive green	Earthy brown	Dark brownish blue	Dark blue
Powder + Glacial Acetic Acid	Olive green	Pale brown	Pale blue	Dark brown	Blackish green	Dark brown
Powder + Picric Acid	Yellowish green	Brown	Pale yellow	Dark brown	Pale yellow	Black
Powder + Formic Acid	Green	Brown	Greenish blue	Brown	Dark green	Dark brown
Powder + Benzene	Olive green	Dark brown	Olive	Dark brown	Greenish black	Fuscous black
Powder + Butanol	Green	Brownish-yellow	Dark green	Dark brown	Greenish black	Blackish blue
Powder + Iodine	Pale green	Earthy brown	Dark sky blue	Bluish-green	Bluish-brown	Dark brown
Powder + Aniline	Reddish brown	Dark brown	Olive green	Dark brown	Blackish red	Reddish black
Powder + Ammonia	Pale green	Light brown	Verdant Green	Dark brown	Blackish green	Earthy brown
Powder + n-Hexane	Dark green	Dark brown	Greenish black	Dark brown	Greenish black	Reddish black
Powder + Diethyl ether	Olive green	Brown	Greenish brown	Brown	Brownish-yellow	Dark brown
Powder + Isopropyl alcohol (2 Propanol)	Brownish blue	Fuscous black	Dark blue	Dark brown	Brownish green	Dark brown
Powder + NaOH	Greenish orange	Black	Greenish yellow	Fuscous black	Brownish green	Brown
Powder + KOH	Light green	Dark brown	Blackish green	Black	Bluish-green	Black
Powder + HCl	Greenish yellow	Yellowish brown	Dark yellow	Brownish red	Yellowish brown	Brownish black
Powder + $AgNO_3$	Bluish black	Brownish black	Yellowish green	Dark brown	Olive green	Blackish brown
Powder + HNO_3	Greenish black	Earthy brown	Olive green	Fuscous black	Yellowish blue	Dark brown
Powder + H_2SO_4	Greenish yellow	Brownish-yellow	Greenish yellow	Black	Yellowish red	Dark brown
Powder + $CaCl_2$	Green	Pale brown	Bluish yellow	Mint green	Dark green	Black
Powder + $FeCl_3$	Olive green	Brownish-yellow	Greenish yellow	Dark brown	Dark yellow	Brown
Powder + Liquid NH_3	Light green	Pale brown	Light green	Pale brown	Olive green	Dark brown
Powder + Potassium dichromate solution	Mint green	Deep yellow	Forest green	Yellowish brown	Blackish green	Black

Table 4.5: Fluorescence analysis of leaf and bark extracts of *Syzygium occidentale*

Syzygium occidentale extracts	Visible light		254 nm UV light		366 nm UV light	
	Leaves	Bark	Leaves	Bark	Leaves	Bark
Petroleum ether extract	Olive green	Brown	Olive green	Dark brown	Olive green	Bluish brown
Chloroform extract	Pale green	Light brown	Mint green	Yellowish black	Green	Brownish blue
Ethyl acetate extract	Moss green	Light brown	Pastel green	Light brown	Dark moss green	Blackish brown
Methanol extract	Dark green	Dark brown	Greenish black	Brownish blue	Greenish blue	Blackish blue
Distilled water extract	Dark green	Syrup brown	Dark green	Brownish black	Dark green	Chocolate brown

Table 4.6: Fluorescence analysis of leaf and bark dry powders of *Syzygium palghatense*

Syzygium palghatense dry powder with reagents	Visible light		254 nm UV light		366 nm UV light	
	Leaves	Bark	Leaves	Bark	Leaves	Bark
Powder alone	Green	Brown	Olive green	Brownish black	Olive green	Dark brown
Powder + Ethanol	Reddish blue	Dark brown	Bluish-red	Fuscous black	Bluish-green	Black red
Powder + Acetone	Dark green	Dark green	Dark green	Dark brown	Bluish black	Bluish black
Powder + Acetonitrile	Green	Brownish green	Dark green	Dark brown	Dark blue	Dark blue
Powder + Glacial Acetic Acid	Greenish yellow	Muddy brown	Bluish-green	Dark brown	Blackish blue	Dark brown
Powder + Picric Acid	Yellowish orange	Brown	Yellowish green	Dark brown	Brownish red	Black
Powder + Formic Acid	Forest green	Brownish black	Dark green	Brown	Dark green	Dark brown
Powder + Benzene	Moss green	Brownish blue	Olive green	Dark brown	Blackish green	Fuscous black
Powder + Butanol	Green	Dark brown	Dark green	Dark brown	Dark green	Blackish blue
Powder + Iodine	Pale green	Dark brown	Dark blue	Bluish-green	Bluish-brown	Dark brown
Powder + Aniline	Reddish green	Dark brown	Olive green	Blackish green	Bluish black	Dark brown
Powder + Ammonia	Green	Earthy brown	Dark green	Bluish brown	Blackish yellow	Earthy brown
Powder + n-Hexane	Dark green	Dark brown	Greenish blue	Dark brown	Greenish blue	Reddish black
Powder + Diethyl ether	Light green	Brown	Greenish brown	Brown	Brownish-yellow	Dark brown
Powder + Isopropyl alcohol (2-Propanol)	Brownish blue	Brownish orange	Dark green	Dark brown	Brownish green	Dark brown
Powder + NaOH	Greenish orange	Blackish brown	Greenish yellow	Fuscous black	Dark green	Brown
Powder + KOH	Light green	Dark brown	Blackish green	Black	Dark green	Blackish brown

Powder + HCl	Greenish yellow	Yellowish black	Dark yellow	Brownish black	Yellowish brown	Dark brown
Powder + $AgNO_3$	Bluish black	Brownish black	Yellowish green	Dark brown	Olive green	Blackish brown
Powder + HNO_3	Greenish blue	Dark brown	Orange green	Yellowish black	Yellowish blue	Dark brown
Powder + H_2SO_4	Greenish orange	Brownish-yellow	Greenish blue	Blackish orange	Yellowish green	Dark brown
Powder + $CaCl_2$	Green	Dark brown	Bluish-green	Dark brown	Dark green	Black
Powder + $FeCl_3$	Olive green	Brownish-red	Greenish blue	Dark brown	Yellowish green	Brown
Powder + Liquid NH_3	Light green	Brown	Light green	Dark brown	Olive green	Brownish black
Powder + Potassium dichromate solution	Forest green	Greenish brown	Dark green	Yellowish brown	Blackish blue	Black

Table 4.7: Fluorescence analysis of leaf and bark extracts of *Syzygium palghatense*

Syzygium palghatense extracts	Visible light		254 nm UV light		366 nm UV light	
	Leaves	Bark	Leaves	Bark	Leaves	Bark
Petroleum ether extract	Light green	Brown	Moss green	Dark brown	Dark green	Bluish brown
Chloroform extract	Mint green	Brown	Pale green	Reddish black	Green	Brownish black
Ethyl acetate extract	Light green	Coffee brown	Forest green	Brown	Dark green	Dark blue
Methanol extract	Greenish black	Greenish black	Black	Black	Blackish blue	Blackish blue
Distilled water extract	Blackish green	Blackish brown	Black	Black	Bluish black	Bluish black

solvent, while the extracts of *S. palghatense* show relatively more distinctive colours, mint green and sandy brown. All three species show fluorescence when illuminated with UV light; *S.* palghatense has comparatively lighter and brighter colours compared to extracts of *S. laetum* and *S. occidentale*, which tend to show darker shades. This indicates that the fluorescence characteristics of these plants are dependent on their species, the form (powder or extract), and the reagents utilized.

4.3.3. Physicochemical and nutritional evaluation

The results of the physicochemical analysis demonstrate (Table 4.8) that the three types of *Syzygium* species exhibit different chemical and nutritional profiles. Before initiating research on a specific herb, it is crucial to perform a detailed evaluation of its physicochemical parameters. *S. laetum* has the highest extractive content, particularly in water-soluble and alcohol-soluble extracts, along with notable Vitamin C levels in its leaves. The highest crude fibre, sodium, calcium, and manganese content was shown by *S. occidentale* (the bark), with relatively high potassium and zinc content. *S. palghatense* has distinct high copper (leaf and bark) and lower ash than the other species. *S. laetum* and *S. palghatense* contain significantly less sulphated ash, whereas *S. occidentale* has a relatively higher ash content than other species, especially in the bark. These differences hint at each species' specific nutritional and chemical properties, indicating varied potential uses in both medicinal and dietary realms.

The physicochemical analysis of leaves and bark of *Syzygium* species demonstrates significant variation in extractive values, fibre content, vitamin contents, minerals, and ash components. The data were analyzed using independent two-sample t-tests to compare means between different species and plant parts.

Statistical analysis revealed highly significant differences across nearly all parameters ($P < 0.001$), indicating genuine variability rather than random variation. For example, the water-soluble extractive values in leaves ranged from 9.92% in *S. occidentale* to 30.51% in *S. palghatense*, with corresponding significant F values confirming robust interspecies differences. This pattern persisted for alcohol-soluble

extractives, petroleum ether, and ethyl acetate extractives, illustrating distinct phytochemical profiles among species.

Mineral contents (e.g., copper, manganese, zinc) also varied markedly, with *S. palghatense* leaves showing notably higher copper levels (4.83 mg/100 g) compared to *S. laetum* (0.43 mg/100 g) and *S. occidentale* (0.37 mg/100 g). Heavy metals such as lead, arsenic, cadmium, and mercury were detected in trace amounts well below toxic thresholds, indicating safe usage potential. Ash values (total, acid-insoluble, water-soluble, and sulphated) further emphasize species-specific differences in mineralization and inorganic content, crucial for quality control and authentication.

The use of independent t-tests and reporting of critical difference (CD) values support the reliability of these physicochemical distinctions. Overall, the results validate the unique biochemical compositions in leaves and bark of these three *Syzygium* species, underpinning their considerable ethnopharmacological importance and justifying further bioactivity evaluation.

Figure 4.1 displays the hierarchical cluster analysis of physicochemical parameters for three *Syzygium* species: *S. laetum*, *S. occidentale*, and *S. palghatense*. The analysis created groups based on the similarity of 21 measured characteristics by using the Euclidean distance and average linkage method. The dendrogram illustrates how samples cluster together; those joined at lower heights share more similarities, while those connected at higher distances are less alike.

The samples formed three main clusters. Cluster I contains *S. laetum* leaf and bark along with *S. palghatense* leaf, indicating these samples have closely related physicochemical profiles. Cluster II groups *S. occidentale* leaf and bark, showing they are similar but distinct from others. Cluster III, with *S. palghatense* bark, is most distinct, highlighting unique variations in its parameters.

Intra-cluster distances (within the same cluster) showed that Cluster II had the highest internal variation (4.846), indicating more diversity among its samples. The inter-cluster distances (between different clusters) were greatest between Clusters II and III (7.403), showing these clusters are the most different from each other.

Table 4.8: Physicochemical analysis (a)-(e) of leaves and bark of *Syzygium laetum*, *Syzygium occidentale,* and *Syzygium palghatense* (f) Independent two-sample t-test

(a)

Parameters	Water-soluble extractive	Alcohol-soluble extractive	Petroleum ether extractive	Ethyl acetate soluble extractive	Crude fibre
SLL	28.56±1.120^{c}	23.89±1.100^{b}	9.03±0.111^{d}	11.82±1.082^{c}	13.55±0.671^{de}
SLB	29.02±1.190^{c}	24.18±1.111^{b}	10.11±1.053^{c}	12.30±1.061^{b}	13.79±1.091^{d}
SOL	9.92±0.230^{e}	11.03±1.010^{d}	5.54±0.101^{e}	6.19±0.093^{e}	20.12±1.011^{a}
SOB	12.78±0.580^{d}	17.21±1.022^{c}	1.13±0.060^{f}	1.06±0.763^{f}	18.71±1.051^{b}
SPL	30.51±1.591^{b}	31.86±1.680^{a}	17.87±1.131^{a}	13.72±1.045^{a}	15.39±1.031^{c}
SPB	32.87±1.750^{a}	32.43±1.711^{a}	10.51±0.851^{b}	8.11±0.761^{d}	13.10±0.661^{e}
F Value	2485.4	1504.3	4157.4	2428.9	360.65
P Value	<0.001	<0.001	<0.001	<0.001	<0.001
CD Value	0.591	0.637	0.257	0.286	0.462

(SLL: *Syzygium laetum* leaves; SLB: *Syzygium laetum* bark; SOL: *Syzygium occidentale* leaves; SOB*: Syzygium occidentale* bark; SPL: *Syzygium palghatense* leaves; SPB: *Syzygium palghatense* bark)

(b)

Parameters	Vitamin A	Vitamin C	Sodium	Potassium	Calcium
SLL	-	628±0.551[b]	2.012±0.008[e]	5.103±0.004[d]	2.30±0.013[c]
SLB	-	655±0.680[a]	4.203±0.005[d]	5.810±0.005[c]	2.64±0.007[b]
SOL	0.061±0.004[b]	198±1.231[c]	6.559±0.124[c]	4.802±0.011[e]	0.43±0.020[f]
SOB	-	-	8.323±0.040[a]	5.301±0.001[d]	2.10±0.005[d]
SPL	-	659±0.812[a]	7.101±0.002[b]	6.521±0.001[b]	1.80±0.006[e]
SPB	0.850±0.003[a]	-	8.230±0.031[a]	8.931±0.001[a]	3.50±0.014[a]
F Value		988.25	3971.7	349.78	1494.3
P Value	<0.001	<0.001	<0.001	<0.001	<0.001
CD Value		22.063	0.117	0.242	0.078

(SLL: *Syzygium laetum* leaves; SLB: *Syzygium laetum* bark; SOL: *Syzygium occidentale* leaves; SOB*: Syzygium occidentale* bark; SPL: *Syzygium palghatense* leaves; SPB: *Syzygium palghatense* bark)

(c)

Parameters	Copper	Manganese	Zinc	Lead	Arsenic
SLL	0.4330±0.003[d]	1.8100±0.002 [c]	1.1350±0.012[b]	0.0123±0.001[a]	0.0107±0.001[a]
SLB	0.4860±0.002[c]	1.8890±0.006[c]	1.2130±0.013[a]	0.0111±0.001[b]	0.0100±0.001[b]
SOL	0.3707±0.001[e]	10.9385±1.005[a]	1.0405±0.010[d]	0.0014±0.002[d]	0.0023±0.001[d]
SOB	0.4172±0.004 [d]	9.5248±1.010[b]	0.7023±0.001[f]	0.0035±0.001[c]	0.0003±0.001[f]
SPL	4.8280±0.005[b]	0.4600±0.002[d]	1.0820±0.003[c]	0.0004±0.001[e]	0.0008±0.001[e]
SPB	4.9230±0.002[a]	0.2550±0.001[e]	0.7550±0.001[e]	0.0005±0.001[e]	0.0045±0.001[c]
F Value	22253.0	8323.6	675.13	5260.8	7575.4
P Value	<0.001	<0.001	<0.001	<0.001	<0.001
CD Value	0.046	0.156	0.024	0.0002	0.0002

(SLL: *Syzygium laetum* leaves; SLB: *Syzygium laetum* bark; SOL: *Syzygium occidentale* leaves; SOB*: Syzygium occidentale* bark; SPL: *Syzygium palghatense* leaves; SPB: *Syzygium palghatense* bark)

(d)

Parameters	Cadmium	Mercury	Total ash	Acid-insoluble ash	Water-soluble ash
SLL	0.0006±0.001^{c}	0.0004±0.001^{b}	5.64±0.100^{c}	0.68±0.001^{b}	2.67±0.011^{b}
SLB	0.0024±0.001^{b}	0.0001±0.001^{e}	6.35±0.008^{b}	0.76±0.001^{a}	2.94±0.021^{a}
SOL	0.0005±0.001^{d}	0.0003±0.001^{c}	4.84±0.002^{e}	0.26±0.001^{d}	1.80±0.001^{d}
SOB	0.0032±0.001^{a}	0.0001±0.001^{e}	8.14±0.002^{a}	0.18±0.001^{f}	1.53±0.001^{e}
SPL	0.0001±0.001^{f}	0.0002±0.001^{d}	3.30±0.003^{f}	0.53±0.001^{c}	2.54±0.101^{c}
SPB	0.0003±0.001^{e}	0.0005±0.001^{a}	5.30±0.002^{d}	0.21±0.001^{e}	1.82±0.101^{d}
F Value	3416.0	3284.2	958.45	1105.6	506.48
P Value	<0.001	<0.001	<0.001	<0.001	<0.001
CD Value	0.000	0.000	0.155	0.023	0.076

(SLL: *Syzygium laetum* leaves; SLB: *Syzygium laetum* bark; SOL: *Syzygium occidentale* leaves; SOB*: Syzygium occidentale* bark; SPL: *Syzygium palghatense* leaves; SPB: *Syzygium palghatense* bark)

(e)

Parameters	Sulphated ash
SLL	4.84±0.111^{d}
SLB	4.95±0.012^{d}
SOL	6.45±0.022^{c}
SOB	12.56±0.122^{a}
SPL	3.67±0.013^{e}
SPB	7.43±0.015^{b}
F Value	3729.7
P Value	<0.001
CD Value	0.155

(SLL: *Syzygium laetum* leaves; SLB: *Syzygium laetum* bark; SOL: *Syzygium occidentale* leaves; SOB*: Syzygium occidentale* bark; SPL: *Syzygium palghatense* leaves; SPB: *Syzygium palghatense* bark)

(f)

Variable	Conditions	Mean values	t-stat	P value
Vitamin A	**SOL**	0.061	841.11	<0.001
	SPB	0.850		

(SOL: *Syzygium occidentale* leaves; SPB: *Syzygium palghatense* bark)

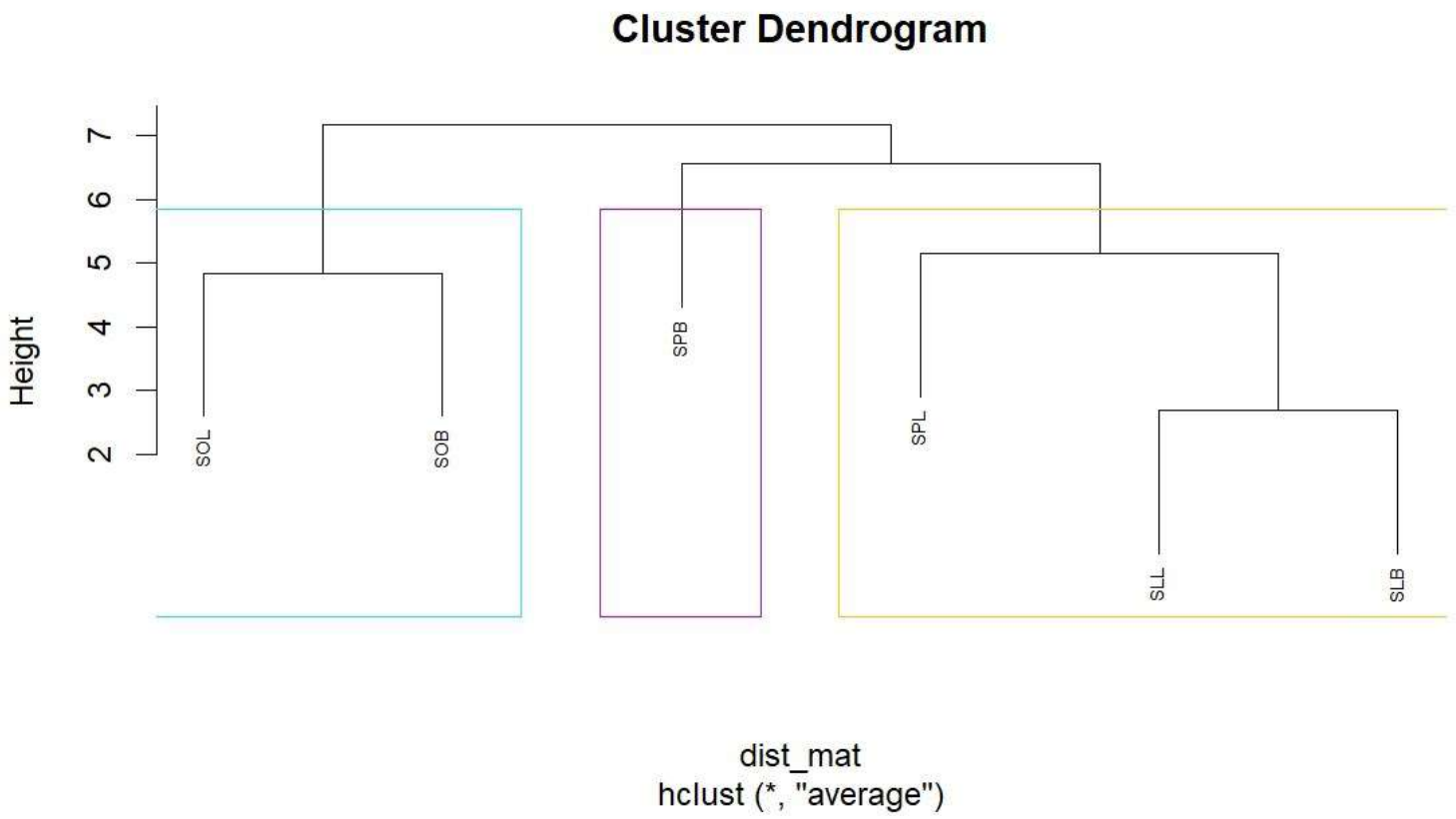


Figure 4.1: Cluster analysis of physicochemical parameters of *Syzygium* species (*S. laetum*, *S. occidentale,* and *S. palghatense*)

Overall, the analysis clearly separates the samples into three distinct groups based on their physicochemical traits, with Cluster II exhibiting the most internal diversity and Clusters II and III being the most dissimilar. The intra-cluster distances measure similarities within each group, with Cluster II showing the greatest internal diversity. The inter-cluster distances reveal how distinct each cluster is from the others, with the largest difference between Clusters II and III. Overall, this analysis identifies clear grouping patterns among the *Syzygium* samples, reflecting the underlying physicochemical relationships without overlap or mixing of distinct sample types. The diagonal values represent the intra-cluster distance and were found to be highest in cluster II. The off-diagonal values represent the inter-cluster distance and were found to be highest between clusters II and III (Tables 4.9-4.10).

This biplot presents the results of a Principal Component Analysis (PCA) of *Syzygium* samples (Figure 4.2), summarizing the relationships between samples and measured variables. The two principal components, PC1 (45.8%) and PC2 (30.2%), together explain a substantial proportion of the variance in the data. Samples positioned near each other in the plot share similar profiles, while those far apart differ more. The direction and length of each arrow represent how strongly and in which direction each variable contributes to the components: variables pointing in a similar direction are positively correlated, and those pointing in opposite directions are negatively correlated. In this plot, *S. occidentale* bark and *S. palghatense* bark are distinctly separated, indicating they have unique physicochemical characteristics compared to the other samples. The arrangement of arrows shows which variables influence the grouping and separation of samples, providing insight into the most significant contributors to sample differences.

In Principal Component Analysis (PCA), an eigenvalue signifies how much of the total variation in the data is accounted for by a specific principal component. Each principal component corresponds to an eigenvalue that measures the significance of that component in representing the dataset's variance. Larger eigenvalues indicate that the component captures more of the original information, making it more important for summarizing the data and reducing dimensionality.

Table 4.9. The hierarchical clusters of six samples

Cluster I	Cluster II	Cluster III
Syzygium laetum Leaf *Syzygium laetum* Bark *Syzygium palghatense* Leaf	*Syzygium occidentale* Leaf *Syzygium occidentale* Bark	*Syzygium palghatense* Bark

Table 4.10: The intra-cluster and inter-cluster distances

	Cluster I	Cluster II	Cluster III
Cluster I	4.327	-	
Cluster II	7.104	4.846	-
Cluster III	6.557	7.403	0.00

Table 4.11: Eigenvalues of principal components

PC1	PC2	PC3	PC4	PC5	PC6
3.103	**2.517**	**1.781**	**1.265**	0.516	6.047e-16

Table 4.12: Variance explained by principal components

Component	PC1	PC2	PC3	PC4
Standard deviation	3.1029	2.5169	1.7808	1.26478
Proportion of Variance	0.4585	0.3017	0.1510	0.07617
Cumulative Proportion	0.4585	0.7601	0.9111	0.98732

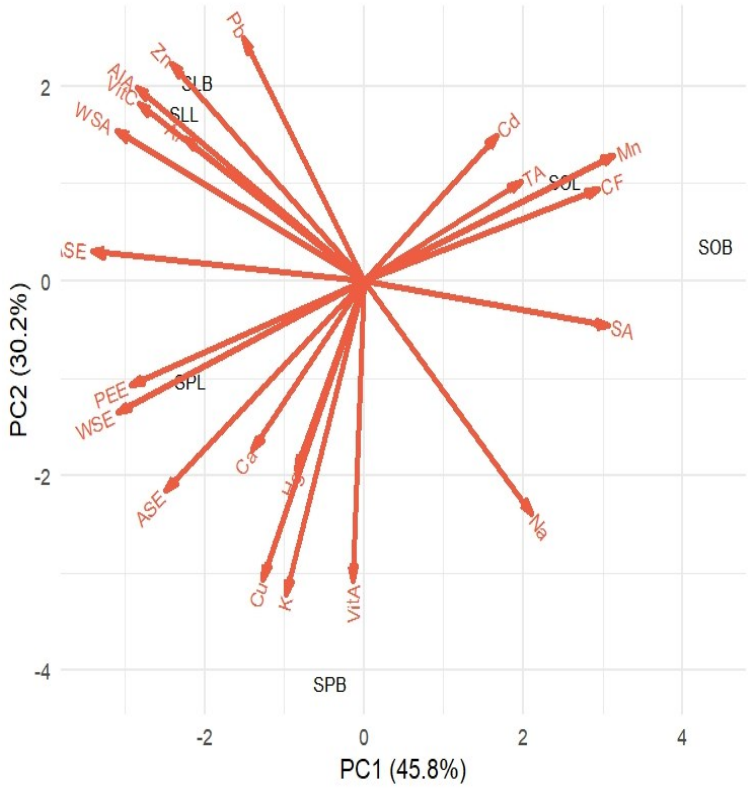


Figure 4.2: Principal Component Analysis (PCA) biplot of *Syzygium* species physicochemical parameters

The Principal Component Analysis (PCA) generated six principal components with corresponding eigenvalues. Applying the eigenvalue criterion (Kaiser-Guttman rule), only components with eigenvalues greater than 1 are considered significant for data interpretation. In this case, the first four components meet this criterion (PC1 = 3.103, PC2 = 2.517, PC3 = 1.781, PC4 = 1.265), and together they explain the majority of the total variance in the dataset. Components with eigenvalues less than 1 (PC5 and PC6) capture less variance than an individual variable and are thus not retained for further analysis. This approach ensures that the dimensionality reduction preserves as much relevant information as possible while minimizing data loss (Tables 4.11-4.12).

4.4. Discussion

Syzygium species are found mostly on the windward side of the Western Ghats, at elevations ranging from 100 to 2400 meters above sea level (Sujanapal & Kunhikannan, 2017). For the purpose of identifying species and genera, leaf anatomy and micromorphology are beneficial (Retamales & Scharaschkin, 2015). The major significance of powder microscopy is comparable to that of T.S. of leaves (Prasad et al., 2021). The leaf powders had different grinding characteristics; *S. laetum* and *S. palghatense* ground easily, whereas *S. occidentale* needed a significant amount of grinding effort.

The proximate composition, physical, and chemical properties of *S. laetum, S. occidentale*, and *S. palghatense* are not well documented in the literature. Thus, reference data from other *Syzygium* species will be used. Dark green (*S. laetum*), light green (*S. occidentale*), and pale green (*S. palghatense*) were among the various colour variations. The bark of the tree or shrub *S. polyanthum* is glabrous or greenish brown (Abdulrahman et al., 2021). Since ancient times, aromatherapy has made extensive use of the fragrance compounds found in natural leaves and flowers, indicating that they have some positive health effects in addition to their pleasing fragrance. Aroma compounds were mostly investigated from the perspective of flavour and scent chemistry until recently. Aroma compounds' therapeutic properties, including their antioxidant properties, have recently been identified (Lee & Shibamoto, 2001). During the organoleptic examination, the distinctive scent was discovered in the bark powders, and all of the leaf powders were found to have aromatic qualities.

In *Syzygium* leaves, four stomatal types, anisocytic, anomocytic, cyclo-staurocytic, and paracytic that can occur separately or in combination are identified. The existence or lack of the adaxial phloem division distinguishes the two main vascular systems. Subgeneric groups can be identified by a combination of non-unique leaf anatomical characteristics, such as stomatal categories, crystal types and frequency, and the midrib vascular system (adaxial phloem division) (Soh & Parnell, 2011). The powdered leaves of *S. laetum* contained vessels, fibers, starch grains, oil droplets, mesophyll fragments, parenchymatous and collenchymatous cells, and stone

cells. The powder microscopic analysis of *S. occidentale* leaf powder showed the presence of three types of calcium oxalate crystals (rosette, prismatic, and rod), as well as characteristic epidermal features, including adaxial and abaxial surfaces, stomata type, palisade cells, and vascular strands. Stomata, sclereids, fibers, vessels, starch granules, and crystals were found in the powdered leaves of *S. palghatense*. In the leaf of *S. cumini*, spiral vessels, fibre fragments, and a calcium oxalate crystal sheath were observed by powder microscopy (Prasad et al., 2021). Important features of the leaf blades included their base, edge, domatia, and petiole vascular arch (de Oliveira et al., 2018).

Syzygium is a useful plant in timber industry having greyish brown thick colour bark (Abdulrahman et al., 2021). In contrast to *S. palghatense*, which displayed brutally pungent leaf and bark powders, *S. laetum* and *S. occidentale* displayed astringent leaf powders and bark powders. Due to the presence of tannins bark powder retained their coarse and fibrous texture. In experimental animals, tannins have also been linked to lower food intake, net metabolizable energy, growth rate, and protein digestibility. These factors may possibly account for the animals' decreased body weight. The tannins found in *S. cumini* stem bark may have antioxidative, anticarcinogenic, antimutagenic, and antibacterial properties in addition to lowering blood pressure, promoting blood coagulation, lowering serum cholesterol levels, and influencing immunological responses (Prasad et al., 2016).

The current study showed that the bark powder of *S. laetum* includes cork, cortical cells, and various crystals, crystal fibers, septate fibers with odd projections or outgrowths, reddish-brown parenchyma cells, sclereids, and stone cells. The bark powder of *S. occidentale* contained calcium oxalate crystals, fibre pieces, sclereids, pigment cells, starch grains, cork cells in various orientations, and pitted parenchyma cells. The powdered bark of *S. palghatense* contained cork cells, medullary ray cells, thick-walled parenchyma cells with a reddish-brown substance, crystal fibers, and stone cells that are frequently connected to starch grains. Sathe & Dighe (2016) observed that the dried powder of *S. jambos* stem bark contained multicellular trichomes, there were cork cells with thick walls and a flat polygonal shape, as well

as slightly elongated, compact epidermal cells with a polygonal shape, vessels with thickening spirals, distinct tracheids, simple fibers, and starch granules with tapering, lignified ends were observed. Species characteristics offer useful taxonomic markers for identifying species and even evaluating their quality. For species identification and authentication, overlapping powder microscopic characteristics serve as reliable taxonomic markers.

S. laetum, S. occidentale, and *S. palghatense* exhibit distinct fluorescence patterns in their dry powders and extracts. Fluorescence can be defined by emission at longer wavelengths and absorption of photons at a specific wavelength (Sharma et al., 2017). When the samples of these species are exposed to the UV light, they show fluorescence. But the extract of *S. palghatense* was shown to have a lighter and brighter colour compared to *S. laetum* and *S. occidentale*. UV light analysis reveals such pronounced fluorescence differences that the varieties are clearly differentiated from one another (Vijayalakshmi & Mohammed, 2024).

According to Gayathri and Kiruba (2015) study, the fluorescence characteristics of the leaf powder in both *Psidium guajava* and *Citrus aurantium* used for medicinal purposes displayed a range of colours, including green, pale green, dark green, brown, and yellow, under various chemical treatments. The drugs *Crataeva adansonii* demonstrated distinct fluorescence in both short and long wavelengths, respectively, 256 nm and 365 nm UV rays, and in regular daylight. Bibi & Din (2020) carried out fluorescence investigation after treatment of the powdered drug with various reagents, such as ethanol, methanol, acetic acid, n-hexane, HCl, nitric acid, carrageenan, glacial acetic acid, diethyl ether, and picric acid, a variation in colour was noted.

Fluorescence is a significant characteristic of many phytoconstituents found in plant substances. In daylight, some exhibit visible fluorescence. Many natural compounds that do not exhibit visible fluorescence in daytime undergo fluorescence when exposed to ultraviolet radiation. Even though some substances are not fluorescent, they can frequently be transformed into fluorescent derivatives using various chemical reagents and chemicals; as a result, we can frequently use

fluorescence, the most crucial pharmacognostical evaluation parameter, to qualitatively evaluate some crude drugs (Ranjith, 2018).

S. cumini (jamun) was used as a carbon source in a simple, inexpensive, and environmentally friendly hydrothermal process by Bhamore et al. (2016) to create fluorescent carbon nanocrystals (NCs) at 180 °C for six hours. Under a UV lamp, carbon NCs exhibited brilliant blue light after exciting them at 365 nm. In the present study, colours like olive and verdant green was produced by *S. laetum* and *S. occidentale* with chemicals like acetone and benzene. *S. palghatense* also exhibits light green and pale brown hues when exposed to various solvents. In terms of extracts, *S. palghatense* extracts display comparatively more distinctive colours, such as mint green and sandy brown, whereas *S. laetum* and *S. occidentale* extracts produce fluorescent colours, such as green, brown, and olive green, when exposed to petroleum ether and chloroform solvent. These findings indicate that the fluorescence behaviour depends on species, form of sample, i.e., powder or extract, and the type of reagent used.

S. laetum was found to have the highest extractive content, particularly in water-soluble and alcohol-soluble extracts, in addition to having notable levels of vitamin C in its leaves. Jaiswal et al. (2015) stated that *S. cumini* is a good source of vitamins, minerals, and antioxidants and also have various therapeutic properties. Chiteva et al. (2023) provide an example of how *S. cumini* can be used as a substitute feed additive to improve food security. The physicochemical characteristics, including fruit breadth, ash, pH, and important minerals like Na, Mg, Mn, Cu, and Zn, varied significantly with the different microclimatic conditions. Compared to oranges, pineapples, pears, peaches, and apples, the fruits have more than enough minerals. According to Ali et al. (2024), when compared to leaves and flowers, bark exhibited the least amount of antibacterial potential against pathogenic microorganisms. In food and medicines, the leaves, flowers, and bark extract are a good source of fibre, proteins, and antimicrobial substances.

The Malay apple fruit (*Syzygium malaccense*) has the potential to be a good source of antioxidant chemicals with potential health benefits, according to Nunes et

al. (2016). The peel had higher levels of total phenolics and total anthocyanins. In addition to having a higher concentration of bioactive chemicals and antioxidant activity, the peel is a source of vitamin C. Furthermore, a positive synergistic impact of peel extracts was noted, and peel extracts showed a stronger oxidation inhibition capability than edible part extracts.

S. occidentale fruits are high in vitamins, lipids, protein, and reducing sugars. Fruits of *S. occidentale* are a suitable dietary supplement because they contain high levels of lipid and amino acids. Additionally, it has excellent levels of vitamin A and vitamin C, making this fruit a useful nutritious supplement (Varghese et al., 2025). In the present study, we found that the bark extract of *S. occidentale* had the highest fibre and mineral content compared to other tested species. The highest fibre content in *S. occidentale* can be a responsible factor for significant grinding effort.

According to the results of the present study, lesser ash content and high copper content was present in the leaves and bark of *S. palghatense* compared to *S. occidentale* which have higher ash content especially in the bark. These variations shows that different *Syzygium* species have distinct chemical and nutritional characteristics so, retain different applications in the field of medicine and nutrition. According to Ghosh et al. (2017), information on various characteristics (physical, chemical and mechanical) of fruit and seeds of *S. cumini* provides a better understanding in industrial processes.

4.5. Conclusion

The study concludes that *S. laetum, S. occidentale,* and *S. palghatense* are nutritionally valuable Myrtaceae members based on the combined powder microscopy, fluorescence, physicochemical, and nutritional data. Their physical features support a complicated taxonomy of *Syzygium* and demonstrate the usefulness of several characteristics for species identification. Characteristics of species are helpful taxonomic indicators for recognizing species and even assessing their quality. Overlapping features in powder microscopy are important taxonomic identifiers for species identification and authenticity.

The fluorescence analysis provided additional authentication factors by revealing species-specific colour changes based on chemical treatment and light conditions. Findings of the study indicates that the fluorescence behaviour of leaf or bark samples depends on species, form of sample, i.e., powder or extract, and the type of reagent used. The extract of plants exhibited a range of fluorescence characteristics, which is an essential indicator for standardizing medicinal plants.

According to physicochemical analysis, different extractive values are displayed; the bark of *S. palghatense* exhibits the highest water-soluble and alcohol-soluble extractive values. It also shows higher copper content and lower ash levels, while *S. occidentale* has the highest ash content, especially in the bark. The comparatively low sulphated ash in *S. laetum* and *S. palghatense* highlights distinct nutritional and chemical profiles, indicating diverse potential applications in medicine and nutrition. Nutritionally, the bark and leaves are rich in antioxidants, vitamins, fibre, and various minerals.

The current study provides a thorough baseline about *S. laetum, S. palghatense*, and *S. occidentale*. The findings enable the correct identification, quality control, and medicinal applications of these unique species by providing pharmacognostic standards. Future research should investigate the isolation of bioactive compounds and their agronomic potential. Further investigation into pharmacological activities could improve understanding.

5

PHYTOCHEMICAL PROIFLING



CHAPTER 5
PHYTOCHEMICAL PROFILING

5.1. Introduction

Phytochemical profiling is an essential strategy that utilizes high-throughput methods alongside conventional screening and analytical tools to characterize plant-based metabolites. Due to their relationship with human health, these phytochemicals have attracted extensive attention, with medicinal plants systematic analysis of secondary metabolites involving diverse extraction approaches and analytical techniques (De Silva et al., 2017).

Phytochemicals are naturally occurring bioactive compounds in plants that provide a myriad of health benefits. Such compounds are called secondary metabolites, frequently produced by altered primary metabolites or pathways originating from (or sharing substrates with) primary metabolites. These compounds, including alkaloids, flavonoids, tannins, saponins, and phenolics, show numerous biological activities that underpin their application in traditional and modern medicine. The identification and characterization of bioactive compounds in plants responsible for their biological properties are derived from recent advances in phytochemical profiling, which have been instrumental in determining a plants chemical diversity. They have antioxidant, anti-inflammatory, anti-cancer, and anti-bacterial properties (De Silva et al., 2017; Kabera et al., 2014; Saxena et al., 2013; Tiwari et al., 2011).

Medicinal plants have several benefits, especially economic ones within Indian subcontinent. Record of traditional learning, particularly of the medicinal plant usage throughout history, has resulted in the discover of multiple drugs in the modern society. India has a historical identity as a rich treasure cum repository of medicinal plants. The main reserve of several aromatic and medicinal plants is the forest chosen to collect raw materials for manufacturing drugs and perfumery items. As many as 8,000 herbal remedies have been recorded and utilized in AYUSH systems in the

country. The well-known systems of indigenous medicines are known to include, Unani, Siddha, Ayurveda, and Folk (tribal) treatments. Among them, Ayurveda and Unani Medicine are the developed and widely practiced systems of medicine in India (Jain et al., 2012; Parthasarathy et al., 2006; Suman et al., 2021).

The history of medicine goes as far back as the history of human civilization itself. Natural products (or secondary metabolites) and natural product-derived compounds have historically been the primary sources of new drugs (Lahlou, 2013). A renaissance in natural product research has been happening recently because this approach to drug discovery has not produced so many hit compounds in important therapeutic areas such as immune suppression, anti-invectives and metabolic diseases. Many of these approved substances are chemically diverse and have further highlighted the importance of natural products in drug discovery efforts today (Chin et al., 2006).

Multiple biological and pharmacological activities have been associated with polyphenolic compounds, particularly antioxidant activity, in edible and nonedible therapeutic plants (Ghareeb et al., 2017; Kähkönen et al., 1999; Mohamed et al., 2011; Mukherjee, 2003). In recent years, the focus has been on multiple species of *Syzygium* with significant medicinal potential. Several pharmacological reviews have been conducted in *Syzygium* species (Prabhakaran et al., 2011).

Phytochemicals are bioactive compounds of plant origin, and they can be divided into two categories, primary constituents or secondary metabolites, based on their involvement in plant metabolism. Primary components include common sugars, amino acids, proteins, chlorophyll, etc. Secondary components contain alkaloids, terpenes, and phenolics. As research progresses, phytochemicals have been found to offer even more remarkable benefits that suggest their nutritional and disease-fighting potential. Many analytical methods, including HPTLC, FTIR, HPLC, and GC/MS, along with NMR, have been developed over the past decade, which are highly effective in separating, identifying, and elucidating the structure of phytochemicals (Sweetlin & Daniel, 2020).

Designed to handle a broader range of integrated, automated sample preparation and extraction systems than ever before with even more advanced instrumentation, as exemplified by the new high-performance GC-MS instruments, are now becoming workhorses in analytical labs due to the increased robustness for varying types of matrices all while improving selectivity over common matrix interferences that possess lower risk and an increasing opportunity for multi-compound approaches. The high performance of GC is defined by its capability for separating mixture signals and instantaneous signal response, which is well suited to be easily deconvoluted. With fused silica columns, the power and potential of GC surpassed all synonymous methods to date when applied to problems involving complex mixtures. Since multi-methods or multi-component analyses are more common these days, GC MS is the best to be used (Annal et al., 2024; Hübschmann, 2015).

Active components can be derived from any plant part, such as leaves, bark, flowers, fruits, and roots. Any bioprospecting study is based on systematic screening of plant species aiming at identifying novel bioactive compounds. The fruits of wild edible plants are rich sources of vitamins (β-carotene, vitamins C and E), flavonoids, and other polyphenolic compounds with high free-radical scavenging activity (Wong et al., 2016).

The bioactive components have a range of medicinal significance and are most likely responsible for curing or decreasing the harmful effects of the diseases. Hence, the qualitative screening of these phytochemicals would provide a glimpse of the diverse chemical pattern of the plant material, and the quantitative screening aims to extract, isolate, purify, and characterize the bioactive component of medicinal importance to mankind (Banu & Cathrine, 2015; Hameed et al., 2014).

Various bioactive compounds, especially flavonoids, phenolic acids, and triterpenoids, have been reported to have excellent pharmacological and biological properties of plants. Tannins are helpful for wound healing and inflamed mucosal membranes. Glycosides, which have purgative characteristics, treat skin diseases and are classified as anticancer agents. The saponins, alkaloids, and flavonoids have

beneficial effects on neurodegenerative disorders and oxidative stress (Zhang et al., 2016).

Screening plant species to find newer compounds that are bioactive in nature is well-known across several labs. The method of plant components' scientific analysis is a pragmatic or a more logical method. Plants are collected randomly or based on leads provided by local healers in the regions where the plants are found fresh or dried plant materials can be used as a source for the extraction of secondary plant components. Several authors have described preparing plant extracts from fresh plant tissues. The premise behind this was the ethno-medicinal application of fresh plant materials by the traditional and tribal communities. However, traditional healers have traditionally used many plants in dry form or as aqueous extract. Because different parts of the plant contain varying amounts of water, plants are typically air-dried to constant weight before extraction (Parekh et al., 2006).

The findings on phytochemical screening of various *Syzygium* species, specifically of solvent extracts, reflected several studies on diverse bioactive compounds and their possible usage as therapeutics. *S. reticulatum* study was performed using GC-MS analysis to identify the main components of methanol extract, namely Diisooctyl phthalate and 2-methyltetracosane, which represented strong antioxidant activity and cytotoxic activities that indicate the presence of bioactive compounds with high potential (Das et al., 2024).

S. cumini has been studied extensively for its phytochemicals due to its high phenolics and flavonoids content, which also gave it good antioxidant and anti-diabetic activities (Rathod et al., 2020; Salomi & Parimala, 2023). Several species of *Syzygium*, especially *S. griffithii* and *S. syzygioides*, exhibit appreciable antioxidant activities in methanol extracts, which indicates the therapeutic potential of the genus in antioxidants (Abdullah & Jamil, 2020). Furthermore, *S. aromaticum* showed that its methanolic extracts contained tannins, alkaloids, and flavonoids connected to its antimicrobial properties, highlighting the significance of these phytochemicals in traditional medicine (Leonard, 2022). Many bioactive compounds, including flavanone derivatives and terpenoids, have been confirmed in the *Syzygium* genus,

responsible for their pharmacological events, like antimicrobial and antioxidant properties (Uddin et al., 2022b). Collectively across studies, advanced analytical techniques like GC-MS and LC-MS have significantly contributed to the identification and characterization of a variety of phytochemicals found in all *Syzygium* species, providing evidence for their use in the development of pharmaceuticals and nutraceuticals (Onukwuli et al., 2024; Sinan et al., 2023).

In this current research, phytochemical profiling was conducted using preliminary qualitative and quantitative tests to identify the various metabolites in the solvent extracts of selected endemic species of *Syzygium*. Analytical techniques such as GC-MS and LC-MS QTOF analysis were also employed to ascertain the volatile and non-volatile compounds in the particular solvent extracts.

- **Objectives**

- To perform systematic solvent extraction of leaves and bark from three endemic *Syzygium* species (*S. laetum*, *S. occidentale*, and *S. palghatense*) using Soxhlet extraction with solvents of increasing polarity (petroleum ether, chloroform, ethyl acetate, methanol, and distilled water).
- To conduct qualitative phytochemical screening to identify the presence of various metabolites in the solvent extracts.
- To perform quantitative phytochemical analysis to determine the concentration of bioactive compounds in the selected *Syzygium* species.
- To characterize volatile compounds using Gas Chromatography-Mass Spectrometry (GC-MS) analysis.
- To identify and analyze non-volatile compounds through Liquid Chromatography-Mass Spectrometry Quadrupole Time-of-Flight (LC-MS QTOF) analysis.

5.2. Materials and methods

5.2.1. Extraction of plant samples

Soxhlet extraction is a common technique to extract bioactive compounds from plant materials with selective solvents. This type of extraction is frequently performed when the desired compound is either insoluble in water or only exists in relatively low concentrations. The Soxhlet method was named after its inventor, the German scientist Franz von Soxhlet (1848-1926), who designed this device. In this method, dried and powdered plant material is placed in a cellulose thimble inside a Soxhlet apparatus and continuously extracted by refluxing with heated solvent at a particular temperature of the solvent based on its boiling point, allowing the solvent to flush the plant material through the sample repeatedly. This method is particularly effective as it allows for repeated cycling of fresh solvent through the plant material, efficiently extracting both polar and non-polar compounds. The extraction will usually take 16-24 hours, during which the solvent will be continuously evaporated, condensed, and siphoned back through the sample. Although this conventional approach works well, it can be very non-automated and time-consuming when dealing with many samples. During Soxhlet extraction, extractive value is the quantitative estimate of the amount of soluble compounds extractable from plant materials with distinct solvents. It represents the active ingredients obtained from a certain amount of plant material during extraction.

The leaves and bark powders of *S. laetum*, *S. occidentale*, and *S. palghatense* were placed in a cellulose extraction thimble and inserted into a Soxhlet device (Rotek). The extraction was continued for 24 hours for each solvent at 60-100°C with petroleum ether (non-polar compounds), chloroform (moderately polar), ethyl acetate (moderately polar), methanol (polar), and distilled water (highly polar). A rotary evapourator (LabTech EV311 Plus) was used to evapourate the solvents, after extraction. The formula shown below was used to calculate the total extractive values on a dry-weight basis (Maldonado et al., 2020):

$$\text{Percentage of extractive value (Yield Percentage)} = \frac{\text{Weight of crude extract}}{\text{Weight of the sample taken}} \text{ X } 100$$

The extracts were stored in amber-coloured glass bottles at 4°C for further experiments.

5.2.2. Qualitative phytochemical analysis

Qualitative tests are needed to demonstrate the presence of pharmacologically active compounds prior to more advanced quantitative or biological activity tests. Preliminary screening results often both correlate to medicinal uses in traditional medicine and help validate ethnomedicinal claims while providing suitable scope for more detailed phytochemical investigations and potential drug development (Gul et al., 2017). This value is crucial for the quality control of crude drugs and lays the standardization criteria when biological assay methods cannot be applied. The more active constituents in the plant material, the higher the extractive value. The qualitative phytochemical analysis might provide insights into validating traditional medicinal uses and identifying specific bioactive compounds for advanced drug development (Uddin et al., 2022).

The preliminary phytochemical analyses were carried out to determine the presence or absence of secondary phytoconstituents responsible for the biological properties of the plants.

The petroleum ether, chloroform, ethyl acetate, methanol, and distilled water extracts of leaves and bark of three plant samples were qualitatively analyzed using standard chemical tests (Chowdhury et al., 2016; Edeoga et al., 2005; Harborne, 1998; Mulla & Paramjyothi, 2010; Santhi & Sengottuvel, 2016; Shanmugam et al., 2019; Sofowora, 1993; Trease & Evans, 2002).

5.2.2.1. Test for alkaloids

- **Mayer's test:** The different solvent extracts of the plant samples were dissolved in dilute H_2SO_4 and filtered. The 2 mL of the filtrate was treated

with Mayer's reagent (Appendix 1). The appearance of the cream colour indicates the presence of alkaloids.

- **Hager's test:** 2 mL of plant extracts were mixed with 2 mL of Hager's reagent (Appendix 2). An eye-catching yellow precipitate pointed to a positive result.
- **Dragendorff's test:** 2 mL of plant extracts were mixed with 2 mL of Dragendorff's reagent (Appendix 3). The presence of an orange-brown colour gives a positive result for the alkaloids.
- **Wagner's test:** 2 mL of Wagner's reagent (Appendix 4) was added to 2 mL of plant extract. A reddish-brown precipitate indicates the presence of an alkaloid.

5.2.2.2. Test for flavonoids

- **Alkaline reagent test:** A few drops of sodium hydroxide solution were added to 2 mL of the test sample. This produced an intense yellow colour, which disappeared upon the addition of dilute hydrochloric acid.
- **Shinoda's test:** 1 mL of concentrated hydrochloric acid was combined with a fraction of the extract, and magnesium ribbon was then added. The development of a pink colouration was taken as proof that flavonoids were present.
- **Lead acetate test:** Two milliliters of the sample were mixed with a few drops of lead acetate solution. The development of a yellow precipitate confirmed the presence of flavonoids.

5.2.2.3. Glycosides Test

- **Borntrager's test:** The plant extracts were first subjected to acid hydrolysis. After that, 2 millilitres of hydrolysate was combined with 3 millilitres of chloroform, shaken thoroughly, and left to stand until two distinct layers formed. To the chloroform layer, an equal amount of 10% ammonia solution

was added. The appearance of a pinkish-red colour indicated the presence of anthraquinone glycosides.

- **Keller-Killani test:** Two milliliters of the plant extract were mixed with 1 mL of glacial acetic acid. A few drops of 5% ferric chloride solution and concentrated sulfuric acid were then carefully added along the sides of the test tube. Formation of a reddish-brown ring at the interface of the two layers confirmed the presence of cardiac glycosides.

5.2.2.4. Test for saponins

- **Foam test:** 2 mL of the extracts were mixed with 10 mL of distilled water and mixed vigorously. Observation of persistent foam indicated a positive result.

5.2.2.5. Test for Carbohydrate

- **Molisch's test:** To 5 mL of the sample, a few drops of Molisch's reagent **(**Appendix 5) were added. The test tube was then inclined, and 1 mL of sulfuric acid was carefully introduced along the side to the bottom. Formation of a reddish-violet ring at the interface of the two layers indicated the presence of sugars.

- **Fehling's test:** One millilitre of the filtrate was heated in a water bath with 1 mL each of Fehling's solutions A and B (Appendix 6). Appearance of a red coloured precipitate confirmed there was sugars present that were reducing in nature.

5.2.2.6. Test for tannins

- **Gelatin test:** Tannins in the extract were identified by adding a few drops of 1% gelatin solution prepared in 10% sodium chloride to 1 mL of the plant extract. The appearance of a white precipitate signified a positive test.

- **Braymer's test:** 2 mL of the extracts were treated with a few drops of 10 % alcoholic ferric chloride solution. The precipitate with a dark green colour indicates the presence of tannins.

- **Lead acetate test:** To the 5 mL of the test solution, a few drops of 1 % lead acetate solution were added. The appearance of a yellow precipitate gives the positive results for the tannins.

5.2.2.7. Test for reducing sugar

- **Fehling's test:** About 0.5 g of plant extract was dissolved in distilled water and filtered. The obtained filtrate was then heated with 5 mL of Fehling's solution A and B in equal proportions. The appearance of a red cuprous oxide precipitate confirmed the presence of reducing sugars.

5.2.2.8. Test for Starch

- **Iodine test**: 0.5 g of plant extracts were taken in a clean test tube. 2-3 drops of iodine solution were added and mixed. The formation of blue-black coularation was taken as the presence of starch.

5.2.2.9. Test for Phenolics

- **Phosphomolybdic acid test:** 1 mL of the extract was spotted on a filter paper. A few drops of phosphomolybdic acid were added to the spot and then exposed to ammonium vapours. The formation of blue colouration in the spotted area was taken as an indication of the presence of phenols.

5.2.2.10. Test for Anthraquinone

- **Borntrager's test:** To a small quantity of extracts, H_2SO_4 and CCl_4 or ether were added. The organic layer formed was separated and shaken with dilute ammonia. The rose-pink colour of the ammonia layer indicates the presence of anthraquinone.

5.2.2.11. Tests for fats and oils

- **Stain test:** By pressing a small quantity of each extract between two filter papers, the stain on the filter papers indicates the presence of the oils.
- **Saponification test:** To check for oils and fats, a few drops of 0.5 N alcoholic potassium hydroxide were added to each extract along with a single drop of phenolphthalein. The mixtures were heated in a water bath for 1–2 hours. The appearance of soap-like material or a reduction in alkalinity signified the presence of lipids.

5.2.2.12. Test for essential oils

The plant extracts were treated with Sudan Red III (Appendix 7). The appearance of red colour indicates the presence of essential oils in the sample.

5.2.2.13. Test for proteins

- **Biuret test:** Added 4 % NaOH and a few drops of 1 % $CuSO_4$ solution to the 3 mL of the extracts. The appearance of violet or pink colour indicates the presence of proteins.
- **Millon's test:** In the aqueous solution of the extract, 2 to 3 mL of Millon's reagent (Appendix 8) was added separately. The formation of pink colour reveals the presence of proteins.

5.2.2.14. Test for amino acids

Ninhydrin test: 2 mL of the extracts were mixed with 1 mL of 5 % ninhydrin solution (Appendix 9). Boiled for 5 minutes in a water bath. The blue-purple colour indicates the presence of amino acids.

5.2.2.15. Test for steroids and triterpenoids

- **Libermann Burchard's test:** The extracts were combined with chloroform and subsequently filtered. Into the filtrate, a small volume of acetic anhydride was introduced, after which the mixture was boiled and then cooled. A few

drops of concentrated sulfuric acid were carefully added. Development of a brownish ring at the interface was taken as evidence for steroids. A positive outcome for triterpenoids and steroids was further confirmed by the appearance of a deep red colouration in the lower layer and a green tint in the upper layer.

5.2.2.16. Test for Coumarin

- **NaOH test:** 3 mL of 10 % NaOH was added to 2 mL of the extracts. The appearance of dark yellow colour indicates coumarins.
- **Ferric chloride test:** 1 mL of the extract was treated with 1 mL of ferric chloride solution. The appearance of a deep yellow colour is an indication of the presence of coumarins.

5.2.3. Quantitative phytochemical analysis

Quantification studies of phytochemicals in the *Syzygium* genus are important for understanding the medicinal and therapeutic efficacy of its different species. Various phytochemical investigations in *Syzygium* endemics have shown the existence of a variety of useful phytochemicals like total phenol, reducing sugar, tannin, carbohydrate, saponins, glycosides, alkaloids and flavonoids, that're known to be responsible for the pharmacological activity.

The preliminary qualitative phytochemical evaluation of the four distinct solvent extracts such as chloroform, ethyl acetate, distilled water, and methanol, made from the leaves and bark of the three plant species showed that the methanol and distilled water extracts of the plant samples included more phytocomponents. In the majority of the preliminary phytochemical assays, the methanolic extract demonstrated the highest quantity of bioactive phytoconstituents and the highest amount of precipitation and colour intensity, suggesting a greater amount of secondary metabolites. The methanol extracts showed higher extractive value. As a result, methanol was chosen as the solvent to be employed for every subsequent study of the present investigation. The required amount of leaves and bark of the methanol

extracts was prepared by the Soxhlet extraction method followed by rotary evaporation.

The quantification of major phytoconstituents revealed from the preliminary qualitative analysis of leaves and bark of the plant samples was estimated by following phytochemical quantitative analysis using standard protocols and all the samples were quantitatively estimated in triplicates.

5.2.3.1. Total alkaloids

1 mg of the plant extracts (1 mg/mL) and different concentrations of the standard solution of atropine were prepared. It was mixed with 2 N HCl, followed by filtration. To this reaction mixture, 5 mL phosphate buffer (Appendix 10) and 5 mL bromocresol green (BCG) solution (Appendix 11) were added. The reaction mixture was shaken well and sequentially combined with 1, 2, 3, and 4 mL of chloroform. The chloroform layer containing the alkaloid was separated by removing the bromocresol green layer. The absorbance of the complex in chloroform was measured at 470 nm against the blank without a sample (Shamsa et al., 2008). The total alkaloid content of the extract was measured and expressed in milligrams of atropine equivalent per gram of dry weight (mg AE/g DW).

5.2.3.2. Total flavonoids

The total available content of Flavonoid was calculated with the help of the aluminium chloride colorimetric method. Standard quercetin solutions (twenty, forty, sixty, eighty, and hundred µg/mL) were prepared. For the assay, 1 mg/mL of the extract and varying concentrations of the standards were mixed with 0.5 mL distilled water and 0.3 mL of 5% sodium nitrate (w/v), then incubated at 25 °C for 5 minutes. After incubation, 0.3 mL of 10% $AlCl_3$ (w/v) was added, and the mixture was shaken well. To this, 2 mL of 1 M sodium hydroxide was added, and the volume was adjusted to 10 mL with distilled water. The absorbance of both test and standard samples was measured against a reagent blank at 510 nm using a UV-Visible spectrophotometer. The calibration curve of quercetin was plotted, and the total flavonoid content was

calculated and expressed as mg quercetin equivalent per gram of dry weight (mg QE/g DW) using a regression equation (Har & Intan, 2012; Oueslati et al., 2012).

5.2.3.3. Total glycosides

The quantity of the glycoside in the plant extracts was estimated using Baljet's reagent method (Appendix 12). 10 mL of 70 % alcohol was used to soak 1 g of each sample for the entire night before filtering. Subsequently, 12.5 percent lead acetate and 4.77 percent Na_2HPO_4 solution were used to purify the extracts, and then freshly made Baljet's reagent was added. Baljet's reagent causes the digitalis cardiac glycosides to turn orange-red. The amount of glycoside present determines how intense the colour becomes. To quantify the amount of cardiac glycoside present, this colour formation is utilized. The colour intensity obtained against blank at 495 nm with the help of a spectrophotometer was noted. The standard graph is prepared using a varying concentration of standard digitoxin (2-14 µg) (Oluwaniy & Ibiyemi, 2007).

5.2.3.4. Total saponins

Saponin levels in the plant extract were determined through the vanillin–sulfuric acid assay. In this procedure, 0.1 g/mL of the sample was mixed with 0.25 mL of 0.8% (w/v) vanillin reagent **(**Appendix 13**)** and 2.5 mL of 72% (v/v) sulfuric acid solution. The mixture was incubated at 60 °C in a shaking water bath for 15 minutes. After incubating for 10 minutes, the reaction tubes were transferred into an ice-cold bath for 3–4 minutes to stop the reaction. The absorbance of the standards and extracts was measured at 544 nm using a UV/VIS spectrophotometer (Jain & Shrivastava, 2017).

5.2.3.5. Total carbohydrate

A 100-milligram portion size of the sample was placed in the test tube and hydrolyzed in a boiling water bath with 5 mL of 2.5 N HCl for 2–3 hours, then allowed to cool to room temperature. The solution was neutralized using solid sodium carbonate until effervescence stopped. The volume was adjusted to 100 mL, centrifuged, and the clear supernatant was collected. Aliquots of 0.5 mL and 1 mL were used for analysis. Standard solutions were prepared by pipetting 0.2–1 mL of a

glucose stock solution (10 mg/100 mL) and diluting to 1 mL with distilled water. A blank was prepared using 1 mL of distilled water. To each tube, 4 mL of anthrone reagent (Appendix 14) was added, and the mixtures were heated in a boiling water bath for 8–10 minutes before cooling. Cool rapidly and notice and note the modifications in the colour from green-dark green at 630 nm. The concentration of glucose in the sample was calculated (Hedge & Hofreiter, 1962).

5.2.3.6. Total tannin

A volumetric flask (10 mL) was charged with 0.10 mL extract, followed by 7.5 mL DI water and 0.50 mL FC (Folin phenol) reagent. Next, 1.0 mL Na_2CO_3 (35% w/v) was introduced and the solution was brought to the mark with water. After thorough mixing, the reaction stood at ambient temperature (~25 °C) for 30 min. A gallic-acid calibration (20–100 μg mL^{-1}) was prepared in the same manner. Absorbance at 725 nm (A_{725}) for standards and samples was read on a UV–Vis spectrophotometer using a reagent-only blank. The tannin content was expressed in terms of mg of GAE /g of extract (Singh et al., 2012).

5.2.3.7. Total reducing sugar

To a beaker, add 100–500 mg sample and 5 mL warm ethanol (EtOH); mix with a glass stirrer for 15–20 min. Decant the supernatant into a centrifuge tube. Extract the residue twice more with 3 mL EtOH each and pool the supernatants. Remove solvent at 70–80 °C in a water bath until dry, then reconstitute the residue (sugars) with 10 mL deionized water (DI). Clarify by centrifugation at 1,000–1,200 rpm for 15–20 min. Prepare a seven-point calibration of the standard (0–3.0 mL in 0.5 mL increments) in labeled tubes. Place 1.0 mL of the sample extract into duplicate tubes. Bring every tube to a total of 3.0 mL with DI water (adjust volumes accordingly). Add 3.0 mL alkaline DNS reagent (3,5-dinitrosalicylic acid) to each tube. Incubate for 5 min in a bath of boiling water. While still hot, add 1.0 mL sodium–potassium tartrate solution to every tube. After proper mixing and cooling, the absorbance of orange-red colour read at 510 nm (Miller, 1959).

5.2.3.8. Total phenol

Total phenolics in plant extract were quantified with the Folin–Ciocalteu (FC) colorimetric assay. A volumetric flask (25 mL) was charged with extract (1.0 mL) and DI water (9.0 mL). FC reagent (1.0 mL) was then introduced and the mixture vortex-mixed vigorously. After 5 min, Na_2CO_3 solution (7% w/v, 10 mL) was added, and the contents were brought to the mark with water (25 mL total). A calibration series of gallic-acid (GA) standards at 20, 40, 60, 80, and 100 μg mL^{-1} was prepared in parallel. Following a 90 min incubation at ambient temperature (~25 °C), A_{550} for samples and standards was recorded relative to a reagent-only blank on a UV–Vis spectrophotometer. Total phenol content was expressed as mg of GAE/g of extract (Xu & Chang, 2008; Ghasemzadeh *et al*., 2010; Rasool et al., 2011)

5.2.4. Gas Chromatography-Mass Spectrometry (GC-MS) analysis

The GC-MS analysis is a crucial area of the study of *Syzygium* species since it serves as a medium for detailed insights into their chemical compositions and potential applications. The GC-MS technique is useful for finding several compounds from the leaves and bark of the *Syzygium* that are widely used for therapeutic activity.

The volatile components in the methanol extracts of the leaves and bark of *Syzygium* endemics, with therapeutic importance, were identified through GC-MS analysis using Shimadzu QP2010S equipment.

- **Instrumentation**

GC-MS analysis was performed using a Shimadzu QP2010S system, with a gas chromatograph connected to a mass spectrometer under the following conditions, utilizing an Elite-5 MS capillary column (30 mL x 0.25 mm ID x 0.25 μm df).

- **GC condition**

The injector was maintained at 260 °C, while the column followed a temperature program starting at 80 °C (isothermal for 4 minutes), then rising at 5 °C per minute until reaching 280 °C, where it was held for 6 minutes. Helium gas of

99.9995% purity served as the carrier at a flow rate of 1 mL per minute. A split ratio of 50 was applied.

- **Identification of components**

Identification of compounds was based on molecular weight, molecular structure, and predicted fragment patterns. Data interpretation involved mass spectral comparison with reference compounds from the Wiley 8 and NIST 11 (National Institute of Standards and Technology) libraries. Retention times were aligned, and the relative concentrations of each component were expressed as percentage peak areas in relation to the overall peak area. Only selected peaks with a similarity index of 70 % and above with Wiley and NIST libraries were chosen and identified (Mir et al., 2020).

5.2.5. Liquid Chromatography-Mass Spectrometry Quadrupole Time of Flight (LC-MS QTOF) analysis

The application of LC-MS QTOF analysis in the study of *Syzygium* species leads to the delivery of an extensive chemical profile and the identification of pharmacologically active constituents. As a useful tool for identifying secondary metabolites such as phenolic acids, flavonoids, and other bioactive compounds, this highly analytical method provides an efficient means to ensure proper annotation of such compounds. The system has high mass resolution and mass accuracy, allowing for obtaining information on the detailed structure of complex compounds as well as the detection of known and unknown metabolites of methanol extracts of the leaves and bark of the *Syzygium* endemics.

100 mg of the methanol extracts of leaves and bark of the selected plants were dissolved in methanol and water (1:1) and diluted sufficiently for instrument (Instrument Model-1260 Infinity, Agilent USA) acquisition. The mobile phase consists of 0.1% formic acid and 0.1 % acetic acid in acetonitrile. The chromatographic separation was performed on column C18 (3.0 x 100 mm, 2.7 microns). The mobile phase was supplied at a flow rate of 0.25 mL per minute. For the MS/MS QTOF 6545 (Agilent USA), the gas temperature was 325°C with 2.0 Kv Capillary Volt, nebulizer

60 psi, and dry gas provided was 6 L/minutes in positive mode. The relative abundances indicated as the area of each annotated peak in each sample were produced as a data matrix after the analytical operation (Rocchetti et al., 2019).

5.2.6. Statistical analysis

All experimental data were analyzed using one-way analysis of variance (ANOVA) to determine significant differences among treatment means. Six replicates were maintained for each treatment to ensure statistical reliability. Critical difference (CD) values were calculated to evaluate the minimum significant difference between means at the chosen confidence level. Post hoc multiple comparison tests were performed following ANOVA to identify specific group differences. Additionally, Principal Component Analysis (PCA) was conducted to reduce data dimensionality and to explore the relationships and variations among phytochemical constituents across solvent extracts. Statistical analyses were carried out using R 4.2.0, with significance levels set at $p < 0.05$.

5.3. Results

5.3.1. The percentage of yield

The percentage yield of leaf and bark extracts of *S. laetum*, *S. occidentale,* and *S. palghatense* in different solvents are presented in Tables 5.1 to 5.3. The maximum yield percentage was obtained in the methanol extracts of the leaves and bark.

The percentage yield of extracts from three *Syzygium* species shows that *S. palghatense* yielded maximum extractive values among the three with the highest yields in methanol (leaves: 49.16 % and bark: 49.23 %) followed by distilled water (leaves: 30.86 % and bark: 34.36 %). Although *S. laetum* produces intermediate yields with methanol (43.28 % leaves and 41.67 % bark) and distilled water (41.18 % leaves and 45.85 % bark), *S. occidentale* exhibited the lowest yield of the three species exhibited at 39.23 % (leaves) and 39.40 % (bark) in methanol, and 26.73 % (leaves) and 27.10 % (bark) in distilled water. As Table 5.1 to 5.3 shows, for all three species, the sequence of extraction yield remains the same: methanol > distilled water > ethyl acetate > petroleum ether > chloroform. Across all species and solvents, bark extracts produce slightly higher yields than leaf extracts. Chloroform extraction gave the lowest yields in *S. occidentale* (leaves: 0.23 % and bark: 0.26 %), while methanol extraction yielded the highest in *S. palghatense*. Across the three species, the yields obtained from the non-polar solvents used (petroleum ether and chloroform) were consistently lower (<1 %) compared to those obtained from the polar solvents (methanol and distilled water). The colour of extracts varies from light green to blackish green for leaves, and from brown to blackish brown for bark, with darker colours usually resulting from higher yields. The optimal combined extraction yields for all five solvent polarities were associated with higher mineral contents and lower acid-insoluble ash, which improves extraction efficiency, especially with polar solvents such as methanol and water.

5.3.2. Qualitative phytochemical analysis

Tables 5.4 depict the heatmap of preliminary qualitative analysis of different extracts of leaves and bark of *S. laetum*, *S. occidentale*, and *S. palghatense*.

Screening of phytochemical constituents in three *Syzygium* species (*S. laetum*, *S. occidentale,* and *S. palghatense*) using different solvent systems showed a comprehensive metabolite profile. Both methanol and distilled water extracts were effective for all three species, with non-polar extracts showing limited utility. Interestingly, essential oils were the sole group of bioactive compounds that were observed in all species across all the solvent extracts, whereas most of the other bioactive compounds were accumulated mainly in the polar extracts. The methanolic extracts consistently affected alkaloids, flavonoids, glycosides, carbohydrates, tannins, reducing sugars, phenolics, and steroids/triterpenoids positive. The profiles of the aqueous extracts were similar but were glycosides and steroids/triterpenoids were notably absent from these extracts, whereas they were uniquely contained saponins. For example, ethyl acetate extracts had a moderate extraction efficiency and mainly isolated glycosides, phenolics and steroids/triterpenoids from leaves, and tannins from bark. The compounds which were consistently absent in all extracts of all three species were starch, anthraquinones, fats and oils, proteins, and amino acids. Methanolic bark extracts of *S. laetum* and *S. palghatense* showed the exclusive presence of coumarins. Most bioactive compounds in the corresponding extract can be obtained at higher recoveries through polar solvents, indicating that in addition to common metabolite distribution patterns in leaves and bark, phytochemical profiles run parallel. Such a comprehensive study categorizes these *Syzygium* species as phenomenal sources of diverse secondary metabolites, especially in their polar extracts, which need to be explored systematically for possible pharmacological applications.

5.3.3. Quantitative phytochemical analysis

Quantification of the phytochemicals present in the methanol and distilled water extracts of *Syzygium* species were statistically analyzed using one-way ANOVA to determine significant differences among treatments, with six replicates per sample. Post hoc comparisons were conducted using the critical difference (CD) method to identify statistically distinct groups ($p < 0.05$). Additionally, Principal Component Analysis (PCA) was applied to reduce dimensionality and explore patterns among

Table 5.1: Percentage of yield of different extracts of *Syzygium laetum* leaves and bark

Solvents	Weight of plant materials (g)		Colour of extracts		Weight of dried extracts (g)		Extractive values (%)	
	Leaves	Bark	Leaves	Bark	Leaves	Bark	Leaves	Bark
Petroleum ether	30	30	Green	Brown	0.22	0.26	0.73	0.86
Chloroform	30	30	Pastel green	Sandy brown	0.12	0.16	0.40	0.53
Ethyl acetate	30	30	Mint green	Light brown	0.63	0.66	2.10	2.20
Methanol	30	30	Dark green	Mocha brown	12.50	13.62	41.66	45.40
Distilled water	30	30	Dark green	Brown	8.49	9.67	28.30	32.23

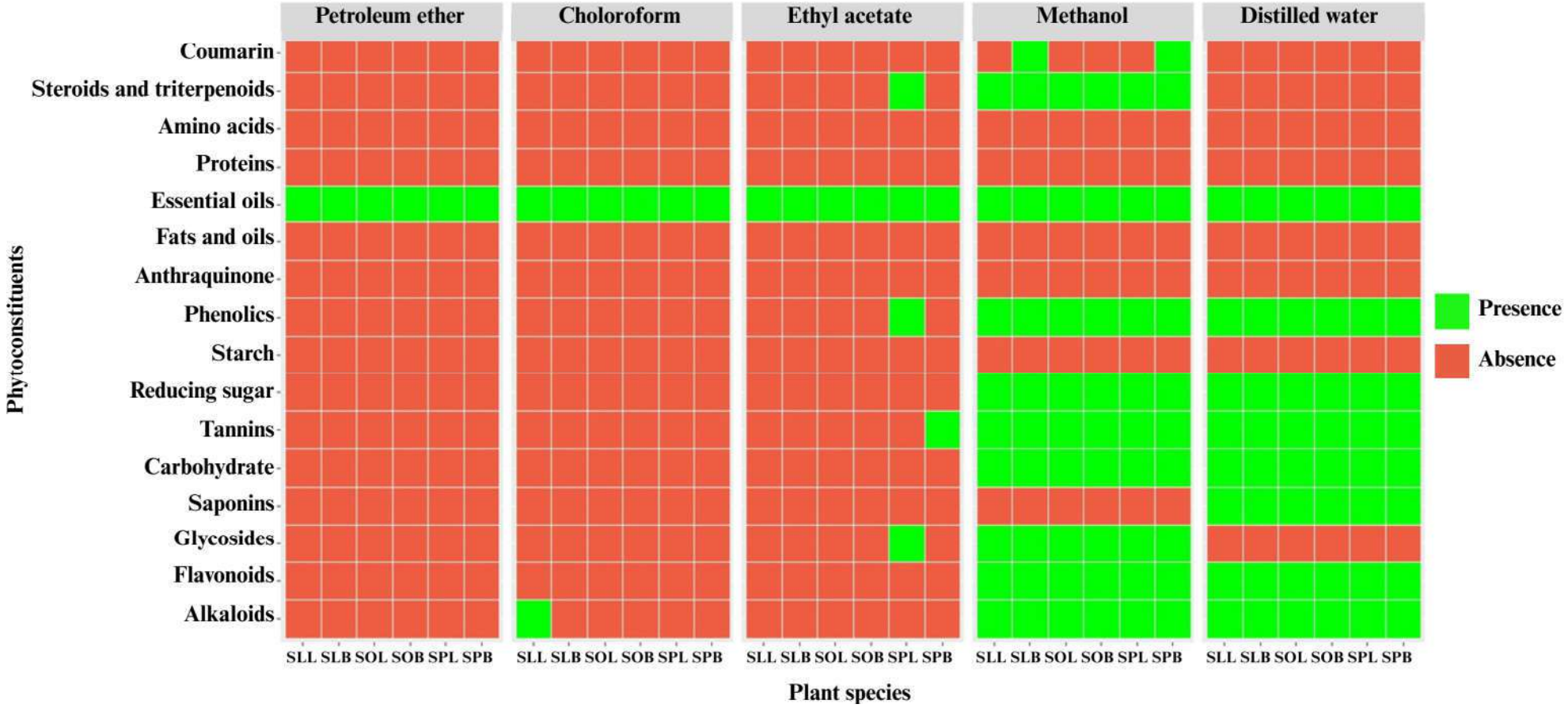
Table 5.2: Percentage of yield of different extracts of *Syzygium occidentale* leaves and bark

Solvents	Weight of plant materials (g)		Colour of extracts		Weight of dried extracts (g)		Extractive values (%)	
	Leaves	Bark	Leaves	Bark	Leaves	Bark	Leaves	Bark
Petroleum ether	30	30	Olive green	Brown	0.12	0.15	0.40	0.50
Chloroform	30	30	Pale green	Light brown	0.07	0.08	0.23	0.26
Ethyl acetate	30	30	Moss green	Light brown	0.16	0.19	0.53	0.63
Methanol	30	30	Dark green	Dark brown	11.77	11.82	39.23	39.40
Distilled water	30	30	Dark green	Syrup brown	8.02	8.13	26.73	27.10

Table 5.3: Percentage of yield of different extracts of *Syzygium palghatense* leaves and bark

Solvents	Weight of plant materials (g)		Colour of extracts		Weight of dried extracts (g)		Extractive values (%)	
	Leaves	Bark	Leaves	Bark	Leaves	Bark	Leaves	Bark
Petroleum ether	30	30	Light green	Brown	0.30	0.32	1	1.06
Chloroform	30	30	Mint green	Brown	0.26	0.28	0.86	0.93
Ethyl acetate	30	30	Light green	Coffee brown	0.65	0.69	2.16	2.30
Methanol	30	30	Greenish black	Greenish black	14.75	14.77	49.16	49.23
Distilled water	30	30	Blackish green	Blackish brown	9.26	10.31	30.86	34.36

Table 5.4: Heatmap of phytoconstituents in various solvent extracts of leaves and bark of *Syzygium laetum*, *Syzygium occidentale*, and *Syzygium palghatense* (SLL: *Syzygium laetum* leaves; SLB: *Syzygium laetum* bark; SOL: *Syzygium occidentale* leaves; SOB: *Syzygium occidentale* bark; SPL: *Syzygium palghatense* leaves; SPB: *Syzygium palghatense* bark)



phytochemical variables. PCs with eigenvalues greater than one were retained based on the Kaiser criterion, and factor loadings were examined to interpret variable contributions. PCA results were visualized through biplots to illustrate relationships and clustering within the data. All analyses were performed using R statistical software with a significance level set at 0.05 (Piepho, 2004).

One-way ANOVA and Post-Hoc Analysis Revealed Significant differences among the six treatments for all phytochemicals analyzed in both solvents ($p < 0.001$). One-way ANOVA results indicated strong treatment effects with F-values ranging from 181.12 to 2142.2 across different phytochemicals. Post hoc critical difference (CD) tests identified statistically distinct groups. The methanol extracts of glycosides varied significantly between treatments, ranging from 125.12 ± 1.02 to 183.97 ± 1.01 mg/g, with SPB exhibiting the highest concentration. Similarly, distilled water extracts showed glycoside concentrations ranging from 59.20 ± 0.12 to 86.25 ± 1.00 mg/g, with SPB again being the highest. Flavonoids, alkaloids, and phenolics followed similar trends, with SPB treatment consistently showing the highest values.

Tables 5.5 to 5.20 and Figures 5.1 to 5.8 depict the quantitative estimation of phytochemicals in *S. laetum*, S. *occidentale,* and *S. palghatense*

5.3.3.1. Estimation of alkaloid

Quantitative comparisons concerning total alkaloid content among the three species (*S. laetum*, *S. occidentale,* and *S. palghatense*) were made using atropine as the reference standard. The standard calibration curve showed a satisfactory linearity from 20 to 100 µg/ml (absorbance 0.018-0.086 at 470 nm) of the regression equation, $y = 0.0008x + 0.0019$ and $R^2 = 0.9989$. Regarding methanolic leaf extract, *S. palghatense* showed higher alkaloid content (197.66 ± 1.153 mg/g) than bark extract (147.63 ± 1.146 mg/g), unlike the other two species. Methanol extracts of *S. laetum* revealed the highest amount of alkaloids present in the bark (148.70 ± 1.142 mg/g), followed by leaf methanol extract (126.80 ± 1.130 mg/g) and the lowest alkaloid concentrations were observed in their distilled water extracts (bark: 77.80 ± 1.041 mg/g; leaf: 48 ± 1.035 mg/g); similar findings were obtained from *S. occidentale* (bark: 138.15 ± 1.133 mg/g; leaf: 117.56 ± 1.121 mg/g) with the lowest concentration

of alkaloids in its distilled water extracts (bark: 38.71 ± 1.022 mg/g; leaf: 47.50 ± 1.032 mg/g). The absorbance readings at 470 nm correlated well with the estimated alkaloid concentrations for all samples. Methanol extracts were consistently extracted more efficiently than distilled water extracts in all three species, indicating that methanol was a preferred solvent for alkaloid extraction. Alkaloid content showed a significant difference between species, plant part, and extraction solvent, suggesting that these factors should be considered as the first step in optimizing alkaloid extraction from *Syzygium* species.

5.3.3.2. Estimation of flavonoids

The total flavonoid content of three distinct *Syzygium* species was quantified using quercetin as a standard reference. Generally, the linear calibration curve ranged from 20-100 mg/ml, with absorbance values at 510 nm varying from 0.011 to 0.078, showing a high correlation. With respect to flavonoids, *S. palghatense* methanolic leaf extract had the highest value (167.77 ± 1.142 mg/g), followed by methanol bark extract (137.77 ± 1.135 mg/g) and aqueous leaf extract (133.33 ± 1.130 mg/g). The bark methanol extract also had the highest flavonoid content in *S. laetum* (144.57 ± 1.131 mg/g), followed by leaf methanol extract (122.13 ± 1.125 mg/g) and leaf aqueous extract (117.07 ± 1.120 mg/g) and the lowest concentration in bark aqueous extract (58.32 ± 1.054 mg/g). *S. occidentale* exhibited a similar pattern as the highest content was found in its leaf methanol extract (138.48 ± 1.129 mg/g), followed by leaf aqueous extract (120.15 ± 1.118 mg/g) and bark methanol extract (105.05 ± 1.110 mg/g), whereas bark aqueous extract showed the least concentration (47.22 ± 1.042 mg/g). All the samples tested revealed a positive relationship between the absorbance measurements obtained at 510 nm and the flavonoid content calculated. Across all three species, methanol extracts were consistently more effective than aqueous extracts, implying that methanol is the more effective solvent for the extraction of flavonoids. This detailed study concludes that the solvent and the part of the plant are deciding factors for flavonoid extraction from the various species of *Syzygium* and that *S. palghatense* is the richest flavonoid source compared to the other species.

5.3.3.3. Estimation of total glycosides

The quantitative analysis regarding the total glycoside content of three *Syzygium* species showed that the standard curve established by digitoxin had a good linearity of concentration of 2-14 mg/ml, absorbance value 0.002 to 0.041 at 495 nm. The highest glycoside content was shown by methanolic leaf extract of *S. palghatense* (183.97 ± 1.015 mg/g digitoxin equivalents), which was followed by that of bark methanol extract (135.97 ± 1.012 mg/g) leaves and bark distilled water extracts were at lower concentrations (86.25 ± 1.005 mg/g and 72.25 ± 0.121 mg/g distilled water extracts from leaves and bark respectively). For *S. laetum*, glycoside content was the highest in the bark methanol extract (170.11 ± 1.123 mg/g), followed by the leaf methanol extract (140.11 ± 1.101 mg/g). In contrast, distilled water extracts had significantly lower concentrations in the leaf (60.20 ± 0.125 mg/g) and bark (59.20 ± 0.120 mg/g). Among the studied plants, *S. occidentale* showed moderate glycoside content, with 135.97 ± 1.135 mg/g from leaf methanol extract, 125.12 ± 1.023 mg/g in bark methanol extract, and lower concentration in distilled water leaf (73.22 ± 0.133 mg/g) and bark (62.20 ± 0.120 mg/g) extracts. All samples had a robust relationship between the measured absorbance at 495 nm and the calculated glycoside concentrations. Methanol extracts showed higher extraction efficiency over all three species than the distilled water extracts, indicating methanol as a preferable solvent for glycoside extraction. Moreover, this study thoroughly explains the impact of solvent choice and plant part on glycoside extraction from the three *Syzygium* species examined, with *S. palghatense* being the richest source of glycosides of the three species investigated.

5.3.3.4. Estimation of total saponin

Diosgenin was dissolved in methanol to obtain 20-100 mg/ml concentrations, and the absorbances (0.023 to 0.308) were noted at 544 nm. In this regard, the maximum amount of saponin was obtained to be 150.22 ± 1.210 mg/g of the sample in the leaf extract of *S. palghatense*, which was closely followed by 140.31 ± 1.136 mg/g in the leaf extract of *S. laetum*, and then followed by 135.85 ± 1.128 mg/g in the leaf extract of *S. occidentale*. In all of the three plant species, the leaf extracts have

shown greater concentrations of saponins as compared to the bark extracts, namely, 42.23 ± 0.018 mg/g, 38.59 ± 0.025 mg/g, and 26.32 ± 0.017 mg/g were observed in the extracts of bark of *S. laetum*, *S. palghatense*, and *S. occidentale*, respectively. Thus, the leaves of the *Syzygium* species are superior due to their extract having higher saponin content than their bark; thus, the *S. palghatense* leaf is the best source of saponin among the three species.

5.3.3.5. Estimation of total carbohydrate

The study was carried out based on a glucose standard calibration curve with 20 to 100 mg/mL concentrations by measuring absorbance values (0.151 to 0.883) at 630 nm. This enables quantifying the carbohydrate content of each species' leaf and bark powder samples. Results showed similar patterns for all three species, where leaf powders contained higher carbohydrate levels than bark powders. The *S. palghatense* recorded the highest carbohydrate content in leaf (130 ± 1.102 mg/g) and bark (81.25 ± 0.220 mg/g) samples compared to *S. laetum* and *S. occidentale*. The result showed the carbohydrate content of *S. laetum* leaf powder was 124 ± 1.011 mg/g, while its bark powder showed 70.14 ± 0.121 mg/g; *S. occidentale* leaf powder had the lowest carbohydrate content of 110 ± 1.003 mg/g, and its bark powder had 60.11 ± 0.110 mg/g. The absorbance readings at a wavelength of 630 nm showed a positive correlation with carbohydrate concentrations, in line with the standard calibration curve. Good precision was observed in the measurements, as the standard deviation values for both absorbance and concentration were small. The results of this study provide important prospective information regarding the content of carbohydrates in *Syzygium* species and plant parts, which may be a cornerstone for studies from botany, pharmacology, or nutrition.

5.3.3.6. Estimation of total tannin

The total tannin content of three *Syzygium* species, *S. laetum*, *S. occidentale*, and *S. palghatense*, have been studied. The results shown in this study start with a classic calibration curve with the help of gallic acid (GA) as a reference standard with various concentrations between 20 and 100 mg/ml and their corresponding absorbance values (0.186 to 0.843) at 725 nm. This calibration enables the assessment

of tannin content in plant extracts. Methanol and distilled water extracts were prepared from leaf and bark samples for each *Syzygium* species. *S. palghatense* (leaves- 233.62 ± 1.108 mg/g; bark- 220.56 ± 1.106 mg/g) had the highest tannin value across all extracts. *S. laetum* was next in order at 133.62 ± 1.105 mg/g leaf and 165.32 ± 1.108 mg/g bark methanol extracts. Compared to *S. occidentale*, it showed the lowest tannin conte nt among the three species, yielding 98.05 ± 0.105 mg/g for leaf and 65.30 ± 0.021 mg/g for bark via methanol extract. Methanol extracts exhibited consistently higher tannin concentrations across all species than distilled water extracts. This indicates that methanol extracts tannins from these plant materials more effectively. Except for *S. laetum* methanol extract, which had a marginally higher tannin content in the bark than leaf extracts, leaf extracts displayed higher tannin content than bark extracts. The absorbance values measured at 725 nm positively correlated with the tannin concentrations provided in the standard calibration curve. Absorbance and concentration values showed relatively low standard deviations, indicating good measurement precision. The comprehensive characterization of the tannin profiles of *Syzygium* species will be beneficial for uses in several industries such as pharmacology, natural product chemistry, and plant biology, with striking variations in tannin levels found not only across *Syzygium* species, but also within various sections of the plant and through different extraction techniques.

5.3.3.7. Estimation of total reducing sugar

The data presented here represent the total reduced sugar content of three *Syzygium* species: *S. laetum*, *S. occidentale*, and *S. palghatense*. The standard calibration curve was performed, where glucose was utilized as a standard for reference with concentrations from 50 to 250 mg/ml and absorbance values at 510 nm (0.023 to 0.449). With this calibration, the quantity of reducing sugar present in different plant extracts can be quantified. Leaf and bark powders of each *Syzygium* species were assessed. The highest reducing sugar content was observed in the leaf powder of *S. palghatense* (4.77 ± 0.015 mg/g), followed by *S. laetum* (2.66 ± 0.011 mg/g) and *S. occidentale* (2.22 ± 0.016 mg/g). *S. laetum* recorded maximum content in bark powder (4.75 ± 0.014 mg/g) when compared to *S. palghatense* (2.80 ± 0.012

mg/g) and *S. occidentale* (1.81 ± 0.014 mg/g). The species showed variable redistribution of the reducing sugar between leaf and bark powders. The average concentration of reducing sugars in bark powder fractions of *S. laetum* was significantly higher than that observed in leaf powder fractions. The reverse was observed for *S. palghatense* and *S. occidentale*, where leaf powders possessed comparatively higher concentrations than bark powders. The absorbance values obtained from the readings at 510 nm increased positively with the reducing sugar concentrations and followed the standard calibrating curve. Results obtained for each measurement had good precision, as indicated by the relatively small standard deviation for both assessable absorbance and concentration values. These results on the reducing sugar profiles of *Syzygium* species are vital for researchers in various fields like food science, plant physiology, and biochemistry. The differences in sugar content between different *Syzygium* species and separate parts of the same plant species reflect complexity of the carbohydrate distribution profile of these plants and provide significant insights for further plant-nutritional and metabolic studies.

5.3.3.8. Estimation of total phenol

The experiment starts with a standard calibration curve with gallic acid as the reference standard, with a concentration of 20 to 100 mg/ml and corresponding absorbance values of 550 nm (0.29 to 0.905). The phenol content of different plant extracts can be quantified using this calibration. A total of two extracts, methanol and distilled water, were used to analyse leaf and bark samples from each *Syzygium* species. Among all extracts, *S. palghatense* showed the highest phenol content with methanol extracts in particular showing high concentrations (leaf: 102.78 ± 1.015 mg/g; bark: 100.74 ± 1.014 mg/g). *S. laetum*: The methanol leaf and bark extracts possess 72.16 ± 0.018 mg/and 80.35 ± 0.027 mg/g, respectively. Methanol extracts of S. occidentale had 60.18 ± 0.012 mg/g (leaf) and 44.56 ± 0.007 mg/g (for bark), the lowest among the three species. Methanol extracts consistently showed a higher phenol concentration than distilled water extracts across species, indicating that methanol is a more effective solvent for phenol extraction from these plant materials. The bark methanol extract of *S. laetum* and *S. palghatense* contained slightly higher

Table 5.5: Standard calibration data for total alkaloid content determination

Reference Standard: Atropine (1 mg/ml stock solution)

Concentrations of Atropine (mg/ml)	Absorbance (OD 470 nm)
20 ± 0.022	0.018 ± 0.006
40 ± 0.030	0.036 ± 0.010
60 ± 0.036	0.054 ± 0.013
80 ± 0.040	0.069 ± 0.016
100 ± 0.047	0.086 ± 0.018

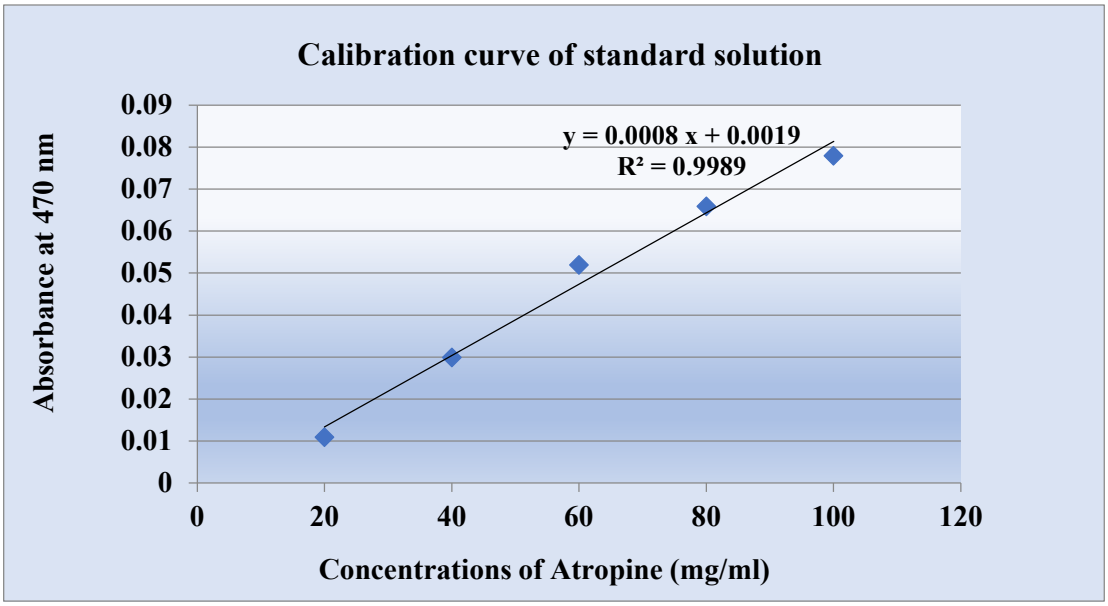


Figure 5.1: Standard calibration curve for total alkaloid content using atropine as reference standard

Table 5.6: Quantitative estimation of total alkaloid content (mg/g) in different extracts of *Syzygium laetum*, *Syzygium occidentale*, and *Syzygium palghatense*

Plant species	Alkaloids in distilled water	Alkaloids in methanol
SLL	48.23 ± 1.035b	126.80 ± 1.130^{d}
SLB	49.80 ± 1.041b	144.70 ± 1.142^{b}
SOL	37.50 ± 1.032c	117.56 ± 1.121^{e}
SOB	38.71 ± 1.022c	138.15 ± 1.133^{c}
SPL	90.70 ± 1.048a	147.63 ± 1.146^{b}
SPB	92.61 ± 1.038a	197.66 ± 1.153^{a}
F Value	1186.8	241.72
p value	<0.001	<0.001
CD Value	2.18	5.34

(SL: *Syzygium laetum*; SO: *Syzygium occidentale*; SP: *Syzygium palghatense*; L Leaves; B: Bark)

Table 5.7: Standard calibration data for total flavonoid content (mg/g) determination Reference Standard: Quercetin (1 mg/ml stock solution)

Concentrations of Quercetin (mg/ml)	Absorbance (OD 510 nm)
20 ± 0.014	0.011 ± 0.002
40 ± 0.018	0.030 ± 0.011
60 ± 0.025	0.052 ± 0.012
80 ± 0.028	0.066 ± 0.014
100 ± 0.030	0.078 ± 0.016

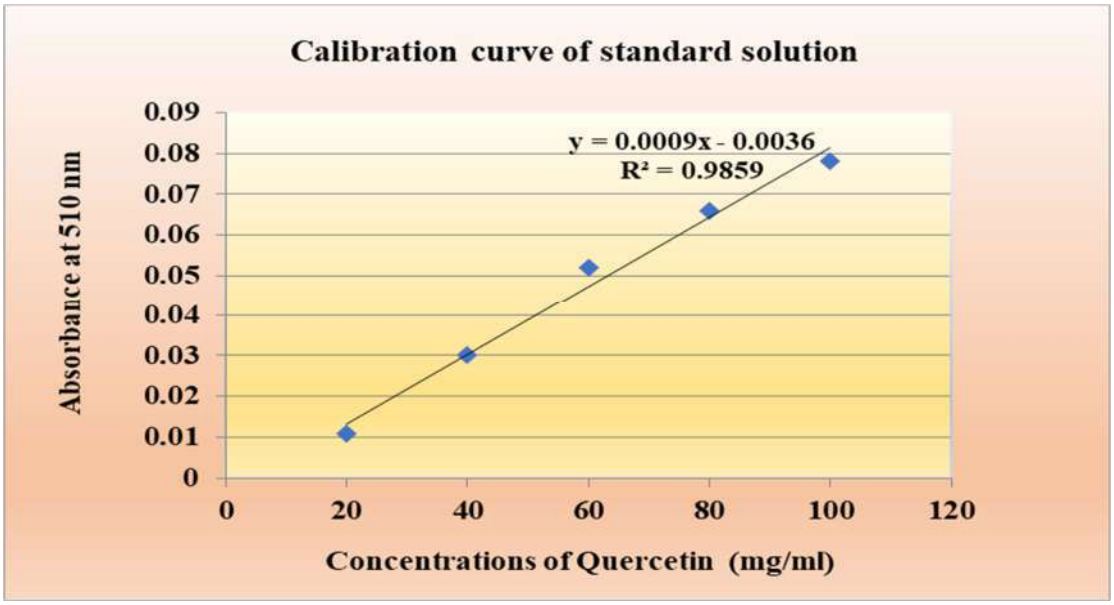


Figure 5.2: Standard calibration curve for total flavonoid content using quercetin as reference standard

Table 5.8: Quantitative estimation of total flavonoid content (mg/g) in different extracts of *Syzygium laetum, Syzygium occidentale,* and *Syzygium palghatense*

Plant species	Flavonoids in distilled water	Flavonoids in methanol
SLL	58.32 ± 1.054e	122.13± 1.125^{d}
SLB	117.07 ± 1.120c	144.57± 1.131^{b}
SOL	47.22 ± 1.042f	105.05 ± 1.110^{e}
SOB	120.15 ± 1.118b	138.48 ± 1.129^{c}
SPL	62.22 ± 1.065d	137.77 ± 1.135^{c}
SPB	133.33 ± 1.130a	167.77± 1.142^{a}
F Value	1885.4	208.37
p value	<0.001	<0.001
CD Value	2.58	4.36

(SL: *Syzygium laetum*; SO: *Syzygium occidentale*; SP: *Syzygium palghatense*; L Leaves; B: Bark)

Table 5.9: Standard calibration data for total glycoside content determination Reference Standard: Digitoxin (0.02 %, 1 mg/ml stock solution)

Concentrations of Digitoxin (mg/ml)	Absorbance (OD 495 nm)
2 ± 0.010	0.002 ± 0.001
4 ± 0.018	0.005 ± 0.001
6 ± 0.021	0.014 ± 0.002
8 ± 0.028	0.020 ± 0.002
10 ± 0.034	0.027 ± 0.003
12 ± 0.038	0.037 ± 0.004
14 ± 0.042	0.041 ± 0.004

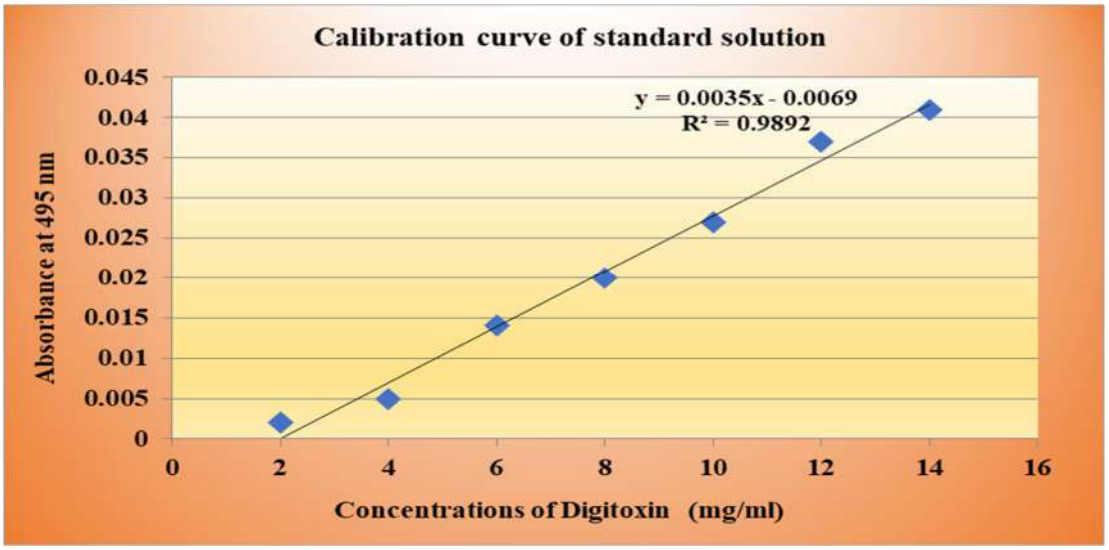


Figure 5.3: Standard calibration curve for total glycoside content using digitoxin as reference standard

Table 5.10: Quantitative estimation of total glycoside content (mg/g) in different extracts of *Syzygium laetum, Syzygium occidentale,* and *Syzygium palghatense*

Plant species	Glycoside in distilled water	Glycosides in methanol
SLL	59.20 ± 0.120d	140.11 ± 1.101^{c}
SLB	60.20 ± 0.125cd	170.11 ± 1.123^{b}
SOL	62.20 ± 0.120c	125.12 ± 1.023^{d}
SOB	73.22 ± 0.133b	135.97 ± 1.135^{c}
SPL	72.25 ± 0.121b	135.97 ± 1.012^{c}
SPB	86.25 ± 1.005a	183.97 ± 1.015^{a}
F Value	219.31	181.12
p value	<0.001	<0.001
CD Value	2.10	5.09

(SL: *Syzygium laetum*; SO: *Syzygium occidentale*; SP: *Syzygium palghatense*; L Leaves; B: Bark)

Table 5.11: Standard calibration data for total saponin content determination Reference Standard: Diosgenin (1 mg/ml stock)

Concentrations of Diosgenin (mg/ml)	Absorbance (OD 544 nm)
20 ± 0.014	0.023 ± 0.002
40 ± 0.016	0.145 ± 0.024
60 ± 0.018	0.170 ± 0.036
80 ± 0.102	0.256 ± 0.101
100 ± 0.104	0.308 ± 0.103

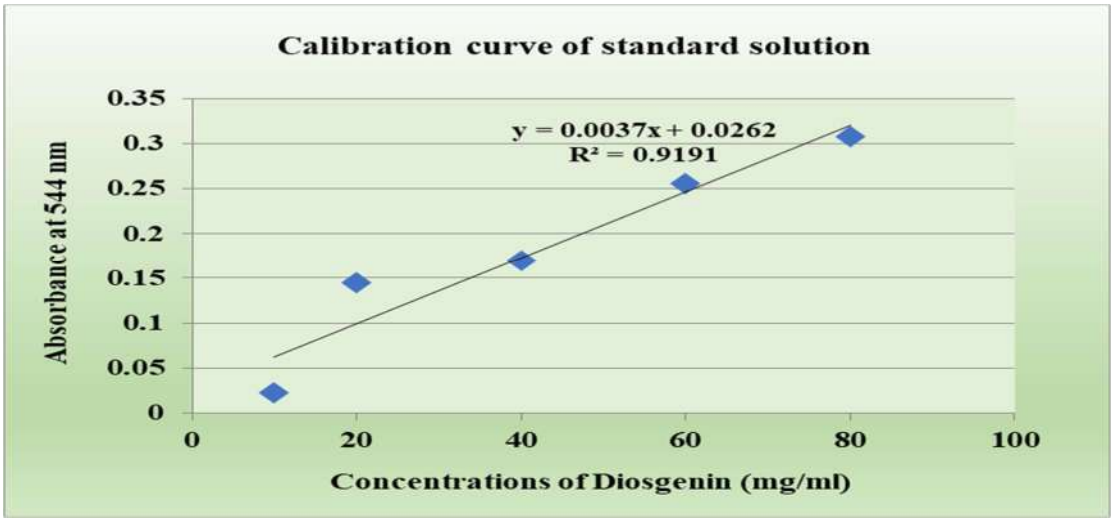


Figure 5.4: Standard calibration curve for total saponin content using diosgenin as reference standard

Table 5.12: Quantitative estimation of total saponin content (mg/g) in distilled water extracts of *Syzygium laetum, Syzygium occidentale,* and *Syzygium palghatense*

Plant species	Saponin
SLL	140.31 ± 1.136[b]
SLB	42.23 ± 0.018[e]
SOL	135.85 ± 1.128[c]
SOB	26.32 ± 0.017[f]
SPL	150.22± 1.210[a]
SPB	48.59± 0.025[d]
F Value	1574.7
p value	<0.001
CD Value	4.28

(SL: *Syzygium laetum*; SO: *Syzygium occidentale*; SP: *Syzygium palghatense*; L Leaves; B: Bark)

Table 5.13: Standard calibration data for total carbohydrate content determination Reference Standard: Glucose (1 mg/ml stock)

Concentrations of Glucose (mg/ml)	Absorbance (OD 630 nm)
20 ± 0.021	0.151 ± 0.020
40 ± 0.026	0.345 ± 0.024
60 ± 0.028	0.50 ± 0.027
80 ± 0.032	0.694 ± 0.028
100 ± 0.068	0.883 ± 0.031

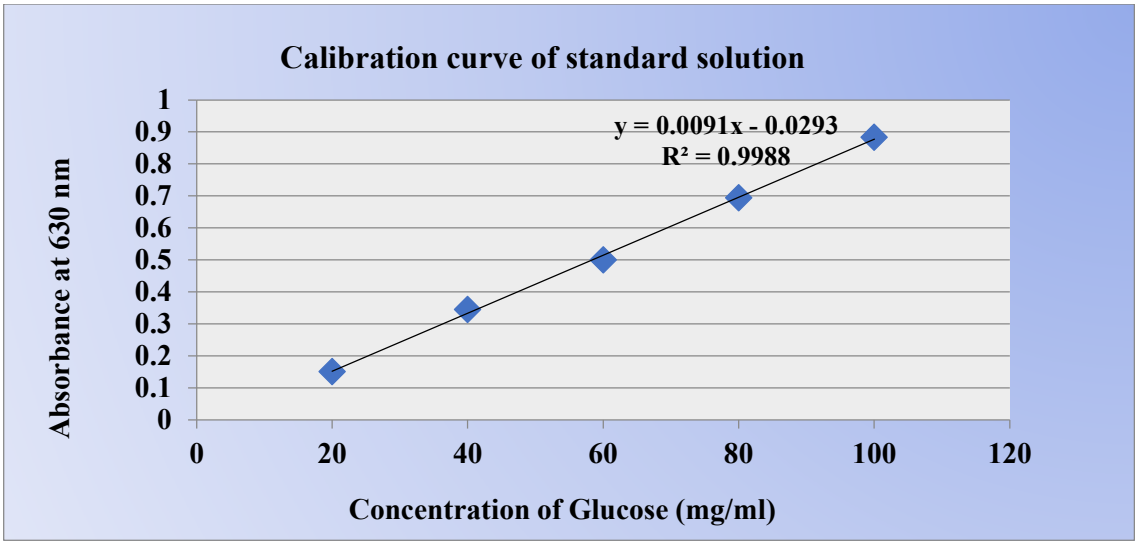


Figure 5.5: Standard calibration curve for total carbohydrate using glucose as reference standard

Table 5.14: Quantitative estimation of total carbohydrate (mg/g) in leaf and bark powders of *Syzygium laetum*, *Syzygium occidentale*, and *Syzygium palghatense*

Plant species	Carbohydrate
SLL	70.14 ± 0.121^{e}
SLB	124.00 ± 1.011^{b}
SOL	60.11 ± 0.110^{f}
SOB	110.00 ± 1.003^{c}
SPL	81.25 ± 0.220^{d}
SPB	130.00 ± 1.102^{a}
F Value	561.48
p value	<0.001
CD Value	3.68

(SL: *Syzygium laetum*; SO: *Syzygium occidentale*; SP: *Syzygium palghatense*; L Leaves; B: Bark)

Table 5.15: Standard calibration data for total tannin content determination Reference Standard: Gallic acid (1 mg/ml stock)

Concentrations of Gallic acid (mg/ml)	Absorbance (OD 725 nm)
20 ± 0.011	0.186 ± 0.002
40 ±0.020	0.283 ± 0.004
60 ± 0.028	0.494 ± 0.012
80 ±0.045	0.661 ± 0.025
100 ± 0.071	0.843 ± 0.029

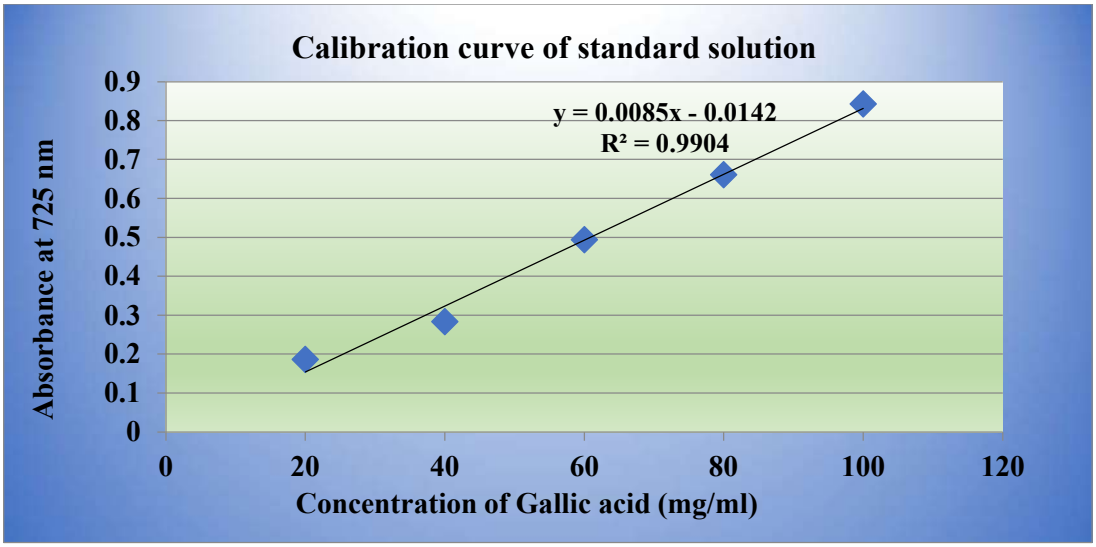


Figure 5.6: Standard calibration curve for total tannin content using gallic acid as reference standard

Table 5.16: Quantitative estimation of total tannin content (mg/g) in different extracts of *Syzygium laetum*, *Syzygium occidentale*, and *Syzygium palghatense*

Plant species	Tannin in distilled water	Tannin in methanol
SLL	50.68 ± 0.008d	133.62 ± 1.105^{d}
SLB	73.86 ± 0.036c	165.32 ± 1.108^{c}
SOL	48.61 ± 0.007d	65.30 ± 0.021^{f}
SOB	73.86 ± 0.036c	98.05 ± 0.105^{e}
SPL	120.68 ± 1.008b	220.56 ± 1.106^{b}
SPB	173.86 ± 1.101a	233.62 ± 1.108^{a}
F Value	2142.2	886.99
p value	<0.001	<0.001
CD Value	3.11	6.66

(SL: *Syzygium laetum*; SO: *Syzygium occidentale*; SP: *Syzygium palghatense*; L Leaves; B: Bark)

Table 5.17: Standard calibration data for total reducing sugar content determination Reference Standard: Glucose (1 mg/ml stock)

Concentrations of Glucose (mg/ml)	Absorbance (OD 510 nm)
50 ± 0.012	0.023 ± 0.003
100 ± 0.105	0.157 ± 0.004
150 ± 0.112	0.287 ± 0.006
200 ± 0.116	0.388 ± 0.015
250 ± 0.118	0.449 ± 0.017

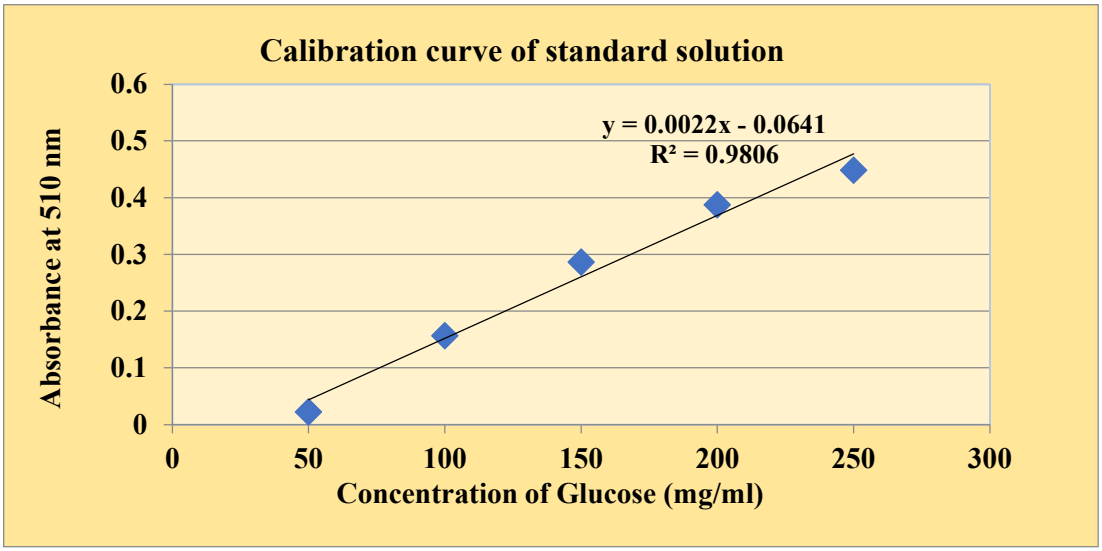


Figure 5.7: Standard calibration curve for total reducing sugar using glucose as the reference standard

Table 5.18: Quantitative estimation of total reducing sugar (mg/g) in leaf and bark powders of *Syzygium laetum*, *Syzygium occidentale*, and *Syzygium palghatense*

Plant species	Reducing sugar
SLL	2.66 ± 0.011^{c}
SLB	4.75± 0.014^{a}
SOL	1.81 ± 0.014^{e}
SOB	2.22 ± 0.016^{d}
SPL	2.80 ± 0.012^{b}
SPB	4.77 ± 0.015^{a}
F Value	1529.7
p value	<0.001
CD Value	0.097

(SL: *Syzygium laetum*; SO: *Syzygium occidentale*; SP: *Syzygium palghatense*; L Leaves; B: Bark)

Table 5.19: Standard calibration data for total phenol content determination Reference Standard: Gallic acid (1 mg/ml stock)

Concentrations of Gallic acid (mg/ml)	Absorbance (OD 550 nm)
20 ± 0.023	0.229 ± 0.015
40 ± 0.25	0.656 ± 0.018
60 ± 0.28	0.791 ± 0.020
80 ± 0.31	0.832 ± 0.023
100 ± 0.37	0.905 ± 0.027

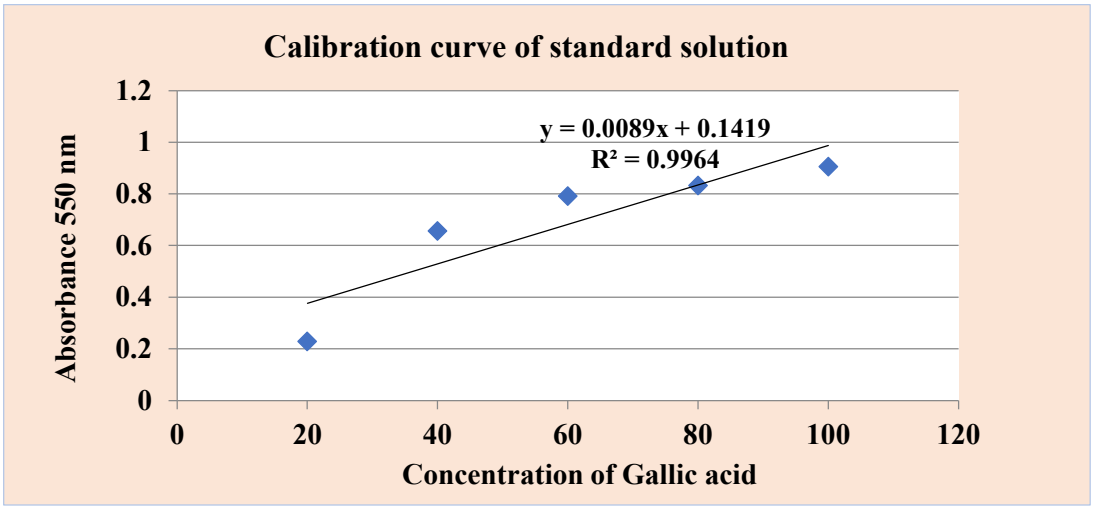


Figure 5.8: Standard calibration curve for total phenol content using gallic acid as reference standard

Table 5.20: Quantitative estimation of total phenol content (mg/g) in different extracts of *Syzygium laetum*, *Syzygium occidentale*, and *Syzygium palghatense*

Plant species	Phenol in distilled water	Phenol in methanol
SLL	58.66 ± 0.012c	59.16± 0.018^{c}
SLB	60.12± 0.014c	80.35± 0.027^{b}
SOL	40.12 ± 0.005e	44.56 ± 0.007^{d}
SOB	55.14± 0.010d	60.18± 0.012^{c}
SPL	76.29 ± 0.132b	100.74 ± 1.014^{a}
SPB	83.66 ± 0.140a	102.78 ± 1.015^{a}
F Value	523.33	1142.6
p value	<0.001	<0.001
CD Value	2.02	2.10

(SL: *Syzygium laetum*; SO: *Syzygium occidentale*; SP: *Syzygium palghatense*; L Leaves; B: Bark)

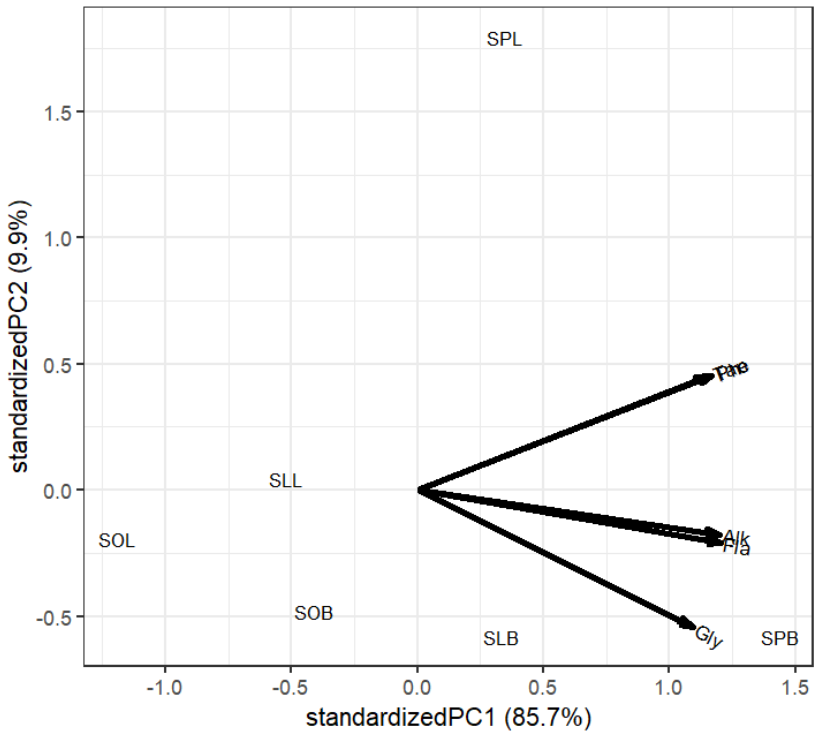


Figure 5.9: Principal Component Analysis (PCA) biplot showing variable contributions for methanol samples

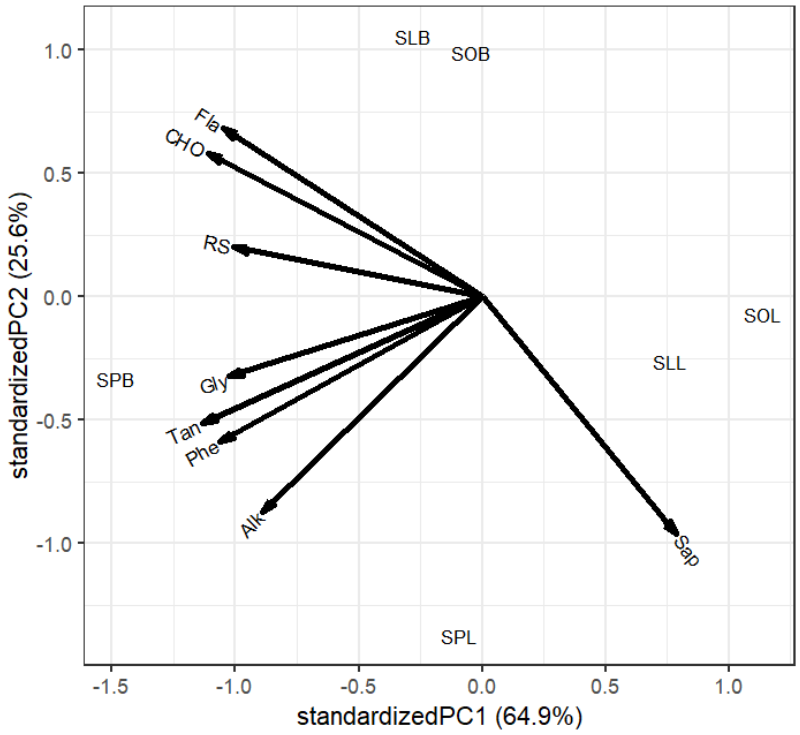


Figure 5.10: Principal Component Analysis (PCA) biplot showing variable contributions for distilled water samples

Table 5.21: Eigenvalues of principal components for methanol

Principal component	Eigenvalue
PC1	2.0701
PC2	0.7024
PC3	0.3745
PC4	0.2626
PC5	0.1098

Based on the eigenvalue criterion (>1), only the first component (PC1) is significant.

Table 5.22: Variability explanation by principal components for methanol

Principal component	Standard deviation	Proportion of variance	Cumulative proportion
PC1	2.0701	0.8571	0.8571
PC2	0.7024	0.0987	0.9557
PC3	0.3745	0.0281	0.9838
PC4	0.2626	0.0138	0.9976
PC5	0.1098	0.0024	1.0000

phenol content than leaf methanol extract, whereas this was reversed in *S. occidentale*. The absorbance values at 550 nm were positively correlated with the phenol concentrations and were consistent with the standardized calibration curve. Absorbance and concentration value standard deviations were fairly small, indicating good precision between measurements. This is the first complete phenol profiling of *Syzygium* species showcasing appreciable differences in phenol content between different species in addition to the rate of extraction in each species and plant part, enabling potential application in natural products chemistry, pharmacology, and plant biology.

The Principal Component Analysis (PCA) results for methanol show that the first principal component (PC1) explains the vast majority (85.7%) of the total variance in the data. This means that most of the underlying structure of the data can be captured by a single dimension, simplifying further analysis and interpretation. The remaining components (PC2 to PC5) each explain very small portions of variance and can generally be disregarded according to the eigenvalue >1 criterion, which considers only PC1 significant.

The standard deviation associated with PC1 is highest, reaffirming its dominant contribution to the data variability. The cumulative proportion indicates that PC1 alone captures over 85% of the variability, suggesting strong data cohesion along this axis. Overall, this analysis implies that, for the methanol dataset, the majority of chemical variation is summarized by one main factor, which can simplify interpretation, modeling, or classification tasks involving this data.

Methanol Extracts PCA exhibited a single principal component (PC1) with an eigenvalue of 2.07 was retained, explaining 85.7% of the total variance. Factor loadings indicated strong positive contributions from glycosides (0.42), flavonoids (0.46), alkaloids (0.46), phenolics (0.44), and tannins (0.45), suggesting these phytochemicals co-vary in methanol extracts. The biplot (Figure 5.9-5.10) visually represents these relationships. In the Distilled Water Extracts, two principal components (PC1 and PC2) were retained, with eigenvalues of 2.28 and 1.43, accounting for a cumulative 90.41% of the variance. PC1 showed negative loadings

for glycosides, flavonoids, alkaloids, phenolics, tannins, carbohydrates, and reducing sugars, while saponins were positively loaded. PC2 differentiated carbohydrates and saponins distinctly. Together, these PCA biplots provide clear visualizations of the major chemical factors driving variation among samples in methanol and distilled water solvents. They aid in simplifying complex multivariate data into interpretable patterns based on component contributions and variable relationships, supporting more informed chemical analysis and differentiation of sample groups (Tables 5.21-5.22).

5.3.4. Gas Chromatography-Mass Spectrometry (GC-MS) analysis

GC-MS chromatogram and details of the compounds of *S. laetum*, *S. occidentale* and *S. palghatense* leaves and bark were displayed in Tables 5.23-5.28 and Figures 5.11-5.22

GC-MS Screening of bioactive compounds in the leaves and bark methanol extracts of *S. laetum* showed a variety of compounds with medicinal properties. The leaf extract had four major compounds: neophytadiene (0.68%), 2,2-dimethyl-3-vinyl-bicyclo (2.2.1), heptane (13.02%), methyl 2-hydroxy-octadeca-9,12,15-trienoate (76.56 %) and lupeol (9.74 %). These compounds display several biological activities, such as anti-inflammatory, antimicrobial, antioxidant, and anticancer properties (Babu & Jayaraman, 2020; Wal et al., 2011).

The bark extract had a more complex profile with thirteen identified compounds. Some of these were as follows: 2-carboxymethyl-3-n-hexyl-maleic anhydride (16.22 %), methyl palmitate (16.81 %), linoleic acid methyl ester (11.74 %), 9-octadecenoic acid (z)-, methyl ester (11.86 %), β-sitosterol (10.46 %), and lupeol (8.66%). The minor compounds also showed multiple bioactivities, including methoxy eugenol, phthalic acid butyl undecyl ester, methyl stearate, octa decanal, glycerol β-palmitate, cholesta-4,6-dien-3-ol benzoate, vitamin E, etc., which exhibit various biological conditions, examples being antimicrobial, antioxidant, anticancer, anti-inflammatory, and cardioprotective conditions. Some also contribute to metabolic regulation, immune modulation, and cellular signaling pathways (Brigelius-Flohé, 2021; Nakaziba et al., 2022).

A wider range of bioactive constituents in the leaves and bark indicates the possibility of *S. laetum* containing various medicinal properties. Nonetheless, further research would be required to explain these extracts' therapeutic potential and safety completely.

There are several peaks in the chromatogram with different heights. A single, prominent peak of extremely high intensity, probably corresponding to methyl 2-hydroxy-octadeca-9,12,15-trienoate, was detected. The peak falls somewhere around 41 minutes. Several smaller peaks along the chromatogram indicate other constituents present in lower amounts. The bark extract chromatogram shows a more complex profile with several peaks throughout the retention time. There appear to be some important peaks of moderate intensity in the 28-32-minute range. The difference in phytochemical profiles of *S. laetum* leaves and bark is illustrated in these chromatograms, aligning with the intensive compound identification results obtained in GC-MS analyses. The leaf extract had one predominant compound, whereas the bark extract had a more balanced compound distribution.

Based on the GC-MS analysis of methanol extracts of *S. occidentale* leaves and bark, this study demonstrated a wide variety of bioactive compounds with considerable pharmacological potential. In leaf extract, a total of five compounds were identified; among them, two with the highest concentration were 3-Pentadecylphenol (42.72 %) and Cyclogallipharaol (46.67 %). These amphiphilic phenolic lipids show strong antioxidant, antimicrobial, and potential anti-obesity activity. Other significant components of the leaf extract were Neophytadiene and phytol acetate, which are diterpenes with different biological activities such as anti-inflammatory, antioxidant, and antimicrobial activity.

The bark extract presented a more complex profile with ten compounds identified, with fatty acid methyl esters as the highest number. Methyl Palmitate (32.16 %), Methyl octadec-10-enoate (26.45 %), and Linoleic acid methyl ester (16.81 %) were the major constituents. Fatty acid methyl esters (FAMEs) are known for their anti-inflammatory, antioxidant, and potential anticancer activities. In addition to Methyl Palmitate, Methyl Myristate, Methyl Stearate, Methyl Arachate, and Methyl

Behenate were present in minor amounts in the bark extract, each characterized by a varying pharmacological profile adding to the overall biological activity of the extract alongside anti-inflammatory, antimicrobial, cardiovascular actions, etc.

It was found in leaf and bark extracts, reinforcing its significance in plants' holistic biological activity. These bioactive compounds substantiate the traditional medicinal applications of *S. occidentale*. Also, it highlights its potential use for developing new therapeutic agents for different types of health issues, such as inflammatory diseases, microbial infections, and metabolic disorders. Nevertheless, more studies, such as *in vivo* and clinical studies, would still be needed to understand these compounds' synergistic impacts comprehensively and validate their therapeutic potential and safety for different health applications.

The leaf extract' chromatogram displays two major rises in the later retention time suggestive of 3-pentadecylphenol and cyclogallipharaol. There are several smaller peaks throughout this, indicating less prominent compounds. In comparison, the chromatogram for the bark extract illustrates a more complex profile for the retention time, as multiple peaks are noted at these times. The chromatogram of bark has several notable peaks of medium intensity, particularly in the mid ranges, most likely due to the presence of various fatty acid methyl esters and other compounds. The unique phytochemical content of *S. occidentale* leaves and bark is illustrated through the chromatogram, where the extract of leaves presents two dominant parts, and the bark extract has a more diversified and balanced percentage of various parts.

The methanol extract of *S. palghatense* leaves exhibited a rich phytochemical profile dominated by sesquiterpenes, hydrocarbons, terpenoids, and fatty acid methyl esters. Key bioactive compounds such as (-)-spathulenol and neophytadiene showed anti-inflammatory and antioxidant properties. Terpenoids like 3,7,11,15-tetramethyl-2-hexadecen-1-ol demonstrated antimicrobial effects. Fatty acid methyl esters, including methyl palmitate, linoleic acid methyl ester, and 9-octadecenoic acid methyl ester contributed to anti-inflammatory and antioxidant activities. The presence of phytol, methyl stearate, squalene, and γ-tocopherol further enhances the extract's

Table 5.23: GC-MS profile of methanol extract of *Syzygium laetum* leaves

Compound name	Type	Molecular formula	Retention time	Peak area (%)	Molecular weight (g/mol)	Biological activities	References
Neophytadiene	Diterpene	$C_{20}H_{38}$	26.620	0.68	278.524	Anti-inflammatory, antimicrobial, antioxidant, cytotoxic, neuropharmacological effects	Koeduka et al., 2014
2,2-Dimethyl-3-vinyl-bicyclo [2.2.1] heptane	Bicyclic hydrocarbon	$C_{11}H_{18}$	41.121	13.02	150.26	Antimicrobial, antioxidant potential, potential genotoxicity, anticancer activity	Pinto et al., 2017
Methyl 2-hydroxy-octadeca-9,12,15-trienoate	Fatty acid methyl ester	$C_{19}H_{32}O_3$	41.297	76.56	308.5	Antioxidant activity, anti-inflammatory effects, play a role in lipid metabolism and cellular signaling pathways, role in enzyme inhibition and induction	Babu & Jayaraman (2020)
Lupeol	Pentacyclic triterpenoid	$C_{30}H_{50}O$	42.955	9.74	426.7	Anti-inflammatory effects, antioxidant properties, anticancer potential, antimicrobial activity, cardioprotective effects, hepatoprotective properties	Wal et al., 2011

Table 5.24: GC-MS profile of methanol extract of *Syzygium laetum* bark

Compound name	Type	Molecular formula	Retention time	Peak area (%)	Molecular weight (g/mol)	Biological activities	References
Methyl palmitate	Fatty acid methyl ester	$C_{17}H_{34}O_2$	28.395	16.81	270.5	Anti-inflammatory effects, antifibrotic properties, antioxidant activity, and modulates immune responses.	Saeed et al., 2012
2-Carboxymethyl-3-n-hexyl-maleic anhydride	Cyclic dicarboxylic anhydride	$C_{12}H_{16}O_5$	18.832	16.22	240.25	Metabolite found in *Aspergillus niger* and *Arthrinium* species; role in crop growth promotion.	Geiger et al., 2014
9-octadecenoic acid (z)-, Methyl ester	Fatty acid methyl ester	$C_{19}H_{36}O_2$	31.720	11.86	296.4879	Anti-inflammatory, antioxidant, antimicrobial, cancer preventive, and help in lowering blood cholesterol levels.	Krishnamoorthy & Subramaniam (2014)
Linoleic acid, Methyl ester	Fatty acid methyl ester	$C_{19}H_{34}O_2$	31.620	11.74	294.48	Antioxidant activity, antifungal properties, Reactive oxygen species (ROS) production, anti-inflammatory effects, anticancer activity, metabolic regulation.	Taha 2020
β-Sitosterol	Phytosterol	$C_{29}H_{50}O$	40.509	10.46	414.7	Anti-inflammatory properties, antioxidant activity, anticancer potential, anti-diabetic activity, cholesterol-	Babu & Jayaraman (2020).

						lowering effects, wound healing property.	
Lupeol	Triterpenoid	$C_{30}H_{50}O$	42.933	8.66	426.7	Anti-inflammatory effects, antioxidant properties, anticancer potential, antimicrobial activity, cardioprotective effects, hepatoprotective properties.	Wal et al., 2011
Cholesta-4,6-dien-3-ol, Benzoate, (3. beta.)-	Steroid	$C_{34}H_{48}O_2$	47.274	4.63	488.7	Anti-inflammatory properties, antifungal activity, antioxidant effects.	Choudhary et al., 2019
Glycerol β-palmitate	Palmitic acid monoglyceride	$C_{19}H_{38}O_4$	38.658	4.34	330.5.	Anti-inflammatory properties, antioxidant activities, improved fat and calcium absorption.	Litmanovitz et al., 2013
Methyl stearate	Fatty acid methyl ester	$C_{19}H_{38}O_2$	32.174	4.13	298.5	Antimicrobial activity, antifoaming agent, serves as a nutrient in fermentation processes, role in stabilizing cellular membranes, and is used as an emulsifier and stabilizer in various applications.	Nakaziba et al., 2022
Vitamin E	Alpha-tocopherol	$C_{29}H_{50}O_2$	48.327	4.13	430.7	Antioxidant activity, immune system support, cell signaling.	Brigelius-Flohé (2021).
Phthalic acid, Butyl undecyl ester	Phthalic acid ester	$C_{23}H_{36}O_4$	29.240	3.06	376.5	Antimicrobial, anti-inflammatory, and potential anticancer	Ahmed et al., 2019

						properties, suppresses uric acid production, and promotes amino acid decarboxylase activity.	
Methoxy eugenol	Allylbenzene and eugenol derivative	$C_{11}H_{14}O_3$	23.957	2.63	194.23	Antioxidant activity, anti-inflammatory effects, hepatoprotective effects, anticancer potential, antimicrobial activity.	Kowalewska, & Majewska-Smolarek (2023).
Octadecanal	Long-chain fatty aldehyde	$C_{18}H_{36}O$	37.284	1.34	268.5	Act as a membrane stabilizer; serves as an energy source and storage molecule in organisms, antimicrobial activity.	Pinto et al., 2017.

Table 5.25: GC-MS profile of methanol extract of *Syzygium occidentale* leaves

Compound name	Type	Molecular formula	Retention time	Peak area (%)	Molecular weight (g/mol)	Biological activities	References
Cyclogallipharaol	Amphiphilic phenolic lipid	$C_{21}H_{36}O$	44.389	46.67	304.51	Antioxidant activity, potential anti-inflammatory effects, antimicrobial properties, inhibit α-glucosidase enzyme activity, potentially helping regulate body weight.	Martins et al., 2022.
3-Pentadecylphenol	Amphiphilic phenolic lipid	$C_{21}H_{36}O$	41.440	42.72	304.51	Antioxidant, antimicrobial, cytotoxic, function as an antiobesity agent by inhibiting α-glucosidase enzyme activity, altering membrane properties and organization.	Sarkar & Chattopadhyay (2021).
1-Tert-butoxy-3-methylbenzene	Aromatic ether	$C_{11}H_{16}O$	41.525	5.48	164.25	Molecular signaling, potential for developing specialized pharmaceutical compounds, interacts with biological targets.	Nakaziba et al., 2022.
Neophytadiene	Diterpene	$C_{20}H_{38}$	26.615	2.59	278.5	Anti-inflammatory effects, antioxidant activity,	Selmy et al., 2023.

						antimicrobial activity, cardioprotective effects, cytotoxic activity, analgesic and antipyretic properties.	
Phytol, acetate	Diterpene	$C_{22}H_{42}O_2$	31.947	2.54	338.6	Antimicrobial effects, antioxidant activity, anti-inflammatory properties, cytotoxic potential, immunomodulatory effects, metabolism modulation, autophagy, and apoptosis induction.	Sujatha et al., 2017.

Table 5.26: GC-MS profile of methanol extract of *Syzygium occidentale* bark

Compound name	Type	Molecular formula	Retention time	Peak area (%)	Molecular weight (g/mol)	Biological activities	References
Methyl palmitate	Fatty acid methyl ester	$C_{17}H_{34}O_2$	28.398	32.16	270.5	Anti-inflammatory effects; acts as a metabolite and has been shown to inhibit phagocytic activity.	Babu & Jayaraman (2020).
Methyl octadec-10-enoate	Fatty acid methyl ester	$C_{19}H_{36}O_2$	31.720	26.45	296.5	Anti-inflammatory, antifungal, antimicrobial properties, anticancer, hypocholesterolemic effects, act as a 5-Alpha reductase inhibitor, and the enzyme is involved in steroid metabolism, insect-repellent properties.	Hájek et al., 2023.
Linoleic acid, methyl ester	Fatty acid methyl ester	$C_{19}H_{34}O_2$	31.617	16.81	294.5	Antioxidant effects, anti-inflammatory and skin benefits, cholesterol regulation, antidiabetic effects, lower the risk of cardiovascular disease, a vital component of cell membranes, and is necessary for proper growth and development.	Saeed et al., 2012.
Methyl stearate	Fatty acid methyl ester	$C_{19}H_{38}O_2$	32.170	8.16	298.5	Anti-inflammatory effects, cholesterol regulation, neuroprotection, skin benefits.	Chen et al., 2020.
Benzene, 1-chloro-4-methoxy-	Aromatic organic compound	C_7H_7ClO	16.618	4.24	142.58	Antimicrobial activity, antioxidant effects, low acute toxicity, potentially affecting metabolic processes.	Choudhary et al., 2019.
3-Pentadecylphenol	Amphiphilic phenolic lipid	$C_{21}H_{36}O$	44.391	3.71	304.5	Antioxidant activity, antimicrobial potential, anti-obesity effects, cell culture applications, used as a reference in GC-MS analysis of certain	Stasiuk & Kozubek (2010).

						plant extracts and archaeological samples, cytotoxic activity.	
2-(4'-Methoxyphenyl)-2-(2'-methoxyphenyl) propane	Aromatic ethers	$C_{17}H_{20}O_2$	17.037	3.38	256.34	Anti-inflammatory effects; cytotoxic activity, act as a scaffold for drug development targeting hydrophobic binding sites.	Nakaziba et al., 2022.
Methyl behenate	Fatty acid methyl ester	$C_{23}H_{46}O_2$	38.839	2.06	354.6	Anti-inflammatory effects, antioxidant activity, cell culture applications, skin benefits.	Saleh et al., 2021.
Methyl myristate	Saturated fatty acid methyl ester	$C_{15}H_{30}O_2$	24.245	1.60	242.40	Anti-tumour agents, cardiovascular agents, anti-inflammatory properties.	Saeed et al., 2012.
Methyl arachate	Fatty acid methyl ester	$C_{21}H_{42}O_2$	35.638	1.44	326.6	Anti-inflammatory effects, metabolic precursor, antimicrobial activity, skin benefits.	Tallima & El Ridi (2017).

Table 5.27: GC-MS profile of methanol extract of *Syzygium palghatense* leaves

Compound Name	Type	Molecular Formula	Retention Time (min)	Peak Area (%)	Molecular Weight (g/mol)	Biological activities	References
(-)-Spathulenol	Sesquiterpene	$C_{15}H_{24}$	21.158	4.68	220.35	Anti-inflammatory, Antimicrobial	Babu & Jayaraman (2020).
Neophytadiene	Hydrocarbon	$C_{20}H_{38}$	26.618	5.62	278.52	Antioxidant	Hájek et al., 2023.
3,7,11,15-Tetramethyl-2-hexadecen-1-ol	Terpenoid	$C_{20}H_{40}O$	27.493	2.25	296.53	Antimicrobial	Saeed et al., 2012.
Methyl Palmitate	Fatty acid methyl ester	$C_{17}H_{34}O_2$	28.388	4.11	270.45	Anti-inflammatory, Antimicrobial	Chen et al., 2020.
Linoleic acid, methyl ester	Fatty acid methyl ester	$C_{19}H_{34}O_2$	31.610	2.08	294.49	Anti-inflammatory	Choudhary et al., 2019.
9-Octadecenoic acid (Z)-, methyl ester	Fatty acid methyl ester	$C_{19}H_{36}O_2$	31.712	4.27	296.50	Antioxidant	Babu & Jayaraman (2020).
Phytol	Diterpene alcohol	$C_{20}H_{40}O$	31.950	5.41	296.53	Anti-inflammatory	Hájek et al., 2023.
Methyl Stearate	Fatty acid methyl ester	$C_{19}H_{38}O_2$	32.166	1.85	298.53	Antimicrobial	Saeed et al., 2012.
Squalene	Triterpene	$C_{30}H_{50}$	43.217	39.14	410.70	Antioxidant	Chen et al., 2020.
γ-Tocopherol (Vitamin E)	Vitamin	$C_{29}H_{50}O_2$	46.747	4.55	430.71	Antioxidant, Anti-inflammatory	Choudhary et al., 2019.

Table 5.28: GC-MS profile of methanol extract of *Syzygium palghatense* bark

Compound name	Type	Molecular formula	Retention time (min)	Peak area (%)	Molecular weight (g/mol)	Biological activities	References
5-Hydroxymethylfurfural	Furan derivative	$C_6H_6O_3$	12.408	28.67	97.05	Antioxidant, anti-inflammatory	Babu & Jayaraman (2020).
3-{[Tert-Butyl (Dimethyl)Silyl]Oxy}-4-Hexenal	Silane derivative	$C_{12}H_{26}OSi$	15.521	2.51	101.05	Antimicrobial	Hájek et al., 2023.
3-Furanacetic Acid, 4-Hexyl-2,5-Dihydro-2,5-Dioxo-	Organic acid	$C_{12}H_{18}O_6$	18.832	7.96	126.05	Antioxidant	Saeed et al., 2012.
D-Allose	Sugar	C6H12O6	19.517	9.66	60.00	Antifungal	Chen et al., 2020.
Phenol, 2,6-Dimethoxy-4-(2-Propenyl)-	Phenolic compound	$C_{11}H_{14}O_3$	23.957	1.29	194.05	Antimicrobial, antioxidant	Choudhary et al., 2019.
Hexadecanoic Acid, Methyl Ester	Fatty acid methyl ester	$C_{17}H_{34}O_2$	28.395	8.25	74.00	Antioxidant, anti-inflammatory	Babu & Jayaraman (2020).
Phthalic Acid, Butyl Undecyl Ester	Ester	$C_{24}H_{38}O_4$	29.240	1.50	149.00	Antimicrobial	Hájek et al., 2023.
Cis-Linoleic Acid Methyl Ester	Fatty acid methyl ester	$C_{19}H_{34}O_2$	31.620	5.76	67.05	Antimicrobial, antioxidant	Saeed et al., 2012.
9-Octadecenoic Acid (Z)-, Methyl Ester	Fatty acid ester	$C_{19}H_{36}O_2$	31.720	5.82	55.05	Antimicrobial, antioxidant	Chen et al., 2020.
Methyl Stearate	Fatty acid methyl ester	$C_{19}H_{38}O_2$	32.174	2.03	74.05	Antioxidant, anti-inflammatory	Choudhary et al., 2019.
Octadecanal	Aldehyde	$C_{18}H_{36}O$	37.284	0.66	57.05	Anticancer	Babu & Jayaraman (2020).
Glycerol 1-Palmitate	Fatty acid ester	$C_{19}H_{38}O_4$	38.658	2.13	57.05	Anthelmintic	Hájek et al., 2023.

Stigmast-5-En-3-Ol, (3.Beta.)-	Steroid	$C_{29}H_{50}O$	40.509	5.13	57.05	Antioxidant, anti-inflammatory	Saeed et al., 2012.
Lupeol	Triterpene	$C_{30}H_{50}O$	42.933	4.25	95.10	Anti-inflammatory, anticancer	Brigelius-Flohé (2021)
D:B-Friedo-B':A'-Neogammacer-5-En-3-One	Triterpene derivative	$C_{30}H_{48}O$	44.065	6.93	95.10	Antioxidant	Brigelius-Flohé (2021
Stigmast-4-En-3-One	Steroid	$C_{29}H_{48}O$	45.919	3.14	124.10	Antidiabetic	Brigelius-Flohé (2021
Cholesta-4,6-Dien-3-Ol, Benzoate, (3.Beta.)-	Steroid ester	$C_{36}H_{50}O_4$	47.274	2.27	135.10	Anticancer	Brigelius-Flohé (2021
Vitamin E	Tocopherol	$C_{29}H_{50}O_2$	48.327	2.03	430.7	Antioxidant, anti-inflammatory, immune support	Brigelius-Flohé (2021)

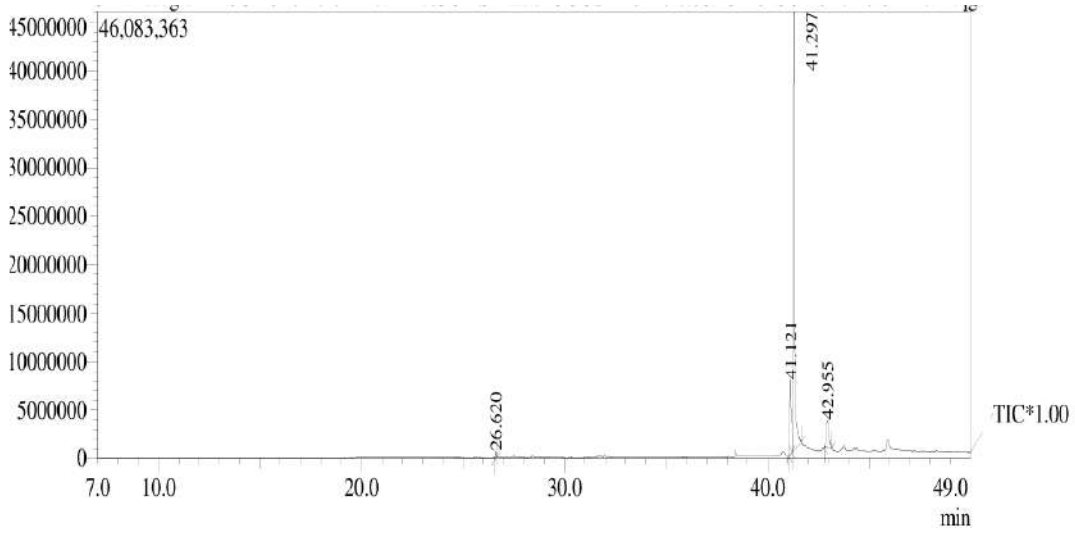


Figure 5.11: GC-MS chromatogram of methanolic extract of *Syzygium laetum* leaves

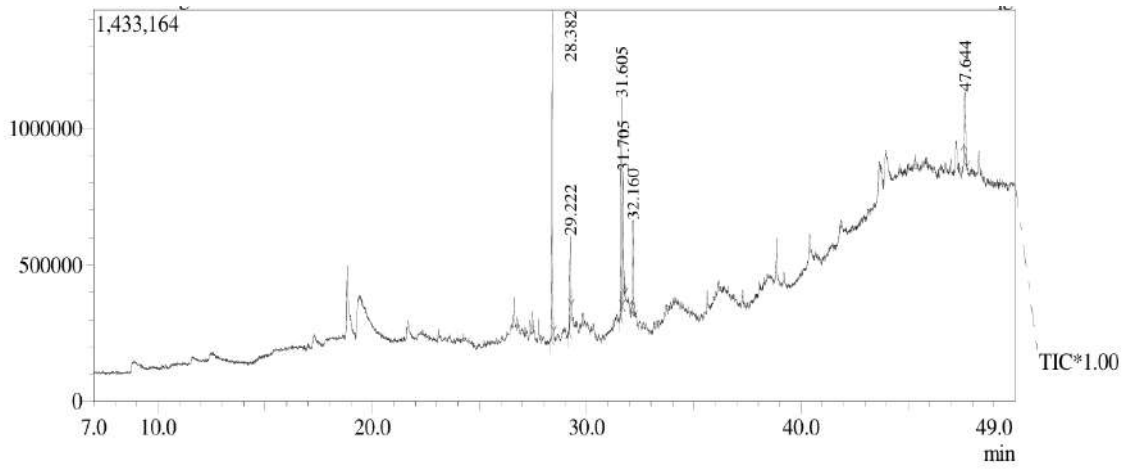


Figure 5.12: GC-MS chromatogram of methanolic extract of *Syzygium laetum* bark

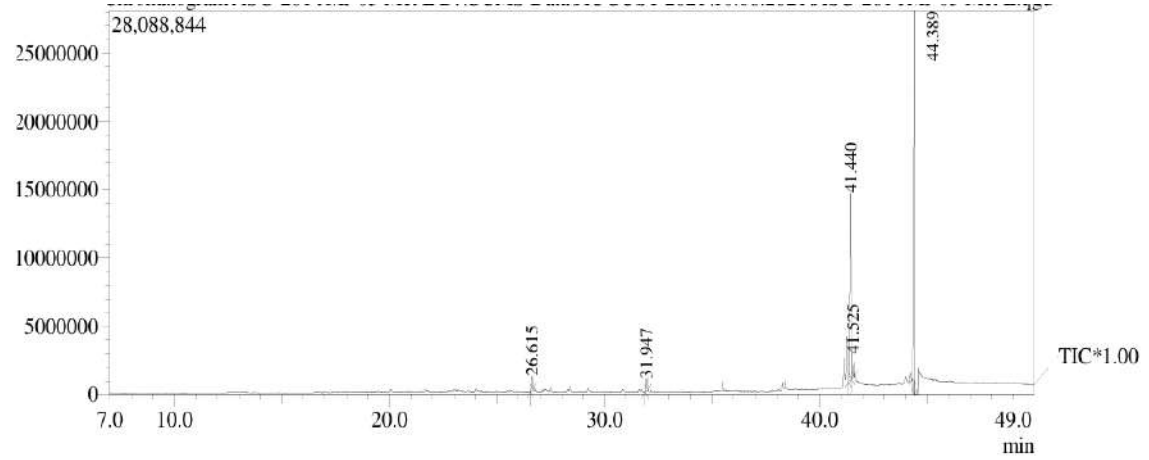


Figure 5.13: GC-MS chromatogram of methanolic extract of *Syzygium occidentale* leaves

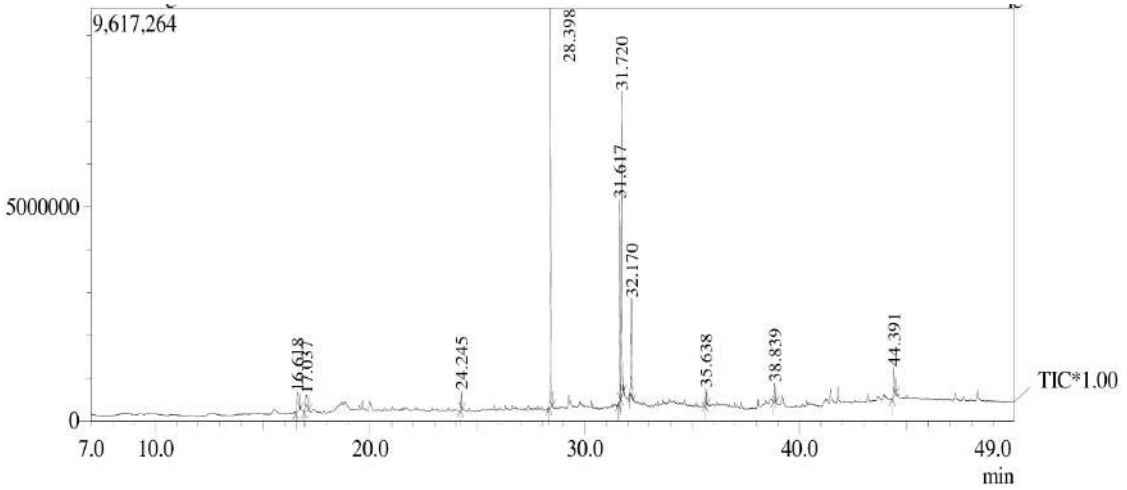


Figure 5.14: GC-MS chromatogram of methanolic extract of *Syzygium occidentale* bark

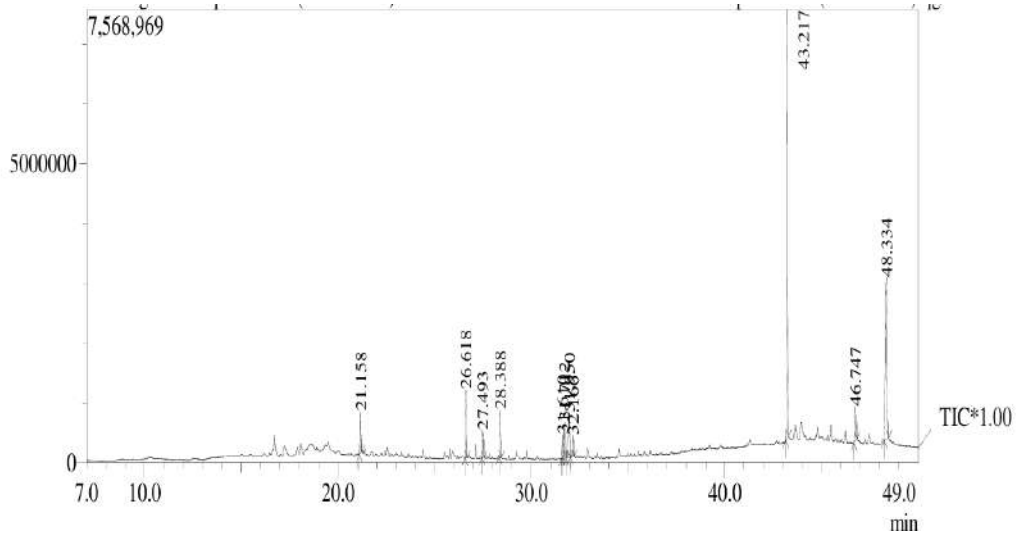


Figure 5.15: GC-MS chromatogram of methanolic extract of *Syzygium palghatense* leaves

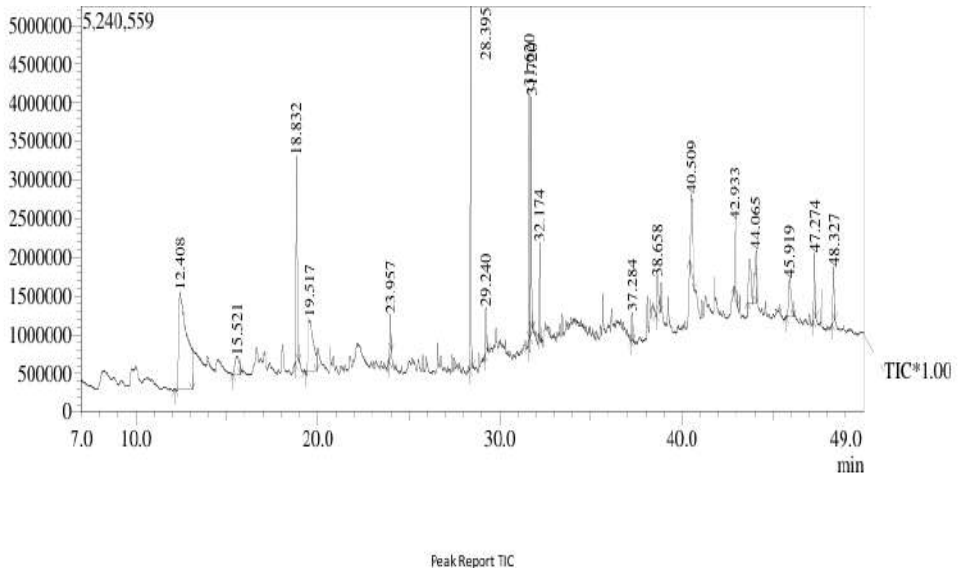
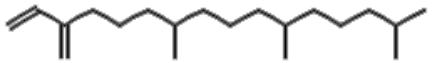
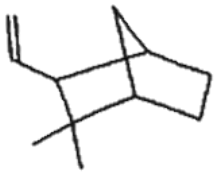


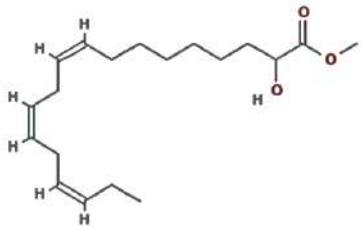
Figure 5.16: GC-MS chromatogram of methanolic extract of *Syzygium palghatense* bark



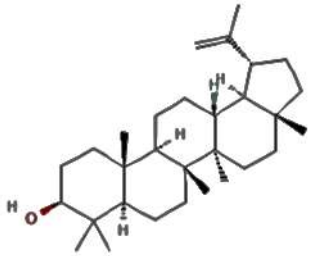
Neophytadiene



2,2-Dimethyl-3-vinyl-bicyclo [2.2.1] heptane



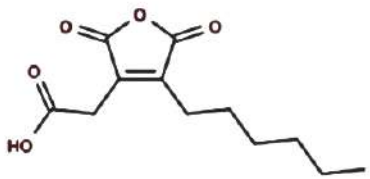
Methyl 2-hydroxy-octadeca-9,12,15-trienoate



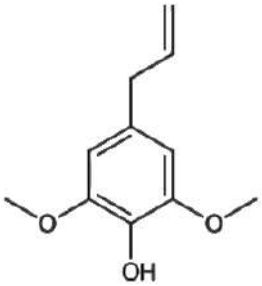
Lupeol

Figure 5.17: Chemical structures of phytochemical compounds identified by GC-MS analysis of *Syzygium laetum* leaf extract

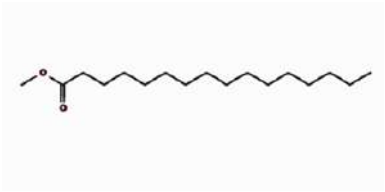
(Source: PubChem, National Centre for Biotechnology Information, U.S. National Library of Medicine, USA)



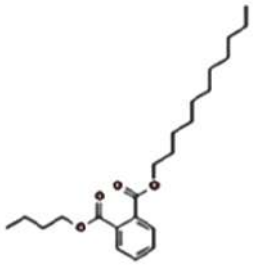
2-Carboxymethyl-3-n-hexyl-maleic anhydride ester



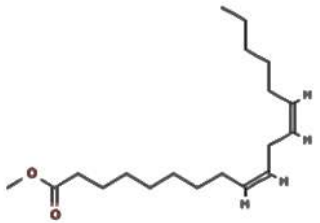
Methoxy eugenol



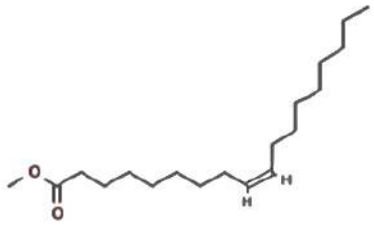
Methyl palmitate



Phthalic acid, Butyl undecyl



Linoleic acid, Methyl ester



9-octadecenoic acid (z)-, Methyl ester



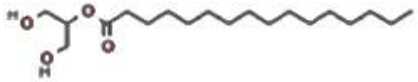
Methyl stearate



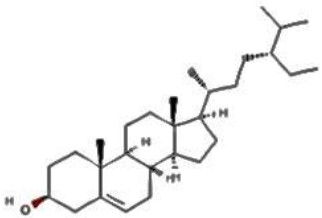
Octadecanal

Figure 5.18a: Chemical structures of phytochemical compounds identified by GC-MS analysis of *Syzygium laetum* bark extract

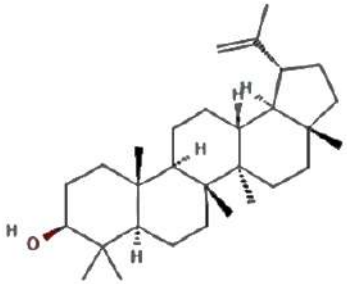
(Source: PubChem, National Centre for Biotechnology Information, U.S. National Library of Medicine, USA)



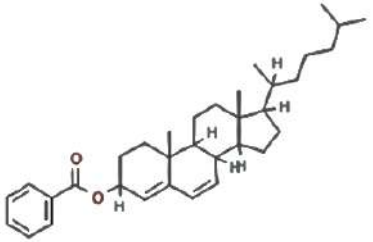
Glycerol β-palmitate



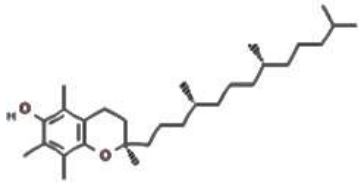
β-Sitosterol



Lupeol



Cholesta-4,6-dien-3-ol, Benzoate, (3. beta.)-



Vitamin E

Figure 5.18b: Chemical structures of phytochemical compounds identified by GC-MS analysis of *Syzygium laetum* bark extract

(Source: PubChem, National Centre for Biotechnology Information, U.S. National Library of Medicine, USA)

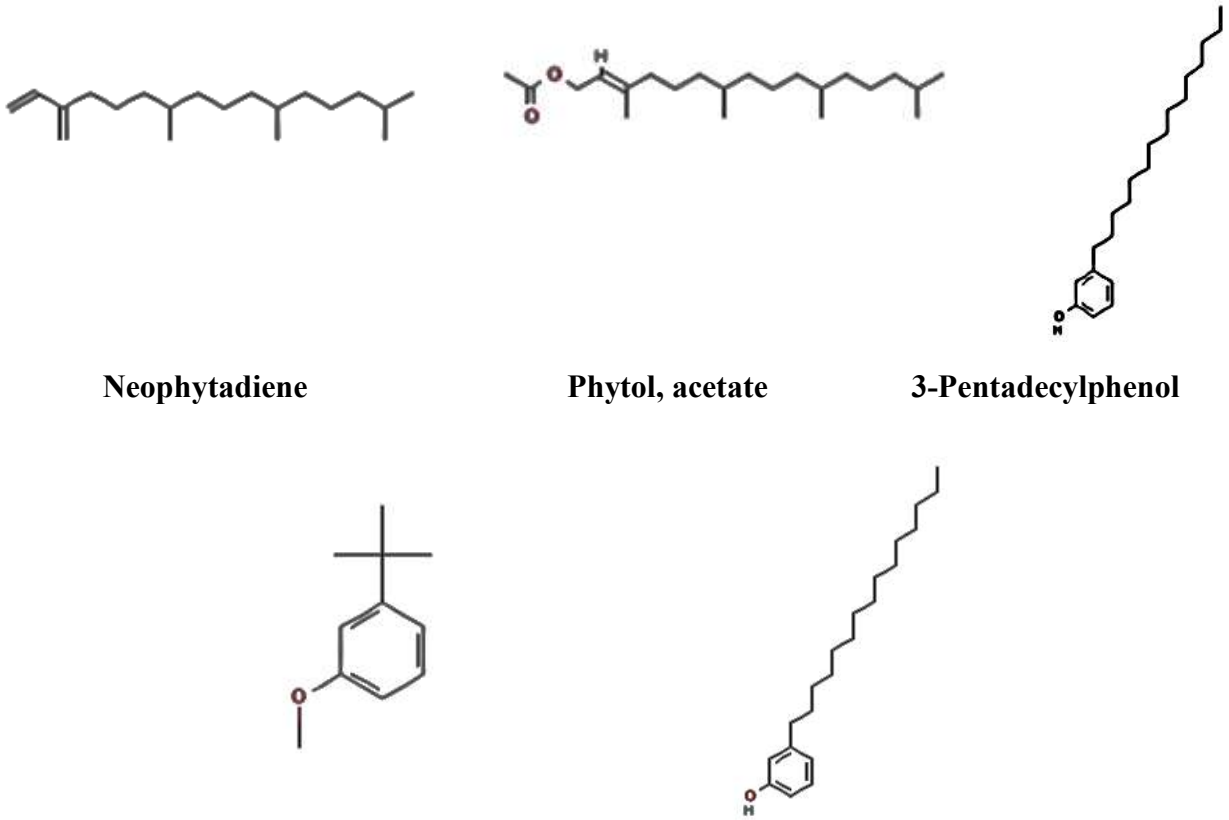
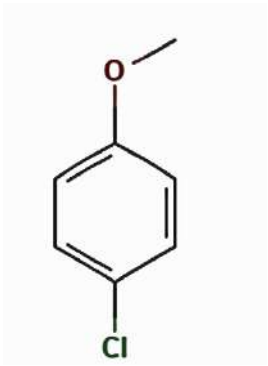
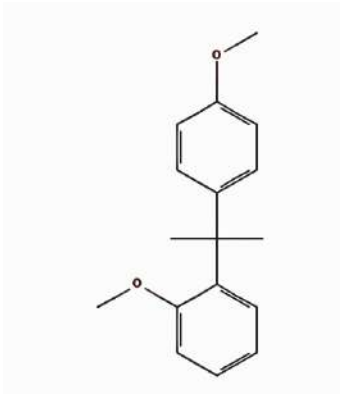


Figure 5.19: Chemical structures of phytochemical compounds identified by GC-MS analysis of *Syzygium occidentale* leaf extract

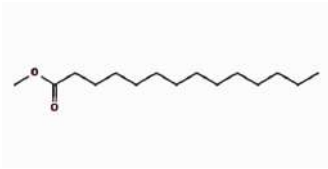
(Source: PubChem, National Centre for Biotechnology Information, U.S. National Library of Medicine, USA)



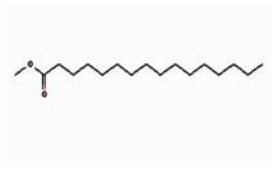
Benzene, 1-chloro-4-methoxy-



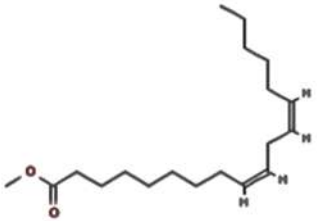
2-(4'-Methoxyphenyl)-2-(2'-methoxyphenyl) propane



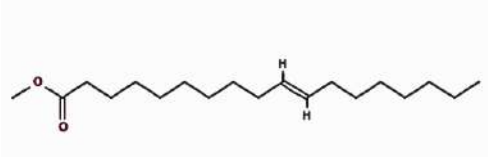
Methyl myristate



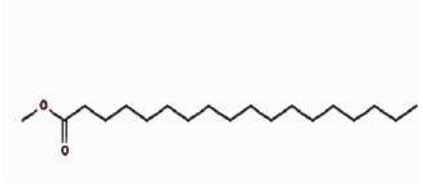
Methyl palmitate



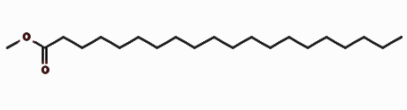
Linoleic acid, methyl ester



Methyl octadec-10-enoate



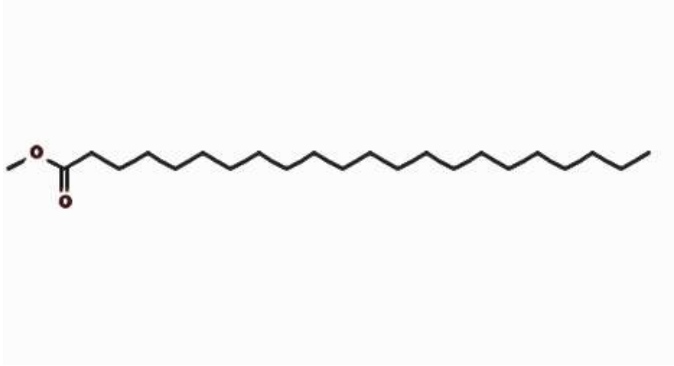
Methyl stearate



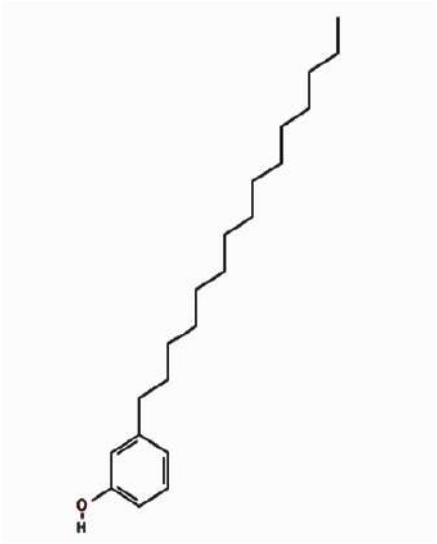
Methyl arachate

Figure 5.20a: Chemical structures of phytochemical compounds identified by GC-MS analysis of *Syzygium occidentale* bark extract

(Source: PubChem, National Centre for Biotechnology Information, U.S. National Library of Medicine, USA)



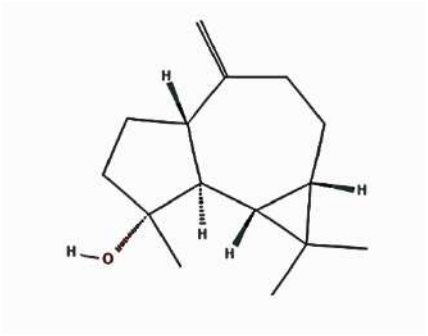
Methyl behenate



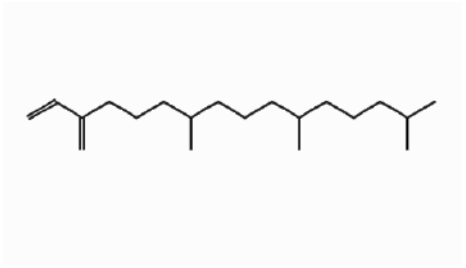
3-Pentadecylphenol

Figure 5.20b: Chemical structures of phytochemical compounds identified by GC-MS analysis of *Syzygium occidentale* bark extract

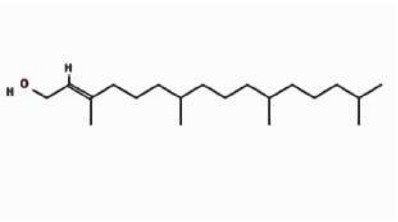
(Source: PubChem, National Centre for Biotechnology Information, U.S. National Library of Medicine, USA)



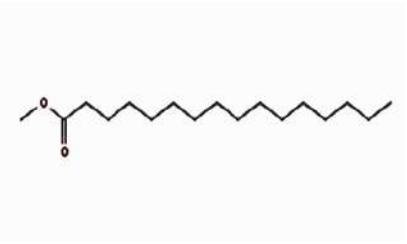
(-)-Spathulenol



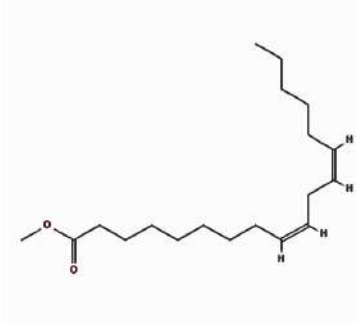
Neophytadiene



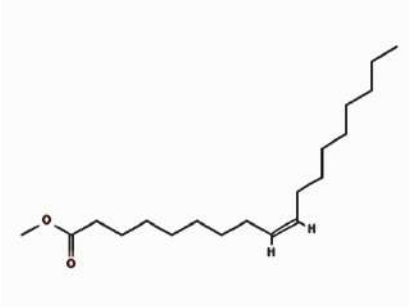
3,7,11,15-Tetramethyl-2-hexadecen-1-ol



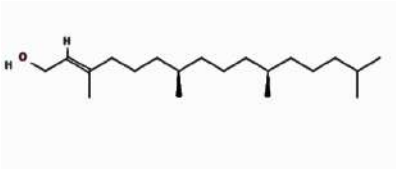
Methyl palmitate



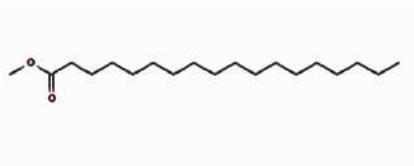
Linoleic Acid, methyl ester



9-octadecenoic Acid (Z)-, methyl ester



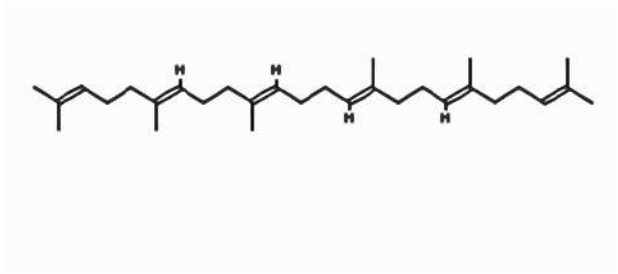
Phytol



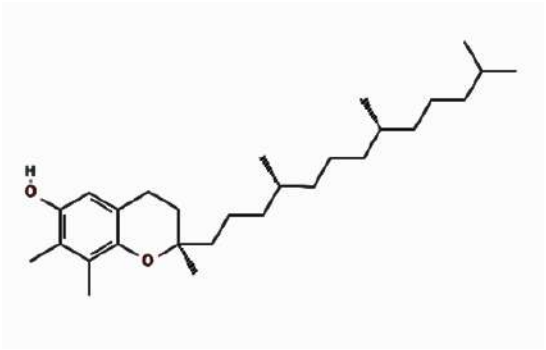
Methyl stearate

Figure 5.21a: Chemical structures of phytochemical compounds identified by GC-MS analysis of *Syzygium palghatense* leaf extract

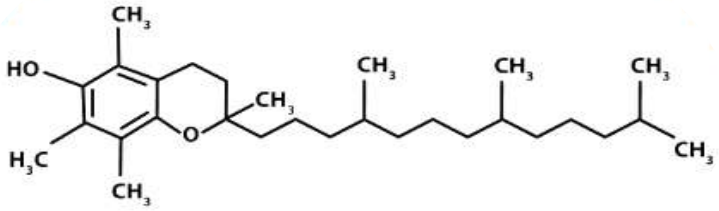
(Source: PubChem, National Centre for Biotechnology Information, U.S. National Library of Medicine, USA)



Squalene



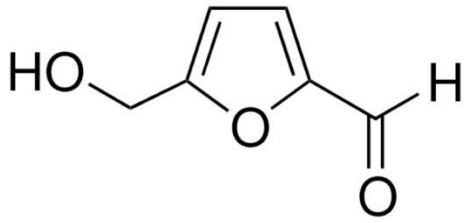
Gamma-Tocopherol



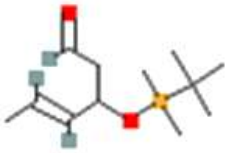
Vitamin E

Figure 5.21b: Chemical structures of phytochemical compounds identified by GC-MS analysis of *Syzygium palghatense* leaf extract

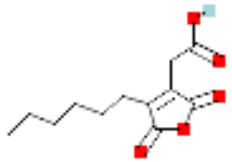
(Source: PubChem, National Centre for Biotechnology Information, U.S. National Library of Medicine, USA)



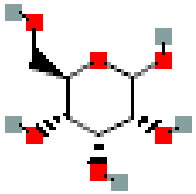
5-Hydroxymethylfurfural



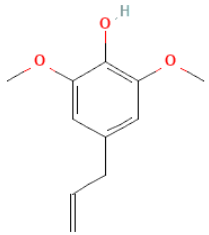
3-{[Tert-Butyl(Dimethyl)Silyl]Oxy}-4-Hexenal



3-Furanacetic Acid, 4-Hexyl-2,5-Dihydro-2,5-Dioxo-



D-Allose



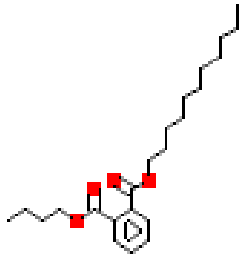
Phenol, 2,6-Dimethoxy-4-(2-Propenyl)-



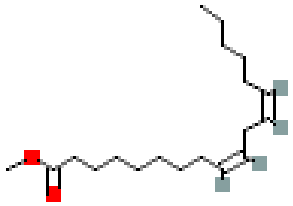
Hexadecanoic Acid, Methyl Ester

Figure 5.22a: Chemical structures of phytochemical compounds identified by GC-MS analysis of *Syzygium palghatense* bark extract

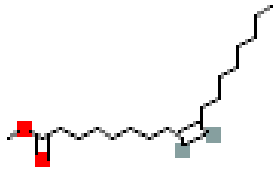
(Source: PubChem, National Centre for Biotechnology Information, U.S. National Library of Medicine, USA)



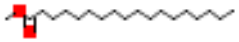
Phthalic Acid, Butyl Undecyl Ester



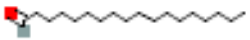
CIS-LINOLEIC ACID METHYL ESTER



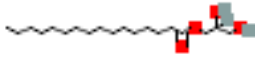
9-OCTADECENOIC ACID (Z)-, METHYL ESTER



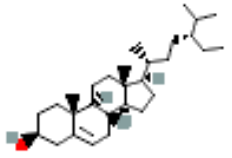
Methyl Stearate



Octadecanal



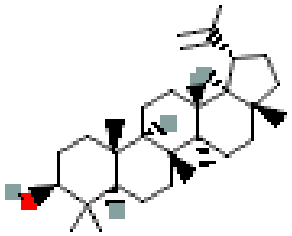
Glycerol 1-Palmitate



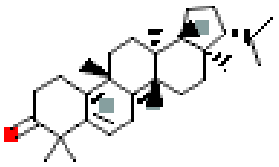
Stigmast-5-En-3-Ol, (3.Beta.)-

Figure 5.22b: Chemical structures of phytochemical compounds identified by GC-MS analysis of *Syzygium palghatense* bark extract

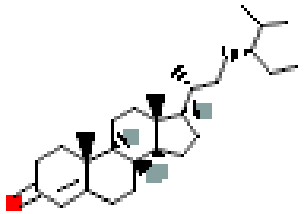
(Source: PubChem, National Centre for Biotechnology Information, U.S. National Library of Medicine, USA)



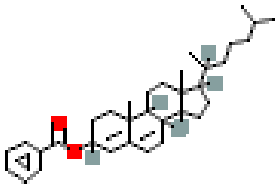
Lupeol



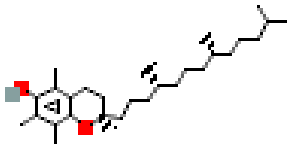
D:B-Friedo-B':A'-Neogammacer-5-En-3-One



Stigmast-4-En-3-One



Cholesta-4,6-Dien-3-Ol, Benzoate, (3.Beta.)-



Vitamin E

Figure 5.22c: Chemical structures of phytochemical compounds identified by GC-MS analysis of *Syzygium palghatense* bark extract

(Source: PubChem, National Centre for Biotechnology Information, U.S. National Library of Medicine, USA)

antioxidant and anti-inflammatory potential, supporting its medicinal value and therapeutic applications.

The GC-MS profile of the methanol extract from *S. palghatense* bark reveals a diverse range of bioactive compounds with significant biological activities. Dominant compounds like 5-Hydroxymethylfurfural (28.67% peak area) exhibit strong antioxidant and anti-inflammatory potential, indicating the extract's capability to counter oxidative stress and inflammation. Other notable constituents include fatty acid methyl esters such as Hexadecanoic acid methyl ester and cis-Linoleic acid methyl ester, which contribute antimicrobial, antioxidant, and anti-inflammatory effects, highlighting the extract's potential in combating microbial infections and inflammation.

The presence of phytochemicals such as Lupeol and stigmasterol derivatives further enhances the therapeutic profile, with demonstrated anti-inflammatory, anticancer, and antidiabetic properties. Steroids and tocopherols, including Vitamin E, add antioxidant and immune-supportive benefits, suggesting comprehensive protective bioactivities.

Overall, these findings suggest that the methanol extract of *S. palghatense* bark is rich in compounds that can provide multifaceted health benefits, particularly through antioxidant, antimicrobial, anti-inflammatory, and potential anticancer activities. This chemical profile underpins the plant's medicinal potential and warrants further investigation for pharmaceutical and nutraceutical applications.

GC-MS profiling of the bark and leaves of *S. laetum*, *S. occidentale*, and *S. palghatense* showed distinct phytochemical profiles with the potential to be further explored as sources of prospective pharmaceuticals. In contrast, *S. laetum* leaf showed a predominant methyl 2-hydroxy-octadeca-9,12,15-trienoate which comprised 76.56 %, while the bark sample presented a complex configuration of fatty acid methyl esters with β-sitosterol. *S. occidentale* leaves contained abundant phenolic lipids (3-pentadecylphenol and cyclogallipharaol), and its bark was concentrated in fatty acid methyl esters. *S. palghatense* leaves were rich in squalene (39.14 %) and vitamin E (26.05 %), its bark had a varied profile like *S. laetum* bark. Of the three species, *S.*

palghatense was found to be the most promising candidate owing to its most balanced and diversified phytochemical profile from both leaves and bark. The unique combination of squalene and vitamin E in the leaves with a huge range of bioactive compounds in the bark indicates the highest potential for different therapeutic applications. However, each species provides different compounds that might be beneficial for treating specific diseases, and they are all worth investigating in pharmaceutical studies.

5.3.5. Liquid Chromatography-Mass Spectrometry Quadrupole Time of Flight (LC-MS QTOF) analysis

LC-MS QTOF chromatogram and details of the compounds of *S. laetum*, *S. occidentale* and *S. palghatense* leaves and bark were displayed in Tables 5.29-5.34 and Figures 5.23-5.34.

LC-MS analysis of methanol extract of *S. laetum* leaf and bark on a QTOF instrument detected different phytochemical profiles. The leaf extract detected 11 qualified compounds of 29 targets. The major compounds detected are cinnamic acid (RT 33.751, Score 92.07), neomycin (RT 37.323, Score 85.66), tryptophan (RT 8.381, Score 93.65), and afzelin (RT 6.388, Score 81.50). The high scores of tryptophan (93.65) and cinnamic acid (92.07) reflect confident identification. Other compounds of interest detected are alpha-pinene (detected at two retention times: 11.388 and 10.491 with scores 86.39 and 87.76, respectively) and isoliquiritin (RT 7.966, Score 82.05).

The bark extract detected 12 qualified compounds of 23 targets and reflects a slightly different chemical composition. Major compounds detected are cinnamic acid (RT 33.828, Score 92.57), mecillinam (RT 32.881, Score 90.51), lanosterol (RT 24.059, Score 90.87), and erucic acid (RT 30.937, Score 86.33). The bark extract also had different compounds, such as beta-tocopherol (RT 30.355, Score 81.91) and phytol (RT 31.734, Score 83.29). Detecting these high-score compounds reflects a broad phytochemical profile with potential biological activities.

The two extracts had some common compounds but slightly different retention times, which could be due to the matrix effect. The analysis was performed under the same conditions (3 µL injection volume, using the general profiling method) for both samples and thus, the result is comparable. The data acquisition was performed with the help of 6200 series TOF/6500 series Q-TOF 10.1 software, with a successful IRM status reflecting a reliable mass accuracy during the analysis. This LC-MS report provides information regarding the chemical makeup of *S. laetum* leaf and bark extracts. It provides a foundation for understanding their potential pharmacological activities.

For *S. occidentale* leaves and bark, the extracts contain prominent phenolic acids like gallic acid and ellagic acid, flavonoids such as quercetin, and various fatty acids, including stearic acid and oleic acid. These compounds are known for their strong antioxidant, anti-inflammatory, and antimicrobial activities, highlighting the extracts' potential for therapeutic and nutraceutical applications. The presence of steroids and triterpenes further enhances the pharmacological profile, contributing anticancer and cardioprotective effects.

2The LC-MS QTOF profile of the methanol extract of *S. palghatense* leaf identified several key phytochemicals, phenolic acids (gallic acid, ellagic acid, chlorogenic acid), flavonoids (quercetin, kaempferol, myricetin, rhamnetin), fatty acids (stearic acid, lauric acid, myristic acid, palmitic acid, oleic acid, linoleic acid), and triterpenoids (oleanolic acid, maslinic acid). These compounds are known for their antioxidant, anti-inflammatory, anticancer, and antimicrobial activities, contributing to the therapeutic potential of the plant. The presence of these phytochemicals supports the ethnopharmacological uses of *S. palghatense* and warrants further pharmacological investigation.

The LC-MS QTOF profile for the methanol extract of *S. palghatense* bark reveals a diverse set of phytochemicals, including notable acids, flavonoids, and phenolic compounds. A highlight of this analysis is the detection of 2-Phenyl-4H-chromen-4-one, a bioactive compound recognized for its potential pharmacological properties, present with high accuracy in the sample profile. Alongside this

compound, the presence of gallic acid, ellagic acid, quercetin, and several fatty acids demonstrates the complex chemical nature of the extract. These results underscore the bark's richness in secondary metabolites with possible antioxidant and therapeutic roles, positioning *S. palghatense* as a promising candidate for further pharmacognostic and bioactivity research. 2-Phenyl-4h-chrome-4-one has confirmed antimicrobial and anti-inflammatory properties. This chemical richness validates the traditional medicinal use of *S. palghatense* and supports its potential in drug discovery.

Table 5.29: LC-MS QTOF profile of methanol extract of *Syzygium laetum* leaves

Compound name	Formula	RT	Mass	Mass (Tgt)	Diff (Tgt, ppm)	Score
Cinnamic acid	$C_9H_8O_2$	33.751	148.0534	148.0524	6.44	92.07
Neomycin	$C_{23}H_{46}N_6O_{13}$	37.323	614.3096	614.3123	-4.39	85.66
2-Methyl-3-hydroxybutyric acid	$C_5H_{10}O_3$	5.740	118.0629	118.0630	-0.40	80.36
Dicentrinone	$C_{19}H_{13}NO_5$	7.584	335.0795	335.0794	0.27	83.50
alpha-Pinene	$C_{10}H_{16}$	11.388	136.1255	136.1252	2.44	86.39
alpha-Pinene	$C_{10}H_{16}$	10.491	136.1250	136.1252	-1.29	87.76
6-Methyl-5-hepten-2-one	$C_8H_{14}O$	7.285	126.1054	126.1045	7.66	85.39
N-Methylcorydaldine	$C_{12}H_{15}NO_3$	11.604	221.1006	221.1052	-20.63	84.23
Tryptophan	$C_{11}H_{12}N_2O_2$	8.381	204.0900	204.0899	0.79	93.65
Isoliquiritin	$C_{21}H_{22}O_9$	7.966	418.1240	418.1264	-5.61	82.05
Afzelin	$C_{21}H_{20}O_{10}$	6.388	432.1053	432.1056	-0.72	81.50

Table 5.30: LC-MS QTOF profile of methanol extract of *Syzygium laetum* bark

Compound name	Formula	RT	Mass	Mass (Tgt)	Diff (Tgt, ppm)	Score
Cinnamic acid	$C_9H_8O_2$	33.828	148.0534	148.0524	6.45	92.57
Neomycin	$C_{23}H_{46}N_6O_{13}$	37.350	614.3111	614.3123	-1.92	82.72
p-Cymene	$C_{10}H_{14}$	20.952	134.1092	134.1096	-2.54	83.21
Erucic acid	$C_{22}H_{42}O_2$	30.937	338.3175	338.3185	-3.00	86.33
Mecillinam	$C_{15}H_{23}N_3O_3S$	32.881	325.1457	325.1460	-1.06	90.51
Dicentrinone	$C_{19}H_{13}NO_5$	2.493	335.0800	335.0794	1.96	83.26
Terpinolene	$C_{10}H_{16}$	32.349	136.1252	136.1252	-0.31	85.31
6-Methyl-5-hepten-2-one	$C_8H_{14}O$	1.746	126.1046	126.1045	0.87	85.69
N-Methylcorydaldine	$C_{12}H_{15}NO_3$	13.608	221.1068	221.1052	7.17	85.28
beta-Tocopherol	$C_{28}H_{48}O_2$	30.355	416.3656	416.3654	0.43	81.91
Phytol	$C_{20}H_{40}O$	31.734	296.3015	296.3079	-21.60	83.29
Lanosterol	$C_{30}H_{50}O$	24.059	426.3875	426.3862	3.07	90.87

Table 5.31: LC-MS QTOF profile of methanol extract of *Syzygium occidentale* leaves

Compound name	Formula	RT	Mass	Mass (Tgt)	Diff (Tgt, ppm)	Score
Cinnamic acid	$C_9H_8O_2$	33.761	148.0533	148.0524	6.16	92.91
Neomycin	$C_{23}H_{46}N_6O_{13}$	36.602	614.3093	614.3123	-4.82	84.48
Guaiacol	$C_7H_8O_2$	2.477	124.0499	124.0524	-20.44	82.06
Liquiritigenin	$C_{15}H_{12}O_4$	12.113	256.0728	256.0736	-2.87	83.28
Stigmasterol	$C_{29}H_{48}O$	36.586	412.3673	412.3705	-7.76	89.65
2-Methyl-3-hydroxybutyric acid	$C_5H_{10}O_3$	1.746	118.0636	118.0630	4.83	80.15
p-Cymene	$C_{10}H_{14}$	16.748	134.1086	134.1096	-7.11	81.04
Erucic acid	$C_{22}H_{42}O_2$	30.937	338.3171	338.3185	-3.95	81.43
alpha-Pinene	$C_{10}H_{16}$	16.532	136.1249	136.1252	-2.40	82.28
alpha-Pinene	$C_{10}H_{16}$	9.737	136.1248	136.1252	-2.63	81.16
6-Methyl-5-hepten-2-one	$C_8H_{14}O$	1.779	126.1044	126.1045	-0.31	85.60

Table 5.32: LC-MS QTOF profile of methanol extract of *Syzygium occidentale* bark

Compound name	Formula	RT	Mass	Mass (Tgt)	Diff (Tgt, ppm)	Score
Cinnamic acid	$C_9H_8O_2$	33.753	148.0535	148.0524	7.24	92.00
Liquiritigenin	$C_{15}H_{12}O_4$	12.154	256.0732	256.0736	-1.23	84.04
Maslinic acid	$C_{30}H_{48}O_4$	28.337	472.3572	472.3553	4.02	90.50
Serine	$C_3H_7NO_3$	22.771	105.0440	105.0426	13.01	81.43
Mecillinam	$C_{15}H_{23}N_3O_3S$	18.351	325.1437	325.1460	-7.04	81.32
Kanamycin	$C_{18}H_{36}N_4O_{11}$	34.667	484.2383	484.2381	0.57	82.92
Tretinoin	$C_{20}H_{28}O_2$	19.415	300.2099	300.2089	3.15	95.94
Dicentrinone	$C_{19}H_{13}NO_5$	18.368	335.0788	335.0794	-1.73	80.63
Terpinolene	$C_{10}H_{16}$	32.341	136.1255	136.1252	2.30	84.99
Carvone	$C_{10}H_{14}O$	14.630	150.1062	150.1045	11.83	81.96

Table 5.33: LC-MS QTOF profile of methanol extract of *Syzygium palghatense* leaves

Compound name	Formula	RT	Mass	Mass (Tgt)	Diff (Tgt, ppm)	Score
Gallic acid	$C_7H_6O_5$	2.137	170.0225	170.0215	5.56	80.18
Ellagic acid	$C_{14}H_6O_8$	3.018	302.0063	302.0063	-0.02	99.80
Quercetin	$C_{15}H_{10}O_7$	2.120	302.0423	302.0436	-1.26	81.57
Stearic acid	$C_{18}H_{36}O_2$	29.900	284.2721	284.2715	2.01	98.21
Lauric acid	$C_{12}H_{24}O_2$	13.302	200.1776	200.1776	0.05	99.73
Myristic acid	$C_{14}H_{28}O_2$	22.722	228.2087	228.2089	-0.82	98.22
Palmitic acid	$C_{16}H_{32}O_2$	26.760	256.2408	256.2402	2.23	98.47
Oleic acid	$C18H_{34}O_2$	35.715	282.2558	282.2559	-0.12	98.63
Linoleic acid	$C_{18}H_{32}O_2$	29.052	280.2402	280.2402	-0.44	99.53
Oleanolic acid	$C_{30}H_{48}O_3$	31.760	456.3587	456.3603	-3.60	92.40
Chlorogenic acid	$C_{16}H_{18}O_9$	21.493	354.0975	354.0951	6.77	87.10
Cinnamic acid	$C_9H_8O_2$	31.262	148.0527	148.0507	1.88	99.63
Rhamnetin	$C_{16}H_{12}O_7$	2.519	316.0533	316.0583	-15.70	72.68
Kaempferol	$C_{15}H_{10}O_6$	21.775	286.0480	286.0477	0.79	79.95
Myricetin	$C_{15}H_{10}O_8$	17.140	318.0374	318.0376	-0.52	98.10
Maslinic acid	$C_{30}H_{48}O_4$	32.674	472.3544	472.3553	-1.83	98.46
Ferulic acid	$C_{10}H_{10}O_4$	9.962	194.0573	194.0602	-3.29	85.61

Table 5.34: LC-MS QTOF profile of methanol extract of *Syzygium palghatense* bark

Compound name	Formula	RT	Mass	Mass (Tgt)	Diff (Tgt, ppm)	Score
Gallic acid	$C_7H_6O_5$	2.137	170.0225	170.0215	5.56	80.18
Ellagic acid	$C_{14}H_6O_8$	3.018	302.0063	302.0063	-0.02	99.80
Quercetin	$C_{15}H_{10}O_7$	2.120	302.0423	302.0436	-1.26	81.57
Stearic acid	$C_{18}H_{36}O_2$	29.900	284.2721	284.2715	2.01	98.21
Lauric acid	$C_{12}H_{24}O_2$	13.302	200.1776	200.1776	0.05	99.73
Myristic acid	$C_{14}H_{28}O_2$	22.722	228.2087	228.2089	-0.82	98.22
Palmitic acid	$C_{16}H_{32}O_2$	26.760	256.2408	256.2402	2.23	98.47
Oleic acid	$C_{18}H_{34}O_2$	35.715	282.2558	282.2559	-0.12	98.63
Linoleic acid	$C_{18}H_{32}O_2$	29.052	280.2402	280.2402	-0.44	99.53
Oleanolic acid	$C_{30}H_{48}O_3$	31.760	456.3587	456.3603	-3.60	92.40
Chlorogenic acid	$C_{16}H_{18}O_9$	21.493	354.0975	354.0951	6.77	87.10
Cinnamic acid	$C_9H_8O_2$	31.262	148.0527	148.0507	1.88	99.63
Vanillin	$C_8H_8O_3$	9.497	152.0473	152.0473	0.00	98.07
Rhamnetin	$C_{16}H_{12}O_7$	2.519	316.0533	316.0583	-15.70	72.68
Kaempferol	$C_{15}H_{10}O_6$	21.775	286.0480	286.0477	0.79	79.95
Myricetin	$C_{15}H_{10}O_8$	17.140	318.0374	318.0376	-0.52	88.10
Maslinic acid	$C_{30}H_{48}O_4$	32.674	472.3544	472.3553	-1.83	98.46
Ferulic acid	$C_{10}H_{10}O_4$	9.962	194.0573	194.0602	-3.29	85.61
Gentisic acid	$C_7H_6O_4$	1.871	154.0266	154.0266	-0.28	96.75
2-Phenyl-4H-chromen-4-one	$C_{15}H_{10}O_2$	8.200	222.0732	222.0732	0.00	97.00

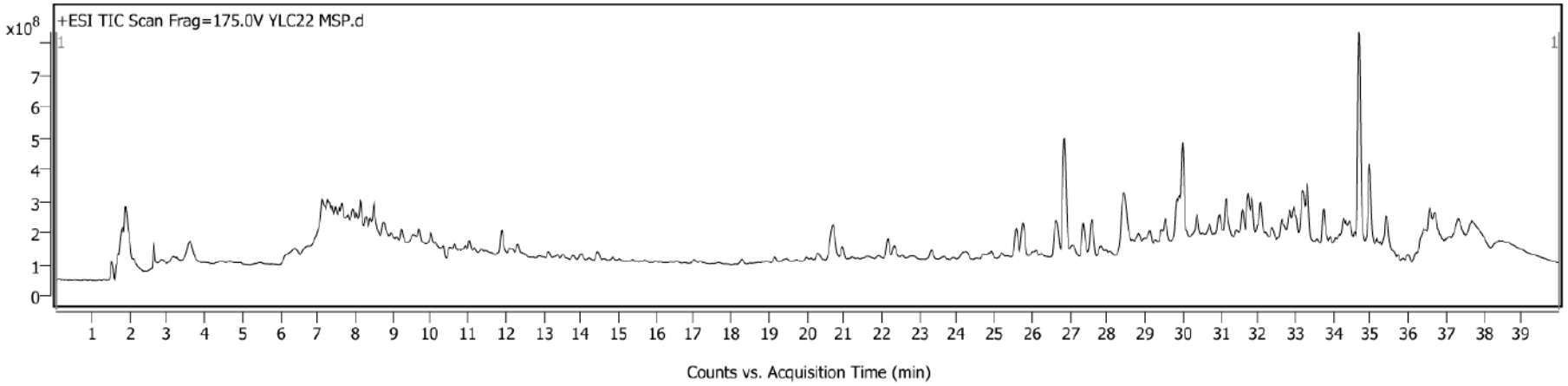


Figure 5.23: Total Ion Chromatogram (TIC) of methanolic extract of *Syzygium laetum* leaves by LC-MS QTOF Analysis

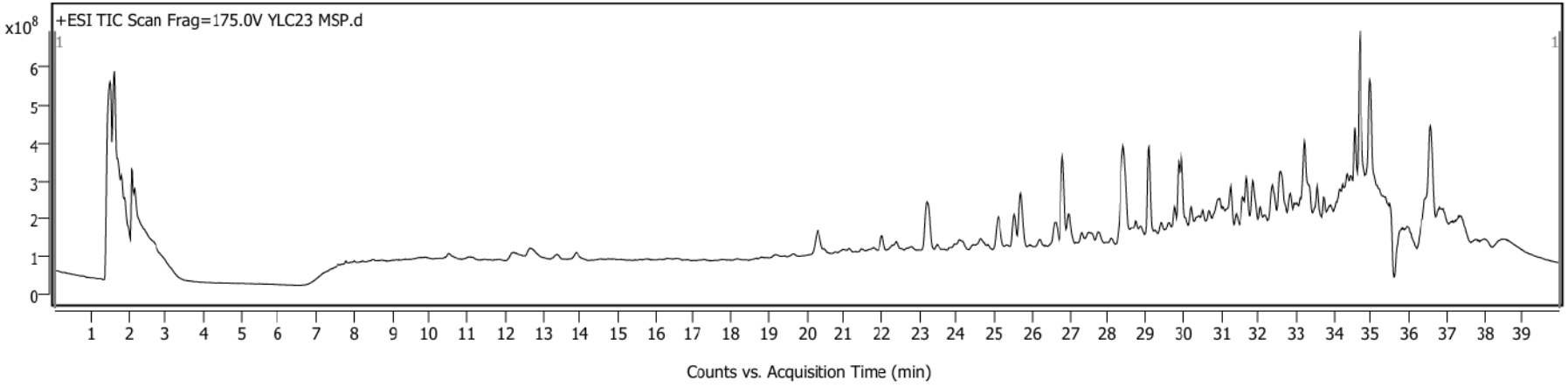


Figure 5.24: Total Ion Chromatogram (TIC) of methanolic extract of *Syzygium laetum* bark by LC-MS QTOF Analysis

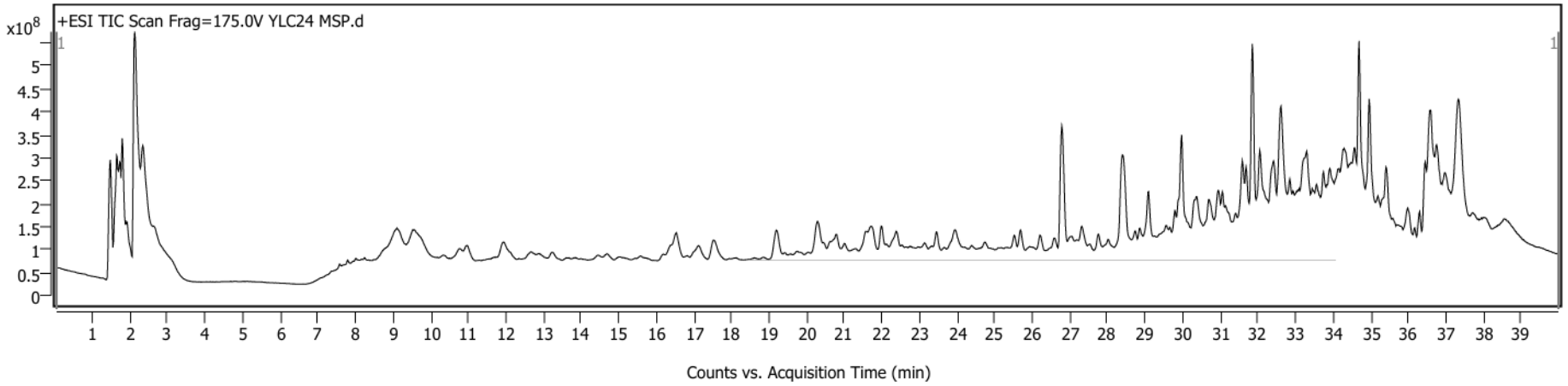


Figure 5.25: Total Ion Chromatogram (TIC) of methanolic extract of *Syzygium occidentale* leaves by LC-MS QTOF Analysis

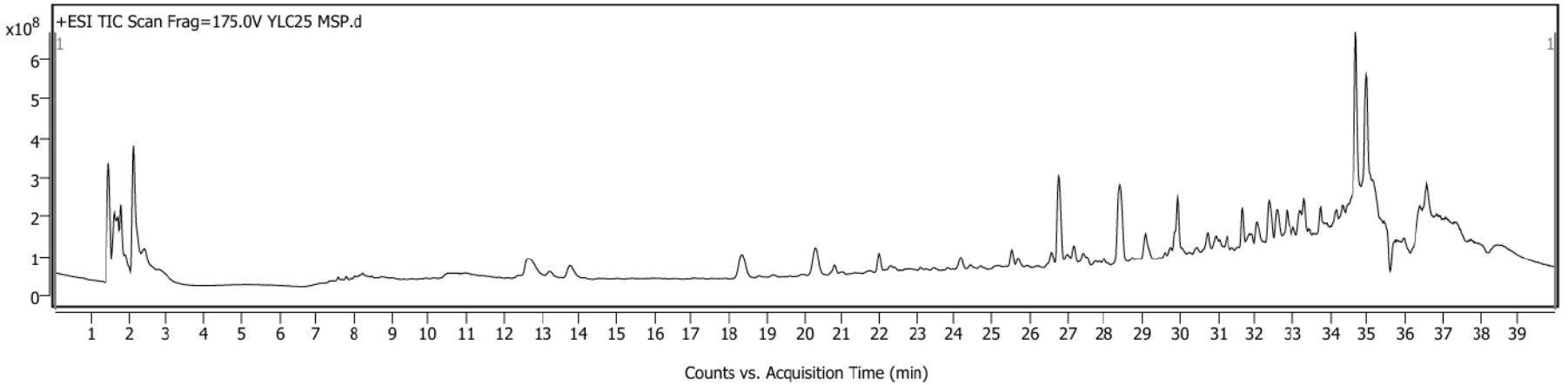


Figure 5.26: Total Ion Chromatogram (TIC) of methanolic extract of *Syzygium occidentale* bark by LC-MS QTOF Analysis

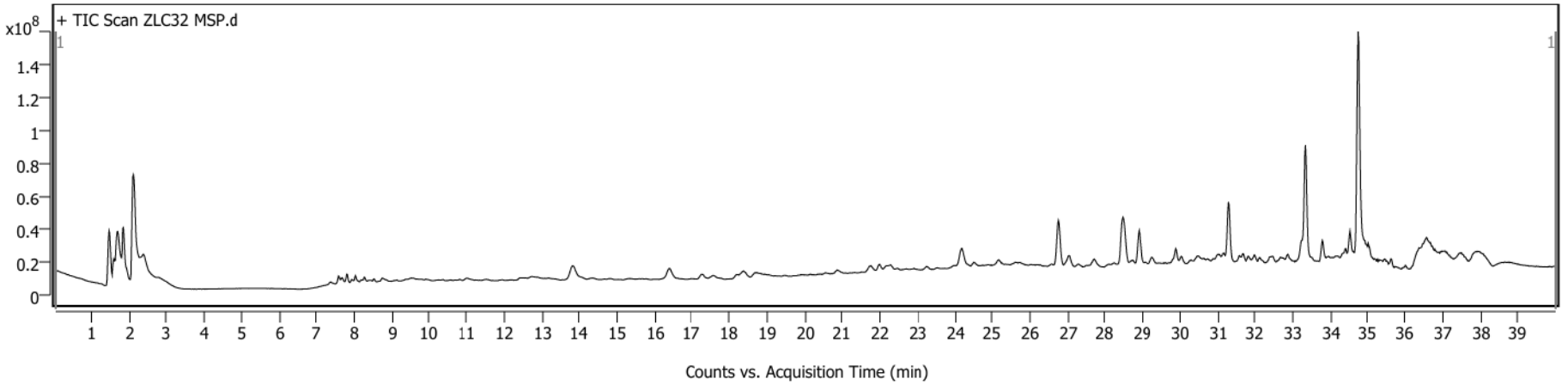


Figure 5.27: Total Ion Chromatogram (TIC) of methanolic extract of *Syzygium palghatense* leaves by LC-MS QTOF Analysis

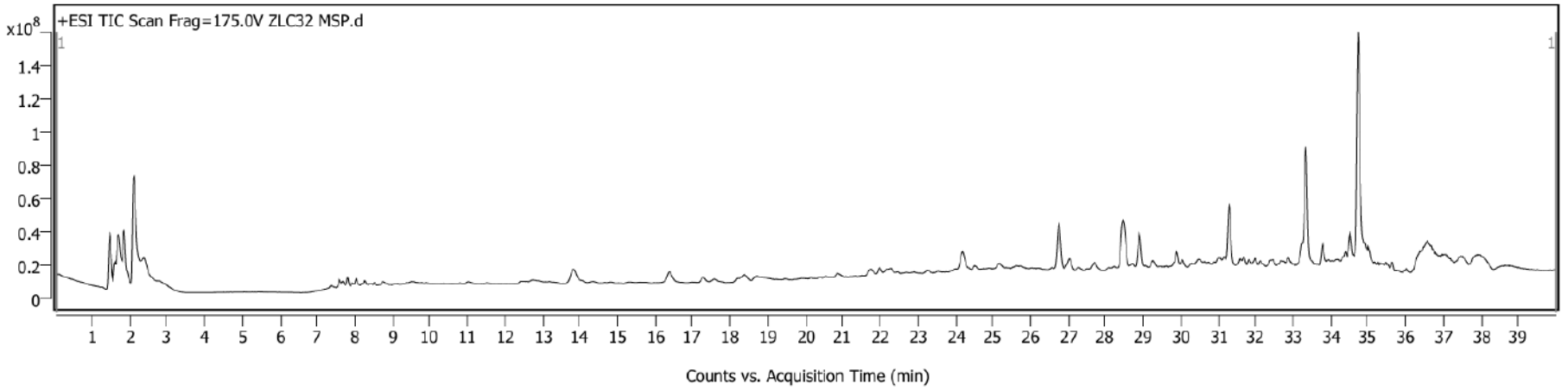
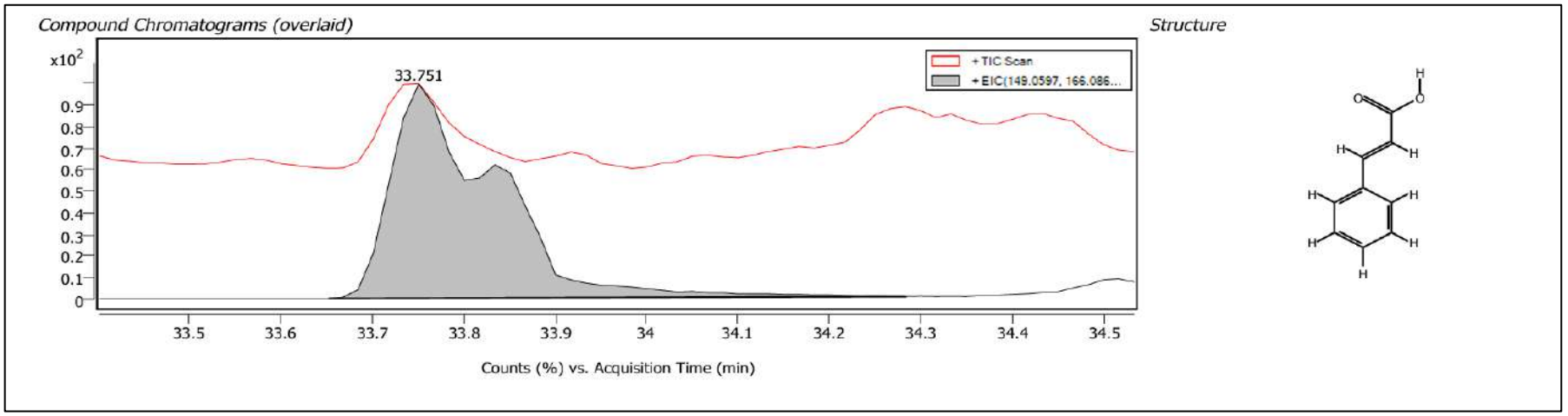
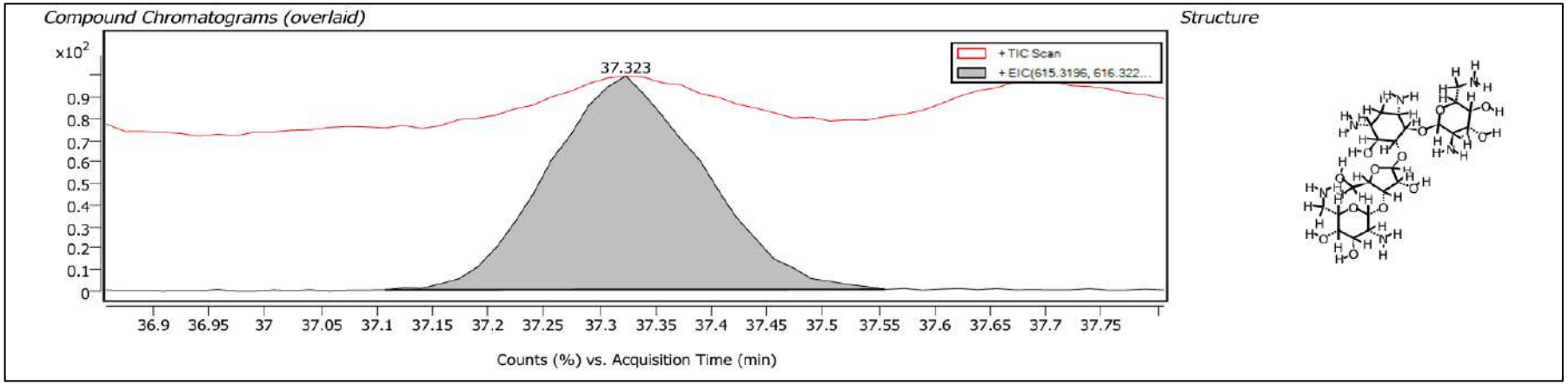


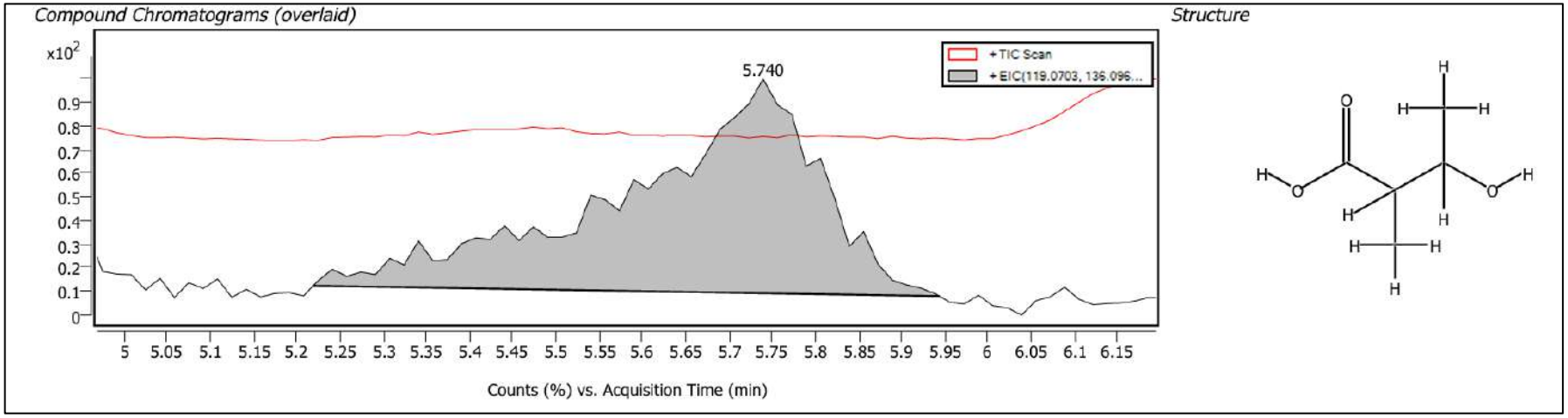
Figure 5.28: Total Ion Chromatogram (TIC) of methanolic extract of *Syzygium palghatense* bark by LC-MS QTOF Analysis



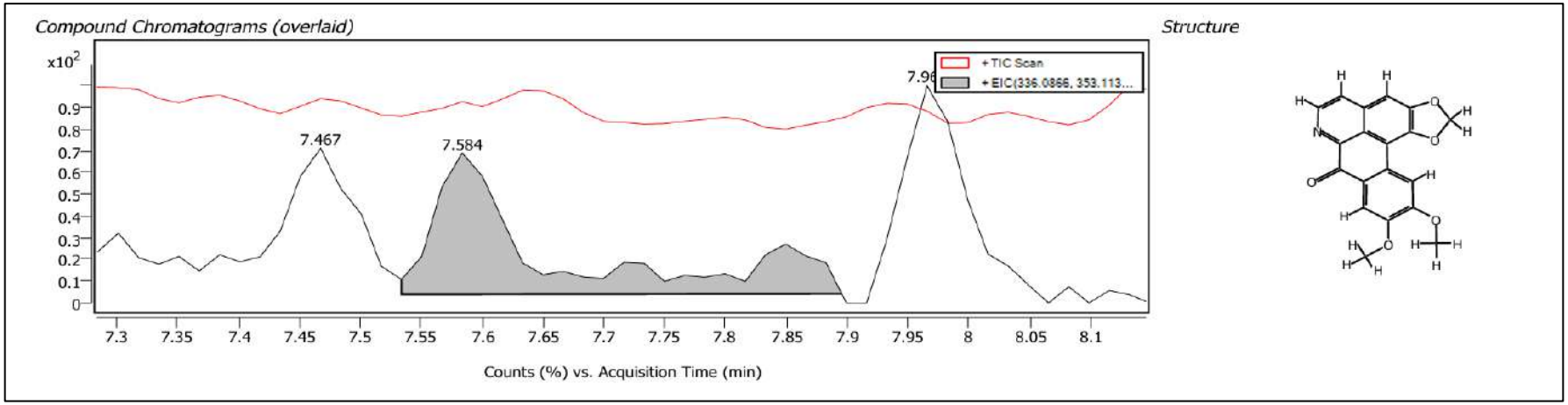
(a) Cinnamic acid



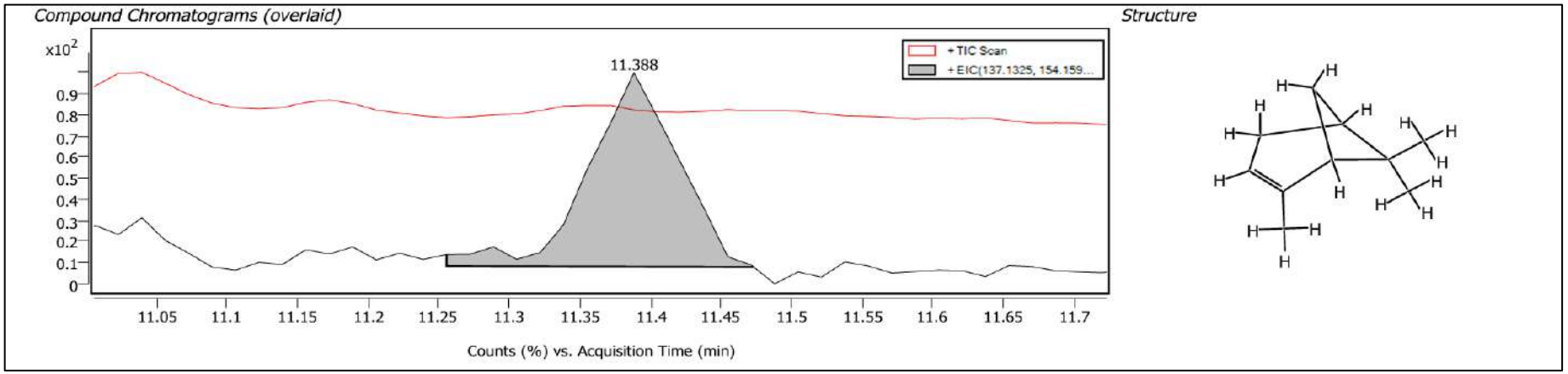
(b) Neomycin



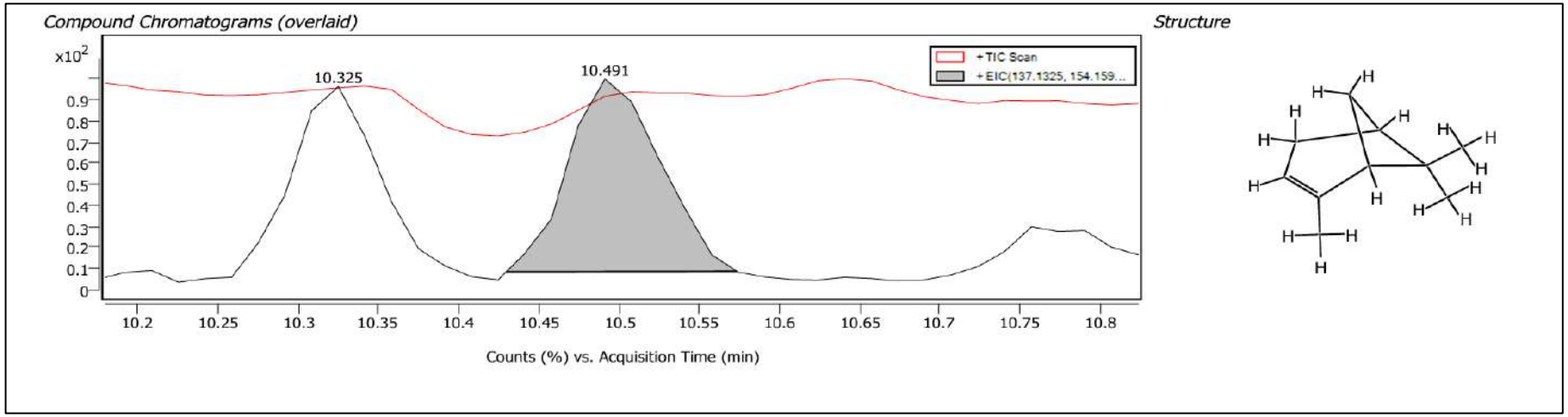
(c) 2-Methyl-3-hydroxybutyric acid



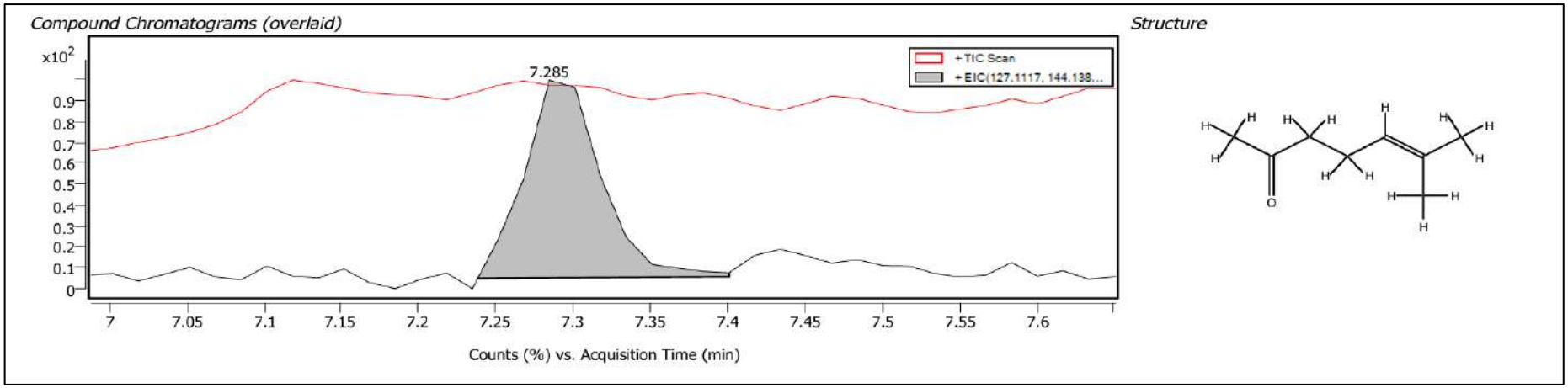
(d) Dicentrinone



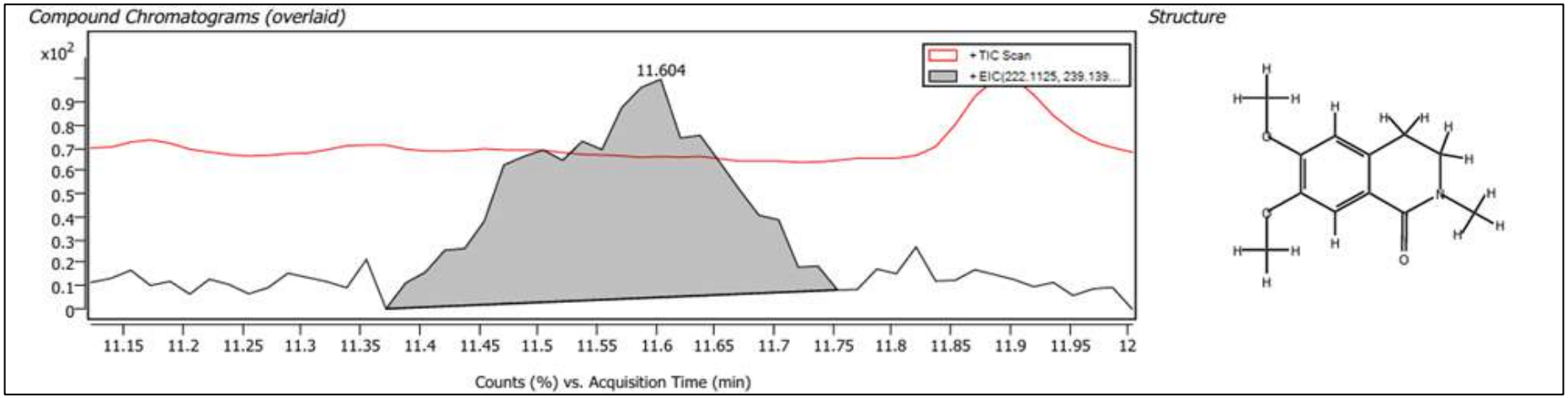
(e) Alpha-Pinene



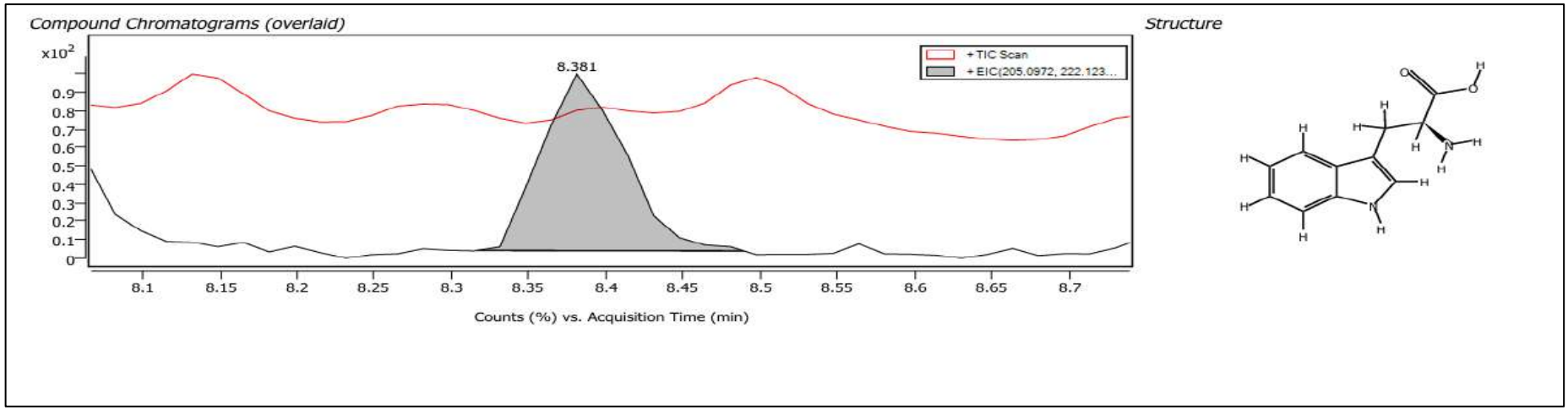
(f) Alpha-Pinene



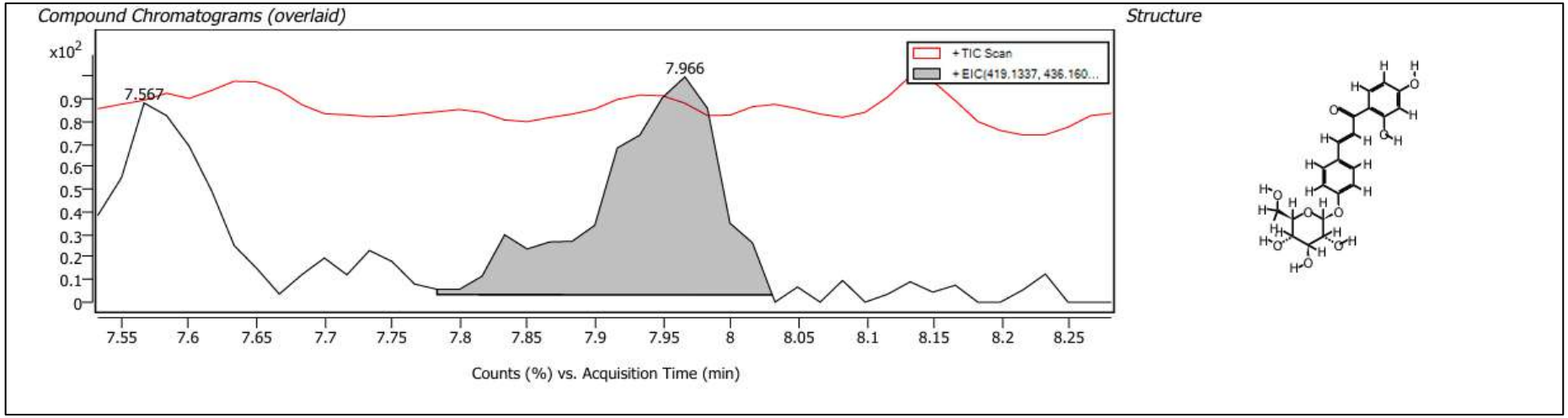
(g) 6-Methyl-5-hepten-2-one



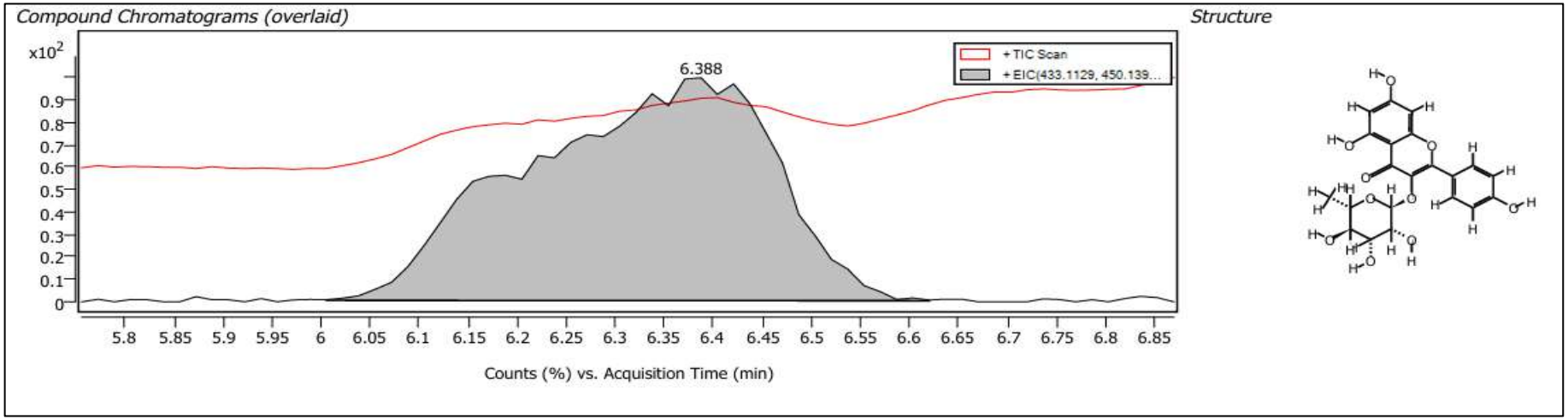
(h) N-Methylcorydaldin



(i) Tryptophan

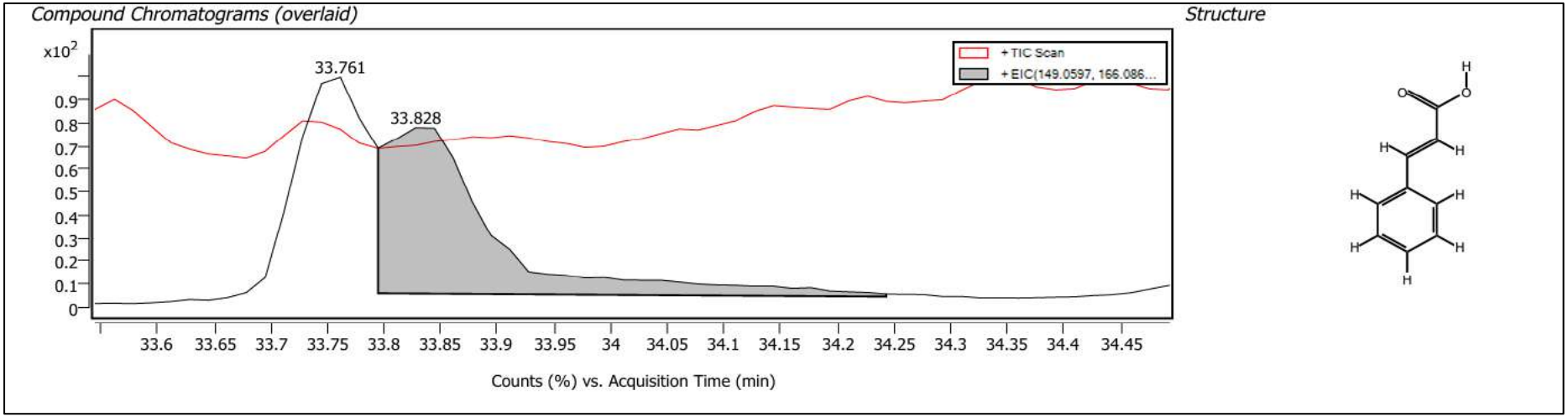


(j) Isoliquiritin

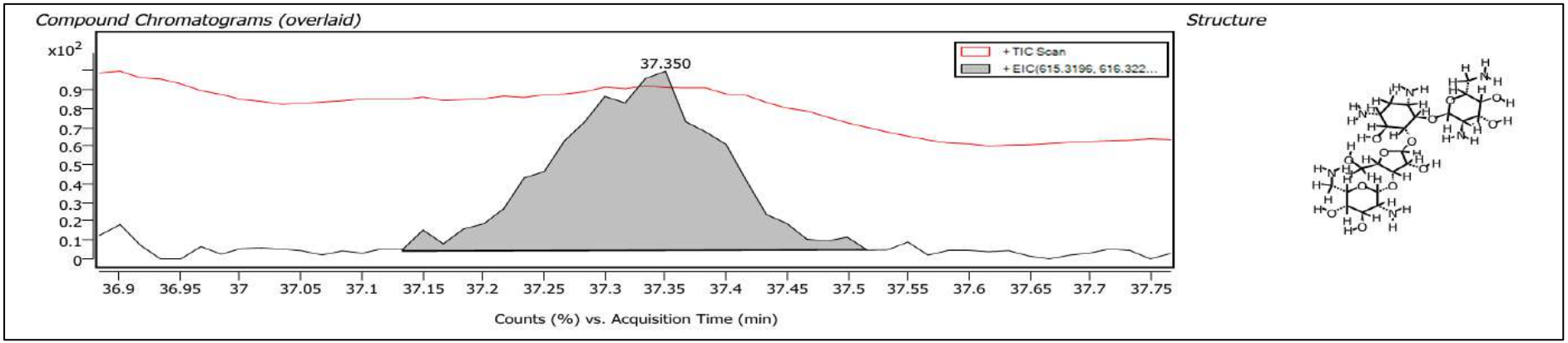


(k) Afzelin

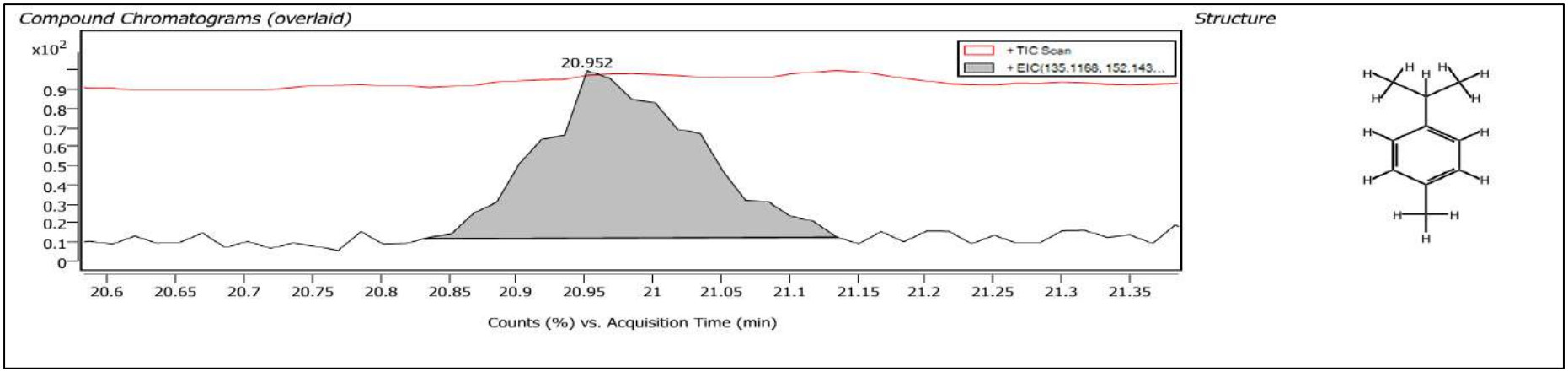
Figure 5.29: (a-k) Phytochemical constituents identified by LC-MS QTOF analysis of *Syzygium laetum* leaves



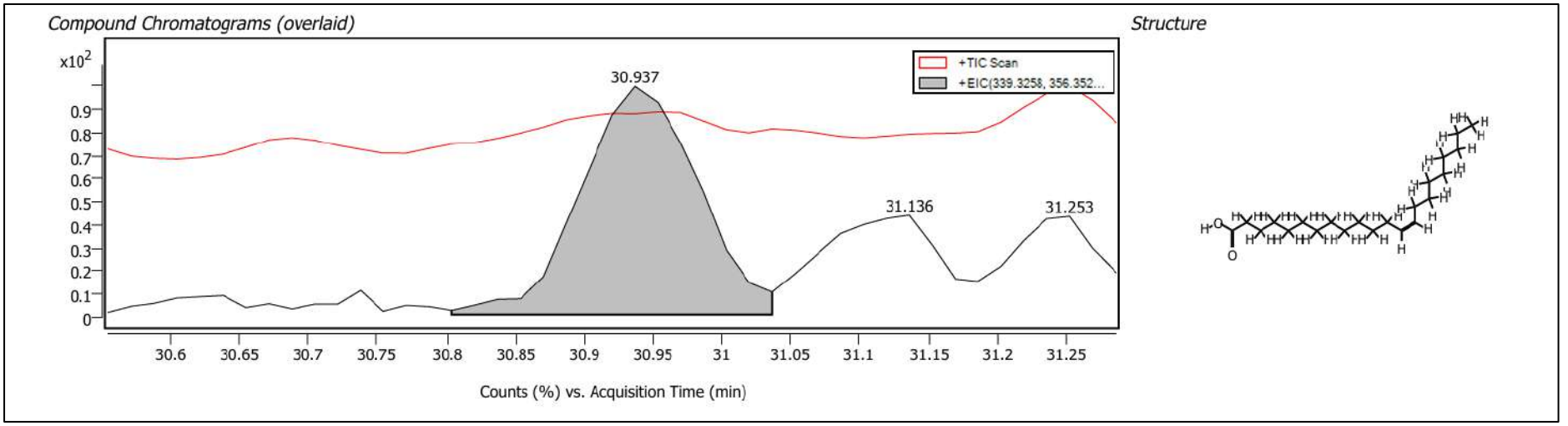
(a) Cinnamic acid



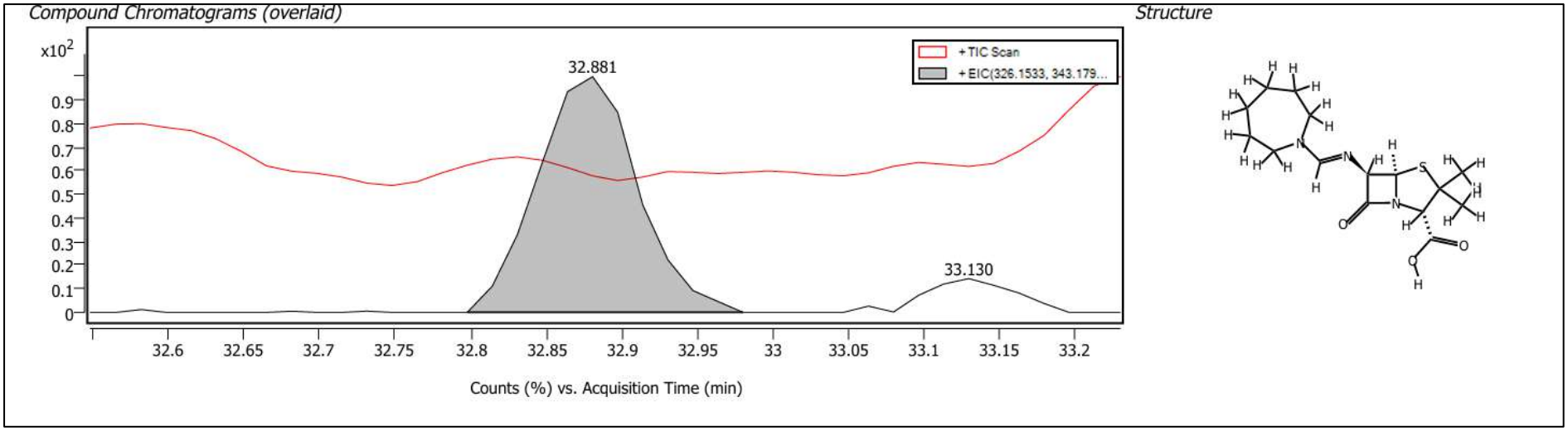
(b) Neomycin



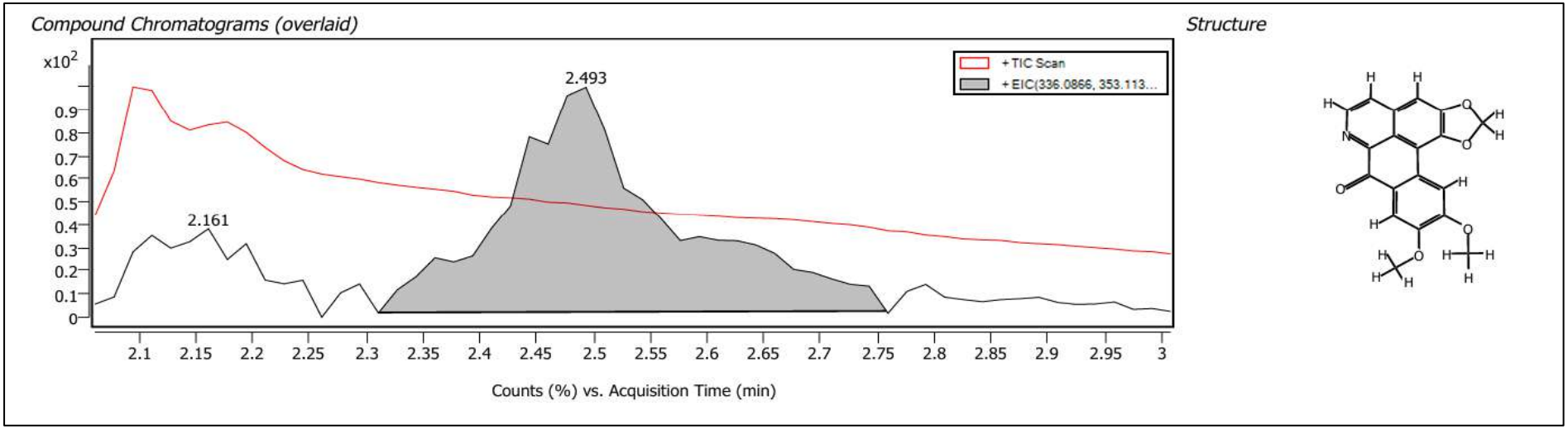
(c) p-Cymene



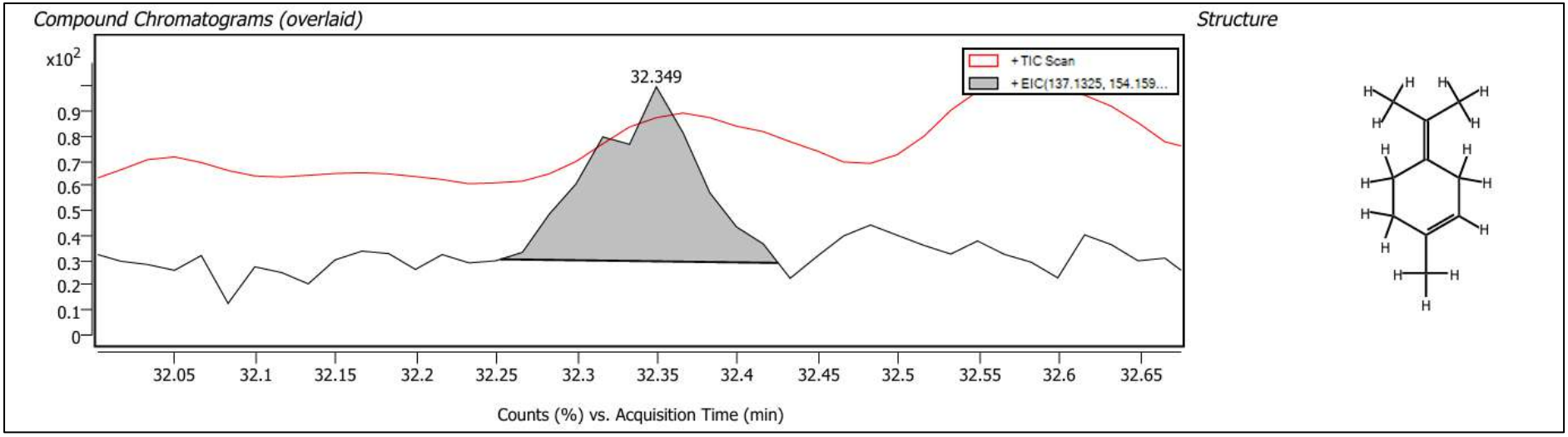
(d) Erucic acid



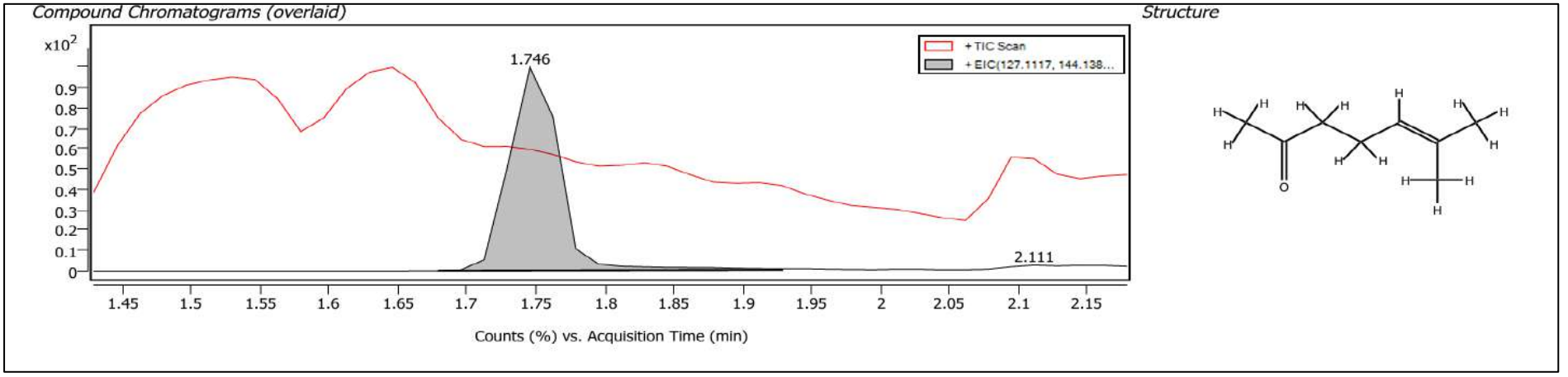
(e) Mecillinam



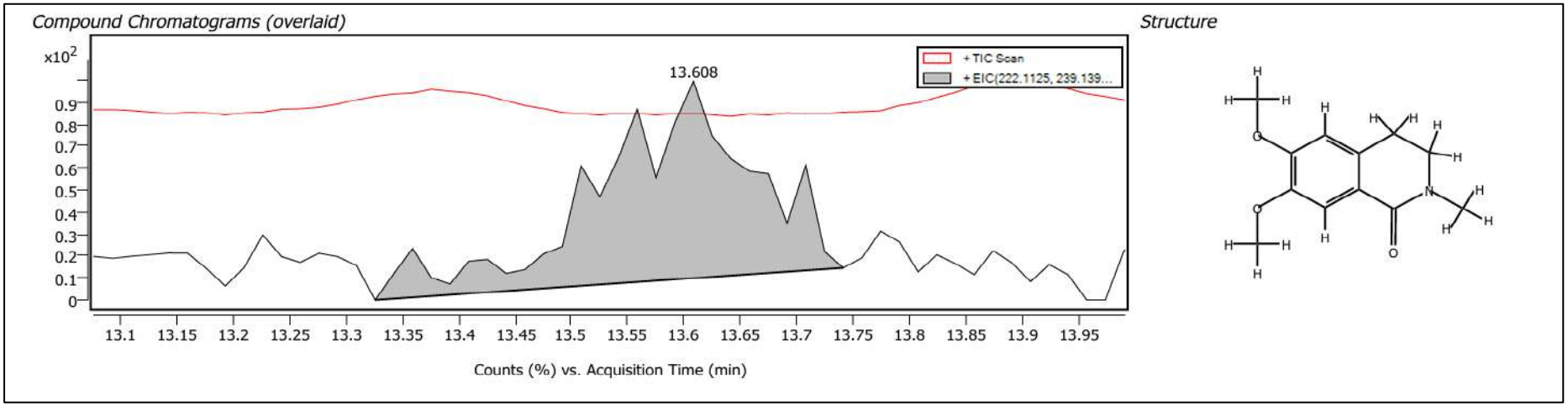
(f) Dicentrinone



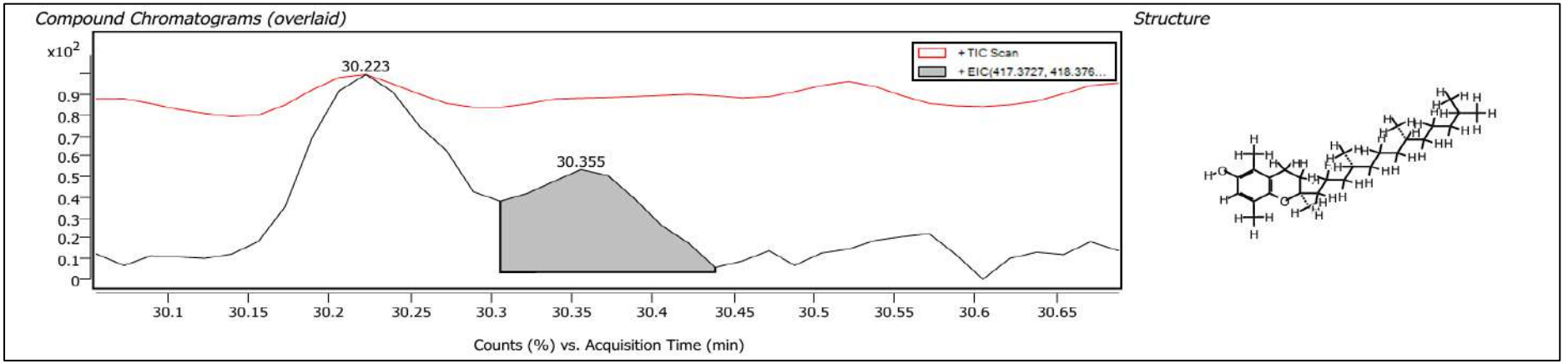
(g) Terpinolene



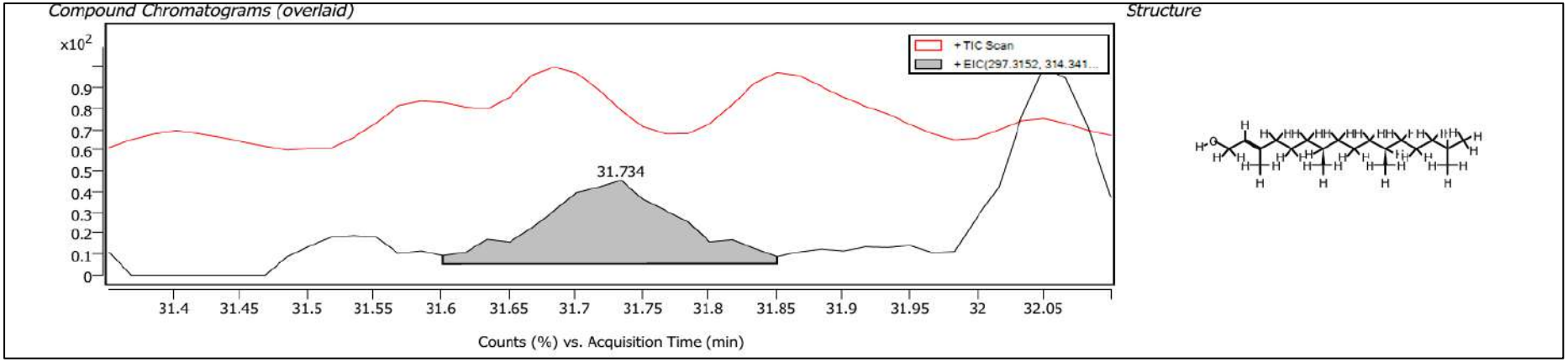
(h) 6-Methyl-5-hepten-2-one



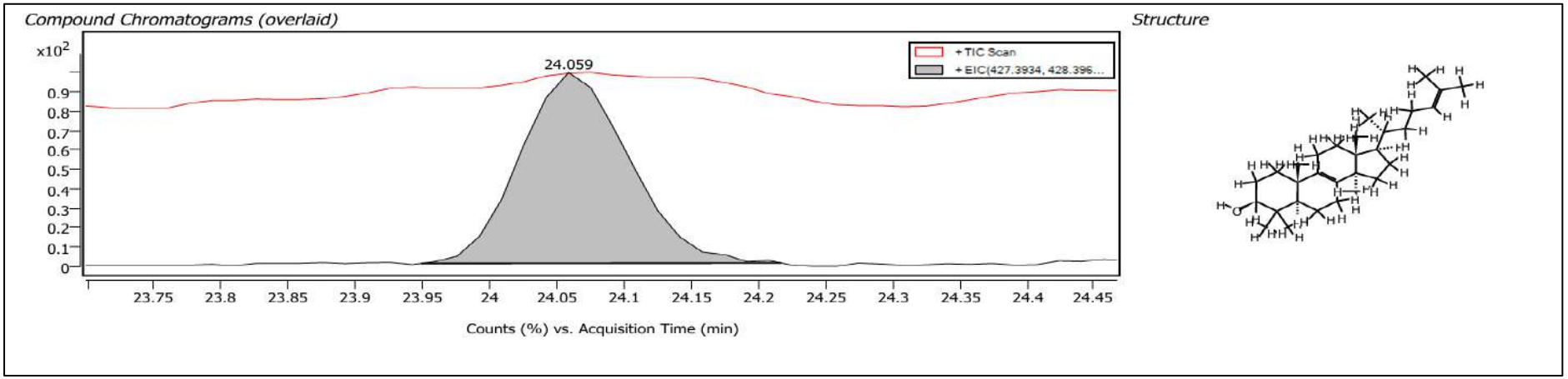
(i) N-Methylcorydaldine



(j) beta-Tocopherol

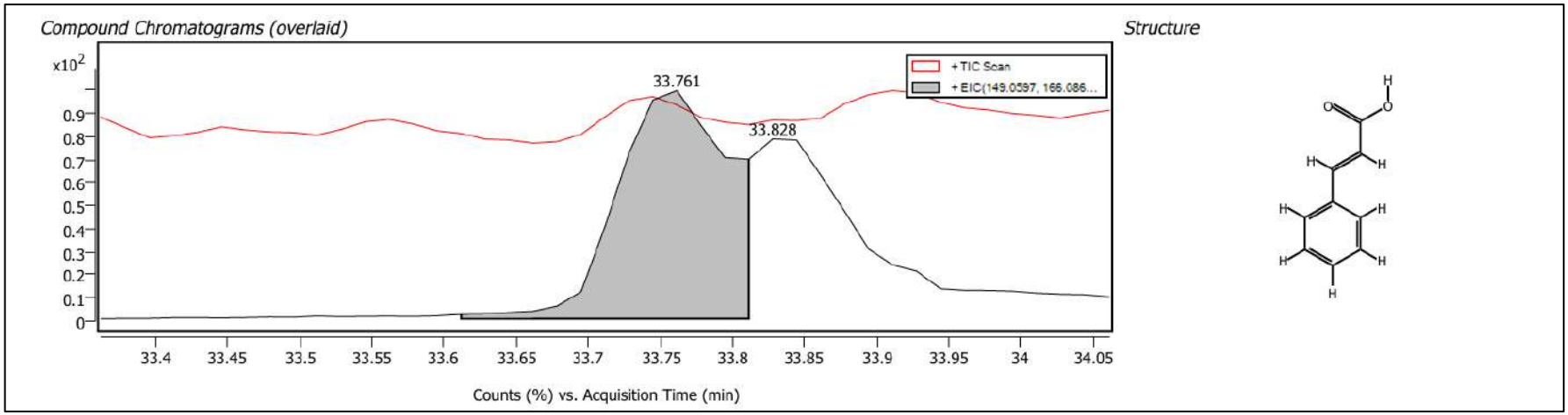


(k) Phytol

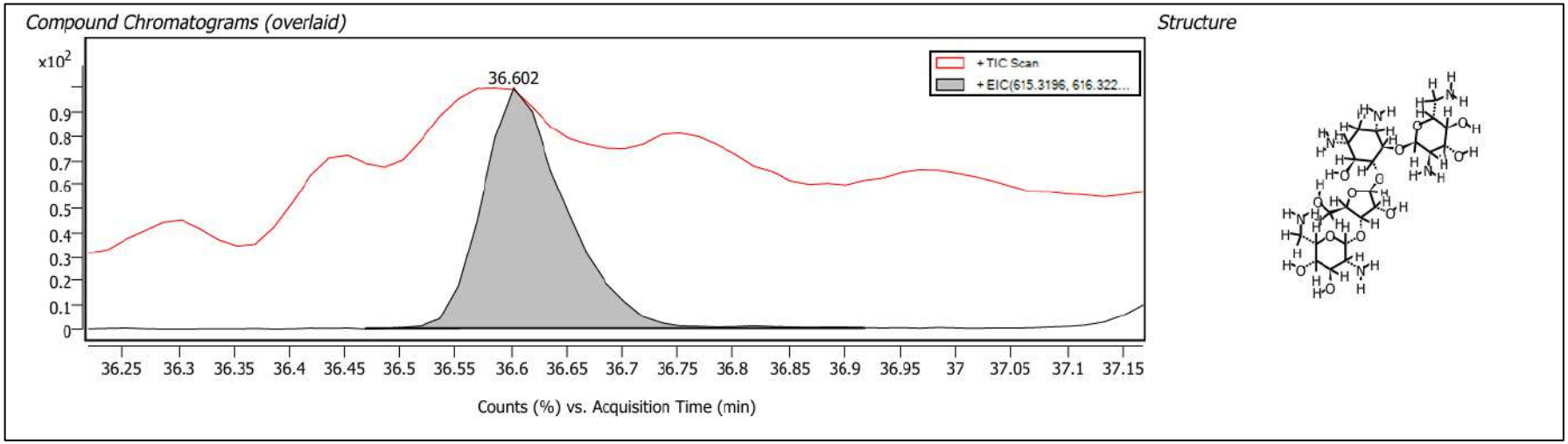


(l) Lanosterol

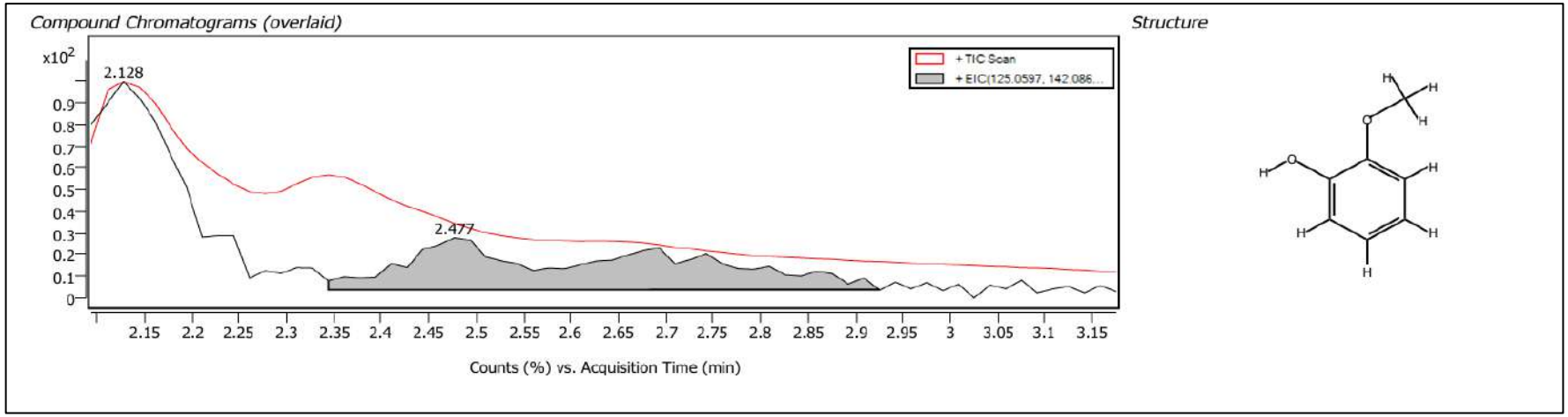
Figure 5.30: (a-l) Phytochemical constituents identified by LC-MS QTOF analysis of *Syzygium laetum* bark



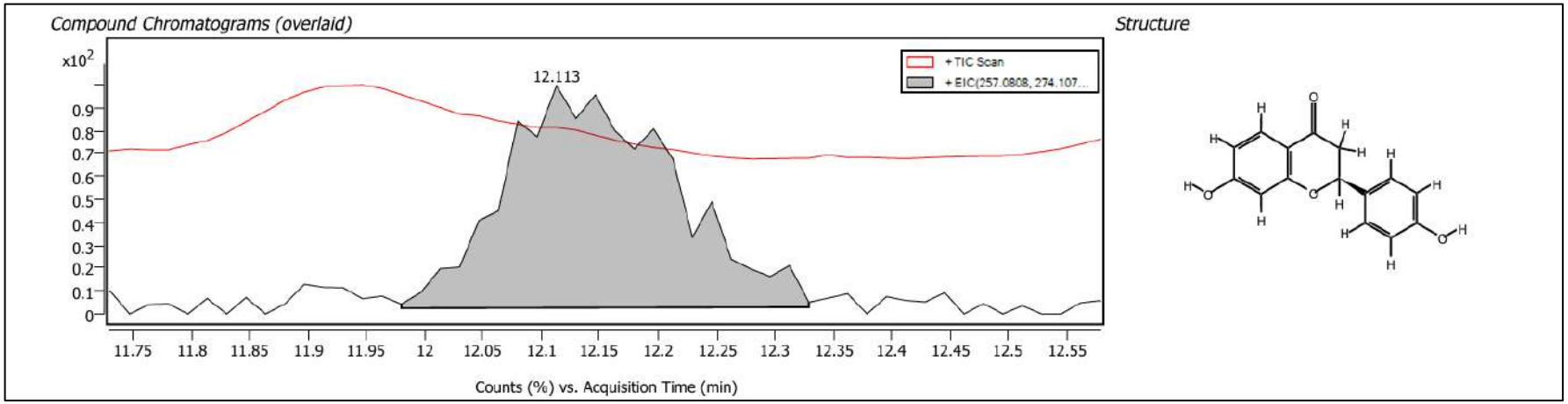
(a) Cinnamic acid



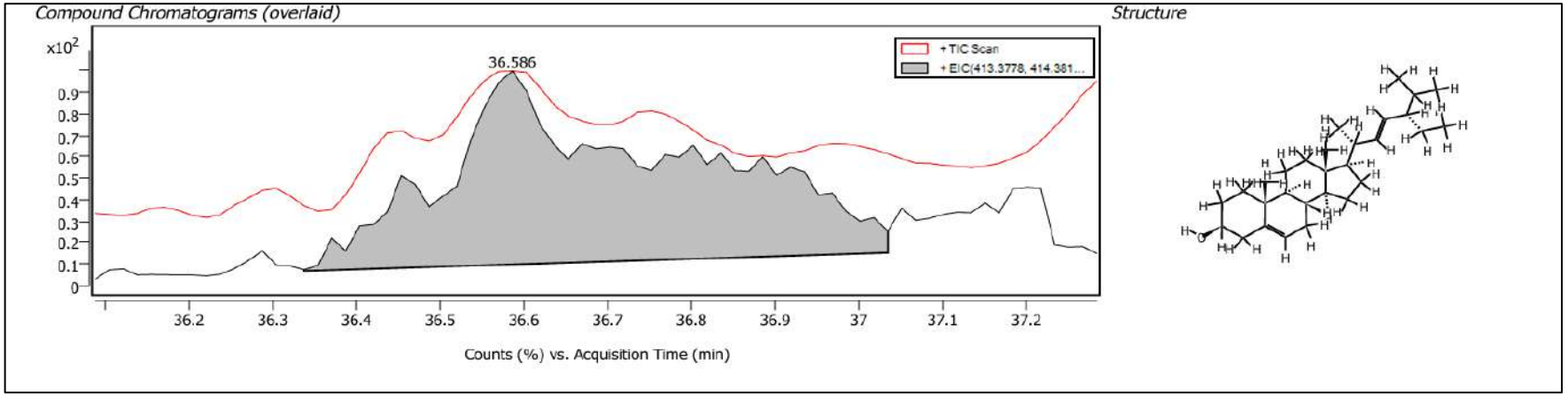
(b) Neomycin



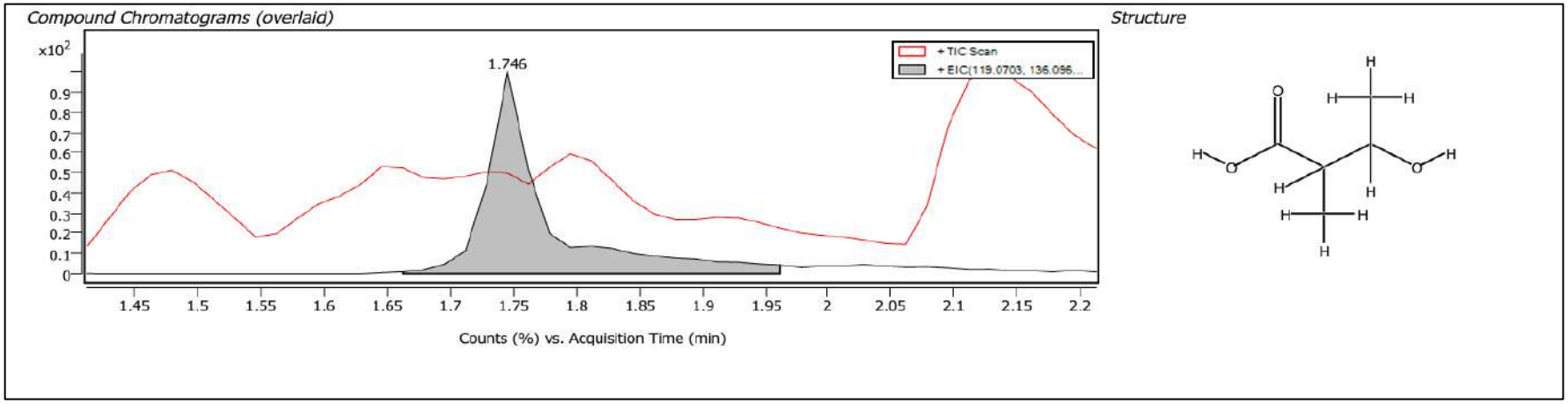
(c) Guaiacol



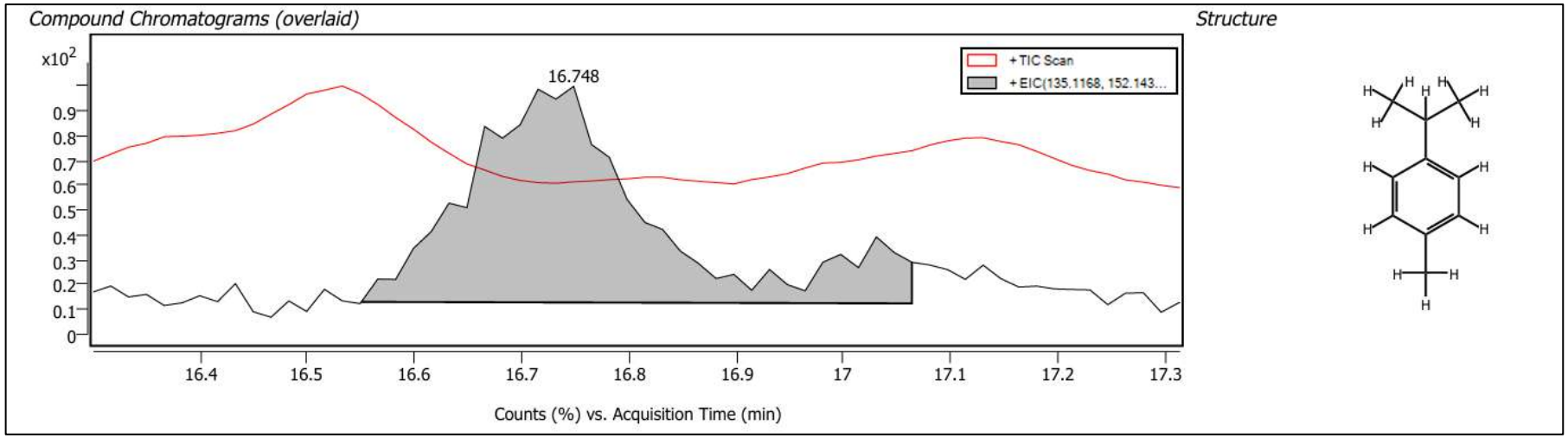
(d) Liquiritigenin



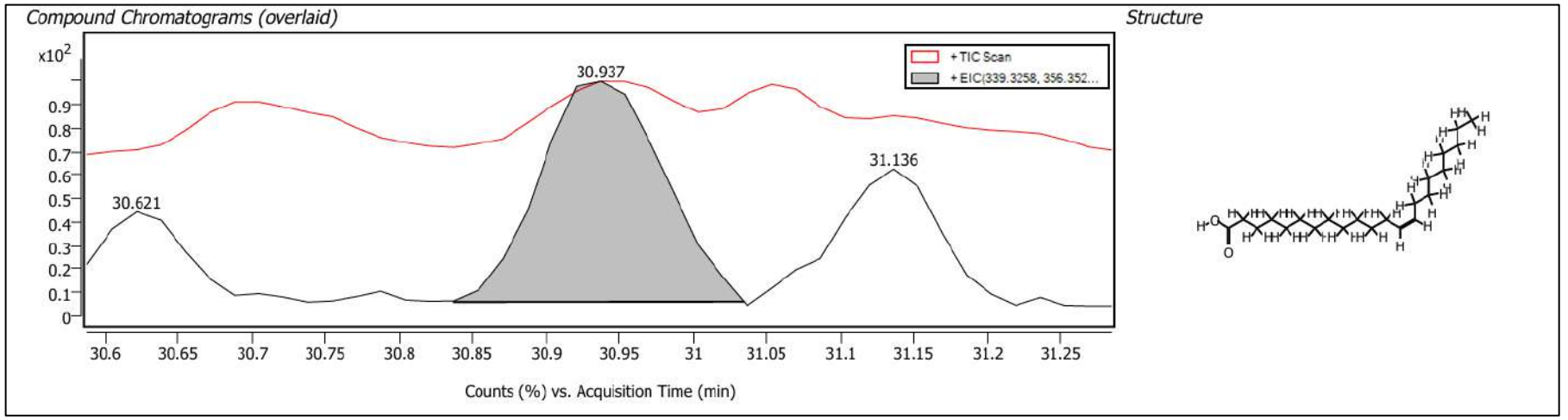
(e) Stigmasterol



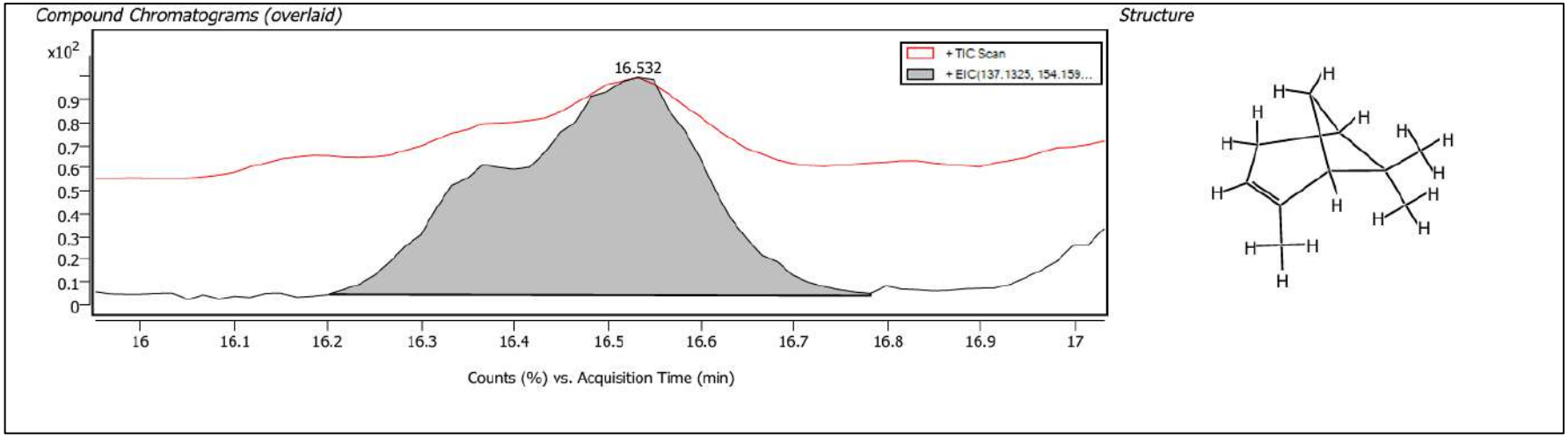
(f) 2-Methyl-3-hydroxybutyric acid



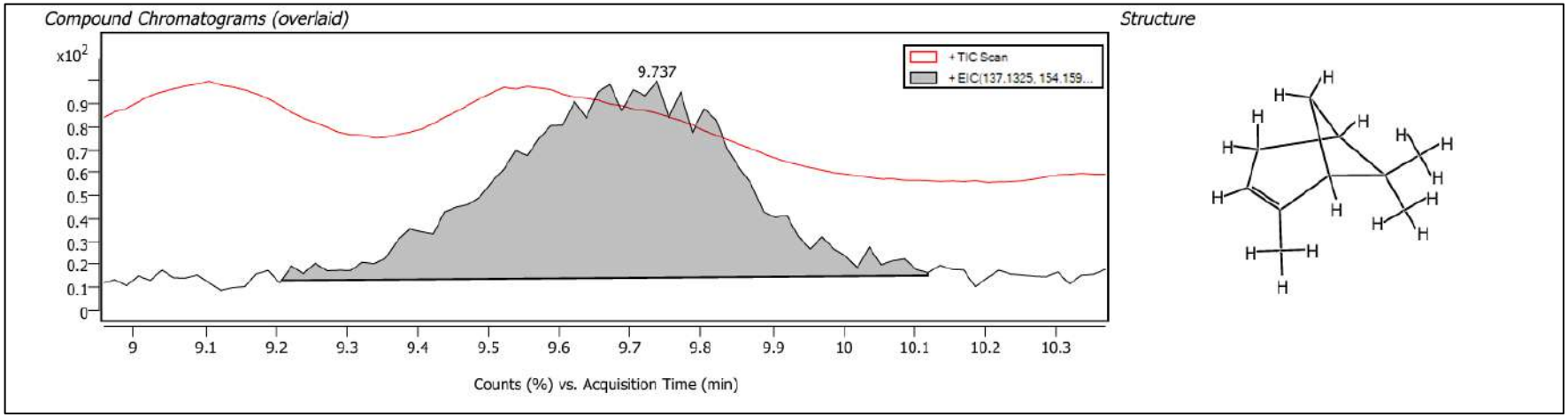
(g) p-Cymene



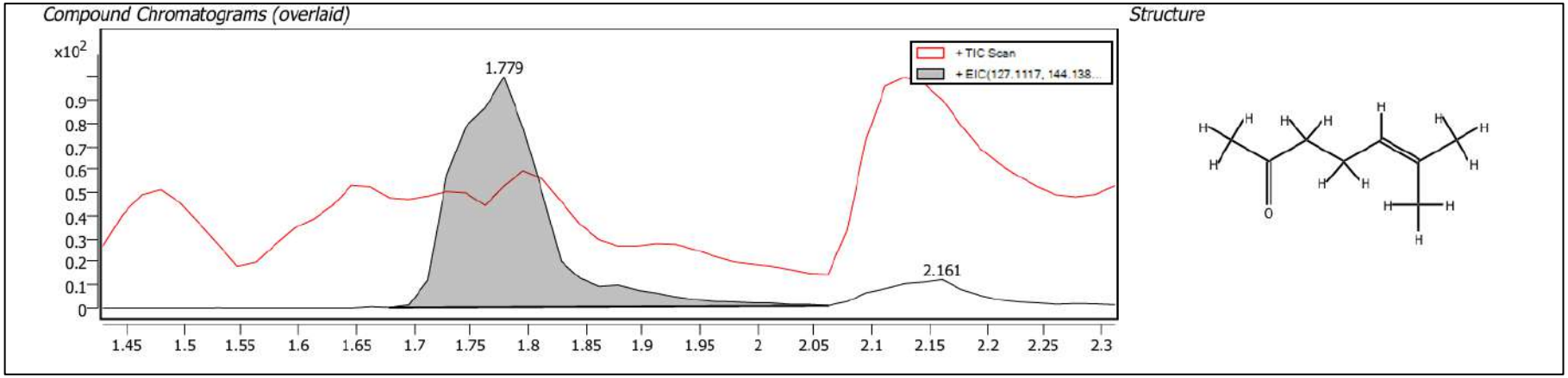
(h) Erucic acid



(i) alpha-Pinene

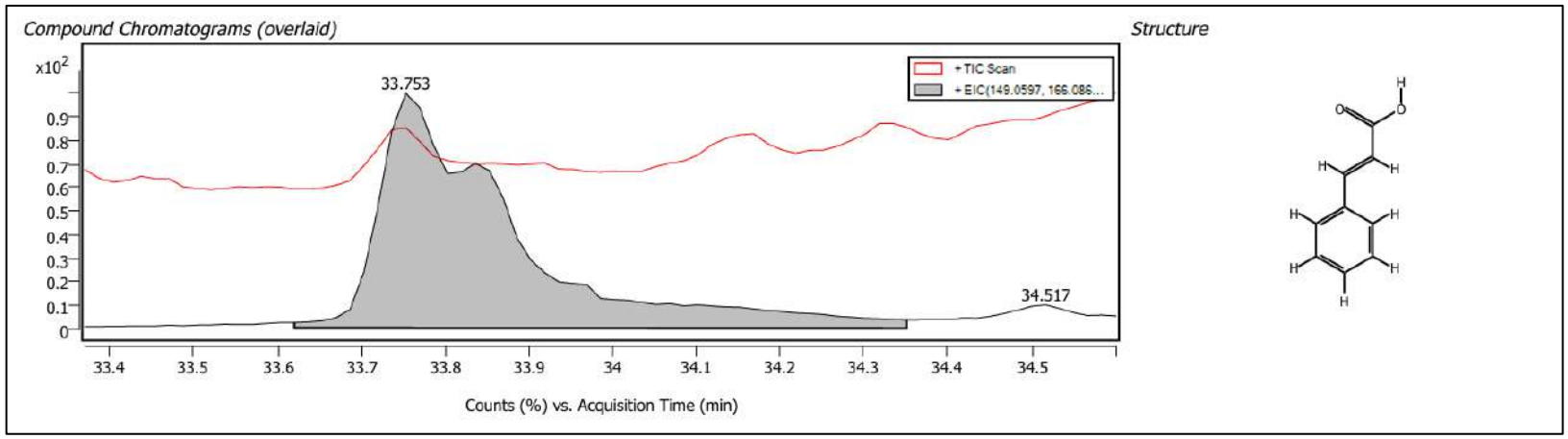


(j) alpha-Pinene

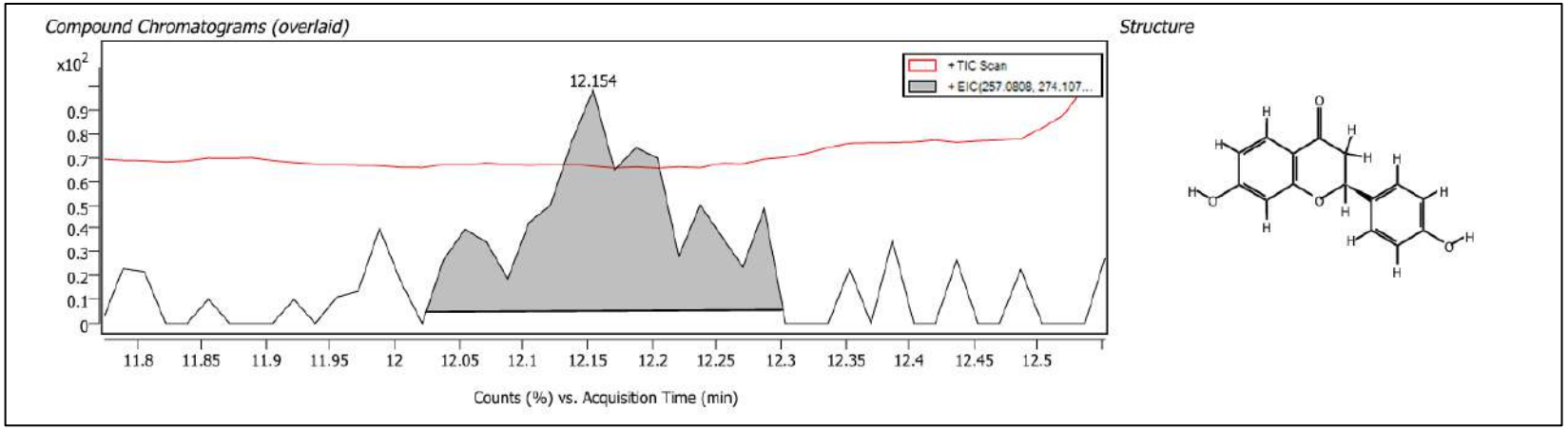


(k) 6-Methyl-5-hepten-2-one

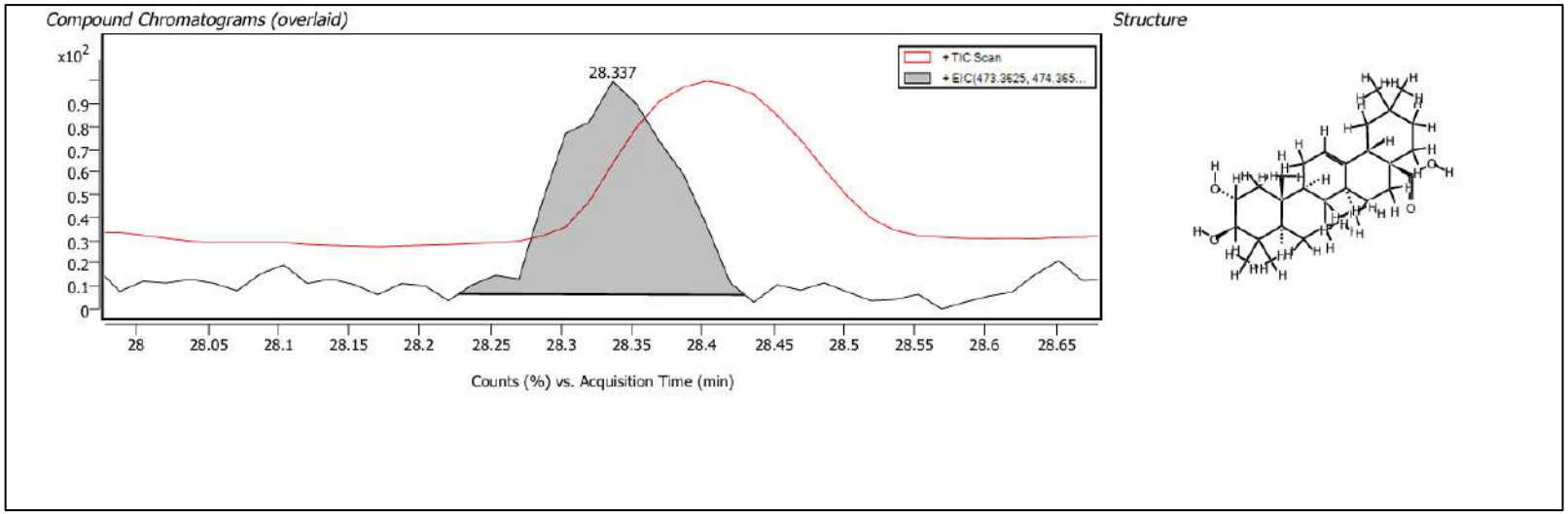
Figure 5.31: (a-k) Phytochemical constituents identified by LC-MS QTOF analysis of *Syzygium occidentale* leaves



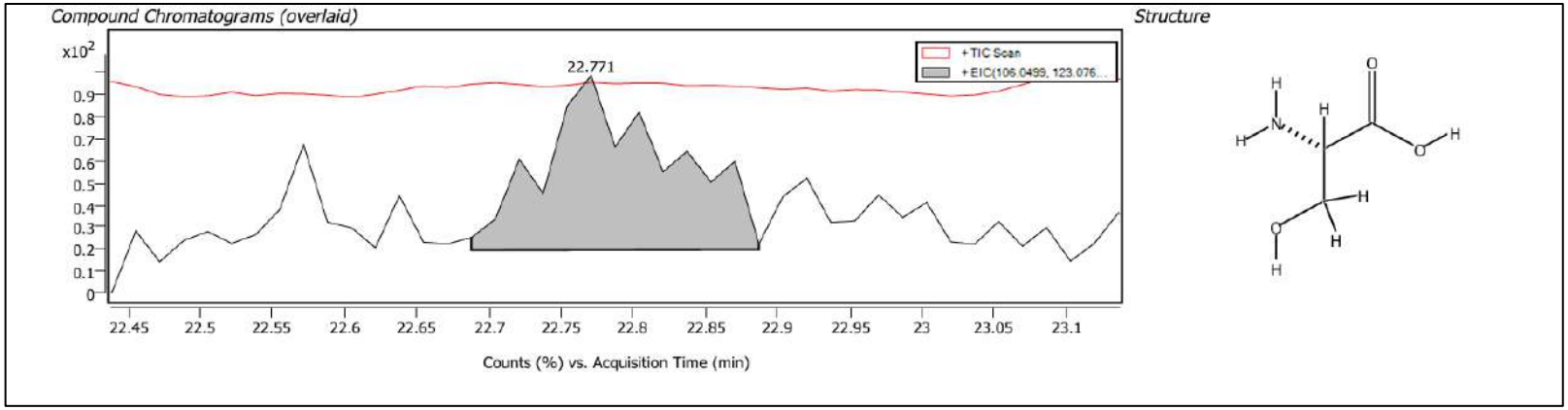
(a) Cinnamic acid



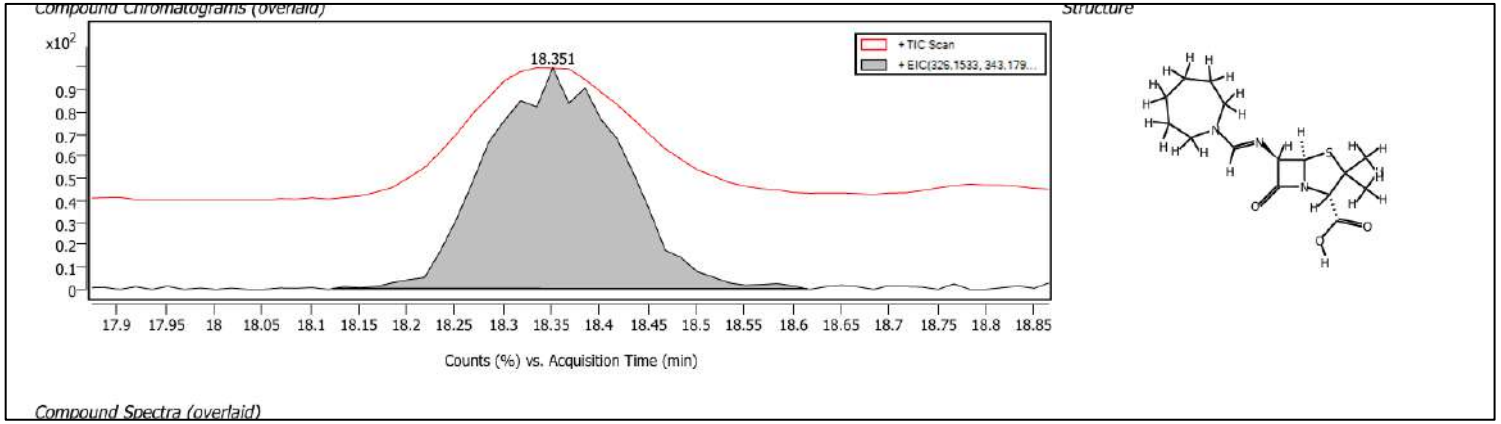
(b) Liquiritigenin



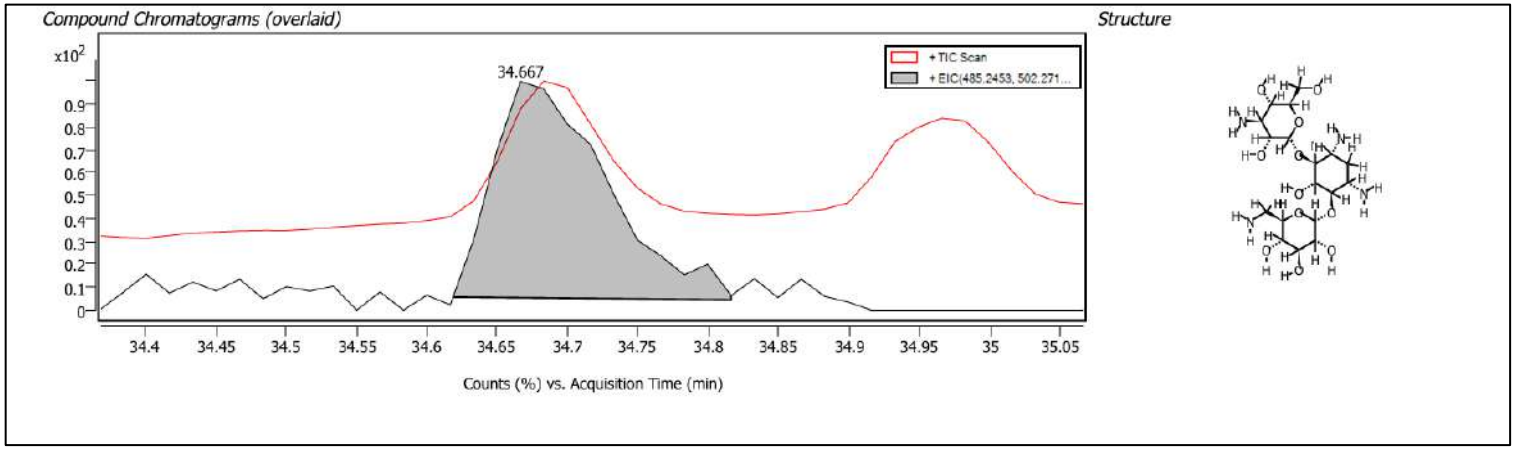
(c) Maslinic acid



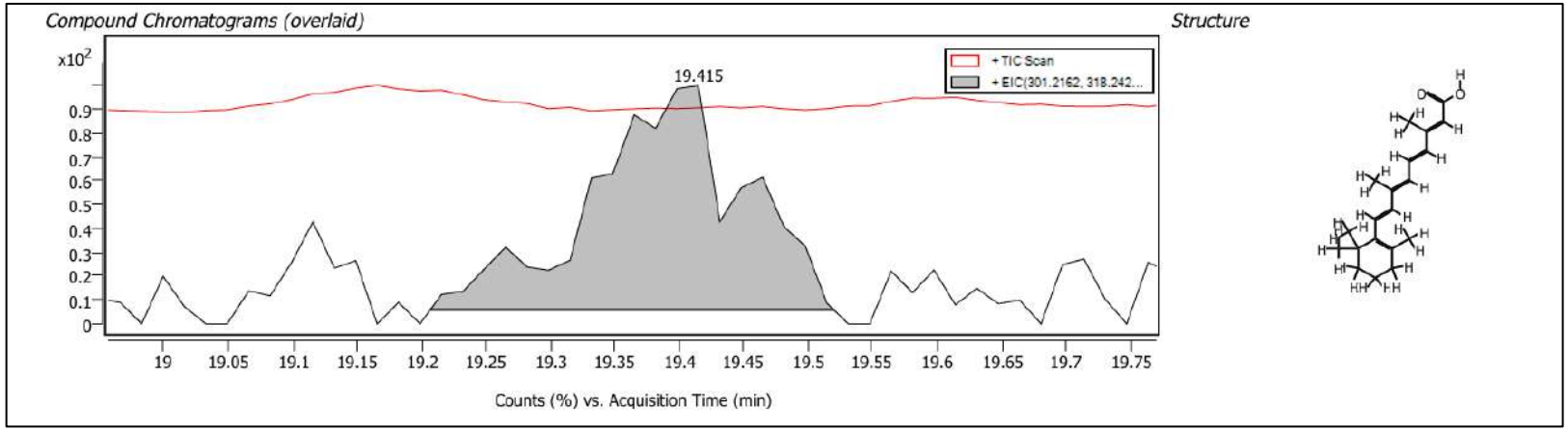
(d) Serine



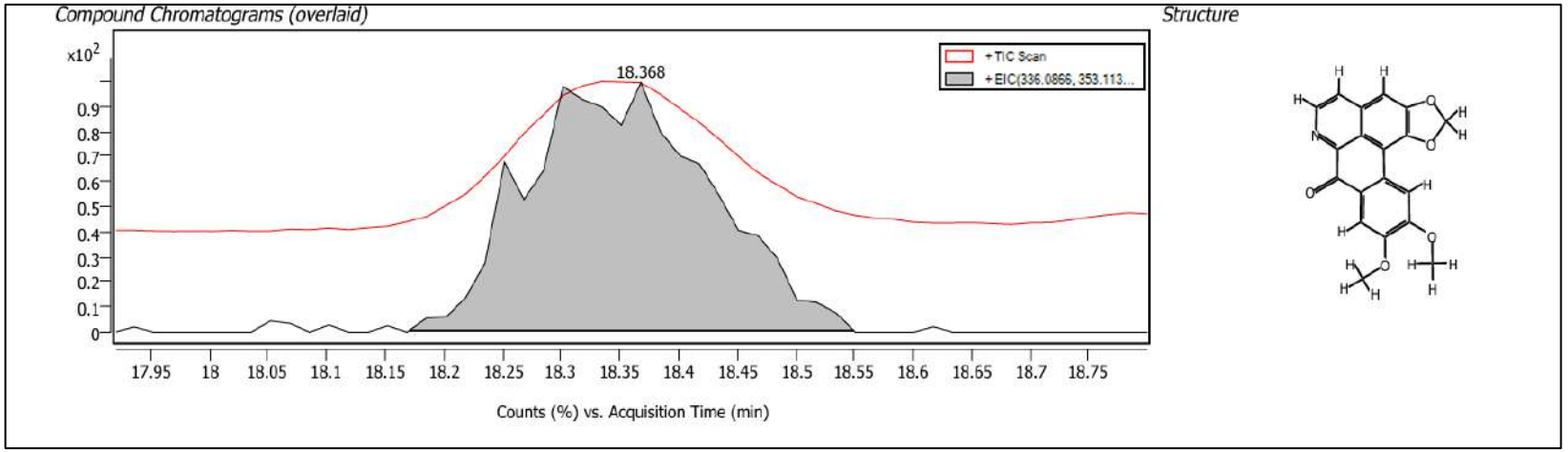
(e) Mecillinam



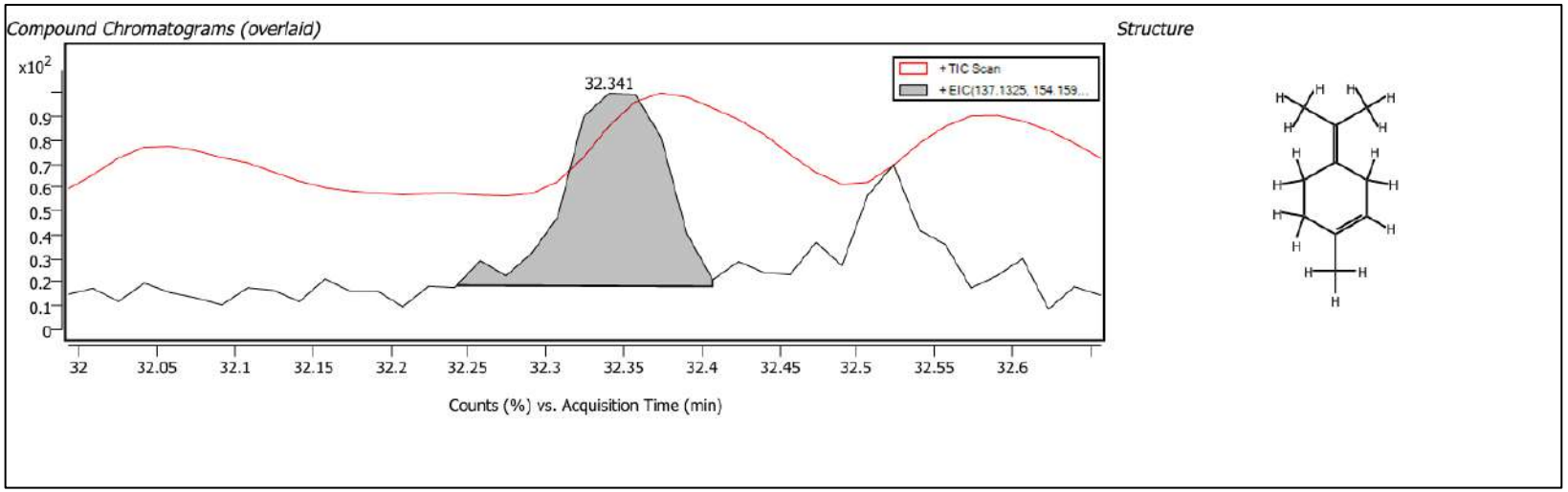
(f) Kanamycin



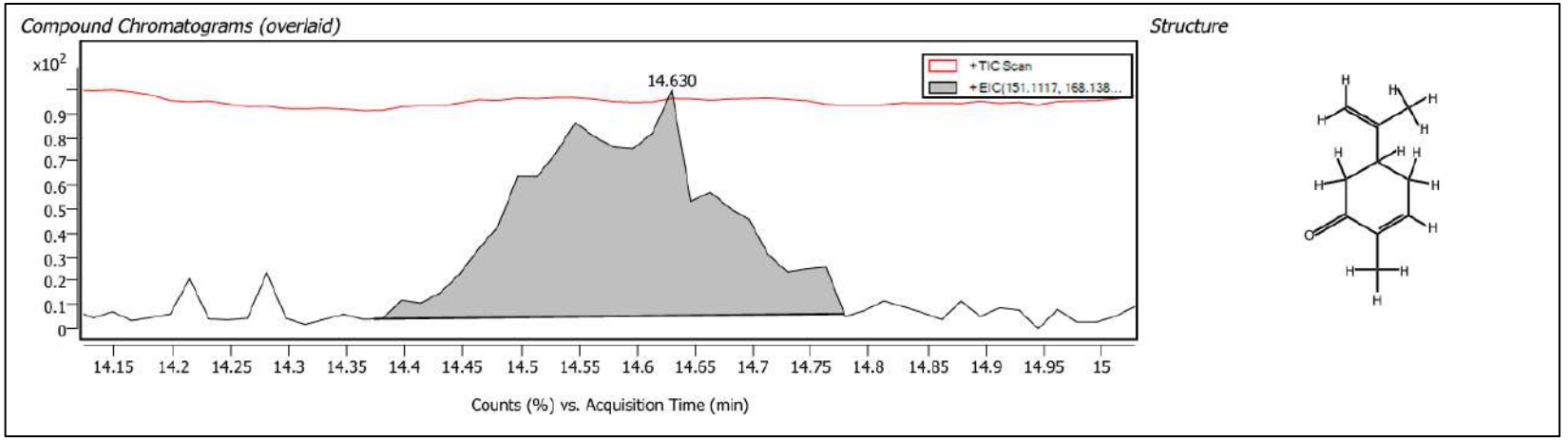
(g) Tretinoin



(h) Dicentrinone

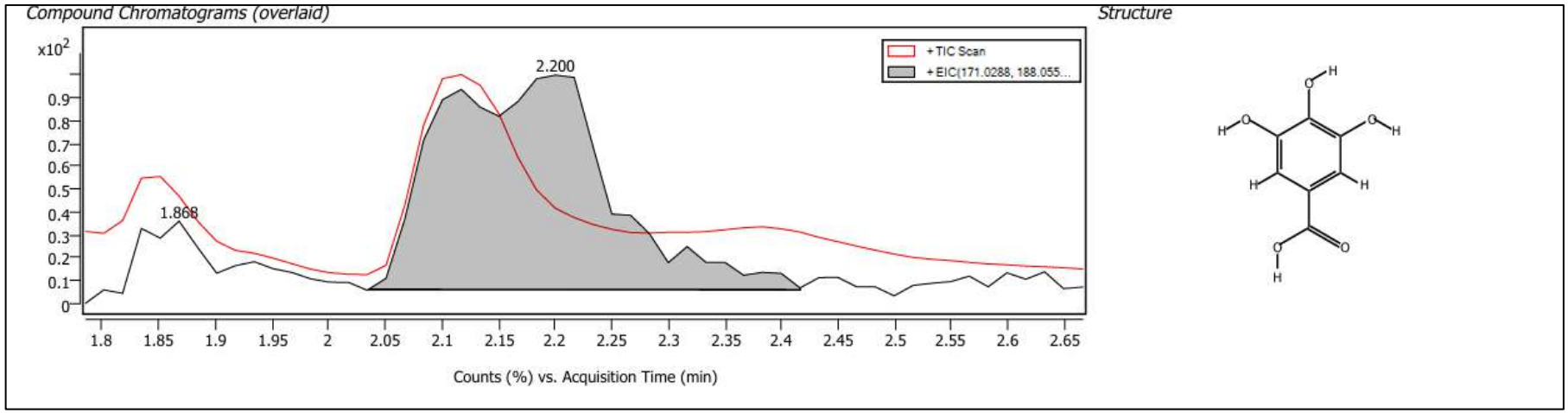


(i) Terpinolene

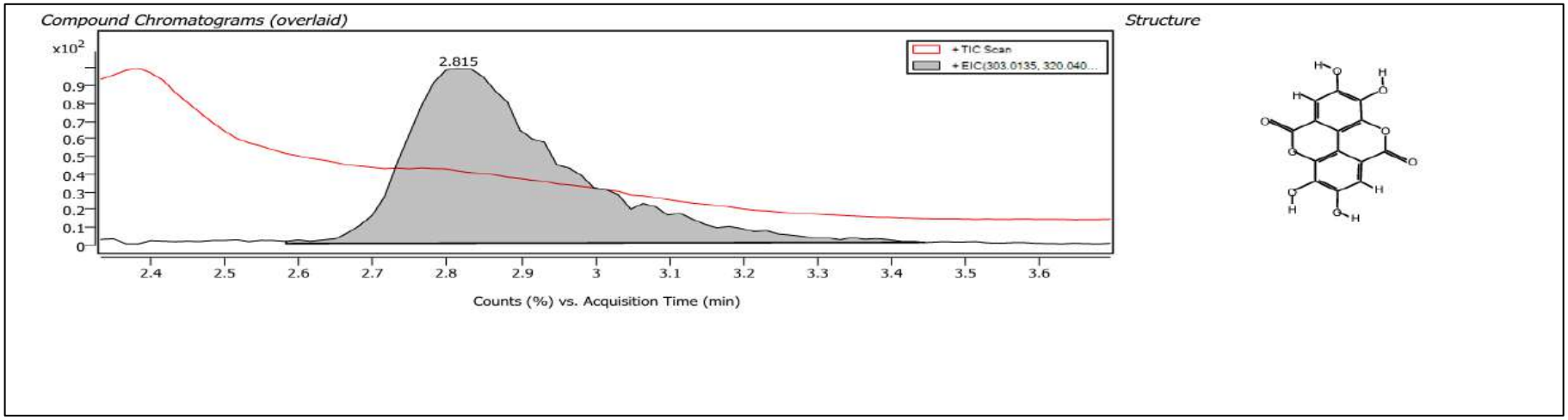


(j) Carvone

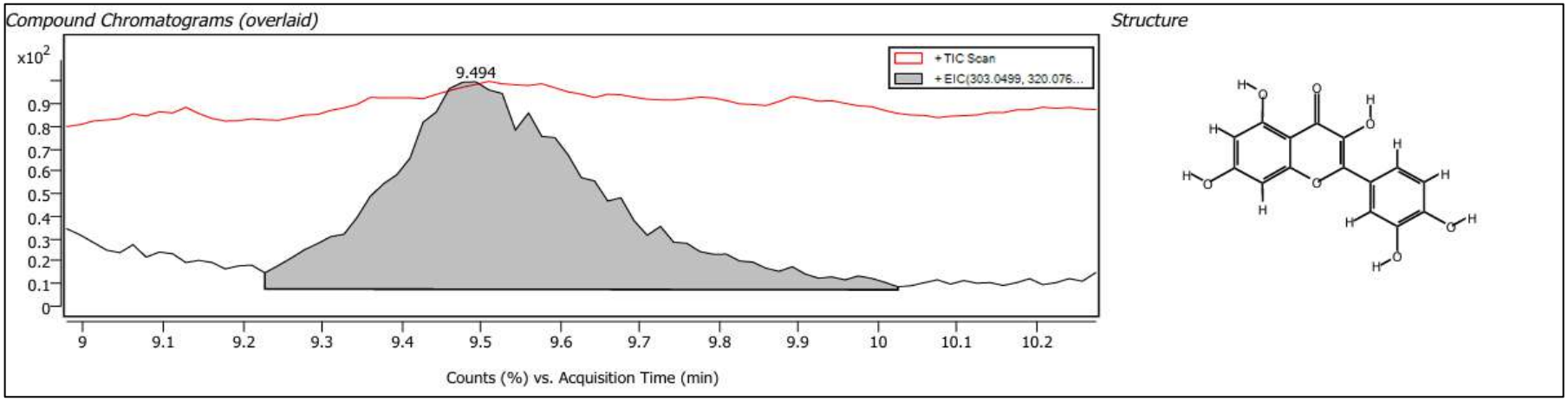
Figure 5.32: (a-j) Phytochemical constituents identified by LC-MS QTOF analysis of *Syzygium occidentale* bark



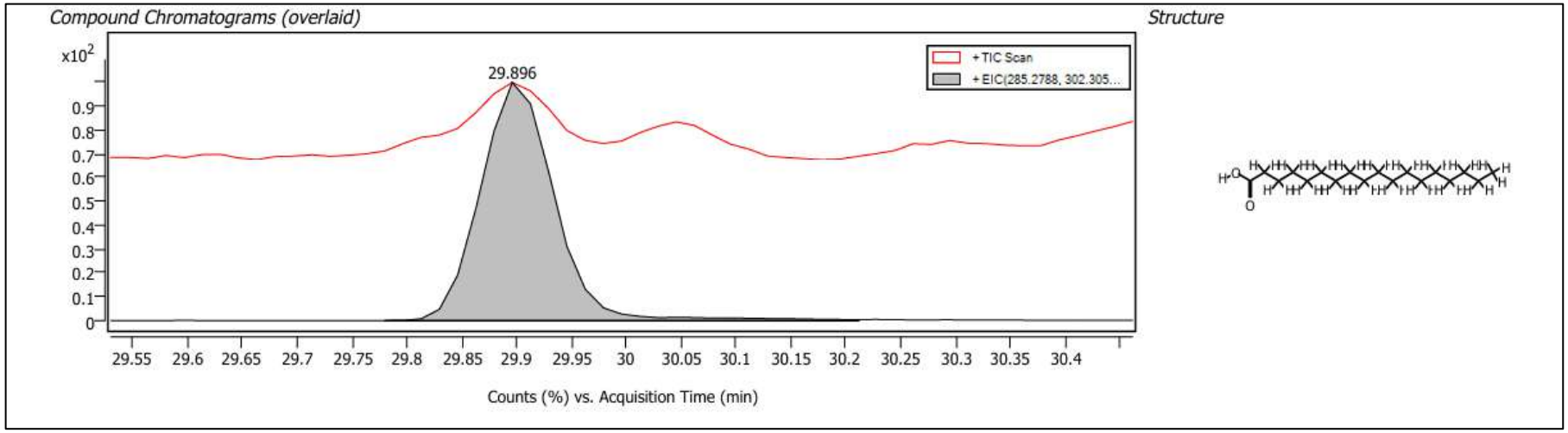
(a) Gallic acid



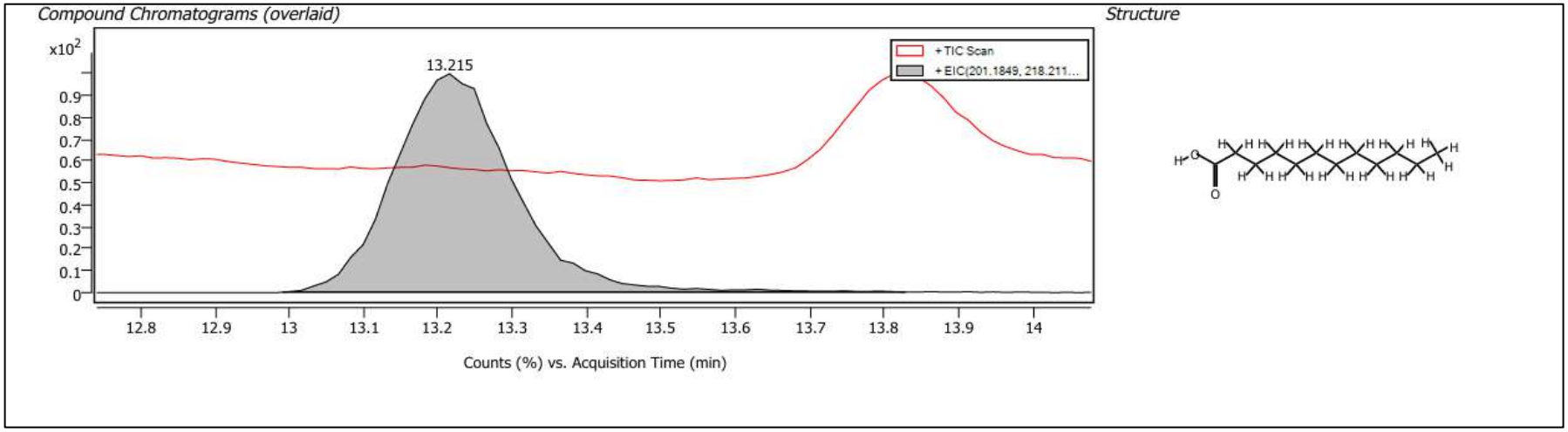
(b) Ellagic acid



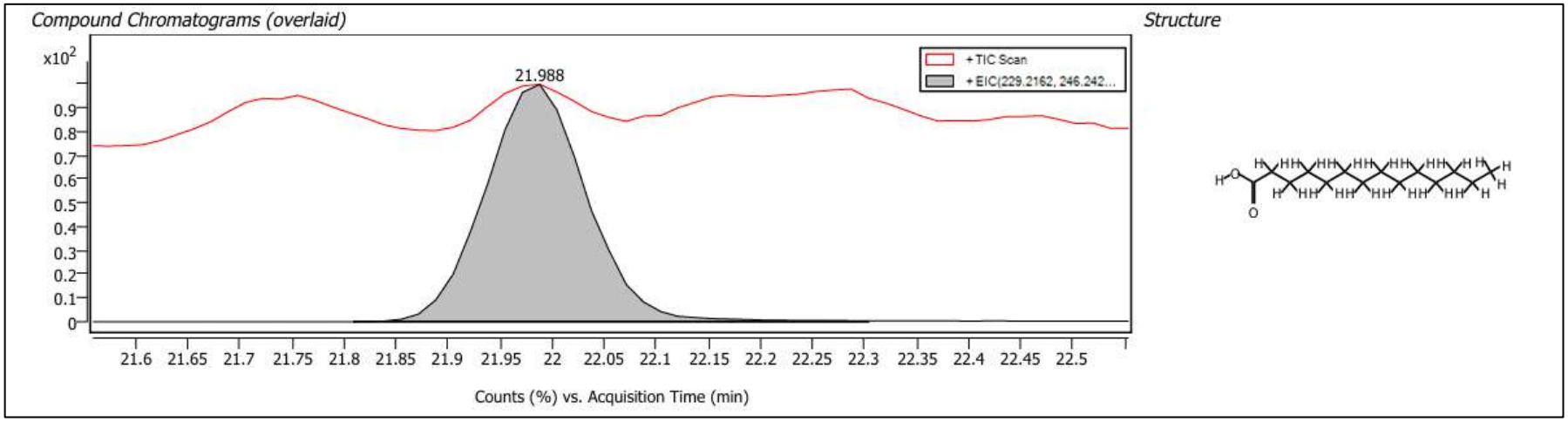
(c) Quercetin



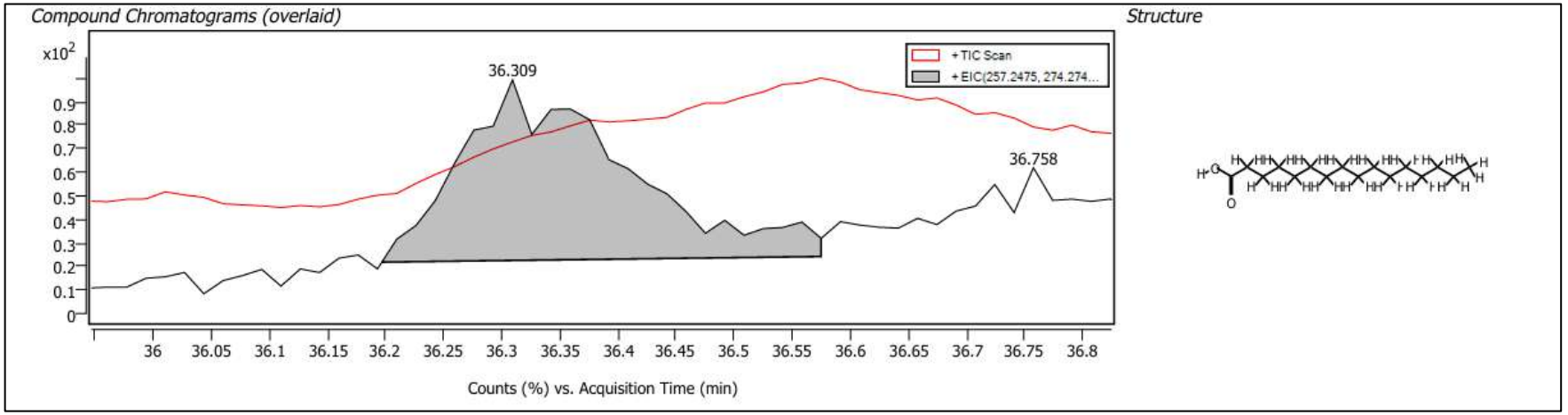
(d) Stearic acid



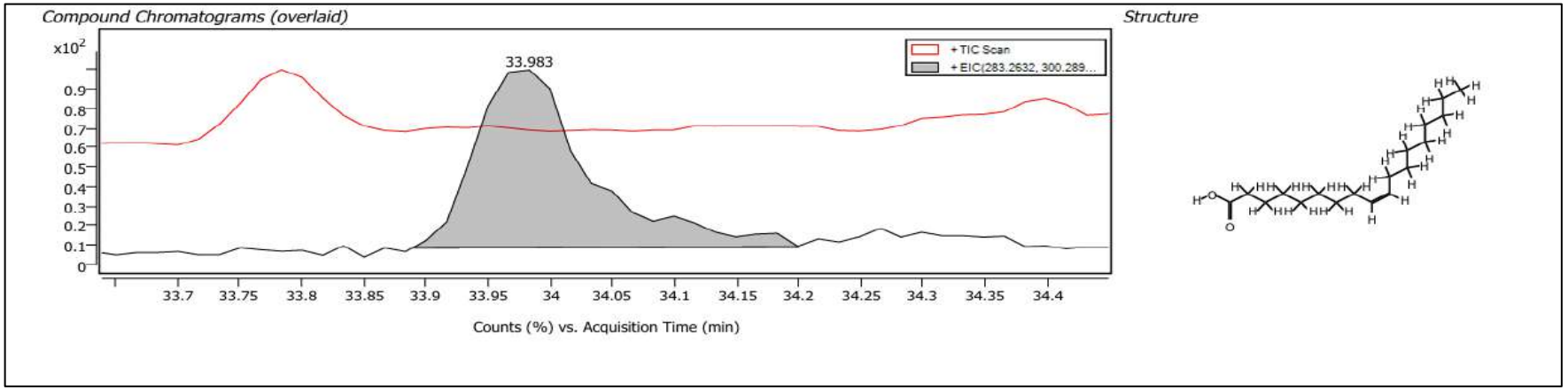
(e) Lauric acid



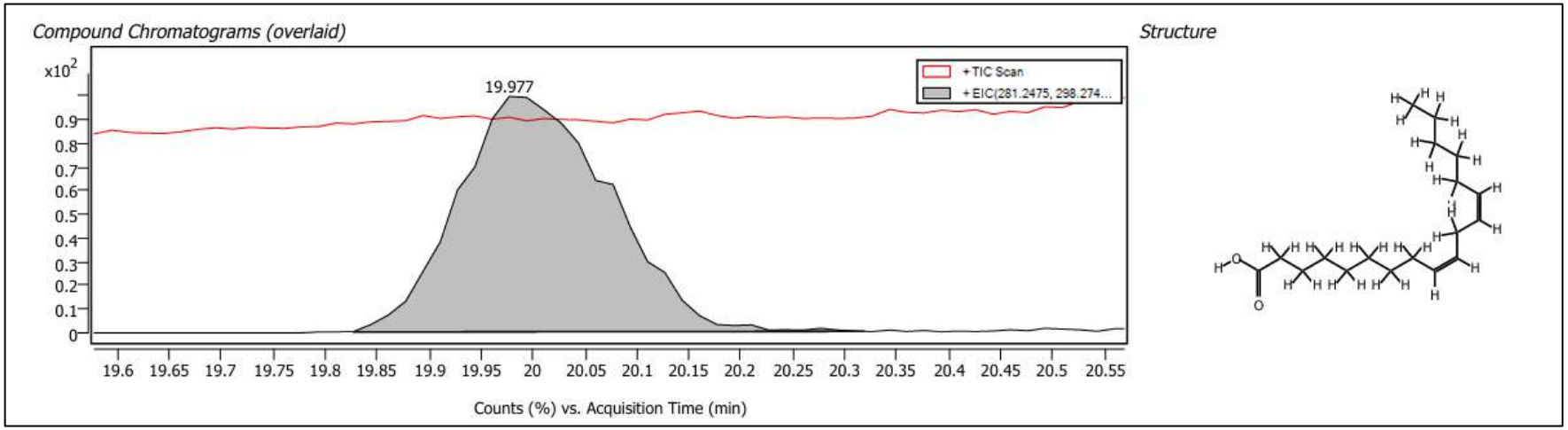
(f) Myristic acid



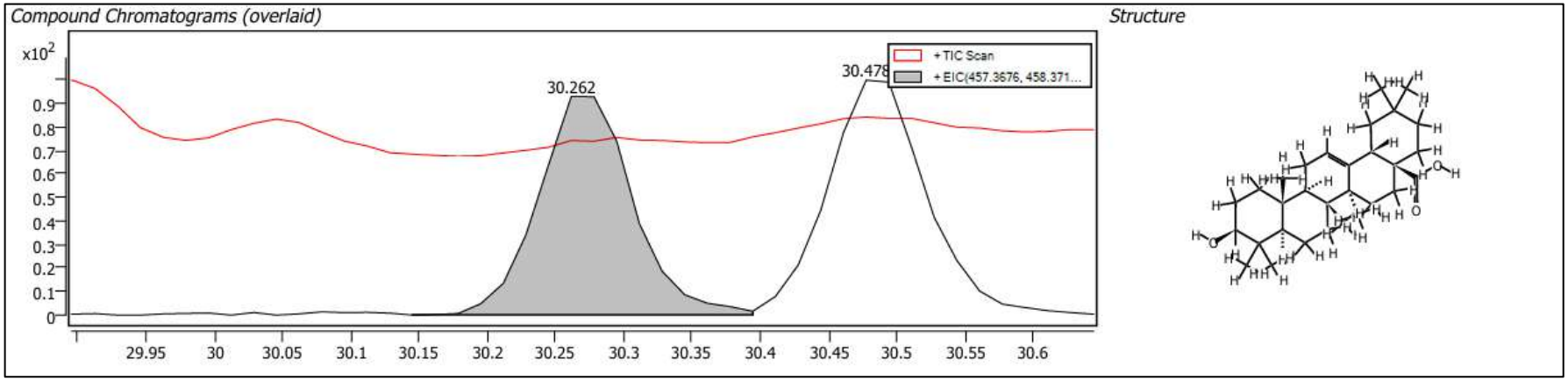
(g) Palmitic acid



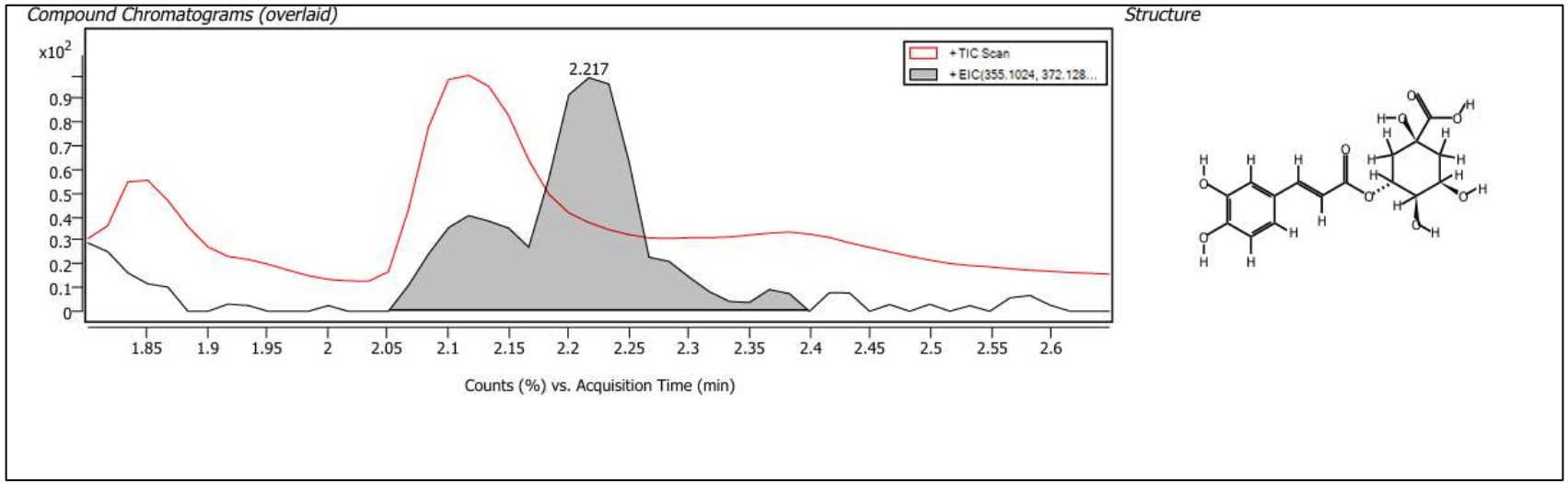
(h) Oleic acid



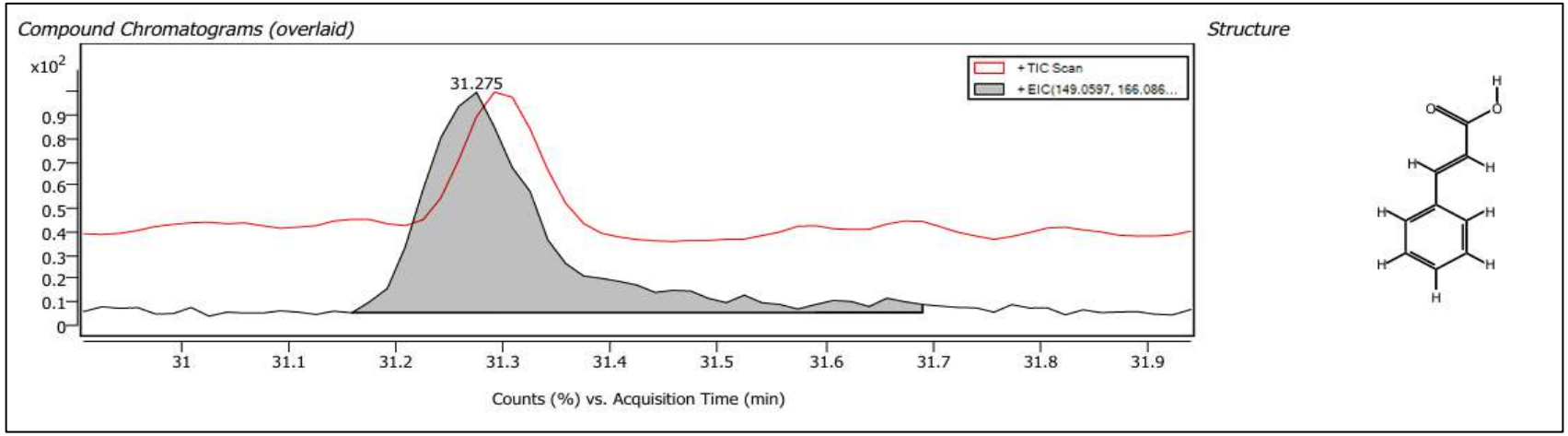
(i) Linoleic acid



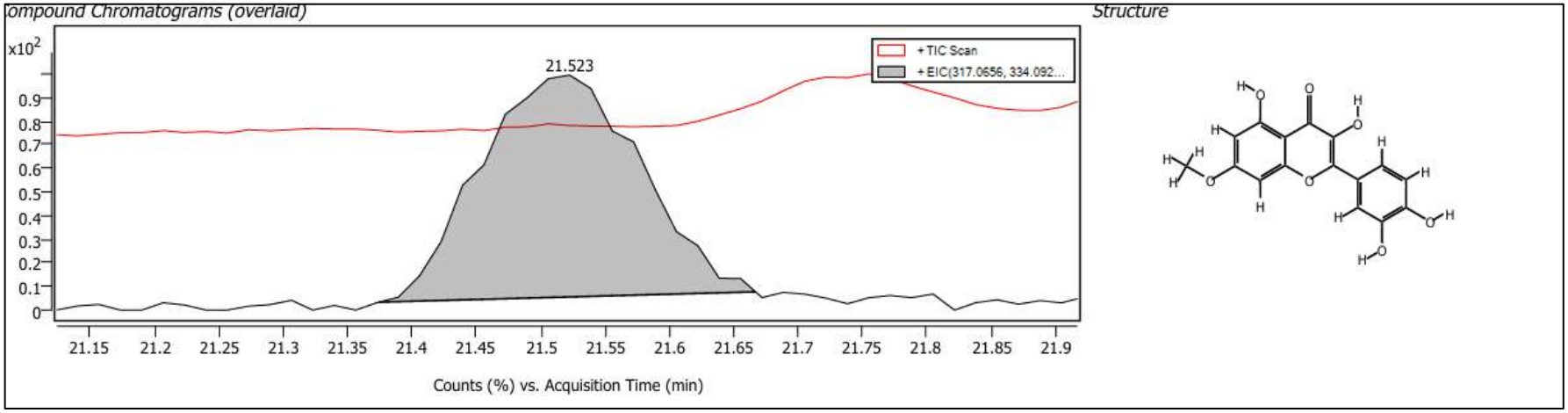
(j) Oleanolic acid



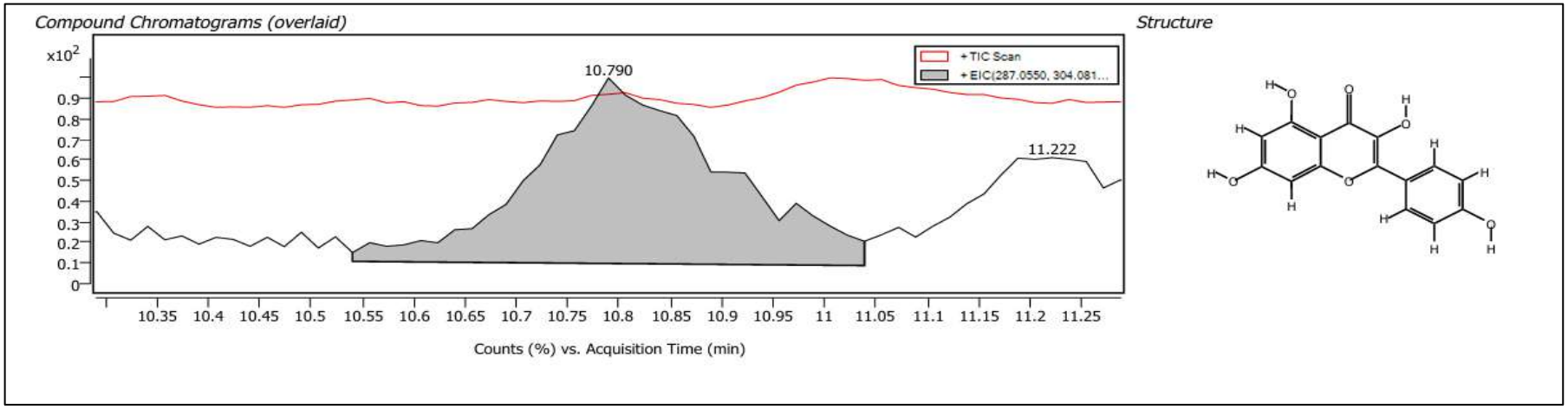
(k) Chlorogenic acid



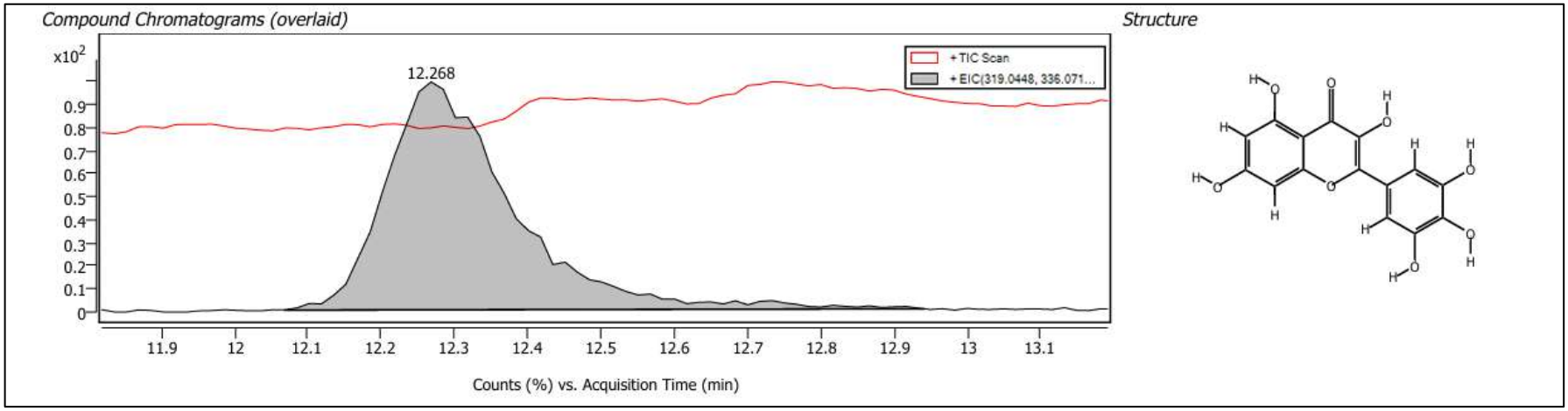
(l) Cinnamic acid



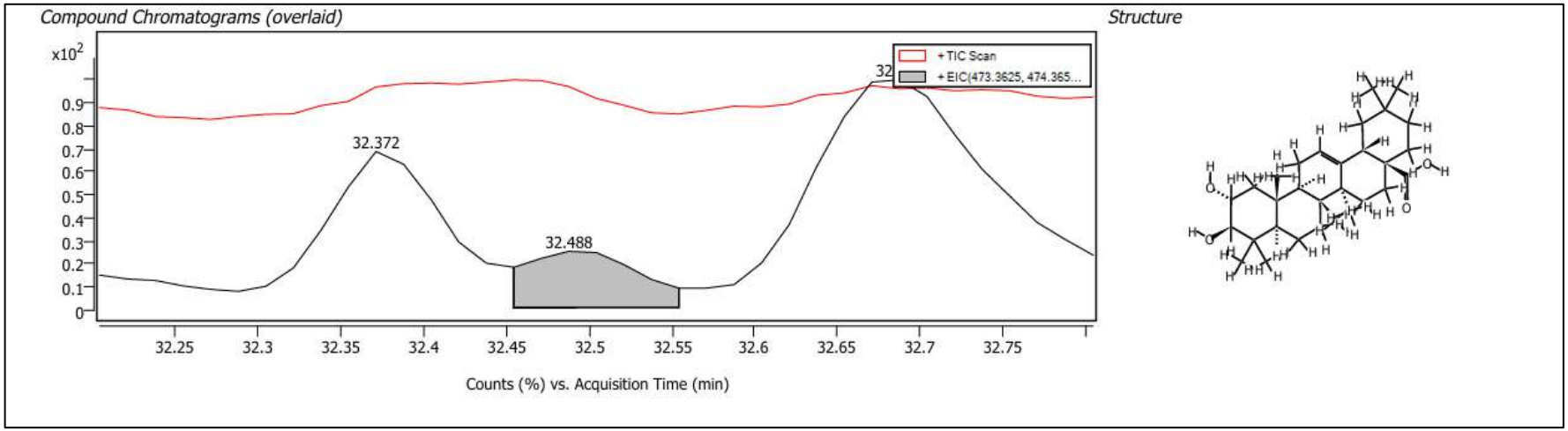
(m) Rhamnetin



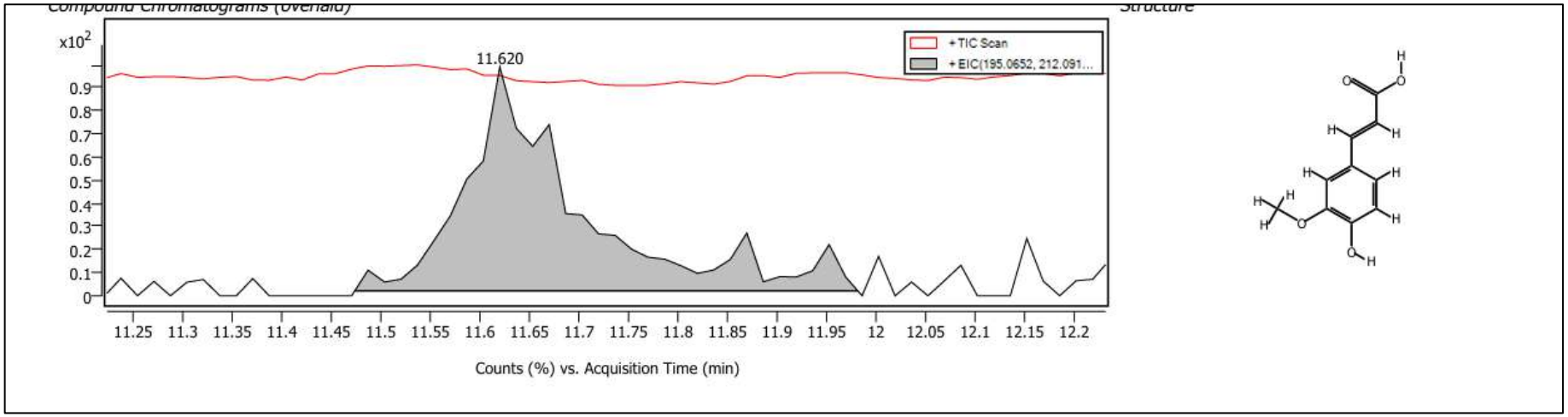
(n) Kaempferol



(o) Myricetin

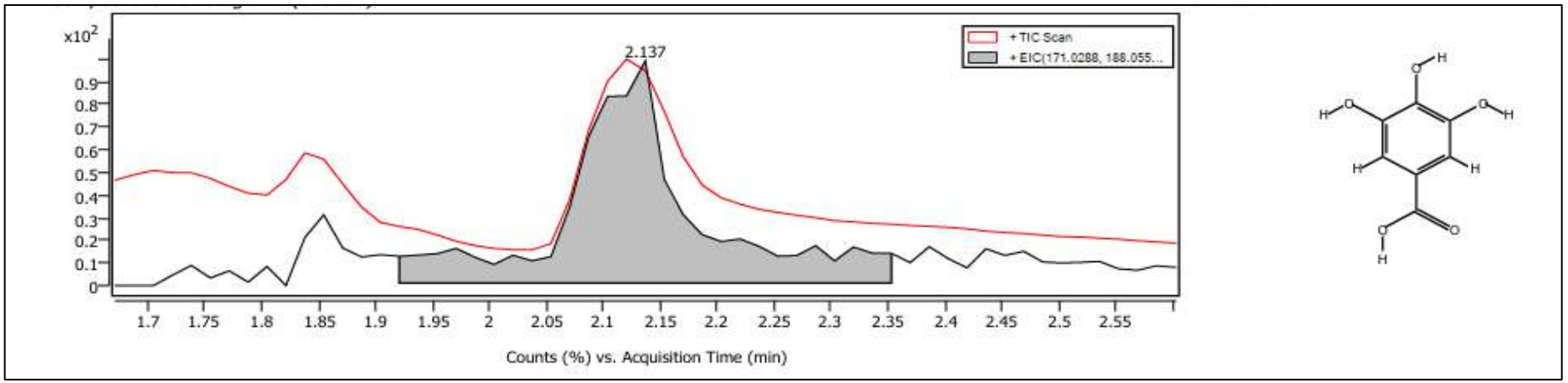


(p) Maslinic acid

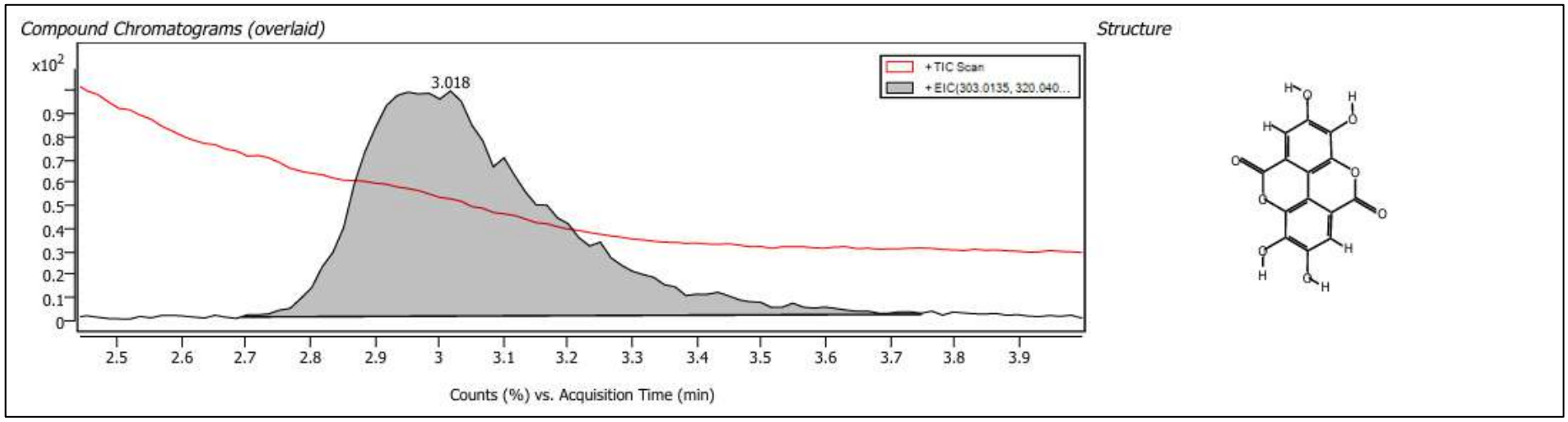


(q) Ferulic acid

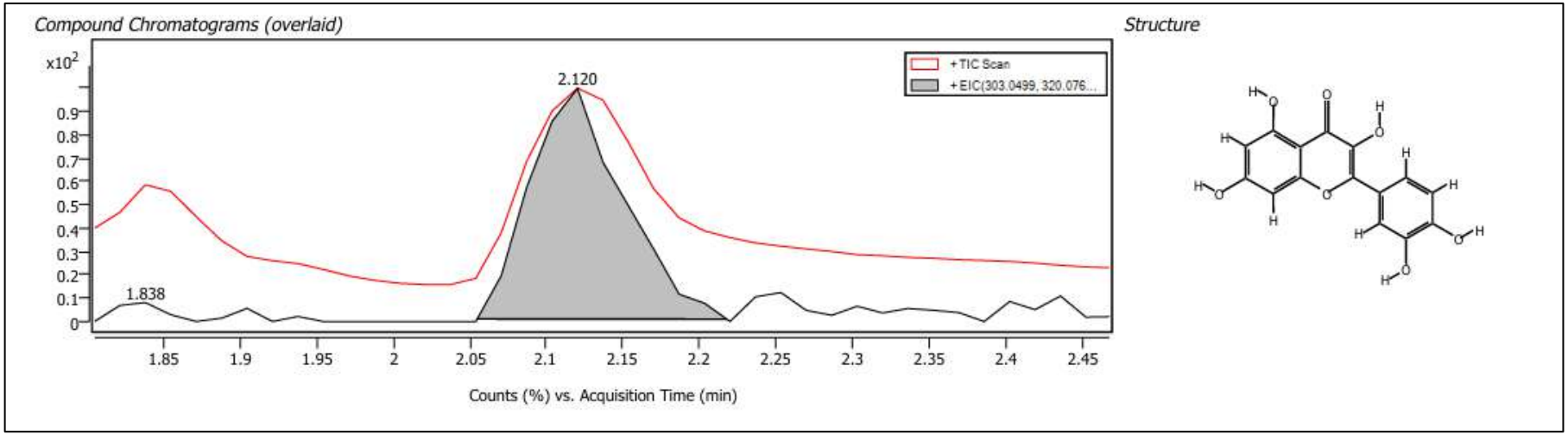
Figure 5.33: (a-q) Phytochemical constituents identified by LC-MS QTOF analysis of *Syzygium palghatense* leaves



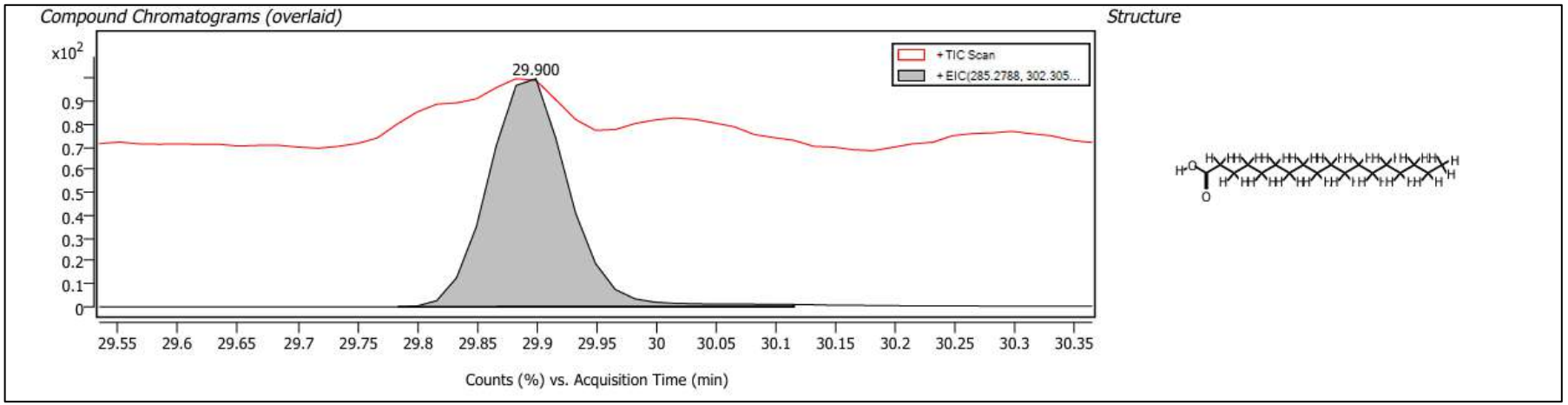
(a) Gallic acid



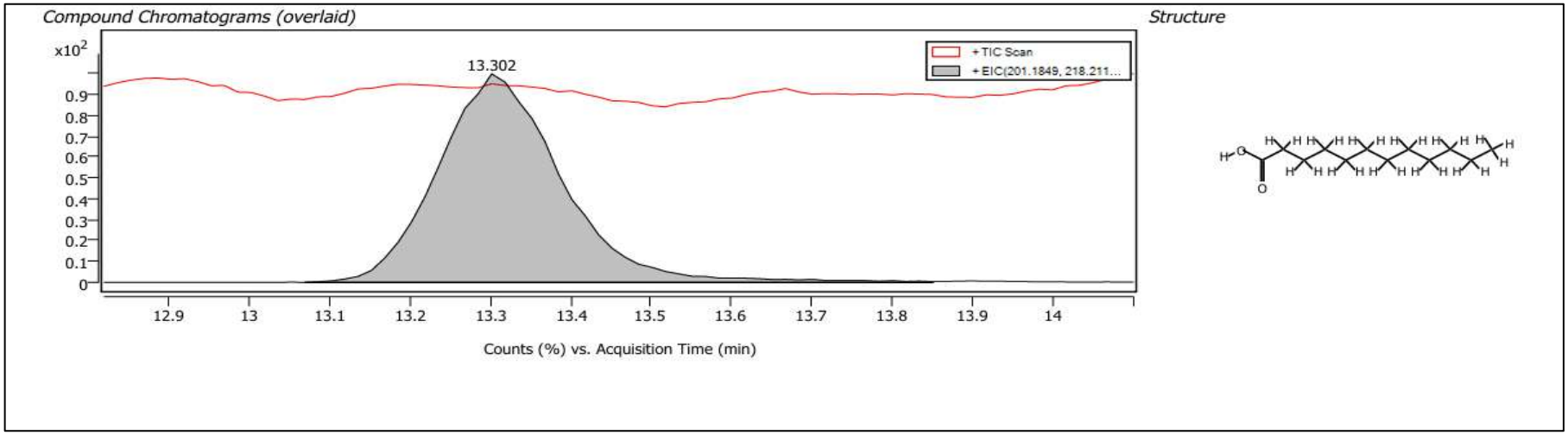
(b) Ellagic acid



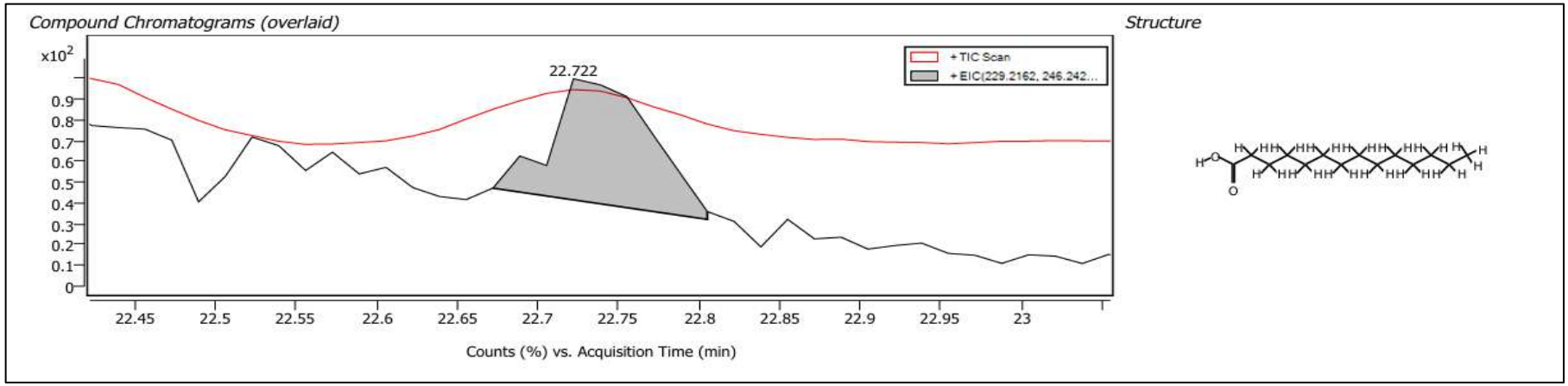
(c) Quercetin



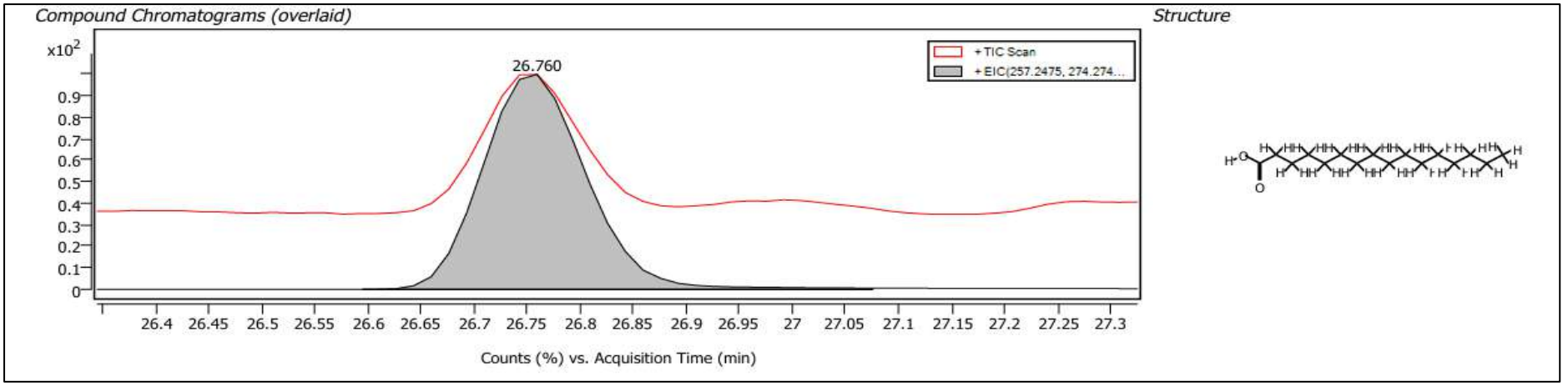
(d) Stearic acid



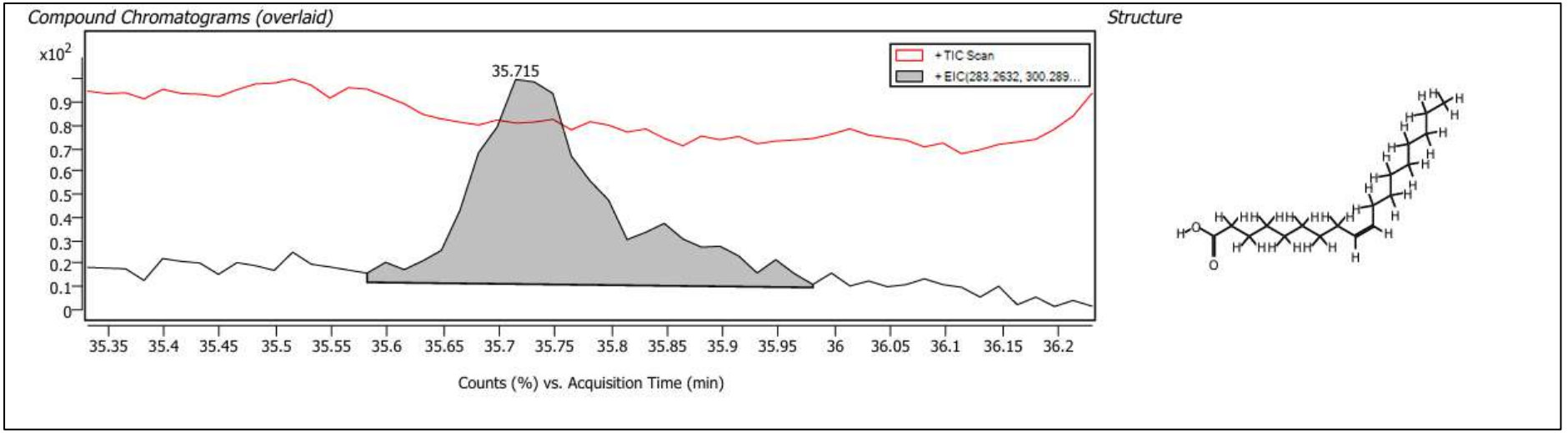
(e) Lauric acid



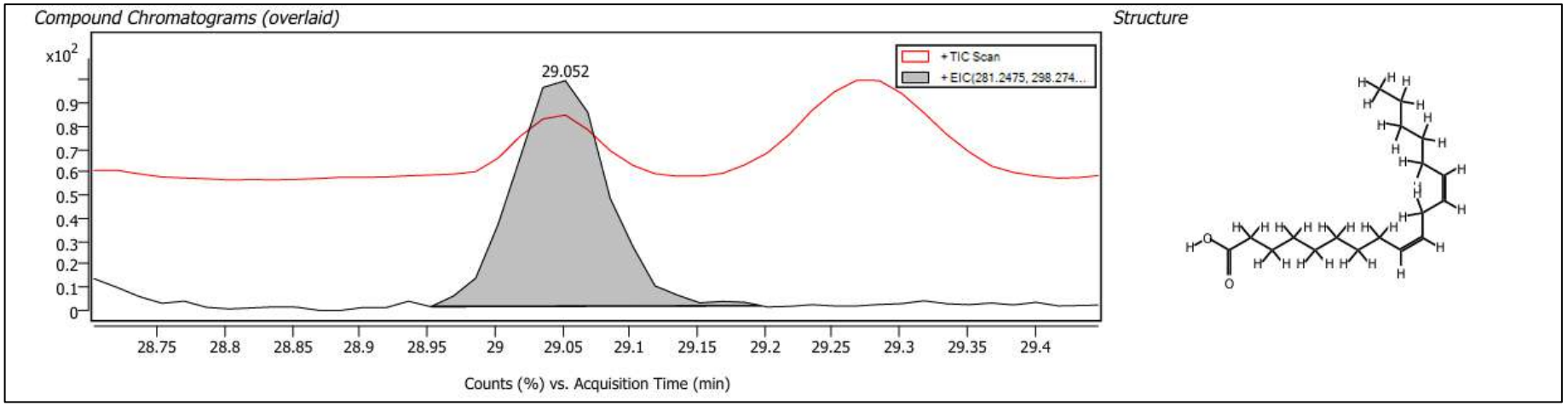
(f) Myristic acid



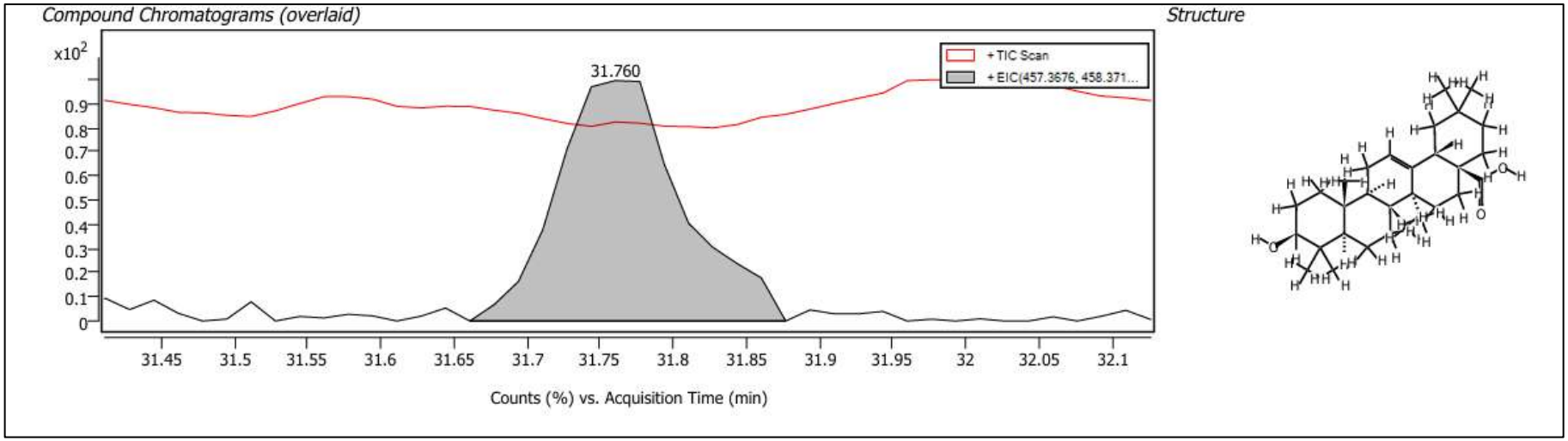
(g) Palmitic acid



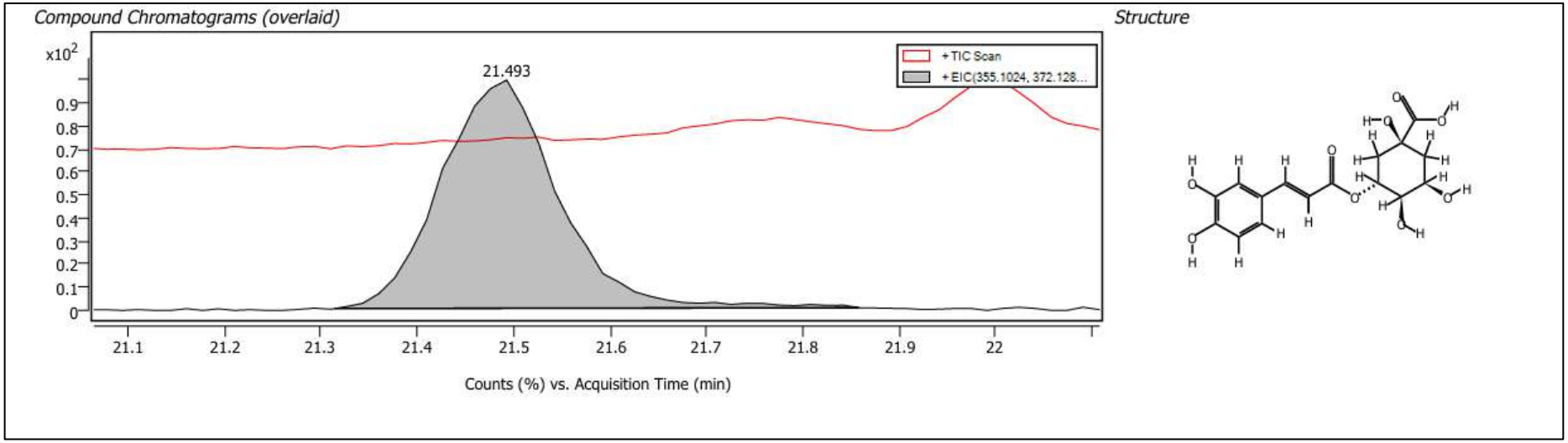
(h) Oleic acid



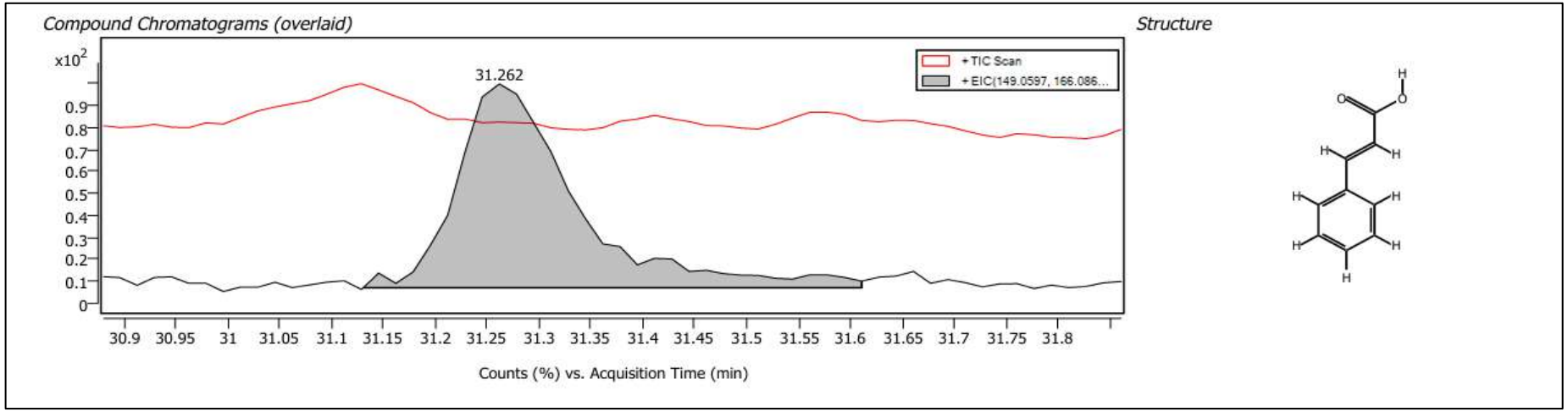
(i) Linoleic acid



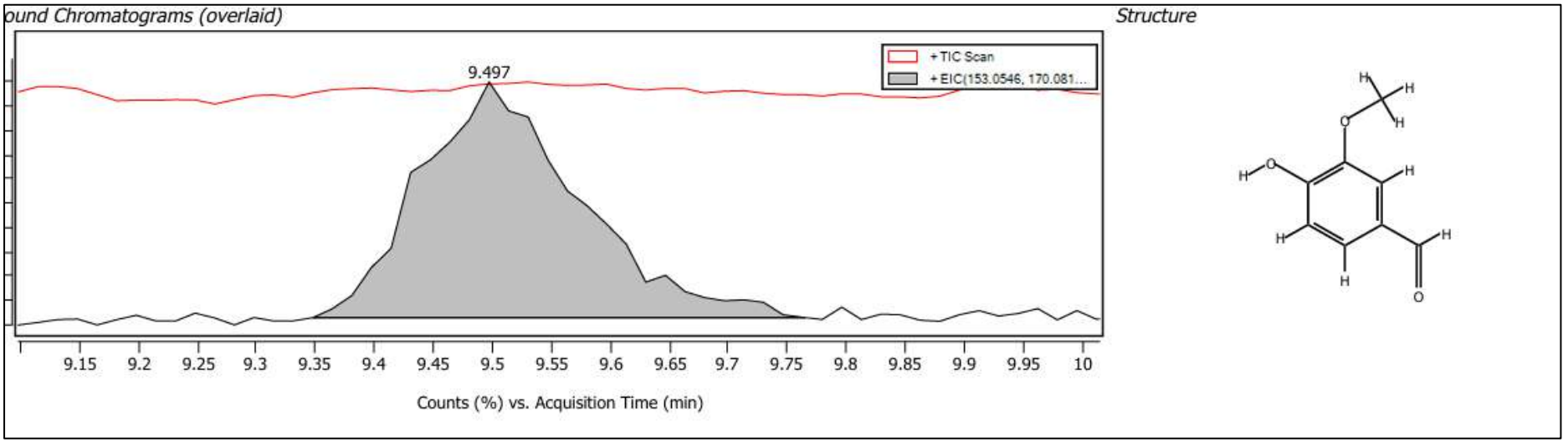
(j) Oleanolic acid



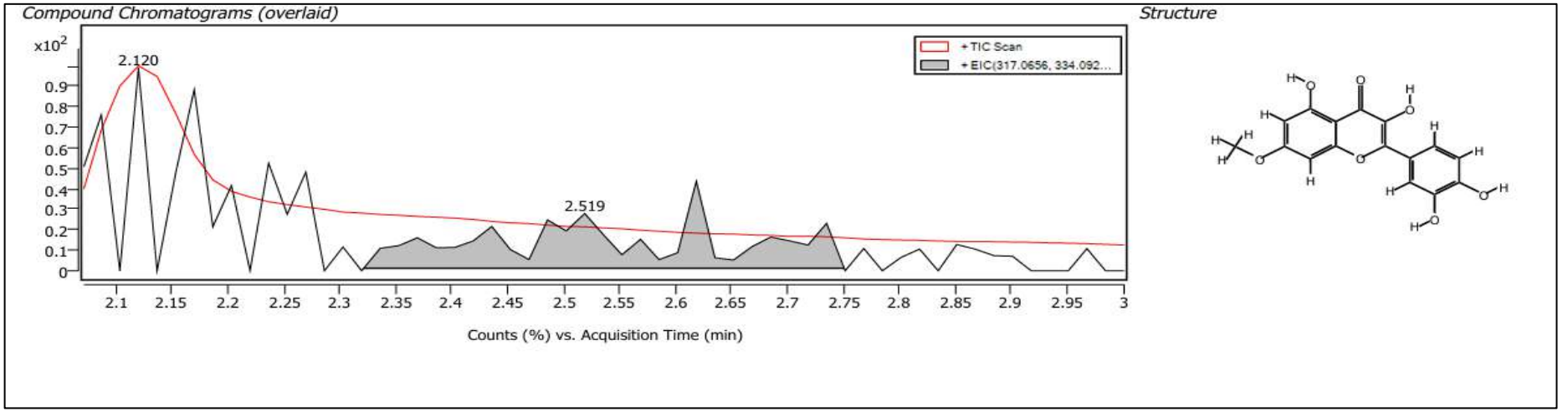
(k) Chlorogenic acid



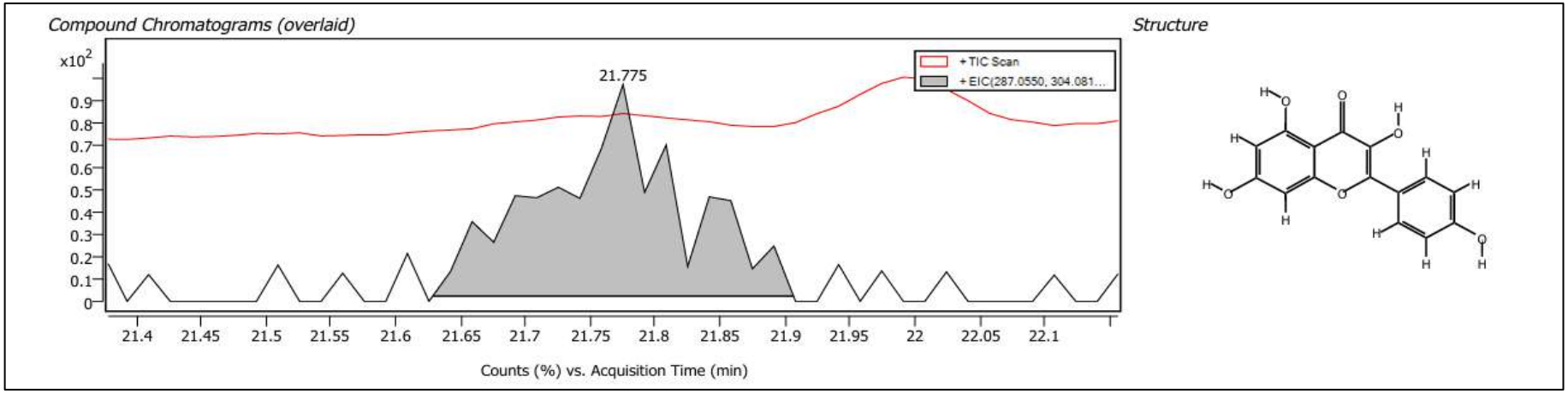
(l) Cinnamic acid



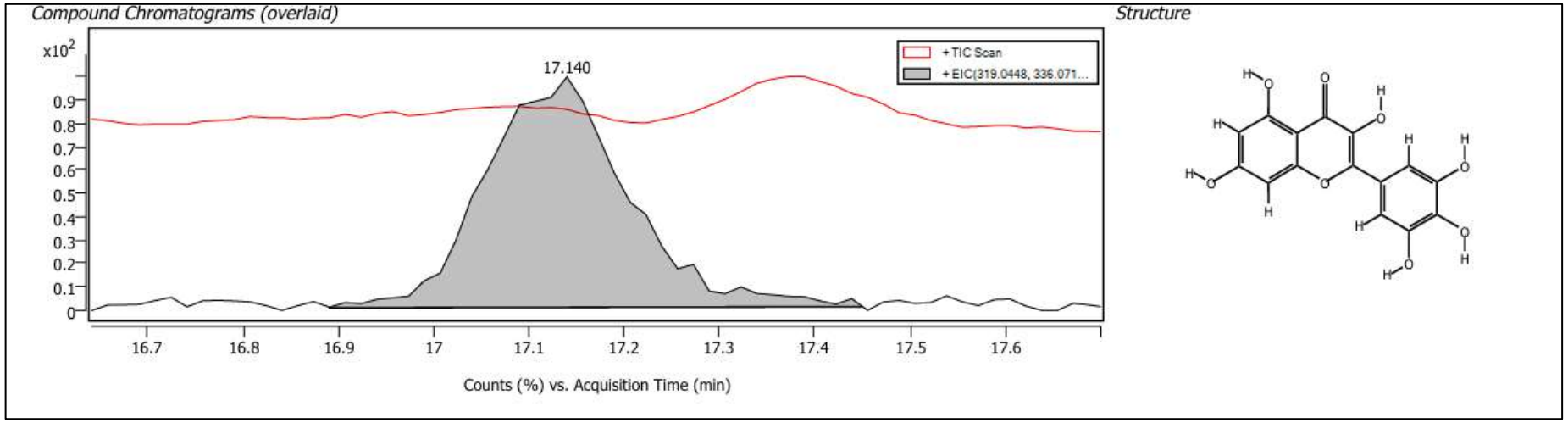
(m) Vanillin



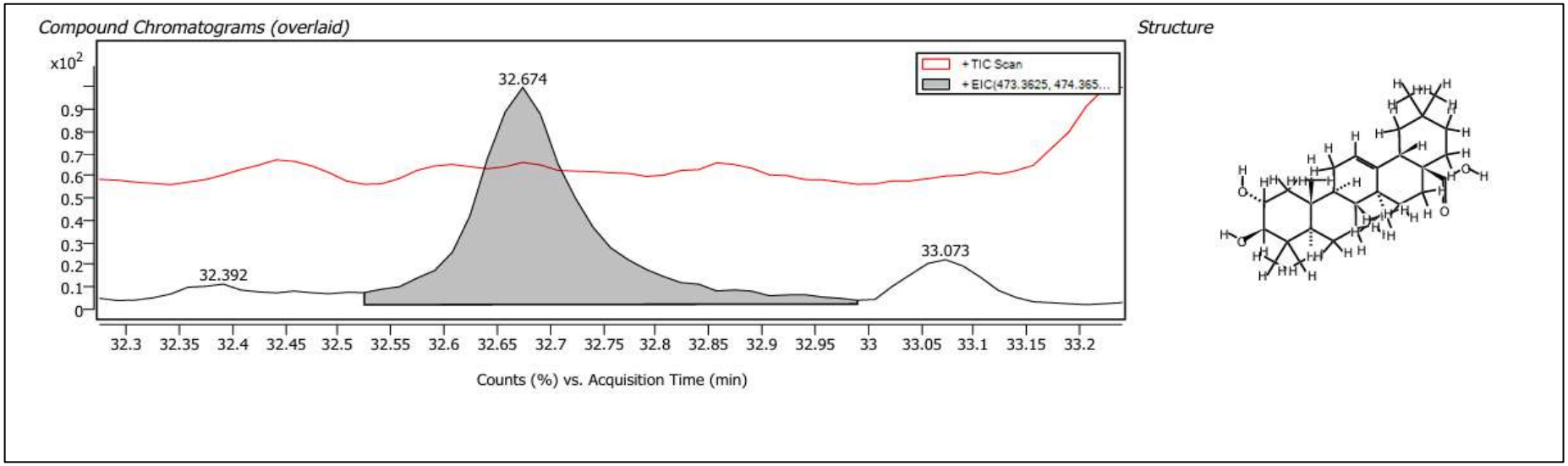
(n) Rhamnetin



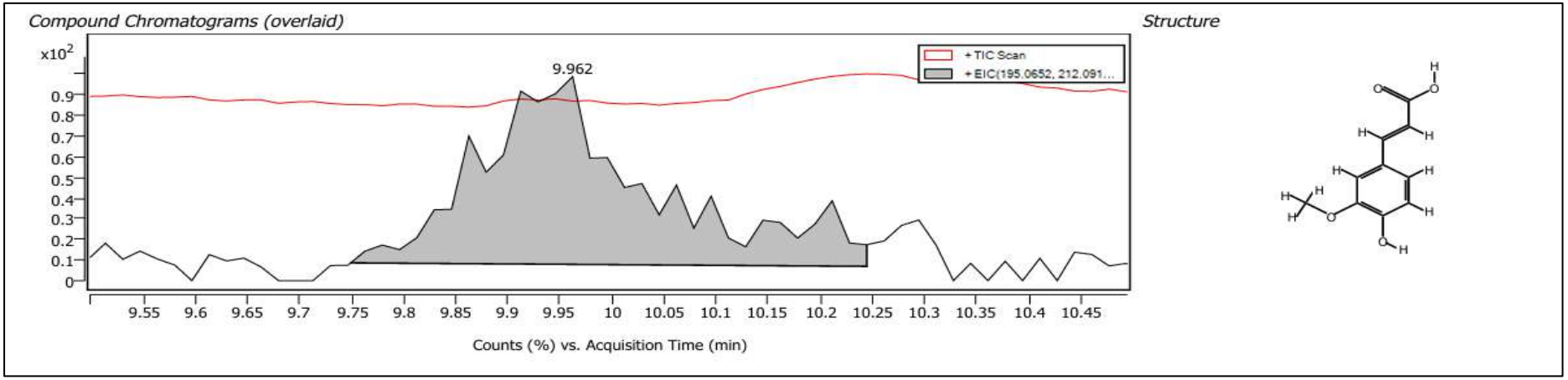
(o) Kaempferol



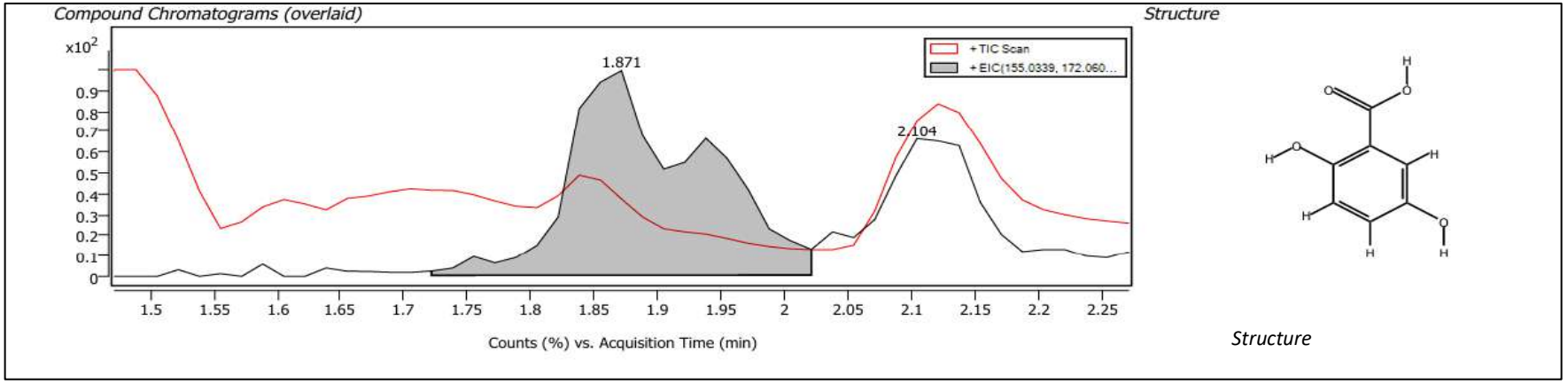
(p) Myricetin



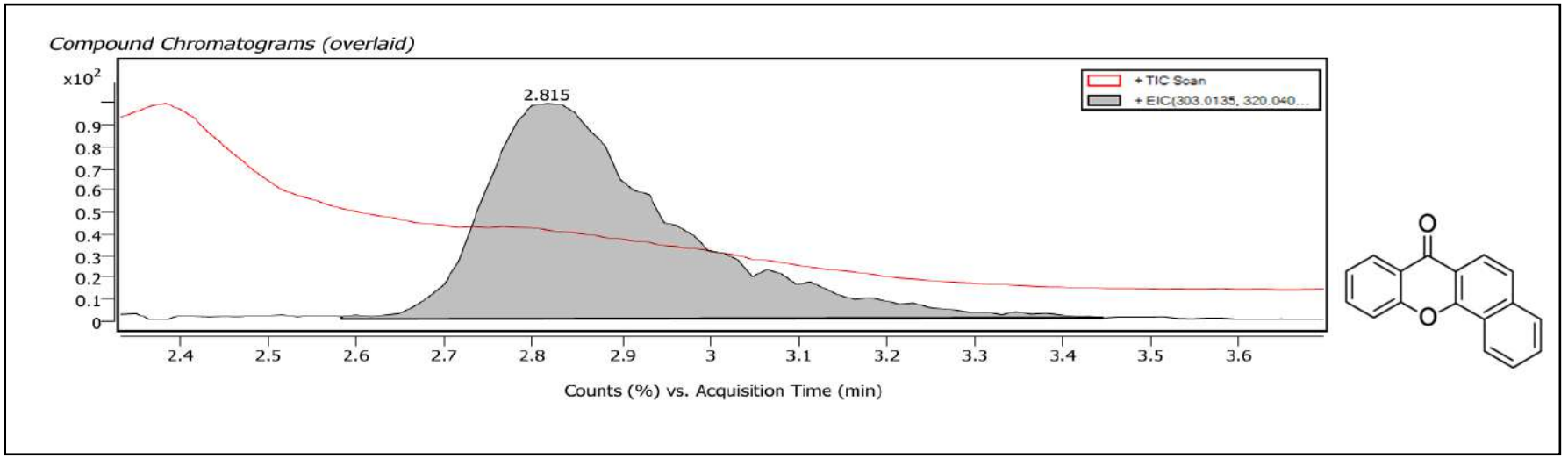
(q) Maslinic acid



(r) Ferulic acid



(s) Gentisic acid



(t) 2-Phenyl-4H-chromen-4-one

Figure 5.34: (a-t) Phytochemical constituents identified by LC-MS QTOF analysis of *Syzygium palghatense* bark

5.4. Discussion

For centuries, humans have become attracted by the many uses of phytochemicals belonging to the *Syzygium* genus (Myrtaceae) (Chandra et al., 2020). The greatest yield percentage of *S. laetum, S. occidentale*, and *S. palghatense* leaf and bark extracts was achieved in the leaf and bark methanol extracts. The highest extractive values of the three were obtained from *S. palghatense.* For all three species, the extraction yield sequence was the same i.e., methanol followed by distilled water, ethyl acetate, petroleum ether and chloroform. For all five solvent polarities, the best combined extraction yields were linked to reduced acid-insoluble ash and higher mineral concentrations, which enhance extraction efficiency, particularly using solvents that are polar in nature, including like methanol and water. Bark extracts give somewhat greater yields than leaf extracts across all species and solvents in present study *S. palghatense* leaves exhibit a high level of activity toward all of the biological characteristics examined when compared to bark.

Irulandi et al. (2016) discovered that, in comparison to other solvent extracts, the methanolic extract of *S. laetum* exhibited good antibacterial activity against *Bacillus subtilis, Pseudomonas aeruginosa*, and *Klebsiella pneumoniaee*, while the ethyl acetate extract displayed the least zone of inhibition against all tested pathogens. The yields from the polar solvents (methanol and distilled water) were consistently higher than those from the non-polar solvents (petroleum ether and chloroform) for all three species.

Higher yields typically result in deeper extract colours, which range from light green to blackish green for leaves and from brown to blackish brown for bark. Higher mineral concentrations and lower acid-insoluble ash increases extraction efficiency, particularly with polar solvents like methanol and water, were linked to the best combined extraction yields for all five solvent polarities.

A comprehensive metabolite profile was revealed by screening the phytochemical contents of three *Syzygium* species (*S. laetum, S. occidentale*, and *S. palghatense*) using several solvent systems. Various secondary metabolites were identified in all the three studied species. All extracts and species had consistent levels

of essential oils. Bioactive chemicals were more effectively extracted by polar (methanol and aqueous) extracts than by non-polar ones. More phytocomponents are present in the methanol extracts of *S. laetum* bark compared with the distilled water extracts. In the study of John et al. (2015) *Memecylon randerianum* exhibited the highest number of examined phytochemicals, followed by *S. laetum*. Rocchetti *et al*. (2019) discovered that leaves from six different species of *Syzygium* were found to have distinct phenolic profiles.

Alkaloids, flavonoids, glycosides, carbohydrates, tannins, reducing sugars, phenolics, and steroids/triterpenoids were all detected in methanol extracts. A total of eight phytoconstituents were identified by Irulandi et al. (2016) from the methanolic extract of *S. laetum* including alkaloids, tannins, flavonoids, phenols, steroids, terpenoids, saponins, and coumarins. Coumarins were uniquely found in methanolic bark extracts of *S. laetum* and *S. palghatense* in the present study. The phytochemical analysis of *S. laetum* leaves revealed the presence of several similar pharmacologically active bioactive compounds, which may be the source of their bioactivity.

The results of the phytochemical screening of the bark of *S. laetum* and the methanolic extract of *S. palghatense* leaves and bark also showed the presence of tannin, alkaloids, glycosides, reducing sugar, carbohydrates, saponins, and phenolics were present. Aqueous extracts were similar in our results; however, they contained saponins exclusively and lacked glycosides and steroids/triterpenoids. Moderately isolated glycosides, phenolics, steroids/triterpenoids (leaves), and tannins (bark) are all extracted by ethyl acetate. Starch, anthraquinones, fats/oils, proteins, and amino acids were consistently lacking. Leaf extract (e.g., ellagic acid; caffeic acid), bark extract (e.g., 3,3-di-O-methyl ellagic acid; 3,3,4-tri-O-methyl ellagic acid), seed extract (e.g., ferulic acid), and other plant components of *S. cumini* had a small amount of phenolic chemicals. TLC, IR, MS, and CC analysis revealed the presence of several triterpenoid chemicals in the fruit, bark, and wood extracts of *S. cordatum* (Uddin et al., 2022).

Flavonoids, terpenoids, tannins, glycosides, and phenolics are among the phytochemical ingredients that are abundant in the leaves, seeds, fruits, bark, and flower buds of the *Syzygium* species. There have been reports of cytotoxic, antibacterial, anti-inflammatory, anticancer, antidiabetic, antioxidant, and anthelmintic properties in a variety of extracts (methanol, ethanol, and aqueous) from distinct *Syzygium* species. (Aung et al., 2020). It was found that alkaloids (197.66 mg/g), flavonoids (167.77 mg/g), tannins (233.62 mg/g), glycosides (183.97 mg/g), carbohydrate (130 mg/g), reducing sugars (4.77 mg/g) and phenols (102.78 mg/g) were highest in *S. palghatense* leaf methanol extract. Builds upon previous reports on *S. palghatense* leaves extracted in methanol contain 128.8 µg/mg alkaloid, 180 µg/mg flavonoids, 318.5 µg/mg glycosides, and 237.4 µg/mg tannin. *S. cumini* was discovered to have high levels of phenols (16.88%) and flavonoids (7.44%) (Bigoniya *et al*., 2012).

It was discovered by Sathe & Dighe (2016) that while cardiac glycosides and steroids were lacking from the dried powder of *S. jambos* stem bark, tannins, alkaloids, saponins, terpenoids, and flavonoids were present. Present study found bark had higher alkaloids than leaves for *S. laetum* and *S. occidentale*, but the opposite for *S. palghatense*. Saponins possess unique distribution pattern and was highest in leaves of all species. According to the finding of present study methanol extracts were consistently superior to aqueous extracts. Similar trends were observed by Carrera-Cevallos *et al.* (2025), where *S. paniculatum* ethanol extracts demonstrated higher bioactive profiles than aqueous extracts, with notable antioxidant capacity.

GC-MS screening in the methanol extracts of the leaves and bark of the investigated *Syzygium* species revealed a range of bioactive compounds with therapeutic qualities. Leaves of *S. laetum* are dominated by methyl 2-hydroxy-octadeca-9,12,15-trienoate (76.56%). Other compounds: lupeol, neophytadiene, 2,2-dimethyl-3-vinyl-bicyclo-heptane. Similar trends were observed by Chandra et al. (2020), where Methyl 2-hydroxy-octadeca-9,12,15-trienoate and 2,2-Dimethyl-3-vinyl bicyclo[2.2.1] heptane contributes 71.82% and 12.22% respectively.Cholest-4-en-3-one, Lupeol, and 3-Pentadecylphenol were also present among the eleven peaks

found in the GC-MS study of *S. laetum* leaf chromatograms. Bark of *S. laetum* has more complex profile in our study, including methyl palmitate, linoleic acid methyl ester, β-sitosterol, lupeol, vitamin E. The bark chromatograms of the indigenous *S. laetum* showed six peaks in the GC-MS study. The main components are methyl palmitate (33.66%) and methyl octadeca 9,12-dienoate (22.85%) (Chandra et al., 2020).

Leaves of *S. occidentale* are rich in 3-pentadecylphenol (42.72%) and cyclogallipharaol (46.67%), amphiphilic phenolic lipids. These compounds exhibit antioxidant, antimicrobial, and anti-obesity properties. Their bark extract contains high levels of fatty acid methyl esters (FAMEs), methyl palmitate, methyl octadecenoate, linoleic acid methyl ester known for anti-inflammatory and cardioprotective activities.

Leaves of *S. palghatense* are Squalene (39.14%) and vitamin E (26.05%) dominated. Known for antioxidant, antimicrobial, anticancer, and skin-protective properties and bark are rich mixture of compounds including Gallic acid, 2-hyphenyl-4H-chromen-4-one and ellagic acid. It stood out as the most diverse and balanced species in phytochemical composition. Squalene is one of the major compounds present in *S. polyanthum*. Squalene, phytol, hentriacontane, palmitic acid, α-pinene, nerolidol, linalool, α-tocopherol, and β-tocopherol were among the chemicals found in the extracts of *S. polyanthum* that were known to be bioactive which has therapeutic significance (Abd Rahim et al., 2018). Alpha-pinene, alpha-cubenene, 1H-Cyclopropa [a] naphthalene, nerolidol, humulene epoxide II, phytol, 9,12,15-Octadecatrien-1-ol, squalene, alpha-tocopherol, beta-sitosterol, azulene, valence, azulene, and beta-Panasinen were detected in the GC-MS test results of *S. polianthum* leaf extract by Rochmat et al. (2022). GC-MS examination of methanol extracts of stem barks, leaves, and fruits revealed over 40 different types of compounds, indicating that *S. alternifolium* has a high phenol content (Uddin et al., 2022).

Leaf extract of *S. laetum* identified 11 compounds and the key compounds were cinnamic acid, tryptophan, neomycin, afzelin, alpha-pinene, isoliquiritin and the bark extract of *S. laetum* identified 12 compounds. The key compounds were cinnamic

acid, lanosterol, mecillinam, erucic acid, beta-tocopherol, phytol. Results showed distinct leaf vs. bark chemical composition, but cinnamic acid is common in both. Compounds indicate antioxidant, antimicrobial, metabolic, and potential anti-inflammatory properties.

Quercetin, syringic acid, cinnamic acid, ellagic acid, ferulic acid, and gallic acid were detected by phenolic profiling of *S. cumini* fractions using HPLC by Syama et al. (2018), these were then verified by LC–QTOF (MS/MS). The main phenolics that were found were docked with the enzymes under study and examined. All of the findings indicate to the great potential of S. *cumini* seed fractions in the treatment of diabetes.

Because of their profusion of bioactive phytochemicals, plants like *Syzygium* species are frequently used as the basis for complementary therapies. Many natural substances that come from *Syzygium* species, including dimethyl cardamonins, phenolics, oleanolic acids, and betulinic acids, have been shown to have anticancer properties (Chua et al., 2019).

According to Ali et al. (2024), quercetin, epicatechin, isovitexin, cinnamic acid, and catechin are the most prevalent phenolic chemicals in Australian myrtles (*Syzygium anisatum*, *Backhousia citriodora*, and *Backhousia myrtifolia*). The study presents a novel perspective on the powerful bioactive phenolic chemicals found in Australian myrtles. This may also have implications in functional, nutraceutical, as well as medicinal fields.

The variation in phenolics across various sections was demonstrated through twelve compounds that were detected by LC-ESI-QTOF-MS/MS screening in the stem, leaf, and root of *S. cumini*. Flavonoids, phenolic acids, other polyphenols, and lignans comprised the majority of the substances. Notable substances that demonstrated the medicinal potential of various fractions of *S. cumini* included naringin 4'-O-glucoside, 3,4-O-dimethylgallic acid, scutellarein, and demethyloleuropein. The findings showed that *S. cumini* fractions had better antioxidant activity because they included a significant amount of phenolics (Imran et al., 2025).

5.5. Conclusion

The *Syzygium* genus is well known for its therapeutic qualities. The analysis from the study showed that the three species (*S. laetum, S. occidentale*, and *S. palghatense*) varies in terms of the yields, bioactive compounds, and phytochemical compositions. These variations leads to different pharmacological properties. Methanol extracts of leaf and bark showed the highest production of the yield for all three species.

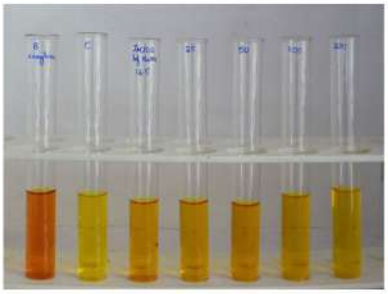
Quantitative phytochemical analysis showed that *S. palghatense* has the highest concentration of alkaloids, flavonoids, glycosides, saponins, phenols, and tannins compared to *S. laetum, S. occidentale*. *Syzygium* species, particularly in polar extracts, are potential sources of a variety of bioactive chemicals. Through numerous pathways, the combined action of phytochemicals may improve a range of biological characteristics.

Different metabolic fingerprints unique to each species were identified using GC-MS. One main derivative of fatty acids dominates *S. laetum*. The leaves of *S. occidentale* are rich in phenolic lipids, while its bark is dominated by Fatty Acid Methyl Esters (FAME). *S. palghatense* was rich in phytocompounds, most pharmacologically active and well-balanced. *S. palghatense* yielded the greatest extractive values out of the three. Relatively few studies have isolated or identified derivatives of bioactive chemicals, and the majority of the information now available on a number of *Syzygium* species is based on extracts or fractions. Future studies are needed to validate these findings. This work provides a strong foundation for advancing the pharmacological utilization of *Syzygium* species and underscores their importance in natural product chemistry and drug development. LC-MS QTOF analysis revealed the presence of various phytocompounds with significant medicinal properties like 2-Phenyl-4H-chromen-4-one.

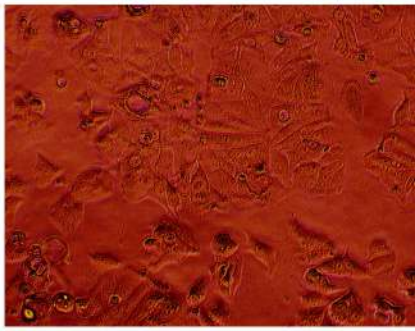
6

BIOLOGICAL ACTIVITIES









CHAPTER 6
BIOLOGICAL ACTIVITIES

6.1. Introduction

The biological potential of the different solvent extracts of *S. laetum*, *S. occidentale,* and *S. palghatense* were analyzed using antioxidant, antimicrobial, anthelmintic, anti-inflammatory, antidiabetic, and antitumor activities. When it comes to *in vitro* and *in vivo*, pharmacological screening was implemented to ascertain the biological activities. The current research attempts to offer a complete overview of the various pharmacological activities of this endemic *Syzygium* species, thus establishing a scientific basis for their possible beneficial applications. Antioxidant activity was measured using a variety of assays, including ferric-reducing antioxidant power (FRAP) tests, hydroxyl radical scavenging, superoxide radical scavenging, and DPPH radical scavenging. These tests gauged the extracts' capacity to neutralize different free radicals and their overall antioxidant power. The agar well diffusion method was brought in use for determining anti-bacterial activity in a panel of bacteria and fungus, includes both type of bacteria Gram-negative and Gram-positive. The minimum inhibitory concentration (MIC), minimum fungicidal concentration (MFC), and minimum bactericidal concentration (MBC) of the active extracts were screened.

The study also investigated biofilm formation and specifically examined *Pseudomonas aeruginosa*. Biofilm inhibition was determined using congo red agar assay, semi-qualitative adherence assay, and quantification of biofilm loss by crystal violet staining. Furthermore, advanced microscopy techniques like bacterial-live-dead assay using SYTO 9 and propidium iodide were performed and used to visualize biofilm formation as well as the effects of plant extracts on bacterial viability. The anthelmintic activity of *Lubricus terrestris* was tested, and extracts were contrasted with the common medication albendazole. Biochemical assays, including protein denaturation inhibitory and proteinase inhibitory activity, were performed to screen for the anti-inflammatory properties. The strongest extract was then tested using RAW

264.7 macrophage cells and its effects on enzyme cyclooxygenase (COX), and lipoxygenase, (LOX) activities, myeloperoxidase, MPO, and nitric oxide production.

Results from the current studies have given insights regarding the possible medicinal use of plant extracts to manage inflammatory conditions. Finally, the extracts were evaluated for their antidiabetic potential using α-amylase and α-glucosidase inhibition assays that are known to have role in carbohydrate metabolism. These detailed reviews present an assessment of the therapeutic value of the chosen *Syzygium* species, laying the groundwork for more studies directed toward drug development and pharmacological applications.

The capacity of substances to neutralize or scavenge free radicals is known as antioxidant activity. Unpaired electrons in free radicals make them very reactive molecules that can harm biological systems by causing oxidative stress. Antioxidants, as free radical scavengers, prevent free radicals from causing excess oxidation and damage within the cells of the body. Popular genera include *Syzygium polyanthum*, *S. malaccense*, and *S. cumini*, which are associated with high levels of antioxidant activity. In traditional medicine, *S. polyanthum* has well-documented antioxidant properties, with very low IC_{50} values in DPPH and ABTS assays, suggesting that the plant has potent free radical scavenging capabilities (Sabandar et al., 2022; Widyawaty et al., 2021). In parallel, leaf extracts of *S. malaccense* have shown high total content of phenols and good radical scavenging in DPPH and ABTS assays. Other species of this genus, *S. cumini*, also has been well studied for their antioxidant potential, displaying strong antioxidant activity in distinct parts of the plant (wood stem, bark, leaf galls), possibly because phenolics, flavonoids, and other bioactive compounds were present. The current study elucidates the potential for *Syzygium* species as natural sources of antioxidants that may be harnessed to develop therapeutic agents and functional foods against oxidative stress-induced disorders. The wide range of antioxidant activities observed in various *Syzygium* species highlights their significance in traditional medicine and their potential roles in contemporary health and nutrition practices.

The capacity to eradicate or fully restrict the growth of micro-organisms, such as viruses, fungus, or bacteria, is known as antimicrobial activity. This property is key to developing a treatment for infections, particularly those caused by multidrug-resistant (MDR pathogens. *S. aromaticum*, *S. caryophyllatum*, and *S. samarangense* have been reported to possess antimicrobial activity. *S. aromaticum* (clove) has shown substantial antimicrobial activity against a large spectrum of bacteria and fungi, attributed to the high percentage of eugenol (65.3%) found in its essential oil (Das et al., 2021; Maggini et al., 2024).

Substances that prevent or disrupt biofilms are referred to as antibiofilm agents. Biofilms are organized microorganism communities that adhere to an object's surface and are surrounded by an outer protective matrix. They are significant problems in medical and industrial conditions, as they exhibit increased resistance against antimicrobial agents and mediate chronic infections. Scientific research focuses extensively on *S. aromaticum* as an active *Syzygium* species, demonstrating significant antibiofilm properties. The essential oil obtained from *S. aromaticum*, which consists of high eugenol content, possesses strong antibiofilm activities, causing inhibition of biofilm formation and the destruction of mature biofilms of pathogens such as *Candida albicans* and *Staphylococcus aureus* (Shahina et al., 2024; Kačániová et al., 2021).

Anthelmintic activity means expelling or destroying parasitic worms, also called helminths, from the host. These parasitic worms can lead to myriad of helminthiasis in humans and animals. Based on their chemical makeup and modes of action, anthelmintic agents are categorized; the most prevalent classes are benzimidazoles, such as albendazole, which targets the energy metabolism of the parasite, ultimately causing paralysis and death of the worms (Bereda, 2022). *Syzygium* species, particularly *S. cumini*, have shown considerable anthelmintic activity, as reported in several studies. Methanol and ethyl acetate extracts of *S. cumini* demonstrate anthelmintic activity against *Lumbricus terrestris* in a dose-dependent mode. When given in doses of 50-200 mg/kg of the body weight, the extract was effective in paralyzing and killing the worms, with better efficacy observed with

increasing concentration, especially at higher concentrations comparable to the standard drug albendazole. It is suggestive that the extract has bioactive compounds that disrupt the neuromuscular function of the worms, as shown in the dose-dependent paralytic effect (Lakshmi et al., 2022).

The capacity of material to combat inflammation, a biological process brought on by pathogens, damaged cells, and irritants, is known as anti-inflammatory activity. This process is essential for the regulation of different inflammatory disorders and diseases. Different species of *Syzygium* have been well studied for anti-inflammatory properties. Examples of this include *S. caryophyllatum* and *S. nervosum* leaf extracts, which exhibit significant activity against one or more anti-inflammatory targets correlating with superior anti-inflammatory effects when compared to standard therapeutic agents such as Acetyl Salicylic acid at certain concentrations tested (Kavitha & Poonguzhali, 2024).

Antidiabetic activity means that the compound can reduce or control blood glucose levels of diabetes mellitus, a chronic metabolic disorder characterized by hyperglycemia consequent to defects in insulin secretion, insulin action, or both (Zulcafli et al., 2020). Related species have been identified by studying *S. jambolanum*, *S. cumini* and others as potential anti-diabetic agents. These plants have historically been utilized in several cultures to control diabetes, and recent scientific studies have elucidated their mechanisms of action. *S. jambolanum* has been reported to reduce blood glucose, enhance insulin sensitivity, and protect beta cells of the pancreas (Shanmugam, 2024).

Antitumor activity means its ability to prevent or reduce the growth and spread of tumors. This activity is the most important component of cancer treatment, leading the malignant cells to shrink, thus preventing metastasis formation. Recent studies on *Syzygium* species, especially *S. aqueum*, *S. samarangense*, and *S. cumini*, have manifested significant antitumor activity. These plants contain bioactive phytochemicals like phenolics, oleanolic acids, and betulinic acids, which play a role in their anticancer effect by restricting the proliferation and activating apoptosis (Abdulrahman & Hama, 2023; Chua et al., 2019).

The genus *Syzygium* (Myrtaceae) has received a lot of scientific attention because of its pharmacological properties and traditional therapeutic uses. This study investigated the therapeutic potencies of three endemic species of *Syzygium*, namely *S. laetum*, *S. occidentale*, and *S. palghatense*, by performing various biological assays on them. Although several *Syzygium* species are regarded as possessing antioxidant, antimicrobial, and antidiabetic properties, these endemic species are understudied despite their potential medicinal value. This systematic study is especially relevant since *S. palghatense* is endemic to Palakkad, Kerala, India, and faces habitat loss threats, whereas *S. laetum* and *S. occidentale* are unexplored species of this medicinally important genus. This comprehensive study contributes to the much-needed documentation and validation of the biological activities exhibited by endemic plant species, which may yield novel bioactive compounds for pharmaceutical exploitation.

- **Objectives**

- Evaluate the antioxidant potential of *S. laetum*, *S. occidentale*, and *S. palghatense* leaf and bark extracts using multiple *in vitro* assays.
- Assess antimicrobial activities of *Syzygium* extracts against selected pathogens.
- Investigate anthelmintic efficacy using *Lumbricus terrestris*
- Examine anti-inflammatory properties through *in vitro* assays and *in vivo* models.
- Determine antidiabetic potential via α-amylase and α-glucosidase enzyme inhibition assays.
- Screen for potential antitumor properties.

6.2. Materials and Methods

6.2.1. Antioxidant activities

Antioxidants are essential components that are mediators to nullify harmful reactive oxygen species (ROS) and their derivatives to avoid cell damage and oxidative stress (Birben et al., 2012; Huang et al., 2015). Such defensive molecules act through various frontline strategies like inhibiting new radicals, scavenging them once formed, and repairing old, damaged membranes (Arora et al., 2000; Gill & Tuteja, 2010). For instance, enzymes like glutathione peroxidases, catalase, and superoxide dismutase (SOD) make up the antioxidant defense system, as well as nonenzymatic antioxidants, which in turn maintain cellular redox homeostasis (Schieber & Chandel, 2014). During metabolic activities, the human body generates unstable molecules known as free radicals. The higher production of free radicals induces oxidative stress, which leads to many serious health issues, such as cardiovascular disease, neurological problems, asthma, premature aging, stroke, arthritis, and diabetes.

Three endemic *Syzygium* species leaves and bark were selected for the current study, and their ability to scavenge free radicals was assessed employing a variety of *in vitro* assays with different amounts of petroleum ether, chloroform, methanol, ethyl acetate, and distilled water extracts. Because each experiment was conducted in six replications (n=6), which are shown by standard error bars, statistical reliability was guaranteed (mean ± SE).

6.2.1.1. DPPH radical scavenging assay

A quick and easy way to gauge antioxidant capacity is to look at DPPH radical-reducing activity. The various solvent extracts (petroleum ether, chloroform, ethyl acetate, methanol, and distilled water) of leaves and bark of the *S. laetum, S. occidentale*, and *S. palghatense* were tested for their scavenging activity against the DPPH (2, 2-diphenyl-1-picrylhydrazyl) according to the method suggested by Aquino et al. (2001) with modifications. The reduced DPPH-H is created when the odd electrons in the stable DPPH free radical combine with hydrogen from an antioxidant.

The decolourization that results is stochiometric to the quantity of electrons that are caught. DPPH is pink, but when antioxidants scavenge it, it turns yellow. The extent of discoluration reflects the antioxidant compound's scavenging capacity. The freshly made DPPH (187 µl) was transferred to various test tubes that were shielded from the sun. Stock concentration, 1 mg/mL of methanol extracts was utilized to create various concentrations ("1, 2, 3, 4, and 5 µg/mL") that were added to this solution. The methanol was used to increase the volume up to about 1 millilitre. The reaction mix was left to rest in complete darkness for twenty minutes in room temperature. Using methanol as a blank, the absorbance of the sample was measured at 517 nm. The methanol (813 µl) with DPPH solution (187 µl) was taken as control. The standard that was employed was ascorbic acid. The required concentration of IC_{50} was determined, and % suppression of the DPPH radical's scavenging ability was represented. The results are given in Mean ± SD, and each experiment was run six times.

$$\text{Percentage of inhibition} = \frac{Ac - As}{Ac} X100$$

Where As, is the absorbance of the sample and Ac is the control's absorbance.

A preliminary screening of antioxidant potential (DPPH) across various solvent fractions (methanol, petroleum ether, chloroform, & distilled water) identified the methanolic extract as the most promising candidate for further biological studies due to its superior bioactive profile compared to the other solvent extracts tested. This compelling evidence led to the strategic selection of methanol extracts for subsequent comprehensive antioxidant and other analyses, optimizing both research efficiency and reliability of results.

6.2.1.2. Superoxide radical scavenging assay

Superoxide is a biologically significant radical. However, excessive generation of this radical can result in a redox imbalance that has detrimental effects on the body. The nitro blue tetrazolium, NBT reduction method of McCord & Fridovich (1969) was used to assess the methanol extracts of the plant sample's

capacity to scavenge superoxide anion radicals. The assay relies on a drug's capacity to prevent superoxide, which is produced by the system's photoreduction of riboflavin, from reducing NBT. The NBT is reduced to a blue-coloured complex by the superoxide radical that is thus produced. The standard used was ascorbic acid.The various concentrations of the methanol extracts (20, 40, 60, 80, and 100 µg/mL) were added to the reaction mixture consisting of 2 ml EDTA, 0.3 mM NaCN in 0.1 M EDTA, 0.05 ml riboflavin (0.12 mM), 0.1 ml NBT (1.5 mM), and 2.64 ml phosphate buffer (0.067 M, pH 7.8) making up the volume to a total of 3 ml. A control with all reagents except the plant extract and an equivalent distilled water's quantity had to be taken. Ascorbic acid acted as a standard. The NBT and riboflavin were added in the dark condition, and every tube was light in a uniform fashion with the help of an incandescent lamp for 15 min. Optical density measured at 560 nm both before and after the illumination. Absorbance readings of the experimental and control tubes were compared in order to measure the percentage inhibition. It was determined what the IC_{50} (drug concentration needed to scavenge 50% superoxide anion) value was. Six tests were performed on each sample, and the mean values were determined.

$$\text{Percentage of inhibition} = \frac{Ac - As}{Ac} X100$$

Where Ac stands for absorbance of the control.

As stands for absorbance of the sample.

6.2.1.3. Hydroxyl radical scavenging activity

The hydroxyl radical scavenging activity of the methanol extracts of the various plant samples was measured as per the protocol of Saldanha et al. (1990). This test measures the capacity of different plant extract concentrations to scavenge the hydroxyl radicals produced by the Fe3+-ascorbate-EDTA-H_2O_2 system, The Fenton reaction. The hydroxyl group attack on deoxyribose. This ultimately results in formation of thiobarbituric acid reaction substances, TBARs. In a final volume of 1 ml, the reaction mixture contained different concentrations of the methanol extracts of the plant samples (20, 40, 60, 80, and 100 µg/mL), ferric chloride (100 µM), EDTA

(100 µM), deoxy-2-ribose (2800 µM), phosphate buffer (100 µM, pH 7.4), hydrogen peroxide (100 µM), and ascorbic acid (100 µM). For one hour, the reaction mixture was incubated at 37℃. At the end of incubation, discard 0.6 ml from the reaction mixture of each test tube, then add 1.5 ml of acetic acid (20%, pH 3.5), 0.2 ml of sodium dodecyl sulphate (SDS, 8.1%), 1.5 ml of TBA (0.8%) and 0.4 ml distilled water. After proper mixing, this reaction mixture was incubated at 100ºC. After cooling, the absorbance was measured at 532 nm (Ohkawa, 1979). All the experiments were carried out six times, and the percent inhibition was calculated by the formula,

$$\text{Percentage of inhibition} = \frac{Ac - As}{Ac} X100$$

Ac and As are the absorbance of the control and sample, respectively.

6.2.1.4. Ferric reducing antioxidant power assay

Based on the ferric ion, the ferric-reducing antioxidant power (FRAP) method calculates the test compounds reducing capacity. In order to preserve iron solubility, the FRAP assay was carried out at an acidic pH of 3.6. A change in primary reaction mechanism results from the reaction at low pH, that increases redox potential & reduces the ionization potential which is responsible for propelling electron transfer. An strong blue colour with an absorption maximum of 595 nm is produced when a ferric tripyridyl triazine (Fe III-TPTZ) complex is reduced to a ferrous (Fe II) form at low pH. The FRAP reagent was freshly prepared, and 900 µl was mixed with different concentrations of the plant extract, and made up to 1 ml with acetate buffer. Fifteen minutes was the time for which the reaction mixture was incubated at a temperature of 37ºC. The reading was taken against the blank, the acetate buffer at 595 nm. The increase in the percentage of ferric-reducing activity was then calculated (Pulido et al., 2000).

6.2.2. Antimicrobial activities

Antimicrobial activity is the capacity of an agent to kill or inhibit microorganisms, such as bacteria, viruses, fungi and algae. This process is vital for fighting infection and represents an exciting target in pursuing novel therapeutic agents, particularly in the face of rising antimicrobial resistance, AMR (Atallah et al., 2022; García et al., 2024).

The methanol extracts of the leaves and bark of the three chosen *Syzygium* species were tested for anti-fungal and anti-bacterial activities using the agar well diffusion method. The active plant extracts' MBC, MFC, and MIC against the strains were ascertained. The standard/ATCC bacterial and fungal strains were used to measure antimicrobial activity.

6.2.2.1. Test microorganisms

The following reference strains were used to evaluate the antimicrobial activity of the methanol extract of leaves and bark of *S. laetum*, *S. occidentale*, and *S. palghatense.* Fungi: *Aspergillus niger* (ATCC 16404), and *Candida albicans* (ATCC 10231); Gram-positive bacteria: *Staphylococcus aureus* (ATCC 25923), *Streptococcus mutans* (MTCC 890), and *Enterococcus fecalis* (ATCC 2912); Gram-negative bacteria: *Escherichia coli* (ATCC 25922), and *Pseudomonas aeruginosa* (ATCC 27853).

The test microorganisms were obtained from the Microbial Type Culture Collection (MTCC) at the Institute of Microbial Technology (IMTECH), Chandigarh, and the American Type Culture Collection (ATCC), Manassas, Virginia.

6.2.2.2. Nutrient medium used

The antimicrobial activity was tested using Potato Dextrose Agar Medium, PDA, Potato Dextrose Broth, PDB, Sabouraud Dextrose Agar, SDA, Mueller Hinton Agar, MHA, and Muller Hinton Broth, MHB, procured from HiMedia Laboratories Pvt. Ltd., Mumbai, India.

6.2.2.3. Concentrations of the sample

Different concentrations were prepared using a two-fold dilution method for antimicrobial and minimum inhibitory concentration activity.

6.2.2.4. Inoculation

The fungal inoculum of each strain was suspended in Potato Dextrose Broth, and the bacterial strain was Muller-Hinton Broth and incubated for 8 -12 hours at 37°C.

6.2.2.5. Antifungal activity

The antifungal effect of methanolic extracts prepared from leaves and bark of selected plant species was tested against Aspergillus niger and Candida albicans using the agar well-diffusion method. For medium preparation, 39 g of commercially available Potato Dextrose Agar Medium (Hi-Media) was dissolved in 1000 mL of distilled water. The solution was autoclaved for 15 minutes at 121 °C and 15 psi, thoroughly mixed, and then dispensed (20 mL/plate) into sterile Petri plates (90 mm).

For broth, 24 g of Potato Dextrose Medium (Hi-Media) was dissolved in 1000 mL of distilled water, boiled to ensure complete solubilization, and sterilized again by autoclaving at 121 °C for 15 minutes at 15 psi. Overnight cultures of A. niger and C. albicans were maintained in Potato Dextrose Broth Medium and subsequently inoculated onto PDA plates.

The plant extracts were dissolved in Dimethyl Sulfoxide (DMSO) at a stock concentration of 10 mg/mL. Agar wells (~10 mm diameter) were prepared using a sterile borer, and different concentrations of the extract (250 µg, 500 µg, and 1000 µg) were added. Plates were incubated at room temperature overnight, and inhibition zones were compared with those produced by the reference antifungal agent Clotrimazole (10 mg/mL). Each concentration was tested in six replicates to validate the results (Patel et al., 2014).

6.2.2.5.1. Minimal inhibitory concentration (MIC) and minimal fungicidal concentration (MFC)

The MIC values for filamentous fungi were determined using broth macro dilution protocols based on the CLSI reference documents with minor modifications (CLSI, 2012). In brief, methanol extract of leaves and bark was tested using two-fold serial dilutions in DMSO with final test concentrations ranging from 10-300 µg/mL. Inoculums were made by counting conidia in a haemocytometer from 7-day-old Potato Dextrose Agar cultures and then adjusting to the appropriate final density (Shehata *et al*., 2008). For *Aspergillus niger* and *Candida albicans*, results were read after 48 hrs of incubation, and MICs were defined as the lowest test concentrations that inhibited growth completely. MFC (Minimum Fungicidal Concentration) values were determined by subculturing 20 ml samples from all optically clear tubes (total growth suppression) and the final tube exhibiting growth on SDA Petri dishes after the matching MIC values had been read. For at least three days, or until growth was apparent in the control samples, the dishes were incubated at 35°C. The lowest concentration of plant extracts where in no noticeable growth was seen was used to determine MFC values. The experiments were duplicated and repeated six times independently, yielding essentially the same results each time (Pinto et al., 2009).

6.2.2.6. Antibacterial activity

An antibacterial assay was performed using "Mueller-Hinton Agar" (MHA) plates and the agar well diffusion method. MHA medium was created after dissolving 33.8 g in 1 L of distilled water, autoclaved at on hundred and twenty-one degrees Celsius for fifteen minutes, and poured in ninety mm Petri plates (20 mL each). Nutrient broth was created by dissolving thirteen grams in 1 litre of water, boiled, and sterilized under similar conditions. Test units grown in the broth and incubated for overnight (37 °C) to match 0.5 McFarland standards (1.5×10^8 CFU/mL). Plant extracts (10 mg/mL) were prepared in DMSO. MHA plates seeded with *Staphylococcus aureus, Streptococcus mutans, Enterococcus faecalis, Escherichia coli,* and *Pseudomonas aeruginosa* were used. Wells of about 10 mm were filled with sample concentrations of 250 µg, 500 µg, and 1000 µg. Plates were incubated at 37

°C for 24 hours, and antibacterial activity was assessed by measuring inhibition zone diameters Streptomycin (10 mg/mL) was used as a positive control (Jani et al., 2012).

6.2.2.6.1. Minimal inhibitory concentration (MIC) and minimal bactericidal concentration (MBC)

The MIC and MBC values were calculated using a standard protocol (CLSI, 2012). MIC was executed inside of 96-well U-shaped microtiter plate that had a two-fold standard broth microdilution method along with the inoculum of approximately 10^6-10^8 CFU/ml. In the medium containing inoculum, methanol extracts of three selected plant species with a 10 mg/mL concentration were mixed and diluted two-fold. The minimal inhibitory concentration (MIC) was defined as the lowest concentration of antimicrobial agent capable of inhibiting visible growth, whereas the minimal bactericidal concentration (MBC) was the lowest concentration of antimicrobial agent capable of completely killing culture growth (Rukayadi, 2008).

6.2.3. Anthelmintic activities

Anthelmintic activity is the capability of substances to expel parasitic worms (helminths) from the body by either stunning or killing (vermicide) them without causing significant damage to the host. Human and veterinary use of anthelmintics is particularly high in developing countries, where mass deworming campaigns and livestock management are common. Anthelmintics treat helminthiasis in both humans and animals, particularly in mass deworming campaigns in developing countries and for livestock management. The most common drugs against soil-transmitted helminths are mebendazole and albendazole, while praziquantel is preferred for schistosomiasis and tapeworms (Bhattacharya, 2019). *In vitro* tests using earthworms are often used to study anthelmintic activity due to their anatomical and physiological similarities with intestinal roundworms, where time to paralysis and death measurements are used for assessment.

The earthworms *Lumbricus terrestris* were procured from IRTC, Mundur, for anthelmintic studies. The anthelmintic activity was evaluated using methanolic and aqueous extracts of leaves and bark of *S. laetum*, *S. occidentale*, and *S. palghatense*.

Stock solutions of 100 mg/mL for each extract were prepared, and different concentrations (25, 50, 75, and 100 mg/mL) were made for testing. Albendazole (20 mg/mL, Glaxo Smith Kline) was used as a standard reference drug. The assay was performed on adult earthworms due to their anatomical and physiological resemblance with the intestinal roundworm parasites of humans. Fourteen groups of approximately equal-sized earthworms were placed in Petri plates containing 50 mL of the respective test solutions: Group I (Control, distilled water), Group II (Standard, Albendazole), and Groups III-XIV (various concentrations of methanolic and aqueous extracts of leaves and bark of the three *Syzygium* species, *S. laetum*, *S. occidentale,* and *S. palghatense*). Observations on the time taken by parasite for paralysis and death were recorded for individual worms. Paralysis was recorded when there is no movement except the worms were shaken vigorously. Death time was recorded after the confirmation that the worm neither moved when shaken vigorously nor dipped in the warm water (50°C), followed by fading of their body colours. All results were expressed as mean ± standard deviation (Patel et al., 2011).

$$\text{Inhibition \%} = (\text{Control death time} - \text{sample death time}) \times 100$$

6.2.4. Anti-inflammatory activities

6.2.4.1. *In vitro* Human Red Blood Cell (HRBC) membrane stabilization method

The anti-inflammatory activity of the methanolic extract of *S. laetum, S. occidentale,* and *S. palghatense leaves and* bark were assessed using the *in vitro* HRBC membrane stabilization assay as described by James et al. (2009) with slight modifications.

Fresh human blood was collected from healthy individuals in compliance with institutional ethical guidelines and mixed in an equal volume of Alsever's solution, which contained 0.05% citric acid, 2% dextrose, 0.8% sodium citrate, and 0.42% sodium chloride to prevent coagulation. The mixture was centrifuged at 3000 rpm for 10 minutes, and the packed red blood cells (RBCs) were washed three times with isosaline (0.85%, pH 7.2). A 10% (v/v) suspension of RBCs was prepared in isosaline.

Different concentrations of the methanolic extract (10, 20, 30, 40, 50, 60, 70, 80, 90, and 100 µg/mL) were taken separately and mixed with an equal amount of volume of phosphate buffer (pH 7.4) and the 10% HRBC suspension. Mixtures were incubated for 30 minutes (37°C) and subsequently centrifuged at the speed of 3000 rpm (10 mins). The absorbance of the supernatant was recorded at 560 nm using a UV–Visible spectrophotometer to estimate the amount of hemoglobin released due to hemolysis.

6.2.4.2. *In vivo* anti-inflammatory studies

6.2.4.2.1. Carrageenan-induced acute paw edema

Female BALB/c mice (25-30 g) were divided into 4 groups. Group 1 was kept as control (carrageenan alone) and Group II received diclofenac (25 mg/kg b. wet.). Group III (low dose) and IV (high dose) were treated with 100 and 200 µL of plant samples respectively. The animals were pretreated with the respective drug or diclofenac dose for 4 days. On the 5th day 1 hour after plant sample or diclofenac administration, inflammation was induced by sub plantar injection of 0.2 mL of 11% carrageenan in 0.1% carboxy methyl cellulose into the right hind paw of all the animals. Paw thickness was measured using Vernier caliper 1 hour prior and for every hour up to 6th consecutive hours after carrageenan injection. The percentage of inhibition was calculated.

6.2.4.2.2. Formalin-induced acute paw edema

Female BALB/c mice (25-30 g) were pretreated for 7 days with the respective drug or diclofenac and continued for the next 7 consecutive days. On the 8th day, chronic inflammation was induced by sub plantar injection of 0.2 mL of 1% formalin 1 hour after plant extract or diclofenac administration. Paw thickness was measured using Vernier caliper 1 hour prior and continued for the next 6 consecutive days after formalin injection. The percentage of inhibition was calculated.

6.2.5. Anti-diabetic activity

6.2.5.1. α-amylase inhibitory assay

A 1% phosphate buffer and starch solution were prepared and incubated with 500 µL of α-amylase for 10 minutes at 37 °C. Subsequently, 1 mL of pooled fractions (20–100 µg/mL) from methanolic extracts of S. palghatense leaves and bark was added. The reaction was stopped using 2 M NaOH, followed by the addition of 1 mL dinitro salicylic acid and heating in a water bath for 5 minutes. After cooling under running water, the volume was adjusted to 10 mL with sterile distilled water, and absorbance was recorded at 540 nm. Acarbose served as the reference standard.

6.2.5.2. α- Glucosidase inhibition assay

One milligram of α-glucosidase (from Saccharomyces cerevisiae) was suspended in 100 mL of neutral phosphate-buffered saline containing 200 mg bovine serum albumin. Different concentrations (20–100 µg/mL) of pooled fractions from methanolic extracts of leaves and bark of three plants were combined with a reaction mix consisting of 10 µL phosphate buffer (pH 6.8) and 490 µL 5 mM p-NPG. After incubation at 37 °C for 5 minutes, 250 µL of α-glucosidase (0.15 U/mL) was added, and the mixture was incubated again for 15 minutes. The reaction was stopped by adding 2 mL of 200 mM sodium carbonate after cooling. Enzyme inhibition activity was determined at 405 nm, with acarbose used as the reference standard.

Percentage calculation

Percentage of free radical scavenging, α-amylase and α-glucosidase inhibition were measured with the formula: Percentage Inhibition/scavenging activity = $[(A_{control} - A_{sample})/ (A_{control})] \times 100$. Where A = absorbance.

6.2.6. Anticancer study

6.2.6.1. Cytotoxicity evaluation of methanol extract of *S. palghatense* bark using the Trypan Blue Exclusion method

The cytotoxicity of the methanolic bark extract of *S. palghatense* was evaluated using the trypan blue exclusion method. Dalton's Lymphoma Ascites (DLA) cells were isolated and incubated with various concentrations of the extract for

3 hours (37°C). After the incubation, trypan blue dye was added to distinguish viable (unstained) from dead (blue-stained) cells, and the percentage cell death was calculated as the ratio of dead cells to total cells multiplied by 100. This method quantitatively assessed the cytotoxic effects of the extract on DLA cells, demonstrating its antiproliferative potential through the induction of cell death (Hussein & Mohsin, 2019).

$$\text{Percentage cell death} = \frac{\text{Number of dead cells}}{(\text{Number of viable cells} + \text{Number of dead cells})} \times 100$$

6.2.6.2. Acute toxicity study

The acute toxicity of *S. palghatense* methanol bark extract was evaluated in an animal model following standard ethical guidelines. Adult Wistar rats were randomly allocated into groups, including a control group receiving no treatment and groups administered with the extract at a dose of 1 g/kg body weight via oral gavage. The dose for each animal was calculated based on its individual weight to ensure precise administration. Animals were observed continuously for the first 4 hours post-treatment and then twice daily for 14 days for any signs of toxicity, abnormal behavior, physical changes, or mortality (Hussein & Mohsin, 2019).

Animal dose calculation =

Animal weight/1000 x drug dose x No. of animals x No. of days

6.2.7. Statistical analysis

A generalized statistical method for plant extract analysis involves presenting data as mean ± standard error (SE) with an appropriate number of replicates (usually $n \geq 3$). The data was analysed with analysis of variance (ANOVA) to assess significant differences among different treatments or sample groups. When ANOVA shows significance ($p < 0.05$), post-hoc multiple comparison tests, such as Least Significant Difference (LSD) test are applied to determine which means differ significantly. Prior to ANOVA, data are tested for normality and homogeneity of variance to satisfy parametric test assumptions. For concentration-dependent assays, nonlinear regression is used to estimate IC_{50} or similar inhibitory values. This approach is widely applicable for quantitative analysis in phytochemical, antioxidant, antimicrobial, and other biological activity studies of plant extracts.

6.3. Results

6.3.1. Antioxidant studies

The antioxidant activities of the methanolic extracts of *S. laetum*, *S. occidentale*, and *S. palghatense* leaves and bark were quantitatively compared using DPPH, superoxide (SRSA), hydroxyl (HRSA), and FRAP assays, with results expressed as Mean ± SE and statistical significance tested by ANOVA and LSD/CD post-hoc analysis. In the DPPH assay, *S. laetum* leaf and bark showed IC_{50} values of 44.50 ± 0.71 µg/mL and 41.70 ± 0.14 µg/mL, while *S. occidentale* leaf and bark were 54.24 ± 1.10 µg/mL and 52.58 ± 1.03 µg/mL, and *S. palghatense* leaf and bark exhibited markedly lower IC_{50}s at 2.31 ± 0.13 µg/mL and 1.45 ± 0.04 µg/mL, indicating superior radical scavenging potency. In the superoxide and hydroxyl assays, similar trends appeared: *S. palghatense* extracts had the lowest IC_{50}s (SPL: 4.45 ± 0.07 µg/mL, SPB: 1.63 ± 0.04 µg/mL for SRSA; SPL: 63 ± 1.41 µg/mL, SPB: 52 ± 0.38 µg/mL for HRSA), outperforming *S. laetum* and *S. occidentale*. The FRAP assay also showed outstanding potency for *S. palghatense* (SPL: 1.98 ± 0.11 µg/mL, SPB: 1.35 ± 0.07 µg/mL). F-values for all assays were highly significant ($p < 0.001$), confirming real differences among samples.

These results demonstrate that while all *Syzygium* extracts exhibit notable antioxidant activity, *S. palghatense* (both leaf and bark) consistently achieves the lowest IC_{50} values and highest percentage inhibition across all tested assays and concentrations. *S. laetum* and *S. occidentale* extracts, although less potent than *S. palghatense*, still show appreciable antioxidant effects, especially in their bark extracts. Overall, the study establishes *S. palghatense* bark as the most effective antioxidant source among the evaluated *Syzygium* species (Tables 6.1-6.4; Figures 6.1-6.5).

6.3.2. Antimicrobial studies

The comparative antimicrobial activity of three *Syzygium* species (*S. laetum*, *S. occidentale*, and *S. palghatense*) was reported (Tables 6.5-6.7) using methanolic extracts of leaf and bark parts. The study tested antifungal and antibacterial efficacy

Table 6.1: Statistical comparison of antioxidant activity between the methanol extracts of *Syzygium laetum*, *Syzygium occidentale* and *Syzygium palghatense* leaf and bark expressed as Mean ± Standard Error (SE), with statistical significance (F-value, P-value, and Critical Difference)

Parameters	DPPH	SRSA	HRSA	FRAP
SLL	44.50 ± 0.7071^{c}	59 ± 1.8210^{e}	81 ± 1.3690^{d}	38 ± 1.3010^{c}
SLB	41.70 ± 0.1414^{b}	57 ± 1.2901^{d}	78 ± 4.2401^{c}	31 ± 1.2202^{b}
SOL	54.24 ± 1.1010^{e}	61 ± 1.8210^{f}	84 ± 0.3750^{e}	50 ± 1.2010^{e}
SOB	52.58 ± 1.0301^{d}	54 ± 1.2102^{c}	80 ± 1.4140^{cd}	48 ± 1.2110^{d}
SPL	2.305 ± 0.1340^{a}	4.45 ± 0.0707^{b}	63 ± 1.4140^{b}	1.975 ± 0.1060^{a}
SPB	1.447 ± 0.0411^{a}	1.625 ± 0.0350^{a}	52 ± 0.3750^{a}	1.35 ± 0.0707^{a}
Standard	56 ± 0.013^{f}	63 ± 0.124^{g}	86 ± 0.231^{e}	50 ± 0.140^{e}
F Value	1912.3	3299.58	245.44	1823.4
p-value	<0.001	<0.001	<0.001	<0.001
CD Value	1.611	1.401	2.356	1.483

Table 6.2: Statistical comparison of antioxidant activity of methanol extracts of *Syzygium laetum*, *Syzygium occidentale,* and *Syzygium palghatense* leaf and bark expressed as Mean ± Standard Error (SE), with statistical significance (F-value, P-value, and Critical Difference)

Treatments	Mean ± SE
SLL	55.6250 ± 9.529^{d}
SLB	51.9250 ± 10.198^{c}
SOL	62.3100 ± 7.576^{f}
SOB	58.6450 ± 7.233^{e}
SPL	17.9325 ± 15.033^{b}
SPB	14.1055 ± 12.632^{a}
F Value	6084.17
p-value	<0.001
CD Value	0.778

(SLL: *Syzygium laetum* leaves; SLB: *Syzygium laetum* bark; SOL: *Syzygium occidentale* leaves; SOB: *Syzygium occidentale* bark; SPL: *Syzygium palghatense* leaves; SPB: *Syzygium palghatense* bark)

Table 6.3: Comparative antioxidant activity of methanol extracts of *Syzygium laetum, Syzygium occidentale, and Syzygium palghatense* leaf and bark across multiple assays (DPPH, SRSA, HRSA, FRAP) expressed as Mean ± Standard Error (SE), with statistical significance (F-value, P-value, and Critical Difference)

Assays	Mean ± SE
DPPH	32.7953 ± 9.967^{b}
SRSA	39.5125 ± 11.579^{c}
HRSA	73.00 ± 5.164^{d}
FRAP	28.3875 ± 8.906^{a}
F Value	8062.16
p-value	<0.001
CD Value	0.636

(DPPH: 2,2-diphenyl-1-picrylhydrazyl Radical Scavenging Assay; SRSA: Superoxide Radical Scavenging Assay; HRSA: Hydroxyl Radical Scavenging Assay; FRAP: Ferric Reducing Antioxidant Power Assay)

Table 6.4: IC_{50} values (Mean ± SE) for antioxidant activity of the methanol extracts of *Syzygium laetum, Syzygium occidentale,* and *Syzygium palghatense* leaf and bark and standard controls across multiple assays (DPPH, SRSA, HRSA, FRAP) with statistical significance (F-value, P-value, and Critical Difference)

Interaction	Mean ± SE
SLL: DPPH	44.50 ± 0.7071^{f}
SLL: SRSA	59 ± 1.8210^{m}
SLL: HRSA	81 ± 1.3690^{q}
SLL: FRAP	38 ± 1.3010^{d}
SLB: DPPH	41.70 ± 0.1414^{e}
SLB: SRSA	57 ± 1.2901^{l}
SLB: HRSA	78 ± 4.2401^{p}
SLB: FRAP	31 ± 1.2202^{c}
SOL: DPPH	54.24 ± 1.1010^{k}
SOL: SRSA	61 ± 1.8210^{n}
SOL: HRSA	84 ± 0.3750^{r}
SOL: FRAP	50 ± 1.2010^{h}
SOB: DPPH	52.58 ± 1.0301^{ij}
SOB: SRSA	54 ± 1.2102^{jk}
SOB: HRSA	80 ± 1.4140^{q}
SOB: FRAP	48 ± 1.2110^{g}
SPL: DPPH	2.305 ± 0.1340^{a}
SPL: SRSA	4.45 ± 0.0707^{b}
SPL: HRSA	63 ± 1.4140^{o}
SPL: FRAP	1.975 ± 0.1060^{a}
SPB: DPPH	1.447 ± 0.0411^{a}
SPB: SRSA	1.625 ± 0.0350^{a}
SPB: HRSA	52 ± 0.3750^{i}
SPB: FRAP	1.35 ± 0.0707^{a}
F Value	198.11
P Value	<0.001
CD Value	1.557

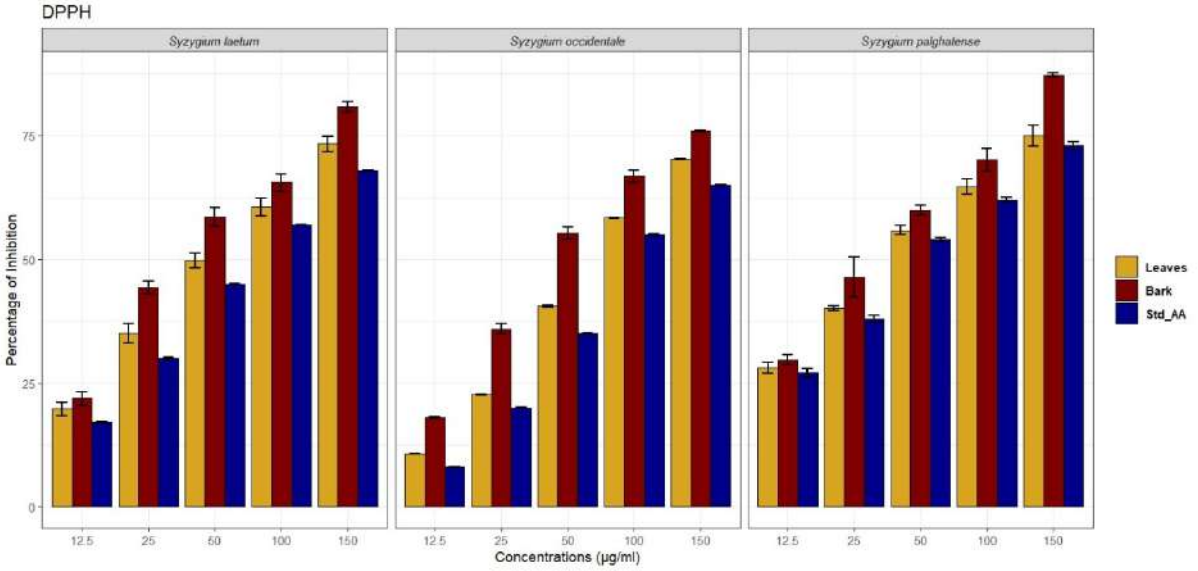


Figure 6.1: DPPH radical scavenging activity of methanolic leaf and bark extracts of *Syzygium laetum*, *Syzygium occidentale*, and *Syzygium palghatense* compared to standard ascorbic acid (Mean ± SE, n=6)

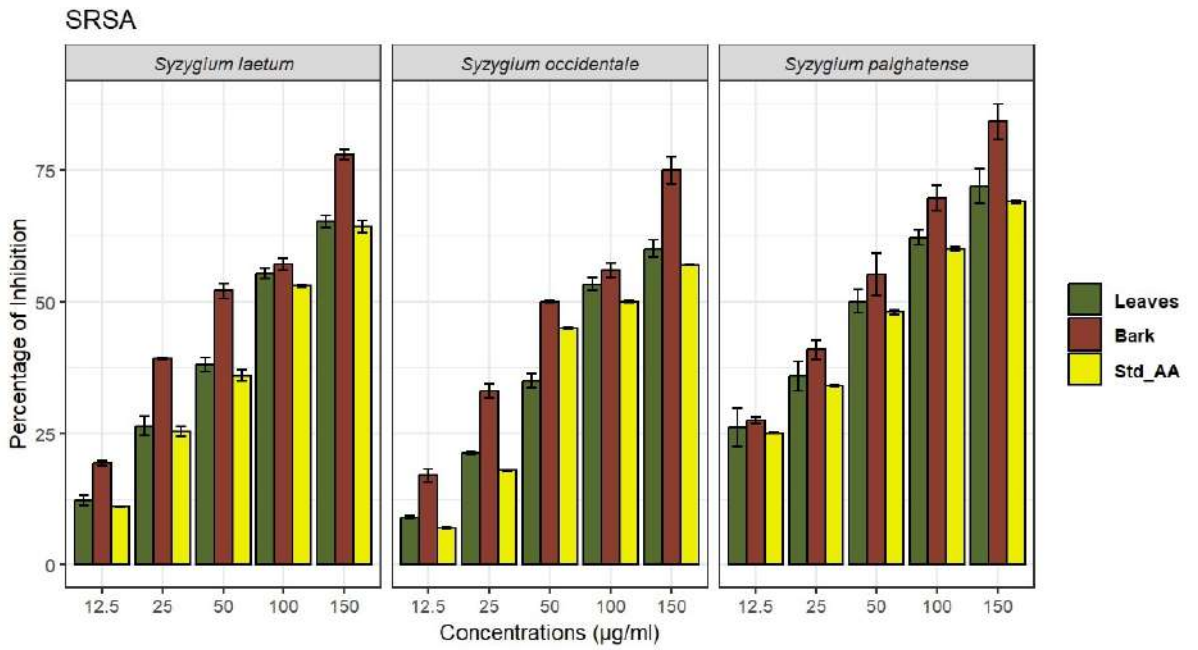


Figure 6.2: Superoxide radical scavenging activity (SRSA) of methanolic leaf and bark extracts of *Syzygium laetum*, *Syzygium occidentale*, and *Syzygium palghatense* compared to standard ascorbic acid (Mean ± SE, n=6)

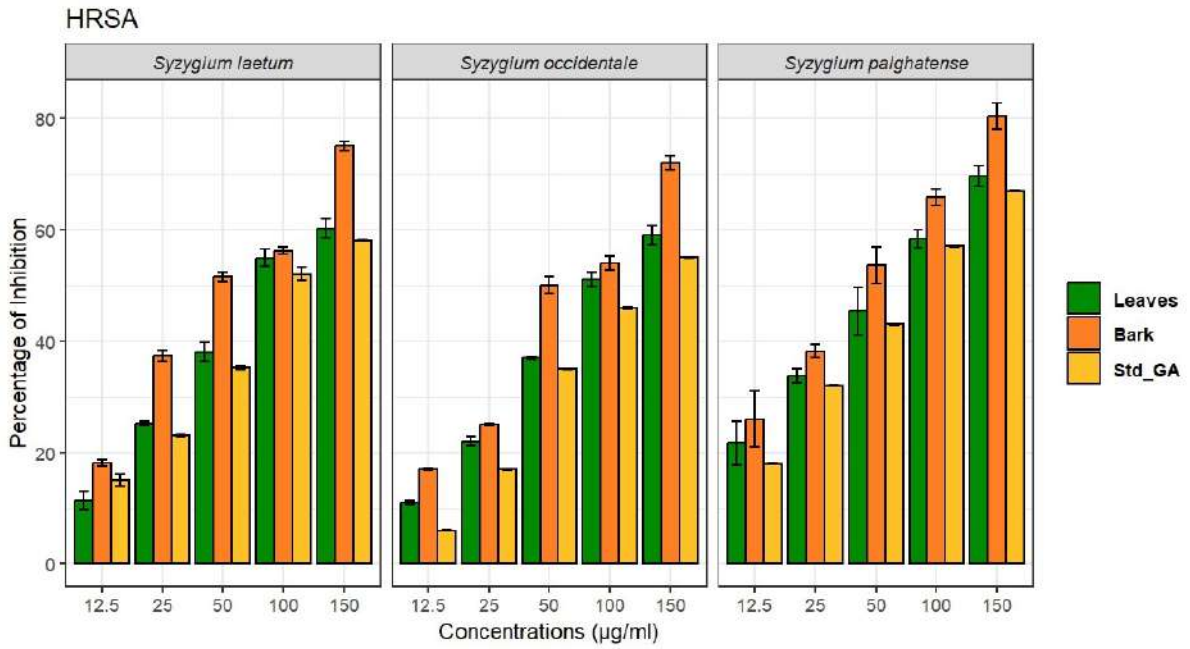


Figure 6.3: Hydroxyl radical scavenging activity (HRSA) of methanolic leaf and bark extracts of *Syzygium laetum*, *Syzygium occidentale*, and *Syzygium palghatense* compared to standard gallic acid (Mean ± SE, n=6)

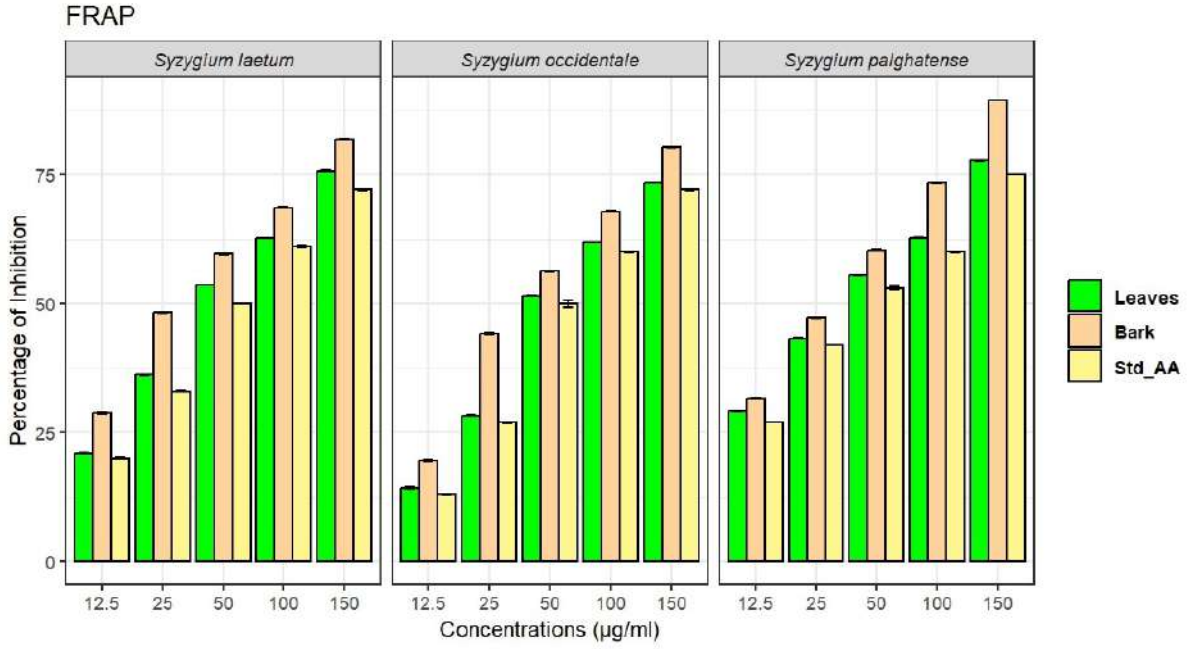


Figure 6.4: Ferric reducing antioxidant power (FRAP) of methanolic leaf and bark extracts of *Syzygium laetum*, *Syzygium occidentale*, and *Syzygium palghatense* compared to standard ascorbic acid (Mean ± SE, n=6)

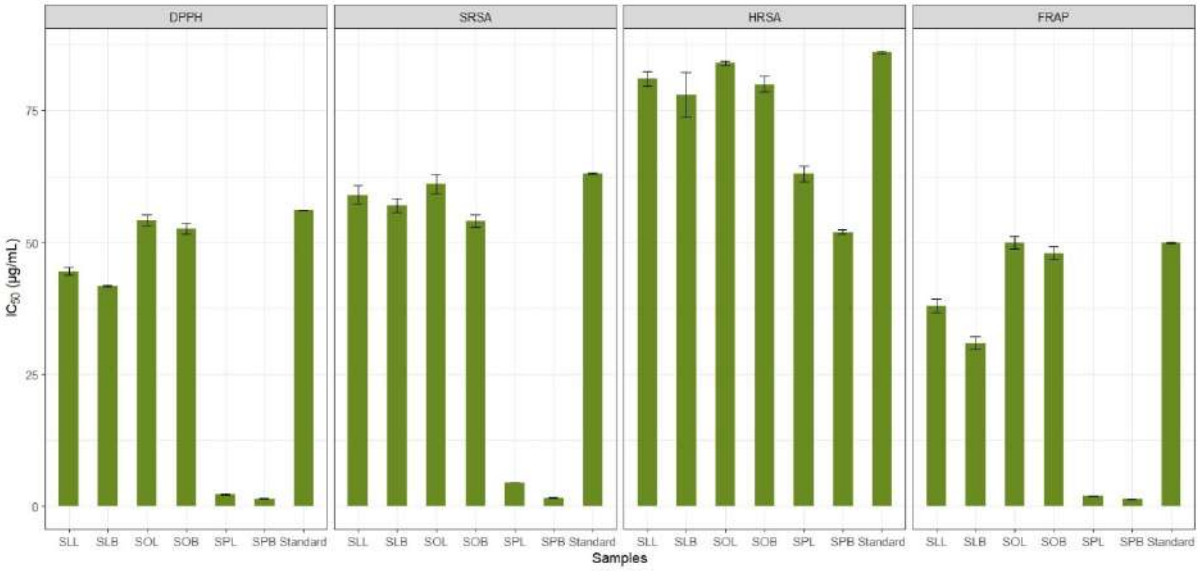


Figure 6.5: Comparative IC_{50} values (µg/mL) of methanolic leaf and bark extracts of *Syzygium laetum*, *Syzygium occidentale*, and *Syzygium palghatense* and standard controls in DPPH, Superoxide (SRSA), Hydroxyl (HRSA), and FRAP Assays (Mean ± SE, n=6)

with two fungi pathogens (*Aspergillus niger* and *Candida albicans*) and five bacterial strains (*Staphylococcus aureus*, *Streptococcus mutans*, *Enterococcus fecalis*, *Escherichia coli* and *Pseudomonas aeruginosa* at standardized concentrations (250, 500 and 1000 µg/mL).

It showed considerable antifungal efficacy in the case of fungal pathogens, while *S. palghatense* exhibited the highest action, notably its bark extract to *A. niger* (18 ± 0.19 mm at 1000 µg/mL). The antifungal activity was always lower than the standard Clotrimazole (23 ± 0.45 mm) but exhibited promising potential. With respect to the bacterial pathogens, the maximum susceptible species were *Pseudomonas aeruginosa* by *S. palghatense* bark extract (18±0.12 mm at 1000 µg/mL) and *S. aureus* by *S. palghatense* bark extract (18 ± 0.13 mm at 1000 µg/mL). *E. fecalis* was particularly sensitive to the bark extracts (18 ± 0.14 mm at 1000 µg/mL for *S. palghatense*). In contrast, *S. aureus* and *S. mutans* showed less sensitivity and higher concentrations were needed for their inhibition (Figures 6.6-6.7).

In all evaluations, bark extracts exhibited higher antimicrobial properties than leaf extracts, with activity proportional to concentration. The antimicrobial activity displayed significant potential for therapeutic applications with a zone of inhibition less than reference antimicrobials (Streptomycin: 25-28 mm). Of the three species, *S. palghatense* displayed the greatest broad-spectrum antimicrobial activity, most prominently in its bark extract, suggesting therapeutic potential for future pharmaceutical applications (Plates 6.1-6.3).

The Principal Component Analysis (PCA) biplot shows that the first principal component (PC1) accounts for 73.7% of the variability in antifungal activity of methanolic extracts of *Syzygium* species against *Aspergillus niger* and *Candida albicans*, while PC2 accounts for 20.1%. The samples inhibiting *A. niger* tightly cluster on the left side of the plot, closely associated with higher concentrations of clotrimazole and extracts, indicating strong antifungal effectiveness. Conversely, samples inhibiting *C. albicans* cluster separately on the right, reflecting different inhibition patterns likely due to the fungal species and extract response. The increasing concentration vectors direct towards enhanced activity, confirming

concentration-dependent antifungal effects. Similarly, the PCA of antibacterial activity explains 67.3% of variance with PC1 and 20.0% with PC2 among extracts tested against five bacteria, including *Staphylococcus aureus*, *Streptococcus mutans*, *Enterococcus faecalis*, *Escherichia coli*, and *Pseudomonas aeruginosa*. Each pathogen clusters distinctly, with *Pseudomonas aeruginosa* showing unique sensitivity. The vectors representing increasing extract and antibiotic concentrations correspond to stronger antibacterial activity. Overall, PCA effectively discriminates the extracts' species-specific antimicrobial profiles and concentration dependencies, elucidating their efficacy against diverse microbial pathogens in this study (Figures 6.8-6.9).

MIC and minimum fungicidal/bactericidal concentration (MFC/MBC) of methanolic leaf and bark extracts against pathogenic microorganisms were studied. On the fungal pathogens, all three species revealed very high levels of antifungal action on *Aspergillus niger* and *Candida albicans*. Antifungal studies demonstrated the relative superiority of *S. palghatense* compared to *S. laetum* and *S. occidentale*, particularly its bark extract. MIC and MFC values were stable for all species, which confirmed the prominent fungicidal mechanism of bark extracts compared to leaf extracts.

With respect to bacterial pathogens, methanolic extracts showed varying degrees of efficacy for both type of bacteria i.e., Gram-positive & Gram-negative *S. palghatense* had remarkable activity. Out of all species, *Pseudomonas aeruginosa* consistently exhibited the highest sensitivity to the extracts, particularly to bark extract. This Gram-negative bacterium exhibited the lowest MIC (113 µg/mL) and MBC values (114 µg/mL) among the microorganisms tested in this study, indicating better susceptibility than other tested microorganisms. Next to *P. aeruginosa*, *Enterococcus fecalis* exhibited high sensitivity (lowest MIC = 116 µg/mL and MBC = 117 µg/mL) against mainly bark extracts. In contrast, *Staphylococcus aureus* and *Streptococcus mutans* were consistently the least sensitive species, with inhibition and bactericidal concentrations (220-239 µg/mL). Of the fungal pathogens tested, both *Aspergillus niger* and *Candida albicans* exhibited moderate sensitivity, with *A. niger* tending to respond slightly better than *C. albicans* to the extracts. Accordingly, *P.*

Table 6.5: Antimicrobial activity of methanol extracts of the leaves and bark of *Syzygium laetum* against the pathogenic microorganisms

Fungus	Concentrations (Zone of inhibition in mm)							
	Clotrimazole (100 µg/ml)		250 (µg/ml)		500 (µg/ml)		1000 (µg/ml)	
	Leaves	Bark	Leaves	Bark	Leaves	Bark	Leaves	Bark
Aspergillus niger	34±0.35	34±0.33	19±0.22	14±0.19	22±0.20	19±0.15	28±0.21	29±0.25
Candida albicans	30±0.31	30±0.29	11±0.16	Nil	12±0.11	12±0.10	13±0.11	14±0.10
Bacteria	**Streptomycin (100 µg)**		**250 (µg/ml)**		**500 (µg/ml)**		**1000 (µg/ml)**	
	Leaves	**Bark**	**Leaves**	**Bark**	**Leaves**	**Bark**	**Leaves**	**Bark**
Staphylococcus aureus	26±0.17	26±0.19	12±0.09	12±0.06	13±0.12	13±0.11	14±0.13	14±0.12
Streptococcus mutans	25±0.16	25±0.15	Nil	11±0.08	11±0.10	12±0.11	12±0.08	13±0.10
Enterococcus fecalis	21±0.18	21±0.17	Nil	19±0.15	Nil	20±0.14	12±0.10	23±0.20
Escherichia coli	24±0.22	24±0.16	Nil	Nil	Nil	11±0.13	Nil	13±0.16
Pseudomonas aeruginosa	32±0.21	32±0.24	12±0.09	11±0.10	13±0.11	12±0.13	16±0.14	14±0.18

Values are mean ± Standard Deviation (SD)

Table 6.6: Antimicrobial activity of methanol extracts of the leaves and bark of *Syzygium occidentale* against the pathogenic microorganisms

Fungus	Concentrations (Zone of inhibition in mm)							
	Clotrimazole (100 µg/ml)		250 (µg/ml)		500 (µg/ml)		1000 (µg/ml)	
	Leaves	Bark	Leaves	Bark	Leaves	Bark	Leaves	Bark
Aspergillus niger	36 ± 0.28	34 ± 0.26	23 ± 0.20	11 ± 0.11	26 ± 0.18	13 ± 0.18	31 ± 0.30	17 ± 0.19
Candida albicans	31 ± 0.29	30 ± 0.27	11 ± 0.13	11 ± 0.12	12 ± 0.17	12 ± 0.16	13 ± 0.17	13 ± 0.12
Bacteria	**Streptomycin (100 µg/ml)**		**250 (µg/ml)**		**500 (µg/ml)**		**1000 (µg/ml)**	
	Leaves	**Bark**	**Leaves**	**Bark**	**Leaves**	**Bark**	**Leaves**	**Bark**
Staphylococcus aureus	26 ± 0.14	26 ± 0.14	Nil	Nil	11 ± 0.10	Nil	12 ± 0.11	11 ± 0.09
Streptococcus mutans	25 ± 0.21	25 ± 0.23	Nil	Nil	11 ± 0.08	Nil	12 ± 0.07	11 ± 0.05
Enterococcus fecalis	21 ± 0.14	21 ± 0.17	Nil	Nil	Nil	Nil	Nil	Nil
Escherichia coli	25 ± 0.12	25 ± 0.18	Nil	11 ± 0.05	11 ± 0.08	12 ± 0.14	12 ± 0.07	13 ± 0.11
Pseudomonas aeruginosa	32 ± 0.20	32 ± 0.19	Nil	Nil	11 ± 0.07	11 ± 0.10	12 ± 0.10	12 ± 0.09

Values are mean ± Standard Deviation (SD)

Table 6.7: Antimicrobial activity of methanol extracts of the leaves and bark of *Syzygium palghatense* against the pathogenic microorganisms

Fungus	Concentrations (Zone of inhibition in mm)							
	Clotrimazole (100 µg/ml)		250 (µg/ml)		500 (µg/ml)		1000 (µg/ml)	
	Leaves	Bark	Leaves	Bark	Leaves	Bark	Leaves	Bark
Aspergillus niger	23 ± 0.45	23 ± 0.61	13 ± 0.45	13 ± 0.31	15 ± 0.25	15 ± 0.22	16 ± 0.33	16 ± 0.19
Candida albicans	20 ± 0.57	20 ± 0.13	13 ± 0.21	12 ± 0.61	14 ± 0.16	14 ± 0.18	16 ± 0.28	15 ± 0.17
Bacteria	**Streptomycin (100 µg)**		**250 (µg/ml)**		**500 (µg/ml)**		**1000 (µg/ml)**	
	Leaves	**Bark**	**Leaves**	**Bark**	**Leaves**	**Bark**	**Leaves**	**Bark**
Staphylococcus aureus	27 ± 0.24	27 ± 0.47	11 ± 055	Nil	12 ± 0.44	Nil	13 ± 0.27	11 ± 0.24
Streptococcus mutans	27 ± 0.14	27 ± 014	Nil	Nil	11 ± 0.25	11 ± 0.27	12 ± 0.24	11 ± 0.28
Enterococcus fecalis	25 ± 0.26	25 ± 0.31	12 ± 0.22	13 ± 0.21	13 ± 0.19	14 ± 0.31	14 ± 0.16	17 ± 0.14
Escherichia coli	28 ± 0.16	28 ± 0.21	12 ± 0.14	11 ± 0.21	13 ± 0.21	13 ± 0.17	14 ± 0.15	14 ± 0.12
Pseudomonas aeruginosa	28 ± 0.13	28 ± 0.14	12 ± 0.13	13 ± 0.16	13 ± 0.15	15 ± 0.14	15 ± 0.89	18 ± 0.12

Values are mean ± Standard Deviation (SD)

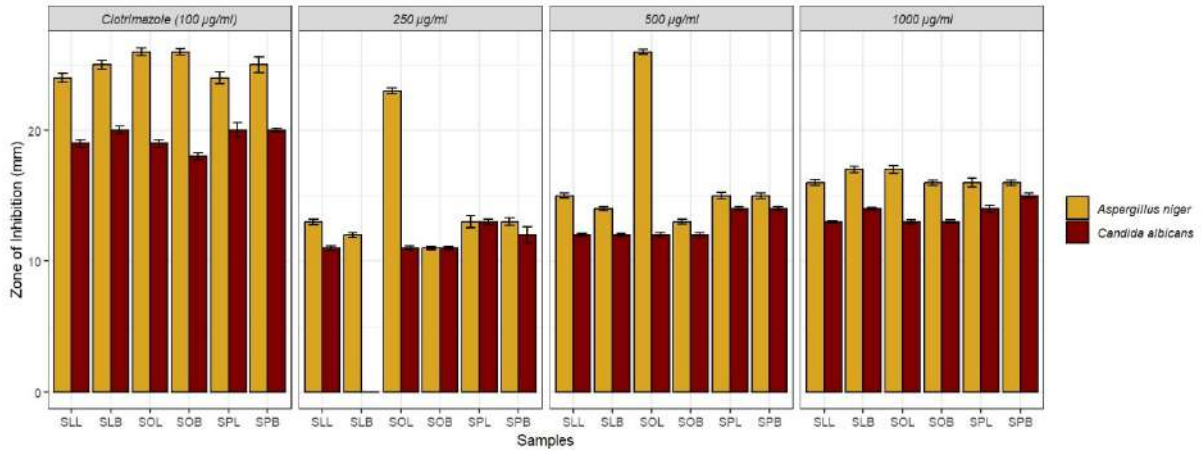


Figure 6.6: Antifungal activity (zone of inhibition, mm) of methanolic leaf and bark extracts of *Syzygium laetum*, *Syzygium occidentale*, and *Syzygium palghatense* against *Aspergillus niger* and *Candida albicans* at different concentrations, compared to clotrimazole (Mean ± SE, n=6)

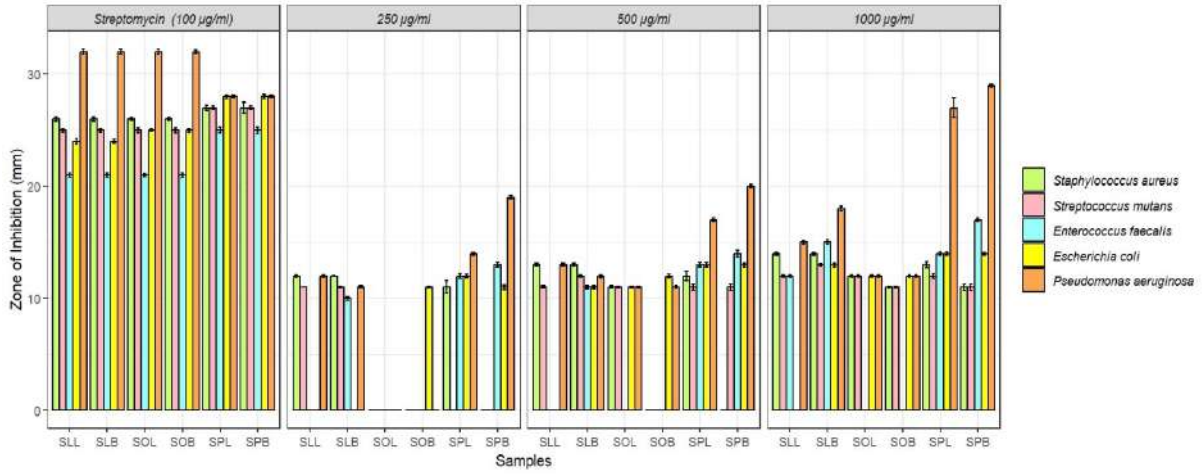


Figure 6.7: Antibacterial activity (zone of inhibition, mm) of methanolic leaf and bark extracts of *Syzygium laetu*m, *Syzygium occidentale*, and *Syzygium palghatense* against selected bacterial pathogens at different concentrations, compared to streptomycin (Mean ± SE, n=6)

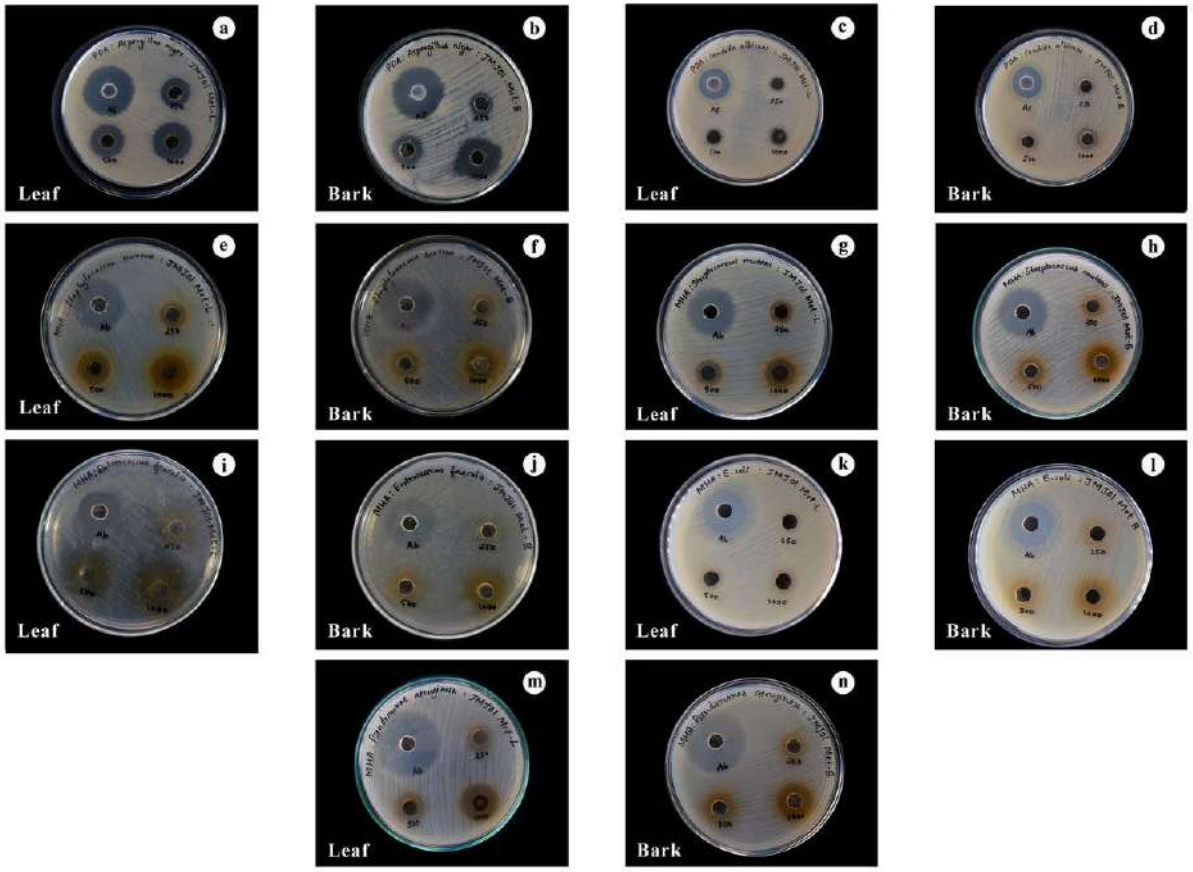


Plate 6.1: The inhibition zone (mm) of methanol extracts of leaves and bark of *Syzygium lateum* against (a & b) *Aspergillus niger* (c & d) *Candida albicans* (e & f) *Staphylococcus aureus* (g & h) *Streptococcus mutans* (i & j) *Enterococcus fecalis* (k & l) *Escherichia coli* and (m & n) *Pseudomonas aeruginosa* by agar well diffusion method

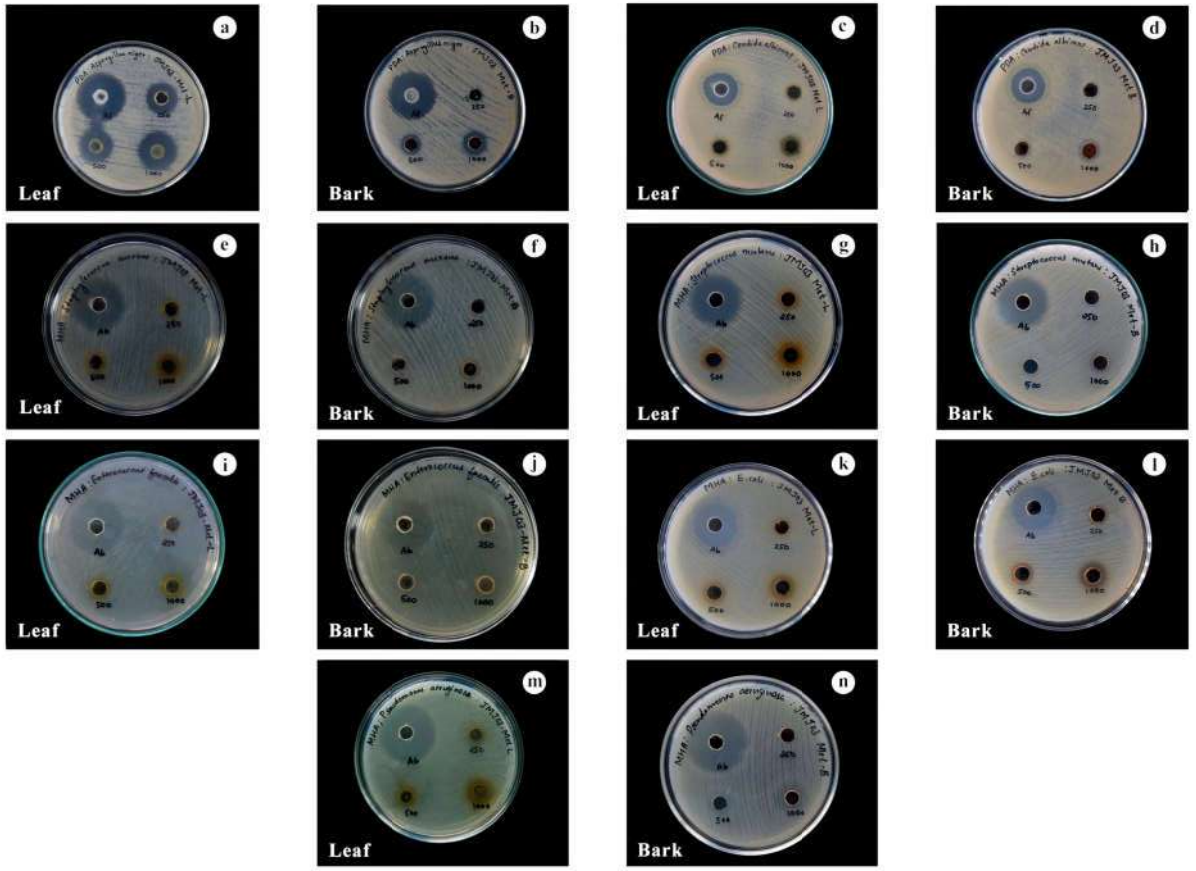


Plate 6.2: The inhibition zone (mm) of methanol extracts of leaves and bark of *Syzygium occidentale* against (a & b) *Aspergillus niger* (c & d) *Candida albicans* (e & f) *Staphylococcus aureus* (g & h) *Streptococcus mutans* (i & j) *Enterococcus fecalis* (k & l) *Escherichia coli* and (m & n) *Pseudomonas aeruginosa* by agar well diffusion method

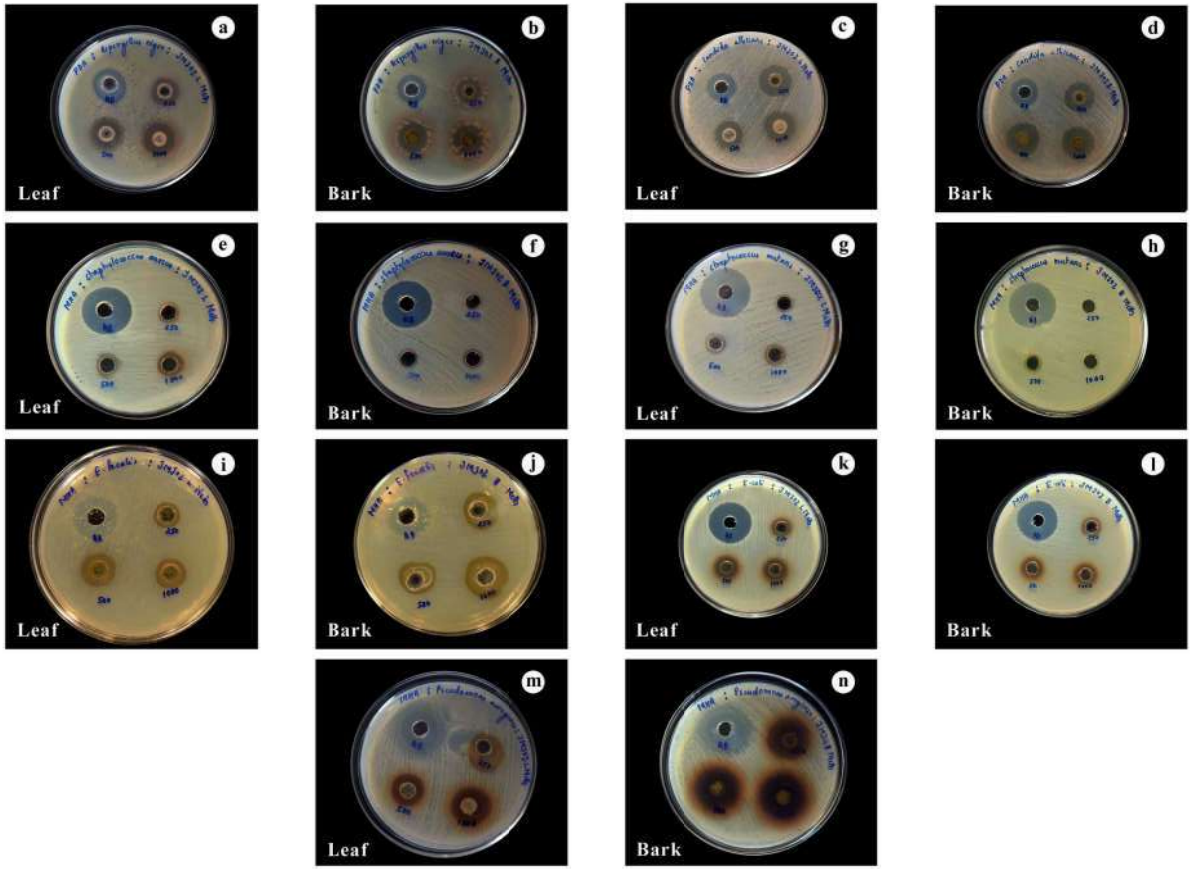


Plate 6.3: The inhibition zone (mm) of methanol extracts of leaves and bark of *Syzygium palghatense* against (a & b) *Aspergillus niger* (c & d) *Candida albicans* (e & f) *Staphylococcus aureus* (g & h) *Streptococcus mutans* (i & j) *Enterococcus fecalis* (k & l) *Escherichia coli* and (m & n) *Pseudomonas aeruginosa* by agar well diffusion method

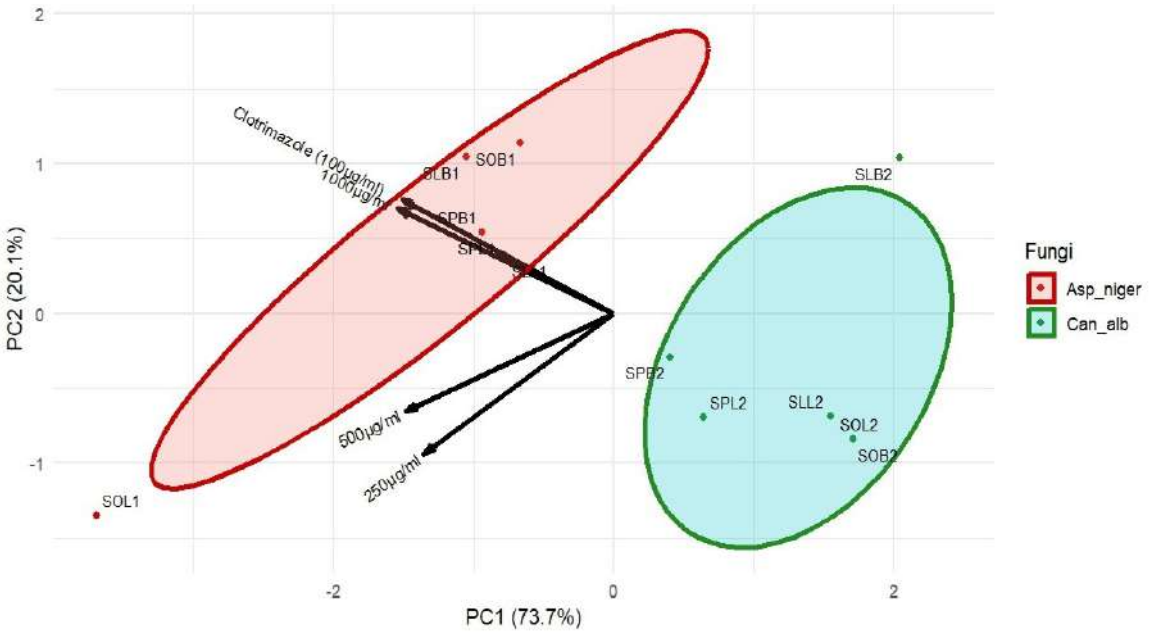


Figure 6.8: Principal Component Analysis (PCA) biplot of antifungal activity of methanolic leaf and bark extracts of *Syzygium* species (*S. laetum*, *S. occidentale*, *S. palghatense*) against *Aspergillus niger* and *Candida albicans* at different concentrations

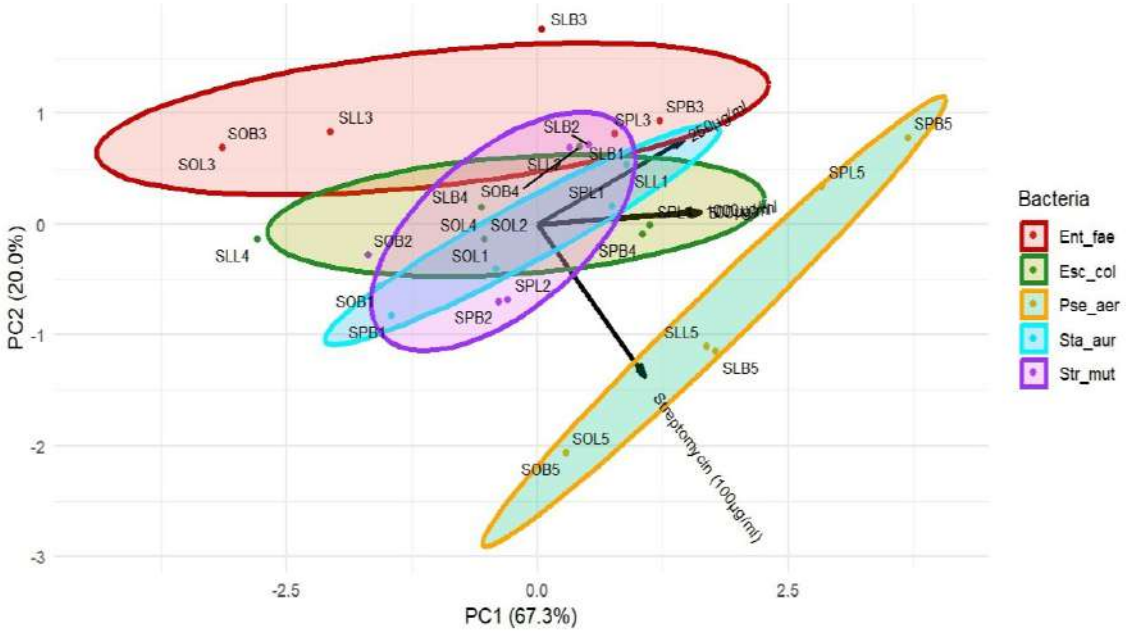


Figure 6.9: Principal Component Analysis (PCA) biplot of antibacterial activity of methanolic leaf and bark extracts of *Syzygium* species (*S. laetum*, *S. occidentale*, *S. palghatense*) against five bacterial pathogens (*Staphylococcus aureus*, *Streptococcus mutans*, *Enterococcus faecalis*, *Escherichia coli* and *Pseudomonas aeruginosa*) at different concentrations

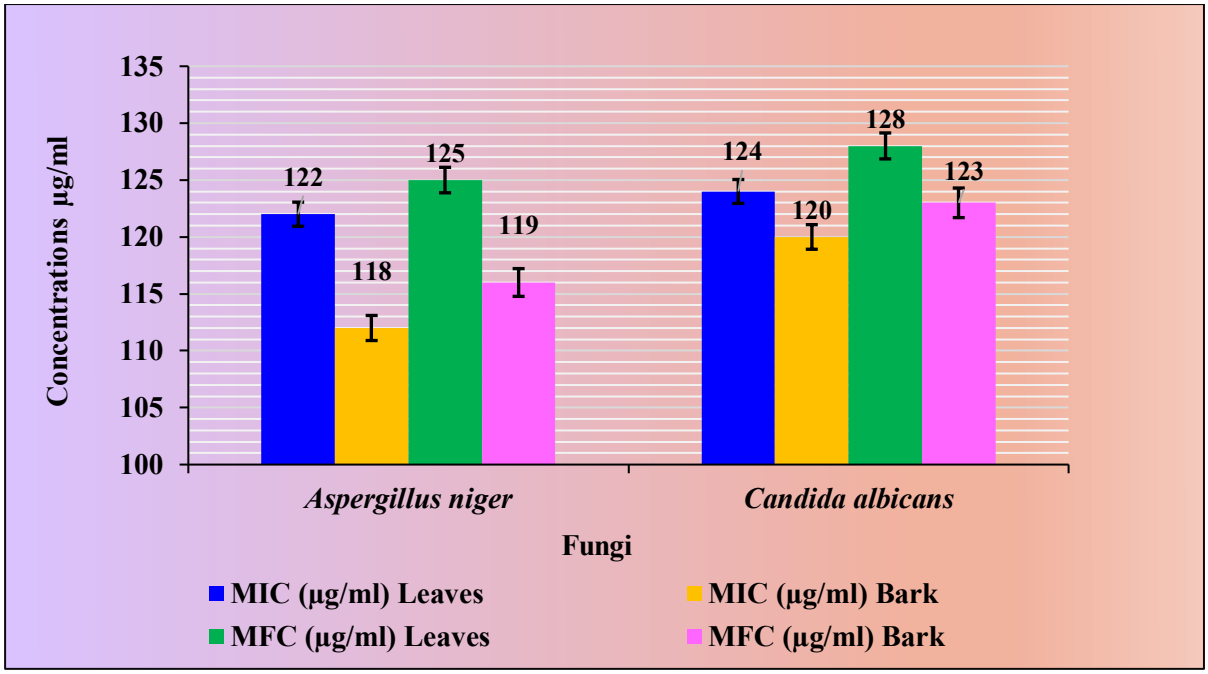


Figure 6.10: Minimum inhibitory and fungicidal concentrations of leaves and bark of methanol extracts of *Syzygium laetum* (Mean ± SE, n=6)

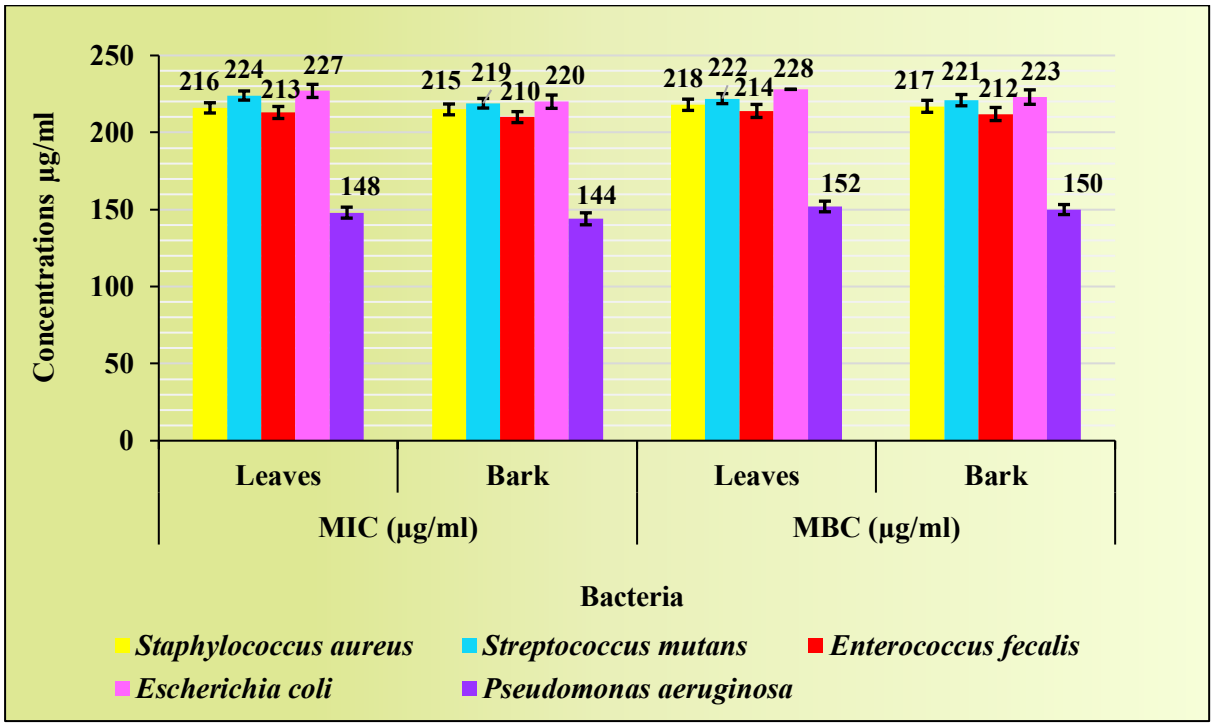


Figure 6.11: Minimum inhibitory and bactericidal concentrations of leaves and bark of methanol extracts of *Syzygium laetum* (Mean ± SE, n=6)

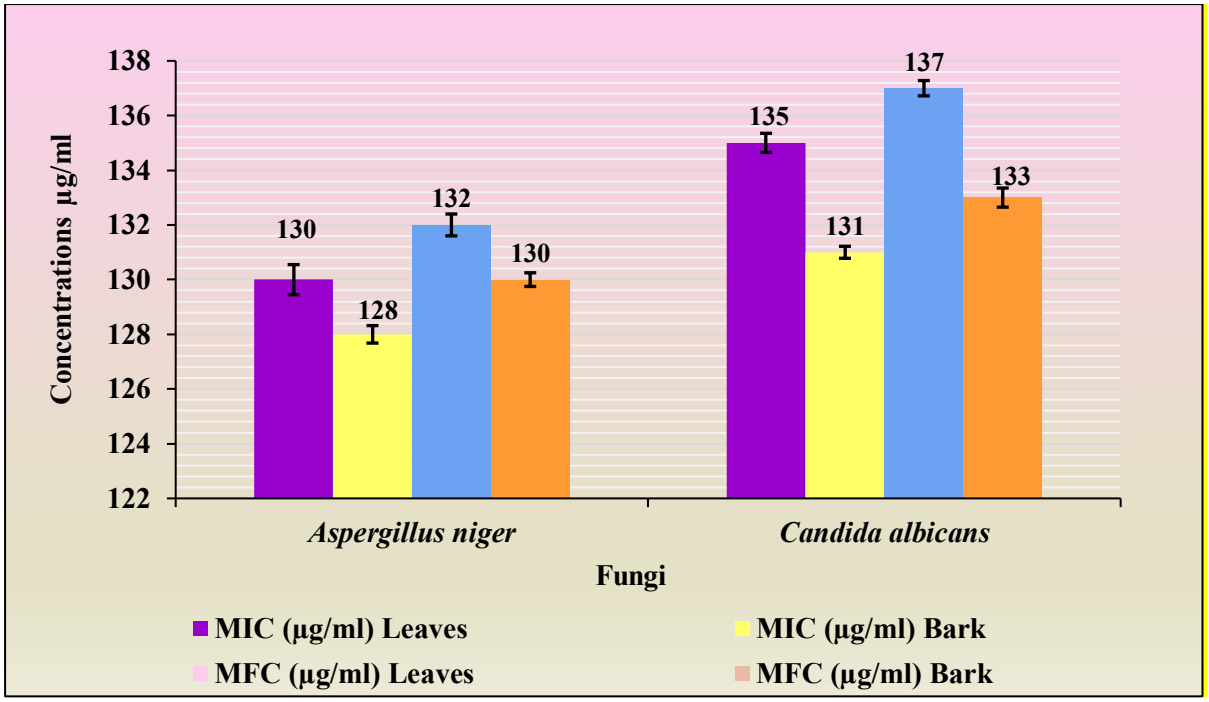


Figure 6.12: Minimum inhibitory and fungicidal concentrations of leaves and bark of methanol extracts of *Syzygium occidentale* (Mean ± SE, n=6)

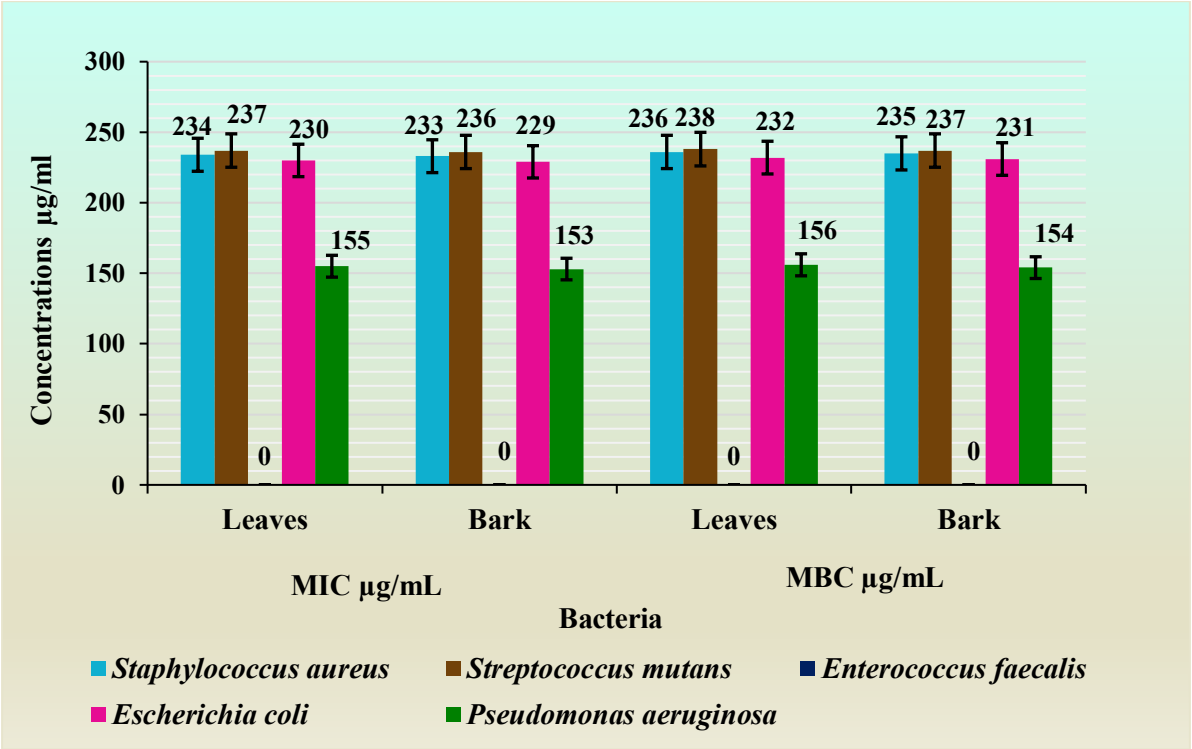


Figure 6.13: Minimum inhibitory and bactericidal concentrations of leaves and bark of methanol extracts of *Syzygium occidentale* (Mean ± SE, n=6)

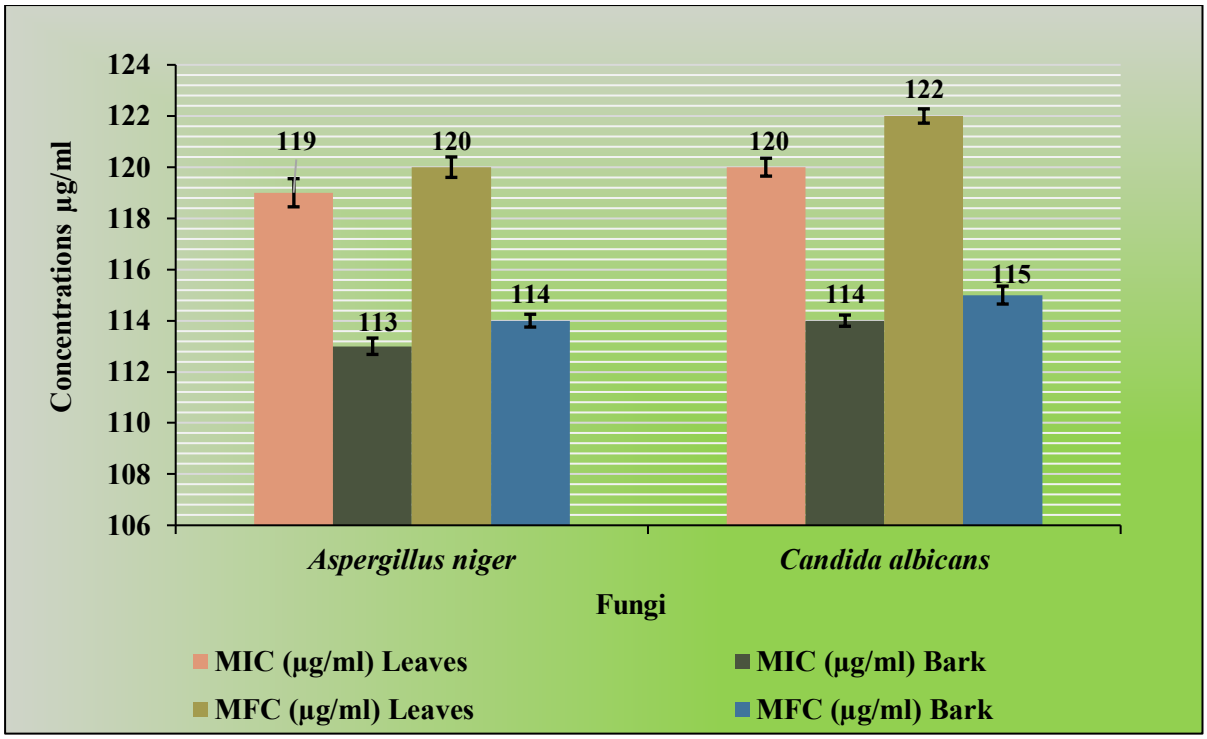


Figure 6.14: Minimum inhibitory and fungicidal concentrations of leaves and bark of methanol extracts of *Syzygium palghatense* (Mean ± SE, n=6)

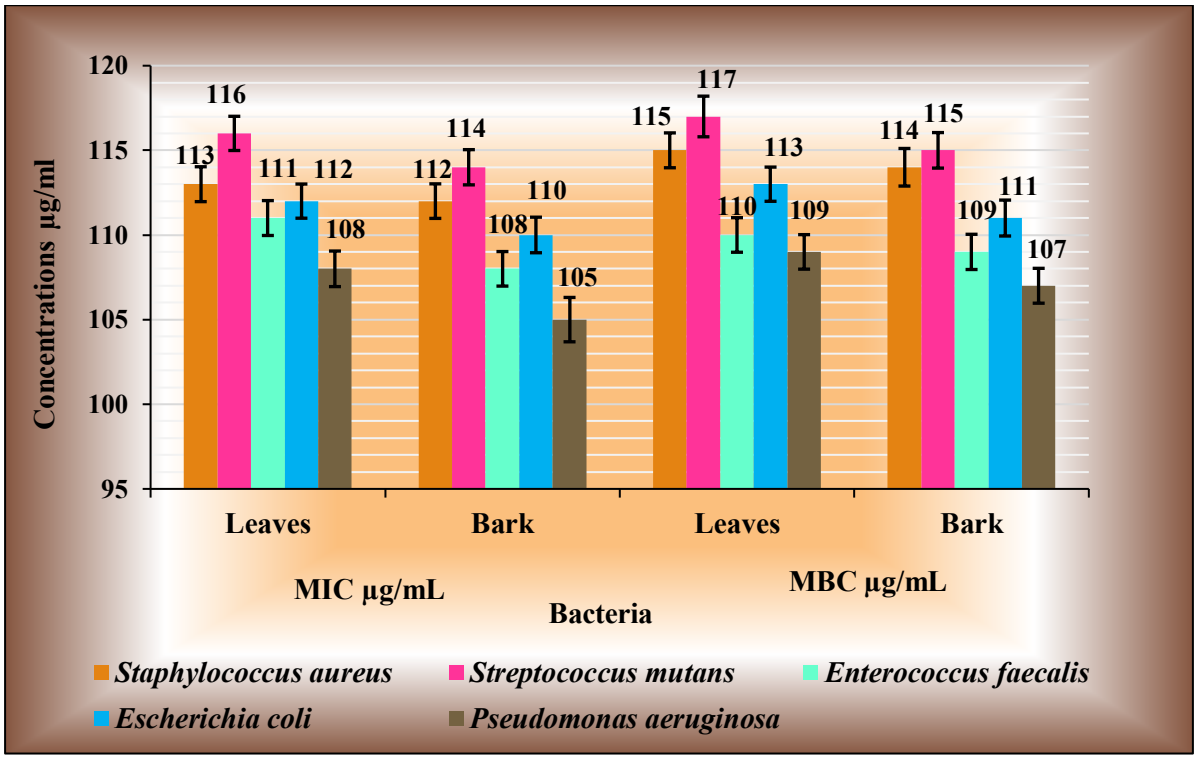


Figure 6.15: Minimum inhibitory and bactericidal concentrations of leaves and bark of methanol extracts of *Syzygium palghatense* (Mean ± SE, n=6)

aeruginosa represents the most susceptible microorganism to the antimicrobial activity generated by all three species of *Syzygium*, especially in the case of the bark extracts.

The antimicrobial activity data represented identifiable patterns, showing that bark extracts of all three species were found to have more potency than leaf extracts. The high bactericidal and fungicidal activity, with a minimal difference between the MIC and MBC/MFC values, indicates the potential of these extracts to enhance the static effect. Data were validated with six replicates (n=6) and expressed with standard error values for reliability. *S. palghatense* has exhibited marginally higher broad-spectrum antimicrobial activity, especially the bark extract, thus proving therapeutic potential from the three species (Figures 6.10-6.15).

6.3.3. Anthelmintic activities

The anthelmintic activity of methanolic extracts and distilled water extracts of leaves and bark of *S. laetum*, *S. occidentale*, and *S. palghatense* was assessed against *Lumbricus terrestris* and compared with albendazole (20 mg/mL), a standard reference drug. Paralysis and death times markedly reduced depending on the concentrations of extracts (25 to 100 mg/mL), revealing significant and dose-dependent anthelmintic activity by all extracts (Table 6.8). The *S. palghatense* bark methanolic extract showed significant anthelmintic activity compared to all the species tested, with paralysis in 2.45 ± 0.46 minutes and death in 5.23 ± 0.68 minutes at 100 mg/mL concentration, better than that of the standard albendazole (paralysis 15.36 ± 0.82 minutes and death 20.36 ± 1.05 minutes). Bark extracts consistently showed higher anthelmintic activities than leaf extracts for all three species, while methanolic extracts were more effective than distilled water extracts. In decreasing order, the anthelmintic potency was: *S. palghatense* bark>*S. laetum* bark>*S. occidentale* bark>*S. palghatense* leaf>*S. laetum* leaf>*S. occidentale* leaf. The improved activity of bark extracts could be linked to their relatively high content level of bioactive molecules, including tannins, flavonoids and phenolics, which were reported to interfere with helminth energy generation through uncoupling oxidative phosphorylation or binding α to glycoproteins-like on the parasite cuticle. These

results indicate that the tested plant extracts are far more effective than the conventional drug albendazole and have the potential to be developed as new treatments for helminthic infections, particularly in jurisdictions where resistance to conventional anthelmintics is emerging.

The anthelmintic activity of methanolic leaf and bark extracts of *S. laetum*, *S. occidentale*, and *S. palghatense* revealed significant dose-dependent effects on paralysis and death times of worms compared to standard and control groups. Increasing extract concentrations resulted in decreased time to induce paralysis and death, indicating stronger anthelmintic efficacy. Among the extracts, *S. palghatense* exhibited the most potent activity, followed by *S. occidentale* and *S. laetum*. The percentage inhibition data further supported this trend, where both leaf and bark extracts showed considerable inhibition of worm activity, closely approaching that of the standard reference drug. These findings align with the known presence of bioactive phytochemicals like tannins, and flavonoids in *Syzygium* species, which are reported to impair parasite motility and viability by mechanisms like cuticle disruption and interference with metabolic processes. Overall, this study confirms the promising anthelmintic potential of *Syzygium* methanolic extracts meriting further phytochemical characterization and *in vivo* validation (Figures 6.16-6.18).

6.3.4. Anti-inflammatory activities

6.3.4.1. *In vitro* analysis

The data in Table 6.9 show that the methanolic leaf and bark extracts of *S. laetum*, *S. occidentale*, and *S. palghatense* exhibit significant anti-inflammatory activity in a dose-dependent manner based on Human Red Blood Cell membrane stabilization assay. Percentage inhibition increases consistently with concentration from 10 to 100 µg/mL in all samples. Among the species and plant parts tested, *S. palghatense* bark demonstrates the highest activity, reaching 75.96 ± 0.04% inhibition at 100 µg/mL, followed closely by its leaf extract at 55.96 ± 0.04%. *S. laetum* leaf extracts show the lowest percentage inhibition at the highest concentration (41.24 ± 0.02%), while its bark extract performs better (52.01 ± 0.03%). *S. occidentale* extracts

Table 6.8: Anthelmintic activity of *Syzygium laetum*, *Syzygium occidentale*, and *Syzygium palghatense* methanol extracts against *Lumbricus terrestris*

Treatment	Concentration (mg/mL)	Time taken for paralysis (minutes)	Time taken for death (minutes)	Inhibition percentage (%)
Control (Distilled water)	0	50.00 ± 0.00	73.00 ± 0.00	0.0 ± 0.0
Standard (Albendazole)	20	15.36 ± 0.82	20.36 ± 1.05	72.1 ± 1.44
***Syzygium laetum* leaf methanol extract**	25	24.40 ± 1.18	34.25 ± 1.44	53.1 ± 1.97
	50	16.85 ± 0.95	26.25 ± 1.20	64.0 ± 1.64
	75	12.35 ± 0.82	19.75 ± 1.05	72.9 ± 1.44
	100	8.15 ± 0.66	13.25 ± 0.85	81.8 ± 1.16
***Syzygium laetum* bark methanol extract**	25	28.20 ± 1.30	37.85 ± 1.55	48.1 ± 2.12
	50	20.15 ± 1.05	29.85 ± 1.32	59.1 ± 1.81
	75	15.05 ± 0.92	23.45 ± 1.15	67.9 ± 1.57
	100	10.75 ± 0.76	16.85 ± 0.98	76.9 ± 1.34
***Syzygium occidentale* leaf methanol extract**	25	29.40 ± 1.34	39.15 ± 1.58	46.3 ± 2.16
	50	22.65 ± 1.18	32.25 ± 1.44	55.8 ± 1.97
	75	17.25 ± 0.98	26.45 ± 1.28	63.8 ± 1.75
	100	12.05 ± 0.80	19.35 ± 1.10	73.5 ± 1.51
***Syzygium occidentale* bark methanol extract**	25	33.20 ± 1.42	42.85 ± 1.66	41.3 ± 2.27
	50	25.95 ± 1.25	36.10 ± 1.52	50.5 ± 2.08
	75	20.80 ± 1.10	30.45 ± 1.38	58.3 ± 1.89
	100	15.45 ± 0.92	24.85 ± 1.22	65.9 ± 1.67
***Syzygium palghatense* leaf methanol extract**	25	18.32 ± 0.95	24.53 ± 1.22	66.4 ± 1.67
	50	9.45 ± 0.78	16.78 ± 1.01	77.0 ± 1.38
	75	4.87 ± 0.69	9.65 ± 0.85	86.8 ± 1.16
	100	2.94 ± 0.47	5.87 ± 0.68	91.9 ± 0.93
***Syzygium palghatense* bark methanol extract**	25	22.45 ± 1.12	28.67 ± 1.34	60.7 ± 1.84
	50	11.87 ± 0.89	20.45 ± 1.13	72.0 ± 1.55
	75	6.24 ± 0.71	12.36 ± 0.90	83.1 ± 1.23
	100	4.15 ± 0.58	8.42 ± 0.79	88.5 ± 1.08

Values are expressed as mean ± standard error (n=6). '-' indicates no paralysis/death observed during the experimental period

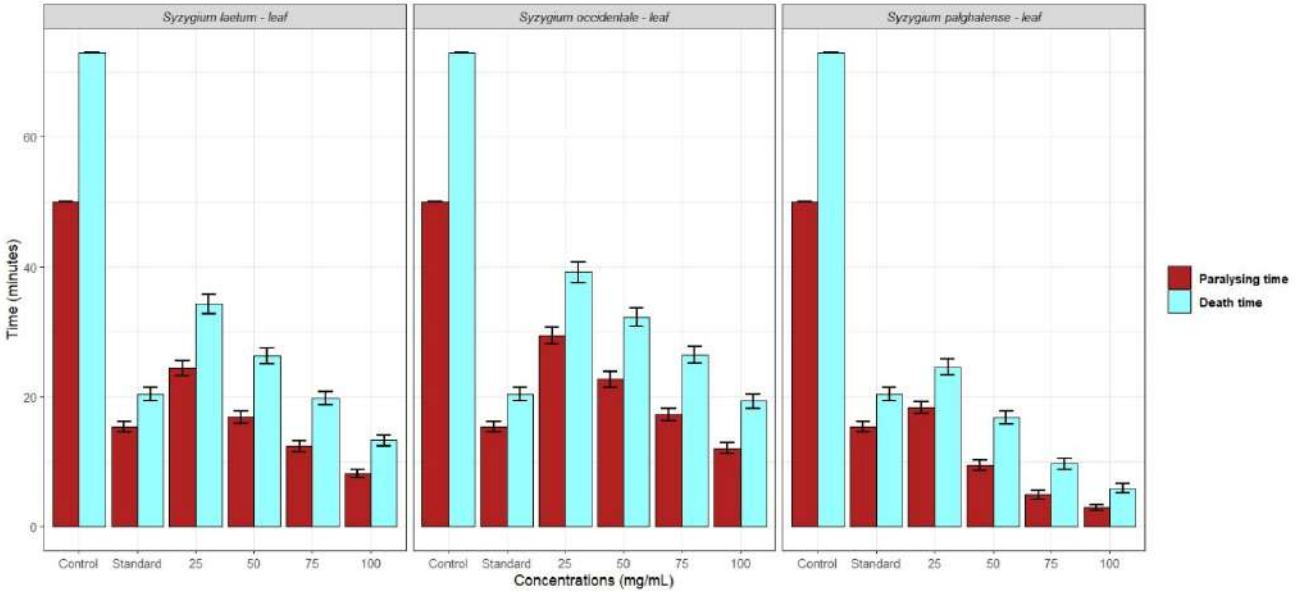


Figure 6.16: Anthelmintic activity of methanolic leaf extracts of *Syzygium laetum*, *Syzygium occidentale,* and *Syzygium palghatense*: paralyzing and death times of worms at different concentrations compared to standard and control (Mean ± SE, n=6)

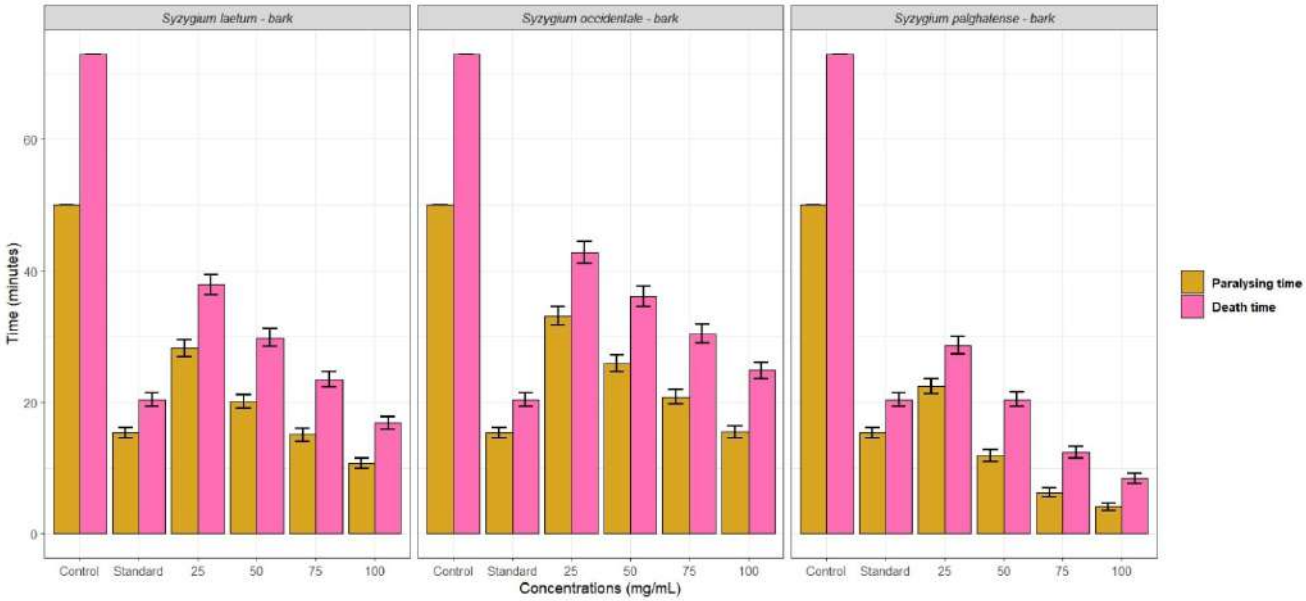


Figure 6.17: Anthelmintic activity of methanolic bark extracts of *Syzygium laetum*, *Syzygium occidentale,* and *Syzygium palghatense*: paralyzing and death times of worms at different concentrations compared to standard and control (Mean ± SE, n=6)

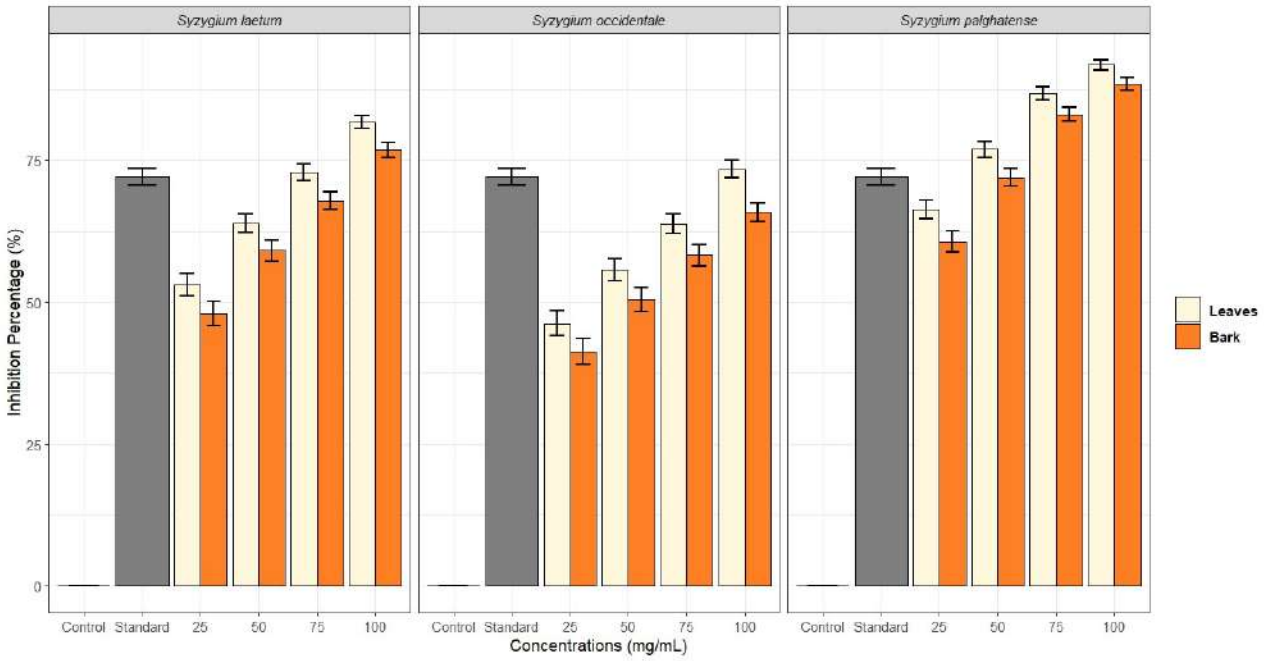


Figure 6.18: Anthelmintic activity-percentage inhibition of methanolic leaf and bark extracts of *Syzygium laetum*, *Syzygium occidentale*, and *Syzygium palghatense* at various concentrations compared to standard and control (Mean ± SE, n=3)

Table 6.9: Dose-dependent anti-inflammatory activity of methanolic leaf and bark extracts of *Syzygium laetum, Syzygium occidentale, and Syzygium palghatense* measured by Human Red Blood Cell membrane stabilization assay

Concentration (µg/mL)	*S. laetum* leaf (%) ± SE	*S. laetum* bark (%) ± SE	*S. occidentale* leaf (%) ± SE	*S. occidentale* bark (%) ± SE	*S. palghatense* leaf (%) ± SE	*S. palghatense* bark (%) ± SE
10	7.85 ± 0.25	8.12 ± 0.26	8.34 ± 0.28	8.50 ± 0.30	12.75 ± 0.39	13.40 ± 0.40
20	15.42 ± 0.30	16.50 ± 0.32	16.95 ± 0.33	17.21 ± 0.35	19.63 ± 0.40	20.10 ± 0.42
30	19.73 ± 0.45	20.10 ± 0.48	20.41 ± 0.50	21.05 ± 0.52	24.87 ± 0.53	25.45 ± 0.55
40	25.31 ± 0.62	26.80 ± 0.64	26.88 ± 0.65	27.50 ± 0.66	29.12 ± 0.58	30.15 ± 0.60
50	29.56 ± 0.57	31.40 ± 0.60	30.15 ± 0.60	31.90 ± 0.62	33.48 ± 0.56	34.25 ± 0.57
60	41.02 ± 0.33	42.15 ± 0.35	42.48 ± 0.37	43.10 ± 0.38	46.55 ± 0.39	47.80 ± 0.41
70	46.26 ± 0.31	48.00 ± 0.33	47.63 ± 0.29	48.05 ± 0.31	51.88 ± 0.31	53.20 ± 0.33
80	52.18 ± 0.08	53.42 ± 0.10	53.82 ± 0.11	54.25 ± 0.13	57.27 ± 0.12	58.70 ± 0.13
90	60.74 ± 0.34	61.30 ± 0.38	61.45 ± 0.38	62.00 ± 0.39	66.38 ± 0.41	67.90 ± 0.42
100	41.24 ± 0.02	52.01 ± 0.03	32.05 ± 0.03	42.80 ± 0.04	55.96 ± 0.04	60.50 ± 0.05
F-Value	2500.23	2550.17	2603.12	2650.89	2901.67	2950.41
P-Value	<0.001	<0.001	<0.001	<0.001	<0.001	<0.001
Critical Difference	1.15	1.18	1.12	1.14	1.20	1.22

Data represents mean percentage inhibition ± standard error (n=6). Statistical significance was evaluated using one-way ANOVA followed by critical difference (CD) test at 5% significance. *Syzygium palghatense* bark extract exhibited the highest anti-inflammatory effect as indicated by the larger percentage inhibition values and highest F-Value.

display intermediate activity between the two, with bark extracts generally more potent than leaves.

The high F-values (ranging from 2500.23 to 2950.41) and p-values (<0.001) indicate that the differences observed are statistically significant. The critical differences of around 1.1 to 1.2 confirm these results' reliability at the 5% significance level.

6.3.4.2. *In vivo* analysis

S. palghatense exhibited increased results *for in vitro* anti-inflammatory studies, thus for *in vivo* studies *S. palghatense* was selected.

Figure 6.19 illustrates the progression of paw edema thickness in rats following carrageenan injection, comparing untreated controls, a standard anti-inflammatory drug, and both low and high doses of the methanolic extract. Edema peaks at 2 hours post-injection, especially in the control group, and then gradually declines. Both LD and HD treatments significantly reduce paw thickness relative to the control, with HD producing results closely comparable to the standard drug throughout the 5-hour observation period. These findings indicate a strong dose-dependent anti-inflammatory effect of the extract, effectively attenuating acute inflammation comparable to conventional pharmacological intervention.

Figure 6.20 presents the changes in paw thickness in rats subjected to a chronic inflammation model across four days. The control group displays a sustained increase in edema, peaking at day 2. Both LD and HD extract treatments significantly limit paw swelling compared to control, with HD showing inhibition of edema nearly equivalent to the standard drug by day 4. These results highlight the methanolic extract's robust, dose-dependent anti-inflammatory efficacy during chronic inflammation, supporting its potential as an effective anti-inflammatory agent.

6.3.5. Antidiabetic studies

S. palghatense bark shows increased activity in other tested experiments; thus, it was taken for antidiabetic analysis.

6.3.5.1. Alpha-amylase activity

The α-amylase inhibitory activity of the methanolic bark extract of *S. palghatense* demonstrates significant enzyme inhibition with increasing concentrations. At 62.5 µg/mL, the extract shows 54.34 ± 0.11% inhibition, which increases gradually to 64.08 ± 0.14% at 1000 µg/mL, comparable to the standard with 73.02 ± 0.03% inhibition. The low optical density values at 540 nm correspond to higher inhibition of the enzyme, confirming potent α-amylase inhibition by the extract. The IC_{50} value for *S. palghatense* bark extract was 347.16 ± 0.20 µg/mL, significantly lower than the standard acarbose's IC_{50} of 620.10 ± 0.30 µg/mL, indicating a stronger potency in this assay. The results, supported by a highly significant F-statistic (40.20) and p-value (<0.001), reveal that the bark extract is an effective α-amylase inhibitor, highlighting its potential therapeutic utility in managing diabetes by slowing carbohydrate digestion and glucose absorption (Tables 6.10-6.11).

6.3.5.2. Alpha-glucosidase activity

The α-glucosidase inhibitory activity of the methanolic bark extract of *S. palghatense* shows a clear dose-dependent increase in percentage inhibition, starting from 14.00 ± 0.11% at 62.5 µg/mL and reaching 65.10 ± 0.21% at 1000 µg/mL, compared to the standard drug acarbose that shows 80.00 ± 0.11% inhibition. The low optical density (OD) values at 540 nm correspond with higher enzyme inhibition. The calculated IC_{50} value for the extract is 165.15 ± 0.10 µg/mL. This is lower than that of acarbose (200.30 ± 0.21 µg/mL), indicating stronger inhibitory potency. Statistical analyses ($F = 40.11$, $p < 0.001$) confirm the significance of these results. Overall, this suggests that *S. palghatense* bark methanol extract is a potent α-glucosidase inhibitor and may serve as a promising natural agent for managing postprandial hyperglycemia in diabetes (Tables 6.12-6.13).

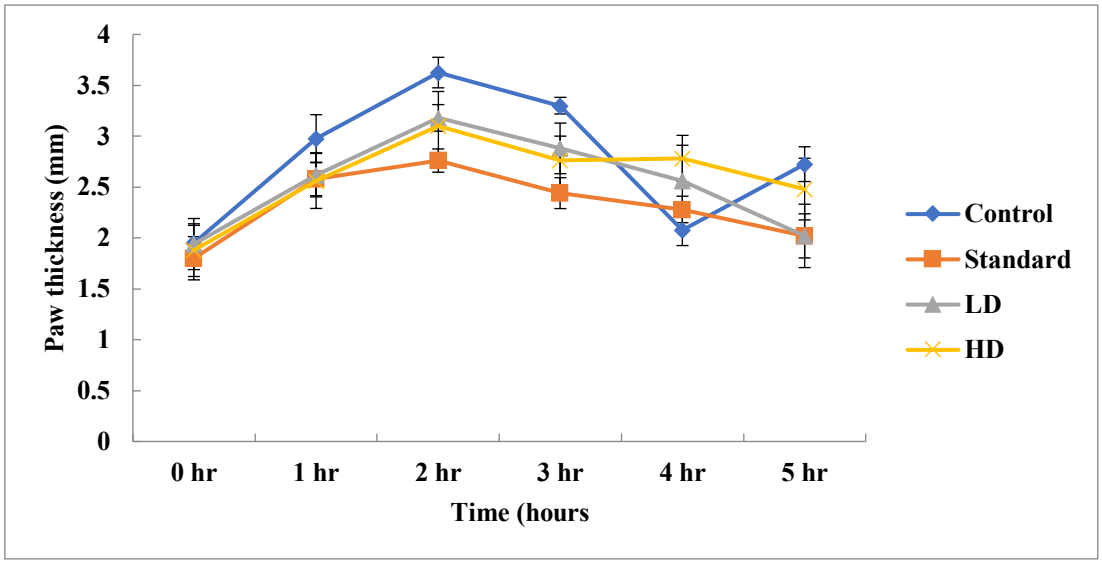


Figure 6.19: Effect of methanolic extract on carrageenan-induced paw edema in rats- comparison of control, standard drug, low dose (LD), and high dose (HD) treatments over 5 hours (Mean ± SE)

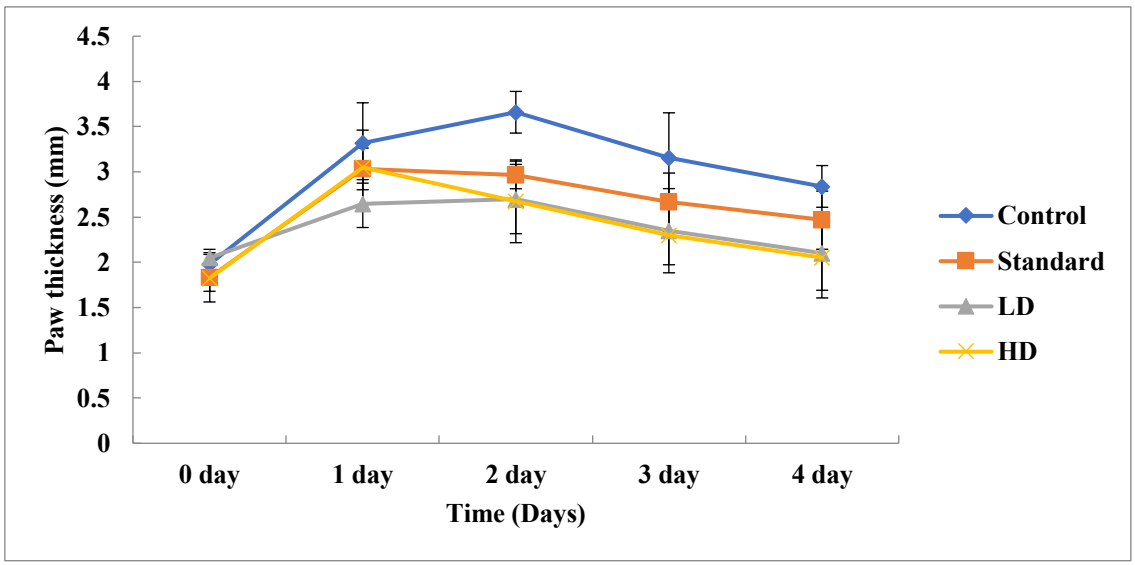


Figure 6.20: Effect of methanolic extract on chronic paw edema in rats- comparison of control, standard drug, low dose (LD), and high dose (HD) treatments over 4 days (Mean ± SE)

Table 6.10: α-Amylase inhibitory activity of methanol extract of *Syzygium palghatense* bark

Sample concentration (µg/mL)	OD at 540 nm	Percentage inhibition (%)
Control	0.2318 ± 0.0121	0
Standard	0.0175 ± 0.0103	73.02 ± 0.0301
62.5	0.1414 ± 0.0520	54.34 ± 0.1050
125	0.1076 ± 0.0362	60.98 ± 0.1151
250	0.0504 ± 0.0541	61.47 ± 0.1272
500	0.0432 ± 0.0210	63.38 ± 0.1187
1000	0.0145 ± 0.0140	64.08 ± 0.1401
F-stat		40.20
P-value		< 0.001
CD at 5%		0.026

Values are expressed as mean ± standard error (n = 6). Statistical significance was evaluated using one-way ANOVA followed by a critical difference (CD) test at the 5% significance level. Differences were considered statistically significant at $p < 0.05$

Table 6.11: IC_{50} value of methanol extract of *Syzygium palghatense* bark in α-Amylase inhibitory activity

Samples	IC_{50} value (%)	F stat	P value	CD at 5%
Standard Acarbose	620.10 ± 0.30	35.87	<0.001	6.05
Methanol extract of *Syzygium palghatense* bark	347.16 ± 0.20	34.45	<0.001	4.12

Values are expressed as mean ± standard error (n = 6). Statistical significance was evaluated using one-way ANOVA followed by a critical difference (CD) test at the 5% significance level. Differences were considered statistically significant at $p < 0.0$

Table 6.12: α-Glucosidase inhibition of methanol extract of *Syzygium palghatense* bark

Sample concentration (µg/mL)	OD at 540 nm	Percentage Inhibition (%)
Control	0.2140 ± 0.0210	0
Standard (Acarbose)	0.0160 ± 0.0110	80.00 ± 0.1121
62.5	0.1240 ± 0.1102	14.00 ± 0.1130
125	0.1060 ± 0.0121	33.33 ± 0.1013
250	0.0350 ± 0.0110	55.00 ± 0.1012
500	0.0310 ± 0.0111	57.33 ± 0.1151
1000	0.0100 ± 0.0102	65.10 ± 0.2110
F-stat		40.11
P-value		< 0.001
CD at 5%		0.016

Values are expressed as mean ± standard error (n = 6). Statistical significance was evaluated using one-way ANOVA followed by a critical difference (CD) test at the 5% significance level. Differences were considered statistically significant at $p < 0.05$

Table 6.13: IC_{50} value of methanol extract of *Syzygium palghatense* bark in α-Glucosidase inhibition assay

Samples	IC_{50} value (%)	F stat	P value	CD at 5%
Standard Acarbose	200.30 ± 0.21	35.45	<0.001	5.23
Methanol extract of *Syzygium palghatense* bark	165.15 ± 0.10	38.12	<0.001	3.45

Values are expressed as mean ± standard error (n = 6). Statistical significance was evaluated using one-way ANOVA followed by a critical difference (CD) test at the 5% significance level. Differences were considered statistically significant at $p < 0$

Table 6.14: Cytotoxicity of methanolic bark extract of *Syzygium palghatense* against Dalton's Lymphoma Ascites (DLA) Cells

Concentration (µg/mL)	Percentage Cell Death (%)
0	1.38
20	9.81
40	28.02
60	35.32
80	37.11
100	40.12



Plate 6.4: Acute oral toxicity assessment of *Syzygium palghatense* methanol bark extract in Wistar rats

6.3.6. Anticancer study

6.3.6.1. Cytotoxicity by the trypan blue exclusion method

The cytotoxic effects of *S. palghatense* bark methanolic extract were assessed by measuring the percentage of cell death in Dalton's Lymphoma Ascites (DLA) cells after treatment. The extract showed a dose-dependent increase in cytotoxicity, starting from 1.38% cell death at 1 µg/mL concentration to 40.12% at 100 µg/mL. This indicates that the extract exerts low cytotoxic activity. The increase in cell death with increasing concentration supports the extract's promise as a natural anticancer agent. Further detailed mechanistic studies are warranted to confirm its therapeutic potential (Table 6.14).

6.3.6.2. Acute toxicity studies

No deaths or adverse behavioral changes were observed during the study. At the end of the observation period, vital organs were examined histologically, revealing no significant pathological alterations. Biochemical parameters also remained normal compared to controls, indicating the extract's safety at the tested dose. This study confirms that the methanol bark extract of *S. palghatense* has no acute toxic effects in the tested animals (Plate 6.4).

6.4. Discussion

The present investigation comprehensively evaluated the pharmacological potential of three endemic *Syzygium* species- *S. laetum*, *S. occidentale*, and *S. palghatense*- through *in vitro* and *in vivo* assays targeting antimicrobial, antibiofilm, anthelmintic, anti-inflammatory, antidiabetic, and antitumor activities. The findings not only validate the traditional ethnomedicinal uses of *Syzygium* species but also highlight the therapeutic promise of these underexplored plants. This discussion integrates the observed results with previously reported studies on *Syzygium* and other related medicinal plants, emphasizing the mechanisms of action, clinical relevance, and potential applications.

Oxidative stress, driven by an imbalance between reactive oxygen species (ROS) and antioxidant defenses, underlies the pathogenesis of numerous chronic conditions, including diabetes, cancer, and neurodegenerative diseases (Birben et al., 2012; Schieber & Chandel, 2014). In the present study, methanolic extracts of *Syzygium* species demonstrated strong antioxidant potential across multiple assays, mentiones above. The methanol extracts consistently outperformed other solvent fractions, reflecting their higher concentration of polar phenolic and flavonoid compounds.

These results align with previous studies on *S. cumini*, *S. polyanthum*, and *S. malaccense*, which have demonstrated high total phenolic content and potent radical scavenging activities (Eshwarappa et al., 2014; Widyawaty et al., 2021). For example, *S. cumini* bark and leaf galls exhibited robust antioxidant activity attributed to tannins and flavonoids. Similarly, *S. polyanthum* showed low IC_{50} values in DPPH and ABTS assays, further supporting the genus as a natural antioxidant reservoir. Collectively, these findings suggest that the endemic *Syzygium* species evaluated here can serve as promising sources of natural antioxidants with potential applications in mitigating oxidative stress-mediated disorders.

The methanol extracts of the tested *Syzygium* species showed numerous antimicrobial activity against both types of bacteria (Gram-positive and Gram-negative bacteria), and fungi, as evidenced by significant inhibition zones, MIC,

MBC, and MFC values. The antimicrobial activity can be attributed to bioactive compounds such as phenolics, tannins, and terpenoids, which interfere with bacterial cell walls, membranes, and metabolic enzymes. This is consistent with recent systematic reviews, such as Valarezo et al. (2025), which underscore the efficacy of clove essential oil in preserving meat products by inhibiting microbial growth (e.g., *Listeria*, *E. coli*, *Pseudomonas*).

Supporting this, Wadi (2025) reports broad-spectrum antibacterial effects of clove aqueous extracts against both types of bacteria, Gram-negative and Gram-positive, identifying eugenol as the dominant active compound (over 53% by composition) through GC–MS analysis.

Further, Alanazi et al.'s (2022) *in vivo* studies demonstrated significant antibacterial and wound-healing efficacy of clove bud oil against methicillin-resistant *Staphylococcus aureus* (MRSA), reinforcing its therapeutic value beyond *in vitro* assays.

Mechanistically, the high eugenol concentration in clove oil (approximately 60–90%) contributes to its antimicrobial action- disrupting microbial membranes and inhibiting growth. Various oil types (bud, leaf, stem) share this bioactivity, with minor constituents like caryophyllene enhancing the effects

Comparable antimicrobial potential has been reported in *S. aromaticum* (clove), which exhibits substantial antibacterial and antifungal activity due to its high eugenol content (Maggini et al., 2024). Similarly, *S. samarangense* and *S. caryophyllatum* have displayed inhibitory activity against *Staphylococcus aureus* and *Escherichia coli* (Kavitha & Poonguzhali, 2024). Importantly, the extracts in this study shows activity against pathogens which are resistant to multiple drugs, including *Pseudomonas aeruginosa*, underscoring their clinical significance in an era of escalating antimicrobial resistance.

The anthelmintic assays demonstrated dose-dependent paralysis and death of *Lumbricus terrestris* following exposure to *Syzygium* extracts, with efficacy comparable to albendazole at higher concentrations. The mode of action may involve

interference with the worms' neuromuscular activity and energy metabolism, similar to the mechanism of benzimidazoles (Dube et al., 2022).

These findings are supported by earlier reports on *S. cumini*, whose methanolic extracts effectively immobilized worms in a dose-dependent manner (Lakshmi et al., 2022). Such activity substantiates the ethnomedicinal use of *Syzygium* species for treating helminthiasis and presents potential for developing plant-based anthelmintic formulations, especially in regions with limited access to conventional drugs.

Inflammation, a double-edged sword in host defense, becomes detrimental when chronic, leading to conditions like arthritis, cardiovascular disease, and cancer (Ferrero-Miliani et al., 2007). In this study, *Syzygium* extracts demonstrated anti-inflammatory effects in both *in vitro* and *in vivo* models. Similar results have been reported with *S. caryophyllatum* and *S. nervosum*, whose extracts inhibited inflammatory mediators with efficacy comparable to acetylsalicylic acid (Kavitha & Poonguzhali, 2024). The mechanistic basis likely involves suppression of NF-κB signaling and downregulation of pro-inflammatory cytokines (Ghasemian et al., 2016). Collectively, the findings support *Syzygium* species' potential as a species that has both natural and anti-inflammatory agents that exhibit less negative effects when it comes to comparing them with synthetic drugs.

Diabetes mellitus remains a major global health burden, and natural α-amylase and α-glucosidase inhibitors have emerged as effective strategies for controlling postprandial hyperglycemia (Ayyanar & Subash-Babu, 2012). The extracts of *Syzygium* species in this study exhibited significant enzyme inhibitory activity, highlighting their potential in glycemic control. Furthermore, although not yet completed, glucose uptake assays and inhibition of endogenous glucose production are anticipated to reinforce these antidiabetic effects.

Previous studies have established *S. cumini* and *S. jambolanum* as potent antidiabetic plants, capable of enhancing insulin sensitivity and protecting pancreatic β-cells (Shanmugam, 2024). The presence of polyphenols and flavonoids likely contributes to improved glucose metabolism and reduced oxidative stress in pancreatic tissue. The current findings extend these benefits to endemic *Syzygium*

species, suggesting potential in functional foods or phytopharmaceuticals for managing type 2 diabetes.

The preliminary evaluation of *Syzygium* extracts suggested antitumor potential, which will be strengthened by forthcoming assays. Previous research on *S. aqueum*, *S. cumini*, and *S. samarangense* demonstrated cytotoxicity against cancer cell lines mediated by bioactive compounds like betulinic acid and oleanolic acid (Abdulrahman & Hama, 2023). These compounds activate caspase-dependent apoptosis, disrupt mitochondrial potential, and cause cell cycle arrest at G0/G1 or G2/M phases. If similar results are confirmed in the endemic *Syzygium* species, they could emerge as valuable candidates for natural anticancer drug development.

The acute toxicity study shows that the methanol bark extract of *S. palghatense* is safe at the tested dose of 1 g/kg body weight, as no mortality, adverse clinical signs, or toxic effects were observed in treated animals.

The results highlight the multifaceted pharmacological properties of *Syzygium* species, encompassing antioxidant, antimicrobial, antibiofilm, anthelmintic, anti-inflammatory, antidiabetic, and anticancer effects. The convergence of these activities is particularly important, as oxidative stress, inflammation, and microbial infections are interconnected with diabetes and cancer progression. Thus, the extracts act on multiple therapeutic targets, offering holistic benefits. Importantly, the endemic nature of *S. laetum*, *S. occidentale*, and *S. palghatense* underscores their uniqueness and potential as novel reservoirs of bioactive molecules.

6.5. Conclusion

The present investigation comprehensively evaluated the pharmacological potential of three endemic *Syzygium* species *S. laetum*, *S. occidentale*, and *S. palghatense* with emphasis on their antioxidant, antimicrobial, antibiofilm, anthelmintic, anti-inflammatory, antidiabetic, and anticancer properties. The study confirmed that all tested species possess significant free radical scavenging activity, attributable to their high phenolic and flavonoid contents, thereby validating their role as natural antioxidants.

The extracts also demonstrated broad-spectrum antimicrobial and antibiofilm activity, notably against *Pseudomonas aeruginosa* and *Candida albicans*, suggesting their utility in addressing microbial resistance and biofilm-associated infections. The anthelmintic assays revealed a dose-dependent effect comparable to albendazole, underscoring their traditional use in parasitic infestations. Anti-inflammatory evaluation, both *in vivo* and *in vitro*, confirmed effective inhibition of inflammatory mediators, aligning with their ethnomedicinal applications in inflammatory disorders.

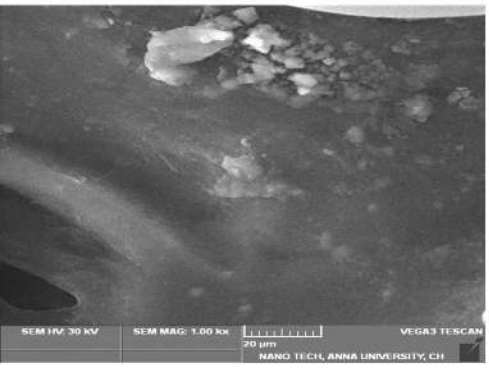
Furthermore, the extracts exhibited promising antidiabetic activity by inhibiting the α-glucosidase enzymes along with α-amylase, while preliminary anticancer analyses indicated cytotoxic potential against selected cancer cell lines. These findings suggest that the pharmacological efficacy of these *Syzygium* species arises from synergistic actions of diverse phytochemicals.

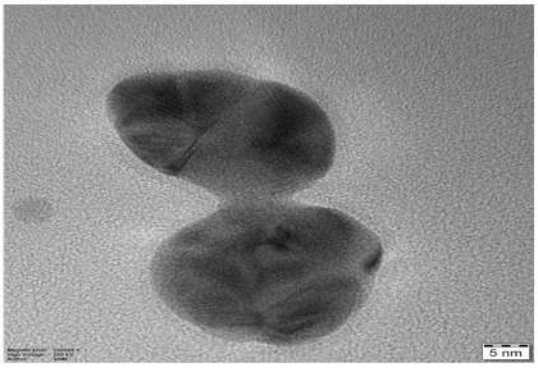
Taken together, the study highlights the therapeutic promise of *S. laetum*, *S. occidentale*, and *S. palghatense* as potential sources for natural drug leads. Importantly, this work adds novel evidence to the relatively unexplored pharmacological profile of these lesser-studied *Syzygium* species, thereby expanding the scientific understanding of the genus.

Future studies involving bioassay-guided isolation of active compounds, detailed mechanistic investigations (e.g., apoptosis, cell cycle regulation, caspase pathways), and advanced *in vivo* models are justified to validate the discoveries and enable the development of plant-based therapeutics.

7

GREEN SYNTHESIS, CHARACTERIZATION, AND BIOACTIVE EFFICACY OF SILVER NANOPARTICLES







CHAPTER 7

GREEN SYNTHESIS, CHARACTERIZATION, AND BIOACTIVE EFFICACY OF SILVER NANOPARTICLES

7.1. Introduction

Silver nanoparticles (AgNPs), due to their unique physicochemical and biological properties, have garnered significant attention for their applications in medicine, pharmaceuticals, and environmental science (Sati et al., 2025). The biological synthesis of silver nanoparticles (AgNPs), particularly from medicinal plants such as those in the genus *Syzygium*, offers a green, sustainable, and cost-effective alternative to conventional chemical and physical methods that often involve toxic reagents and harsh conditions (Almatroudi et al., 2020). Extracts from *Syzygium* species, rich in bioactive phytochemicals like phenols, flavonoids, and terpenoids, not only facilitate the reduction of silver ions (Ag^{+}) to metallic silver (Ag^{0}), but also stabilize the nanoparticles by capping, leading to uniform, stable nanoscale materials (Chakravarty et al., 2022; Yugandhar et al., 2015).

Green synthesis typically involves mixing aqueous or methanolic *Syzygium* extracts with silver nitrate solution under ambient conditions, where the reduction process is visually indicated by a colour shift due to surface plasmon resonance (SPR). The morphology and size of nanoparticles are influenced by parameters such as extract concentration, pH, temperature, and reaction time (Htwe et al., 2019). Characterization techniques, including UV-Visible spectroscopy, X-Ray Diffraction (XRD), Transmission Electron Microscopy (TEM), Scanning Electron Microscopy (SEM), Atomic Force Microscopy (AFM), Fourier Transform Infrared Spectroscopy (FTIR), and Energy Dispersive X-ray Spectroscopy (EDS), confirm nanoparticle synthesis, size distribution (mostly 5–50 nm), crystalline nature, surface chemistry, and elemental composition, ensuring reproducibility and understanding of bioactivity (Almatroudi et al., 2020; Ojo et al., 2018).

The synthesized silver nanoparticles (AgNPs) exhibit significant biological activities, notably antimicrobial effects against Gram-positive and Gram-negative bacteria, disrupting microbial cell walls and generating reactive oxygen species for bactericidal effects (Sati et al., 2025). The antifungal potential against pathogens like *Candida albicans* further expands their biomedical relevance (Ojo et al., 2018). Moreover, their antioxidant properties, assessed via various *in vitro* assays, anti-inflammatory, antidiabetic, and anticancer assays demonstrate their ability to neutralize free radicals and protect against oxidative stress-related cellular damage, positioning these silver nanoparticles (AgNPs) as promising agents for therapeutic applications (Chakravarty et al., 2022; Yugandhar et al., 2015).

Environmental factors and synthesis parameters profoundly affect nanoparticle characteristics, which in turn influence their biological efficacy, highlighting the importance of careful optimization in green synthesis protocols. The incorporation of *Syzygium*-derived silver nanoparticles (AgNPs) into nanomedicine and environmental applications offers a sustainable path forward, though future studies must address scalability, stability, precise mechanistic actions, and safety profiles to fully harness their potential.

The green synthesis of silver nanoparticles (AgNPs) from plant extracts is an eco-friendly, cost-effective, and sustainable approach increasingly favoured over conventional chemical and physical methods due to its simplicity and reduced environmental impact (Shankar et al., 2005). Among various plant species explored for nanoparticle synthesis, the genus *Syzygium* has attracted considerable attention owing to its rich reservoir of bioactive compounds such as polyphenols, flavonoids, and tannins, which act as natural reducing and stabilizing agents in nanoparticle formation (Yugandhar et al., 2015). The methanolic bark extract of *S. palghatense*, a less-studied species, has demonstrated promising biological activities through both *in vitro* and *in vivo* assays, making it an excellent candidate for green synthesis of silver nanoparticles to harness and possibly enhance these activities.

In this work, silver nitrate ($AgNO_3$) was employed as the precursor for silver nanoparticles (AgNPs) synthesis, with the bark extract serving as a reductant and

capping agent. The biosynthesis procedure involved dropwise addition of the extract into a 1 mM aqueous $AgNO_3$ solution, followed by incubation at elevated temperatures (60–80°C) for one hour, during which a visible colour change from dark brown to reddish-brown indicated nanoparticle formation an established indicator of surface plasmon resonance excitation in silver nanoparticles (Shankar et al., 2005; Yugandhar et al., 2015).

Characterization techniques such as UV-Visible spectroscopy (UV-VIS), Fourier Transform Infrared (FTIR) spectroscopy, Atomic force Microscopy (AFM), Scanning Electron Microscopy (SEM), Transmission Electron Microscopy (TEM), X-ray diffraction (XRD), and provide insights into the reduction process, nanoparticle size, shape, crystallinity, and surface chemistry. UV-VIS spectroscopy allows monitoring of silver ion reduction by characteristic absorption peaks within 200–800 nm (Shankar et al., 2005). FTIR spectroscopy identifies functional groups from the plant extract responsible for nanoparticle capping and stabilization (Ghadially, 1996). XRD analysis confirms the crystalline, face-centred cubic structure of the synthesized nanoparticles and determines average crystallite size using the Scherrer equation (Ghadially, 1996). TEM provides morphological analysis with high resolution, allowing for the assessment of size distribution and shape, which are critical for understanding biological interactions (Ajaykumar et al., 2023).

This multidisciplinary approach not only facilitates the synthesis of biologically active silver nanoparticles from *S. palghatense* but also offers an effective pathway to explore the potential pharmaceutical and environmental applications of these green-synthesized nanomaterials.

- **Objectives**

❖ To synthesize silver nanoparticles (AgNPs) using the methanolic extract of *S. palghatense* bark, leveraging its potent bioactive compounds for effective nanoparticle formation.

❖ To perform comprehensive physicochemical characterization of the synthesized silver nanoparticles (AgNPs) utilizing advanced analytical

techniques such as UV-Visible spectroscopy (UV-Vis) for surface plasmon resonance analysis, Fourier-transform infrared spectroscopy (FTIR) for identifying functional groups, Scanning and Transmission Electron Microscopy (SEM and TEM) for detailed morphology and size examination, Atomic Force Microscopy (AFM) for nanoscale surface topography, and X-Ray Diffraction (XRD) for crystallographic structure determination.

- To evaluate the biological potential of the *S. palghatense* bark-derived silver nanoparticles (AgNPs) through rigorous *in vitro* assessments encompassing antioxidant activity, antimicrobial efficacy against pathogenic bacteria and fungi, antibiofilm capabilities, as well as anthelmintic, anti-inflammatory, antidiabetic, and anticancer properties.

7.2. Materials and methods

7.2.1. Precursor preparation

The methanolic bark extract of *S. palghatense* demonstrated significant biological activity in both *in vitro* and *in vivo* assays. Based on these findings, *S. palghatense* was selected for the green synthesis of silver nanoparticles, followed by their physicochemical characterization and validation of associated biological properties.

Silver nitrate ($AgNO_3$) was used as a precursor for the synthesis of silver nanoparticles from the *S. palghatense* bark methanol extract. 1 mM solution of silver nitrate was prepared by using the double-distilled water which was stored at 4°C.

7.2.2. Biosynthesis of Silver Nanoparticles

The green synthesis method was used for the synthesis of AgNPs. For the reduction of Ag^+ ions, 1 mL *S. palghatense* bark methanol extract was added dropwise into 100 mL of 1 mM aqueous solution of $AgNO_3$ and heated at 60-80°C for 1 hour. The change in colour was observed from dark brown to reddish-brown, indicating the formation of silver nanoparticles. Similarly, 0.5, 1, 2, and 2.5 mL of *S. palghatense* bark methanol extract were suspended for the preparation of silver nanoparticles (Shankar et al., 2005).

7.2.3. UV-Visible Absorbance Spectroscopy (UV-Vis)

UV-Visible spectroscopy analysis was carried out on a Jasco UV absorption spectrophotometer V-650 with a resolution of ±1 nm between 200 and 800 nm, processing a scanning speed of 200 nm/minutes. Equal amounts of the suspension (0.5 mL) were taken and analyzed at room temperature. The progress of the reaction between metal ions and the *S. palghatense* bark methanol extract was monitored by UV-Visible spectra of silver nanoparticles in aqueous solution with different wavelengths in nanometers from 200 to 800 nm. The reduction of silver ions and formation of silver nanoparticles occurred after 24 hours of reaction. Control was maintained by using $AgNO_3$ (Shankar et al., 2005).

7.2.4. Fourier Transforms Infrared Spectroscopy (FTIR)

For FTIR measurements, the synthesized silver nanoparticles solution was centrifuged at 10000 rpm for 30 minutes. The pellet was washed three times with 5 mL of deionized water to remove free proteins or enzymes that were not capping the silver nanoparticles. The pellet was dried using a vacuum drier. It was analysed by FTIR (Ghadially, 1996).

7.2.5. Scanning Electron microscopy (SEM) Analysis

SEM study was done using electron microscope (JSM-6610 LV, Jeol Asia PTE Ltd, Japan). Silver nanoparticles that were synthesized were centrifuged at 10,000 rpm (15 minutes). The pellets were re-dispersed in sterile double-distilled water and centrifuged at 10,000 rpm (10 minutes). The purified pellets were dried at 50°C in an oven, and thin films of the dried samples were prepared on a carbon-coated copper grid by dropping a very small amount of the sample onto the grid. By using blotting paper extra solutions of the samples were removed. The films on the carbon-coated copper grid (SEM grid) were allowed to dry by placing them under a mercury lamp for 5 minutes. The morphological features, micrograph images, size, and structure of synthesized nanoparticles from plant extract were analyzed and recorded (Ajaykumar et al., 2023).

7.2.6. Transmission Electron Microscopy (TEM) Analysis

In TEM analysis, the maximum thickness allowable depends on the electron scattering factor of the material. A general rule of thumb is that the higher the atomic number of the elements in the sample, the greater the electron scattering factor and the thinner the specimen needs to be. Therefore, under identical conditions, an aluminium (Al) sample could be more than 10 times thicker than a uranium (U) sample to achieve the same TEM picture quality. For amorphous samples under 100-kV electrons, a few hundred nanometres of Al and a few tens of nanometres of Uranium are often the limits for regular TEM analysis. Higher accelerating voltages can tolerate thicker specimens. When the sample is crystalline, the thickness requirement need not be as stringent. Bragg reflection at certain crystal orientations

allows electrons to penetrate anomalously thick regions of the sample. All thinning techniques aim to prepare foils or regions of foils that are approximately 0.1 to 10 micrometres (μm) in thickness. The transverse features and size of the synthesized nanoparticles from the plant extract were analyzed and recorded (Ajaykumar et al., 2023).

7.2.7. Atomic Force Microscopy (AFM)

AFM allows for 3D characterization of nanoparticles with sub-nanometer resolution. Nanoparticle characterization using Atomic Force Microscopy has a number of advantages over dynamic light scattering, electron microscopy and optical characterization methods (Hoo et al., 2008).

7.2.8. X-Ray Diffraction (XRD) Analysis

It was used for the structural analysis of the synthesized AgNPs, an X-ray powder diffractometer (D-max IIA, Rigaku, Japan) was used. Diffraction data were collected over a range of 2θ angles. The average crystalline domain size (D) was calculated using the Scherrer equation (Ghadially, 1996).

$$D=K\lambda / \beta \text{Cos}\theta$$

Where, D = average crystalline domain size, β denotes Full Width Half Maximum (FWHM);

K = 0.94, λ = wavelength of X-ray (1.54 A^0) and θ is the Brag's angle

7.2.9. Bioactivity screening of *S. palghatense* silver nanoparticles (AgNPs)

7.2.9.1. Antioxidant assay of *S. palghatense* silver nanoparticles (AgNPs)

The antioxidant capacity of *S. palghatense* bark silver nanoparticles was evaluated using four standard *in vitro* assays. DPPH Radical Scavenging was performed following Aquino et al. (2001), where 0.1 mM DPPH solution was mixed with various sample concentrations, incubated for 20 min in the dark, and absorbance was measured at 517 nm. Superoxide Radical Scavenging followed McCord and Fridovich (1969), using riboflavin–NBT photoreduction, with absorbance read at

560 nm after 15 min illumination. Hydroxyl Radical Scavenging was assessed using Fenton reaction (Saldanha et al., 1990; Ohkawa, 1979), measuring thiobarbituric acid reactive substances at 532 nm after heating with TBA reagent. FRAP Assay was done per Pulido et al. (2000), mixing samples with freshly prepared FRAP reagent, incubating at 37 °C for 15 min, and reading at 595 nm. All tests were repeated six times for accuracy.

7.2.9.2. Antimicrobial potential of *S. palghatense* silver nanoparticles (AgNPs)

The antimicrobial activity of silver nanoparticles (AgNPs) synthesized from *S. palghatense* bark methanol extract can be evaluated using standardized *in vitro* methods adapted from plant extract studies.

The agar well diffusion method is commonly employed, where AgNPs at various concentrations are applied to wells bored in agar plates inoculated with standard microbial strains, such as *Staphylococcus aureus*, *Escherichia coli, Candida albicans*, and *Pseudomonas aeruginosa* (Atallah et al., 2022; Patel et al., 2014). Zones of inhibition are measured after incubation to assess antimicrobial potency. Minimal inhibitory concentration (MIC) and minimal bactericidal or fungicidal concentration (MBC/MFC) are determined by two-fold broth dilution methods following CLSI guidelines, with MIC defined as the lowest concentration inhibiting visible microbial growth, and MBC/MFC as the lowest concentration killing the organism (CLSI, 2012; Pinto et al., 2009). For biofilm studies, particularly against *Pseudomonas aeruginosa*, anti-biofilm assays involve quantifying biofilm inhibition or disruption by AgNPs using crystal violet staining or similar assays, given the significance of biofilms in antimicrobial resistance (Rukayadi, 2008). These methods provide precise and reproducible measurements of the antimicrobial efficacy of *S. palghatense*-derived AgNPs, offering valuable data for assessing their therapeutic potential.

7.2.9.2.1. Minimal Inhibitory Concentration (MIC) and Minimal Fungicidal Concentration (MFC)

MIC values of silver nanoparticles synthesized from *S. palghatense* bark methanol extract were assessed using broth macrodilution following CLSI guidelines

(2012) with slight modifications. Two-fold serial dilutions (10–300 µg/mL) were prepared in DMSO and inoculated with conidial suspensions adjusted from 7-day-old PDA cultures (Shehata et al., 2008). For *Aspergillus niger* and *Candida albicans*, MIC was recorded after 48 hours as the lowest concentration that fully prevented visible growth. To determine MFC, 20 µL from tubes showing no growth at and above the MIC was plated onto SDA and incubated at 35 °C for up to three days. MFC was defined as the lowest concentration at where no colonies developed. All assays were performed in duplicate and repeated six times independently with consistent outcomes (Pinto et al., 2009).

7.2.9.2.2. Minimal Inhibitory Concentration (MIC) and Minimal Bactericidal Concentration (MBC)

MIC and MBC of the synthesized silver nanoparticles were determined by broth microdilution in 96-well U-bottom plates, according to CLSI protocols (2012). Inocula containing ~10^6–10^8 CFU/mL were prepared, and nanoparticles were serially diluted two-fold from a 10 mg/mL stock solution in the growth medium (Rukayadi, 2008). MIC was defined as the lowest nanoparticle concentration that prevented visible bacterial growth. MBC was identified by subculturing wells with no visible growth onto fresh agar plates and incubating until control growth was evident. The lowest concentration with no surviving colonies was recorded as the MBC.

7.2.9.2.3. Biofilm studies

Silver nanoparticles (AgNPs) synthesized from the methanolic extract of *S. palghatense* bark have shown higher antimicrobial activity; thus, this study was designed to investigate their advanced anti-biofilm potential. Among the tested pathogens, *Pseudomonas aeruginosa* (ATCC 27853) was selected for biofilm studies as it was most sensitive to antimicrobial activity.

Antibiofilm activity is the capacity of a substance to inhibit or disintegrate biofilms, which are organized microbial communities that attach to surfaces and are enclosed in a protective extracellular matrix. Biofilms are well-known for their increased resistance against antimicrobials and persistent infections; the two major

problems faced worldwide in the industrial and medical fields (Donlan & Costerton, 2002).

7.2.9.2.3.1. Congo red agar assay

Among different screening approaches, the Congo Red agar assay is most commonly used to detect biofilm formation in microorganisms, specifically bacterial species. The Congo Red dye is mixed with brain heart infusion agar with glucose. Hence, this approach provides a differential medium for guiding biofilm producers *in vitro*. On this medium, biofilm-producing strains will form black or dark red colonies with a dry-crystalline morphology because they are able to produce extracellular polymeric substances, EPS. In contrast, non-biofilm-producing strains will produce pink or lighter-coloured colonies that have smooth surfaces. Black colouration intensity directly relates to biofilm formation ability and allows for a qualitative measure of biofilm-generating capacity. This assay is very useful due to its simplicity, cost-effectiveness, and reliability for the high-throughput evaluation of clinical isolates for their biofilm-forming capacity. It is a valuable tool for microbiological research and diagnostics. Results are generally interpreted after incubating for 24-48 hours at 37°C, where a positive result may suggest virulence factors present in pathogenic organisms.

Thus, Congo red agar assay was used to assess the capacity of bacteria to create a biofilm. The details regarding the media composition, preparation of the medium, and procedure adopted for the technique are explained below (Hassan et al., 2011).

7.2.9.2.3.1.1. Materials required

Congo Red Agar (CRA) medium, Brain Heart Infusion Broth (BHIB) (Oxoid, UK), sucrose (50 g/L), and agar no. 1 (10 g/L) (Oxoid, UK), congo red indicator (Oxoid, UK), *Pseudomonas aeruginosa* (ATCC 27853).

7.2.9.2.3.1.2. Preparation of brain heart infusion broth (BHIB)

13 g of Nutrient Broth media (Hi-Media) was dissolved in 1000 ml of distilled water and sterilized by autoclaving at 121°C and 15 psi for 15 minutes.

7.2.9.2.3.1.3. Preparation of congo red agar plates

The Congo Red Agar (CRA) medium was prepared by mixing brain heart infusion broth (37 g/L), sucrose (50 g/L), and agar no. 1 (10 g/L) in distilled water. Congo red indicator (8 g/L) was prepared separately. It was dissolved in a minimal volume of sterile distilled water, and all aliquots of the dye were sterilized by autoclaving at 121°C, 15 psi for 15 minutes. The sterilized Congo red solution was aseptically added when the brain heart infusion agar with sucrose was cooled to 55°C.

7.2.9.2.3.1.4. Culture of the test organism

The bacterial suspension of *Pseudomonas aeruginosa* was adjusted to 0.5 McFarland standard, approximately 1.5×10^8 CFU/Ml.

7.2.9.2.3.1.5. Procedure

A standardized suspension of *Pseudomonas aeruginosa* was prepared from a culture in brain heart infusion broth, and an aliquot was inoculated onto Congo Red Agar (CRA) medium and incubated aerobically at 37°C for 24 hours. Biofilm formation was indicated by colony morphology and pigmentation characteristics: colonies with black or dark red pigmentation and dry crystalline were considered positive for biofilm production, while colonies that retained a bright red colour with smooth surfaces were considered negative. Each experiment was performed six times (n = 6), and all aseptic techniques were employed to ensure reproducibility and statistical validity.

7.2.9.2.3.2. Semi-quantitative adherence assay

One of the most common methods to measure biofilm formation and bacterial adherence is the semi-quantitative assay employing crystal violet staining. This approach utilizes 96-well tissue culture plates to assess biofilm formation by optical

density measurements. The method was popularized due to its relative ease and reproducibility with respect to quantifying biofilm formation. Experiments focusing on biofilm formation can be statistically analyzed to show significant differences between biofilm formation and different strains or conditions. This method enables all scientists to examine the potential of different compounds in preventing or disrupting biofilm formation in various bacteria, which is crucial for fundamental biological studies and therapeutic development (Ben Abdallah et al., 2009).

The potential of *Pseudomonas aeruginosa* (ATCC 27853) to form biofilm was assessed by semi-quantitative adherence assay in 96-well tissue culture plates (Nunc, Roskilde, Denmark) as described by Kouidhi et al. (2010). The bacterium was cultured in Brain Heart Infusion Broth, BHIB (Bio-Rad, France).

7.2.9.2.3.2.1. Materials required

Pseudomonas aeruginosa (ATCC 27853), brain heart infusion broth (BHIB), sterile phosphate buffer saline (PBS), crystal violet (5% w/v), ethanol (95% v/v), dimethyl sulphoxide (DMSO), 96-well microtiter plate (Nunc, Roskilde, Denmark), ELISA plate reader (ERBA, Lisa Scan).

7.2.9.2.3.2.2. Preparation of brain heart infusion broth (BHIB)

Brain Heart Infusion Broth (37 g/L) was dissolved in 1000 mL of distilled water and sterilized by autoclaving at 121°C and 15 psi for 15 minutes.

7.2.9.2.3.2.3. Preparation of bacterial inoculum

The bacterial suspension of *Pseudomonas aeruginosa* (ATCC 27853) was adjusted to 0.5 McFarland standard (approximately 1.5×10^8 CFU/mL).

7.2.9.2.3.2.4. Procedure

The semi-quantitative adherence assay was performed using the crystal violet staining method. The bacterial inoculum of *Pseudomonas aeruginosa* was prepared, and the growth was adjusted to 0.5 McFarland standard. A portion of sterile BHIB was distributed into 96-well microtiter plate wells. A standard bacterial inoculum (20

µL) was mixed with Silver nanoparticles (AgNPs) synthesized from the methanolic extract of *S. palghatense* bark for respective concentrations (62.5, 125, 250, 500, and 1000 µg/mL) in each well. Control wells were filled with sterile BHIB (negative control) and bacterial suspension without extract (positive control). Afterwards, the plates were placed at 37°C for 24 hours incubation. All tests were done in hexaplicate (n=6).

Non-adherent cells were washed off three times with sterile phosphate-buffered saline (7 mM Na_2HPO_4, 3 mM NaH_2PO_4, 130 mM NaCl, pH 7.4). Plates were inverted and dried for 30 minutes at 60°C. Biofilms developed on the plates were fixed with 95% ethanol (v/v) and stained using a crystal violet solution (100 µL, 5% w/v, Merck, France) for 5 minutes. Plates were air-dried overnight, following a triple wash with sterile PBS. 200 µL dimethyl sulfoxide (DMSO) was used to solubilize adherent cells. Optical density was recorded at 570 nm with an ELISA plate reader (ERBA, Lisa Scan). The biofilm formation was classified by reading the OD values at 570 nm. Samples with $OD_{570} < 0.1$ were considered negative for biofilm formation; samples with OD_{570} values between 0.1 and 1 ($0.1 \leq OD_{570} < 1$) were classified as low-grade positive; $OD_{570} \geq 1$ were classified as strongly positive for biofilm (Kitti et al., 2019).

7.2.9.2.3.3. Inhibition assay of initial and pre-formed biofilm

Inhibition assay of initial and pre-formed biofilm is important in assessing antimicrobial efficacy at varying levels of biofilm development. The analysis assesses preventive capacity against biofilm formation and the ability to disrupt established biofilms, which is particularly important for understanding antimicrobial resistance mechanisms (Hassan et al., 2011).

7.2.9.2.3.3.1. Materials required

Pseudomonas aeruginosa (ATCC 27853), sterile phosphate buffer saline (PBS), 96-well microtiter plate (Nunc, Roskilde, Denmark), 10% dimethyl sulphoxide (DMSO), 95 % Ethanol, 5% crystal violet, brain heart infusion broth (BHIB), ELISA plate reader (ERBA, Lisa Scan).

7.2.9.2.3.3.2. Initial biofilm formation assay

The bacterial suspension of *Pseudomonas aeruginosa* was prepared, and growth was standardized to 0.5 McFarland standard. Nutrient Broth was prepared and sterilized by autoclaving at 121°C and 15 lbs for 15 minutes. 20 µL of standardized inoculum were added to each well of a sterile flat-bottom 96-well microtiter plate and incubated at 37°C for 96 hours for biofilm formation. After incubation, fresh media was seeded to each well, with varying concentrations of test samples (62.5, 125, 250, 500, and 1000 µg/mL). The growth control wells contained 100 µL inoculum and 100 µL 5-10% DMSO without test samples. The plates were incubated at 37°C for 24 hours.

7.2.9.2.3.3.3. Pre-formed biofilm inhibition assay

The inhibition of the pre-formed biofilm was carried out according to Taufiq & Darah (2020) with some modifications. 100 µL of bacterial suspension was inoculated into the wells containing 100 µL BHIB. The microtiter plate was incubated at 37°C for 24 hours. The wells were rinsed thrice with 200 µL sterile phosphate-buffered saline (PBS). An aliquot of 100 µL of fresh BHIB was added to biofilm-containing wells with 100 µL of test samples at concentrations ranging from 62.5 to 1000 µg/mL. The sterile BHIB served as a negative control. After 24 hours of incubation at 37°C, the biofilms were quantified.

7.2.9.2.3.4. Quantification of biofilm

Biofilm formation can be measured using many standardized methods. The crystal violet (CV) assay is commonly employed due to its high reliability and simplicity, as the dye binds to both viable and non-viable bacteria, as well as the extracellular polymeric matrix. Optical density at 570 nm (OD_{570}) provides quantitative data on biofilm biomass. A visual assessment of antimicrobial activity can be achieved using the agar well diffusion method, as indicated by the zone of inhibition. However, combining these techniques allows for an extensive quantification of biofilm formation and inhibition, with results commonly expressed in percentage inhibition compared to untreated controls (O'Toole, 2011).

7.2.9.2.3.4.1. Materials required

Pseudomonas aeruginosa (ATCC 27853), 10% dimethyl sulphoxide (DMSO), 95 % Ethanol, 5% crystal violet, brain heart infusion broth (BHIB), sterile phosphate buffer saline (PBS), 96-well microtiter plate (Nunc, Roskilde, Denmark), ELISA plate reader (ERBA, Lisa Scan).

7.2.9.2.3.4.2. Biofilm formation and inhibition assay

Pseudomonas aeruginosa (ATCC 27853) bacterial suspension was made, and growth was regulated to the 0.5 McFarland standard. The nutrient broth was prepared and sterilized by autoclaving at 121°C and 15 psi for 15 minutes and then distributed into each well of a sterile 96-well microtiter plate. After adding 20 µL of inoculum to each well, the plate was incubated for 72 hours at 37°C to allow biofilm formation. The biofilm was applied with varying sample quantities (62.5, 125, 250, 500, and 1000 µg). No sample was added to the control well.

7.2.9.2.3.4.3. Biofilm quantification

The plate was in the incubator for a full day. The 96-well microtiter plate was gently flipped to remove the contents from the wells after the incubation period. Before removing the unattached bacteria, the entire microtiter plate was inserted at a 45° angle into a large beaker containing sterilized PBS solution (pH 7.2).

The biofilms were heat-fixed for 1 hour in an oven at 60°C. 100 µL of 0.5% crystal violet was used to stain the well-containing biofilm for 15 minutes, and the crystal violet was subsequently discarded. The 96-well microtiter plate was allowed to air dry at room temperature (30 ± 2°C) for 15 minutes after the wells were rinsed with sterile distilled water. 100 µL acetic acid (30%, v/v) was added into each well to solubilize the stained biofilm and incubated for 10 minutes at room temperature (30 ± 2°C) in an assay shaker with a 50 rpm agitation speed. The absorbance was measured at 570 nm after the crystal violet solution containing the solubilized biofilm was transferred to a different 96-well plate. All the experiments were performed six times (Chaieb et al., 2011; Kwasny & Opperman, 2010).

The inhibition activity was expressed in terms of the percentage of biofilm inhibited compared to the untreated control biofilms and was determined using the following formula: [(OD control-OD sample)/OD control] x 100. The lowest concentration of silver nanoparticles that exhibited 50% inhibition on the biofilm formation was designated the biofilm inhibition concentration (BIC_{50}).

7.2.9.2.3.5. Bacterial live/dead assay using SYTO 9 and propidium iodide

SYTO 9 and propidium iodide are advanced dual-staining fluorescence methods that can be carried out to assess bacterial viability quickly via the evaluation of membrane integrity. The assay uses SYTO 9, a green fluorescent nucleic acid stain permeant to all bacterial membranes, and propidium iodide, which can only enter cells with compromised membranes. When applied sequentially, the two dyes make a clear visual distinction: bacteria with intact membranes take up the first dye and appear green (live), and those with compromised membranes take up the second dye and appear red (dead). This approach offers a more efficient yet reliable and reproducible alternative to existing, time-consuming culture-based methods for assessing bacterial viability across various genera. These techniques provide several benefits, such as quick results within minutes, the ability to visualize mixed bacterial populations simultaneously, and the ability to perform qualitative and quantitative analyses with microscopy, cell flow cytometry, or microplate readers (Robertson et al., 2019).

7.2.9.2.3.5.1. Material required

Nutrient broth, 96-well plates, sterile phosphate buffer saline, 3.34 mM SYTO 9, and 20 mM propidium iodide (1:1).

7.2.9.2.3.5.2. Bacterial culture

The bacterial inoculum of *Pseudomonas aeruginosa* (ATCC 27853) was prepared, and growth was regulated to the 0.5 McFarland standard. Nutrient broth media (13 g) was dissolved in 1000 mL of distilled water, autoclaved at 121°C for 15 minutes at 15 lbs, and dispersed to each well of a 96-well microtiter plate. 20 µL of inoculum was added to each well, and the plate was incubated for 72 hours at 37°C to allow biofilm formation.

7.2.9.2.3.5.3. Sample addition

After 72 hours, biofilms were treated with IC_{50} concentrations of test samples. No sample was added to the control well. The plate was then incubated for an additional 24 hours at 37°C.

7.2.9.2.3.5.4. Live/dead assay

A staining solution was prepared by mixing SYTO9 3.34 mM in propidium iodide 20 mM at equal volumes in a microfuge tube. The biofilms were washed twice with sterile PBS pH 7.2 before air-drying. 3 µl of the dye solution was added to each well and incubated in the dark for 15 minutes at a room temperature of 22-25°C. Following the incubation, the excess dye was poured out with sterile PBS. The dye was observed using an Olympus CKX41 fluorescent microscope equipped with an Optika pro5 CCD camera and appropriate filters (Stiefel et al., 2015), which were used for SYTO9 (excitation/emission: 485/498 nm) and propidium iodide (excitation/emission: 535/617 nm).

7.2.9.2.3.6. Bacterial cell adherence assay

Bacterial cell adherence assay is a fundamental tool for assessing the initial attachment phase of biofilm formation, which serves as the first step in the colonization of surfaces by bacteria. In this assay, bacterial adhesion to substrates is quantified by measuring CFU after treatment with a potential inhibitory agent. The assay can identify potential anti-biofilm compounds that prevent biofilm development by inhibiting the initial attachment phase, which is critical for biofilm formation. This approach is especially relevant for screening potential therapeutic agents against biofilm-forming pathogens such as *Pseudomonas aeruginosa*, which mediate chronic infections by forming surface-attached communities with increased antibiotic resistance (Merritt et al., 2011).

7.2.9.2.3.6.1. Materials required

Luria-Bertani broth (LB broth, Hi-Media), Luria-Bertani agar (LB agar, Hi-Media), *Pseudomonas aeruginosa* (ATCC 27853), 48-well tissue culture plates,

sterile phosphate-buffered saline (PBS, pH 7.4), Sterile distilled water, digital colony counter, micropipettes and sterile tips, and petri plates.

7.2.9.2.3.6.2. Preparation of Luria-Bertani Broth (LB Broth)

LB broth (25 g/L) was prepared by dissolving 2.5 g of Luria-Bertani broth media (Hi-Media) in 100 mL of distilled water and was sterilized by autoclaving at 121°C and 15 psi for 15 minutes.

7.2.9.2.3.6.3. preparation of Luria Bertani Agar (LB Agar)

LB agar (25 g/L) (Appendix 15) was prepared by dissolving 25 g in 1000 mL of distilled water and sterilized by autoclaving at 121°C and 15 psi for 15 minutes. The media was allowed to cool to 50°C without any disturbance and was aseptically poured into sterile, labeled petri plates and allowed to solidify in a laminar airflow cabinet with UV sterilization.

7.2.9.2.3.6.4. Biofilm formation

Pseudomonas aeruginosa (ATCC 27853), was standardized to 0.5 McFarland standard (approximately 1.5×10^8 CFU/mL). LB broth was dispensed into 48-well tissue culture plates, and 20 µL of standardized inoculum was added to each well. Plates were incubated at 37°C for 72 hours to allow biofilm formation.

7.2.9.2.3.6.5. Sample treatment

After 72 hours, established biofilms were treated with silver nanoparticles (AgNPs) synthesized from the methanolic extract of *S. palghatense* bark at concentrations of 250 and 1000 µg/mL. Control wells received no treatment. Plates were incubated for an additional 24 hours at 37°C.

7.2.9.2.3.7. Quantification of adherent bacteria

The plate wells were washed thrice with sterile distilled water to remove non-adherent bacterial cells. Adherent cells were removed by adding 300 µL of sterile PBS into each well after air-drying at room temperature (22-25°C). The bacterial suspensions were then serially diluted to 10^{-3} and incubated at 37°C for 10 minutes.

From each dilution, 20 µL was spot-inoculated on LB agar plates, followed by dispersion of the suspension with a sterile spreader. The LB agar plates were incubated at 37°C for 24 hours. Following incubation, colony-forming units (CFUs) were enumerated using a digital colony counter and expressed as CFU/mL (Chenicheri et al., 2022).

7.2.9.2.3.8. Drug efflux assay by ethidium bromide

The ethidium bromide drug efflux assay is a fluorescence-based technique employed to evaluate bacterial efflux pump activity, known to play a vital role in antimicrobial resistance and biofilm development. This technique involves measuring the accumulation or efflux of ethidium bromide, a fluorescent substrate for several bacterial efflux systems, into bacterial cells. The assay relies on exposing bacterial cultures to ethidium bromide, which normally does not penetrate cell membranes but can bind to nucleic acids when it does enter a cell and fluoresce. When efflux pumps are active, they remove ethidium bromide from the cell, reducing fluorescence, whereas when efflux pumps are inhibited, ethidium bromide accumulates within cells, enhancing fluorescence. The intensity of fluorescence in arbitrary units (a.u.) is a quantitative measure of activity or inhibition of efflux pumps. It is particularly well-suited for the initial screening of potential efflux pump inhibitors, which could potentially help to overcome antimicrobial resistance by blocking the ejection of such drugs from bacterial cells (Bohnert et al., 2010; Paixão et al., 2009).

7.2.9.2.3.8.1. Materials required

Nutrient Broth (13 g of nutrient broth was dissolved in 1000 mL distilled water and sterilized by autoclaving at 121°C and 15 psi for 15 minutes), Luria-Bertani (LB) Broth (2.5 g of Luria-Bertani broth media (Hi-Media) in 100 mL of distilled water and was sterilized by autoclaving at 121°C and 15 psi for 15 minutes), Ethidium Bromide solution (10 mg/mL), Phosphate Buffered Saline (PBS, pH 7.4), Antibiotics (Penicillin and tetracycline discs), *Pseudomonas aeruginosa* (ATCC 27853), and Qubit Fluorometer with blue filter (excitation/emission: 510/595 nm).

7.2.9.2.3.8.2. Procedure

An overnight culture of *Pseudomonas aeruginosa* (ATCC 27853) was inoculated into 5 mL Luria-Bertani broth and incubated at 37°C until turbidity reached approximately 0.5 McFarland standard. 25 mL of nutrient broth was added and incubated at 37°C for 4 hours. The culture (*E. coli* broth) was divided into four sterile microcentrifuge tubes (1 mL each). For the antibiotic efflux pump assay, two tubes were treated with resistant antibiotic discs (penicillin and tetracycline, respectively) and incubated overnight at 37°C to induce the expression of efflux pumps. The other two tubes were untreated controls.

Antibiotic discs were carefully removed from the treated samples after incubation. The four samples were centrifuged at 6000 rpm for 10 minutes, and the supernatants were removed. The pellets of bacteria were resuspended, and 5 µL ethidium bromide (10 mg/mL) was added to each tube. Suspensions were mixed well and incubated in the dark at room temperature (22-25°C) for 10 minutes to permit ethidium bromide uptake. After incubation, the samples were centrifuged at 6000 rpm for 5 minutes. The pellets were washed and resuspended in 200 µL PBS. The fluorescence of the supernatant was measured using a Qubit fluorometer with blue LED excitation (430-495 nm) and green emission detection (510-580 nm). For the test organisms, fluorescence intensity was determined, and the efflux ability of the test organisms was measured and compared, wherein less fluorescence intensity indicated higher efflux activity (Paixao et al., 2009).

7.2.9.2.3.9. Bacterial MTT assay-Total cell response to compound

The bacterial MTT (3-(4,5-dimethylthiazol-2-yl)-2,5-diphenyltetrazolium bromide) assay is a colorimetric method used to assess the viability and metabolic activity of bacteria in the presence of antimicrobial compounds. This assay is based on the ability of metabolically active bacteria to reduce the yellow tetrazolium salt MTT (3-(4,5-dimethylthiazol-2-yl)-2,5-diphenyltetrazolium bromide) into purple formazan crystals. When testing compounds are added to cultures of bacteria, functionally dead cells lose their ability to reduce MTT due to a lack of metabolic activity, and thus produce less formazan than viable counterparts; the crystal

efficiently dissolves in solubilization solvent (dimethyl sulfoxide, DMSO) allowing for the quantification of formazan by spectrophotometry at 595 nm (when MTT reduction occurs, the more viable cells produce more absorbance due to a higher quantity of formazan being present when dissolved in DMSO). The assay generates quantitative information about the bacterial response toward antimicrobial agents, and results are usually reported as percentage viability compared to untreated controls. Moreover, this approach is advantageous through its sensitivity, reproducibility, and suitability for high-throughput screening. It provides a means to screen for new antimicrobial compounds against various bacterial pathogens, including biofilm-producing bacteria (Benov, 2019; Wang et al., 2010).

7.2.9.2.3.9.1. Material required

Nutrient Broth (13 g of nutrient broth was dissolved in 1000 mL distilled water and sterilized by autoclaving at 121°C and 15 psi for 15 minutes), MTT (3-(4,5-dimethylthiazol-2-yl)-2,5-diphenyltetrazolium bromide) 5 mg/mL in PBS, DMSO (Dimethyl sulphoxide, Sigma Aldrich, USA), 96-well microtiter plates and *Pseudomonas aeruginosa* (ATCC 27853).

7.2.9.2.3.9.2. Procedure

After 24-hour bacterial culture incubation with test samples, 30 µL of reconstituted MTT solution (5 mg/mL) was added to each test and cell control well. The plate was shaken gently and then incubated for 4 hours at 37°C before collecting the supernatant and centrifuging at 6000 rpm for 10 minutes. The pellet was then resuspended in 100 µL of MTT solubilization solution (DMSO) to solubilize the formazan crystals. Wells were mixed gently by pipetting up and down. Five minutes of 6000 rpm centrifugation were applied to harvest supernatants. Absorbance was detected at 595 nm with a microplate reader (Benov, 2019; Walter et al., 2017).

The percentage of growth inhibition was calculated using the formula:

$$\text{Percentage of cell viability} = \frac{\text{Mean OD samples}}{\text{Mean OD of a control group}} \text{X } 100$$

7.2.9.2.3.10. Determination of bacterial load using acridine orange (AO) staining

Acridine orange (AO), a nucleic acid-binding fluorescent dye, was used to morphologically detect viable cells and determine bacterial load. AO can cross the bacterial cell membrane, intercalate into double-stranded DNA, and emit green fluorescence (excitation/emission: 500/526 nm).

7.2.9.2.3.10.1. Material Required

Nutrient Broth (13 g Nutrient Broth (Hi Media) dissolved in 1000 mL of distilled water and sterilized by autoclaving at 121°C, 15 psi for 15 minutes), *Pseudomonas aeruginosa* (ATCC 27853), 96 well plates, Acridine Orange (1 mg/mL in sterile distilled water), Sterile phosphate-buffered saline (PBS, pH 7.4).

7.2.9.2.3.10.2. Biofilm formation

Pseudomonas aeruginosa (ATCC 27853) inoculum was standardized to a 0.5 McFarland standard (approximately 1.5×10^8 CFU/mL). Sterile nutrient broth was dispensed into 96-well tissue culture plates, and 20 µL of standardized inoculum was added to each well. Plates were incubated at 37°C for 72 hours to allow biofilm formation.

7.2.9.2.3.10.3. Sample treatment

Biofilms established for 72 hours were treated with silver nanoparticles (AgNPs) synthesized from the methanolic extract of *S. palghatense* bark at 1000 µg/mL. Control wells were treated with no agents. Plates were further incubated at 37°C for 24 hours.

7.2.9.2.3.10.4. Acridine orange staining

After incubation, the culture medium was gently removed without disturbing the biofilms. The biofilms were subsequently air-dried for 10 minutes at room temperature (22-25°C). Wells were washed twice with sterile PBS to remove non-adherent cells and excess media. Add 10-20 µL of acridine orange solution to each well of the plate, and incubate the plate at room temperature for 15-20 minutes in the

dark. Wells were washed twice with sterile PBS to remove excess stain after incubation. Fluorescence was observed using an Olympus CKX41 fluorescent microscope with an Optika pro5 CCD camera, equipped with appropriate filters for acridine orange (excitation/emission: 500/526 nm).

7.2.9.2.3.11. Gene expression study

Bacterial inoculum of *Pseudomonas aeruginosa* (ATCC 27853) was prepared, and growth was adjusted to 0.5% McFarland standard (approximately 1.5×10^8 CFU/mL). Nutrient broth was prepared and sterilized by autoclaving at 121°C, 15 psi for 15 minutes. It was then dispensed to each well in a 12-well tissue culture plate. 20 µL of inoculum was added to each well, and the plate was kept for incubation at 37°C for 72 hours for the formation of biofilm. After 72 hours, 100 µL /mL silver nanoparticles (AgNPs) synthesized from the methanolic extract of *S. palghatense* bark were added to the well. The control well was kept without the addition of a sample. The plate was incubated for 24 hours at 37°C (O'Toole, 2011).

7.2.9.2.3.11.1. Isolation of Total RNA (TRIzol Method)

Total RNA was isolated using the TRIzol reagent (Invitrogen, USA) total RNA isolation kit according to the manufacturer's instructions (Invitrogen, Product code 10296010). The addition of TRIzol solution causes cell disruption and the release of RNA. Following chloroform extraction and centrifugation, RNA remains exclusively in the aqueous phase while proteins partition to the interphase and organic phase. RNA is subsequently precipitated from the aqueous phase using isopropanol, forming a white pellet on the side and bottom of the tube.

After incubation, the media was removed aseptically, and 200 µL of TRIzol reagent (Appendix 16) was added to the culture well plate. The plate was then incubated for 5 minutes at room temperature (22-25°C). The contents were then transferred to a fresh sterile microcentrifuge tube. 200 µL of chloroform was added, and the tubes were shaken vigorously for 15 seconds and then incubated for 2-3 minutes at room temperature. This was followed by centrifugation at 14,000 rpm for 15 minutes at 4°C. The upper aqueous layer was carefully collected, and 500 µL of

100% isopropanol was added. The sample was incubated for 10 minutes at room temperature and then centrifuged at 14,000 rpm for 15 minutes at 4℃. The supernatant was discarded, and the RNA pellet thus obtained was washed with 200 µL of 75% ethanol (Merck). Samples were centrifuged at 14,000 rpm for 5 minutes at 4℃ in a cooling centrifuge (Remi CM12). The RNA pellet was air-dried for 5-10 minutes and resuspended in nuclease-free TE buffer. RNA concentration and purity were determined spectrophotometrically by measuring absorbance at 260 and 280 nm.

7.2.9.2.3.11.2. cDNA synthesis

Total RNA was extracted using TRIzol reagent. The purity and concentration of the extracted RNA were determined. Complementary DNA (cDNA) was synthesized using the cDNA preparation kit (G BIOSCIENCES, product codes 786-5019s and 786-5020, master premix for first-strand cDNA synthesis). The reaction mixture consisted of 5 µL of RT Easy mix (Appendix 17), 0.5 µL of oligo (dT) primers, and 2 µL of RNA template (0.5 µg of total RNA) in an RNase-free tube (Appendix 18). The total reaction volume was adjusted to 10 µL with nuclease-free water. The solution was mixed by pipetting gently up and down. cDNA synthesis was performed in a thermal cycler (Eppendorf Master Cycler) programmed with the following conditions (Table 7.1): 42°C for 20 minutes (reverse transcription) followed by 85°C for 5 minutes (enzyme inactivation).

Table 7.1: Thermal cycling conditions for first-strand cDNA synthesis

Steps	Temperature ℃	Time (minutes)	Number of cycles
cDNA synthesis	42	20	1
Inactivation	85	5	1

7.2.9.2.3.11.3. Gene expression analysis by RT-qPCR

Real-Time quantitative reverse transcription PCR (RT-qPCR) analysis was carried out using SYBR® Green Master Mix (G BIOSCIENCES, product code 786-5062) on a LightCycler® 96 instrument (Roche). All reactions were performed in six

separate replicates and data were analyzed according to the ΔΔCt method (Appendix 19) using LightCycler® 96 SW 1.1 Software.

7.2.9.2.3.11.4. Thermal cycling conditions for RT-qPCR

Gene expression analysis was conducted by Real-time quantitative Reverse Transcriptase PCR (RT-qPCR) using SYBR® Green Master Mix (G BIOSCIENCES, Product code-786-5062) on the LightCycler® 96 (Roche) instrument. Thermal cycling parameters were optimized for amplification of the target genes. The protocol consisted of an initial activation step at 95°C for 2 minutes, followed by 40 cycles of a three-step PCR (denaturation: 95°C for 10 seconds; annealing: 58°C for 1 minute; extension: 72°C for 1 minute/kb expected amplicon length. A final extension step at 68°C for 5 minutes, followed by an indefinite hold at 4°C, was performed after cycling. All reactions were done in six times, and data were analyzed by ΔΔCt method with LightCycler® 96 SW 1.1 Software. In the ΔΔCt method, the relative gene expression was determined. It enables the identification of specific molecular targets that exhibit a differential response to *S. palghatense* silver nanoparticles in *Pseudomonas aeruginosa*. The genes targeted (lasR and rhlR) are master regulators of the expression of quorum-sensing-controlled virulence factors and biofilm, which are important determinants of pathogenicity; therefore, the importance of these genes as mediators of the potential of the extract to disrupt communication systems essential to bacterial pathogenicity is evident. Target gene-specific primer sequences were thoroughly developed to have comparable melting temperatures (Tm) to facilitate the amplification of the different gene products with the same efficiency. Agarose gel electrophoresis of PCR products verified the amplification specificity. The various steps involved, the time taken, and the temperature of each step are given in Table 7.2.

Table 7.2: Thermal Cycling Conditions for SYBR® Green-Based RT-qPCR

Steps	Time	Temperature (℃)
Initial activation step	2 minutes	95
3-step cycling (40 cycles)		
Denaturation	10 seconds	95
Annealing	1 minute	58
Extension	1 minute/kb	72
Final extension	5 minutes	68
Hold (End of PCR cycling)	Indefinite	4

7.2.9.2.3.11.5. Primer sequences

RT-qPCR reactions were performed with gene-specific primers designed with optimal properties for amplification efficiency. The reference gene was ldh, and the targeted genes were lasR and rhlR, which are important quorum-sensing regulators in *Pseudomonas aeruginosa*. Melting temperature (Tm) of primer pairs designed is between the range of 57-64.4°C, which is recommended for qPCR applications (52-58°C for most primers, with ldh (lactate dehydrogenase) being slightly higher). Each primer pair had low differences in Tm between the forward and reverse primers (≤1.7°C for ldh, 0°C for lasR and 0°C for rhlR), ensuring that the primers anneal in synchrony across the thermal cycles. The rhlR gene symbol has been changed from the original "Rhir", to comply with the standard nomenclature for *P. aeruginosa* quorum sensing genes, and all gene symbols have been italicized according to scientific convention (Taylor et al., 2019). Primer sequences used for RT-qPCR analysis were listed in Table 7.3.

Table 7.3: Primer sequences used for RT-qPCR analysis

Target gene	Forward primer (5'→3')	Tm (℃)	Reverse primer (5'→3')	Tm (℃)
Ldh	TTGGCGACGCTCTTGATCTTAG	64.4	GTCAGCATCCGCACAGTCTTC	62.7
lasR	AAGGAAGTGTTGCAGTGGTG	58	GAGCAGTTGCAGATAACCGA	58
Rhir	GACCAGGAGTTCGACCAGTT	57	GGTAGGCGAAGACTTCCTTG	57

Tm (℃): Melting temperature

7.2.9.2.3.11.6. Agarose gel electrophoresis

Agarose gel electrophoresis is a method for separating and visualizing DNA fragments based on their size. When subjected to an electric field, the fragments are separated by charge and size and move through the agarose gel matrix. The smaller fragments move faster than the larger ones. The electric field is generated by applying a potential across an electrolyte solution (buffer). When boiled in an aqueous buffer, agarose dissolves and solidifies to a gel upon cooling. A 1.5% (w/v) agarose gel was prepared by dissolving agarose powder in 1× TAE buffer (40 mM Tris, 20 mM acetic acid, 1 mM EDTA, pH 8.0) and heating in a water bath at 90°C until completely dissolved. The melted agarose was cooled to approximately 55°C before adding 6 µL of ethidium bromide solution (10 mg/mL) as a nucleic acid stain. The mixture was then poured into a gel casting apparatus with the gel comb. After the gel solidified (approximately 30 minutes at room temperature), the comb was removed, and the gel was placed in an electrophoresis tank containing 1× TAE buffer, ensuring the gel was completely submerged. DNA samples mixed with loading dye (containing glycerol and tracking dyes) were loaded into the wells alongside a DNA ladder as a size reference. Electrophoresis was performed at 50 V for 30 minutes (Lee et al., 2012). The DNA fragments, intercalated with ethidium bromide, were visualized under UV light using a gel documentation system (E-Gel Imager, Invitrogen).

7.2.9.2.3.12. EPS quantification

Extracellular polysaccharides (EPS) are high molecular weight natural polymers excreted by microorganisms and represent the basic component influencing the biofilm physicochemical properties. EPS provides both functional and structural integrity to biofilms by providing compositional support and protection from harsh environments (Seviour et al., 2019). Quantitative measurement of EPS as a biofilm characteristic is crucial for evaluating anti-biofilm strategies and elucidating the biofilm-forming mechanisms of clinically important pathogens, such as *Pseudomonas aeruginosa*.

Extracellular polysaccharide (EPS) constitutes the basic unit of biofilm matrix. EPS in biofilm was quantified using the phenol-sulphuric acid method. To quantify

EPS production, the test organism was grown in nutrient broth for 10 days in 24-well tissue culture plates to establish mature biofilms. After biofilm formation, 10 mg/mL of silver nanoparticles (AgNPs) synthesized from the methanolic extract of *S. palghatense* bark was added to the wells and incubated for 3 days. After the treatment period, the culture medium was carefully removed, and biofilms were washed with PBS (pH 7.4) to remove planktonic cells and media components (Jiao et al., 2010).

For the quantification of EPS, 0.5 mL of a 5% phenol solution (dissolved in 0.1 N HCl) was added to each well, followed by the rapid addition of 2.5 mL of concentrated sulfuric acid. The reaction mixture was incubated at room temperature for 20 minutes to achieve complete colour development. The absorbance at 490 nm was determined by a spectrophotometer. The EPS inhibition percentages were determined by comparing the absorbances of treated samples with those of untreated controls. A control without silver nanoparticles and a blank without an organism were also maintained throughout the experiment. EPS content was determined using a standard curve prepared with glucose (0-140 μg) as a reference standard.

7.2.9.3. Anthelmintic activity of *S. palghatense* silver nanoparticles (AgNPs)

The anthelmintic efficacy of *S. palghatense*-derived silver nanoparticles was assessed using *Lumbricus terrestris* as experimental models, following established protocols (Patel et al., 2011). Silver nanoparticles (AgNPs) were suspended in distilled water to prepare test solutions at concentrations of 25, 50, 75, and 100 mg/mL. Earthworms of comparable size were divided into groups and exposed to 50 mL of each test solution in separate Petri dishes. Negative (distilled water) and positive (albendazole, 20 mg/mL) controls were included. The time to onset of paralysis (cessation of all movement except upon vigorous shaking) and time to death (no movement even after exposure to warm water at 50 °C and appearance of body discoluration) were recorded for each worm. Results were expressed as mean ± standard error for each group.

7.2.9.4. Anti-Inflammatory activity of *S. palghatense* silver nanoparticles (AgNPs)

Anti-inflammatory activity is the ability of substances to suppress inflammation, or the protective response to an injury or infection, marked by redness, swelling, pain, and loss of function. That is important because chronic inflammation is the root of many ailments, including arthritis, cardiovascular disease, neurodegenerative disease, and cancer. Anti-inflammatory agents block inflammatory mediators (i.e., prostaglandins, cytokines) or interrupt inflammatory signaling pathways (Ferrero-Miliani et al., 2007). Great anti-inflammatory agents can be obtained from plant-derived compounds, comprising multiple bioactive constituents that can simultaneously target various aspects of inflammation while potentially having fewer side effects than synthetic counterparts (Ghasemian et al., 2016). Identifying novel anti-inflammatory compounds from natural sources offers alternative options for treating inflammatory diseases when conventional treatment fails or causes undesirable side effects (Maroon et al., 2010).

Various biochemical assays were employed to screen the anti-inflammatory properties of the silver nanoparticles (AgNPs) synthesized from the methanol extract of *S. palghatense* bark. Then, carefully examined for its ability to inhibit inflammation in RAW 264.7 macrophage cells stimulated with lipopolysaccharide (LPS).

7.2.9.4.1. *In vitro* anti-inflammatory activity screening by biochemical methods

The ability of the silver nanoparticles (AgNPs) synthesized from the methanol extract of *S. palghatense* bark to inhibit inflammatory processes is estimated *in vitro* by biochemical methods using techniques such as Human Red Blood Cell (HRBC) membrane stabilization method, protein denaturation inhibition, membrane stabilization, protease inhibition, and cyclooxygenase inhibition assays. Cell-based models using macrophage cell lines (RAW 264.7) which quantitatively determine the inhibition of pro-inflammatory mediators such as nitric oxide (NO) after stimulation of LPS. These models offer preliminary data on anti-inflammatory potential, allow identification of the most promising candidates for further mechanistic investigation, and elucidate the molecular pathways through which AgNPs may have anti-

inflammatory potential, thereby reducing the need for time-consuming and costly initial animal studies (Arulselvan et al., 2016).

The anti-inflammatory activity of the silver nanoparticles (AgNPs) synthesized from the methanol extract of *S. palghatense* bark was assessed using *in vitro* biochemical tests. The silver nanoparticles (AgNPs) with the highest level of effectiveness were found by estimating the percentage of inhibition.

7.2.9.4.1.1. Human Red Blood Cell (HRBC) membrane stabilization method

The anti-inflammatory potential of silver nanoparticles (AgNPs) synthesized from the methanolic extract of *S. palghatense* bark was evaluated using the *in vitro* HRBC membrane stabilization method. Fresh blood was drawn from healthy volunteers following ethical guidelines and mixed in an equal volume with Alsever's solution (containing 2% dextrose, 0.8% sodium citrate, 0.05% citric acid, and 0.42% sodium chloride) to inhibit coagulation. The mixture was centrifuged at 3000 rpm for 10 minutes, and the packed red blood cells were washed three times with isosaline (0.85%, pH 7.2). A 10% (v/v) HRBC suspension was prepared in isosaline.

Various concentrations of silver nanoparticles (AgNPs) (10, 20, 30, 40, 50, 60, 70, 80, 90, and 100 µg/mL) were added to equal volumes of the HRBC suspension and phosphate buffer (pH 7.4). The mixtures were incubated at 37°C for 30 minutes, followed by centrifugation at 3000 rpm for 10 minutes. The absorbance of the supernatant was measured at 560 nm using a spectrophotometer to determine the amount of haemoglobin released due to haemolysis. The percentage of membrane stabilization, indicative of anti-inflammatory activity, was calculated by comparing the absorbance of the test samples with that of a control containing distilled water (James et al., 2009).

7.2.9.4.1.2. Inhibition of protein denaturation

The ability of the silver nanoparticles (AgNPs) synthesized from the methanol extract of *S. palghatense* bark to prevent denaturation of proteins was evaluated according to the method described by Mizushima and Kobayashi (1968). The various AgNPs concentrations (62.5, 125, 250, and 500 µg/mL) were prepared from the stock

solution of 10 mg/mL DMSO. The reaction mixture (0.5 mL) consisted of the test sample and 1% aqueous bovine serum albumin solution. The control in this assay consisted of the reaction mixture with BSA and phosphate buffer subjected to the same incubation and heating conditions, but without the addition of either AgNPs or diclofenac sodium. The diclofenac sodium was used as the standard reference drug. The pH of each solution was adjusted to 6.3 using 1 N HCl. The AgNPs were incubated at 37^0C for 20 minutes and then heated at 57°C for 3 minutes to induce protein denaturation. After cooling, 2.5 mL of phosphate buffer was added to each tube. The turbidity was measured spectrophotometrically at 416 nm. The percentage inhibition of protein denaturation was calculated using the formula,

$$\text{Percentage inhibition} = \frac{(\text{Absorbance of control} - \text{Absorbance of sample})}{\text{Absorbance of Control}} \text{X100}$$

7.2.9.4.1.3. Proteinase inhibitory activity

Proteinase inhibitory activity is the capacity of a compound or extract to inhibit the work of proteases (enzymes that separate proteins into peptides or amino acids). This activity is vital in many biological functions such as inflammation, wound healing, and disease prevention where excess protease action can cause harm and lead to the development of something pathological like arthritis or cancer (Laskowski & Kato, 1980). Proteinase inhibitors can be applied therapeutically to combat situations where protease functionality is harmful. Molecules, such as protease inhibitors, play an essential role in HIV therapy by blocking viral proteases crucial for viral replication (Flexner, 1998).

Different concentrations of the AgNPs (62.5, 125, 250, and 500 µg/mL) were prepared from a stock solution of 10 mg/mL in DMSO to evaluate proteinase inhibitory activity. Diclofenac sodium served as the standard solution. The reaction mixture consisted of 1 mL of the test sample at various concentrations in phosphate buffer (pH 7.4). To this, 1 mL of Tris-HCl buffer (20 mM, pH 7.4) (Appendix 20) containing trypsin (0.06 mg) was added, and the mixture was incubated at 37°C for 5 minutes. Following incubation, 1 mL of 0.8% (w/v) casein was added as substrate, and the reaction mixture was incubated for an additional 20 minutes at 37°C. The

reaction was terminated by adding 2 mL of 70% perchloric acid, resulting in a cloudy suspension. This suspension was centrifuged at 3000 rpm for 10 minutes to remove the precipitated protein. The control in this proteinase inhibitory activity assay is the reaction mixture that includes trypsin enzyme and casein substrate, but does not contain any of the test compounds or inhibitors such as AgNPs or diclofenac sodium. The absorbance of the supernatant was measured spectrophotometrically at 280 nm against buffer as blank (Oyedepo & Femurewa, 1995). The percentage inhibition of proteinase activity was calculated using the formula:

$$\text{Percentage inhibition} = \frac{(\text{Absorbance of control} - \text{Absorbance of sample})}{\text{Absorbance of Control}} \text{X100}$$

7.2.9.4.2. Anti-inflammatory activity on RAW 264.7 macrophage cell line

The RAW 264.7 macrophage cells have been widely used to evaluate anti-inflammatory activity, giving insight into the mechanisms by which silver nanoparticles (AgNPs) synthesized from the methanol extract of *S. palghatense* bark modulate inflammatory responses. Derived from murine macrophages, this cell line represents an optimal model to study inflammatory processes since macrophages are pivotal in initiating and maintaining inflammation. The cells respond to lipopolysaccharide (LPS) stimulation by producing inflammatory mediators, including interleukins, TNF-α, iNOS, and COX-2, which allows researchers to study various aspects of inflammation and test potential anti-inflammatory compounds (Ghasemian et al., 2016).

The effect of the silver nanoparticles (AgNPs) synthesized from the methanol extract of *S. palghatense* bark on cyclooxygenase (COX) activity, lipoxygenase (LOX) activity, myeloperoxidase (MPO) activity, cellular nitrite level (NO), and inducible nitric oxide synthase (iNOS) activity was determined using standard protocols.

7.2.9.4.2.1. Cell culture

RAW 264.7 murine macrophage cells were obtained from the National Centre for Cell Sciences (NCCS), Pune, India. The cells were maintained in Dulbecco's Modified Eagle's Medium (DMEM) (Sigma Aldrich, USA) supplemented with 10% foetal bovine serum (FBS), 2 mM L-glutamine, 1.5 g/L sodium bicarbonate (Merck, Germany), and an antibiotic-antimycotic solution containing penicillin (100 U/mL), streptomycin (100 µg/mL), and amphotericin B (0.25 µg/mL). The cultures were maintained at 37°C in a humidified atmosphere with 5% CO_2 (NBS Eppendorf, Germany).

For experiments, cells were plated in 24-well plates and allowed to grow to 60-70% confluency. They were stimulated with lipopolysaccharide (LPS, 1 µg/mL) to produce an inflammatory response. After stimulation with LPS, the cells were treated with different concentrations (25, 50, 100 µg/mL) of silver nanoparticles (AgNPs) synthesized from the methanol extract of *S. palghatense* bark and incubated for 24 hours. Supernatants were collected from the culture after the incubation period for a nitrite assay, and the cells were lysed for anti-inflammatory assays such as assays to measure COX, LOX, MPO, and iNOS activity. Each of the experiments was performed six times.

7.2.9.4.2.2. Cyclooxygenase (COX) activity

The COX activity assay can be used to determine the inhibition of prostaglandin synthesis, which suggests potential anti-inflammatory effects of the silver nanoparticles (AgNPs) synthesized from the methanol extract of *S. palghatense* bark, like that of non-steroidal anti-inflammatory drugs. COX activity was measured using a modified method of Walker & Gierse (2010). 100 µL of cell lysate were mixed with Tris-HCl buffer (pH 8.0), 5 mM glutathione, and 5 mM haemoglobin and incubated at 25°C for 1 minute. Reaction was started by addition of 200 µM arachidonic acid. After incubation at 37°C for 20 minutes, the reaction was terminated by adding 200 µL of 10% trichloroacetic acid in 1 N hydrochloric acid. After centrifugation, 200 µL of 1% thiobarbiturate acid was added to the supernatant and boiled for 20 minutes. Indomethacin is used as a standard. The control is the reaction

mixture prepared under the same conditions but without the addition of the test inhibitor (silver nanoparticles or indomethacin). The control is the reaction mixture prepared under the same conditions but without the addition of the test inhibitor (silver nanoparticles or indomethacin). Following incubation and centrifugation (3 minutes at 3000 rpm), absorbance was determined at 632 nm with a spectrophotometer to measure COX activity.

Percentage inhibition of the enzyme was calculated as,

$$\text{Percentage inhibition} = \frac{(\text{Absorbance of control} - \text{Absorbance of sample})}{\text{Absorbance of Control}} X100$$

7.2.9.4.2.3. Lipoxygenase (LOX) activity

LOX activity assessment determines the extract's ability to inhibit the leukotriene production that mediates inflammatory and allergic reactions. LOX activity tested according to a modified method by Axelrod et al. (1981). The reaction mixture (2 mL) contained Tris-HCl buffer (pH 7.4), 50 µL of cell lysate, and 200 µL of sodium linoleate substrate. LOX activity was assessed spectrophotometrically by detecting the increase in absorbance at 234 nm, indicating the production of 5-hydroxyeicosatetraenoic acid (5-HETE). The standard used was Nordihydroguaiaretic acid (NDGA). The control is the reaction mixture prepared under the same conditions but without the addition of any inhibitor (such as Nordihydroguaiaretic acid, NDGA, or test samples like AgNPs). The percentage of inhibition of LOX activity was determined by using the following equation:

$$\text{Percentage inhibition} = \frac{(\text{Absorbance of control} - \text{Absorbance of sample})}{\text{Absorbance of Control}} X100$$

7.2.9.4.2.4. Myeloperoxidase (MPO) activity

Myeloperoxidase (MPO) activity, a measure of neutrophil function and an indicator of oxidative stress, was evaluated with the method of Bradley et al. (1982) after slight modification. The cell lysate was resuspended in a mixture of 50 mM potassium phosphate buffer (pH 6.0) and 0.57% hexadecyltrimethylammonium

bromide (HTAB) and homogenized. The homogenate was centrifuged at 2000 g for 30 minutes at 4 °C, and the supernatant was harvested for MPO activity analysis.

MPO activity was assessed by mixing 50 µL of the supernatant with 950 µL of 50 mM phosphate buffer (pH 6.0) consisting of 0.167 mg/mL guaiacol and 0.0005% hydrogen peroxide (H_2O_2). The increase in absorbance at 460 nm was recorded spectrophotometrically over 3 minutes at 25 °C. MPO activity was measured using the molar extinction coefficient of guaiacol (26.6 $mM^{-1}cm^{-1}$) and expressed as units/mg protein. Control is the blank reaction mixture without MPO enzyme. The standard used in myeloperoxidase (MPO) activity assays is typically purified Myeloperoxidase enzyme. One unit of MPO activity was defined as the quantity of enzyme catalyzing the oxidation of 1 µmol guaiacol per minute at 25°C. Protein concentration in the supernatant was measured using the Bradford method, with bovine serum albumin as the standard (Bradford, 1976).

$$\text{MPO Activity}\left(\text{U / mL}\right) = \frac{\Delta\text{OD} \times \text{Vt} \times \text{dilution factor}}{\text{L} \times \varepsilon \times \Delta\text{t} \times \text{Vs}}$$

Where:

ΔOD = change in absorbance at 460 nm, Vt = total volume of reaction mixture (mL), L = path length of the cuvette (1 cm), ε = molar extinction coefficient of guaiacol (26.6 $mM^{-1}\cdot cm^{-1}$), Δt = time of reaction in minutes, Vs = volume of sample (mL)

One unit of MPO is defined as the amount of enzyme that catalyses the oxidation of 1 µmol of guaiacol per minute at 25 °C.

7.2.9.4.2.5. Inducible Nitric Oxide Synthase (iNOS) activity

Inducible Nitric Oxide Synthase (iNOS) activity was assessed to evaluate the silver nanoparticles (AgNPs) synthesized from the methanol extract of *S. palghatense* bark effect on nitric oxide (NO) production, a key inflammatory mediator, using the method described by Salter et al. (2016). The cell lysate was homogenized in 2 mL of HEPES buffer (pH 7.4) (Appendix 21). The reaction mixture (1 mL) contained L-Arginine (2 µM), manganese chloride (4 µM), dithiothreitol, DDT (10 mM), NADPH

(1 mM), tetrahydrobiopterin (4 µM), oxygenated haemoglobin (10 µM), and 0.1 mL of the cell lysate as the enzyme source. The reaction was initiated by adding the cell lysate, and the increase in absorbance at 401 nm was monitored spectrophotometrically at 37°C for 3 minutes. iNOS activity was calculated using the molar extinction coefficient of oxyhaemoglobin (77,000 $M^{-1}cm^{-1}$) and expressed as nmol/min/mg protein. Recombinant or purified Inducible Nitric Oxide Synthase (iNOS) enzyme serves as a positive standard to calibrate and quantify enzyme activity in the assay. Negative control is a Reaction mixture without cell lysate or heat-inactivated lysate to measure background absorbance. LPS (Lipopolysaccharide) is used in iNOS studies because it stimulates the immune cells to produce inducible nitric oxide synthase (iNOS). Protein concentration in the enzyme source was determined using the Bradford method. This assay provides insights into the extract's potential to modulate iNOS activity and reduce nitric oxide (NO) production, which is critical in inflammatory responses.

$$\text{Percentage inhibition} = \frac{(\text{Absorbance of control} - \text{Absorbance of sample})}{\text{Absorbance of Control}} \text{X100}$$

7.2.9.4.2.6. Estimation of cellular nitrite levels

As an indirect marker of nitric oxide (NO) production, cellular nitrite levels were estimated to assess the effect of silver nanoparticles (AgNPs) synthesized from the methanol extract of *S. palghatense* bark on inflammatory pathways. The assay was based on the method of Lepoivre et al. (2019), with minor changes. A 0.5 mL aliquot of the cell lysate was deproteinized by adding 0.1 mL of 3% sulfosalicylic acid, vortexing for 30 minutes. The mixture was centrifuged at 5,000 rpm for 15 minutes at 4°C, and the protein-free supernatant (200 µL) was mixed with 30 µL of 10% NaOH and 300 µL of Tris-HCl buffer (pH 7.4). 530 µL of Griess reagent (Appendix 22) (1% sulphanilamide, 0.1% N-1-naphthyl ethylene diamine dihydrochloride in 2% phosphoric acid) was added. For 15 minutes, the reaction mixture was incubated in the dark at room temperature. The absorbance was read spectrophotometrically at 540 nm versus a Griess reagent blank. Sodium nitrite solutions (0-100 µM) generated a standard curve. Nitrite concentrations in samples were measured by interpolation from the standard curve. Control is the baseline cell

lysate without LPS or treatment to represent normal nitrite levels. LPS is used in cellular nitrate level studies because it stimulates immune cells to produce nitric oxide (NO), which quickly converts to nitrate and nitrite in the body, allowing for measurement of inflammation and immune response levels. In other words, LPS induces the production of nitrate as a marker of nitric oxide generation during inflammation. Results were presented as μmol nitrite per μg protein. Protein concentration was measured using the Bradford method (Bradford, 1976). Combined with the iNOS activity assessment, these assays offered a broad overview of the extract's potential to modulate nitric oxide (NO) production and its implicating anti-inflammatory effects at the cellular and molecular levels.

7.2.9.5. Histopathology and wound healing studies of *S. palghatense* silver nanoparticles (AgNPs)

Inflammation constitutes a critical early phase in fish wound healing, orchestrating immune responses essential for tissue repair and regeneration. Upon injury, immune cells such as neutrophils are rapidly recruited to the wound site, releasing pro-inflammatory cytokines including tumour necrosis factor-alpha (TNF-α) and interleukin-1 beta (IL-1β), which facilitate clearance of debris and infection control (Chablais & Jazwinska, 2016). Macrophages follow, producing cytokines like interleukin-6 (IL-6) and interleukin-12 that further modulate inflammation and initiate tissue remodelling (Richardson et al., 2013). Adaptive immune cells, including T- and B-lymphocytes, contribute through cytokine release and antibody production, respectively, enhancing the immune defense during regeneration (Renshaw et al., 2006). Anti-inflammatory cytokines such as interleukin-10 (IL-10) and transforming growth factor-beta (TGF-β) subsequently act to resolve inflammation, promoting tissue regeneration and remodelling (Shaw & Martin, 2009). Zebrafish serve as an excellent vertebrate model for studying these processes due to their conserved immune pathways and rapid regenerative capacity, with inflammation tightly coordinated with re-epithelialization, granulation tissue formation, and neovascularization (Lisse et al., 2016; Renshaw & Trede, 2012).

Adult zebrafish (*Danio rerio*, AB strain, 3–6 months old) were obtained from local suppliers and acclimatized in laboratory aquaria for 15 days under standard conditions (28–33 °C, 14 hours light/10 hours dark cycle). The caudal fins of the fish were amputated using a sterile scalpel, making a precise cut parallel to the dorsal and ventral fin axes. Following amputation, the fish were allocated into two groups: Group 1 (control) was provided normal fish feed, while Group 2 (treated) received normal feed supplemented with synthesized nanoparticles at a concentration of 1 mg/mL in the tank water.

Fish were observed over a period of 15 days, with regenerative growth monitored and documented at six time points: 0, 3, 6, 9, 12, and 15 days post-amputation. Anaesthesia was administered using 0.016% tricaine methane sulfonate prior to imaging and sample collection. Regenerating caudal fins were imaged using a Leica M205C stereomicroscope, and fin area measurements were obtained by analyzing images with ImageJ software following manufacturer guidelines.

The regeneration efficiency (%) was calculated by using the following formula, Regeneration efficiency (%) = (Regenerated fin area/Fin area at control) x 100. The experiments were done in six times, and the data were represented as mean ± standard error.

Selected regenerated fin tissues were fixed in 4% paraformaldehyde, embedded in paraffin, sectioned, and stained with Haematoxylin and Eosin (H&E) to assess histological features corresponding to tissue repair and regeneration (Ganesh et al., 2025).

7.2.9.6. Anti-diabetic activity of *S. palghatense* bark silver nanoparticles (AgNPs)

The anti-diabetic potential of silver nanoparticles (AgNPs) was evaluated using α-amylase and α-glucosidase inhibitory assays, following standard protocols with minor modifications.

7.2.9.6.1. α-Amylase inhibition

The α-amylase inhibitory activity of silver nanoparticles (AgNPs) synthesized from *S. palghatense* bark was assessed using a modified 3,5-dinitrosalicylic acid (DNS) method. Initially, a 1% starch solution and phosphate buffer were prepared. The enzymatic reaction was started by incubating 500 µL of α-amylase with varying concentrations of AgNPs (20–100 µg/mL) at 37 °C for 10 minutes, followed by the addition of starch solution. The reaction was stopped by adding 2 M NaOH, then 1 mL of DNS reagent was added, and the mixture was heated in a water bath for 5 minutes to develop colour. After cooling and diluting the mixture to 10 mL with distilled water, the absorbance was measured at 540 nm. Acarbose was used as a reference standard. In this assay, the control refers to the reaction mixture where the α-amylase enzyme and starch substrate are incubated without the silver nanoparticles (AgNPs) or any inhibitor (Ali et al., 2016). The percentage inhibition was calculated by comparing the absorbance of the test samples to the control using the formula:

Percentage Inhibition = [(A control – A sample)/A control] × 100.

Where A = absorbance.

7.2.9.6.2. α-Glucosidase inhibition assay

The α-glucosidase inhibitory activity of AgNPs from *S. palghatense* bark was determined by incubating varying concentrations of the nanoparticles (20–100 µg/mL) with a reaction mixture containing phosphate buffer and the substrate p-nitrophenyl-α-D-glucopyranoside (p-NPG). After an initial incubation at 37 °C for 5 minutes, α-glucosidase enzyme was added, and the mixture was further incubated for 15 minutes. The reaction was terminated by adding 200 mM sodium carbonate, and the absorbance was measured at 405 nm. Acarbose served as the reference standard. In this αassay, the control is the reaction mixture containing the α-glucosidase enzyme and the substrate p-nitrophenyl-α-D-glucopyranoside (p-NPG) without the silver nanoparticles (AgNPs) or any inhibitor (Tadera et al., 2006). The percentage of enzyme inhibition was calculated using the following formula:

Percentage Inhibition = [(A control – A sample)/A control] × 100.

Where A = absorbance.

7.2.9.6.3. Determination of *in vitro* glucose uptake assay

L6 rat myoblast cells (National Centre for Cell Sciences, Pune, India) were cultured in Dulbecco's Modified Eagle's Medium (DMEM; Sigma Aldrich, USA) supplemented with 10% fetal bovine serum (FBS), L-glutamine, sodium bicarbonate (Merck, Germany), and an antibiotic solution containing penicillin (100 U/mL), streptomycin (100 µg/mL), and amphotericin B (2.5 µg/mL). Cells were maintained in a humidified incubator at 37°C with 5% CO_2. The cells were trypsinized using 0.025% trypsin in phosphate-buffered saline (PBS) with 0.5 mM EDTA (Invitrogen) for 2 minutes under aseptic conditions and seeded into 24-well plates. Upon reaching 80% confluency, the cells were starved in glucose-free DMEM (Appendix 23) for 24 hours (Zhang et al., 2018; Zhou et al., 2017).

Subsequently, silver nanoparticles synthesized from the methanolic extract of *S. palghatense* bark were added to the cells at final concentrations of 25, 50, and 100 µg/mL, prepared from a 1 mg/mL stock solution. Cells were then incubated in DMEM containing 300 mM glucose for 24 hours. A high-glucose untreated control group was maintained under identical conditions. Pioglitazone is used as a standard. After incubation, cells were harvested by centrifugation at 6000 rpm for 10 minutes, and the supernatant was discarded. Cell lysis was performed by adding 200 µL of lysis buffer containing 1 M Tris-HCl, 0.25 M EDTA, 2 M NaCl, and 0.5% Triton X-100, followed by incubation at 4°C for 30 minutes.

Glucose uptake was quantified using a high-sensitivity glucose oxidase assay kit (Coral Clinical Systems, Lot No. RGLU1091), following the manufacturer's protocol. The total glucose concentration was determined spectrophotometrically, and the percentage of glucose uptake was calculated using the formula:

$$\text{Total Glucose}\left(\text{mg / dL}\right) = \frac{\text{Absorbance of Test}}{\text{Absorbance of standard}} \times 100$$

Percentage glucose uptake:

$$\frac{(\text{Glucose concentration in control}) - (\text{Glucose concentration in sample})}{(\text{Glucose concentration in control})} \times 100$$

This method effectively evaluates the potential of AgNPs derived from *S. palghatense* bark to enhance cellular glucose uptake, contributing to the understanding of their anti-diabetic effects.

7.2.9.6.4. Endogenous inhibition of glucose production in the liver

HepG2 liver hepatic cells were procured from NCCS Pune and cultured in Dulbecco's Modified Eagle's Medium (DMEM, Sigma Aldrich) supplemented with 10% fetal bovine serum (FBS, Invitrogen). Cells were maintained at 37°C in a humidified atmosphere with 5% CO_2 until confluent. For subculturing, cells were trypsinized using 500 µL of 0.025% trypsin in PBS containing 0.5 mM EDTA (Gibco, Invitrogen) for 2 minutes under sterile conditions and seeded into T-flasks. Subsequently, cells were transferred to 24-well plates for experimental treatment (Zhou et al., 2001).

Once cultures reached approximately 80% confluency, the cells were washed and incubated in glucose-free DMEM containing AgNPs synthesized from the methanol extract of *S. palghatense* bark at final concentrations of 25 µg/mL, 50 µg/mL, and 100 µg/mL, prepared from a 1 mg/mL stock solution. This treatment was administered for 30 minutes prior to incubation with 100 nM glucagon to induce glucose production. After 6 hours of incubation under these conditions, both treated and untreated control cells (without glucose in the media) were collected by centrifugation at 6000 rpm for 10 minutes. The supernatant was discarded, and 200 µL of cell lysis buffer (composition: 1 M Tris HCl, 0.25 M EDTA, 2 M NaCl, 0.5% Triton) was added to lyse the cells. The lysate was incubated at 4°C for 30 minutes to ensure complete lysis.

The glucose content in the cell lysate was then quantified using a commercial glucose estimation kit (Erba Mannheim, Germany) by measuring the absorbance at

505 nm with a microplate reader (Agilent, USA). All experimental procedures were performed in six times, and the mean values were used for further analysis.

The total glucose concentration (mg/dL) in each sample was calculated using the formula:

$$\text{Total Glucose}\left(\text{mg / dL}\right) = \frac{\text{Absorbance of Test}}{\text{Absorbance of standard}} \times 100$$

Percentage glucose uptake:

$$\frac{\left(\text{Glucose concentration in control}\right) - \left(\text{Glucose concentration in sample}\right)}{\left(\text{Glucose concentration in control}\right)} \times 100$$

7.2.9.6.5. Determination of effects of AgNPs synthesized from the methanol extract of *S. palghatense* bark on gene expression in HepG2 cells by Real-Time PCR analysis

7.2.9.6.5.1. Cell culture and treatment

HepG2 cells (a hepatocellular carcinoma cell line) were cultured according to standard cell culture protocols. Cells were seeded at a density of 1×10^5 cells per well in 24-well culture plates. Upon reaching confluency, cells were washed and incubated in glucose-free DMEM medium containing synthesized AgNPs derived from the methanol extract of *S. palghatense* bark at a concentration of 100 µg/mL. Metformin (32.06 µg/mL) was used as the standard reference control. Following a 30-minute pre-treatment, cells were stimulated with 100 nM glucagon and maintained at 37°C in a humidified atmosphere with 5% CO_2 for 24 hours. Parallel cultures treated with glucose-free DMEM alone and untreated cells served as controls.

7.2.9.6.5.2. Total RNA isolation by TRIzol method

Total RNA was isolated from treated and control HepG2 cells using the TRIzol reagent according to the manufacturer's instructions (Invitrogen, Product code 10296010). 1 mL of TRIzol reagent was added directly to the cell culture wells and incubated for 5 minutes at room temperature to lyse the cells and release RNA. The lysate was transferred to RNase-free microcentrifuge tubes, followed by the addition

of 200 µL chloroform. After thorough mixing and incubation at room temperature, samples were centrifuged at 14,000 rpm for 15 minutes at 4°C. The aqueous phase containing RNA was carefully collected, and RNA was precipitated by adding 500 µL of isopropanol, followed by incubation at room temperature for 10 minutes. Samples were centrifuged again at 14,000 rpm for 15 minutes at 4°C to pellet the RNA. The RNA pellet was washed with 200 µL of 75% ethanol, centrifuged at 14,000 rpm for 5 minutes at 4°C, air-dried, and resuspended in Tris-EDTA buffer (TE) for downstream applications (Appendix 24).

7.2.9.6.5.3. cDNA synthesis

Complementary DNA (cDNA) synthesis was performed using the iScript cDNA synthesis kit (Biorad, Cat# 1708891). A reaction mix containing 4 µL of 5x iScript reaction mix, 1 µL of iScript reverse transcriptase, and 0.5 µg of total RNA template was prepared in RNase-free tubes. The final volume was adjusted to 20 µL with nuclease-free water. The reaction was gently mixed and incubated in a thermal cycler with the following program: priming at 25°C for 5 minutes, reverse transcription at 46°C for 20 minutes, and enzyme inactivation at 95°C for 1 minute (Table 7.4).

Table 7.4: Thermal cycler conditions for cDNA synthesis

Step	Temperature °C	Time (minutes)	Number of cycles
Priming	25	5	1
cDNA synthesis	46	20	1
Inactivation	95	1	1

7.2.9.6.5.4. Real-Time Quantitative PCR (RT-qPCR) Amplification

Gene expression analysis was conducted using SYBR Green Master Mix (G BIOSCIENCES, Product code 786-5062) (Appendix 25) on a LightCycler 96 instrument (Roche). Each sample was analyzed in six times. Amplification was performed with an initial denaturation at 95°C for 2 minutes followed by 40 cycles of denaturation at 95°C for 10 seconds, annealing at 57°C for 1 minute, and extension at 72°C (1 minute per kb of amplicon size). After amplification, samples were held at 4°C indefinitely (Table 7.5). Data were analyzed using the ΔΔCt method with LightCycler 96 software version 1.1.

Table 7.5: Thermal cycling parameters for Real-Time PCR amplification

Steps	Time required	Temperature
Initial activation step	2 minutes	95°C
3-step cycling		
Denaturation	10 seconds	95°C
Annealing	1 minutes	57°C
Extension	1 min/kb	72°C
Number of cycles	40 cycles	
End of PCR cycling	Indefinite	4°C

7.2.9.6.5.5. Primers used for RT-qPCR

Primers targeting PGC-1α (Peroxisome Proliferator-Activated Receptor Gamma Coactivator 1-Alpha) and GAPDH (Glyceraldehyde 3-Phosphate Dehydrogenase) were designed (Table 7.6) as shown below: Tm means melting temperature.

Table 7.6: Primer sequences and melting temperatures for RT-qPCR

OLIGO name	FORWARD		REVERSE	
	SEQUENCE (5' ->3')	Tm	SEQUENCE (5' ->3')	Tm
PGC-1α	TAAACTGAGCTACCCTTGGG	57.3	CTCGACACGGAGAGTTAAAGGAA	60.6
GAPDH	ACTCAGAAGACTGTGGATGG	57.3	GTCATCATACTTGGCAGGTT	55.3

7.2.9.6.5.6. Agarose Gel Electrophoresis for PCR product verification

PCR products were verified by electrophoresis on a 1.5% agarose gel prepared in 1x TE buffer. Agarose was melted in a water bath at 90°C, cooled to approximately 45°C, and stained with ethidium bromide (10 mg/mL, 6 µL per gel). Gels were cast with combs for sample wells. The samples (PCR products) were loaded and electrophoresed at 50 V for 30 minutes in 1x TAE buffer. The gel was visualized using a ChemiDoc imaging system (Biorad) to confirm the expected amplicon size (Wittwer et al., 2003).

7.2.9.6.6. Effect of AgNPs synthesized from the methanol extract of *S. palghatense* bark on insulin secretion in pancreatic cells

7.2.9.6.6.1. Cell culture

Pancreatic β-cell line INS-1 (Insulinoma-1), which is a rat pancreatic β-cell line commonly used to study insulin secretion, was cultured in RPMI-1640 medium supplemented with 10% fetal bovine serum (FBS), 1% penicillin-streptomycin, and 50 μM β-mercaptoethanol at 37°C in a humidified 5% CO_2 incubator.

7.2.9.6.6.2. Treatment

Cells were seeded in 24-well plates at a density of 1 × 10^5 cells/well and allowed to adhere overnight. The cells were then treated with the test samples at concentrations of 10, 50, and 100 μg/mL for 24 hours. A positive control group was treated with 100 μM metformin. Untreated cells served as the negative control.

7.2.9.6.6.3. Glucose stimulation and insulin secretion assay

After treatment, cells were washed with Krebs-Ringer bicarbonate buffer containing low glucose (2.8 mM) and pre-incubated for 1 hour. Subsequently, cells were incubated in buffer containing high glucose (16.7 mM) for 1 hour to stimulate insulin secretion.

The culture supernatants were collected, and insulin levels were quantified using a commercially available rat/mouse insulin ELISA kit following the manufacturer's instructions (Lenzen, 2008).

7.2.9.7. Anticancer activity of *S. palghatense* bark silver nanoparticles (AgNPs)

The anticancer potential of silver nanoparticles (AgNPs) was evaluated using *in vitro* cytotoxicity by the trypan blue exclusion method, MTT (3-(4,5-dimethylthiazol-2-yl)-2,5-diphenyltetrazolium bromide), and XTT assays, following standard protocols with minor modifications.

At a concentration of 100 μg/mL, AgNPs synthesized from *S. palghatense* bark induced substantial cytotoxicity in DLA cells, as evidenced by a high percentage

of cell death observed using the trypan blue exclusion method. This pronounced cytotoxic effect suggests that these AgNPs exhibit strong antitumor activity against DLA tumour cells.

7.2.9.7.1. Cytotoxicity evaluation of *S. palghatense* bark silver nanoparticles (AgNPs) using the Trypan Blue Exclusion method

The cytotoxicity of silver nanoparticles (AgNPs) synthesized from *S. palghatense* bark was evaluated using the trypan blue exclusion method. Dalton's Lymphoma Ascites (DLA) cells were isolated from the peritoneal cavity of mice and suspended in PBS (pH 7.4). After repeated centrifugation and washing, the cell suspension was incubated with various concentrations of AgNPs samples at 37°C for 3 hours. Following incubation, trypan blue dye was added, and both viable (unstained) and dead (blue-stained) cells were counted using a hemacytometer. The percentage of cell death was calculated as the ratio of dead cells to the total number of cells (viable plus dead), multiplied by 100. This method provided a quantitative assessment of cytotoxic effects induced by the AgNPs on DLA cells (Hussein & Mohsin, 2019).

$$\text{Percentage cell death} = \frac{\text{Number of dead cells}}{\left(\text{Number of viable cells} + \text{Number of dead cells}\right)} \text{ x } 100$$

7.2.9.7.2. MTT (3-(4,5-dimethylthiazol-2-yl)-2,5-diphenyltetrazolium bromide) assay

MCF-7(Human Breast Cancer) cell line was initially procured from National Centre for Cell Sciences (NCCS), Pune, India, and maintained in Dulbecco's modified Eagle's medium, DMEM (Sigma Aldrich, USA).

The cell line was cultured in a 25 cm^2 tissue culture flask with DMEM supplemented with 10% FBS, L-glutamine, sodium bicarbonate (Merck, Germany), and antibiotic solution containing: Penicillin (100U/ml), Streptomycin (100µg/ml), and Amphotericin B (2.5µg/ml). Cultured cell lines were maintained at 37 °C in a humidified 5% CO_2 incubator (NBS Eppendorf, Germany).

The viability of cells was evaluated by direct observation of cells using an Inverted phase contrast microscope, followed by the MTT assay method.

7.2.9.7.2.1. Cells seeding in 96 well plate

Two days old confluent monolayer of cells was trypsinized, and the cells were suspended in 10% growth medium. 100 µL cell suspension ($5x10^3$ cells/well) was seeded in 96 well tissue culture plate and incubated at 37ºC in a humidified 5% CO_2 incubator.

7.2.9.7.2.2. Preparation of stock

1mg of sample was weighed and dissolved in 1 mL of 0.1% DMSO using a cyclomixer. The sample solution was filtered through a 0.22 µM Millipore syringe filter to ensure sterility. Cisplatin was used as a standard drug in the MTT assay.

7.2.9.7.2.3. Anticancer evaluation

After 24 hours, the growth medium was removed, and freshly prepared silver nanoparticles (AgNPs) synthesized from the methanol extract of *S. palghatense* bark were added at concentrations of 100 µg/ml, 50 µg/ml, 25 µg/ml, 12.5 µg/ml, and 6.25 µg/ml of DMEM. Each concentration was added in six times to the respective wells and incubated at 37ºC in a humidified 5% CO_2 incubator. Untreated control cells were also maintained.

7.2.9.7.2.4. Anticancer assay by direct microscopic observation

The entire plate was observed after 24 hours of treatment in an inverted phase contrast tissue culture microscope (Olympus CKX41 with Optika Pro5 CCD camera), and microscopic observations were recorded as images. Any detectable changes in the morphology of the cells, such as rounding or shrinking of cells, granulation, and vacuolization in the cytoplasm of the cells, were considered as indicators of cytotoxicity.

7.2.9.7.2.5. Anticancer assay by MTT method

15 mg of MTT (Sigma, M-5655) was reconstituted in 3 ml PBS until completely dissolved and sterilized by filter sterilization.

After 24 hours of incubation period, the sample content in wells were removed and 30 µL of reconstituted MTT solution was added to all test and cell control wells. The plate was gently shaken well, then incubated at 37ºC in a humidified 5% CO_2 incubator for 4 hours. After the incubation period, the supernatant was removed and 100 µL of MTT Solubilization Solution (Dimethyl sulphoxide, DMSO, Sigma Aldrich, USA) was added, and the wells were mixed gently by pipetting up and down in order to solubilize the formazan crystals. The absorbance values were measured by using a microplate reader at a wavelength of 540 nm (Mosmann, 1983).

The percentage of growth inhibition was calculated using the formula:

$$\text{Percentage of viability} = \frac{\text{Mean OD Samples}}{\text{Mean OD of the control group}} \times 100$$

7.2.9.7.3. XTT assay

In the XTT 2,3-Bis(2-methoxy-4-nitro-5-sulfophenyl)-2H-tetrazolium-5-carboxanilide assay, Caco-2 (Human Colon Cancer) cells and MCF-7 (Human Breast Cancer) were initially procured from the National Centre for Cell Sciences (NCCS), Pune, India, and maintained in Dulbecco's modified Eagle's medium, DMEM (Sigma Aldrich, USA). The cell line was cultured in a 25 cm^2 tissue culture flask with DMEM supplemented with 10% FBS, L-glutamine, sodium bicarbonate (Merck, Germany), and antibiotic solution containing: Penicillin (100 U/mL), Streptomycin (100 µg/mL), and Amphotericin B (2.5µg/mL). Cultured cell lines were kept at 37ºC in a humidified 5% CO_2 incubator (NBS Eppendorf, Germany).

The viability of cells was evaluated by direct observation of cells using an Inverted phase contrast microscope and followed by the MTT assay method.

7.2.9.7.3.1. Cells seeding in 96 well plate

Two-day-old confluent monolayer of cells were trypsinized and the cells were suspended in 10% growth medium. 100 µL cell suspension ($5x10^3$ cells/well) was seeded in 96 well tissue culture plate and incubated at 37ºC in a humidified 5% CO_2 incubator.

7.2.9.7.3.2. Preparation of stock

1mg of sample was weighed and dissolved in 1mL DMEM using a cyclomixer. The sample solution was filtered through a 0.22 µm Millipore syringe filter to ensure sterility.

7.2.9.7.3.3. Anticancer evaluation

After 24 hours, the growth medium was removed, and freshly prepared samples were added at concentrations of 100 µg/mL, 50 µg/mL, 25 µg/mL, 12.5 µg/mL, and 6.25 µg/mL in DMEM. Each concentration was added in six times to the respective wells and incubated at 37°C in a humidified 5% CO_2 incubator. Untreated control cells were also maintained.

7.2.9.7.3.4. Anticancer assay by direct microscopic observation

The entire plate was observed after 24 hours of treatment in an inverted phase contrast tissue culture microscope (Olympus CKX41 with Optika Pro5 CCD camera), and microscopic observations were recorded as images. Any detectable changes in the morphology of the cells, such as rounding or shrinking of cells, granulation, and vacuolization in the cytoplasm of the cells, were considered as indicators of cytotoxicity.

7.2.9.7.3.5. Anticancer assay by XTT method

The PMS solution (Phenazine Methosulfate) was prepared by dissolving 3 mg of PMS in 1 mL of 1× PBS. The XTT solution was then prepared by dissolving 4 mg of XTT in 4 mL of cell culture medium. 10 µL of the PMS solution was added to 4 mL of XTT to create the detection solution. Immediately, 50 µL of the detection

solution prepared in the previous step was added to each well. Incubated for 2-5 hours at 37°C. The reaction is mixed on a shaker for a short period to incorporate the dye into the solution. The absorbance was measured at 450 nm (Huyck et al., 2012).

The percentage of growth inhibition was calculated using the formula:

$$\text{Percentage of viability} = \frac{\text{Mean OD samples}}{\text{Mean OD of the control group}} \times 100$$

7.2.9.7.4. Protein estimation by the Bradford method

The protein in solution can be measured quantitatively by different methods. The method described by Bradford uses the capacity of protein to bind a dye quantitatively. The method is simple, rapid, and inexpensive.

The assay is based on the ability of proteins to bind Coomassie brilliant blue G250 and form a complex whose extinction coefficient is significantly greater than that of the free dye.

7.2.9.7.4.1. Procedure

100 µL of the silver nanoparticles (AgNPs) synthesized from the methanol extract of *S. palghatense* bark were mixed with 5 mL of diluted Bradford dye. It was mixed well and allowed the colour to develop for at least 5 minutes but no longer than 30 minutes. Absorbance was read at 595nm (UV-VIS Spectrophotometer-SHIMADZU-UV-1900i) after incubation. A standard graph was plotted, and the protein concentration was determined using the standard curve. Bovine serum albumin was used as the standard (Bradford, 1976).

7.2.9.7.5. Apoptosis FACS (Fluorescence-Activated Cell Sorting)/Annexin V apoptosis assay by flow cytometry

Apoptosis, or programmed cell death, is an important and actively regulated pathway that controls cell growth and proliferation. Cells respond to specific induction signals by initiating intracellular processes resulting in characteristic physiological changes. These include the externalization of phosphatidylserine (PS)

to the outer surface of the cell membrane, cleavage and degradation of specific cellular proteins, compaction and fragmentation of nuclear chromatin, and, in later stages, loss of membrane integrity. Annexin V is a calcium-dependent phospholipid-binding protein with a high affinity for PS, which is normally localized to the inner leaflet of the cell membrane. Early in the apoptotic pathway, PS molecules are translocated to the outer surface of the cell membrane, where Annexin V can readily bind to them (Elmore et al., 2007).

The Muse™ Annexin V and Dead Cell Assay utilize Annexin V to detect phosphatidylserine (PS) on the external membrane of apoptotic cells. A dead cell marker, such as propidium iodide (PI), is also used to indicate loss of cell membrane integrity. This marker is excluded from live, healthy cells and early apoptotic cells but penetrates late apoptotic and dead cells. Four populations of cells can be distinguished in this assay: non-apoptotic cells (Annexin V negative, PI negative), early apoptotic cells (Annexin V positive, PI negative), late-stage apoptotic and dead cells (Annexin V positive, PI positive), and mostly nuclear debris (Annexin V negative, PI positive) (Vermes et al., 1995).

7.2.9.7.5.1. Procedure

MCF-7 (Human Breast Cancer) cell line was cultured as per standard procedures and treated with LD (Lethal Dose) 50 concentration of the sample: 105.623 µg/ml and incubated for 24 hours. Non-treated controls were also maintained and then incubated at 37 °C in a humidified 5% CO_2 incubator for 24 hours.

The cell sample was transferred to a 12 × 75 mm polystyrene tube. The minimum recommended number of cells for fixation in a tube is 1×10^6 cells. The sample, silver nanoparticles (AgNPs) synthesized from the methanol extract of *S. palghatense* bark, were then centrifuged at 3000 rpm for 5minutes. The supernatant was removed without disturbing the pellet. After centrifugation, the cell pellet forms either a visible pellet or a white film on the bottom of the tube.

To each tube, added 100 µL of the Muse™ Annexin V and Dead Cell Reagent. The tubes were mixed thoroughly by pipetting up and down or vortexing at a medium

speed for 3 to 5 seconds, followed by incubation for 20 minutes at room temperature in the dark. The cells were analyzed using a flow cytometer and processed with Muse flow cytometry software. Cells were gated against untreated control cells and analyzed for apoptosis using Muse FCS 3.0 software (Vermes et al., 1995).

7.2.9.7.6. Indirect ELISA (Enzyme-Linked Immunosorbent Assay)

MCF-7 cells were initially procured from the National Centre for Cell Sciences (NCCS), Pune, India, and maintained in Dulbecco's modified Eagle's medium, DMEM (Sigma Aldrich, USA).

The cell line was cultured in a 25 cm^2 tissue culture flask with DMEM supplemented with 10% FBS (Fetal Bovine Serum), L-glutamine, sodium bicarbonate (Merck, Germany), and antibiotic solution containing: Penicillin (100 U/mL), Streptomycin (100 µg/mL), and Amphotericin B (2.5 µg/mL). Cultured cell lines were maintained at 37 °C in a humidified 5% CO_2 incubator (NBS Eppendorf, Germany).

The cells were grown to 60% confluency, followed by activation with 1 µL of Lipopolysaccharides (LPS: 1 µg/mL). LPS-stimulated cells were exposed to the sample (Sample-105.623 µg/ml, Cisplatin–9.832 µg/ml) from a stock of 1 mg/mL and incubated for 24 hours at 37ºC in a humidified 5% CO_2 incubator. Non-treated control cells were also maintained.

After incubation, the supernatant was collected, and 100 µL of each was added to the 96-well plate and kept in incubation at 37°C overnight. The following day, the wells were drained and washed with PBS twice. 200 µL of freshly prepared blocking buffer (0.2% gelatin in 0.05% Tween 20 in PBS) was added and incubated for 1 hour at room temperature. It was washed twice with PBS-Tween. 100 µL of primary antibody, Caspase-9 (Santa Cruz, USA), Cysteine-Aspartic Protease 9, an initiator caspase enzyme involved in apoptosis, was added to each well and incubated for 2 hours at room temperature. After incubation, it was washed twice with PBS-Tween. 100 µL of secondary antibody (HRP Conjugate, Santa Cruz, USA) was added and incubated for 1 hour at room temperature. It was then washed twice with PBS-Tween. 200 µL of O-dianisidine hydrochloride (1 mg/100 mL methanol + 21 mL citrate

buffer, pH 5 + 60 mL H2O2; Sigma Aldrich, USA) was added and incubated for 30 minutes at room temperature. The reaction was stopped by adding 50 µL of 5N HCl. OD was read at 415 nm in an ELISA reader. The concentration of protein was also estimated. It was calculated using the following formula (Surendran et al., 2023):

Activity of Antibody = OD Value / Protein Concentration.

7.2.9.7.7. Analysis of DNA content and cell cycle distribution using the cell cycle kit by flow cytometry

Monitoring a cell's ability to proliferate is critical for assessing a cell's health during toxicity studies. The most accurate method of doing this is by directly measuring DNA synthesis. The basic principle of the MUSE cell cycle kit (ready-to-use flow cytometry kit) is a standard ethanol fixation and detergent permeabilization, which is sufficient to gain access to the DNA during the active cell cycle. The kit utilizes a premixed reagent which includes the nuclear DNA intercalating stain propidium iodide (PI), which discriminates cells at different stages of the cell cycle based on the differential DNA content in the presence of RNAase to increase the specificity of DNA staining in each phase (G_0/G_1, S, and G_2/M).

MCF-7 (Human Breast Cancer) cell line was cultured as per standard procedures described earlier and treated with LD 50 concentration of Cisplatin: 9.832 µg/ml and incubated for 24 hours. Non-treated controls were also maintained and then incubated at 37ºC in a humidified 5% CO_2 incubator for 24 hours.

The cell sample was transferred to a 12 × 75 mm polystyrene tube. The minimum recommended number of cells for fixation in a tube is 1×10^6 cells. The samples were then centrifuged at 3000 rpm for 5minutes. The supernatant was removed without disturbing the pellet. After centrifugation, the cell pellet forms either a visible pellet or a white film on the bottom of the tube.

An appropriate volume of PBS (Phosphate Buffered Saline) was added to each tube (i.e., 1 mL of PBS per 1×10^6 cells), and the contents were mixed by pipetting several times or gently vortexing. The cells were centrifuged at 3000 rpm for 5 minutes. The supernatant was discarded without disturbing the cell pellet, leaving

approximately 50 µL of PBS per 1 × 10^6 cells. Resuspend the pellet in the residual PBS by repeated pipetting several times or gently vortexing. The resuspended cells were added dropwise to the tube containing 1 mL of ice-cold 70% ethanol while vortexing at medium speed. Cap and freeze the tube at -20ºC (Jerard et al., 2020).

7.2.9.7.7.1. Staining of the cell cycle

After overnight incubation, the samples were centrifuged at 3000 rpm for 5 minutes at room temperature. The supernatant was removed, and 250 µL PBS was added to the pellet. Then, the centrifugation was repeated at the same rpm and time. The pellet was resuspended after discarding the supernatant; 250 µL of cell cycle reagent was then added. This was incubated in the dark for 30 minutes (which is light sensitive). After this, it was analyzed using a Flow Cytometer. Gating was performed with reference to untreated control cells, and samples were analyzed (Jerard et al., 2020).

7.2.9.8. Formulation of a cream from silver nanoparticles (AgNPs) synthesized from the methanol extract of *S. palghatense* bark

The cream formulation was prepared by initially melting 5 g of shea butter, serving as the emulsifying agent, at a controlled temperature to prevent degradation of its constituents. Concurrently, the aqueous phase was prepared by combining 1.5 mL of silver nanoparticles (AgNPs) synthesized from the methanol extract of *S. palghatense* bark, known for its wound healing, anti-inflammatory, and antibacterial properties, with 2 mL of aloe vera gel, recognized for its acne-reducing effects, and 9.5 mL of liquid paraffin, which functions as a lubricating agent. Sterile distilled water was added to the aqueous mixture in sufficient quantity to adjust the final volume to 18g. The aqueous phase was then gradually added to the melted shea butter under continuous stirring to facilitate emulsification. The mixture was homogenized using a mechanical stirrer until a uniform cream consistency was achieved, ensuring stable emulsion formation and preventing phase separation. The cream was subsequently cooled to ambient temperature with gentle stirring to maintain homogeneity. Finally, the formulated cream was transferred into sterile containers for further evaluation and

storage. All steps were performed under aseptic conditions to preserve the formulation's integrity (Pal et al., 2014).

7.2.9.8.1. Antimicrobial assay by agar well diffusion method

Standardized microbial cultures were prepared by inoculating test organisms in Nutrient broth and incubating overnight at 37°C to achieve turbidity equivalent to 0.5 McFarland standard, yielding approximately 1.5 × 10^8 CFU/mL. Mueller Hinton Agar (MHA) plates were uniformly inoculated with this microbial suspension. Wells were bored into the agar, and each well was filled with different concentrations (100, 150, and 200 for fungus and 75, 100, and 150 µg/mL for bacteria) of the test samples. Streptomycin (25 µg) was used as the positive control, while 100% DMSO served as the solvent/negative control. The plates were allowed to stand at room temperature for 30 minutes to facilitate diffusion of the samples into the agar. Subsequently, plates were incubated at 37°C for 18-24 hours. Following incubation, zones of inhibition (clear areas around the wells indicating antimicrobial activity) were measured in millimetres (mm). This method follows the guidelines outlined by the Clinical and Laboratory Standards Institute (CLSI) (Wayne, 2015).

7.2.10. Statistical analysis

All experimental data were analyzed using one-way analysis of variance (ANOVA) to determine significant differences among treatment means. Six replicates were maintained for each treatment to ensure statistical reliability. Critical difference (CD) values were calculated to evaluate the minimum significant difference between means at the chosen confidence level. Post hoc multiple comparison tests were performed following ANOVA to identify specific group differences.

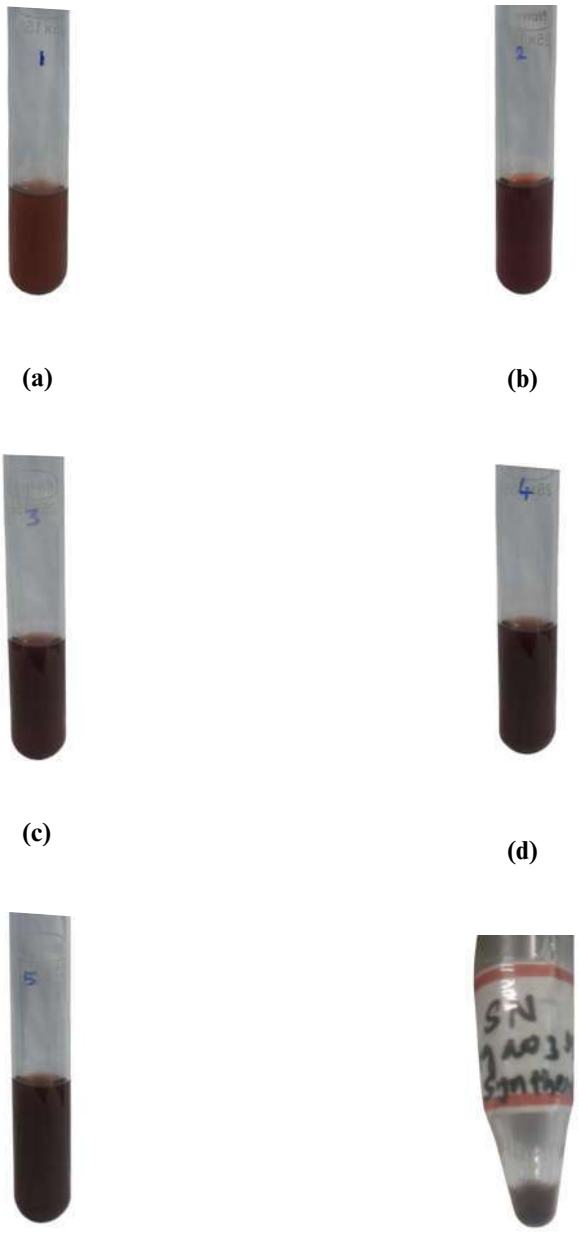
7.3. Results

Green synthesis of silver nanoparticles (AgNPs) was performed using *S. palghatense* methanol extract serving as both a reducing agent and stabilizer. The UV–vis spectrophotometer is one of the most efficient tools for identifying metal oxide NPs. The characteristic peak of the extract appeared at about 410 nm, which is mainly attributed to the presence of polyphenols that are involved in reducing and stabilizing the metal nanoparticles. While the silver nanoparticles synthesized extract showed the characteristic peak at 440 nm, which is the characteristic band of Ag nanoparticles due to Surface Plasmon Resonance (SPR).

The synthesis of silver nanoparticles (AgNPs) was further optimized by using various concentrations of the methanol extract of *S. palghatense* bark (1mg/mL) and silver nitrate (1 mM) concentration. Among the concentrations (2 mg, 4 mg,6 mg,8 mg, and 10 mg) carried out for the study (Plate 7.1), results indicate the maximum absorbance of surface plasmon resonance for the 6 mg/ml concentration. When the concentration of the extract was further increased, the absorbance was decreased, while no shift of the SPR was observed, indicating that lower and higher extract volumes were not sufficient for the maximum reduction of silver nitrate molecules.

7.3.1. UV-Visible analysis

The synthesis of silver nanoparticles (AgNPs) was further optimized by using various concentrations of the methanol extract of *S. palghatense* bark (1mg/mL) and silver nitrate (1mM) concentration. The effect of various concentrations of the extract on the synthesis of nanoparticles is provided in Figure 7.1. Among the concentrations, 2 mg, 4 mg, 6 mg, 8 mg, and 10mg were carried out for the study, results indicate the maximum absorbance of surface plasmon resonance for 6 mg/ml concentration. When the concentration of the extract was further increased, the absorbance was decreased while no shift of the SPR, indicating lower and higher extract volume was not sufficient for the maximum reduction of silver nitrate molecules.



(a) **(b)**

(c) **(d)**

(e) **(f)**

Plate 7.1: Silver nano particles (AgNPs) synthesized from the methanol extract of *Syzygium palghatense* bark at different extract concentrations: (a) 2 mg (b) 4 mg (c) 6 mg (d) 8 mg (e) 10 mg (f) Silver nanoparticles in Eppendorf tubes.

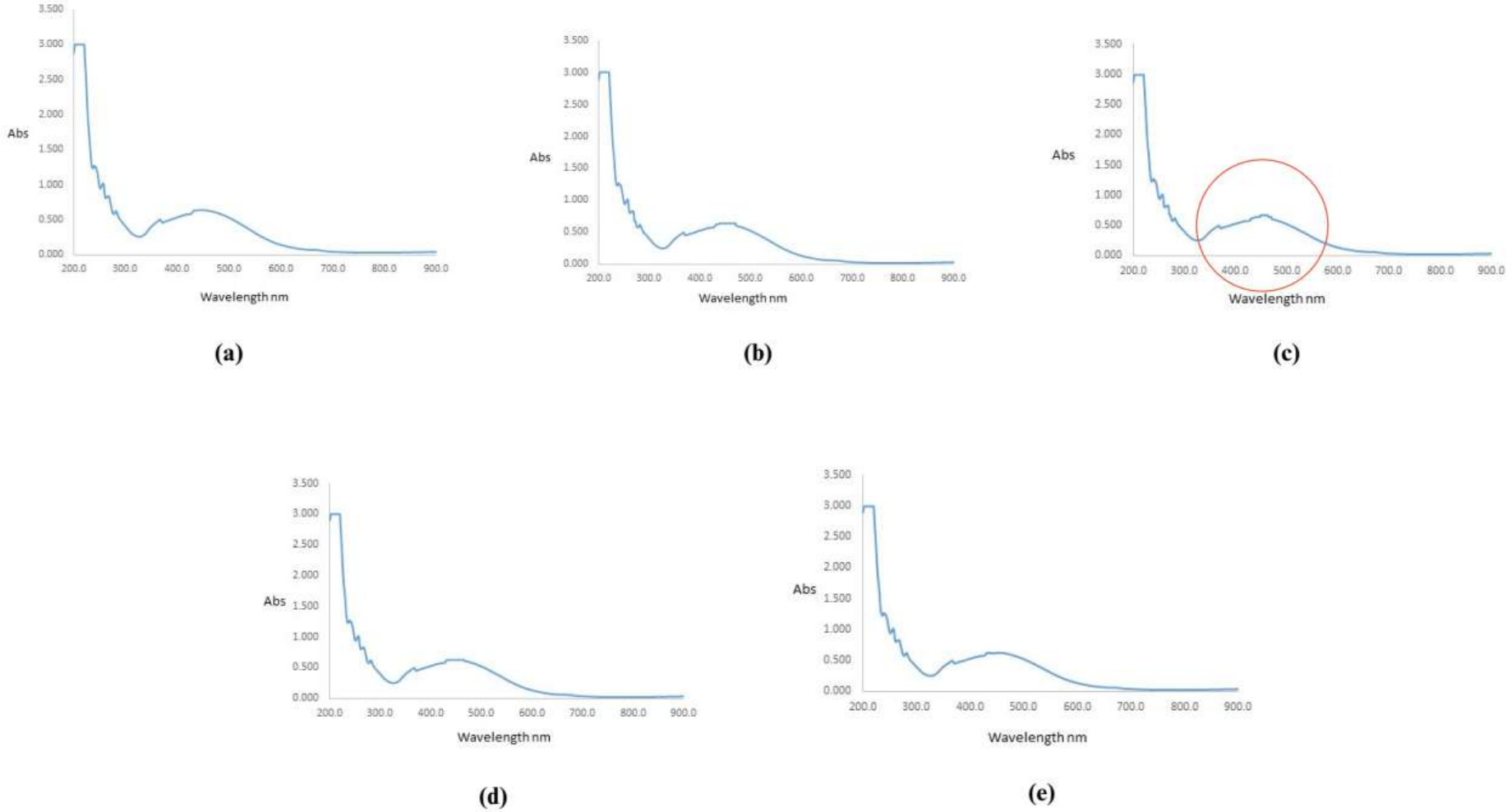


Figure 7.1: Ultraviolet-Visible (UV-Vis) analysis of silver nanoparticles (AGNPs) synthesized from *Syzygium palghatense* bark methanol extract at different concentrations: (a) 2 mg (b) 4 mg (c) 6 mg (d) 8 mg (e) 10 mg

7.3.2. FT-IR analysis

FTIR studies were performed to detect potential biomolecules in the aqueous extract, the basic material responsible for the reduction and stabilization of the nanoparticle solution. In the study, the FTIR spectrum of the *S. palghatense* bark methanol extract exhibits prominent absorption bands at 3439 cm-1 and 1633 cm-1, corresponding to the free O-H groups and carbonyl stretching, respectively, present in the extract.

While the peak at 1051 cm-1 arises due to the C=C stretching, with C-O stretching frequency. The FTIR spectrum of silver nanoparticles (AgNPs) of the extract represents the stretching vibrations of O-H and C=O groups of the extract appeared at 3439 cm^{-1} and 1633 cm^{-1} respectively with a decrease in intensity indicating the involvement of the respective functional groups in reducing silver nitrate to yield silver oxide NPs. The peak at 1051 cm^{-1} arises due to the C=C stretching with C-O stretching frequency. The FTIR spectrum of silver nanoparticles (AgNPs) of the extract represents the stretching vibrations of O-H and C=O groups of the extract appeared at 3439 cm^{-1} and 1633 cm-^{1,} respectively, with a decrease in intensity indicating the involvement of the respective functional groups in reducing silver nitrate to yield silver oxide NPs. The distinct peaks at 418 cm^{-1} revealed the successful synthesis of silver oxide NPs stabilized by the methanol extract. It has been reported that phenolic groups are known to stabilize iron oxide nanoparticles through electrostatic interactions. Typically, the formation of distinctive metal-oxygen bonds occurs between 400–4000 cm^{-1} (Figure 7.2). FT-IR study confirmed the bio-reduction of silver nitrate nanoparticles via reduction by the capping material of aqueous extract.

7.3.3. SEM analysis

The surface morphology, size, and shape of the silver nanoparticles were analyzed by Scanning Electron Microscope. The SEM images show individual silver nanoparticles, which are predominantly spherical in shape, as well as a number of aggregates with no defined morphology. The presence of biomolecules in the *S.*

palghatense extract has resulted in the synthesis of spherical silver nanoparticles, and the aggregation may be due to the presence of secondary metabolites in the *S. palghatense* methanol extract of bark. The SEM image shows the size of the silver nanoparticles ranging from 60 to 85 nm. The Energy Dispersive X-ray Spectroscopy (EDX) showed peak values at 1.043 and 3.431 keV (Plate 7.2).

7.3.4. TEM analysis

TEM images of regions with a higher density of atoms are darker due to more incident electrons are blocked by the objective aperture (OBJ aperture). Crystalline state materials are dominated by the scattering effect. TEM analysis revealed that silver nanoparticles (AgNPs) exhibit a narrow size distribution. The formation of bead-like structure is supported by the existence of SPR coupling at 450 nm in the UV-Visible absorption spectrum of the *S. palghatense* extract AgNPs nanoconjugates. The Selected Area Electron Diffraction (SAED) pattern of the AgNPs nanoconjugates shows well-defined diffraction spots of AgNPs, and the diffraction pattern is assigned to a face-centred cubic crystal structure (Plate 7.3).

7.3.5. AFM analysis

The atomic force microscope (AFM) indicated the synthesized nanoparticles morphology and size. The size range of silver nanoparticles formed from *S. palghatense* ranges from 10 to 100 nm and is almost spherical in shape, as shown in Table 7.7 and Plate 7.4.

Atomic Force Microscopy (AFM) provides high-resolution 3D surface characterization of silver nanoparticle (AgNP) films deposited on a glass substrate with sub-nanometre precision. The AFM images reveal well-dispersed nanoparticle grains with sizes smaller than 100 Å (10 nm), confirming nanoscale synthesis. The electrostatic interactions between biomolecules (such as anesthetics) and the negatively charged AgNPs surfaces at the working pH strongly influence film behaviour and stability. Additionally, the hydrophobic and hydrogen bonding interactions between the coated nanoparticles and the molecular species contribute to the formation of the nanoparticle film and its structural characteristics. When

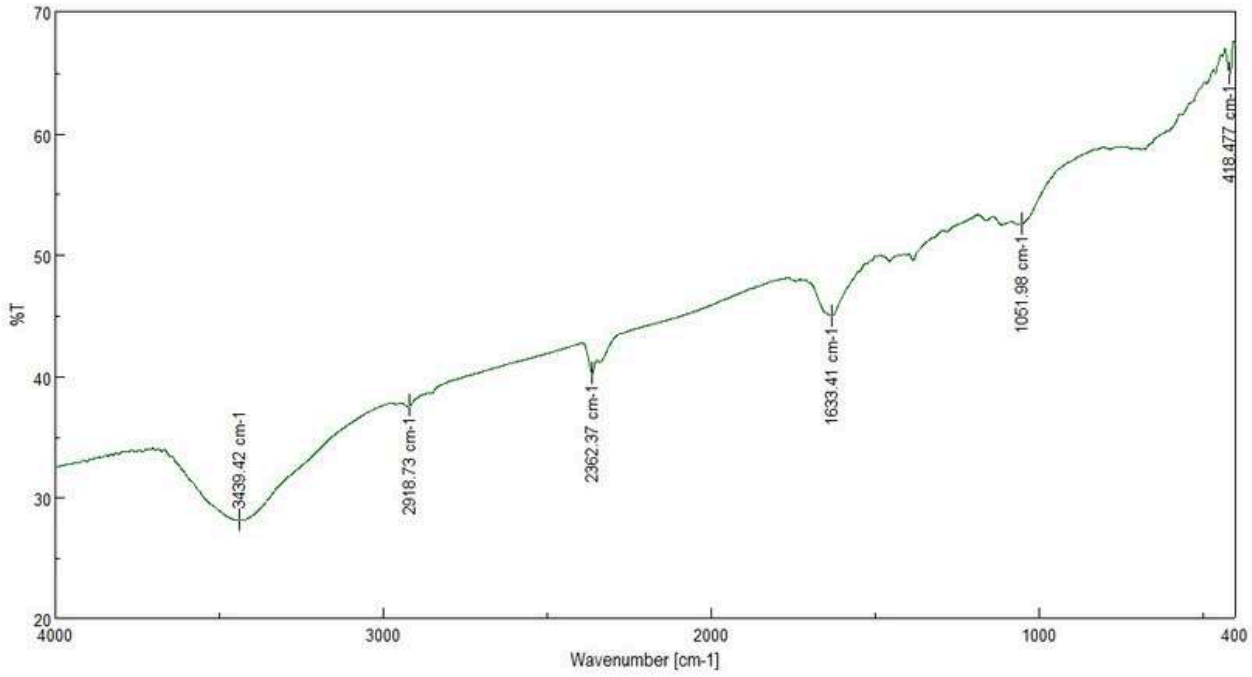
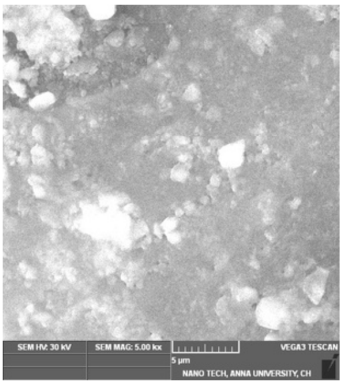
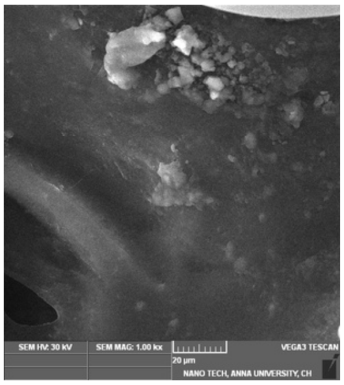


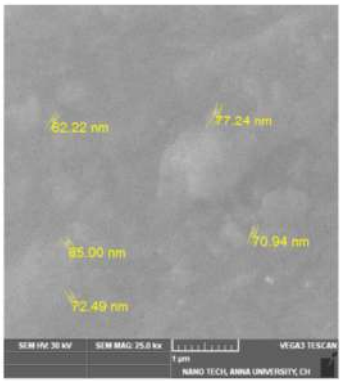
Figure 7.2: Fourier Transform Infrared (FT-IR) Spectroscopy analysis of silver nanoparticles (AgNPs) synthesized from the methanol extract of *Syzygium palghatense* bark at 6 mg concentration



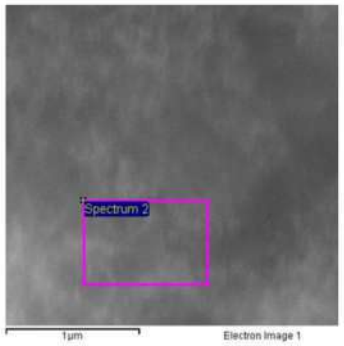
(a)



(b)



(c)

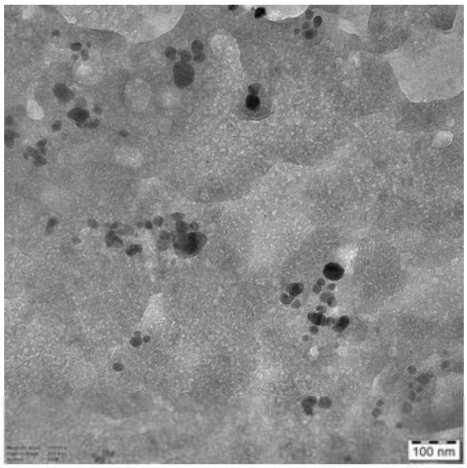


(d)

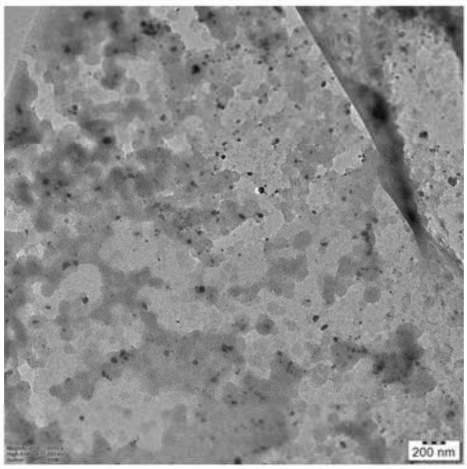


(e)

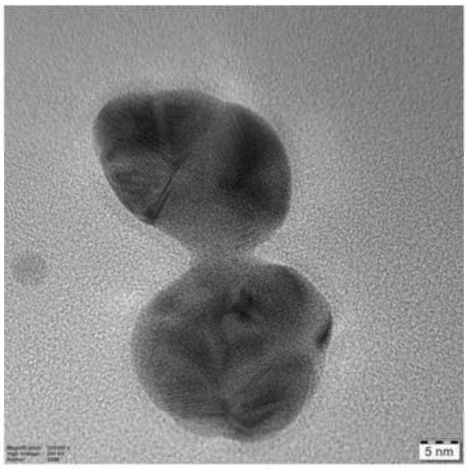
Plate 7.2: Scanning Electron Microscopy (SEM) analysis of silver nanoparticles (AgNPs) synthesized from the methanol extract of *Syzygium palghatense* bark: (a) Surface morphology at 5000 × magnification (b) Aggregated nanoparticles at 1000× magnification (c) Nanoparticle size distribution (62–85 nm) at 25000× magnification (d) & (e) Energy Dispersive X-ray Spectroscopy (EDX) spectrum of the selected SEM area



(a)



(b)



(c)

Plate 7.3: Transmission Electron Microscopy (TEM) analysis of silver nanoparticles (AgNPs) synthesized from the methanol extract of *Syzygium palghatense* bark at different magnifications: (a) Scale bar: 100 nm (b) Scale bar: 200 nm (c) Scale bar: 5 nm, High-resolution TEM image at 500,000× magnification

Table 7.7: Elemental composition of silver nanoparticles by Energy Dispersive X-ray Spectroscopy (EDX), complementing AFM morphological analysis

Element	Standard Compound	Weight %	Atomic %
C (Carbon) K	$CaCO_2$ (Calcium Carbonate)	73.82	79.32
O (Oxygen) K	SiO_2 (Silicon Dioxide)	25.59	20.64
Au (Gold) M	Au (Gold)	0.59	0.04
Totals		100.00	—

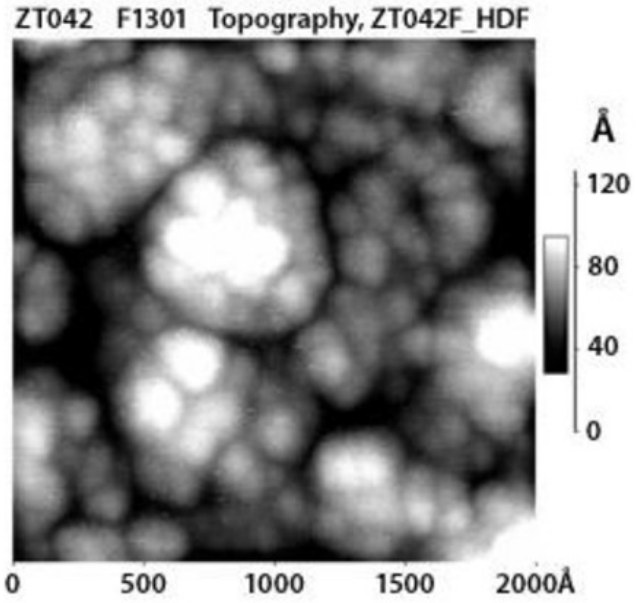


Plate 7.4: Atomic Force Microscopy (AFM) topography image of silver nanoparticle film synthesized from the methanol extract of *Syzygium palghatense* bark, showing surface morphology at the nanoscale (Scale: 0–2000 Å, Height: 0–120 Å)

operating in contact mode, frictional forces between the AFM tip and the sample induce twisting of the cantilever, causing lateral movement of the laser beam on the photodetector. This lateral deflection is harnessed in lateral force microscopy to distinguish different phases on the sample surface that may have similar topography, providing insight into surface chemistry and mechanical properties.

The accompanying elemental composition table (Table 7.7) shows the normalized weight and atomic percentages of carbon (C), oxygen (O), and gold (Au) detected in the analyzed sample area. The predominance of carbon and oxygen is consistent with organic residues from the biosynthesis process and substrate materials. Trace amounts of gold likely reflect the conductive coating or artifacts of sample preparation. This compositional information complements the AFM morphological data by confirming the elemental constituents present on the nanoparticle surfaces.

7.3.6. XRD analysis

Analysis of the structure and crystalline size of the synthesized silver nanoparticles were carried out by XRD. The XRD analysis of synthesized silver nanoparticles from *S. palghatense* extract showed diffraction peaks at = 32.7°, 38.3°, 44.4°, 64.6°, and 76.8°, respectively. The obtained XRD spectrum confirmed that the synthesized silver nanoparticles were in nanocrystal form and crystalline in nature. The peaks can be assigned to the planes (124), (116), (198), (220), (246), and (216) facets of silver crystal, respectively (Figure 7.3). The high peaks in the XRD analysis indicated the active silver composition with the indexing. The results indicate that the silver nanoparticles are face-centered cubic and crystalline in nature. The broadening of Bragg's peaks around their bases indicates the formation of small silver nanoparticles. A few unassigned peaks observed could be due to the presence of some bioorganic compounds/protein(s) in the *S. palghatense* bark extract, and crystallize on the surface of the silver nanoparticles formed.

7.3.7. Antioxidant properties

The antioxidant potential of silver nanoparticles (AgNPs) synthesized from the methanolic extract of *S. palghatense* bark was evaluated using DPPH, superoxide,

hydroxyl radical scavenging, and ferric reducing antioxidant power (FRAP) assays. The percentage of inhibition increased dose-dependently in all assays for AgNPs, consistently outperforming the standard ascorbic acid at each concentration tested.

Table 7.8-7.10 lists the statistical comparison of antioxidant activity between silver nanoparticles (AgNPs) synthesized from the methanol extracts of *S. palghatense* bark and standard controls, presented as mean ± standard error (SE) includes one-way ANOVA results showing F-value, P-value, and Critical Difference (CD) for evaluation of significant differences

In the DPPH assay, AgNPs exhibited radical scavenging activity ranging from 32% ± 0.33 to 89% ± 0.05 across concentrations of 12.5 to 150 µg/mL, compared to ascorbic acid's 29% ± 0.21 to 75% ± 0.21. The superoxide radical scavenging assay showed inhibition of 31% ± 0.03 to 86% ± 0.15 for AgNPs, higher than the standard range of 27% ± 0.26 to 73% ± 0.20. Similarly, for hydroxyl radical scavenging, AgNPs demonstrated inhibition ranging from 28% ± 0.12 to 83% ± 0.11, exceeding the standard's range of 23% ± 0.24 to 70% ± 0.21. The FRAP assay highlighted the reducing power of AgNPs, with values ranging from 33% ± 0.33 to 90% ± 0.05, surpassing those of ascorbic acid, which ranged from 30% ± 0.21 to 78% ± 0.21(Figure 7.4).

The IC_{50} values (concentration for 50% inhibition) further attest to the superior antioxidant efficiency of AgNPs, with notably lower values than the standard across all assays: 1.311 ± 0.123 µg/mL vs. 53 ± 0.010 µg/mL (DPPH), 1.521 ± 0.301 µg/mL vs. 60 ± 0.114 µg/mL (superoxide), 48 ± 0.145 µg/mL vs. 80 ± 0.201 µg/mL (hydroxyl), and 1.204 ± 0.102 µg/mL vs. 48 ± 0.140 µg/mL (FRAP). These data confirm a potent antioxidant capacity of the biosynthesized AgNPs (Figure 7.5).

In all assays, the AgNPs demonstrated a clear dose-dependent increase in percentage inhibition, consistently outperforming the standard ascorbic acid across the tested concentrations. Notably, the FRAP assay demonstrated the highest antioxidant activity, with AgNPs achieving up to 90% inhibition at 150 µg/mL, indicating a strong ferric ion-reducing capacity. Correspondingly, the IC_{50} values highlighted the potent antioxidant efficacy of these nanoparticles, with the lowest

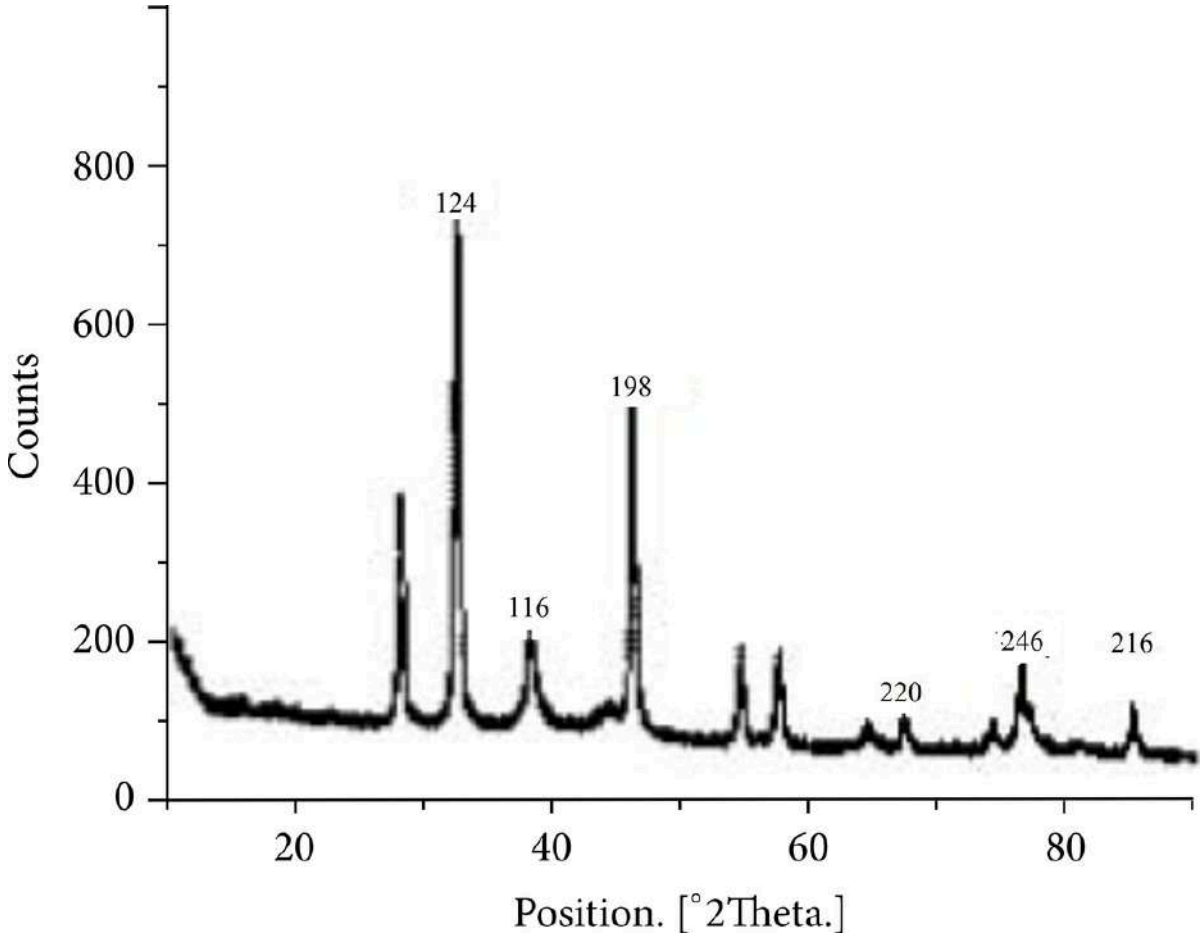


Figure 7.3: X-Ray Diffraction (XRD) analysis of silver nanoparticles (AgNPs) synthesized from the methanol extract of *Syzygium palghatense* bark

Table 7.8: Statistical comparison of antioxidant activity between silver nanoparticles (AgNPs) synthesized from the methanol extracts of *Syzygium palghatense* bark expressed as Mean ± Standard Error (SE), with statistical significance (F-value, P-value, and Critical Difference)

Treatments	Mean ± SE
AgNPs	13.009±11.66[a]
Standard	60.25±7.03[b]
F Value	13932.58
P Value	<0.001
CD Value	0.826

Table 7.9: Comparative antioxidant activity of silver nanoparticles (AgNPs) synthesized from the methanol extracts of *Syzygium palghatense* bark across multiple assays (DPPH, SRSA, HRSA, FRAP) expressed as Mean ± Standard Error (SE), with statistical significance (F-value, P-value, and Critical Difference)

Assays	Mean ± SE
DPPH	27.1555±25.84[b]
SRSA	30.7605±29.24[c]
HRSA	64.00±16.00[d]
FRAP	24.602±23.40[a]
F Value	2118.47
P Value	<0.001
CD Value	1.168

(DPPH: 2,2-diphenyl-1-picrylhydrazyl Radical Scavenging Assay; SRSA: Superoxide Radical Scavenging Assay; HRSA: Hydroxyl Radical Scavenging Assay; FRAP: Ferric Reducing Antioxidant Power Assay)

Table 7.10: IC_{50} values (Mean ± SE) for antioxidant activity of silver nanoparticles (AgNPs) synthesized from the methanol extracts of *Syzygium palghatense* bark and standard controls across multiple assays (DPPH, SRSA, HRSA, FRAP) with statistical significance (Mean ± Standard Error (SE), F-value, P-value, and Critical Difference)

Interaction	Mean ± SE
AgNPs: DPPH	1.311 ± 0.123^{a}
AgNPs: SRSA	1.521 ± 0.301^{a}
AgNPs: HRSA	48 ± 0.145^{b}
AgNPs: FRAP	1.204 ± 0.102^{a}
Standard: DPPH	53 ± 0.010^{c}
Standard: SRSA	60 ± 0.114^{d}
Standard: HRSA	80 ± 0.201^{e}
Standard: FRAP	48 ± 0.140^{b}
F Value	196.95
P Value	<0.001
CD Value	1.652

(DPPH: 2,2-diphenyl-1-picrylhydrazyl Radical Scavenging Assay; SRSA: Superoxide Radical Scavenging Assay; HRSA: Hydroxyl Radical Scavenging Assay; FRAP: Ferric Reducing Antioxidant Power Assay)

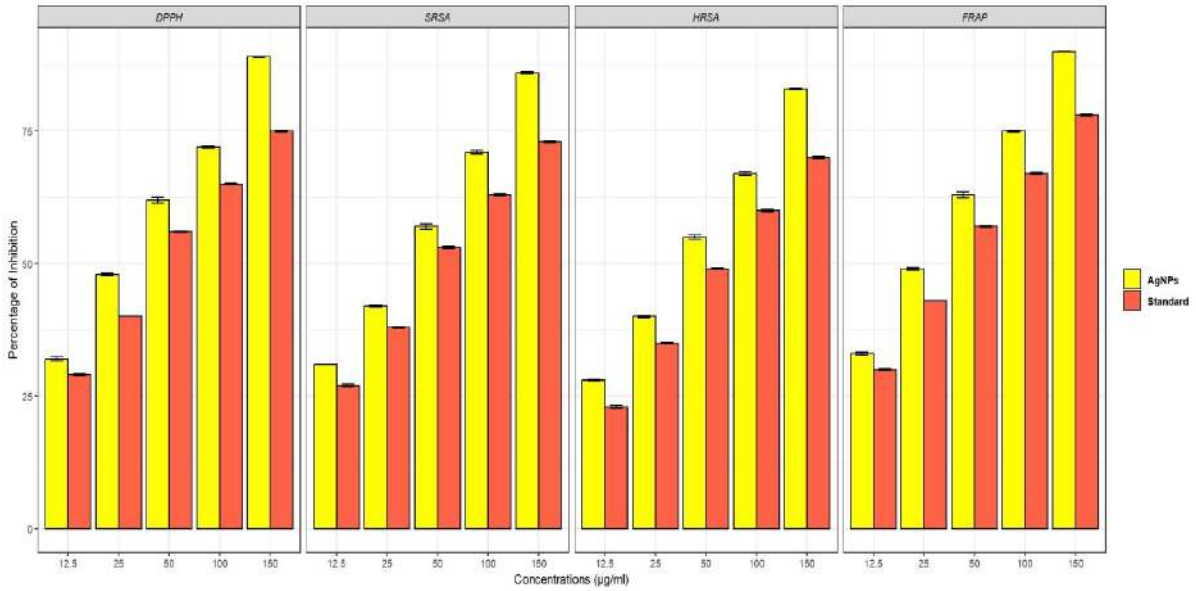


Figure 7.4: Comparative antioxidant activities of silver nanoparticles (AgNPs) synthesized from the *Syzygium palghatense* bark across different concentrations in DPPH, SRSA, HRSA, and FRAP assays (DPPH: 2,2-diphenyl-1-picrylhydrazyl Radical Scavenging Assay; SRSA: Superoxide Radical Scavenging Assay; HRSA: Hydroxyl Radical Scavenging Assay; FRAP: Ferric Reducing Antioxidant Power Assay)

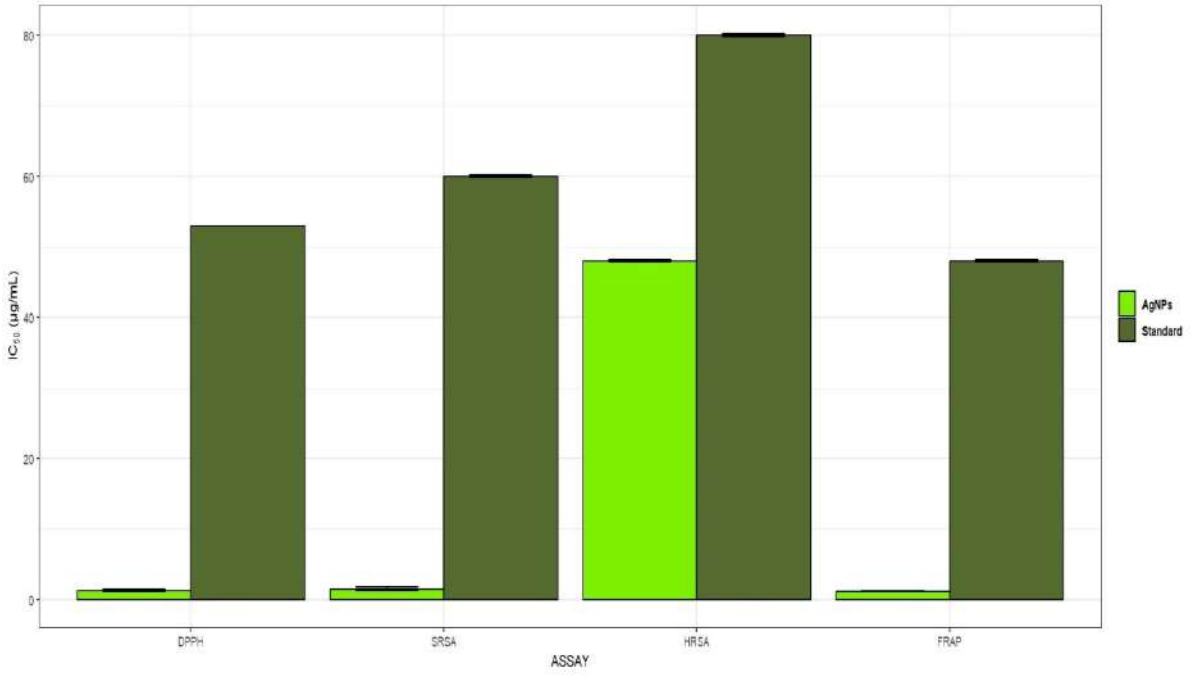


Figure 7.5: Comparative IC_{50} values of silver nanoparticles (AgNPs) synthesized from the *Syzygium palghatense* bark across different concentrations in DPPH, SRSA, HRSA, and FRAP assays (DPPH: 2,2-diphenyl-1-picrylhydrazyl Radical Scavenging Assay; SRSA: Superoxide Radical Scavenging Assay; HRSA: Hydroxyl Radical Scavenging Assay; FRAP: Ferric Reducing Antioxidant Power Assay)

value observed in the FRAP assay (1.204 ± 0.102 µg/mL), followed closely by DPPH (1.311 ± 0.123 µg/mL) and SRSA (1.521 ± 0.301 µg/mL), while HRSA exhibited a comparatively higher IC_{50}. These findings suggest that the biosynthesized AgNPs possess robust free radical scavenging and reducing abilities, as underscored by the FRAP assay results, which highlight their superior electron-donating antioxidant power, making them promising candidates for applications where oxidative stress mitigation is critical.

7.3.8. Antimicrobial properties

The antimicrobial efficacy of silver nanoparticles (AgNPs) derived from *S. palghatense* bark was evaluated against fungi (*Aspergillus niger*, *Candida albicans*) and bacteria (*Staphylococcus aureus*, *Streptococcus mutans*, *Enterococcus faecalis*, *Escherichia coli*, and *Pseudomonas aeruginosa*) using different concentrations represented by the zone of inhibition (mm) assay (Plate 7.5).

Compared to the antifungal standard clotrimazole (100 µg/mL), which showed inhibition zones of 29 mm for *A. niger* and 33 mm for *C. albicans*, AgNPs exhibited concentration-dependent but lower antifungal activity. At 1000 µg/mL, AgNPs created inhibition zones of 19 mm (*A. niger*) and 22 mm (*C. albicans*), demonstrating moderate antifungal potency. Lower concentrations (250 and 500 µg/mL) showed smaller inhibition zones, indicating a dose-dependent response (Figure 7.6).

Against bacterial strains, the standard antibiotic streptomycin (100 µg) showed zones of inhibition ranging from 27 mm to 33 mm across the tested bacteria, confirming its strong antimicrobial efficacy. The AgNPs showed no inhibition at 250 µg/mL but exhibited increasing antibacterial activity at concentrations of 500 and 1000 µg/mL. Notably, *Pseudomonas aeruginosa* was the most susceptible, with a maximum inhibition zone of 31 mm at 1000 µg/mL, surpassing other bacterial strains, such as *Staphylococcus aureus* (14 mm) and *Escherichia coli* (20 mm), at the same concentration. The broad-spectrum activity and significant zones at higher dosages underscore the potency of AgNPs against resistant and opportunistic bacteria (Figure 7.7).

These results indicate that biosynthesized silver nanoparticles possess effective antimicrobial activity, particularly at higher concentrations. Although standard drugs outperform AgNPs at lower dosages, the nanoparticles demonstrate promising inhibitory effects against both fungi and bacteria, especially Gram-negative bacteria such as *Pseudomonas aeruginosa*. The antimicrobial mechanism likely involves the disruption of microbial cell walls and metabolic interference through the release of silver ions and reactive oxygen species. Despite having lower antifungal potency compared to clotrimazole, AgNPs offer multi-targeted activity, with potential applications in both biomedical and environmental antimicrobial fields (Dakal et al., 2016).

7.3.8.1. Minimal Inhibitory Concentration (MIC) and Minimal Fungicidal Concentration (MFC)

The silver nanoparticles demonstrated strong antifungal activity against *Aspergillus niger* and *Candida albicans*. The MIC values were 0.36 µg/mL and 0.38 µg/mL, respectively, showing effective growth inhibition at low concentrations. The MFC values (0.47 µg/mL for *A. niger* and 0.48 µg/mL for *C. albicans*) and corresponding fungicidal concentrations (0.52 µg/mL and 0.54 µg/mL) confirmed that the nanoparticles could effectively kill the fungal cells at slightly higher concentrations. Among the fungi tested, *A. niger* was slightly more sensitive, as indicated by its consistently lower MIC and MFC values. These findings suggest the AgNPs possess potent fungicidal properties, making them promising antifungal agents (Figure 7.8).

7.3.8.2. Minimal Inhibitory Concentration (MIC) and Minimal Bactericidal Concentration (MBC)

The silver nanoparticles exhibited potent antibacterial activity across all tested bacteria. *Pseudomonas aeruginosa* was the most sensitive, with the lowest MIC (0.25 µg/mL), MBC (0.3 µg/mL), and bactericidal concentration (0.32 µg/mL), indicating strong susceptibility. *Escherichia coli* also showed high sensitivity with MIC of 0.27 µg/mL and MBC of 0.36 µg/mL. Gram-positive bacteria, including *Enterococcus faecalis*, *Staphylococcus aureus*, and *Streptococcus mutans,* showed slightly higher

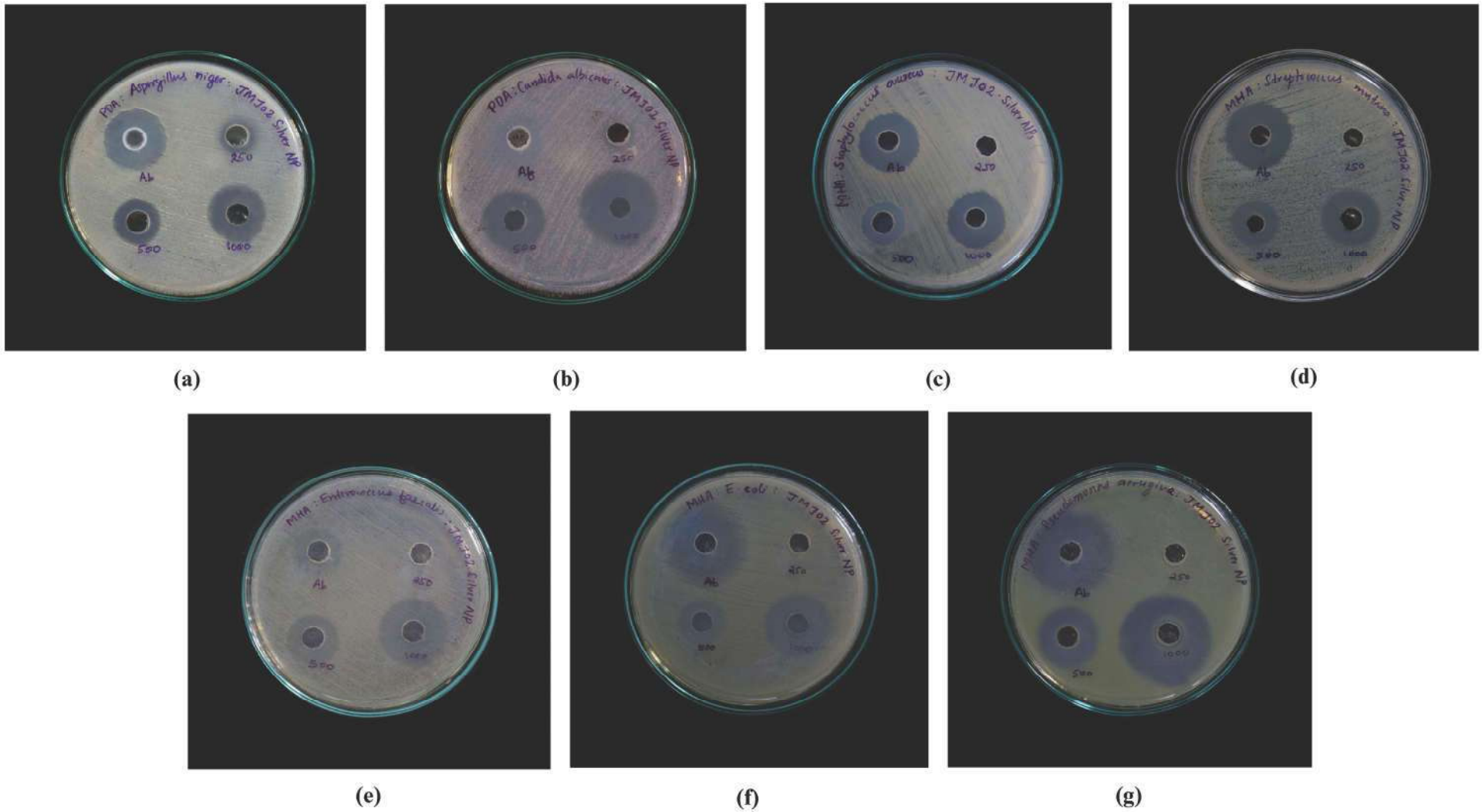


Plate 7.5: The inhibition zone (mm) of silver nanoparticles (AgNPs) synthesized from the methanol extract of *Syzygium palghatense* bark against (a) *Aspergillus niger* (b) *Candida albicans* (c) *Staphylococcus aureus* (d) *Streptococcus mutans* (e) *Enterococcus faecalis* (f) *Escherichia coli* and (g) *Pseudomonas aeruginosa* by agar well diffusion method

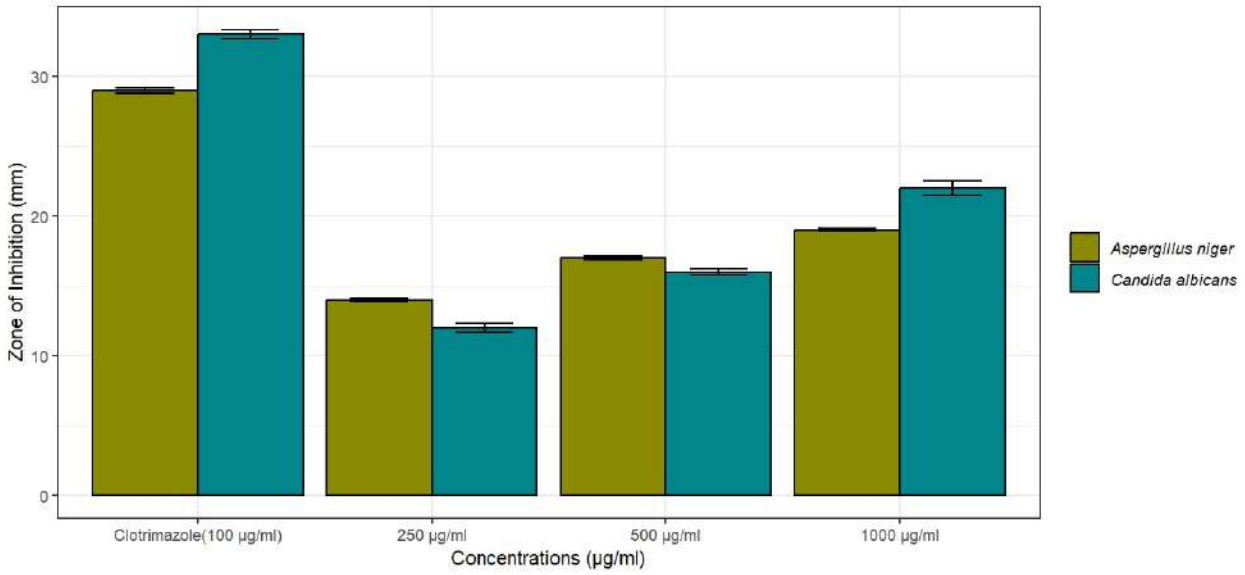


Figure 7.6: Antifungal activity of silver nanoparticles (AgNPs) synthesized from the methanol extract of *Syzygium palghatense* bark against pathogenic fungi, compared to clotrimazole

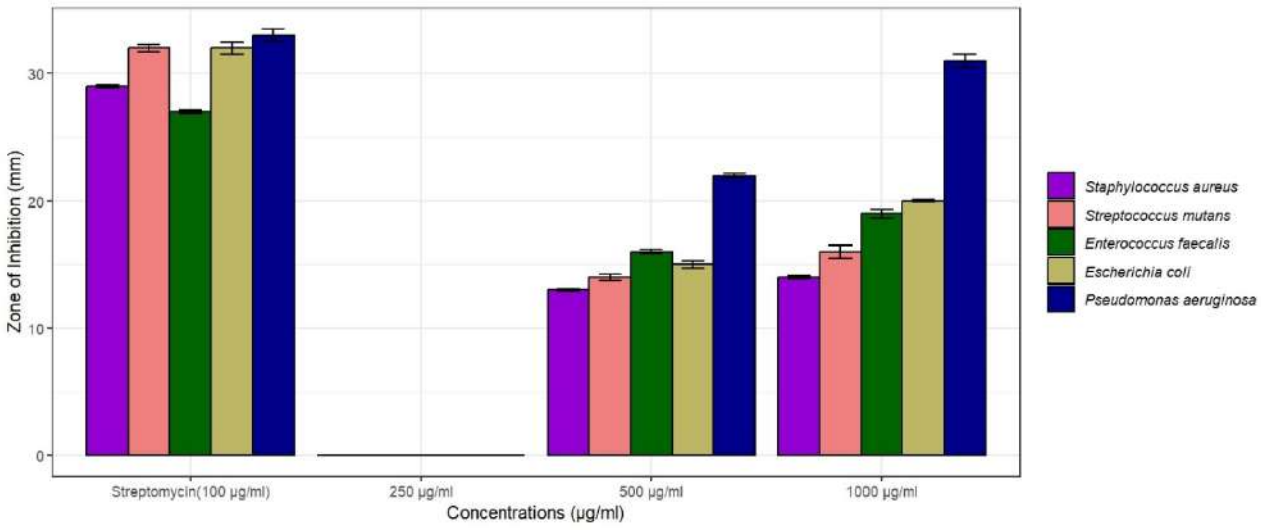


Figure 7.7: Antibacterial activity of silver nanoparticles (AgNPs) synthesized from the methanol extract of *Syzygium palghatense* bark against pathogenic bacteria, compared to streptomycin

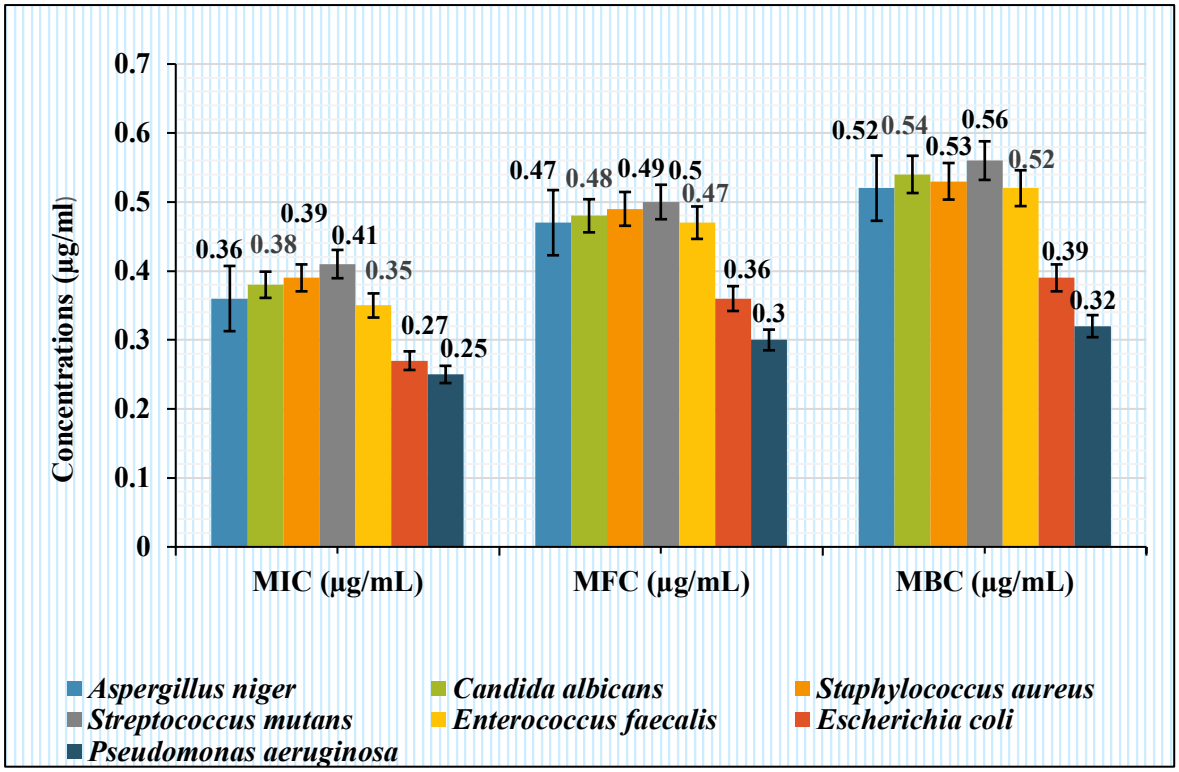


Figure 7.8: Minimum inhibitory (MIC), fungicidal (MFC), and bactericidal (MBC) concentrations of silver nanoparticles (AgNPs) synthesized from the methanol extract of *Syzygium palghatense* bark (Mean ± SE, n=6)

MICs ranging from 0.35 to 0.41 μg/mL, with bactericidal effects at concentrations between 0.47 and 0.56 μg/mL. The close MIC and MBC values indicate that the nanoparticles have bactericidal rather than merely bacteriostatic effects. These results demonstrate the broad and effective antibacterial potential of *S. palghatense* bark-derived AgNPs (Figure 7.8).

7.3.8.3. Biofilm studies

Biofilms, which are structures that consist of clusters of microorganisms embedded in an extracellular polymeric substance, represent some of the most significant clinical challenges owing to their capability to survive antimicrobial treatment and cause chronic infection in medical devices, including catheters, prostheses, and heart valves. Utilizing microorganisms to produce secondary metabolites that have demonstrated the ability to dismantle biofilm structures and inhibit quorum-sensing-mediated biofilms, ultimately leading to a reduction in biofilm-related infections when incorporated into medical device coatings, has emerged as a promising approach (Chakraborty & Chakraborty, 2024). *Pseudomonas aeruginosa* was selected for advanced antimicrobial studies, including biofilm formation assays, due to its significant zone of inhibition observed in preliminary tests.

7.3.8.3.1. Congo red agar assay

The red colour of the agar turns almost blackish. The presence of dark red coloured rough colonies on Congo red agar confirms the biofilm-forming ability of *Pseudomonas aeruginosa* (ATCC 27853) used in this study.

Plate 7.6 represents the Congo red agar (CRA) assay performed to assess *Pseudomonas aeruginosa* biofilm. A clear transition from the red of the Congo red agar in the petri dish and a change to dark black colouration, especially notable in the middle portion, where only red colouration remains at the edges of the petri dish. Such a colour shift, red to black, following some crystallization, demonstrates positive biofilm accumulation by *P. aeruginosa* under the test conditions (37°C for 24 hours). Black pigmentation was detected due to the interaction between Congo red dye and

extracellular polymeric substances (EPS) synthesized during biofilm development. The increasing gradient of black to red in the image indicates differences in biofilm production throughout the culture, with the darkest areas demonstrating the best formation of biofilm. This positive result demonstrates the biofilm formation ability of *P. aeruginosa*, which is one of the important virulence factors associated with *P. aeruginosa*, pathogenicity and multi-drug resistance.

7.3.8.3.2. Semi-quantitative adherence assay

Using a semi-quantitative adherence assay, silver nanoparticles synthesized from the methanol extract of *S. palghatense* bark (SPB AgNPs) inhibited *Pseudomonas aeruginosa* (ATCC 27853) biofilm formation (Table 7.11). There was greater biofilm formation in untreated controls with 0.3210 ± 0.1054 optical density for silver nanoparticles. The result showed dose-dependent inhibition at 62.5 and 1000 µg/mL concentrations. AgNPs SPB (62.5 µg/mL) resulted in 20.24 ± 1.0240% inhibition (OD_{570}: 0.2341 ± 0.0035). The inhibition was concentration-dependent, with a maximum inhibition of 1000 µg/mL, where the AgNPs SPB showed higher activity (64.44 ± 1.1305%, OD_{570}: 0.1018 ± 0.0015). The IC_{50} values were found to be 1.25 µg/mL for AgNPs SPB, which demonstrates the strong anti-biofilm potential.

7.3.8.3.3. Inhibition assay of initial and pre-formed biofilm

As shown in Table 7.11, SPB AgNPs exhibited substantial anti-biofilm activity against *Pseudomonas aeruginosa* (ATCC 27853). There is clear dose-dependent inhibitory activity from 62.5 to 1000 µg/mL. SPB AgNPs (optical density 1.3015 ± 0.0214) exhibited significant biofilm formation in the control samples. The SPB AgNPs exhibited moderate inhibition at the lowest tested concentration (62.5 µg/mL), of which an inhibition percentage was higher for SPB AgNPs at 25.12 ± 1.0332%. Notably, at the 500 µg/mL concentration, a significant elevation in inhibition occurred, with SPB AgNPs achieving an inhibition rate of 75.21 ± 1.2251% (OD_{570}: 0.2581 ± 0.0014). The maximum inhibition was recorded at 1000 µg/mL for SPB AgNPs, which showed excellent activity (86.33 ± 1.2300%, OD_{570}: 0.1756 ± 0.0005). The IC_{50} result of 1.22 µg/mL for SPB AgNPs confirms the enhanced anti-



Plate 7.6: Detection of biofilm formation by *Pseudomonas aeruginosa* using congo red agar assay

Table 7.11: Semi-Quantitative Adherence Assay (SQAA), Initial Biofilm Inhibition Assay (IAIPB), and Biofilm Quantification (BQ) of silver nanoparticles (AgNPs) synthesized from the methanol extracts of *Syzygium palghatense* bark expressed as Mean ± Standard Error (SE), with statistical significance (F-value, P-value, and Critical Difference)

Biofilm	Concentration (µg/mL)	SQAA		IBIA		BQ	
		Optical density (OD, 570 nm)	Percentage of inhibition (%)	Optical density (OD, 570 nm)	Percentage of inhibition (%)	Optical density (OD, 570 nm)	Percentage of inhibition (%)
	Control	0.321 ± 0.1054^{a}	0 ± 0^{f}	$1.302 \pm 0.0.214^{a}$	0 ± 0^{f}	0.825 ± 0.0714^{a}	0 ± 0^{f}
	62.5	0.234 ± 0.0035^{b}	27.07 ± 1.0240^{e}	1.201 ± 0.2101^{b}	25.12 ± 1.0332^{e}	0.655 ± 0.0410^{b}	35.01 ± 1.2017^{e}
	125	0.210 ± 0.0038^{c}	34.65 ± 1.2062^{d}	1.002 ± 0.1401^{c}	36.15 ± 1.1232^{d}	0.411 ± 0.0350^{c}	49.32 ± 1.5101^{d}
	250	0.183 ± 0.0027^{d}	47.36 ± 1.0547^{c}	0.684 ± 0.1021^{d}	48.32 ± 1.2060^{c}	0.258 ± 0.0276^{d}	64.23 ± 1.5204^{c}
	500	0.155 ± 0.0090^{e}	53.01 ± 1.1254^{b}	0.258 ± 0.0014^{e}	75.21 ± 1.2251^{b}	0.103 ± 0.0147^{e}	68.56 ± 1.5650^{b}
	1000	0.102 ± 0.0015^{f}	64.44 ± 1.1305^{a}	0.176 ± 0.0005^{f}	86.33 ± 1.2300^{a}	0.102 ± 0.0011^{e}	79.27 ± 1.6102^{a}
F Stat		**1130.2**	**854.41**	**1560.6**	**1177.92**	**19987**	**1102.02**
p-value		**<0.05**	**<0.05**	**<0.05**	**<0.05**	**<0.05**	**<0.05**
CD @ 5%		**0.007**	**1.50**	**0.04**	**2.23**	**0.006**	**1.54**

biofilm activity. The increased activity is illustrated by the formation of wider inhibition zones in the agar well diffusion assay, indicating that the synergistic effect of methanol with silver nanoparticles from the bark potentially contained greater quantities of potent bioactive compounds that can interfere with *P. aeruginosa* biofilm formation. Further confirmation of this observation is given by the image (Plate 7.5 g) corresponding to greater inhibition zones for SPB AgNPs, which was found to be more effective against biofilm at significantly higher concentrations.

7.3.8.3.4. Quantification of biofilm

Quantitative assessment of biofilm formation indicates that methanolic SPB AgNPs exhibit potent inhibitory activity against biofilm formation of *Pseudomonas aeruginosa* (ATCC 27853). The data reveal a clear concentration-dependent inhibition pattern from 62.5-1000 µg/mL. The optical density values for SPB AgNPs in control samples were 0.8254 ± 0.0714, indicating significant biofilm growth. The difference in inhibition at the lowest concentration tested (62.5 µg/mL) also indicates that SPB AgNPs were significantly higher (35.01 ± 1.20%), which demonstrates the strong initial anti-biofilm activity of the SPB AgNPs. At 250 µg/mL, an increase in inhibition was seen with SPB AgNPs, where SPB AgNPs displayed 64.23 ± 1.5204% (OD_{570}: 0.2580 ± 0.0276) inhibition. At 1000 µg/mL, maximum inhibition was achieved, with SPB AgNPs displaying marginally greater activity (79.27 ± 1.6102%, OD_{570}: 0.1018 ± 0.0011). The IC_{50} values of 1.46 µg/mL for SPB AgNPs also confirm the higher anti-biofilm activity. The data align with the visual representation of these findings in Table 7.11, whereby SPB AgNPs have wider inhibition zones against *P. aeruginosa*, indicating that the bioactive compounds are more potent within the bark tissue.

7.3.8.3.5. Bacterial live/dead assay using SYTO 9 and propidium iodide

Fluorescence microscopy images demonstrate the efficacy of SPB AgNPs in reducing biofilm viability of *Pseudomonas aeruginosa* (ATCC 27853) as visualized using LIVE/DEAD BacLight™ Bacterial Viability Kit (Plate 7.7). The untreated control displayed predominantly green fluorescence due to SYTO 9 staining of viable

bacterial cells with intact cell membranes. Compared to the control, the samples treated with SPB AgNPs in propidium iodide staining exhibit pronounced red fluorescence, indicating the disruption of cell membranes and the presence of non-viable bacteria. More cells seem to have their membrane damaged in the bark extract treatment, as indicated by the greater number of red-stained cells. It agrees with the quantitative biofilm inhibition data, indicating that the SPB AgNPs have higher antimicrobial activity. The sharp visual contrast between live (green) and dead (red) cells confirms that the extracts disrupt the integrity of the bacterial cell membrane and decrease biofilm viability. The findings provide visual evidence of the anti-biofilm action of *S. palghatense* silver nanoparticles and mechanistic information on their mode of action, which involves membrane disruption, a process that is especially important for devising strategies against biofilm-mediated infections.

7.3.8.3.6. Bacterial cell adherence assay

SPB AgNPs showed potent inhibition on *Pseudomonas aeruginosa* biofilm formation as reflected in bacterial cell adherence assay (Table 7.12, Plate 7.8). One hundred forty-six colonies in the control group were counted. At 250 µg/mL concentration, colony count was reduced to 75 colonies (3.4×10^3 CFU/mL), a 48.6% decrease. Indeed, at a higher 1000 µg/mL concentration, SPB AgNPs completely inhibited the growth of bacteria (no detectable colonies), indicating 100% inhibition of bacterial adherence. The results demonstrate a significant dose-dependent antibacterial effect of SPB AgNPs, with marginally better inhibitory activity observed at lower concentrations tested. The high concentration confirms that SPB AgNPs contain strong bioactive molecules that can interfere with bacterial cell adherence, a crucial early stage in biofilm development, as demonstrated by the LIVE/DEAD BacLight™ assay (Plate 7.7).

7.3.8.3.7. Drug efflux assay by ethidium bromide

The drug efflux assay using ethidium bromide showed that the SPB AgNPs are significantly inhibitory of efflux in *Pseudomonas aeruginosa* (ATCC 27853). Fluorescence intensity (arbitrary units, a.u.) shows a concentration-dependent response for SPB AgNPs (Table 7.13). The SPB AgNPs showed more effective

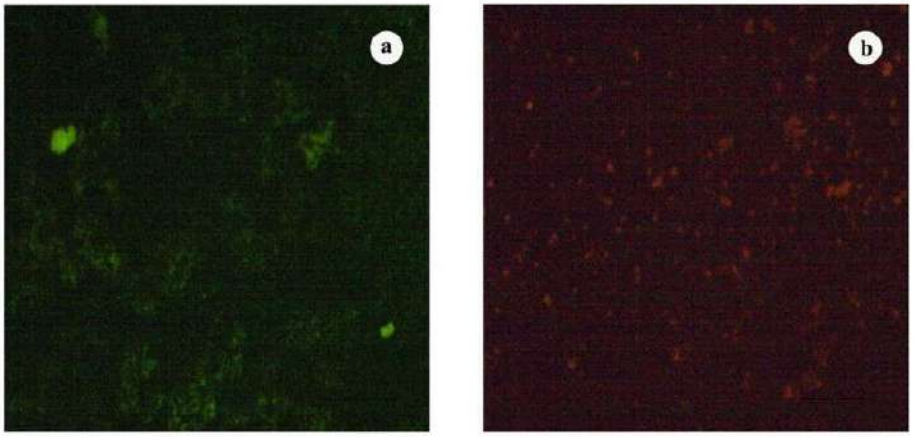


Plate 7.7: Determination of bacterial viability using LIVE/DEAD BacLight™ bacterial viability kit for *Pseudomonas aeruginosa* biofilms treated with silver nanoparticles (AgNPs) synthesized from the methanol extracts of *Syzygium palghatense* bark

(a) Untreated control (green fluorescence- viable cells)

(b) AgNPs treated (red fluorescence- non-viable cells)

Table 7.12: Bacterial cell adherence assay of methanolic extracts of silver nanoparticles (AgNPs) synthesized from the methanolic extracts of *Syzygium palghatense* bark against *Pseudomonas aeruginosa*

Concentrations (µg/mL)	Number of colonies counted	CFU/mL
Control	146	7.3×10^3
250	75	3.4×10^3
1000	Nil	Nil

Table 7.13: Drug efflux assay by ethidium bromide on methanolic extracts of silver nanoparticles (AgNPs) synthesized from the methanolic extracts of *Syzygium palghatense* bark against *Pseudomonas aeruginosa*

Concentrations (µg/mL)	Fluorescence (Green emission, a.u.)
Control	3729.31
250	2200.15
1000	1365.33

Table 7.14: Bacterial MTT assay-total cell response of *Pseudomonas aeruginosa* to silver nanoparticles (AgNPs) of methanolic extracts of *Syzygium palghatense* bark

Concentration (µg/mL)	Optical density (OD 570 nm)	Average viability (%)
Control	2.1023 ± 0.1021	100.00 ± 0.0001
62.5	1.8260 ± 0.1001	65.21 ± 1.0040
125	0.6920 ± 0.0541	33.24 ± 1.0035
250	0.5721 ± 0.0031	24.01 ± 1.0011
500	0.4513 ± 0.0022	17.33 ± 0.0008
1000	0.2105 ± 0.0011	12.36 ± 0.0004

Values are expressed as mean ± standard error (n=6)

Table 7.15: Quantification of extracellular polysaccharides (EPS) in *Pseudomonas aeruginosa* biofilms treated with silver nanoparticles (AgNPs) of methanolic extracts of *Syzygium palghatense* bark

Treatments	Absorbance (OD at 490 nm)	EPS content (µg/mL)	Inhibition percentage (%)
Control	1.5023 ± 0.0021	2907.6 ± 1.1450	Nil
AgNPs	0.5200 ± 0.0140	942.3 ± 1.0651	67.6 ± 0.0712

Values are expressed as mean ± standard error (n=6)

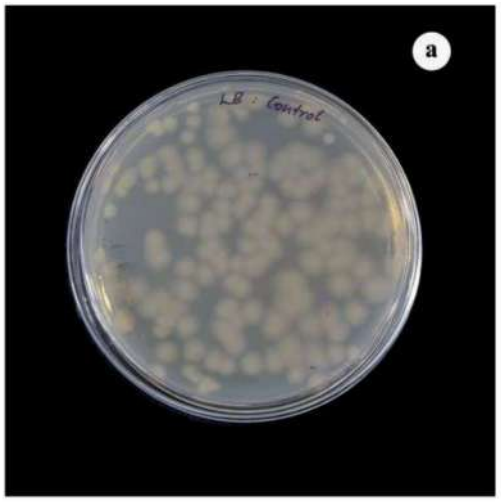




Plate 7.8: Bacterial cell adherence assay of silver nanoparticles (AgNPs) synthesized from the methanol extract of *Syzygium palghatense* bark against *Pseudomonas aeruginosa*: (a) Control (b) Treated with AgNPs

inhibition, as evidenced by a decrease in fluorescence from 3729.31 a.u. (control) to 2200.15 a.u. at 250 µg/mL (41.0% reduction) and 1365.33 a.u. at 1000 µg/mL (63.4% reduction). The lower the fluorescence value, the more ethidium bromide is retained within bacterial cells, thus confirming the effective inhibition of membrane-bound efflux pumps. This inhibits key bacterial processes, including quorum-sensing molecule transport, outer biofilm polymeric substances secretion, and resistance mechanisms to antimicrobials, which are crucial during biofilm development and maintenance. The superior efflux pump inhibitory activity of SPB AgNPs correlates with the improved antibiofilm activity demonstrated in earlier adherence and biofilm inhibition assays. *S. palghatense* is rich in bioactive phytochemicals that target bacterial membrane transport systems as their primary mechanism of action. This approach may lead to the future development of novel anti-biofilm agents against the clinically significant pathogen *P. aeruginosa*.

7.3.8.3.8. Bacterial MTT assay-Total cell response to compound

The bacterial MTT assay demonstrated that SPB AgNPs inhibited the growth of *Pseudomonas aeruginosa* (ATCC 27853) in a concentration-dependent manner. Viable bacterial cells are capable of reducing MTT to formazan and provide OD values that directly correlate with bacterial viability (Table 7.14). SPB AgNPs exhibited a concentration-dependent reduction in OD values from 2.1023 ± 0.1021 (control) to 0.2105 ± 0.0011 (1000 µg/mL), with viabilities measured from 100% to 12.36 ± 0.0004%. SPB AgNPs caused significant inhibition at 125 µg/mL and higher, reducing viability to approximately one-third the control value. The reproducibility of the assay is underscored by both the dose-dependent response being qualitatively similar across the independent experiments and low standard deviations accompanying all measurements. The results are consistent with previous studies relating to biofilm inhibition and bacterial adherence assay. The *S. palghatense* extracts were reported to contain bioactive agents that inhibit bacterial metabolism, with marginally better activity of the bark extract against *P. aeruginosa*.

7.3.8.3.9. Determination of bacterial load using acridine orange (AO) staining

The results of acridine orange staining reflect the antibacterial activity of SPB AgNPs against *Pseudomonas aeruginosa* biofilms (Plate 7.7). In the control, a large amount of green fluorescence suggests high cell density of viable bacterial cells with intact membranes and double-stranded DNA. This signifies the successful growth of resilient *P. aeruginosa* biofilm under experimental situations. The treated SPB AgNPs exhibited drastically reduced green fluorescence, thereby inhibiting bacterial and biofilm formation. The bacterial cells are more spread out with reduced fluorescent intensity, which correlates with loss of viability. The treated SPB AgNPs showed even more pronounced inhibition with almost no visible green fluorescence, indicating a greater antibacterial activity. This progressive decrease in fluorescence intensity from control to SPB AgNPs follows, as seen in previous quantitative assays, the dose-dependent antibacterial effect of *S. palghatense* extracts. The microscopic evaluation supports direct visual validation for the extracts in reducing bacterial load and inhibiting biofilm formation, with the SPB AgNPs displaying slightly better inhibitory effects toward *P. aeruginosa*.

7.3.8.3.10. Gene expression study

RT-qPCR analysis showing specific roles of SPB AgNPs on lasR gene expression in *Pseudomonas aeruginosa* (Figure 7.9). The SPB AgNPs showed an impressive downregulation in lasR with an end fold change of 0.55, meaning a 45% decrease in the lasR level. This differential response indicates that the bioactive compounds in the bark extract are more potent in inhibiting the Las quorum-sensing system. The higher Ct values observed in bark extract-treated samples (21.10 for lasR) further confirm the inhibitory effect of bark constituents on gene expression.

The results shown in Figure 7.10 highlight an upregulated response of the *Pseudomonas aeruginosa* rhlR gene in response to the SPB AgNPs. Results from RT-qPCR analysis indicated treatment-specific differences in Ct values. Results for the rhlR gene showed that control samples had the least Ct values on average (average 19.36), indicating the highest initial template abundance. The SPB AgNPs demonstrate significantly higher Ct values (average 22.01), accounting for the

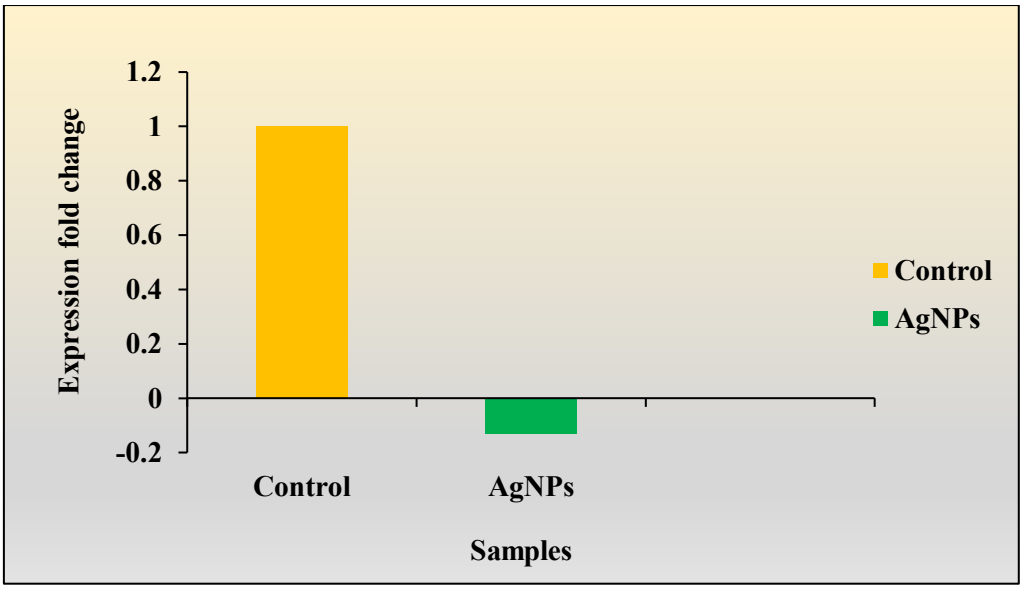


Figure 7.9: RT-qPCR analysis of lasR gene expression in *Pseudomonas aeruginosa* treated with silver nanoparticles (AgNPs) synthesized from the methanol extract of *Syzygium palghatense* bark

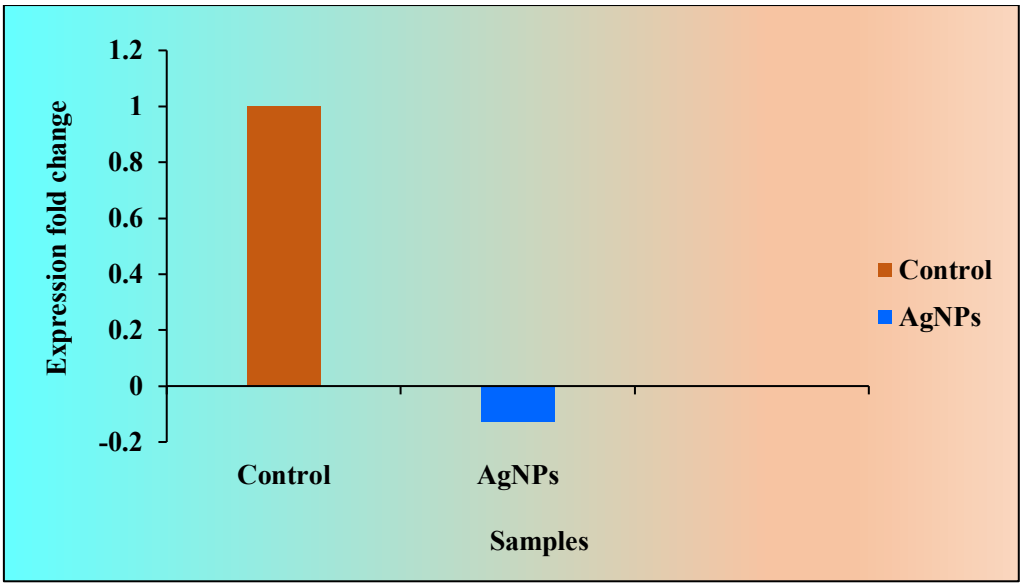


Figure 7.10: RT-qPCR analysis of rhlR gene expression in *Pseudomonas aeruginosa* treated with silver nanoparticles (AgNPs) synthesized from the methanol extract of *Syzygium palghatense* bark

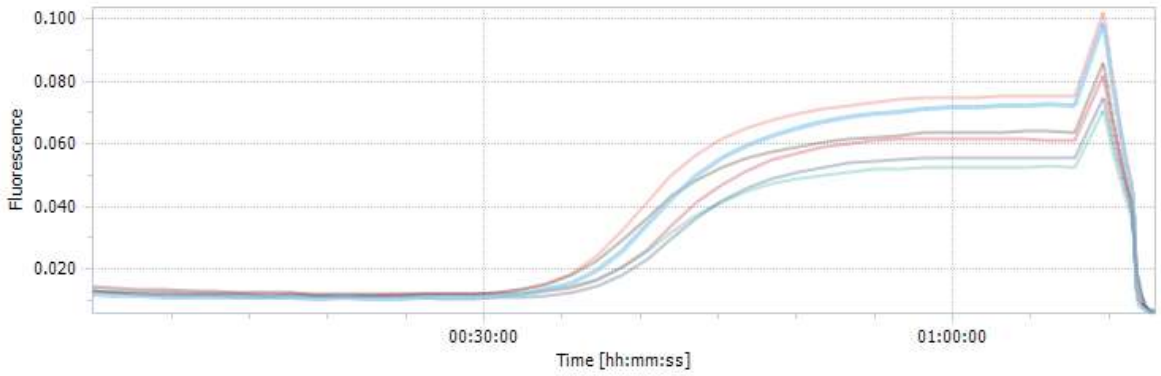


Figure 7.11: Fluorescence curve for the lasR gene

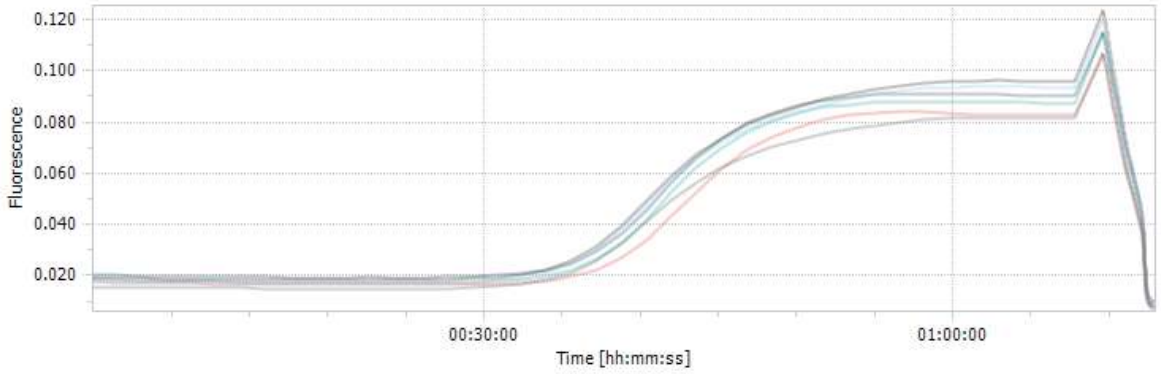


Figure 7.12: Fluorescence curve for the rhIR gene

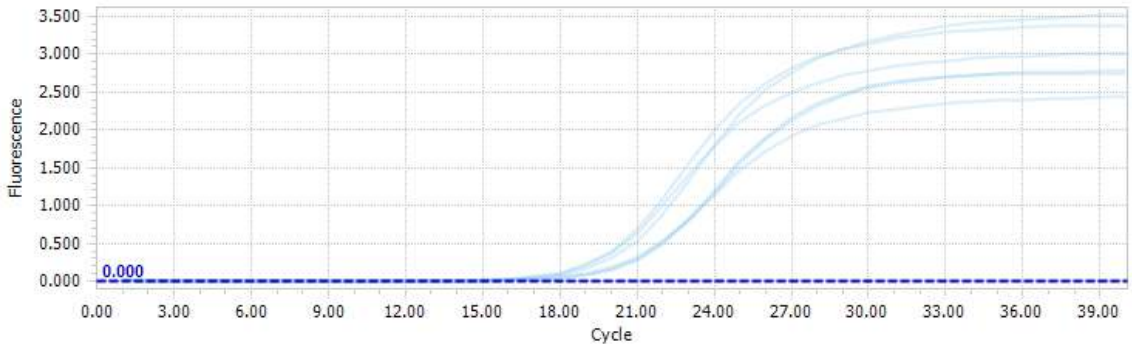


Figure 7.13: PCR Amplification curve for the lasR gene

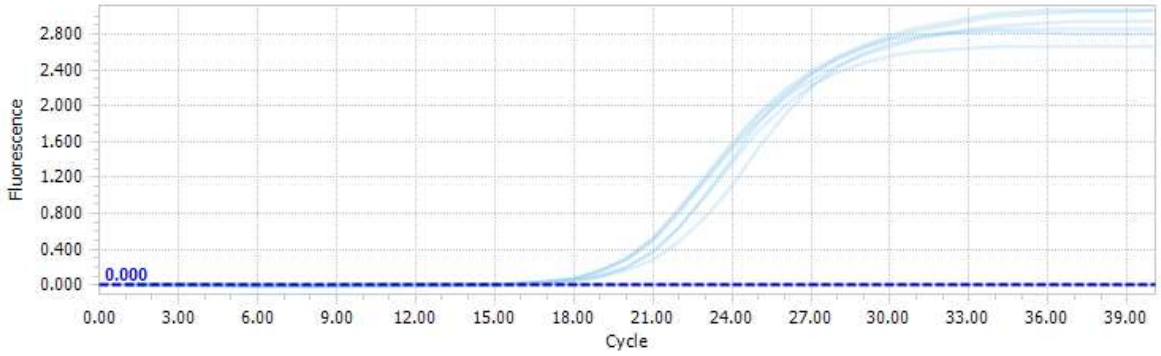


Figure 7.14: PCR Amplification curve for the rhlR gene

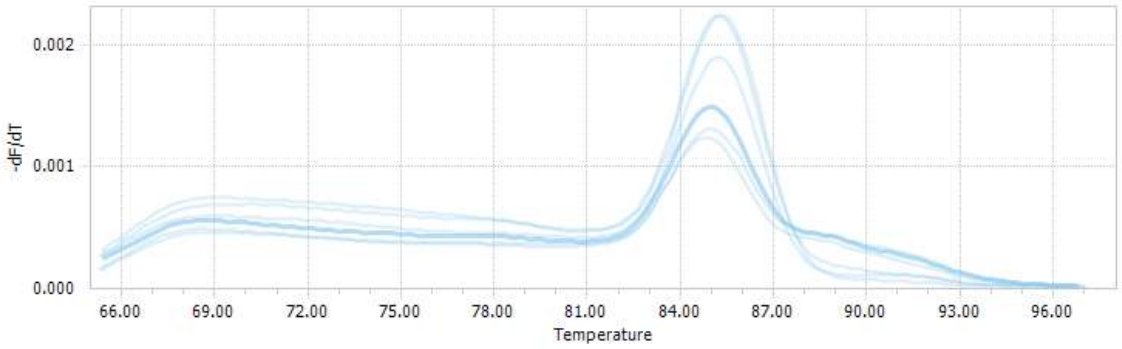


Figure 7.15: Melting peaks for the lasR gene

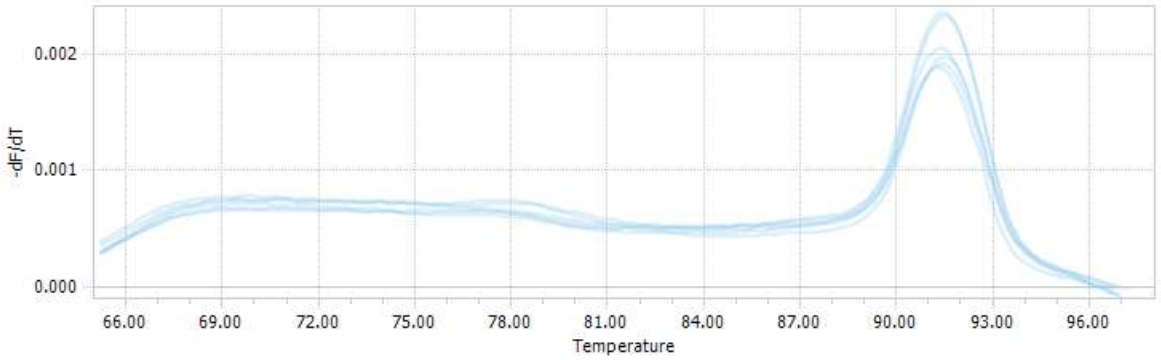


Figure 7.16: Melting peaks for the rhlR gene

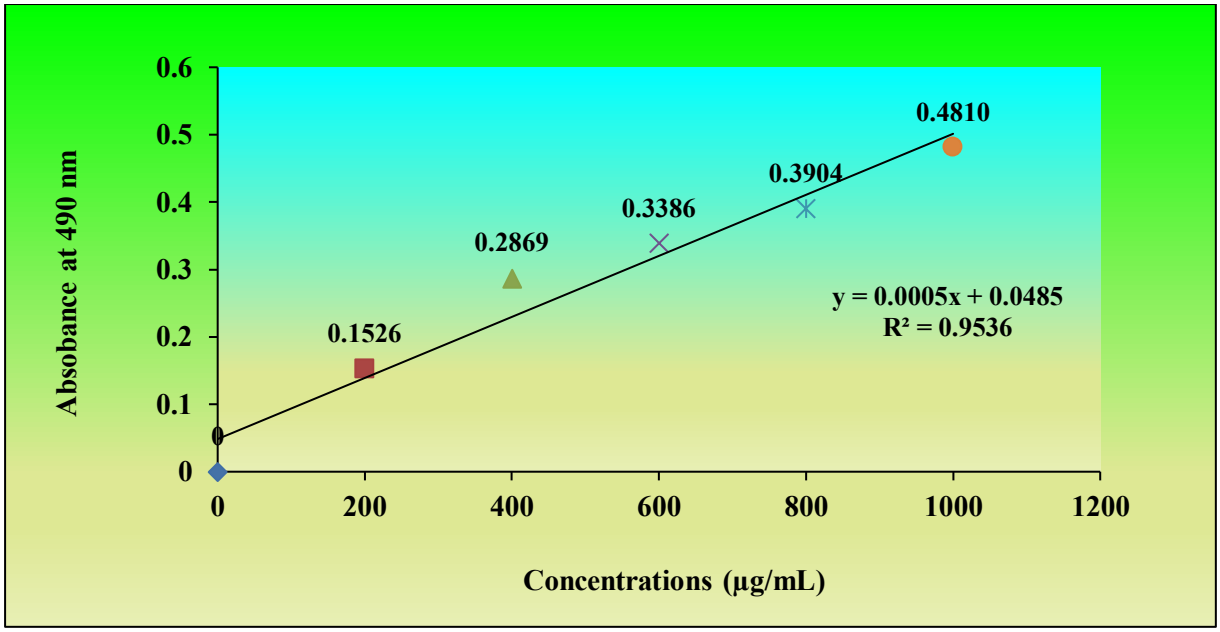


Figure 7.17: Standard calibration curve of glucose for the estimation of carbohydrates in the Extracellular polysaccharide (EPS) quantification

observed greater inhibitory effect of the bark-isolated constituents for rhlR expression. Such a striking difference in the regulation of genes suggests that the bioactive compounds in the SPB AgNPs are more potent against down-regulating the rhIR quorum-sensing system.

Figures 7.11 to 7.16 show the fluorescence curves, amplification curves and melting peaks for the lasR and rhlR genes, respectively.

7.3.8.3.11. EPS quantification

Figure 7.17 presents a standard calibration curve for glucose estimation used in EPS quantification, displaying a strong linear relationship ($R^2 = 0.9536$) between glucose concentration (0-1000 µg/mL) and absorbance at 490 nm. The linear regression equation $y = 0.0005x + 0.0485$ enables accurate conversion of spectrophotometric readings to glucose equivalent concentrations. The concentration points (0, 200, 400, 600, 800, and 1000 µg/mL) with corresponding absorbance values (0, 0.1526, 0.2869, 0.3386, 0.3904, and 0.4810) establish a reliable reference for quantifying extracellular polysaccharides in *Pseudomonas aeruginosa* biofilm samples treated with SPB AgNPs. The high coefficient of determination indicates that the phenol-sulfuric acid method provides consistent and reproducible results for carbohydrate quantification in biofilm analysis.

SPB AgNPs exhibited incredible anti-biofilm activity against EPS production in *Pseudomonas aeruginosa* biofilms, as shown in Table 7.15. Over 2907.6 ± 1.1450 µg/mL of EPS was produced by untreated control biofilms. SPB AgNPs showed the best anti-biofilm activity, with EPS diminished to 942.3 ± 1.0651 µg/mL (67.6% inhibition). SPB AgNPs have higher quantities of bioactive compounds that block EPS biosynthesis pathways. The reduction highlighted here demonstrates the potential of the silver nanoparticles synthesized from the bark methanolic extract to affect biofilm-targeted degradation and reduce its persistence and pathogenicity. Furthermore, since EPS is primarily involved in biofilm architecture and antimicrobial resistance, our results suggest the efficacy of SSPB AgNPs as a potential anti-biofilm agent for *P. aeruginosa* infections.

7.3.9. Anthelmintic properties

The anthelmintic efficacy of silver nanoparticles (AgNPs) synthesized from the methanolic extract of *S. palghatense* bark was evaluated against *Lumbricus terrestris* by measuring paralysis and death times at various concentrations (25–100 mg/mL), compared to albendazole (20 mg/mL) and a distilled water control. The control group showed paralysis and death times of 120.00 ± 2.50 and 150.00 ± 3.10 minutes, respectively. Albendazole exhibited significantly shorter paralysis and death times of 12.25 ± 0.74 and 17.95 ± 0.88 minutes, correlating with an inhibition percentage of 92.0 ± 0.80% (Table 7.16). The AgNP treatments demonstrated a clear dose-dependent activity. At 25 mg/mL, paralysis and death occurred at 18.32 ± 0.95 and 24.53 ± 1.22 minutes, with 83.65 ± 1.24% inhibition. These times significantly decreased with increasing nanoparticle concentration; at 50 mg/mL, the times were 9.45 ± 0.78 and 16.78 ± 1.01 minutes (88.81 ± 1.35% inhibition), while at 75 mg/mL, further reductions to 4.87 ± 0.69 and 9.65 ± 0.85 minutes were observed (93.56 ± 0.25% inhibition). The highest concentration of 100 mg/mL induced the most rapid paralysis and death, at 2.94 ± 0.47 and 5.87 ± 0.68 minutes respectively, exceeding the efficacy of albendazole with an inhibition percentage of 96.08 ± 1.06%. Statistical analysis confirmed that differences in paralysis time, death time, and inhibition percentages among groups were highly significant (F-statistics: paralysis time = 9321.80, death time = 4573.60, inhibition = 1315.20; all $p < 0.001$). The critical difference values at 5% significance level were 1.398 for paralysis time, 2.439 for death time, and 3.058 for inhibition percentage (Figure 7.18-7.19). These findings underline the potent, concentration-dependent anthelmintic activity of silver nanoparticles synthesized from *S. palghatense* bark, suggesting their valuable potential as alternative antiparasitic agents.

7.3.10. Anti-inflammatory properties

7.3.10.1. Human Red Blood Cell membrane stabilization assay (HRBC)

The anti-inflammatory activity of silver nanoparticles (AgNPs) synthesized from the methanol extract of *S. palghatense* bark was assessed by the *in vitro* Human Red Blood Cell membrane stabilization assay (HRBC). The assay was conducted at

Table 7.16: Anthelmintic activity of silver nanoparticles synthesized from the methanol extract of *Syzygium palghatense* bark against *Lumbricus terrestris*

Treatment	Concentration (mg/mL)	Time taken for paralysis (minutes)	Time taken for death (minutes)	Inhibition percentage (%)
Control (Distilled water)	0	120.00 ± 2.50^{a}	150.00 ± 3.10^{a}	0.0 ± 0.00^{e}
Standard (Albendazole)	20	12.25 ± 0.74^{c}	17.95 ± 0.88^{c}	92.0 ± 0.80^{b}
Silver nanoparticles (AgNps)	25	18.32 ± 0.95^{b}	24.53 ± 1.22^{b}	83.65 ± 1.24^{d}
	50	9.45 ± 0.78^{d}	16.78 ± 1.01^{c}	88.81 ± 1.35^{c}
	75	4.87 ± 0.69^{e}	9.65 ± 0.85^{d}	93.56 ± 0.25^{ab}
	100	2.94 ± 0.47^{f}	5.87 ± 0.68^{e}	96.08 ± 1.06^{a}
F-stat		9321.80	4573.60	1315.20
P-value		<0.001	<0.001	<0.001
CD value at 5%		1.398	2.439	3.058

Values are expressed as mean ± standard error (n = 6). Statistical significance was determined by one-way ANOVA followed by the critical difference (CD) test at the 5% significance level. Different superscript letters within each column indicate significant differences ($p < 0.05$)

Table 7.17: Anti-inflammatory activity of silver nanoparticles synthesized from *Syzygium palghatense* bark methanolic extract assessed by Human Red Blood Cell membrane stabilization assay (HRBC)

Concentration (µg/mL)	Percentage inhibition
10	9.47 ± 0.32
20	16.34 ± 0.34
30	21.09 ± 0.49
40	26.66 ± 0.67
50	31.40 ± 0.61
60	43.76 ± 0.36
70	48.60 ± 0.30
80	53.95 ± 0.09
90	63.29 ± 0.36
100	74.02 ± 0.03
F-stat	2753.88
P-value	<0.001
CD at 5%	1.20

Values are expressed as mean ± standard error (n = 6). Statistical significance was evaluated using one-way ANOVA followed by a critical difference (CD) test at the 5% significance level. Differences were considered statistically significant at $p < 0.05$

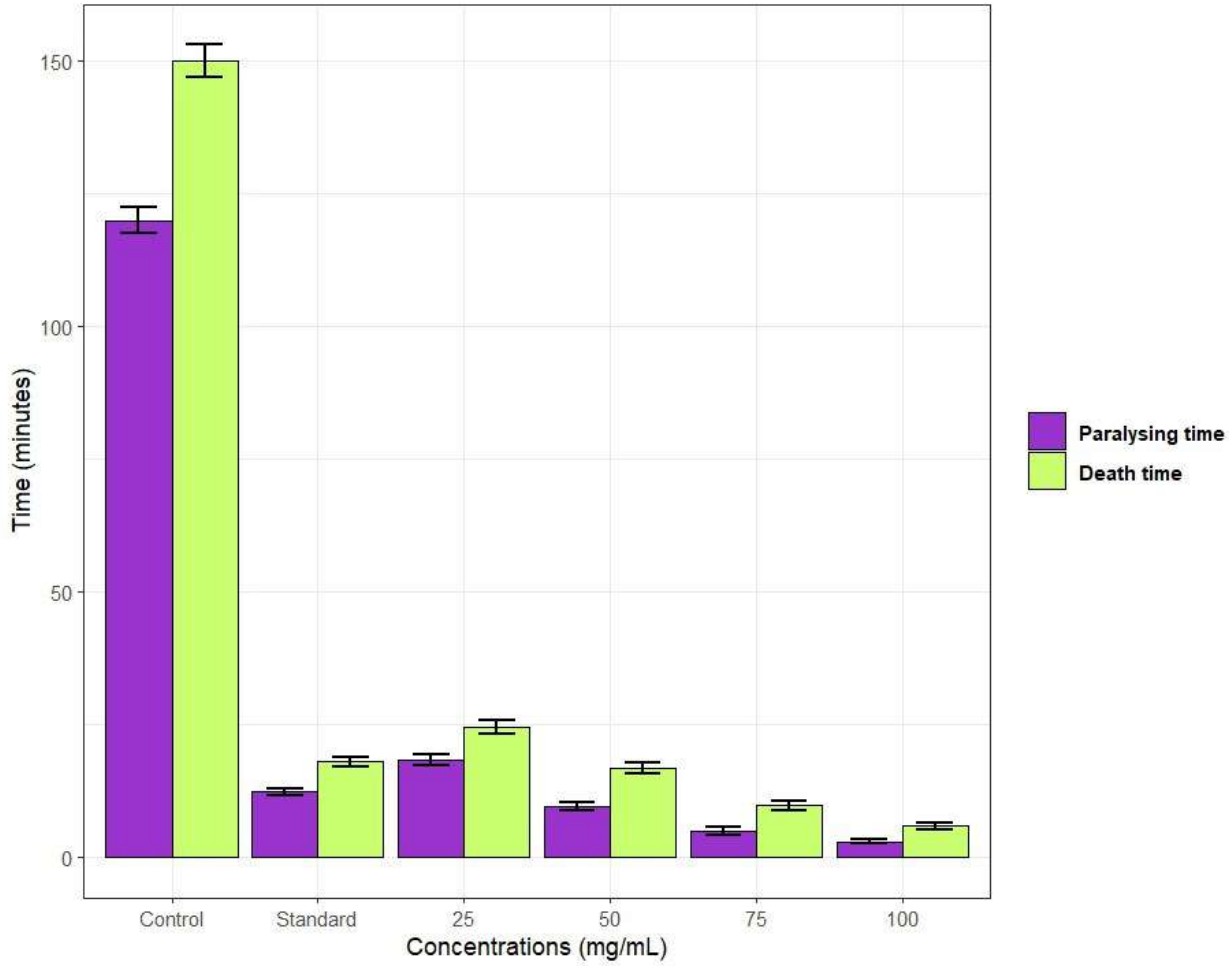


Figure 7.18: Dose-dependent anthelmintic efficacy of silver nanoparticles synthesized from the methanol extract *of Syzygium palghatense* bark against *Lumbricus terrestris*, expressed as paralysis and death time at increasing concentrations (mean ± SE, n = 6)

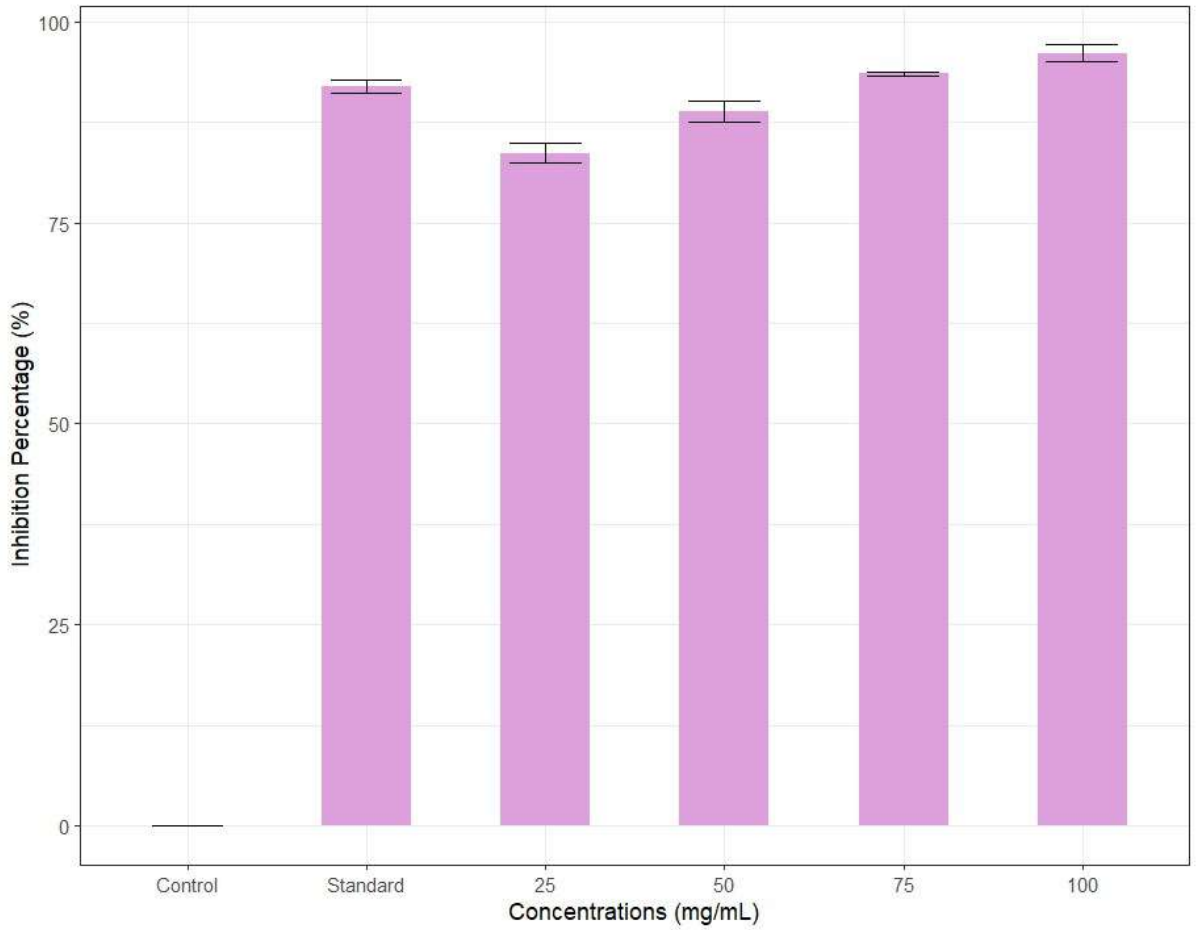


Figure 7.19: Dose-dependent anthelmintic efficacy of silver nanoparticles synthesized from the methanol extract of *Syzygium palghatense* bark against *Lumbricus terrestris*, expressed as inhibition percentage at increasing concentrations (mean ± SE, n=6)

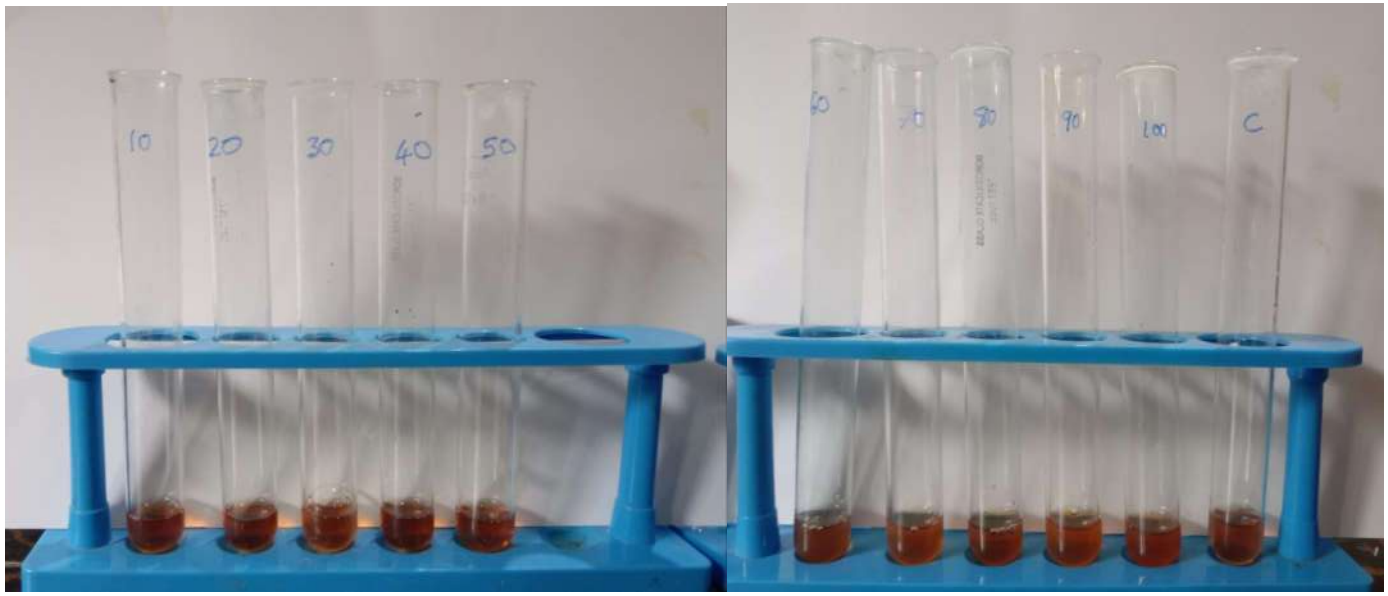


Plate 7.9: Demonstration of anti-inflammatory activity by silver nanoparticles synthesized from *Syzygium palghatense* bark using the Human Red Blood Cell membrane stabilization assay (HRBC). Test tubes display varying degrees of haemolysis inhibition at increasing nanoparticle concentrations (10–100 µg/mL) and the control

concentrations ranging from 10 to 100 µg/mL, where the percentage inhibition of haemolysis was measured as an indicator of membrane stabilization (Plate 7.9). Results showed a concentration-dependent increase in membrane stabilization, with inhibition values ranging from approximately 9% at 10 µg/mL to about 74% at 100 µg/mL. These findings suggest that the AgNPs effectively protect the HRBC membrane against hypotonic stress-induced lysis, reflecting their potential as potent anti-inflammatory agents through membrane-stabilizing mechanisms (Table 7.17).

7.3.10.2. Inhibition of protein denaturation

The protein denaturation inhibition assay is a widely used preliminary *in vitro* method to evaluate the anti-inflammatory potential of compounds by measuring their ability to prevent the denaturation of proteins under heat stress. This assay mimics the inflammatory response where protein denaturation leads to tissue damage, and inhibition of this process correlates with anti-inflammatory activity (Arulselvan et al., 2016).

In this study, silver nanoparticles (AgNPs) synthesized from *S. palghatense* bark demonstrated a clear, concentration-dependent increase in protein denaturation inhibition. The percentage inhibition of denaturation by AgNPs ranged from 20.47% ± 0.69 at 62.5 µg/mL to a maximum of 85.10% ± 0.38 at 500 µg/mL. These findings indicate strong stabilization of protein structure and significant anti-inflammatory potential of the AgNPs at higher concentrations.

For comparison, standard diclofenac sodium, a known non-steroidal anti-inflammatory drug (NSAID), also showed concentration-dependent inhibition ranging from 18.5% ± 0.5 to 78.0% ± 1.1 in the same concentration range. Notably, AgNPs exhibited slightly superior inhibition at each concentration, especially at 500 µg/mL, highlighting their promising efficacy.

Statistical analysis using one-way ANOVA revealed highly significant differences in protein denaturation inhibition across the tested concentrations for both diclofenac sodium ($F = 28.45$, $p < 0.001$) and AgNPs ($F = 42.17$, $p < 0.001$). The Critical Difference (CD) values at 5% significance level were 3.12 for diclofenac

sodium and 2.97 for AgNPs, confirming that the observed dose-dependent differences are statistically meaningful (Table 7.18).

The lower IC_{50} value of AgNPs indicates higher potency as it requires a lower concentration to inhibit 50% of the protein denaturation compared to diclofenac sodium. The higher F-statistic for AgNPs suggests greater variance explained by treatment concentration, confirming a stronger effect size in this group. With p-values less than 0.001 for both samples, the differences observed are statistically highly significant. The critical differences (CD) confirm that the differences in inhibition percentages between concentration groups are meaningful and not due to random variation (Table 7.19).

Therefore, silver nanoparticles derived from *S. palghatense* bark exhibit significantly greater anti-inflammatory efficacy than the standard diclofenac sodium under the conditions tested, endorsing their potential for future therapeutic development (Khan et al., 2019).

7.3.10.3. Proteinase inhibitory activity

The data show that silver nanoparticles (AgNPs) synthesized from *S. palghatense* bark exhibit significant proteinase inhibitory activity compared to standard diclofenac sodium. Percentage inhibition increased with concentration for both AgNPs and diclofenac sodium, with AgNPs consistently showing higher inhibition at each concentration tested. At 500 µg/mL, AgNPs achieved 67.10% ± 0.20 inhibition, while diclofenac sodium achieved 65.21% ± 1.21 (Table 7.20).

Statistical analysis confirmed significant differences among concentration groups for both treatments. The F-statistic for AgNPs (38.17) was higher than that of diclofenac sodium (22.45), indicating a stronger effect size. Both yielded p-values < 0.001, signifying highly significant results. The critical difference (CD) values at 5% significance were 2.84 for AgNPs and 3.03 for diclofenac, confirming that the variations between groups are statistically meaningful.

Additionally, the IC_{50} value for AgNPs was notably lower (20 µg/mL) than that of diclofenac sodium (58 µg/mL), demonstrating that AgNPs are more potent

Table 7.18: Protein denaturation inhibition by silver nanoparticles (AgNPs) Synthesized from *Syzygium palghatense* bark

Concentration (µg/mL)	Standard Diclofenac sodium Percentage of inhibition (%)	AgNPs Percentage of inhibition (%)
Control	0	0
62.5	18.5 ± 0.5	20.47 ± 0.69
125	35± 0.7	38.65 ± 0.58
250	56.0 ± 0.9	57.34 ± 0.49
500	78.0 ± 1.1	85.10 ± 0.38
F-stat	28.45	42.17
P-value	<0.001	<0.001
CD at 5%	3.12	2.97

Values are expressed as mean ± standard error (n = 6). Statistical significance was evaluated using one-way ANOVA followed by a critical difference (CD) test at the 5% significance level. Differences were considered statistically significant at $p < 0.05$

Table 7.19: IC_{50} value of silver nanoparticles (AgNPs) synthesized from *Syzygium palghatense* bark in Protein denaturation inhibition

Samples	IC_{50} value (%)	F stat	P value	CD at 5%
Standard Diclofenac sodium	55 ± 0.103	27.56	<0.001	3.10
Silver nanoparticles (AgNPs) synthesized from *Syzygium palghatense* bark	12 ± 0.420	40.12	<0.001	2.85

Values are expressed as mean ± standard error (n = 6). Statistical significance was evaluated using one-way ANOVA followed by a critical difference (CD) test at the 5% significance level. Differences were considered statistically significant at $p < 0.05$

Table 7.20: Proteinase inhibitory activity by silver nanoparticles (AgNPs) Synthesized from *Syzygium palghatense* bark

Concentration (µg/mL)	Standard Diclofenac sodium Percentage of inhibition (%)	AgNPs Percentage of inhibition (%)
Control	0	0
62.5	15.5 ± 0.45	19.47 ± 0.59
125	28.01± 0.62	28.65 ± 0.48
250	44.05 ± 0.59	47.14 ± 0.40
500	65.21 ± 1.21	67.10 ± 0.20
F-stat	22.45	38.17
P-value	<0.001	<0.001
CD at 5%	3.03	2.84

Values are expressed as mean ± standard error (n = 6). Statistical significance was evaluated using one-way ANOVA followed by a critical difference (CD) test at the 5% significance level. Differences were considered statistically significant at $p < 0.05$

inhibitors of proteinase activity. This is further supported by the higher F-statistic (38.11) and lower CD (2.65) for AgNPs in the IC_{50} analysis, all pointing to statistically significant and biologically relevant differences (Table 7.21).

These results collectively suggest that silver nanoparticles derived from *S. palghatense* bark have a stronger proteinase inhibitory effect and potentially greater anti-inflammatory activity compared to standard diclofenac sodium. The enhanced efficacy of the biosynthesized AgNPs highlights their promise as alternative or complementary agents in inflammation-related therapies.

7.3.10.4. Cyclooxygenase (COX) activity

The cyclooxygenase (COX) activity assay results revealed that silver nanoparticles (AgNPs) synthesized from *S. palghatense* bark exhibit significant COX inhibition, indicating their potential anti-inflammatory effects. The percentage of inhibition increased progressively with concentration; at 500 µg/mL, AgNPs achieved 64.10% inhibition, slightly higher than the 63.11% observed for the standard indomethacin. Statistical analysis demonstrated significant differences among groups, with an F-statistic of 31.10 and a p-value less than 0.001 for AgNPs, confirming reliable inhibition (Table 7.22).

Furthermore, the IC_{50} value for AgNPs (25 µg/mL) was markedly lower than that of indomethacin (60 µg/mL), highlighting the higher potency of the nanoparticles in inhibiting COX activity. The corresponding F-statistic and critical difference (CD) values also underscored the significance of the inhibitory effect. These findings suggest that AgNPs from *S. palghatense* possess potent cyclooxygenase inhibitory activity comparable or superior to indomethacin, positioning them as promising candidates for anti-inflammatory therapeutic applications (Table 7.23).

7.3.10.5. Lipoxygenase (LOX) activity

The lipoxygenase (LOX) activity assay results demonstrate that silver nanoparticles (AgNPs) synthesized from *S. palghatense* bark exhibit significant LOX inhibitory activity, which is crucial in mediating inflammatory and allergic reactions. The percentage inhibition increased with concentration for both the AgNPs and the

standard Nordihydroguaiaretic acid (NDGA), with AgNPs showing consistently higher inhibition. At the highest concentration of 500 µg/mL, AgNPs inhibited LOX activity by 74.50% ± 0.1 compared to 66.11% ± 1.05 inhibition by NDGA (Table 7.24).

Statistical analysis showed strong significance, with F-statistics of 35.10 for AgNPs and 25.15 for NDGA, both with p-values less than 0.001. The critical difference (CD) values of 3.81 for AgNPs and 4.01 for NDGA further support the reliability of these findings.

Moreover, the IC_{50} value of AgNPs (19 µg/mL) was substantially lower than that of NDGA (57 µg/mL), indicating the superior potency of the synthesized nanoparticles in inhibiting LOX activity. The higher F-statistic and comparable CD value for AgNPs reinforce the statistical robustness of this enhanced effect (Table 7.25).

Overall, these results suggest that silver nanoparticles derived from *S. palghatense* bark possess strong lipoxygenase inhibitory activity, even surpassing the standard NDGA, highlighting their potential as effective anti-inflammatory agents.

7.3.10.6. Myeloperoxidase (MPO) activity

Table 7.26 shows that the ΔOD (absorbance) and MPO enzyme activity decrease progressively with increasing concentrations of AgNPs, from 62.5 to 500 µg/mL, compared to control and standard samples. This decline illustrates a dose-dependent inhibition of MPO activity by these silver nanoparticles. The F-statistic of 45.32 and a highly significant p-value less than 0.001 confirm that the differences observed between sample groups are statistically significant. The Critical Difference (CD) at 5% (0.0025) further validates that the reduction in enzyme activity with AgNP treatment is meaningful and not due to chance.

Table 7.27 compares the IC_{50} values, showing that AgNPs have a substantially lower IC_{50} (36%) than the standard MPO enzyme inhibitor (57%). This indicates that the synthesized AgNPs from *S. palghatense* bark are more potent inhibitors of MPO

Table 7.21: IC_{50} value of silver nanoparticles (AgNPs) Synthesized from *Syzygium palghatense* bark in Proteinase inhibitory activity

Samples	IC_{50} value (%)	F stat	P value	CD at 5%
Standard Diclofenac sodium	58 ± 0.102	25.16	<0.001	2.90
Silver nanoparticles (AgNPs) synthesized from *Syzygium palghatense* bark	20 ± 0.302	38.11	<0.001	2.65

Values are expressed as mean ± standard error (n = 6). Statistical significance was evaluated using one-way ANOVA followed by a critical difference (CD) test at the 5% significance level. Differences were considered statistically significant at $p < 0.0$

Table 7.22: Cyclooxygenase (COX) activity by silver nanoparticles (AgNPs) Synthesized from *Syzygium palghatense* bark

Concentration (µg/mL)	Standard Indomethacin Percentage of inhibition (%)	AgNPs Percentage of inhibition (%)
Control	0	0
62.5	14.1 ± 0.40	17.47 ± 0.59
125	25.01± 0.12	26.15 ± 0.28
250	43.05 ± 0.29	45.14 ± 0.10
500	63.11 ± 1.01	64.10 ± 0.10
F-stat	21.35	31.10
P-value	<0.001	<0.001
CD at 5%	3.01	2.80

Values are expressed as mean ± standard error (n = 6). Statistical significance was evaluated using one-way ANOVA followed by a critical difference (CD) test at the 5% significance level. Differences were considered statistically significant at $p < 0.05$

Table 7.23: IC_{50} value of silver nanoparticles (AgNPs) synthesized from *Syzygium palghatense* bark in Cyclooxygenase (COX) activity

Samples	IC_{50} value (%)	F stat	P value	CD at 5%
Standard Indomethacin	60 ± 0.120	24.16	<0.001	2.80
Silver nanoparticles (AgNPs) synthesized from *Syzygium palghatense* bark	25 ± 0.350	35.11	<0.001	2.55

Values are expressed as mean ± standard error (n = 6). Statistical significance was evaluated using one-way ANOVA followed by a critical difference (CD) test at the 5% significance level. Differences were considered statistically significant at $p < 0.0$

Table 7.24: Lipoxygenase (LOX) activity by silver nanoparticles (AgNPs) Synthesized from *Syzygium palghatense* bark

Concentration (µg/mL)	Standard Nordihydroguaiaretic acid Percentage of inhibition (%)	AgNPs Percentage of inhibition (%)
Control	0	0
62.5	24.1 ± 0.10	27.37 ± 0.51
125	35.01± 0.10	36.05 ± 0.22
250	56.05 ± 0.22	65.34 ± 0.14
500	66.11 ± 1.05	74.50 ± 0.11
F-stat	25.15	35.10
P-value	<0.001	<0.001
CD at 5%	4.01	3.81

Values are expressed as mean ± standard error (n = 6). Statistical significance was evaluated using one-way ANOVA followed by a critical difference (CD) test at the 5% significance level. Differences were considered statistically significant at $p < 0.05$

Table 7.25: IC_{50} value of silver nanoparticles (AgNPs) synthesized from *Syzygium palghatense* bark in Lipoxygenase (LOX) activity

Samples	IC_{50} value (%)	F stat	P value	CD at 5%
Standard Nordihydroguaiaretic acid	57 ± 0.012	34.11	<0.001	3.99
Silver nanoparticles (AgNPs) synthesized from *Syzygium palghatense* bark	19 ± 0.302	38.18	<0.001	3.85

Values are expressed as mean ± standard error (n = 6). Statistical significance was evaluated using one-way ANOVA followed by a critical difference (CD) test at the 5% significance level. Differences were considered statistically significant at $p < 0.0$

Table 7.26: Myeloperoxidase (MPO) activity by silver nanoparticles (AgNPs) synthesized from *Syzygium palghatense* bark

Concentration (µg/mL)	ΔOD (Absorbance at 460 nm)	MPO activity (U/mL)
Control	0.0237 ± 0.0101	0.007821 ± 0.0010
Standard	0.0201 ± 0.0145	0.007010 ± 0.0014
62.5	0.0156 ± 0.0126 ±	0.005148 ± 0.0013
125	0.0134 ± 0.0135	0.004422 ± 0.0014
250	0.0034 ± 0.0150	0.001122 v 0.0016
500	0.0021 ± 0.0125	0.001011 ± 0.0011
F-stat		45.32
P-value		<0.001
CD at 5%		0.0025

Values are expressed as mean ± standard error (n = 6). Statistical significance was evaluated using one-way ANOVA followed by a critical difference (CD) test at the 5% significance level. Differences were considered statistically significant at $p < 0.05$

Table 7.27: IC_{50} value of silver nanoparticles (AgNPs) synthesized from *Syzygium palghatense* bark in Myeloperoxidase (MPO) activity

Samples	IC_{50} value (%)	F stat	P value	CD at 5%
Standard Myeloperoxidase enzyme	57 ± 0.012	22.85	<0.001	2.60
Silver nanoparticles (AgNPs) synthesized from *Syzygium palghatense* bark	36 ± 0.123	38.11	<0.001	2.55

Values are expressed as mean ± standard error (n = 6). Statistical significance was evaluated using one-way ANOVA followed by a critical difference (CD) test at the 5% significance level. Differences were considered statistically significant at $p < 0.0$

Table 7.28: Inducible Nitric Oxide Synthase (iNOS) activity by silver nanoparticles (AgNPs) Synthesized from *Syzygium palghatense* bark

Concentration (µg/mL)	OD at 0 minutes	OD at 5 minutes	ΔOD (OD0 - OD5)	Percentage of inhibition
LPS	0.1245 ± 0.051	0.1042 ± 0.020	0.0203 ± 0.015	
Control	0.1234 ± 0.025	0.1040 ± 0.010	0.0201 ± 0.012	0
Standard	0.1179 ± 0.001	0.1008 ± 0.012	0.0171 ± 0.013	15.76 ± 0.014
62.5	0.1232 ± 0.014	0.1106 ± 0.030	0.0126 ± 0.002	37.93 ±0.124
125	0.1135 ± 0.042	0.1025 ± 0.015	0.0110 ± 0.014	37.70 ± 0.415
250	0.1100 ±0.020	0.1045 ± 0.015	0.0075 ± 0.013	50.99 ±0.230
500	0.1294 ± 0.010	0.1195 ± 0.014	0.0099 ± 0.018	51.23 ± 0.145
F-stat				28.45
P-value				<0.001
CD at 5%				0.0028

Values are expressed as mean ± standard error (n = 6). Statistical significance was evaluated using one-way ANOVA followed by a critical difference (CD) test at the 5% significance level. Differences were considered statistically significant at $p < 0.05$

Table 7.29: IC_{50} value of silver nanoparticles (AgNPs) synthesized from *Syzygium palghatense* bark in Inducible Nitric Oxide Synthase (iNOS) activity

Samples	IC_{50} value (%)	F stat	P value	CD at 5%
Standard Recombinant or purified iNOS	55 ± 0.102	22.75	<0.001	2.60
Silver nanoparticles (AgNPs) synthesized from *Syzygium palghatense* bark	35 ± 0.125	38.20	<0.001	2.4

Values are expressed as mean ± standard error (n = 6). Statistical significance was evaluated using one-way ANOVA followed by a critical difference (CD) test at the 5% significance level. Differences were considered statistically significant at $p < 0.0$

activity. The statistical parameters ($F = 38.11$, $p < 0.001$, $CD = 2.55$) also support the significant difference in inhibitory effects between AgNPs and the standard.

Overall, these findings reveal that silver nanoparticles biosynthesized from *S. palghatense* bark effectively inhibit MPO activity in a dose-dependent manner with statistically significant potency surpassing that of the standard enzyme inhibitor. This supports their potential application as anti-inflammatory agents by modulating MPO-related oxidative processes.

7.3.10.7. Inducible Nitric Oxide Synthase (iNOS) activity

The data in Table 7.28 shows a progressive decrease in iNOS activity, as indicated by the decreasing OD difference (ΔOD) with increasing concentrations of AgNPs, compared to the control and standard. The percentage of inhibition increases with higher AgNP concentrations, reaching a maximum of around 51% inhibition at 500 µg/mL. This demonstrates a dose-dependent inhibitory effect of the synthesized AgNPs on iNOS activity, which is significant since iNOS plays a crucial role in producing nitric oxide, a mediator in inflammatory responses.

The statistical analysis supports these findings, with an F-statistic value of 28.45 and a p-value less than 0.001, indicating significant differences in iNOS activity between sample groups. The critical difference (CD) value of 0.0028 at 5% significance level confirms that the observed changes in enzyme activity with treatment are statistically meaningful.

Table 7.29 compares the IC_{50} values of AgNPs and standard recombinant or purified iNOS enzyme inhibitors in suppressing iNOS activity. The AgNPs exhibit a lower IC_{50} value (35%) than the standard (55%), suggesting that the silver nanoparticles have a stronger inhibitory effect on iNOS. This is further supported by the higher F-statistic (38.20) and similarly significant p-value (< 0.001) for AgNPs compared to the standard. The CD at 5% (2.4) indicates the threshold for significant differences in this comparison.

In summary, the synthesized silver nanoparticles from *S. palghatense* bark effectively inhibit iNOS activity in a dose-dependent manner with statistically

significant potency exceeding that of the standard inhibitor. These findings highlight the potential of these nanoparticles as anti-inflammatory agents by mitigating nitric oxide-mediated inflammation.

7.3.10.8. Estimation of Cellular Nitrite Levels

The data presented in Table 7.30 shows that silver nanoparticles (AgNPs) synthesized from *S. palghatense* bark significantly reduce cellular nitrite levels in a dose-dependent manner compared to the LPS-stimulated positive control. The progressive decrease in both optical density (OD) and nitrite concentration with increasing AgNP concentration from 62.5 to 500 µg/mL indicates effective inhibition of nitric oxide production, which is a key marker of inflammation. The statistical analysis confirms this conclusion, with a high F-statistic value of 35.72 and a highly significant p-value (<0.001), demonstrating that the differences among different concentrations are statistically meaningful. The critical difference (CD) at 5% of 8.75 µg nitrite further confirms that the observed inhibitory effects exceed the threshold for significance.

Table 7.31 further supports the potency of these AgNPs by comparing their half-maximal inhibitory concentration (IC_{50}) values with that of a standard recombinant or purified inducible nitric oxide synthase (iNOS). The AgNPs show a significantly lower IC_{50} value (35% ± 0.251) than the standard (55% ± 0.241), indicating stronger inhibitory activity against nitric oxide production. This is corroborated by corresponding statistical values (F-statistic of 38.20, p-value <0.001, CD at 5% of 2.4), emphasizing the efficacy and reliability of the AgNPs in modulating iNOS activity.

Together, these results demonstrate that AgNPs derived from *S. palghatense* possess potent anti-inflammatory properties by effectively suppressing iNOS-mediated nitric oxide production. This suggests their therapeutic potential in managing inflammation-related conditions through natural, biogenic nanoparticle interventions.

Table 7.30: Estimation of cellular nitrite levels silver nanoparticles (AgNPs) Synthesized from *Syzygium palghatense* bark

Concentration (µg/mL)	OD	Concentration of Nitrite (µg)
LPS	0.0964 ± 0.0012	477.18 ± 0.010
Control	0.0742 ± 0.0120	367.29 ± 0.123
Standard	0.0511 ± 0.0130	252.945± 0.201
62.5	0.0325 ± 0.0140	160.875 ± 0.304
125	0.0321 ± 0.0144	159.213 ± 0.325
250	0.0200 ± 0.0125	155.210 ± 0.324
500	0.0129 ± 0.0120	145.023 ± 0.652
F-stat		35.72
P-value		<0.001
CD at 5%		8.75

Values are expressed as mean ± standard error (n = 6). Statistical significance was evaluated using one-way ANOVA followed by a critical difference (CD) test at the 5% significance level. Differences were considered statistically significant at $p < 0.05$

Table 7.31: IC_{50} value of silver nanoparticles (AgNPs) synthesized from *Syzygium palghatense* bark in cellular nitrite levels

Samples	IC_{50} value (%)	F stat	P value	CD at 5%
Standard Recombinant or purified iNOS	55 ±0.241	22.75	<0.001	2.60
Silver nanoparticles (AgNPs) synthesized from *Syzygium palghatense* bark	35 ± 0.251	38.20	<0.001	2.4

Values are expressed as mean ± standard error (n = 6). Statistical significance was evaluated using one-way ANOVA followed by a critical difference (CD) test at the 5% significance level. Differences were considered statistically significant at $p < 0.0$

Table 7.32: Caudal fin regeneration (cm) in Zebrafish over 15 days post-amputation for control and silver nanoparticles synthesized from the methanol extract of *Syzygium palghatense* bark-treated groups

Day	Group – 1 (Control)	Group – 2 (Treated)
0th d	2.5 cm	2.3 cm
3rd d	2.5 cm	2.7 cm
6th d	2.6 cm	2.9 cm
9th d	2.6 cm	2.9 cm
12th d	2.9 cm	3.0 cm
15th d	3.0 cm	3.2 cm

(Group 1 fishes were fed normal fish food; Group 2 fishes were treated with a combination of normal fish food and synthesized nanoparticles (1 mg/mL). Measurements were recorded at specified days post-amputation)

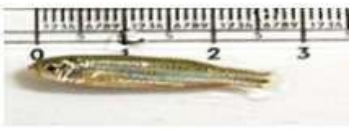
Day	Group – 1 (Control)	Group – 2 (Treated)
0th d		
3rd d		
6th d		
9th d		
12th d		
15th d		

Plate 7.10: Caudal fin regeneration (cm) in Zebrafish over 15 days post-amputation for control and silver nanoparticles synthesized from the *Syzygium palghatense* bark - treated groups

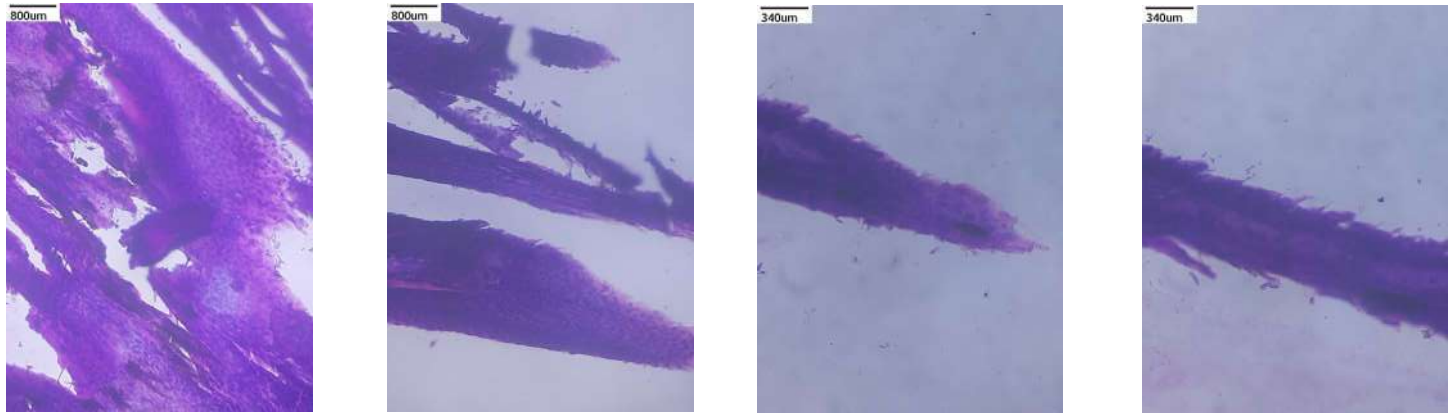


Plate 7.11: Baseline histological sections of zebrafish caudal fin tissue before treatment, stained with Haematoxylin and Eosin (H&E). Micrographs at 10X and 40X magnification show intact tissue architecture and normal cellular organization. Scale bars represent 800 µm and 340 µm

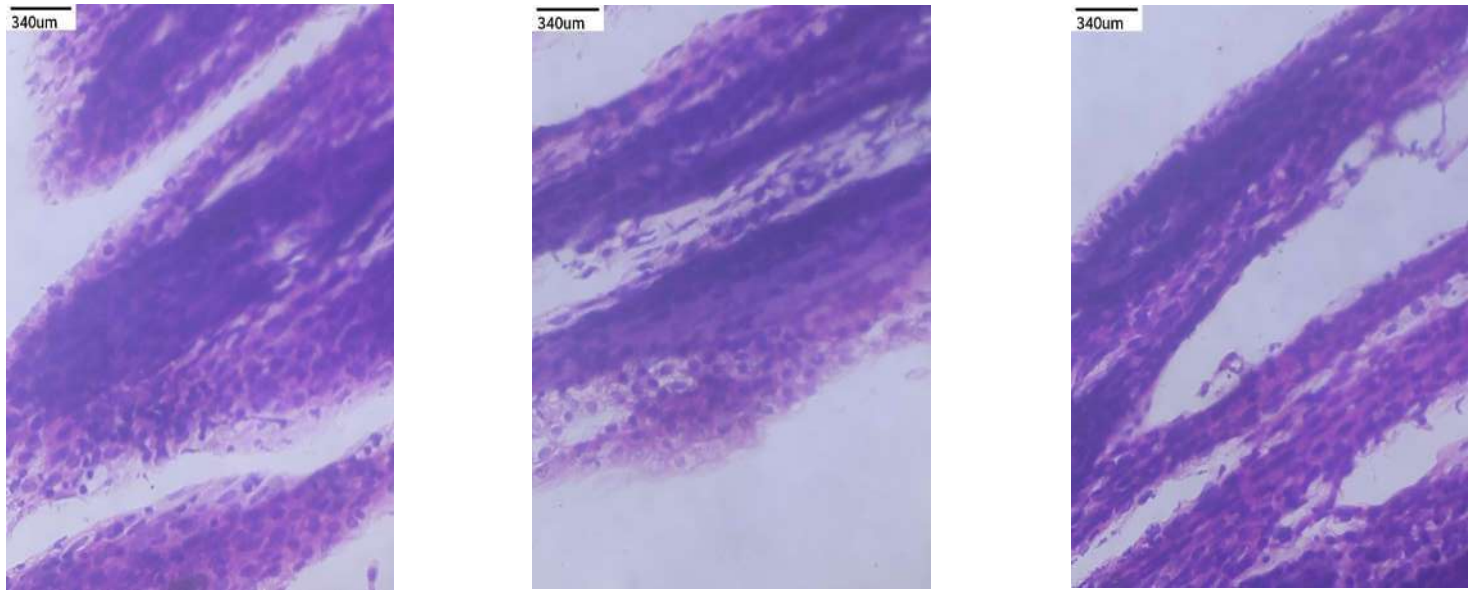


Plate 7.12: Histological sections of zebrafish caudal fin tissue after treatment, stained with Haematoxylin and Eosin (H&E). Images captured at 40X magnification display regenerated tissue architecture and cellular organization following experimental intervention. Scale bar: 340 µm

7.3.11. Histopathology and wound healing studies

The zebrafish in the treated group, exposed to silver nanoparticles synthesized from *S. palghatense* bark, exhibited enhanced caudal fin regeneration compared to the control group. Measurements revealed a progressive increase in fin length, from approximately 2.3 cm at day 0 to 3.2 cm at day 15 in treated fish, surpassing the control group's 3.0 cm fin length by day 15. Notably, treated fish demonstrated faster regeneration rates during the first 9 days post-amputation (Table 7.32).

Histological analysis showed well-organized tissue architecture in regenerated fins from treated fish, including the formation of new blood vessels and no signs of cellular disruption or atypia. These observations indicate that nanoparticles promote effective tissue regeneration and vascularization without cytotoxic effects.

The accelerated regeneration in the treated group supports the hepatoprotective and pro-regenerative potential of the nanoparticles synthesized, contributing to improved wound healing in zebrafish.

Images of caudal fins after amputation and treatment with nanoparticles are shown in Plate 7.10. Group 1 refers to control fish fed with normal fish food; Group 2 refers to fish treated with normal fish food supplemented with synthesized silver nanoparticles (1 mg/mL). Measurements were recorded at 0, 3, 6, 9, 12, and 15 days post-amputation. The results showed that caudal fins treated with nanoparticles were significantly regenerated compared to the control group. The 1 mg/mL treatment had the highest and fastest regenerative rate. These data indicated that the regeneration of caudal fin tissue was accelerated when the silver nanoparticles synthesized from the *S. palghatense* bark concentrations were increased.

Plate 7.11 displays the baseline histological morphology of zebrafish caudal fin tissue prior to experimental treatment. The haematoxylin and eosin-stained sections, captured at both 10X and 40X magnifications, illustrate an intact and well-organized tissue architecture characterized by uniformly arranged cells and clearly defined fin rays. This morphology is indicative of healthy fin tissue, with no evidence of injury or regenerative activity.

In contrast, Plate 7.12 depicts histological sections following treatment with synthesized nanoparticles. The micrographs at 40X magnification reveal pronounced tissue regeneration, demonstrated by increased cellular density, reformation of fin ray structures, and active cellular proliferation. These features suggest successful tissue remodelling and regeneration post-amputation. The regenerated tissue exhibits normal cellular organization, consistent with the restoration of functional fin architecture, which supports the efficacy of the treatment in promoting fin regeneration.

Collectively, these histological findings confirm the regenerative potential of the nanoparticle treatment, demonstrated by the transition from baseline tissue morphology to actively regenerating fin tissue, aligning with previous literature on zebrafish fin regeneration mechanisms.

7.3.12. Antidiabetic properties

7.3.12.1. α-Amylase inhibition

The α-amylase inhibitory activity of silver nanoparticles (AgNPs) synthesized from *S. palghatense* bark was evaluated using a standard colorimetric assay based on the reduction of 3,5-dinitrosalicylic acid. The results revealed a dose-dependent inhibition of α-amylase activity, with percentage inhibition increasing significantly from 14.34% at 62.5 µg/mL to 93.08% at 1000 µg/mL, which is comparable to the standard inhibitor acarbose. Statistical analysis further supported these findings, with a high F-statistic value (45.23) and a p-value less than 0.001, indicating that the inhibitory effects observed were statistically significant. The critical difference (CD) at 5% was 0.025, confirming that the changes in enzyme inhibition across different concentrations were meaningful (Table 7.33).

Furthermore, the IC_{50} value of the AgNPs was found to be 247.06 µg/mL, which is notably lower than that of acarbose (720.15 µg/mL), demonstrating the higher potency of the nanoparticles in inhibiting α-amylase activity. These findings highlight the potential of *S. palghatense*-derived silver nanoparticles as effective natural agents for controlling postprandial hyperglycaemia by inhibiting

Table 7.33: α-Amylase inhibitory activity of silver nanoparticles synthesized from *Syzygium palghatense* bark

Sample concentration (µg/mL)	OD at 540 nm	Percentage inhibition (%)
Control	0.2818 ± 0.0121	0
Standard	0.0195 ± 0.0103	95.02 ± 0.1301
62.5	0.2414 ± 0.0520	14.34 ± 0.1250
125	0.1776 ± 0.0362	36.98 ± 0.1351
250	0.0804 ± 0.0541	71.47 ± 0.1572
500	0.0412 ± 0.0210	85.38 ± 0.1587
1000	0.0195 ± 0.0140	93.08 ± 0.1475
F-stat		45.23
P-value		< 0.001
CD at 5%		0.025

Values are expressed as mean ± standard error (n = 6). Statistical significance was evaluated using one-way ANOVA followed by a critical difference (CD) test at the 5% significance level. Differences were considered statistically significant at $p < 0.05$

Table 7.34: IC_{50} value of silver nanoparticles (AgNPs) synthesized from *Syzygium palghatense* bark in α-Amylase inhibitory activity

Samples	IC_{50} value (%)	F stat	P value	CD at 5%
Standard Acarbose	720.15 ± 0.31	25.87	<0.001	7.05
Silver nanoparticles (AgNPs) synthesized from *Syzygium palghatense* bark	247.06 ± 0.24	33.45	<0.001	5.12

Values are expressed as mean ± standard error (n = 6). Statistical significance was evaluated using one-way ANOVA followed by a critical difference (CD) test at the 5% significance level. Differences were considered statistically significant at $p < 0.0$

Table 7.35: α-Glucosidase inhibition assay of silver nanoparticles synthesized from *Syzygium palghatense* bark

Sample concentration (µg/mL)	OD at 540 nm	Percentage inhibition (%)
Control	0.3000 ± 0.0210	0
Standard (Acarbose)	0.0180 ± 0.0220	95.89 ± 0.1021
62.5	0.2280 ± 0.135	24.00 ± 0.1130
125	0.1400 ± 0.0124	53.33 ± 0.1043
250	0.0750 ± 0.0120	75.00 ± 0.2012
500	0.0380 ± 0.0131	87.33 ± 0.2151
1000	0.0180 ± 0.0128	94.00 ± 0.3010
F-stat		52.87
P-value		< 0.001
CD at 5%		0.018

Values are expressed as mean ± standard error (n = 6). Statistical significance was evaluated using one-way ANOVA followed by a critical difference (CD) test at the 5% significance level. Differences were considered statistically significant at $p < 0.05$

carbohydrate-digesting enzymes, offering promising applications in the management of diabetes mellitus (Table 7.34).

7.3.12.2. α-Glucosidase inhibition assay

The α-glucosidase inhibitory activity of silver nanoparticles (AgNPs) synthesized from *S. palghatense* bark was assessed through a spectrophotometric assay measuring enzyme inhibition across a range of concentrations. The data demonstrated a clear concentration-dependent inhibition pattern, with percentage inhibition increasing from 24.00% at 62.5 µg/mL to a maximum of 94.00% at 1000 µg/mL, which matches the inhibitory capacity of the standard inhibitor, acarbose. The optical density values decreased correspondingly, confirming reduced enzyme activity. Statistical analysis indicated a highly significant difference between treatment groups, with an F-statistic of 52.87 and a p-value less than 0.001, and the critical difference at the 5% level being 0.018, indicating the reliability of these results (Table 7.35).

Further analysis of the half-maximal inhibitory concentration (IC_{50}) values showed that the synthesized AgNPs had an IC_{50} of 110.25 µg/mL, which is substantially lower than that of acarbose (200.30 µg/mL). This finding indicates that the AgNPs possess stronger inhibitory activity against α-glucosidase. The statistical measures reinforced the significance of this difference, with an F-statistic of 40.10, a p-value below 0.001, and a critical difference of 3.85 at the 5% significance level. Collectively, these results highlight the promising potential of *S. palghatense*-derived silver nanoparticles as effective α-glucosidase inhibitors, supporting their application in controlling postprandial hyperglycaemia and managing type 2 diabetes (Table 7.36).

7.3.12.3. *In vitro* glucose uptake assay

Table 7.37 shows the *in vitro* glucose uptake by silver nanoparticles (AgNPs) synthesized from *S. palghatense* bark, compared with the standard drug Pioglitazone at concentrations of 25, 50, and 100 µg/mL. For Pioglitazone, glucose uptake increased from 42.36% ± 1.02 at 25 µg/mL to 80.36% ± 1.29 at 100 µg/mL, with

corresponding glucose levels rising from 35.68 ± 0.55 mg/dL to 104.70 ± 0.75 mg/dL. The AgNPs demonstrated even higher glucose uptake, ranging from 48.70% ± 0.98 at 25 µg/mL to 85.00% ± 1.10 at 100 µg/mL, with glucose concentrations increasing from 39.00 ± 0.48 mg/dL to 116.00 ± 0.62 mg/dL. Both treatments showed statistically significant increases compared to the control (20.56 ± 0.41 mg/dL glucose, 0% uptake), as indicated by one-way ANOVA (Pioglitazone: $F = 38.14$, $p < 0.001$; AgNPs: $F = 39.45$, $p < 0.001$). The high F-values and very low p-values confirm that the glucose uptake enhancement with increasing concentrations is significant. These findings indicate that the silver nanoparticles possess strong glucose uptake activity, comparable to or better than the standard Pioglitazone drug. All results are mean ± standard error from six replicates, with significance confirmed by a critical difference test at the 5% level.

Furthermore, the calculated EC_{50} values indicate that the AgNPs are markedly more potent, with an EC_{50} of 35.22 ± 0.40%, substantially lower than Pioglitazone's 93.54 ± 0.50%, meaning that the AgNPs achieve half-maximal glucose uptake at a much lower concentration. This enhanced potency is statistically significant ($F = 42.10$, $p < 0.001$). Together, these findings highlight the strong potential of *S. palghatense* bark-derived silver nanoparticles as effective enhancers of glucose uptake, thereby suggesting their promising application in improving glycemic control and managing diabetes (Table 7.38).

7.3.12.4. Endogenous inhibition of glucose production in the liver

The results in Tables 7.39 and 7.40 demonstrate the significant endogenous inhibition of glucose production in liver cells by silver nanoparticles (AgNPs) synthesized from *S. palghatense* bark, compared to the standard antidiabetic drug, Metformin. It outlines how AgNPs dose-dependently inhibit glucose production, with percentage inhibitions of 45.45%, 61.54%, and 84.53% at 25, 50, and 100 µg/mL, respectively, markedly surpassing Metformin's corresponding inhibitions of 23.30%, 34.68%, and 50.81%. The statistical analyses indicate highly significant differences among the groups and concentrations, with F-statistics ranging from 50.33 to 54.67 and p-values less than 0.001, confirming the robustness of these findings.

Table 7.36: IC_{50} value of silver nanoparticles (AgNPs) synthesized from *Syzygium palghatense* bark in α-Glucosidase inhibition assay

Samples	IC_{50} value (%)	F stat	P value	CD at 5%
Standard Acarbose	200.30 ± 0.30	28.40	<0.001	5.80
Silver nanoparticles (AgNPs) synthesized from *Syzygium palghatense* bark	110.25 ± 0.22	40.10	<0.001	3.85

Values are expressed as mean ± standard error (n = 6). Statistical significance was evaluated using one-way ANOVA followed by a critical difference (CD) test at the 5% significance level. Differences were considered statistically significant at p < 0

Table 7.37: *In vitro* glucose uptake by silver nanoparticles (AgNPs) Synthesized from *Syzygium palghatense* Bark

Concentration (µg/mL)	Absorbance (OD)	Glucose (mg/dL)	% Glucose uptake
Control	0.0634 ± 0.005	20.56 ± 0.41	0
Standard Pioglitazone			
25	0.1100 ± 0.007	35.68 ± 0.55	42.36 ± 1.02
50	0.1628 ± 0.008	52.81 ± 0.66	61.06 ± 1.15
100	0.3228 ± 0.009	104.70 ± 0.75	80.36 ± 1.29
F-stat	35.12		38.14
P-value	<0.001		<0.001
OD at 5%	4.09		2.10
***Syzygium palghatense* bark- AgNPs**			
25	0.1200 ± 0.006	39.00 ± 0.48	48.70 ± 0.98
50	0.1700 ± 0.007	58.00 ± 0.57	69.00 ± 1.05
100	0.3500 ± 0.008	116.00 ± 0.62	85.00 ± 1.10
F-stat	37.12		39.45
P-value	<0.001		<0.001
OD at 5%	4.15		2.20

Values are expressed as mean ± standard error (n = 6). Statistical significance was evaluated using one-way ANOVA followed by a critical difference (CD) test at the 5% significance level. Differences were considered statistically significant at p < 0.05

Table 7.38: EC_{50} value of silver nanoparticles (AgNPs) synthesized from *Syzygium palghatense* bark in glucose uptake assay

Samples	EC_{50} value (%)	F stat	P value	CD at 5%
Standard Pioglitazone	93.54 ± 0.50	38.25	<0.001	5.20
Silver nanoparticles (AgNPs) synthesized from *Syzygium palghatense* bark	35.22 ± 0.40	42.10	<0.001	3.50

Values are expressed as mean ± standard error (n = 6). Statistical significance was evaluated using one-way ANOVA followed by a critical difference (CD) test at the 5% significance level. Differences were considered statistically significant at p < 0.0

Table 7.39: Endogenous inhibition of glucose production in the liver by silver nanoparticles (AgNPs) Synthesized from *Syzygium palghatense* bark

Concentration (µg/mL)	Absorbance (OD)	Glucose (mg/dL)	% Glucose uptake
Control	0.2275	66.42	0.00
Standard Metformin			
25	0.1745	50.95	23.30
50	0.1486	43.39	34.68
100	0.1119	32.67	50.81
F-stat	50.12	53.21	49.25
P-value	<0.001	<0.001	<0.001
OD at 5%	3.12	3.15	2.03
***Syzygium palghatense* bark- AgNPs**			
25	0.1241	36.23	45.45
50	0.0875	25.55	61.54
100	0.0352	10.28	84.53
F-stat	52.11	54.67	50.33
P-value	<0.001	<0.001	<0.001
OD at 5%	4.15	3.90	2.20

Values are expressed as mean ± standard error (n = 6). Statistical significance was evaluated using one-way ANOVA followed by a critical difference (CD) test at the 5% significance level. Differences were considered statistically significant at $p < 0.05$

Table 7.40: IC_{50} values and statistical analysis of metformin and silver nanoparticles (AgNPs) synthesized from *Syzygium palghatense* bark in endogenous inhibition of glucose production in the liver

Samples	IC_{50} value (%)	F stat	P value	CD at 5%
Standard Metformin	50.81 ± 0.75	45.32	<0.001	4.20
Silver nanoparticles (AgNPs) synthesized from *Syzygium palghatense* bark	35.22 ± 0.40	52.10	<0.001	3.50

Values are expressed as mean ± standard error (n = 6). Statistical significance was evaluated using one-way ANOVA followed by a critical difference (CD) test at the 5% significance level. Differences were considered statistically significant at $p < 0.0$

Furthermore, Table 7.40 presents the IC_{50} values, which quantify the concentration required to achieve 50% inhibition of glucose production. The AgNPs exhibit a markedly lower IC_{50} value of 35.22 ± 0.40 µg/mL compared to Metformin's 50.81 ± 0.75 µg/mL. This lower IC_{50} value signifies that the AgNPs are more potent, requiring a significantly lower concentration to inhibit hepatic glucose production by half. The associated F-statistic of 52.10 and p-value < 0.001 further reinforce the statistical significance of this enhanced potency, supported by a critical difference (CD) value of 3.50.

Together, these data strongly suggest that silver nanoparticles synthesized from *S. palghatense* bark possess superior efficacy and potency in suppressing endogenous glucose production in liver cells compared to a standard antidiabetic drug. This highlights the therapeutic potential of these nanoparticles as promising candidates for managing hyperglycemia and diabetes.

7.3.12.5. Impact of *S. palghatense* bark silver nanoparticles (AgNPs) on PGC-1α expression in HepG2 cells by Real-Time PCR analysis

The bar graph displays the fold-change in PGC-1α (Peroxisome Proliferator-Activated Receptor Gamma Coactivator 1-Alpha) gene expression across four groups (Figure 7.20). The control group shows a fold change of 1.0representing baseline gene expression. Under glucose-starved conditions, PGC-1α expression rises sharply to approximately 1.7, highlighting the gene's activation during metabolic stress. In contrast, the sample group treated with *S. palghatense* bark AgNPs and the standard group treated with metformin both exhibit a fold change of approximately -0.0376 and -0.0281, respectively, indicating a strong suppression of PGC-1α expression. These findings demonstrate that both AgNPs and metformin effectively inhibit PGC-1α upregulation, even under stress conditions that usually activate this gene.

The image (Plate 7.13) displays results from a 1.5% agarose gel electrophoresis assessing gene expression in HepG2 cells. Bands for PGC-1α are strongest in the glucose-starved group, moderately visible in the control, and substantially weaker in the AgNPs-treated and standard-treated samples, indicating reduced gene expression after treatment. In contrast, GAPDH (Glyceraldehyde 3-

Phosphate Dehydrogenase) bands remain consistently strong across all lanes, serving as a loading control and confirming equal sample input and RNA quality. Overall, the gel illustrates that *S. palghatense* AgNPs and metformin treatments suppress PGC-1α expression in HepG2 cells.

Fluorescence curves in real-time PCR show the increase in fluorescent signal as the target gene is amplified during each PCR cycle. Here, fluorescence curves for PGC-1α and GAPDH indicate the accumulation of their respective PCR products over time (Figures 7.21-7.22). GAPDH serves as the housekeeping gene with stable expression, providing a control for normalization. The shape, slope, and threshold cycle (Ct) of these curves reflect gene expression levels: a steeper curve or earlier Ct suggests higher initial template quantity (more gene expression), while a delayed or flatter curve indicates lower expression. Thus, comparing the fluorescence curves of PGC-1α to GAPDH allows assessment of relative changes in PGC-1α expression in HepG2 cells under different conditions. Fluorescence curves show the increase in signal over time.

The amplification curves represent the progress of PCR product accumulation during real-time qPCR cycles for PGC-1α and GAPDH genes (Figures 7.23-7.24). Each curve shows three distinct phases: a baseline phase with minimal fluorescence, an exponential amplification phase where fluorescence increases sharply, and a plateau phase where the reaction saturates. The cycle threshold (Ct) value is indicated where the curve rises above background fluorescence. A lower Ct value corresponds to higher initial gene expression. GAPDH curves serve as internal control with stable expression, while PGC-1α curves indicate variable expression depending on the sample condition. Steeper and earlier rising curves for PGC-1α reflect higher gene expression; conversely, delayed or flattened curves suggest downregulation or lower transcript abundance. These curves quantify differential gene expression in HepG2 cells under different treatments. Amplification curves highlight the exponential increase and Ct values.

Melting curve analysis is a post-PCR method used to evaluate the specificity of amplified products by gradually increasing the temperature and monitoring the decrease in fluorescence as double-stranded DNA melts into single strands. Each DNA amplicon has a specific melting temperature (Tm) at which 50% of the DNA

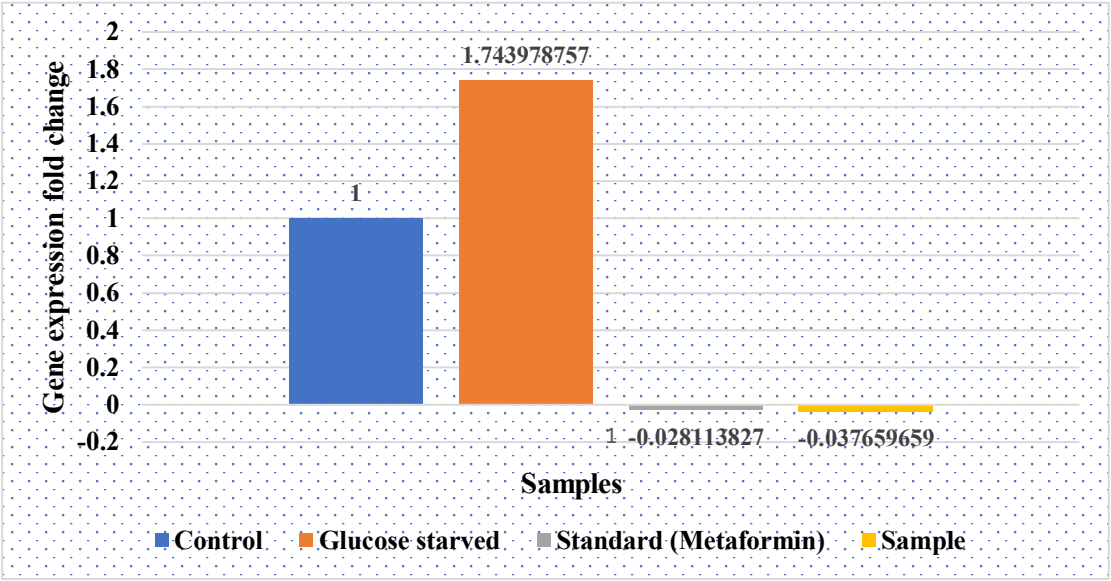


Figure 7.20: Suppression of PGC-1α expression by *Syzygium palghatense* bark AgNPs in HepG2 cells by Real-Time PCR analysis

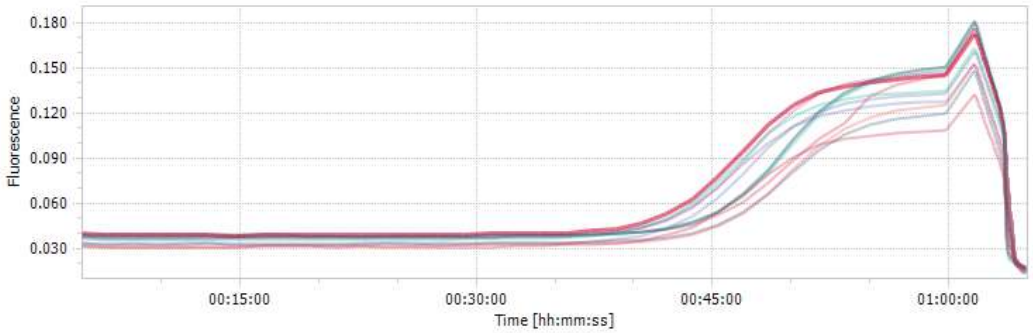


Figure 7.21: Real-Time PCR Fluorescence Amplification curves for PGC-1α (Peroxisome Proliferator-Activated Receptor Gamma Coactivator 1-Alpha)

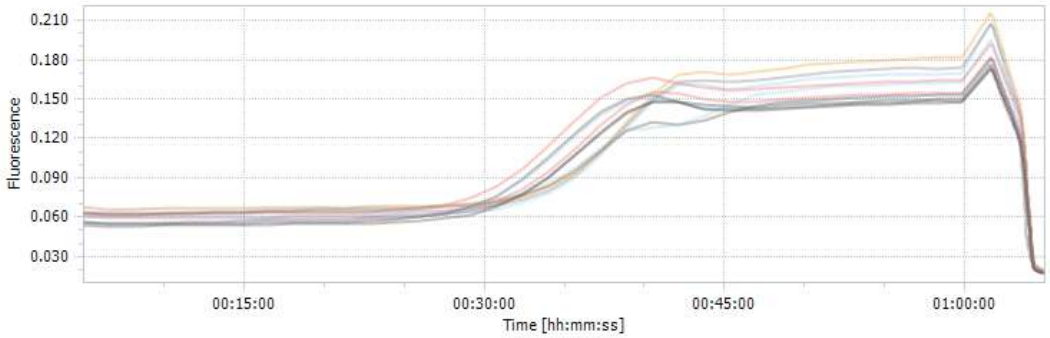


Figure 7.22: Real-Time PCR Fluorescence Amplification curves for GAPDH (Glyceraldehyde 3-Phosphate Dehydrogenase)

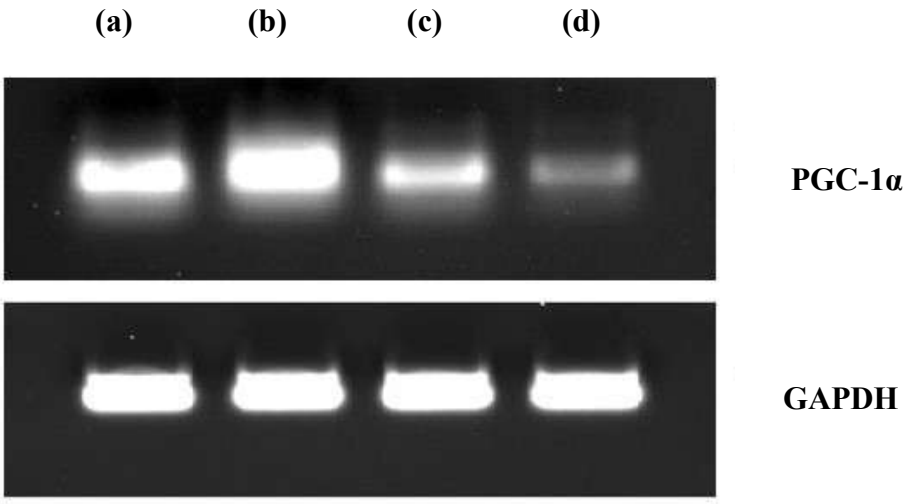


Plate 7.13: Photomicrograph of a typical 1.5% agarose gel depicting the gene expression pattern of PGC-1α (Peroxisome Proliferator-Activated Receptor Gamma Coactivator 1-Alpha) and housekeeping gene GAPDH (Glyceraldehyde 3-Phosphate Dehydrogenase) in HepG2 cells (a) Control (b) Glucose starved (c) AgNPs (d) Standard. The gel image was captured by the ChemiDoc imaging system, Biorad

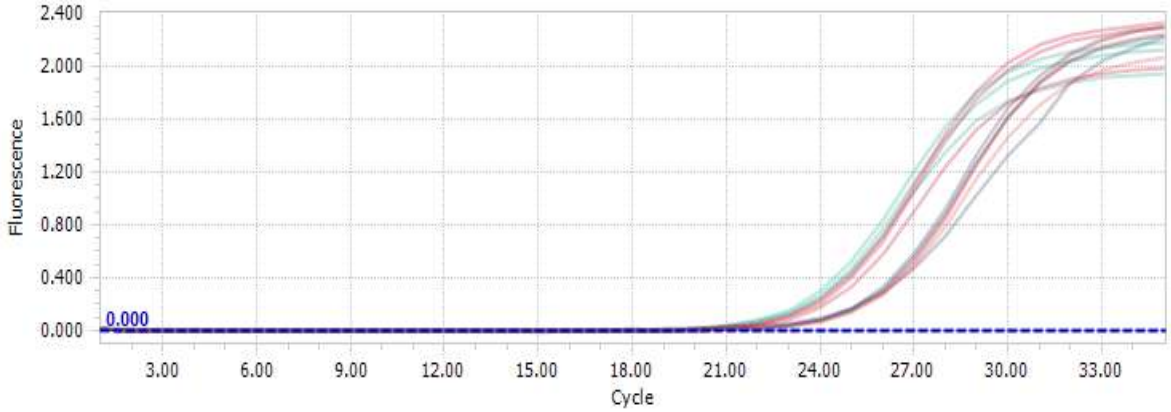


Figure 7.23: Real-Time PCR Amplification curves for PGC-1α (Peroxisome Proliferator-Activated Receptor Gamma Coactivator 1-Alpha)

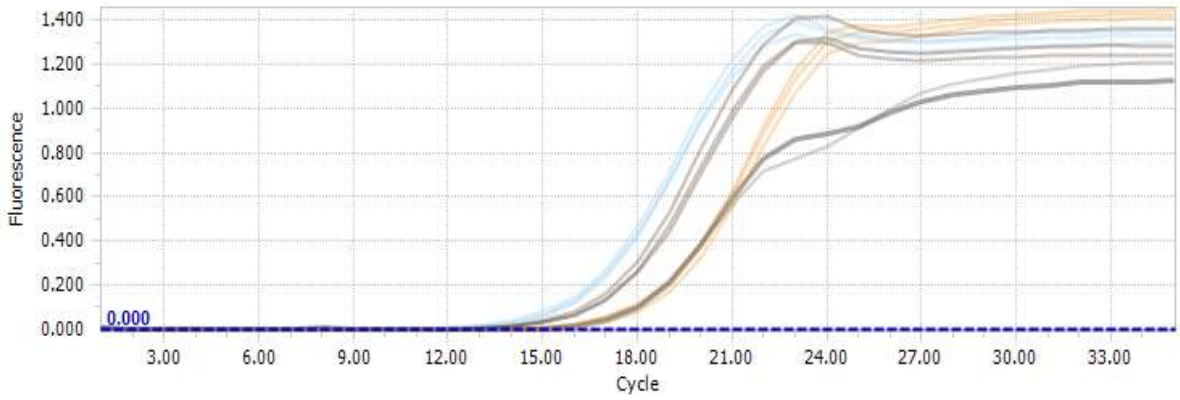


Figure 7.24: Real-Time PCR Amplification curves for GAPDH (Glyceraldehyde 3-Phosphate Dehydrogenase)

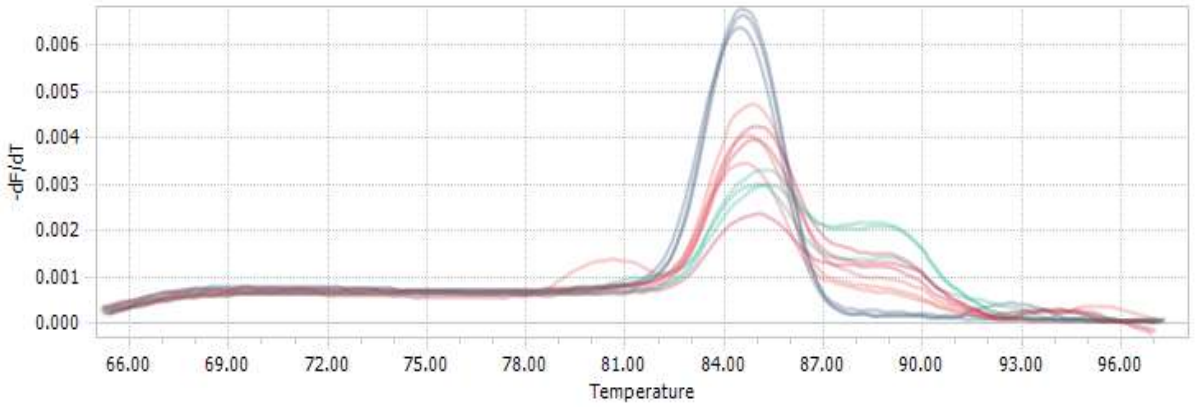


Figure 7.25: Real-Time PCR Melting curves for PGC-1α (Peroxisome Proliferator-Activated Receptor Gamma Coactivator 1-Alpha)

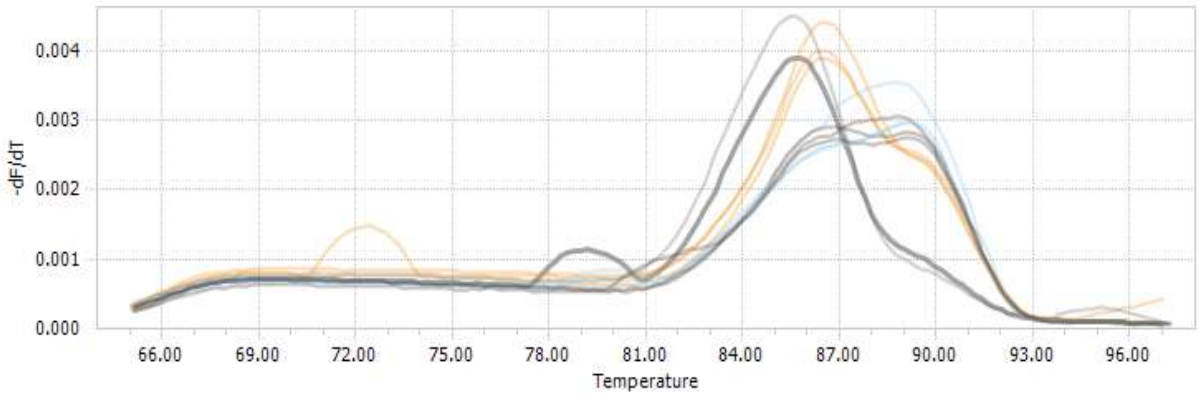


Figure 7.26: Real-Time PCR Melting curves for GAPDH (Glyceraldehyde 3-Phosphate Dehydrogenase)

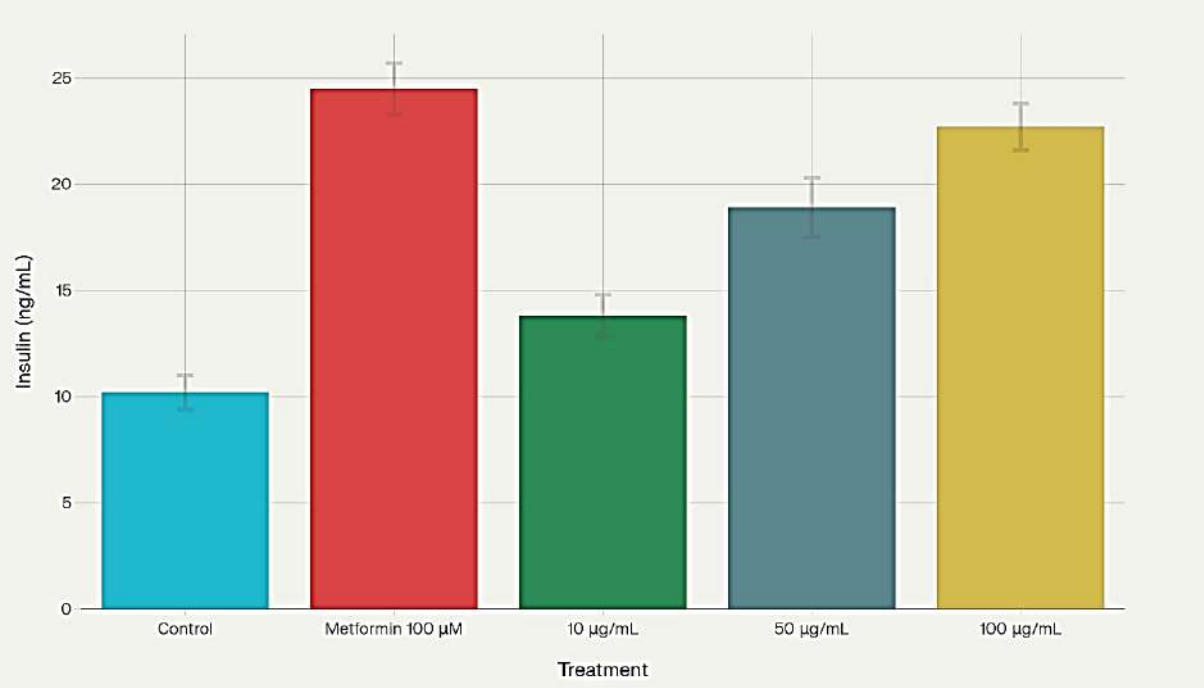


Figure 7.27: Effect of different treatments on Insulin Secretion in INS-1 (Insulinoma-1) Pancreatic β-cells

denatures, which is observed as a sharp decrease in fluorescence. A single, sharp peak in the melting curve corresponds to a specific, homogeneous PCR product, while multiple peaks or shoulders indicate non-specific products or primer-dimers. Melting curves confirm the specificity of the amplified products. For PGC-1α and GAPDH, the presence of single melt peaks confirms the specificity of amplification and absence of artifacts, validating the reliability of the qPCR data. This ensures that the gene expression measurements reflect true target amplification rather than primer-dimer or non-specific products (Figures 7.25-7.26).

7.3.12.6 Impact of *S. palghatense* bark silver nanoparticles (AgNPs) on Insulin secretion

Figure 7.27 illustrates the effect of various treatments on insulin secretion by INS-1 (Insulinoma-1) pancreatic β-cells. The data show a significant increase in insulin release in response to metformin, which serves as a positive control, compared to untreated cells. Treatment with the test sample at concentrations of 10, 50, and 100 µg/mL also dose-dependently enhanced insulin secretion, with the highest concentration eliciting an effect close to that of metformin. These findings indicate that the test AgNPs synthesized from the methanol extract of *S. palghatense* bark effectively stimulate insulin secretion in pancreatic β-cells, suggesting potential therapeutic benefits for improving β-cell function and glucose regulation. The results are supported by statistical significance, highlighting the samples capacity to modulate insulin release *in vitro*.

7.3.13. Anticancer properties

7.3.13.1. Cytotoxicity of *S. palghatense* bark silver nanoparticles (AgNPs) by Trypan Blue Assay

Figure 7.28 shows a clear dose-dependent increase in percentage cell death of DLA (Dalton's Lymphoma Ascites) cells with rising concentrations of AgNPs. At lower concentrations (0–20 µg/mL), cytotoxicity is minimal, while significant increases are observed starting from 40 µg/mL. Maximum cell death, 77%, is achieved at 100 µg/mL, indicating that AgNPs from *S. palghatense* bark exhibit strong cytotoxic effects against DLA cells *in vitro*. This trend suggests potent antitumor

activity at higher nanoparticle concentrations, as assessed by the trypan blue exclusion assay.

7.3.13.2. MTT assay

The MTT assay results presented in Table 7.41 demonstrate the effect of standard cisplatin and silver nanoparticles (AgNPs) synthesized from *S. palghatense* bark on cell viability across different concentrations. For cisplatin, cell viability decreased significantly from 56.81% ± 1.15 at 6.25 µg/mL to 15.39% ± 0.15 at 100 µg/mL. Similarly, the AgNPs showed a dose-dependent reduction in viability from 76.89% ± 1.03 at 6.25 µg/mL to 27.83% ± 1.23 at 100 µg/mL (Plates 7.14-7.15). Statistical analysis using one-way ANOVA revealed highly significant differences in cell viability among concentrations for both cisplatin ($F = 372.86$, $p < 0.001$) and AgNPs ($F = 386.76$, $p < 0.001$), confirming that the reductions in viability were statistically meaningful. These findings indicate potent cytotoxic effects of both treatments, with cisplatin exhibiting somewhat greater cytotoxicity at lower concentrations compared to the nanoparticles.

Table 7.42 summarizes the IC_{50} values and associated statistical parameters for the same samples. The IC_{50} for standard cisplatin was 40.71% ± 0.75, indicating the concentration at which half of the cells remain viable. For the silver nanoparticles, the IC_{50} was higher at 55.12% ± 0.40, suggesting a slightly lower cytotoxic potency compared to cisplatin. Both samples showed significant statistical differences as indicated by F-statistics of 65.32 and 72.13 with p-values less than 0.001. The critical difference (CD) values at the 5% significance level were 4.25 for cisplatin and 5.50 for the AgNPs, supporting the reliability and significance of these comparisons. Overall, the data confirm the cytotoxic efficacy of both standard cisplatin and *S. palghatense* bark AgNPs, with cisplatin showing marginally higher potency in the tested assay.

7.3.13.3. XTT assay

The data presented in Table 7.43 demonstrate the effect of standard cisplatin and silver nanoparticles (AgNPs) synthesized from *S. palghatense* bark on the

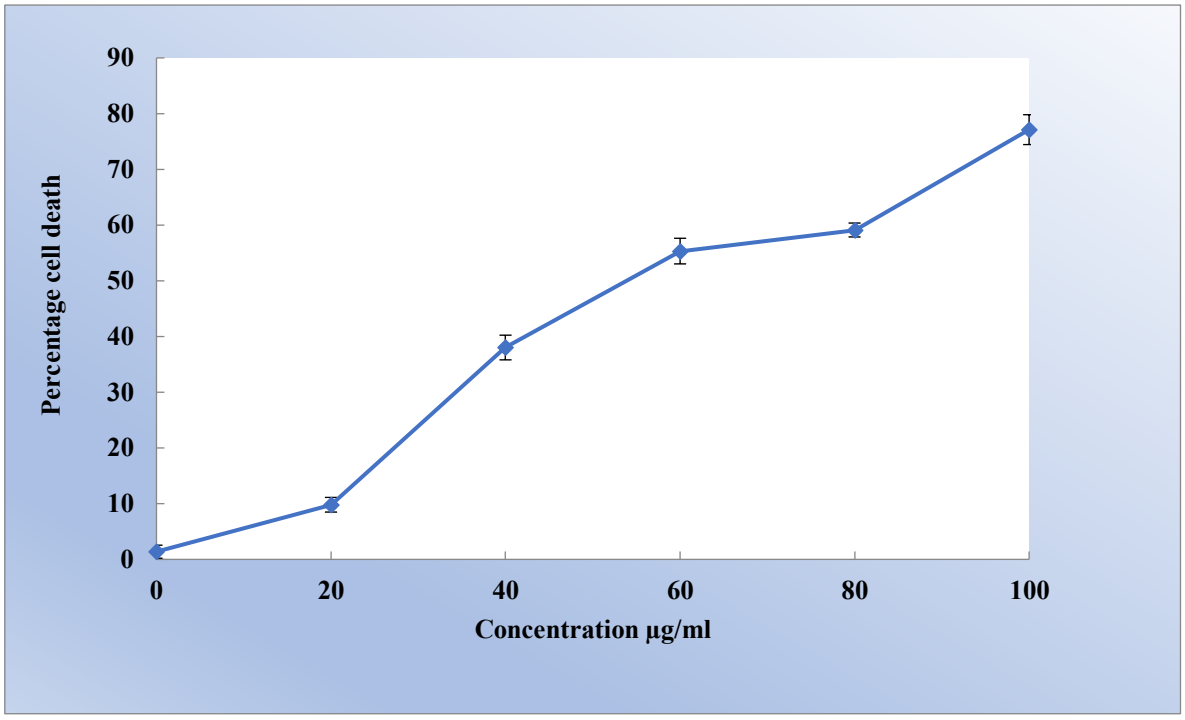


Figure 7.28: Dose-dependent cytotoxicity of *Syzygium palghatense* bark silver nanoparticles (AgNPs) on DLA (Dalton's Lymphoma Ascites) cells determined by Trypan Blue Exclusion Assay

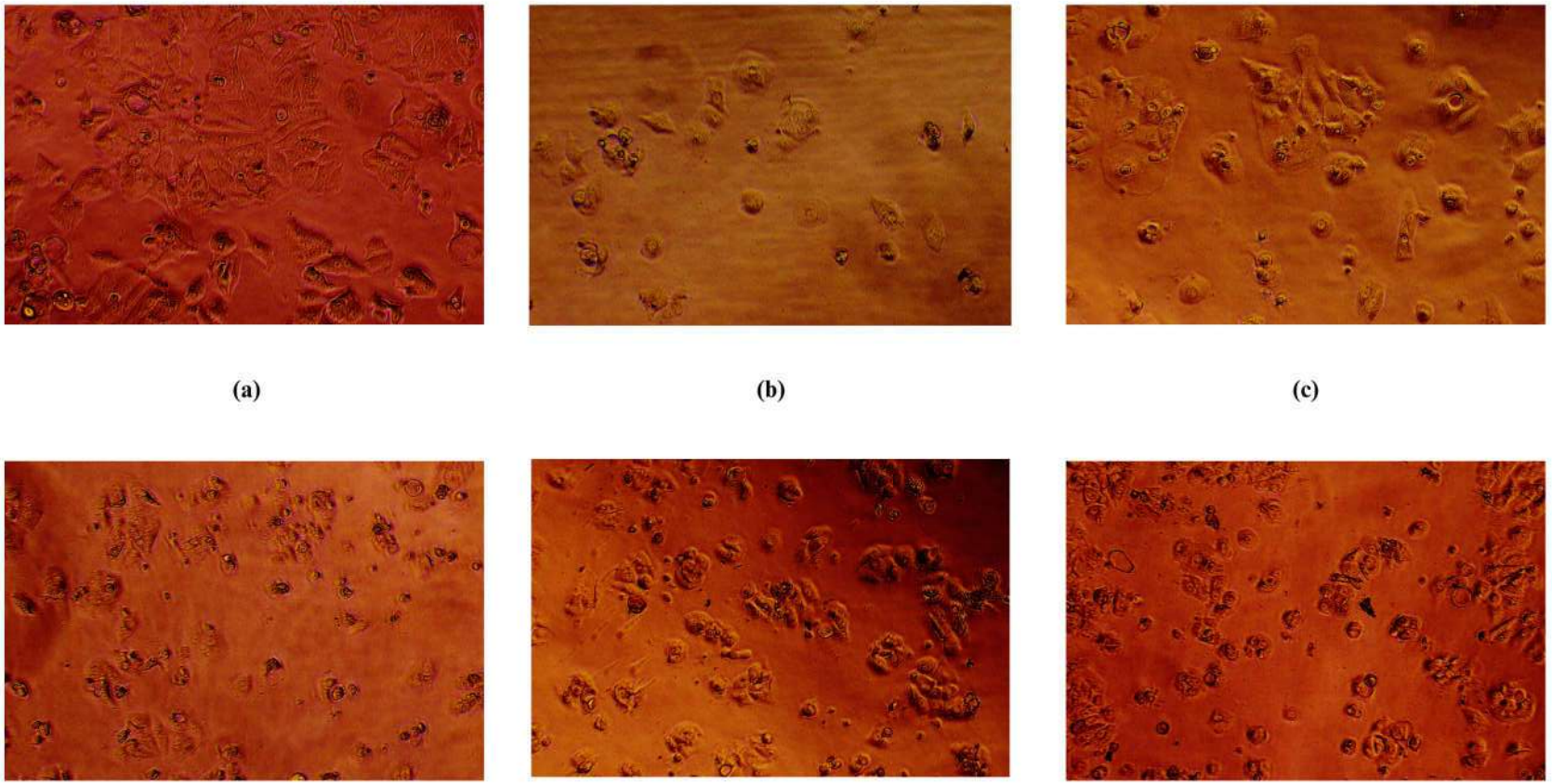
Table 7.41: Effect of standard cisplatin and *Syzygium palghatense* bark silver nanoparticles (AgNPs) on cell viability at different concentrations measured by MTT assay

Sample Concentration (µg/mL)	Average absorbance (OD at 540 nm)	Percentage viability (%)
Control	0.7590	100.00
Standard Cisplatin		
6.25	0.4312 ± 0.0104	56.81 ± 1.1485
12.5	0.3410 ± 0.0253	44.93 ± 1.192
25	0.2634 ± 0.0520	34.71 ± 1.0251
50	0.1775 ± 0.0470	23.39 ± 1.0542
100	0.1168 ± 0.0264	15.39 ± 0.1456
F-stat		372.86
P-value		<0.001
***Syzygium palghatense* bark AgNPs**		
6.25	0.7354 ± 0.0101	76.89 ± 1.0321
12.5	0.6604 ±0.0152	67.01 ± 1.0214
25	0.5708 ± 0.0150	55.20 ± 1.1120
50	0.4925 ± 0.0122	34.88 ± 1.1031
100	0.4389 ± 0.0111	27.83 ± 1.230
F-stat		386.76
P-value		<0.001

Values are expressed as mean ± standard error (n = 6). Statistical significance was evaluated using a one-way ANOVA. Differences were considered statistically significant at $p < 0.05$

Table 7.42: IC_{50} values, and statistical analysis of Cisplatin and *Syzygium palghatense* bark silver nanoparticles (AgNPs) in MTT assay

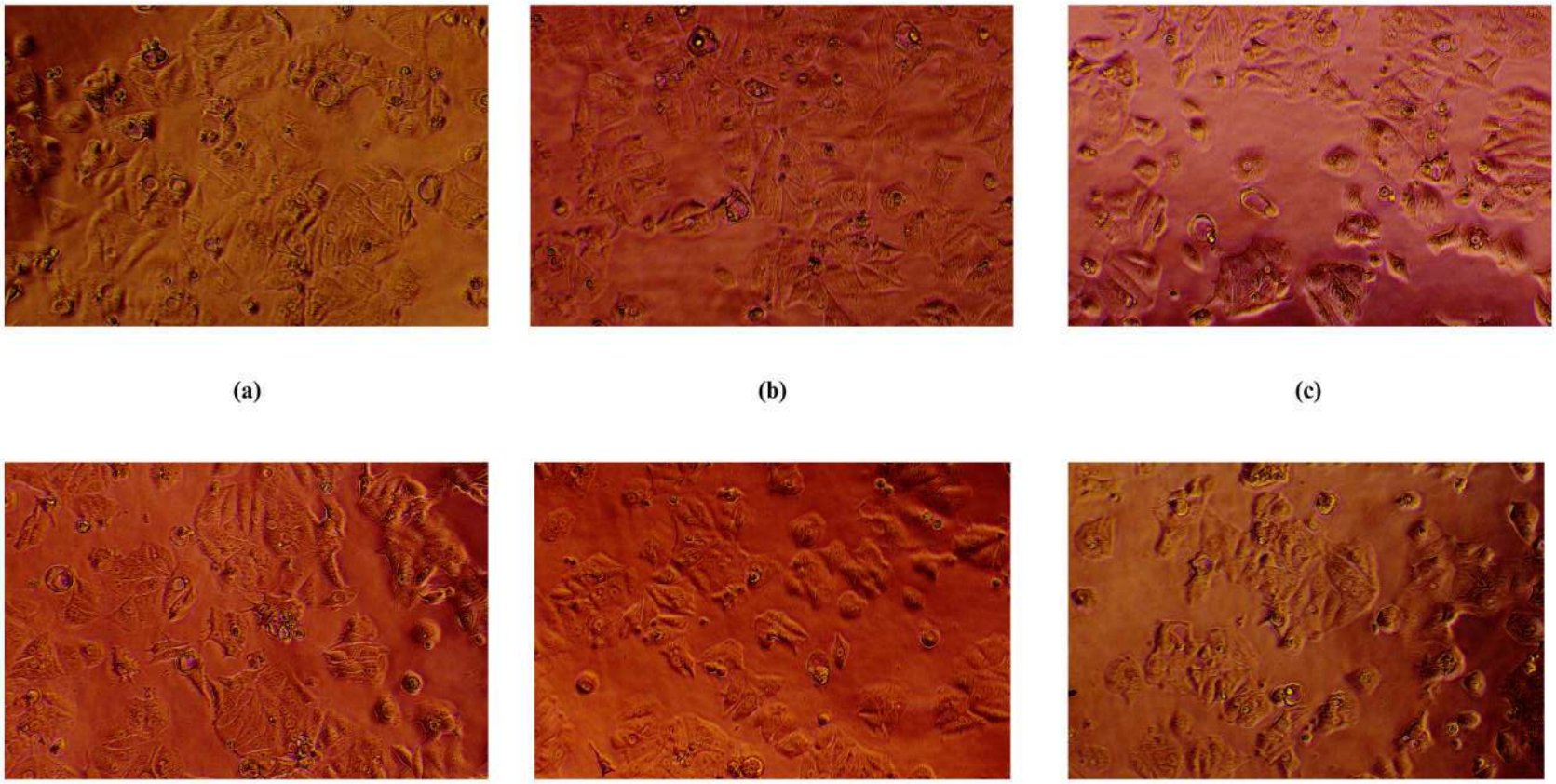
Samples	IC_{50} value (%)	F stat	P value	CD at 5%
Standard Cisplatin	40.71 ± 0.75	65.32	<0.001	4.25
Silver nanoparticles (AgNPs) synthesized from *Syzygium palghatense* bark	55.12 ± 0.40	72.13	<0.001	5.50



(a) (b) (c)

(d) (e) (f)

Plate 7.14: Photomicrographs depicting standard cisplatin-treated cells in MTT assay at different concentrations: (a) Untreated control (b) 6.25 µg/mL (c) 12.5 µg/mL (d) 25 µg/mL (e) 50 µg/mL (f) 100 µg/mL



(a) (b) (c)

(d) (e) (f)

Plate 7.15: Photomicrographs depicting silver nanoparticles synthesized from the methanol extract of *Syzygium palghatense* bark-treated cells in MTT assay at different concentrations: (a) Untreated control (b) 6.25 µg/mL (c) 12.5 µg/mL (d) 25 µg/mL (e) 50 µg/mL (f) 100 µg/mL

Table 7.43: Effect of standard cisplatin and *Syzygium palghatense* bark silver nanoparticles (AgNPs) on cell viability at different concentrations measured by XTT assay with Caco-2 (Human Colon Cancer) cells

Sample Concentration (µg/mL)	Average absorbance (OD at 540 nm)	Percentage viability (%)
Control	0.4701	100.00
Standard Cisplatin		
6.25	0.2722 ± 0.0114	57.91 ± 1.0485
12.5	0.2054 ± 0.0213	43.69 ± 1.1201
25	0.1676 ± 0.0522	35.66 ± 1.1251
50	0.1207 ± 0.0370	25.68 ± 0.1542
100	0.0712 ± 0.0164	15.15 ± 0.1256
F-stat		549.29
P-value		<0.001
***Syzygium palghatense* bark AgNPs**		
6.25	0.9653 ± 0.0111	89.68 ± 1.0121
12.5	0.8867 ± 0.0122	77.21 ± 1.0114
25	0.8266 ± 0.0130	65.30 ± 1.1125
50	0.7593 ± 0.0108	49.18 ± 1.2031
100	0.6881 ± 0.0151	35.13 ± 1.130
F-stat		425.15
P-value		<0.001

Values are expressed as mean ± standard error (n = 6). Statistical significance was evaluated using a one-way ANOVA. Differences were considered statistically significant at $p < 0.05$

Table 7.44: IC_{50} values, and statistical analysis of Cisplatin and *Syzygium palghatense* Bark silver nanoparticles (AgNPs) in XTT assay with Caco-2 (Human Colon Cancer) cells

Samples	IC_{50} value (%)	F stat	P value	CD at 5%
Standard Cisplatin	10.11 ± 0.20	43.12	<0.001	3.28
Silver nanoparticles (AgNPs) synthesized from *Syzygium palghatense* bark	21.12 ± 0.12	60.10	<0.001	5.10

Values are expressed as mean ± standard error (n = 6). Statistical significance was evaluated using one-way ANOVA followed by a critical difference (CD) test at the 5% significance level. Differences were considered statistically significant at $p < 0.0$

viability of Caco-2 (Human Colon Cancer) cells, as measured by the XTT assay. The results show a clear dose-dependent decrease in cell viability for both treatments. Cisplatin caused a pronounced reduction in viability, decreasing from 57.91% ± 1.05 at 6.25 µg/mL to 15.15% ± 0.13 at 100 µg/mL. Similarly, the AgNPs reduced viability from 89.68% ± 1.01 to 35.13% ± 1.13 over the same concentration range, indicating cytotoxicity, but to a lesser extent than Cisplatin. Statistical analysis using one-way ANOVA revealed highly significant differences across concentrations for both Cisplatin ($F = 549.29$, $p < 0.001$) and the AgNPs ($F = 425.15$, $p < 0.001$), confirming the strong impact of increasing doses on cell viability.

Table 7.44 summarizes key potency parameters from the same assay by presenting IC_{50} values along with associated statistical measures. The IC_{50} for Cisplatin was 10.11% ± 0.20, indicating high potency in inhibiting cancer cell viability, whereas the AgNPs showed an IC_{50} of 21.12% ± 0.12, reflecting lower potency compared to Cisplatin but still significant activity. Both agents exhibited statistically significant efficacy as indicated by F-statistics of 43.12 and 60.10 and p-values below 0.001. The critical differences (CD) at the 5% significance level were 3.28 for Cisplatin and 5.10 for the AgNPs, supporting reliable differentiation of effects between tested concentrations. Together, these findings demonstrate that both cisplatin and *S. palghatense* bark AgNPs effectively reduce colon cancer cell viability, with Cisplatin showing greater potency under the experimental conditions.

The data presented in Tables 7.45 and 7.46 illustrate the cytotoxic effects of standard cisplatin and silver nanoparticles (AgNPs) synthesized from *S. palghatense* bark on MCF-7 (Human Breast Cancer) cell viability, measured using the XTT assay. Table 7.45 shows a clear decrease in cell viability with increasing concentrations of both treatments. Cisplatin significantly reduced cell viability from 56.11 ± 1.04 at 6.25 µg/mL to 14.10 ± 0.13 at 100 µg/mL. Similarly, AgNPs decreased viability from 70.68% ± 1.01 to 31.11% ± 1.02 across the same concentration range, demonstrating cytotoxicity that was less potent than cisplatin but still substantial. One-way ANOVA analysis confirmed the statistical significance of these findings with F-values of 439.21 and 417.10 for Cisplatin and AgNPs respectively, and p-values less than 0.001.

Table 7.46 summarizes the potency of these treatments through IC_{50} values and supporting statistical analyses. The IC_{50} for cisplatin was 10.11% ± 0.20, indicating higher potency compared to the AgNPs, which had an IC_{50} of 19.15% ± 0.12. Both treatments showed statistically significant differences as indicated by F-statistics of 40.18 and 56.11, with p-values remaining below 0.001. Critical difference (CD) values of 3.26 for Cisplatin and 5.06 for the AgNPs further support that the differences between treatment concentrations were meaningful. These results collectively demonstrate that both cisplatin and the *S. palghatense* bark AgNPs effectively reduce breast cancer cell viability, with cisplatin exhibiting stronger cytotoxic effects under the tested conditions.

The anticancer effects are depicted in Plates 7.16-7.18, which shows the impact of different concentrations of standard and silver nanoparticles on Caco-2 and MCF-7 cells, respectively.

7.3.13.4. Protein estimation by the Bradford method

The protein estimation assay using the Bradford method are presented based on absorbance measurements at 595 nm. The standard curve was generated using bovine serum albumin concentrations ranging from 0.1 to 1 mg/mL, with corresponding absorbance values from 0.277 to 0.613 (Figure 7.29). Sample absorbance values were then measured, and protein concentrations calculated from this curve. The control sample showed an absorbance of 0.8671, corresponding to a protein concentration of 1.62284 mg/mL, indicating the highest protein content. The test sample, which contained silver nanoparticles synthesized from *S. palghatense* bark, exhibited an absorbance of 0.6887 and a protein concentration of 1.15558 mg/mL. The standard sample recorded an absorbance of 0.5725 with a protein concentration of 0.85123 mg/mL. These results demonstrate that treatment with silver nanoparticles affected the protein concentration, which was notably lower than in the control but higher than in the standard, suggesting a modulation of protein levels due to the nanoparticle treatment.

The protein estimation results show that the control sample has an absorbance of 0.8671, corresponding to a protein concentration of 1.62284 mg/mL. The sample treated with silver nanoparticles exhibits an absorbance of 0.6887, corresponding to a protein concentration of 1.15558 mg/mL. The standard sample displays an absorbance

Table 7.45: Effect of standard cisplatin and *Syzygium palghatense* bark silver nanoparticles (AgNPs) on cell viability at different concentrations measured by XTT assay with MCF-7 (Human Breast Cancer)

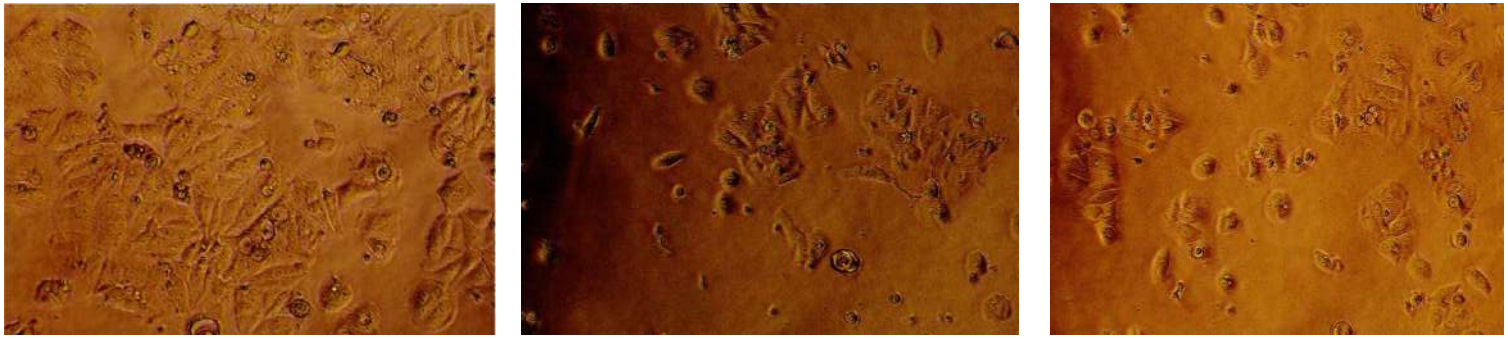
Sample Concentration (µg/mL)	Average absorbance (OD at 540 nm)	Percentage viability (%)
Control	0.4701	100.00
Standard Cisplatin		
6.25	0.2622 ± 0.0112	56.11 ± 1.0410
12.5	0.2004 ± 0.0214	43.29 ± 1.1101
25	0.1071 ± 0.0510	34.36 ± 1.1051
50	0.1237 ± 0.0340	24.01 ± 0.1342
100	0.0512 ± 0.0364	14.10 ± 0.1356
F-stat		439.21
P-value		<0.001
***Syzygium palghatense* bark AgNPs**		
6.25	0.7700 ± 0.0011	70.68 ± 1.0120
12.5	0.7132 ± 0.0102	57.20 ± 1.1114
25	0.6447 ± 0.0110	64.20 ± 1.1026
50	0.5154 ± 0.0104	43.58 ± 1.2131
100	0.4841 ± 0.0151	31.11 ± 1.020
F-stat		417.10
P-value		<0.001

Values are expressed as mean ± standard error (n = 6). Statistical significance was evaluated using a one-way ANOVA. Differences were considered statistically significant at $p < 0.05$

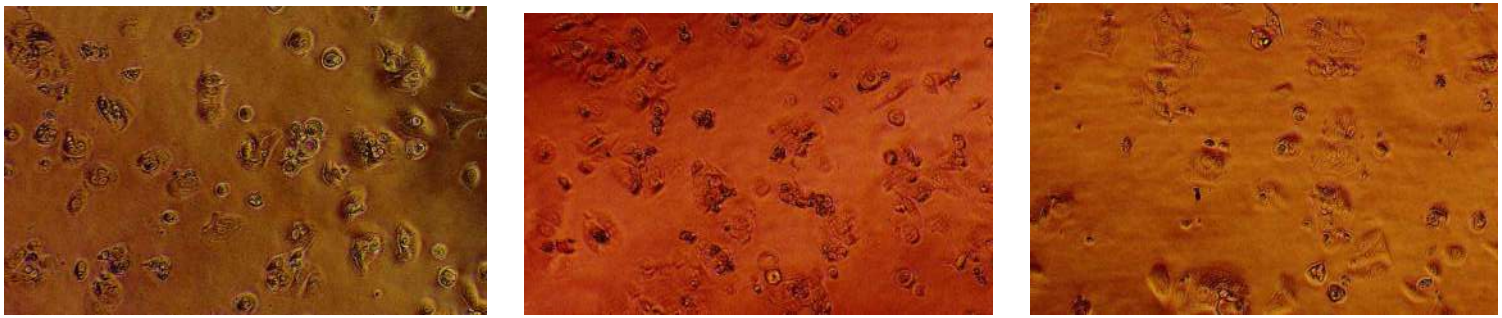
Table 7.46: IC_{50} values, and statistical analysis of Cisplatin and *Syzygium palghatense* Bark silver nanoparticles (AgNPs) in XTT assay with MCF-7 (Human Breast Cancer)

Samples	IC_{50} value (%)	F stat	P value	CD at 5%
Standard Cisplatin	10.11 ± 0.20	40.18	<0.001	3.26
Silver nanoparticles (AgNPs) synthesized from *Syzygium palghatense* bark	19.15 ± 0.12	56.11	<0.001	5.06

Values are expressed as mean ± standard error (n = 6). Statistical significance was evaluated using one-way ANOVA followed by a critical difference (CD) test at the 5% significance level. Differences were considered statistically significant at $p < 0.0$



(a) **(b)** **(c)**



(d) **(e)** **(f)**

Plate 7.16: Photomicrographs depicting standard cisplatin-treated cells in XTT assay at different concentrations: (a) Untreated control (b) 6.25 µg/mL (c) 12.5 µg/mL (d) 25 µg/mL (e) 50 µg/mL (f) 100 µg/mL

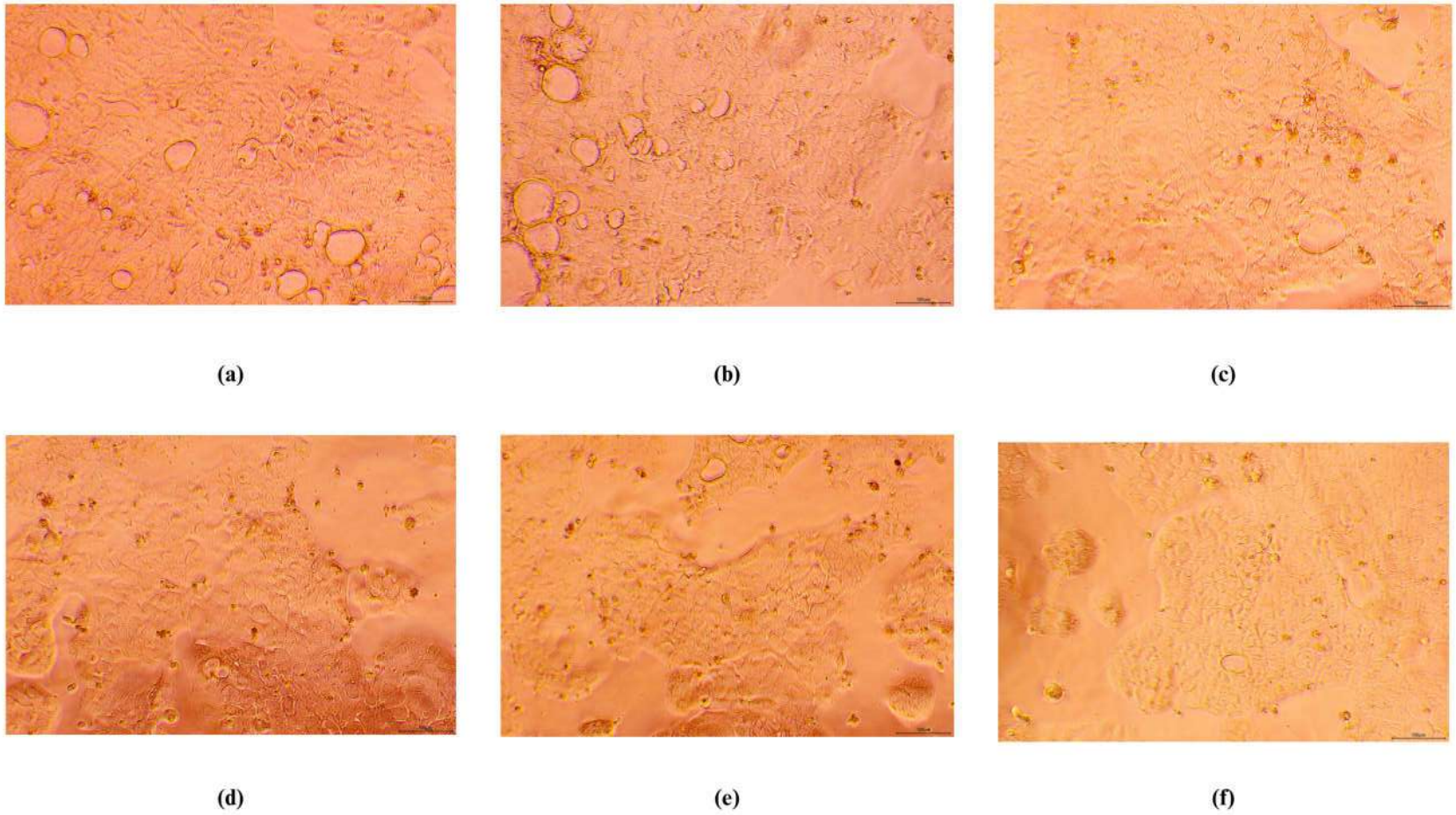
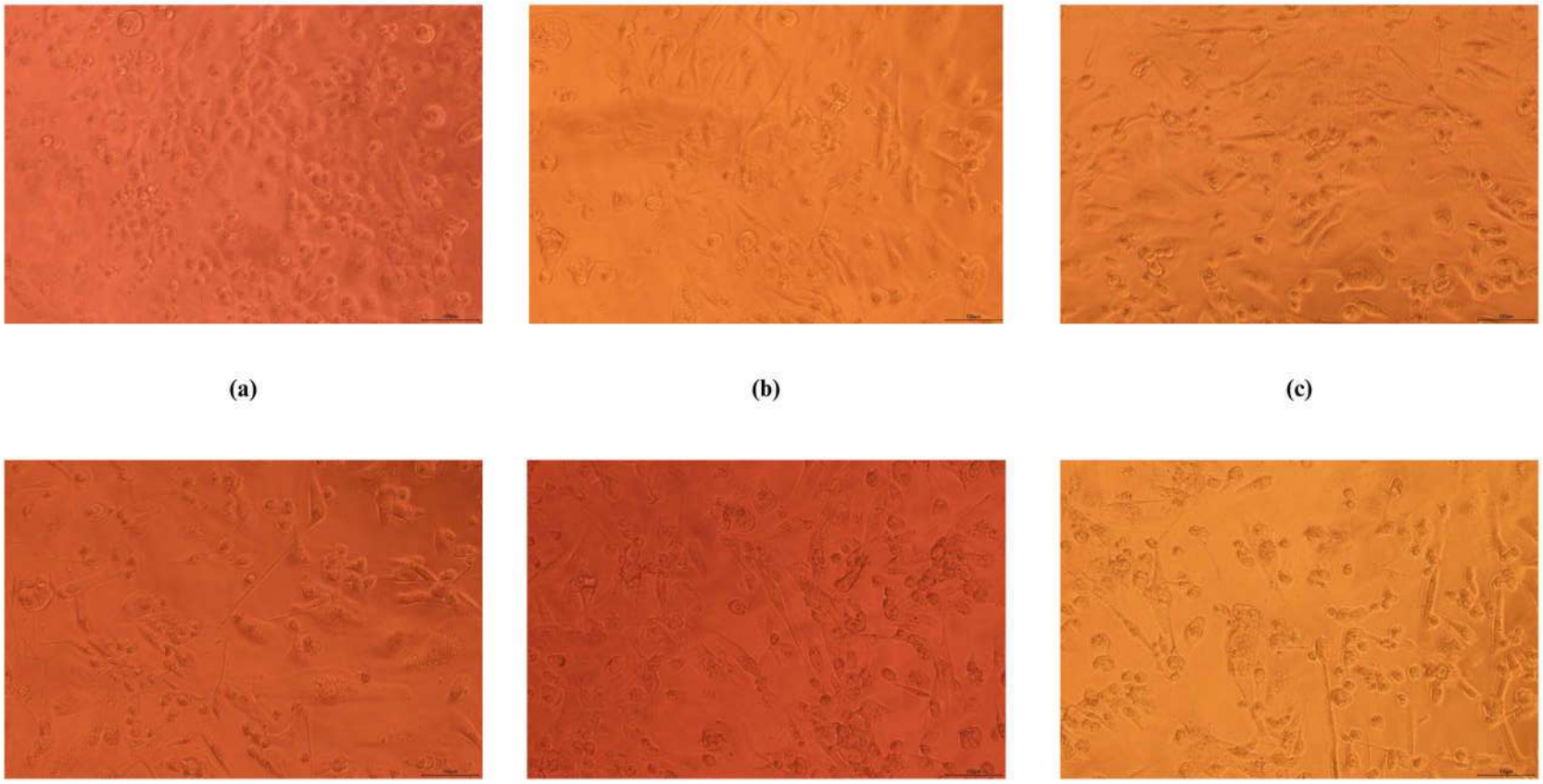


Plate 7.17: Photomicrographs depicting the anticancer effect of the silver nanoparticles (AgNPs) synthesized from the methanol extract of *Syzygium palghatense* bark on cultured Caco-2 (Human Colon Cancer) cells: (a) Untreated control (b) 6.25 µg/mL (c) 12.5 µg/mL (d) 25 µg/mL (e) 50 µg/mL (f) 100 µg/mL



(a) (b) (c)

(d) (e) (f)

Plate 7.18: Photomicrographs depicting the anticancer effect of the silver nanoparticles (AgNPs) synthesized from the methanol extract of *Syzygium palghatense* bark on cultured MCF-7 (Human Breast Cancer) cells: (a) Untreated control (b) 6.25 µg/mL (c) 12.5 µg/mL (d) 25 µg/mL (e) 50 µg/mL (f) 100 µg/mL

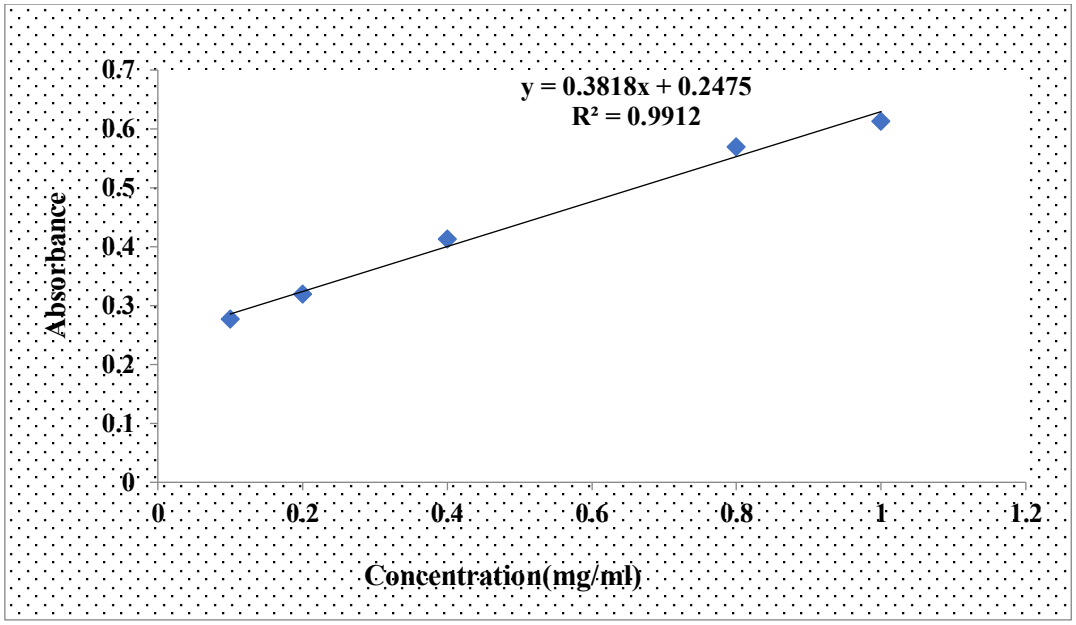


Figure 7.29: Standard Curve for Protein Estimation by Bradford Method

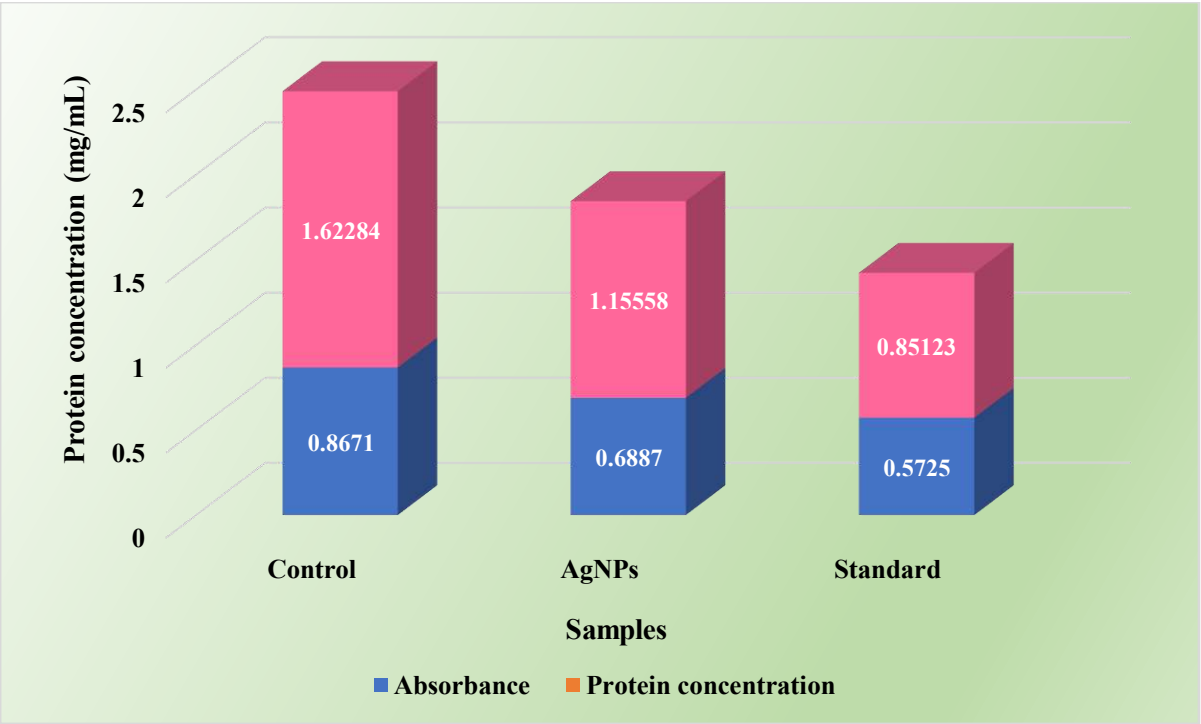


Figure 7.30: Comparison of absorbance and protein concentration in control, AgNPs, and standard samples

value of 0.5725 and a corresponding protein concentration of 0.85123 mg/mL. These values indicate that the protein content is highest in the control group, reduced in the nanoparticle-treated sample, and lowest in the standard. This quantification reflects the effect of the silver nanoparticle treatment on protein concentration in comparison to both the untreated control and the standard (Figure 7.30).

7.3.13.5. Apoptosis FACS (Fluorescence-Activated Cell Sorting)/Annexin V apoptosis assay by flow cytometry

Flow cytometry is a technology that simultaneously measures and then analyzes multiple physical characteristics of single particles, usually cells, as they flow in a fluid stream through a beam of light. The properties measured include a particle's relative size, relative granularity or internal complexity, and relative fluorescence intensity. These characteristics are determined using an optical-to-electronic coupling system that records how the cell or particle scatters incident laser light and emits fluorescence (Shapiro, 2003).

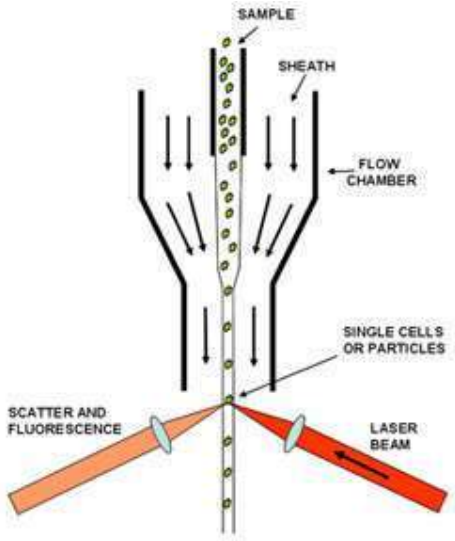


Figure 7.31: Schematic representation of flow cytometric analysis of cells

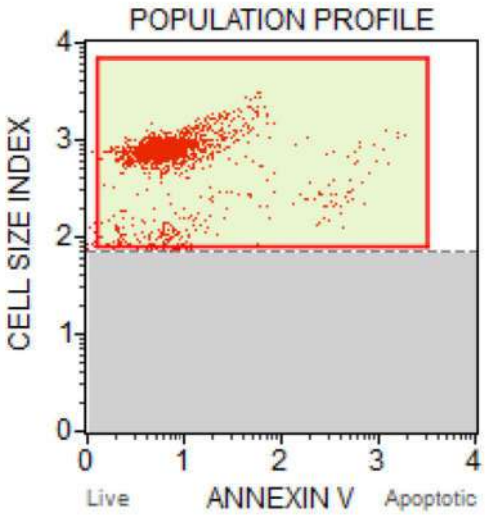
Apoptosis is a carefully regulated process of cell death that occurs as a normal part of development. Inappropriately regulated apoptosis is implicated in disease states, such as Alzheimer's disease and cancer. Apoptosis is distinguished from necrosis, or accidental cell death, by characteristic morphological and biochemical

changes, including compaction and fragmentation of the nuclear chromatin, shrinkage of the cytoplasm, and loss of membrane asymmetry (Kroemer et al., 2007).

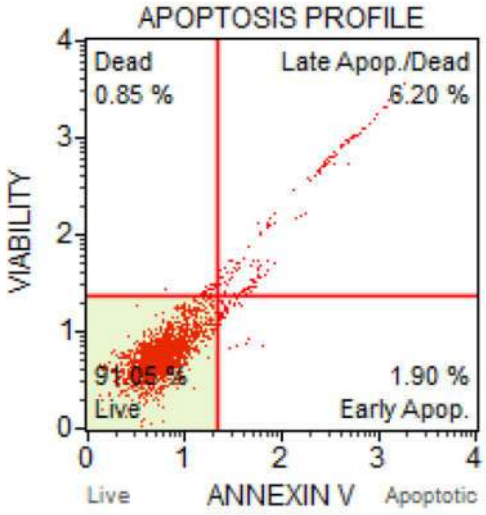
The Alexa Fluor-488 Annexin V/Dead Cell Apoptosis Kit with Alexa Fluor-488 annexin V and PI (red-fluorescent propidium iodide) for flow cytometry provides a rapid and convenient assay for apoptosis. The kit contains recombinant annexin V conjugated to fluorescein (Alexa Fluor-488), as well as a ready-to-use solution of the red-fluorescent propidium iodide (PI) nucleic acid binding dye. PI is impermeant to live cells and apoptotic cells, but stains dead cells with red fluorescence, binding tightly to the nucleic acids in the cell. After staining a cell population with Alexa Fluor-488 annexin V and PI in the provided binding buffer, apoptotic cells show green fluorescence, dead cells show red and green fluorescence, and live cells show little or no fluorescence (Figure 7.31). These populations can easily be distinguished using a flow cytometer with the 488 nm line of an argon-ion laser for excitation (Kroemer et al., 2007).

The flow cytometry results for untreated control cells demonstrate a predominant population of healthy, viable cells, as indicated by the 91.05% found in the live quadrant. A smaller fraction of the cells, 1.90%, are in early apoptosis, exhibiting Annexin V positivity without loss of membrane integrity, while 6.20% are classified as late apoptotic or dead, marked by both Annexin V and PI staining. The remaining 0.85% represents cell debris. This distribution is consistent with a cell population maintained under optimal conditions, showing minimal spontaneous apoptosis and strong viability. The population profile further reflects a uniform cell size index, supporting overall cellular health in control samples (Plate 7.19).

Treatment with silver nanoparticles (AgNPs) synthesized from the methanol extract of *S. palghatense* bark caused major changes in the cell population. The flow cytometry results show that only 32.40% of cells remain viable after exposure, indicating a significant reduction in cell survival compared to controls. Most of the cells, 60.45%, are identified in the late apoptotic/dead quadrant, reflecting strong cytotoxic effects induced by the nanoparticles. Early apoptotic cells represent 1.45%, and 5.70% of debris is observed, showing increased cell damage and fragmentation.



(a)



(b)

	Cell Conc. (Cells / mL)	% Gated
Live (LL) :	4.01E+05	91.05 %
Early Apoptotic (LR) :	8.36E+03	1.90 %
Late Apop./ Dead (UR) :	2.73E+04	6.20 %
Debris (UL) :	3.74E+03	0.85 %
Total Apoptotic :	3.56E+04	8.10 %

(c)

Plate 7.19: Flow cytometry analysis of cell population, apoptosis profiles, and cell distribution in control cells: (a) Population profile of untreated control cells (b) Apoptosis profile of untreated control cells (c) Cell distribution analysis of untreated control cells

The population profile also reveals considerable heterogeneity in cell size and a shift away from healthy cell morphology, consistent with extensive apoptosis and cell death following AgNPs treatment. These results demonstrate the potent anti-proliferative and apoptosis-inducing properties of AgNPs against the tested cell line (Plate 7.20).

7.3.13.6. Indirect ELISA (Enzyme-Linked Immunosorbent Assay)

Figure 7.32 shows the Caspase-9 enzyme activity, expressed as units per milligram of protein, across three different sample groups: the control, silver nanoparticles (AgNPs) synthesized from *S. palghatense* bark-treated group, and a standard reference. The control group exhibits the lowest Caspase-9 activity, indicating baseline enzyme levels without treatment. Treatment with AgNPs leads to a moderate increase in enzyme activity compared to the control, suggesting a stimulatory effect of these nanoparticles on Caspase-9. The standard sample shows the highest activity, serving as a reference for maximal enzyme response. This data implies that AgNPs derived from *S. palghatense* bark can enhance Caspase-9 activity, which may have implications for cellular processes involving this enzyme.

7.3.13.7. Analysis of DNA content and cell cycle distribution using the cell cycle kit by flow cytometry

The analysis of untreated control MCF-7 cells using flow cytometry and the MUSE Cell Cycle Kit demonstrates a typical healthy cell cycle distribution. The population profile plot shows a concentrated distribution of cells within the gated region, indicating a well-defined and viable cell population (Plate 7.21 a). The DNA content profile reveals that most cells are in the G0/G1 phase (71.7%), with a smaller proportion in the S phase (11.2%) and G2/M phase (15.5%) (Plate 7.22 b). This suggests that the majority of control cells are either resting or preparing for DNA synthesis, with only a small fraction actively synthesizing DNA or undergoing mitosis. (Plate 7.21)

The result summarizing the percentages, means, and coefficients of variation for each phase confirms these findings, with low percentage coefficient of variation

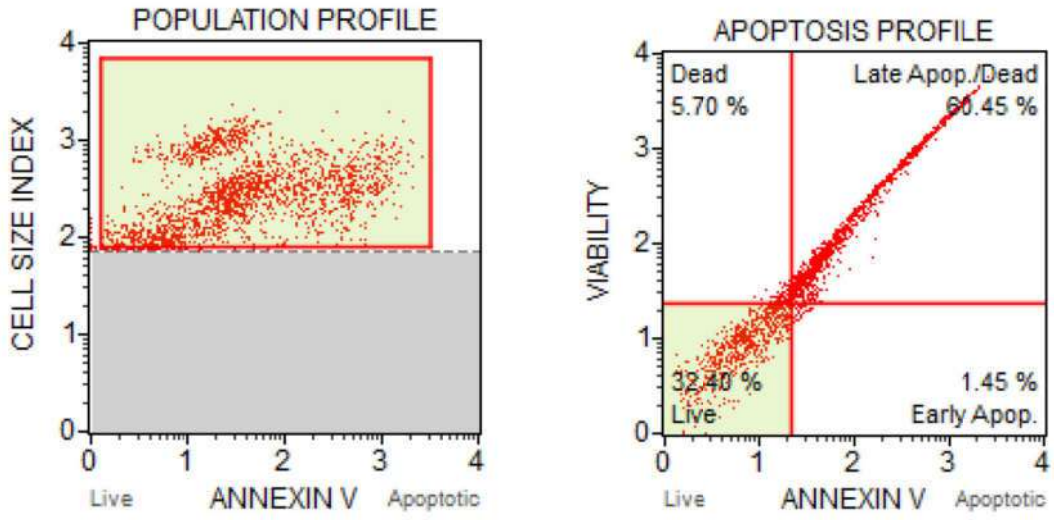
(CV) values supporting precise discrimination between cell cycle phases. The data overall indicate a normal cell cycle progression, with minimal stress or arrest, as would be expected in healthy untreated controls (Plate 7.21 c). This baseline distribution provides a reliable reference point for assessing changes in cell cycle progression following treatment or experimental manipulation. The cell cycle of standard cisplatin and the sample are displayed in Plates 7.22 and 7.23.

7.3.14. Formulation of a cream from the methanol extract of *S. palghatense* bark silver nanoparticles (AgNPs)

This cream formulation incorporates silver nanoparticles (AgNPs) synthesized from the methanol extract of *S. palghatense* bark, combined with skin-soothing and moisturizing agents such as aloe vera gel, shea butter, and liquid paraffin. The sterile distilled water is added as needed to achieve the desired consistency. Together, these ingredients aim to create a topical product that leverages the antimicrobial and therapeutic properties of green-synthesized silver nanoparticles with natural emollients for enhanced skin care and potential healing benefits (Table 7.47).

This cream contains silver nanoparticles synthesized from the methanol extract of *S. palghatense* bark, which provides wound healing, anti-inflammatory, and antibacterial benefits due to the unique bioactivity of the nanoparticles. Aloe vera gel contributes to reducing acne and soothing the skin, while shea butter acts as an emulsifying agent to stabilize the cream's texture. Liquid paraffin functions as a lubricating agent, enhancing smooth application, and sterile distilled water serves as the vehicle to adjust the formulation consistency (Table 7.48). Together, these ingredients create a multifunctional topical cream aimed at promoting skin healing, reducing inflammation, and protecting against microbial infections (Ahmed et al., 2016).

The cream prepared using silver nanoparticles derived from the methanol extract of *S. palghatense* bark shows a consistent and smooth texture, indicating proper blending of the nanoparticles within the cream base. It has a white to off-white appearance, which is common for creams containing nanoparticles and is acceptable for both cosmetic and medical purposes. The pH of the cream is maintained between



	Cell Conc. (Cells / mL)	% Gated
Live (LL) :	9.76E+04	32.40 %
Early Apoptotic (LR) :	4.37E+03	1.45 %
Late Apop./ Dead (UR) :	1.82E+05	60.45 %
Debris (UL) :	1.72E+04	5.70 %
Total Apoptotic :	1.86E+05	61.90 %

(a) **(b)** **(c)**

Plate 7.20: Flow cytometry analysis of cell population, apoptosis profiles, and cell distribution in silver nanoparticles (AgNPs) synthesized from the methanol extract of *Syzygium palghatense* bark: (a) Population profile of AgNPs (b) Apoptosis profile of AgNPs (c) Cell distribution analysis of AgNPs

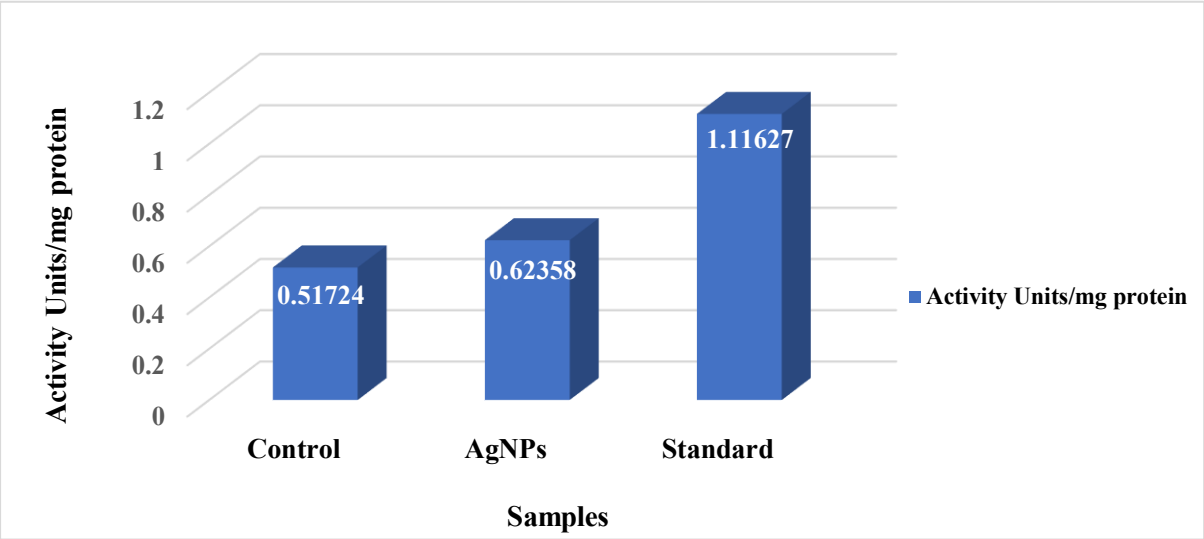
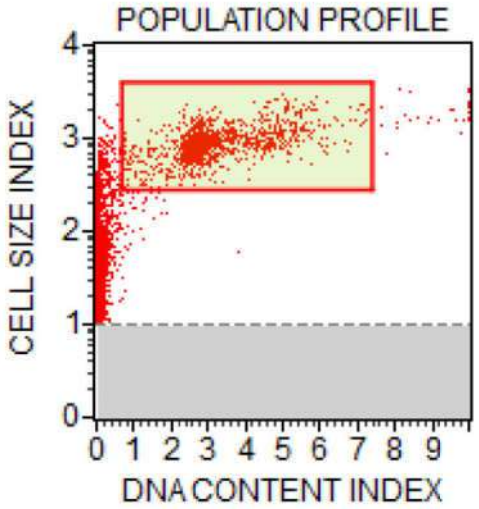
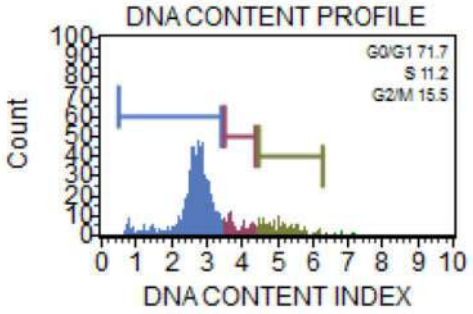


Figure 7.32: Caspase-9 activity (Units/mg protein) in Control, silver nanoparticles (AgNPs) from *Syzygium palghatense* bark-treated, and Standard samples measured by ELISA (Enzyme-Linked Immunosorbent Assay)



(a)

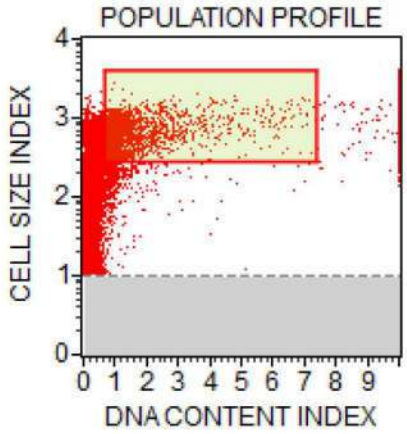


(b)

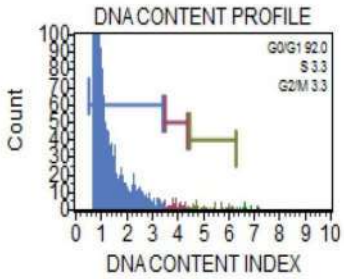
	G0/G1	S	G2/M
% Gated :	71.7	11.2	15.5
Mean :	2572.4	3893.4	5122.2
% CV :	22.9	7.6	9.3

(c)

Plate 7.21: Analysis of (a) Cell population (b) DNA content, and (c) Cell cycle distribution in untreated control



(a)

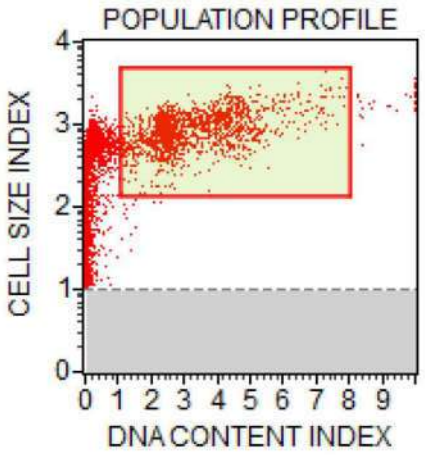


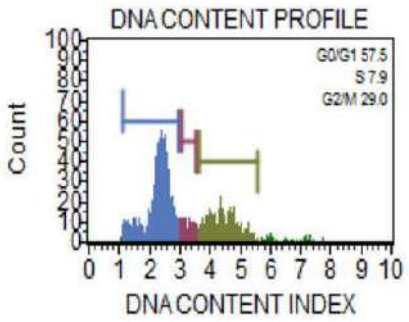
(b)

	G0/G1	S	G2/M
% Gated :	92.0	3.3	3.3
Mean :	1277.6	3901.3	5306.7
% CV :	49.4	6.6	10.2

(c)

Plate 7.22: Analysis of (a) Cell population (b) DNA content, and (c) Cell cycle distribution in standard cisplatin





	G0/G1	S	G2/M
% Gated :	57.5	7.9	29.0
Mean :	2263.3	3286.7	4431.2
% CV :	19.2	5.1	10.9

Plate 7.23: Analysis of (a) Cell population (b) DNA content, and (c) Cell cycle distribution in silver nanoparticles (AgNPs) synthesized from the methanol extract of *Syzygium palghatense* bark

Table 7.47: Ingredients and quantities in silver nanoparticle (AgNPs)-infused cream formulation from *Syzygium palghatense* bark

Ingredients	Quantity
Silver nanoparticles (AgNPs) synthesized from the methanol extract of *Syzygium palghatense* bark	1.5 mL
Aloe vera gel	2.00 mL
Shea butter	5.00 g
Liquid paraffin	9.5 mL
Sterile distilled water	q.s. (quantity sufficient)

Table 7.48: Ingredients and their roles in silver nanoparticle-based cream formulation from *Syzygium palghatense* bark

Ingredients	Roles
Silver nanoparticles (AgNPs) synthesized from the methanol extract of *Syzygium palghatense* bark	Wound healing, anti-inflammatory, and anti-bacterial properties
Aloe vera gel	Reduce acene
Shea butter	Emulsifying agent
Liquid paraffin	Lubricating agent
Sterile Distilled Water	Vehicle

(References: **Ahmed et al., 2016)**

Table 7.49: Antifungal activity of formulated cream of silver nanoparticles (AgNPs) synthesized from the methanol extract of *Syzygium palghatense* bark

Organism	Zone of Inhibition (in mm)			Antibiotic Fluconazole (in mm)
	100 µg/mL	150 µg/mL	200 µg/mL	
Candida albicans	10 ± 0.2031	12 ± 0.2014	13 ± 0.3011	11 ± 0.2451

Values are mean ± Standard Error (SE)

Table 7.50: Antibacterial activity of formulated cream of silver nanoparticles (AgNPs) synthesized from the methanol extract of *Syzygium palghatense* bark

Organism	Zone of Inhibition (in mm)			Antibiotic – Streptomycin (in mm)
	100 µg/mL	150 µg/mL	200 µg/mL	
Pseudomonas aeruginosa	14 ± 0.3021	17 ± 0.3564	19 ± 0.4125	9 ± 0.3145
Staphylococcus aureus	10 ± 0.1025	12 ± 0.2563	15 ± 0.2341	12 ± 0.2314

Values are mean ± Standard Error (SE)

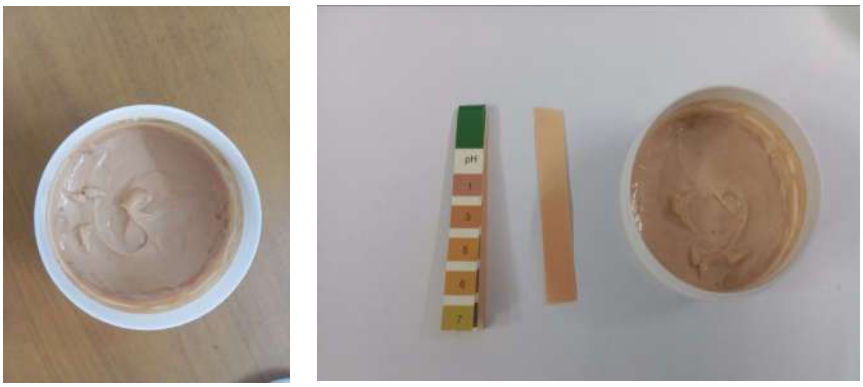


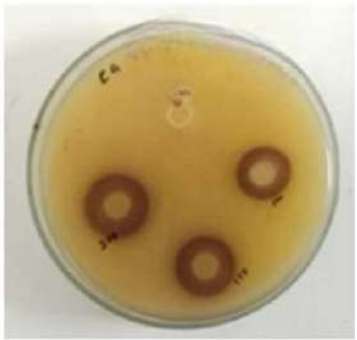
Plate 7.24: Formulated cream from the silver nanoparticles synthesized from the methanol extract of *Syzygium palghatense* bark: (a) Cream (b) Cream showing pH range



(a)



(b)



(c)

Plate 7.25: Zone of inhibition (mm) of silver nanoparticles synthesized from the methanol extract of *Syzygium palghatense* bark against: (a) *Pseudomonas aeruginosa* (b) *Staphylococcus aureus* (c) *Candida albicans*

4.5 and 6.5, aligning well with the skin's natural pH level. This balance helps prevent skin irritation and supports the skin's protective barrier. These characteristics suggest that the cream is stable, safe to use on the skin, and effective for delivering the silver nanoparticles topically (Plate 7.24).

7.3.14.1. Antimicrobial activity of formulated cream of silver nanoparticles synthesized from the methanol extract of *S. palghatense* bark

The antifungal activity of the formulated cream containing silver nanoparticles synthesized from the methanol extract of *S. palghatense* bark was evaluated against *Candida albicans*. The zones of inhibition (ZOI) ranged between 10 ± 0.2031 mm to 13 ± 0.3011 mm, indicating moderate antifungal efficacy of the cream formulation (Table 7.49, Plate 7.25).

The antibacterial activity of the same formulated cream was assessed against *Pseudomonas aeruginosa* and *Staphylococcus aureus* at concentrations of 100, 150, and 200 µg/mL. The zone of inhibition for *P. aeruginosa* increased from 14 ± 0.3021 mm at 100 µg/mL to 19 ± 0.4125 mm at 200 µg/mL, with the antibiotic streptomycin showing a 9 ± 0.3145 mm zone. For *S. aureus*, the respective zones were 10 ± 0.1025 mm, 12 ± 0.2563 mm, and 15 ± 0.2341 mm, compared with 12 ± 0.2314 mm for streptomycin (Table 7.50).

The results demonstrate dose-dependent antimicrobial properties of the silver nanoparticle cream, showing increased efficacy with higher concentrations. The efficacy against both fungal and bacterial pathogens suggests that the cream may serve as a potential topical antimicrobial agent.

7.4. Discussion

Previously, only chemical and physical techniques were used to produce nanoparticles. Chemical synthesis methods frequently result in the surface absorption of some hazardous chemicals that might have negative effects in medical applications. That is not a problem for nanoparticles that are biosynthesized using the green synthesis method. Plant extracts (also known as phytochemicals) and microbial enzymes often cause metal compounds to be reduced into their corresponding nanoparticles due to their reducing or antioxidant qualities (Ramya & Subapriya, 2012). In the present study, AgNPs were successfully synthesized by *S. palghatense* methanol extract as a reducing and stabilizing agent.

To the best of our knowledge, this is the first investigation into the synthesis of AgNPs with *S. palghatense*. However, earlier research of comparable nature has been done with other species of the *Syzygium* genus, therefore we utilize that articles in this section. A study was carried out by Kumar et al. (2010) to examine the biomolecules of *S. cumini* that are used in the production of silver nanoparticles which discovered that SNP production is exclusively caused by highly polar soluble molecules. Earlier, the green approach was used to generate Ag NPs using *S. aromaticum* (Vijayaraghavan et al., 2012) and fruit extract from *S. cumini* (Chakravarty et al., 2022)

The study of *S. palghatense* methanol bark extract revealed significant potential in green synthesis of silver nanoparticles (AgNPs), demonstrating distinctive physicochemical properties and robust biological activities. The synthesized AgNPs exhibited characteristic surface plasmon resonance at 440 nm, confirming successful nanoparticle formation facilitated by polyphenolic compounds acting as reducing and stabilizing agents. These nanoparticles were primarily spherical with sizes ranging between 10 and 100 nm, consistent with the morphology reported for other *Syzygium* species nanoparticles, such as *S. cumini*, which also show effective capping by phytochemicals that influence shape and size distribution (Ahmed et al., 2016; Khan et al., 2019).

In the UV-Vis region, spectroscopy is a quick, convenient, cost-effective, and ubiquitous technique for detection and qualitative and quantitative characterization (Abdolkarimi-Mahabadi et al., 2021). UV-Vis spectroscopy was used for the confirmation of AgNPs formation. UV-Vis peak for extract appeared at 410 nm and for the synthesized AgNPs showed the characteristic peak at 440 nm (SPR band). Concentration 6 mg/mL extract gave the highest absorbance. The UV spectra of the silver nanoparticles made from *S. cumini* seeds showed the highest absorbance at around 450 nm after a 24-hour incubation period (Banerjee & Narendhirakannan, 2011). A characteristic peak at 443 nm from Ag NPs of *S. cumini* (fruit extract) was reported by Chakravarty et al. (2022).

FTIR analyses were conducted to identify various biomolecules in the *S. palghatense* bark aqueous extract, which is the key element that stabilizes and reduces the nanoparticle solution. Functional groups -OH (3439 cm^{-1}) and C=O (1633 cm^{-1}) were involved in reduction and stabilization. Shonekan et al. (2019) reported similar absorption peaks in the methanol extract of *S. guineenses* at 3341 cm^{-1} (-OH) for alcohol, 1736 cm^{-1} (C=O) for the carbonyl group, 1161.83 cm^{-1}, and 1036.49 cm^{-1} (C-O) for esters. According to Idris et al. (2023), chemometric studies when combined with FTIR and GC-MS can be utilized as a quick way to distinguish between bioactive structural functionalities and their biological activity.

Numerous important parameters, such as size distribution, shape, surface chemistry, surface charge, and the presence of capping agents, affect the biological activity of inorganic nanoparticles. These factors are important to show that how these nanoparticles responsible for performing various therapeutic functions and how they interact with the biological systems (Muruganandham et al., 2023). Morphology of the synthesized *S. palghatense*-derived AgNPs was also studied using various techniques. It was found that the synthesized AgNPs are mainly spherical in shape and the size is between 60 nm to 85 nm. Variations in the size of *S. aromaticum* derived AgNPs was reported by Vijayaraghavan et al. (2012) with 20 to 149 nm with almost spherical shape. *S. alternifolium* (aqueous fruit extract) derived AgNPs also are spherical in shape with size ranging from 5 nm to 68 nm and are polydispersed

(Yugandhar & Savithramma, 2016). Chakravarty et al. (2022) reported the 47 nm size of the *S. cumini* (fruit extract) derived Ag NPs with spherical shape. The morphology and form of nanoparticles can affect their ability to behave biologically. For example, research has shown that various forms, such as cubes, spheres, or rods, can result in varied biodistribution patterns and cellular reactions (Albanese et al., 2012; Yaqub et al., 2023). It was found that the synthesized silver nanoparticles are crystalline and face-centered cubic.

The methanolic extract of bark and leaves of *S. palghatense* possesses potential antioxidant, antidiabetic compounds, and also important therapeutic properties. In the present study, AgNPs synthesized from the methanolic extract of *S. palghatense* bark showed stronger antioxidant potential than ascorbic acid in DPPH, superoxide, hydroxyl, and FRAP assays. Highest activity observed in FRAP assay with 90% inhibition at 150 µg/mL. According to Shonekan et al. (2019), the methanol extract of *S. guineenses* has a greater potential for phytochemicals and antioxidants. According to Dos Santos et al. (2024) the antioxidant activity of phenolic components from *S. cumini* was enhanced by nanoencapsulation by up to 110% compared to the crude extract.

S. palghatense-derived AgNPs demonstrated superior antioxidant capacity across multiple assays (DPPH, superoxide, hydroxyl radical scavenging, and FRAP) compared to the standard ascorbic acid, with notably lower IC_{50} values suggesting enhanced free radical scavenging potential relative to some *Syzygium* extracts previously reported (Dakwal et al., 2016).

Moderate antifungal activity (against *Aspergillus niger* (19 mm) and *Candida albicans* (22 mm)) at 1000 µg/mL and a strong dose-dependent antibacterial effect with the highest inhibition against *Pseudomonas aeruginosa* (31 mm zone) at 1000 µg/mL was recorded in the present study. Yugandhar & Savithramma (2016) found high toxicity against various bacterial and fungal isolates is shown by the antimicrobial study of Ag NPs from the aqueous fruit extract of *S. alternifolium.* Using fruit extract from *S. alternifolium*, Yugandhar et al. (2018) manufactured copper oxide nanoparticles (CuO NPs) and assessed their antiviral effectiveness against Newcastle

Disease Virus (NDV) and discovered that they may have a growth-inhibiting impact on the virus. Based on Desalegn et al. (2021) antibacterial test results, *S. guineense*-Ag NPs have the potential to treat infectious diseases carried by the tested pathogens. They demonstrated a synergistic effect against Gram-positive bacteria, *S. aureus*, as well as Gram-negative bacteria, *P. aeruginosa, E. coli*, and *E. aerogenes.* Similarly, Ag NPs from fruit extract of *S. cumini* shown antibacterial qualities against numerous bacterial species (gram-positive and gram-negative) and strong anti-inflammatory and antioxidant properties were also discovered by Chakravarty et al. (2022). Muruganandham et al. (2023) found that compared to the aqueous extract, *S. aromaticum*-Ag NPs shown a greater degree of effectiveness in preventing the development of bacteria and fungus. The antimicrobial profile of these nanoparticles showed promising but moderate antifungal effects and significant antibacterial efficacy, especially against Gram-negative bacteria such as *Pseudomonas aeruginosa*, which aligns with findings for other *Syzygium* species nanoparticle preparations, though variations in potency depend on the species and extraction method (Chakraborty, 2024).

The emergence of antibiotic resistance and infections linked to microbial biofilms is being seen as major public health issues (Del Pozo, 2017). Advanced antibacterial tests were done on *Pseudomonas aeruginosa*, SPB Ag NPs significantly inhibited biofilm formation in a dose-dependent manner. They showed significant antibiofilm effects, reducing microbial resistance mechanisms. Because biofilms on biomaterials are more resistant to host immune responses and antimicrobial treatment, they can have significant clinical consequences. By using AgNPs-HEScL, Bernardo et al. (2022) found substantial effects against combined cell adhesion and mixed biofilm production of *S. aureus* and *S. epidermidis.* The safety and effectiveness of Sa-Ag NPs for a variety of antibacterial and antibiofilm applications are further supported by the results of a study conducted by Makky et al. (2023). Diksha et al. (2023) carried out similar investigations and discovered a notable decrease in motility patterns as suggested by the action of AgNPs made using *S. cumini* leaf extract towards *P. aeruginosa* and *A. baumannii*. Therefore, a greener way of synthesizing AgNPs might be confirmed as a workable alternative for getting treatment of

infections brought on by nosocomial microorganisms that are resistant to several drugs.

With potential uses in animal health, nanotechnology is a scientific discipline with tremendous potential (Kaiaty et al., 2023). Kavitha et al. (2011) was the first study to report on the anthelmintic activity of methanolic and aqueous extracts of the bark of *S. cumini*. According to their research, the methanolic extract of *S. cumini* bark has the potential to be effective as an anthelmentic, whereas the aqueous extract has modest anthelmentic action. Synthesized AgNPs was also found to exhibited significant anthelmintic activity in a concentration-dependent manner in the present study**.** According to Maregesi et al. (2016), who reported similar findings, *S. guineense* fruits are an excellent source of macro and micronutrients and may also have antihelmintic properties.

The anti-inflammatory potential of *S. palghatense* AgNPs was also remarkable, exhibiting dose-dependent inhibition of relevant enzymes like COX and LOX, surpassing standard drugs such as indomethacin, which positions this species as a potentially superior source for anti-inflammatory agents within the genus

According to the findings, Ag NPs successfully shield the HRBC membrane from lysis brought on by hypotonic stress, indicating their potential as strong anti-inflammatory drugs via membrane-stabilizing processes. AgNPs exhibited superior anti-inflammatory potential compared to standard drugs. Prior research by Akolkar et al. (2025) emphasizes the advantages of sustainable nanoparticle production and suggests that *S. stocksii*-mediated Ag NPs may have biomedical uses. Synthesized Ag NPs showed promising anti-inflammatory effects (20.26% inhibition in the hemolysis model at 300 µg/mL) and moderate antioxidant activity (24.69% DPPH inhibition at 1000 µg/mL), according to biological assessment. It was also found in the present study that AgNPs promote wound healing and tissue regeneration effectively in zebrafish, as the treated groups showed faster caudal fin regeneration and histology showed enhanced tissue remodeling, angiogenesis, and no cytotoxic effects**.**

Bhavi et al. (2024) examined the possibility of *Syzygium*-based AgNPs as a novel strategy for managing diabetes and discovered that they could successfully control blood glucose levels in a manner comparable to those of traditional drugs. They can lower oxidative stress, increase insulin sensitivity, and improve glucose metabolism. It was recorded that *S. palghatense*-derived AgNPs exhibit potent antidiabetic effects by inhibiting carbohydrate-digesting enzymes, enhancing glucose uptake, reducing hepatic glucose production, downregulating PGC-1α, and stimulating insulin secretion**.** Their efficacy is greater than or comparable to standard drugs like acarbose, Pioglitazone, and Metformin. Fatima et al. (2025) found that with the biological extract of *S. cumini*, the antidiabetic test of silver nanoparticles (AgNPs) showed 54.6% inhibition of the α-glucosidase enzyme at an optimal dose of 50 µg/mL. A study conducted by Nadar and Sellappan (2025) shows that *S. salicifolium* is useful as a sustainable precursor for multifunctional nanoparticles. In comparison to diclofenac, the hypoglycemic activity demonstrated inhibition of α-amylase and α-glucosidase, as well as a good anti-inflammatory impact against albumin denaturation and membrane stabilization.

Numerous compounds produced from plants have been shown to exhibit strong anticancer activity against a variety of human and animal cancer cell lines (Lin et al., 2003). In the present study, AgNPs exhibit significant anticancer activity by inducing apoptosis, reducing cell viability, altering protein levels, and activating Caspase-9 pathways**.** While cisplatin remains slightly more potent**,** AgNPs offer a natural, less toxic alternative for cancer therapy. The possible anticancer effect of green produced AgNPs against A549 tumor cell lines was examined by Thampi & Shalini (2015). It suggested that a wide range of potential uses, including targeted medication administration to tumor cells, are made possible by metal-based nanoparticles and a deeper comprehension of specific chemical pathways. Aqueous leaf extract from *S. jambolanum* was used in the manufacture of silver nanoparticles by Madakka et al. (2021). In a cytotoxic experiment, these NPs had antihemolytic action at lower concentrations and demonstrated potent anti-cancerous activity against the MCF-7 breast cancer cell line. According to Vishal et al. (2023), *S. aromaticum* has been shown to have potential anticancer properties. The *in vitro* evaluation of CL-

AgNPs' anticancer activity in the MCF-7 cell line strengthens the *in-silico* research by demonstrating the active interactions between the phytochemicals in clove and the breast cancer target proteins. Abdulrahman & Hama (2023) anticancer test examination revealed that the genus, particularly *S. aqueum, S. samarangense*, and *S. cumini*, showed great potential as an anticancer agent *in vitro* against a number of cancer cell lines. According to Ibrahim et al. (2023), the plant *S. aromaticum* has the ability to activate immune cells and can be employed as an immune-stimulatory agent to combat tumors and their growth.

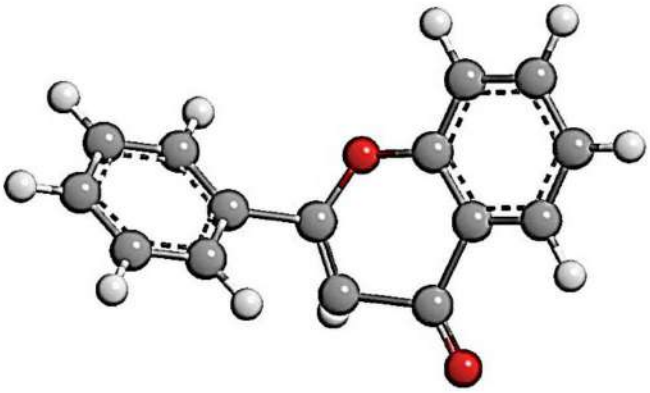
Additionally, the nanoparticle formulation in cream form maintained favorable physicochemical properties, including a pH compatible with the skin, enhancing topical applicability, which has parallels in formulations involving *S. aromaticum* extracts used in dermatological applications. Overall, *S. palghatense* distinguishes itself through its enhanced nanoparticle synthesis facilitated by its unique phytochemical profile, along with potent antioxidant, antimicrobial, anti-inflammatory, and wound-healing activities compared to closely related *Syzygium* species, making it a valuable candidate for further pharmacological development (Ahmed et al., 2016; Khan et al., 2019).

7.5. Conclusions

Syzygium plants are used in "green synthesis" to produce AgNPs, which are safe and environmentally friendly. Green synthesis has several advantages over chemical and physical processes, including being inexpensive, environmentally friendly, and simple to scale up for large-scale synthesis. AgNPs provide a supplemental strategy that increases the efficacy of current therapies when used in combination with conventional medications. In this study, AgNPs mediated by *S. palghatense* were effectively produced and evaluated for a range of therapeutic effects.

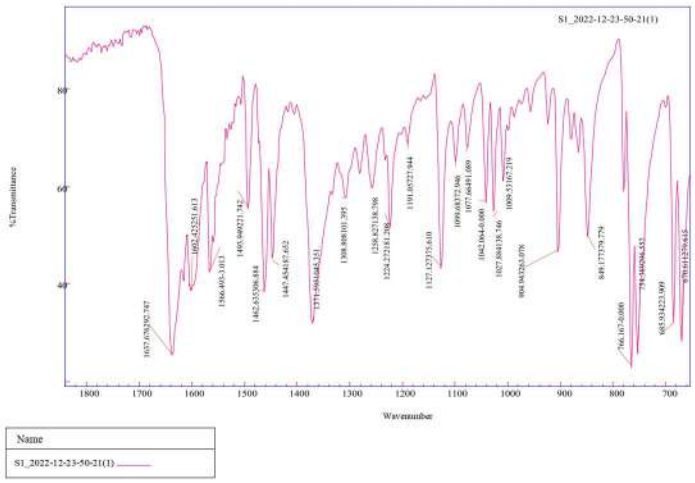
According to the results, it had strong anti-biofilm and quorum-sensing inhibition effects, particularly against *Pseudomonas aeruginosa*; significant anthelmintic properties that outperformed the standard medication albendazole; and significant anticancer activity by causing apoptosis, lowering cell viability, changing protein levels, and activating Caspase-9 pathways. *S. palghatense*-derived AgNPs also exhibit potent antidiabetic effects by inhibiting carbohydrate-digesting enzymes, enhancing glucose uptake, reducing hepatic glucose production, downregulating PGC-1α, and stimulating insulin secretion. These multifaceted properties of AgNPs produced from *S. palghatense* demonstrate their prospective uses in nanotherapeutics, pharmaceuticals, and biomedicine. They are appropriate for further development as innovative therapeutic agents due to their efficacy across a variety of biological processes.

Although there are several studies on the synthesis of AgNPs from other *Syzygium* species, there wasn't any prior research on *S. palghatense*. With the use of its bark extract, this work offers an initial demonstration of the green synthesis and characterisation of *S. palghatense*-AgNPs as well as information on their biological potential. Future research is necessary to investigate the medicinal uses of AgNPs generated from *S. palghatense*, as this might lead to new opportunities for their application in antimicrobial treatment, nanomedicine, and chemicals. The formulated cream has potential wound-healing and antimicrobial properties.



8

ISOLATION AND BIOACTIVITY VALIDATION OF PHYTOCOMPOUNDS



CHAPTER 8

ISOLATION AND BIOACTIVITY VALIDATION OF PHYTOCOMPOUNDS

8.1. Introduction

Bioactive chemicals produced from medicinal plants are well recognized for their role in primary healthcare as a source of novel drugs for a variety of treatments (Ahmad et al., 2014). Many of the pharmaceuticals we use on a daily basis in modern medicine are produced from phytocompounds, which are substances obtained from plants and their metabolites (Wang, 2021). Plant-based foods can help in the prevention or lower the threat of chronic diseases like cancer, diabetes mellitus, arterial hypertension, and cardiovascular disease because they contain biologically active plant compounds called phytochemicals, according to increasing data from scientific, *in vitro*, *in vivo*, and clinical test results. Phytocompounds affect systemic, cellular, and molecular processes (Portincasa & Calamita, 2019). People across the world depend on herbal plants, which are a treasured gift from nature to humanity. These plants contain a variety of phytoconstituents that have been passed down to the next generation and used to treat illnesses. Medicinal plants may produce a wide range of low molecular weight (MW) chemical molecules known as secondary metabolites, which typically have complex and distinctive structures (Devakumar et al., 2017)

Plants and plant-based products play a vital role in the human diet in addition to being a significant source of physiologically active chemicals, including antioxidants, dietary fiber, vitamins, and molecules that decrease cholesterol (Velavan, 2015). Phytocompounds are beneficial substances (phenolic, amino acids, vitamins, and minerals) found in a variety of plant materials that have therapeutic potential for a range of biological activities, including the prevention and treatment of cardiovascular disease, cancer, and other chronic illnesses (Muhamad et al., 2017). Around the world, traditional medicines made from medicinal plants have been used to cure a variety of illnesses. Recently, there has been a growing interest in learning

more about the medicinal properties of plants that are found across the world (Mujawah et al., 2023).

Some bioactive phytocompounds (containing coumarin, thiosulfonate, proanthocyanidin, steroid, polysaccharide, alkaloid, tannin, lignin, terpene, quinone, flavonoid, saponin, and polyphenol) are known to possess inhibitory effects against a number of viral diseases (Mohanty et al., 2023). A growing body of research indicates that the natural products and bioactive components of many plants have promising anticancer efficacy and are less harmful than traditional anticancer medications. Their water solubility, lack of stability, absorption, bioavailability, and selective targeting, however, significantly limit their broad application in cancer therapy (Bozzuto et al., 2024).

Numerous secondary metabolites, including terpenoids, flavonoids, alkyl phloroglucinols, chalcones, lignans, hydrolyzable tannins, and chromone derivatives, are found in the *Syzygium* genus (Memon et al., 2015; Aung et al., 2020). A genus of economic and ecological significance, *Syzygium* species are grown for their fruits on a commercial basis (*S. cumini*, *S. jambos*), timbers (*S. aqueum*, *S. malaccense*), or as spices or for medical purposes (*S. aromaticum*) (Sreekumar et al., 2020). Genus *Syzygium* is thought to have over 1200 species, is the largest genus under the family Myrtaceae. Many species of this genus are grown in various places for their delicious fruits and medicinal qualities (Parnell et al., 2007; Byng et al., 2015; Eswarappa & Somashekar, 2020). There are 54 species of *Syzygium,* which are known in India (Govaerts et al., 2008; Sreekumar et al., 2020). Largest diversity of *Syzygium,* with 48 species, are found in the Western Ghats, from which 27 are endemic to there (Sujanapal & Kunhikannan, 2017; Sreekumar et al., 2020).

The *Syzygium* flourishes in the forests of Western Ghats, particularly in the tropical wet evergreen forests and higher altitude Shola peaks. Species such as *S. palghatense* are recognized from a single location (Sreekumar et al., 2020). *S. palghatense* represents a small to medium-sized evergreen tree that may grow up to 15 meters in height. It has only been found in one place in the Anamalai region of the southern Western Ghats. *S. palghatense* was believed to be extinct, but after 140 years,

it was found again near the original site. Between 1,100 and 1,524 meters above sea level, only three mature specimens were recorded inside the boundaries of Kerala's Parambikulam Tiger Reserve. The most recent evaluation of *S. palghatense* for listing on the IUCN Red List of Threatened Species was conducted in 2022. The criteria have classified *S. palghatense* as Critically Endangered (Amitha Bachan & Devika, 2023).

Traditional remedies are largely used in developing countries. Various plant extracts or their bioactive components are used in this traditional medication (Aravindhan et al., 2009). Plants have therapeutic significance because of certain chemicals that have specific physiological effects on humans. The most significant bioactive components found in plants include phenolic chemicals, alkaloids, flavonoids, and tannins (Doss, 2009). Plant-based medications are widely accessible, reasonably priced, safe, effective, and rarely cause adverse effects (Yadav & Agarwala, 2011). The secondary metabolites that are produced also have significant characteristics for both ornamental and food plants, such as flavour, colour, and fragrance. Furthermore, many plants secondary metabolites, including flavonoids, alkaloids, steroids, tannins, saponins, terpenoids, rotenoids, etc., have been used commercially as flavoring agents, fragrances, drugs, dyes, and insecticides (Velavan, 2015).

Medicinal herbs have been used for centuries to treat a variety of ailments and epidemics. Numerous biological actions are demonstrated by them, including antioxidant, antibiotic, anti-inflammatory, anti-parasitic, anti-insecticidal, and anti-hemolytic qualities. Various bioactive chemicals found in medicinal plants are crucial for both disease prevention and the production of pharmaceuticals. Consequently, populations across the world greatly benefit from phytochemicals (Mondal et al., 2024). Nowadays, plants play a significant role in homeopathy, herbal medicine, allopathic treatment, and aromatherapy. Medicinal herbs are the source of many significant contemporary medications (Ajayi et al., 2011). Numerous techniques, including extraction, separation, purification, identification, structural clarification, physical and chemical property evaluation, biosynthesis, and quantification, can be

used to investigate the phytochemicals present in a plant (Anulika et al., 2016; Aung et al., 2020).

Extracts derived from plants can have various uses, especially in food and medicines. Characterizing the bioactive compounds from the plant for the physical and chemical nature can helps in identifying the various applications it can offer (Muhamad et al., 2017). The important section for studying the medicinal properties of medicinal plants are the isolation and characterization of the phytoconstituents they possess (Saxena, 2023). A number of chromatographic techniques are available to tackle this problem, like thin-layer chromatography (Sindhu et al., 2021). These chromatographic techniques used for the isolation of the compounds from a mixture of chemicals (Raaman, 2006; Shah, 2018). TLC provides a fast, sensible and cost-effective method for the identification of the compound also helps in purification of the compounds (Cai, 2014).

Gas chromatography and mass spectrometry are both used in GC-MS analysis. Gas chromatography provides the analysis of the compound in an extract (Khan et al., 2017), while mass spectrometry helps in the identification and identifying the molecular and chemical properties of the substance. For identifying the functional group present in a compound, FTIR can be used, as well as for determining its structure. Other techniques like Nuclear Magnetic Resonance Spectroscopy offer the chemical, biological as well as physical properties of the substance. The structure of the chemical substance can also be formed by the 2D NMR technique (Ingle et al., 2017).

Whether it is purified or not, the phytocompounds can be used for medicinal purposes (Sruthi et al., 2023). However, there are new approaches for the improvement of these but traditional approaches are also being used, which include maceration, percolation, as well as Soxhlet extraction. But the more yield are given by the modern techniques, which includes SFE (supercritical fluid extraction), PLE (pressurized liquid extraction), UAE (ultrasound-assisted extraction) and MAE (microwave-assisted extraction). As the biochemicals have been extracted, they must be identified. For the separation and measurement of the bioactive phytochemicals, chromatographic techniques such as GC and HPLC can be used. In addition to those

spectroscopic approaches, like MS (Mass spectrometry) and NMR (nuclear magnetic resonance) provide the information about the structure of the compounds (Saxena, 2023).

Natural substances are a good source for creating molecules that are active in many diseases, including cancer (Bozzuto et al., 2024). Because the bioactive chemicals found in plant material are multi-component combinations, there continue to be issues with their extraction, identification, and determination. The majority of them must, in practice, be purified using a combination of various chromatographic techniques and other purification processes in order to isolate the bioactive ingredient (Ingle et al., 2017).

Individuals from different parts of the world are now interested in plants because of the growing need for various chemicals in screening programs and the search for medicinal medications made from natural materials. An effective extraction technique is essential to drug development as it is the fundamental first step in phytochemistry, pharmacognosy, and medicinal plant research to obtain the desired molecule (Sruthi et al., 2023). Since these types of secondary metabolites are frequently present in minute levels in plants, the primary limiting factor after the identification of any potential metabolite is the capacity to produce sufficient material for application in both industrial and medicinal contexts (Saifi et al., 2024).

The long extraction time, significant solvent consumption, and the possibility of sensitive chemical degradation are some disadvantages of traditional extraction techniques. Effective separation, identification, and quantification of bioactive plant chemicals have been made possible by liquid chromatography (LC), gas chromatography (GC), and their hyphenated forms, such as LC–mass spectrometry (LC-MS) and GC–mass spectrometry (GC-MS). The technique known as high-performance LC (HPLC) is widely utilized because of its effectiveness, sensitivity, and adaptability. Accurate and rapid identification of bioactive substances has been made feasible by the combination of tandem mass spectrometry and HPLC. Along with the advancement of cutting-edge technology, the development of more environmentally friendly and efficient methods has advanced the area of natural substance discovery and made it easier to identify possible lead compounds for therapeutic applications and drug development (Ogbole et al., 2025).

Although bioactive chemicals generated from plants have a protective function for plants, they may also alter a number of physiological functions in plant consumers. Since they interact with the molecular signaling pathways that underlie vital processes like apoptosis, cell growth and differentiation, inflammation, autophagy, cell volume regulation, metabolic homeostasis, redox balance, and energy balance, a wide range of phytochemicals have been discovered to be health-promoting in the past few years (Tesse et al., 2018).

S. palghatense bark shows an incredible amount of various phytochemicals from GC-MS, LC-MS QTOF. Biological activity study through various methods also revealed that *S. palghatense* bark is potentially more active than *S. laetum* and *S. occidentale*. Numerous studies on *Syzygium* species have been published, but little is known about *S. palghatense*.

For these reasons, this study was conducted in order to separate and identify the bioactive phytochemicals from the methanolic bark extract of *S. palghatense*. Purified compounds were obtained by TLC, PTLC, and silica gel column chromatography, and they were then characterized by UV, IR, NMR, and ESI-MS studies. The information provided by this study on *S. palghatense* phytocompounds may help guide further pharmacological analyses.

✓ Objectives

- To isolate and characterize bioactive phytocompounds from the methanol extract of *S. palghatense* bark using chromatographic and spectroscopic techniques.
- To evaluate the antioxidant, antimicrobial, anthelmintic, anti-inflammatory, antidiabetic, and anticancer activities of the isolated phytocompounds through standardized *in vitro* and *in vivo* assays.
- To compare the bioactive efficacy of *S. palghatense* bark extract with extracts from other *Syzygium* species.
- To provide scientific validation for the traditional medicinal use of *S. palghatense* based on phytochemical composition and biological activities

8.2. Materials and methods

8.2.1. Isolation of and characterization of bioactive phytocompounds from the methanol extract of *S. palghatense* bark

GC-MS and LC-MS-QTOF analyses revealed that the bark of *S. palghatense* contains a higher concentration of bioactive phytocompounds compared to *S. laetum* and *S. occidentale*. These phytochemical profiles may underlie the significant biological activities observed. Subsequent *in vitro*, *in vivo*, and silver nanoparticle studies demonstrated that the methanolic extract (bark) of *S. palghatense* was more potent than the extracts of the other two species. Based on these findings, the methanolic bark extract of *S. palghatense* was selected for compound isolation and further investigation.

8.2.1.1. Preparation of extract

All glassware (Borosil) used in the study was initially immersed in a cleaning solution for several hours, after that, give it a thorough wash with normal water. After that, a detergent solution was used to wash the glassware, and distilled water was used to rinse it. After cleaning, the glassware was dried in a hot air oven and properly stored to prevent contamination. Analytical grade chemicals from reputable suppliers such as Hi-Media, Loba, S.D. Fine Chemicals, Qualigens, E. Merck, and Sigma Chemicals (U.S.A.) were utilized throughout the experiments. For the preparation of the extract, the collected *S. palghatense* bark was cleaned under running water, let to dry in the shade, and then ground into a coarse powder using a motorized pulverizer. 20 g of the powdered bark was subjected to Soxhlet extraction with methanol at room temperature. with a solvent-to-solid ratio of 4:1 (v/w) and allowed to extract for 24 hours (Sukhdev et al., 2008).

8.2.1.2. Thin layer chromatography (TLC)

Compounds are separated using thin-layer chromatography (TLC) according to how differently they partition between a stationary and a mobile phase. The chemicals included in a fractional extract are separated using this method. The separation depends on the choice and ratio of solvents used as the mobile phase. A

drug solution (1 mg/mL) was spotted on TLC plates and allowed to dry. The plates were then developed using different solvent ratios. The spots were visualized under UV light, visible light, and in an iodine chamber. Each spot's Rf (Retention factor) value was determined by dividing the solute's travel distance by the solvent front's travel distance, by the formula:

R_f = Distance travelled by the solute/Distance travelled by the solvent

Compounds corresponding to the spots were scraped off and used for further screening (Deinstrop, 2000).

8.2.1.3. Column chromatography

Concentrated methanolic extract of *S. palghatense* bark was dissolved in methanol and mixed in silica gel (100–200 mesh, 60 Å) for the preparation of a slurry of crude extract-silica gel, which was air-dried overnight in a hot air oven at 50 °C. Methanolic extract was fractionated using silica gel column chromatography with a glass column measuring 2.5 cm in diameter and 75 cm in length. Silica gel (100–200 mesh, 60 Å) was activated by drying at 80 °C for 3 hours, then packed into the column up to a length of 50 cm. The packing volume was calculated using the formula $V=\pi r^2 h$ (V- packing volume of column; π- 3.14; r^2- multiply the radius of column; h- total length of column). The column was initially washed with 100 mL of hexane. The methanol extract-silica gel slurry was then placed on the column and eluted first with 100% hexane, followed by solvents of gradually increasing polarity, and finally with 100% methanol. Solvents used is based on the polarity of the solvents. The use of solvents have been gradually increased from low-polar solvents to high-polar solvents (Table 8.1).

TLC was used to identify if chemicals were present after fractions of 100 mL each were collected. At an evaporation temperature of 50 °C, fractions exhibiting comparable spots were scraped, pooled, and focused using a speed vacuum operating at low pressure. Based on purity and quantity, further purification was carried out using preparative thin-layer chromatography (PTLC). Separation of compounds was monitored under UV light at 254 nm and 365 nm. The value of Rf was determined by

Table 8.1: Solvent gradient for column chromatography fractions

Fractions	Solvents used
Fraction 1	Hexane – 100% (100 mL)
Fraction 2	Hexane : Chloroform (90:10)
Fraction 3	Hexane : Chloroform (80:20)
Fraction 4	Hexane : Chloroform (70:30)
Fraction 5	Hexane : Chloroform (60:40)
Fraction 6	Hexane : Chloroform (50:50)
Fraction 7	Hexane : Chloroform (40:60)
Fraction 8	Hexane : Chloroform (30:70)
Fraction 9	Hexane : Chloroform (20:80)
Fraction 10	Hexane : Chloroform (10:90)
Fraction 11	Chloroform – 100%
Fraction 12	Chloroform : Ethyl acetate (90:10)
Fraction 13	Chloroform : Ethyl acetate (80:20)
Fraction 14	Chloroform : Ethyl acetate (70:30)
Fraction 15	Chloroform : Ethyl acetate (60:40)
Fraction 16	Chloroform : Ethyl acetate (50:50)
Fraction 17	Chloroform : Ethyl acetate (40:60)
Fraction 18	Chloroform : Ethyl acetate (30:70)
Fraction 19	Chloroform : Ethyl acetate (20:80)
Fraction 20	Chloroform : Ethyl acetate (10:90)
Fraction 21	Ethyl acetate – 100%
Fraction 22	Ethyl acetate : Methanol (90:10)
Fraction 23	Ethyl acetate : Methanol (80:20)
Fraction 24	Ethyl acetate : Methanol (70:30)
Fraction 25	Ethyl acetate : Methanol (60:40)
Fraction 26	Ethyl acetate : Methanol (50:50)
Fraction 27	Ethyl acetate : Methanol (40:60)
Fraction 28	Ethyl acetate : Methanol (30:70)
Fraction 29	Ethyl acetate : Methanol (20:80)
Fraction 30	Ethyl acetate : Methanol (10:90)
Fraction 31	Methanol – 100%

dividing the solute's travel distance by the solvent front's travel distance. The purified fractions isolated by PTLC were subjected to structural elucidation using various spectral analyses, including IR (Infrared), UV (Ultraviolet), NMR (Nuclear Magnetic Resonance), and ESI-MASS (Electrospray Ionization Mass) spectroscopy (Jóźwiak & Hajnos, 2007).

8.2.1.4. Preparative Thin Layer Chromatography (PTLC)

PTLC was performed on glass plates measuring 50 mm × 100 mm, precoated with silica gel Si 60 HF_{254} (Merck) at thicknesses of 0.25, 0.5, or 2 mm. The isolated compound was applied using a capillary tube. The large surface area of silica gel, combined with its mildly acidic nature, may promote air oxidation of sensitive functional groups such as aldehydes, amines, and reactive double bonds. Additionally, this method is relatively expensive and is generally suited for small-scale separations. The methanolic extract of the isolated compound was spotted on the plate and developed in a specific solvent system. Developed plates were examined under a UV chamber to visualize spots of interest, which were then scraped off, collected, and used for further analysis. Isolated compounds from the methanolic extract of *S. palghatense* bark were further characterized using various spectral techniques **(**Jóźwiak & Hajnos, 2007).

8.2.1.5. Ultraviolet spectrum

Ultraviolet spectral studies of the isolated compounds were recorded on a SHIMADZU (UV-160A) UV-visible spectrophotometer (Skoog et al., 2017).

8.2.1.6. FTIR (Fourier-Transform Infrared) spectrum

Infrared spectral studies of the compounds isolated were done using a FTIR-NICOLET spectrophotometer over the wavenumber range from 500 to 4000 cm^{-1}. The IR spectra were recorded on a Perkin Elmer spectrophotometer using potassium bromide (KBr) discs as the sample matrix (Smith, 2011).

8.2.1.7. Nuclear Magnetic Resonance (NMR) spectrum

8.2.1.7.1. ^{1}H NMR (Proton Nuclear Magnetic Resonance) spectrum

^{1}H NMR spectra of the isolated compounds were recorded in $CDCl_3$ (Deuterated chloroform) using a 500 MHz Bruker instrument at the Sophisticated Analytical Instrumentation Facility (SAIF), Chennai, India (Claridge, 2016).

8.2.1.7.2. ^{13}C NMR (Carbon-13 Nuclear Magnetic Resonance) spectrum

^{13}C NMR spectra of the isolated compounds were recorded between 0 and 200 ppm at 100.4 MHz in $CDCl_3$ using a 400 MHz Bruker instrument at the Sophisticated Analytical Instrumentation Facility (SAIF), Chennai, India (Claridge, 2016).

8.2.1.7.3. Mass Spectrum (MS) analysis

Mass spectral analysis was performed using an electron spray ionization (ESI) source functioning with either positive or negative spray polarity. The following parameters were established (positive/negative): shield voltage – 600 V, needle voltage – 3500 V / +5000 V, capillary voltage ± 50 V, drying gas (nitrogen) at 20 psi (138 kPa) and 250°C and mobilizing gas (air/nitrogen) at 50 psi (345 kPa). The complete scan mode was adopted in the MS analyzer over a mass range of m/z 100-1000, with a scan speed of 5000 Da/s, averaging 3 scans. The multiplier voltage was set to 1385 V. Data acquisition was performed using the MS Workstation and MS Data Review 6.9 software Varian (Gross, 2017).

8.2.2. Validation of the biological activities of an isolated compound

The compound isolated was tested for its biological activities

8.2.2.1. Antioxidant activity

Antioxidant activity of the compound isolated from the methanolic extract (bark) of *S. palghatense* was evaluated using several *in vitro* assays. The DPPH radical scavenging assay was performed by incubating varying concentrations of the compound with DPPH solution in the dark and measuring the decrease in absorbance at 517 nm to calculate the percentage of inhibition (Aquino et al., 2001). Superoxide

radical scavenging activity was assessed using the riboflavin–NBT–NBT photoreduction method, where the compound's ability to inhibit NBT reduction by superoxide radicals was measured at 560 nm (McCord & Fridovich, 1969). Hydroxyl radical scavenging was determined by the deoxyribose degradation assay, involving the Fenton reaction, with inhibition of thiobarbituric acid reactive substances formation measured at 532 nm (Ohkawa et al., 1979; Saldanha et al., 1990). The ferric reducing antioxidant power (FRAP) assay evaluated the compound's ability to reduce Fe (III)-TPTZ complex to Fe (II), with absorbance recorded at 595 nm (Pulido et al., 2000). A positive control was ascorbic acid **i**n all assays, and results were expressed as mean ± SD of sextuplicate determinations with IC_{50} values calculated for comparison.

8.2.2.2. Antimicrobial activity

The antimicrobial activity of the isolated compound from *S. palghatense* was evaluated using different concentrations prepared by two-fold dilution. The compound stock solution was made in dimethyl sulfoxide (DMSO) at a concentration of 10 mg/mL, and working concentrations of 250 µg, 500 µg, and 1000 µg per well were used for agar well diffusion assays against bacterial and fungal strains. Fungal inocula were prepared in Potato Dextrose Broth (PDB) and inoculated on Potato Dextrose Agar (PDA), while bacterial cultures were grown in Mueller-Hinton Broth (MHB) and seeded onto Mueller-Hinton Agar (MHA). Plates were incubated at room temperature overnight for fungi and at 37 °C for 24 hours for bacteria. The minimal inhibitory concentration (MIC) and minimal fungicidal/bactericidal concentrations (MFC/MBC) were determined by broth microdilution using two-fold serial dilutions of the compound ranging from 10 µg/mL to 300 µg/mL. MIC was defined as the lowest concentration inhibiting visible microbial growth, while MFC and MBC were identified as the lowest concentrations preventing growth after subculturing (Clinical and Laboratory Standards Institute [CLSI], 2012; Patel et al., 2014; Rukayadi, 2008). Clotrimazole (10 mg/mL) and streptomycin (10 mg/mL) were used as standard antifungal and antibacterial controls, respectively.

8.2.2.3. Anthelmintic activity

Anthelmintic activity of the isolated compound from the bark of *S. palghatense* was evaluated using adult earthworms (*Lumbricus terrestris*) due to their physiological similarity to human intestinal roundworms. Stock solutions of the compound were prepared at 100 mg/mL, and testing was conducted at concentrations of 25, 50, 75, and 100 mg/mL. Albendazole (20 mg/mL) was used as the standard reference drug. Groups of earthworms were exposed to these solutions, and the time taken for paralysis and death was recorded. Paralysis was confirmed when worms showed no movement except under vigorous shaking, and death was established when no movement was observed even after shaking and exposure to warm water (50°C), accompanied by body colour fading. The percentage inhibition of death time was calculated relative to the control (distilled water) and expressed as mean ± standard deviation (Patel et al., 2011).

8.2.2.4. Anti-Inflammatory activity

The isolated compound's anti-inflammatory properties from the methanolic bark extract of *S. palghatense* was evaluated using the *in vitro* Human Red Blood Cell (HRBC) membrane stabilization method. In accordance with ethical standards, fresh blood was drawn from healthy participants and combined with an equivalent volume of Alsever's solution to stop coagulation. Centrifugation was done at 3000 rpm for 10 minutes, and the packed red blood cells were washed three times with isosaline (0.85%, pH 7.2). A 10% (v/v) HRBC suspension was prepared in isosaline. Different concentrations of the isolated compound (10 to 100 µg/mL) were mixed with equal volumes of the HRBC suspension and phosphate buffer (pH 7.4). The samples were incubated at 37°C for 30 minutes and then centrifuged at 3000 rpm for 10 minutes. The supernatant’s absorbance was measured at 560 nm to determine haemoglobin release due to haemolysis. Percentage membrane stabilization, reflecting anti-inflammatory activity, was calculated by comparing sample absorbance with that of the control containing distilled water (James et al., 2009).

8.2.2.5. Antidiabetic activity

8.2.2.5.1. Alpha-amylase activity

The α-amylase inhibitory activity of the isolated compound from the methanolic bark extract of *S. palghatense* was evaluated by incubating 500 µL of α-amylase with 1% phosphate buffer and starch solution at 37 °C for 10 minutes. A 1 mL concentration of the isolated chemical, ranging from 20 to 100 µg/mL, was then added. 2 M NaOH was added to stop the reaction, and then 1 mL of dinitro salicylic acid reagent was added. The mixture was then heated in a water bath for five minutes. After cooling under running water, the absorbance at 540 nm was measured, and the volume was adjusted to 10 mL using sterile distilled water. Acarbose served as the standard.

8.2.2.5.2. Alpha-glucosidase activity

For the α-glucosidase inhibition assay, α-glucosidase from *Saccharomyces cerevisiae* (1 mg) was suspended in 100 mL of neutral phosphate-buffered saline containing 200 mg bovine serum albumin. Various concentrations of the isolated compound (20–100 µg/mL) were incubated with 10 µL phosphate buffer (pH 6.8) and 490 µL of 5 mM p-nitrophenyl-α-D-glucopyranoside (p-NPG) at 37 °C for 5 minutes. Then, 250 µL of α-glucosidase (0.15 U/mL) was added and incubated for an additional 15 minutes. To stop the reaction 2 mL of 200 mM sodium carbonate was added after cooling, and the absorbance was recorded at 405 nm. Acarbose served as the reference standard in this assay.

The percentage of α-amylase and α-glucosidase inhibition and free radical scavenging was determined using the following formula:

$$\text{Percentage Inhibition/scavenging activity} = [(A_{control} - A_{sample})/ (A_{control})] \times 100.$$

Where A = absorbance.

8.2.2.6. Anticancer activity

Trypan blue exclusion and MTT tests were used for the assessment of the cytotoxicity of the chemical that was isolated from the methanolic bark extract of *S. palghatense*.

8.2.2.6.1. Trypan blue exclusion method

In this method, Dalton's Lymphoma Ascites (DLA) cells isolated from the peritoneal cavity of mice were suspended in phosphate-buffered saline (PBS, pH 7.4), washed, and incubated with varying concentrations of the isolated compound at 37 °C for 3 hours. Following incubation, trypan blue dye was added, and viable (unstained) and dead (blue-stained) cells were counted using a hemocytometer. The percentage of cell death was calculated as the ratio of dead cells to total cells multiplied by 100, providing a quantitative measure of cytotoxicity **(**Hussein & Mohsin, 2019).

8.2.2.6.2. MTT (3-(4,5-dimethylthiazol-2-yl)-2,5-diphenyltetrazolium bromide) assay

For the MTT assay, Dulbecco's Modified Eagle's Medium (DMEM), supplemented with 10% fetal bovine serum and antibiotics, was used to cultivate the MCF-7 human breast cancer cell line. The culture was kept in a humidified atmosphere at 37 °C with 5% CO2. After being seeded at a density of 5×10^3 cells/well in 96-well plates, the cells were left to adhere for an entire day. The isolated compound was prepared in 0.1% DMSO at various concentrations (6.25 to 100 µg/mL) and added to the wells, followed by incubation for 24 hours. After treatment, the medium was removed, and 30 µL of MTT reagent was added to each well, incubated for 4 hours to allow formazan crystal formation. The crystals were dissolved using DMSO, and absorbance was measured at 540 nm for the determination of cell viability. Percentage viability was calculated relative to untreated controls, providing an assessment of the compound's anticancer activity (Mosmann, 1983).

8.2.3. Statistical analysis

All experimental data were analyzed using one-way analysis of variance (ANOVA) to determine significant differences among treatment means. Six replicates were maintained for each treatment to ensure statistical reliability. Critical difference (CD) values were calculated to evaluate the minimum significant difference between means at the chosen confidence level. Post hoc multiple comparison tests were performed following ANOVA to identify specific group differences. Additionally,

Principal Component Analysis (PCA) was conducted to reduce data dimensionality and to explore the relationships and variations among phytochemical constituents across solvent extracts. Statistical analyses were carried out using R 4.2.0, with significance levels set at $p < 0.05$.

8.3. Results

8.3.1. Soxhlet extraction of *S. palghatense* bark

Two kilograms of finely dried, coarsely ground *S. palghatense* bark were extracted using methanol in the ratio of 1:4 w/v for 72 hours for three consecutive days, and the process of extraction was carried out till the colour of the extract was pale. The yield of methanolic extract was 4.163 g (Plates 8.1). The extract obtained were stored in a sealed glass jar for further use.

8.3.2. Isolation of bioactive compounds from *S. palghatense* bark

The methanolic bark extract of *S. palghatense* displayed the occurrence of phytocomponents by the TLC method. The plant was subjected to column chromatography with the organic solvents according to the polarity (Plates 8.2). The fractions obtained were pooled, condensed using a rotary evaporator, and a single compound with Rf value of 0.95 was obtained through the preparative thin layer chromatography (PTLC) method. The compound showed a blue fluorescent spot in TLC with an Rf value of 0.95 under 365 nm under the solvent system ethyl acetate and methanol (3:7). The purified compound was subjected to structure characterization and further analysis **(**Plates 8.3-8.4).

Methanol extract of 3g was loaded in the silica gel column. A total of 31 fractions were collected. From the fractions collected, fractions 25, 26, and 27 were selected for further study, as they showed similar spots with the same Rf value of 0.95. The fractions were pooled, and the Rf value was spot 0.95. The weight of the isolated compound was 7 mg **(**Plate 8.2).

8.3.3. Characterization of compound

8.3.3.1. Physical characteristics

The purified compound was pale yellow and waxy in nature, with a melting point observed between 93 °C and 96 °C. It showed the Rf value of 0.95 in the TLC solvent system of ethyl acetate and methanol (3:7). The compound was found to be



Plate 8.1: Methanol extract of *Syzygium palghatense* bark



(a) (b) (c) (d) (e) (f)



(g) (h)

Plate 8.2: Column chromatography setup for the methanol extract of *Syzygium palghatense* bark: (a) Column chromatography apparatus (b)-(h) Fractions collected in separate containers/test tubes



Plate 8.3: Fractions collected (1-31) were viewed under visible light by the thin layer chromatography (TLC) method

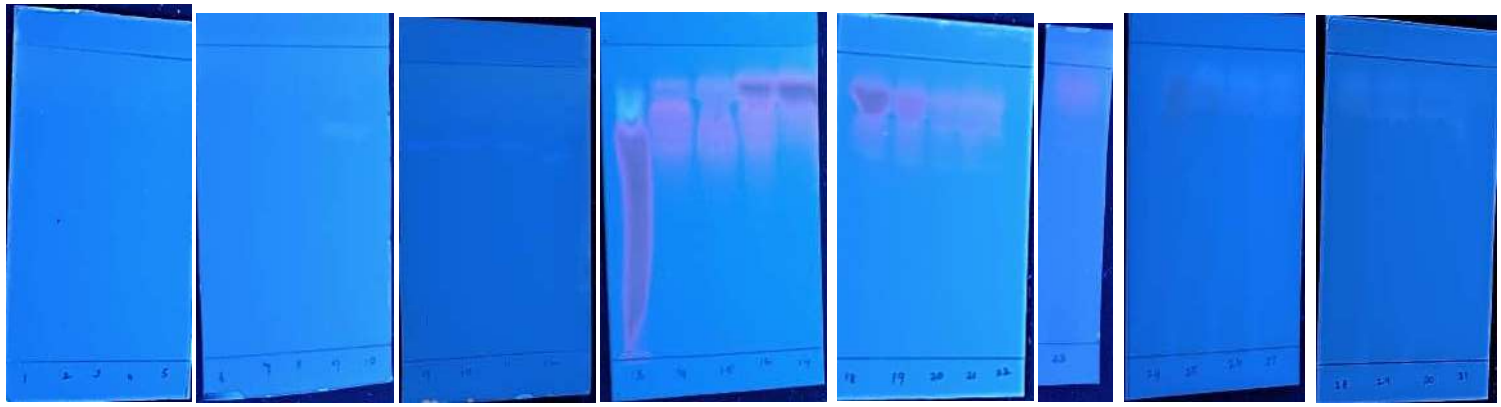


Plate 8.4: Fractions collected (1-31) viewed under ultraviolet (UV) light at 365 nm by the thin layer chromatography (TLC) method

soluble in methanol and other alcohols, and insoluble in water. Under the UV at 365 nm, a fluorescent blue spot was observed.

8.3.3.2. UV spectrum

UV-visible spectrum shown in Figure 8.1 presents the ultraviolet description of the compound isolated from the methanol bark extract of *S. palghatense*. The spectrum exhibits distinct absorption peaks, indicating the presence of conjugated systems in the compound. The absorption in the UV region typically corresponds to electronic transitions. These transitions are characteristic of compounds containing aromatic rings, conjugated double bonds, or functional groups like carbonyls, which are common in plant-derived secondary metabolites, including flavonoids, phenolics, and other polyphenolic compounds. The position and intensity of the absorption maxima can offer valuable insights into the degree of conjugation and the nature of the chromophores present in the molecule. The UV absorption pattern thus supports the presence of aromatic and conjugated structures in the isolated compound from *S. palghatense* bark, which may correlate with its biological activities and chemical properties (Figure 8.1).

The absorption peak appears close to the region around 290–300 nm. The highest absorbance (maximum peak) is indeed located at or near 294 nm.

8.3.3.3. FT-IR spectrum

The FTIR (Fourier-Transform Infrared) spectrum depicting the percentage transmittance versus wavenumber for the sample labeled S1_2022-12-23-50-21(1). The strong and broad absorption band around 1637 cm^{-1} likely indicates the occurrence of C=C stretching (typical for alkenes or aromatic rings), or possibly a conjugated carbonyl group. The peaks between 1500–1450 cm^{-1} are attributed to C=C and C–H bending vibrations of aromatic rings, while the region around 1380–1310 cm^{-1} may correspond to C–H methyl bending or other aliphatic deformations. The numerous sharp bands between 1300–1000 cm^{-1} are characteristic of C–O stretching, suggesting the occurrence of ethers, alcohols, or esters. Additional peaks in the

fingerprint region (900–700 cm^{-1}) provide further evidence for substituted benzene rings or other aromatic systems.

The absorption regions for the compound were 1637 (C=C), 1566, 1493, 1462, 1371, 1224, 1127, 1027, 904, 766, 685 (C-H) cm-1 **(**Figure 8.2).

8.3.3.4. Nuclear Magnetic Resonance (NMR) spectrum

8.3.3.4.1. ^{1}H NMR spectrum

^{1}H NMR data for the isolated compound from the methanol extract of *S. palghatense* bark reveals major aromatic characteristics. The chemical shifts mainly fall between 7.93 and 6.83 ppm, indicating the presence of multiple aromatic protons in distinct electronic environments, suggestive of substituted benzene rings or related aromatic systems. This distribution of peaks implies that the compound consists predominantly of aromatic or unsaturated structures. Notably, there are minimal to no signals in the aliphatic region, reinforcing that the compound is rich in aromatic moieties. The NMR spectrum was recorded on a 400 MHz instrument with $CDCl_3$ solvent at around 297 K, ensuring high resolution of these proton environments. While a few anomalous negative chemical shift values appear, these likely result from referencing artifacts and do not detract from the overall interpretation. This data supports the conclusion that the compound is an aromatic, consistent with bioactive phenolic or flavonoid constituents typically found in *Syzygium* species. Further structural elucidation using complementary spectroscopic techniques would provide a more complete understanding of its molecular framework (Figure 8.3).

^{1}H NMR spectrum for the compound isolated from the methanol extract of *S. palghatense* bark was recorded at 400 MHz in $CDCl_3$ solvent at a temperature of 296.9 K. The spectrum shows multiple chemical shifts primarily in the aromatic region between approximately 6.83 and 8.25 ppm, indicating the presence of several aromatic protons consistent with substituted benzene rings or aromatic moieties. The clustering of chemical shift values, such as peaks between 7.4 to 7.9 ppm, reflects a complex pattern with likely overlapping signals from protons in different electronic

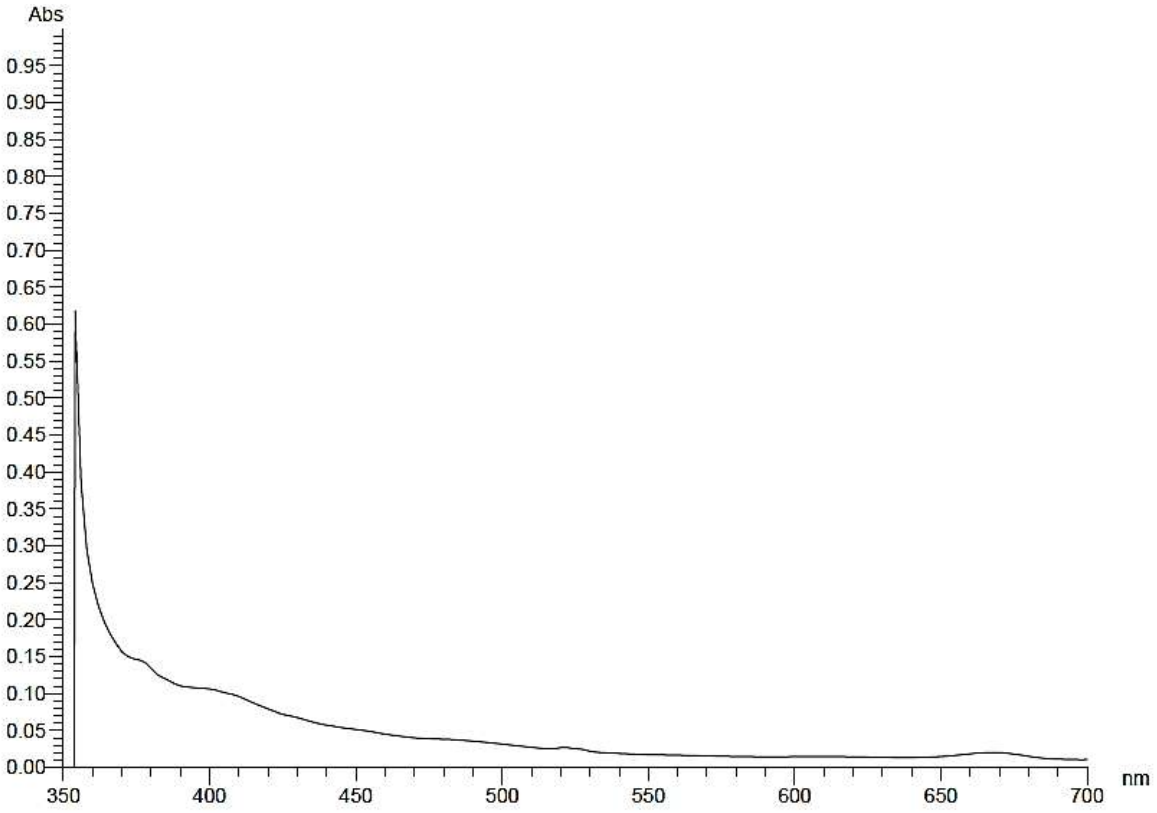


Figure 8.1: UV (ultraviolet) characterization of the compound isolated from the methanol extract of *Syzygium palghatense* bark

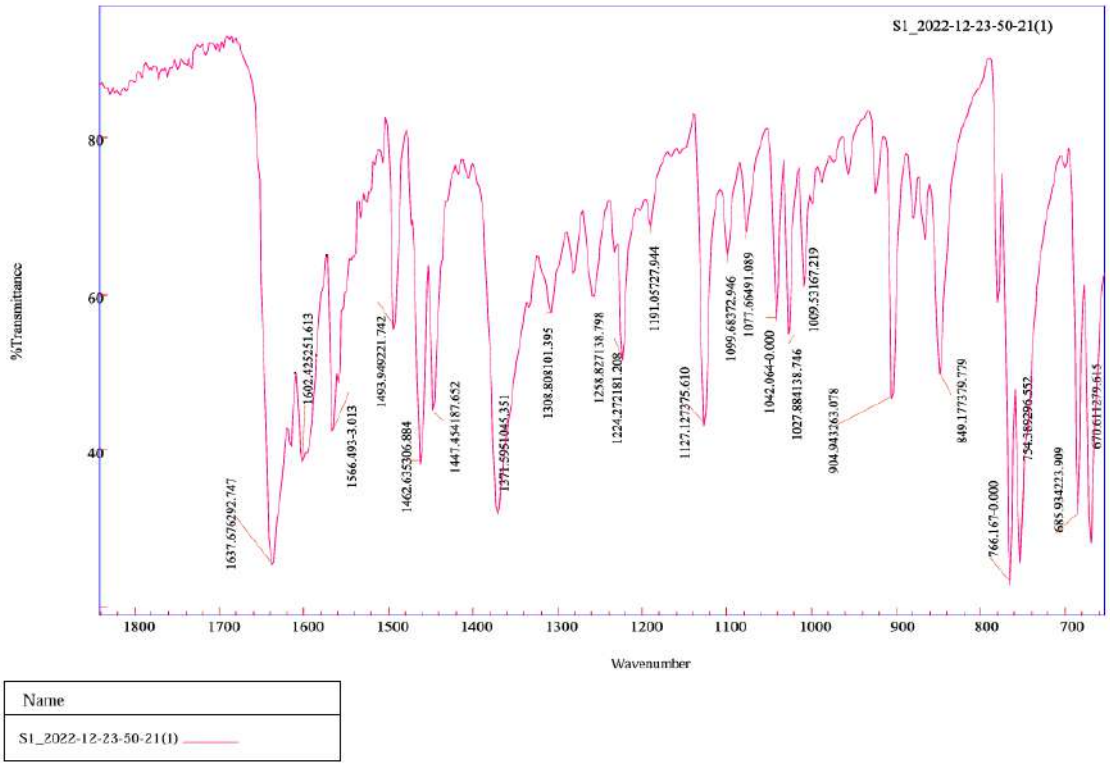


Figure 8.2: FTIR (Fourier-Transform Infrared) characterization of the compound isolated from the methanol extract of *Syzygium palghatense* bark

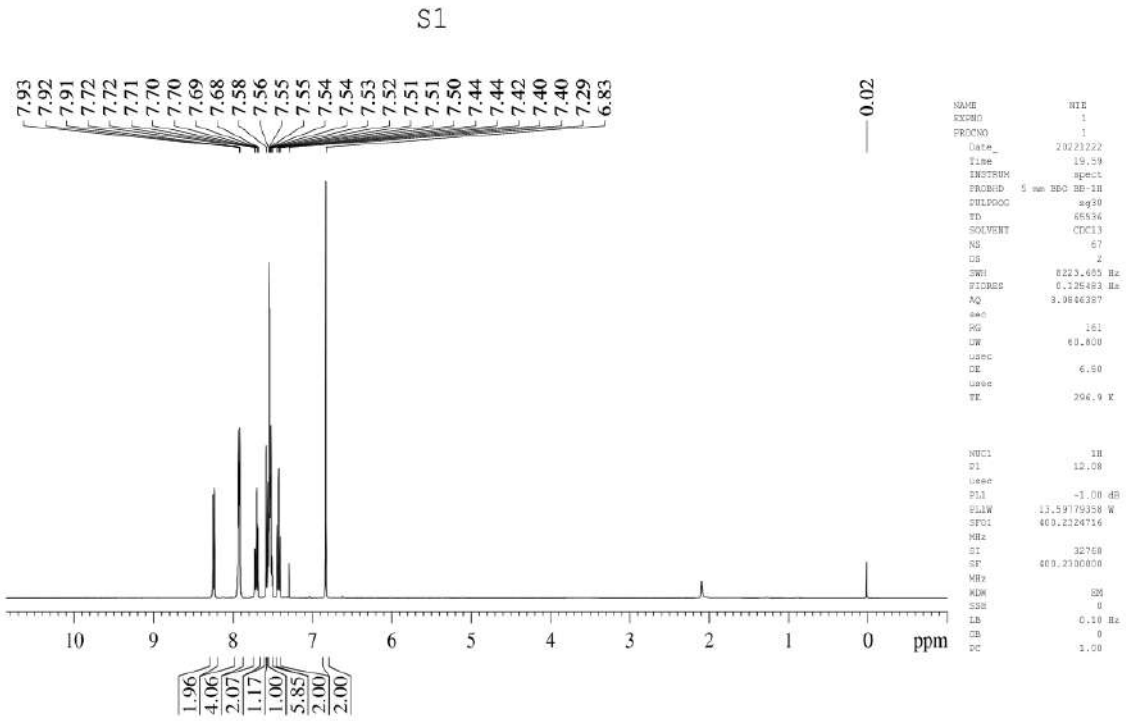


Figure 8.3: Experimental details and ^{1}H NMR (Proton Nuclear Magnetic Resonance) spectral data of the purified compound, isolated from the methanol extract of *Syzygium palghatense* bark

environments around the aromatic rings, typical of poly-substituted aromatic compounds.

The absence of significant signals downfield of 6.8 ppm or upfield of 2 ppm suggests the compound mainly consists of aromatic and possibly olefinic protons without notable aliphatic groups. Experimental parameters, including a spectral width of 8223.7 Hz, acquisition time of roughly 3.98 seconds, and 67 scans, ensured good spectral resolution and sensitivity for detailed proton analysis. The data, therefore, confirm that the compound is an aromatic-rich compound, which aligns well with the known phytochemical nature of *Syzygium* species that often contain abundant phenolic and flavonoid structures.

This spectral data forms a basis for further structural elucidation, ideally combined with complementary techniques like ^{13}C NMR spectroscopy and 2D NMR methods to fully define the molecular structure and substitution pattern of the compound (Figure 8.4).

The ^{1}H NMR spectral data for the isolated compound, recorded at 400 MHz in $CDCl_3$ solvent and measured at 296.9 K, indicate the existence of aromatic protons predominantly in the downfield region between approximately 7.9 and 8.25 ppm. These chemical shifts are characteristic of aromatic ring systems, likely containing electron-withdrawing substituents or extended conjugation that cause deshielding. The well-resolved signals in this region suggest a substituted aromatic or heteroaromatic structure. With experimental parameters such as a spectral width of 8223.7 Hz, an acquisition time of about 4 seconds, and 67 scans, the spectrum was recorded under conditions that optimize resolution and sensitivity. Overall, the data support that the compound is an aromatic-rich compound with substitution patterns typical of plant-derived secondary metabolites, consistent with expected phytochemicals from *Syzygium* species. Further spectral analysis using complementary techniques would be necessary to fully elucidate the precise structure of the chemical (Figure 8.5).

$_{1}H$ NMR spectrum of the isolated compound was recorded at 400 MHz using $CDCl_3$ as the solvent at a temperature of 296.9 K. The spectrum shows a series of

distinct signals primarily in the aromatic region between 7.40 and 7.75 ppm, indicating the occurrence of multiple aromatic protons. These closely spaced peaks reflect various proton environments on substituted aromatic rings, suggesting a complex aromatic structure with different electronic effects. Additionally, signals are observed at lower chemical shifts around 1.00, 1.17, 2.00, 2.07, and 5.85 ppm, which may correspond to aliphatic or olefinic protons linked to the aromatic core. The experimental conditions included 67 scans, a spectral width of 8223.7 Hz, and a high-resolution acquisition time of approximately 3.98 seconds, providing a well-resolved and sensitive spectrum. Overall, the data indicate that the compound is predominantly aromatic with aliphatic or olefinic substituents, consistent with secondary metabolites from plants, such as flavonoids or phenolic substances isolated from *S. palghatense*.

The ^{1}H-NMR spectrum of the isolated compound shows distinct signals characteristic of both aliphatic and aromatic protons. The sharp multiplets between δ 2.72 and 2.93 ppm (including two doublets of doublets) correspond to aliphatic methylene protons. The doublet of doublets at δ 5.30 ppm indicates a proton likely attached to a carbon bearing electronegative substituents or in an olefinic environment. The aromatic region between δ 7.10 and 7.73 ppm displays multiple complex multiplets, typical of aromatic protons on substituted benzene rings. This pattern aligns well with structural features expected in bioactive plant compounds, confirming the presence of aromatic and aliphatic groups. Overall, the spectrum is consistent with the pure substance that was separated from the methanol extract of *S. palghatense* bark (Figure 8.6).

8.3.3.4.2. ^{13}C-NMR spectrum

The spectroscopic data for the isolated compound from the methanol extract of *S. palghatense* bark suggest a comprehensive analysis likely involving ^{13}C and ^{1}H NMR parameters, sample preparation details, and operational conditions. The NMR chemical shifts, given in ppm, span from 76.79 to 178.41 ppm, which is indicative of a range of carbon environments commonly observed in polyphenolic or aromatic structures. The presence of chemical shifts above 150 ppm generally corresponds to conjugated or carbonyl carbons, signifying the possible existence of ester, aldehyde,

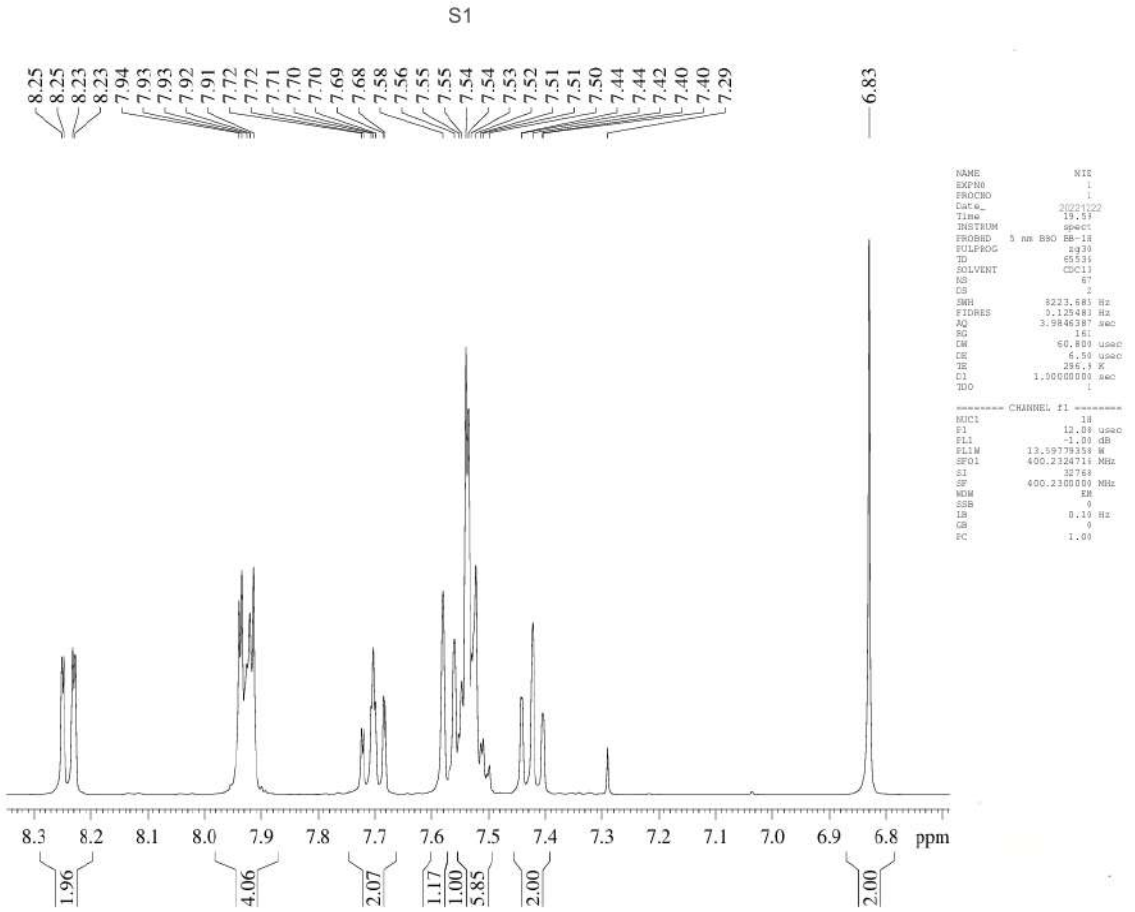


Figure 8.4: Parameters and ^{1}H NMR (Proton Nuclear Magnetic Resonance) spectral analysis of the compound isolated from the methanol extract of *Syzygium palghatense* bark

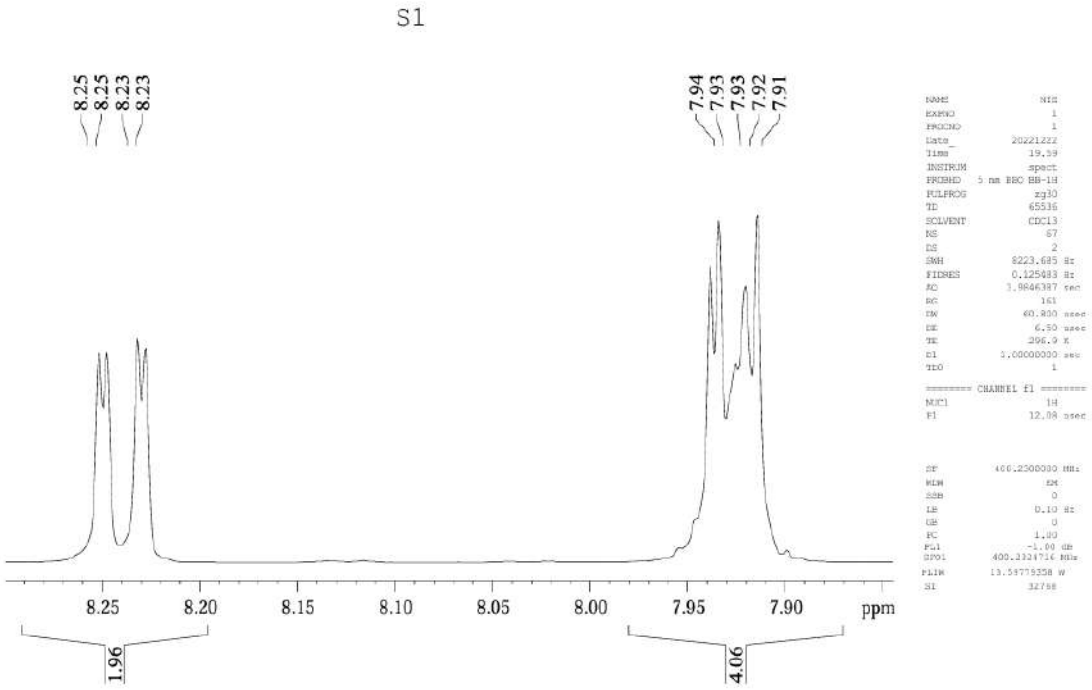


Figure 8.5: Nuclear Magnetic Resonance (NMR) spectral data and experimental parameters for a compound isolated from the methanol extract of *Syzygium palghatense* bark

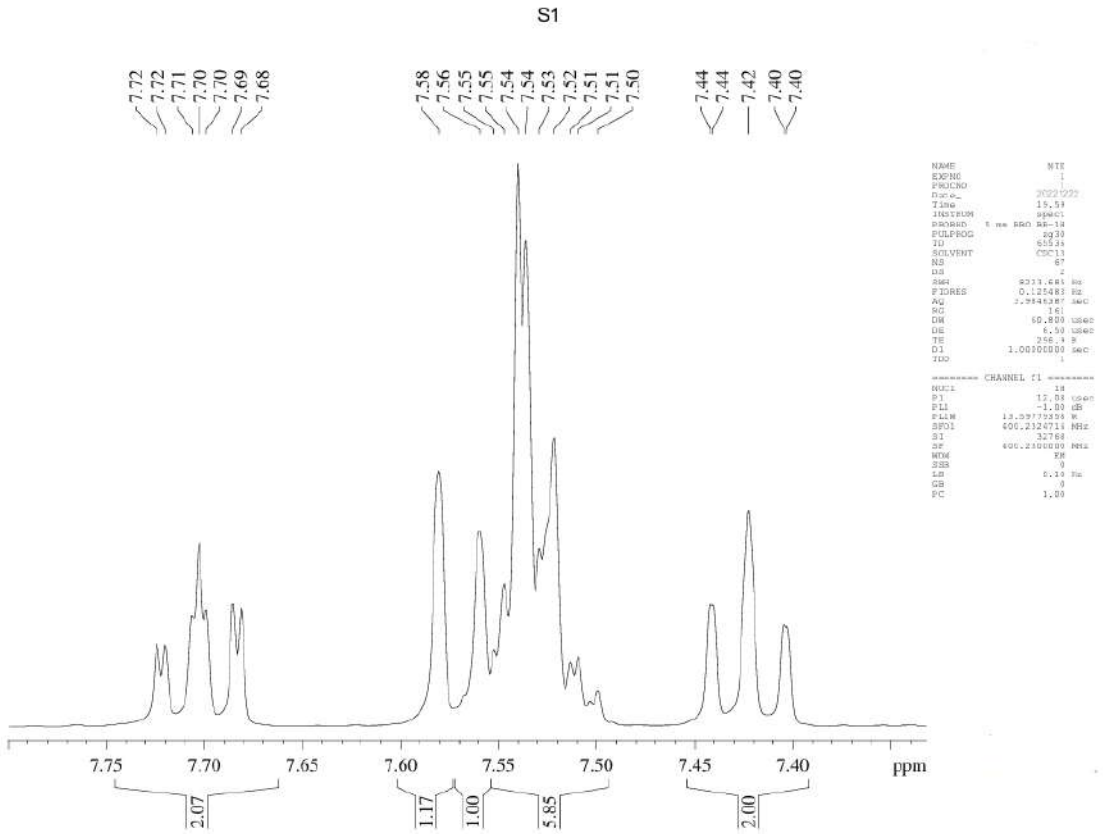


Figure 8.6: Aromatic-focused ^{1}H NMR (Proton Nuclear Magnetic Resonance) spectral data and experimental parameters for the isolated compound, showing enhanced resolution analysis from the methanol extract of *Syzygium palghatense* bark

or ketone functionalities. The choices of pulse programs and solvent ($CDCl_3$), alongside the sample temperature and acquisition parameters, confirm that a standard NMR protocol for organic compound identification was followed. With several signals in the region of 120–140 ppm, the compound likely features aromatic rings, consistent with plant-derived secondary metabolites. The isolated compound from the bark can thus be interpreted as a structurally diverse molecule with multiple aromatic and possibly conjugated or carbonyl-bearing functional groups, supporting its probable role as a bioactive secondary metabolite characteristic of *S. palghatense* bark extracts (Figure 8.7).

Figure 8.8 depicts the NMR experimental parameters for a ^{13}C and ^{1}H nuclear magnetic resonance analysis of an isolated compound dissolved in $CDCl_3$ solvent. The experiment was conducted on a 5 mm BBO (Broadband Observe probe) broadband probe at a temperature of approximately 295.6 K, using a zgpg30 pulse program optimized for ^{13}C observation with proton decoupling (waltz16). Acquisition parameters, such as a spectral width of around 24 kHz and a data size of 65,536 points, were configured to ensure high resolution, while the relaxation delay and acquisition times (D1 = 2.0 sec, AQ ≈ 1.36 sec) were chosen to optimize signal sensitivity and resolution. The ^{13}C spectrum is made simpler by the proton decoupling that occurs during acquisition, which collapses multiplets into singlets, improving the clarity of the carbon signals. With 3,072 scans collected, the spectrum would exhibit good signal-to-noise ratios for detailed structural elucidation. These conditions indicate that the isolated compound's carbon framework was rigorously analyzed to identify various carbon environments, which is crucial in confirming molecular structure and functional groups present in the compound extracted from *S. palghatense* bark. Overall, the data reflect a well-executed NMR experiment tailored for detailed chemical characterization.

The NMR experimental data provided for the isolated compound from the methanol extract of *S. palghatense* bark reflect a detailed ^{13}C NMR spectral analysis recorded in $CDCl_3$ solvent using a 5 mm BBO broadband probe. The spectrum displays chemical shifts ranging approximately from 107.57 to 133.77 ppm, which

are characteristic of carbons in aromatic and possibly olefinic environments. These chemical shifts suggest the compound contains aromatic ring systems; indicative of phenolic or polyphenolic components typically found in plant secondary metabolites. The absence of signals in lower ppm regions may imply limited aliphatic carbons or that the focus is on aromatic carbons in this spectrum. The NMR acquisition parameters, including proton decoupling (waltz16), optimize signal clarity by removing proton-carbon splitting, thus simplifying the spectrum for easier interpretation. This data supports that the isolated compound is likely an aromatic-rich molecule, consistent with bioactive compounds from *S. palghatense* bark that may exhibit antimicrobial or other pharmacological properties. Overall, the spectrum confirms the presence of multiple aromatic carbons, fundamental in elucidating the molecular framework of the isolated secondary metabolite from the bark extract.

The ^{13}C-NMR spectrum of the purified compound from the methanol extract of *S. palghatense* bark shows peaks mainly in the aromatic region (118.15, 123.38761, 127.09, 44.405, 121.08, 126.23306, 126.23306, 128.92353, 128.49229, 128.49229, 131.33934, 139.202, ppm), indicating the presence of aromatic rings typical for plant secondary metabolites. The downfield peak at 191.75 ppm suggests a carbonyl group, while the signal at 78.595 ppm corresponds to carbons bonded to oxygen, such as alcohol or ether groups. A peak at 44.40 ppm indicates aliphatic carbons possibly adjacent to functional groups. The repeated peaks reflect symmetrical carbons or overlapping signals in the aromatic system. Overall, this confirms the compound contains aromatic, carbonyl, oxygenated, and aliphatic carbons consistent with bioactive molecules from *S. palghatense* bark (Figure 8.9).

8.3.3.4.3. GC-MS (Gas Chromatography-Mass Spectrometry)

Figure 8.10 is a mass spectrum (GC-MS) of a compound isolated from the methanol extract of *S. palghatense* bark. The spectrum shows several prominent peaks, with the most intense (base peak) at m/z 84.5701, indicating that this fragment is the most stable and abundant ion produced during ionization. Other significant peaks appear at m/z 96.7382, 110.7598, 124.7356, 145.5690, 153.6215, 167.5612, 190.4954, and 222.3272. The presence of these specific mass-to-charge ratios

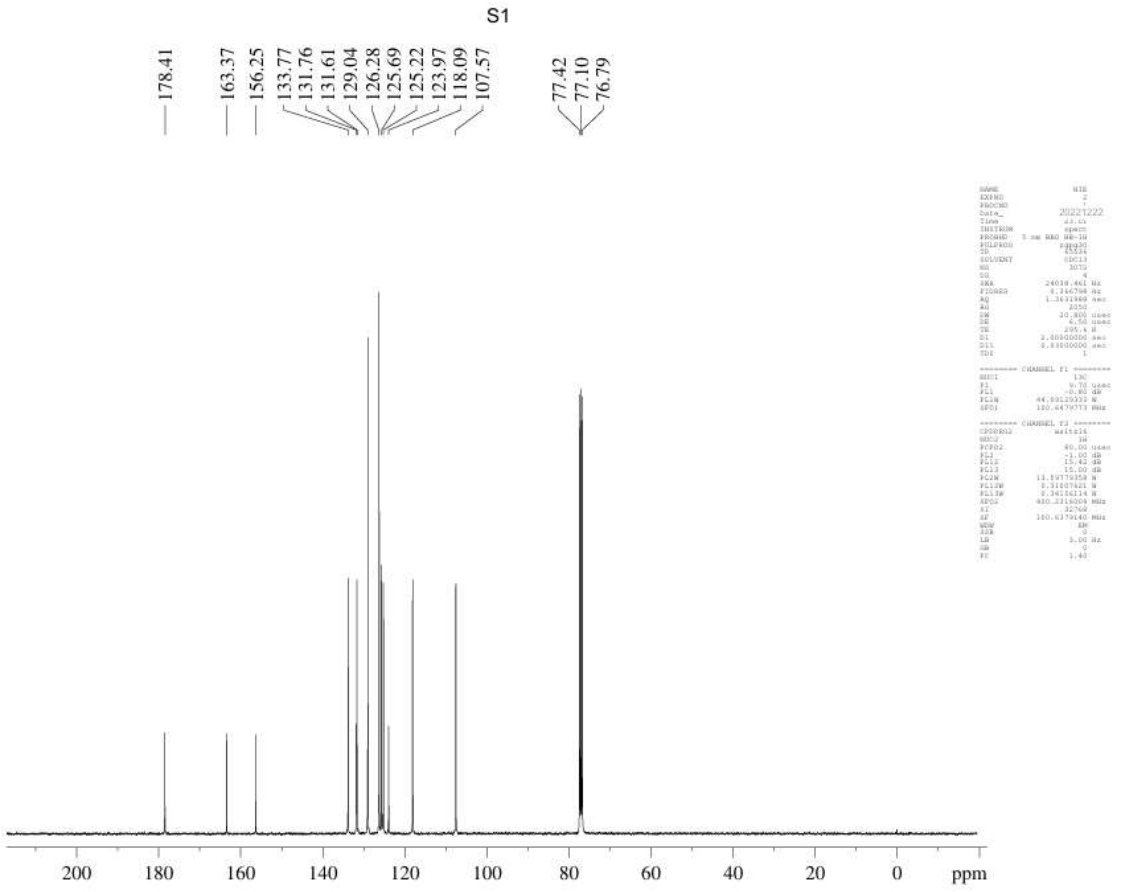


Figure 8.7: ^{13}C NMR (Carbon-13 Nuclear Magnetic Resonance) spectrum of the isolated compound from the methanol extract of *Syzygium palghatense* bark

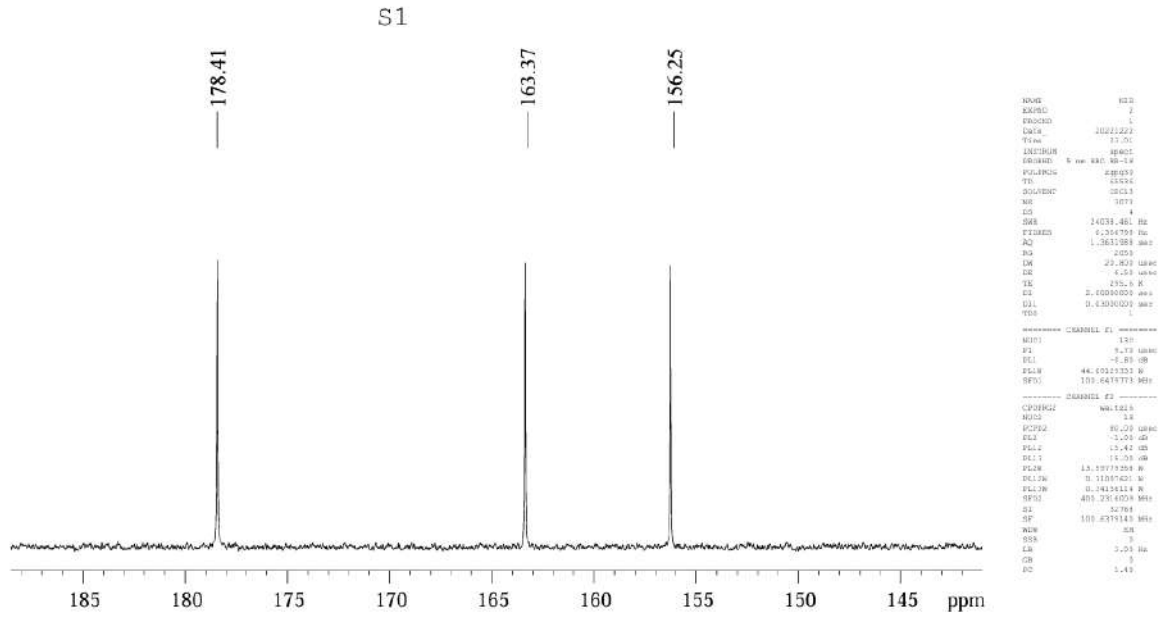


Figure 8.8: NMR Experimental Parameters for the ^{13}C NMR (Carbon-13 Nuclear Magnetic Resonance) spectrum of the isolated compound from *Syzygium palghatense* bark

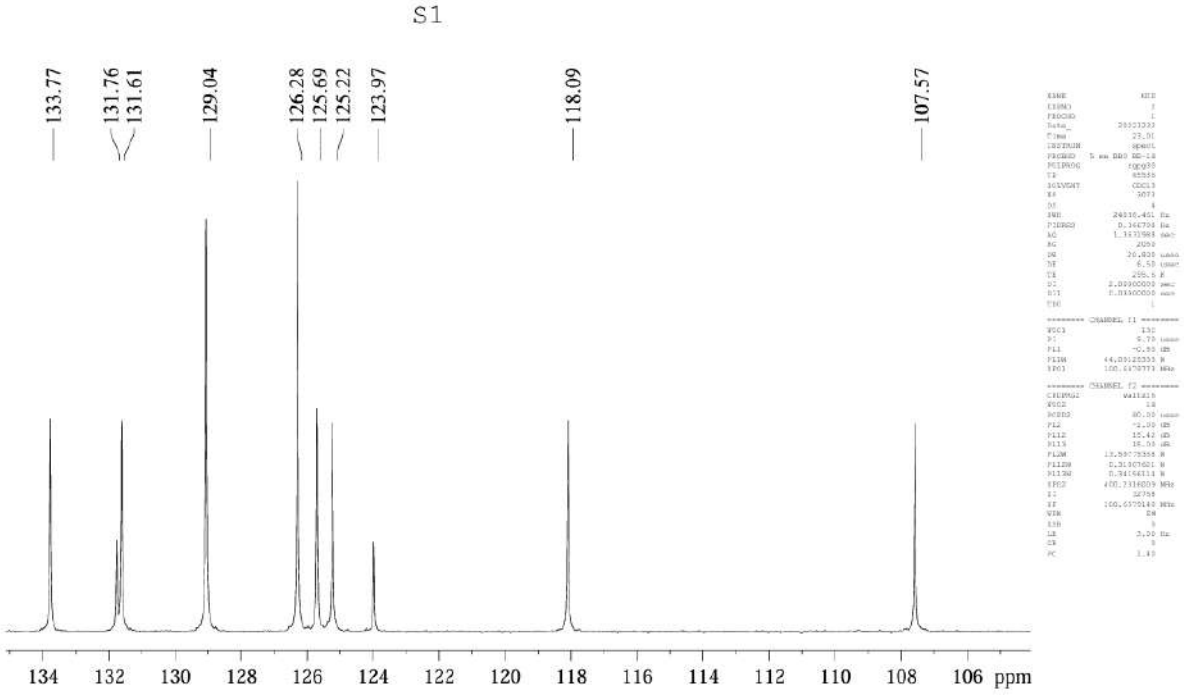


Figure 8.9: Carbon-13 NMR spectral analysis of the bioactive compound isolated from the methanol extract of *Syzygium palghatense* bark, highlighting aromatic carbon resonances

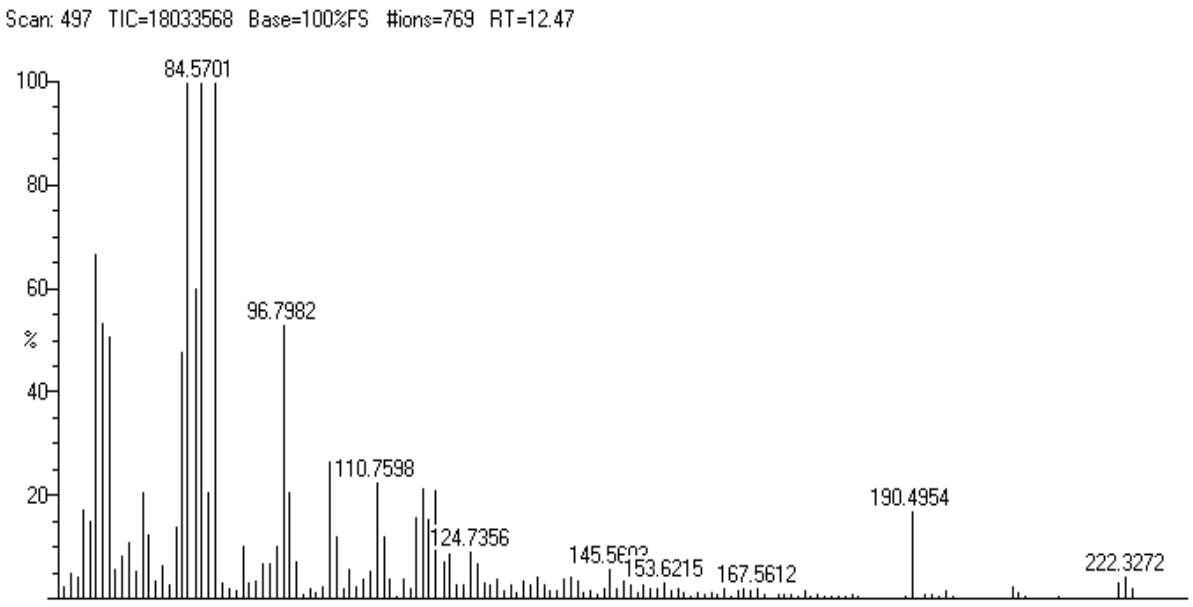
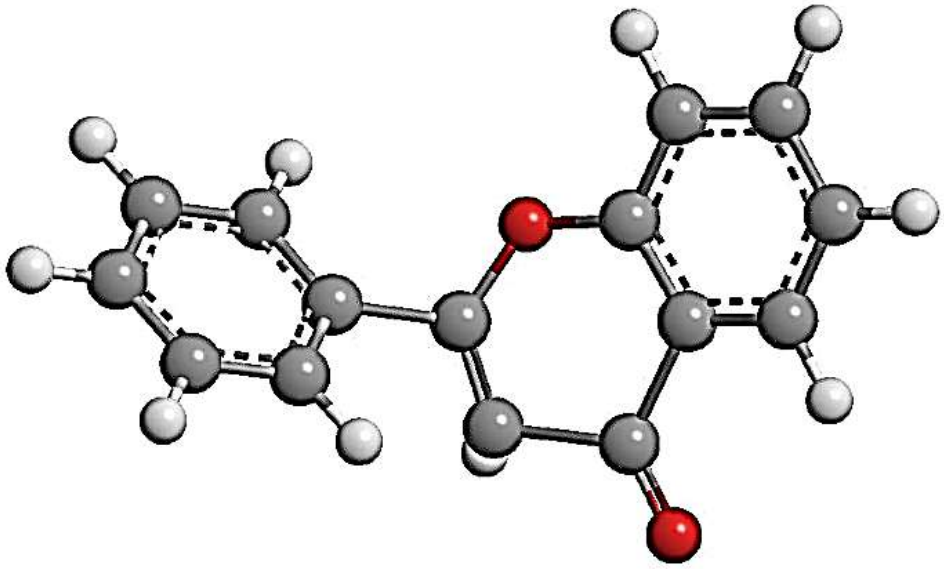
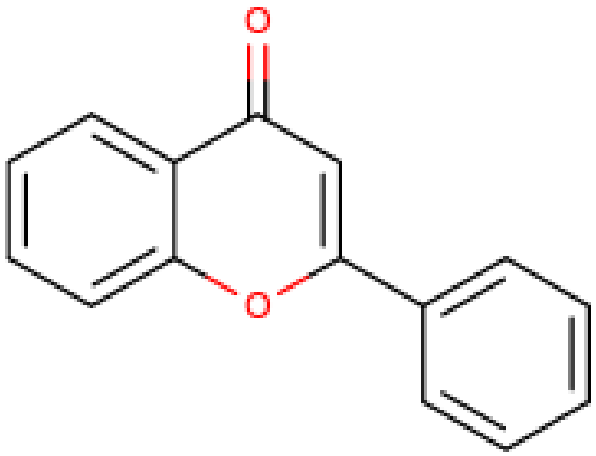


Figure 8.10: GC-MS spectrum of the compound isolated from the methanol extract of *Syzygium palghatense* bark



(a)



(b)

Figure 8.11: Three-dimensional (3D) and two-dimensional (2D) structure of 2-Phenyl-4H-Chromen-4-One

suggests the stepwise fragmentation of the parent molecule, revealing information about the possible substructures present. The molecular ion peak likely appears at the highest m/z value with significant intensity (here at 222.3272), providing an estimated molecular weight for the compound. The pattern of fragments with increases of 14 or 16 Da hints at common losses such as CH2 or O atoms, typical for natural compounds with aliphatic and oxygenated substituents. Overall, this spectrum supports the presence of a moderately high molecular weight compound with both aliphatic and functionalized components, consistent with secondary metabolites such as flavonoids or phenolics found in *S. palghatense* bark.

The molecular weight of the purified compound is 222.243, which is supported by a peak at m/z 222.3272 and molecular formula $C_{15}H_{10}O_2$. Based on the comparison of the physical characteristics and spectral data of the reported compound from related species in the literature, the isolated compound was identified as 2-Phenyl-4H-chromen-4-one from *S. palghatense*. For the first time, this compound is reported from the *S. palghatense,* and the structure of 2-phenyl-4H-chromen-4-one is shown in Figure 8.11.

8.3.4. Biological activities of isolated compounds

8.3.4.1. Antioxidant activity

The antioxidant activities of 2-Phenyl-4H-chromen-4-one isolated from *S. palghatense* bark were evaluated using DPPH, superoxide, hydroxyl radical scavenging, and ferric reducing antioxidant power (FRAP) assays. The compound demonstrated significant, dose-dependent antioxidant activity in all assays, consistently showing higher percentage inhibition compared to standard ascorbic acid at equivalent concentrations. For instance, at 150 µg/mL, it exhibited 87% inhibition in the DPPH assay versus 74% for the standard, and similar superior activity was observed in the other assays. The IC_{50} values further highlight its potency, with 2-Phenyl-4H-chromen-4-one showing notably lower IC_{50} values across DPPH (1.376 µg/mL), superoxide (1.601 µg/mL), and FRAP (1.303 µg/mL) assays compared to the standard, indicating higher antioxidant efficiency. Although the hydroxyl radical

scavenging activity had a relatively higher IC_{50} (49 µg/mL), it was still more effective than the standard. These results confirm the compound's strong antioxidant capability, suggesting it could be a valuable natural agent in combating oxidative stress and related disorders (Figures 8.12-8.13).

8.3.4.2. Antimicrobial activity

The antifungal and antibacterial activities of 2-Phenyl-4H-chromen-4-one isolated from the methanol extract of *S. palghatense* bark were assessed against various pathogenic fungi and bacteria and compared to standard drugs, clotrimazole and streptomycin, respectively **(**Figures 8.14-8.15). The compound showed moderate antifungal activity, with zones of inhibition increasing with concentration from 250 to 1000 µg/mL. For example, against *Aspergillus niger*, inhibition zones increased from 13 mm at 250 µg/mL to 18 mm at 1000 µg/mL, while *Candida albicans* showed no inhibition at 250 µg/mL but showed zones of 15 and 16 mm at higher concentrations. In antibacterial tests, the compound exhibited dose-dependent activity against pathogens such as *Streptococcus mutans*, *Staphylococcus aureus*, *Enterococcus faecalis*, *Escherichia coli*, and *Pseudomonas aeruginosa*. Notably, *Pseudomonas aeruginosa* showed substantial sensitivity, with inhibition zones increasing from no inhibition at 250 µg/mL to 30 mm at 1000 µg/mL. Although the compound's antimicrobial effects were generally less potent than the standards, the results indicate promising antimicrobial potential of 2-Phenyl-4H-chromen-4-one. These results suggest its antimicrobial potential against various fungal and bacterial pathogens, which may contribute to novel therapeutic interventions against infections (Plate 8.5).

Figure 8.16 depicts the minimum fungicidal concentration (MFC), minimum inhibitory concentration (MIC), and minimum bactericidal concentration (MBC) values (in µg/mL) for 2-Phenyl-4H-chromen-4-one against various microbial strains. Across all tested microorganisms, including fungi (*Aspergillus niger*, *Candida albicans*) and several bacteria (*S. mutans*, *E. faecalis*, *S. aureus*, *E. coli*, and *P. aeruginosa*), the MIC values range from approximately 0.51 to 0.62 µg/mL, with the lowest inhibition observed for *P. aeruginosa* (0.51 µg/mL) and the highest for *S.*

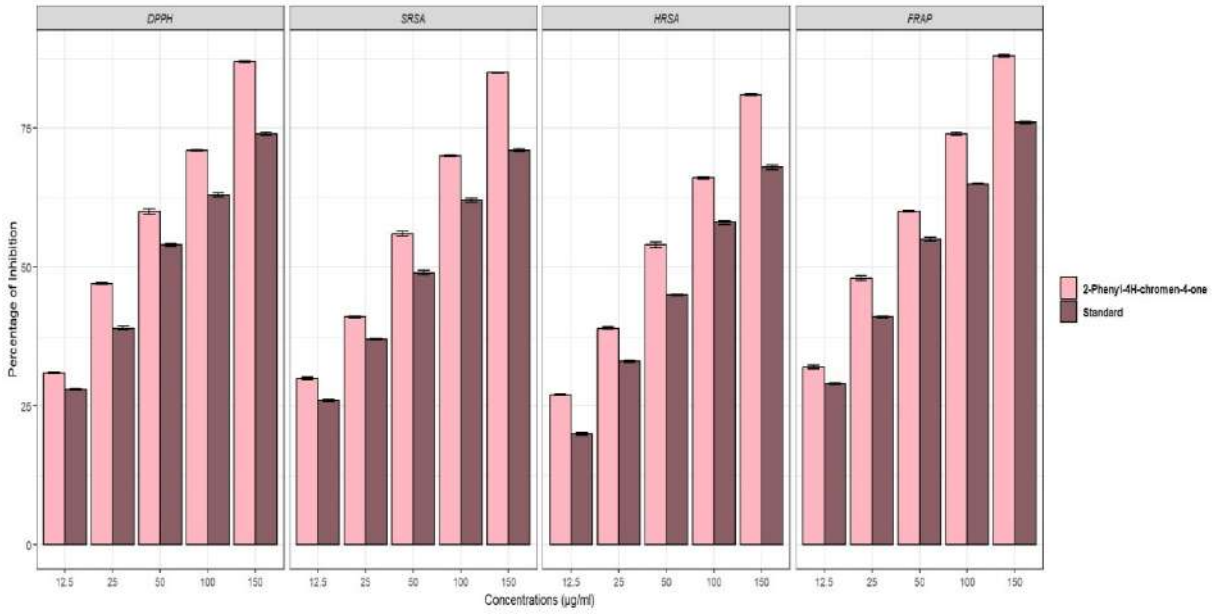


Figure 8.12: Comparative antioxidant activities of 2-Phenyl-4H-chromen-4-one, isolated from the methanol extract of *Syzygium palghatense* bark across different concentrations in DPPH, SRSA, HRSA, and FRAP assays (DPPH: 2,2-diphenyl-1-picrylhydrazyl Radical Scavenging Assay; SRSA: Superoxide Radical Scavenging Assay; HRSA: Hydroxyl Radical Scavenging Assay; FRAP: Ferric Reducing Antioxidant Power Assay)

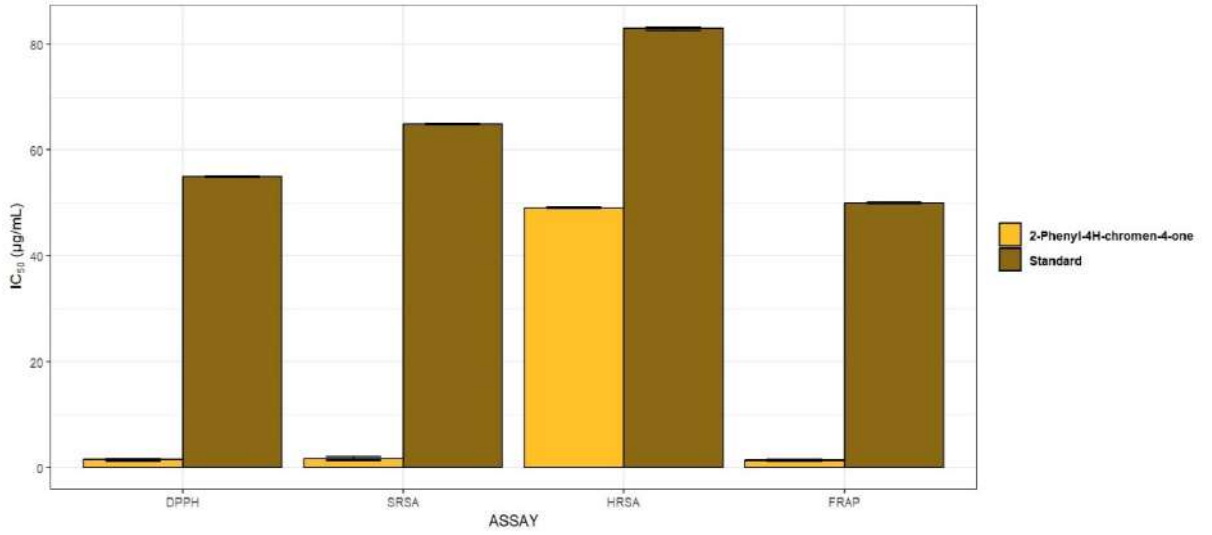


Figure 8.13: Comparative IC50 values of 2-Phenyl-4H-chromen-4-one, isolated from the methanol extract of *Syzygium palghatense* bark across different concentrations in DPPH, SRSA, HRSA, and FRAP assays (DPPH: 2,2-diphenyl-1-picrylhydrazyl Radical Scavenging Assay; SRSA: Superoxide Radical Scavenging Assay; HRSA: Hydroxyl Radical Scavenging Assay; FRAP: Ferric Reducing Antioxidant Power Assay)

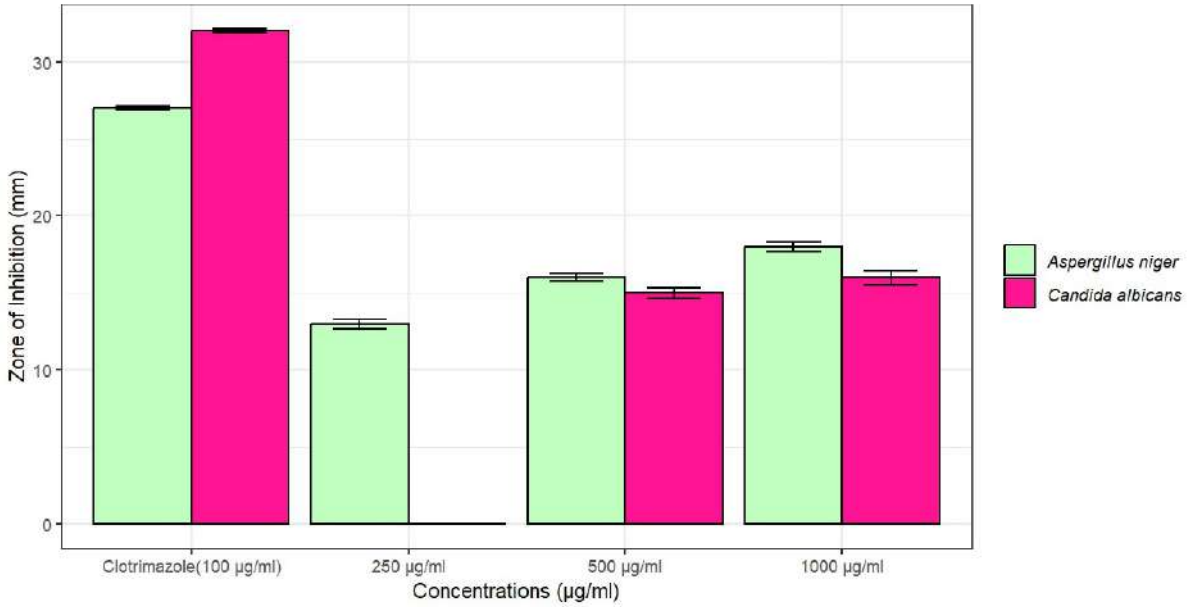


Figure 8.14: Antifungal activity of 2-Phenyl-4H-chromen-4-one isolated from the methanol extract of *Syzygium palghatense* bark against pathogenic fungi, compared to clotrimazole

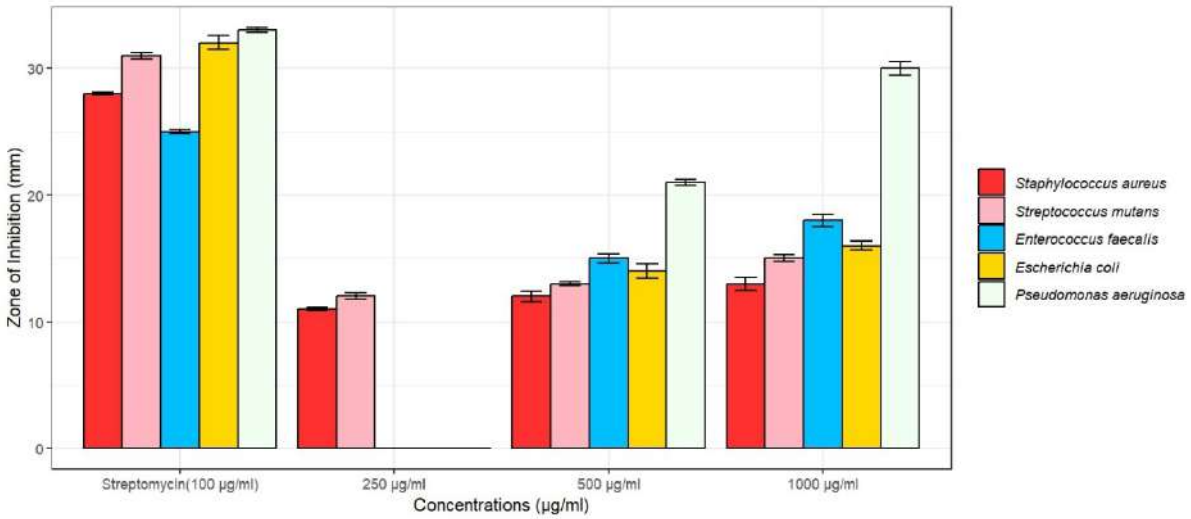


Figure 8.15: Antibacterial activity of 2-Phenyl-4H-chromen-4-one isolated from the methanol extract of *Syzygium palghatense* bark against pathogenic bacteria, compared to streptomycin

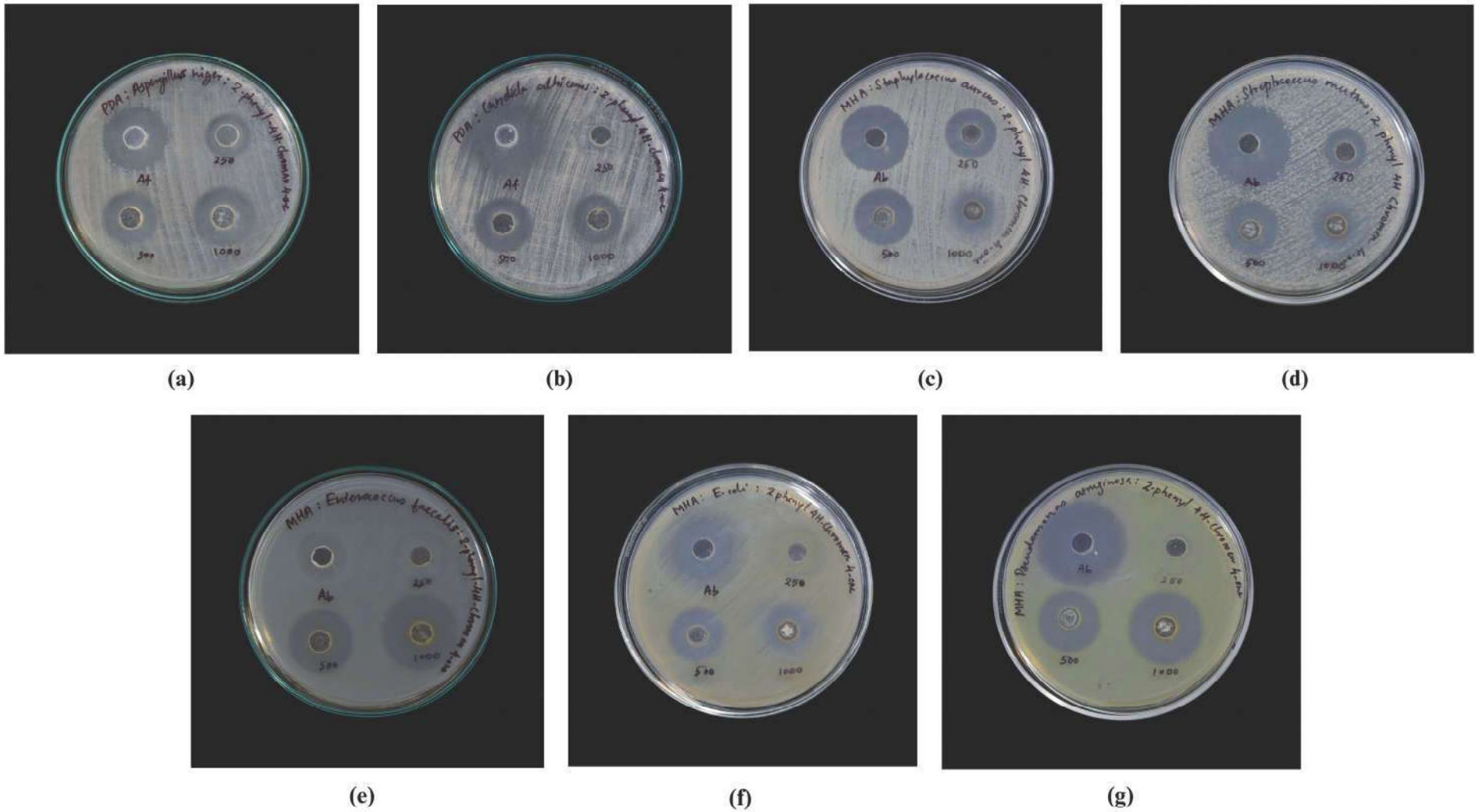


Plate 8.5: The inhibition zone (mm) of 2-Phenyl-4H-chromen-4-one isolated from the methanol extract of *Syzygium palghatense* bark against (a) *Aspergillus niger* (b) *Candida albicans* (c) *Staphylococcus aureus* (d) *Streptococcus mutans* (e) *Enterococcus faecalis* (f) *Escherichia coli* and (g) *Pseudomonas aeruginosa* by agar well diffusion method

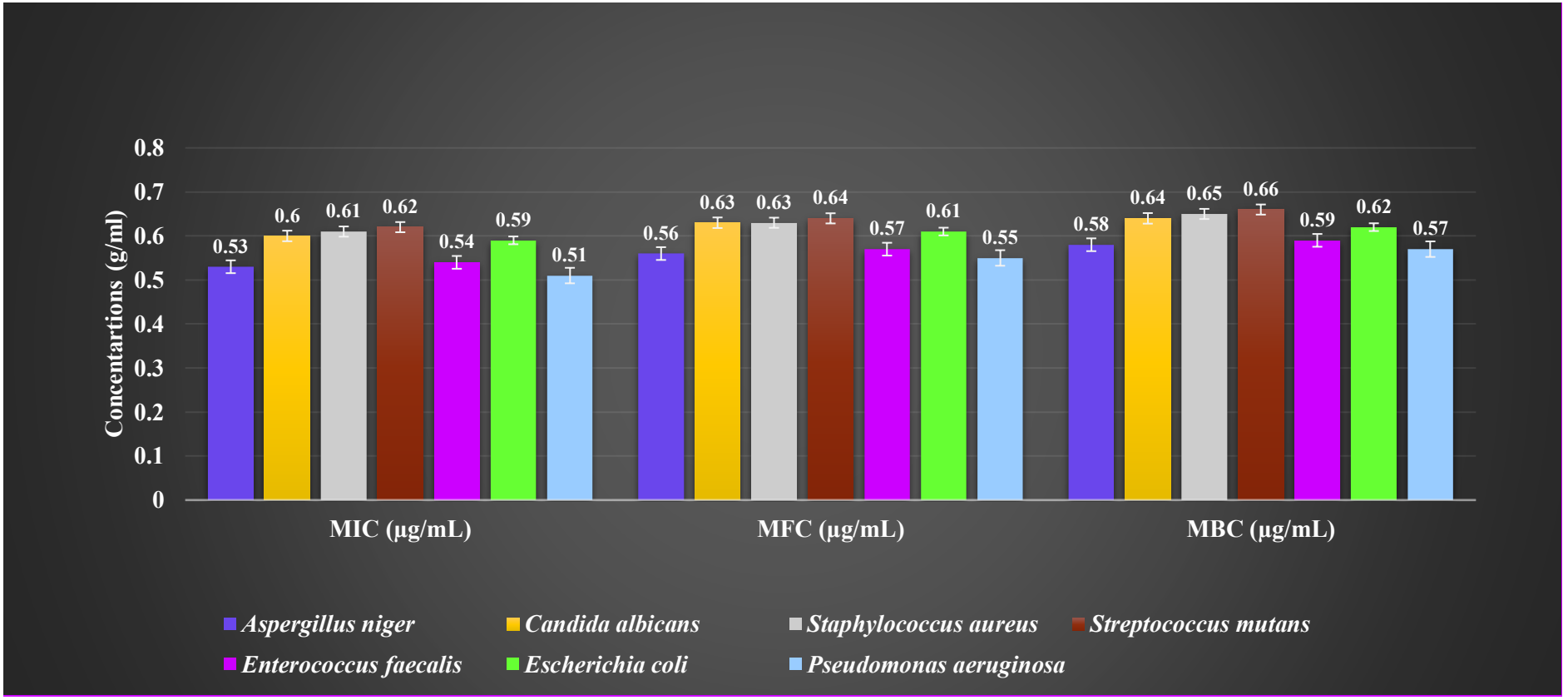


Figure 8.16: Minimum inhibitory (MIC), fungicidal (MFC), and bactericidal (MBC) concentrations of 2-Phenyl-4H-chromen-4-one isolated from the methanol extract of *Syzygium palghatense* bark (Mean ± SE, n=6)

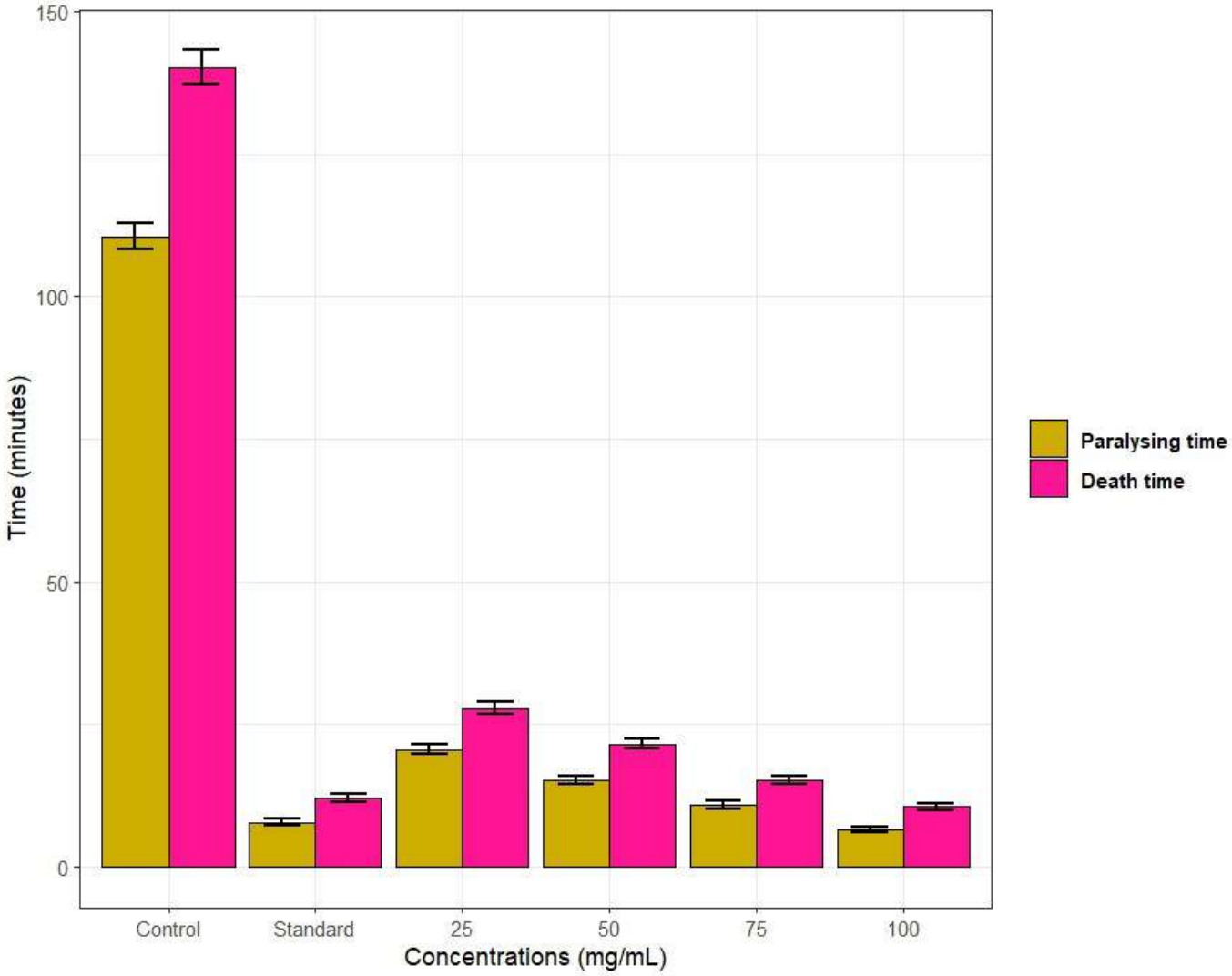


Figure 8.17: Dose-dependent anthelmintic efficacy of 2-Phenyl-4H-chromen-4-one isolated from the methanol extract of *Syzygium palghatense* bark against *Lumbricus terrestris*, expressed as paralysis and death time at increasing concentrations (mean ± SE, n = 6)

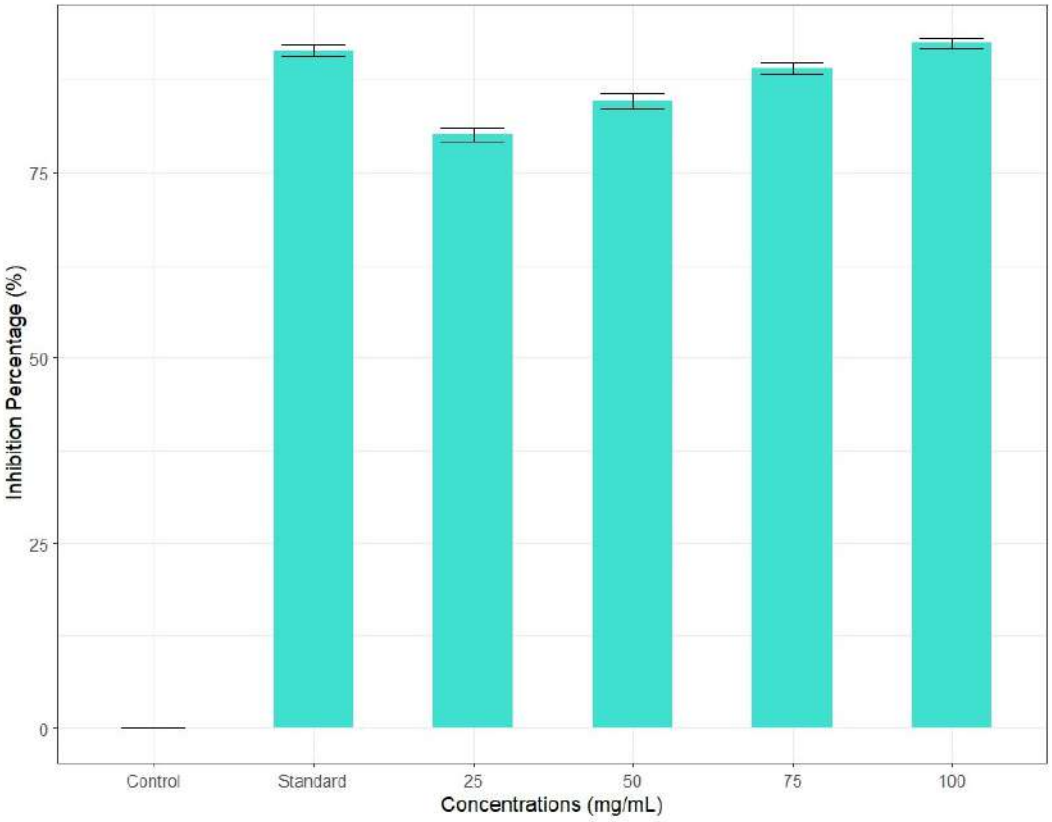


Figure 8.18: Dose-dependent anthelmintic efficacy of 2-Phenyl-4H-chromen-4-one isolated from the methanol extract of *Syzygium palghatense* bark against *Lumbricus terrestris*, expressed as inhibition percentage at increasing concentrations (mean ± SE, n=6)

aureus (0.62 µg/mL). MFC and MBC values follow a similar trend, typically falling slightly above the corresponding MIC for each microorganism. The data indicate that 2-Phenyl-4H-chromen-4-one exhibits substantial antimicrobial activity, with relatively low concentrations being sufficient to inhibit and kill both fungal and bacterial pathogens. Notably, the antimicrobial action is broad-spectrum, as evidenced by consistently effective concentrations across diverse strains, suggesting this compound could serve as a potent therapeutic agent for controlling a range of pathogenic microbes. The error bars reflect good reproducibility and reliability of the results, emphasizing the robustness of the findings.

8.3.4.3. Anthelmintic activity

Figure 8.17 shows that 2-Phenyl-4H-chromen-4-one, isolated from the methanol extract of *S. palghatense* bark, exhibits significant anthelmintic activity against *Lumbricus terrestris*, with the activity being both dose-dependent and comparable to the standard drug Albendazole. As the concentration of 2-Phenyl-4H-chromen-4-one increases from 25 to 100 mg/mL, the time required for both paralysis and death of the worms decreases substantially, indicating greater efficacy at higher doses. Specifically, at the highest tested dose (100 mg/mL), the time taken for paralysis (6.50 ± 0.55 minutes) and death (10.50 ± 0.63 minutes) approaches that seen with Albendazole (7.80 ± 0.60 minutes for paralysis; 12.00 ± 0.65 minutes for death) and is far superior to the control (110.50 ± 2.30 minutes and 140.20 ± 3.00 minutes, respectively).

In addition, the percentage inhibition increases with the concentration of 2-Phenyl-4H-chromen-4-one, reaching a maximum of 92.51 ± 0.65% at 100 mg/mL, which is very close to the inhibition observed with Albendazole (91.44 ± 0.80%). This suggests that the isolated compound is highly effective at higher concentrations and could be a promising candidate for anthelmintic therapy. The control group showed negligible inhibition and much longer times to paralysis and death, confirming the specificity and potency of the treatment. Overall, the findings demonstrate that 2-Phenyl-4H-chromen-4-one has strong dose-dependent anthelmintic activities, closely matching the performance of the current standard treatment (Figure 8.18).

8.3.4.4. Anti-inflammatory activity

The anti-inflammatory activity of isolated compound from the methanol extract of *S. palghatense* bark was assessed through the HRBC membrane stabilization assay (Plate 8.6). This test evaluates the compound's ability to stabilise the membrane of red blood cells against lysis (rupture), which reflects its potential to prevent the membrane destabilization that occurs during inflammation. Since the erythrocyte and lysosomal membranes are comparable, stabilization of HRBC membranes suggests that the compound may also stabilize lysosomal membranes, prevent the release of inflammatory mediators, and thereby exert anti-inflammatory effects.

The results show a clear dose-dependent increase in percentage inhibition, with inhibition rising from 8.40 ± 0.12% at 10 µg/mL to 70.13 ± 0.01% at 100 µg/mL. This indicates that 2-Phenyl-4H-chromen-4-one increasingly protects the HRBC membranes from lysis as its concentration increases, suggesting stronger anti-inflammatory activity at higher doses. The statistical analysis using one-way ANOVA yielded an F-statistic of 2640.71with a p-value less than 0.001, confirming that the differences in inhibition at different concentrations are highly statistically significant. The critical difference (CD) value at 5% significance was 1.11, indicating the minimum significant difference between means (Table 8.2).

Overall, these findings demonstrate that 2-Phenyl-4H-chromen-4-one has significant and dose-dependent anti-inflammatory properties by stabilizing the HRBC membrane, which is an *in vitro* indicator of its potential to reduce inflammation by protecting cell membranes from damage or lysis during inflammatory processes. This supports its potential as an effective anti-inflammatory agent.

8.3.4.5. Antidiabetic activity

8.3.4.5.1. α-Amylase activity

The α-amylase inhibitory activity of 2-Phenyl-4H-chromen-4-one isolated from the methanol extract of *S. palghatense* bark was evaluated based on its ability to inhibit the enzyme α-amylase, which is key in carbohydrate digestion and glucose

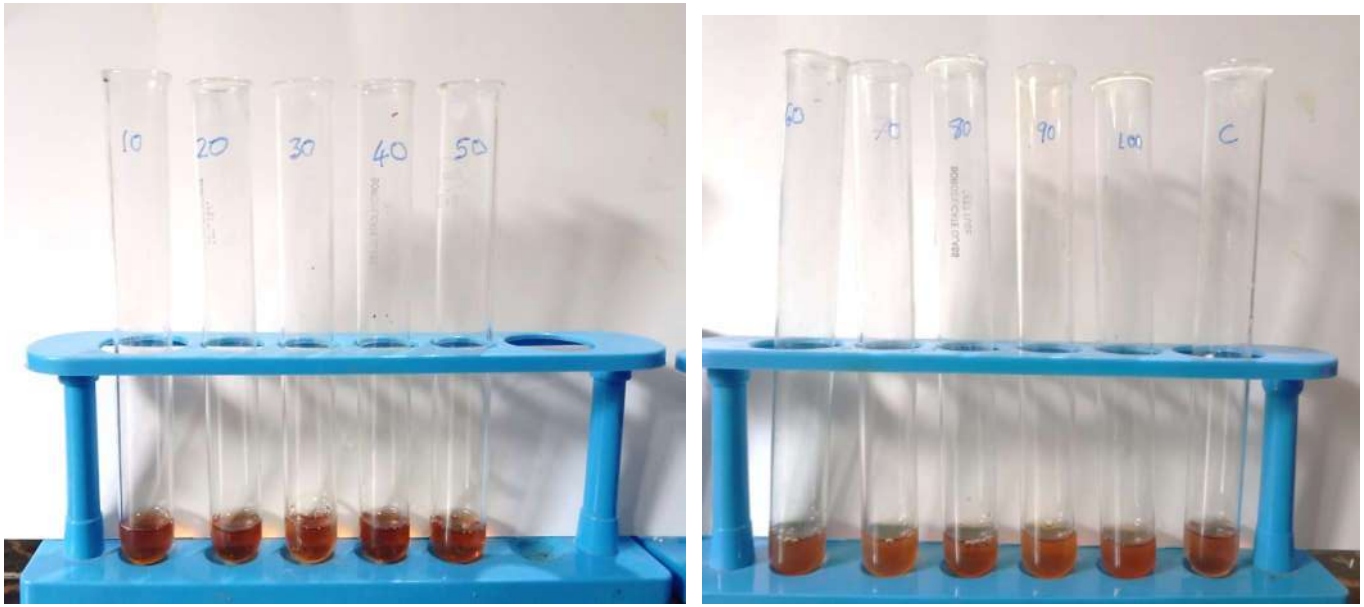


Plate 8.6: Demonstration of anti-inflammatory activity by 2-Phenyl-4H-chromen-4-one isolated from the methanol extract of *Syzygium palghatense* bark using the Human Red Blood Cell membrane stabilization assay (HRBC). Test tubes display varying degrees of haemolysis inhibition at increasing nanoparticle concentrations (10–100 µg/mL) and the control

Table 8.2: Anti-inflammatory activity of 2-Phenyl-4H-chromen-4-one isolated from the methanol extract of *Syzygium palghatense* bark methanolic extract assessed by Human Red Blood Cell membrane stabilization assay (HRBC)

Concentration (µg/mL)	Percentage inhibition (%)
10	8.40 ± 0.12
20	15.14 ± 0.14
30	20.09 ± 0.41
40	25.60 ± 0.17
50	28.30 ± 0.21
60	40.16 ± 0.31
70	43.10 ± 0.31
80	51.15 ± 0.07
90	61.19 ± 0.20
100	70.13 ± 0.01
F-stat	2640.71
P-value	<0.001
CD at 5%	1.11

Values are expressed as mean ± standard error (n = 6). Statistical significance was evaluated using one-way ANOVA followed by a critical difference (CD) test at the 5% significance level. Differences were considered statistically significant at $p < 0.05$

Table 8.3: α-Amylase inhibitory activity of 2-Phenyl-4H-chromen-4-one isolated from the methanol extract of *Syzygium palghatense* bark

Sample Concentration (µg/mL)	OD at 540 nm	Percentage Inhibition (%)
Control	0.2100 ± 0.0101	0
Standard	0.0182 ± 0.0100	91.01 ± 0.1211
62.5	0.2102 ± 0.0320	12.14 ± 0.1130
125	0.1316 ± 0.0201	33.11 ± 0.0251
250	0.1212 ± 0.0511	51.17 ± 0.1410
500	0.1101 ± 0.0202	65.30 ± 0.1320
1000	0.1005 ± 0.0130	83.13 ± 0.1420
F-stat		41.13
P-value		< 0.001
CD at 5%		0.021

Values are expressed as mean ± standard error (n = 6). Statistical significance was evaluated using one-way ANOVA followed by a critical difference (CD) test at the 5% significance level. Differences were considered statistically significant at $p < 0.05$

release. The results indicate that the compound exhibits dose-dependent inhibitory effects, with percentage inhibition increasing as the concentration rises. At the lowest tested concentration of 62.5 µg/mL, inhibition was 12.14 ± 0.11%, while the highest concentration of 1000 µg/mL showed a substantial inhibition of 83.13 ± 0.14%. These results demonstrate that the compound effectively reduces α-amylase activity, potentially contributing to blood glucose regulation.

The control sample, which had no inhibitor, showed an optical density (OD) at 540 nm of 0.2100 ± 0.0101, corresponding to 0% inhibition, while the standard inhibitor exhibited a high inhibition of 91.01 ± 0.12%, confirming the assay's validity. Statistical analysis via one-way ANOVA yielded a significant F-statistic of 41.13 ($p < 0.001$), and the critical difference (CD) at 5% was 0.021, confirming the significance of the concentration-dependent inhibition.

Furthermore, the IC_{50} value (the concentration causing 50% inhibition) for 2-Phenyl-4H-chromen-4-one was 233.06 ± 0.14 µg/mL, which is lower than that of the standard drug Acarbose (720.11 ± 0.21 µg/mL), indicating a stronger α-amylase inhibitory potential of the isolated compound compared to the standard. The IC_{50} results were statistically significant ($F = 30.15$, $p < 0.001$), emphasizing the potent α-amylase inhibition exerted by 2-Phenyl-4H-chromen-4-one (Tables 8.3-8.4).

Taken together, these findings suggest that 2-Phenyl-4H-chromen-4-one possesses effective α-amylase inhibitory activity, making it a promising candidate for managing postprandial hyperglycemia and type 2 diabetes through enzymatic control of carbohydrate digestion.

8.3.4.5.2. α-Glucosidase activity

The α-glucosidase inhibitory activity of 2-Phenyl-4H-chromen-4-one isolated from the methanol extract of *S. palghatense* bark was evaluated through measurement of enzyme activity inhibition at various concentrations. The compound demonstrated a strong dose-dependent inhibitory effect, with percentage inhibition increasing from 24.00 ± 0.12% at 62.5 µg/mL to 90.10 ± 0.20% at 1000 µg/mL, indicating enhanced enzyme inhibition with higher concentrations. The control showed no inhibition,

confirming assay validity, while the standard drug Acarbose exhibited 92.00 ± 0.11% inhibition (Table 8.5).

Statistical analysis via one-way ANOVA produced an F-statistic of 50.14 with a p-value less than 0.001, signifying that the differences between inhibition at various concentrations are highly significant. The critical difference (CD) at 5% was 0.015, indicating the minimum detectable difference between group means.

Importantly, the IC_{50} value of 2-Phenyl-4H-chromen-4-one was found to be 105.15 ± 0.10 µg/mL, which is significantly lower than that of the standard Acarbose, whose IC_{50} was 190.30 ± 0.21 µg/mL. This lower IC_{50} indicates that 2-Phenyl-4H-chromen-4-one is a more potent α-glucosidase inhibitor than Acarbose under the tested conditions (Table 8.6).

Overall, these findings suggest that 2-Phenyl-4H-chromen-4-one from *S. palghatense* bark exhibits strong α-glucosidase inhibitory activity, offering potential as a natural agent for managing postprandial hyperglycemia and diabetes by slowing carbohydrate digestion and glucose absorption. The data support its higher efficacy compared to the standard drug, making it a promising candidate for further development as an antidiabetic compound.

8.3.4.6. Anticancer activity

8.3.4.6.1. Cytotoxicity of 2-Phenyl-4H-chromen-4-one isolated from the methanol extract of *S. palghatense* bark by Trypan Blue assay

The results from the Trypan Blue Exclusion assay indicate that 2-Phenyl-4H-chromen-4-one, isolated from the methanol extract of *S. palghatense* bark, exhibits a clear dose-dependent cytotoxic effect against Dalton's Lymphoma Ascites (DLA) cells. At the lowest tested concentration (20 µg/mL), the compound produced only minimal cytotoxicity (8.1%). However, as the dose increased, cell death rose progressively, reaching 32.0% at 40 µg/mL, 50.3% at 60 µg/mL, and 54.1% at 80 µg/mL. At the highest concentration tested (100 µg/mL), cytotoxicity peaked at 59.1%. This steady increase demonstrates a concentration-dependent response, suggesting that the compound effectively inhibits the viability of DLA cells. The

Table 8.4: IC_{50} value of 2-Phenyl-4H-chromen-4-one isolated from the methanol extract of *Syzygium palghatense* bark in α-Amylase inhibitory activity

Samples	IC_{50} value (%)	F stat	P value	CD at 5%
Standard Acarbose	720.11 ± 0.21	21.77	<0.001	6.01
of 2-Phenyl-4H-chromen-4-one isolated from *Syzygium palghatense* bark	233.06 ± 0.14	30.15	<0.001	5.02

Values are expressed as mean ± standard error (n = 6). Statistical significance was evaluated using one-way ANOVA followed by a critical difference (CD) test at the 5% significance level. Differences were considered statistically significant at $p < 0.0$

Table 8.5: α-Glucosidase inhibition of 2-Phenyl-4H-chromen-4-one isolated from the methanol extract of *Syzygium palghatense* bark

Sample Concentration (µg/mL)	OD at 540 nm	Percentage inhibition (%)
Control	0.2100 ± 0.0211	0
Standard (Acarbose)	0.0170 ± 0.0110	92.00 ± 0.1121
62.5	0.1140 ± 0.1102	24.00 ± 0.1230
125	0.1020 ± 0.0124	53.33 ± 0.1013
250	0.0650 ± 0.0110	75.00 ± 0.1012
500	0.0340 ± 0.0111	87.33 ± 0.1151
1000	0.0150 ± 0.0108	90.10 ± 0.2010
F-stat		50.14
P-value		< 0.001
CD at 5%		0.015

Values are expressed as mean ± standard error (n = 6). Statistical significance was evaluated using one-way ANOVA followed by a critical difference (CD) test at the 5% significance level. Differences were considered statistically significant at $p < 0.05$

Table 8.6: IC_{50} value of 2-Phenyl-4H-chromen-4-one isolated from the methanol extract of *Syzygium palghatense* bark in α-Glucosidase inhibition assay

Samples	IC_{50} value (%)	F stat	P value	CD at 5%
Standard Acarbose	190.30 ± 0.21	25.45	<0.001	5.23
2-Phenyl-4H-chromen-4-one isolated from *Syzygium palghatense* bark	105.15 ± 0.10	39.12	<0.001	3.45

Values are expressed as mean ± standard error (n = 6). Statistical significance was evaluated using one-way ANOVA followed by a critical difference (CD) test at the 5% significance level. Differences were considered statistically significant at $p < 0$

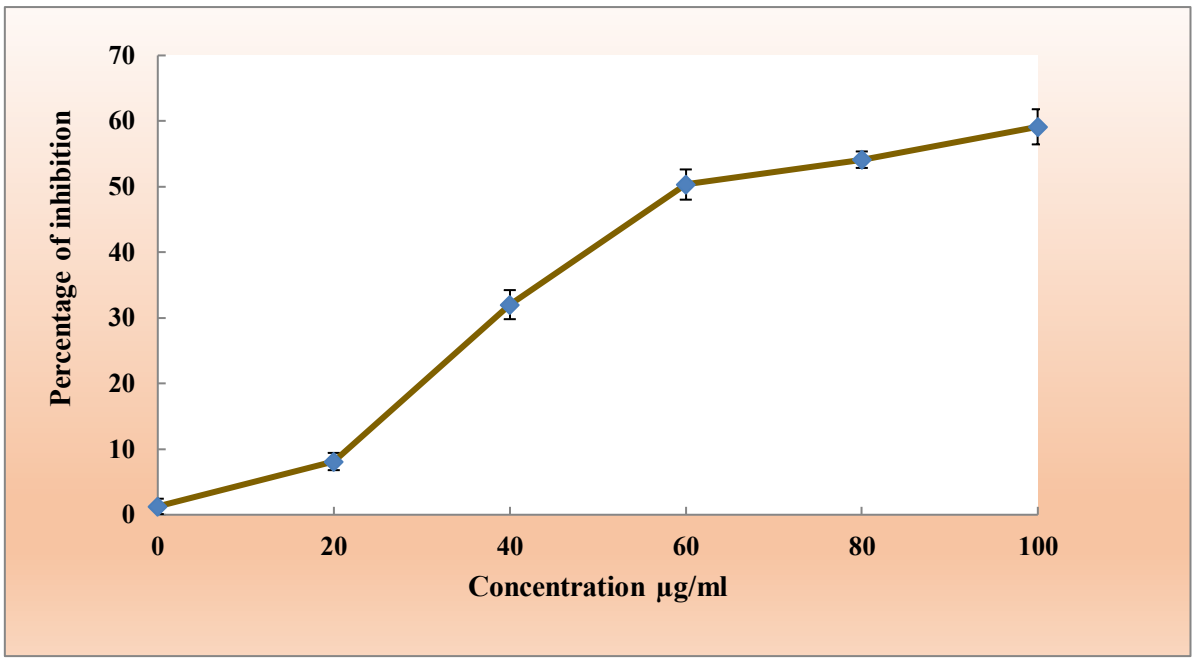


Figure 8.19: Dose-dependent cytotoxicity of 2-Phenyl-4H-chromen-4-one isolated from the methanol extract of *Syzygium palghatense* bark on DLA (Dalton's Lymphoma Ascites) cells determined by Trypan Blue Exclusion Assay

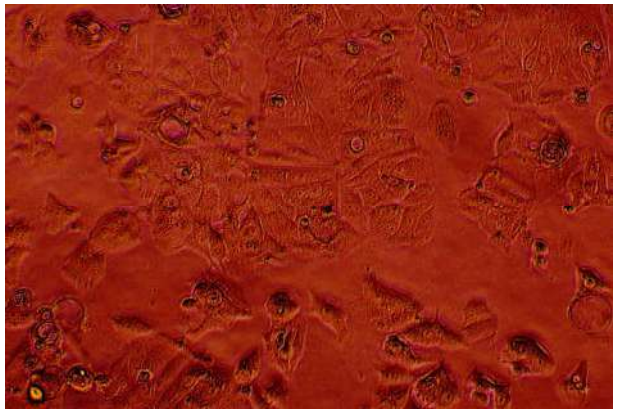
Table 8.7: Effect of standard cisplatin and of 2-Phenyl-4H-chromen-4-one isolated from the methanol extract of *Syzygium palghatense* bark on cell viability at different concentrations measured by MTT assay

Sample Concentration (µg/mL)	Average absorbance (OD at 540 nm)	Percentage viability (%)
Control	0.7590	100.00
Standard Cisplatin		
6.25	0.4395 ± 0.0110	57.90 ± 1.1522
12.5	0.3486 ± 0.0241	45.92 ± 1.182
25	0.2689 ± 0.0485	35.42 ± 1.0315
50	0.1834 ± 0.0460	24.15 ± 1.0441
100	0.1215 ± 0.0272	16.01 ± 0.1523
F-stat		368.42
P-value		<0.001
2-Phenyl-4H-chromen-4-one		
6.25	0.7052 ± 0.0121	82.95 ± 1.0421
12.5	0.6563 ± 0.0132	76.40 ± 1.0315
25	0.5815 ± 0.0174	67.00 ± 1.1102
50	0.4928 ± 0.0186	54.90 ± 1.1044
100	0.2732 ± 0.0152	36.00 ± 1.0822
F-stat		315.72
P-value		<0.001

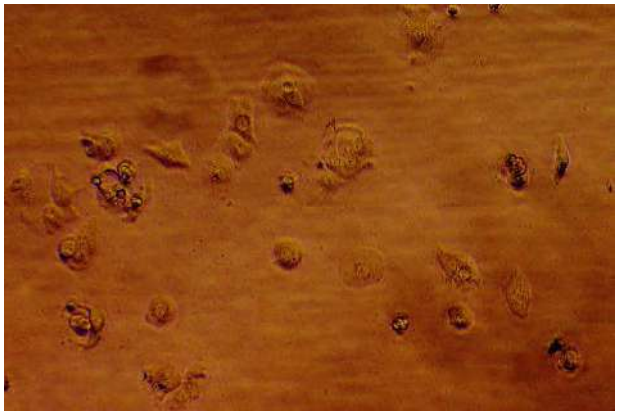
Values are expressed as mean ± standard error (n = 6). Statistical significance was evaluated using a one-way ANOVA. Differences were considered statistically significant at $p < 0.05$

Table 8.8: IC_{50} values and statistical analysis of Cisplatin and of 2-Phenyl-4H-chromen-4-one isolated from the methanol extract of *Syzygium palghatense* bark in MTT assay

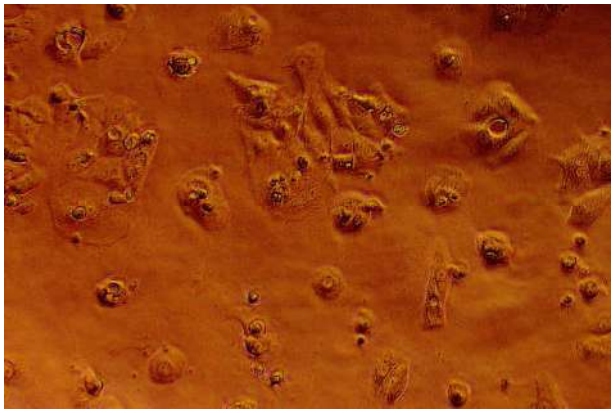
Samples	IC_{50} value (%)	F stat	P value	CD at 5%
Standard Cisplatin	41.05 ± 0.72	64.18	<0.001	4.32
2-Phenyl-4H-chromen-4-one isolated from the methanol extract of *Syzygium palghatense* bark	56.02 ± 0.47	71.25	<0.001	5.62



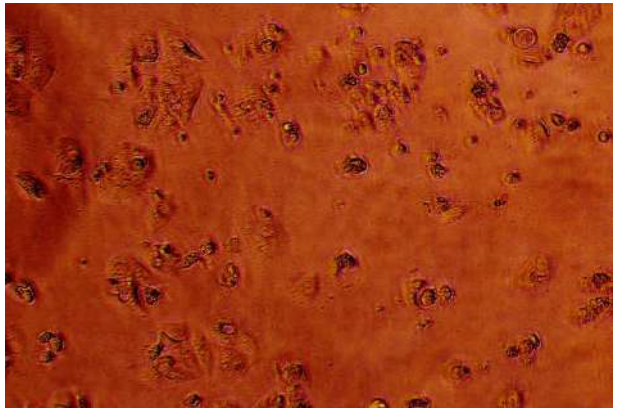
(a)



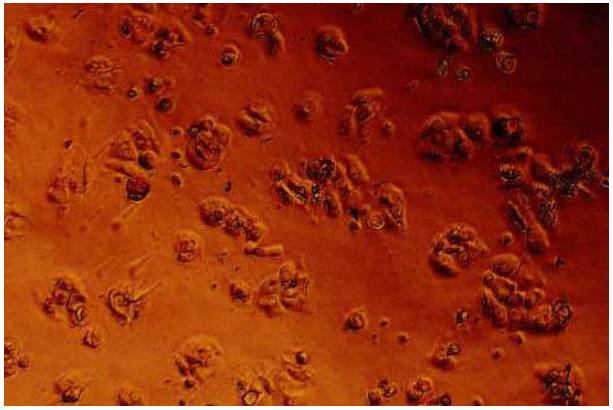
(b)



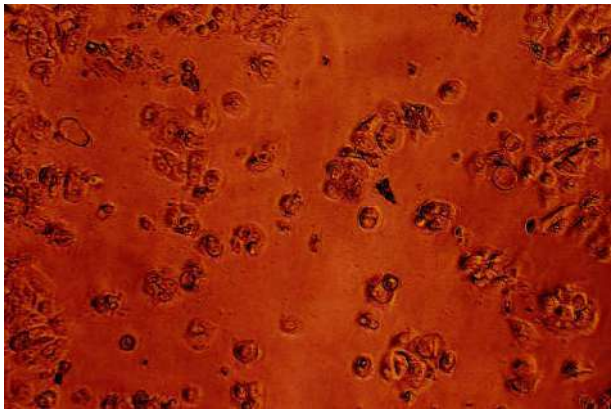
(c)



(d)

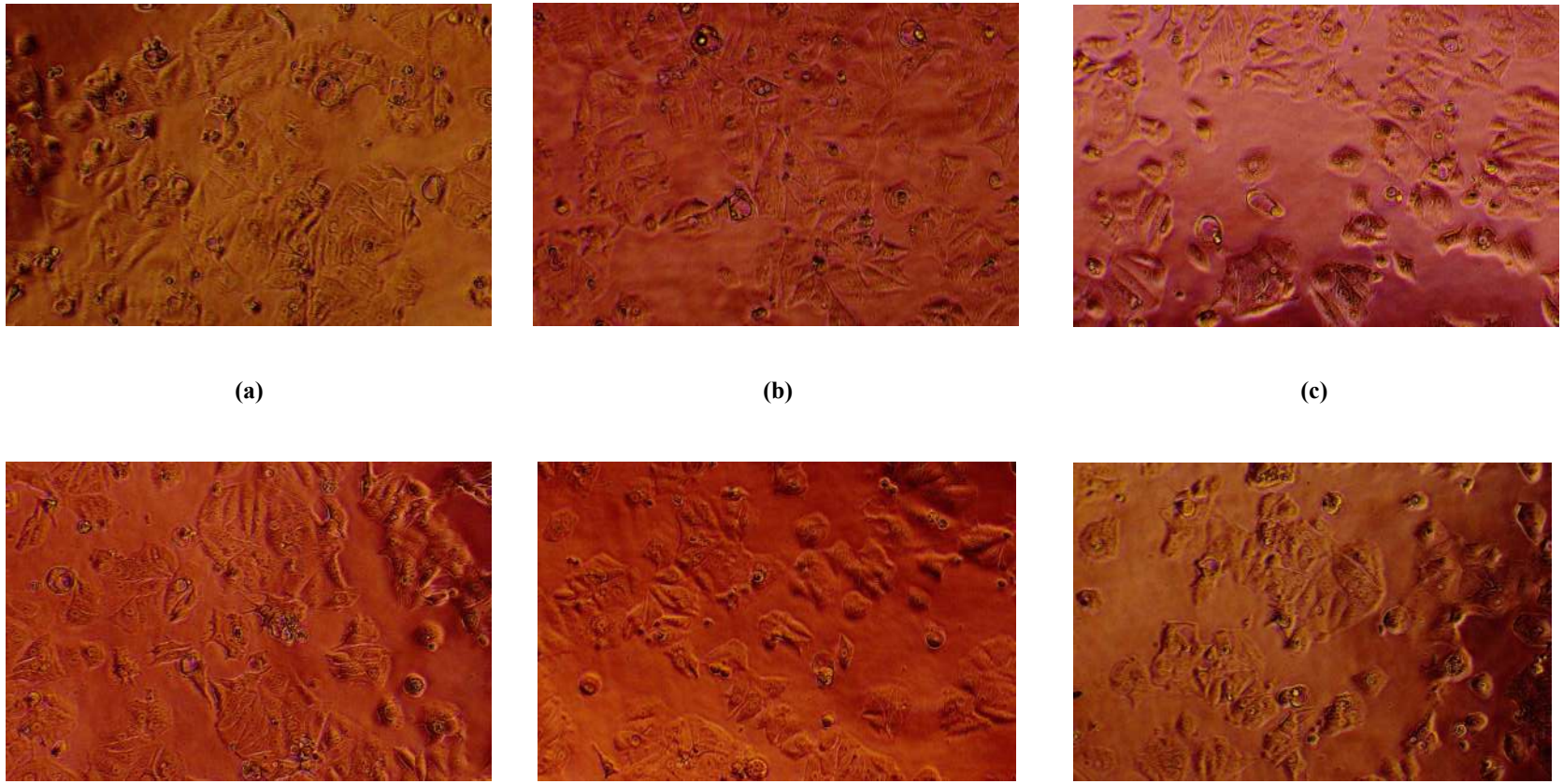


(e)



(f)

Plate 8.7: Photomicrographs depicting standard cisplatin-treated cells in MTT assay at different concentrations: (a) Untreated control (b) 6.25 µg/mL (c) 12.5 µg/mL (d) 25 µg/mL (e) 50 µg/mL (f) 100 µg/mL



(a) **(b)** **(c)**

(d) **(e)** **(f)**

Plate 8.8: Photomicrographs depicting 2-Phenyl-4H-chromen-4-one isolated from the methanol extract of *Syzygium palghatense* bark-treated cells in MTT assay at different concentrations: (a) Untreated control (b) 6.25 µg/mL (c) 12.5 µg/mL (d) 25 µg/mL (e) 50 µg/mL (f) 100 µg/mL

findings support the potential anticancer activity of the flavonoid derivative, with stronger effects at higher doses, though complete cytotoxicity was not achieved even at 100 µg/mL (Figure 8.19).

8.3.4.6.2. MTT assay

The MTT assay results presented in Tables 8.7 and 8.8 clearly demonstrate a dose-dependent cytotoxic effect of both standard cisplatin and the compound isolated from the methanol extract of *S. palghatense* bark, against cancer cells. Cisplatin exhibited a strong and progressive reduction in cell viability, decreasing from 57.9% at 6.25 µg/mL to as low as 16.0% at 100 µg/mL, reflecting its potent cytotoxicity (Plates 8.7-8.8). In comparison, 2-Phenyl-4H-chromen-4-one also showed inhibitory activity on cell viability, but to a lesser extent: it reduced cell survival from 82.9% at 6.25 µg/mL to 36.0% at 100 µg/mL. The IC_{50} values further emphasize this difference in potency, with cisplatin having a lower IC_{50} of 41.05 µg/mL, indicating stronger cytotoxic potential, while the isolated compound displayed a higher IC_{50} of 56.02 µg/mL, suggesting moderate anticancer activity. Both treatments were statistically significant ($p < 0.001$), confirming the reliability of the observed effects. These findings indicate that, while cisplatin remains a more effective cytotoxic agent, 2-Phenyl-4H-chromen-4-one also possesses appreciable anticancer potential and could serve as a valuable phytochemical candidate for further investigation.

Comparing the methanol extract, silver nanoparticles (AgNPs), and 2-Phenyl-4H-chromen-4-one of *S. palghatense*

When comparing the biological activities, including antioxidant, antimicrobial, anthelmintic, anti-inflammatory, antidiabetic, and anticancer properties, between the methanol extract of *S. palghatense* bark, silver nanoparticles synthesized from the methanol extract of *S. palghatense* bark, and the compound 2-Phenyl-4H-chromen-4-one isolated from *S. palghatense*, the *Syzygium*-derived silver nanoparticles showed the highest activity, followed by the isolated compound and then the methanol extract.

A comprehensive evaluation of the antioxidant properties of *S. palghatense* bark methanol extract, its silver nanoparticles, and the isolated compound 2-Phenyl-4H-chromen-4-one reveals that the silver nanoparticles consistently exhibit the highest activity across all assays and concentrations.

In the DPPH radical scavenging assay (Figure 8.20), the percentage inhibition for silver nanoparticles (AgNPs) reached approximately 89% at 150 µg/ml, surpassing both the methanol extract (~81%) and the isolated compound (~85%) at the same concentration, with all samples outperforming the standard ascorbic acid (Std_AA) which showed around 74% inhibition. In the superoxide radical scavenging assay (SRSA) (Figure 8.21), a similar trend was observed: AgNPs achieved nearly 87% inhibition at the highest concentration tested, while the methanol extract reached ~80% and the isolated compound ~82%, with standard ascorbic acid giving lower values (~71%). The hydroxyl radical scavenging assay (HRSA) (Figure 8.22) demonstrated AgNPs again led the group, reaching over 84% inhibition at 150 µg/ml, whereas the methanol extract and the isolated compound achieved approximately 82% and 81%, respectively, both exceeding the standard gallic acid (Std_GA; ~67%). The ferric reducing antioxidant power (FRAP) assay (Figure 8.23) further confirmed this ranking of activity, with AgNPs showing around 88% inhibition at the highest dose, followed by the isolated compound (~85%), methanol extract (~83%), and standard ascorbic acid (~75%).

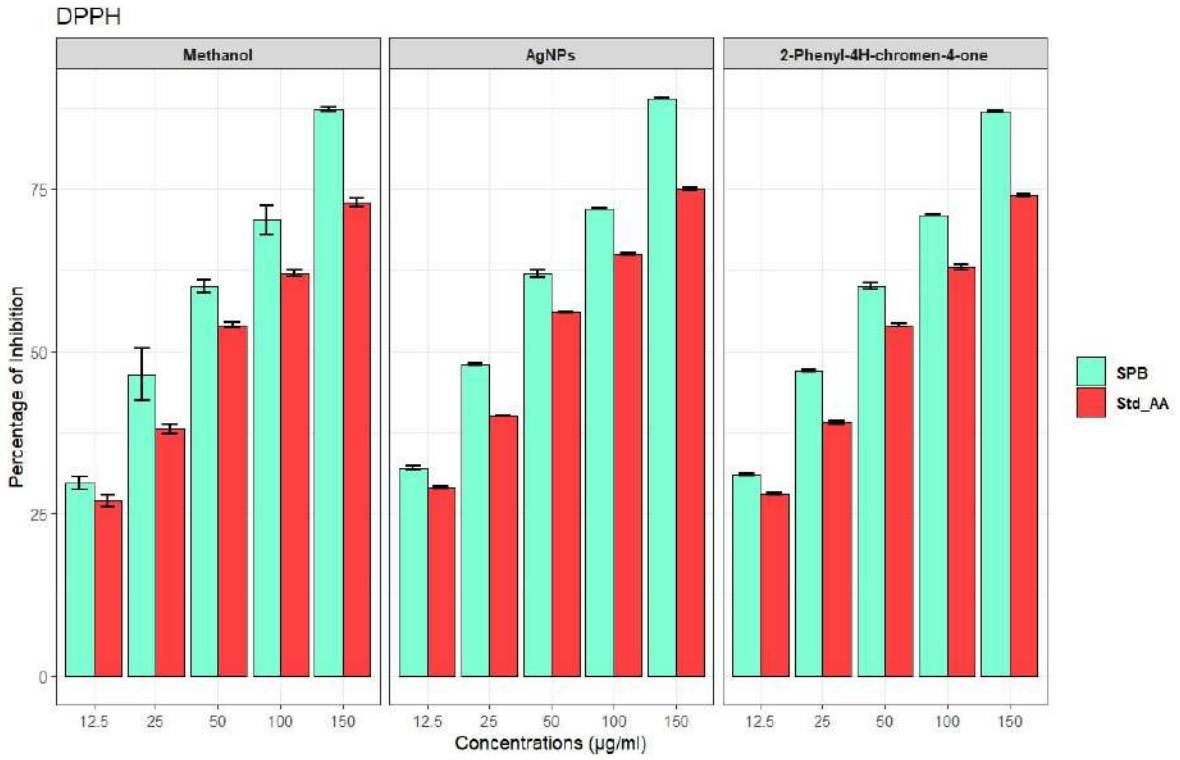


Figure 8.20: DPPH Radical Scavenging activity of methanol extract, AgNPs, and 2-Phenyl-4H-chromen-4-one isolated from *Syzygium palghatense* bark

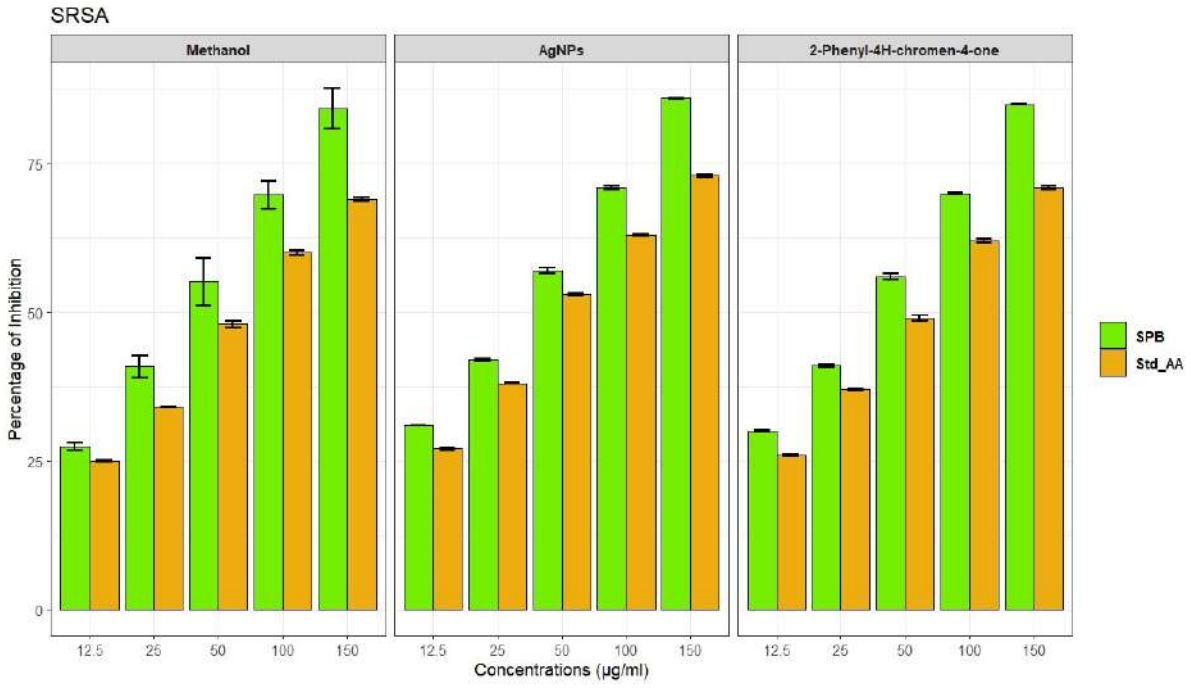


Figure 8.21: Superoxide Radical Scavenging assay (SRSA) of methanol extract, AgNPs, and 2-Phenyl-4H-chromen-4-one isolated from *Syzygium palghatense* bark

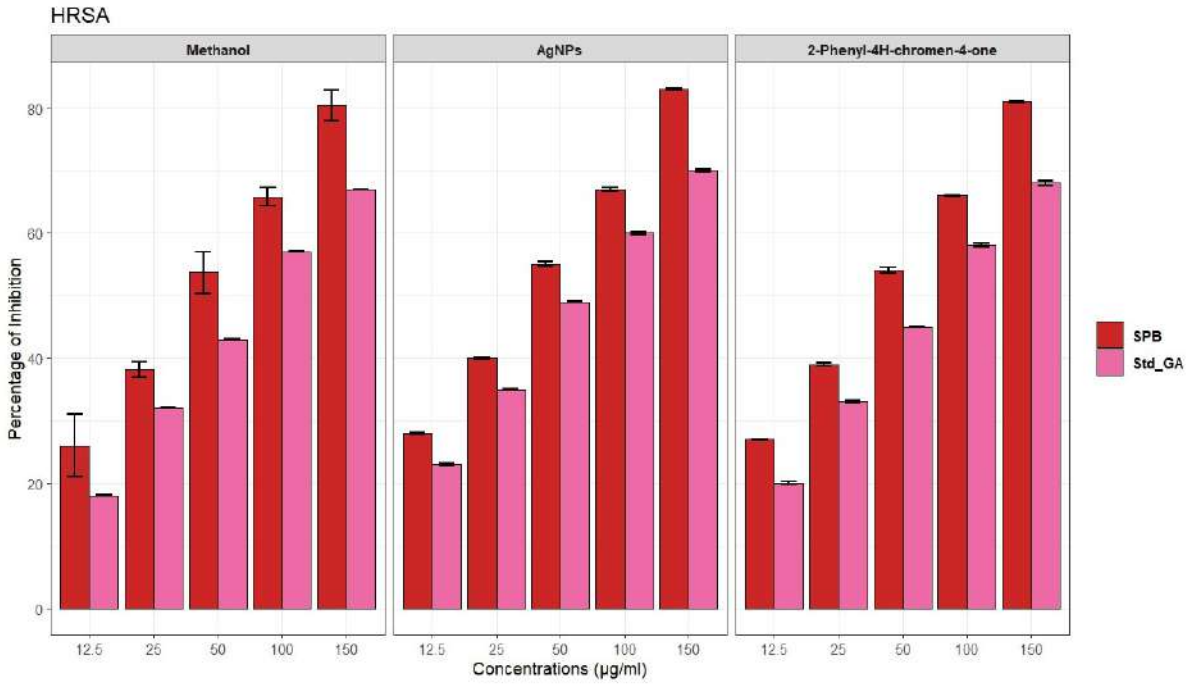


Figure 8.22: Hydroxyl Radical Scavenging assay (HRSA) of methanol extract, AgNPs, and 2-Phenyl-4H-chromen-4-one isolated from *Syzygium palghatense* bark

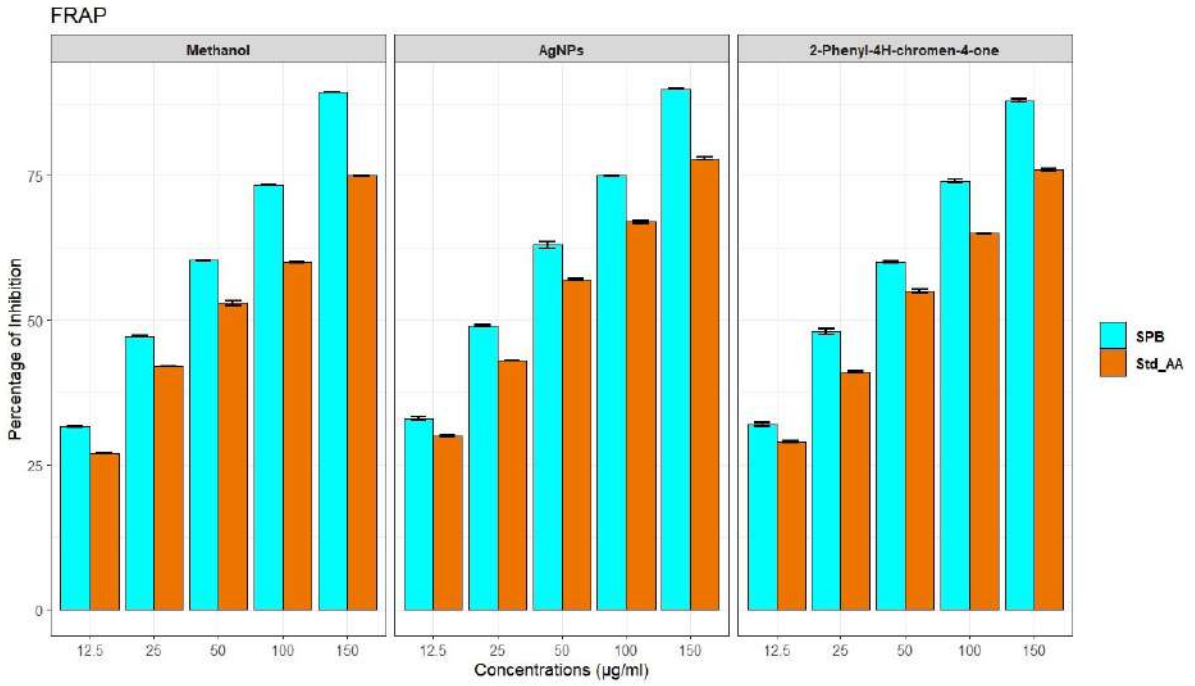


Figure 8.23: Ferric Reducing Antioxidant Power (FRAP) assay of methanol extract, AgNPs, and 2-Phenyl-4H-chromen-4-one isolated from *Syzygium palghatense* bark

The IC_{50} comparison chart (Figure 8.24) unambiguously supports these results: across all assays, the lowest IC_{50} values (μg/ml) were observed for the silver nanoparticles, followed by 2-Phenyl-4H-chromen-4-one, and then the methanol extract. Standards exhibited significantly higher IC_{50} values than all *Syzygium* palghatense-derived samples.

Collectively, these findings demonstrate that synthesizing silver nanoparticles from *S. palghatense* bark markedly enhances antioxidant efficacy compared to using either the crude methanol extract or the isolated compound alone. The nanoparticles show the most potent radical scavenging and ferric-reducing power, making them a promising approach for boosting the antioxidant value of plant-based therapies.

Figure 8.25 represents the antifungal activity (zone of inhibition in mm) of methanol extract, synthesized AgNPs (silver nanoparticles), and 2-Phenyl-4H-chromen-4-one compound from *Syzygium* species against *Aspergillus niger* (purple) and *Candida albicans* (green), compared with the standard Clotrimazole (100 μg/ml). Across all treatments, Clotrimazole exhibited the highest inhibition zones (Methanol: 24 ±1 mm for *A. niger*, 20 ±1 mm for *C. albicans*; AgNPs: 29 ±2 mm for *A. niger*, 33 ±2 mm for *C. albicans*; 2-Phenyl-4H-chromen-4-one: 27 ±2 mm for *A. niger*, 33 ±2 mm for *C. albicans*). With increasing concentrations of extracts (250, 500, 1000 μg/ml), the inhibition zones increased modestly, notably for AgNPs, which generally exhibited higher antifungal activity (up to 25 ±1 mm for *A. niger* at 1000 μg/ml) compared to methanol extract (up to 18 ±1 mm) and 2-Phenyl-4H-chromen-4-one (up to 20 ±1 mm for *Candida*).

Figure 8.26 summarizes the antibacterial activity (zone of inhibition in mm) of methanol extract, AgNPs, and 2-Phenyl-4H-chromen-4-one against five bacterial strains: *Staphylococcus aureus* (blue), *Streptococcus mutans* (green), *Enterococcus faecalis* (brown), *Escherichia coli* (red), and *Pseudomonas aeruginosa* (yellow), with Streptomycin (100 μg/ml) as a standard. Streptomycin demonstrated the highest inhibition (Methanol: 28 ±1 mm for *E. coli*; AgNPs: 30 ±2 mm for *P. aeruginosa*; 2-Phenyl-4H-chromen-4-one: 32 ±2 mm for *P. aeruginosa*). Among extracts, AgNPs

generally showed superior antibacterial activity, with maximum inhibition against *P. aeruginosa* reaching 27 ±1 mm at 1000 µg/ml. This was followed by 2-Phenyl-4H-chromen-4-one and methanol extract, both showing moderate activity at similar concentrations (typically between 15–22 mm). *P. aeruginosa* consistently exhibited the highest susceptibility across treatments, while *E. faecalis* and *S. mutans* showed lower zones of inhibition (around 13–17 mm at the highest extract concentrations). These trends suggest that AgNPs synthesized from *Syzygium* exhibit pronounced broad-spectrum antimicrobial effects, with both antifungal and antibacterial activity increasing in a concentration-dependent manner and being most effective against *C.* albicans and *P. aeruginosa*.

Figure 8.27 compares the paralyzing time and death time of worms (in minutes) exposed to different concentrations (25, 50, 75, 100 mg/mL) of Methanol extract, AgNPs, and 2-Phenyl-4H-chromen-4-one, along with control and standard treatments. For all three test substances, both paralyzing and death times decrease as the concentration increases, indicating higher potency at higher doses. Among the three, the standard drug consistently showed lower (faster) paralyzing and death times than the extracts, demonstrating higher efficacy. At 100 mg/mL, all test samples achieved markedly faster performance compared to controls, with AgNPs and 2-Phenyl-4H-chromen-4-one approaching the standard in efficacy. This suggests concentration-dependent anthelmintic activity, with nanoparticles or pure compounds possibly offering enhanced potency relative to crude plant extract.

Figure 8.28 presents a comparative analysis of inhibition percentages exhibited by the methanolic extract, silver nanoparticles (AgNPs), and 2-Phenyl-4H-chromen-4-one at different concentrations (25, 50, 75, and 100 mg/mL), alongside control and standard references. In all three test groups, the control consistently shows negligible inhibition, while the standard demonstrates close to 100% inhibition, indicating its role as a positive control. The methanolic extract reveals a concentration-dependent increase in inhibition percentage, starting moderately and rising to around 88% at the highest concentration. In contrast, AgNPs display markedly higher inhibitory activity across all concentrations, consistently remaining

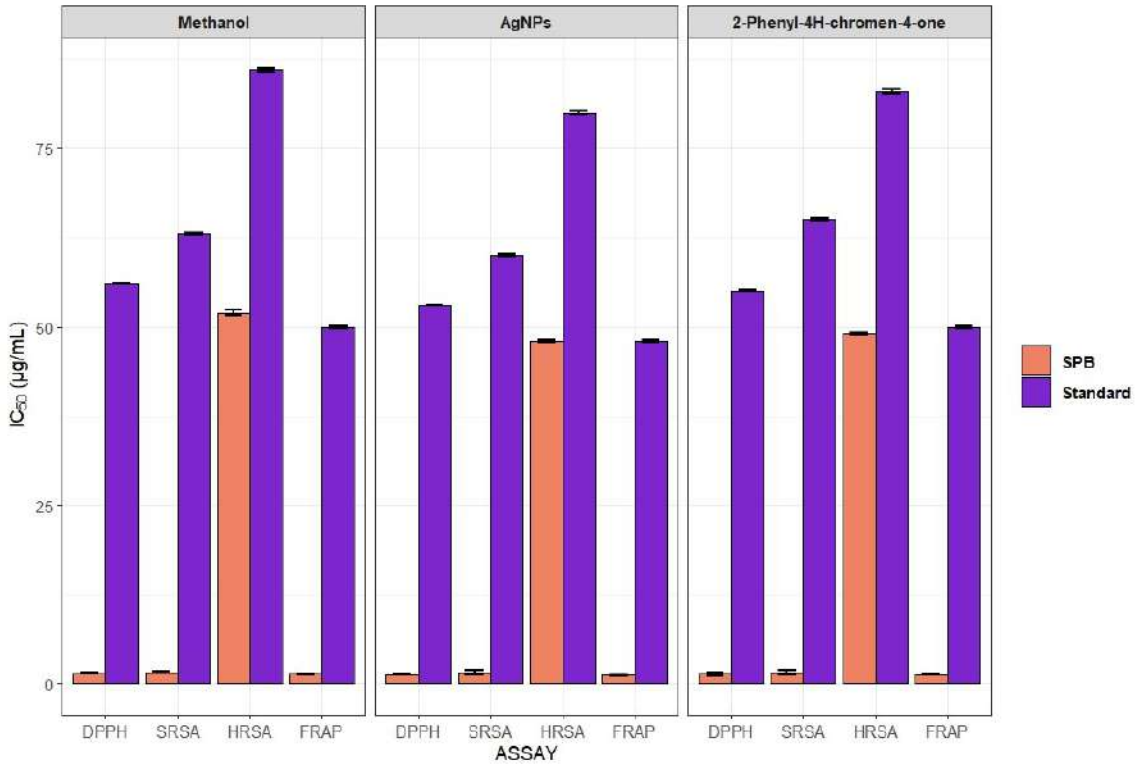


Figure 8.24: IC_{50} Comparison of antioxidant assays (DPPH, SRSA, HRSA, FRAP) between methanol extract, AgNPs, 2-Phenyl-4H-chromen-4-one, and standards

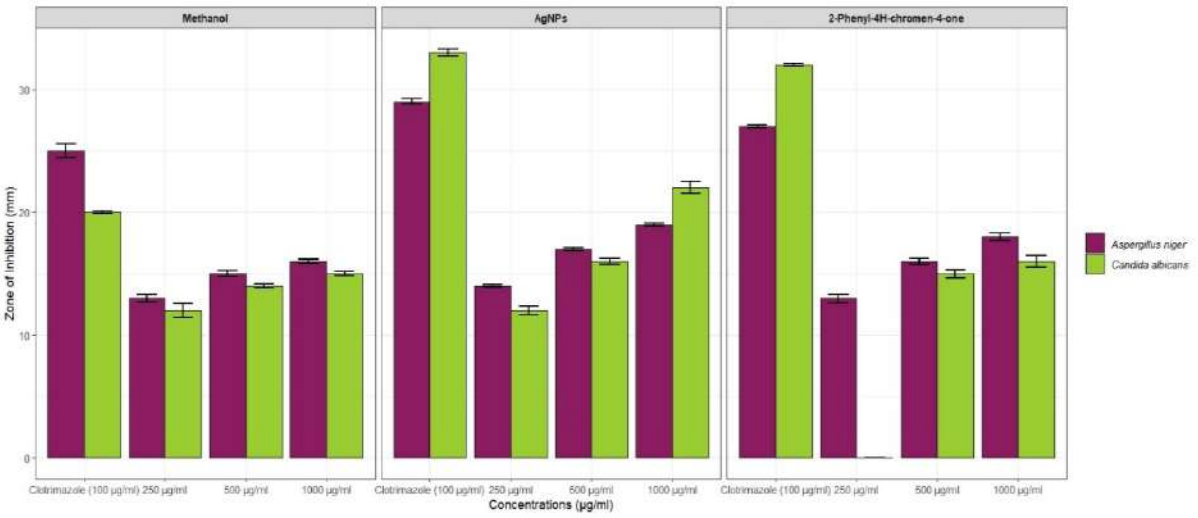


Figure 8.25: Antifungal activity of *Syzygium* methanol extracts, AgNPs, and 2-Phenyl-4H-chromen-4-*one* against pathogenic fungi

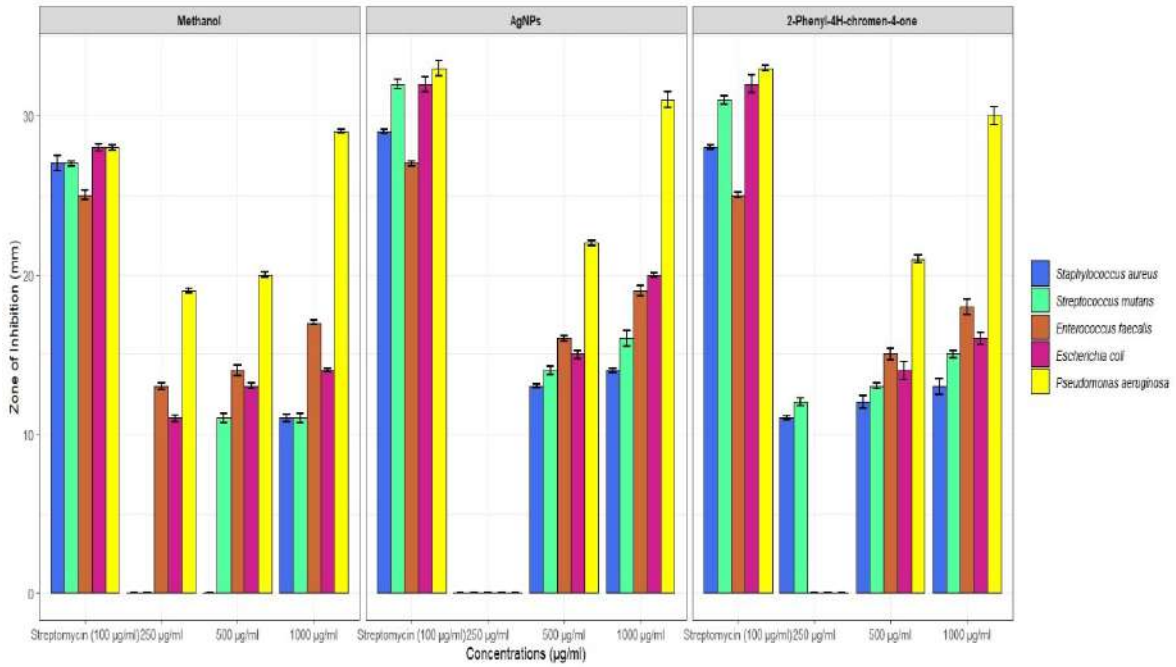


Figure 8.26: Antibacterial activity of *Syzygium* methanol extracts, AgNPs, and 2-Phenyl-4H-chromen-4-*one* against pathogenic bacteria

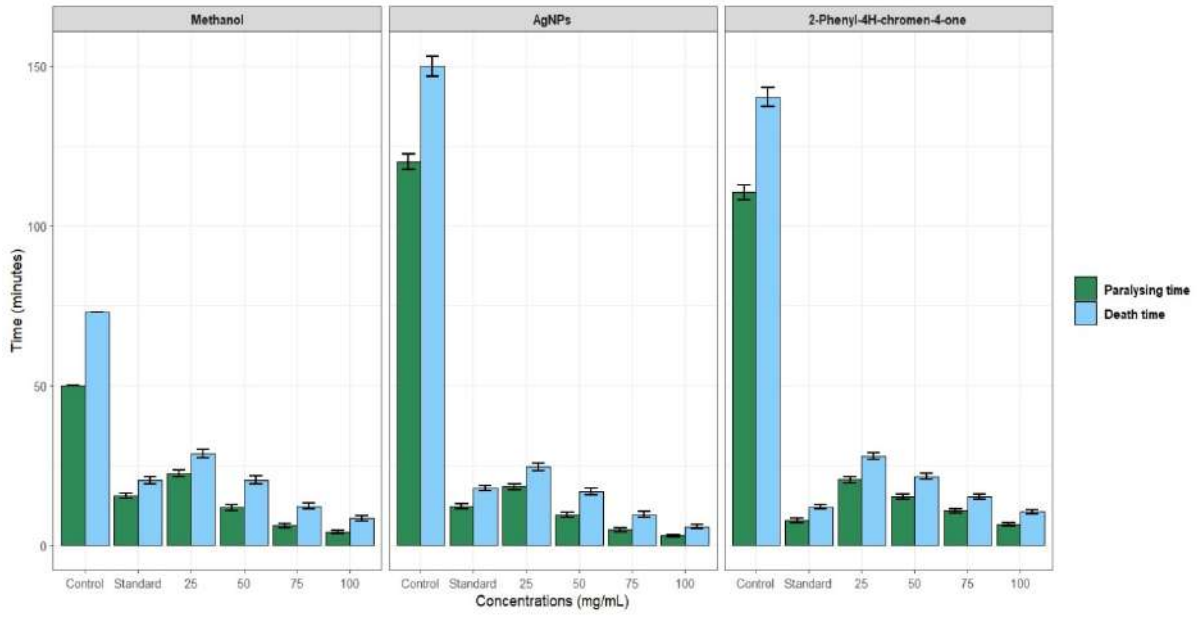


Figure 8.27: Anthelmintic activity of methanol extract, AgNPs, and 2-Phenyl-4H-chromen-4-one

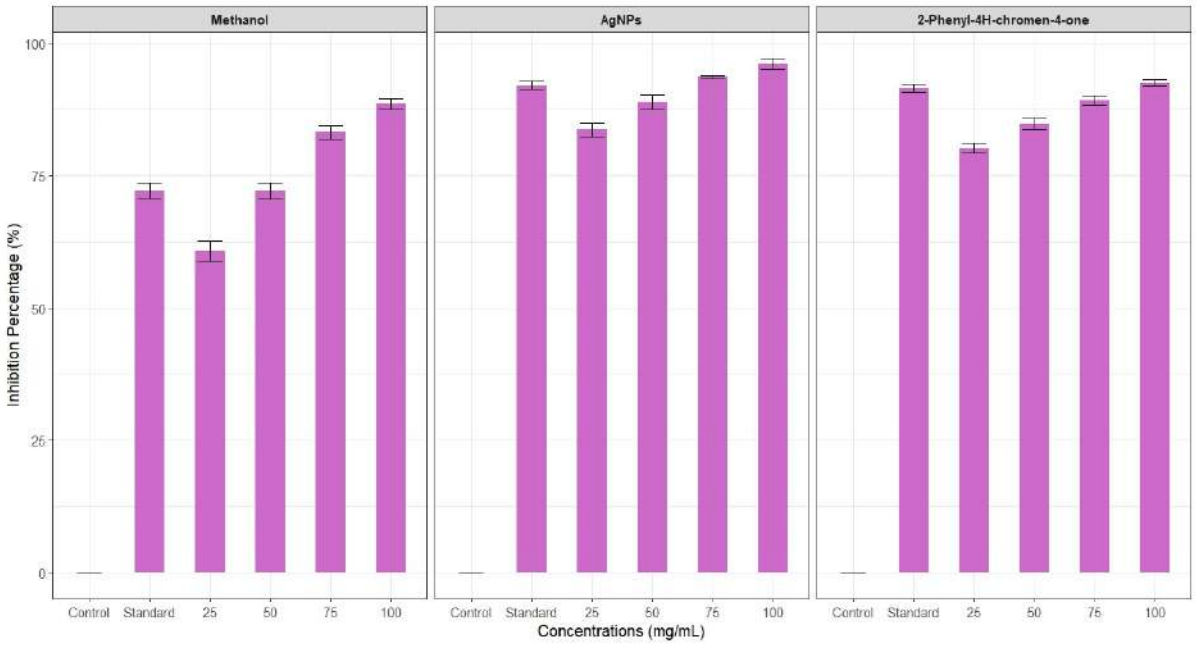


Figure 8.28: Comparative analysis of inhibition percentage for methanolic extract, AgNPs, and 2-Phenyl-4H-chromen-4-one at different concentrations

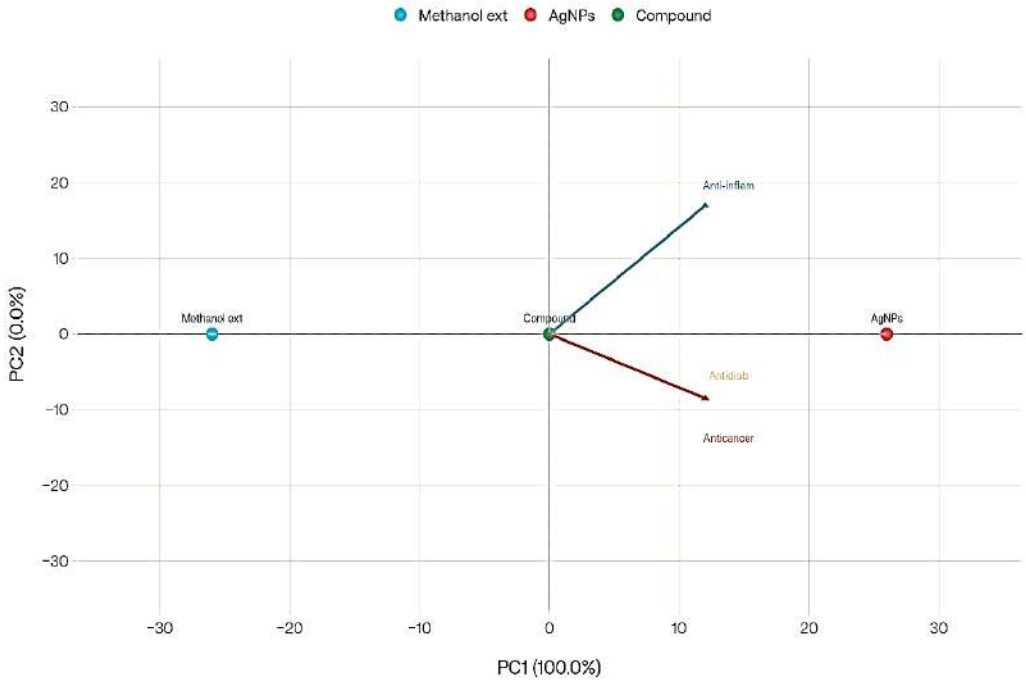


Figure 8.29: PCA plot showing anti-inflammatory, antidiabetic and anticancer activity of methanolic extract, AgNPs, and 2-Phenyl-4H-chromen-4-one at different concentrations

above 85% and closely aligning with the standard's efficacy. Similarly, 2-Phenyl-4H-chromen-4-one maintains a high inhibition profile above 80% at each concentration tested, suggesting strong and consistent biological activity. These data collectively indicate that AgNPs and 2-Phenyl-4H-chromen-4-one are more potent inhibitors compared to the crude methanolic extract, particularly evident at lower concentrations, thereby underscoring their potential as promising agents in pharmacological research.

Figure 8.29 represents the PCA biplot was constructed using anti-inflammatory, antidiabetic, and anticancer activities for the three samples: silver nanoparticles, 2-Phenyl-4H-chromen-4-one, and Methanol extract. The plot shows that silver nanoparticles cluster farthest along both principal components, indicating the highest combined bioactivity in all domains, followed by the compound, and then the methanol extract. The vectors (arrows) for each activity point toward the region dominated by silver nanoparticles, confirming their superior efficacy across the tested parameters. This visualization illustrates clear separation and ranking in bioactivities, supporting that silver nanoparticles > Compound > Methanol extract in biological potency.

8.4. Discussion

Plants contain naturally occurring, physiologically active chemical compounds called phytochemicals that are beneficial for human health (Velavan, 2015). Bioactive compound 2-Phenyl-4H-chromen-4-one was successfully isolated, characterised, and assessed for its biological activities. This compound has been identified for the first time in *S. palghatense*. 2-Phenyl-4H-chromen-4-one have the molecular weight of 222.243 Da with molecular formula $C_{15}H_{10}O_2$. It shows maximum absorption near 294 nm in the UV spectrum. Singh et al. (2018) developed, synthesized, and assessed the poly-functionality of a series of 2-Phenyl-4H-chromen-4-one and its related compounds. Given their wide range of pharmacological actions, these substances may be used as a foundation for the creation of powerful medications to treat diseases like Alzheimer's disease.

Previously, Zarghi and Kakhki (2014) reported the synthesis and biological analysis of an array of 2-phenyl 4H-chromen-4-one derivatives with different replacements at the C-3 chromene moiety and a methylsulfonyl pharmacophore at the para position of the C-4 phenyl ring. They discovered moderate to high COX-2 inhibitory action was showed by all of the target substances. Additionally, the results showed that the size and type of the substituent at position 3 of the chromene scaffold are crucial for the inhibitory effects of COX-2. Xiao et al. (2022) synthesized twelve novel 2-phenyl 4H-chromen-4-one derivatives. These compounds' anti-inflammatory properties were then assessed both *in vitro* and *in vivo*. The majority of the compounds demonstrated favorable NO inhibitory activity and minimal toxicity in RAW264.7 cells, according to the initial assessment results. More significantly, a compound showed efficacy against inflammation by suppressing the production of pro-inflammatory cytokines in RAW264.7 cells by blocking the TLR4/MAPK signaling pathways.

It should be recognized that evaluating the circumstances of the extraction of the bioactive substances in any natural product is crucial for conducting a thorough investigation of its biological characteristics (Savi et al., 2020). Ever since the beginning of time, medicinal plants have been historically used to treat illnesses, and

they are now employed as a guide for assistance in the development of new drugs. The flavonoids are one of the primary classes of phenolic chemicals present in plants (de Oliveira et al., 2016). Eugenol is the primary phytochemicals in clove oil, with eugenyl acetate and β-caryophyllene following closely after. Their compounds have various biological advantages. Apart from its widespread application as a flavoring element in food, clove oil has been used for centuries as an oral analgesic in dentistry (Mittal et al., 2014). Because phenolic chemicals have been linked to protection against several illnesses and sensory perception, they have gained importance.

The n-butanol extract of *S. jambos* (Family Myrtaceae) yielded eight distinct compounds (quercetin 3-O-rutinoside, prenylbenzoic acid 4-β-D-glucoside, morolic acid 3-O-caffeate, 5,4'-dihydroxy, 7-methoxy, 6-methyl-flavone, 3,4,5-trihydroxybenzoic acid, quercetin, isoetin-7-O-β-D-glucopyranoside, and 4′ Hydroxy-3′-methoxyphenol- β- D- [6-O- (4″-hydroxy-3″, 5″-dimethoxybenzoate)] glucopyranoside which are having natural antioxidant and antimicrobial potential (Ghareeb et al., 2017). According to GC-MS research, the methanolic leaf extract of *S. jambos* contains 45 active compounds with antipyretic and antiparasitic properties (Devakumar et al., 2017). Myrigalone-G pentoside, Myricetin rhamnoside, quercetin galloyl-pentoside, and cryptostrobin were among the 87 distinct flavonoid-rich compounds found in the methanol extract of *S. aqueum* leaves. The main flavonoid compounds in this extract were myrigalone-B and myrigalone-G (Ahmed et al., 2021; Sobeh et al., 2018).

The natural compounds known as flavonoids, which have a variety of phenolic structures, can be found in fruits, tea, wine, vegetables, bark, stems, roots, grains, and flowers. These natural compounds have been regarded for being good for the body, and attempts are going on to separate these components. Many pharmaceutical, cosmetic, nutraceutical, and medical applications now view flavonoids as an essential ingredient (Panche et al., 2016). Commonly referred to as flavones, 2-Phenyl-4H-chromen-4-one is a member of the flavonoid class and is found in an array of plants. Because of the double bond among C2 and C3 within the structure and the absence of substituents at the C3 location, flavones vary from other flavonoids (Devi et al., 2022).

Many species of the genus *Syzygium* have been found to contain bioactive substances, including terpenoids, ellagic acid derivatives, flavanone derivatives, and other polyphenolics. However, more thorough research on the phytochemical components and mechanism-based pharmacological actions is required for numerous species in the genus *Syzygium* (Uddin et al., 2022).

According to several studies, flavonoids contain biological properties such as vasodilating, antiviral, antiallergenic, and anti-inflammatory effects. The antioxidant properties of flavonoids, on the other hand, has drawn the greatest attention because of its capacity to scavenge and prevent the production of free radicals (Pietta et al., 2000). When attempting to measure the antioxidant capabilities of chemicals derived from plants, suitable techniques that concentrate on the kinetics of the processes involving the antioxidants as well as the underlying mechanisms of antioxidant activity, are required (Amorati & Valgimigli, 2018). In the present study, the antioxidant activity of the isolated compound was assessed by DPPH, superoxide, hydroxyl radical scavenging, and ferric reducing antioxidant power (FRAP) assays. It showed dose-dependent antioxidant activity in all assays, outperformed ascorbic acid in most tests.

The compound also possesses a broad spectrum of antimicrobial and antifungal effects. Moderate inhibition against *Aspergillus niger* and *Candida albicans*. Similar to research by de Oliveira et al. (2016), who stated that 2-phenyl-4H-chromen-4-one may be an alternative medication for treating *Candida*-caused fungal infections. It has the capability of breaking down chitin, which aids in the creation of fungal membranes. Compounds containing lipophilic electron-withdrawing groups had strong antifungal activity when compared to fluconazole (Devi et al., 2022). Methanol extracts of *S. jambos* (leaf), *S. australe* (leaf), and *S. luehmannii* (leaf and fruit) shown strong antifungal action by preventing the development of human dermatophytes (Noé et al., 2019).

Antimicrobial agent resistance is becoming a more significant and urgent worldwide issue (Cushnie & Lamb, 2005). The present study indicates that it has potential as an antimicrobial agent as it possesses strong activity, especially against

Pseudomonas aeruginosa. Findings from Thebti et al. (2023) demonstrated that chalcones were more effective than flavones and flavanones and that the majority of tested flavonoids had moderate to high antibacterial activity, especially against Staphylococcus aureus, with minimum inhibitory concentrations (MIC) ranging from 31.25 to 125 µg/mL. MIC recorded in the present study ranged from 0.51 to 0.62 µg/mL. According to Silva et al. (2024), the essential oil of the *S. cumini* (EOSC) shows potential as an investigation material for compounds with antifungal and anti-*Trichomonas vaginalis* properties. According to their findings, nerol and α-pinene are the primary phytochemical components of the EOSC. Its effectiveness in treating microbial infections and its capacity to boost fluconazole's effects are also encouraging, suggesting that it can be used as a supplemental treatment. This study also reported its anti-*Trichomonas vaginalis* action for the first time. According to Biharee et al. (2020), flavonoids have the potential to resolve this new crisis since they are a class of natural chemicals that may be a viable therapy for pathogenic infections because they exhibit antimicrobial activity through different pathways than traditional medications.

The use of herbal plants as a substitute for anthelmintics must be investigated since anthelmintic resistance has become a significant issue in parasite management (Anggrahini et al., 2020). Anthelmintic activity of the isolated compound was tested against *Lumbricus terrestris,* with the action being dose-dependent and similar to that of the common medication albendazole. According to Chander et al. (2014), who investigated the anthelmintic properties of *Barleria buxifolia* leaves in order to determine their total flavonoid content, the leaf extract exhibited good anthelmintic activity. Kavitha et al. (2011) provide the first study on the anthelmintic properties of methanolic and aqueous extracts of the bark of *S. cumini*. According to the results of the experiment by Anggrahini et al. (2020), bay leaf extract (*S. polyanthum*) may have anthelmintic properties against *A. galli*. To ascertain the optimal dose, more study needs to be done.

Anti-inflammatory activity assessed by HRBC membrane stabilization assay, suggesting a strong anti-inflammatory potential. In Bangladesh, *S. jambos* has long

been used as an ancient treatment for inflammatory conditions. Hossain et al. (2016) found *that S. jambos* have acute anti-inflammatory and antioxidant properties, which are caused by phenolic and flavonoid components. The aqueous root extract of *S. caryophyllatum*, which is cultivated in Sri Lanka, has strong *in vitro* anti-inflammatory properties, as reported by Heendeniya et al. (2018). This action may be mediated by flavonoids, tannins, and alkaloids. According to Qamar et al. (2021), fruit extracts from *S. cumini* are a rich source of bioactive chemicals that demand more research as potential leads for the development of anti-inflammatory drugs. *S. polyanthum* was identified by Zawawi & Sahidin (2022) as a possible source of medicinal compounds having antioxidant and anti-inflammatory properties.

Many chemicals from various classes that were isolated from various *Syzygium* species showed antidiabetic properties (Uddin et al., 2022). The results indicate that the isolated compound has significant α-glucosidase inhibitory activity and excellent α-amylase inhibitory activity, making it a potential option for the enzymatic regulation of carbohydrate digestion in the management of postprandial hyperglycemia and type 2 diabetes. The ethanolic extracts of *S. aqueum* leaves were shown to be successful in blocking the enzymes that hydrolyze carbohydrates, α-glucosidase and α-amylase; they were also able to inhibit aldose reductase, a critical enzyme in the polyol pathway (Manaharan et al., 2012). Kiruthiga et al. (2018) conducted an *in silico* library and designed phenyl-4H-chromen-one that targets many diabetes enzymes. It was noticeable from the docking result that these compounds had a strong correlation with the predicted anti-diabetic effectiveness.

Many plants' natural compounds and bioactive ingredients show promising anticancer activity and are less toxic than conventional anticancer drugs, according to an expanding field of research. However, their extensive applicability in cancer therapy is severely limited by their water solubility, lack of stability, absorption, bioavailability, and selective targeting (Bozzuto et al., 2024). Anticancer activity was evaluated against Dalton’s Lymphoma Ascites (DLA) cells using Trypan Blue and MTT assay, which indicates its potential as an anticancer agent. Although cisplatin is still a more potent cytotoxic drug, the results show that 2-phenyl-4H-chromen-4-one

has significant anticancer potential and may be a useful phytochemical option for further research.

With a variety of biological activities, including anti-cancer ones, flavonoids may prove to be effective preventative and therapeutic agents for cancer. According to Mindawati et al. (2024), *S. cumini* can serve in anticancer therapy of breast cancer because it contains numerous bioactive chemicals, namely flavonoids, phenolic compounds, and anthocyanins, which are known to have anticancer properties. These chemicals can stop the development of cancerous cells by inducing apoptosis or other methods.

Research on pharmacological activities provided evidence in favor of this genus's medicinal significance. More thorough research on the phytochemical components and mechanism-based pharmacological actions is necessary for several *Syzygium* species. Additionally, before conducting clinical investigations, *in vitro* and *in vivo* animal studies are required to confirm the safety, clarify the effective dosages, and determine the mechanisms of action (Uddin et al., 2022).

8.5. Conclusion

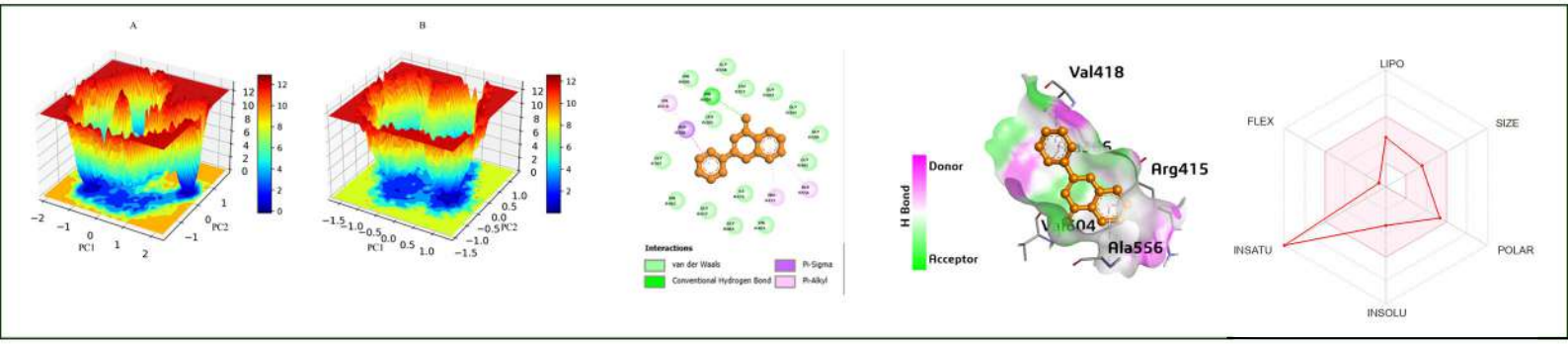
In the present study, the bioactive flavonoid derivative, 2-Phenyl-4H-chromen-4-one, was discovered in the bark extract of *S. palghatense* for the first time. It was effectively isolated, characterized, and evaluated for its biological properties using comprehensive spectroscopic analyses, such as UV, FT-IR, NMR, and GC-MS techniques. It belongs to the flavonoid class and is present in a variety of plants. It is commonly referred to as flavones. The molecule was identified as a light yellow waxy flavonoid derivative with a molecular weight of 222.24 Da and a molecular formula $C_{15}H_{10}O_2$. Its categorization as a secondary metabolite originating from plants was confirmed by its notable conjugation and aromaticity.

The 2-phenyl-4H-chromen-4-one demonstrated several pharmacological characteristics. It was shown that 2-phenyl-4H-chromen-4-one exhibited dose-dependent antioxidant, antibacterial, antifungal, anthelmintic, anti-inflammatory, antidiabetic (by inhibiting α-glucosidase and α-amylase), and anticancer properties. All of these results point to 2-Phenyl-4H-chromen-4-one as a distinctive bioactive compound derived from plants with a wide range of therapeutic potential, indicating that it may be used to create natural anticancer, antimicrobial, antidiabetic, anti-inflammatory, and anthelmintic agents. Prior to therapeutic applications, more *in vivo* research and mechanistic analyses are necessary to confirm its pharmacological effectiveness and safety.

As far as we are aware, this is the first report of this substance being isolated from *S. palghatense* bark, which offers important new information on the pharmacological and phytochemical potential of this uncommon species. These comprehensive investigations will open the door for this naturally occurring molecule to potentially be translated into potent therapeutic agents for the treatment of conditions linked to oxidative stress, infectious illnesses, diabetes, inflammation, parasite infections, and even cancer. In conclusion, this work demonstrates the considerable pharmacological promise of *S. palghatense* as a useful source of new plant-based medicinal chemicals and establishes a solid scientific basis for future drug development efforts utilizing 2-Phenyl-4H-chromen-4-one.

9

MOLECULAR DOCKING AND DYNAMICS OF PHYTOCOMPOUNDS AGAINST KEY TARGETS



CHAPTER 9

MOLECULAR DOCKING AND DYNAMICS OF PHYTOCOMPOUNDS AGAINST KEY TARGETS

9.1. Introduction

Throughout history, researchers have always looked at substances from nature for potential new avenues for pharmaceutical development (Yaacob et al., 2010; Sindhu et al., 2011). Essential nutrients and functionally useful substances are abundant in plants. The phytochemical components have great promise for the treatment of human and plant ailments (Ralte et al., 2022). The utilization of molecular modeling tools for predicting a protein's interactions with tiny molecules (ligands) is known as molecular docking (Roy & Paul, 2010). The binding process may be investigated using molecular docking, and the activity of chemicals obtained from plants can be correlated with the docking score (Sindhu et al., 2011). Effective lead identification requires the establishment of a computational chemical library (Glick & Jacoby, 2011). Drug development trends nowadays center on understanding disease processes, then identifying targets and finding lead compounds. Chemoinformatic methods, which facilitate the integration of information at several levels to improve the dependability of data results, provide enormous promise to revolutionize in silico drug design and discovery (Katsila et al., 2016). A computer-generated three-dimensional structure of tiny ligands may be positioned into a receptor structure via molecular docking in a number of different orientations, conformations, and locations. This approach offers knowledge about molecular recognition and is helpful in medicinal chemistry and drug development. Docking is now a crucial component of CADDD, or computer-aided drug design and discovery (Jakhar et al., 2020).

Finding bioactive compounds is a lengthy and expensive endeavor, and new approaches are continually sought to streamline the process. One of the more recent approaches that has been investigated for the discovery of potential bioactive

compounds is virtual screening (VS) (da Silva Rocha et al., 2019). It is one important step in the drug design and development process. VS is usually thought of as the process of employing computational techniques to pick promising drug candidates from vast libraries of chemical structures (Sousa et al., 2010). In the early stages of drug and probe development, structure-based docking screens using large chemical libraries are becoming typical. Compound libraries have expanded and computer efficiency has increased, making it possible for small computer clusters to screen hundreds of millions or perhaps billions of compounds. As a result, a large chemical space may be quickly and affordably explored and categorized into a subset that is rich in possible hits for a particular target (Bender et al., 2021).

The use of molecular dynamics (MD) simulations in drug discovery and molecular biology has grown significantly in the last several years. The availability of experimental structure data, together with significant advancements in simulating speed, precision, and accessibility, has made biomolecular modeling more attractive to experimentalists. The development and optimization of small molecules, such as peptides and proteins, as well as the understanding of the functional processes of proteins and other biomolecules, have all benefited from the use of simulations (Hollingsworth & Dror, 2018). However, there is information about *Syzygium* species and its medicinal importance, but the data for the computational analysis and docking studies are limited. Therefore, this work provides details on its pharmacokinetic profile, toxicity prediction, and molecular docking to assess the compounds' eligibility for possible development as therapeutic agents.

Oxidative stress plays a critical role in the pathophysiology of numerous chronic diseases, including cancer, neurodegeneration, diabetes, and cardiovascular disorders (Forman & Zhang, 2021). The human body is equipped with an elaborate antioxidant defense system composed of enzymatic and non-enzymatic components that work in concert to mitigate oxidative damage caused by reactive oxygen species (ROS) (Jomova et al., 2023). The enzymatic regulation of oxidative stress plays a critical role in cellular homeostasis. Central to this regulatory network are antioxidant enzymes such as Superoxide Dismutase (SOD1) (Islam et al., 2022), Catalase (CAT)

(Gusti et al., 2021), Glutathione Peroxidase 1 (GPx1) (Pei et al., 2023), the Kelch-like ECH-associated protein 1 (KEAP1) (Guo et al., 2021), and the Thioredoxin (TRX)-Thioredoxin-interacting protein (TXNIP) complex (Qayyum et al., 2021). These proteins function in concert to neutralize reactive oxygen species (ROS), thereby maintaining redox balance and protecting cellular components from oxidative damage.

SOD1 catalyzes the dismutation of superoxide radicals into hydrogen peroxide, which is subsequently decomposed by CAT into water and molecular oxygen. GPx1 facilitates the reduction of hydrogen peroxide and organic hydroperoxides using glutathione as a cofactor, supporting intracellular detoxification. KEAP1, through its interaction with NRF2, modulates the transcriptional activation of antioxidant response elements, acting as a key regulator of oxidative stress signaling. The TRX-TXNIP complex is involved in redox control and has been implicated in oxidative damage-related cellular responses through modulation of thiol-disulfide exchange reactions. Phytochemicals of plant origin are known to possess diverse redox-modulating properties, making them attractive candidates for therapeutic targeting of oxidative stress pathways. In the present study, a structure-based virtual screening approach was employed to identify phytocompounds with binding potential against five key antioxidant enzymes: SOD1, CAT, GPx1, KEAP1, and the TRX-TXNIP complex. Molecular docking, pharmacokinetic prediction, and toxicity assessment were used to evaluate the suitability of selected natural compounds for further investigation as redox-targeted therapeutic agents (Lu & Holmgren, 2014).

Antimicrobial resistance (AMR) has emerged as a pressing global health concern, undermining the effectiveness of conventional antibiotics and complicating the management of infectious diseases (Tang et al., 2023). Pathogenic bacteria employ diverse molecular strategies to withstand antimicrobial pressure, including the alteration of cell wall biosynthesis, modulation of quorum-sensing pathways, and the establishment of biofilms that protect against host defenses and therapeutic agents.

Targeting the essential bacterial proteins governing these processes offers a promising avenue for novel drug discovery (Okeke et al., 2024).

D-Alanine–D-Alanine ligase (DDLA) is a key enzyme in bacterial peptidoglycan biosynthesis, catalyzing the ATP-dependent formation of the D-Ala–D-Ala dipeptide, which serves as a critical building block for cell wall crosslinking (Nocentini, 2024). Inhibiting this enzyme compromises cell wall integrity, leading to bacterial death. In *Pseudomonas aeruginosa*, quorum sensing is mediated through regulators such as LasR (Crémet et al., 2021) and RhlR (Asfahl et al., 2022), which respond to specific autoinducers to control virulence gene expression, biofilm formation, and pathogenicity. The PqsR (MvfR) regulator (Sabir et al., 2021), operating within a parallel quorum-sensing pathway, governs the production of quinolone signaling molecules, further modulating virulence and persistence. Penicillin-binding protein 3 (PBP3), a transpeptidase critical for septum formation during cell division (Long et al., 2025), catalyzes the crosslinking of peptidoglycan strands, making it a major target of β-lactam antibiotics.

Phytochemicals derived from medicinal plants have demonstrated the capacity to inhibit bacterial enzymes, disrupt quorum-sensing networks, and interfere with cell wall synthesis. Their structural diversity and multi-target potential position them as attractive candidates for the development of novel anti-infective agents capable of counteracting resistance mechanisms. In this study, a structure-based virtual screening strategy was applied to evaluate the binding potential of selected phytocompounds against five critical antimicrobial targets: DDLA ligase, LasR, PqsR (MvfR), PBP3, and RhlR. Computational docking, pharmacokinetic profiling, and toxicity prediction were conducted to identify natural compounds with favourable drug-like properties for subsequent *in vitro* and *in vivo* validation.

Helminth infections are a significant global health concern, particularly in tropical and subtropical regions, contributing to chronic morbidity, malnutrition, and impaired cognitive and physical development. These parasitic diseases, caused by nematodes, trematodes, and cestodes, persist through complex life cycles and sophisticated immune evasion mechanisms (Arrais et al., 2022). The pathophysiology

of helminthiasis involves host–parasite interactions that disrupt normal physiological processes, leading to tissue damage, metabolic stress, anaemia, and inflammation. Resistance to conventional anthelmintic drugs, combined with their potential adverse effects, underscores the urgent need for novel, safe, and effective therapeutic strategies (Loukas et al., 2021).

The survival and pathogenicity of helminths depend on a highly coordinated network of metabolic enzymes and stress-response proteins that sustain their energy production, structural stability, and defense against host immune responses. Among the most promising therapeutic targets are ATP synthase (Carvalho-Kelly et al., 2022), Cytochrome c oxidase (Monteiro et al., 2025), Heat Shock Protein 70 **(**Alipour et al., 2024), NADH-ubiquinone oxidoreductase (Reed & Smith, 2024), and Extracellular Globin-3/Erythrocruorin (David et al., 2021). ATP synthase subunit a and NADH-ubiquinone oxidoreductase are critical components of the mitochondrial oxidative phosphorylation pathway, essential for ATP generation and parasite viability. Cytochrome c oxidase subunit 1 plays a central role in the electron transport chain, facilitating oxygen reduction and energy conversion. HSP70 is a molecular chaperone that safeguards parasite proteins under stress conditions, promoting survival within the hostile host environment. Extracellular globins, such as erythrocruorin, are specialized oxygen-binding proteins that enable parasites to thrive in low-oxygen niches within the host.

Bioactive phytochemicals from medicinal plants have emerged as promising candidates for targeting these vital parasitic proteins, owing to their structural diversity, multitarget activity, and reduced toxicity compared to synthetic drugs. In this study, a structure-based virtual screening approach was employed to identify phytocompounds with inhibitory potential against these five key anti-helminthic targets. Molecular docking was integrated with pharmacokinetic profiling and toxicity prediction to evaluate the drug-likeness, therapeutic potential, and safety profiles of the selected candidates, aiming to advance the development of plant-derived anthelmintic agents.

Inflammation is a complex biological response that serves as a protective mechanism against infection, injury, and other harmful stimuli **(**Yeung et al., 2018). While acute inflammation is essential for tissue repair and host defense, chronic or dysregulated inflammation contributes to the pathogenesis of numerous disorders, including autoimmune diseases, cancer, neurodegeneration, and cardiovascular conditions (Mendes et al., 2018). The inflammatory cascade is mediated by a network of signaling molecules and enzymes that regulate the production of cytokines, chemokines, and reactive mediators, ultimately influencing immune cell recruitment, proliferation, and survival (Rajendran et al., 2018).

Among the central regulators of inflammation are transcription factors, cytokines, and enzymatic mediators such as Nuclear Factor kappa B (NF-κB) p50 (Alharbi et al., 2021), Tumor Necrosis Factor-alpha (TNF-α) (Jang et al., 2021), Human Inducible Nitric Oxide Synthase (iNOS) (Cinelli et al., 2020), Janus Kinase 2 (JAK2) (Purohit et al., 2023), and Human Cyclooxygenase-2 (COX-2) (Ferrer et al., 2019). These proteins play pivotal roles in inflammatory signaling pathways, making them critical therapeutic targets. NF-κB p50 functions as a transcriptional regulator, modulating the expression of genes involved in immune and inflammatory responses. TNF-α is a pro-inflammatory cytokine that triggers apoptosis, immune cell activation, and the release of other inflammatory mediators. iNOS catalyzes the production of nitric oxide, a reactive nitrogen species with both antimicrobial and pro-inflammatory effects. JAK2 acts as a key kinase in the JAK-STAT signaling pathway, mediating cytokine receptor signaling and immune regulation. COX-2 catalyzes the conversion of arachidonic acid to prostaglandins, which are potent lipid mediators involved in pain, fever, and inflammation.

Natural phytochemicals have been widely recognized for their anti-inflammatory potential, acting through diverse mechanisms including the inhibition of pro-inflammatory mediators, modulation of signaling pathways, and suppression of oxidative stress-linked inflammation (Andrade & Valentão, 2018). In the present study, a structure-based virtual screening approach was employed to identify phytocompounds with strong binding potential against five key anti-inflammatory

proteins: NF-κB p50, TNF-α, iNOS, JAK2, and COX-2. Molecular docking, pharmacokinetic prediction, and toxicity assessment were performed to evaluate the suitability of selected natural compounds for potential therapeutic development targeting chronic inflammation.

Diabetes mellitus is a chronic metabolic disorder characterized by persistent hyperglycemia resulting from impaired insulin secretion, insulin action, or both. The long–term complications of diabetes affect multiple organ systems, leading to cardiovascular disease, neuropathy, nephropathy, and retinopathy (Tomic et al., 2022). The pathophysiology of diabetes involves a complex interplay of hormonal imbalances, metabolic dysregulation, oxidative stress, and inflammation. In particular, insulin resistance and defective glucose metabolism are central to disease progression and therapeutic failure (Antar et al., 2023). Over the past decades, attention has increasingly turned to molecular targets involved in glycemic control for the development of more effective and safer antidiabetic therapies (Abel et al., 2024).

The human body relies on a tightly regulated network of enzymes and signaling proteins to modulate glucose homeostasis. Among the most promising therapeutic targets are Dipeptidyl Peptidase 4 (DPP4) (Shao et al., 2024), Insulin Receptor (IR) (Bao et al., 2021), Pancreatic Alpha–Amylase (PAA) (Kaur et al., 2021), Peroxisome Proliferator–Activated Receptor Gamma (PPARG) (Mohajan & Mohajan, 2024), and Protein Tyrosine Phosphatase 1B (PTP1B) (Teimouri et al., 2022). These proteins play pivotal roles in insulin signaling, glucose absorption, and lipid metabolism. DPP4 is an exopeptidase that degrades incretin hormones such as GLP–1, thereby influencing insulin secretion and postprandial glucose regulation. The insulin receptor ectodomain facilitates the binding of insulin and subsequent activation of downstream pathways essential for glucose uptake. Pancreatic alpha–amylase is a digestive enzyme responsible for the breakdown of dietary starch into glucose; its inhibition is a validated strategy for managing postprandial hyperglycemia. PPARG is a nuclear receptor involved in adipocyte differentiation and insulin sensitization, while PTP1B negatively regulates insulin receptor signaling and is thus a major contributor to insulin resistance (Saltiel & Kahn, 2001).

Phytochemicals derived from medicinal plants have attracted significant interest due to their multi–targeted mechanisms, minimal side effects, and potential to modulate key proteins implicated in diabetes pathogenesis (Aravindakshan et al., 2024). In the present study, a structure–based virtual screening strategy was employed to identify bioactive phytocompounds with inhibitory potential against five major antidiabetic targets: DPP4, IR, PPA, PPARG, and PTP1B. Molecular docking, pharmacokinetic profiling, and toxicity prediction were carried out to evaluate the drug–likeness and therapeutic suitability of selected compounds as candidate agents for diabetes management.

Cancer is a multifactorial disease characterized by uncontrolled cell proliferation, evasion of apoptosis, sustained angiogenesis, and metastatic potential. The initiation and progression of cancer are driven by a complex interplay of genetic mutations, dysregulated signaling pathways, and altered cellular metabolism (Soerjomataram & Bray, 2021). While conventional therapies such as chemotherapy, radiotherapy, and targeted agents have improved patient outcomes, drug resistance, toxicity, and tumour recurrence remain significant clinical challenges (Ferlay et al., 2021). Several key proteins act as central regulators in cancer development and progression, making them critical therapeutic targets. These include AKT1**,** Epidermal Growth Factor Receptor (EGFR)**,** Kirsten Rat Sarcoma Viral Oncogene Homolog (KRAS)**,** Mitogen-Activated Protein Kinase 1 (MAPK1)**,** and Tumour Protein p53**.**

AKT1 is a serine/threonine kinase involved in cell survival, growth, and metabolism, with hyperactivation linked to tumour proliferation and resistance to apoptosis (George et al., 2022). EGFR is a receptor tyrosine kinase that regulates cell division and survival through downstream pathways, including PI3K-AKT and RAS-RAF-MAPK, with mutations and overexpression contributing to multiple cancer types (Wang et al., 2022). KRAS is a small GTP-binding protein that acts as a molecular switch in cell signaling, with oncogenic mutations driving uncontrolled proliferation and therapeutic resistance (Singhal et al., 2024). MAPK1 (ERK2) functions in the MAPK/ERK signaling cascade, promoting cell cycle progression and

differentiation, while aberrant activation supports tumorigenesis (Wang et al., 2023). p53 is a pivotal tumour suppressor that governs DNA repair, cell cycle arrest, and apoptosis; its inactivation is one of the most common events in human cancers (Hassin & Oren, 2023).

Natural phytochemicals are increasingly recognized for their anticancer potential, acting through diverse mechanisms such as inhibition of oncogenic signaling, induction of apoptosis, suppression of metastasis, and modulation of the tumour microenvironment (Ang et al., 2023; Castañeda et al., 2022). In the present study, a structure-based virtual screening approach was undertaken to identify phytocompounds with strong binding potential against five key anti-cancer proteins, AKT1, EGFR, KRAS, MAPK1, and p53. Molecular docking, pharmacokinetic profiling, and toxicity prediction were performed to evaluate the suitability of these compounds for potential development as anticancer agents.

❖ **Objectives**

- To retrieve and prepare the three-dimensional crystal structures of five key antioxidant-related target proteins (SOD1, Catalase, GPx1, KEAP1, and the TRX–TXNIP complex), antimicrobial-related proteins (D-alanyl-D-alanine ligase, LasR, PqsR (MvfR), PBP3, and RhlR), anthelminthic target proteins (ATP synthase subunit a, Cytochrome c oxidase, Heat Shock Protein, NADH-ubiquinone oxidoreductase, and Extracellular Globin-3/Erythrocruorin), anti-inflammatory target proteins (NF-κB p50, TNF-α, iNOS, JAK2, and COX-2), antidiabetic target proteins, (Dipeptidyl Peptidase 4 (DPP4), Insulin Receptor (IR), Pancreatic Alpha–Amylase (PAA), Peroxisome Proliferator–Activated Receptor Gamma (PPARG), and Protein Tyrosine Phosphatase 1B (PTP1B)), and anti-cancer target proteins (AKT1, EGFR, KRAS, MAPK1, and p53) for molecular docking analysis.
- To evaluate the binding affinity and molecular interaction profiles of selected phytocompounds with the aforementioned antioxidant, antimicrobial,

anthelmintic, anti-inflammatory, antidiabetic, and anticancer targets using structure-based molecular docking approaches.

- To assess the pharmacokinetic attributes of the top-performing compounds via *in silico* ADMET (Absorption, Distribution, Metabolism, Excretion, and Toxicity) profiling tools.
- To predict the toxicity potential of the shortlisted phytocompounds using computational toxicity models to determine their safety profiles.
- To identify and recommend promising natural compounds with potential antioxidant, antimicrobial, anthelmintic, anti-inflammatory, antidiabetic, anticancer, and redox-modulating activity for *in vitro* and *in vivo* validation studies.

9.2. Materials and Methods

9.2.1. Selection and preparation of target proteins

S. palghatense leaf and bark phytochemicals and compounds isolated from the *S. palghatense* bark were selected for the study. Methanolic extract consistently showed the highest activity across all bioassays. Bark exhibits higher activity in both *in vitro* and *in vivo* studies, except for anthelmintic activity. Molecular docking was not performed on silver nanoparticles, as silver acts as a metallic carrier and lacks discrete ligand-receptor interaction mechanisms typical of organic phytochemicals. Docking studies are more appropriate for structurally defined small molecules, not for metallic NPs, which exhibit bulk interaction rather than site-specific binding.

9.2.1.1. Antioxidant target proteins

Five therapeutically relevant antioxidant-related protein targets (SOD1, Catalase, GPx1, KEAP1, and the TRX–TXNIP complex) were selected for structural and functional evaluation (Table 9.1).

9.2.1.2. Antimicrobial target proteins

Five molecular targets with established roles in bacterial survival, virulence regulation, and antimicrobial resistance were selected (D-alanyl-D-alanine ligase, LasR, PqsR (MvfR), PBP3, and RhlR) for structural and functional evaluation (Table 9.2).

9.2.1.3. Anthelmintic target proteins

Five therapeutically significant protein targets associated with helminth survival and pathogenicity were selected ATP synthase subunit a, Cytochrome c Oxidase, Heat Shock Protein, NADH-ubiquinone oxidoreductase, and Extracellular Globin-3/Erythrocruorin) for structural and functional analysis (Table 9.3).

9.2.1.4. Anti-inflammatory target proteins

Five protein targets of established therapeutic significance in inflammation (NF-κB p50, TNF-α, iNOS, JAK2, and COX-2) were chosen for structural and functional assessment (Table 9.4).

9.2.1.5.Antidiabetic target proteins

Five therapeutically relevant protein targets implicated in type 2 diabetes mellitus were selected (Dipeptidyl Peptidase 4 (DPP4), Insulin Receptor (IR), Pancreatic Alpha–Amylase (PAA), Peroxisome Proliferator–Activated Receptor Gamma (PPARG), and Protein Tyrosine Phosphatase 1B (PTP1B)), for structural and functional evaluation (Table 9.5).

9.2.1.6. Anticancer target proteins

Five protein targets of recognized therapeutic relevance in cancer biology were selected (AKT1, EGFR, KRAS, MAPK1, and p53) for structural and functional evaluation (Table 9.6).

The three-dimensional (3D) structures of these proteins were retrieved from the RCSB Protein Data Bank (PDB) in .pdb format using their respective PDB IDs. High-resolution crystal structures with complete or near-complete chain data were prioritized for selection. All the protein structures were obtained from the RCSB Protein Data Bank as high-resolution X-ray crystallography models with minimal missing residues. Prior to computational analysis, each structure was refined by removing crystallographic water molecules, co-crystallized ligands, and heteroatoms using molecular visualization tools such as PyMOL and BIOVIA Discovery Studio. This preprocessing ensured that only the polypeptide backbone and relevant structural features were retained, enabling uniform preparation and compatibility across all molecular docking workflows (Burley et al., 2022).

9.2.2. Physicochemical property prediction using ProtParam

Physicochemical properties provide fundamental insights into the biochemical behaviour of proteins, including their solubility, stability, charge, molecular weight, isoelectric point (pI), and hydrophobicity, which are essential for understanding their biological function and druggability. The ProtParam tool, part of the ExPASy Bioinformatics Resource Portal, allows *in silico* computation of these parameters from the primary amino acid sequence of a protein (Azimi et al., 2024).

Table 9.1: Overview of selected proteins for antioxidant *in silico* analysis

Proteins	Abbreviations	PDB ID	Method	Resolution (Å)	PDB DOI
Human Cu, Zn Superoxide Dismutase	SOD1	1PU0	X-ray diffraction	1.70	10.2210/pdb1PU0/pdb
Human Erythrocyte Catalase	CAT	1DGB	X-ray diffraction	2.20	10.2210/pdb1DGB/pdb
Human Glutathione Peroxidase 1	GPx1	2F8A	X-ray diffraction	1.50	10.2210/pdb2F8A/pdb
KEAP1 Kelch Domain	KEAP1 Kelch	4L7B	X-ray diffraction	2.41	10.2210/pdb4L7B/pdb
Thioredoxin and TXNIP Complex	Trx-TXNIP	4LL1	X-ray diffraction	2.00	10.2210/pdb4LL1/pdb

Table 9.2: Overview of selected proteins for antimicrobial *in silico* analysis

Proteins	Abbreviation	PDB ID	Method	Resolution (Å)	PDB DOI
D-alanyl-D-alanine ligase (D-ALA:D-ALA Ligase)	Ddl	1IOV	X-ray Diffraction	2.20	https://doi.org/10.2210/pdb1IOV/pdb
LasR ligand-binding domain	LasR	2UV0	X-ray Diffraction	1.80	https://doi.org/10.2210/pdb2UV0/pdb
PqsR coinducer-binding domain	PqsR (MvfR)	4JVD	X-ray Diffraction	2.95	https://doi.org/10.2210/pdb4JVD/pdb
Penicillin-Binding Protein 3	PBP3	3OC2	X-ray Diffraction	1.97	https://doi.org/10.2210/pdb3OC2/pdb
Regulatory protein RhlR	RhlR	-	-	93.87 (Plddt)	-

Table 9.3: Overview of selected proteins for anthelmintic *in silico* analysis

Proteins	Abbreviations	predicted Local Distance Difference (pLDDT)
ATP synthase subunit a	ATP synthase	81
Cytochrome c Oxidase subunit 1	COX1	97.19
Heat Shock Protein 70	HSP70	91.12
NADH-Ubiquinone Oxidoreductase chain 1	Complex I	89.36
Extracellular Globin-3 /Erythrocruorin	Ext. Globin-3	89.93

Table 9.4: Overview of selected proteins for anti-inflammatory *in silico* analysis

Proteins	Abbreviations	PDB ID	Method	Resolution (Å)	PDB DOI
Nuclear Factor kappa B p50	NF-κB p50	1SVC	X-Ray Diffraction	2.60 Å	https://doi.org/10.2210/pdb1SVC/pdb
Tumour Necrosis Factor-alpha	TNF-α	2AZ5	X-Ray Diffraction	2.10 Å	https://doi.org/10.2210/pdb2AZ5/pdb
Human Inducible Nitric Oxide Synthase	iNOS	4NOS	X-Ray Diffraction	2.25 Å	https://doi.org/10.2210/pdb4NOS/pdb
Janus Kinase 2	JAK2	2B7A	X-Ray Diffraction	2.00 Å	https://doi.org/10.2210/pdb2B7A/pdb
Human Cyclooxygenase-2	COX-2	5IKR	X-Ray Diffraction	2.34 Å	https://doi.org/10.2210/pdb5IKR/pdb

Table 9.5: Overview of selected proteins for anti-diabetic *in silico* analysis

Proteins	Abbreviation	PDB ID	Method	Resolution (Å)	DOI / Link
Dipeptidyl Peptidase 4	DPP4	5YRK	X-Ray Diffraction	2.51 Å	https://doi.org/10.1016/j.bbrc.2017.10.101
Insulin Receptor Ectodomain	IR	7QID	Cryo-Electron Microscopy	5.00 Å	https://doi.org/10.1083/jcb.201907210
Pancreatic Alpha-Amylase	PAA	6Z8L	X-Ray Diffraction	1.40 Å	https://doi.org/10.1039/d0sc04297h
Peroxisome Proliferator-Activated Receptor Gamma	PPARG	9F7X	X-Ray Diffraction	1.63 Å	https://doi.org/10.3390/biom14060640
Protein Tyrosine Phosphatase 1B	PTP1B	8SKL	X-Ray Diffraction	1.55 Å	https://doi.org/10.1038/s41467-023-40170-8

Table 9.6: Overview of selected proteins for anticancer *in silico* analysis

Protein Name	Abbreviation	PDB ID	Method	Resolution	PDB DOI
AKT serine/threonine kinase	AKT1	6NPZ	X-Ray Diffraction	2.12 Å	https://doi.org/10.2210/pdb6NPZ/pdb
Epidermal Growth Factor Receptor	EGFR	8TJL	X-Ray Diffraction	2.70 Å	https://doi.org/10.2210/pdb8TJL/pdb
Kirsten Rat Sarcoma Viral Oncogene Homolog	KRAS	6GJ8	X-Ray Diffraction	1.65 Å	https://doi.org/10.2210/pdb6GJ8/pdb
Mitogen-Activated Protein Kinase 1	MAPK1	8ZJV	X-Ray Diffraction	1.80 Å	https://doi.org/10.2210/pdb8ZJV/pdb
Tumour Protein p53	TP53	8WD2	X-Ray Diffraction	1.85 Å	https://doi.org/10.2210/pdb8WD2/pdb

ProtParam calculates these properties based on established experimental formulae such as:

- **Molecular weight**: Sum of the average isotopic masses of amino acid residues and water.
- **Theoretical pI**: Calculated using the Bjellqvist method, based on pKa values of ionizable groups.
- **Instability Index**: Predicts protein stability under *in vitro* conditions; a value >40 suggests instability.
- **Aliphatic Index**: Reflects thermal stability based on aliphatic side chains (Ala, Val, Ile, Leu).
- **GRAVY (Grand Average of Hydropathicity)**: Indicates solubility; negative values denote hydrophilicity.
- **Extinction Coefficient**: Used to estimate protein concentration in solution, based on aromatic residues (Trp, Tyr, Cys).

Methodology: The amino acid sequence of each protein was retrieved from the corresponding .pdb file or UniProtKB entry. The sequence was submitted to the ProtParam server. Parameters, including molecular weight, theoretical pI, amino acid composition, atomic composition, instability index, aliphatic index, GRAVY score, and extinction coefficient, were computed. The results were then recorded for comparative interpretation across all five target proteins for each biological activity.

9.2.3. Secondary structure prediction using Prosite

Accurate prediction and quantification of secondary structure elements provide a structural basis for understanding enzyme mechanisms, binding specificity, and drug interaction sites (Alsulaimany, 2023). The Prosite server interprets secondary structure from 3D coordinates using DSSP–like algorithms. These algorithms classify each residue into one of several structural motifs based on hydrogen bonding patterns and geometric constraints.

Methodology:

- The .pdb structures of each protein were uploaded to the server
- Secondary structure assignments were computed, reporting the number and type of:
    - Sheets
    - β–Hairpins
    - β–Bulges
    - Strands
    - Helices
    - Helix–Helix Interactions
    - Turns (β–turns and γ–turns)
- The data were interpreted to determine the dominant structural class (e.g., α–helical, β–rich, or mixed α/β) of each protein.

9.2.4. Ramachandran plot analysis using PROCHECK

To evaluate the stereochemical quality of each protein model, Ramachandran plot analysis was performed using the PROCHECK server, developed by EMBL–EBI. The Ramachandran plot is a well–established method to assess the backbone dihedral angles, phi (ϕ) and psi (ψ), of amino acid residues in a protein structure. It categorizes each residue based on its angular positioning into most favoured, additionally allowed, generously allowed, or disallowed regions. High percentages of residues within the most favoured and allowed regions indicate that the protein adopts a physically and sterically plausible conformation, consistent with energetically stable secondary structures (Bhardwaj et al., 2024). Each .pdb file was submitted individually to the PROCHECK server, which automatically parses the protein backbone and generates a detailed Ramachandran plot. Models with residues in

disallowed regions were closely examined to ensure these deviations were not within active sites or structurally conserved motifs (Bhardwaj et al., 2024).

Methodology:

The refined .pdb files of each target protein were submitted to the PROCHECK server. Ramachandran plots were generated for each protein, showing:

- Most favoured regions (A, B, L),
- Additionally allowed regions (a, b, l, p),
- Generously allowed regions, and
- Disallowed regions.

The percentage of residues in each region was recorded. Additional metrics such as G–factors for dihedral angles and bond geometry were collected to evaluate model accuracy. Any residue falling in disallowed regions was manually inspected for structural anomalies.

9.2.5. Retrieval of bark phytocompounds

The phytocompounds present in the bark were identified through GC–MS and LC–MS QTOF analysis and confirmed through a literature review. They were subsequently retrieved from the PubChem database, a freely accessible chemical information resource maintained by the National Centre for Biotechnology Information (NCBI) and the National Institutes of Health (NIH). PubChem hosts a comprehensive repository of chemical structures, identifiers, physicochemical properties, biological activities, toxicity profiles, and safety data for both small molecules and complex macromolecules (Kim et al., 2022). Each selected compound was located in the database using its name or PubChem Compound Identifier (CID). The corresponding 3D structures in Structure Data File (SDF) format were downloaded for computational analysis. The retrieved structures were used as the starting point for subsequent molecular docking, pharmacokinetic profiling, and toxicity prediction workflows. This ensured the use of standardized, validated

molecular information for all computational experiments. Out of 37 phytocompounds identified from the bark. Top 5 phytocompounds based on the docking score selected for further analysis.

9.2.6. Docking with PyRx

Molecular docking simulations were conducted to re-evaluate the binding potential of selected phytocompounds against five human antioxidant-related protein targets: Cu, Zn Superoxide Dismutase (SOD1, PDB ID: 1PU0)**,** Erythrocyte Catalase (CAT, PDB ID: 1DGB)**,** Glutathione Peroxidase 1 (GPx1, PDB ID: 2F8A)**,** KEAP1 Kelch Domain (PDB ID: 4L7B)**,** and the Thioredoxin–TXNIP Complex (PDB ID: 4LL1)**,** five antimicrobial protein targets: D-Alanine–D-Alanine Ligase (DDLA Ligase/Ddl), LasR ligand-binding domain, PqsR coinducer-binding domain (PqsR/MvfR), Penicillin-Binding Protein 3 (PBP3), and Regulatory Protein (RhlR), five therapeutically relevant anthelminthic protein targets: ATP synthase subunit a (UniProt ID: Q34946), Cytochrome c Oxidase (UniProt ID: A0A0N9H6J3), Heat Shock Protein 70 (HSP70; UniProt ID: B9TY08), NADH-Ubiquinone Oxidoreductase (UniProt ID: Q37546), and Extracellular Globin-3/Erythrocruorin (UniProt ID: P11069), five key human anti-inflammatory protein targets: 0Nuclear Factor kappa B p50 (PDB ID: 1SVC), Tumour Necrosis Factor-alpha (PDB ID: 2AZ5), Human Inducible Nitric Oxide Synthase (PDB ID: 4NOS), Janus Kinase 2 (PDB ID: 2B7A), and Human Cyclooxygenase-2 (PDB ID: 5IKR), five human antidiabetic protein targets: Dipeptidyl Peptidase 4 (PDB ID: 5Y7K), Insulin Receptor Ectodomain (PDB ID: 7QID), Pancreatic Alpha–Amylase (PDB ID: 6Z8L), Peroxisome Proliferator–Activated Receptor Gamma (PDB ID: 9F7X), and Protein Tyrosine Phosphatase 1B (PDB ID: 8SKL), and five key human anti-cancer protein targets: AKT1 (PDB ID: 6NPZ), Epidermal Growth Factor Receptor – EGFR (PDB ID: 8TJL), Kirsten Rat Sarcoma Viral Oncogene Homolog – KRAS (PDB ID: 6GJ8), Mitogen-Activated Protein Kinase 1 – MAPK1 (PDB ID: 8ZJV), and Tumour Protein p53 (PDB ID: 8WD2) (Tables 9.7-9.12).

The docking protocol was executed using PyRx 0.9, which integrates AutoDock Vina 2.0, to refine and validate binding poses and estimate binding free

Table 9.7: Molecular docking grid coordinates and box dimensions of antioxidant target proteins

Protein	PDB ID	Centre			Dimensions		
		X	Y	Z	X	Y	Z
Human Cu, Zn Superoxide Dismutase	1PU0	57.91	43.50	16.76	34.25	44.59	42.30
Human Erythrocyte Catalase	1DGB	20.92	39.36	63.06	73.12	86.58	75.80
Human Glutathione Peroxidase 1	2F8A	4.68	16.27	28.88	47.31	36.15	47.56
KEAP1 Kelch Domain	4L7B	9.59	-16.41	-11.91	49.90	47.14	51.95
Thioredoxin and TXNIP Complex	4LL1	-39.86	-0.12	31.81	91.45	42.89	88.40

Table 9.8: Molecular docking grid coordinates and box dimensions of antimicrobial target proteins

Protein	PDB ID	Centre			Dimensions		
		X	Y	Z	X	Y	Z
D-alanyl-D-alanine ligase (D-ALA:D-ALA Ligase)	1IOV	13.96	6.40	44.98	42.92	55.02	55.10
LasR ligand-binding domain	2UV0	51.81	9.92	69.04	35.27	44.52	50.01
PqsR coinducer-binding domain	4JVD	-27.14	64.36	9.92	48.28	44.89	47.71
Penicillin-Binding Protein 3	3OC2	5.80	20.55	2.24	53.06	67.20	96.34
Prepared Regulatory protein RhIR	-	0.89	2.51	1.50	57.41	50.84	61.20

Table 9.9: Molecular docking grid coordinates and box dimensions of anthelmintic target proteins

Protein	PDB ID	Centre			Dimensions		
		X	Y	Z	X	Y	Z
ATP synthase subunit a	Q34946	-2.38	0.65	0.41	62.19	68.28	67.56
Cytochrome c Oxidase subunit 1	A0A0N9H6J3	0.3	-0	0.18	56.22	42.89	64.74
Heat Shock Protein 70	B9TY08	-0	0.81	1.35	58.86	33.07	54.91
NADH-Ubiquinone Oxidoreductase chain 1	Q37546	-2.90	3.6	0.31	58.55	49.02	62.63
Extracellular Globin-3/Erythrocruorin	P11069	-1.02	-0.73	1.12	42.78	36.66	41.00

Table 9.10: Molecular docking grid coordinates and box dimensions of anti-inflammatory target proteins

Protein	PDB ID	Centre			Dimensions		
		X	Y	Z	X	Y	Z
Nuclear Factor kappa B p50	1SVC	42.46	14.65	38.04	70.86	61.52	55.72
Tumour Necrosis Factor-alpha	2AZ5	-26.53	65.90	41.94	43.69	41.01	36.67
Human Inducible Nitric Oxide Synthase	4NOS	-2.15	94.73	17.16	57.28	70.45	47.77
Janus Kinase 2	2B7A	108.76	68.97	0.42	60.91	55.49	52.52
Human Cyclooxygenase-2	5IKR	31.88	6.84	58.94	75.95	60.13	63.92

Table 9.11: Molecular docking grid coordinates and box dimensions of antidiabetic target proteins

Proteins	PDB ID	Centre			Dimensions		
		X	Y	Z	X	Y	Z
Dipeptidyl Peptidase 4	5Y7K	43.88	-13.84	53.52	75.58	78.17	77.31
Insulin Receptor Ectodomain	7QID	176.44	167.19	130.53	98.76	69.74	70.22
Pancreatic Alpha-Amylase	6Z8L	-8.16	21.24	-18.87	55.43	73.30	54.57
Peroxisome Proliferator-Activated Receptor Gamma	9F7X	7.23	8.51	17.08	42.21	47.86	65.03
Protein Tyrosine Phosphatase 1B	8SKL	-36.82	29.91	-14.99	52.91	58.29	41.96

Table 9.12: Molecular docking grid coordinates and box dimensions of anticancer target proteins

Protein	PDB ID	Centre			Dimensions		
		X	Y	Z	X	Y	Z
AKT serine/threonine kinase	6NPZ	-25.22	0.38	24.44	48.32	48.40	63.75
Epidermal Growth Factor Receptor	8TJL	58.56	-8.09	25.21	46.96	65.20	54.70
Kirsten Rat Sarcoma Viral Oncogene	6GJ8	16.52	16.56	-5.16	43.44	43.47	41.34
Mitogen-Activated Protein Kinase 1	8ZJV	-35.34	12.11	2.22	67.97	52.05	44.92
Tumour Protein p53	8WD2	-0.66	14.64	22.92	40.24	46.09	50.35

energies for the ligands. From the initial virtual screening, the top five phytocompounds exhibiting the highest binding affinities for each protein were shortlisted for docking. Protein and ligand structures were prepared in PDBQT format by adding polar hydrogens, calculating Gasteiger charges, and assigning torsional flexibility to ligands, ensuring compatibility with Vina. A blind docking approach was employed, enabling ligands to explore the complete protein surface rather than being restricted to predefined active sites. This approach facilitated the identification of both orthosteric and potential allosteric binding sites (Kondapuram et al., 2021). Docking outputs were ranked by binding free energy (kcal/mol), and the top–scoring conformations were selected for post–docking analysis. The protein–ligand complexes were visualized and analyzed using BIOVIA Discovery Studio Visualizer to identify hydrogen bonds, hydrophobic interactions, and π–interactions critical for molecular stabilization within the binding site (Ayodele et al., 2023).

9.2.7. Visualization

Following the completion of molecular docking, the resulting receptor–ligand complexes were analyzed for their interaction profiles and spatial orientations using BIOVIA Discovery Studio Visualizer. This software provides a comprehensive platform for visualizing atomic–level interactions, including hydrogen bonds, π–π stacking, hydrophobic associations, and salt bridge formations. The top–ranked binding conformations for each ligand were imported to evaluate their fit within the protein's binding pocket. Emphasis was placed on identifying and examining the key amino acid residues responsible for stabilizing the ligand–protein complex (Ayodele et al., 2023).

9.2.8. Post-docking analysis

To further characterize the molecular interactions between protein targets and their respective ligands, the Protein–Ligand Interaction Profiler (PLIP) was employed. PLIP enables detailed detection of non-covalent interactions within biomolecular complexes, delivering atom-specific insights into binding behaviour. The tool identifies various interaction types, including hydrogen bonds, hydrophobic contacts, π–stacking, and salt bridges, alongside high-quality graphical

representations and machine-readable output formats. For this study, the PLIP web interface was utilized, offering a user-friendly environment ideal for efficient examination of individual complex structures without requiring command-line input (Schake et al., 2025).

9.2.9. Pharmacokinetic profiling of top–hit ligands

To identify phytochemical candidates with optimal pharmacokinetic properties for antioxidant, antimicrobial, anthelmintic, anti-inflammatory, antidiabetic, and anticancer targets intervention, ADME (Absorption, Distribution, Metabolism, and Excretion) profiling was conducted on the top-performing ligands obtained from molecular docking studies against key therapeutic proteins of each biological activity. The SwissADME web server was utilized as the primary computational platform for this evaluation.

SwissADME offers an integrated suite of predictive algorithms that estimate essential pharmacokinetic and physicochemical attributes relevant to drug discovery. Parameters such as lipophilicity (LogP), aqueous solubility, gastrointestinal (GI) absorption potential, and blood–brain barrier (BBB) permeability were assessed. Additionally, the drug–likeness of each compound was evaluated using widely accepted filters, including Lipinski's Rule of Five, Ghose, Veber, Egan, and Muegge criteria (Riyadi et al., 2021). To enhance accuracy, SwissADME also incorporates proprietary models like iLOGP for refined lipophilicity estimation. Each ligand showing high binding affinity with the antioxidant, antimicrobial, anthelmintic, anti-inflammatory, antidiabetic, and anticancer targets was individually subjected to SwissADME analysis. The resulting profiles served to prioritize phytocompounds that not only bind effectively to target proteins but also exhibit pharmacokinetic features conducive to therapeutic efficacy and safety. This integrated approach aids in the early–stage selection of lead compounds with potential for further *in vivo* and clinical validation (Riyadi et al., 2021).

9.2.10. Toxicity profiling

Evaluating the potential toxicity of small molecules is a crucial step in the drug development process. In this study, the ProTox 3.0 web–based platform was employed to predict the toxicological profiles of the top–ranked phytochemicals targeting each biological activity protein. ProTox offers a high–throughput, *in silico* alternative to traditional animal testing methods, significantly accelerating toxicity screening while aligning with ethical guidelines by minimizing *in vivo* experimentation.

ProTox 3.0 integrates advanced computational frameworks, including machine learning algorithms, molecular fragment analysis, chemical similarity measures, and frequent structural feature profiling. The tool comprises 61 independently trained predictive models designed to evaluate a wide spectrum of toxicological endpoints. These include acute toxicity, organ–specific toxicity, toxicity pathways (e.g., Tox21), molecular initiating events, metabolic fate, adverse outcomes, and specific toxicity targets (Banerjee et al., 2024). The acute toxicity of compounds is quantified using the LD_{50} metric (median lethal dose), expressed in mg/kg body weight. This value reflects the estimated dose required to cause mortality in 50% of a test population. Based on LD_{50}, ProTox classifies compounds into six globally harmonized toxicity classes (GHS criteria), as follows:

- **Class I**: Highly toxic or fatal if ingested ($LD_{50} \leq 5$ mg/kg)
- **Class II**: Fatal upon ingestion ($5 < LD_{50} \leq 50$ mg/kg)
- **Class III**: Toxic when swallowed ($50 < LD_{50} \leq 300$ mg/kg)
- **Class IV**: Harmful if ingested ($300 < LD_{50} \leq 2000$ mg/kg)
- **Class V**: Possibly harmful if swallowed ($2000 < LD_{50} \leq 5000$ mg/kg)
- **Class VI**: Practically non–toxic ($LD_{50} > 5000$ mg/kg)

The ProTox results provided a comprehensive toxicity assessment, aiding in the identification of phytocompounds with minimal risk profiles suitable for further pharmacological development.

9.2.11. Docking with a marketed drug

To establish a reference for assessing the binding efficiency of the screened phytocompounds, molecular docking was also performed with a marketed drug that exhibits antioxidant, antimicrobial, anthelmintic, anti-inflammatory, antidiabetic, and anticancer properties. The procedure followed the same docking protocol outlined earlier, ensuring consistency and enabling direct comparison of binding affinities and interaction profiles (Tables 9.13-9.18). Protein structures were prepared using identical preprocessing steps, and the marketed drug was retrieved in three–dimensional format from the PubChem database. Following geometry optimization, the ligand was docked into the active site of each target protein using the same grid parameters applied to the phytocompounds. The docking scores and key binding interactions, including hydrogen bonds and hydrophobic contacts, were then compared to identify common residues and evaluate relative binding performance against a clinically validated standard (Meng et al., 2011).

9.2.12. Trajectory–based structural analysis

Molecular dynamics (MD) simulations were conducted using GROMACS 2023.1 to evaluate the structural stability, conformational flexibility, and dynamic interaction patterns of protein–ligand complexes under near–physiological conditions. For each target protein, the protein–ligand complex exhibiting the highest binding affinity from molecular docking was selected for simulation. In addition, the protein–drug complex corresponding to a marketed reference drug was also simulated for comparative analysis of interaction stability and binding dynamics (Joshi et al., 2022).

The CHARMM36 force field was employed for accurate modelling of bonded and non–bonded interactions within the protein, while ligand parameters were generated using the CHARMM General Force Field (CGenFF) via the CGenFF server to provide a precise description of the ligand's topology and partial atomic charges.

Table 9.13. Molecular docking grid coordinates and box dimensions of the marketed antioxidant drug target proteins

Protein	PDB ID	Centre			Dimensions		
		X	Y	Z	X	Y	Z
KEAP1 Kelch Domain	4L7B	9.59	-16.41	-11.91	49.90	47.14	51.95

Table 9.14. Molecular docking grid coordinates and box dimensions of the marketed antimicrobial drug target proteins

Protein	PDB ID	Centre			Dimensions		
		X	Y	Z	X	Y	Z
LasR Ligand	2UV0	51.81	9.92	69.04	35.27	44.52	50.01

Table 9.15. Molecular docking grid coordinates and box dimensions of the marketed anthelmintic drug target proteins

Protein	ID	Centre			Dimensions		
		X	Y	Z	X	Y	Z
Extracellular Globin-3/Erythrocruorin	P11069	-1.02	-0.73	1.12	42.78	36.66	41.00

Table 9.16. Molecular docking grid coordinates and box dimensions of the marketed anti-inflammatory drug target proteins

Protein	PDB ID	Centre			Dimensions		
		X	Y	Z	X	Y	Z
Human Inducible Nitric Oxide Synthase	4NOS	-2.15	94.73	17.16	57.28	70.45	47.77

Table 9.17. Molecular docking grid coordinates and box dimensions of the marketed antidiabetic drug target proteins

Protein	PDB ID	Centre			Dimensions		
		X	Y	Z	X	Y	Z
Peroxisome Proliferator-Activated Receptor Gamma	9F7X	7.23	8.51	17.08	42.21	47.86	65.03

Table 9.18. Molecular docking grid coordinates and box dimensions of the marketed anticancer drug target proteins

Protein	PDB ID	Centre			Dimensions		
		X	Y	Z	X	Y	Z
Kirsten Rat Sarcoma Viral Oncogene Homolog	6GJ8	16.52	16.56	-5.16	43.44	43.47	41.34

Each prepared complex was placed in a triclinic simulation box, maintaining a minimum distance of 1.0 nm between the protein surface and the box edges to minimize periodic boundary artifacts. The systems were solvated with explicit TIP3P water molecules, and counter–ions (Na^+or Cl^-) were added to achieve electrostatic neutrality (Huang & MacKerell, 2013).

Energy minimization was performed to remove steric clashes, followed by NVT equilibration at 310 K using a velocity–rescaling thermostat and NPT equilibration at 1 atm using the Parrinello–Rahman barostat. The production MD runs were performed for 100 ns with a 2–fs integration time step under periodic boundary conditions. Long–range electrostatics were calculated using the Particle Mesh Ewald (PME) method with a real–space cut–off of 1.2 nm, while the Verlet cut–off scheme was applied for short–range interactions. All bond lengths involving hydrogen atoms were constrained using the LINCS algorithm, enabling stable simulations with the selected time step.

Trajectory snapshots were saved every 10 ps for post–simulation analyses, including root mean square deviation (RMSD), root mean square fluctuation (RMSF), radius of gyration (Rg), hydrogen bond profiling, and free energy landscape (FEL) mapping to assess the stability and conformational states of the complexes.

9.2.13. Conformational sampling and landscape analysis

Following molecular dynamics simulations, Principal Component Analysis (PCA) was employed to extract and characterize the dominant collective motions within the protein–ligand systems. Trajectory coordinates were projected onto the principal eigenvectors, enabling the identification of large–scale conformational shifts and dominant motion patterns that occurred during the simulation period.

To further investigate conformational preferences, the Free Energy Landscape (FEL) was constructed using the first two principal components (PC1 and PC2) as reaction coordinates, with Gibbs free energy values mapped across the conformational space (Azmal et al., 2024). This representation allowed visualization of energy basins corresponding to stable structural states and provided a comparative view of flexibility

and stability between the highest binding affinity protein–ligand complex and the protein–drug complex. The location, depth, and distribution of energy minima in the FEL indicated preferred binding conformations and potential intermediate states sampled during the simulation.

9.2.14. Binding free energy analysis

Binding free energies for all simulated complexes were evaluated using the Molecular Mechanics/Poisson–Boltzmann Surface Area (MM/PBSA) approach implemented in g_mmpbsa. Equilibrated trajectory frames were extracted at defined intervals to ensure representative sampling of the bound state. The total binding free energy (ΔG_bind) was calculated as the sum of van der Waals, electrostatic, polar solvation, and non-polar solvation contributions (Sahoo et al., 2025). This analysis was conducted for both the highest binding affinity protein–ligand complex and the protein–marketed drug complex, enabling direct comparison of their energetic stability. The results provided quantitative validation of molecular docking predictions and offered insights into the dominant energetic components driving stable ligand–protein association in each system.

9.2.15. Normal mode analysis

Normal Mode Analysis (NMA) is a computational technique widely used to study the intrinsic dynamics and conformational flexibility of biomolecules, particularly proteins, based on their three-dimensional structures. It operates on the principle that protein motion can be decomposed into a set of collective oscillations, or "normal modes," each representing a potential movement pattern around the equilibrium conformation. These modes often correspond to biologically relevant motions such as domain shifts, loop flexibility, or active-site rearrangements, which are essential for protein function. Unlike molecular dynamics simulations, NMA requires fewer computational resources while still providing valuable insights into low-frequency, large-scale motions that dominate functional conformational changes. In this study, NMA was performed for the top-ranked protein using the iMODS server, which evaluates deformability, B-factors, eigenvalues, covariance matrices, and elastic network models to characterize motion patterns. The eigenvalue reflects the

stiffness of motion, with lower values indicating higher flexibility and greater potential for conformational change (Islam et al., 2023). This analysis is important as it reveals the protein's dynamic stability, flexibility, and potential interaction adaptability, factors critical for understanding ligand binding, allosteric regulation, and druggability.

9.2.16. Density Functional Theory (DFT) studies

Density Functional Theory (DFT) calculations were performed to analyse the frontier molecular orbitals, Highest Occupied Molecular Orbital (HOMO) and Lowest Unoccupied Molecular Orbital (LUMO), of the selected ligand. Geometry optimization was carried out using the B3LYP/6-31G(d,p) level of theory to obtain the most stable molecular conformation. The energy gap ($\Delta E = E_LUMO - E_HOMO$) was determined to assess the electronic stability and chemical reactivity of the compound. HOMO and LUMO visualizations were further examined to identify electron-donating and electron-accepting regions, offering insight into potential interaction hotspots within the target protein's binding environment (Yele et al., 2021).

9.3. Results

9.3.1. Selection and preparation of target proteins

Structurally resolved models of five key antioxidant, antimicrobial, anthelmintic, anti-inflammatory, antidiabetic, and anticancer proteins were curated to facilitate downstream computational analysis. Each protein was individually processed to remove bound ligands, crystallographic water molecules, and non-essential heteroatoms, thereby standardizing the structures for docking and simulation. This preprocessing step was carried out using molecular visualization and editing platforms, ensuring that only the biologically relevant polypeptide chains were retained. The resulting clean protein models served as the foundation for accurate receptor–ligand interaction profiling and pharmacokinetic assessment (Plates 9.1 to 9.6).

9.3.2. Physicochemical properties of target proteins

Physicochemical properties describe the intrinsic chemical and physical characteristics of proteins, such as amino acid composition, molecular weight, isoelectric point (pI), hydrophobicity, and stability indices. These parameters are essential for understanding how a protein behaves in physiological and experimental environments, influencing folding, interactions with ligands, and enzymatic functions (Gasteiger et al., 2005).

Antioxidant proteins play a crucial role in mitigating oxidative stress by neutralizing reactive oxygen species (ROS). Their physicochemical properties, such as molecular weight, isoelectric point (pI), amino acid composition, stability indices, and hydrophobicity, are vital in understanding their structural resilience and functional adaptability. For antioxidant enzymes like catalase, these parameters influence substrate binding, catalytic efficiency, and stability under varying cellular environments. Evaluating such properties provides key insights into how these proteins withstand oxidative damage while maintaining catalytic activity, thereby contributing to cellular defense mechanisms and potential therapeutic applications (Nandi et al., 2019).

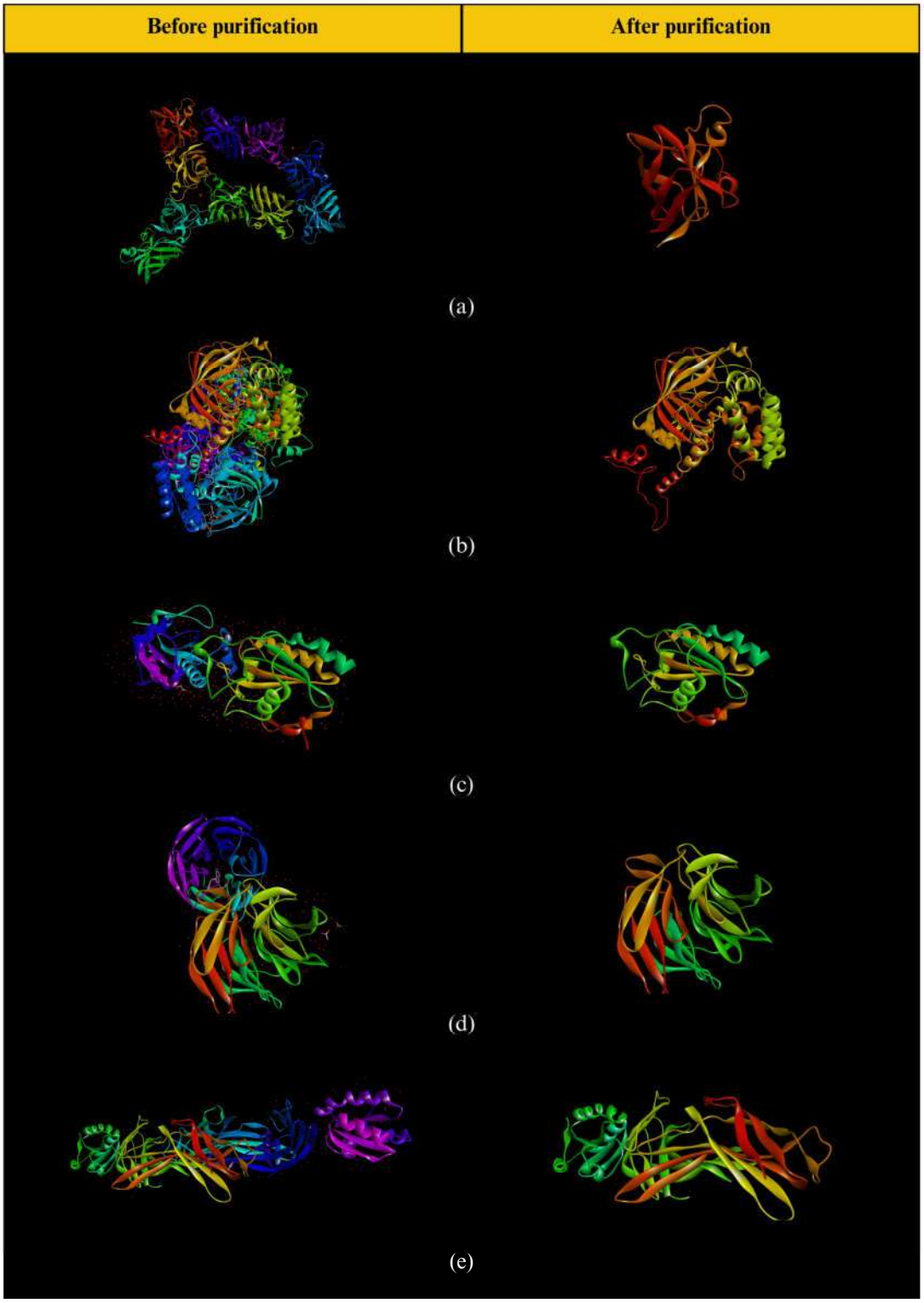


Plate 9.1: Molecular visualization of ligand interactions with antioxidant proteins before and after purification for (a) Human Cu, Zn Superoxide Dismutase (SOD1) (b) Human Erythrocyte Catalase (CAT) (c) Human Glutathione Peroxidase 1 (GPx1) (d) KEAP1 Kelch Domain (KEAP1 Kelch) (e) Thioredoxin and TXNIP complex (Trx-TXNIP)

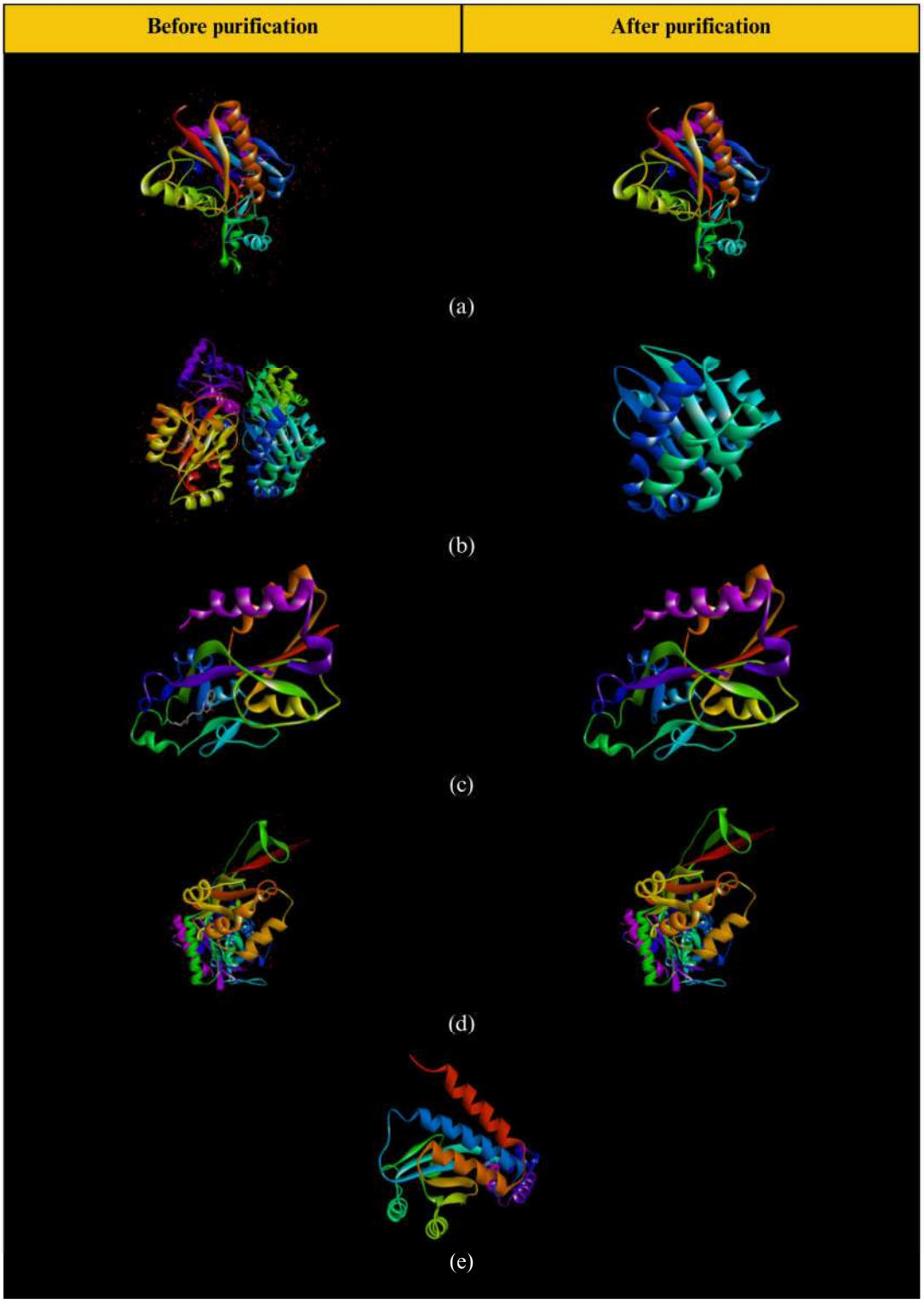


Plate 9.2: Molecular visualization of ligand interactions with antimicrobial proteins before and after purification for (a) D-alanyl-D-alanine ligase (Ddl) (b) LasR ligand-binding domain (LasR) (c) PqsR/MvfR coinducer-binding domain (PqsR/MvfR) and (d) Penicillin-Binding Protein 3 (PBP3) (e) Prepared Regulatory Protein RhlR (RhIR)

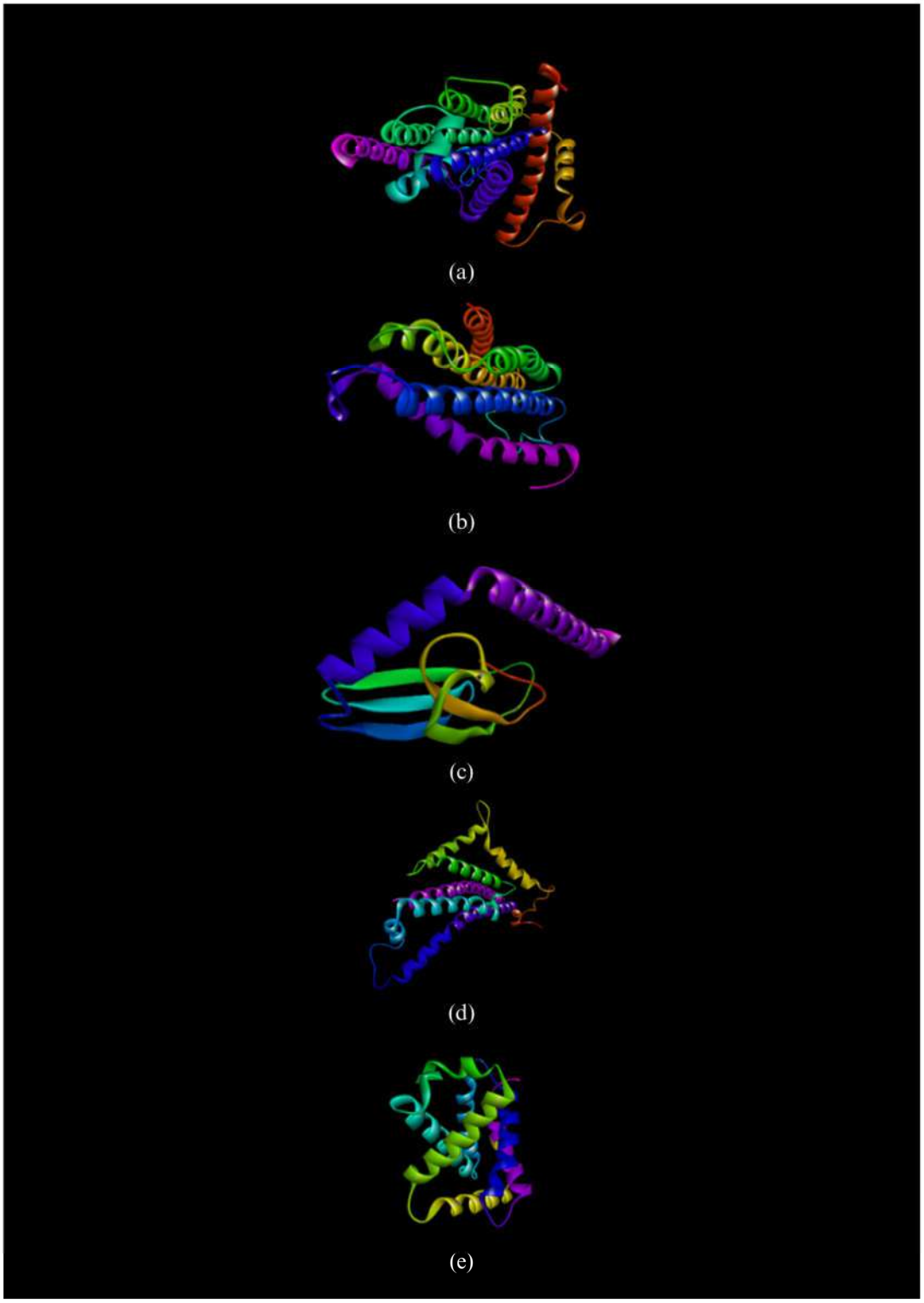


Plate 9.3: Prepared anthelmintic protein structures of (a) ATP synthase subunit a (UniProt ID: Q34946) (b) Cytochrome c Oxidase subunit 1 (COX1) (c) Heat Shock Protein 70 (HSP70; UniProt ID: B9TY08) (d) NADH-Ubiquinone Oxidoreductase chain 1 (Complex I; UniProt ID: Q37546) (e) Extracellular Globin-3/Erythrocruorin (Ex. Globin-3; UniProt ID: P11069)

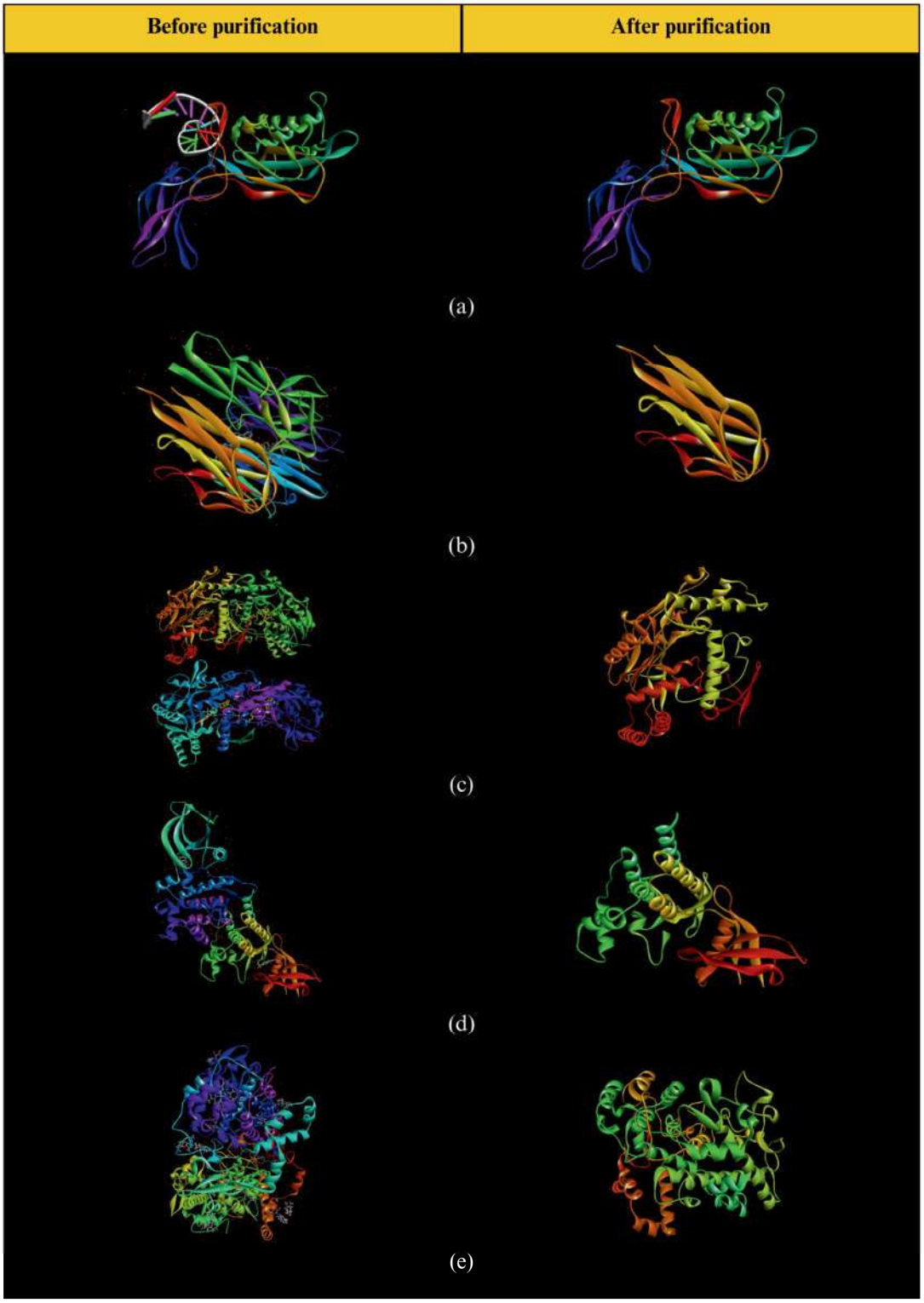


Plate 9.4: Molecular visualization of ligand interactions with anti-inflammatory proteins before and after purification for (a) Nuclear Factor kappa B p50 (NF-κB p50) (b) Tumour Necrosis Factor-alpha (TNF-α) (c) Human Inducible Nitric Oxide Synthase (iNOS) (d) Janus Kinase 2 (JAK2) (e) Human Cyclooxygenase-2 (COX-2)

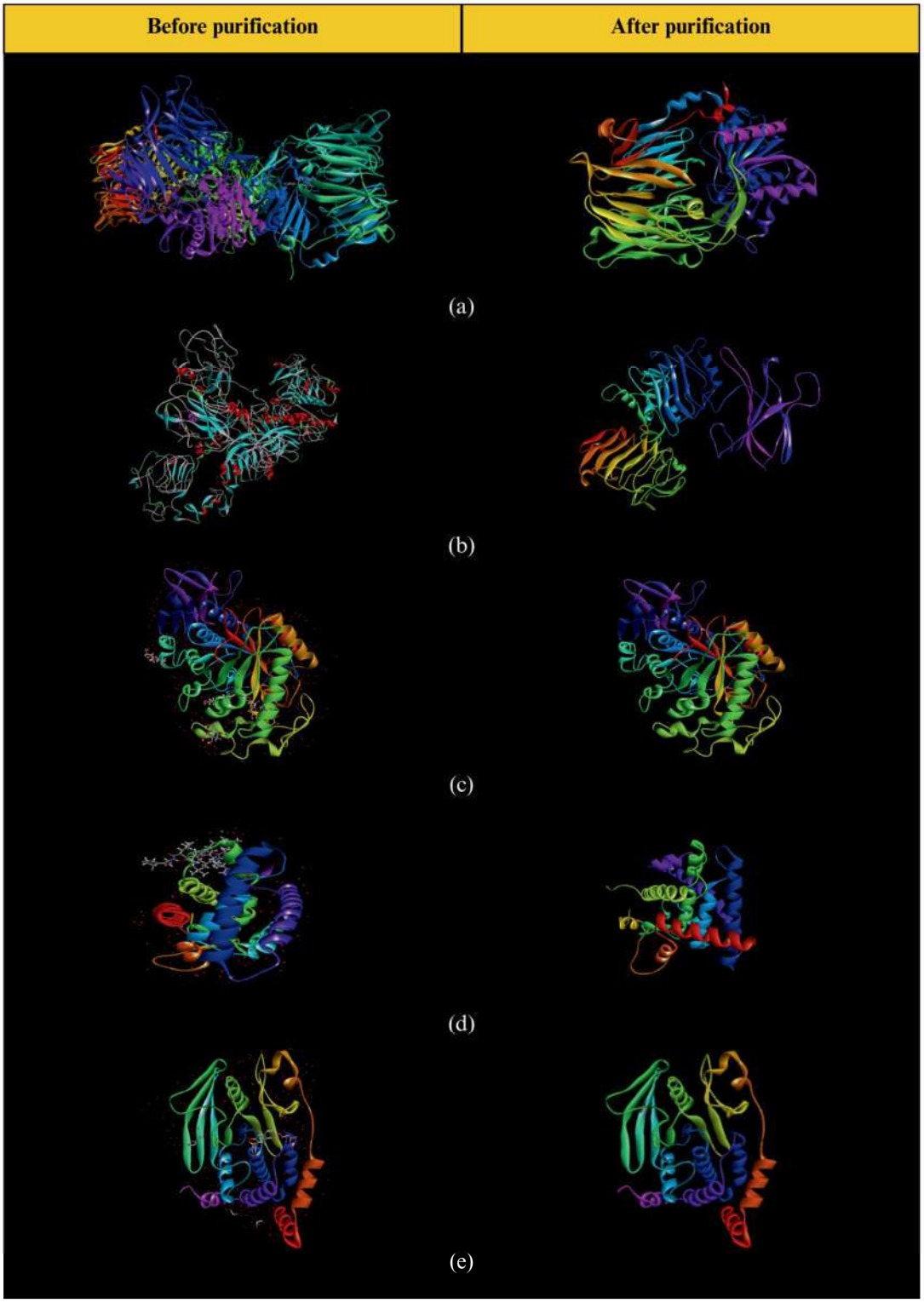


Plate 9.5: Molecular visualization of ligand interactions with proteins before and after purification for (a) Dipeptidyl Peptidase 4 (DPP4) (b) Insulin Receptor Ectodomain (IR) (c) Pancreatic Alpha-Amylase (PAA) (d) Peroxisome Proliferator-Activated Receptor Gamma (PPARG) (e) Protein Tyrosine Phosphatase 1B (PTP1B)

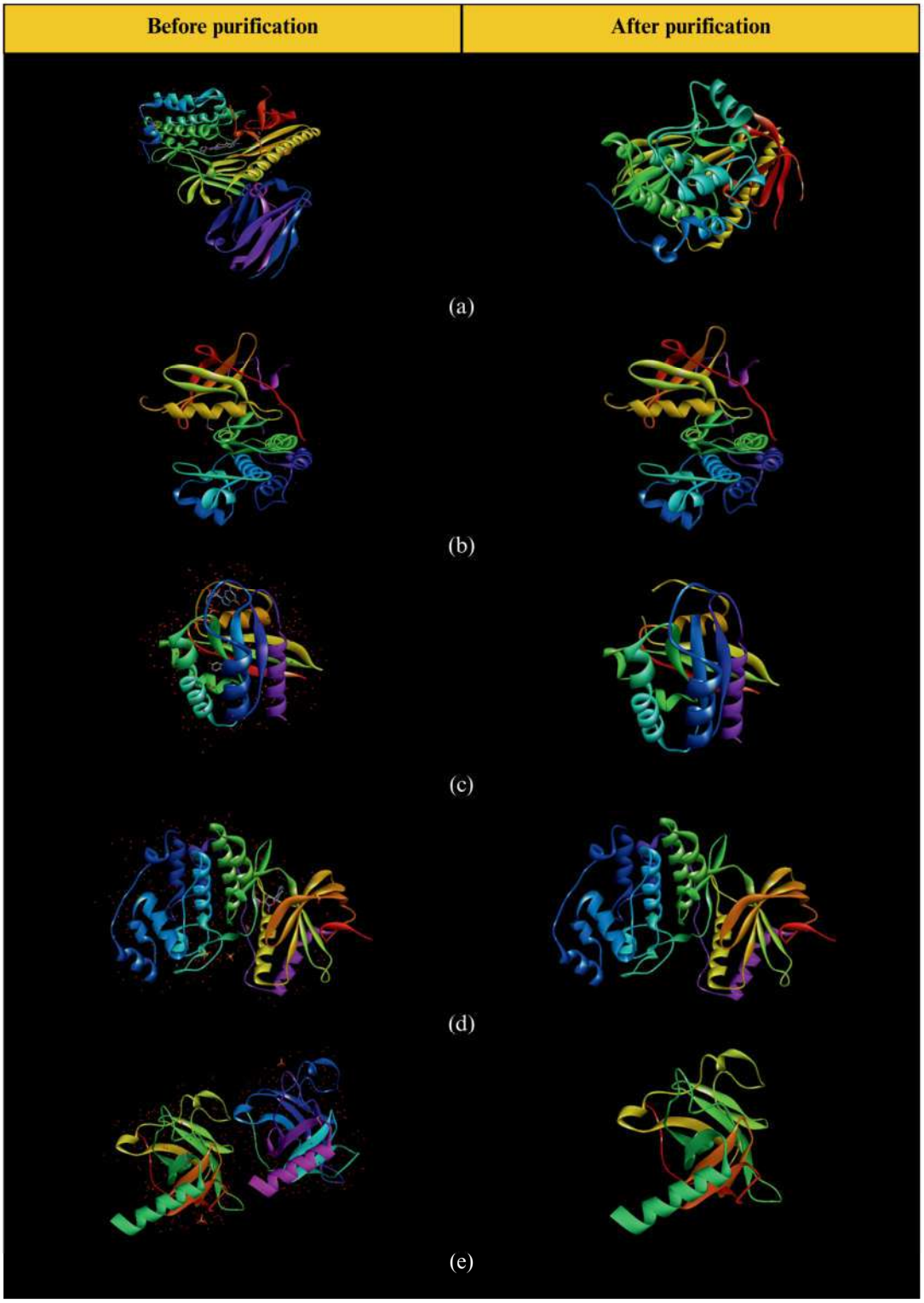


Plate 9.6: Molecular visualization of ligand interactions with anticancer proteins before and after purification for (a) AKT serine/threonine kinase (AKT1) (b) Epidermal Growth Factor Receptor (EGFR) (c) Kirsten Rat Sarcoma Viral Oncogene Homolog (KRAS) (d) Mitogen-Activated Protein Kinase 1 (MAPK1) (e) Tumour Protein p53 (TP53)

In the context of antimicrobial proteins, such physicochemical characteristics can reveal enzyme efficiency, substrate affinity, membrane interaction potential, and resilience to hostile environments encountered in microbial cells or during immune responses. For example, proteins with a high aliphatic index are typically more thermostable, which may enhance survival in variable host environments. Similarly, the pI can dictate the electrostatic interactions with bacterial membranes or cell wall components, influencing antimicrobial activity. By analyzing these parameters, researchers can better understand the mechanistic basis of antimicrobial action and identify structural features critical for designing more effective inhibitors or mimetics (Nguyen et al., 2011).

In anthelmintic proteins, physicochemical properties help predict how these molecules behave in the parasite's cellular environment, influencing their role in energy metabolism, stress response, structural integrity, or defense mechanisms. Moreover, insights into these parameters can guide the design of drugs targeting these proteins or help optimize recombinant production for research and therapeutic purposes (Madhivardhana et al., 2025).

Physicochemical properties provide valuable insight into the structural stability, solubility, and functional tendencies of proteins. Parameters like molecular weight and theoretical pI can guide purification and separation techniques, while amino acid composition offers clues about hydrophobicity, flexibility, and potential binding affinities. Charged residues play a pivotal role in protein–protein and protein–ligand interactions, which is critical for anti-inflammatory proteins that often mediate signaling cascades. Indices such as the instability index, aliphatic index, and GRAVY score provide predictive assessments of stability, thermostability, and hydrophilicity/hydrophobicity balance, all of which can help understand how these proteins contribute to anti-inflammatory mechanisms. For instance, stability in varied environments can influence how long a protein remains active during inflammatory responses (Gasteiger et al., 2005).

In the context of antidiabetic proteins, such characteristics can provide insights into their stability, activity, and interaction with therapeutic compounds,

which is crucial for designing effective inhibitors or modulators in diabetes management (Gasteiger et al., 2005).

For anticancer targets, physicochemical profiling can reveal potential binding site environments, predict protein behaviour under physiological conditions, and identify biophysical constraints for therapeutic molecule design. Evaluating these parameters ensures structural integrity in computational modelling and enhances the reliability of virtual screening campaigns (Lionta et al., 2014).

9.3.2.1. Physicochemical properties of antioxidant proteins

9.3.2.1.1. Human Cu, Zn Superoxide Dismutase (SOD1)

Human Cu, Zn Superoxide Dismutase (SOD1) is a compact 153-amino-acid antioxidant enzyme with a molecular weight of 15.80 kDa and a slightly acidic pI of 5.70, aligning with its cytosolic localization, where it must interact with charged superoxide radicals. Its amino acid profile shows a strikingly high glycine content (16.3%), which imparts flexibility to the polypeptide chain, crucial for rapid catalytic turnover. Valine (9.2%) and leucine/isoleucine combined (~11.8%) suggest a hydrophobic core that stabilizes the structure, while the negatively charged residues (21) exceed the positively charged residues (15), reflecting a net acidic surface optimal for metal ion binding (e.g., Cu/Zn in Cu/Zn-SOD).

The aliphatic index of 78.95 suggests moderate thermostability, while the GRAVY score (-0.358) indicates an overall hydrophilic nature, promoting solubility and efficient diffusion in the cytosol. Its low extinction coefficient (5750 M^{-1} cm^{-1}) suggests fewer aromatic residues, consistent with its small size (Figure 9.1). Importantly, the instability index (20.89) classifies it as highly stable, a necessity for constant protection against oxidative stress. Functionally, SOD catalyzes the dismutation of the toxic superoxide radical into oxygen and hydrogen peroxide, serving as the first line of enzymatic defense against reactive oxygen species, and its physicochemical properties directly enhance catalytic efficiency and substrate accessibility.

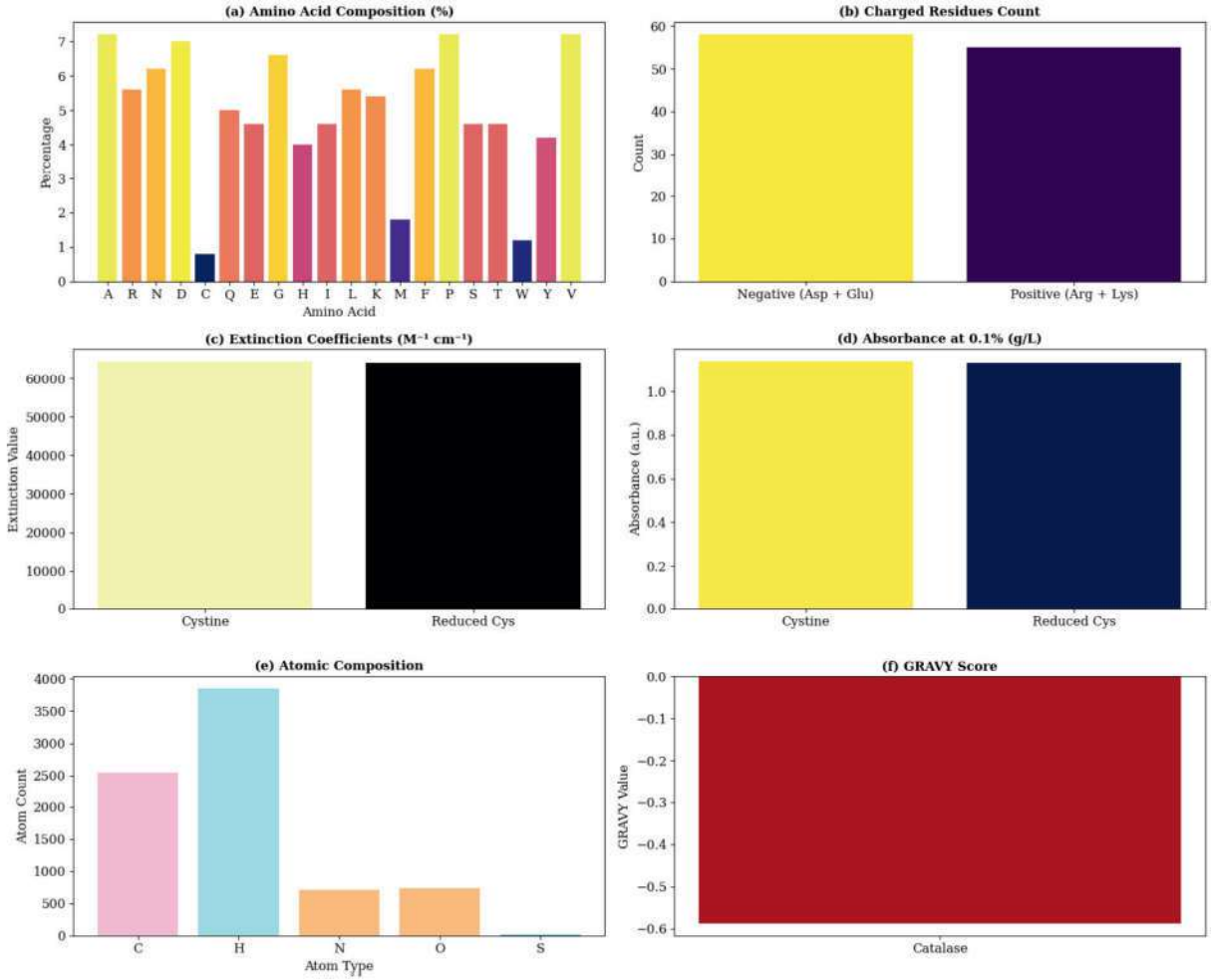


Figure 9.1: Physicochemical profile of Human Cu, Zn Superoxide Dismutase (SOD1): (a) Amino acid distribution (b) Charged residues count (c) Extinction coefficients (d) Absorbance (e) Atomic composition (f) GRAVY Score

9.3.2.1.2. Human Erythrocyte Catalase (CAT)

Human Erythrocyte Catalase (CAT), composed of 498 amino acids and with a molecular weight of 56.63 kDa, shows a near-neutral pI of 6.70, indicating functionality in cytosolic and peroxisomal environments. The amino acid composition reveals balanced proportions of hydrophobic (Leu 5.6%, Val 7.2%) and hydrophilic residues (Asp + Glu = 58 residues, Arg + Lys = 55 residues), essential for maintaining both catalytic activity and solubility. The aliphatic index of 68.13 suggests moderate thermostability, suitable for its function in a wide temperature range within the cell. The negative GRAVY value (-0.587) highlights its hydrophilic nature, consistent with its high aqueous solubility for efficient interaction with hydrogen peroxide. The instability index of 29.79 classifies it as stable, which is crucial for long-term enzymatic activity under oxidative stress. The extinction coefficient of 64,540 M^{-1} cm^{-1} supports its use in spectrophotometric quantification (Figure 9.2). Functionally, these features align with catalase's role in rapidly decomposing hydrogen peroxide into water and oxygen, protecting cells from ROS-induced damage and oxidative stress-linked pathologies (Nandi et al., 2019).

9.3.2.1.3. Human Glutathione Peroxidase 1 (GPx1)

Human Glutathione Peroxidase 1 (GPx1) is a 184-amino-acid enzyme with a molecular weight of 20.31 kDa and an acidic pI of 5.76, indicating optimal activity in slightly acidic to neutral conditions, which matches its cytosolic and mitochondrial environments. Its amino acid profile shows a significant proportion of hydrophobic residues (Leu 12.0%, Ala 7.6%, Val 7.1%) contributing to structural stability, alongside polar residues (Gly 9.2%, Ser 5.4%) that support solubility and interaction with glutathione. The negatively charged residues (21) slightly exceed the positively charged residues (19), suggesting a surface charge balance that favours catalytic efficiency without excessive repulsion from the anionic glutathione substrate.

The aliphatic index of 87.45 denotes moderate thermostability, while the GRAVY score of -0.177 reflects a balanced hydrophilic/hydrophobic character, essential for interaction with both aqueous environments and hydrophobic regions of

membranes (Figure 9.3). However, the instability index of 47.80 classifies GPx1 as unstable, hinting at a reliance on cellular chaperones or dimer/tetramer formation for stability. Its extinction coefficient of 17,085 M^{-1} cm^{-1} supports spectrophotometric monitoring in enzymatic studies. These features align with GPx1's primary role in reducing hydrogen peroxide and lipid peroxides, using glutathione as an electron donor, thereby safeguarding cells from oxidative damage and maintaining redox balance under stress conditions.

9.3.2.1.4. KEAP1 Kelch Domain (KEAP1 Kelch)

KEAP1 Kelch Domain (KEAP1 Kelch), a 291-amino-acid cytoplasmic regulatory protein, has a molecular weight of 31.89 kDa and a slightly acidic pI of 5.66, supporting its function in binding the basic Nrf2 transcription factor under basal conditions. The amino acid profile reveals a high proportion of glycine (12.0%) and valine (9.3%), which together provide structural flexibility and moderate hydrophobicity, critical for Keap1's role in conformational changes during oxidative stress sensing. The negatively charged residues (31) exceed the positively charged residues (23), suggesting a net acidic surface that may aid in electrostatic interaction with Nrf2's basic regions.

The aliphatic index of 77.66 reflects moderate thermal stability, while the GRAVY score of -0.279 indicates a generally hydrophilic nature, suitable for cytoplasmic solubility. The instability index (40.86) classifies Keap1 as unstable, consistent with its role in transient, signal-dependent protein-protein interactions rather than long-term structural persistence. Its high extinction coefficient (58,830 M^{-1} cm^{-1}) supports effective spectrophotometric quantification in biochemical assays (Figure 9.4). Functionally, Keap1 serves as a redox sensor by regulating Nrf2 degradation under normal conditions and releasing it during oxidative stress, thereby activating antioxidant and cytoprotective genes, a process directly tied to its physicochemical adaptability and interaction-prone surface chemistry.

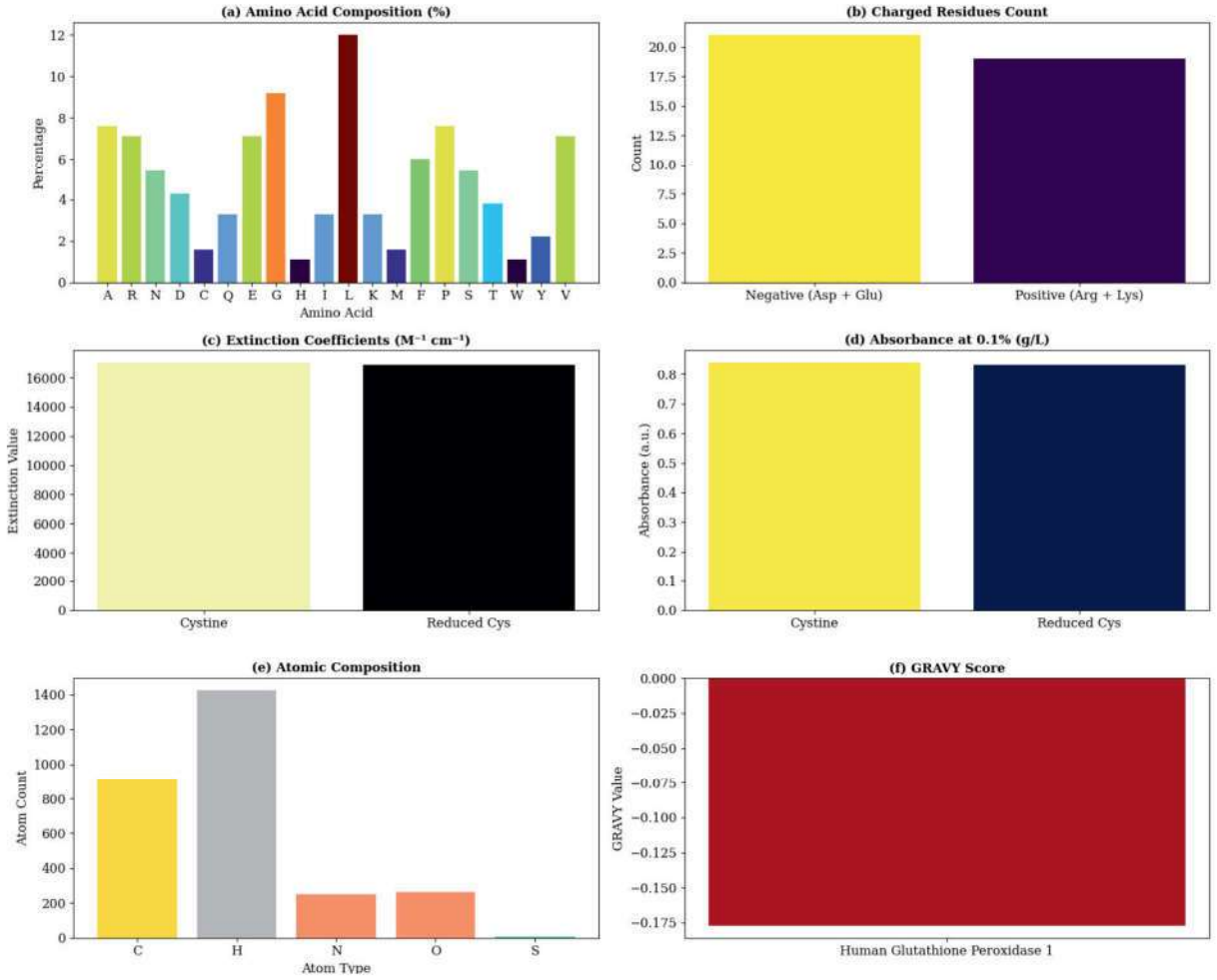


Figure 9.2: Physicochemical profile of Human Erythrocyte Catalase (CAT): (a) Amino acid distribution (b) Charged residues count (c) Extinction coefficients (d) Absorbance (e) Atomic composition (f) GRAVY Score

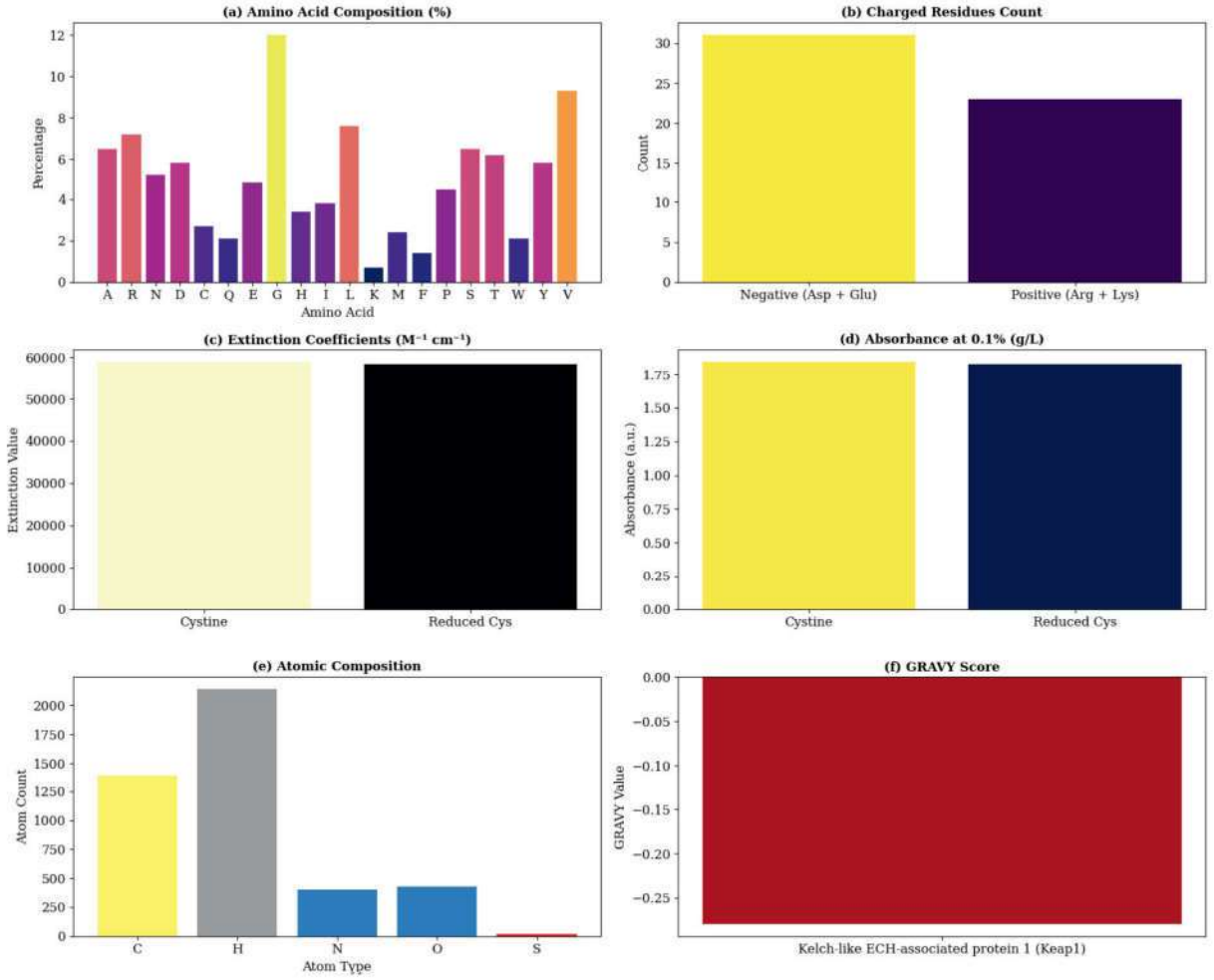


Figure 9.3: Physicochemical profile of Human Glutathione Peroxidase 1 (GPx1): (a) Amino acid distribution (b) Charged residues count (c) Extinction coefficients (d) Absorbance (e) Atomic composition (f) GRAVY Score

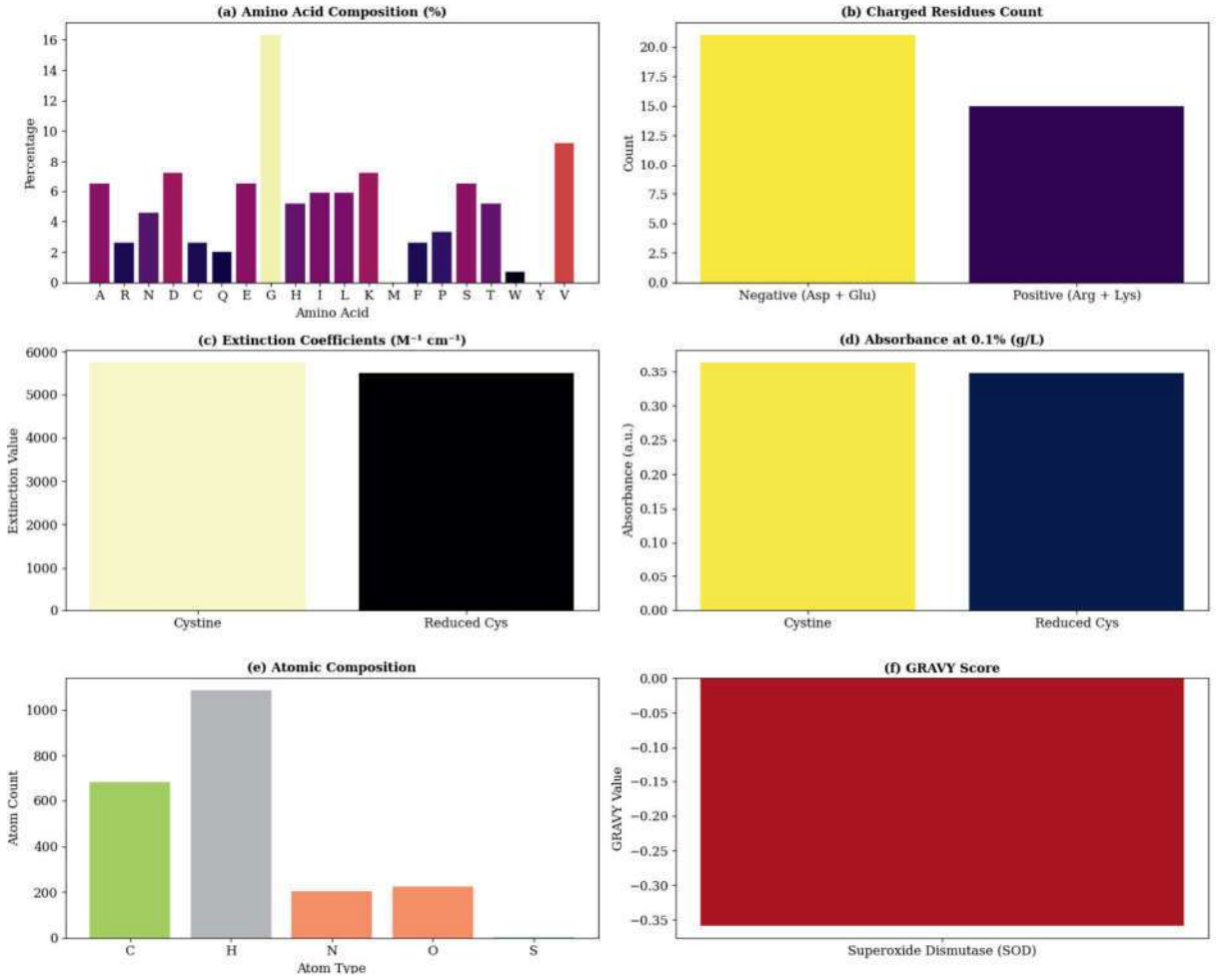


Figure 9.4: Physicochemical profile of KEAP1 Kelch Domain (KEAP1 Kelch): (a) Amino acid distribution (b) Charged residues count (c) Extinction coefficients (d) Absorbance (e) Atomic composition (f) GRAVY Score

9.3.2.1.5. Thioredoxin and TXNIP Complex (Trx-TXNIP)

Thioredoxin and TXNIP Complex (Trx-TXNIP) is a moderately large 278-amino-acid redox-regulating protein with a molecular weight of 30.97 kDa and a basic pI of 9.29, indicating a strong net positive charge at physiological pH. This property facilitates electrostatic interactions with the negatively charged thioredoxin, enabling efficient binding and regulation of cellular redox states. The protein shows a high valine content (11.5%), contributing to hydrophobic stability, along with serine (8.6%) and glycine (7.6%), which provide flexibility for conformational adaptation during protein-protein interactions. The positively charged residues (40) significantly exceed the negatively charged residues (30), aligning with its role in binding acidic surfaces of target proteins.

The aliphatic index (90.32) suggests high thermostability, while the GRAVY score (-0.203) indicates balanced hydrophilicity for solubility without compromising hydrophobic core stability (Figure 9.5). The instability index (24.94) classifies TXNIP as stable, important for its function as a long-term regulator of oxidative stress responses. The extinction coefficient (31650 M^{-1} cm^{-1}) allows moderate UV absorbance, supporting detection in biochemical assays. Functionally, TXNIP negatively regulates thioredoxin, increasing oxidative stress and influencing apoptosis, inflammation, and metabolism. Its physicochemical features, especially its stability, positive surface charge, and hydrophobic balance, are well-aligned with its role as a redox sensor and modulator.

9.3.2.2. Physicochemical properties of antimicrobial proteins

9.3.2.2.1. D-alanyl-D-alanine ligase (D-ALA:D-ALA Ligase/Ddl)

D-alanyl-D-alanine ligase (D-ALA:D-ALA Ligase/Ddl) from the antimicrobial dataset consists of 306 amino acids with a molecular weight of 32,839.71 Da and an acidic pI of 4.75, suggesting a net negative charge at physiological pH, which can influence substrate binding in the enzymatic active site. The protein is rich in leucine (13.4%) and glycine (10.1%), indicating a balance between hydrophobic stability and structural flexibility. A total of 38 negatively

charged residues (Asp + Glu) compared to 25 positively charged residues (Arg + Lys) further supports its acidic nature, possibly contributing to optimal activity in cytosolic or periplasmic conditions of bacteria (Figure 9.6).

The instability index is 39.03, classifying it as stable, while the aliphatic index of 98.53 points toward substantial thermostability, advantageous for functioning under variable bacterial growth conditions. A GRAVY score of 0.077 reflects mild hydrophobicity, indicating balanced solubility and potential for interactions with both hydrophilic and hydrophobic ligands. The estimated half-life (>20 hours in yeast, 30 hours in mammalian systems) suggests long persistence, which could be vital for sustained antimicrobial effect. Functionally, D-alanine ligase plays a pivotal role in bacterial cell wall biosynthesis, and these properties support efficient catalysis and resilience in diverse environments, making it a critical target for antimicrobial drug development.

9.3.2.2.2. LasR ligand-binding domain (LasR)

LasR ligand-binding domain (LasR), a transcriptional regulator, exhibits distinct physicochemical characteristics that align with its role in quorum sensing and pathogenic regulation in *Pseudomonas aeruginosa*. The protein consists of 162 amino acids with a molecular weight of 17,970.19 Da and a theoretical pI of 5.06, suggesting a mildly acidic nature that may facilitate interactions with DNA and other regulatory proteins under physiological pH. The amino acid profile is enriched with leucine (13.0%) and alanine (11.7%), indicating a significant hydrophobic core that supports structural stability in the ligand-binding domain. Notably, glycine (8.0%) and serine (8.6%) content implies flexibility and potential involvement in conformational changes during signal molecule binding. Charged residue analysis reveals 21 negatively charged and 14 positively charged residues, creating a moderate electrostatic balance favourable for protein–DNA binding specificity. The aliphatic index (88.64) suggests moderate thermal stability, while the GRAVY score (-0.165) indicates an overall hydrophilic character, essential for maintaining solubility in the cytosol. The extinction coefficient (32,430 $M^{-1}cm^{-1}$) denotes a relatively strong aromatic content, contributing to reliable spectrophotometric quantification. With an

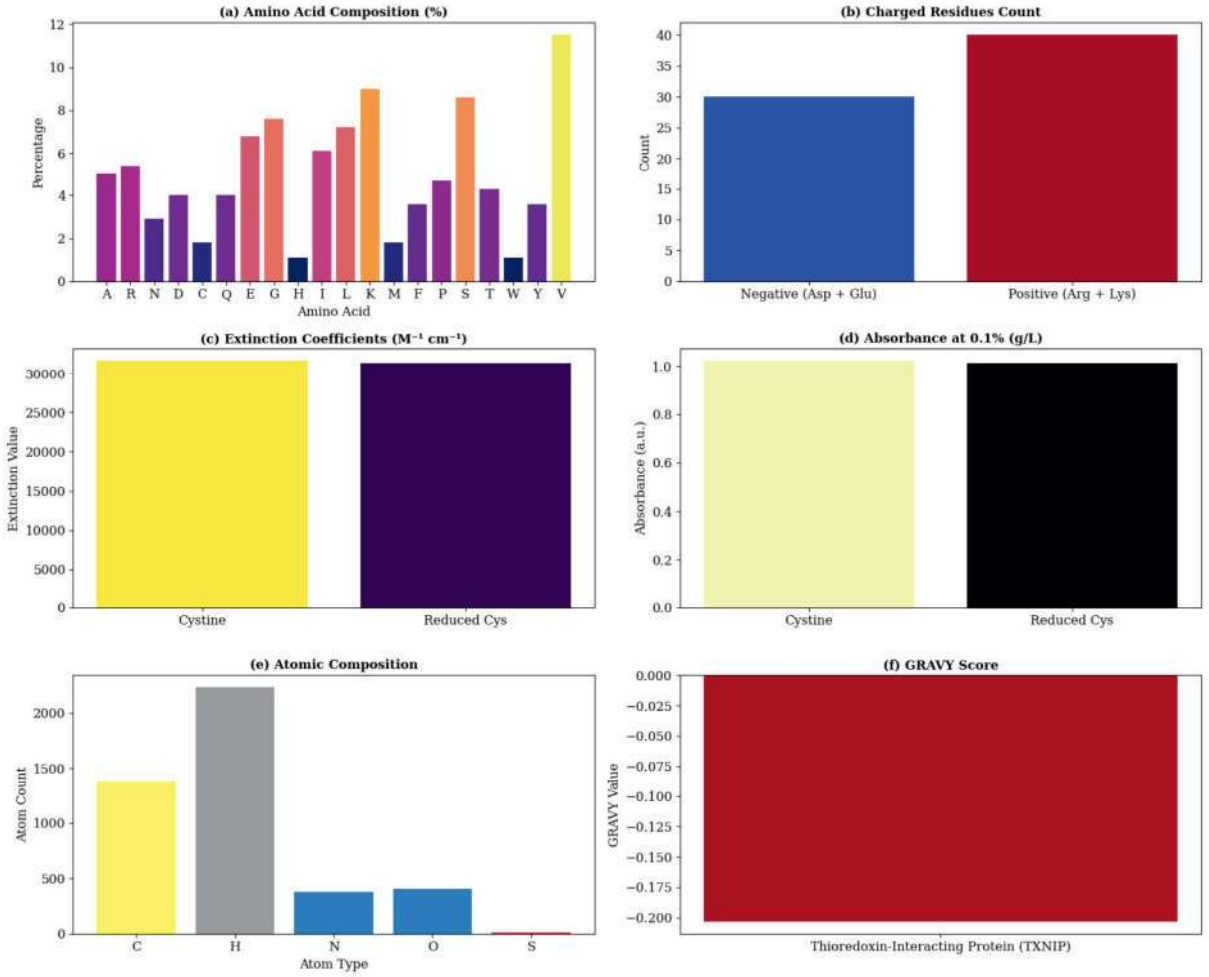


Figure 9.5: Physicochemical profile of Thioredoxin and TXNIP Complex (Trx-TXNIP): (a) Amino acid distribution (b) Charged residues count (c) Extinction coefficients (d) Absorbance (e) Atomic composition (f) GRAVY Score

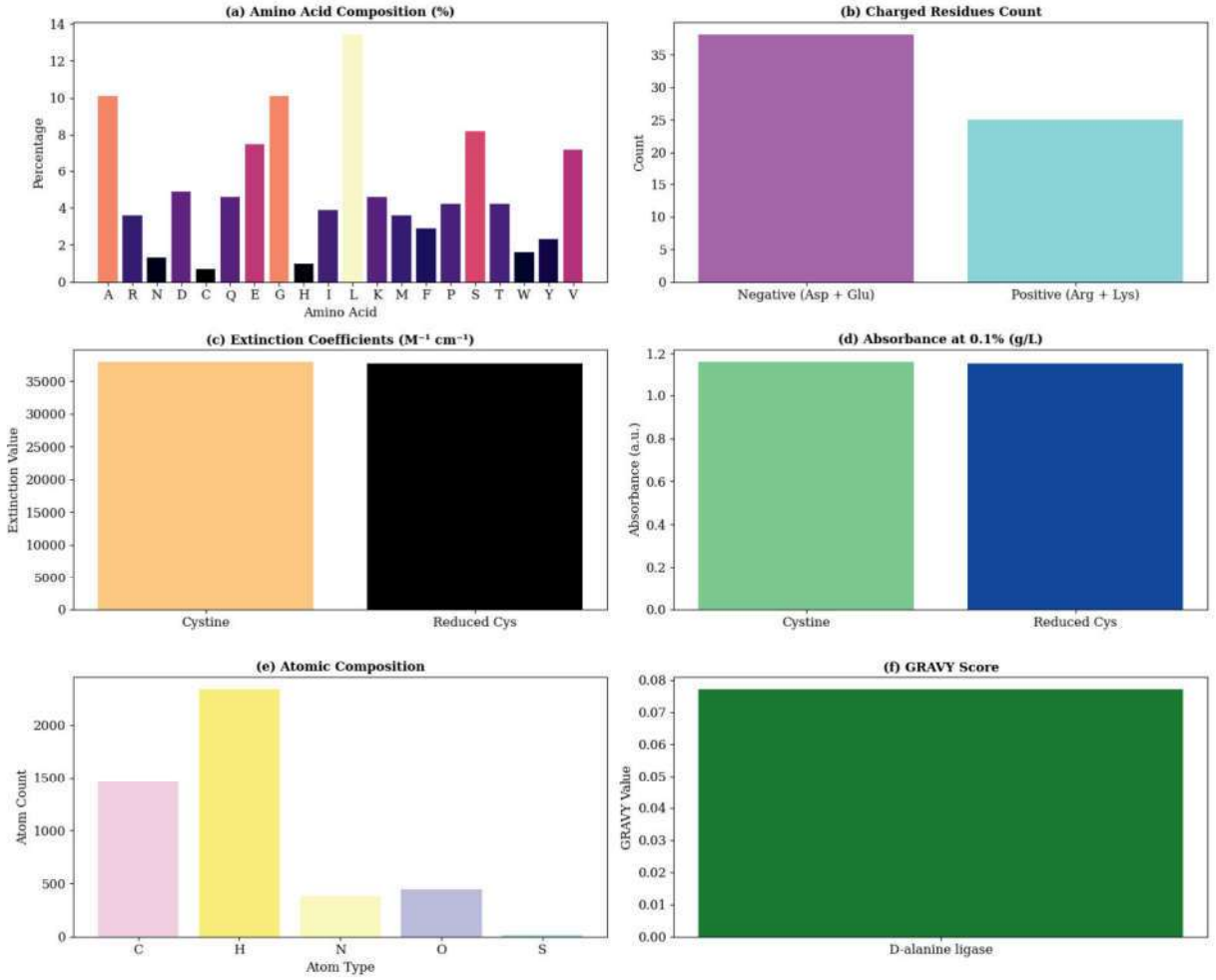


Figure 9.6: Physicochemical profile of D-alanyl-D-alanine ligase (D-ALA:D-ALA Ligase/Ddl): (a) Amino acid distribution (b) Charged residues count (c) Extinction coefficients (d) Absorbance (e) Atomic composition (f) GRAVY Score

instability index of 40.10, LasR is predicted to be unstable *in vitro*, possibly reflecting the need for regulatory turnover in bacterial signal transduction (Figure 9.7). These properties collectively support LasR's functional dynamics in environmental sensing and virulence modulation.

9.3.2.2.3. PqsR coinducer-binding domain (PqsR/MvfR)

The transcriptional regulator PqsR coinducer-binding domain (PqsR/MvfR) is a 203-amino-acid protein with a molecular weight of 22,706.85 Da and a theoretical pI of 5.36, indicating a slightly acidic nature. This pI suggests that PqsR/MvfR will likely carry a net negative charge at physiological pH, which may influence DNA-binding affinity and regulatory interactions in quorum-sensing networks. The protein's composition is dominated by leucine (13.3%), serine (9.4%), and alanine/valine (both 7.4%), which collectively contribute to structural stability, flexibility, and hydrophobic core formation. The serine richness may be linked to its regulatory role, enabling hydrogen bonding with nucleic acids and partner proteins.

Charge distribution analysis reveals 25 negatively charged residues compared to 19 positively charged residues, in line with its acidic pI. The aliphatic index (103.74) indicates high thermal stability, important for functioning under various environmental conditions encountered during bacterial infections. The GRAVY score (-0.023) denotes a nearly neutral hydropathicity, suggesting balanced solubility and membrane interaction potential. The instability index (37.67) places PqsR/MvfR in the stable category, consistent with its requirement for sustained regulatory function in pathogenic bacteria (Figure 9.8). Its extinction coefficient (16,180 $M^{-1}cm^{-1}$) allows moderate spectroscopic detectability. Collectively, these properties explain PqsR/MvfR's resilience and efficiency in regulating virulence gene expression, making it a viable antimicrobial drug target.

9.3.2.2.4. Penicillin-binding Protein 3 (PBP3)

Penicillin-binding protein 3 (PBP3) is a large 495-amino-acid protein with a molecular weight of 53,680.63 Da and a theoretical pI of 9.59, indicating a distinctly basic nature that supports interactions with the negatively charged bacterial cell wall

precursors during peptidoglycan synthesis. The protein's amino acid profile is dominated by alanine (11.1%), valine (9.3%), and glycine (9.1%), suggesting a composition that enhances structural compactness and catalytic efficiency. The relatively high leucine content (8.7%) supports hydrophobic packing, essential for the transpeptidase domain's stability within the bacterial membrane environment.

Electrostatic analysis shows 48 negatively charged versus 59 positively charged residues, reinforcing its basic pI and likely facilitating strong binding to anionic substrates. The aliphatic index (92.42) reflects high thermal stability, an important trait for enzymes operating across diverse bacterial growth conditions. With a GRAVY score of -0.143, PBP3 maintains a mildly hydrophilic character, balancing solubility with membrane association. Its instability index (33.98) categorizes it as stable, supporting its functional persistence during bacterial cell division. The extinction coefficient (46,870 $M^{-1}cm^{-1}$) reflects substantial aromatic amino acid content, enabling accurate spectroscopic tracking (Figure 9.9). These properties collectively illustrate why PBP3 is a prime target for β-lactam antibiotics, its stability, charge profile, and structural composition underpin its critical role in bacterial cell wall biosynthesis.

9.3.2.2.5. Regulatory protein RhlR (RhIR)

The Regulatory Protein RhlR (RhIR) is a 241-amino-acid transcriptional regulator with a molecular weight of 27,577.59 Da and a theoretical pI of 6.66, suggesting it is nearly neutral at physiological pH. This near-neutral charge distribution is confirmed by the balance between 28 negatively charged residues (Asp + Glu) and 27 positively charged residues (Arg + Lys), which could favour dynamic binding and unbinding with DNA or other regulatory proteins. Leucine (11.6%) is the most abundant amino acid, supporting hydrophobic core stability, while alanine, serine, and arginine each contribute significantly to its structural and functional versatility. The GRAVY score (-0.278) indicates moderate hydrophilicity, favouring solubility while retaining some hydrophobic character for structural integrity. The aliphatic index (91.08) reflects good thermal stability, essential for sustained bacterial regulatory activity under stress conditions. However, the instability index (56.53)

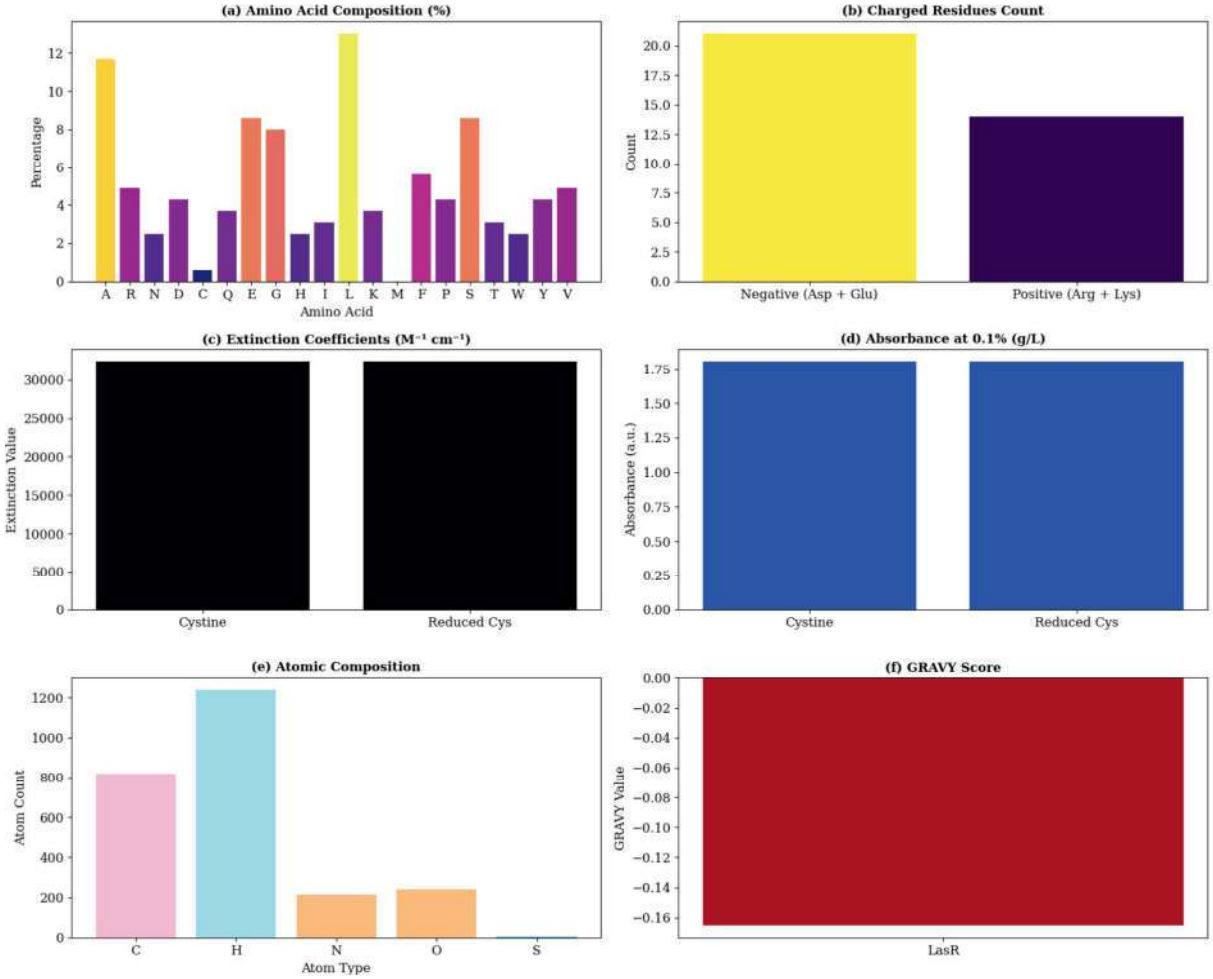


Figure 9.7: Physicochemical profile of LasR ligand-binding domain (LasR): (a) Amino acid distribution (b) Charged residues count (c) Extinction coefficients (d) Absorbance (e) Atomic composition (f) GRAVY Score

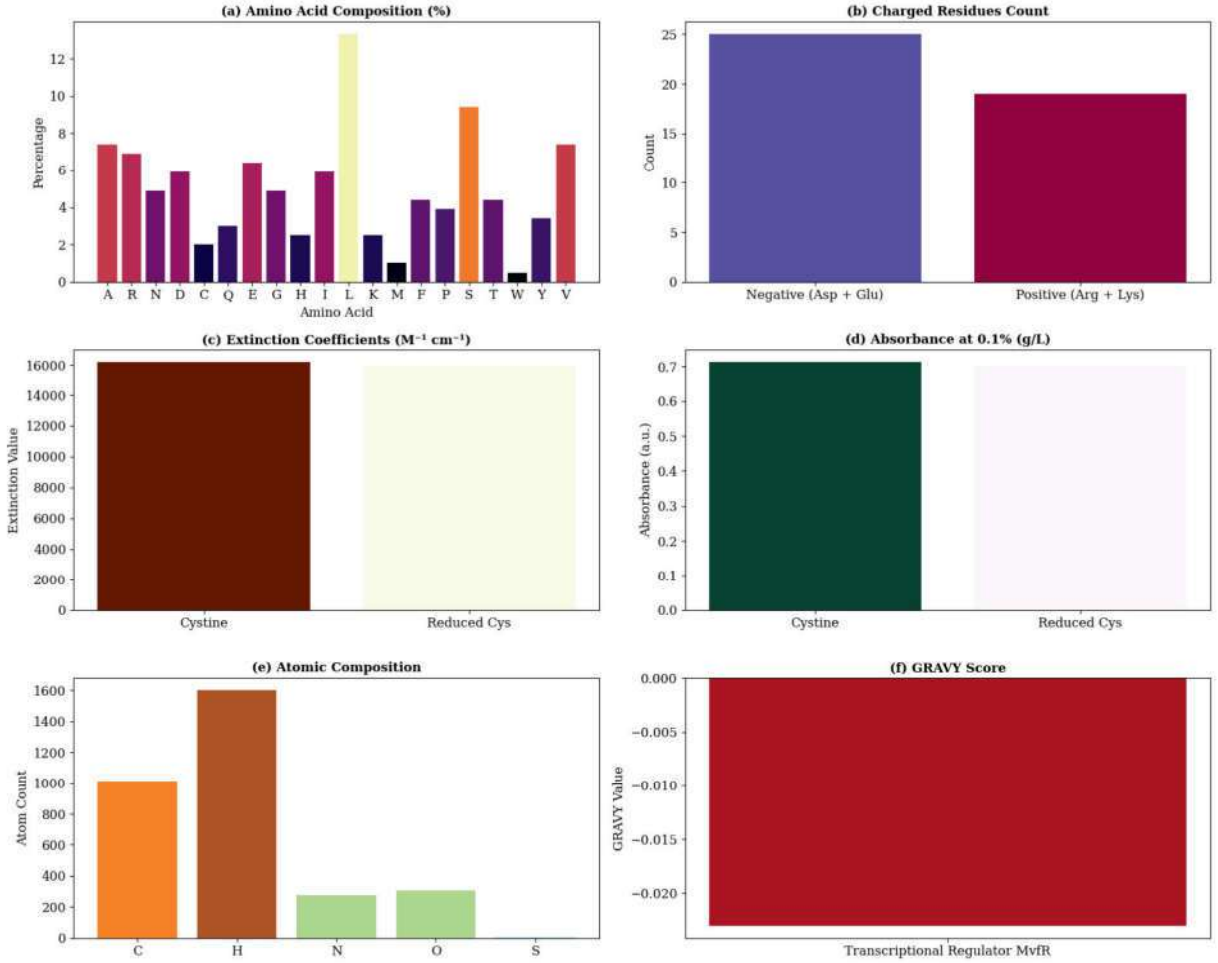


Figure 9.8: Physicochemical profile of PqsR coinducer-binding domain (PqsR/MvfR): (a) Amino acid distribution (b) Charged residues count (c) Extinction coefficients (d) Absorbance (e) Atomic composition (f) GRAVY Score

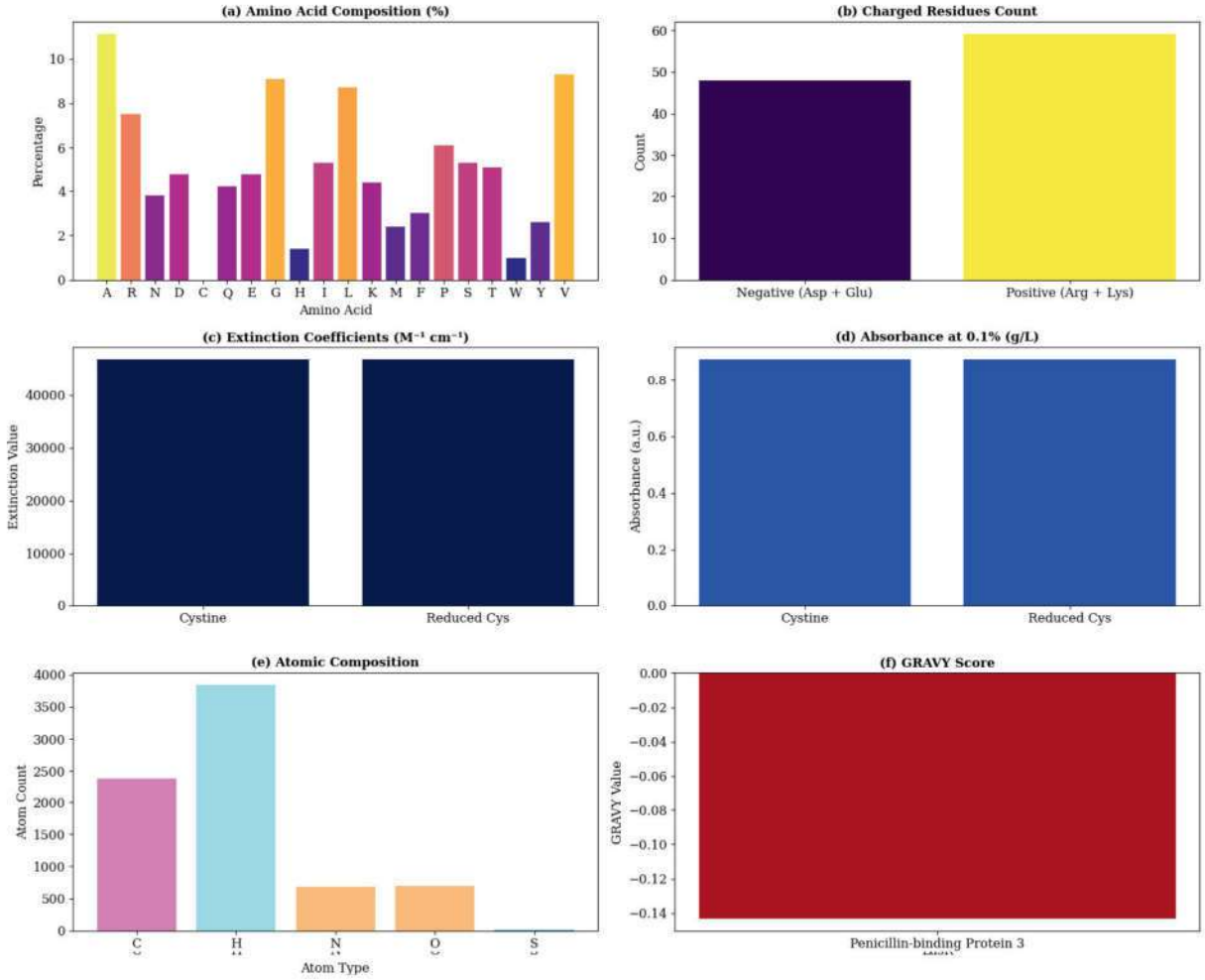


Figure 9.9: Physicochemical profile of Penicillin-Binding Protein 3 (PBP3): (a) Amino acid distribution (b) Charged residues count (c) Extinction coefficients (d) Absorbance (e) Atomic composition (f) GRAVY Score

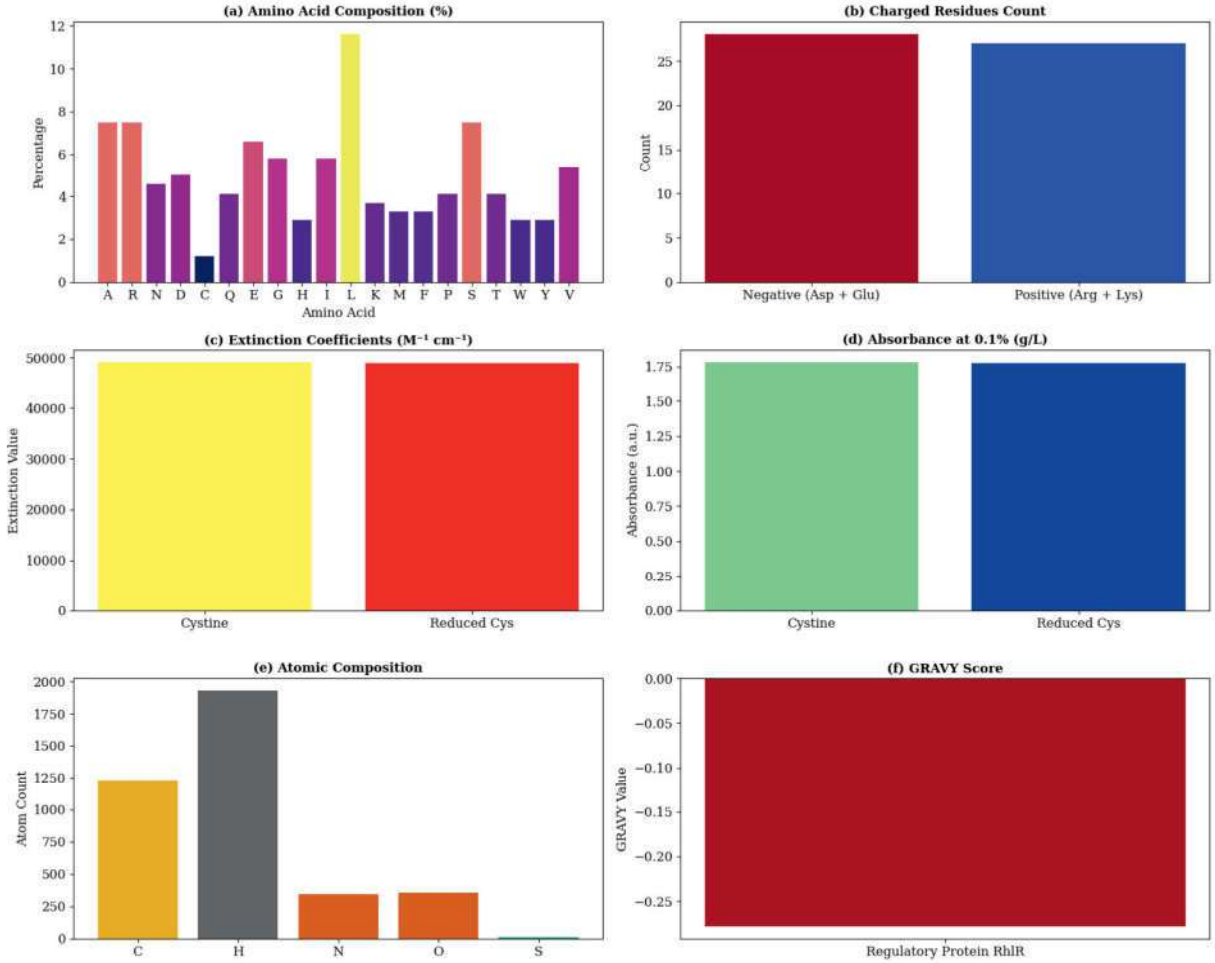


Figure 9.10: Physicochemical profile of Regulatory protein RhlR (RhIR): (a) Amino acid distribution (b) Charged residues count (c) Extinction coefficients (d) Absorbance (e) Atomic composition (f) GRAVY Score

categorizes it as unstable, indicating that it may require protective interactions with DNA, proteins, or small molecules to maintain its functional conformation. The high extinction coefficient (49,055 $M^{-1}cm^{-1}$) means it can be readily monitored spectrophotometrically (Figure 9.10). Combined, these physicochemical traits support RhlR's role in quorum-sensing regulation, where flexibility, DNA-binding capability, and environmental responsiveness are crucial for modulating virulence gene expression in antimicrobial resistance contexts.

9.3.2.3. Physicochemical properties of anthelmintic proteins

9.3.2.3.1. ATP synthase subunit a (ATP synthase)

ATP synthase subunit a is a 231-residue, strongly hydrophobic, transmembrane protein with a molecular weight of 25,678.37 Da and a theoretical pI of 6.63, indicating near-neutral charge under physiological pH. It is rich in leucine (15.6%), serine (12.6%), phenylalanine (9.1%), and threonine (8.7%), along with high isoleucine (8.2%) content, a hallmark of membrane-spanning helices. The GRAVY score (0.821) highlights strong hydrophobicity, essential for embedding in the lipid bilayer of the mitochondrial membrane, where ATP synthesis occurs. With 9 negatively charged and 8 positively charged residues, the charge balance remains nearly neutral, which aids in maintaining structural stability within the hydrophobic environment of the membrane. A high aliphatic index (114.03) suggests strong thermal stability, supporting its function in energy production even under varying temperature conditions. The extinction coefficient (31,065 M^{-1} cm^{-1}) and aromatic amino acid composition make spectrophotometric detection feasible (Figure 9.11). An instability index of 35.36 classifies it as stable, in line with its role as a durable rotary motor subunit in ATP synthesis, a critical process for parasite survival and energy metabolism.

9.3.2.3.2. Cytochrome c oxidase subunit 1 (COX1)

Cytochrome c oxidase subunit 1 (COX1) is a key enzyme in the mitochondrial respiratory chain that catalyzes the reduction of oxygen to water, facilitating ATP production. The provided physicochemical data reveal that this protein has a distinct

amino acid profile optimized for membrane embedding, with a likely high proportion of hydrophobic residues aiding in transmembrane anchoring. Its calculated molecular weight and pI suggest that it operates efficiently in the mitochondrial inner membrane environment, maintaining functional stability in hydrophobic lipid surroundings. The moderate aliphatic index and hydropathicity values indicate adaptability to varying membrane fluidities, which may be crucial for parasitic survival in diverse host conditions. The instability index provides an indication of protein turnover, suggesting this protein maintains sufficient stability to function as a core respiratory complex component, but may require protein chaperones for assembly and repair (Figure 9.12). These physicochemical traits not only highlight its critical role in oxidative phosphorylation but also present potential vulnerabilities, such as dependence on membrane integrity, that could be targeted in anthelmintic therapy.

9.3.2.3.3. Heat Shock Protein 70 (HSP70)

Heat shock protein 70 (HSP70) is a 132-residue chaperone protein with a molecular weight of 14,862.68 Da and a theoretical pI of 5.03, indicating a moderately acidic nature. The amino acid profile shows a predominance of glutamic acid (11.4%), lysine (9.8%), asparagine (7.6%), and threonine (7.6%), reflecting its potential for extensive hydrogen bonding and electrostatic interactions during protein folding. The absence of cysteine and tryptophan suggests limited disulfide-mediated stability and lower intrinsic absorbance accuracy. The protein carries 24 negatively charged residues (Asp + Glu) and 20 positively charged residues (Arg + Lys), indicating a slightly more acidic overall charge. With an instability index of 26.15, HSP70 is predicted to be stable under physiological conditions. Its aliphatic index (67.20) points to moderate thermostability, while a GRAVY score of –0.818 indicates high hydrophilicity, consistent with its role in interacting with unfolded polypeptides in aqueous environments. The estimated half-life (1.1 hours in mammalian cells) suggests a relatively short intracellular persistence, fitting for a stress-induced chaperone that responds quickly to cellular damage (Figure 9.13). Biologically, these properties align with HSP70's function in protein quality control, refolding denatured proteins, and protecting cells from proteotoxic stress during infection or heat shock.

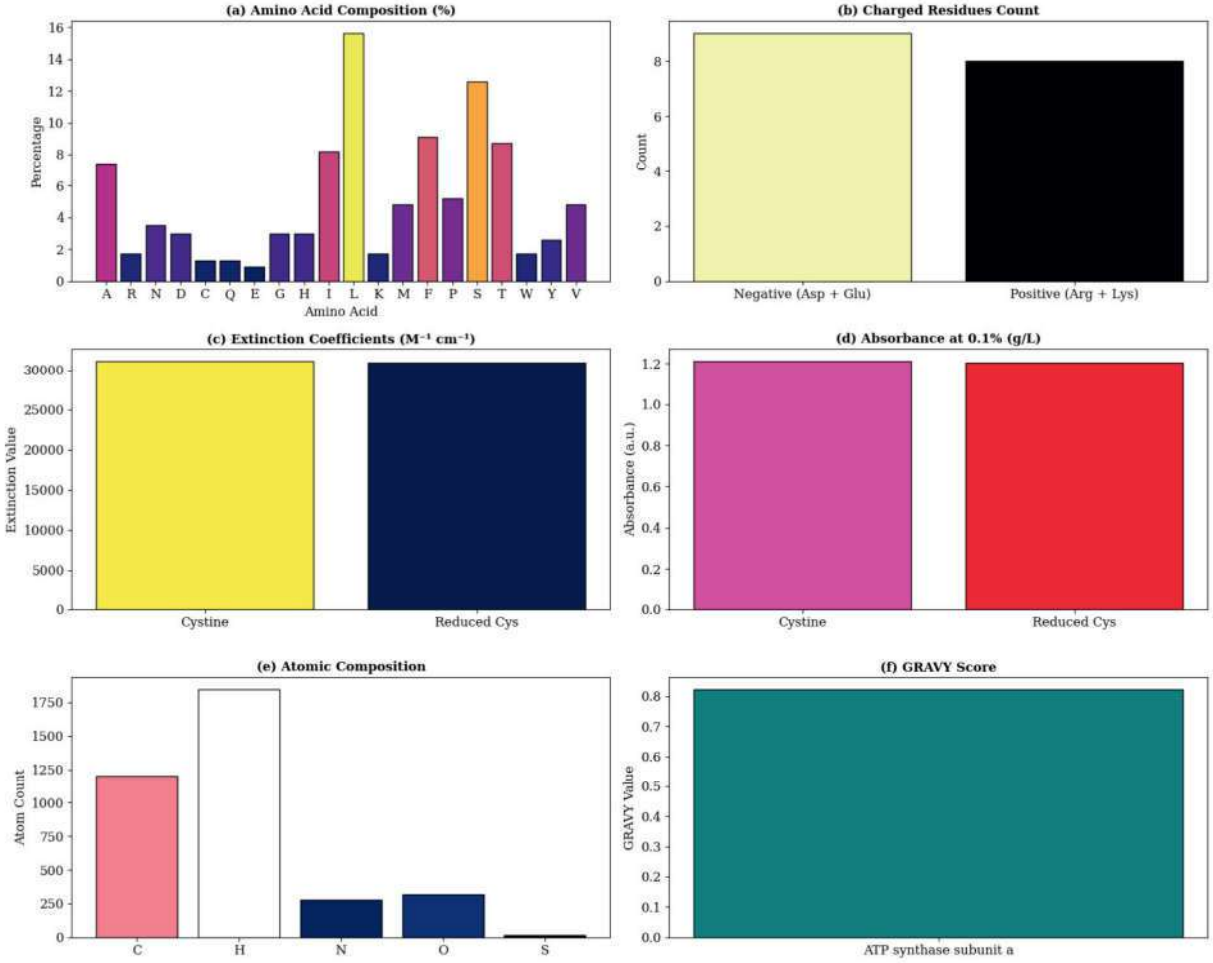


Figure 9.11: Physicochemical profile of ATP synthase subunit a (ATP synthase): (a) Amino acid distribution (b) Charged residues count (c) Extinction coefficients (d) Absorbance (e) Atomic composition (f) GRAVY Score

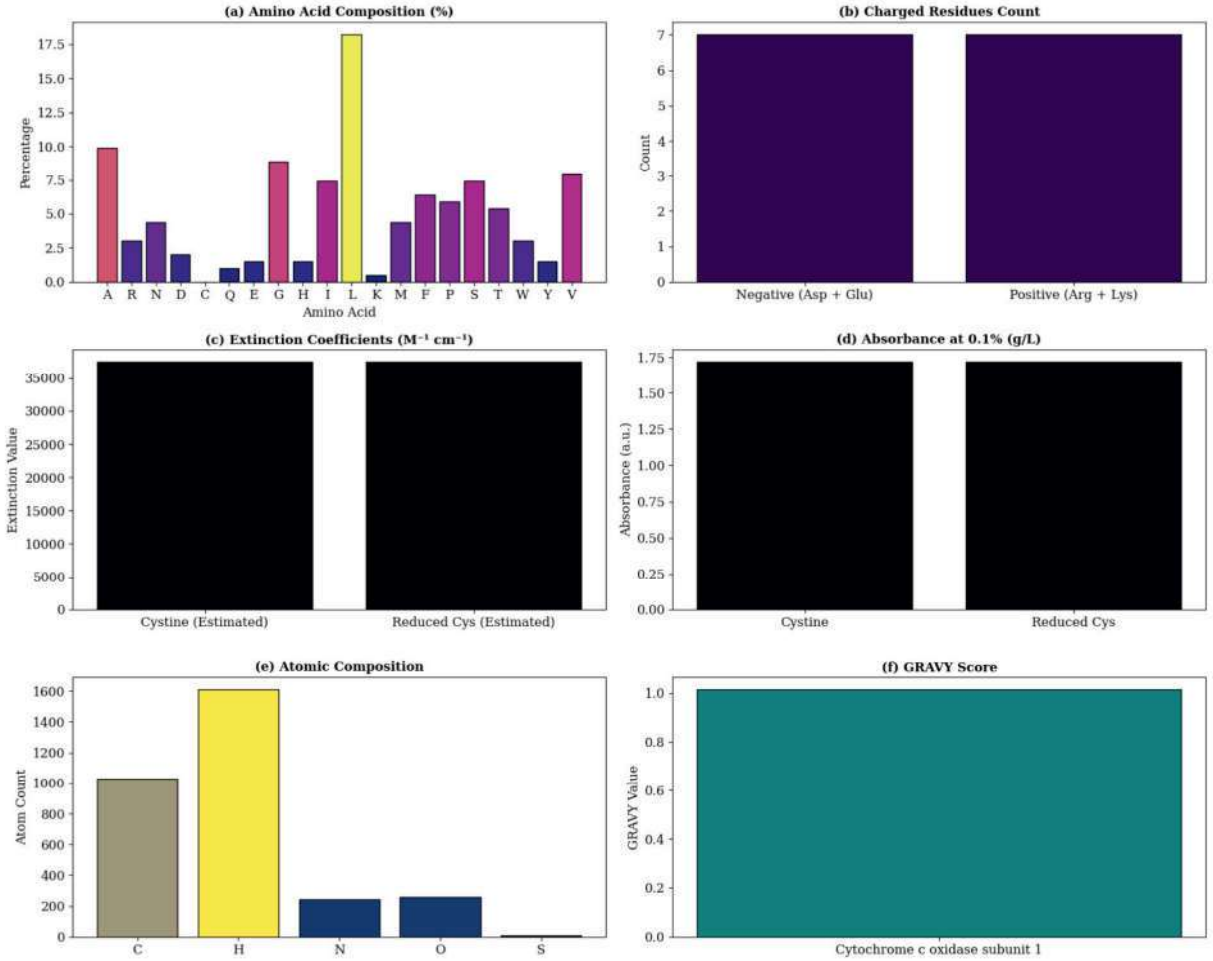


Figure 9.12: Physicochemical profile of Cytochrome c Oxidase subunit 1 (COX1): (a) Amino acid distribution (b) Charged residues count (c) Extinction coefficients (d) Absorbance (e) Atomic composition (f) GRAVY Score

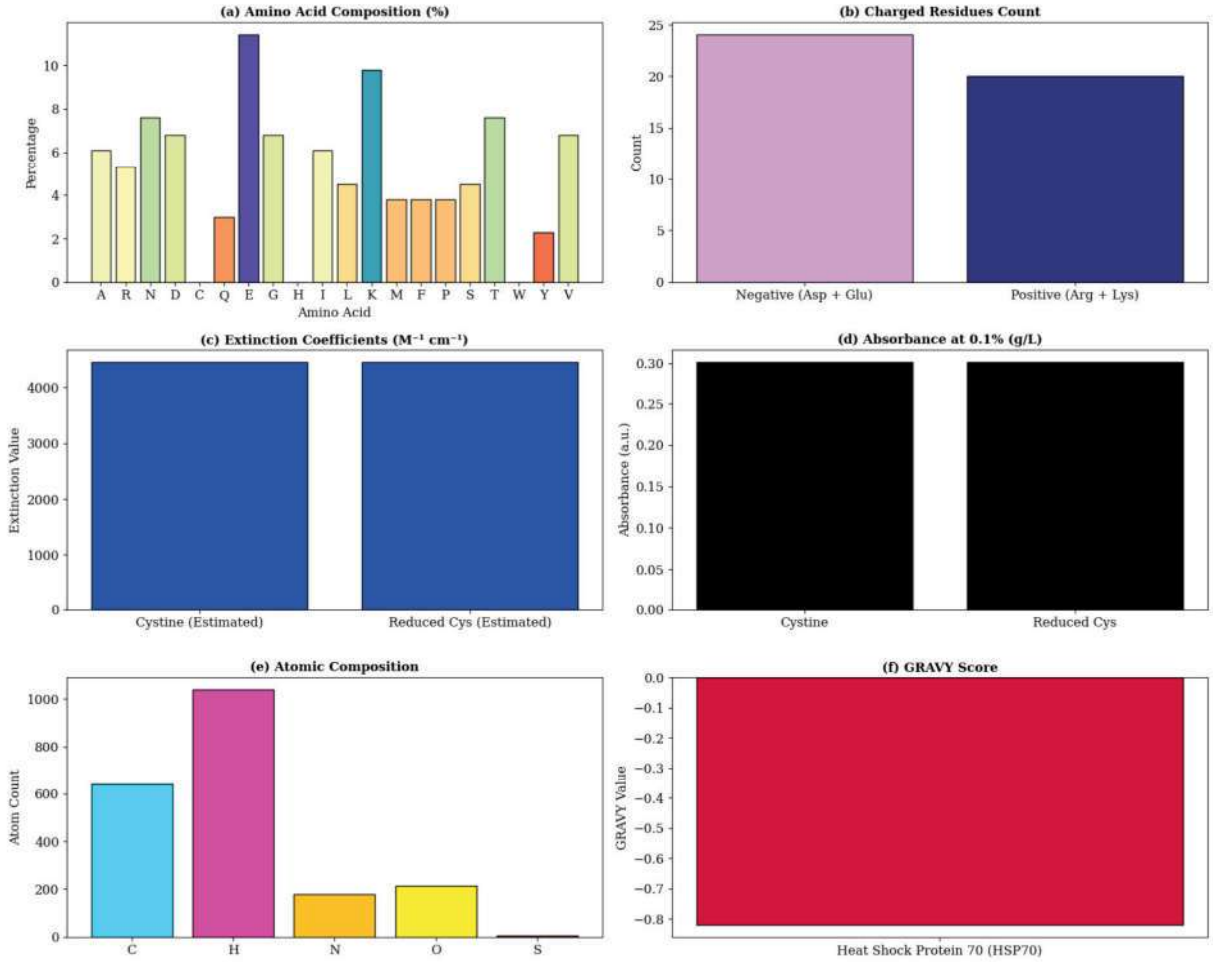


Figure 9.13: Physicochemical profile of Heat Shock Protein 70 (HSP70): (a) Amino acid distribution (b) Charged residues count (c) Extinction coefficients (d) Absorbance (e) Atomic composition (f) GRAVY Score

9.3.2.3.4. NADH-ubiquinone oxidoreductase chain 1 (Complex 1)

NADH-ubiquinone oxidoreductase chain 1 (Complex 1) is a 308-residue, hydrophobic-rich membrane protein with a molecular weight of 34,841.71 Da and a theoretical pI of 8.46, suggesting a predominantly basic nature. It is highly enriched in leucine (15.6%), serine (9.7%), and phenylalanine (9.1%), along with significant alanine (8.1%) and methionine (7.5%) content, a composition consistent with a tightly packed, hydrophobic transmembrane structure. The GRAVY score (0.791) confirms strong hydrophobicity, critical for membrane integration and stability in the lipid bilayer. The charge profile shows 14 negatively charged residues and 16 positively charged residues, maintaining a slight basic tilt. A high aliphatic index (110.84) points to strong thermostability, supporting its function in the mitochondrial respiratory chain under fluctuating cellular conditions. The extinction coefficient (51,005 M^{-1} cm^{-1}) suggests a substantial aromatic amino acid presence, aiding in spectrophotometric tracking. With an instability index of 36.58, it is classified as stable, correlating well with its role as a durable electron transport component in oxidative phosphorylation, a process essential for ATP synthesis and parasite survival in varying environments (Figure 9.14).

9.3.2.3.5. Extracellular Globin-3/Erythrocruorin (Ext. Globin-3)

Extracellular Globin-3/Erythrocruorin (Ext. Globin-3) is a 146-residue protein with a molecular weight of 16,434.86 Da and a theoretical pI of 6.14, indicating a near-neutral to slightly acidic nature. Its amino acid profile is notable for a high leucine content (15.1%), followed by aspartic acid (10.3%) and alanine (9.6%), suggesting a structure with significant hydrophobic core stability and moderate acidic side chain prevalence. The protein contains 23 negatively charged residues (Asp + Glu) and 20 positively charged residues (Arg + Lys), indicating a near-balanced charge distribution, which could contribute to structural stability in extracellular environments. The instability index of 32.57 classifies the protein as stable, with a high aliphatic index (109.66) implying strong thermal stability, a beneficial trait for proteins exposed to variable environmental temperatures. The GRAVY score (-0.275) suggests mild hydrophilicity, allowing balanced interaction between aqueous

surroundings and hydrophobic core regions. The extinction coefficient (17,990 M^{-1} cm^{-1}) indicates moderate aromatic residue content, important for optical detection and quantification (Figure 9.15). These properties align with its presumed role in oxygen transport and extracellular signaling in parasitic organisms, where environmental adaptability and stability are key.

9.3.2.4. Physicochemical properties of anti-inflammatory proteins

9.3.2.4.1. Nuclear Factor kappa B p50 (NF-κB p50)

Nuclear factor kappa-light-chain-enhancer of activated B cells (NF-κB p50) is a 311-amino acid transcription factor with a molecular weight of 34,794.83 Da and a theoretical pI of 8.27, indicating it is predominantly basic under physiological conditions, which supports its strong affinity for the negatively charged DNA backbone. It contains 41 positively charged residues (Arg + Lys) and 39 negatively charged residues (Asp + Glu), reflecting a slight positive bias that enhances nucleic acid binding. Its GRAVY score of -0.390 suggests an overall hydrophilic nature, compatible with its nuclear localization and role in protein-protein/DNA interactions. NF-κB p50 exhibits a moderate extinction coefficient of 23,755 M^{-1} cm^{-1}, making it moderately detectable via UV spectroscopy. The instability index of 39.44 categorizes it as stable, correlating with its requirement for sustained nuclear presence during inflammatory signaling. Residue composition shows enrichment in glycine and leucine (8.4% each), contributing to structural flexibility and stability of its DNA-binding domains. The high aliphatic index (82.09) indicates good thermostability, aligning with its functional resilience during stress responses (Figure 9.16). Functionally, these properties equip NF-κB p50 to act as a rapid-response transcription factor, binding DNA efficiently, resisting degradation, and orchestrating the transcription of multiple pro-inflammatory and survival-related genes.

9.3.2.4.2. Tumour Necrosis Factor-alpha (TNF-α)

Tumour necrosis factor-alpha (TNF-α) is a 132-amino acid cytokine with a molecular weight of 14,628.77 Da and a theoretical pI of 5.50, indicating it is slightly acidic at physiological pH. This charge profile supports its extracellular signaling role,

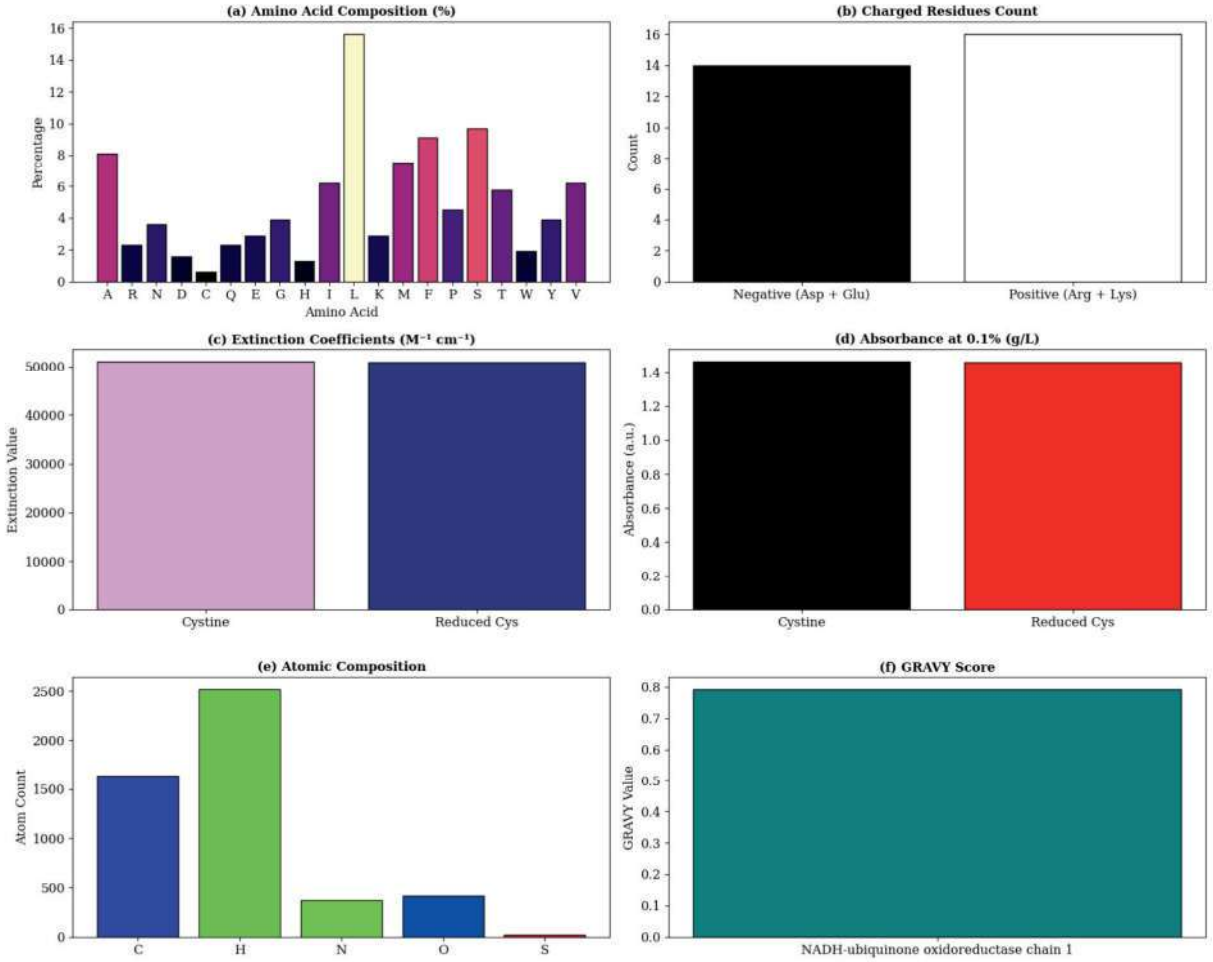


Figure 9.14: Physicochemical profile of NADH-Ubiquinone Oxidoreductase chain 1 (Complex I): (a) Amino acid distribution (b) Charged residues count (c) Extinction coefficients (d) Absorbance (e) Atomic composition (f) GRAVY Score

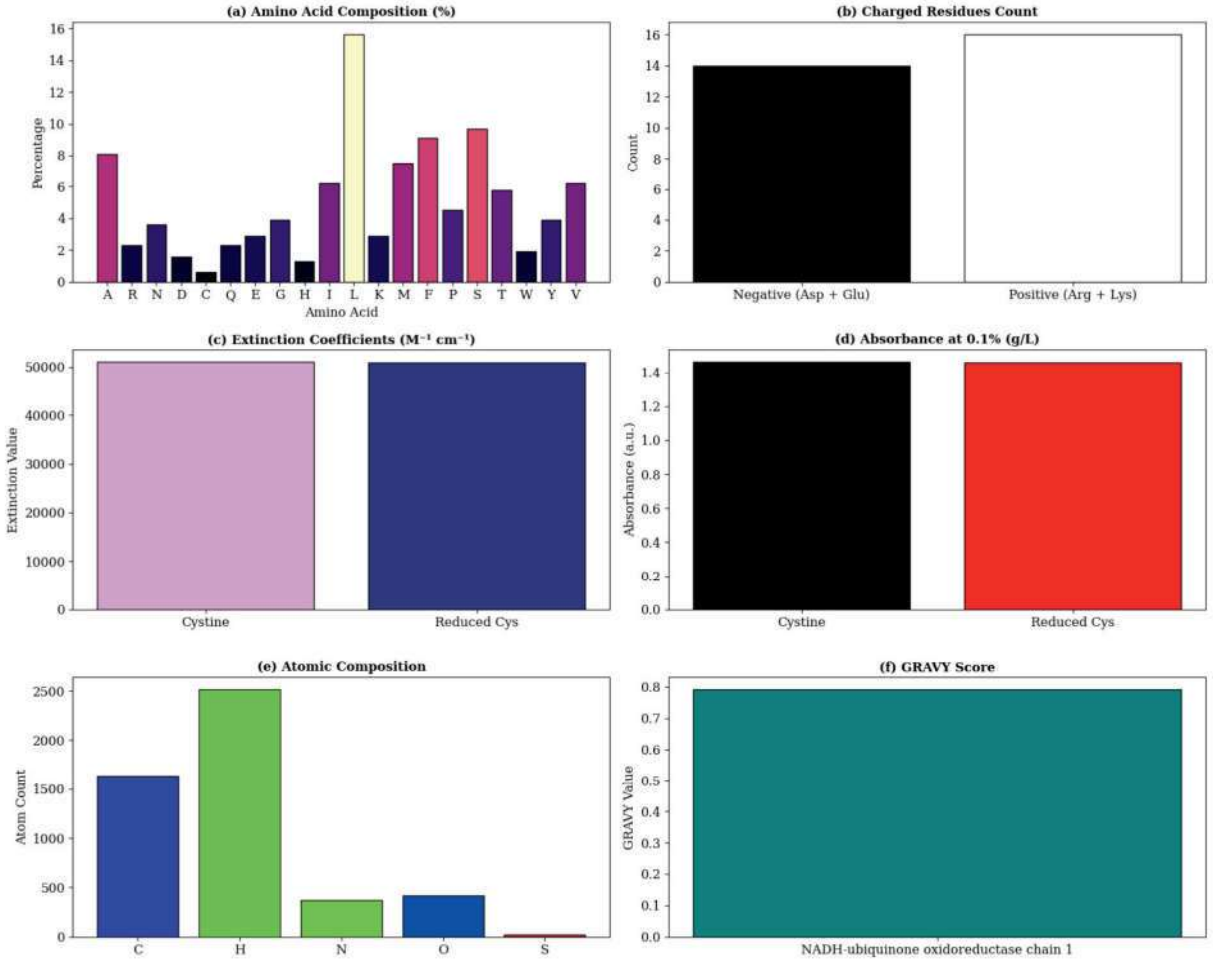


Figure 9.15: Physicochemical profile of Extracellular Globin-3/Erythrocruorin (Ext. Globin-3): (a) Amino acid distribution (b) Charged residues count (c) Extinction coefficients (d) Absorbance (e) Atomic composition (f) GRAVY Score

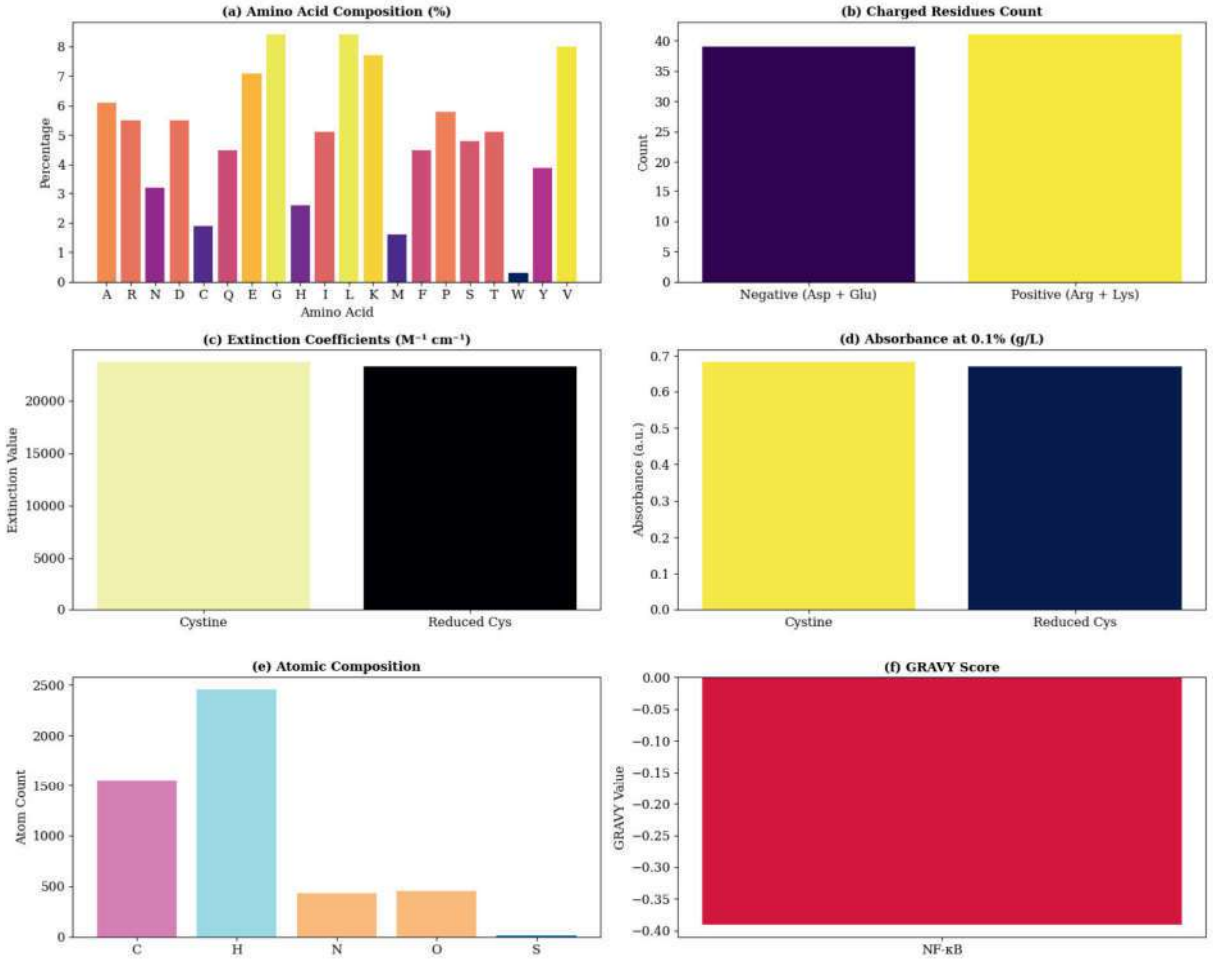


Figure 9.16: Physicochemical profile of Nuclear Factor kappa B p50 (NF-κB p50): (a) Amino acid distribution (b) Charged residues count (c) Extinction coefficients (d) Absorbance (e) Atomic composition (f) GRAVY Score

facilitating interactions with cell-surface TNF receptors via electrostatic complementarity. The ratio of negatively (12) to positively (9) charged residues confirms a modest acidic bias. Its GRAVY score of 0.060 suggests near-neutral hydropathicity, reflecting a balance between hydrophobic and hydrophilic residues, ideal for a protein that requires both soluble transport and stable receptor embedding during inflammation. The high aliphatic index (110.00) indicates exceptional thermostability, consistent with its role in inflammatory cascades where it must remain active under varying physiological conditions. The extinction coefficient (21,555 M^{-1} cm^{-1}) allows for efficient spectrophotometric quantification in laboratory assays. Notably, the instability index (25.98) categorizes TNF-α as stable, reinforcing its reliability as a persistent inflammatory mediator until degraded by cellular regulation (Figure 9.17). Functionally, these physicochemical features make TNF-α a potent and durable pro-inflammatory signaler, capable of enduring extracellular conditions while triggering receptor-mediated pathways that lead to immune activation, apoptosis, or inflammation resolution depending on the cellular context.

9.3.2.4.3. Human Inducible Nitric Oxide Synthase (iNOS)

Human Inducible nitric oxide synthase (iNOS) is a 421-amino acid enzyme with a molecular weight of 48,633.57 Da and a theoretical pI of 6.75, suggesting a nearly neutral charge distribution under physiological conditions. It contains 49 negatively charged residues and 47 positively charged residues, indicating balanced electrostatic characteristics, which can support dynamic interactions with cofactors and substrates. Aromatic residue content is relatively high, as reflected in a strong extinction coefficient of 97,330 M^{-1} cm^{-1}, enabling sensitive UV absorbance-based detection. Compositionally, iNOS is rich in leucine (7.4%), glycine/valine (6.7% each), and arginine (6.4%), contributing to structural flexibility and cofactor binding adaptability. The GRAVY score of -0.403 indicates a predominantly hydrophilic nature, favouring solubility in the cytosolic environment where nitric oxide synthesis occurs (Figure 9.18). Its instability index of 46.80 classifies it as unstable, reflecting a short-lived, tightly regulated nature, consistent with the biological necessity to prevent excessive nitric oxide accumulation and associated oxidative stress. With a

short half-life in yeast and *Escherichia coli*, iNOS is likely transiently expressed during inflammatory responses, tightly controlled at transcriptional and translational levels.

9.3.2.4.4. Janus kinase 2 (JAK2)

Janus kinase 2 (JAK2) is a 284-amino acid kinase fragment with a theoretical pI of 6.79 and a molecular weight of 33,302.23 Da. It shows a near-balanced charge distribution (41 negatively charged vs. 40 positively charged residues), suggesting a neutral electrostatic profile conducive for versatile protein–protein interactions in signaling. Its amino acid composition is enriched in leucine (10.2%) and lysine (8.1%), supporting structural stability and potential for hydrogen bonding. The extinction coefficient (36,120 M^{-1} cm^{-1} in cystine form) indicates moderate aromatic residue content, sufficient for optical quantification. The instability index of 49.46 categorizes JAK2 as unstable, implying that its folding may be sensitive to environmental factors, possibly linked to its role as a tightly regulated kinase in inflammatory cascades. The aliphatic index of 84.37 indicates moderate thermostability, while the GRAVY score of -0.571 reflects hydrophilicity, enhancing solubility in cytosolic conditions. With a short half-life in mammalian cells (0.8 hours), JAK2 activity is likely tightly controlled to prevent aberrant signaling (Figure 9.19). These traits align with JAK2's biological role in cytokine receptor-mediated signal transduction, where rapid activation and deactivation are essential for preventing excessive inflammatory responses.

9.3.2.4.5. Human Cyclooxygenase-2 (COX-2)

Human Cyclooxygenase-2 (COX-2) consists of 528 amino acids, has a theoretical pI of 6.83, and a molecular weight of 60,860.67 Da, indicating it is a moderately acidic and large enzyme. Its amino acid composition is rich in leucine (8.7%) and glycine (6.6%), which can contribute to hydrophobic interactions and flexibility in its catalytic site. The protein contains 56 negatively charged residues and 54 positively charged residues, suggesting a balanced electrostatic profile, which may facilitate diverse substrate and inhibitor interactions. The extinction coefficient (73,730 M^{-1} cm^{-1} for cystine form) reflects a high aromatic amino acid content, useful

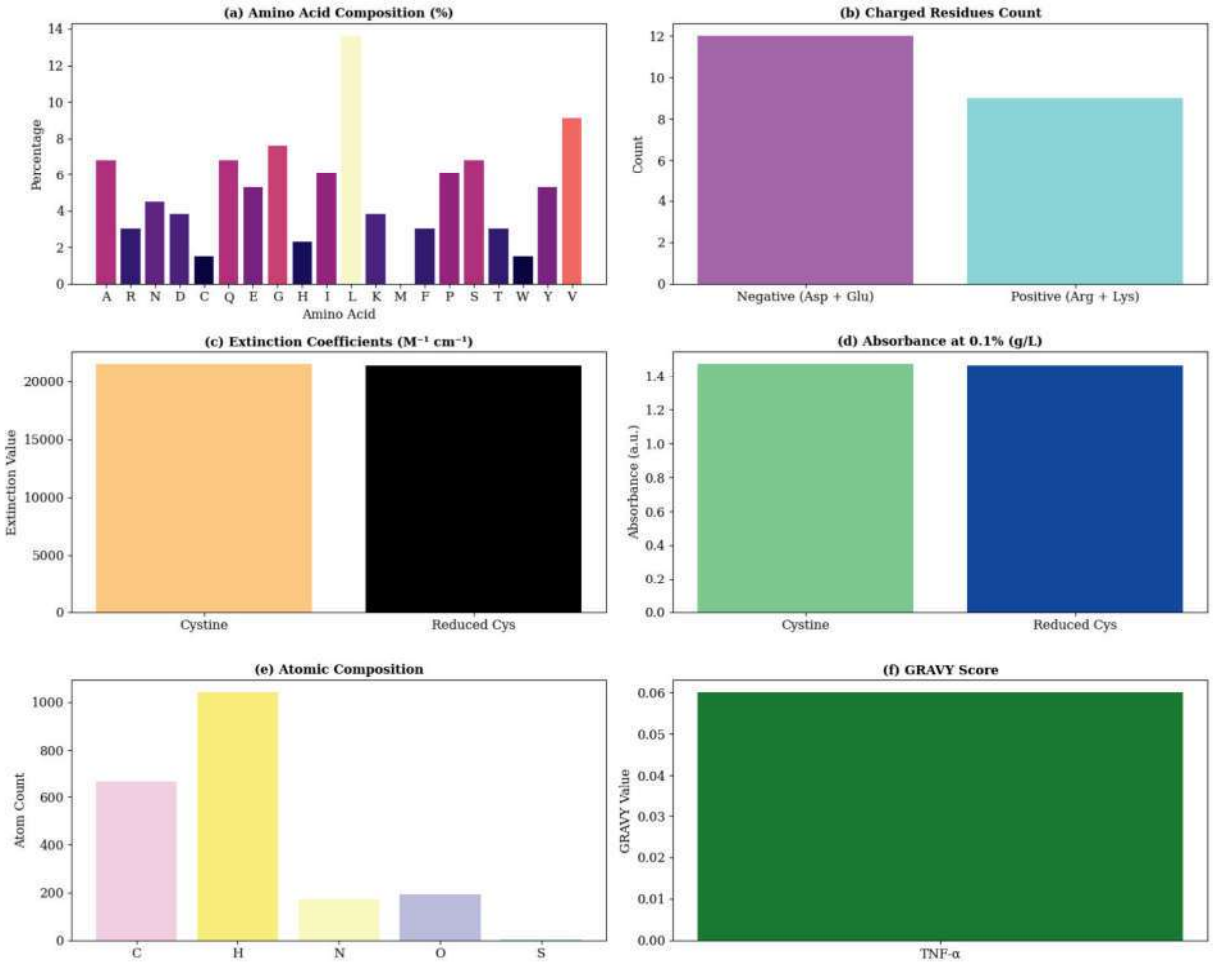


Figure 9.17: Physicochemical profile of Tumour Necrosis Factor-alpha (TNF-α): (a) Amino acid distribution (b) Charged residues count (c) Extinction coefficients (d) Absorbance (e) Atomic composition (f) GRAVY Score

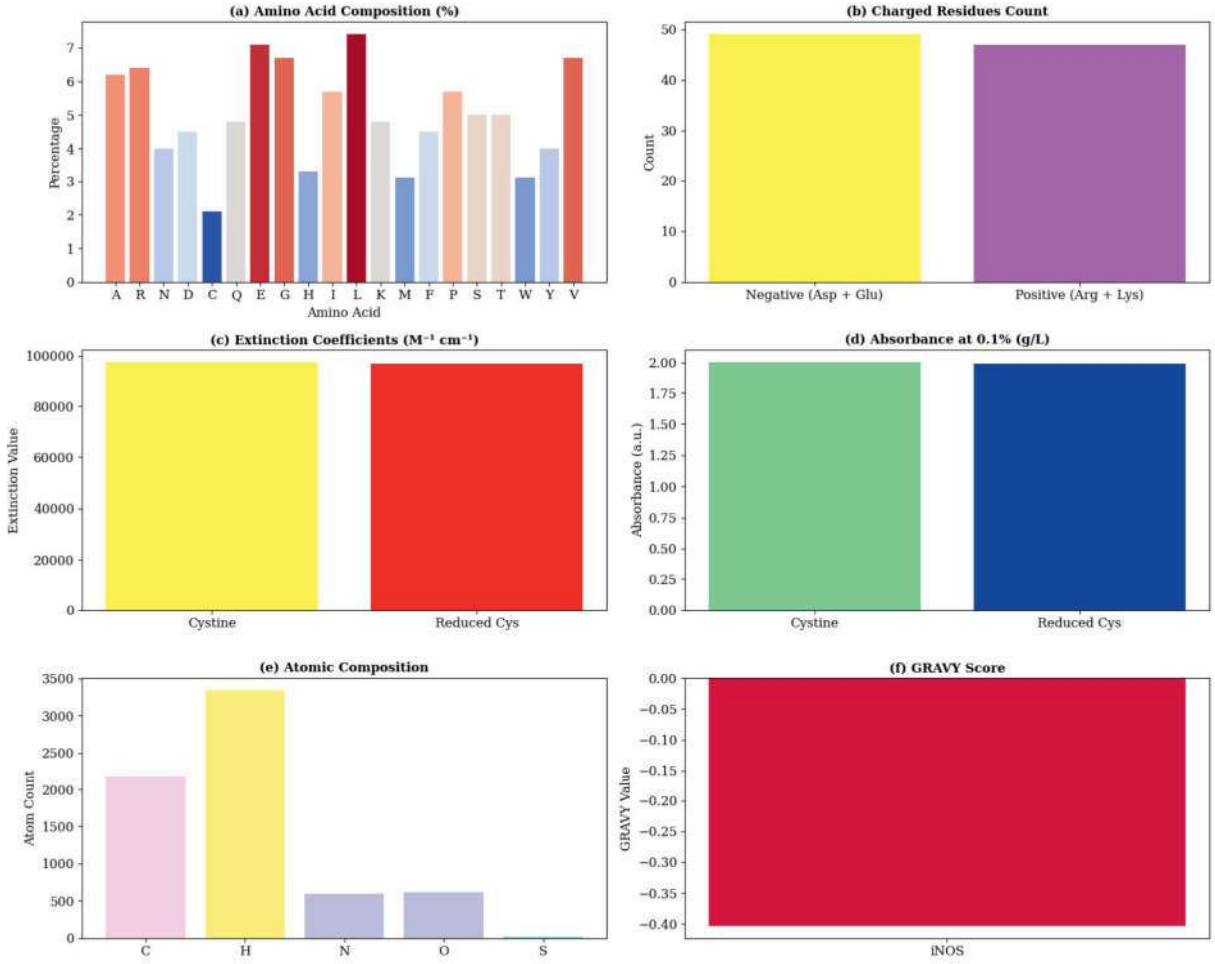


Figure 9.18: Physicochemical profile of Human Inducible Nitric Oxide Synthase (iNOS): (a) Amino acid distribution (b) Charged residues count (c) Extinction coefficients (d) Absorbance (e) Atomic composition (f) GRAVY Score

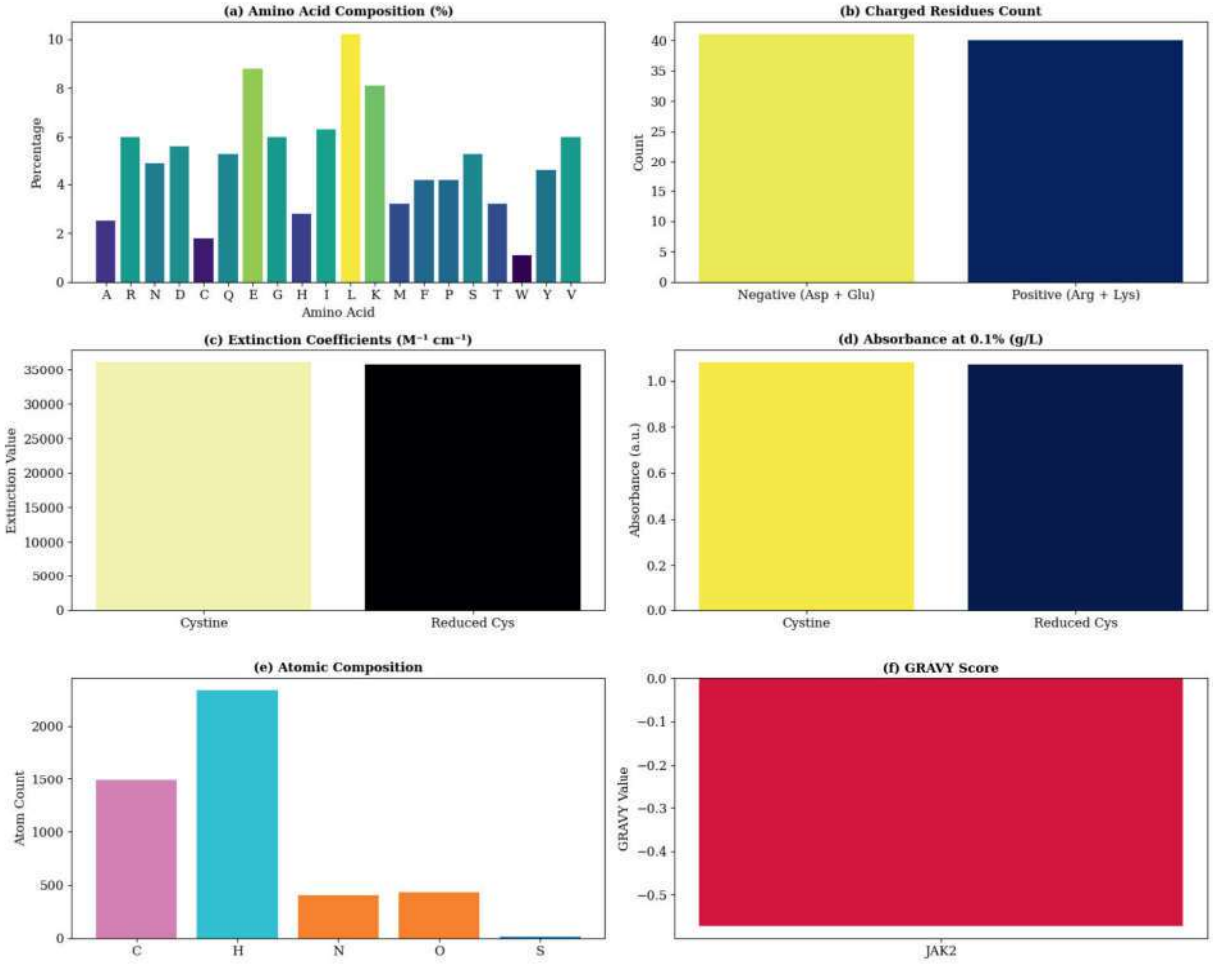


Figure 9.19: Physicochemical profile of Janus Kinase 2 (JAK2): (a) Amino acid distribution (b) Charged residues count (c) Extinction coefficients (d) Absorbance (e) Atomic composition (f) GRAVY Score

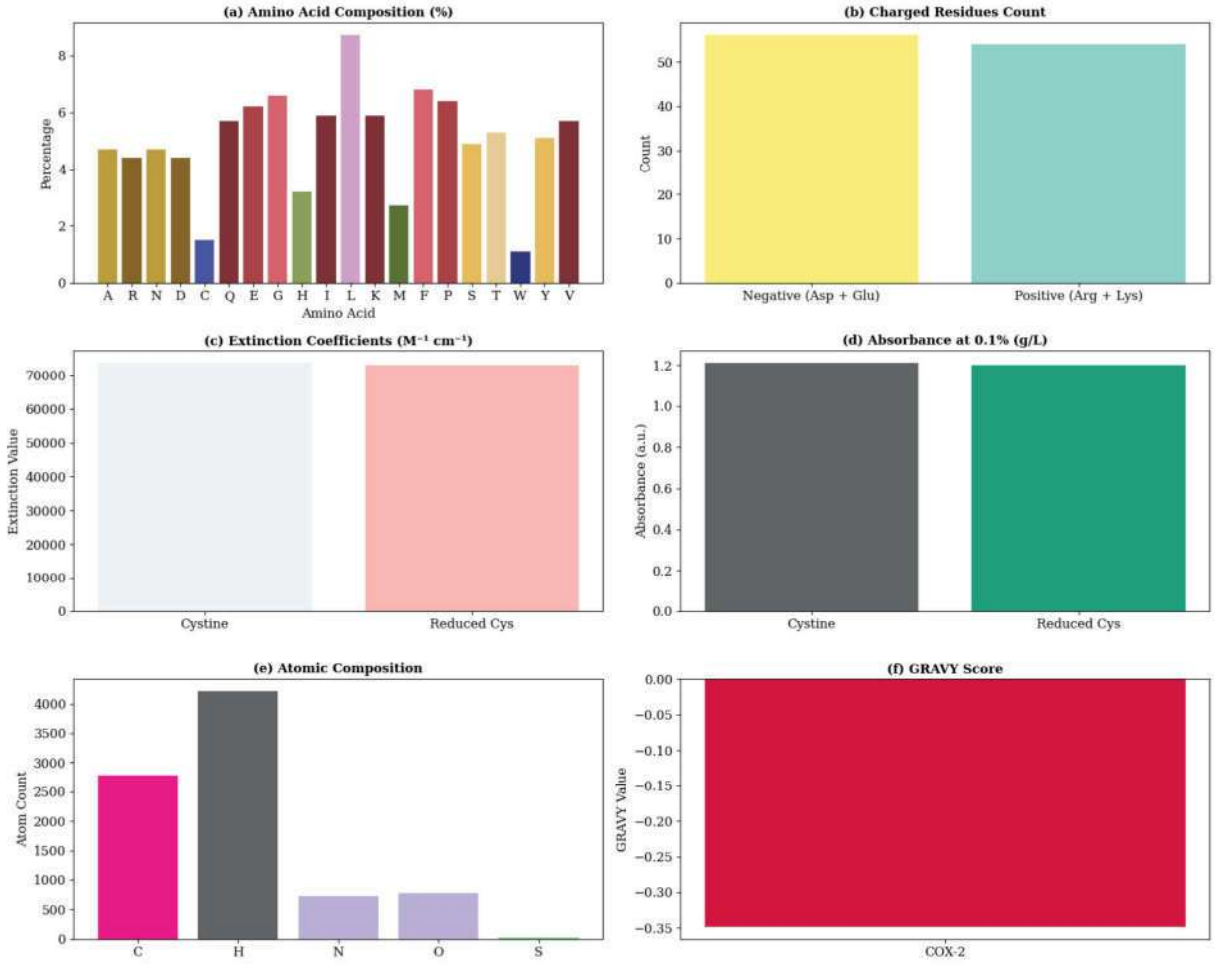


Figure 9.20: Physicochemical profile of Human Cyclooxygenase-2 (COX-2): (a) Amino acid distribution (b) Charged residues count (c) Extinction coefficients (d) Absorbance (e) Atomic composition (f) GRAVY Score

for spectrophotometric quantification. With an instability index of 38.84, COX-2 is classified as stable, while its aliphatic index of 78.09 suggests moderate thermostability. The negative GRAVY score (-0.348) indicates overall hydrophilicity, which may aid in solubility and activity in aqueous cellular environments (Figure 9.20). These physicochemical characteristics are consistent with COX-2's role as a membrane-associated enzyme catalyzing prostaglandin biosynthesis during inflammation, making it a key drug target for anti-inflammatory therapeutics.

9.3.2.5. Physicochemical properties of antidiabetic proteins

9.3.2.5.1. Dipeptidyl Peptidase 4 (DPP4)

Physicochemical properties of Dipeptidyl Peptidase 4 (DPP4) were given in (Figure 9.21) DPP4 (MW: 84,079.58 Da, pI 5.67) contains 725 amino acids with a balanced distribution of polar and nonpolar residues. Serine (8.7%) and tyrosine (7.7%) are notably abundant, suggesting potential roles in catalytic function and ligand binding via hydrogen bonding and aromatic stacking interactions. The protein shows 83 negatively charged residues (Asp + Glu) and 67 positively charged residues (Arg + Lys), indicating a net negative charge at physiological pH, which may influence substrate specificity and inhibitor interaction.

The GRAVY score (-0.406) suggests a moderately hydrophilic nature, favouring aqueous solubility but retaining hydrophobic patches for membrane or substrate interactions. The aliphatic index (76.76) points to moderate thermostability, suitable for functioning under physiological conditions. The extinction coefficient (194,190 M^{-1} cm^{-1}) is exceptionally high, reflecting a significant number of aromatic residues, which facilitates spectrophotometric quantification. However, the instability index (44.32) classifies DPP4 as unstable *in vitro*, which could impact recombinant expression yields and storage stability. Biologically, these properties align with DPP4's function as a serine protease involved in incretin degradation, where the structural balance between hydrophilic and hydrophobic residues and a high aromatic content supports precise substrate recognition and binding (Guruprasad et al., 1990).

9.3.2.5.2. Physicochemical properties of Insulin Receptor

The insulin receptor (MW: 67,731.58 Da, pI 6.55) comprises 590 amino acids with leucine (11.2%) being highly abundant, reflecting its likely role in maintaining hydrophobic core stability and receptor dimerization. Notably, cysteine accounts for 5.6% of residues, forming multiple disulfide bonds essential for extracellular domain stability and the proper ligand-binding conformation. The receptor has 68 negatively charged residues (Asp + Glu) and 64 positively charged residues (Arg + Lys), indicating near-charge balance, which may contribute to maintaining its structural integrity in the extracellular environment (Figure 9.22).

The GRAVY score (-0.319) reflects a moderately hydrophilic nature, consistent with its role as a transmembrane glycoprotein with significant extracellular exposure. The aliphatic index (83.75) suggests moderate thermal stability, which supports functional activity across physiological temperature ranges. A high extinction coefficient (92,760 M^{-1} cm^{-1}), due to aromatic residues, facilitates spectrophotometric detection in protein assays. However, the instability index (45.45) classifies the receptor as unstable *in vitro*, which can be a consideration for recombinant expression and purification. Functionally, these properties are consistent with the insulin receptor's role as a tyrosine kinase receptor that undergoes conformational changes upon insulin binding, triggering downstream glucose uptake pathways. The high cysteine content and charge distribution are particularly important for its dimeric structure and activation mechanism (Hubbard, 2013).

9.3.2.5.3. Physicochemical properties of Pancreatic Alpha Amylase (PAA)

The pancreatic alpha amylase protein consists of 495 amino acids, with a theoretical pI of 6.45 and a molecular weight of 55,791.48 Da. Glycine (10.1%) is the most abundant residue, followed by asparagine (8.5%) and valine (7.1%). The distribution of negatively charged residues (Asp + Glu: 53) is balanced by a similar proportion of positively charged residues (Arg + Lys: 50), suggesting a relatively neutral electrostatic profile at physiological pH. The atomic composition (C: 2492, H: 3727, N: 695, O: 731, S: 21) and moderate aliphatic index (67.72) reflect a protein

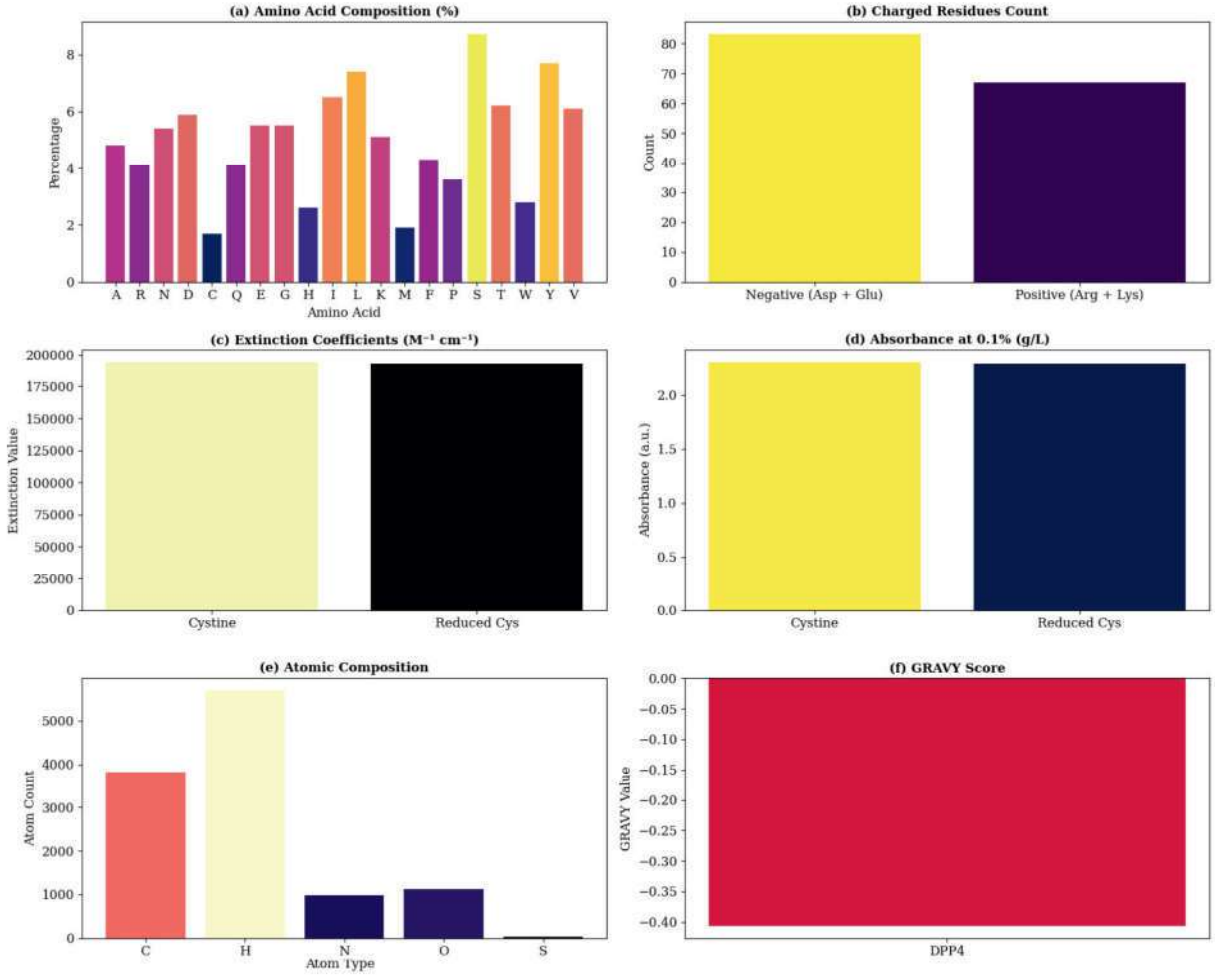


Figure 9.21: Physicochemical profile of Dipeptidyl Peptidase 4 (DPP4): (a) Amino acid distribution (b) Charged residues count (c) Extinction coefficients (d) Absorbance (e) Atomic composition (f) GRAVY Score

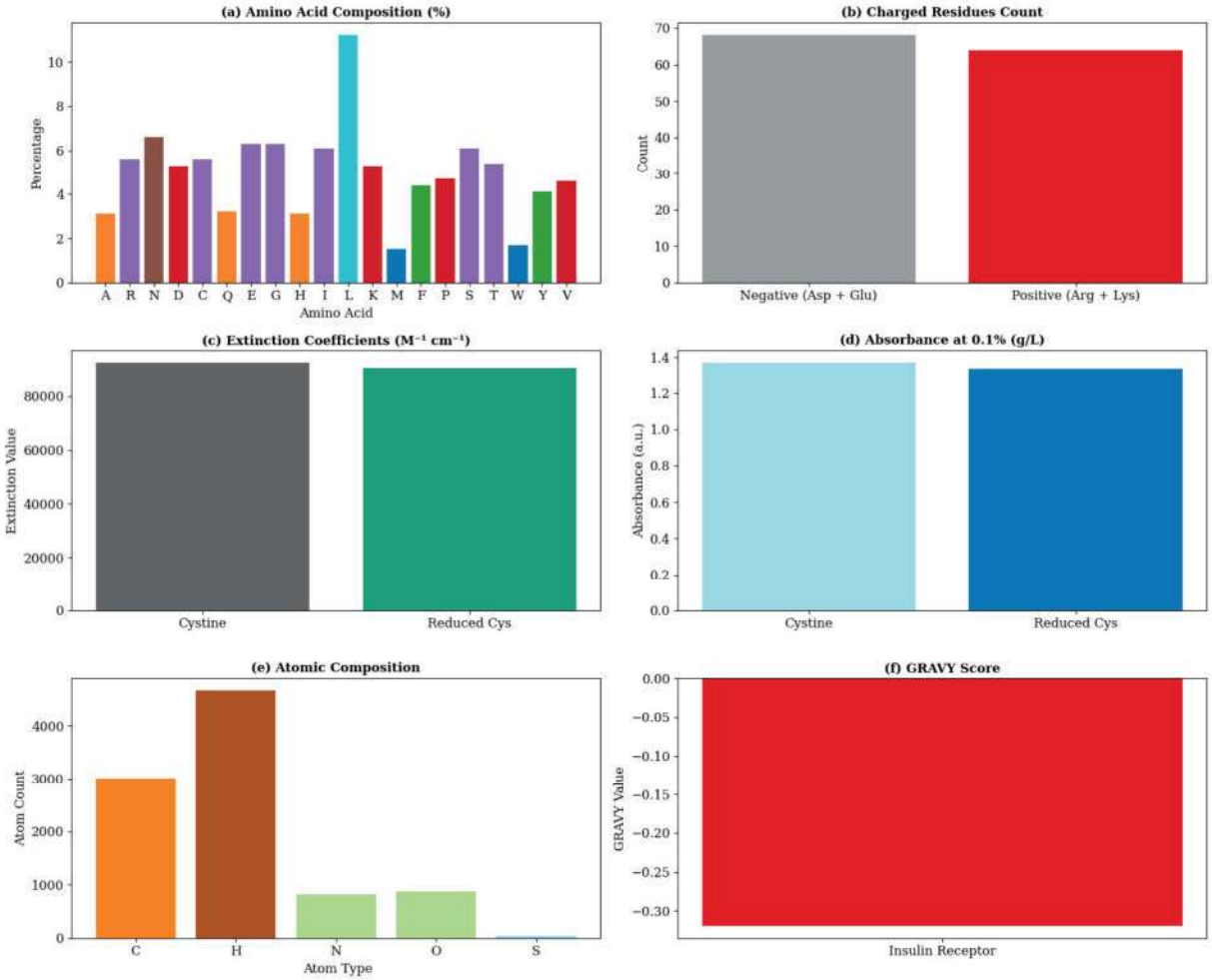


Figure 9.22: Physicochemical profile of Insulin Receptor Ectodomain (IR): (a) Amino acid distribution (b) Charged residues count (c) Extinction coefficients (d) Absorbance (e) Atomic composition (f) GRAVY Score

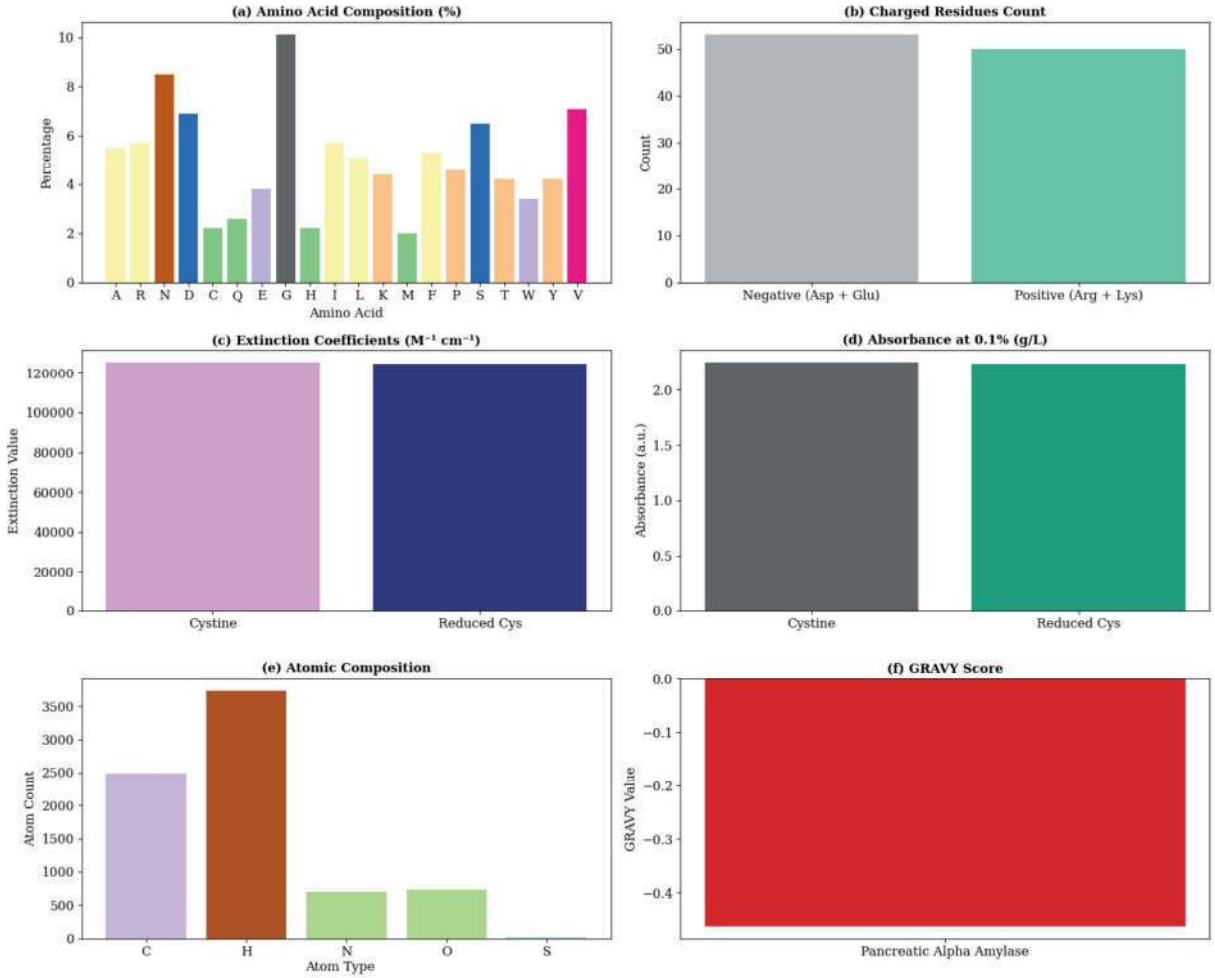


Figure 9.23: Physicochemical profile of Pancreatic Alpha-Amylase (PAA): (a) Amino acid distribution (b) Charged residues count (c) Extinction coefficients (d) Absorbance (e) Atomic composition (f) GRAVY Score

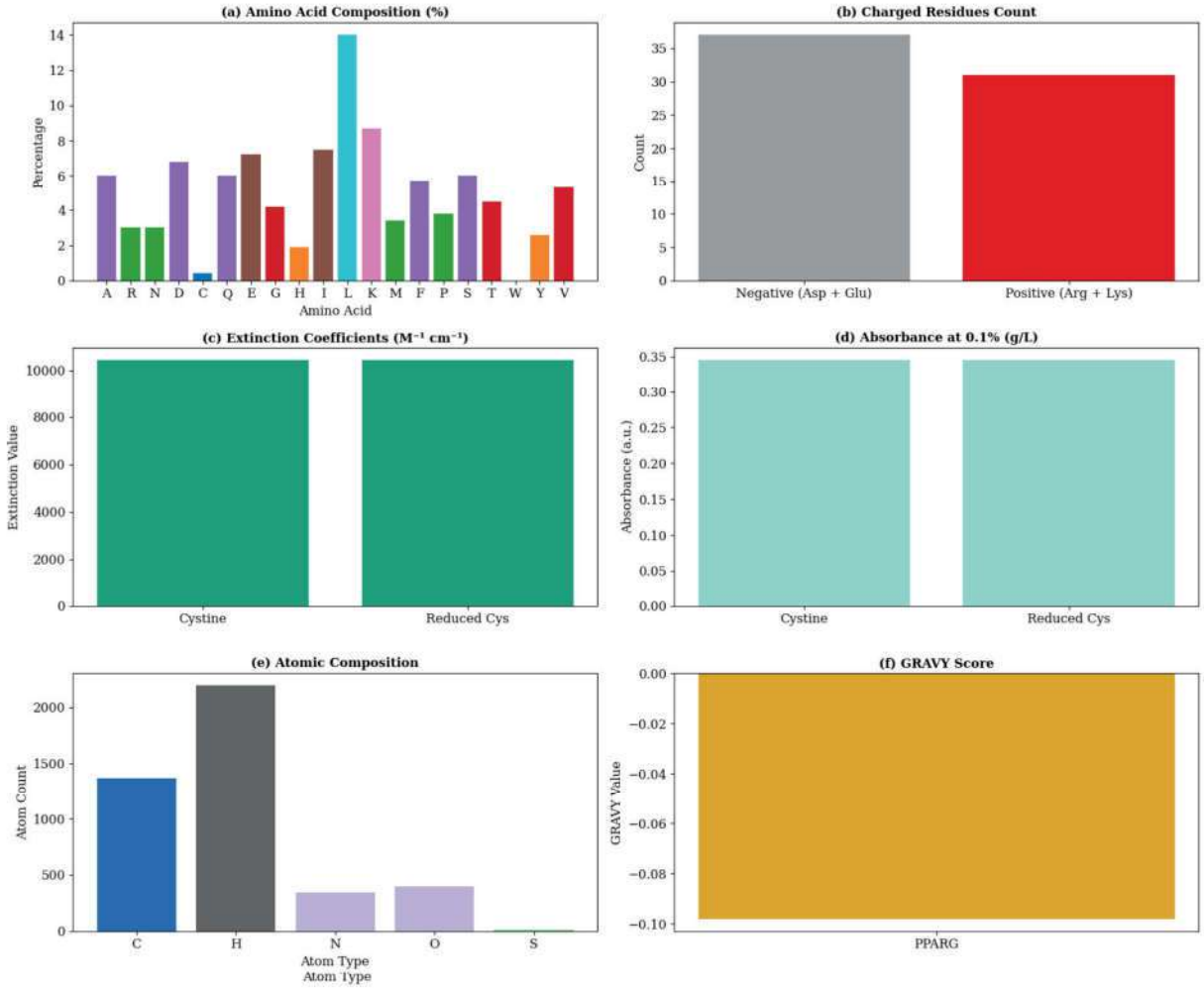


Figure 9.24: Physicochemical profile of Peroxisome Proliferator-Activated Receptor Gamma (PPARG): (a) Amino acid distribution (b) Charged residues count (c) Extinction coefficients (d) Absorbance (e) Atomic composition (f) GRAVY Score

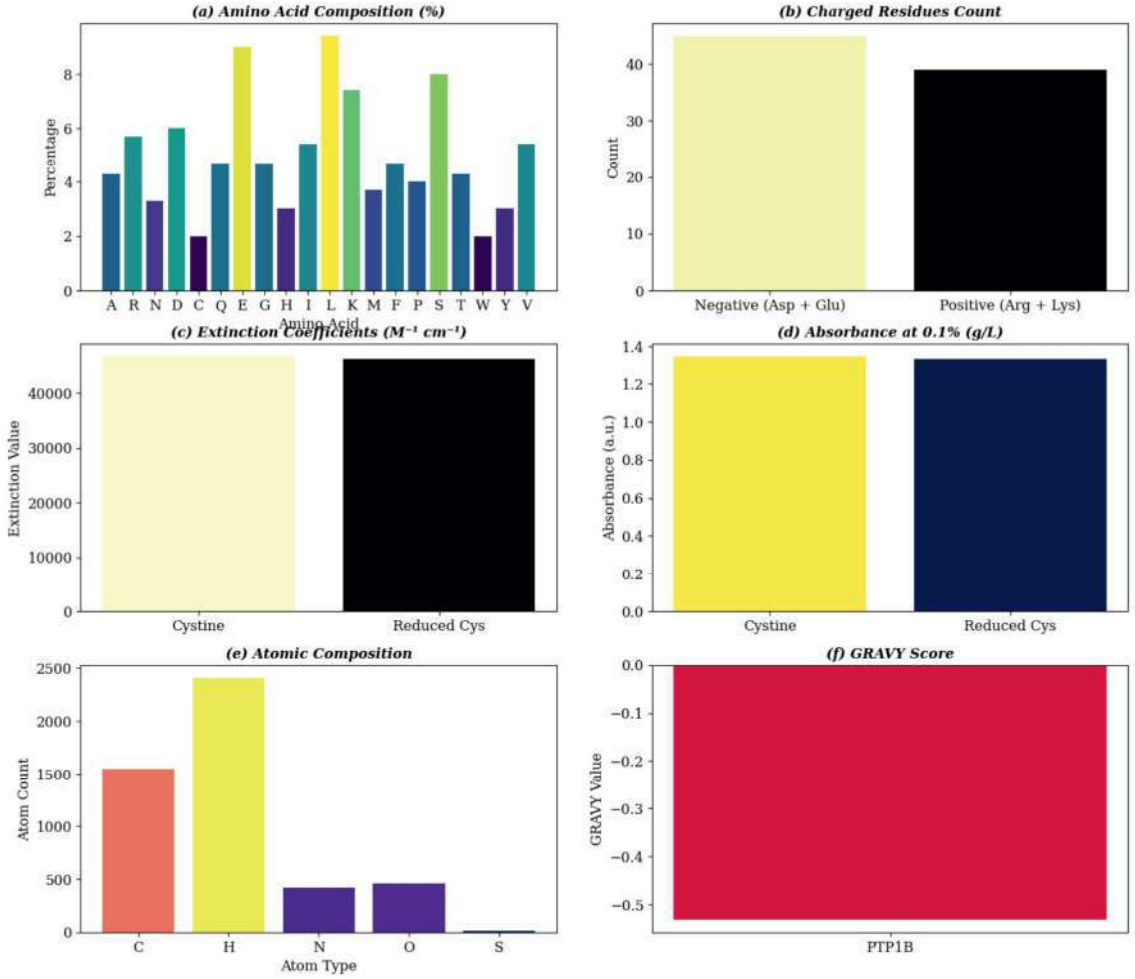


Figure 9.25: Physicochemical profile of Protein Tyrosine Phosphatase 1B (PTP1B): (a) Amino acid distribution (b) Charged residues count (c) Extinction coefficients (d) Absorbance (e) Atomic composition (f) GRAVY Score

that is moderately hydrophobic but maintains flexibility for substrate interaction (Figure 9.23).

The extinction coefficient is high (125,415 M^{-1} cm^{-1} for the cystine form), indicating a strong aromatic content, which is beneficial for spectrophotometric quantification. The GRAVY score (-0.462) indicates an overall hydrophilic nature, which aligns with its role in the aqueous enzymatic digestion of starches. With an instability index of 24.47, this protein is predicted to be stable, a trait essential for its persistent catalytic function in the digestive tract. The short-estimated half-life in yeast and *Escherichia coli* contrasts with a longer *in vitro* stability in mammalian reticulocytes, highlighting environment-specific turnover rates (Guruprasad et al., 1990).

9.3.2.5.4. Physicochemical properties of Peroxisome Proliferator-Activated Receptor Gamma (PPARG)

PPARG is composed of 265 amino acids, with a theoretical pI of 5.49 and a molecular weight of 30,203.14 Da. It shows a high leucine content (14%), followed by lysine (8.7%) and glutamic acid (7.2%). The balance between negatively charged residues (37) and positively charged residues (31) gives it a slightly acidic character, consistent with its pI value (Figure 9.24). Notably, the aliphatic index is very high (105.25), indicating strong thermal stability, beneficial for nuclear receptor proteins that undergo conformational changes during ligand binding.

With a GRAVY score of -0.098, PPARG is near neutral in hydropathicity, suggesting a balance between hydrophilic DNA-binding domains and hydrophobic ligand-binding pockets. The extinction coefficient (10,430 M^{-1} cm^{-1}) is relatively low, partly due to the absence of tryptophan residues, which typically contribute strongly to absorbance. Its instability index (44.48) classifies it as unstable, which might reflect its regulation through degradation in cellular signaling pathways. The estimated half-life of more than 20 hours in mammalian and yeast systems indicates functional persistence, aligning with its role as a transcription factor in metabolic control (Kyte & Doolittle, 1982).

9.3.2.5.5. Physicochemical properties of Protein Tyrosine Phosphatase 1B (PTP1B)

PTP1B contains 299 amino acids, with a theoretical pI of 5.90 and molecular weight of 34,785.70 Da. It has a high leucine content (9.4%) and glutamic acid (9.0%), indicating structural stability and acidic character. The balance between negatively charged residues (45) and positively charged residues (39) aligns with its near-neutral pI. Its aliphatic index of 77.26 suggests good thermostability (Figure 9.25).

GRAVY score of -0.531 indicates a predominance of hydrophilic regions, which is consistent with its cytoplasmic, soluble nature. The extinction coefficient is 46,785 M^{-1} cm^{-1}, enabling effective detection in spectrophotometric assays. Its instability index (35.74) categorizes it as stable, and the estimated half-life (>20 hours in yeast and bacteria, 30 hours in mammalian cells) supports its role in sustained regulation of insulin signaling. This stability and hydrophilicity make PTP1B a robust therapeutic target in type 2 diabetes, where inhibition can enhance insulin receptor activity and improve glucose uptake (Kyte & Doolittle, 1982).

9.3.2.6. Physicochemical properties of anticancer proteins

9.3.2.6.1. AKT1serine/threonine kinase

AKT1 is a serine/threonine kinase integral to the PI3K/AKT/mTOR pathway, where it regulates cell proliferation, survival, and metabolism, functions often dysregulated in cancer. The amino acid profile is balanced, with leucine (10.3%), glutamate (9.1%), and glycine (7.2%) as major contributors, reflecting a mix of hydrophobic and polar residues that support both structural stability and flexibility required for kinase function. Charged residues are equally distributed (46 negative, 46 positive), giving AKT1 a net neutral charge at physiological pH (theoretical pI 7.30), which is favourable for transient interactions with diverse signaling partners. The extinction coefficients (39,100 $M^{-1}cm^{-1}$ for cystine; 38,850 $M^{-1}cm^{-1}$ for reduced cysteine) and corresponding absorbance values (~1.05) indicate a notable aromatic residue content, which stabilizes the protein's fold and may play roles in ATP and substrate binding. The atomic composition shows a carbon-rich core (1,684 C atoms)

with a high hydrogen count (2,599), suggesting a predominantly hydrophobic interior, while the GRAVY score (−0.420) points to an overall hydrophilic surface, well-suited for cytosolic localization. The aliphatic index (78.84) indicates moderate thermostability, and the instability index (28.95) classifies AKT1 as stable, supporting its suitability for *in vitro* biochemical assays (Figure 9.26). Collectively, these properties align with AKT1's role as a dynamic and versatile signaling mediator in cancer biology, capable of engaging multiple protein–protein and protein–ligand interactions critical for oncogenic signaling cascades.

9.3.2.6.2. Epidermal Growth Factor Receptor (EGFR)

Epidermal Growth Factor Receptor (EGFR) is a receptor tyrosine kinase critical for cell proliferation, differentiation, and survival, and is a well-established therapeutic target in multiple cancers. The amino acid profile shows a predominance of leucine (10.5%), isoleucine (8.2%), and valine (7.5%), contributing to a high aliphatic index of 100.33, which suggests substantial thermostability, beneficial for maintaining receptor structure in the hydrophobic environment of the plasma membrane. The negative-to-positive charged residue ratio (42:37) yields an acidic pI of 5.95, indicating the protein would carry a net negative charge under physiological pH, which may influence ligand interactions and receptor dimerization. Extinction coefficients (51,255 $M^{-1}cm^{-1}$ for cystine; 50,880 $M^{-1}cm^{-1}$ for reduced cysteine) and high absorbance values (~1.46) point to an aromatic residue-rich composition, aiding in UV-based detection and quantification.

The atomic composition (1,572 C, 2,492 H, 410 N, 446 O, and 17 S atoms) reflects a balance between hydrophobic and polar residues, consistent with a transmembrane signaling protein. The GRAVY score (−0.136) indicates a slightly hydrophilic overall surface, favouring extracellular ligand binding while maintaining hydrophobic transmembrane segments. The instability index (41.09) classifies EGFR as unstable *in vitro*, suggesting potential reliance on membrane anchoring or interacting partners for stability. The long-predicted half-life, particularly in mammalian and microbial systems, underscores its persistence in signaling roles (Figure 9.27). Collectively, these properties align with EGFR's dual need for

structural rigidity in its membrane-spanning domain and flexibility in its ligand-binding extracellular region, features essential for its role in oncogenic signaling.

9.3.2.6.3. Kirsten Rat Sarcoma Viral Oncogene Homolog (KRAS)

Kirsten Rat Sarcoma Viral Oncogene Homolog (KRAS) is a small GTP-binding protein that functions as a molecular switch in pathways controlling cell proliferation, differentiation, and survival. Mutations in KRAS are among the most common oncogenic drivers in human cancers. The amino acid composition shows a relatively high proportion of acidic residues (Asp 9.5%, Glu 7.7%), giving a low theoretical pI of 5.01 and resulting in a net negative charge at physiological pH. This negative surface potential may influence KRAS's binding affinity for regulatory proteins such as GEFs and GAPs. Hydrophobic residues like valine (8.9%), isoleucine (6.5%), and leucine (6.5%) contribute to the protein's aliphatic index of 81.83, suggesting moderate thermostability suitable for a cytosolic signaling protein.

KRAS has a relatively low extinction coefficient (12,045 $M^{-1}cm^{-1}$ for cystine; 11,920 $M^{-1}cm^{-1}$ for reduced cysteine) due to the absence of tryptophan residues, indicating reduced aromatic absorbance capacity, which could lead to higher error margins in spectrophotometric quantification. The GRAVY score (−0.481) suggests a hydrophilic overall surface, favouring solubility in the cytoplasm. The instability index (41.08) classifies KRAS as unstable *in vitro*, meaning that in a cellular environment, it likely depends on interaction with membranes or binding partners for stability (Figure 9.28). The atomic composition (843 C, 1,333 H, 231 N, 269 O, and 7 S atoms) reflects a compact structure typical of small GTPases, optimized for rapid conformational switching between active and inactive states in cancer signaling pathways.

9.3.2.6.4. Mitogen-Activated Protein Kinase 1 (MAPK1)

Mitogen-Activated Protein Kinase 1 (MAPK1), also known as ERK2, is a key serine/threonine kinase in the MAPK/ERK signaling pathway, which regulates cell growth, differentiation, and survival. The amino acid profile is dominated by leucine (12.3%), isoleucine (8.0%), and aspartic acid (6.9%), contributing to an aliphatic

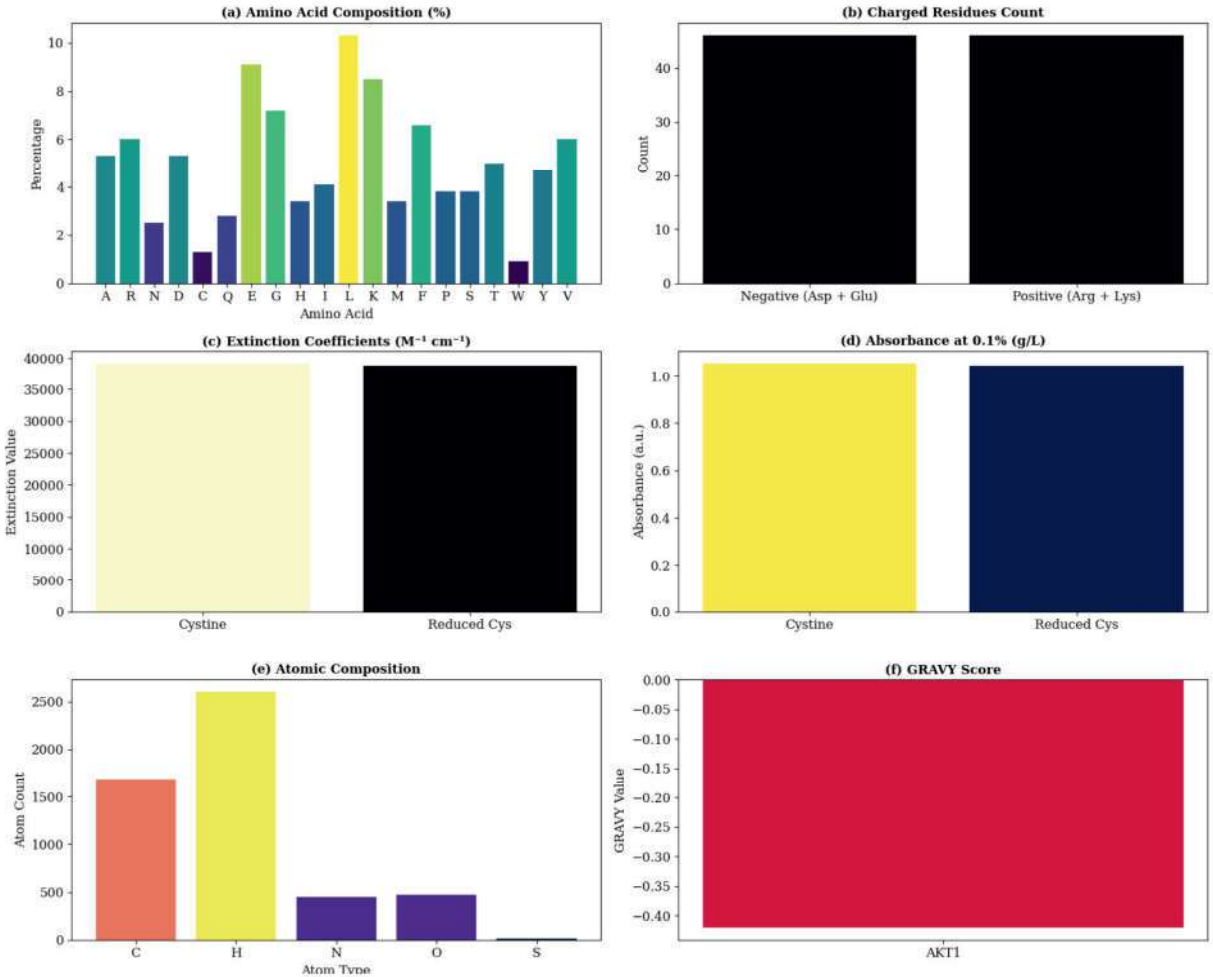


Figure 9.26: Physicochemical profile of AKT serine/threonine kinase (AKT1): (a) Amino acid distribution (b) Charged residues count (c) Extinction coefficients (d) Absorbance (e) Atomic composition (f) GRAVY Score

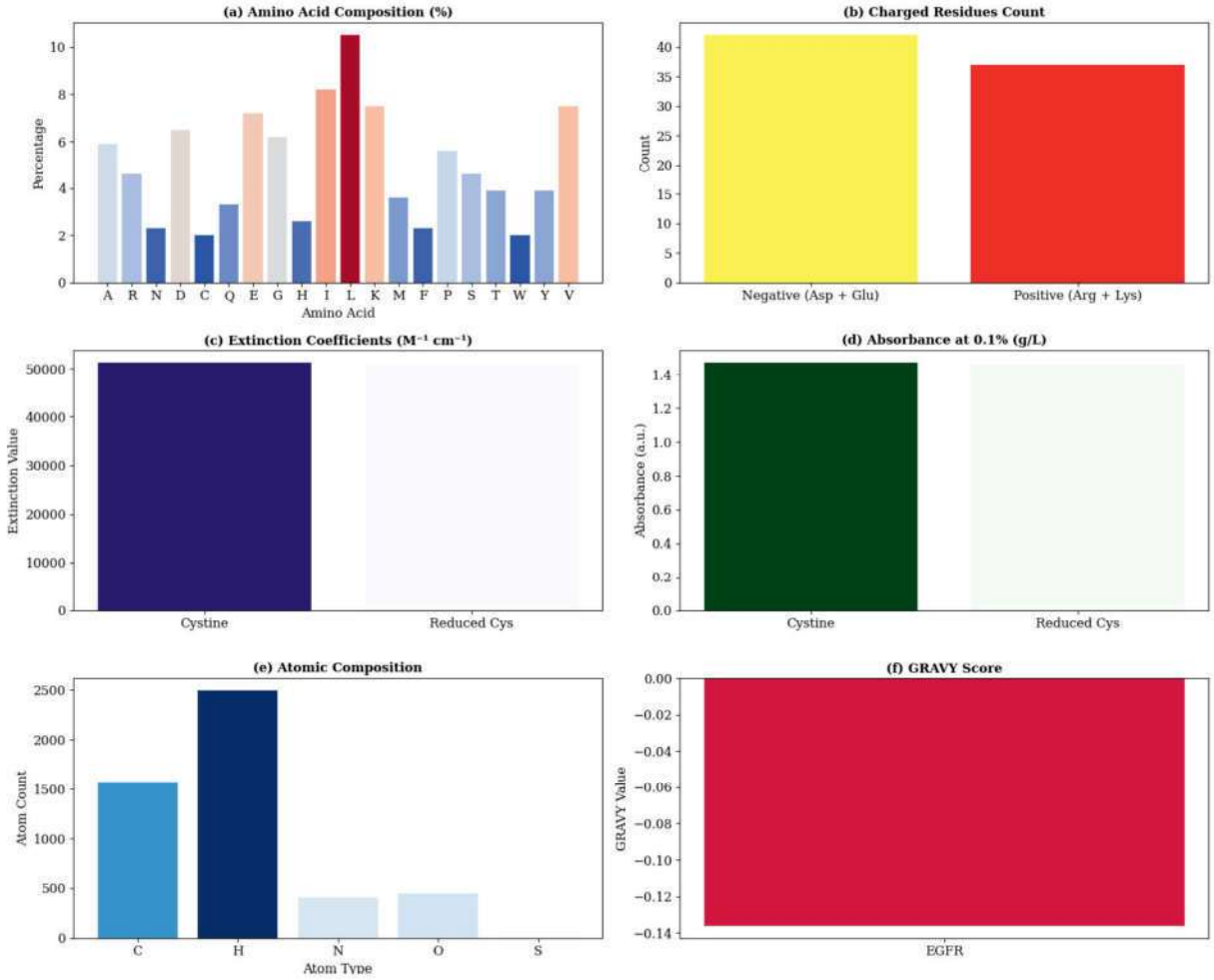


Figure 9.27: Physicochemical profile of Epidermal Growth Factor Receptor (EGFR): (a) Amino acid distribution (b) Charged residues count (c) Extinction coefficients (d) Absorbance (e) Atomic composition (f) GRAVY Score

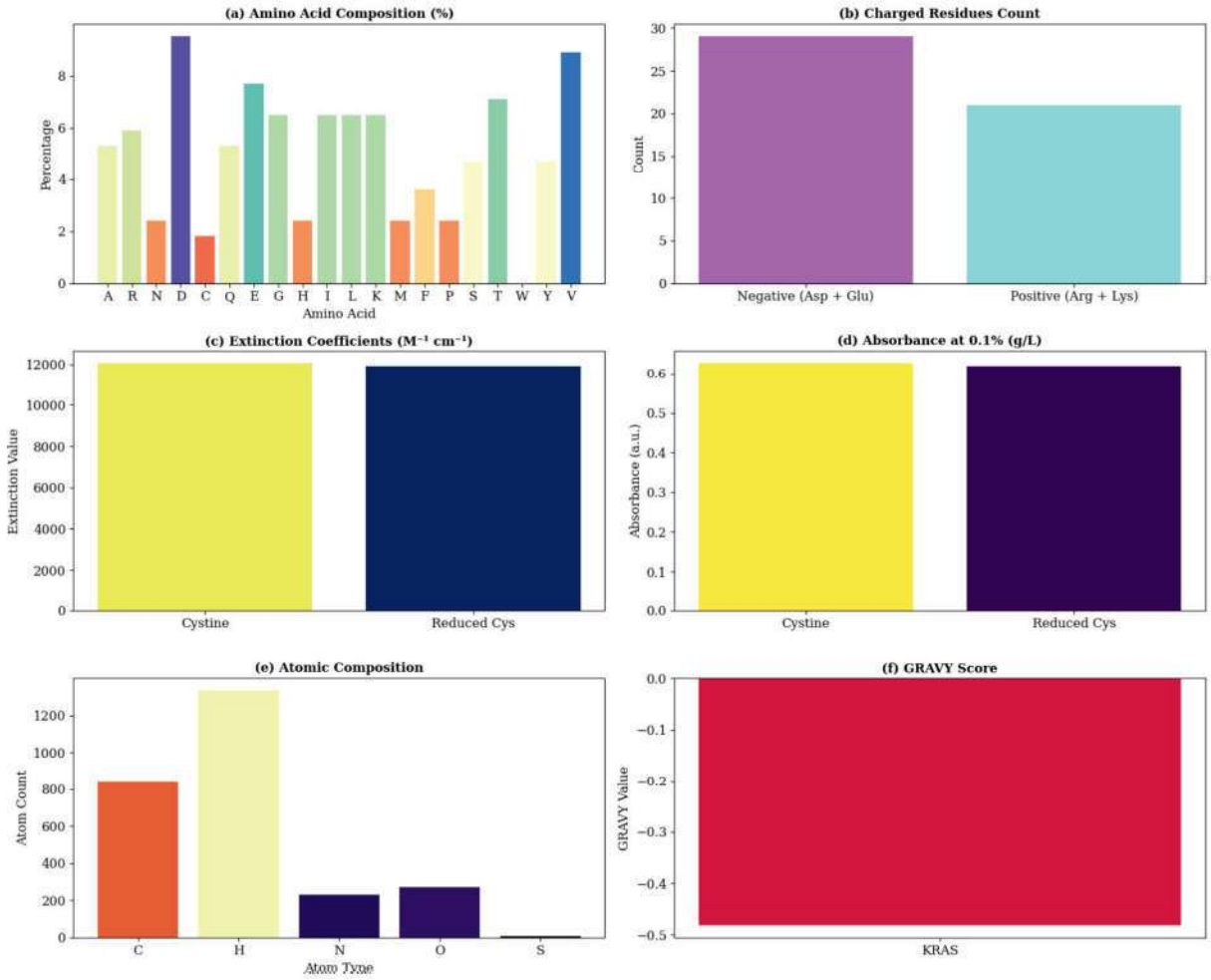


Figure 9.28: Physicochemical profile of Kirsten Rat Sarcoma Viral Oncogene Homolog (KRAS): (a) Amino acid distribution (b) Charged residues count (c) Extinction coefficients (d) Absorbance (e) Atomic composition (f) GRAVY Score

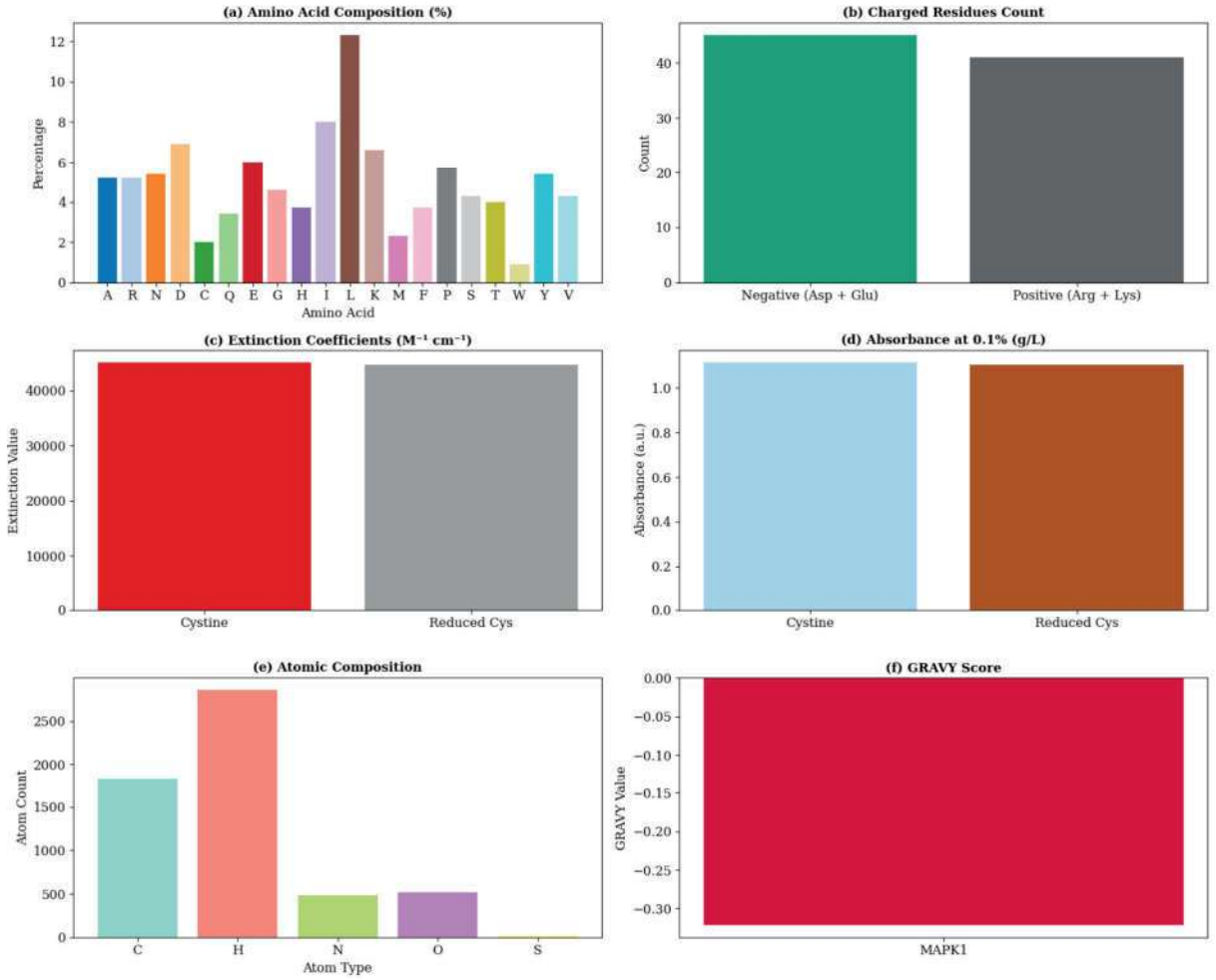


Figure 9.29: Physicochemical profile of Mitogen-Activated Protein Kinase 1 (MAPK1): (a) Amino acid distribution (b) Charged residues count (c) Extinction coefficients (d) Absorbance (e) Atomic composition (f) GRAVY Score

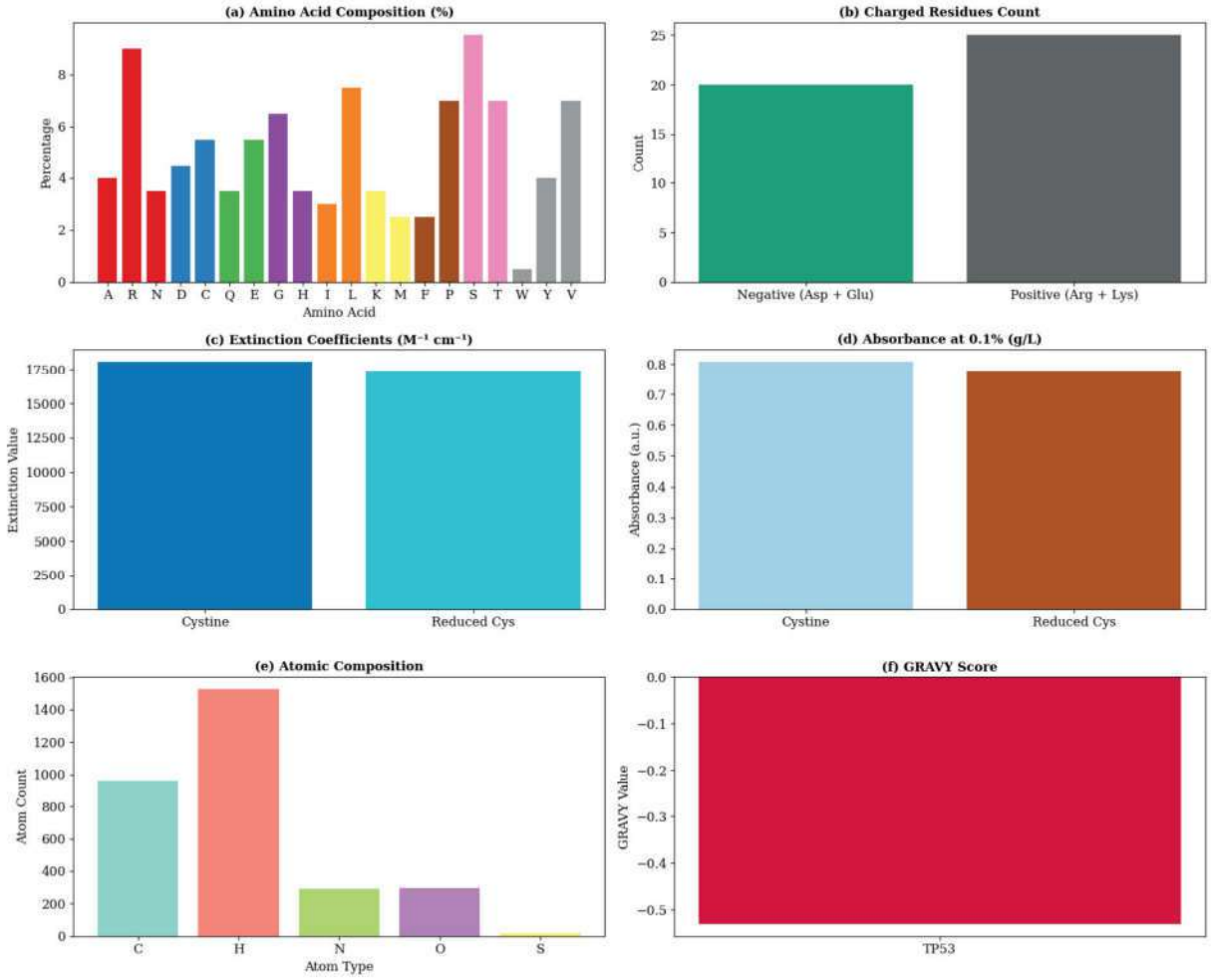


Figure 9.30: Physicochemical profile of Tumour Protein p53 (TP53): (a) Amino acid distribution (b) Charged residues count (c) Extinction coefficients (d) Absorbance (e) Atomic composition (f) GRAVY Score

index of 96.96, indicating substantial thermostability. The balance between acidic (45) and basic (41) residues yields a slightly acidic pI of 6.37, suggesting a net negative charge at physiological pH, which may influence protein–protein interactions within signaling complexes. Extinction coefficients (45,185 $M^{-1}cm^{-1}$ for cystine; 44,810 $M^{-1}cm^{-1}$ for reduced cysteine) and absorbance values (~1.11) reflect significant aromatic content, useful for spectrophotometric detection.

The GRAVY score (−0.321) indicates moderate hydrophilicity, consistent with a cytosolic protein that interacts with both hydrophilic and hydrophobic partners during signaling cascades. The instability index (39.76) classifies MAPK1 as stable, supporting its role in sustained signal relay. Its atomic composition (1,831 C, 2,854 H, 486 N, 519 O, and 15 S atoms) reflects a large, well-folded kinase domain capable of accommodating ATP and diverse substrates (Figure 9.29). These physicochemical characteristics align with MAPK1's need for structural stability and functional flexibility in oncogenic signaling, making it a robust drug target for cancer therapeutics.

9.3.2.6.5. Tumour Protein p53 (TP53)

Tumour Protein p53 (TP53), commonly known as p53, is a tumour suppressor protein that regulates cell cycle arrest, DNA repair, and apoptosis. Mutations in TP53 are present in over half of human cancers, making it one of the most studied anticancer targets. The amino acid composition is notable for its high serine (9.5%), arginine (9.0%), and proline (7.0%) content, reflecting its flexible, intrinsically disordered regions that are crucial for interacting with multiple regulatory partners. The pI of 8.65 indicates a net positive charge at physiological pH, consistent with its strong DNA-binding capacity. The ratio of positively charged (25) to negatively charged residues (20) reinforces this electrostatic profile, enabling TP53 to bind efficiently to negatively charged DNA backbones.

The extinction coefficient (18,045 $M^{-1}cm^{-1}$ for cystine; 17,420 $M^{-1}cm^{-1}$ for reduced cysteine) is moderate, reflecting limited aromatic residue content, which is also evident in the relatively low absorbance values (~0.80). The GRAVY score

(−0.530) confirms strong hydrophilicity, consistent with its nuclear localization and requirement for extensive aqueous solubility. The aliphatic index (65.58) is relatively low, indicating reduced thermostability, and the instability index (72.25) classifies TP53 as unstable *in vitro*, explaining why it is prone to misfolding without stabilizing interactions from binding partners (Figure 9.30). The atomic composition (961 C, 1,525 H, 289 N, 295 O, 16 S atoms) reflects a mid-sized protein with substantial flexibility, aligning with its biological role as a transcription factor that needs to adapt its conformation to various DNA sequences and cofactors.

9.3.3. Secondary structural analysis of target proteins

Secondary structural analysis provides insight into the folding patterns, stability, and functional adaptability of proteins. Elements such as β-sheets, α-helices, β-hairpins, β-bulges, helix-helix interactions, β-turns, and γ-turns collectively determine the protein's stability, flexibility, and binding capabilities. In membrane proteins, helices often dominate due to their role in spanning lipid bilayers, whereas soluble proteins may exhibit higher β-sheet content to support globular folding. The number of helix-helix interactions can indicate how tightly packed and stable a helical domain is, while beta turns and gamma turns contribute to directional changes in the peptide chain, enabling complex folding.

In antioxidant proteins, secondary structure elements often support redox catalysis, substrate accessibility, and interaction with regulatory partners. For example, beta sheets and alpha helices contribute to structural rigidity, enabling the protein to retain its conformation during oxidative stress, while beta turns and hairpins provide flexibility and facilitate loop regions important for active site exposure. Disulfide bonds further enhance stability, particularly for enzymes that function in oxidative environments. The secondary structure composition of each antioxidant protein reflects its adaptation to its functional role, from reactive oxygen species scavenging to redox signaling regulation.

For antimicrobial proteins, structural features directly influence substrate binding, catalytic efficiency, regulatory control, and interactions with cell membranes or nucleic acids. For example, β-sheets and β-hairpins can enhance rigidity for stable

binding surfaces, while α-helices often participate in DNA interactions or membrane associations. β-turns and γ-turns provide structural flexibility for conformational adjustments during activity. The analysis of these antimicrobial proteins reveals that while each protein adopts a unique secondary structure profile, they all combine rigidity (β-structures) and flexibility (turns and helices) in a way that supports their respective antimicrobial roles.

In anthelmintic targets, structural stability is vital, as these proteins often operate under challenging physiological conditions in the parasite's environment.

Proteins involved in inflammation often need to be structurally adaptable to interact with multiple binding partners, undergo conformational changes during activation, and withstand extracellular or intracellular environmental variations. The number of helix-helix interactions and disulfide bonds often reflects protein rigidity and thermal stability, whereas β-turns and γ-turns confer structural compactness and flexibility, enabling rapid signaling or catalytic responses.

For antidiabetic proteins, these structural patterns play a critical role in enzymatic activity, receptor binding, and signal transduction, which are essential in regulating blood glucose levels, insulin signaling, and carbohydrate metabolism.

In anticancer targets, these structural motifs often determine substrate specificity, regulatory interactions, and potential binding sites for therapeutic agents. The balance between rigid elements (β-sheets) and flexible motifs (loops, turns) is particularly relevant, as it impacts both catalytic efficiency and adaptability in complex signaling environments.

9.3.3.1. Secondary structural analysis of antioxidant proteins

9.3.3.1.1. Human Cu, Zn Superoxide Dismutase (SOD1)

Human Cu, Zn Superoxide Dismutase (SOD1)'s structure contains 2 sheets, 4 beta hairpins, 3 beta bulges, 9 strands, 2 helices, 14 beta turns, 1 gamma turn, and 1 disulfide bond (Figure 9.31). The dominance of beta structures over helices is characteristic of many metal-binding oxidoreductases, as it allows for a rigid scaffold

to precisely position catalytic metal ions (such as copper and zinc in Cu/Zn SOD). The beta hairpins contribute to the compact barrel-like fold that protects the active site from nonspecific oxidation. The relatively low number of helices (2) indicates that alpha-helical stability is not the primary structural strategy; instead, beta-sheet rigidity ensures consistent active site geometry. The 1 disulfide bond plays a stabilizing role, particularly under oxidative conditions, preventing denaturation. The beta turns (14) and single gamma turn facilitate loop mobility for substrate (superoxide) entry and product release. Overall, this structure supports SOD's role in efficiently dismutating superoxide radicals to hydrogen peroxide and oxygen, maintaining cellular redox balance.

9.3.3.1.2. Human Erythrocyte Catalase (CAT)

Human Erythrocyte Catalase (CAT) consists of 1 sheet, 6 beta hairpins, 4 beta bulges, 10 strands, 22 helices, 18 helix-helix interactions, 41 beta turns, and 10 gamma turns. The abundance of alpha helices (22) provides high structural stability and a well-packed hydrophobic core, which is critical for maintaining active site geometry during high oxidative turnover (Figure 9.32). The presence of beta hairpins and bulges contributes to localized flexibility, allowing the substrate (hydrogen peroxide) efficient access to the heme-containing catalytic centre. The 41 beta turns enhance conformational adaptability, enabling catalase to adjust its active site loops during substrate binding and product release. The significant number of gamma turns (10) adds to the structural compactness, reinforcing folding in regions critical for enzymatic stability. This combination of rigidity (from helices) and flexibility (from turns) is essential for catalase's role in rapidly decomposing hydrogen peroxide into water and oxygen, thereby preventing oxidative damage in cells. Its secondary structure indicates a well-evolved design for durability and high catalytic efficiency under stress conditions.

9.3.3.1.3. Human Glutathione Peroxidase 1 (GPx1)

Human Glutathione Peroxidase 1 (GPx1) features 2 sheets, 2 beta-alpha-beta units, 2 beta hairpins, 3 beta bulges, 7 strands, 10 helices, 5 helix-helix interactions, and 19 beta turns. The beta-alpha-beta units are a hallmark of enzyme catalytic cores,

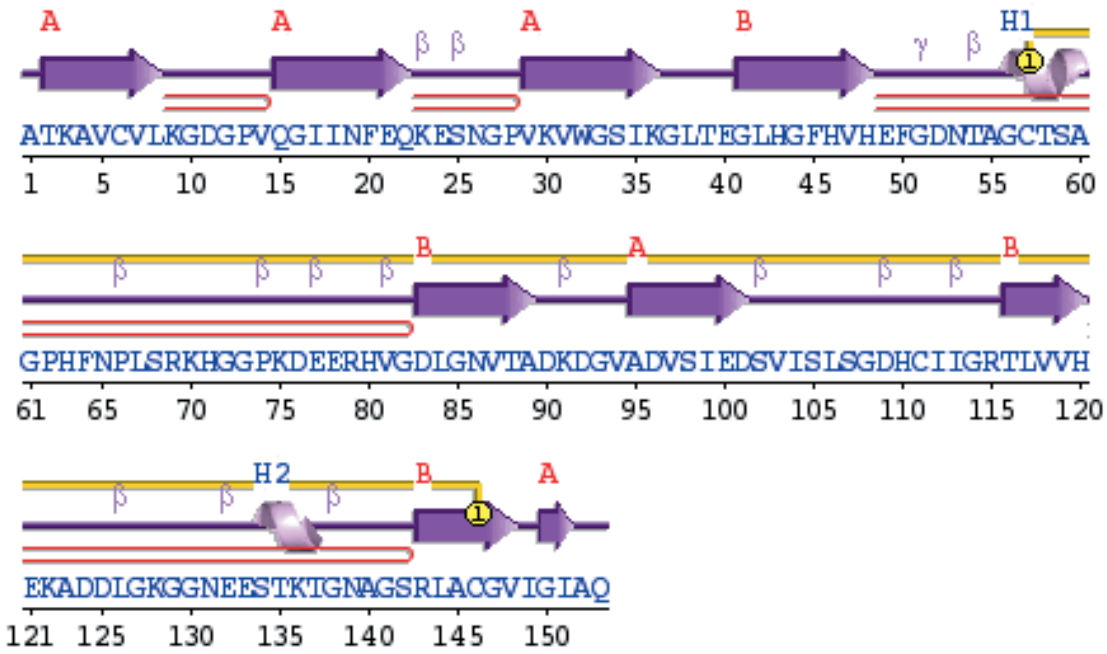


Figure 9.31: Secondary structural analysis of Human Cu, Zn Superoxide Dismutase (SOD1)

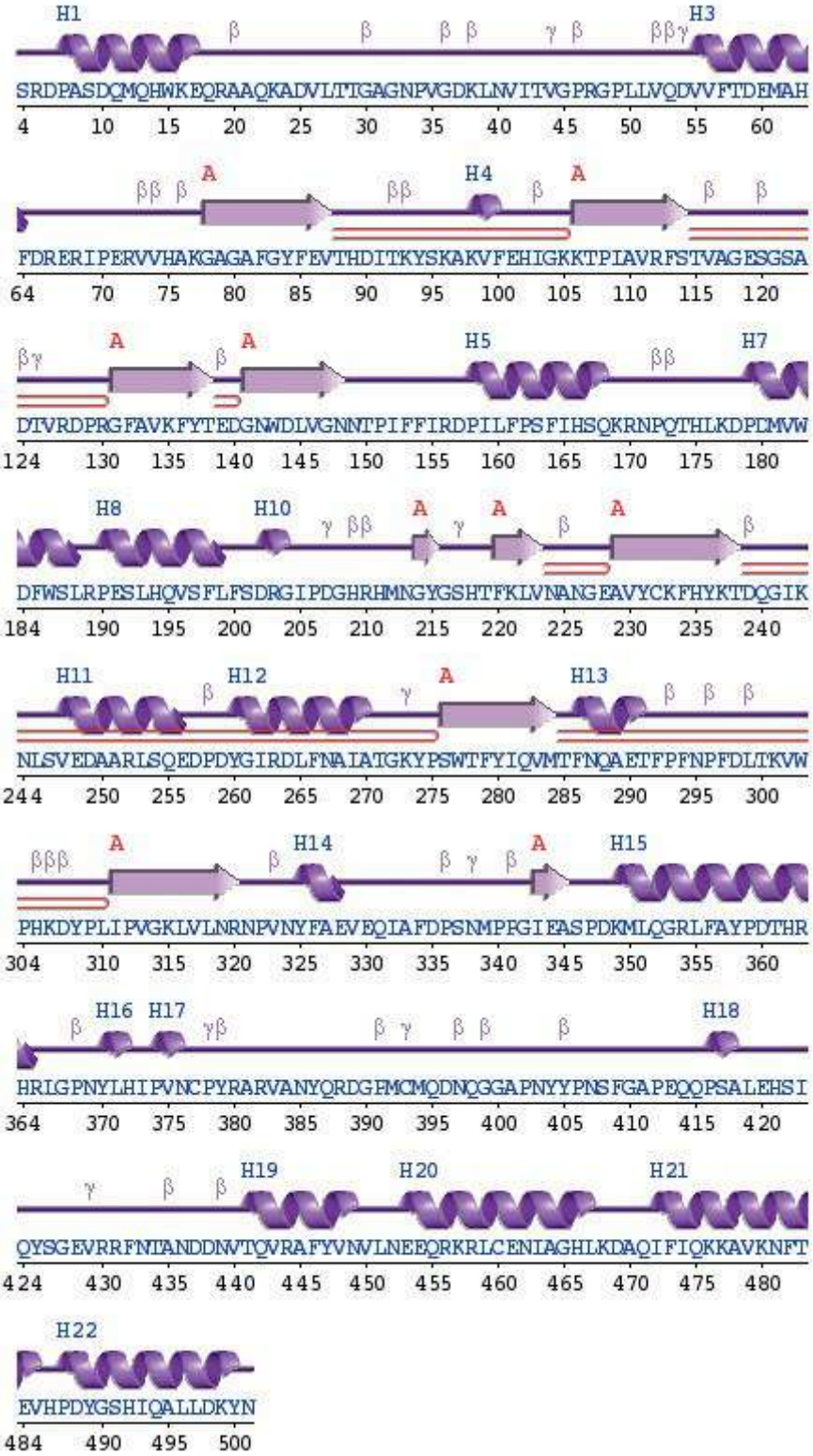


Figure 9.32: Secondary structural analysis of Human Erythrocyte Catalase (CAT)

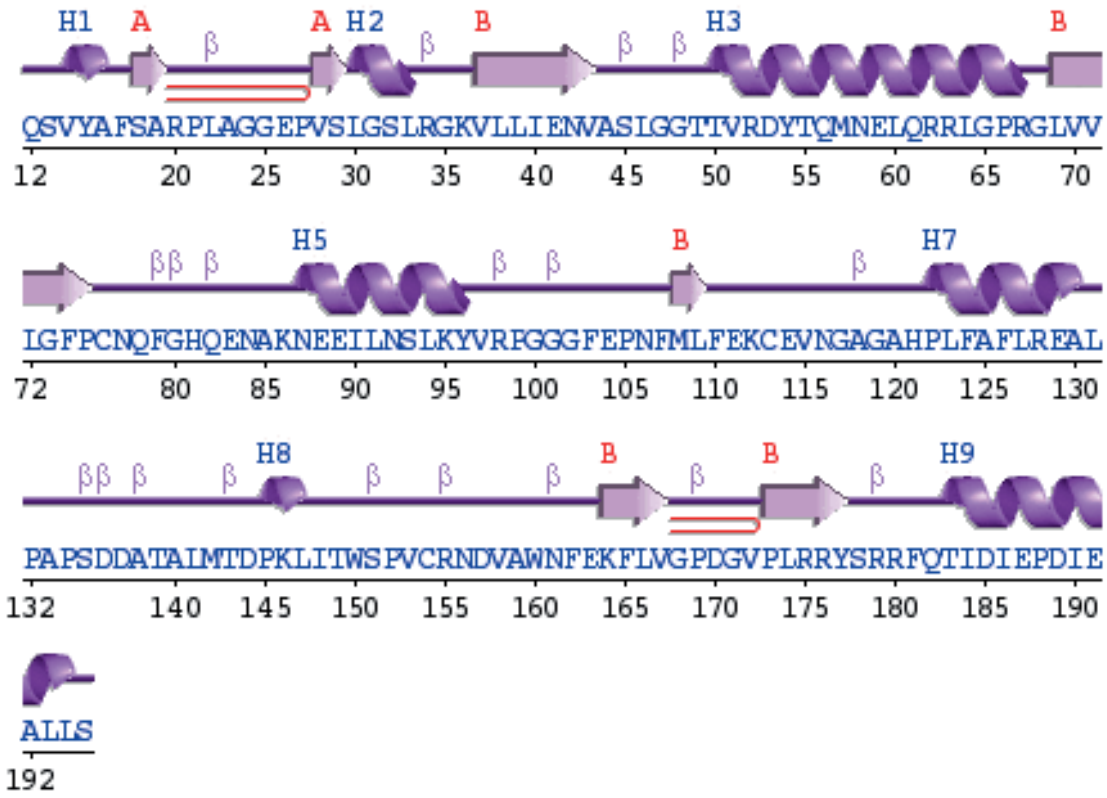


Figure 9.33: Secondary structural analysis of Human Glutathione Peroxidase 1 (GPx1)

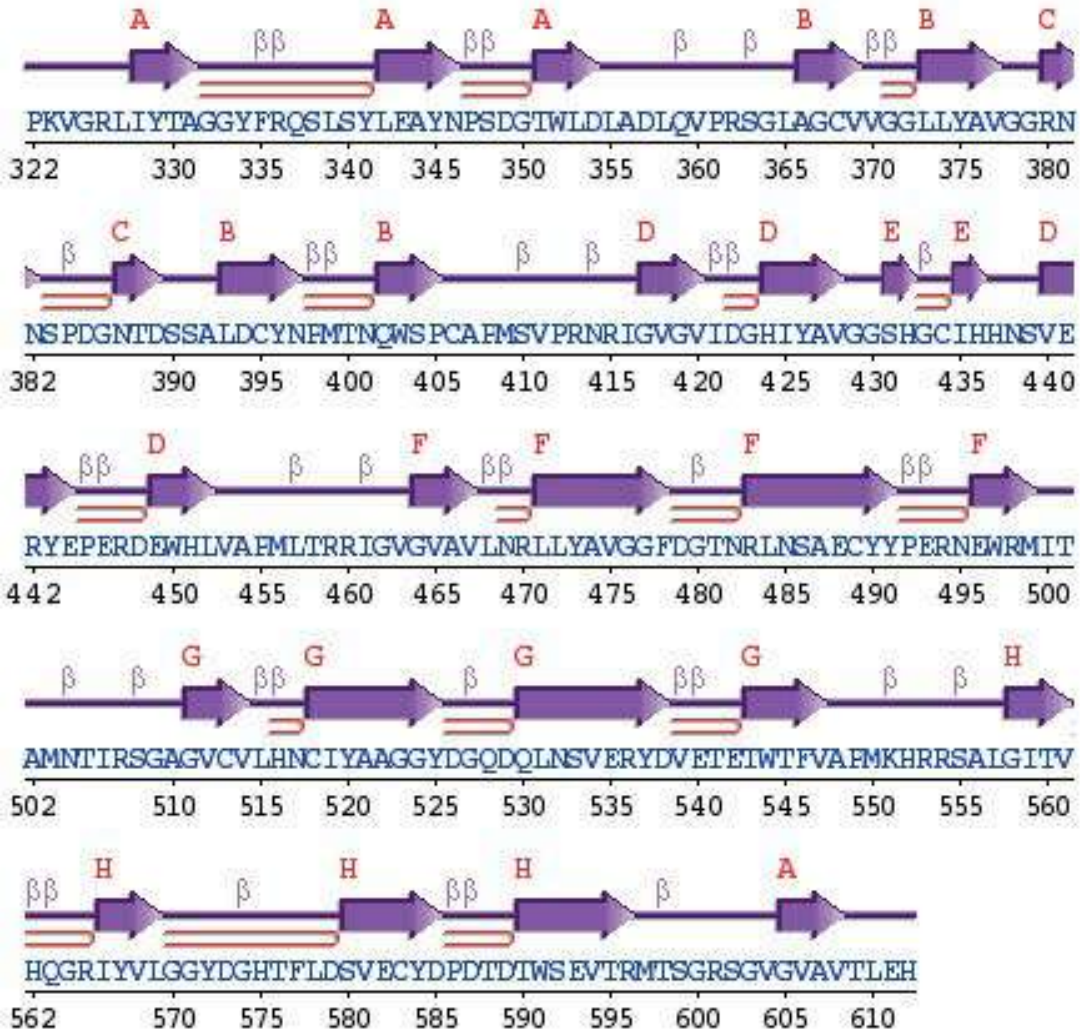


Figure 9.34: Secondary structural analysis of KEAP1 Kelch Domain (KEAP1 Kelch)

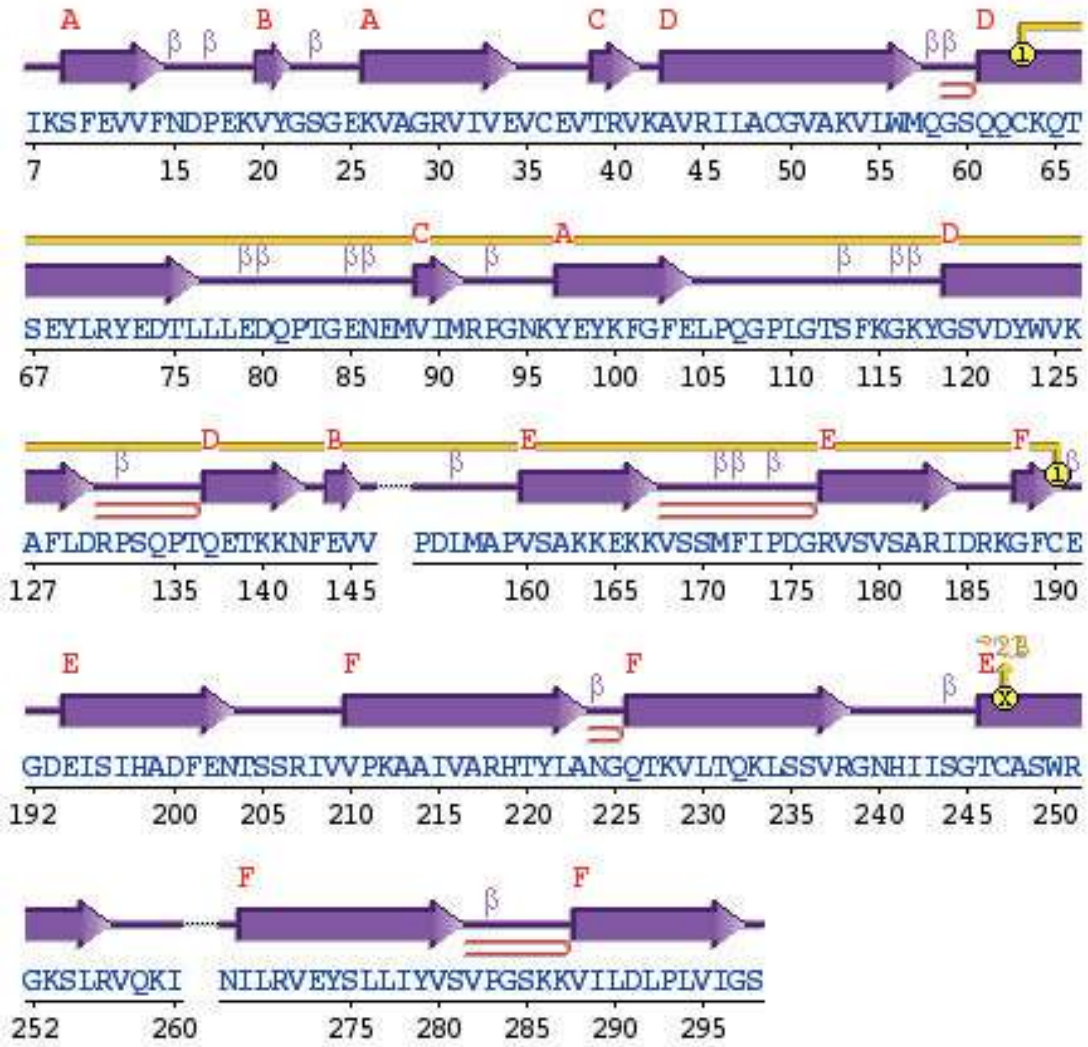


Figure 9.35: Secondary structural analysis of Thioredoxin and TXNIP Complex (Trx-TXNIP)

supporting both structural integrity and proper orientation of catalytic residues, in this case, the selenocysteine-dependent peroxidase active site. The moderate helical content (10 helices) ensures a balance between stability and flexibility, necessary for binding glutathione and reducing peroxides. The beta turns (19) provide mobility to loop regions, aiding in substrate accommodation and product release. The relatively low number of beta bulges (3) suggests minimized distortion in beta-sheet geometry, enhancing packing stability (Figure 9.33). The compact yet flexible fold is well-suited for GPx1's function of neutralizing hydrogen peroxide and lipid hydroperoxides, thus protecting membranes and proteins from oxidative injury. This arrangement reflects an evolutionary optimization for rapid catalytic cycles and adaptability in fluctuating oxidative environments.

9.3.3.1.4. KEAP1 Kelch Domain (KEAP1 Kelch)

KEAP1 Kelch Domain (KEAP1 Kelch) exhibits a highly sheet-rich structure with 8 sheets, 17 beta hairpins, 10 beta bulges, 28 strands, 40 beta turns, and 1 gamma turn. This dense beta-sheet architecture forms the backbone of its Kelch-repeat domain, which is specialized for binding to the Nrf2 transcription factor. The abundance of beta hairpins (17) suggests multiple loop connections between sheets, creating binding grooves with high surface area for protein-protein interactions. The beta bulges (10) add slight distortions to sheet geometry, enhancing flexibility in binding pockets. The 40 beta turns indicate significant conformational adaptability, crucial for accommodating various redox-dependent modifications that regulate Nrf2 release. With no significant helical dominance, KEAP1's structure prioritizes extensive beta-sheet surfaces for stable yet reversible binding. The single gamma turn contributes to local folding stability. (Figure 9.34) Functionally, this secondary structure enables KEAP1 to act as a dynamic redox sensor, adjusting Nrf2 sequestration in response to oxidative stress, thereby regulating the transcription of antioxidant defense genes.

9.3.3.1.5. Thioredoxin and TXNIP Complex (Trx-TXNIP)

Thioredoxin and TXNIP Complex (Trx-TXNIP) displays a complex structure with 6 sheets, 5 beta hairpins, 8 beta bulges, 20 strands, 22 beta turns, 1 gamma turn,

and 2 disulfide bonds. The extensive beta-sheet network provides a stable scaffold for binding interactions, particularly with thioredoxin. The beta bulges (8) introduce localized distortions that may help in modulating binding affinity during redox-regulated conformational changes. The 22 beta turns contribute significant flexibility, enabling TXNIP to undergo structural adjustments during protein-protein recognition. The 2 disulfide bonds enhance oxidative stability, ensuring that TXNIP maintains structural integrity even under high ROS conditions. The relatively high strand count (20) suggests a strong, sheet-dominant core, while the absence of significant helical regions aligns with its role as a regulatory binding protein rather than a catalytic enzyme (Figure 9.35). This secondary structure equips TXNIP to act as a redox-sensitive inhibitor of thioredoxin, thereby influencing apoptosis, inflammation, and metabolic control in oxidative stress contexts.

9.3.3.2. Secondary structural analysis of antimicrobial proteins

9.3.3.2.1. D-alanyl-D-alanine ligase (D-ALA: D-ALA Ligase/Ddl)

D-alanyl-D-alanine ligase (D-ALA: D-ALA Ligase) displays a balanced architecture consisting of 3 β-sheets, 1 β-α-β unit, 4 β-hairpins, and 3 β-bulges, supported by 13 β-strands (Figure 9.36). Its helical content is also substantial, with 13 α-helices stabilized by 9 helix-helix interactions. The presence of 28 β-turns and 5 γ-turns contributes significant flexibility, likely important for substrate recognition and catalysis. The moderate β-sheet content provides a stable scaffold for the active site, while the helices may help in positioning catalytic residues and facilitating ATP binding. The β-α-β motif, a known feature of many ATP-binding enzymes, further supports its role in peptidoglycan synthesis in bacterial cell walls. This combination of stable β-structure and flexible turns is ideal for an enzyme that must accommodate substrate movement during catalysis while maintaining structural integrity.

9.3.3.2.2. LasR ligand-binding domain (LasR)

LasR ligand-binding domain (LasR) has a simpler β-structure profile with 1 β-sheet, 3 β-hairpins, and 2 β-bulges, totaling 6 β-strands. This is complemented by 11 α-helices and 9 helix-helix interactions, alongside 5 β-turns and 3 γ-turns (Figure

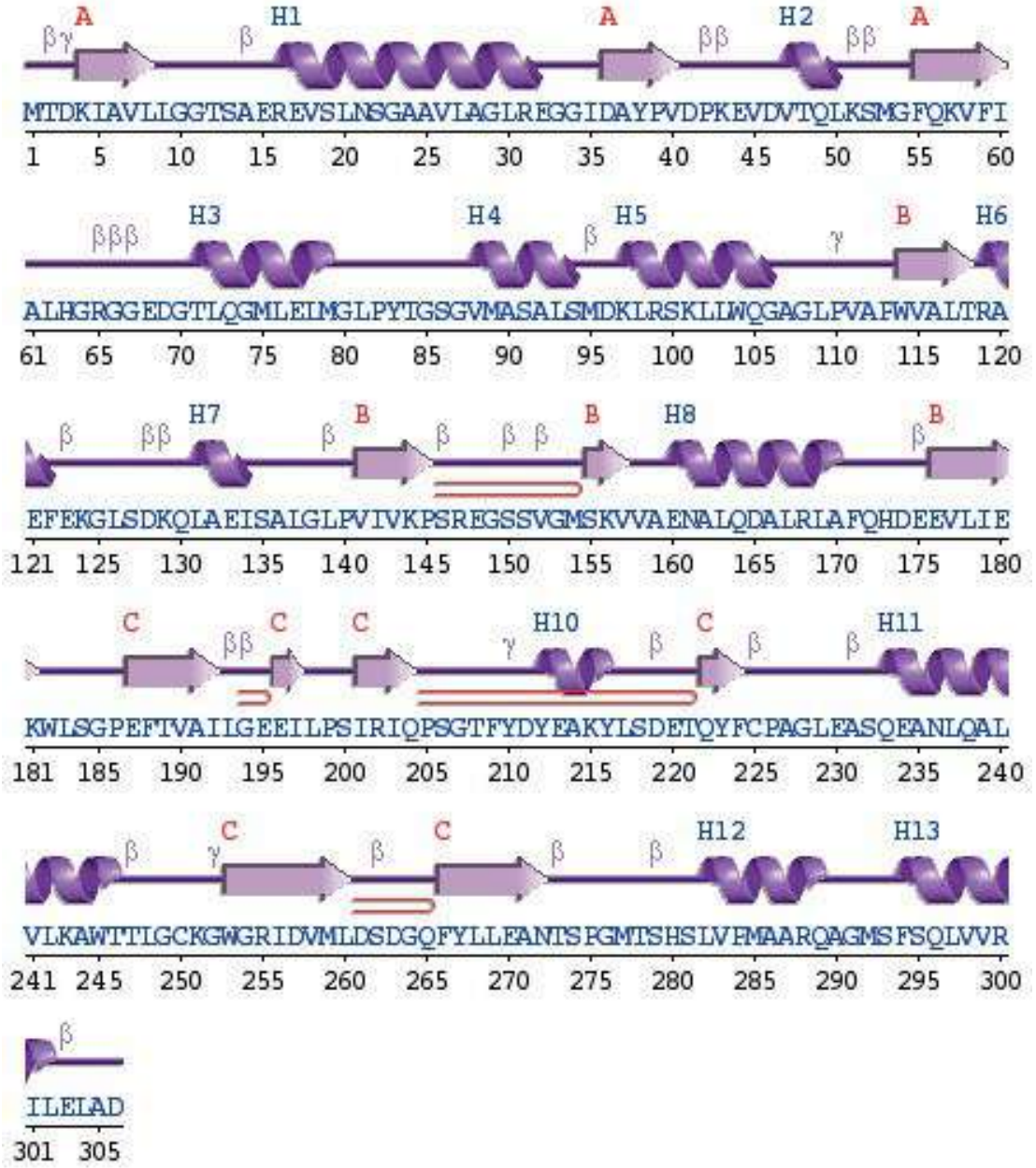


Figure 9.36: Secondary structural analysis of D-alanyl-D-alanine ligase (D-ALA:D-ALA Ligase/Ddl)

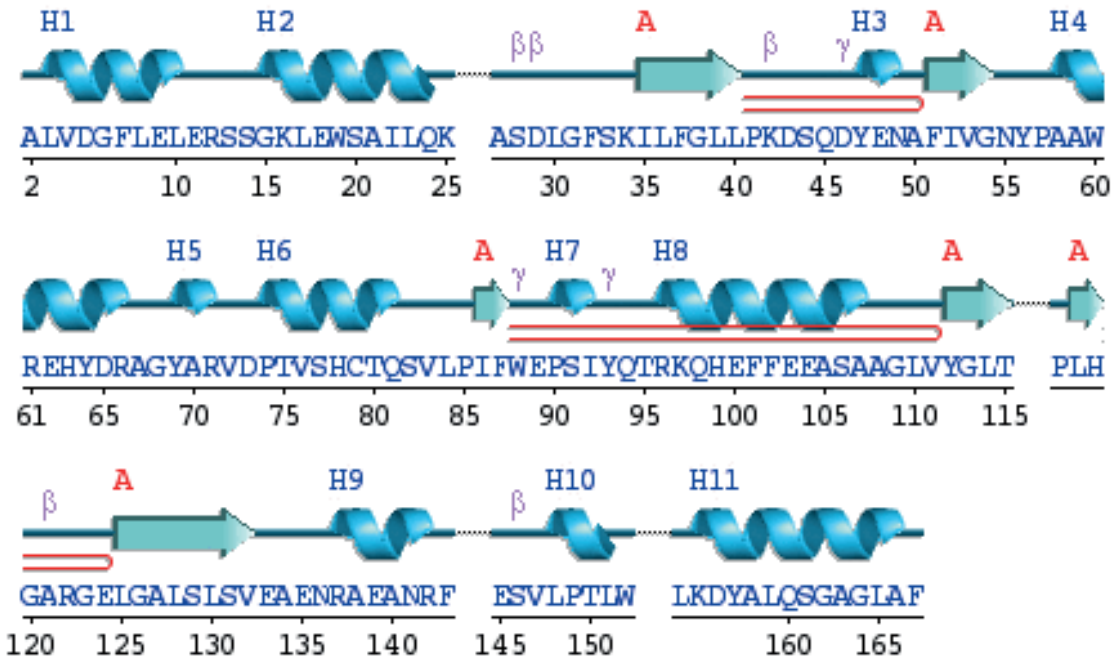


Figure 9.37: Secondary structural analysis of LasR ligand-binding domain (LasR)

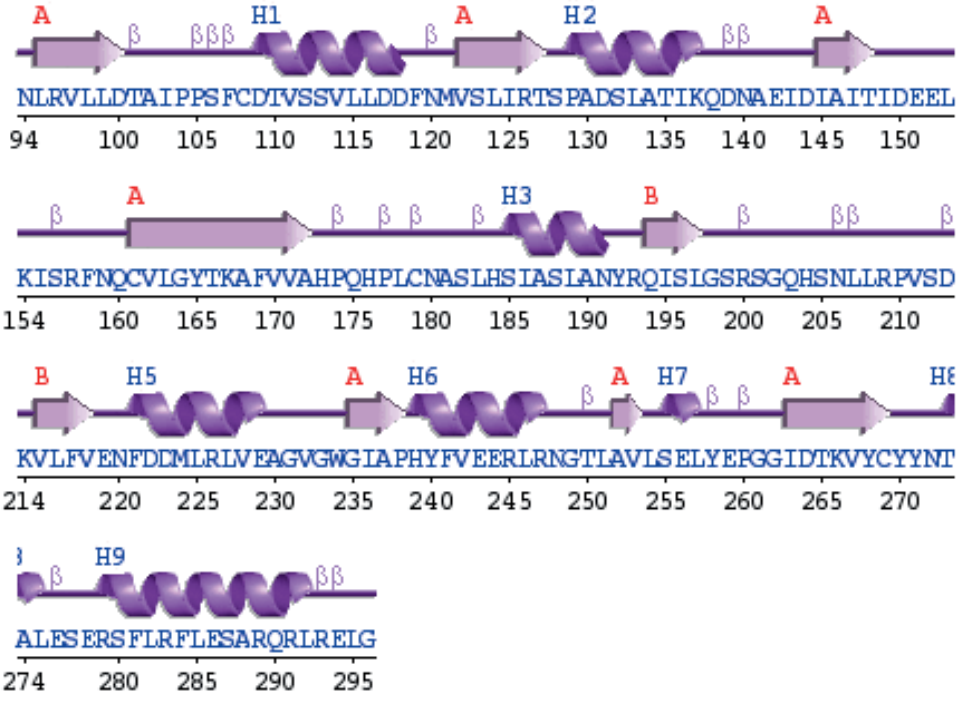


Figure 9.38: Secondary structural analysis of PqsR coinducer-binding domain (PqsR/MvfR)

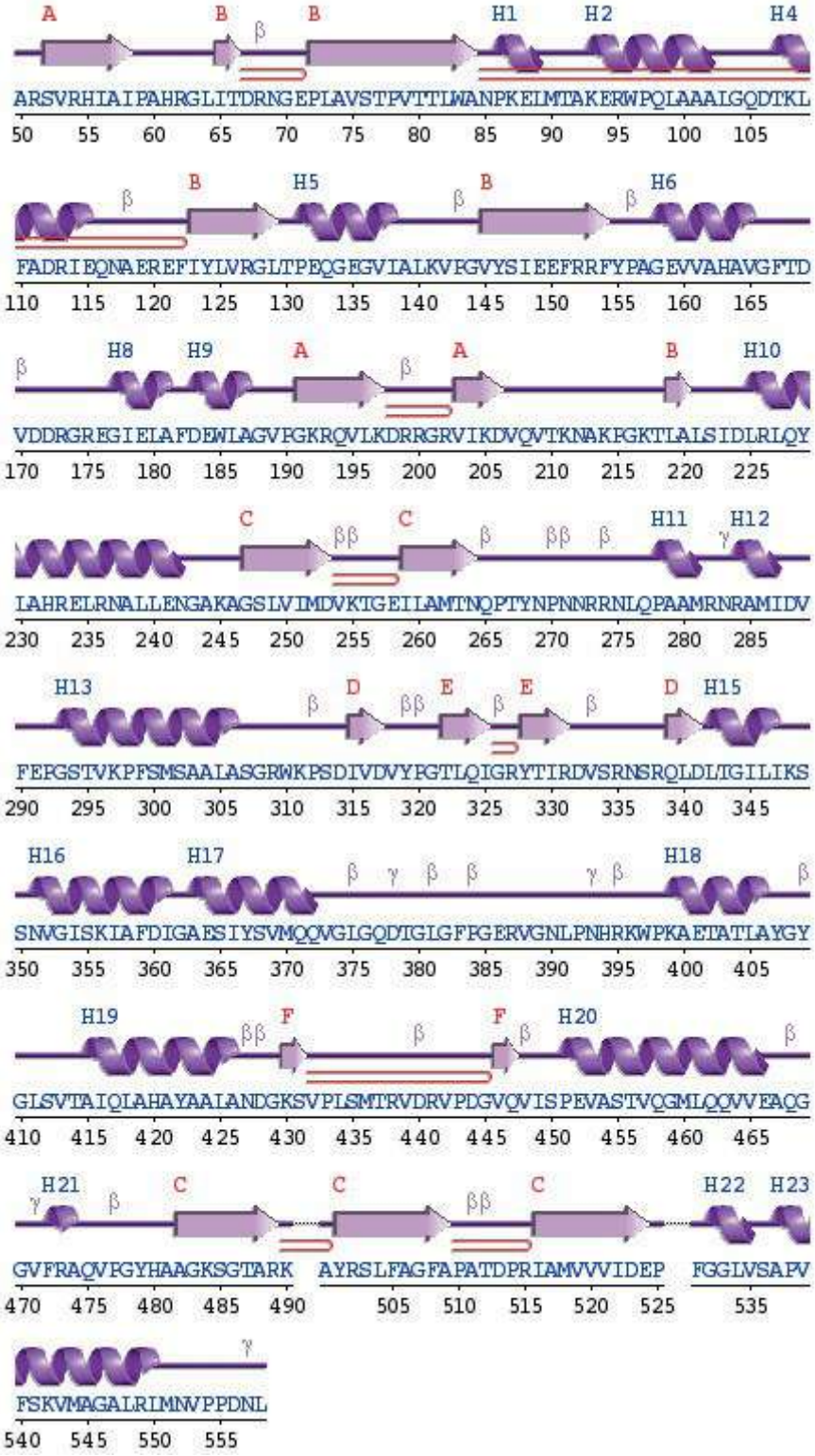


Figure 9.39: Secondary structural analysis of Penicillin-Binding Protein 3 (PBP3)

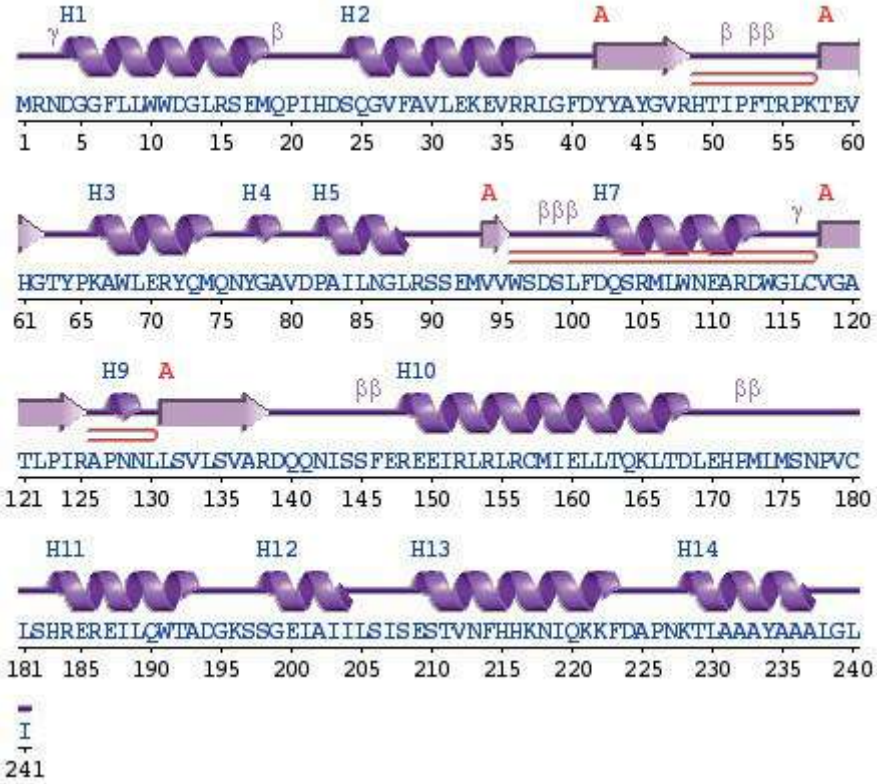


Figure 9.40: Secondary structural analysis of Regulatory Protein RhlR (RhlR)

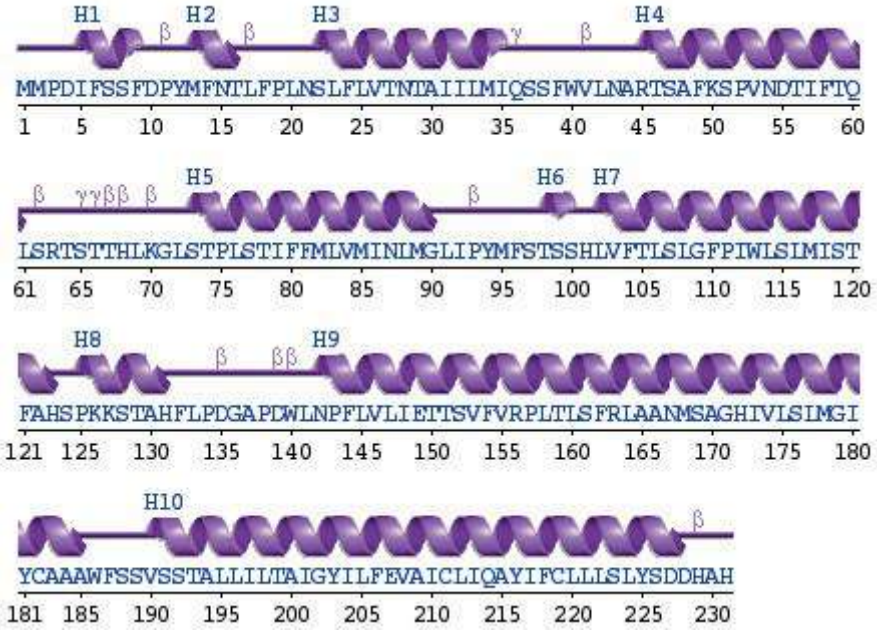


Figure 9.41: Secondary structural analysis of ATP synthase subunit a (ATP synthase)

9.37). The dominance of α-helices suggests strong involvement in DNA binding, as helices can fit into the major groove of DNA during transcriptional regulation. The relatively low β-sheet content indicates a more flexible protein core, which could facilitate conformational changes upon ligand binding. The moderate number of turns provides adaptability in the DNA-binding domains, essential for LasR's role in quorum sensing and controlling virulence gene expression.

9.3.3.2.3. PqsR coinducer-binding domain (PqsR/MvfR)

PqsR coinducer-binding domain (PqsR/MvfR) exhibits a compact yet functional structure with 2 β-sheets, 1 β-α-β unit, and 1 β-bulge, supported by 9 β-strands. The α-helical portion includes 9 helices with 3 helix-helix interactions, while flexibility is provided by 22 β-turns and 1 γ-turn. The limited β-sheet content suggests that PqsR/MvfR relies more on α-helices for stability and functional specificity, especially in DNA binding (Figure 9.38). The β-α-β unit is characteristic of ligand-binding domains, which aligns with its role in quorum-sensing regulation. The high number of β-turns allows for flexible conformations necessary for transcriptional control, where PqsR/MvfR must adjust to different promoter DNA sequences.

9.3.3.2.4. Penicillin-Binding Protein 3 (PBP3)

Penicillin-Binding Protein 3 (PBP3) has the most complex β-structure among the proteins studied, with 6 β-sheets, 8 β-hairpins, and 9 β-bulges, amounting to 19 β-strands. Its α-helical content is equally impressive, with 23 helices and 31 helix-helix interactions. Flexibility is supported by 30 β-turns and 6 γ-turns (Figure 9.39). This extensive β-sheet network provides a rigid framework necessary for the transpeptidase activity involved in bacterial cell wall crosslinking. The large number of helices may form functional domains for substrate accommodation and catalysis. High β-turn content allows conformational adaptability, critical for interacting with various peptidoglycan precursors. This structural richness likely explains its resilience and specificity as a major target for β-lactam antibiotics.

9.3.3.2.5. Regulatory Protein RhlR (RhlR)

Regulatory Protein RhlR (RhlR) is characterized by 1 β-sheet, 3 β-hairpins, and 2 β-bulges, giving a total of 5 β-strands. The α-helical content is substantial, with 14 helices and 12 helix-helix interactions, accompanied by 11 β-turns and 2 γ-turns. This helix-rich composition strongly suggests a role in DNA recognition and binding during transcription regulation. The relatively low β-sheet content provides greater flexibility, which may be advantageous in accommodating various autoinducer molecules and DNA target sites. The moderate number of turns supports domain movement, allowing the protein to adapt conformationally to its regulatory targets in quorum-sensing pathways. (Figure 9.40)

9.3.3.3. Secondary structural analysis of anthelmintic proteins

9.3.3.3.1. ATP synthase subunit a (ATP synthase)

ATP synthase subunit a (ATP synthase) contains 10 helices and 16 helix-helix interactions, along with 12 beta turns and 3 gamma turns. This subunit plays a direct role in proton translocation within the F_0 motor of ATP synthase, and its structure is optimized for this task. The high helical content reflects its integral membrane positioning, while the moderate helix-helix interactions provide stability without overly restricting movement, necessary for the conformational shifts during rotary catalysis (Figure 9.41). The beta turns and gamma turns add localized flexibility, allowing subtle adjustments to the proton channels as they open and close. This structural balance ensures that ATP synthase subunit remains both mechanically robust and dynamically responsive, a requirement for efficient ATP production under the variable physiological conditions experienced by helminths.

9.3.3.3.2. Cytochrome c oxidase subunit 1 (COX1)

Cytochrome c oxidase subunit 1 (COX1) displays 9 helices and 20 helix-helix interactions, a pattern highly consistent with its role as a core subunit of the mitochondrial respiratory complex IV. The dominance of helices reflects its transmembrane nature, allowing the protein to embed firmly in the inner mitochondrial membrane while facilitating proton pumping. The substantial number

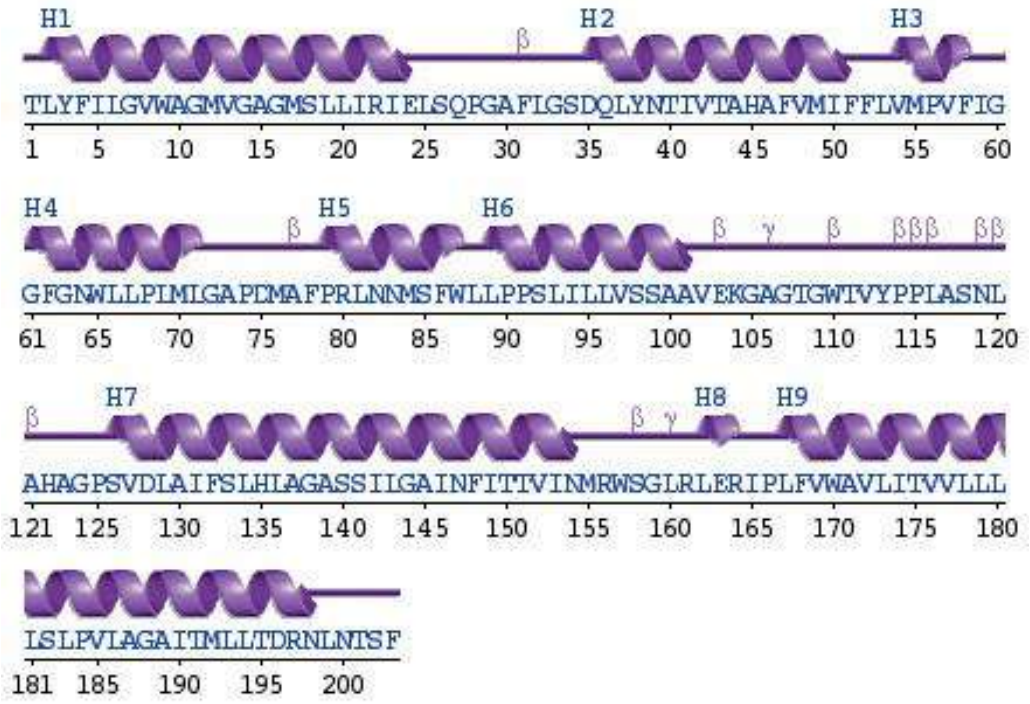


Figure 9.42: Secondary structural analysis of Cytochrome c Oxidase subunit 1 (COX1)

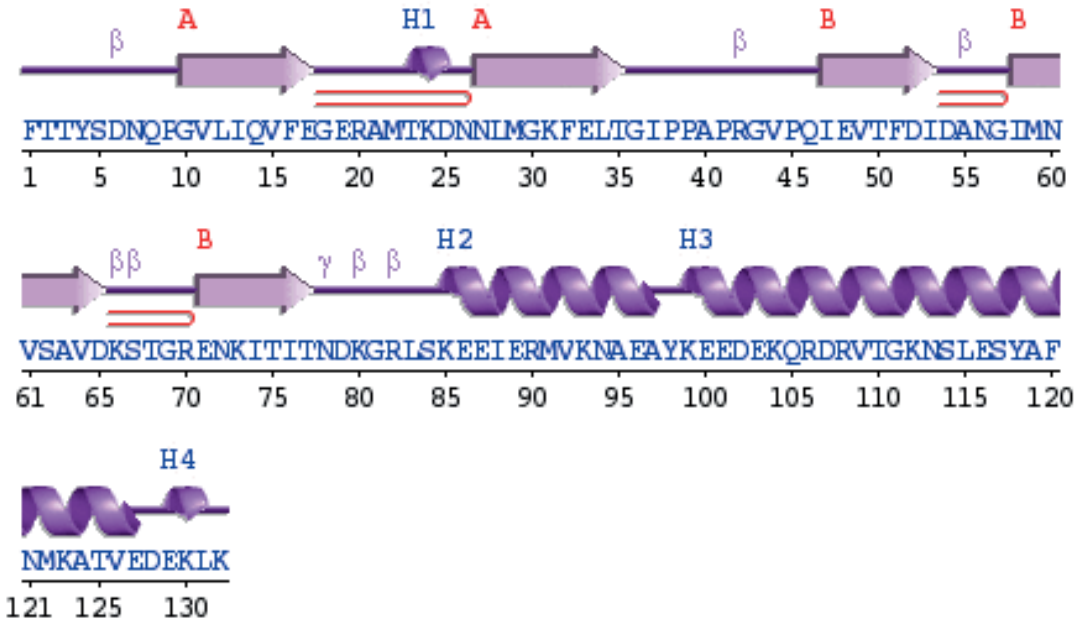


Figure 9.43: Secondary structural analysis of Heat Shock Protein 70 (HSP70)

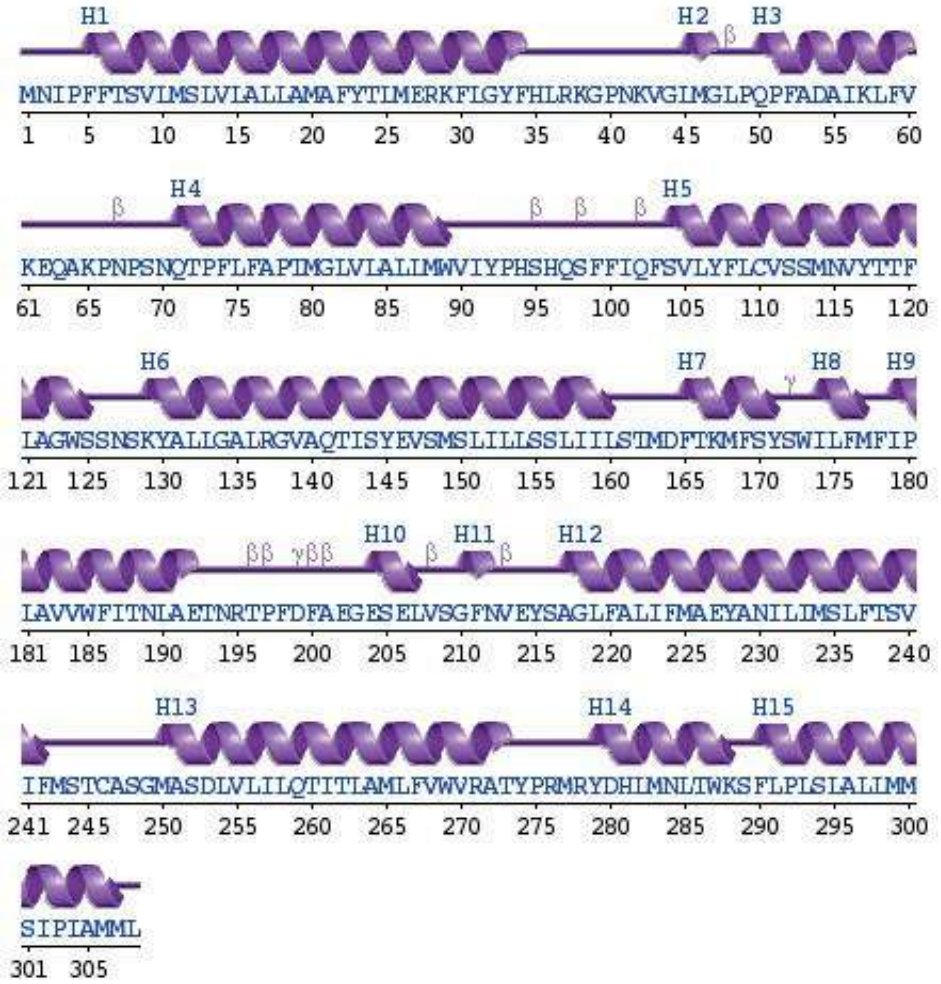


Figure 9.44: Secondary structural analysis of NADH-ubiquinone oxidoreductase chain 1 (Complex 1)

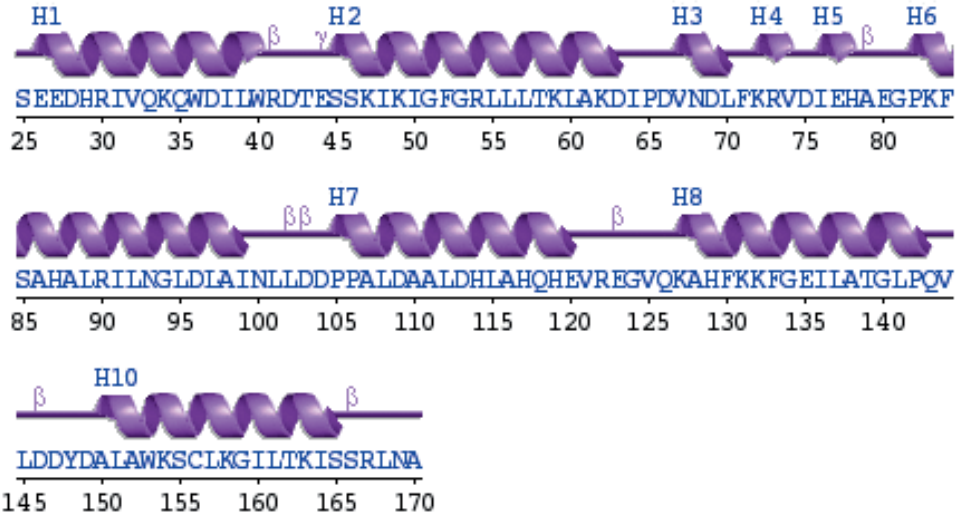


Figure 9.45: Secondary structural analysis of Extracellular Globin-3/Erythrocruorin (Ext. Globin-3)

of helix-helix interactions suggests a tightly packed, hydrophobic core, which is crucial for maintaining structural integrity during the electron transport process. The 11 beta turns and 2 gamma turns are relatively minimal, reflecting its function in maintaining stable membrane-spanning domains rather than adopting flexible or soluble conformations (Figure 9.42). These turns likely occur at loop regions connecting helices, providing minimal but necessary flexibility for conformational shifts during proton translocation. This configuration ensures both structural rigidity for maintaining the proton gradient and subtle flexibility for catalytic cycling, aligning with its vital role in oxidative phosphorylation.

9.3.3.3.3. Heat Shock Protein 70 (HSP70)

Heat shock protein 70 contains 2 sheets, 3 beta hairpins, 3 beta bulges, and 5 strands, alongside 4 helices and only 1 helix-helix interaction. The balance between β- and α-structures here reflects its soluble, cytoplasmic role as a molecular chaperone. The modest β-sheet presence contributes to a stable core for substrate binding, while the relatively low helix content allows for flexibility, critical in accommodating unfolded or partially folded proteins. The 7 beta turns and 1 gamma turn further enhance conformational adaptability, enabling rapid structural rearrangements during the binding and release cycles associated with ATP hydrolysis (Figure 9.43). The low number of helix-helix interactions suggests that helices in HSP70 are not tightly packed but rather arranged to facilitate dynamic movement between the nucleotide-binding and substrate-binding domains. Overall, this structure supports HSP70's role in protein quality control, helping maintain proteostasis under heat stress and other denaturing conditions within parasitic cells.

9.3.3.3.4. NADH-ubiquinone oxidoreductase chain 1 (Complex 1)

NADH-ubiquinone oxidoreductase chain 1 (Complex 1) exhibits 15 helices and 27 helix-helix interactions, supported by 11 beta turns and 2 gamma turns. This architecture reflects its role as part of Complex I in the mitochondrial electron transport chain, where it anchors deeply into the membrane. The abundance of helices is typical of membrane-embedded subunits, providing a stable hydrophobic framework for interacting with lipids and other subunits. The exceptionally high

number of helix-helix interactions indicates an extremely compact and stable structure, vital for maintaining the proton translocation machinery during redox cycling (Figure 9.44). The small number of turns suggests minimal flexibility, aligning with the need for mechanical stability in the energy-conversion process. This rigidity ensures efficient coupling between electron transfer and proton pumping, which is essential for generating the electrochemical gradient that powers ATP synthesis in parasites.

9.3.3.3.5. Extracellular Globin-3/Erythrocruorin (Ext. Globin-3)

Extracellular Globin-3/Erythrocruorin (Ext. Globin-3) is characterized by 10 helices and 13 helix-helix interactions, with 7 beta turns and 1 gamma turn, but no significant β-sheet content. This predominance of α-helices is a hallmark of globin family proteins, which use a compact helical scaffold to create a stable binding pocket for heme groups, enabling oxygen binding and transport. The helix-helix interactions stabilize the helical bundle, ensuring the precise positioning of residues necessary for ligand coordination (Figure 9.45). The modest number of turns suggests that the overall architecture is rigid, with only minimal loop-mediated flexibility, enough to allow small conformational adjustments during oxygen loading and unloading. In a parasitic environment, extracellular globin-3 likely plays a role in oxygen storage or buffering, ensuring survival in fluctuating oxygen conditions. The highly helical, tightly packed design is well-suited for such a function, resisting denaturation while preserving ligand-binding capability in extracellular spaces.

9.3.3.4. Secondary structural analysis of anti-inflammatory proteins

9.3.3.4.1. Nuclear Factor kappa B p50 (NF-κB p50)

Nuclear factor kappa-light-chain-enhancer of activated B cells (Nuclear Factor kappa B p50, NF-κB p50) possesses 5 sheets, 21 strands, and 9 helices, with 6 helix-helix interactions. The high β-sheet content, along with 5 β-hairpins and 7 β-bulges, forms a stable DNA-binding scaffold, enabling specific recognition of κB sites within gene promoters. The 28 β-turns and 2 γ-turns provide localized flexibility in the DNA-binding domain, allowing NF-κB p50 to adapt to different DNA conformations and

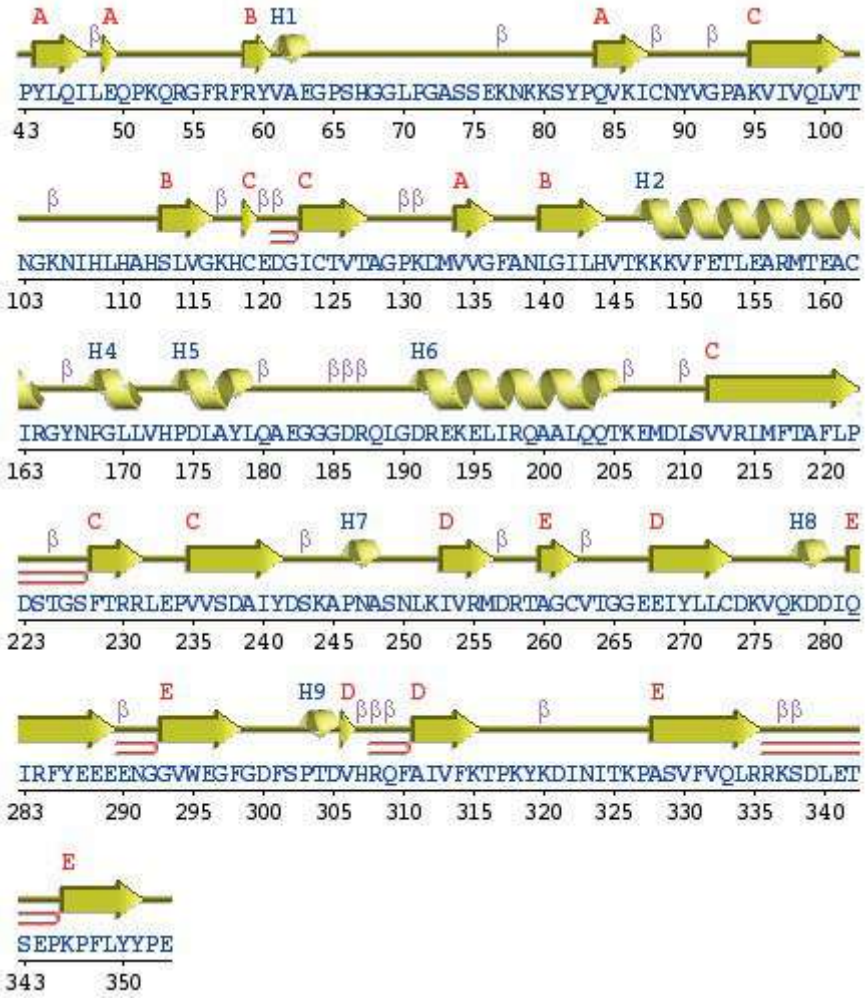


Figure 9.46: Secondary structural analysis of Nuclear Factor kappa B p50 (NF-κB p50)

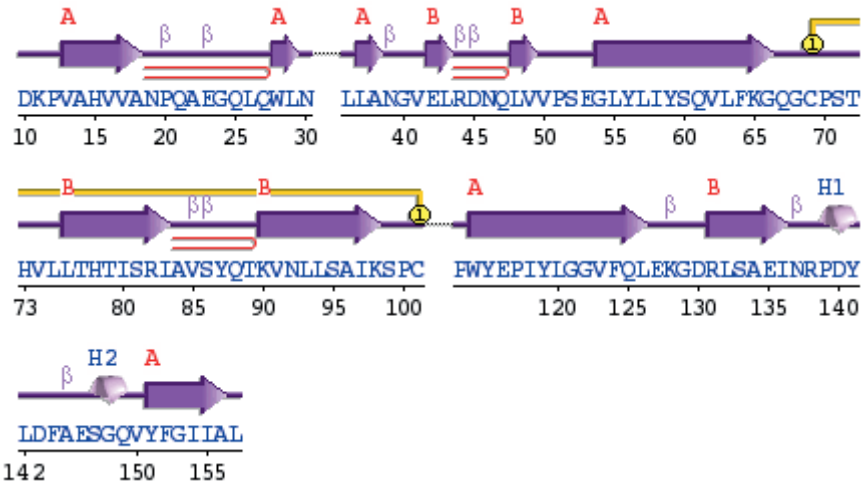


Figure 9.47: Secondary structural analysis of Tumour necrosis factor-alpha (TNF-α)

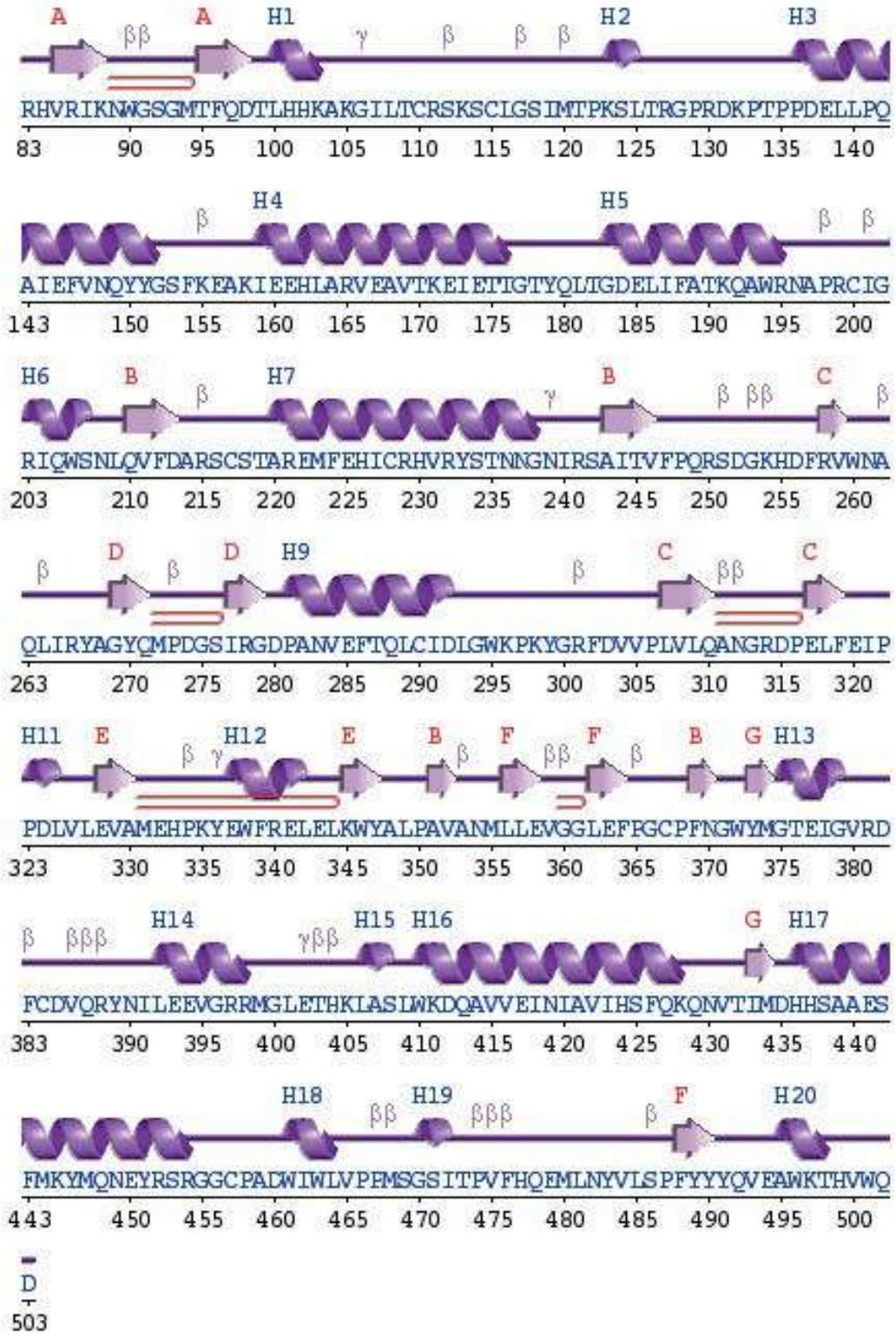


Figure 9.48: Secondary structural analysis of Human Inducible Nitric Oxide Synthase (iNOS)

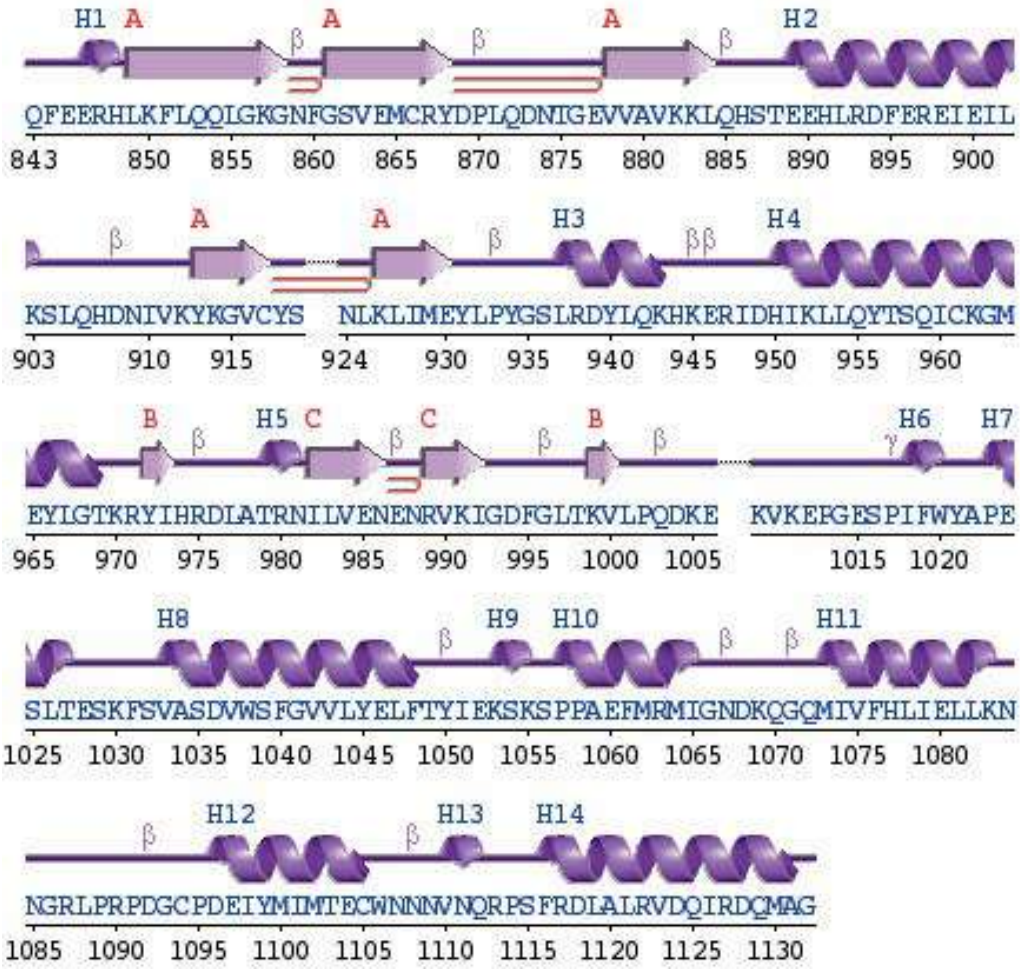


Figure 9.49: Secondary structural analysis of Janus kinase 2 (JAK2)

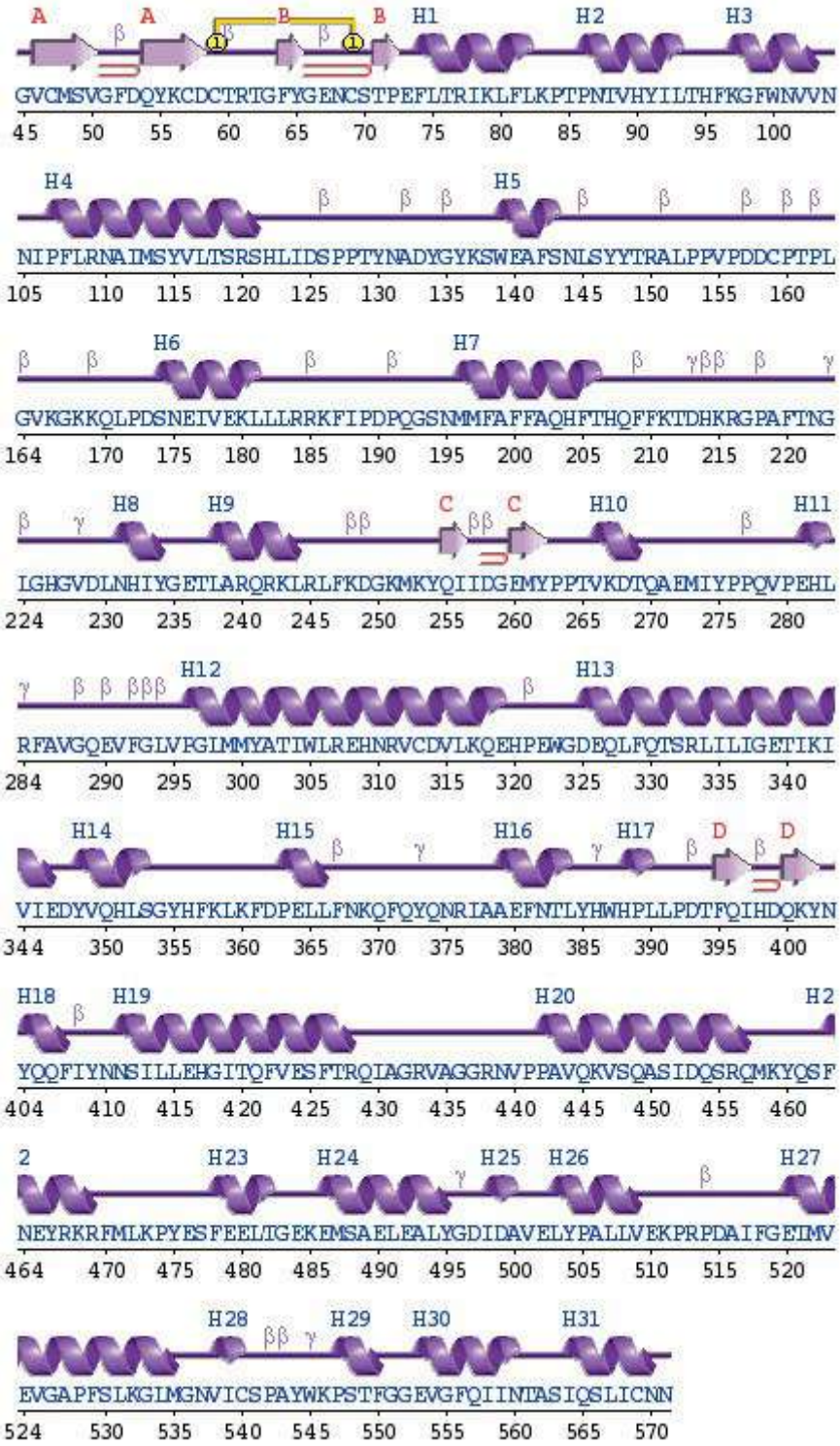


Figure 9.50: Secondary structural analysis of Human Cyclooxygenase-2 (COX-2)

co-factor interactions. This structure is optimized for its role as a transcription factor, allowing it to shuttle between inactive cytoplasmic forms and active nuclear forms upon inflammatory stimulation (Figure 9.46).

9.3.3.4.2. Tumour necrosis factor-alpha (TNF-α)

Tumour necrosis factor-alpha (TNF-α) exhibits a relatively compact structure with 2 sheets, 11 strands, and 2 helices, connected by 10 β-turns. The 3 β-hairpins and 3 β-bulges enhance strand curvature, contributing to its compact trimeric arrangement in the active form. The single disulfide bond is critical for structural integrity, particularly in the extracellular environment where TNF-α must resist proteolytic degradation. This minimal yet stable secondary structure supports TNF-α's role as a cytokine, ensuring that it can maintain functional receptor-binding conformation during transport and upon engagement with target cells in inflammatory pathways (Figure 9.47).

9.3.3.4.3. Human Inducible Nitric Oxide Synthase (iNOS)

Human Inducible Nitric Oxide Synthase (iNOS) exhibits a highly intricate structure with 7 sheets, 18 strands, and 20 helices, supported by 15 helix-helix interactions. The 2 β-α-β units indicate Rossmann-like folds, commonly associated with nucleotide-binding, consistent with iNOS's requirement for cofactors like NADPH. The 5 β-hairpins and 2 β-bulges enhance sheet flexibility, while 35 β-turns and 4 γ-turns confer high structural adaptability, vital for accommodating substrate L-arginine and facilitating electron transfer during NO production. This extensive structural flexibility is critical for iNOS's ability to respond rapidly to pro-inflammatory stimuli, producing nitric oxide as both a defense and signaling molecule during immune activation (Figure 9.48).

9.3.3.4.4. Janus kinase 2 (JAK2)

Janus kinase 2 (JAK2) features 3 sheets, 9 strands, and 14 helices, with 13 helix-helix interactions. Its secondary structure profile indicates a balanced α/β composition, which is typical of cytoplasmic kinases that require structural stability for ATP binding and flexibility for substrate recognition. The 4 β-hairpins and 5 β-

bulges suggest an adaptable β-sheet topology, enhancing the protein's ability to accommodate multiple signaling partners in the JAK-STAT pathway. The 16 β-turns and 1 γ-turn contribute to domain mobility, crucial for the conformational shifts needed during phosphorylation events (Figure 9.49). This combination of structural stability and adaptability ensures that JAK2 can remain functional under diverse intracellular conditions, supporting its central role in transmitting inflammatory cytokine signals.

9.3.3.4.5. Human Cyclooxygenase-2 (COX-2)

Human Cyclooxygenase-2 (COX-2) displays a highly complex secondary structure comprising 4 sheets, 8 strands, and 31 helices, connected by 54 helix-helix interactions. This extensive α-helical content is consistent with COX-2's role as a membrane-associated enzyme, providing structural stability within the hydrophobic lipid bilayer. The presence of 38 β-turns and 8 γ-turns adds flexibility, allowing conformational changes during substrate entry and product release in the prostaglandin synthesis pathway. The single disulfide bond likely contributes to localized structural stabilization, critical for maintaining the catalytic pocket's integrity under oxidative conditions during inflammation. These structural elements collectively support COX-2's enzymatic efficiency and durability, especially under inflammatory stress, where oxidative agents and temperature fluctuations could otherwise destabilize protein structure (Figure 9.50).

9.3.3.5. Secondary structural analysis of antidiabetic proteins

Secondary structural analysis provides insights into the folding patterns and stability of proteins, which are closely linked to their biological function. By examining the distribution of structural motifs such as β-sheets, α-helices, turns, and loops, we can infer how these proteins achieve their specific conformations to interact with ligands, substrates, or other biomolecules. For antidiabetic proteins, these patterns play a critical role in enzymatic activity, receptor binding, and signal transduction, which are essential in regulating blood glucose levels, insulin signaling, and carbohydrate metabolism (Dill & MacCallum, 2012).

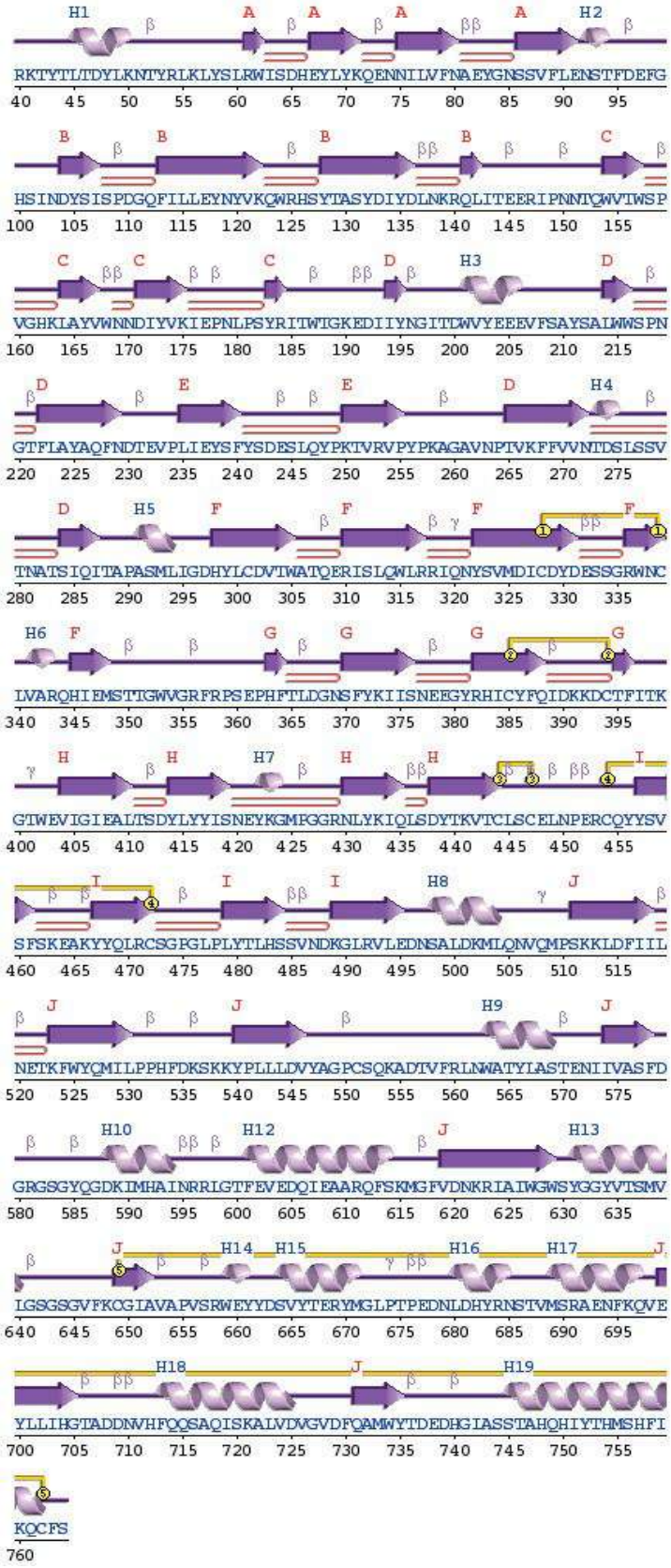


Figure 9.51: Secondary structural analysis of Dipeptidyl Peptidase 4 (DPP4)

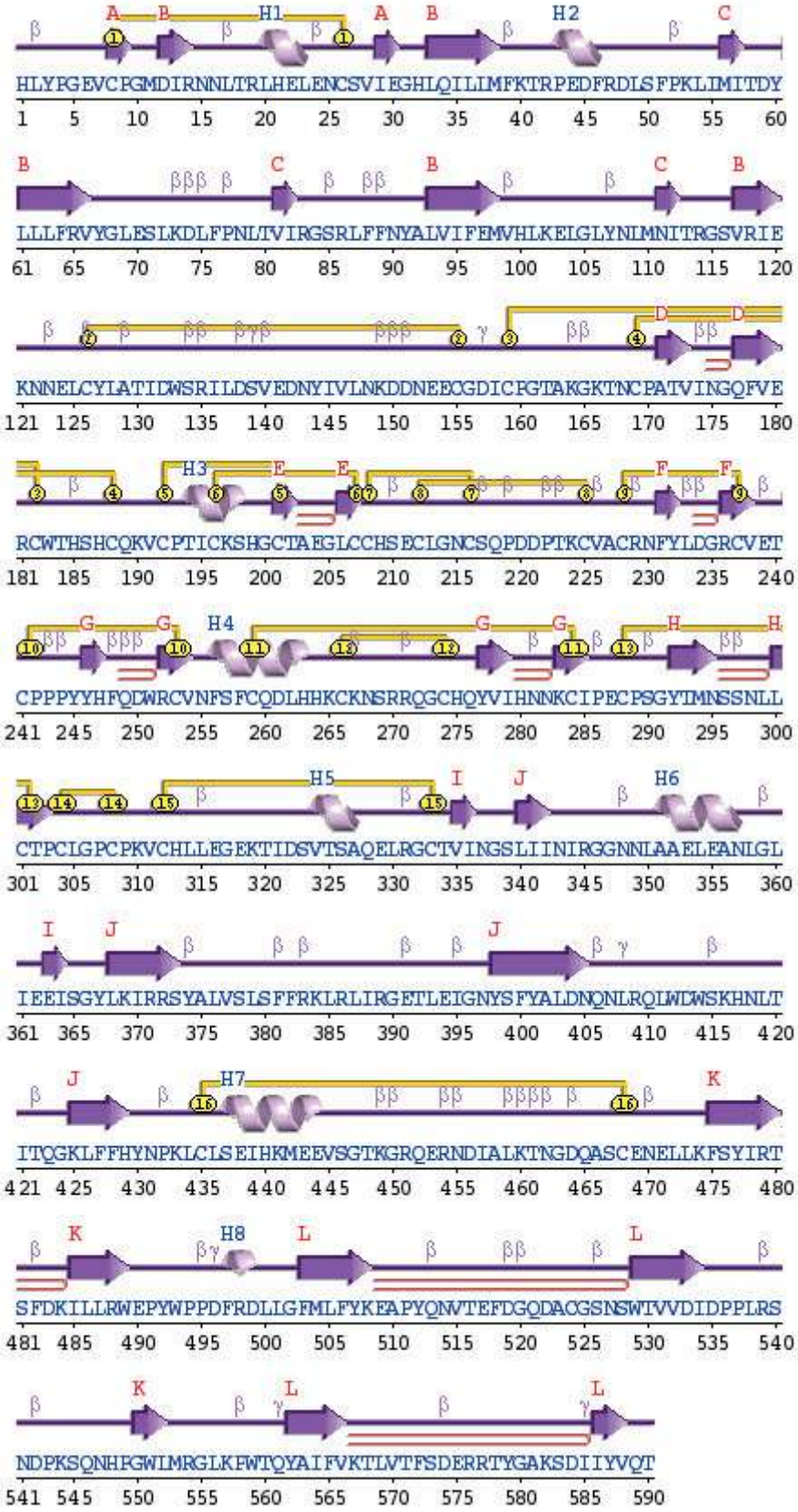


Figure 9.52: Secondary structural analysis of Insulin Receptor Ectodomain (IR)

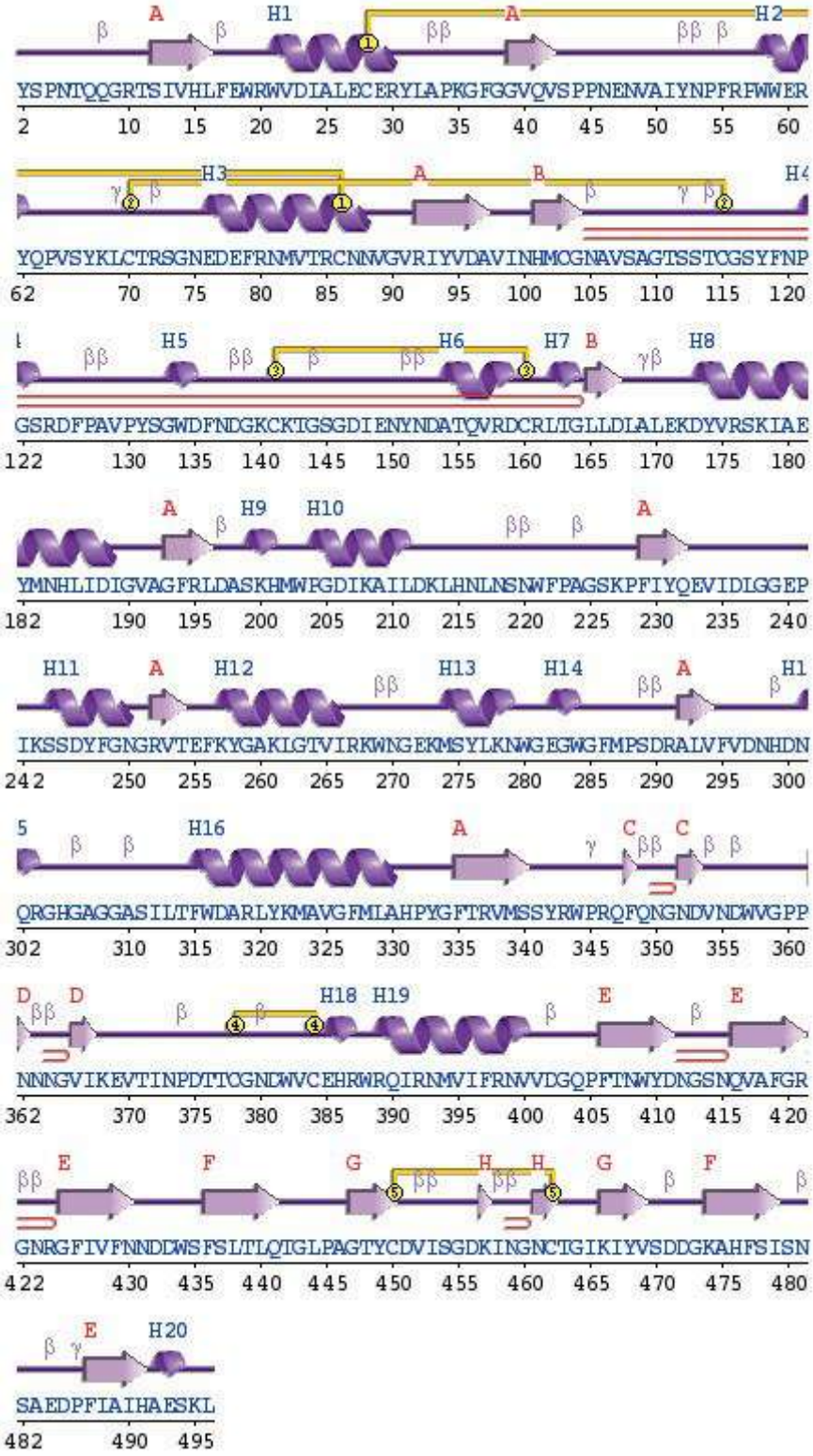


Figure 9.53: Secondary structural analysis of Pancreatic Alpha-Amylase (PAA)

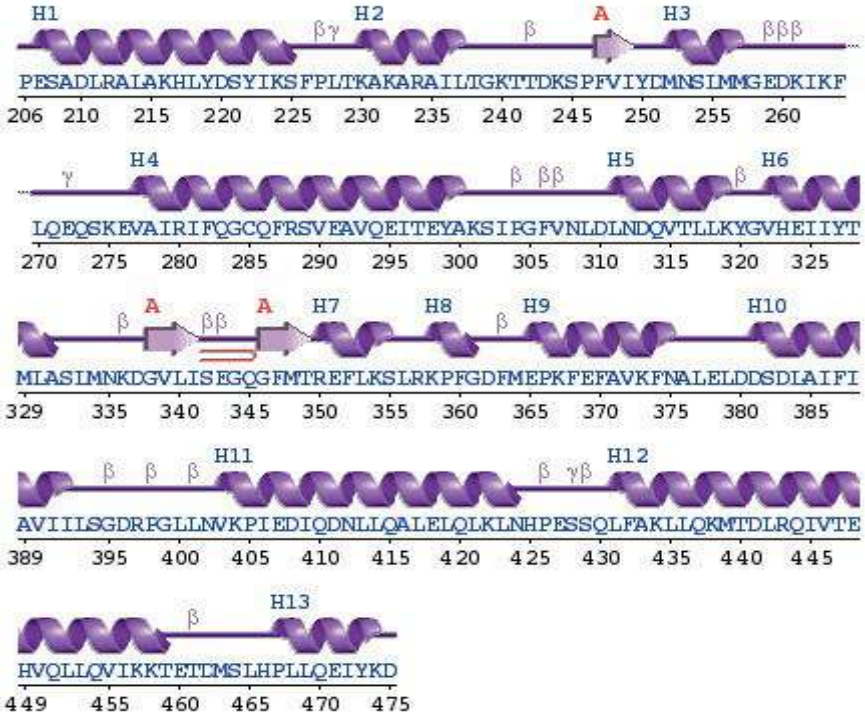


Figure 9.54: Secondary structural analysis of Peroxisome Proliferator-Activated Receptor Gamma (PPARG)

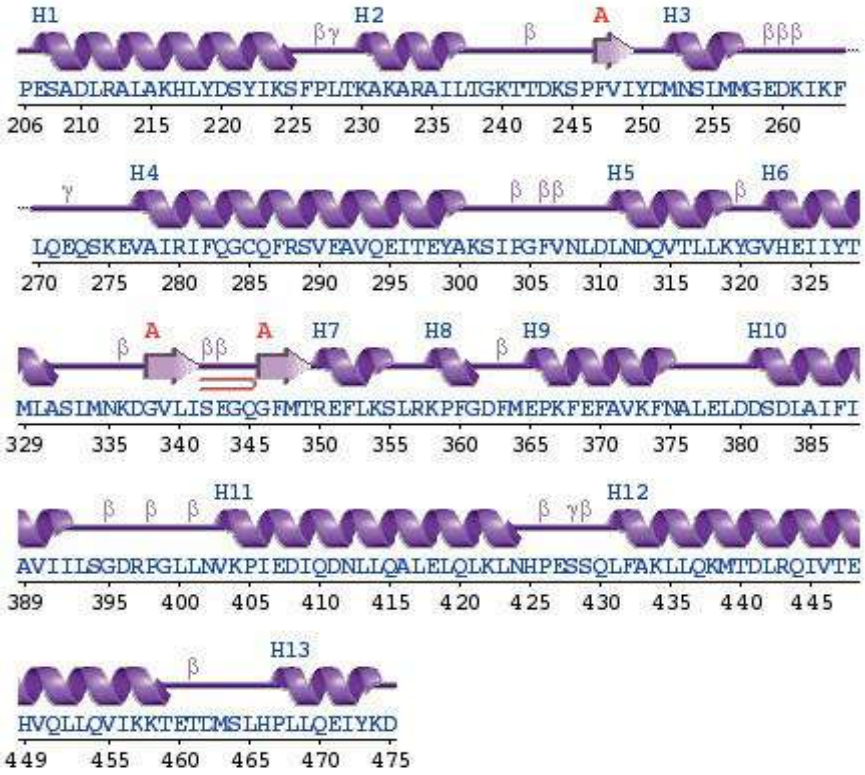


Figure 9.55: Secondary structural analysis of Protein Tyrosine Phosphatase 1B (PTP1B)

9.3.3.5.1. Secondary structural analysis of Dipeptidyl Peptidase 4 (DPP4)

DPP4 displays a highly complex structure with 10 β-sheets, 4 β-α-β units, and an extensive 44 strands, suggesting a large and intricate β-sheet framework crucial for substrate recognition (Figure 9.51). The 25 β-hairpins and 15 β-bulges indicate multiple local folding patterns that may stabilize the binding pocket for peptide substrates like incretins. The 19 α-helices and 11 helix–helix interactions provide a balanced α–β structure, supporting both rigidity and flexibility. The 73 β-turns and 4 γ-turns promote tight directional changes in the polypeptide chain, critical for forming the catalytic site. The 5 disulfide bonds enhance structural integrity, vital for stability in extracellular environments. These structural attributes align with DPP4's role as a membrane-bound serine protease in glucose regulation (Branden & Tooze, 1999).

9.3.3.5.2. Secondary structural analysis of Insulin Receptor Ectodomain

The insulin receptor is characterized by 12 β-sheets and 35 strands, forming a robust β-rich extracellular domain suited for hormone binding (Figure 9.52). The presence of 9 β-hairpins and 7 β-bulges reflects structural adjustments for precise ligand accommodation. The 8 α-helices are fewer than in many receptor kinases, but their presence alongside 2 helix–helix interactions ensure proper intracellular signaling domain stability. With 84 β-turns and 6 γ-turns, the protein maintains the flexibility necessary for conformational shifts upon insulin binding. Notably, 16 disulfide bonds confer high extracellular stability, essential for a receptor exposed to oxidative conditions. This architecture supports the receptor's dual role in insulin binding and activation of intracellular tyrosine kinase domains for glucose homeostasis (Hubbard, 2013).

9.3.3.5.3. Secondary structural analysis of Pancreatic Alpha Amylase (PAA)

Pancreatic alpha-amylase exhibits 8 β-sheets, 5 β-α-β units, and 24 β-strands, forming a mixed α/β hydrolase fold characteristic of carbohydrate-degrading enzymes. Its 6 β-hairpins and 3 β-bulges indicate moderate local β-sheet stabilization, while 20 α-helices dominate the fold, reflecting a strong α-helical framework for catalytic domain organization (Figure 9.53). The 11 helix–helix interactions suggest

significant tertiary packing stability, essential for maintaining active site geometry. With 48 β-turns and 5 γ-turns, the protein can adopt tight loop conformations for substrate entry and product release. Five disulfide bonds provide additional rigidity, enabling the enzyme to withstand harsh digestive conditions while efficiently hydrolyzing starch into maltose and glucose (Branden & Tooze, 1999).

9.3.3.5.4. Secondary structural analysis of Peroxisome Proliferator–Activated Receptor Gamma (PPARG)

PPARG has a relatively simple β-structure with 1 β-sheet and 3 β-strands, alongside 1 β-hairpin and 1 ψ-loop, indicating a minimal β-fold contribution to stability. Instead, the protein is dominated by 13 α-helices and an unusually high 36 helix–helix interactions, reflecting its identity as a ligand-activated nuclear receptor with a predominantly α-helical ligand-binding domain. The 19 β-turns and 3 γ-turns provide flexibility for conformational adjustments during ligand binding and coactivator recruitment (Figure 9.54). Lacking disulfide bonds, PPARG relies on hydrophobic and hydrogen-bond interactions for stability. Its α-helical dominance is consistent with its role in transcriptional regulation of genes involved in glucose and lipid metabolism (Nolte et al., 1998).

9.3.3.5.5. Secondary structural analysis of Protein Tyrosine Phosphatase 1B (PTP1B)

PTP1B's architecture features 2 β-sheets, 11 β-strands, and 6 β-hairpins, forming the core β-structure of its catalytic domain (Figure 9.55). The 5 β-bulges enhance local β-sheet stability, while 11 α-helices and 14 helix–helix interactions contribute to proper folding and enzyme functionality. With 30 β-turns and 3 γ-turns, the structure achieves a balance between rigidity for catalytic precision and flexibility for substrate accommodation. The absence of disulfide bonds is expected for a cytosolic enzyme, reducing oxidative vulnerability. This mixed α/β structure supports PTP1B's role in dephosphorylating the insulin receptor, thereby modulating insulin signaling and glucose metabolism (Barford et al., 1994).

9.3.3.6. Secondary structural analysis of anticancer proteins

9.3.3.6.1. AKT1

AKT1 displays 2 sheets, 8 strands, and 16 helices, with 15 helix-helix interactions indicating a densely packed helical core. The presence of 5 β-hairpins and 6 β-bulges suggests localized β-sheet curvature, contributing to a stable scaffold for its kinase domain. 21 β-turns and 3 γ-turns add structural flexibility, allowing conformational changes essential for activation and substrate recognition. The relatively high helix count supports AKT1's role as a kinase requiring a stable catalytic framework, while the moderate sheet content helps maintain domain rigidity (Figure 9.56). This balance between rigidity and flexibility facilitates precise regulation in the PI3K/AKT/mTOR pathway, allowing AKT1 to adapt to different activation states and interact with multiple partners in oncogenic signaling.

9.3.3.6.2. Epidermal Growth Factor Receptor (EGFR)

Epidermal Growth Factor Receptor (EGFR)'s structure features 4 sheets and 11 strands, supported by 14 helices and 10 helix-helix interactions. The sheet network, reinforced by 5 β-hairpins and 4 β-bulges, forms a stable β-sandwich architecture typical of extracellular ligand-binding and kinase domains. 26 β-turns and 3 γ-turns indicate significant flexibility, likely important for conformational shifts during ligand binding and receptor dimerization. The balanced mix of helices and sheets supports both rigidity for signal transduction and adaptability for activation. EGFR's secondary structure architecture is consistent with its function as a receptor tyrosine kinase that must undergo large conformational rearrangements upon activation while maintaining precise catalytic alignment (Figure 9.57).

9.3.3.6.3. Kirsten Rat Sarcoma Viral Oncogene Homolog (KRAS)

Kirsten Rat Sarcoma Viral Oncogene Homolog (KRAS) presents a relatively simple fold with 1 sheet, 6 strands, and 6 helices, along with 6 helix-helix interactions. The presence of 2 β–α–β units, 1 β-hairpin, and 1 ψ-loop reflects a classical small GTPase topology optimized for rapid conformational switching between active and inactive states. The 10 β-turns and 1 γ-turn contribute to localized flexibility in the

switch regions, which are critical for nucleotide exchange and effector binding (Figure 9.58). KRAS's minimal sheet content emphasizes its reliance on α-helical stability combined with loop flexibility, enabling its function as a dynamic molecular switch in Ras-MAPK signaling and its adaptability for binding to various regulatory proteins in cancer progression.

9.3.3.6.4. Mitogen-Activated Protein Kinase 1 (MAPK1)

Mitogen-Activated Protein Kinase 1 (MAPK1) shows 4 sheets and 12 strands, indicating a robust β-sheet core, complemented by 18 helices and 15 helix-helix interactions for stability. 5 β-hairpins and 6 β-bulges contribute to β-sheet curvature, while 28 β-turns and 2 γ-turns offer flexibility for substrate accommodation and conformational changes during kinase activation. This structure supports MAPK1's dual-domain kinase architecture, where a stable scaffold is essential for ATP binding and catalysis, and flexible loops facilitate substrate entry and phosphorylation events (Figure 9.59). The high helix count strengthens domain packing, while the significant turn content allows for structural adaptability within signaling complexes.

9.3.3.6.5. Tumour Protein p53 (P53)

Tumour Protein p53 (TP53) exhibits 2 sheets and 11 strands, but only 3 helices, reflecting its partially disordered nature, especially in the N-terminal transactivation domain. The β-architecture is reinforced by 3 β-hairpins and 4 β-bulges, while a striking 26 β-turns provide high flexibility, consistent with its ability to bind diverse DNA sequences and partner proteins. The relatively low helix count underscores its flexible, modular nature, enabling TP53 to adapt structurally when interacting with DNA and regulatory cofactors (Figure 9.60). This structural arrangement explains both its versatility in transcriptional regulation and its susceptibility to destabilization upon mutation, which is a hallmark in many cancers.

9.3.4. Ramachandran plot analysis of target proteins

Ramachandran plot analysis evaluates the sterically allowed and disallowed torsional angles (φ and ψ) of amino acid residues in a protein, providing insight into the stereochemical quality of its 3D model. A higher percentage of residues in the

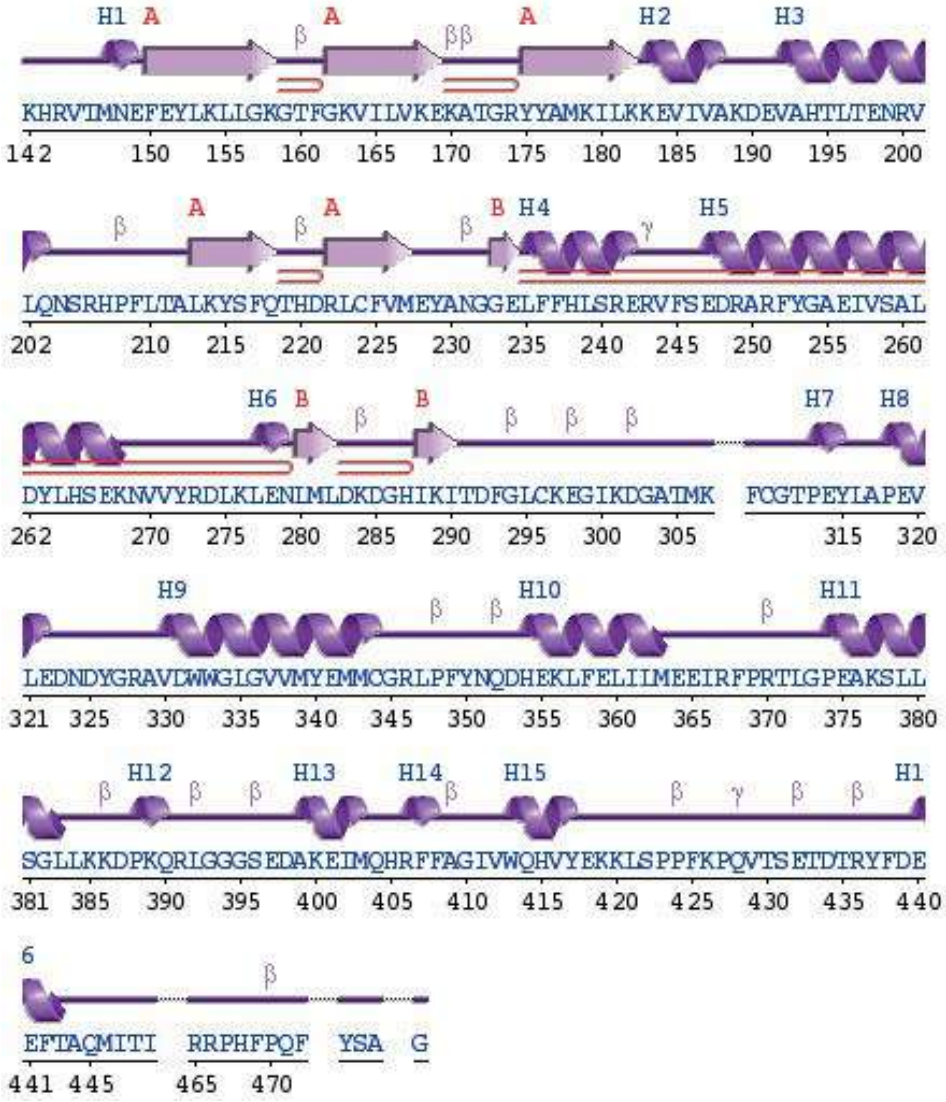


Figure 9.56: Secondary structural analysis of AKT serine/threonine kinase (AKT1)

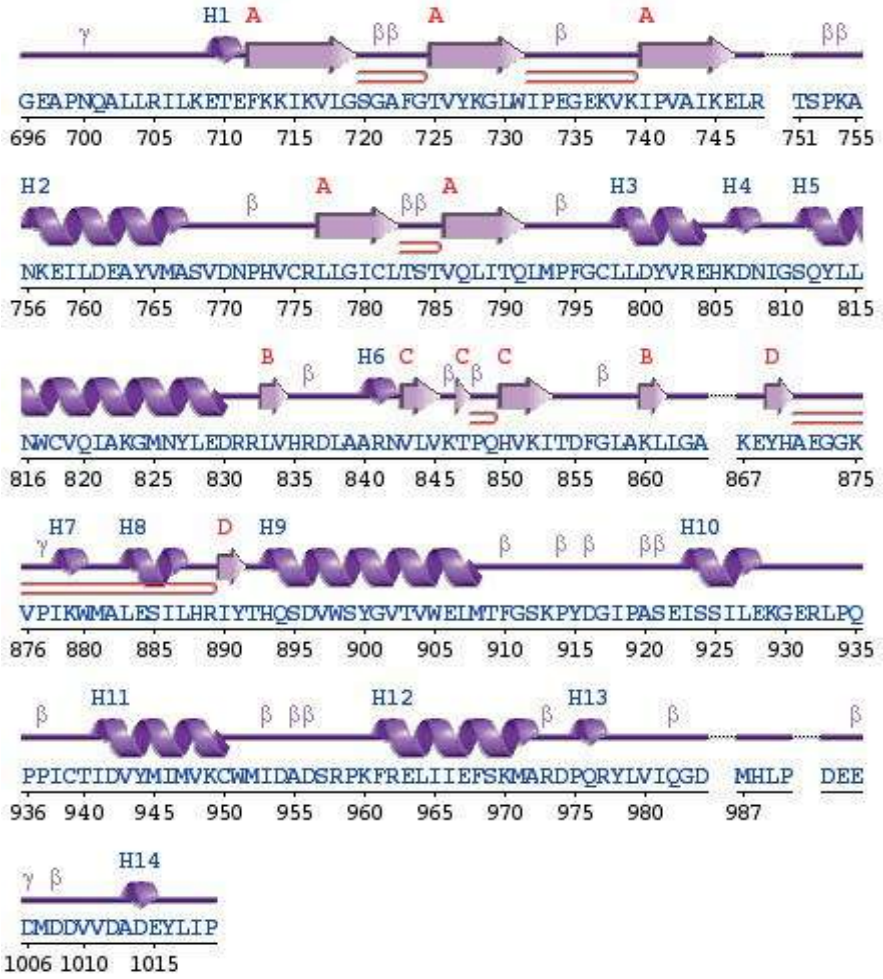


Figure 9.57: Secondary structural analysis of Epidermal Growth Factor Receptor (EGFR)

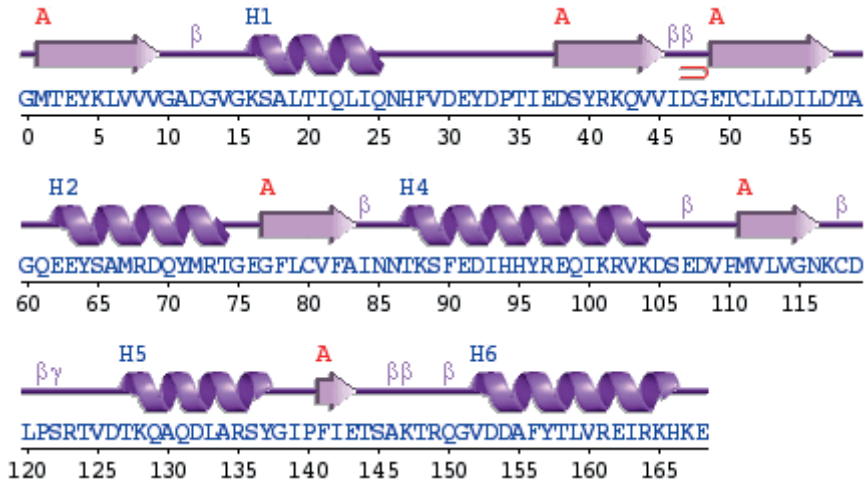


Figure 9.58: Secondary structural analysis of Kirsten Rat Sarcoma Viral Oncogene Homolog (KRAS)

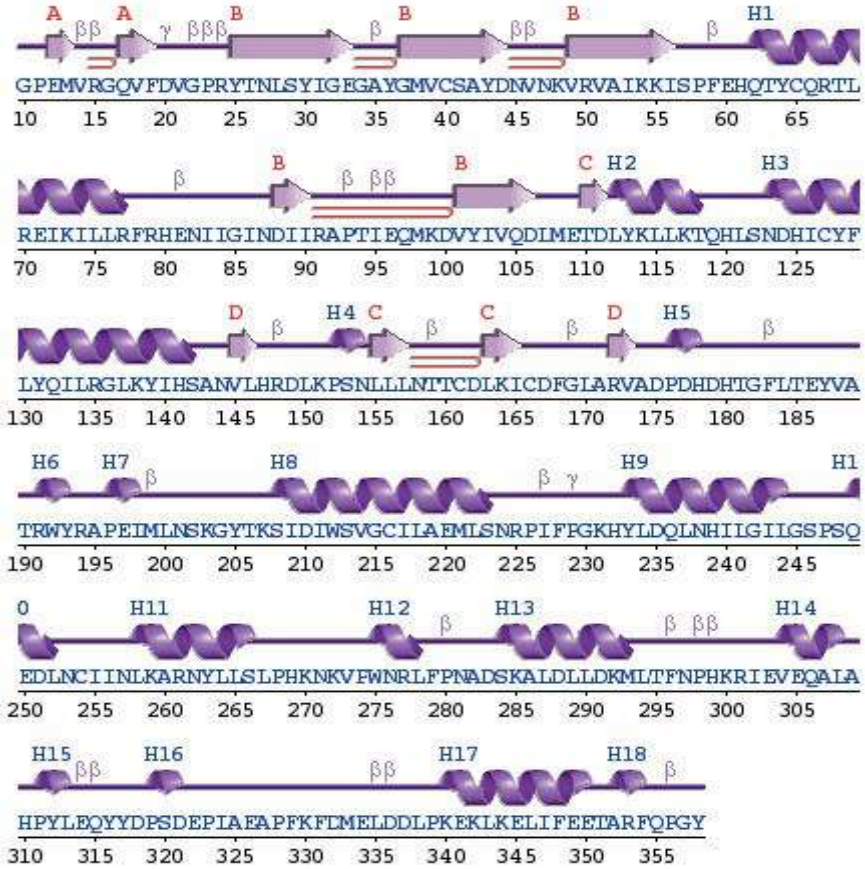


Figure 9.59: Secondary structural analysis of Mitogen-Activated Protein Kinase 1 (MAPK1)

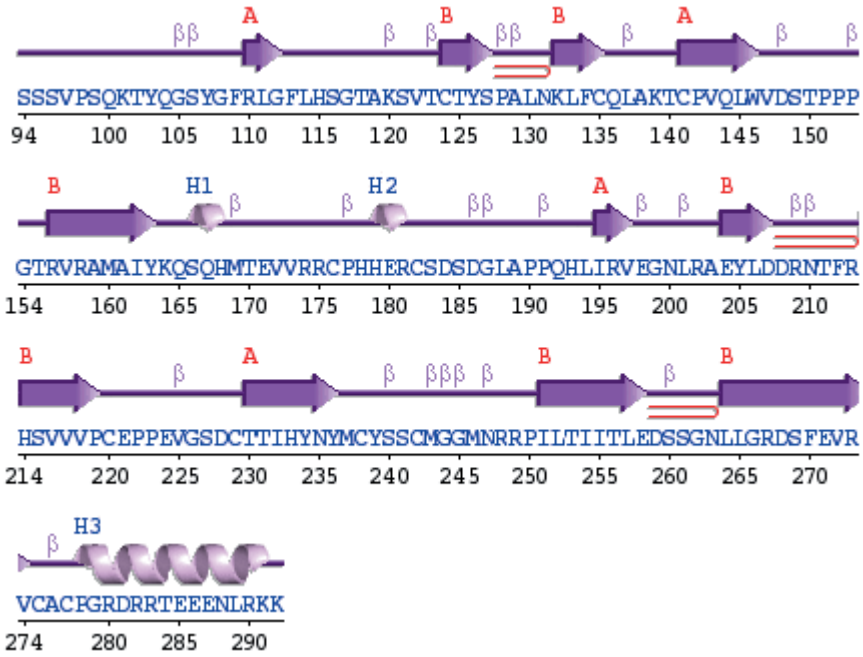


Figure 9.60: Secondary structural analysis of Tumour Protein p53 (P53)

Table 9.19: Ramachandran plot statistics for antioxidant proteins

Parameter	Human Cu, Zn Superoxide Dismutase (SOD1)	Human Erythrocyte Catalase (CAT)	Human Glutathione Peroxidase 1 (GPx1)	KEAP1 Kelch Domain (KEAP1 Kelch)	Thioredoxin and TXNIP Complex (Trx-TXNIP)
Most favoured regions (%)	90.9	84.5	92.1	89.7	91.6
Additional allowed regions (%)	9.1	15.2	7.9	9.9	7.5
Generously allowed regions (%)	0	0	0	0	0.9
Disallowed regions (%)	0	0.2	0	0.4	0
Non-Gly/Pro residues	121	427	151	242	334
Glycine count	25	33	17	35	26
Proline count	5	36	14	13	16
Total residues	153	498	184	291	383

Table 9.20: Ramachandran plot statistics for antimicrobial proteins

Parameter	D-alanyl-D-alanine ligase (D-ALA:D-ALA Ligase/Ddl)	LasR ligand-binding domain (LasR)	PqsR coinducer-binding domain (PqsR/MvfR)	Penicillin-Binding Protein 3 (PBP3)	Regulatory protein RhlR (RhIR)
Most favoured regions (%)	85	91.7	89.7	91.8	93
Additional allowed regions (%)	14.2	8.3	8.2	8	6.5
Generously allowed regions (%)	0	0	1.1	0	0.5
Disallowed regions (%)	0.8	0	1.1	0.2	0
Non-Gly/Pro residues	260	133	184	415	215
Glycine count	31	13	10	45	14
Proline count	13	7	8	30	10
Total residues	306	162	203	495	241

Table 9.21: Ramachandran plot statistics for anthelmintic proteins

Parameter	ATP synthase subunit a (ATP synthase)	Cytochrome c Oxidase subunit 1 (COX1)	Heat Shock Protein 70 (HSP70)	NADH-Ubiquinone Oxidoreductase chain 1 (Complex I)	Extracellular Globin-3/Erythrocruorin (Ext. Globin-3)
Most favoured regions (%)	93.8	93	97.4	93.6	90.8
Additional allowed regions (%)	6.2	6.4	2.6	5.7	9.2
Generously allowed regions (%)	0	0.6	0	0.4	0
Disallowed regions (%)	0	0	0	0.4	0
Non-Gly/Pro residues	210	171	116	280	131
Glycine count	7	18	9	12	8
Proline count	12	12	5	14	5
Total residues	231	203	132	308	146

Table 9.22: Ramachandran plot statistics for anti-inflammatory proteins

Parameter	Nuclear Factor kappa B p50 (NF-κB p50)	Tumour Necrosis Factor-alpha (TNF-α)	Human Inducible Nitric Oxide Synthase (iNOS)	Janus Kinase 2 (JAK2)	Human Cyclooxygenase-2 (COX-2)
Most favoured regions (%)	85.3	92.7	89.4	91.2	90.6
Additional allowed regions (%)	12.4	7.3	10.6	8	9.2
Generously allowed regions (%)	1.5	0	0	0.4	0.2
Disallowed regions (%)	0.8	0	0	0.4	0
Non-Gly/Pro residues	266	109	367	250	458
Glycine count	26	10	28	17	35
Proline count	18	8	24	12	34
Total residues	311	132	421	284	528

Table 9.23: Ramachandran plot statistics for anti-antidiabetic proteins

Parameter	Dipeptidyl Peptidase 4 (DPP4)	Insulin Receptor Ectodomain (IR)	Pancreatic Alpha-Amylase (PAA)	Peroxisome Proliferator-Activated Receptor Gamma (PPARG)	Protein Tyrosine Phosphatase 1B (PTP1B)
Most Favoured Regions (%)	86.9	69.2	88.8	90.5	90.8
Additional Allowed Regions (%)	12.8	30.8	10.7	9.1	8.5
Generously Allowed Regions (%)	0.2	0	0.2	0.4	0.7
Disallowed Regions (%)	0.2	0	0.2	0	0
Non-Gly/Pro Residues	657	523	420	241	271
Glycine Count	40	37	50	11	14
Proline Count	26	28	23	10	12
Total Residues	725	590	495	265	299

Table 9.24: Ramachandran plot statistics for anticancer proteins

Parameters	AKT1	Epidermal Growth Factor Receptor (EGFR)	Kirsten Rat Sarcoma Viral Oncogene Homolog (KRAS)	Mitogen-Activated Protein Kinase 1 (MAPK1)	Tumour Protein p53 (TP53)
Most Favoured Regions (%)	91.3	89.4	90.8	88.8	91.8
Additional Allowed Regions (%)	6.9	9.9	9.2	11.2	8.2
Generously Allowed Regions (%)	1.1	0.8	0	0	0
Disallowed Regions (%)	0.7	0	0	0	0
Non-Gly/Pro Residues	276	263	153	312	170
Glycine Count	23	19	11	16	13
Proline Count	12	17	4	20	14
Total Residues	319	306	169	349	199

most favoured regions indicates a more reliable and well-folded protein structure. Ramachandran plot analysis evaluates the stereochemical quality of a protein structure by mapping φ (phi) and ψ (psi) torsion angles of amino acid residues. The distribution of residues into most favoured, additional allowed, generously allowed, and disallowed regions serves as an indicator of conformational stability and validity of the protein model. Proteins with higher percentages in the most favoured regions are generally well-folded and stable, while the presence of residues in disallowed regions can indicate strained conformations that might be functionally relevant or artefactual (Ramachandran et al., 1963).

For antioxidant proteins, such structural features are vital, as they operate under oxidative stress and require both stability and flexibility for effective redox activity.

For antimicrobial proteins, these stereochemical insights help correlate 3D structure with their catalytic, regulatory, or binding activities in microbial inhibition.

Anthelmintic protein targets, where structural stability is critical to survival under parasitic conditions, Ramachandran analysis provides a measure of how well the protein maintains its functional conformation.

The anti-inflammatory proteins, maintaining a high percentage of residues in most favoured regions ensure structural robustness during dynamic physiological processes like ligand binding, signal transduction, and catalytic activity. Proteins with balanced flexibility can adapt to molecular interactions, which is critical in inflammation, where transient complex formation is frequent.

Ramachandran plot analysis is crucial for antidiabetic proteins, as the conformational integrity of these biomolecules directly influences their ligand-binding efficiency, enzymatic activity, and receptor interactions. Poorly folded or unstable regions could compromise their biological role in glucose regulation and insulin signaling.

In anticancer proteins, maintaining a well-defined backbone conformation is critical for functional integrity, especially in ligand-binding and catalytic domains where precise geometry dictates biological activity.

Ramachandran plot statistics for target proteins were listed in Tables 9.19-9.24

9.3.4.1. Ramachandran plot analysis of antioxidant proteins

Ramachandran plot analysis of antioxidant proteins are demonstrated in Figure 9.61

9.3.4.1.1. Human Cu, Zn Superoxide Dismutase (SOD1)

Human Cu, Zn Superoxide Dismutase (SOD1)'s Ramachandran statistics reveal 90.9% in most favoured regions, 9.1% in additional allowed regions, and 0% in disallowed regions, indicative of a highly refined fold. At 153 residues, this compact enzyme maintains structural precision while incorporating loop flexibility for substrate binding. The 25 glycines enable movement in loops surrounding the catalytic copper/zinc site, while only 5 prolines maintain structural stability without excessive rigidity. The complete absence of disallowed residues reflects evolutionary optimization, allowing SOD to rapidly convert superoxide radicals into less reactive species, thus preventing oxidative damage.

9.3.4.1.2. Human Erythrocyte Catalase (CAT)

Human Erythrocyte Catalase (CAT) Catalase shows 84.5% of residues in most favoured regions, 15.2% in additional allowed regions, and a minimal 0.2% in disallowed regions. This suggests a structurally stable enzyme with regions of flexibility, essential for accommodating hydrogen peroxide at the active site. With 498 residues, including 33 glycines and 36 prolines, catalase combines flexible loops with rigid turns to maintain structural integrity during rapid catalysis. The slight proportion in disallowed regions likely reflects active site loops adopting strained conformations for substrate access. These structural properties are critical for catalase's high turnover capacity, enabling efficient detoxification of hydrogen peroxide under oxidative stress.

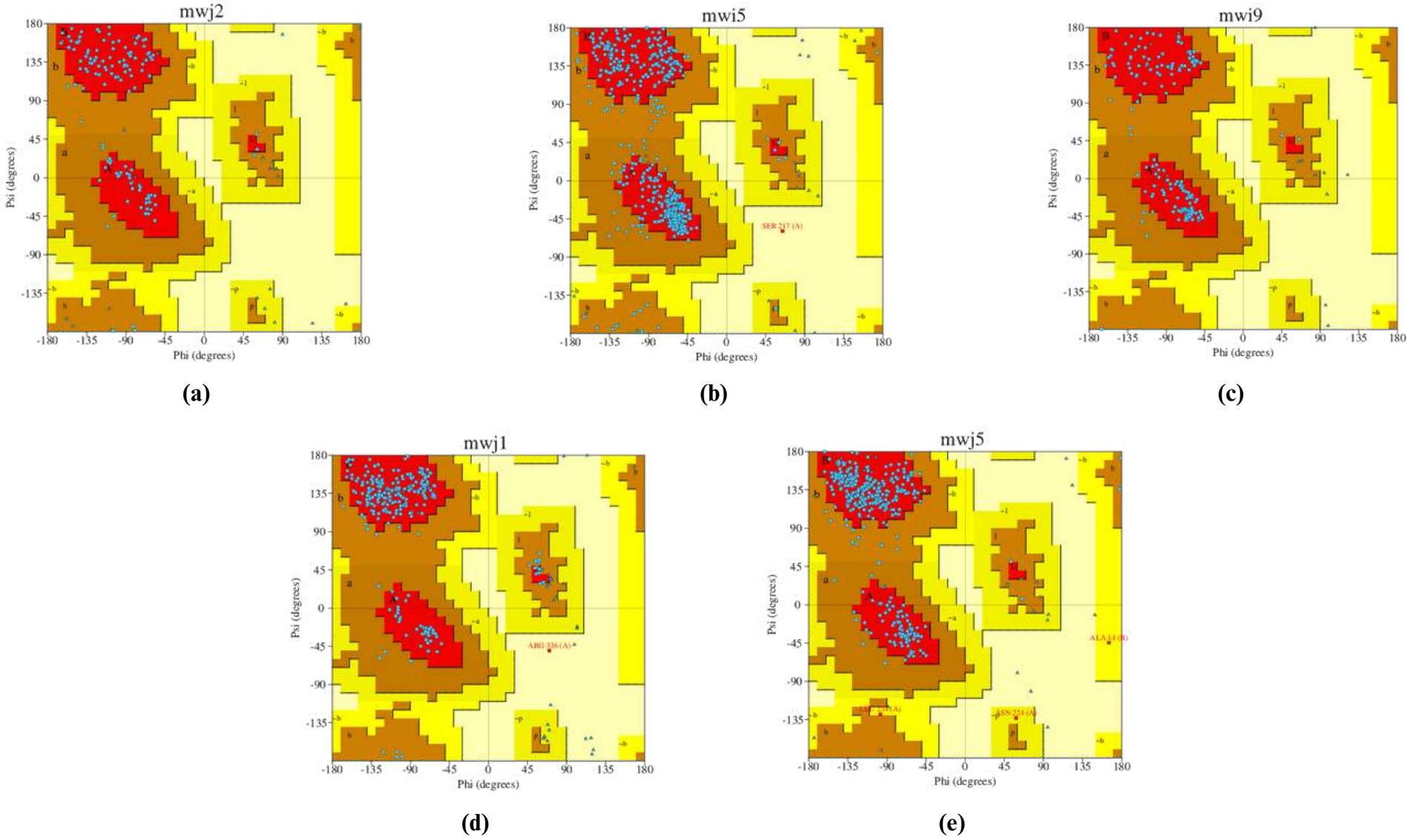


Figure 9.61: Ramachandran plot analysis of antioxidant proteins (a) Human Cu, Zn SuperoxideDismutase (SOD1) (b) Human Erythrocyte Catalase (CAT) (c) Human Glutathione Peroxidase 1 (GPx1) (d) KEAP1 Kelch Domain (KEAP1 Kelch)(e) Thioredoxin and TXNIP Complex (Trx-TXNIP)

9.3.4.1.3. Human Glutathione Peroxidase 1 (GPx1)

Human Glutathione Peroxidase 1 (GPx1) has 92.1% residues in most favoured regions, 7.9% in additional allowed regions, and 0% in disallowed regions, indicating exceptional stereochemical quality. Its compact size (184 residues) and high structural precision ensure reliable peroxide detoxification. The 17 glycines provide flexibility in the glutathione-binding loops, while 14 prolines stabilize key turns near the active site. The absence of disallowed residues suggests minimal structural strain, critical for the reactivity of the catalytic selenocysteine. This structural robustness allows GPx1 to function effectively in protecting cells from hydrogen peroxide and lipid hydroperoxides.

9.3.4.1.4. KEAP1 Kelch Domain (KEAP1 Kelch)

KEAP1 Kelch Domain (KEAP1 Kelch) displays 89.7% of residues in most favoured regions, 9.9% in additional allowed regions, and a negligible 0.4% in disallowed regions. For a 291-residue regulatory protein, this reflects a well-structured core with strategically flexible loops. The 35 glycine residues contribute to conformational adaptability in the Kelch-repeat domains, which are crucial for binding the transcription factor Nrf2. The small fraction in disallowed regions likely corresponds to specific strained conformations at protein–protein interaction sites, enhancing binding specificity. KEAP1's Ramachandran profile supports its role as a dynamic oxidative stress sensor, capable of switching between inactive and active conformations for redox regulation.

9.3.4.1.5. Thioredoxin and TXNIP Complex (Trx-TXNIP)

Thioredoxin and TXNIP Complex (Trx-TXNIP) shows 91.6% of residues in most favoured regions, 7.5% in additional allowed regions, 0.9% in generously allowed regions, and 0% in disallowed regions. With 383 residues, TXNIP achieves a balance of stability and flexibility, aided by 26 glycines for loop mobility and 16 prolines for turn stability. The fraction in generously allowed regions likely reflects conformations enabling thioredoxin binding, crucial for its regulatory function in redox signaling and apoptosis. The lack of disallowed residues indicates a structurally

sound protein capable of maintaining its functional conformation even under oxidative stress**.**

9.3.4.2. Ramachandran plot analysis of antimicrobial proteins

Ramachandran plot analysis of antimicrobial proteins are demonstrated in Figure 9.62

9.3.4.2.1. D-alanyl-D-alanine ligase (D-ALA:D-ALA Ligase/Ddl)

D-alanyl-D-alanine ligase (D-ALA:D-ALA Ligase/Ddl) exhibits 85.0% of residues in the most favoured regions, 14.2% in additional allowed regions, and a minimal 0.8% in disallowed regions. The low disallowed percentage suggests that the majority of the structure adopts energetically stable conformations. With 260 non-glycine/proline residues, the protein maintains a strong backbone geometry, while the 31 glycine residues contribute to localized flexibility, and the 13 proline residues introduce rigidity at turns. The slightly lower "most favoured" percentage compared to other stable enzymes could indicate functionally important conformational adaptability, essential for accommodating both substrates and ATP in its active site during peptidoglycan synthesis. This balance of rigidity and flexibility likely supports its catalytic cycle.

9.3.4.2.2. LasR ligand-binding domain (LasR)

LasR ligand-binding domain (LasR) demonstrates an excellent stereochemical profile with 91.7% of residues in the most favoured regions and no residues in disallowed regions. The 133 non-glycine/proline residues form the well-folded structural core, while 13 glycine residues enhance flexibility for conformational changes during ligand or DNA binding. The 7 prolines likely stabilize the loop and turn regions. The high proportion in the most favoured regions, combined with the absence of disallowed residues, reflects a robust and reliable model suitable for DNA-binding transcription factors. This structural integrity is vital for LasR's role in quorum sensing, ensuring stable helix-turn-helix domains can interact precisely with promoter regions.

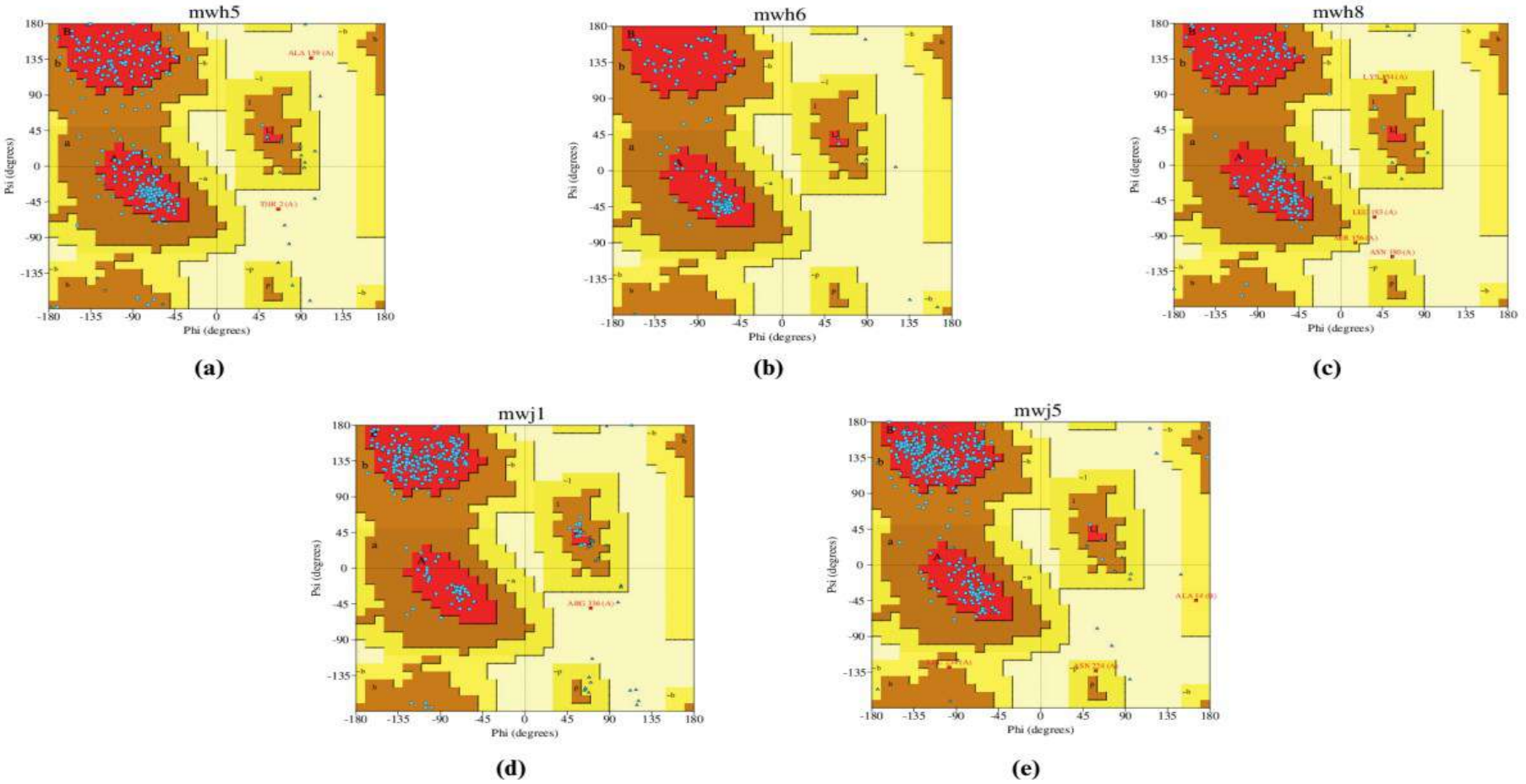


Figure 9.62: Ramachandran plot analysis of antimicrobial proteins (a) D-alanyl-D-alanine ligase (D-ALA:D-ALA Ligase/Ddl)(b) LasR ligand-binding domain (LasR)(c) PqsR coinducer-binding domain (PqsR/MvfR)(d) Penicillin-Binding Protein 3 (PBP3) (e) Regulatory protein RhIR (RhIR)

9.3.4.2.3. PqsR coinducer-binding domain (PqsR/MvfR)

PqsR coinducer-binding domain (PqsR/MvfR) has 89.7% of residues in most favoured regions, 8.2% in additional allowed, 1.1% in generously allowed, and 1.1% in disallowed regions. With 184 non-glycine/proline residues, the structure is largely well-folded but with some minor strain, possibly reflecting functional conformations needed for DNA or ligand binding. The 10 glycines enhance flexibility in binding domains, while 8 prolines introduce rigid kinks that can stabilize specific loop conformations. The slightly elevated disallowed percentage could be due to active-site or regulatory domain mobility, which is often observed in transcription factors that need to adjust to different DNA promoters.

9.3.4.2.4. Penicillin-Binding Protein 3 (PBP3)

Penicillin-Binding Protein 3 (PBP3) shows 91.8% of residues in the most favoured regions, 8.0% in additional allowed, and only 0.2% in disallowed regions. With 415 non-glycine/proline residues, the protein possesses a rigid catalytic framework, while 45 glycine residues provide necessary flexibility for accommodating peptidoglycan substrates. The 30 proline residues help lock specific structural turns in place, maintaining the enzyme's active site geometry. This stereochemical quality supports the protein's function in bacterial cell wall biosynthesis and explains why it is a prime target for β-lactam antibiotics. The minimal disallowed content reinforces the accuracy of the model for inhibitor design.

9.3.4.2.5. Regulatory protein RhIR (RhIR)

Regulatory protein RhIR (RhIR) exhibits 93.0% of residues in most favoured regions, 6.5% in additional allowed, 0.5% in generously allowed, and none in disallowed regions. This high most-favoured percentage indicates an exceptionally well-folded protein. The 215 non-glycine/proline residues form a stable framework, with 14 glycines enabling local flexibility and 10 prolines stabilizing turns in helix-rich domains. Such structural reliability is advantageous for its role as a transcriptional regulator in quorum sensing, ensuring precise conformational control for binding

autoinducers and target DNA. The absence of disallowed residues reflects an optimal geometry with minimal steric strain.

9.3.4.3. Ramachandran plot analysis of anthelmintic proteins

Ramachandran plot analysis of antimicrobial proteins are demonstrated in Figure 9.63

9.3.4.3.1. ATP synthase subunit a (ATP synthase)

ATP synthase subunit a demonstrates 93.8% in most favoured regions and 6.2% in additional allowed regions, with no residues in generously allowed or disallowed regions. This clean stereochemical profile aligns with the functional need for a stable, membrane-embedded proton channel within the F_0 domain of ATP synthase. The modest fraction in additional allowed regions likely reflects the conformational adaptability needed during rotary catalysis. With 7 glycines and 12 prolines, the protein balances rigidity with localized flexibility, ensuring efficient proton translocation without compromising mechanical stability.

9.3.4.3.2. Cytochrome c oxidase subunit 1 (COX1)

Cytochrome c oxidase subunit 1 (COX1) shows 93.0% of residues in most favoured regions, 6.4% in additional allowed regions, and only 0.6% in generously allowed regions, with no residues in disallowed regions. This distribution indicates a highly optimized structure, with minimal deviations from ideal backbone dihedral angles. Given its role as part of mitochondrial Complex IV, such precision in folding is crucial for maintaining the proton translocation pathway and ensuring efficient electron transfer. The balanced presence of 18 glycines and 12 prolines likely contributes to localized flexibility while avoiding excessive conformational strain. Overall, the results suggest a well-packed and stable membrane-bound protein, adapted for the energetically demanding conditions of oxidative phosphorylation.

9.3.4.3.3. Heat Shock Protein 70 (HSP70)

Heat Shock Protein 70 (HSP70) exhibits 97.4% of residues in most favoured regions and only 2.6% in additional allowed regions, with no residues in generously

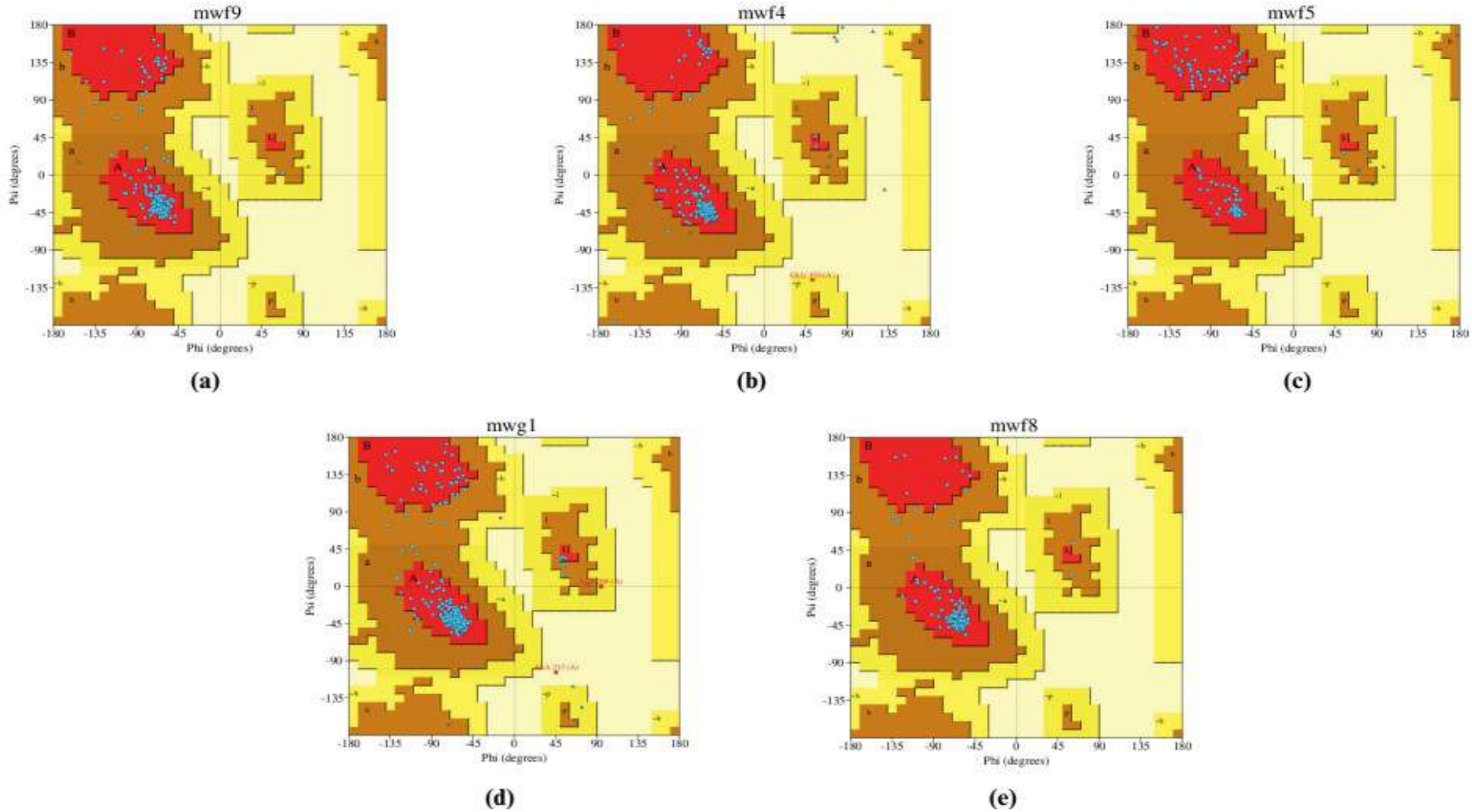


Figure 9.63: Ramachandran plot analysis of anthelmintic proteins (a) ATPsynthase subunit a (ATP synthase)(b) Cytochrome c Oxidase subunit 1 (COX1)(c) Heat Shock Protein 70 (HSP70)(d) NADH-ubiquinone oxidoreductase chain 1 (Complex I) (e)Extracellular Globin-3 / Erythrocruorin (Ext. Globin-3)

allowed or disallowed regions. This exceptionally high percentage of residues in ideal conformations highlights the structural reliability of this chaperone protein. Since HSP70 undergoes repeated binding and release cycles during protein folding, a robust and strain-free backbone is essential for maintaining efficiency over many cycles. The relatively small number of glycines (9) and prolines (5) provides a balance between flexibility and stability, ensuring the protein can adapt its conformation for diverse substrates without destabilizing its structure.

9.3.4.3.4. NADH-ubiquinone oxidoreductase chain 1 (Complex I)

NADH-ubiquinone oxidoreductase chain 1 (Complex I) shows 93.6% in most favoured regions, 5.7% in additional allowed regions, 0.4% in generously allowed regions, and 0.4% in disallowed regions. The extremely small proportion of disallowed residues (only 1 residue) is unlikely to disrupt function, especially given the complex's membrane-embedded environment, where local deviations may be functionally important for proton transfer. The 12 glycines and 14 prolines contribute to precise folding while enabling movement in transmembrane loops. Such high stereochemical accuracy supports its role in Complex I, where tight coupling of electron transport and proton pumping requires exceptional structural integrity.

9.3.4.3.5. Extracellular Globin-3/Erythrocruorin (Ext. Globin-3)

Extracellular Globin-3 / Erythrocruorin (Ext. Globin-3) has 90.8% of residues in most favoured regions and 9.2% in additional allowed regions, with no residues in disallowed regions. While slightly lower than HSP70, this still indicates a high-quality fold. The higher proportion in additional allowed regions may reflect the helical loop transitions necessary for heme binding and oxygen release. The presence of 8 glycines and 5 prolines supports targeted flexibility, ensuring the helical scaffold can accommodate subtle shifts during ligand binding and release. This configuration is well suited to maintaining oxygen transport efficiency in fluctuating parasitic environments.

9.3.4.4. Ramachandran plot analysis of anti-inflammatory proteins

Ramachandran plot analysis of anti-inflammatory proteins are demonstrated in Figure 9.64

9.3.4.4.1. Nuclear Factor kappa B p50 (NF-κB p50)

Nuclear Factor kappa B p50 (NF-κB p50) presents a more flexible stereochemical profile, with 85.3% (227 residues) in most favoured regions, 12.4% (33 residues) in additional allowed regions, 1.5% (4 residues) in generously allowed regions, and 0.8% (2 residues) in disallowed regions. The higher proportion outside the most favoured regions suggests a structure adapted for conformational versatility, crucial for DNA binding and interaction with co-factors. The 26 glycines facilitate tight turns in the DNA-binding domain, while 18 prolines contribute to loop rigidity and stability. The small number of disallowed conformations may occur in high-strain binding pockets, supporting NF-κB's role as a transcriptional regulator capable of adapting to diverse DNA target sites.

9.3.4.4.2. Tumour Necrosis Factor-alpha (TNF-α)

Tumour Necrosis Factor-alpha (TNF-α) demonstrates 92.7% (101 residues) in most favoured regions and 7.3% (8 residues) in additional allowed regions, with no residues in generously allowed or disallowed categories. This high stereochemical quality reflects TNF-α's compact and stable extracellular structure, optimized for receptor binding and trimer formation. The 10 glycines allow for localized flexibility within loop regions, and the 8 prolines contribute to conformational stability under extracellular stress conditions. Such a robust stereochemical framework is vital for maintaining the biologically active conformation during cytokine signaling in inflammatory pathways.

9.3.4.4.3. Human Inducible Nitric Oxide Synthase (iNOS)

Human Inducible Nitric Oxide Synthase (iNOS) displays 89.4% (328 residues) in most favoured regions and 10.6% (39 residues) in additional allowed regions, with no residues in generously allowed or disallowed categories. This slightly

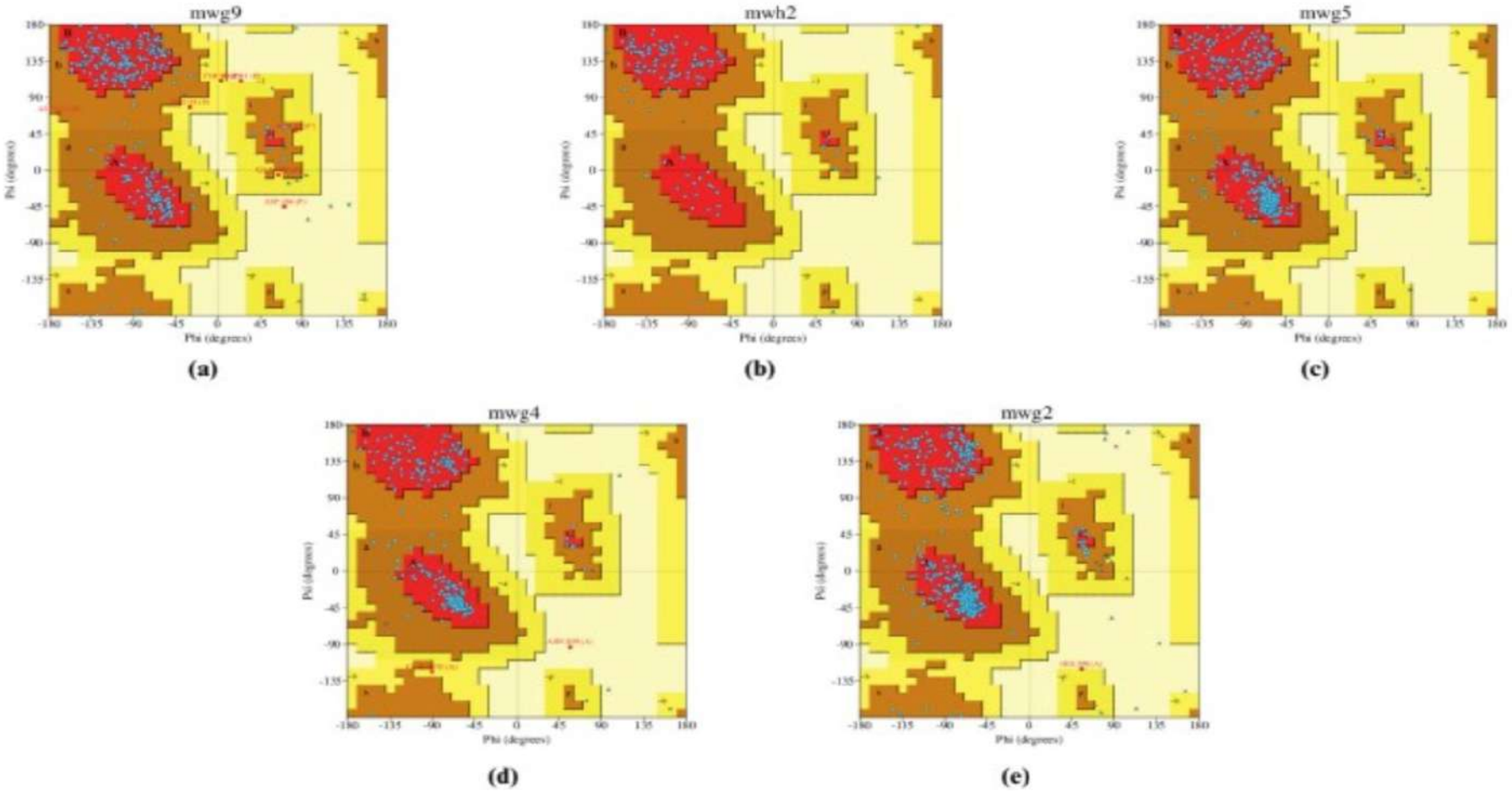


Figure 9.64: Ramachandran plot analysis of anti-inflammatory proteins (a) Nuclear Factor kappa B p50 (NF-κB p50) (b) Tumour Necrosis Factor-alpha (TNF-α) (c) Human Inducible Nitric Oxide Synthase (iNOS) (d) Janus Kinase 2 (JAK2) (e) Human Cyclooxygenase-2 (COX-2)

lower most-favoured percentage compared to COX-2 and JAK2 indicates a modest increase in backbone flexibility, consistent with iNOS's catalytic requirement for dynamic substrate accommodation and electron transfer. The 28 glycines provide rotational adaptability for cofactor binding, while 24 prolines stabilize loops and turns within the large enzyme. Such flexibility may be biologically advantageous, enabling rapid nitric oxide production in response to immune triggers while maintaining structural integrity over sustained catalytic cycles.

9.3.4.4.4. Janus Kinase 2 (JAK2)

Janus Kinase 2 (JAK2) exhibits 91.2% (228 residues) in most favoured regions, 8.0% (20 residues) in additional allowed zones, and 0.4% (1 residue) each in generously allowed and disallowed regions. The presence of a minimal number of disallowed conformations suggests overall good stereochemical quality, with the exceptions likely localized in functional motifs that require structural strain, such as ATP-binding loops. The 17 glycines provide rotational flexibility, while 12 prolines introduce rigid kinks essential for proper domain orientation during phosphorylation events. This balance between rigidity and flexibility supports JAK2's ability to undergo conformational changes upon cytokine receptor activation, a key step in JAK-STAT signaling during inflammatory responses.

9.3.4.4.5. Human Cyclooxygenase-2 (COX-2)

Human Cyclooxygenase-2 (COX-2) demonstrates 90.6% of its non-glycine, non-proline residues in most favoured regions (415 residues), with an additional 9.2% (42 residues) in allowed regions, and only 0.2% in generously allowed zones. No residues fall into disallowed regions, reflecting high stereochemical quality. The protein's 35 glycines and 34 prolines contribute to loop flexibility, essential for accommodating substrate entry and facilitating prostaglandin synthesis. This strong stereochemical profile aligns with COX-2's function as a membrane-associated enzyme, which must remain stable in lipid-rich environments while tolerating conformational shifts during catalysis. The low number of strained conformations ensures minimal structural stress, which likely enhances catalytic efficiency and reduces susceptibility to misfolding in the oxidative inflammatory microenvironment.

9.3.4.5. Ramachandran plot analysis of antidiabetic proteins

Ramachandran plot analysis of antidiabetic proteins are demonstrated in Figure 9.65

9.3.4.5.1. Ramachandran plot analysis of Dipeptidyl Peptidase 4 (DPP4)

DPP4 shows 86.9% of residues in the most favoured regions, 12.8% in additional allowed regions, and only 0.2% each in generously allowed and disallowed categories. With 657 non-glycine/non-proline residues, 40 glycines, and 26 prolines, the structure demonstrates high stereochemical reliability. The small fraction in disallowed regions suggests minor local flexibility, possibly in loop regions important for substrate accommodation. Overall, these values confirm a stable extracellular enzyme conformation, essential for its role in cleaving incretin hormones and modulating postprandial glucose levels.

9.3.4.5.2. Ramachandran plot analysis of Insulin Receptor Ectodomain (IR)

The insulin receptor's statistics show 69.2% of residues in the most favoured regions and a relatively high 30.8% in additional allowed regions, with no residues in disallowed areas. While this is still acceptable, the lower proportion in the most favoured regions suggests a high degree of structural flexibility, especially in ligand-binding domains. This flexibility could facilitate the receptor's large conformational changes upon insulin binding, but it may also make certain regions more susceptible to structural instability. The presence of 37 glycines and 28 prolines supports this flexibility.

9.3.4.5.3. Ramachandran plot analysis of Pancreatic Alpha Amylase (PAA)

This enzyme displays 88.8% of residues in the most favoured regions, 10.7% in additional allowed regions, and only 0.2% each in generously allowed and disallowed categories. With 50 glycines and 23 prolines, the structure balances rigidity with loop flexibility for substrate access. The high proportion of favoured conformations reflects a well-folded hydrolase, capable of efficiently binding and

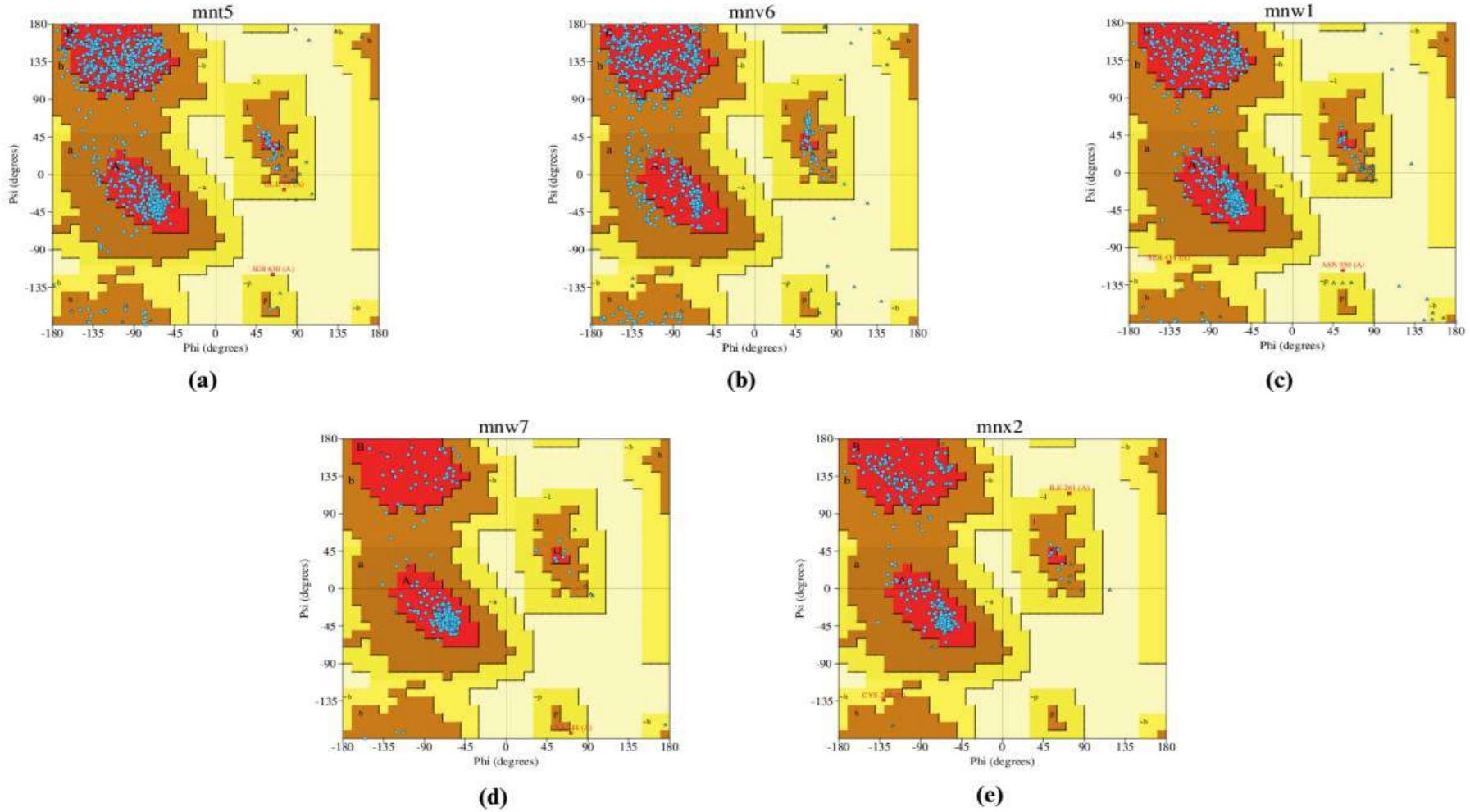


Figure 9.65: Ramachandran plot analysis of antidiabetic proteins (a) Dipeptidyl Peptidase 4 (DPP4) (b) Insulin Receptor Ectodomain (IR) (c) Pancreatic Alpha-Amylase (PAA) (d) Peroxisome Proliferator-Activated Receptor Gamma (PPARG) (e) Protein Tyrosine Phosphatase 1B (PTP1B)

hydrolyzing starch under digestive conditions. Minimal disallowed regions further reinforce the reliability of its structural model.

9.3.4.5.4. Ramachandran plot analysis of Peroxisome Proliferator–Activated Receptor Gamma (PPARG)

PPARG achieves 90.5% in the most favoured regions, 9.1% in additional allowed regions, and just 0.4% in generously allowed regions with no disallowed residues. This indicates a highly stereochemically sound structure, consistent with the stable α-helical framework of nuclear receptors. With relatively few glycines (11) and prolines (10), the protein's fold remains rigid, supporting precise ligand binding and coactivator recruitment in transcriptional regulation of glucose metabolism genes.

9.3.4.5.5. Ramachandran plot analysis of Protein Tyrosine Phosphatase 1B (PTP1B)

PTP1B shows 90.8% most favoured, 8.5% additional allowed, and 0.7% generously allowed regions, with no disallowed residues. This distribution reflects a high-quality model with minimal stereochemical strain. The 14 glycines and 12 prolines allow for controlled loop flexibility within its catalytic domain, facilitating substrate binding and release. Such a reliable fold is essential for its regulatory role in dephosphorylating the insulin receptor and modulating downstream signaling.

9.3.4.6. Ramachandran plot analysis of anticancer proteins

Ramachandran plot analysis of antidiabetic proteins are demonstrated in Figure 9.66

9.3.4.6.1. AKT serine/threonine kinase (AKT1)

AKT1 exhibits 91.3% of residues in the most favoured regions, 6.9% in additional allowed, and only 0.7% in disallowed regions. Out of 276 non-glycine, non-proline residues, only 2 falls in disallowed regions, suggesting overall high stereochemical quality with minor local deviations. The balanced distribution between favoured and allowed regions supports a structurally reliable kinase domain, essential for ATP binding and phosphorylation functions. The low percentage of disallowed

residues indicates minimal strain, maintaining catalytic efficiency. The presence of 23 glycines enhances backbone flexibility in key loop regions, while 12 prolines contribute to rigid turns stabilizing the fold. This stereochemical integrity is crucial for AKT1's role in the PI3K/AKT pathway, where structural fidelity underlies precise signaling regulation.

9.3.4.6.2. Epidermal Growth Factor Receptor (EGFR)

Epidermal Growth Factor Receptor (EGFR)'s structure shows 89.4% of residues in the most favoured regions, 9.9% in additional allowed, and 0% in disallowed regions, indicating an exceptionally well-refined backbone conformation. The slightly lower favoured percentage compared to AKT1 may reflect EGFR's requirement for conformational adaptability during ligand-induced activation and dimerization. With 263 non-glycine, non-proline residues, the absence of outliers suggests a stable model suitable for molecular docking and simulation studies. The 19 glycine residues likely localize to loop and hinge regions, enabling large conformational shifts during kinase activation. The 17 proline residues add rigidity to structural motifs, maintaining domain stability while supporting dynamic extracellular and intracellular conformational changes crucial for signal transduction.

9.3.4.6.3. Kirsten Rat Sarcoma Viral Oncogene Homolog (KRAS)

Kirsten Rat Sarcoma Viral Oncogene Homolog (KRAS) presents 90.8% of residues in the most favoured regions and 9.2% in additional allowed regions, with no disallowed residues. This high-quality stereochemistry reflects the compact and well-defined fold typical of small GTPases. The absence of outliers enhances confidence in its switch I and II regions' geometry, which is essential for nucleotide binding and hydrolysis. The 11 glycine residues impart flexibility critical for conformational cycling between GTP- and GDP-bound states, while 4 proline residues introduce tight turns stabilizing the core. Such precise backbone geometry ensures KRAS maintains functional responsiveness in Ras-MAPK signaling, where even subtle distortions could compromise its regulatory switching mechanism.

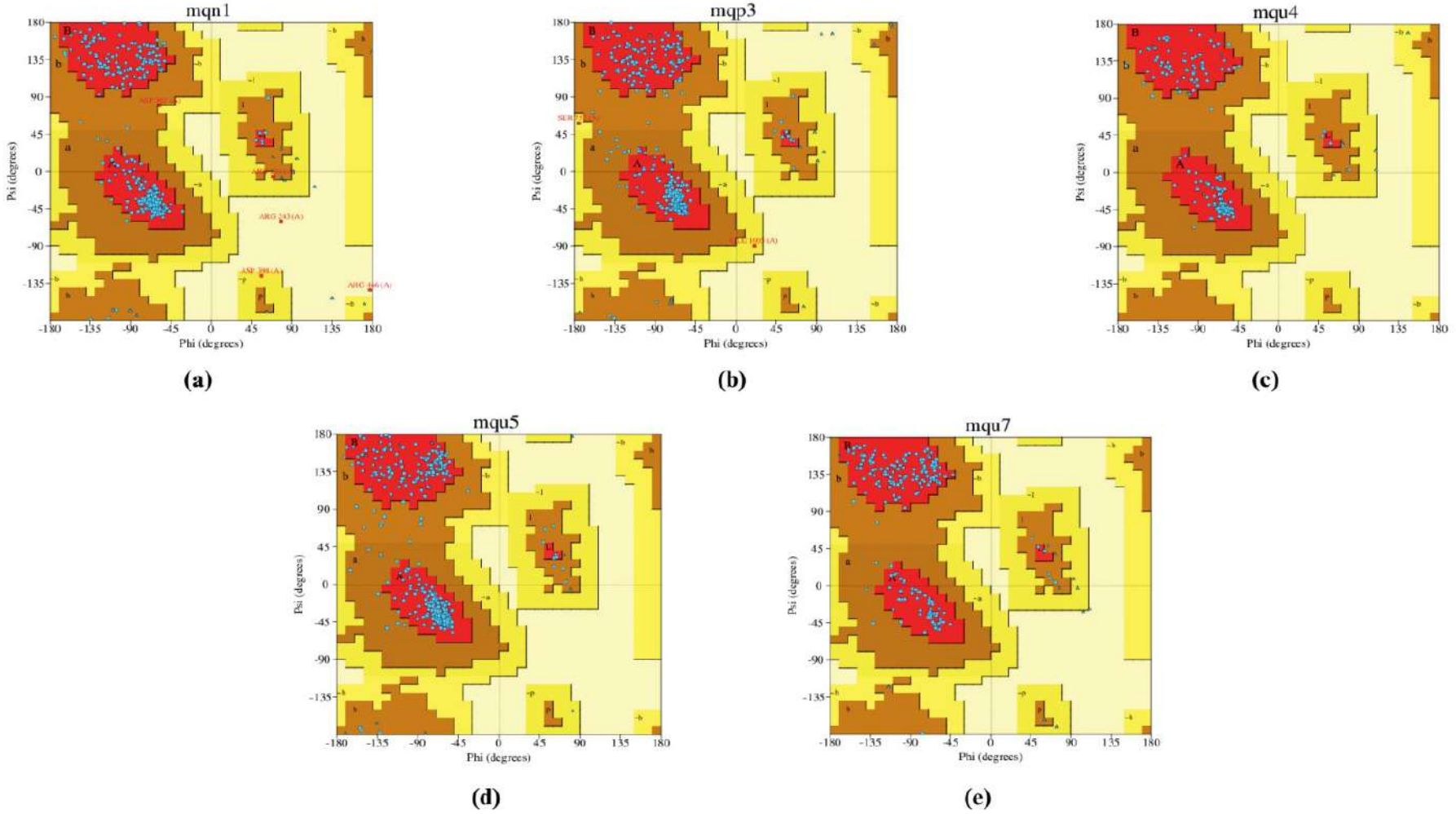


Figure 9.66: Ramachandran plot analysis of anticancer proteins (a) AKT serine/threonine kinase (AKT1) (b) Epidermal Growth Factor Receptor (EGFR) (c) Kirsten Rat Sarcoma Viral Oncogene Homolog (KRAS) (d) Mitogen-Activated Protein Kinase 1 (MAPK1) (e) Tumour Protein p53 (TP53)

9.3.4.6.4. Mitogen-Activated Protein Kinase 1 (MAPK1)

Mitogen-Activated Protein Kinase 1 (MAPK1) has 88.8% of residues in most favoured regions and 11.2% in additional allowed regions, with no disallowed residues. This slightly lower favoured percentage compared to other kinases may reflect increased loop flexibility, necessary for accommodating diverse substrates. With 16 glycines, flexibility is distributed across loop regions connecting its N- and C-terminal lobes, facilitating conformational adjustments during catalysis. 20 proline residues stabilize β-turns and hinge regions, preserving active site alignment. The overall stereochemical profile supports MAPK1's dual-domain kinase structure, allowing both rigidity for ATP binding and adaptability for substrate specificity-critical for its central role in the MAPK/ERK signaling cascade.

9.3.4.6.5. Tumour Protein p53 (TP53)

Tumour Protein p53 (TP53) exhibits 91.8% of residues in most favoured regions and 8.2% in additional allowed regions, with no disallowed residues. This high-quality stereochemistry is notable given TP53's partially disordered nature. The 13 glycine residues are likely concentrated in flexible linkers, enabling structural adaptability for binding diverse DNA sequences and regulatory proteins. 14 proline residues provide structural breaks and rigidity in certain regions, stabilizing protein-DNA interfaces. The absence of disallowed residues underscores the reliability of the resolved structural core, while flexibility in unstructured regions supports TP53's multifunctional roles in transcription regulation, DNA repair, and apoptosis, functions essential for its tumour suppressor activity.

9.3.5. Docking with PyRx

The docking simulations produced a range of binding affinities, reflecting the varying interaction strengths between the 37 bark 29 leaf phytocompounds of *S. palghatense* identified in the GC-MS and LC-MS QTOF results, and the five bioactivity protein targets, including antioxidant, antimicrobial, anthelmintic, anti-inflammatory, antidiabetic, and anticancer properties.

9.3.5.1. Antioxidant

With antioxidant-related target proteins, for Human Cu, Zn Superoxide Dismutase (PDB ID: 1PU0), binding affinities ranged from –3.5 to –7.1 kcal/mol, with DB-Friedo-B'A'-Neogammacer-5-en-3-one (–7.1 kcal/mol) showing the most favourable interaction. Catalase (PDB ID: 1DGB) exhibited stronger binding, with values between –4.6 and –9.9 kcal/mol. Kaempferol demonstrated the highest affinity at –9.9 kcal/mol, followed closely by Maslinic Acid (–9.6 kcal/mol). For Glutathione Peroxidase 1 (GPx1, PDB ID: 2F8A), docking scores ranged from –3.7 to –7.2 kcal/mol, with Maslinic Acid showing the best binding energy at –7.2 kcal/mol. The KEAP1 Kelch Domain (PDB ID: 4L7B) recorded affinities from –4.9 to –10.5 kcal/mol, with Maslinic Acid emerging as the top binder (–10.5 kcal/mol), followed closely by Oleanolic Acid (–9.7 kcal/mol). For the Thioredoxin–TXNIP Complex (PDB ID: 4LL1), docking affinities varied between –3.8 and –8.6 kcal/mol. The most favourable interaction was observed Oleanolic acid (–8.6 kcal/mol) (Tables 9.25-29).

9.3.5.2. Antimicrobial

The docking simulations for anti-microbial proteins demonstrated a diverse range of binding affinities, indicating varying degrees of interaction between the selected phytocompounds and the protein targets. For DDLA Ligase, affinities ranged from –4 to –9.1 kcal/mol, with 2-Phenyl-4H-chromen-4-one (–9.1 kcal/mol) exhibiting the strongest binding potential. The LasR ligand binding domain recorded values between –4.3 and –10.9 kcal/mol, where 2-Phenyl-4H-chromen-4-one (–10.9 kcal/mol) was identified as the top binder. For PqsR, affinities were between –4.8 and –8.8 kcal/mol, with Oleanolic acid (–8.8 kcal/mol) showing the most favourable interaction. Penicillin-Binding Protein 3 showed docking scores ranging from –4.2 to –8.9 kcal/mol, with Ellagic acid (–8.9 kcal/mol) emerging as the top binder. The Regulatory Protein RhlR displayed a comparatively narrower range of –4 to –8.3 kcal/mol, with Cholesta-4,6-dien-3-ol, benzoate, (3.beta.)- (–8.3 kcal/mol) demonstrating the highest binding potential within this target (Tables 30-34).

Table 9.25: Molecular Docking for antioxidant protein Human Cu, Zn Superoxide Dismutase (SOD1)

Ligand	Binding affinity (kcal/mol)
DB-Friedo-B'A'-Neogammacer-5-en-3-one	-7.1
Maslinic acid	-6.9
Oleanolic acid	-6.8
Ellagic acid	-6.7
2-Phenyl-4H-chromen-4-one	-6.6
Lupeol	-6.6
Beta-Sitosterol	-6.6
Cholesta-4,6-dien-3-ol, benzoate, (3.beta.)-	-6.6
Chlorogenic acid	-6.5
Myricetin	-6.4
Quercetin	-6.4
Rhamnetin	-6.3
Kaempferol	-6.2
Stigmast-4-en-3-one	-5.8
3-Furanacetic acid, 4-Hexyl-2,5-Dihydro-2,5-Dioxo-	-5.2
Ferulic acid	-5.0
Gallic acid	-5.0
Vitamin E	-5.0
D-Allose	-4.9
Gentisic acid	-4.7
Phenol, 2,6-Dimethoxy-4-(2-Propenyl)-	-4.7
Vanillin	-4.7
Phthalic acid, butyl undecyl ester	-4.6
Cinnamic acid	-4.5
Glycerol 1-palmitate	-4.3
Linoleic acid	-4.3
Oleic acid	-4.3
Stearic acid	-4.3
5-Hydroxymethylfurfural	-4.1
Cis-Linoleic acid Methyl ester	-4.0
Palmitic acid	-4.0
Myristic acid	-3.9
9-Octadecenoic acid (Z)-, methyl ester	-3.8
Hexadecanoic acid, Methyl ester	-3.8
Lauric acid	-3.7
Octadecanal	-3.7
Methyl Stearate	-3.5

Table 9.26: Molecular Docking for antioxidant protein Human Erythrocyte Catalase (CAT)

Ligand	Binding affinity (kcal/mol)
Kaempferol	-9.9
Maslinic acid	-9.6
Quercetin	-9.3
Myricetin	-9.1
2-Phenyl-4H-chromen-4-one	-8.8
Lupeol	-8.8
Oleanolic acid	-8.8
Stigmast-4-en-3-one	-8.8
Cholesta-4,6-dien-3-ol, benzoate, (3.beta.)-	-8.7
DB-Friedo-B'A'-Neogammacer-5-en-3-one	-8.5
Ellagic acid	-8.4
Phthalic acid, butyl undecyl ester	-8.4
Rhamnetin	-8.1
Cis-Linoleic acid Methyl ester	-7.8
Beta-Sitosterol	-7.8
Vitamin E	-7.7
Hexadecanoic acid, Methyl ester	-7.5
3-Furanacetic acid, 4-Hexyl-2,5-Dihydro-2,5-Dioxo-	-7.4
Chlorogenic acid	-7.4
Ferulic acid	-7.4
Gallic acid	-7.3
Oleic acid	-7.3
9-Octadecenoic acid (Z)-, methyl ester	-7.2
Stearic acid	-7.2
Glycerol 1-palmitate	-7.0
Cinnamic acid	-6.9
Octadecanal	-6.9
Palmitic acid	-6.9
Gentisic acid	-6.7
Phenol, 2,6-Dimethoxy-4-(2-Propenyl)-	-6.7
Vanillin	-6.6
Myristic acid	-6.5
D-Allose	-6.0
Lauric acid	-6.0
Linoleic acid	-6.0
5-Hydroxymethylfurfural	-5.9
Methyl Stearate	-4.6

Table 9.27: Molecular Docking for antioxidant protein Human Glutathione Peroxidase 1 (GPx1)

Ligands	Binding affinity (kcal/mol)
Maslinic acid	-7.2
DB-Friedo-B'A'-Neogammacer-5-en-3-one	-7.1
Beta-Sitosterol	-6.7
Oleanolic acid	-6.3
2-Phenyl-4H-chromen-4-one	-5.9
Lupeol	-5.9
Cholesta-4,6-dien-3-ol, benzoate, (3.beta.)-	-5.9
Rhamnetin	-5.8
Stigmast-4-en-3-one	-5.8
Ellagic acid	-5.7
Myricetin	-5.7
Quercetin	-5.7
Chlorogenic acid	-5.6
Kaempferol	-5.5
Gallic acid	-5.0
3-Furanacetic acid, 4-Hexyl-2,5-Dihydro-2,5-Dioxo-	-4.9
Cinnamic acid	-4.9
Vitamin E	-4.9
Ferulic acid	-4.8
D-Allose	-4.7
Gentisic acid	-4.6
Phenol, 2,6-Dimethoxy-4-(2-Propenyl)-	-4.6
Glycerol 1-palmitate	-4.5
Myristic acid	-4.5
Lauric acid	-4.3
Linoleic acid	-4.3
Oleic acid	-4.3
Vanillin	-4.3
5-Hydroxymethylfurfural	-4.2
Hexadecanoic acid, Methyl ester	-4.1
Phthalic acid, butyl undecyl ester	-4.1
Stearic acid	-4.1
Methyl Stearate	-4.0
Octadecanal	-4.0
Cis-Linoleic acid Methyl ester	-3.8
9-Octadecenoic acid (Z)-, methyl ester	-3.7
Palmitic acid	-3.7

Table 9.28: Molecular Docking for Antioxidant protein KEAP1 Kelch Domain (KEAP1 Kelch)

Ligand	Binding affinity (kcal/mol)
Maslinic acid	-10.5
Oleanolic acid	-9.7
DB-Friedo-B'A'-Neogammacer-5-en-3-one	-9.5
Cholesta-4,6-dien-3-ol, benzoate, (3.beta.)-	-9
2-Phenyl-4H-chromen-4-one	-8.2
Lupeol	-8.2
Chlorogenic acid	-8.1
Myricetin	-8.1
Quercetin	-8
Ellagic acid	-7.9
Kaempferol	-7.9
Stigmast-4-en-3-one	-7.7
Beta-Sitosterol	-7.6
Rhamnetin	-7.5
Vitamin E	-7.2
Ferulic acid	-6.9
Gallic acid	-6.8
3-Furanacetic acid, 4-Hexyl-2,5-Dihydro-2,5-Dioxo-	-6.6
D-Allose	-6.5
Phthalic acid, butyl undecyl ester	-6.4
Gentisic acid	-6.3
Phenol, 2,6-Dimethoxy-4-(2-Propenyl)-	-6.1
Cis-Linoleic acid Methyl ester	-5.9
Cinnamic acid	-5.8
Glycerol 1-palmitate	-5.8
9-Octadecenoic acid (Z)-, methyl ester	-5.7
Oleic acid	-5.6
Vanillin	-5.6
Linoleic acid	-5.5
Palmitic acid	-5.5
Methyl Stearate	-5.4
Hexadecanoic acid, Methyl ester	-5.3
Myristic acid	-5.3
Stearic acid	-5.3
Octadecanal	-5.1
Lauric acid	-5.0
5-Hydroxymethylfurfural	-4.9

Table 9.29: Molecular Docking for antioxidant protein Thioredoxin and TXNIP Complex (Trx-TXNIP)

Ligands	Binding affinity (kcal/mol)
Oleanolic acid	-8.6
Maslinic acid	-8.4
DB-Friedo-B'A'-Neogammacer-5-en-3-one	-8.1
Ellagic acid	-7.5
2-Phenyl-4H-chromen-4-one	-7
Ellagic acid	-6.9
Stigmast-4-en-3-one	-6.9
Cholesta-4,6-dien-3-ol, benzoate, (3.beta.)-	-6.8
Myricetin	-6.8
Quercetin	-6.8
Rhamnetin	-6.7
Beta-Sitosterol	-6.7
Chlorogenic acid	-6.7
Kaempferol	-6.7
Gallic acid	-6.6
Gentisic acid	-6.2
Vitamin E	-5.8
3-Furanacetic acid, 4-Hexyl-2,5-Dihydro-2,5-Dioxo-	-5.5
Ferulic acid	-5.5
Cinnamic acid	-5.1
Phthalic acid, butyl undecyl ester	-4.9
D-Allose	-4.7
Phenol, 2,6-Dimethoxy-4-(2-Propenyl)-	-4.7
Linoleic acid	-4.6
Myristic acid	-4.6
Glycerol 1-palmitate	-4.5
Vanillin	-4.5
Lauric acid	-4.4
Stearic acid	-4.4
Palmitic acid	-4.3
Octadecanal	-4.2
Cis-Linoleic acid Methyl ester	-4.1
Methyl Stearate	-4.1
Oleic acid	-4.1
5-Hydroxymethylfurfural	-4.0
Hexadecanoic acid, Methyl ester	-4.0
9-Octadecenoic acid (Z)-, methyl ester	-3.8

Table 9.30: Molecular Docking for antimicrobial protein D-alanyl-D-alanine ligase (D-ALA:D-ALA Ligase/Ddl)

Ligand	Binding affinity (kcal/mol)
2-Phenyl-4H-chromen-4-one	-9.1
Kaempferol	-8.6
D:B-Friedo-B':A'-Neogammacer-5-en-3-one	-8.5
Maslinic acid	-8.2
Chlorogenic acid	-7.9
Rhamnetin	-7.9
Cholesta-4,6-dien-3-ol, benzoate, (3.beta.)-	-7.9
Oleanolic acid	-7.7
Beta Sitosterol	-7.5
Ellagic acid	-7.5
Stigmast-4-en-3-one	-7.5
Lupeol	-7.2
Quercetin	-7.1
Ferulic acid	-7
Cinnamic acid	-6.7
Myricetin	-6.7
Gallic acid	-6.5
Gentisic acid	-6.4
D-Allose	-6.4
Linoleic acid	-6.3
Phenol, 2,6-Dimethoxy-4-(2-Propenyl)-	-6.2
Vitamin E	-6
Phthalic acid, butyl undecyl ester	-5.8
5-Hydroxymethylfurfural	-5.7
Oleic acid	-5.7
3-Furanacetic acid, 4-Hexyl-2,5-Dihydro-2,5-Dioxo-	-5.7
Methyl Stearate	-5.7
Vanillin	-5.5
Cis-Linoleic acid Methyl ester	-5.3
9-Octadecenoic acid (Z)-, methyl ester	-4.9
Myristic acid	-4.8
Glycerol 1-palmitate	-4.7
Hexadecanoic acid, Methyl ester	-4.6
Palmitic acid	-4.6
Lauric acid	-4.5
Stearic acid	-4.5
Octadecanal	-4

Table 9.31: Molecular Docking for antimicrobial protein LasR ligand-binding domain (LasR)

Ligand	Binding affinity (kcal/mol)
2-Phenyl-4H-chromen-4-one	-10.9
Rhamnetin	-10.8
Quercetin	-10.7
Kaempferol	-10.7
Myricetin	-10.7
Ellagic acid	-10.3
Oleic acid	-8.1
Ferulic acid	-7.6
D:B-Friedo-B':A'-Neogammacer-5-en-3-one	-7.6
Palmitic acid	-7.5
Methyl Stearate	-7.4
Oleanolic acid	-7.3
3-Furanacetic acid, 4-Hexyl-2,5-Dihydro-2,5-Dioxo-	-7.3
Maslinic acid	-7.3
Cholesta-4,6-dien-3-ol, benzoate, (3.beta.)-	-7.3
Myristic acid	-7.2
Gentisic acid	-7.2
Cinnamic acid	-7.2
Lupeol	-7.1
Phenol, 2,6-Dimethoxy-4-(2-Propenyl)-	-7
Chlorogenic acid	-6.9
Gallic acid	-6.8
Beta Sitosterol	-6.6
Stigmast-4-en-3-one	-6.5
Lauric acid	-6.4
Vanillin	-6.3
D-Allose	-5.9
5-Hydroxymethylfurfural	-5.6
Vitamin E	-5.1
Cis-Linoleic acid Methyl ester	-4.8
Glycerol 1-palmitate	-4.8
Octadecanal	-4.6
9-Octadecenoic acid (Z)-, methyl ester	-4.6
Stearic acid	-4.5
Hexadecanoic acid, Methyl ester	-4.4
Phthalic acid, butyl undecyl ester	-4.4
Linoleic acid	-4.3

Table 9.32: Molecular Docking for antimicrobial protein PqsR coinducer-binding domain (PqsR/MvfR)

Ligand	Binding affinity (kcal/mol)
Oleanolic acid	-8.8
Ellagic acid	-8.8
2-Phenyl-4H-chromen-4-one	-8.6
Stigmast-4-en-3-one	-8.4
Vitamin E	-8.2
Beta Sitosterol	-8.2
Kaempferol	-8.1
Quercetin	-7.9
Maslinic acid	-7.8
Lupeol	-7.6
D:B-Friedo-B':A'-Neogammacer-5-en-3-one	-7.5
Cholesta-4,6-dien-3-ol, benzoate, (3.beta.)-	-7.5
Rhamnetin	-7.4
Myricetin	-7.3
Chlorogenic acid	-7.2
Ferulic acid	-6.5
3-Furanacetic acid, 4-Hexyl-2,5-Dihydro-2,5-Dioxo-	-6.5
Oleic acid	-6.3
Cinnamic acid	-6.1
Myristic acid	-6
Phenol, 2,6-Dimethoxy-4-(2-Propenyl)-	-5.9
Methyl Stearate	-5.9
Phthalic acid, butyl undecyl ester	-5.9
Gentisic acid	-5.8
Gallic acid	-5.8
Palmitic acid	-5.8
9-Octadecenoic acid (Z)-, methyl ester	-5.8
Glycerol 1-palmitate	-5.8
Linoleic acid	-5.7
Stearic acid	-5.7
D-Allose	-5.6
Cis-Linoleic acid Methyl ester	-5.6
Octadecanal	-5.6
Lauric acid	-5.5
Hexadecanoic acid, Methyl ester	-5.5
Vanillin	-5.3
5-Hydroxymethylfurfural	-4.8

Table 9.33: Molecular Docking for antimicrobial protein Penicillin-Binding Protein 3 (PBP3)

Ligand	Binding affinity (kcal/mol)
Ellagic acid	-8.9
Oleanolic acid	-8.7
Myricetin	-8.7
D:B-Friedo-B':A'-Neogammacer-5-en-3-one	-8.7
Cholesta-4,6-dien-3-ol, benzoate, (3.beta.)-	-8.6
Beta sitosterol	-8.5
Quercetin	-8.2
Rhamnetin	-8.2
Lupeol	-8.1
Maslinic acid	-8.1
Kaempferol	-8
Vitamin E	-7.8
2-Phenyl-4H-chromen-4-one	-7.6
Stigmast-4-en-3-one	-7.6
Chlorogenic acid	-7.5
Ferulic acid	-6.6
Gallic acid	-6.3
Cinnamic acid	-6.2
3-Furanacetic acid, 4-Hexyl-2,5-Dihydro-2,5-Dioxo-	-6
Gentisic acid	-5.9
Phenol, 2,6-Dimethoxy-4-(2-Propenyl)-	-5.8
D-Allose	-5.8
Phthalic acid, butyl undecyl ester	-5.6
Linoleic acid	-5.5
Vanillin	-5.4
5-Hydroxymethylfurfural	-5.3
Oleic acid	-5.3
Cis-Linoleic acid Methyl ester	-5.3
9-Octadecenoic acid (Z)-, methyl ester	-5.2
Glycerol 1-palmitate	-5.2
Hexadecanoic acid, Methyl ester	-4.9
Methyl Stearate	-4.9
Myristic acid	-4.8
Lauric acid	-4.8
Octadecanal	-4.8
Palmitic acid	-4.6
Stearic acid	-4.2

Table 9.34: Molecular Docking for antimicrobial Regulatory protein RhlR (RhIR)

Ligand	Binding affinity (kcal/mol)
Cholesta-4,6-dien-3-ol, benzoate, (3.beta.)-	-8.3
Lupeol	-7.9
D:B-Friedo-B':A'-Neogammacer-5-en-3-one	-7.8
Ellagic acid	-7.7
Oleanolic acid	-7.3
Beta sitosterol	-7.3
Maslinic acid	-7.2
Quercetin	-7.1
Cinnamic acid	-7
Kaempferol	-7
Myricetin	-7
Rhamnetin	-6.8
2-Phenyl-4H-chromen-4-one	-6.7
Chlorogenic acid	-6.6
Stigmast-4-en-3-one	-6.6
Phenol, 2,6-Dimethoxy-4-(2-Propenyl)-	-6.3
Ferulic acid	-5.9
Vitamin E	-5.8
3-Furanacetic acid, 4-Hexyl-2,5-Dihydro-2,5-Dioxo-	-5.5
5-Hydroxymethylfurfural	-5.3
Phthalic acid, butyl undecyl ester	-5.2
Gallic acid	-5.1
D-Allose	-5.1
Gentisic acid	-5
Cis-Linoleic acid Methyl ester	-4.8
Myristic acid	-4.6
Glycerol 1-palmitate	-4.6
Vanillin	-4.5
Oleic acid	-4.5
Linoleic acid	-4.5
Stearic acid	-4.5
9-Octadecenoic acid (Z)-, methyl ester	-4.5
Palmitic acid	-4.4
Octadecanal	-4.4
Methyl Stearate	-4.4
Lauric acid	-4.1
Hexadecanoic acid, Methyl ester	-4

9.3.5.3. Anthelmintic

The docking simulations for anthelmintic proteins revealed a broad spectrum of binding affinities, reflecting variable interaction strengths between the screened phytocompounds and the target proteins. For ATP Synthase, affinities ranged from –5 to –8.6 kcal/mol, with Oleanolic acid (–8.6 kcal/mol) showing the strongest binding potential. Cytochrome c Oxidase displayed scores between –4.3 and –8.1 kcal/mol, where Oleanolic acid (–8.1 kcal/mol) emerged as the top binder. Heat Shock Protein 70 exhibited docking values from –4.1 to –8.7 kcal/mol, with Oleanolic Acid (–8.7 kcal/mol) demonstrating the highest binding potential. For NADH–Ubiquinone Oxidoreductase, affinities were recorded between –4.4 and –9.3 kcal/mol, with Maslinic Acid (–9.3 kcal/mol) achieving the most favourable interaction. Extracellular Globin-3/Erythrocruorin presented a narrower high-affinity range from –5.6 to –9.4 kcal/mol, with Vitamin E (–9.4 kcal/mol) identified as the strongest binder for this protein target (Tables 35-39).

9.3.5.4. Anti-inflammatory

The docking simulations produced a range of binding affinities, indicating variable interaction strengths between the selected phytocompounds and the five anti-inflammatory protein targets. For NF-κB p50 (1SVC), binding energies ranged from –3.6 to –7.6 kcal/mol, with Maslinic Acid (–7.6 kcal/mol) showing the strongest interaction. TNF-α (2AZ5) recorded affinities between –3.7 and –7.4 kcal/mol, where DB-Friedo-B'A'-Neogammacer-5-en-3-one (–7.4 kcal/mol) emerged as the top binder. iNOS (4NOS) exhibited the highest binding strength overall, with values from –5 to –10.9 kcal/mol, and Cholesta-4,6-dien-3-ol, 3-benzoate, (3beta)- (–10.9 kcal/mol) showing the most favourable interaction. JAK2 (2B7A) showed affinities in the range of –3.9 to –9.8 kcal/mol, with Ellagic Acid (–9.8 kcal/mol) as the strongest binder. For COX-2 (5IKR), docking scores varied from –5 to –9.3 kcal/mol, with Cholesta-4,6-dien-3-ol, 3-benzoate, (3beta)- (–9.3 kcal/mol) displaying the highest binding potential (Tables 9.40-9.44).

9.3.5.5. Antidiabetic

The docking simulations yielded a range of binding affinities, reflecting varying interaction strengths between the selected phytocompounds and each of the five anti-diabetic protein targets. For DPP4 (5YRK), affinities ranged from –4.8 to –9.5 kcal/mol, with DB-Friedo-B'A'-Neogammacer-5-en-3-one (–9.5 kcal/mol) showing the most favourable interaction. IR (7QID) exhibited values between –4.4 and –9 kcal/mol, where DB-Friedo-B'A'-Neogammacer-5-en-3-one (–9.0 kcal/mol) emerged as the top binder. Pancreatic Alpha Amylase (6Z8L) recorded affinities from –4.8 to –10.7 kcal/mol, with Cholesta-4,6-dien-3-ol, 3-benzoate, (3beta)- (–10.7 kcal/mol) showing the strongest binding. PPARG (9F7X) showed a range of –4.9 to –10.6 kcal/mol, with DB-Friedo-B'A'-Neogammacer-5-en-3-one (–10.6 kcal/mol) as the most favourable ligand. For Protein Tyrosine Phosphatase 1B (8SKL), affinities varied from –4.9 to –9.6 kcal/mol, with Cholesta-4,6-dien-3-ol, benzoate, (3.beta.)-(–9.6 kcal/mol) demonstrating the highest binding potential (Tables 9.45-9.49).

9.3.5.6. Anticancer

The molecular docking analysis revealed a diverse range of binding affinities across the selected phytocompounds and the five targeted proteins, reflecting variable interaction strengths and binding preferences. For AKT1 (8UW9), binding affinities ranged from –4.4 to –9.1 kcal/mol, with Chlorogenic acid (–9.1 kcal/mol) showing the strongest interaction. EGFR (8TLJ) recorded affinities between –4.7 and –9.7 kcal/mol, where DB-Friedo-B'A'-Neogammacer-5-en-3-one (–9.7 kcal/mol) emerged as the top binder. KRAS (6GJ8) exhibited binding energies from –5.3 to –8.8 kcal/mol, with Chlorogenic acid (–9.6 kcal/mol) showing the most favourable interaction. MAPK1 (8ZJV) showed affinities in the range of –3.8 to –9.4 kcal/mol, with Ellagic acid (–9.4 kcal/mol) as the strongest binder. For TP53 (8WD2), docking scores varied from –3.7 to –7.5 kcal/mol, with Quercetin (–7.5 kcal/mol) displaying the highest binding potential (Tables 9.50-9.54).

Table 9.35: Molecular Docking for anthelmintic protein ATP synthase subunit a (ATP synthase)

Ligand	Binding Affinity (kcal/mol)
Oleanolic acid	-8.6
2-Phenyl-4H-chromen-4-one	-8.3
Maslinic acid	-8
Kaempferol	-7.9
Squalene	-7.9
Myricetin	-7.8
Rhamnetin	-7.8
Quercetin	-7.7
Ellagic acid	-7.6
.Gamma. -Tocopherol	-7.6
Chlorogenic acid	-7.1
Vitamin E	-6.9
(-)-Spathulenol	-6.6
Gallic acid	-6.4
Neophytadiene	-6.2
3,7,11,15-Tetramethyl-2-hexadecen-1-ol	-6.2
Ferulic acid	-6
Phytol	-6
Cinnamic acid	-5.8
Oleic acid	-5.7
Stearic acid	-5.6
Linoleic Acid, methyl ester	-5.5
Methyl palmitate	-5.4
Linoleic acid	-5.3
Palmitic acid	-5.3
Myristic acid	-5.2
9-octadecenoic Acid (Z)-, methyl ester	-5.2
Methyl stearate	-5.2
Lauric acid	-5

Table 9.36: Molecular Docking for anthelmintic protein Cytochrome c oxidase subunit 1 (COX1)

Ligand	Binding affinity (kcal/mol)
Oleanolic acid	-8.1
Maslinic acid	-8
Ellagic acid	-7.8
Chlorogenic acid	-7.6
2-Phenyl-4H-chromen-4-one	-6.9
Kaempferol	-6.8
Quercetin	-6.7
Myricetin	-6.7
Rhamnetin	-6.6
(-)-Spathulenol	-6.5
Vitamin E	-6.3
Ferulic acid	-6.3
Cinnamic acid	-5.8
Neophytadiene	-5.7
.Gamma. -Tocopherol	-5.5
Gallic acid	-5.2
3,7,11,15-Tetramethyl-2-hexadecen-1-ol	-5
Linoleic Acid, methyl ester	-4.9
Squalene	-4.9
Lauric acid	-4.7
Linoleic acid	-4.7
Myristic acid	-4.6
Oleic acid	-4.6
Phytol	-4.6
Palmitic acid	-4.5
Stearic acid	-4.4
Methyl palmitate	-4.3
9-octadecenoic Acid (Z)-, methyl ester	-4.3
Methyl stearate	-4.3

Table 9.37: Molecular Docking for anthelmintic protein Heat Shock Protein 7 (HSP70)

Ligand	Binding affinity (kcal/mol)
Oleanolic acid	-8.7
Maslinic acid	-8.5
2-Phenyl-4H-chromen-4-one	-6.7
Ellagic acid	-6.7
Chlorogenic acid	-6.6
Myricetin	-6.4
Quercetin	-6.3
Kaempferol	-6.3
Rhamnetin	-6.3
.Gamma. -Tocopherol	-6.2
Squalene	-6
(-)-Spathulenol	-5.9
Ferulic acid	-5.5
Cinnamic acid	-5.4
Vitamin E	-5.3
Oleic acid	-5.3
Phytol	-5.1
Neophytadiene	-4.9
Gallic acid	-4.8
Linoleic acid	-4.8
3,7,11,15-Tetramethyl-2-hexadecen-1-ol	-4.8
Methyl palmitate	-4.7
9-octadecenoic Acid (Z)-, methyl ester	-4.7
Lauric acid	-4.6
Stearic acid	-4.6
Linoleic Acid, methyl ester	-4.5
Palmitic acid	-4.5
Methyl stearate	-4.4
Myristic acid	-4.1

Table 9.38: Molecular Docking for anthelmintic protein NADH-Ubiquinone Oxidoreductase chain 1 (Complex I)

Ligand	Binding affinity (kcal/mol)
Maslinic acid	-9.3
Oleanolic acid	-8.9
Quercetin	-7.5
Ellagic acid	-7.5
Myricetin	-7.4
Kaempferol	-7.3
Chlorogenic acid	-7.1
Rhamnetin	-7.1
2-Phenyl-4H-chromen-4-one	-6.7
(-)-Spathulenol	-6.2
.Gamma. -Tocopherol	-6.2
Vitamin E	-6.1
Squalene	-5.9
Gallic acid	-5.4
Cinnamic acid	-5.4
Neophytadiene	-5.3
Ferulic acid	-5.3
Linoleic acid	-5.2
3,7,11,15-Tetramethyl-2-hexadecen-1-ol	-5.1
Linoleic Acid, methyl ester	-5
Phytol	-4.9
Palmitic acid	-4.9
9-octadecenoic Acid (Z)-, methyl ester	-4.8
Myristic acid	-4.7
Methyl palmitate	-4.7
Lauric acid	-4.6
Stearic acid	-4.6
Methyl stearate	-4.5
Oleic acid	-4.4

Table 9.39: Molecular Docking for anthelmintic protein Extracellular Globin-3 /Erythrocruorin (Ext. Globin-3)

Ligand	Binding affinity (kcal/mol)
Vitamin E	-9.4
.Gamma. -Tocopherol	-9.3
2-Phenyl-4H-chromen-4-one	-9.1
Rhamnetin	-8.8
Quercetin	-8.7
Myricetin	-8.6
Squalene	-8.4
Maslinic acid	-8.3
Oleanolic acid	-8.2
Ellagic acid	-8.1
Chlorogenic acid	-8
Phytol	-8
Kaempferol	-8
Neophytadiene	-7.7
Linoleic acid	-7.4
9-octadecenoic Acid (Z)-, methyl ester	-7.2
Linoleic Acid, methyl ester	-7.1
Oleic acid	-7
Methyl stearate	-6.9
(-)-Spathulenol	-6.8
3,7,11,15-Tetramethyl-2-hexadecen-1-ol	-6.8
Methyl palmitate	-6.8
Stearic acid	-6.8
Palmitic acid	-6.7
Myristic acid	-6.6
Cinnamic acid	-6.5
Ferulic acid	-6.4
Lauric acid	-6.3
Gallic acid	-5.6

Table 9.40: Molecular Docking for anti-inflammatory protein Nuclear Factor kappa B p50 (NF-κB p50)

Ligand	Binding affinity (kcal/mol)
Maslinic acid	-7.6
D:B-Friedo-B':A'-Neogammacer-5-en-3-one	-7.5
Cholesta-4,6-dien-3-ol, benzoate, (3.beta.)-	-7.4
Oleanolic acid	-7.3
Lupeol	-7.2
Chlorogenic acid	-6.9
Beta sitosterol	-6.9
Rhamnetin	-6.9
Ellagic acid	-6.9
Quercetin	-6.7
Myricetin	-6.7
Stigmast-4-en-3-one	-6.7
2-Phenyl-4H-chromen-4-one	-6.6
Kaempferol	-6.6
Gallic acid	-6.1
Ferulic acid	-5.6
Cinnamic acid	-5.5
Gentisic acid	-5.3
3-Furanacetic acid, 4-Hexyl-2,5-Dihydro-2,5-Dioxo-	-5.3
D-Allose	-5.2
5-Hydroxymethylfurfural	-5
Vanillin	-4.9
Vitamin E	-4.9
Phenol, 2,6-Dimethoxy-4-(2-Propenyl)-	-4.9
Lauric acid	-4.8
9-Octadecenoic acid (Z)-, methyl ester	-4.8
Myristic acid	-4.7
Methyl Stearate	-4.7
Cis-Linoleic acid Methyl ester	-4.6
Phthalic acid, butyl undecyl ester	-4.6
Octadecanal	-4.5
Linoleic acid	-4.4
Glycerol 1-palmitate	-4.4
Hexadecanoic acid, Methyl ester	-4.1
Oleic acid	-3.9
Stearic acid	-3.8
Palmitic acid	-3.6

Table 9.41: Molecular Docking for anti-inflammatory protein Tumour Necrosis Factor-alpha (TNF-α)

Ligand	Binding affinity (kcal/mol)
D:B-Friedo-B':A'-Neogammacer-5-en-3-one	-7.4
Stigmast-4-en-3-one	-7
Oleanolic acid	-6.9
2-Phenyl-4H-chromen-4-one	-6.9
Beta sitosterol	-6.9
Lupeol	-6.9
Maslinic acid	-6.9
Ellagic acid	-6.7
Cholesta-4,6-dien-3-ol, benzoate, (3.beta.)-	-6.7
Chlorogenic acid	-6.5
Quercetin	-6.5
Myricetin	-6.4
Kaempferol	-6.3
Rhamnetin	-6.3
Vitamin E	-5.9
Ferulic acid	-5.2
Gentisic acid	-5.1
Cinnamic acid	-5.1
Gallic acid	-4.9
D-Allose	-4.6
3-Furanacetic acid, 4-Hexyl-2,5-Dihydro-2,5-Dioxo-	-4.6
Vanillin	-4.5
Phenol, 2,6-Dimethoxy-4-(2-Propenyl)-	-4.5
9-Octadecenoic acid (Z)-, methyl ester	-4.5
Linoleic acid	-4.3
Cis-Linoleic acid Methyl ester	-4.3
Palmitic acid	-4.3
Phthalic acid, butyl undecyl ester	-4.3
Glycerol 1-palmitate	-4.2
Lauric acid	-4
Oleic acid	-4
Stearic acid	-4
Methyl Stearate	-4
5-Hydroxymethylfurfural	-3.9
Hexadecanoic acid, Methyl ester	-3.9
Octadecanal	-3.9
Myristic acid	-3.7

Table 9.42: Molecular Docking for anti-inflammatory protein Human Inducible Nitric Oxide Synthase (iNOS)

Ligand	Binding affinity (kcal/mol)
Cholesta-4,6-dien-3-ol, benzoate, (3.beta.)-	-10.9
2-Phenyl-4H-chromen-4-one	-10.1
Beta sitosterol	-10
D:B-Friedo-B':A'-Neogammacer-5-en-3-one	-9.8
Kaempferol	-9.5
Stigmast-4-en-3-one	-9.5
Maslinic acid	-9.5
Lupeol	-9.4
Quercetin	-9.2
Myricetin	-8.8
Ellagic acid	-8.8
Oleanolic acid	-8.6
Vitamin E	-8.6
Chlorogenic acid	-8.4
Rhamnetin	-8.4
Cinnamic acid	-7.2
Ferulic acid	-7.2
Phthalic acid, butyl undecyl ester	-7.2
Cis-Linoleic acid Methyl ester	-6.7
3-Furanacetic acid, 4-Hexyl-2,5-Dihydro-2,5-Dioxo-	-6.7
Phenol, 2,6-Dimethoxy-4-(2-Propenyl)-	-6.6
Gallic acid	-6.6
D-Allose	-6.4
Vanillin	-6.3
Palmitic acid	-6.3
Myristic acid	-6.2
Gentisic acid	-6.2
Linoleic acid	-6
Octadecanal	-6
Glycerol 1-palmitate	-6
Stearic acid	-5.9
9-Octadecenoic acid (Z)-, methyl ester	-5.8
Methyl Stearate	-5.8
Lauric acid	-5.6
Oleic acid	-5.4
Hexadecanoic acid, Methyl ester	-5.2
5-Hydroxymethylfurfural	-5

Table 9.43: Molecular Docking for anti-inflammatory protein Janus Kinase 2 (JAK2)

Ligand	Binding affinity (kcal/mol)
Ellagic acid	-9.8
Myricetin	-9.1
Kaempferol	-9
2-Phenyl-4H-chromen-4-one	-8.9
Quercetin	-8.9
Rhamnetin	-8.9
Cholesta-4,6-dien-3-ol, benzoate, (3.beta.)-	-8.1
Oleanolic acid	-7.7
Chlorogenic acid	-7.6
Maslinic acid	-7.6
D:B-Friedo-B':A'-Neogammacer-5-en-3-one	-7.6
Vitamin E	-7.5
Lupeol	-7.2
Beta sitosterol	-7
Ferulic acid	-6.7
Stigmast-4-en-3-one	-6.7
Cinnamic acid	-6.5
Phenol, 2,6-Dimethoxy-4-(2-Propenyl)-	-6.2
Gallic acid	-6.1
Linoleic acid	-6.1
Phthalic acid, butyl undecyl ester	-6
Gentisic acid	-5.9
Vanillin	-5.8
Cis-Linoleic acid Methyl ester	-5.8
3-Furanacetic acid, 4-Hexyl-2,5-Dihydro-2,5-Dioxo-	-5.7
Oleic acid	-5.5
Myristic acid	-5.4
D-Allose	-5.4
Hexadecanoic acid, Methyl ester	-5.4
9-Octadecenoic acid (Z)-, methyl ester	-5.2
Stearic acid	-5.1
Lauric acid	-5
5-Hydroxymethylfurfural	-4.9
Glycerol 1-palmitate	-4.6
Octadecanal	-4.4
Palmitic acid	-4.3
Methyl Stearate	-3.9

Table 9.44: Molecular docking for anti-inflammatory protein Human Cyclooxygenase-2 (COX-2)

Ligand	Binding affinity (kcal/mol)
Cholesta-4,6-dien-3-ol, benzoate, (3.beta.)-	-9.3
2-Phenyl-4H-chromen-4-one	-9.2
Oleanolic acid	-8.7
Maslinic acid	-8.6
D:B-Friedo-B':A'-Neogammacer-5-en-3-one	-8.6
Lupeol	-8.6
Myricetin	-8.1
Chlorogenic acid	-8
Beta sitosterol	-7.9
Vitamin E	-7.6
Rhamnetin	-7.6
Ellagic acid	-7.4
Stigmast-4-en-3-one	-7.4
Quercetin	-7.3
Kaempferol	-7.3
Cinnamic acid	-6.9
Ferulic acid	-6.8
Phenol, 2,6-Dimethoxy-4-(2-Propenyl)-	-6.7
Gentisic acid	-6.5
Phthalic acid, butyl undecyl ester	-6.4
Gallic acid	-6.2
3-Furanacetic acid, 4-Hexyl-2,5-Dihydro-2,5-Dioxo-	-6
Vanillin	-5.9
9-Octadecenoic acid (Z)-, methyl ester	-5.9
Linoleic acid	-5.8
Palmitic acid	-5.6
Methyl Stearate	-5.6
Cis-Linoleic acid Methyl ester	-5.5
Stearic acid	-5.4
Myristic acid	-5.3
D-Allose	-5.3
Hexadecanoic acid, Methyl ester	-5.2
Octadecanal	-5.2
5-Hydroxymethylfurfural	-5.1
Lauric acid	-5.1
Oleic acid	-5
Glycerol 1-palmitate	-5

Table 9.45: Molecular docking for antidiabetic protein Dipeptidyl Peptidase 4 (DPP4)

Ligand	Binding affinity (kcal/mol)
D:B-Friedo-B':A'-Neogammacer-5-en-3-one	-9.5
Maslinic acid	-9.1
Oleanolic acid	-9
Lupeol	-8.9
2-Phenyl-4H-chromen-4-one	-8.8
Ellagic acid	-8.8
Stigmast-5-en-3-ol, (3.beta.)-	-8.6
Cholesta-4,6-dien-3-ol, benzoate, (3.beta.)-	-8.4
Stigmast-4-en-3-one	-8.3
Quercetin	-8.1
Myricetin	-8.1
Rhamnetin	-8
Kaempferol	-7.8
Vitamin E	-7.7
Chlorogenic acid	-7.4
3-Furanacetic acid, 4-Hexyl-2,5-Dihydro-2,5-Dioxo-	-6.5
Gallic acid	-6.4
Phthalic acid, butyl undecyl ester	-6.3
Phenol, 2,6-Dimethoxy-4-(2-Propenyl)-	-6.2
Cinnamic acid	-6.1
D-Allose	-6
Ferulic acid	-6
Oleic acid	-5.8
Linoleic acid	-5.7
Linoleic Acid, methyl ester	-5.7
Palmitic acid	-5.7
Gentisic acid	-5.6
Stearic acid	-5.5
Vanillin	-5.4
Glycerol 1-palmitate	-5.4
9-Octadecenoic acid (Z)-, methyl ester	-5.3
Methyl Stearate	-5.3
Myristic acid	-5.2
Octadecanal	-5.2
5-Hydroxymethylfurfural	-5.1
Lauric acid	-4.9
Hexadecanoic acid, Methyl ester	-4.8

Table 9.46: Molecular docking for antidiabetic protein Insulin Receptor Ectodomain (IR)

Ligand	Binding affinity (kcal/mol)
D:B-Friedo-B':A'-Neogammacer-5-en-3-one	-9
Oleanolic acid	-8.7
Maslinic acid	-8.7
Lupeol	-8.2
2-Phenyl-4H-chromen-4-one	-7.6
Cholesta-4,6-dien-3-ol, benzoate, (3.beta.)-	-7.6
Stigmast-5-en-3-ol, (3.beta.)-	-7.6
Beta-Sitosterol	-7.5
Myricetin	-7.4
Quercetin	-7.3
Ellagic acid	-7.3
Vitamin E	-7.2
Kaempferol	-6.8
Chlorogenic acid	-6.7
Rhamnetin	-6.7
Phthalic acid, butyl undecyl ester	-6.1
Cinnamic acid	-5.9
Ferulic acid	-5.6
Gentisic acid	-5.5
Gallic acid	-5.5
Oleic acid	-5.5
3-Furanacetic acid, 4-Hexyl-2,5-Dihydro-2,5-Dioxo-	-5.5
Vanillin	-5.3
D-Allose	-5.2
Phenol, 2,6-Dimethoxy-4-(2-Propenyl)-	-5.1
9-Octadecenoic acid (Z)-, methyl ester	-5.1
Methyl stearate	-5.1
Linoleic acid	-5
Cis-Linoleic acid Methyl ester	-5
5-Hydroxymethylfurfural	-4.8
Lauric acid	-4.8
Palmitic acid	-4.8
Octadecanal	-4.7
Glycerol 1-palmitate	-4.7
Myristic acid	-4.6
Hexadecanoic acid, Methyl ester	-4.5
Stearic acid	-4.4

Table 9.47: Molecular docking for antidiabetic protein Pancreatic Alpha-Amylase (PAA)

Ligand	Binding affinity (kcal/mol)
Cholesta-4,6-dien-3-ol, benzoate, (3.beta.)-	-10.7
D:B-Friedo-B':A'-Neogammacer-5-en-3-one	-10.2
Lupeol	-9.4
Maslinic acid	-9.3
2-Phenyl-4H-chromen-4-one	-9
Beta-Sitosterol	-9
Quercetin	-9
Myricetin	-9
Rhamnetin	-9
Oleanolic acid	-9
Stigmast-5-en-3-ol, (3.beta.)-	-9
Kaempferol	-8.7
Ellagic acid	-8.7
Vitamin E	-8.2
Chlorogenic acid	-7.8
Ferulic acid	-6.6
3-Furanacetic acid, 4-Hexyl-2,5-Dihydro-2,5-Dioxo-	-6.6
Phthalic acid, butyl undecyl ester	-6.6
Gallic acid	-6.1
D-Allose	-6.1
Cinnamic acid	-6.1
Gentisic acid	-5.9
Oleic acid	-5.6
Glycerol 1-palmitate	-5.6
Phenol, 2,6-Dimethoxy-4-(2-Propenyl)-	-5.5
Linoleic acid	-5.5
Vanillin	-5.4
Cis-Linoleic acid Methyl ester	-5.4
Lauric acid	-5.2
Stearic acid	-5.2
9-octadecenoic Acid (Z)-, methyl ester	-5.2
Myristic acid	-5.1
Palmitic acid	-5.1
Methyl Stearate	-5
5-Hydroxymethylfurfural	-4.9
Methyl palmitate	-4.9
Octadecanal	-4.8

Table 9.48: Molecular docking for antidiabetic protein Peroxisome Proliferator-Activated Receptor Gamma (PPARG)

Ligand	Binding affinity (kcal/mol)
D:B-Friedo-B':A'-Neogammacer-5-en-3-one	-10.6
Cholesta-4,6-dien-3-ol, benzoate, (3.beta.)-	-10.3
Lupeol	-10.1
Stigmast-5-en-3-ol, (3.beta.)-	-9.8
Maslinic acid	-9.8
Oleanolic acid	-9.7
Beta-Sitosterol	-9.6
Rhamnetin	-8.8
Myricetin	-8.7
Ellagic acid	-8.7
Chlorogenic acid	-8.4
Quercetin	-8.4
Vitamin E	-8.2
Kaempferol	-8.2
2-Phenyl-4H-chromen-4-one	-8
3-Furanacetic acid, 4-Hexyl-2,5-Dihydro-2,5-Dioxo-	-6.8
Ferulic acid	-6.7
Gallic acid	-6.5
Cinnamic acid	-6.4
Phenol, 2,6-Dimethoxy-4-(2-Propenyl)-	-6.3
Phthalic acid, butyl undecyl ester	-6.3
Gentisic acid	-6.2
Cis-Linoleic acid Methyl ester	-6
Vanillin	-5.9
Linoleic acid	-5.9
Glycerol 1-palmitate	-5.9
Lauric acid	-5.6
Oleic acid	-5.6
9-octadecenoic Acid (Z)-, methyl ester	-5.6
Methyl stearate	-5.6
D-Allose	-5.5
Palmitic acid	-5.5
Stearic acid	-5.5
Hexadecanoic acid, Methyl ester	-5.4
Octadecanal	-5.4
Myristic acid	-5.3
5-Hydroxymethylfurfural	-4.9

Table 9.49: Molecular docking for antidiabetic protein, Protein Tyrosine Phosphatase 1B (PTP1B)

Ligand	Binding affinity (kcal/mol)
Cholesta-4,6-dien-3-ol, benzoate, (3.beta.)-	-9.6
Quercetin	-8.2
Rhamnetin	-8.2
Maslinic acid	-8.1
2-Phenyl-4H-chromen-4-one	-7.7
Myricetin	-7.7
Cinnamic acid	-7.5
Oleanolic acid	-7.3
Ellagic acid	-7.2
D:B-Friedo-B':A'-Neogammacer-5-en-3-one	-7.2
Beta-Sitosterol	-7.1
Vitamin E	-7
Chlorogenic acid	-7
Ferulic acid	-7
Kaempferol	-6.9
Stigmast-4-en-3-one	-6.9
Lupeol	-6.7
Gentisic acid	-6.4
Vanillin	-6
Gallic acid	-6
3-Furanacetic acid, 4-Hexyl-2,5-Dihydro-2,5-Dioxo-	-5.9
Myristic acid	-5.8
Stearic acid	-5.8
Palmitic acid	-5.7
Linoleic acid	-5.6
Cis-Linoleic acid Methyl ester	-5.6
Phenol, 2,6-Dimethoxy-4-(2-Propenyl)-	-5.5
Lauric acid	-5.5
D-Allose	-5.5
9-Octadecenoic acid (Z)-, methyl ester	-5.5
5-Hydroxymethylfurfural	-5.4
Oleic acid	-5.4
Methyl Stearate	-5.1
Glycerol 1-palmitate	-5.1
Octadecanal	-5
Phthalic acid, butyl undecyl ester	-5
Hexadecanoic acid, Methyl ester	-4.9

Table 9.50: Molecular docking for antidiabetic protein AKT serine/threonine kinase (AKT1)

Ligand	Binding affinity (kcal/mol)
Cholesta-4,6-dien-3-ol, benzoate, (3.beta.)-	-9.1
Oleanolic acid	-9
Vitamin E	-8.7
Ellagic acid	-8.4
2-Phenyl-4H-chromen-4-one	-7.9
Lupeol	-7.9
D:B-Friedo-B':A'-Neogammacer-5-en-3-one	-7.9
Beta Sitosterol	-7.9
Maslinic acid	-7.6
Myricetin	-7.6
Quercetin	-7.4
Chlorogenic acid	-7.4
Kaempferol	-7.4
Rhamnetin	-7
Stigmast-4-en-3-one	-7
Phthalic acid, butyl undecyl ester	-6.8
Ferulic acid	-6.5
3-Furanacetic acid, 4-Hexyl-2,5-Dihydro-2,5-Dioxo-	-6.5
Cinnamic acid	-6.1
Gallic acid	-5.9
Gentisic acid	-5.8
Linoleic acid	-5.7
9-Octadecenoic acid (Z)-, methyl ester	-5.7
Phenol, 2,6-Dimethoxy-4-(2-Propenyl)-	-5.6
Cis-Linoleic acid Methyl ester	-5.6
Myristic acid	-5.5
Vanillin	-5.5
Methyl Stearate	-5.5
Glycerol 1-palmitate	-5.5
Lauric acid	-5.4
Stearic acid	-5.4
D-Allose	-5.3
Oleic acid	-5.2
Methyl palmitate	-5.2
Palmitic acid	-5.1
5-Hydroxymethylfurfural	-4.7
Octadecanal	-4.4

Table 9.51: Molecular docking for anticancer protein Epidermal Growth Factor Receptor (EGFR)

Ligand	Binding affinity (kcal/mol)
D:B-Friedo-B':A'-Neogammacer-5-en-3-one	-9.7
Oleanolic acid	-9.6
Lupeol	-9.6
Beta-sitosterol	-9
2-Phenyl-4H-chromen-4-one	-8.8
Maslinic acid	-8.8
Ellagic acid	-8.8
Cholesta-4,6-dien-3-ol, benzoate, (3.beta.)-	-8.7
Rhamnetin	-8.7
Quercetin	-8.6
Kaempferol	-8.6
Myricetin	-8.6
Chlorogenic acid	-8.3
Vitamin E	-7.9
3-Furanacetic acid, 4-Hexyl-2,5-Dihydro-2,5-Dioxo-	-6.9
Stigmast-4-en-3-one	-6.7
Phthalic acid, butyl undecyl ester	-6.5
Ferulic acid	-6.4
Gentisic acid	-6.3
Linoleic acid	-6.3
Cinnamic Acid	-6.2
Stearic acid	-6.2
Phenol, 2,6-Dimethoxy-4-(2-Propenyl)-	-6.1
Gallic acid	-6.1
Oleic acid	-6.1
Cis-Linoleic acid Methyl ester	-6.1
9-Octadecenoic acid (Z)-, methyl ester	-5.9
Glycerol 1-palmitate	-5.9
Hexadecanoic acid, Methyl ester	-5.8
Methyl Stearate	-5.8
Vanillin	-5.7
Palmitic acid	-5.7
Octadecanal	-5.7
Myristic acid	-5.6
D-Allose	-5.5
Lauric acid	-5.3
5-Hydroxymethylfurfural	-4.7

Table 9.52: Molecular docking for anticancer protein Kirsten Rat Sarcoma Viral Oncogene Homolog (KRAS)

Ligand	Binding affinity (kcal/mol)
Chlorogenic acid	-9.6
Beta sitosterol	-8.8
Quercetin	-8.8
Kaempferol	-8.7
2-Phenyl-4H-chromen-4-one	-8.6
Myricetin	-8.6
Rhamnetin	-8.5
Vitamin E	-8.4
Ellagic acid	-8.4
Cholesta-4,6-dien-3-ol, benzoate, (3.beta.)-	-7.7
D:B-Friedo-B':A'-Neogammacer-5-en-3-one	-7.2
3-Furanacetic acid, 4-Hexyl-2,5-Dihydro-2,5-Dioxo-	-7.1
Oleanolic acid	-7
Stigmast-4-en-3-one	-7
Glycerol 1-palmitate	-6.9
Lupeol	-6.8
Maslinic acid	-6.7
Ferulic acid	-6.6
Phthalic acid, butyl undecyl ester	-6.6
D-Allose	-6.5
Linoleic acid	-6.5
Oleic acid	-6.4
Cis-Linoleic acid Methyl ester	-6.4
9-Octadecenoic acid (Z)-, methyl ester	-6.4
Gentisic acid	-6.3
Gallic acid	-6.3
Lauric acid	-6.2
Cinnamic acid	-6.2
Hexadecanoic acid, Methyl ester	-6.2
Palmitic acid	-6.2
Myristic acid	-6
Phenol, 2,6-Dimethoxy-4-(2-Propenyl)-	-6
Stearic acid	-5.9
Vanillin	-5.8
Methyl Stearate	-5.8
Octadecanal	-5.7
5-Hydroxymethylfurfural	-5.3

Table 9.53: Molecular docking for anticancer protein Mitogen-Activated Protein Kinase 1 (MAPK1)

Ligand	Binding affinity (kcal/mol)
Ellagic acid	-9.4
D:B-Friedo-B':A'-Neogammacer-5-en-3-one	-9.1
Oleanolic acid	-9
Myricetin	-8.9
2-Phenyl-4H-chromen-4-one	-8.6
Vitamin E	-8.6
Maslinic acid	-8.6
Lupeol	-8.6
Quercetin	-8.6
Cholesta-4,6-dien-3-ol, benzoate, (3.beta.)-	-8.4
Kaempferol	-8.1
Beta Sitosterol	-8
Rhamnetin	-7.8
Chlorogenic acid	-7.4
Stigmast-4-en-3-one	-7
3-Furanacetic acid, 4-Hexyl-2,5-Dihydro-2,5-Dioxo-	-6.7
Cinnamic acid	-6.6
Ferulic acid	-6.6
Gallic acid	-6.2
Phenol, 2,6-Dimethoxy-4-(2-Propenyl)-	-6
Gentisic acid	-5.9
Linoleic acid	-5.9
Phthalic acid, butyl undecyl ester	-5.9
Cis-Linoleic acid Methyl ester	-5.8
Vanillin	-5.7
9-Octadecenoic acid (Z)-, methyl ester	-5.7
Methyl palmitate	-5.6
D-Allose	-5.4
Palmitic acid	-5.4
Oleic acid	-5.3
Glycerol 1-palmitate	-5.3
Stearic acid	-5.1
Myristic acid	-4.8
5-Hydroxymethylfurfural	-4.7
Lauric acid	-4.7
Octadecanal	-4.7
Methyl Stearate	-3.8

Table 9.54: Molecular docking for anticancer protein Tumour Protein p53 (TP53)

Ligand	Binding affinity (kcal/mol)
Quercetin	-7.5
Myricetin	-7.4
Kaempferol	-7.3
D:B-Friedo-B':A'-Neogammacer-5-en-3-one	-7.3
2-Phenyl-4H-chromen-4-one	-6.9
Oleanolic acid	-6.9
Ellagic acid	-6.9
Maslinic acid	-6.9
Cholesta-4,6-dien-3-ol, benzoate, (3.beta.)-	-6.8
Chlorogenic acid	-6.8
Rhamnetin	-6.8
Lupeol	-6.6
Stigmast-4-en-3-one	-6.2
Beta sitosterol	-6
Ferulic acid	-5.7
Vitamin E	-5.5
Gallic acid	-5.3
Gentisic acid	-5.2
Phenol, 2,6-Dimethoxy-4-(2-Propenyl)-	-5.1
Cinnamic acid	-5
Vanillin	-4.9
D-Allose	-4.9
3-Furanacetic acid, 4-Hexyl-2,5-Dihydro-2,5-Dioxo-	-4.9
Phthalic acid, butyl undecyl ester	-4.9
5-Hydroxymethylfurfural	-4.5
Linoleic acid	-4.4
Glycerol 1-palmitate	-4.4
Oleic acid	-4.3
Cis-Linoleic acid Methyl ester	-4.3
Stearic acid	-4.3
9-octadecenoic Acid (Z)-, methyl ester	-4.2
Myristic acid	-4
Methyl stearate	-4
Lauric acid	-3.9
Hexadecanoic acid, Methyl ester	-3.9
Palmitic acid	-3.9
Octadecanal	-3.7

9.3.6. Visualization

Although docking scores offer a numerical assessment of ligand–protein binding strength, molecular visualization is crucial for interpreting the qualitative aspects of these interactions. It enables the examination of the specific binding location and mode of a compound within the protein structure, shedding light on the underlying factors influencing affinity, selectivity, and potential biological effects. Ligand -protein complex with a higher docking score was selected for further analysis. Tools like BIOVIA Discovery Studio Visualizer facilitate this process by generating:

- **2D interaction maps** that depict hydrogen bonds, hydrophobic interactions, and π–π stacking with active site residues.
- **3D structural views** that illustrate the spatial orientation of the ligand within the protein's binding pocket.

9.3.6.1. Visualization of antioxidant proteins

Out of 37 bark phytochemicals from *S. palghatense* bark methanol extracts, docked with Human Cu, Zn Superoxide Dismutase (SOD1), D:B-Friedo-B':A'-Neogammacer-5-en-3-one demonstrated the strongest binding affinity. Kaempferol showed the highest affinity in docking with Human Erythrocyte Catalase (CAT). Maslinic acid exhibited the best binding with Human Glutathione Peroxidase 1 (GPx1) and also with the KEAP1 Kelch Domain. Oleanolic acid showed significant binding affinity with the Thioredoxin and TXNIP complex.

9.3.6.1.1. 3D and 2D visualization of Human Cu, Zn Superoxide Dismutase (SOD1) with DB-Friedo-B'A'-Neogammacer-5-en-3-one

The 3D visualization illustrates DB-Friedo-B'A'-Neogammacer-5-en-3-one fitting securely within the hydrophobic cavity of the Human Cu, Zn Superoxide Dismutase (SOD1) protein. The ligand is positioned along the surface groove, engaging predominantly through non-polar contacts, with the semi-transparent molecular surface revealing the complementary shape between the protein's active site and the triterpenoid framework of the ligand. This tight spatial complementarity

suggests a stabilizing fit that may influence the enzyme's activity through steric and hydrophobic effects.

The 2D interaction map highlights the specific amino acid contacts contributing to the ligand's stabilization within the SOD1 binding site. The following interactions were identified:

- Alkyl Interactions (pink spheres)

  LEU144 and LYS122 form non-polar alkyl interactions with hydrophobic regions of the ligand, providing van der Waals-driven stability and contributing to its snug accommodation.

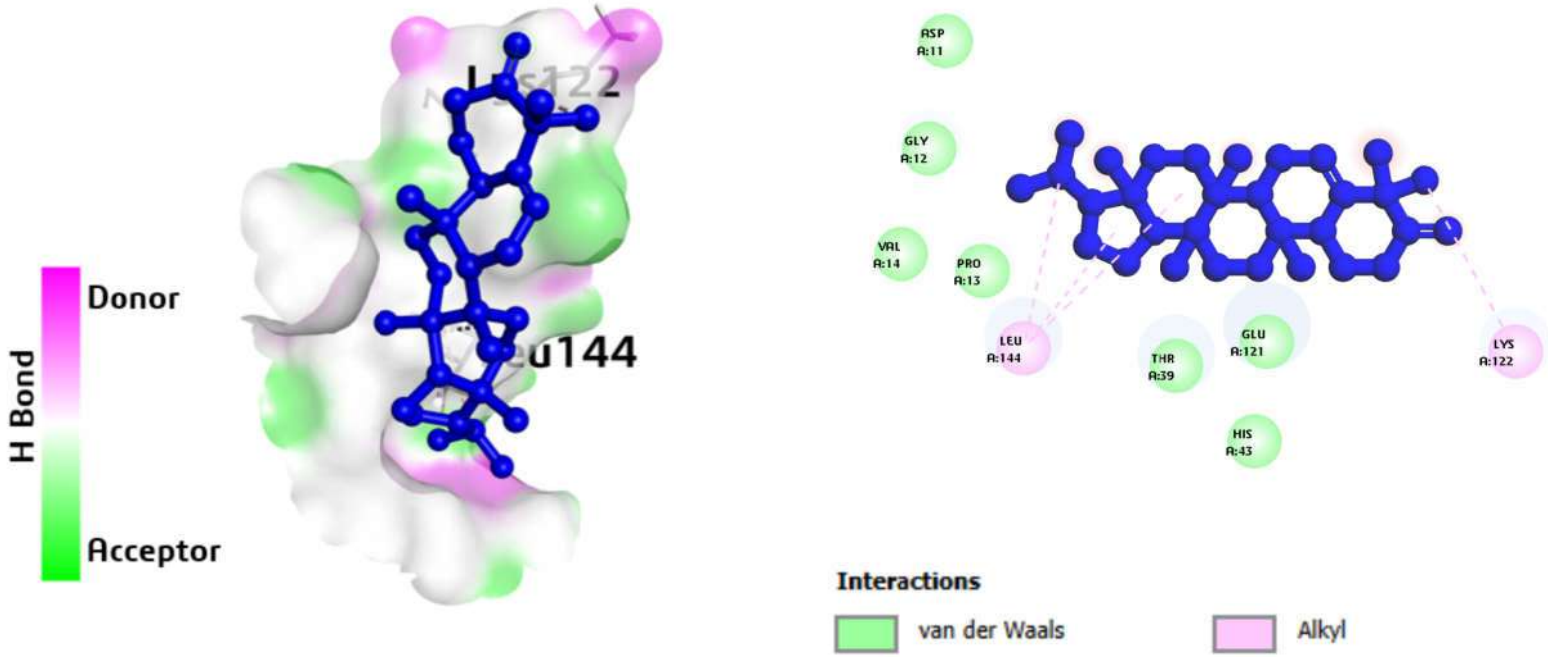
- Van der Waals Interactions (light green spheres)

  Residues such as ASP11, GLY12, VAL14, PRO13, THR39, GLU121, and HIS43 engage in multiple van der Waals contacts, collectively enhancing the shape complementarity and holding the ligand in an energetically favourable position.

This interaction profile indicates that DB-Friedo-B'A'-Neogammacer-5-en-3-one binds to SOD1 primarily through hydrophobic and van der Waals forces, with minimal polar contributions, suggesting a binding mechanism driven by non-polar complementarity rather than strong directional hydrogen bonding (Plate 9.7).

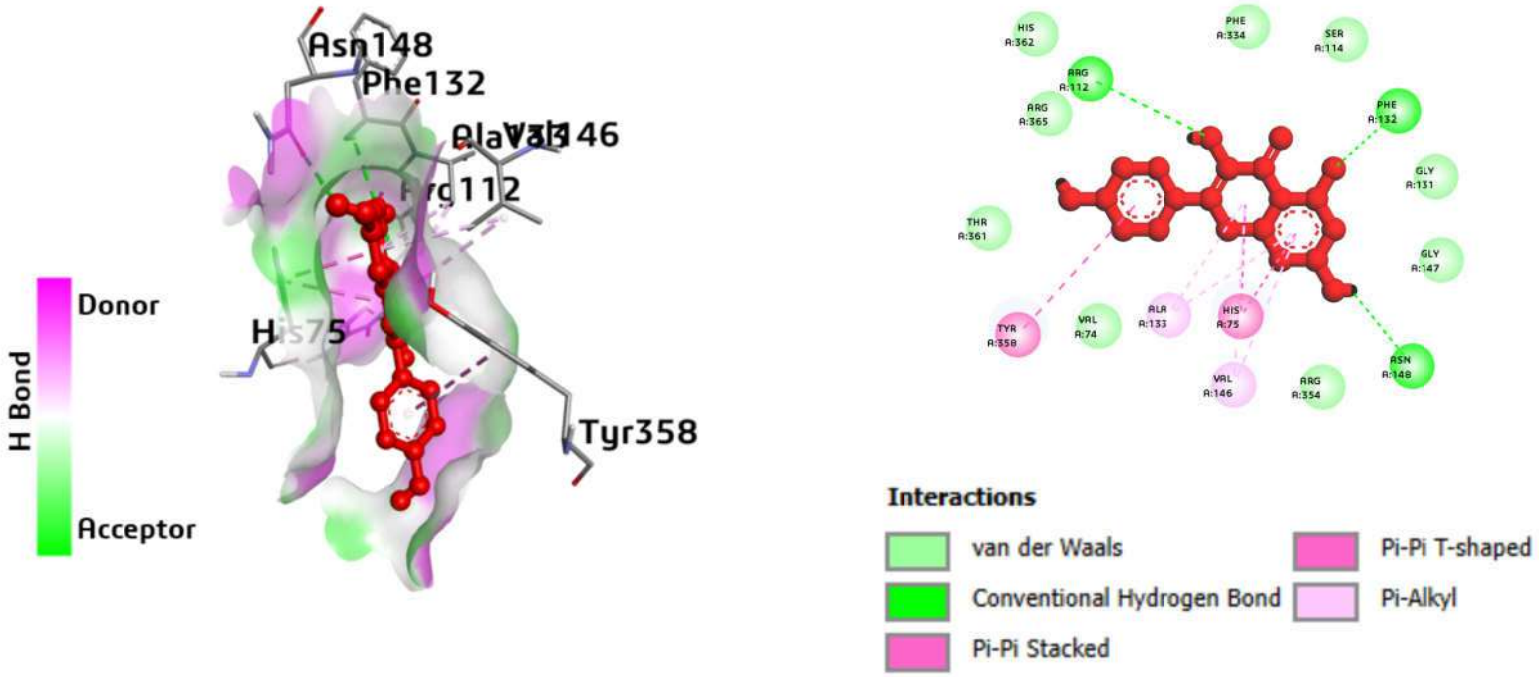
9.3.6.1.2. 3D and 2D visualization of Human Erythrocyte Catalase (CAT) with Kaempferol

The 3D visualization shows Kaempferol occupying a well-defined binding pocket within the Catalase protein. The ligand is oriented along the central groove of the active site, with its planar flavonoid scaffold fitting closely against the semi-transparent protein surface. The surrounding surface patches display alternating hydrophobic and hydrophilic zones, allowing the aromatic rings of Kaempferol to align with π-stacking regions while its hydroxyl groups extend toward polar residues for hydrogen bonding. This spatial complementarity suggests a stable binding mode, where both non-polar packing and polar contacts contribute to ligand stabilization.



(a) (b)

Plate 9.7: Visualization of binding interactions between Human Cu,Zn Superoxide Dismutase (SOD1) and D:B-Friedo-B':A'-Neogammacer-5-en-3-one, showing (a) the three-dimensional (3D) molecular surface and (b) the two-dimensional (2D) interaction diagram



(a) (b)

Plate 9.8: Visualization of binding interactions between Human Erythrocyte Catalase (CAT)and Kaempferol, showing (a) the three-dimensional (3D) molecular surface and (b) the two-dimensional (2D) interaction diagram

The 2D interaction map identifies the specific amino acid interactions involved in ligand stabilization:

- Conventional Hydrogen Bonds (green lines)

  ARG112, PHE132, and ASN148 form directional hydrogen bonds with hydroxyl groups of Kaempferol, anchoring the ligand via polar contacts that enhance specificity.

- Van der Waals Interactions (light green spheres)

  PHE334, SER114, GLY131, GLY147, HIS362, and ARG365 engage in van der Waals interactions, shaping the ligand fit within the binding pocket and contributing to non-covalent stabilization.

- Pi–Pi Stacking and Pi–Pi T-shaped Interactions (magenta and pink spheres)

  HIS75 and TYR358 interact with the aromatic rings of Kaempferol through π-stacking and π–π T-shaped orientations, reinforcing the ligand's position through aromatic ring interactions.

- Pi–Alkyl Interactions (light pink spheres)

  VAL146 and ARG354 form hydrophobic π–alkyl contacts with the aromatic moieties of the ligand, adding further non-polar stabilization.

This interaction profile indicates that Kaempferol binds to Catalase through a synergistic combination of hydrogen bonding, aromatic π-based interactions, and hydrophobic packing, potentially stabilizing the ligand in a conformation that could modulate the enzyme's catalytic activity (Plate 9.8).

9.3.6.1.3. 3D and 2D visualization of Human Glutathione Peroxidase 1 (GPx1) with Maslinic acid

The 3D visualization depicts Maslinic Acid nestled within the hydrophobic cleft of Glutathione Peroxidase 1 (GPx1). The ligand adopts an extended conformation along the binding groove, with its triterpenoid backbone oriented to

maximize surface complementarity with the protein. The semi-transparent molecular surface reveals that the ligand fits snugly, engaging both hydrophobic and polar patches, indicating a balance between van der Waals stabilization and directional hydrogen bonding. This spatial arrangement suggests that Maslinic Acid can achieve stable anchoring within the GPx1 active site, potentially influencing catalytic function through steric modulation.

The 2D interaction diagram highlights the following residue contacts:

- Van der Waals Interactions (light green spheres)

Residues TYR54, ASN58, GLU59, GLY100, GLY101, and GLU104 contribute to multiple van der Waals contacts, forming a stabilizing microenvironment around the ligand.

- Conventional Hydrogen Bonds (bright green spheres)

THR55 and ARG62 establish strong hydrogen bonds with Maslinic Acid, providing directional binding stability and reinforcing the ligand's orientation.

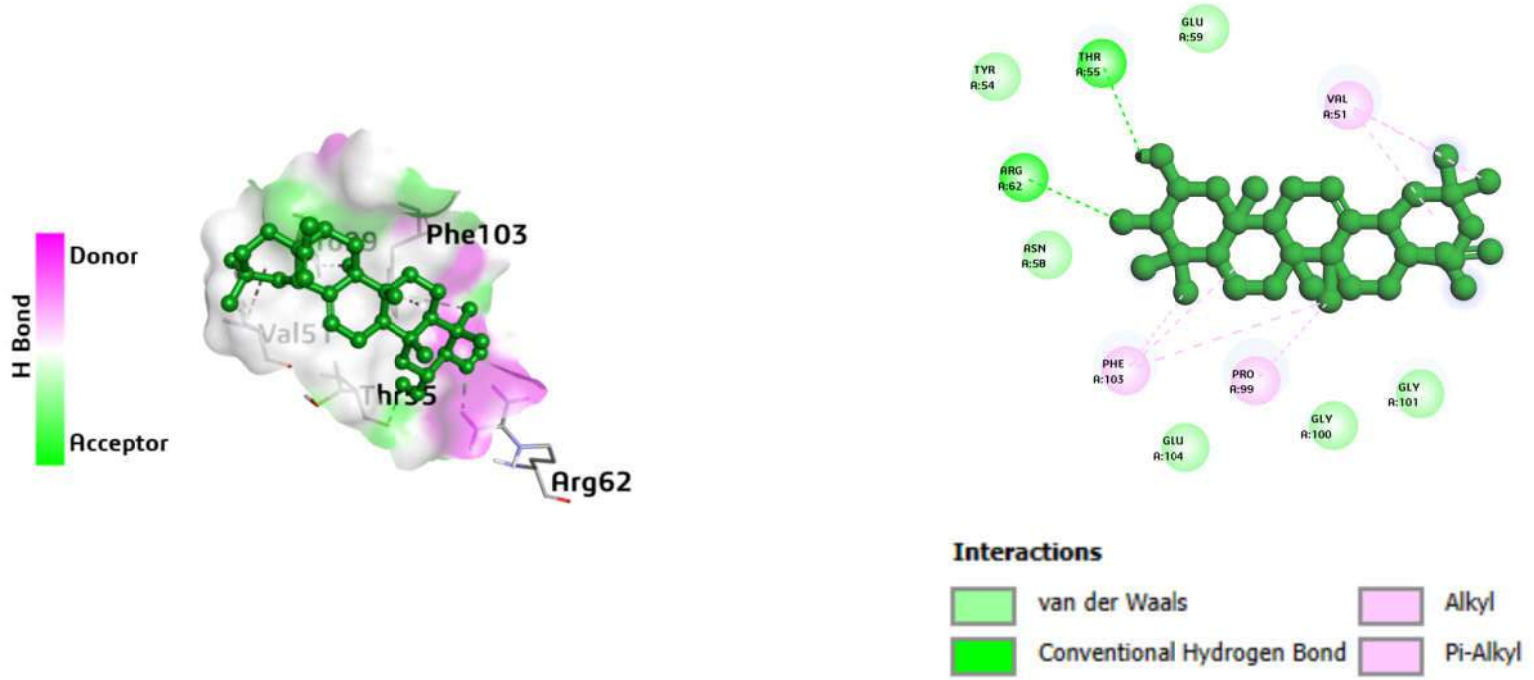
- Alkyl and Pi–Alkyl Interactions (pink spheres)

VAL51, PRO99, and PHE103 participate in hydrophobic alkyl and π–alkyl interactions with the ligand's non-polar moieties, enhancing fit through dispersion forces.

This binding profile indicates that Maslinic Acid interacts with GPx1 through a synergistic network of hydrophobic, van der Waals, and hydrogen-bonding interactions. The predominance of non-polar contacts, complemented by strategic hydrogen bonds, suggests a binding mechanism optimized for structural complementarity rather than high electrostatic contribution (Plate 9.9).

9.3.6.1.4. 3D and 2D visualization of KEAP1 Kelch Domain (KEAP1 Kelch) with Maslinic acid

The 3D visualization shows Maslinic Acid occupying a well-defined hydrophobic channel within the Kelch domain of the Nrf-Keap complex. The ligand's



(a) (b)

Plate 9.9: Visualization of binding interactions between Human Glutathione Peroxidase 1 (GPx1)and Maslinic acid, showing (a) the three-dimensional (3D) molecular surface and (b) the two-dimensional (2D) interaction diagram

pentacyclic triterpenoid scaffold aligns along the binding groove, establishing optimal surface complementarity with the surrounding residues. The molecular surface mapping reveals alternating hydrophobic (magenta) and polar (green) regions, with Maslinic Acid engaging both environments to achieve a stable fit. This spatial arrangement suggests a favorable anchoring mode, enabling the ligand to potentially modulate Nrf2–Keap1 interactions through steric and hydrophobic interference at the binding interface.

The 2D interaction diagram highlights the following contacts:

- Van der Waals interactions (light green)

HIS516, VAL420, VAL467, VAL514, VAL608, GLY419, GLY367, GLY611, CYS513, CYS368, VAL369, and GLU611 form an extensive van der Waals network, creating a stabilizing microenvironment.

- Conventional hydrogen bonds (bright green)

GLY564 and GLN563 form hydrogen bonds with the ligand, reinforcing its orientation within the binding pocket.

- Alkyl and π–alkyl interactions (light pink)

LEU515, VAL561, VAL418, VAL514, and ALA607 contribute hydrophobic stabilization, further securing the ligand in place through dispersion forces.

This binding profile indicates that Maslinic acid stabilizes within the Nrf-Keap active site through a combination of non-polar van der Waals contacts, targeted hydrophobic interactions, and directional hydrogen bonds. The predominance of hydrophobic engagement, complemented by selective polar contacts, suggests a mechanism favouring high structural complementarity and potential interference with Keap1's Nrf2 recognition function (Plate 9.10).

9.3.6.1.5. 3D and 2D visualization of Thioredoxin and TXNIP Complex (Trx-TXNIP) with Oleanolic acid

The 3D visualization depicts Oleanolic Acid snugly accommodated within the hydrophobic cleft of the Thioredoxin–TXNIP complex. The ligand adopts an extended hydrophobic conformation, allowing optimal surface complementarity with the binding pocket. The molecular surface mapping reveals a predominance of hydrophobic (magenta) and van der Waals–favorable (light green) regions, interspersed with hydrogen bond–favourable zones. The ligand's triterpenoid scaffold enables extensive alkyl and Pi–Alkyl contacts, anchoring it deeply into the binding groove, while selective hydrogen bonds stabilize its orientation.

The 2D interaction diagram highlights the following residue contacts:

- Van der Waals Interactions (light green spheres)

ALA52, SER67, SER113, GLY108, GLU273, and PRO293 form non-polar van der Waals contacts that reinforce the ligand's stability in the pocket.

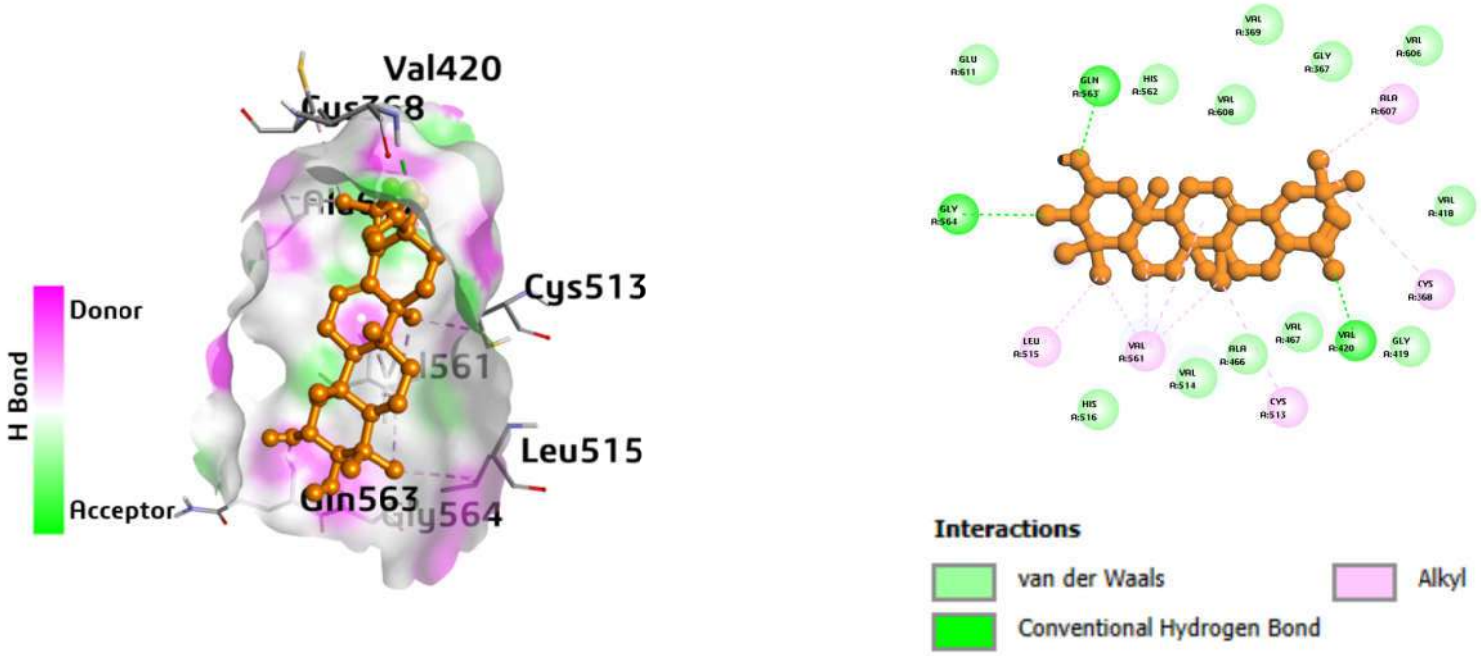
- Conventional Hydrogen Bonds (bright green spheres)

LYS187 and LEU294 establish conventional hydrogen bonds with the ligand, enhancing binding specificity and directional stability.

- Alkyl and Pi–Alkyl Interactions (light pink spheres)

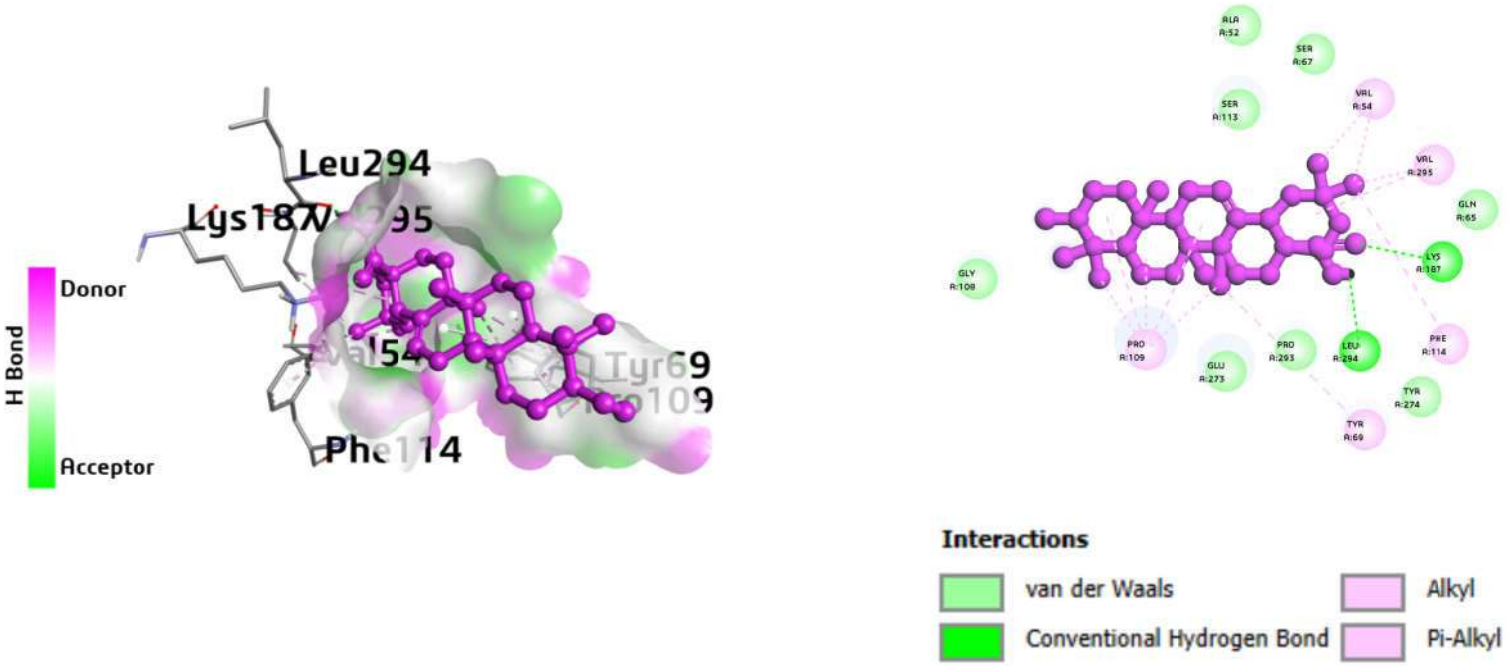
VAL54, VAL295, PRO109, PHE114, TYR69, and TYR274 participate in hydrophobic alkyl and Pi–Alkyl interactions, contributing significantly to the ligand's entrapment and residence time within the active site.

This interaction network indicates that Oleanolic Acid binds to the Thioredoxin–TXNIP complex through a synergistic combination of van der Waals stabilization, hydrophobic packing, and hydrogen bonding. The dominance of hydrophobic and shape-complementary interactions suggests that the binding is primarily driven by non-polar contacts, with hydrogen bonds providing positional reinforcement (Plate 9.11).



(a) (b)

Plate 9.10: Visualization of binding interactions between KEAP1 Kelch Domain (KEAP1 Kelch) and Maslinic acid, showing (a) the three-dimensional (3D) molecular surface and (b) the two-dimensional (2D) interaction diagram



(a) (b)

Plate 9.11: Visualization of binding interactions betweenThioredoxin and TXNIP Complex (Trx-TXNIP) and Oleanolic acid, showing (a) the three-dimensional (3D) molecular surface and (b) the two-dimensional (2D) interaction diagram

9.3.6.2. Visualization of antimicrobial proteins

Out of 37 phytochemicals docked from bark methanol extracts of *S. palghatense*, 2-Phenyl-4H-chromen-4-one showed strong binding with both D-alanyl-D-alanine ligase (D-ALA:D-ALA Ligase/Ddl) and the LasR ligand-binding domain (LasR). Oleanolic acid displayed notable affinity for the PqsR coinducer-binding domain (PqsR/MvfR). Ellagic acid was found to bind effectively with Penicillin-Binding Protein 3 (PBP3), while Cholesta-4,6-dien-3-ol, benzoate, (3.beta)- exhibited strong interaction with the regulatory protein RhlR (RhIR).

9.3.6.2.1. 3D and 2D visualization of D-alanyl-D-alanine ligase (D-ALA:D-ALA Ligase/Ddl) with 2-Phenyl-4H-chromen-4-one

The 3D visualization illustrates 2-Phenyl-4H-chromen-4-one firmly positioned within the binding cavity of DDLA Ligase, enclosed by a semi-transparent surface representing the protein's interaction topology. The ligand is well-aligned in a hydrophobic and moderately polar groove, adopting a stable orientation that allows optimal contact with the surrounding residues. Its positioning is reinforced by a combination of hydrogen bonds, hydrophobic contacts, and aromatic interactions, collectively stabilizing the ligand within the catalytic region of the protein.

The 2D interaction diagram provides a detailed mapping of the intermolecular contacts between 2-Phenyl-4H-chromen-4-one and DDLA Ligase:

- Conventional Hydrogen Bonds (green arrows)

SER151 and TYR210 form hydrogen bonds with the oxygen atoms of the ligand, securing its anchorage within the active site.

- π–Anion Interactions (orange)

GLU187 and ASP257 engage with the aromatic system of the ligand, enhancing electrostatic complementarity.

- π–Sigma Interactions (purple)

LEU269 and MET154 participate in π–sigma interactions with the ligand's aromatic rings, contributing to hydrophobic stabilization.

- π–Sulfur Interactions (yellow)

MET259 forms π–sulfur contacts, adding to the structural stabilization of the binding pose.

- π–Alkyl Interactions (pink)

ILE142 and LEU183 provide additional hydrophobic packing through π–alkyl contacts.

- Van der Waals Interactions (light green)

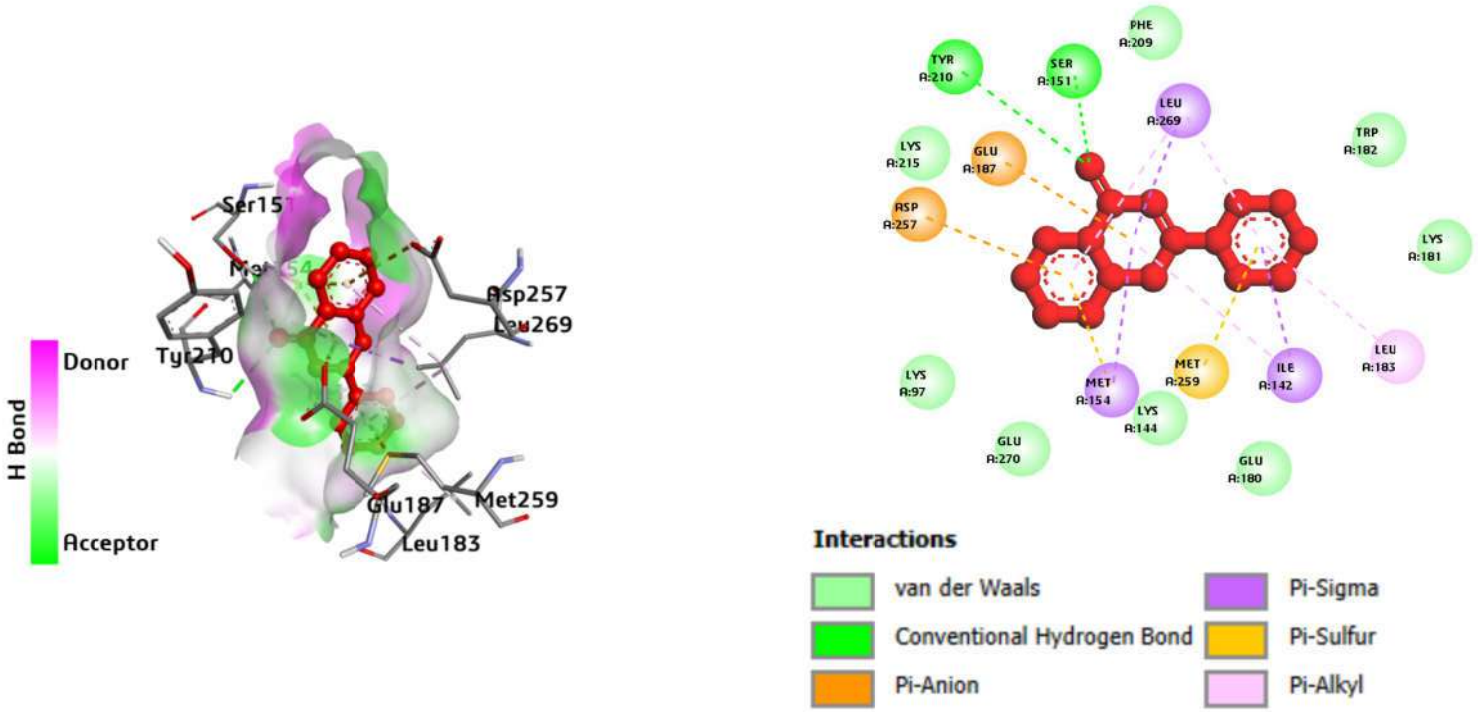
Multiple residues, including LYS144, GLU180, LYS181, TRP182, and PHE209, surround the ligand and maintain close-range stabilizing interactions.

This interaction network highlights the complementary fit of 2-Phenyl-4H-chromen-4-one within the DDLA Ligase/Ddl active pocket, where the interplay of polar contacts, aromatic stacking, and hydrophobic encapsulation ensures a stable and specific binding orientation (Plate 9.12).

9.3.6.2.2. 3D and 2D visualization of LasR ligand-binding domain (LasR) with 2-Phenyl-4H-chromen-4-one

The 3D visualization shows 2-Phenyl-4H-chromen-4-one securely positioned within the hydrophobic cavity of the LasR ligand-binding domain, enveloped by a semi-transparent surface illustrating the topography and chemical nature of the binding pocket. The ligand's planar aromatic scaffold aligns with the hydrophobic groove, while its substituents extend toward peripheral regions, optimizing contact with both aromatic and nonpolar residues. The arrangement facilitates a compact fit, driven largely by π–π stacking and hydrophobic interactions.

The 2D interaction diagram maps the specific molecular contacts stabilizing the complex:



(a) (b)

Plate 9.12: Visualization of binding interactions betweenD-alanyl-D-alanine ligase (D-ALA:D-ALA Ligase/Ddl) and 2-Phenyl-4H-chromen-4-one, showing (a) the three-dimensional (3D) molecular surface and (b) the two-dimensional (2D) interaction diagram

- π–Anion Interaction (orange)

ASP73 engages in a π–anion contact with the ligand's aromatic system, contributing to electrostatic stabilization.

- π–Sigma Interaction (purple)

TYR64 forms a π–sigma bond with the aromatic ring, reinforcing hydrophobic complementarity.

- π–Alkyl Interactions (Pink):

Multiple hydrophobic residues, including VAL76, LEU36, LEU40, LEU125, and LEU127, interact with the aromatic and aliphatic portions of the ligand, enhancing stability.

- π–π Stacked Interactions (bright pink)

TYR47 engages in π–π stacking with the ligand's phenyl ring, supporting strong aromatic stabilization.

- Van der Waals Interactions (light green)

Residues such as GLY38, GLY39, ILE52, ARG61, TYR56, SER129, and THR75 surround the ligand and reinforce its positioning through close-range packing forces.

This interaction network reveals that 2-Phenyl-4H-chromen-4-one achieves stable accommodation in the LasR binding site through a synergy of aromatic stacking, hydrophobic encapsulation, and specific electrostatic contacts, aligning well with the hydrophobic nature of the receptor groove (Plate 9.13).

9.3.6.2.3. 3D and 2D visualization of PqsR coinducer-binding domain (PqsR/MvfR) with Oleanolic acid

The 3D visualization depicts Oleanolic acid accommodated within the hydrophobic cavity of the PqsR regulatory protein, enclosed by a semi-transparent

molecular surface that reflects the polarity and topography of the binding site. The triterpenoid framework of the ligand aligns with the elongated groove, enabling extensive hydrophobic and alkyl interactions, while limited polar contacts contribute to targeted stabilization at specific points within the cavity.

The 2D interaction diagram highlights the molecular contacts stabilizing the complex:

- Conventional Hydrogen Bonds (green arrows)

ALA187 and TYR258 form hydrogen bonds with polar regions of the ligand, anchoring it within the binding site.

- Alkyl Interactions (light pink)

Residues including VAL211 and LEU207 contribute to nonpolar stabilization via alkyl contacts along the hydrophobic surface of the ligand.

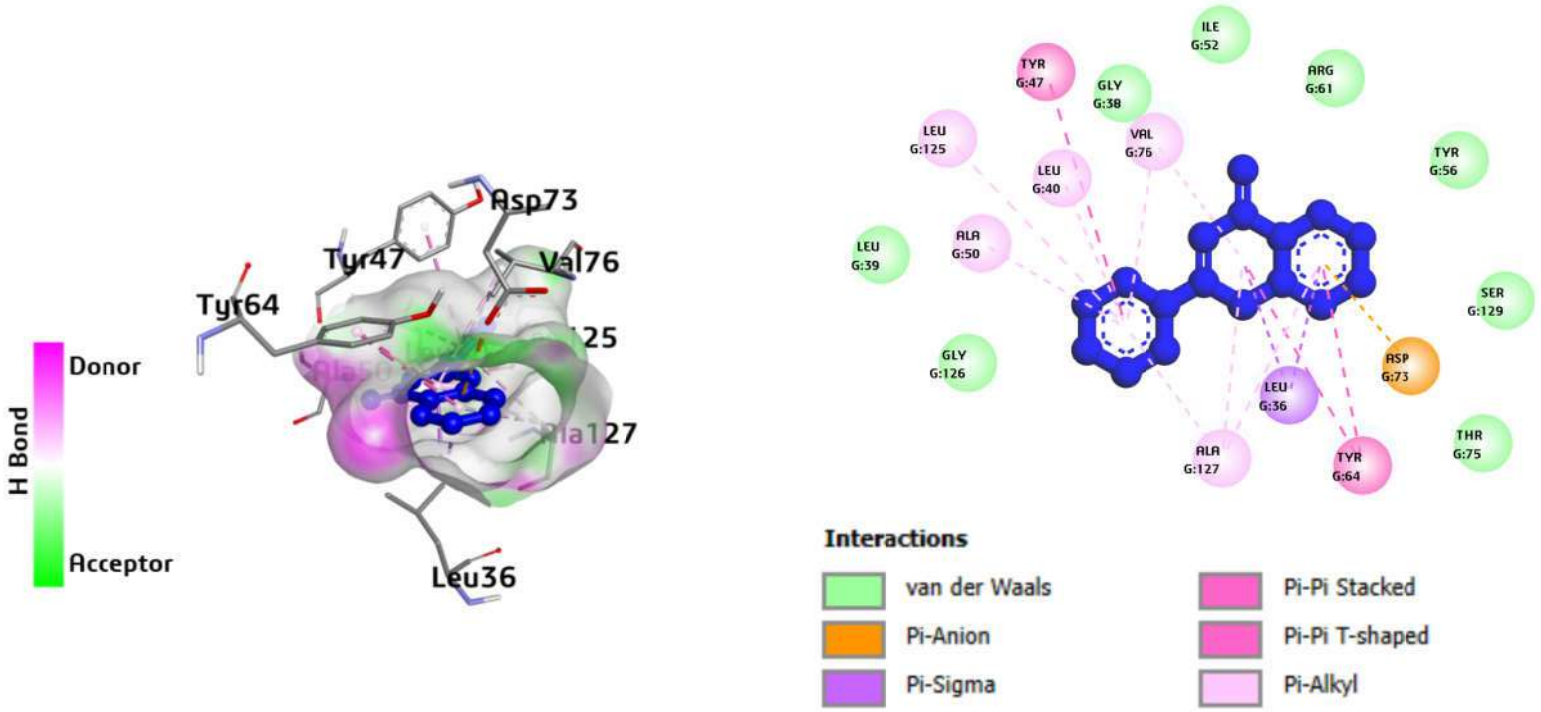
- π–Alkyl Interactions (light purple)

TYR258, ILE263, and ILE256 engage in π–alkyl contacts with the hydrophobic rings of Oleanolic Acid, enhancing compact packing.

- Van der Waals Interactions (light green)

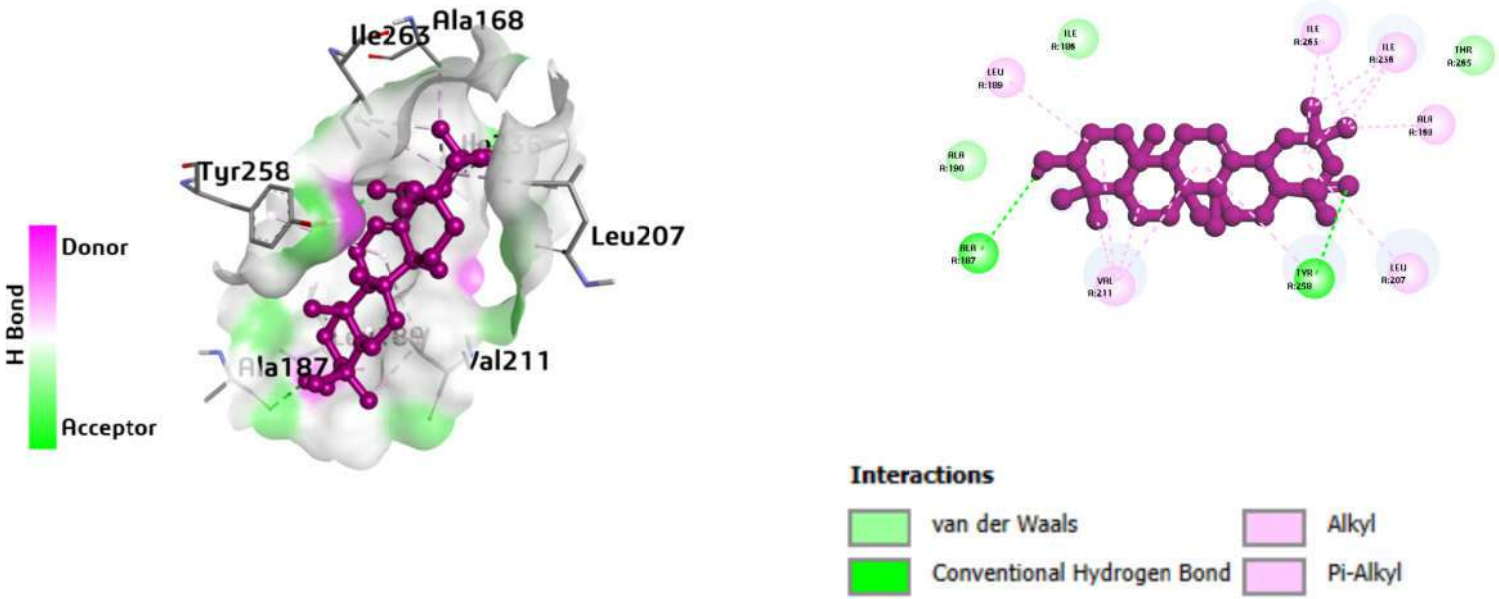
Multiple residues, such as LEU189, ALA190, THR265, ALA168, and ILE186, surround the ligand and reinforce binding through close-range non-covalent forces.

The interaction profile demonstrates that Oleanolic Acid's binding is driven predominantly by hydrophobic and alkyl interactions, complemented by select hydrogen bonds, leading to a stable fit within the PqsR coinducer-binding domain (Plate 9.14).



(a) **(b)**

Plate 9.13: Visualization of binding interactions betweenLasR ligand-binding domain (LasR) and 2-Phenyl-4H-chromen-4-one, showing (a) the three-dimensional (3D) molecular surface and (b) the two-dimensional (2D) interaction diagram



(a) (b)

Plate 9.14: Visualization of binding interactions betweenPqsR coinducer-binding domain (PqsR/MvfR) and Oleanolic acid, showing (a) the three-dimensional (3D) molecular surface and (b) the two-dimensional (2D) interaction diagram

9.3.6.2.4. 3D and 2D visualization of Penicillin-Binding Protein 3 (PBP3) with Ellagic acid

The 3D visualization shows Ellagic Acid fitting securely within the binding cavity of Penicillin-Binding Protein 3 (PBP3), enveloped by a semi-transparent molecular surface that reflects the receptor topology. The ligand positions itself in a strategic orientation, enabling multiple stabilizing interactions with both catalytic and supportive residues. The placement within the groove suggests an optimal conformation for interaction with the protein's active site architecture.

The 2D interaction diagram provides a closer look at the key atomic-level contacts between Ellagic Acid and the surrounding amino acid residues of PBP3:

- Conventional Hydrogen Bonds (green lines)

ARG153, ARG273, and GLU150 form hydrogen bonds with the ligand, anchoring it within the pocket and enhancing polar complementarity. These bonds are essential in maintaining the stability of the ligand within the enzyme's active site.

- π–Cation Interaction (orange line)

ARG152 engages in a π–cation interaction with one of the aromatic rings of Ellagic Acid, contributing to additional electrostatic stabilization.

- π–Sigma and π–Alkyl Interactions (purple and pink lines)

VAL170 participates in π–sigma interactions, while ARG152 contributes to π–alkyl contacts, both of which enhance hydrophobic complementarity between the ligand and the protein.

- Van der Waals Interactions (light green spheres)

Several residues, including TYR155, ASP169, THR168, ASP172, PHE151, ARG127, and THR81, engage in van der Waals interactions, subtly shaping the binding environment and reinforcing the snug fit of the ligand within the pocket.

This interaction profile reveals that Ellagic acid is well-stabilized within PBP3 through a balanced network of hydrogen bonding, electrostatic, hydrophobic, and aromatic interactions, supporting its potential to influence the protein's functional dynamics (Plate 9.15).

9.3.6.2.5. 3D and 2D visualization of Regulatory protein RhlR (RhIR) with Cholesta-4,6-dien-3-ol, benzoate, (3.beta)-

The 3D visualization reveals Cholesta-4,6-dien-3-ol, benzoate, (3.beta)- positioned deep within the hydrophobic binding cavity of the Regulatory Protein RhlR, enclosed by a semi-transparent receptor surface that highlights the spatial topology of the active site. The ligand adopts an elongated conformation, enabling extensive surface contact with the surrounding residues. Notably, its rigid steroidal backbone aligns within the non-polar groove, forming a stable fit aided by complementary shape and surface chemistry. The aromatic benzoate moiety projects towards a pocket enriched in hydrophobic and π-interacting residues, promoting close packing and non-covalent stabilization.

The 2D interaction diagram provides a residue-level map of the molecular contacts between the ligand and RhlR. Key interactions observed include:

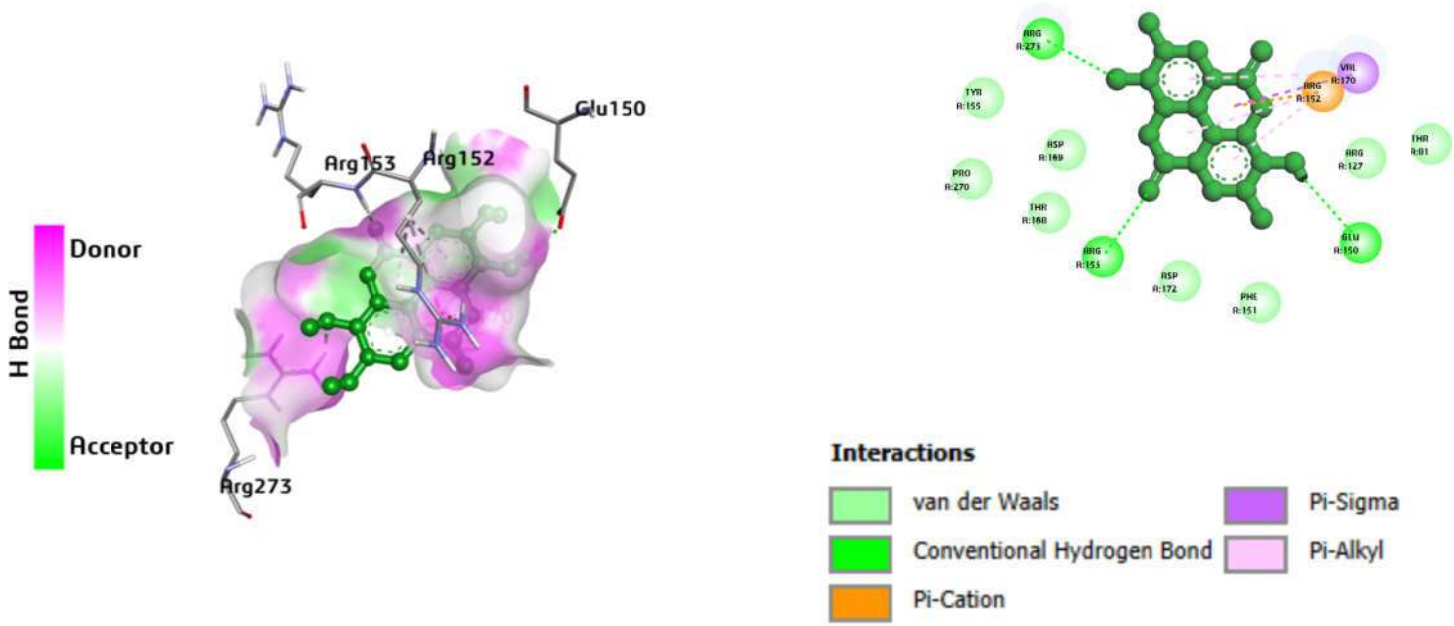
- π–Alkyl Interactions (pink spheres)

Residues such as PHE146, PHE7, ARG2, and LEU153 form multiple π–alkyl contacts with the aromatic core of the ligand, reinforcing ligand anchoring through hydrophobic and dispersive forces.

- Van der Waals Interactions (green spheres)

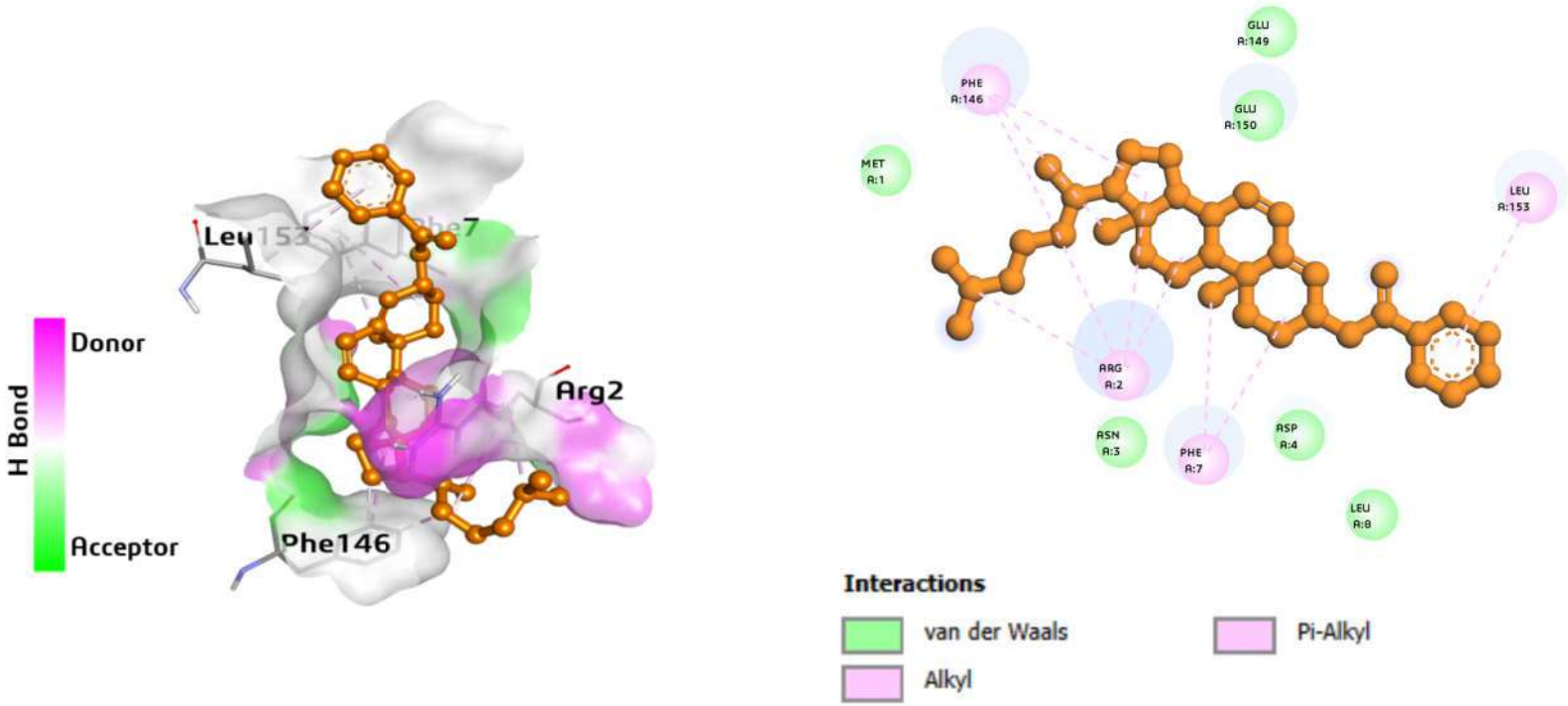
MET1, ASN3, ASP4, LEU8, GLU149, and GLU150 contribute to van der Waals stabilization, subtly shaping the ligand's fit within the active site and enhancing overall pocket complementarity.

This interaction network emphasizes the role of hydrophobic and aromatic stabilization in securing Cholesta-4,6-dien-3-ol, benzoate, (3β)- within the RhlR binding site. The ligand's structural rigidity, coupled with a favorable spatial



(a) (b)

Plate 9.15: Visualization of binding interactions betweenPenicillin-Binding Protein 3 (PBP3) and Ellagic acid, showing (a) the three-dimensional (3D) molecular surface and (b) the two-dimensional (2D) interaction diagram



(a) (b)

Plate 9.16: Visualization of binding interactions betweenRegulatory protein RhlR (RhIR) and Cholesta-4,6-dien-3-ol, benzoate, (3.beta)-, showing (a) the three-dimensional (3D) molecular surface and (b) the two-dimensional (2D) interaction diagram

arrangement of π–alkyl and van der Waals contacts, indicates a strong potential for modulating the protein's regulatory functions (Plate 9.16).

9.3.6.3. Visualization of anthelmintic proteins

Among 29 phytochemicals docked from methanol leaf extracts of *S. palghatense*, Oleanolic acid showed strong binding with ATP synthase subunit a (ATP synthase), Cytochrome c oxidase subunit 1 (COX1), and Heat Shock Protein 70 (HSP70). Maslinic acid displayed significant affinity for NADH-Ubiquinone Oxidoreductase chain 1 (Complex I). Vitamin E interacted notably with Extracellular Globin-3/Erythrocruorin (Ext. Globin-3).

9.3.6.3.1. 3D and 2D visualization of ATP synthase subunit a (ATP synthase) with Oleanolic acid

The 3D visualization depicts Oleanolic acid securely accommodated within the binding cavity of ATP Synthase subunit a, represented by a semi-transparent molecular surface highlighting the receptor topology. The ligand aligns deeply along the hydrophobic groove, establishing multiple stabilizing contacts with both polar and non-polar residues. Notably, the binding pose positions the ligand adjacent to key residues such as TYR92, HIS94, and LEU15, facilitating a snug fit and favourable orientation for interaction within the enzymatic site.

The 2D interaction diagram offers an atomic-level breakdown of the binding profile between Oleanolic Acid and ATP Synthase. The following interaction types were observed:

- π–Alkyl Interactions (pink highlight)

TYR92 and HIS94 form π–alkyl contacts with the ligand's hydrophobic ring systems, reinforcing aromatic packing and contributing to shape complementarity.

Additional alkyl contacts are established with residues such as ILE257, ILE261, and ALA19, enhancing the ligand's hydrophobic stabilization within the pocket.

- Van der Waals Interactions (green highlight)

Residues including LEU15, SER12, TRP89, LEU232, LEU236, and THR260 contribute van der Waals forces that fine-tune the ligand's spatial accommodation, subtly shaping the local microenvironment for optimal fit.

This interaction profile indicates that Oleanolic Acid is predominantly stabilized through non-polar forces, with π–alkyl interactions playing a major role in ligand retention. The deep hydrophobic embedding suggests that ligand modifications introducing additional polar moieties could further enhance specific anchoring and binding affinity to ATP Synthase subunit a (Plate 9.17).

9.3.6.3.2. 3D and 2D visualization of Cytochrome c Oxidase subunit 1 (COX1) with Oleanolic acid

The 3D visualization shows Oleanolic acid deeply accommodated within the hydrophobic pocket of Cytochrome c Oxidase, represented by a semi-transparent molecular surface that outlines the topology of the binding site. The ligand's triterpenoid scaffold aligns closely with multiple non-polar residues, optimizing surface complementarity. Key interactions occur with residues such as TRP110, PHE51, and LEU186, which help stabilize the ligand's position within the cavity through hydrophobic packing and aromatic–aliphatic interactions.

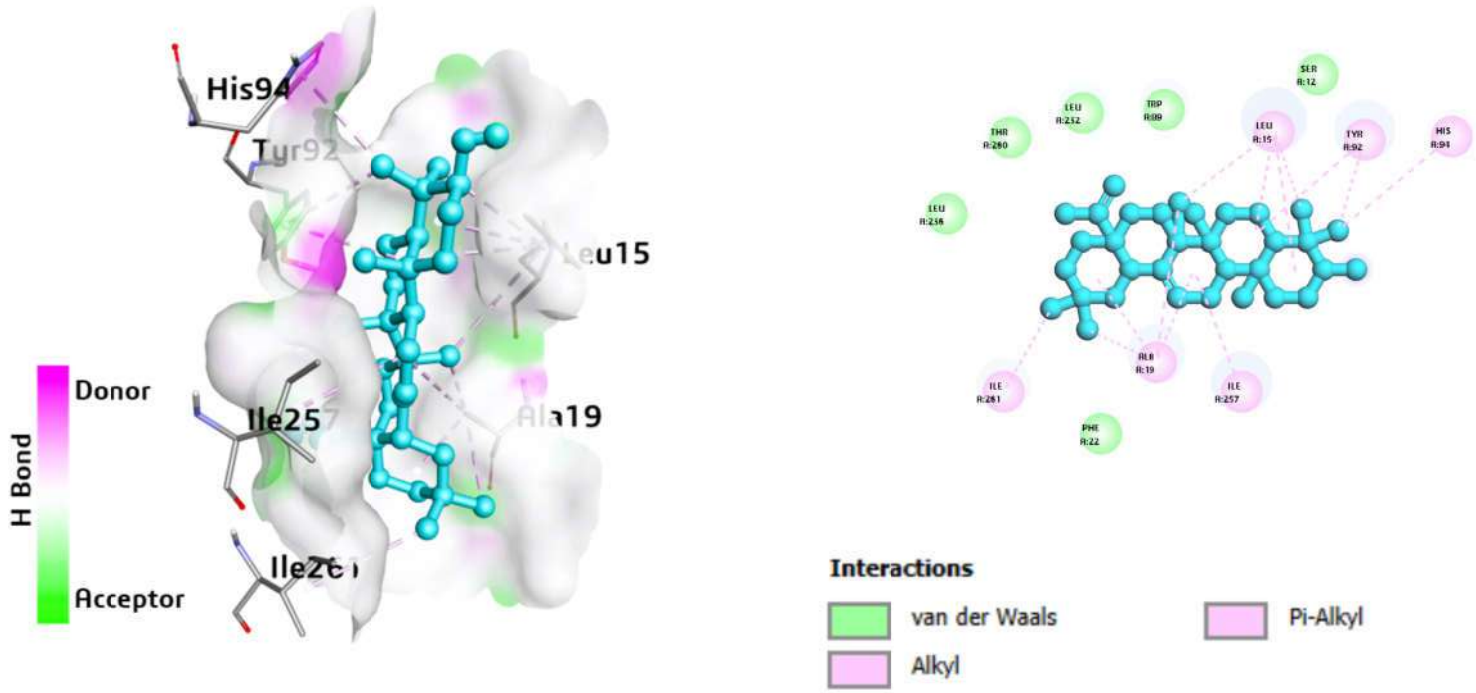
The 2D interaction diagram highlights the following binding interactions:

- π–Alkyl Interactions (light pink)

TRP110, LEU186, PHE51, and LEU193 engage in π–alkyl contacts with the hydrophobic rings of Oleanolic Acid, enhancing non-polar stabilization.

- Alkyl Interactions (lavender)

PRO114 and ALA189 form alkyl contacts, further reinforcing the hydrophobic anchoring of the ligand inside the active site.



(a) (b)

Plate 9.17: Visualization of binding interactions betweenATP synthase subunit a (ATP synthase) and Oleanolic acid, showing (a) the three-dimensional (3D) molecular surface and (b) the two-dimensional (2D) interaction diagram

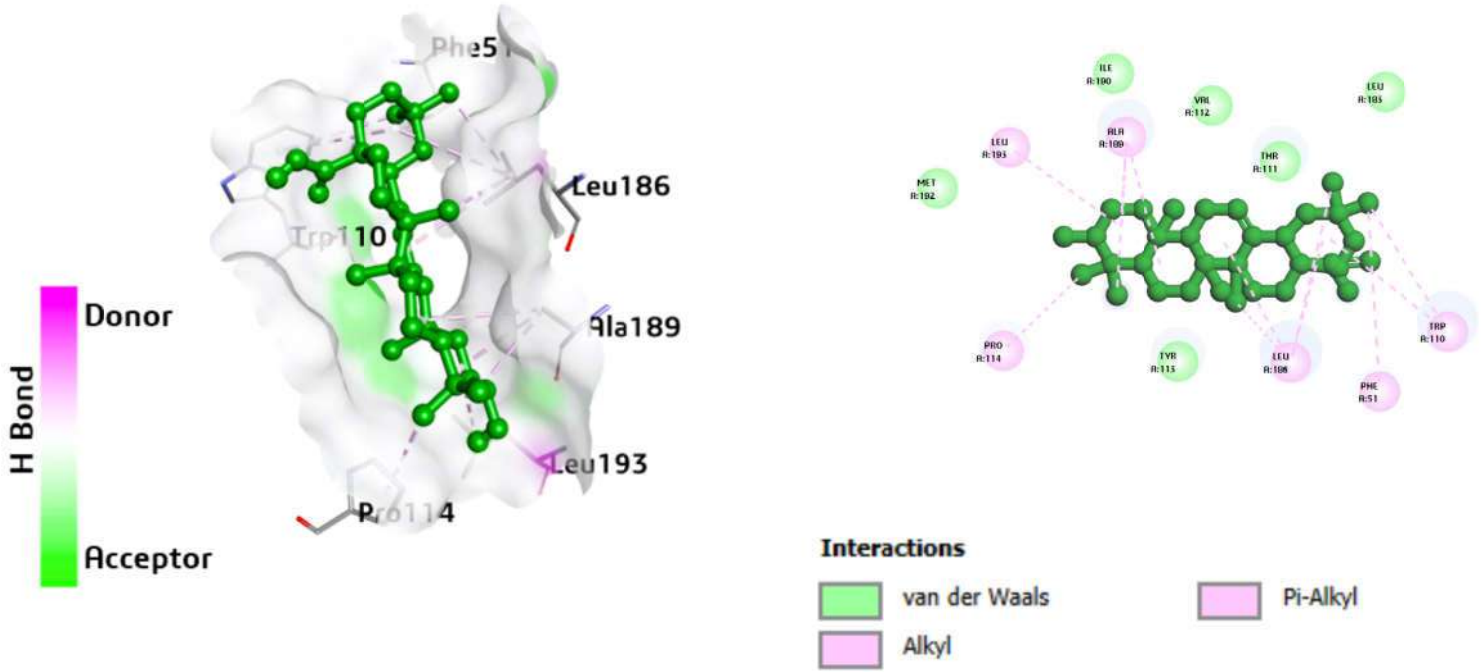


Plate 9.18: Visualization of binding interactions betweenCytochrome c Oxidase subunit 1 (COX1) and Oleanolic acid, showing (a) the three-dimensional (3D) molecular surface and (b) the two-dimensional (2D) interaction diagram

- Van der Waals Interactions (light green)

Residues such as ILE190, VAL112, TYR113, and MET192 provide van der Waals support, ensuring the ligand is securely fitted into the pocket and maintaining favourable molecular orientation.

The interaction profile indicates that Oleanolic Acid is predominantly stabilized by hydrophobic and van der Waals forces within Cytochrome c Oxidase. Its strong fit within the non-polar cavity suggests high binding stability, though the absence of polar interactions means that incorporating hydrogen-bonding groups could potentially enhance specificity and modulate the ligand's functional activity (Plate 9.18).

9.3.6.3.3. 3D and 2D visualization of Heat Shock Protein 70 (HSP70) with Oleanolic acid

The 3D visualization depicts Oleanolic Acid tightly accommodated within the active pocket of the Heat Shock Protein 70 (HSP70), surrounded by a semi-transparent surface representing the receptor topology. The ligand is positioned in a hydrophobic groove, adopting a conformation that maximizes contact with the protein environment. Notably, Oleanolic Acid is oriented to interact with key residues such as PHE16, PHE51, LEU12, and ILE13, facilitating a favorable and stable binding conformation within the cleft.

The 2D interaction diagram provides a detailed mapping of the molecular interactions between Oleanolic Acid and the active site residues of HSP70. The following interaction types were observed:

- Conventional Hydrogen Bonds (green arrows)

PHE16 forms a hydrogen bond, helping stabilize the ligand through polar complementarity.

- π–Sigma Interactions (purple arcs)

PHE1 and PHE51 engage in π–sigma interactions with the ligand's aromatic system, contributing to the hydrophobic packing and improving binding stability.

- π–Alkyl Interactions (pink arcs)

LEU12 and ILE13 interact with the aromatic rings via π–alkyl contacts, enhancing hydrophobic association between the ligand and the protein pocket.

- Van der Waals Interactions (light green spheres)

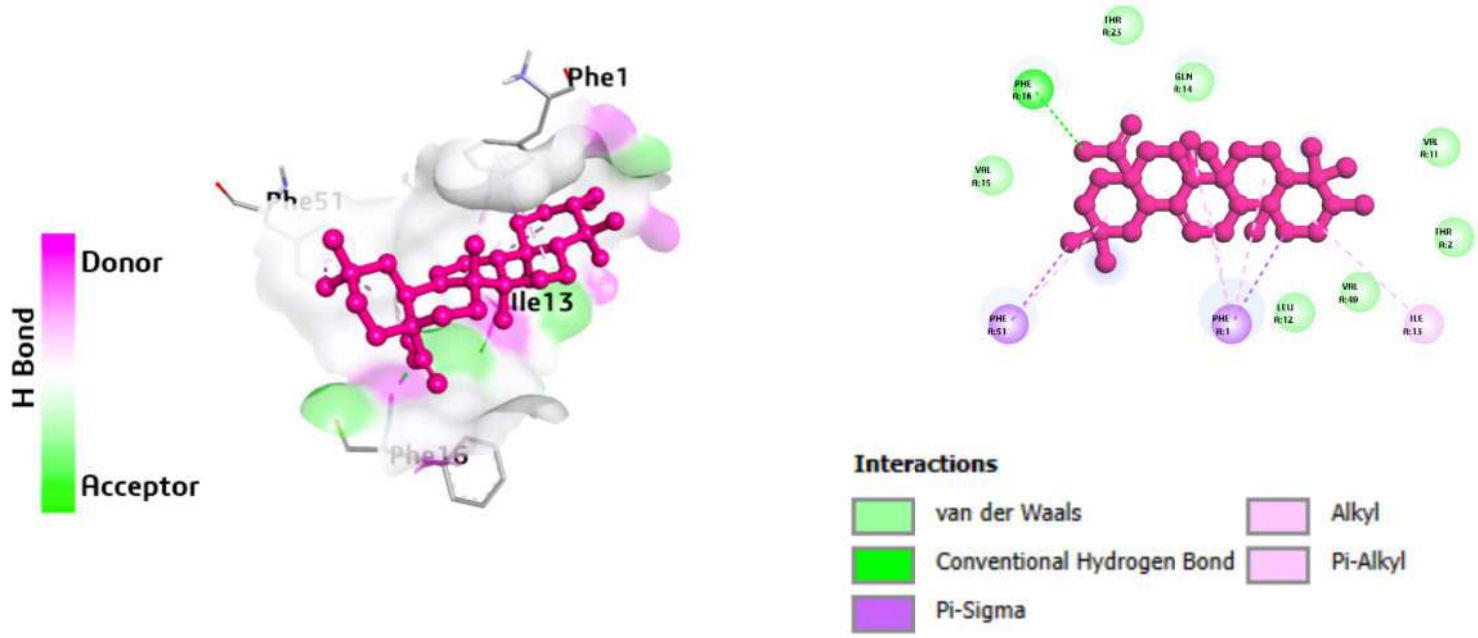
Multiple residues, including GLN14, VAL11, VAL15, THR2, THR23, and VAL49, provide van der Waals contacts, shaping the binding environment and supporting ligand accommodation.

The interaction network demonstrates that Oleanolic acid is stabilized primarily through a combination of hydrophobic interactions (π–alkyl, π–sigma, van der Waals) and specific hydrogen bonding. This balance of non-covalent forces positions the ligand effectively within the HSP70 binding pocket, suggesting potential for modulating the protein's activity through hydrophobic and aromatic complementarity (Plate 9.19).

9.3.6.3.4. 3D and 2D visualization of NADH-Ubiquinone Oxidoreductase chain 1 (Complex I) with Maslinic acid

The 3D visualization depicts Maslinic acid securely accommodated within the active site of the NADH-Ubiquinone Oxidoreductase protein, surrounded by a semi-transparent surface that maps the receptor topology. The ligand aligns snugly within the binding pocket, stabilized by a network of hydrophobic and polar interactions with both catalytic and peripheral residues. Positioned adjacent to critical residues such as ILE92, SER176, and PRO93, Maslinic Acid adopts a favourable binding conformation that complements the geometry of the enzymatic cleft.

The 2D interaction diagram offers a detailed breakdown of atomic-level contacts between Maslinic acid and the active site residues of NADH-Ubiquinone Oxidoreductase. The following interaction types were observed:



(a) **(b)**

Plate 9.19: Visualization of binding interactions betweenHeat Shock Protein 70 (HSP70) and Oleanolic acid, showing (a) the three-dimensional (3D) molecular surface and (b) the two-dimensional (2D) interaction diagram

- Conventional Hydrogen Bonds (green arrows)

ILE92 forms a classical hydrogen bond with the ligand, anchoring it within the pocket and enhancing polar complementarity.

- Pi–Alkyl Interactions (pink lines)

PHE14, TYR94, PRO93, and CYS182 engage in Pi–Alkyl interactions with the aromatic core of Maslinic acid, stabilizing the ligand through hydrophobic contacts.

- Van der Waals Interactions (light green spheres)

Multiple residues, including MET95, LEU91, GLY179, SER176, and LEU175, contribute to van der Waals interactions, which fine-tune the ligand's spatial fit within the binding cavity.

This interaction profile highlights that Maslinic acid is well-stabilized within NADH-Ubiquinone Oxidoreductase through a combination of hydrogen bonding, hydrophobic interactions, and shape complementarity, suggesting a strong potential for modulating the protein's activity (Plate 9.20).

9.3.6.3.5. 3D and 2D visualization of Extracellular Globin-3/Erythrocruorin (Ext. Globin-3) with Vitamin E

The 3D visualization depicts Vitamin E tightly accommodated within the active pocket of the Extracellular Globin-3/Erythrocruorin protein, surrounded by a semi- transparent surface representing the receptor topology. The ligand fits snugly within the hydrophobic groove, stabilized by a network of non-covalent interactions with both hydrophobic and charged residues. Notably, Vitamin E positions itself in proximity to key residues such as ARG75, ARG90, and PHE130, allowing a favourable binding conformation and optimal van der Waals contacts within the binding cleft.

The 2D interaction diagram provides a detailed overview of the atomic-level interactions between Vitamin E and the active site residues of Extracellular Globin-3/Erythrocruorin. The following interaction types were observed:

- Pi-Cation Interactions (orange lines)

ARG75 and ARG122 engage in π–cation interactions with the aromatic moieties of Vitamin E, enhancing electrostatic stabilization within the binding pocket.

- Pi-Sigma Interactions (purple lines)

PHE130, PHE133, and HIS87 form π–sigma interactions with the aromatic rings of the ligand, contributing to spatial complementarity and aromatic stabilization.

- Pi–Pi Stacked Interactions (pink lines)

Multiple aromatic residues, including PHE171 and HIS119, engage in π–π stacking with Vitamin E's aromatic systems, strengthening hydrophobic packing.

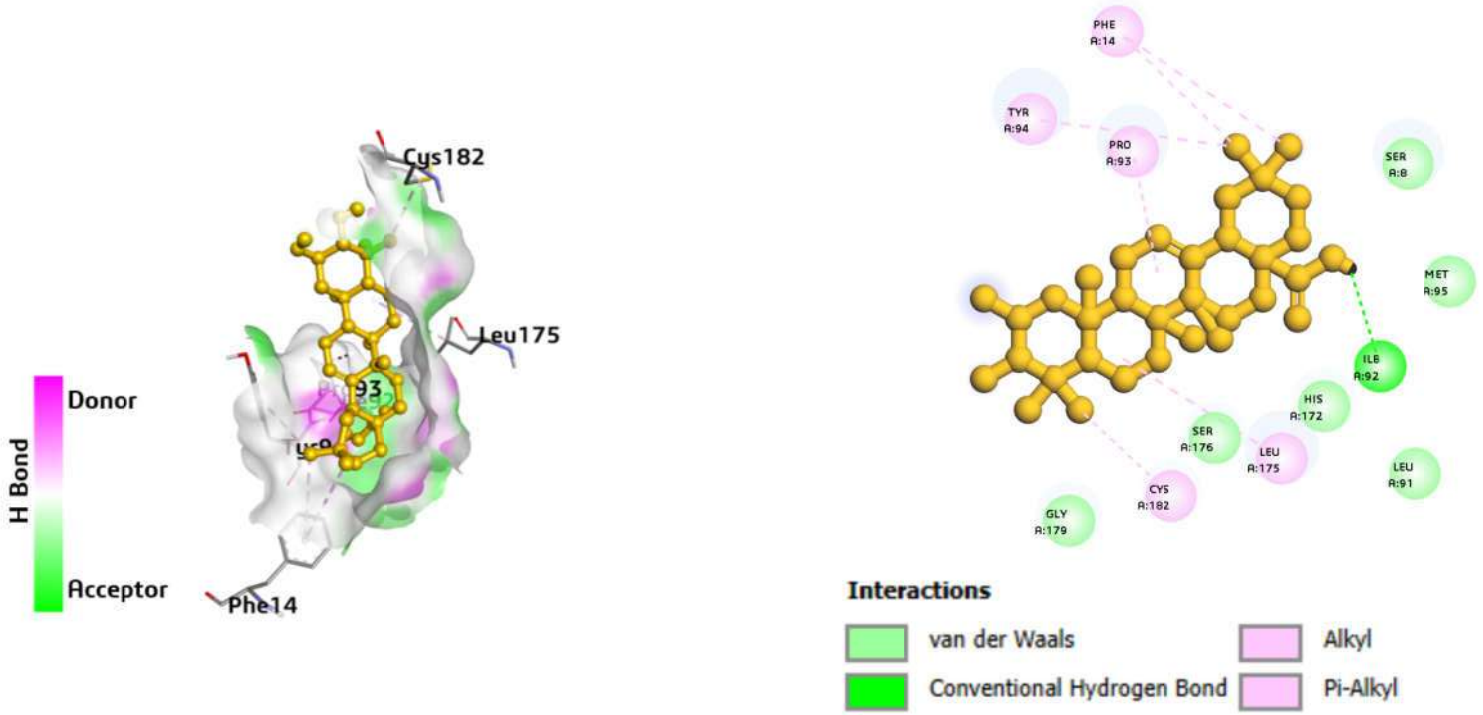
- Pi-Alkyl Interactions (light pink lines)

Residues such as LEU123, LEU125, and VAL74 participate in π–alkyl contacts, further increasing hydrophobic stabilization within the ligand-binding region.

- Van der Waals Interactions (light green spheres)

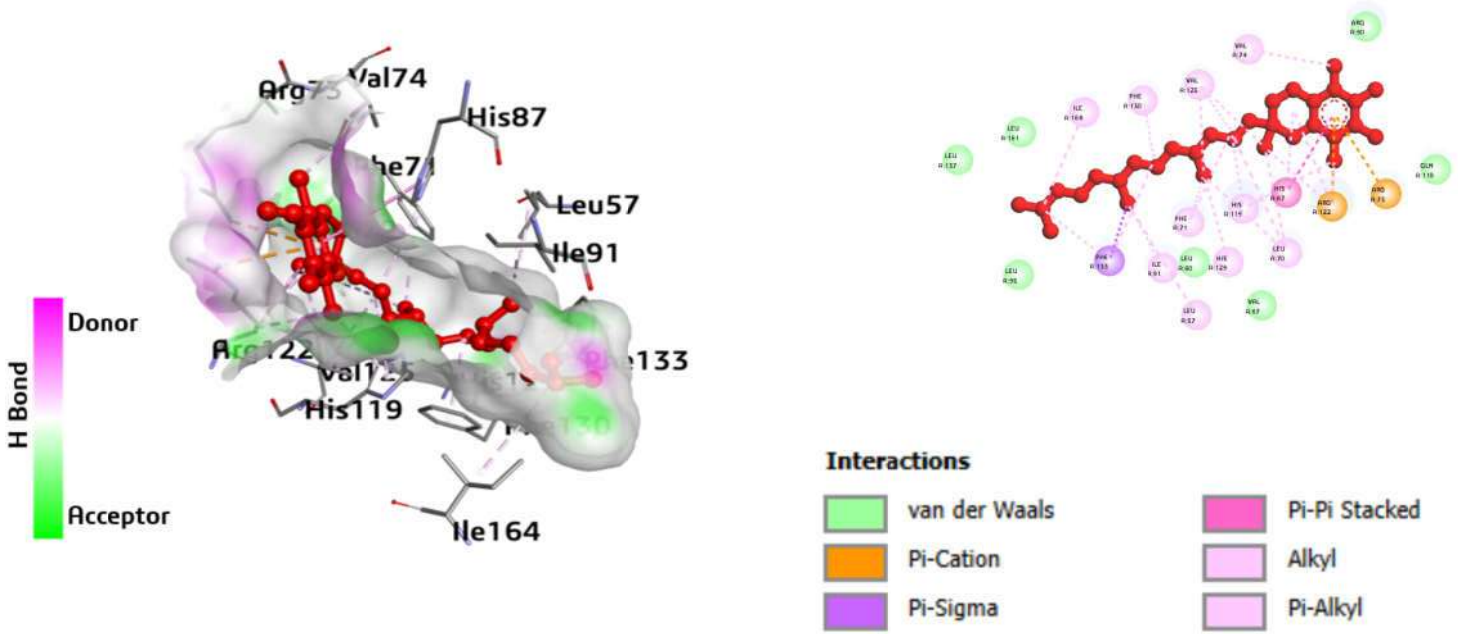
Several residues, including LEU85, LEU137, and GLN118, form van der Waals interactions with Vitamin E, subtly shaping the microenvironment to accommodate the ligand.

The binding profile indicates that Vitamin E is well-stabilized in the Extracellular Globin-3/Erythrocruorin active site through a combination of hydrophobic packing, aromatic stacking, and electrostatic π–cation contacts. These interactions collectively provide a robust and stable ligand-binding conformation, which could play a role in modulating the protein's function (Plate 9.21).



(a) (b)

Plate 9.20: Visualization of binding interactions betweenNADH-Ubiquinone Oxidoreductase chain 1 (Complex I) and Maslinic acid, showing (a) the three-dimensional (3D) molecular surface and (b) the two-dimensional (2D) interaction diagram



(a) (b)

Plate 9.21: Visualization of binding interactions between Extracellular Globin-3/Erythrocruorin (Ext. Globin-3) and Vitamin E, showing (a) the three-dimensional (3D)molecular surface and (b) the two-dimensional (2D) interaction diagram

9.3.6.4. Visualization of anti-inflammatory proteins

Among 37 phytochemicals docked from *S. palghatense* bark methanol extracts, Maslinic acid showed strong binding affinity with Nuclear Factor kappa B p50 (NF-κB p50). D:B-Friedo-B'A'-Neogammacer-5-en-3-one exhibited notable interaction with Tumor Necrosis Factor-alpha (TNF-α). Cholesta-4,6-dien-3-ol, benzoate, (3.beta.)- displayed effective binding with Human Inducible Nitric Oxide Synthase (iNOS) as well as with Human Cyclooxygenase-2 (COX-2). Ellagic acid demonstrated significant affinity for Janus Kinase 2 (JAK2).

9.3.6.4.1. 3D and 2D visualization of Nuclear Factor kappa B p50 (NF-κB p50) with Maslinic acid

The 3D visualization shows Maslinic acid tightly positioned within the binding cavity of the NF-κB p50 protein, enclosed by a semi-transparent molecular surface that highlights the receptor's topology. The ligand is oriented to maximize contact with the hydrophobic and polar regions of the active site, with notable proximity to key residues such as LYS79, LYS80, and PRO71. This spatial arrangement facilitates a stable binding conformation, supported by a combination of polar interactions and hydrophobic contacts within the binding groove.

The 2D interaction diagram reveals the specific atomic-level interactions formed between Maslinic Acid and NF-κB p50:

- Conventional Hydrogen Bonds (green arrows)

LYS79 forms a hydrogen bond with the ligand, enhancing polar stabilization within the binding pocket.

- Alkyl Interactions (pink arcs)

LYS52 and PRO71 engage in alkyl contacts with hydrophobic portions of the ligand, contributing to van der Waals stabilization.

- Van der Waals Interactions (light green spheres)

Multiple residues, including SER74, SER75, GLY72, GLY68, PHE56, ARG57, and HIS67, form van der Waals contacts that reinforce the ligand's snug fit.

The overall interaction profile indicates that Maslinic Acid achieves a well-balanced combination of hydrogen bonding, hydrophobic, and van der Waals forces, supporting its potential as a modulator of NF-κB p50 activity (Plate 9.22).

9.3.6.4.2. 3D and 2D visualization of Tumour Necrosis Factor-alpha (TNF-α) with DB-Friedo-B'A'-Neogammacer-5-en-3-one

The 3D visualization depicts DB-Friedo-B'A'-Neogammacer-5-en-3-one lodged within the binding cavity of TNF-α (2AZ5), enclosed by a semi-transparent molecular surface outlining the receptor topology. The ligand adopts an elongated orientation that allows optimal contact with the hydrophobic groove, engaging key residues such as TYR59, TYR151, and TYR119. These interactions promote a stable binding mode through a combination of aromatic stacking and hydrophobic complementarity.

The 2D interaction diagram details the molecular contacts:

- Pi-Sigma Interactions (purple arcs)

TYR59 participates in π–sigma interactions, providing additional stabilization via aromatic-electron overlap.

- Pi-Alkyl Interactions (pink arcs)

TYR59 also engages in π–alkyl contacts with non-polar regions of the ligand, reinforcing hydrophobic packing.

Van der Waals Interactions (light green spheres)

Residues such as GLY121, TYR119, LEU120, SER60, TYR151, ILE155, and HIS15 contribute to van der Waals forces, fine-tuning the ligand's spatial fit within the pocket.

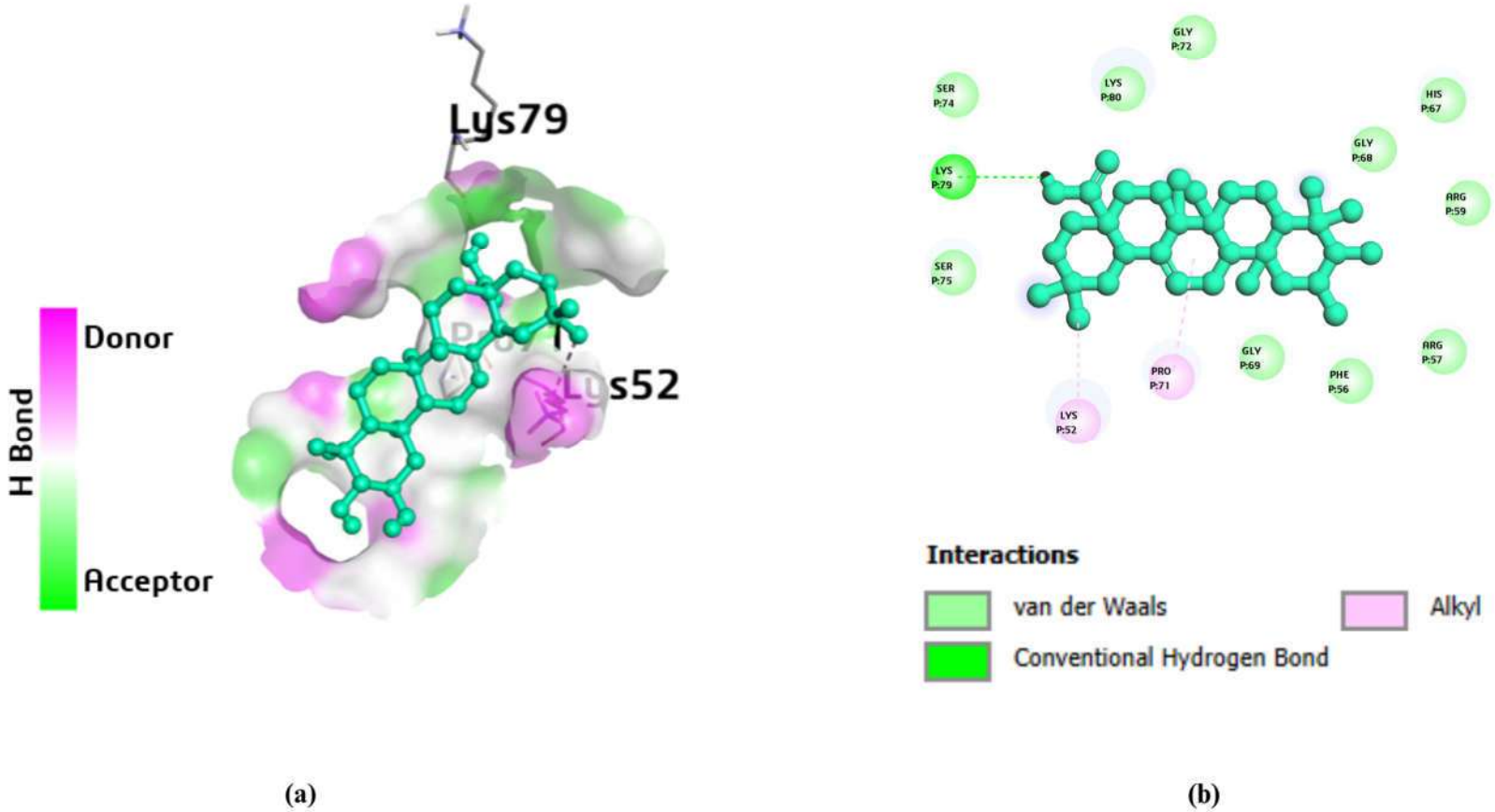


Plate 9.22: Visualization of binding interactions betweenNuclear Factor kappa B p50 (NF-κB p50) and Maslinic acid, showing (a) the three-dimensional (3D) molecular surface and (b) the two-dimensional (2D) interaction diagram

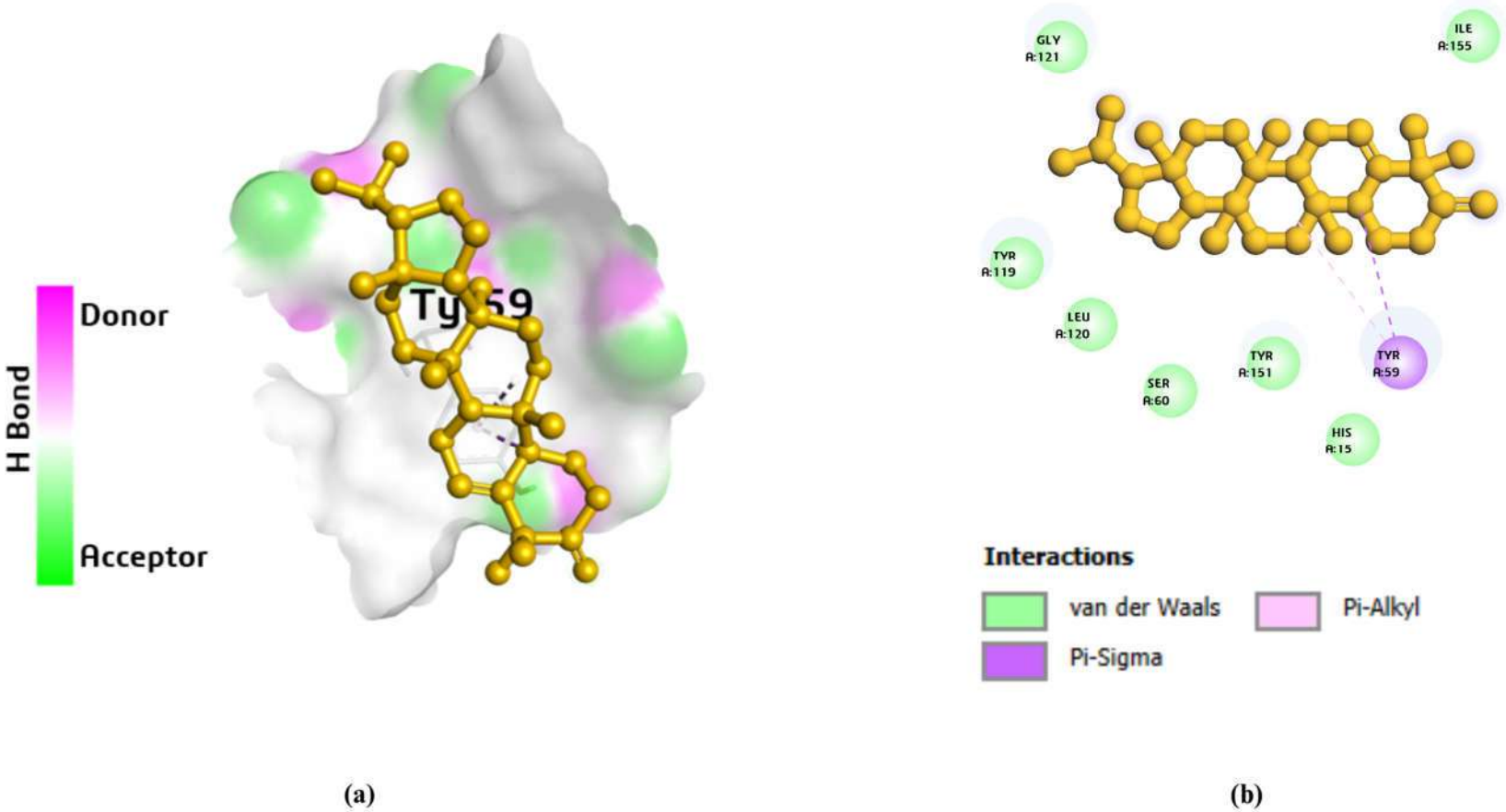


Plate 9.23: Visualization of binding interactions betweenTumour Necrosis Factor-alpha (TNF-α) with DB-Friedo-B'A'-Neogammacer-5-en-3-one, showing (a) the three-dimensional (3D) molecular surface and (b) the two-dimensional (2D) interaction diagram

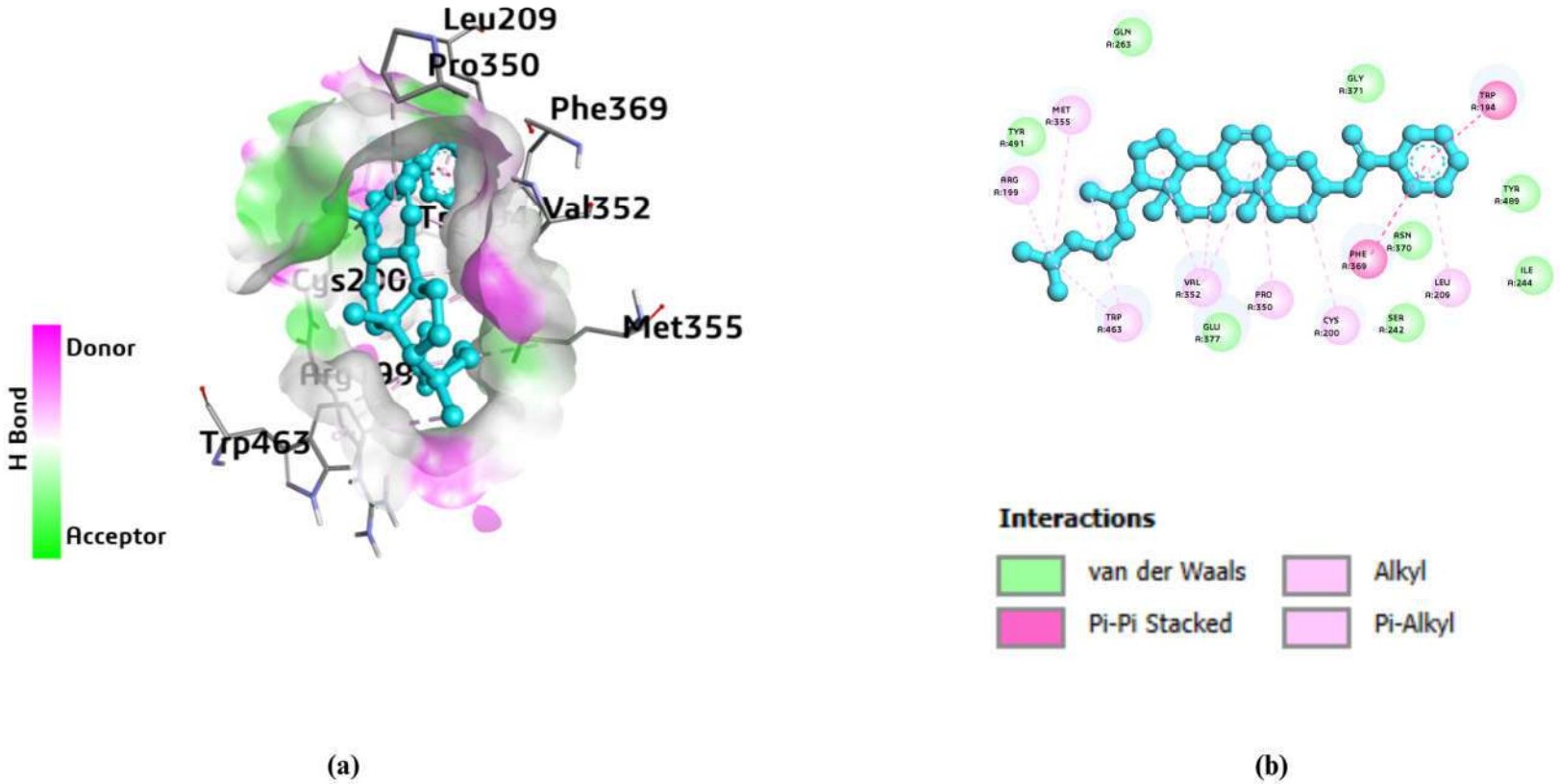


Plate 9.24: Visualization of binding interactions betweenHuman Inducible Nitric Oxide Synthase (iNOS) and Cholesta-4,6-dien-3-ol, benzoate, (3.beta.)-, showing (a) the three-dimensional (3D) molecular surface and (b) the two-dimensional (2D) interaction diagram

This interaction network demonstrates that DB-Friedo-B'A'-Neogammacer-5-en-3-one achieves stable binding with TNF-α through a combination of aromatic interactions and van der Waals stabilization, supporting its potential as an anti-inflammatory agent targeting TNF-α (Plate 9.23).

9.3.6.4.3. 3D and 2D visualization of Human Inducible Nitric Oxide Synthase (iNOS) with Cholesta-4,6-dien-3-ol, benzoate, (3.beta.)-

The 3D visualization shows Cholesta-4,6-dien-3-ol, 3-benzoate, (3beta)-positioned deep within the hydrophobic channel of human inducible nitric oxide synthase (iNOS), surrounded by a semi-transparent molecular surface representing the receptor topology. The ligand aligns longitudinally along the groove, optimizing lipophilic and aromatic contacts, with prominent stabilization provided by residues such as TRP194, MET355, and PHE368. This spatial configuration enables close complementarity between the ligand and the binding site, ensuring strong accommodation and molecular fit.

The 2D interaction diagram reveals the following atomic-level contacts:

- Pi–Pi Stacked Interactions (pink arcs)

TRP194, TRP463, and PHE368 engage in π–π stacking with the ligand's aromatic moieties, reinforcing aromatic stabilization and binding specificity.

- Alkyl and Pi–Alkyl Interactions (light purple arcs)

VAL352, PRO350, LEU209, ILE244, and MET355 form hydrophobic alkyl and π–alkyl contacts, enhancing packing stability within the binding cleft.

- Van der Waals Interactions (light green spheres)

TYR489, TYR491, GLY371, ASN370, GLU377, SER242, and GLN263 contribute to overall stabilization through non-covalent van der Waals forces, supporting optimal orientation of the ligand.

The combined contribution of π–π stacking, hydrophobic, and van der Waals interactions indicates that Cholesta-4,6-dien-3-ol, 3-benzoate, (3beta)- establishes a robust and well-fitted complex with inducible nitric oxide synthase, highlighting its potential as a modulatory scaffold in anti-inflammatory or nitric oxide regulation therapies (Plate 9.24).

9.3.6.4.4. 3D and 2D visualization of Janus Kinase 2 (JAK2) with Ellagic acid

The 3D visualization shows Ellagic acid securely positioned within the binding pocket of Janus Kinase 2 (2B7A), enclosed by a semi-transparent molecular surface that highlights the receptor's structural topology. The ligand orients its aromatic core and polar functional groups to optimize both hydrogen bonding and π-based interactions, with substantial stabilization provided by residues such as LEU855, MET929, and LEU983. This orientation allows Ellagic Acid to align closely with the hydrophobic contour of the active site, ensuring tight binding and spatial complementarity.

The 2D interaction diagram reveals the following atomic-level contacts:

- Conventional Hydrogen Bonds (green arrows)

LEU932 and GLY993 form strong hydrogen bonds with the ligand, enhancing binding specificity and polar stabilization.

- Pi–Sigma Interaction (purple arcs)

VAL863 participates in a π–σ interaction, contributing to electronic stabilization of the aromatic system.

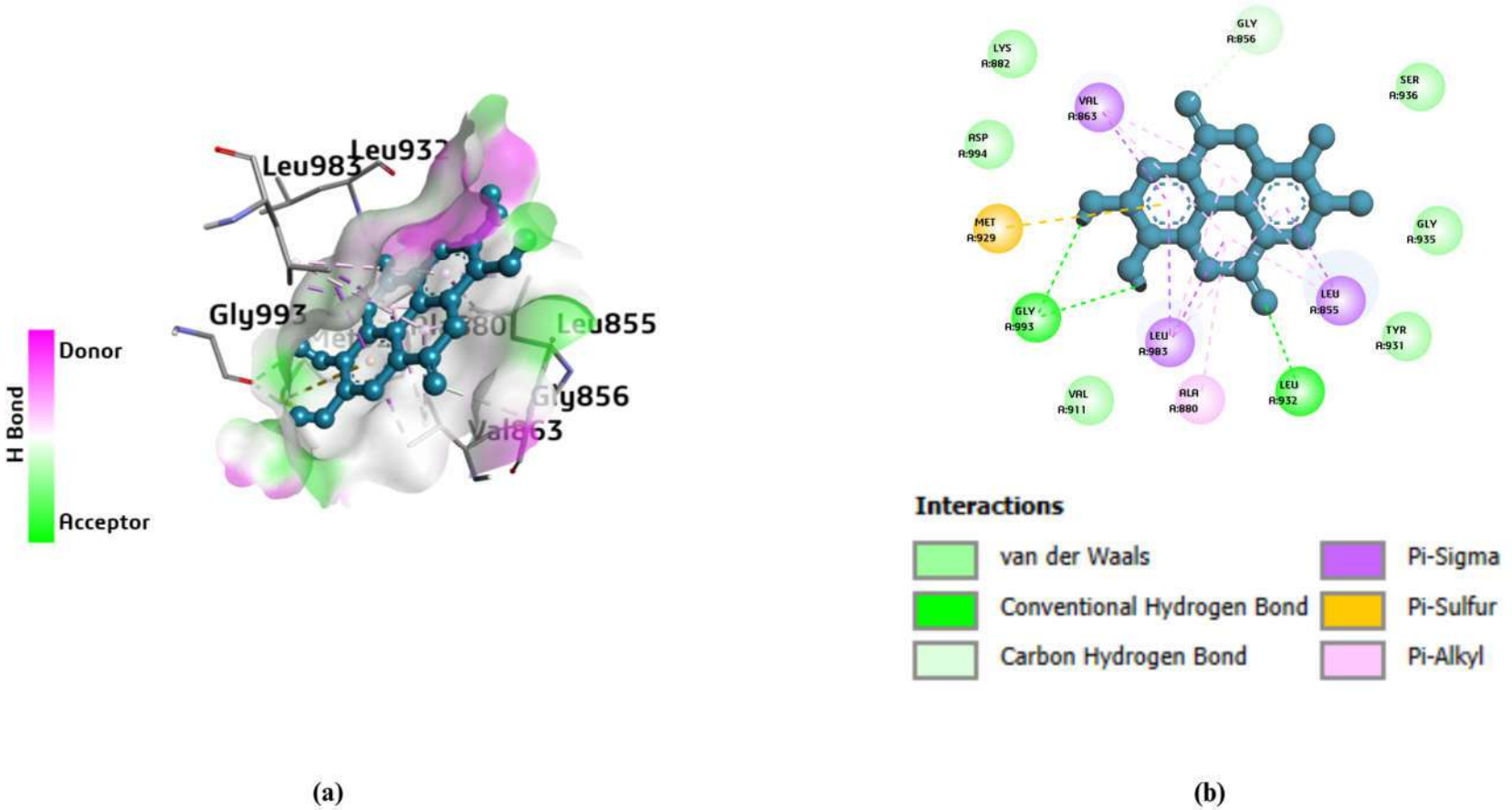
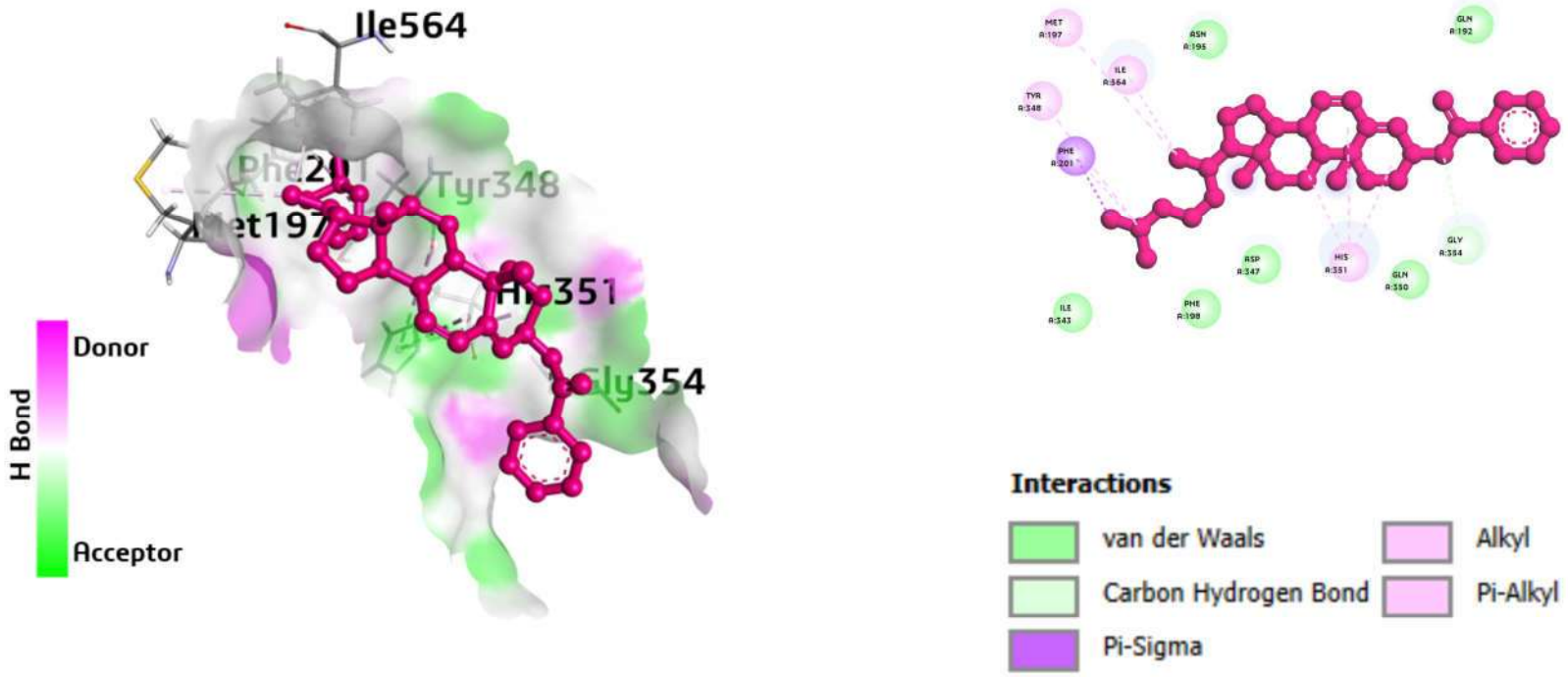


Plate 9.25: Visualization of binding interactions betweenJanus Kinase 2 (JAK2) and Ellagic acid, showing (a) the three-dimensional (3D) molecular surface and (b) the two-dimensional (2D) interaction diagram



(a) (b)

Plate 9.26: Visualization of binding interactions betweenHuman Cyclooxygenase-2 (COX-2) and Cholesta-4,6-dien-3-ol, benzoate, (3.beta.)-, showing (a) the three-dimensional (3D) molecular surface and (b) the two-dimensional (2D) interaction diagram

- Pi–Sulfur Interaction (yellow arcs)

MET929 engages in a π–sulfur contact, reinforcing ligand anchoring within the binding cavity.

- Pi–Alkyl Interactions (pink arcs)

LEU855, LEU983, and ALA880 stabilize the aromatic core via multiple π–alkyl interactions.

- Van der Waals Interactions (light green spheres)

Residues LYS882, ASP994, GLY856, TYR931, SER936, GLY935, and VAL911 provide additional hydrophobic complementarity through van der Waals forces.

The cooperative interplay of hydrogen bonding, π–alkyl, π–σ, π–sulfur, and van der Waals forces indicates that Ellagic Acid forms a stable, well-adapted complex with Janus Kinase 2, supporting its potential as a kinase-targeted therapeutic agent (Plate 9.25).

9.3.6.4.5. 3D and 2D visualization of Human Cyclooxygenase-2 (COX-2) with Cholesta-4,6-dien-3-ol, benzoate, (3.beta.)-

The 3D visualization depicts Cholesta-4,6-dien-3-ol, benzoate, (3.beta.)- securely lodged within the active site of COX-2, enveloped by a semi-transparent molecular surface illustrating the enzyme's binding pocket topology. The ligand's steroidal scaffold is positioned to maximize hydrophobic packing, while the benzoate moiety aligns to facilitate π-based interactions and complementary steric fitting with the catalytic groove. Key residues such as MET197, TYR348, and HIS351 provide stabilizing contacts, anchoring the ligand in an orientation that complements the binding site's hydrophobic and aromatic regions.

The 2D interaction diagram reveals the following molecular contacts:

- Pi–Alkyl Interactions (pink arcs)

MET197, TYR348, and ILE564 engage in π–alkyl interactions, reinforcing hydrophobic stability and maintaining the ligand's rigid orientation within the cavity.

- Pi–Sigma Interaction (purple arc)

PHE201 participates in a π–σ contact with the aromatic portion of the ligand, contributing to electronic stabilization.

- Van der Waals Interactions (light green spheres)

ASN195, GLN192, PHE198, ASP347, ILE343, GLY354, and GLN350 provide extensive van der Waals complementarity, increasing overall binding affinity through distributed non-polar contacts.

- Carbon Hydrogen Bonds (light cyan lines)

HIS351 forms a carbon hydrogen bond, enhancing positional restraint and polar compatibility.

The cooperative effect of π–alkyl, π–σ, hydrogen bonding, and van der Waals forces suggests that Cholesta-4,6-dien-3-ol, benzoate, (3.beta.)- achieves a snug, well-optimized fit within the COX-2 binding site, underscoring its potential as a bioactive modulator of the enzyme (Plate 9.26).

9.3.6.5. Visualization of antidiabetic proteins

From the 37 phytochemicals docked from bark methanol extracts of *S. palghatense*, DB-Friedo-B'A'-Neogammacer-5-en-3-one showed notable binding with Dipeptidyl Peptidase 4 (DPP4), Insulin Receptor Ectodomain (IR), and Peroxisome Proliferator-Activated Receptor Gamma (PPARG). Cholesta-4,6-dien-3-ol, benzoate, (3.beta.)- exhibited strong affinity toward Pancreatic Alpha-Amylase (PAA) and Protein Tyrosine Phosphatase 1B (PTP1B).

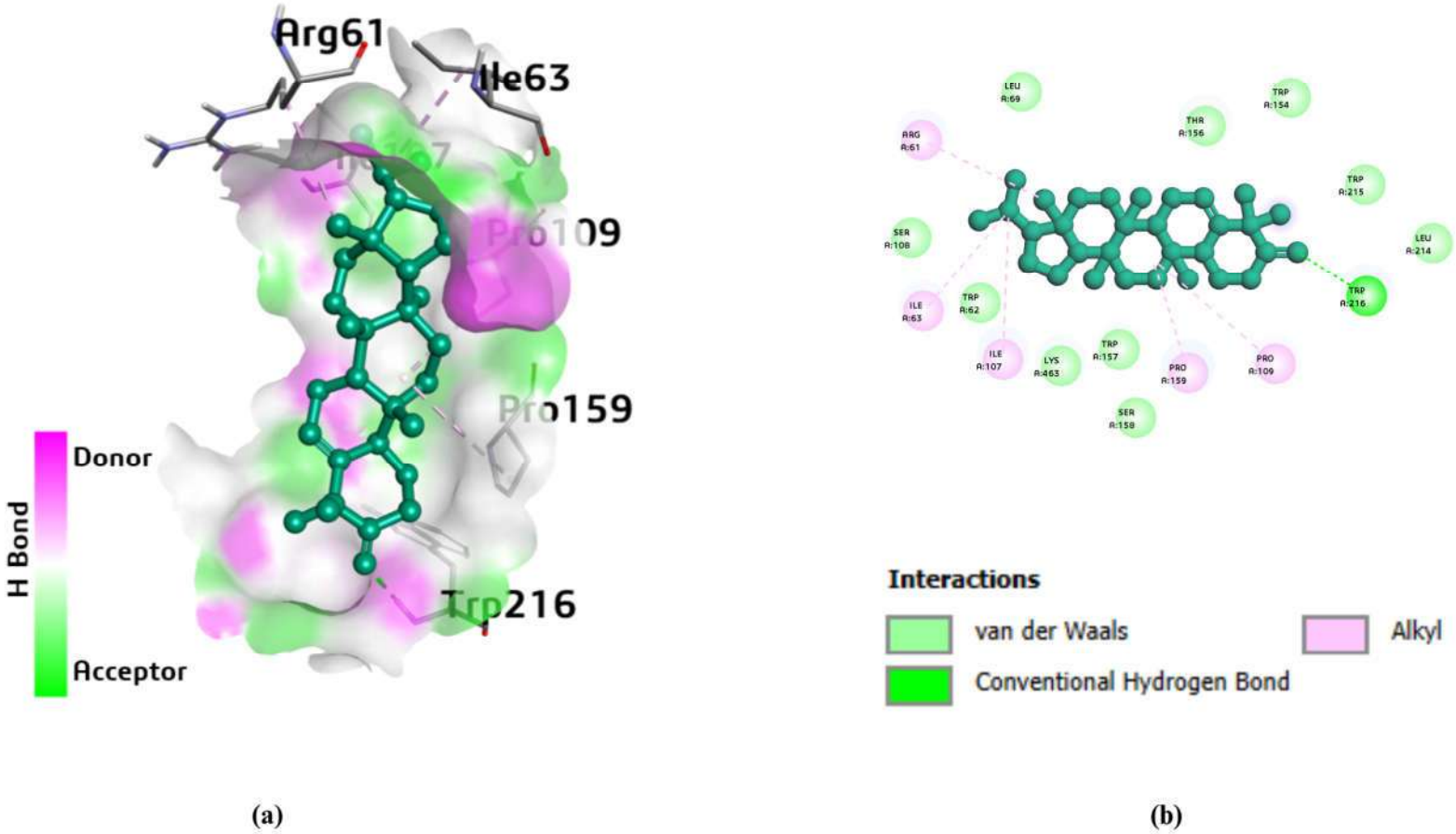


Plate 9.27: Visualization of binding interactions betweenDipeptidyl Peptidase 4 (DPP4) and DB-Friedo-B'A'-Neogammacer-5-en-3-one, showing (a) the three-dimensional (3D) molecular surface and (b) the two-dimensional (2D) interaction diagram

9.3.6.5.1. 3D and 2D Visualization of Dipeptidyl Peptidase 4 (DPP4) with DB-Friedo-B'A'-Neogammacer-5-en-3-one

The 3D visualization reveals DB-Friedo-B'A'-Neogammacer-5-en-3-one deeply embedded within the hydrophobic channel of the Dipeptidyl Peptidase-4 (DPP4) protein, with a significant portion of the ligand surface buried inside the active site pocket. The receptor surface is mapped with colour-coded interaction zones, highlighting a favorable spatial accommodation of the ligand. The elongated and non-polar nature of the ligand enables extensive contact with several nonpolar and aromatic residues, suggesting a strong hydrophobic stabilization mechanism.

The 2D interaction diagram elucidates the various non-covalent interactions contributing to the complex's stability and ligand anchoring within the DPP4 cavity:

- Conventional Hydrogen Bond (green arrows)

TRP216 donates a hydrogen bond to a polar functional group on the ligand, anchoring the terminal region and contributing to directional affinity.

- Alkyl Interactions (light pink lines)

Multiple hydrophobic residues including PRO109, PRO159, and ARG61 engage in alkyl interactions with the saturated steroidal moiety of the ligand. These interactions enhance the lipophilic binding landscape within the pocket.

- Van der Waals Interactions (light green spheres)

Surrounding residues such as ILE63, TRP62, ILE107, SER108, LYS463, TRP157, SER158, LEU69, and TRP215 establish weak, yet cumulative, van der Waals interactions. These contacts help conform the ligand snugly within the binding site and maintain structural complementarity.

The interaction landscape highlights a predominantly hydrophobic and sterically driven accommodation of the ligand, with a single polar anchoring point. This binding profile suggests strong passive retention and favourable binding energy

for DB-Friedo-B'A'-Neogammacer-5-en-3-one within the active site of DPP4 (Plate 9.27).

9.3.6.5.2. 3D and 2D visualization of Insulin Receptor Ectodomain (IR) with DB-Friedo-B'A'-Neogammacer-5-en-3-one

The 3D interaction model of the Insulin Receptor (IR) with DB-Friedo-B'A'-Neogammacer-5-en-3-one reveals that the bulky, non-polar triterpenoid core is stably embedded within a lipophilic groove of the receptor domain. The ligand adopts a linear orientation, allowing maximum surface contact with the surrounding hydrophobic residues. The topography of the binding pocket exhibits a high degree of shape complementarity with the elongated molecular scaffold of the ligand.

The 2D interaction diagram confirms a strong network of stabilizing non-covalent interactions:

- Alkyl Interactions (light pink lines)

Hydrophobic residues such as ILE55, PRO4, and VAL226 engage in alkyl interactions with the triterpenoid rings of the ligand. These contacts dominate the interaction profile and enhance the ligand's retention within the cavity.

- Van der Waals Interactions (light green spheres)

A broad range of residues, including LYS53, PRO52, ASN78, ASN80, ASN108, ASN215, and LEU79, contribute van der Waals forces, supporting the snug fit of the ligand without contributing polar strain.

The absence of hydrogen bonding and polar interactions highlights the hydrophobic character of both the ligand and binding pocket. The stable accommodation of DB-Friedo-B'A'-Neogammacer-5-en-3-one within the IR domain is mediated almost exclusively by van der Waals and alkyl contacts, underlining its potential as a non-polar modulator of insulin receptor activity (Plate 9.28).

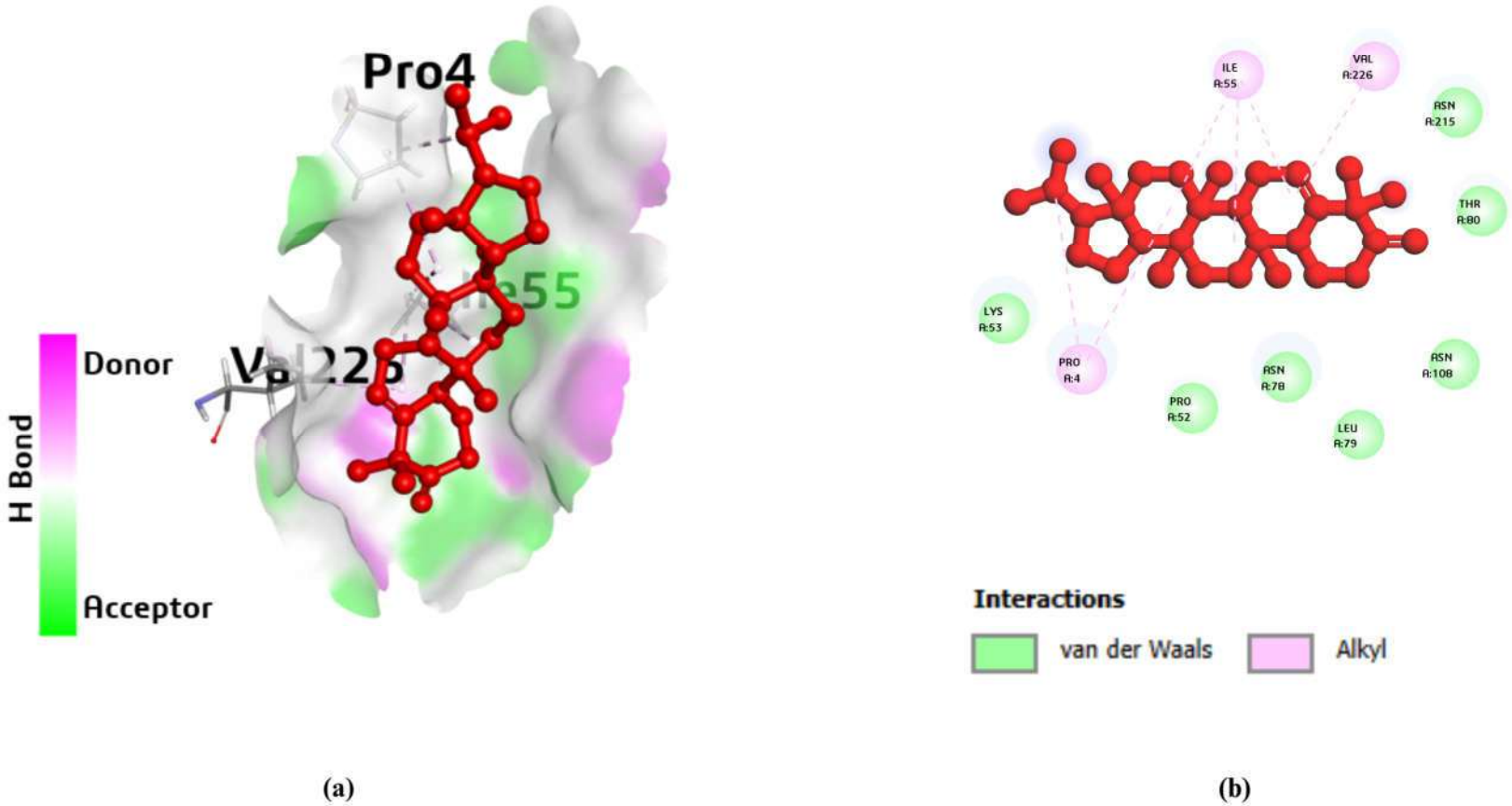


Plate 9.28: Visualization of binding interactions betweenInsulin Receptor Ectodomain (IR) and DB-Friedo-B'A'-Neogammacer-5-en-3-one, showing (a) the three-dimensional (3D) molecular surface and (b) the two-dimensional (2D) interaction diagram

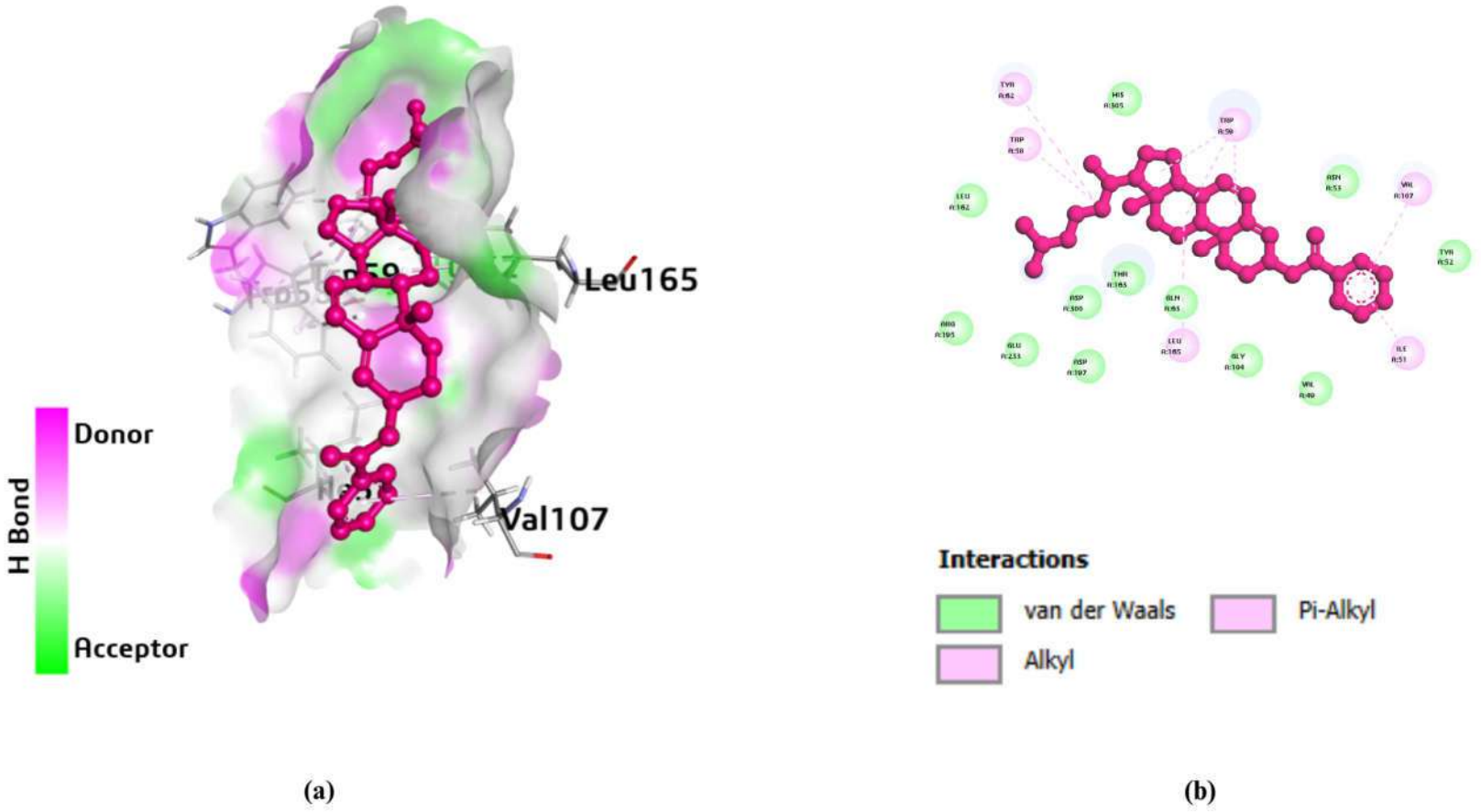


Plate 9.29: Visualization of binding interactions betweenPancreatic Alpha-Amylase (PAA) with Cholesta-4,6-dien-3-ol, benzoate, (3.beta.)-, showing (a) the three-dimensional (3D) molecular surface and (b) the two-dimensional (2D) interaction diagram

9.3.6.5.3. 3D and 2D visualization of Pancreatic Alpha-Amylase (PAA) with Cholesta-4,6-dien-3-ol, benzoate, (3.beta.)-

The 3D surface mapping reveals Cholesta-4,6-dien-3-ol, benzoate, (3β)- tightly enclosed within the catalytic cleft of Pancreatic Alpha-Amylase. The steroidal scaffold is extended vertically through the binding groove, exhibiting strong hydrophobic packing and surface complementarity with key non-polar residues. The benzoate moiety contributes additional interaction potential via π-alkyl contacts, enabling multi-site binding within the pocket.

The 2D interaction diagram provides detailed insights into the ligand's engagement:

- Pi-Alkyl and Alkyl Interactions (pink and violet boxes)

Extensive π-alkyl and alkyl interactions are observed with key hydrophobic residues such as TRP58, TRP59, TYR62, TRP305, LEU165, ILE51, VAL107, GLN63, and TYR52. These interactions dominate the binding mode, stabilizing the compound through hydrophobic anchoring and stacking.

- Van der Waals Interactions (light green spheres)

Complementary van der Waals contacts are provided by ASP197, ASP300, THR163, ASN53, LEU104, ASN78, VAL49, and GLU233. These contacts, while individually weak, contribute collectively to the ligand's snug retention and spatial accommodation.

The interaction landscape confirms that Cholesta-4,6-dien-3-ol, benzoate, (3β)- is stabilized primarily via hydrophobic and aromatic interactions, indicative of strong passive fit within the alpha-amylase catalytic pocket. Its ability to engage multiple residues, including catalytically relevant ones such as TRP59 and HIS305, highlights its potential as a potent inhibitor of carbohydrate metabolism (Plate 9.29).

9.3.6.5.4. 3D and 2D visualization of Peroxisome Proliferator-Activated Receptor Gamma (PPARG) with DB-Friedo-B'A'-Neogammacer-5-en-3-one

The 3D visualization demonstrates that DB-Friedo-B'A'-Neogammacer-5-en-3-one is nestled within the hydrophobic ligand-binding domain of Human PPARG. The planar and extended triterpenoid skeleton aligns along the receptor groove, establishing strong surface complementarity. The spatial conformation reveals efficient hydrophobic encapsulation, favouring a stable ligand accommodation without steric hindrance.

The 2D interaction diagram maps a diverse network of non-covalent interactions:

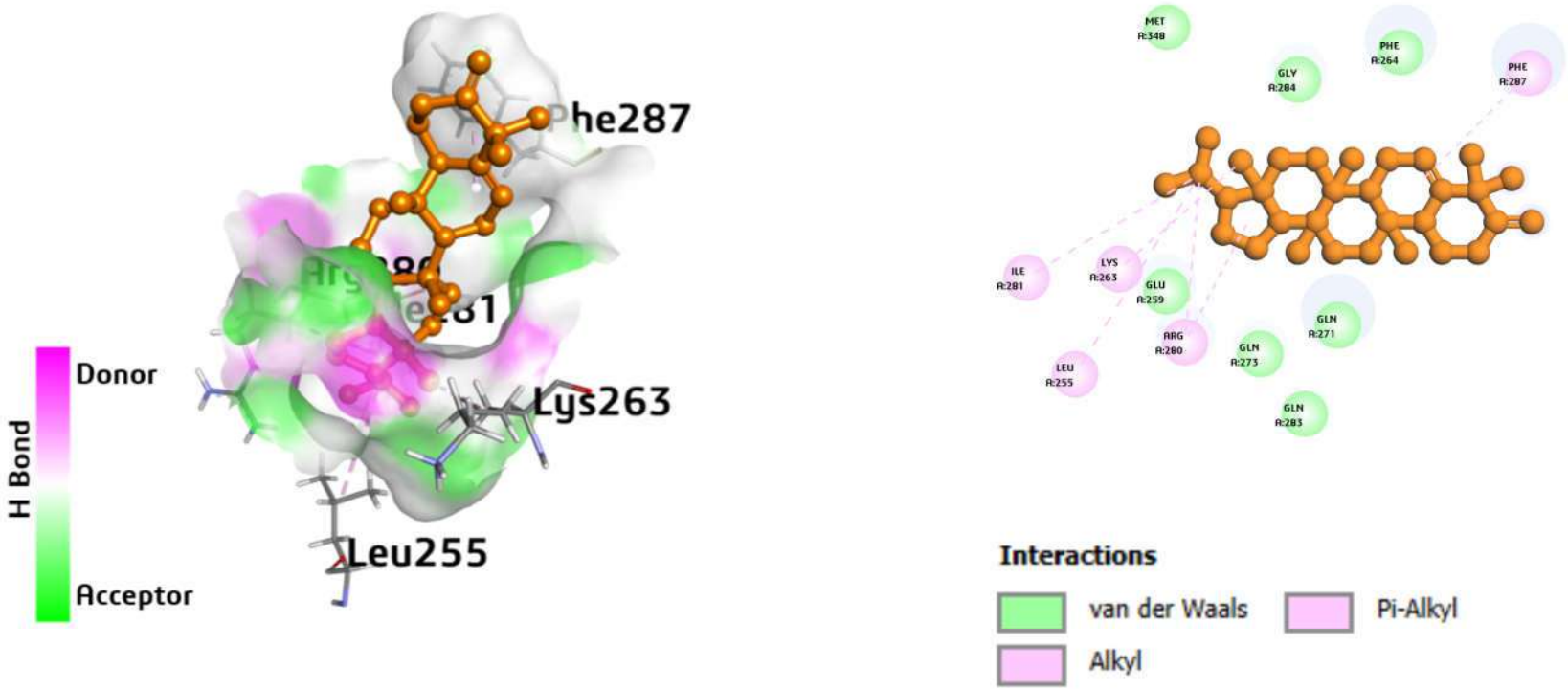
- Pi-Alkyl and Alkyl Interactions (purple and pink lines)

Aromatic and aliphatic residues such as PHE287, ARG280, ILE281, LEU255, and LYS263 engage in π–alkyl and alkyl contacts, effectively stabilizing the rigid triterpenoid core of the ligand within the hydrophobic channel.

- Van der Waals Interactions (light green spheres)

Additional support is provided by GLU259, PHE264, GLY284, GLN271, GLN273, GLN283, and MET348, whose side chains contribute favourable dispersion forces along the ligand surface without forming directional bonds.

This interaction profile highlights that DB-Friedo-B'A'-Neogammacer-5-en-3-one is predominantly stabilized through hydrophobic interactions, particularly π–alkyl and van der Waals contacts. The strategic alignment of the ligand within the non-polar core of the PPARG ligand-binding pocket suggests high affinity and receptor compatibility, supporting its potential as a PPARG modulator (Plate 9.30).



(a) (b)

Plate 9.30: Visualization of binding interactions betweenPeroxisome Proliferator-Activated Receptor Gamma (PPARG) and DB-Friedo-B'A'-Neogammacer-5-en-3-one, showing (a) the three-dimensional (3D) molecular surface and (b) the two-dimensional (2D) interaction diagram

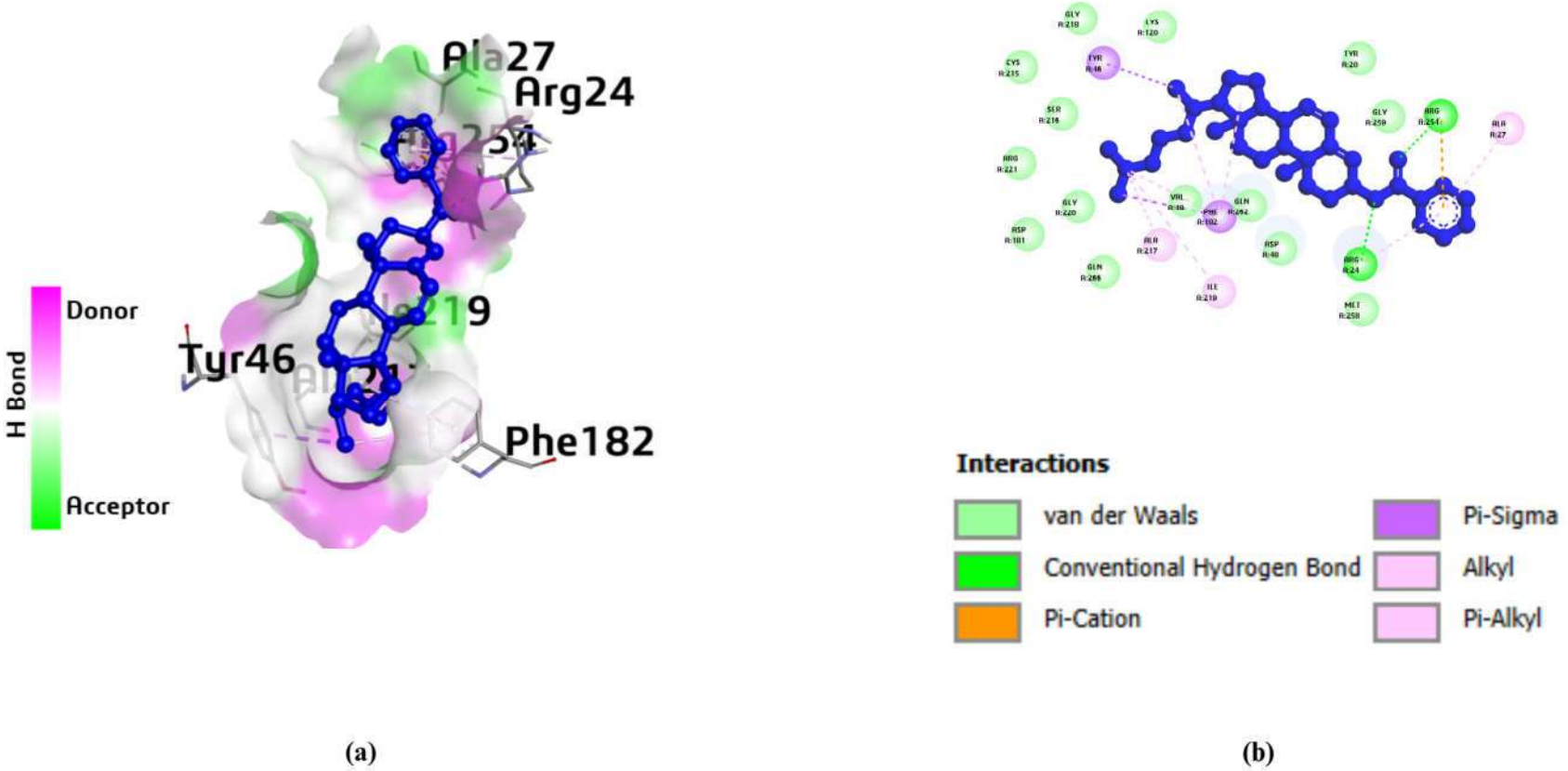


Plate 9.31: Visualization of binding interactions betweenProtein Tyrosine Phosphatase 1B (PTP1B) and Cholesta-4,6-dien-3-ol, benzoate, (3.beta.)-, showing (a) the three-dimensional (3D) molecular surface and (b) the two-dimensional (2D) interaction diagram

9.3.6.5.5. 3D and 2D visualization of Protein Tyrosine Phosphatase 1B (PTP1B) with Cholesta-4,6-dien-3-ol, benzoate, (3.beta.)-

The 3D surface visualization reveals that the ligand Cholesta-4,6-dien-3-ol, benzoate, (3.beta.)- is deeply embedded within a long hydrophobic tunnel of the PTP1B receptor. The ligand's elongated steroidal scaffold aligns along the groove, facilitating extended interaction with multiple non-polar residues. Its rigid fused ring structure complements the receptor's lipophilic cavity, forming a stable hydrophobic fit.

The 2D interaction map details a complex matrix of interactions:

- Pi-Sigma and Pi-Alkyl Interactions (purple and light purple lines)

Residues such as TYR46, ILE219, VAL49, and PHE182 form π–σ and π–alkyl interactions that stabilize the benzoate moiety and the steroidal rings, ensuring tight packing and restricted movement within the active site.

- Alkyl Interactions (pink lines)

Surrounding non-polar residues including ALA217 and ALA27 contribute to additional hydrophobic stabilization of the steroid backbone.

- Pi-Cation and Hydrogen Bonding (orange and green lines)

A pi–cation interaction is observed with ARG254, while ARG24 contributes to a conventional hydrogen bond, further anchoring the ligand at the terminal end.

- Van der Waals Interactions (green spheres)

Widespread van der Waals forces from residues such as GLN262, GLY259, GLY218, MET258, ASP181, and SER216 maintain molecular proximity and complementarity throughout the binding channel.

This interaction landscape demonstrates that Cholesta-4,6-dien-3-ol, benzoate (3β-) is predominantly stabilized by hydrophobic contacts, particularly π–alkyl and alkyl interactions, alongside supportive hydrogen bonding and π–cation effects. These

interactions likely confer significant binding strength and orientation fidelity, reflecting the compound's compatibility with the PTP1B hydrophobic groove (Plate 9.31).

9.3.6.6. Visualization of anticancer proteins

Among the 37 phytochemicals of *S. palghatense* methanol extract of bark docked, Cholesta-4,6-dien-3-ol, benzoate, (3.beta.)- showed strong binding with AKT serine/threonine kinase (AKT1). DB-Friedo-B'A'-Neogammacer-5-en-3-one demonstrated significant affinity toward the Epidermal Growth Factor Receptor (EGFR). Chlorogenic acid displayed notable binding with the Kirsten Rat Sarcoma Viral Oncogene Homolog (KRAS). Ellagic acid bound effectively to Mitogen-Activated Protein Kinase 1 (MAPK1), while Quercetin exhibited strong interactions with Tumour Protein p53 (TP53).

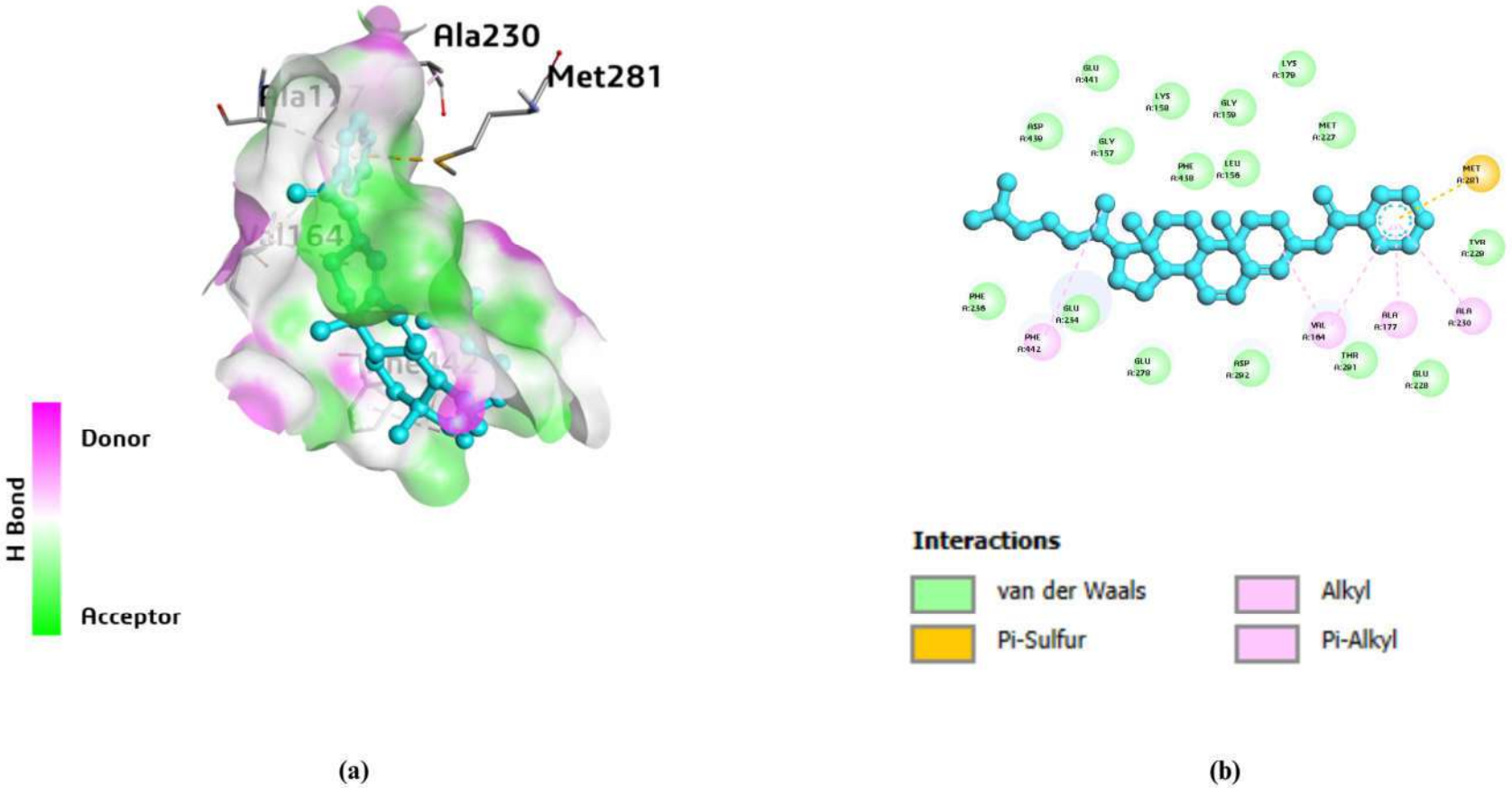
9.3.6.6.1. 3D and 2D visualization of AKT serine/threonine kinase (AKT1) with Cholesta-4,6-dien-3-ol, benzoate, (3.beta.)-

The 3D visualization depicts Cholesta-4,6-dien-3-ol, 3-benzoate, (3β)- embedded within the hydrophobic groove of AKT1, with the surrounding receptor topology rendered as a semi-transparent molecular surface. The ligand orients itself along the contour of the binding cleft, allowing extensive hydrophobic packing and π–alkyl interactions. Key residues such as VAL164, ALA177, and MET281 contribute to anchoring the ligand through close-range hydrophobic and π–sulfur contacts, enhancing its positional stability within the binding cavity.

The 2D interaction diagram details the specific atomic-level contacts:

- Pi–Sulfur Interaction (yellow lines)

MET281 forms a π–sulfur contact with the ligand's aromatic ring, contributing to enhanced non-covalent stabilization.



(a) (b)

Plate 9.32: Visualization of binding interactions betweenAKT serine/threonine kinase (AKT1) and Cholesta-4,6-dien-3-ol, benzoate, (3.beta.)-, showing (a) the three-dimensional (3D) molecular surface and (b) the two-dimensional (2D) interaction diagram

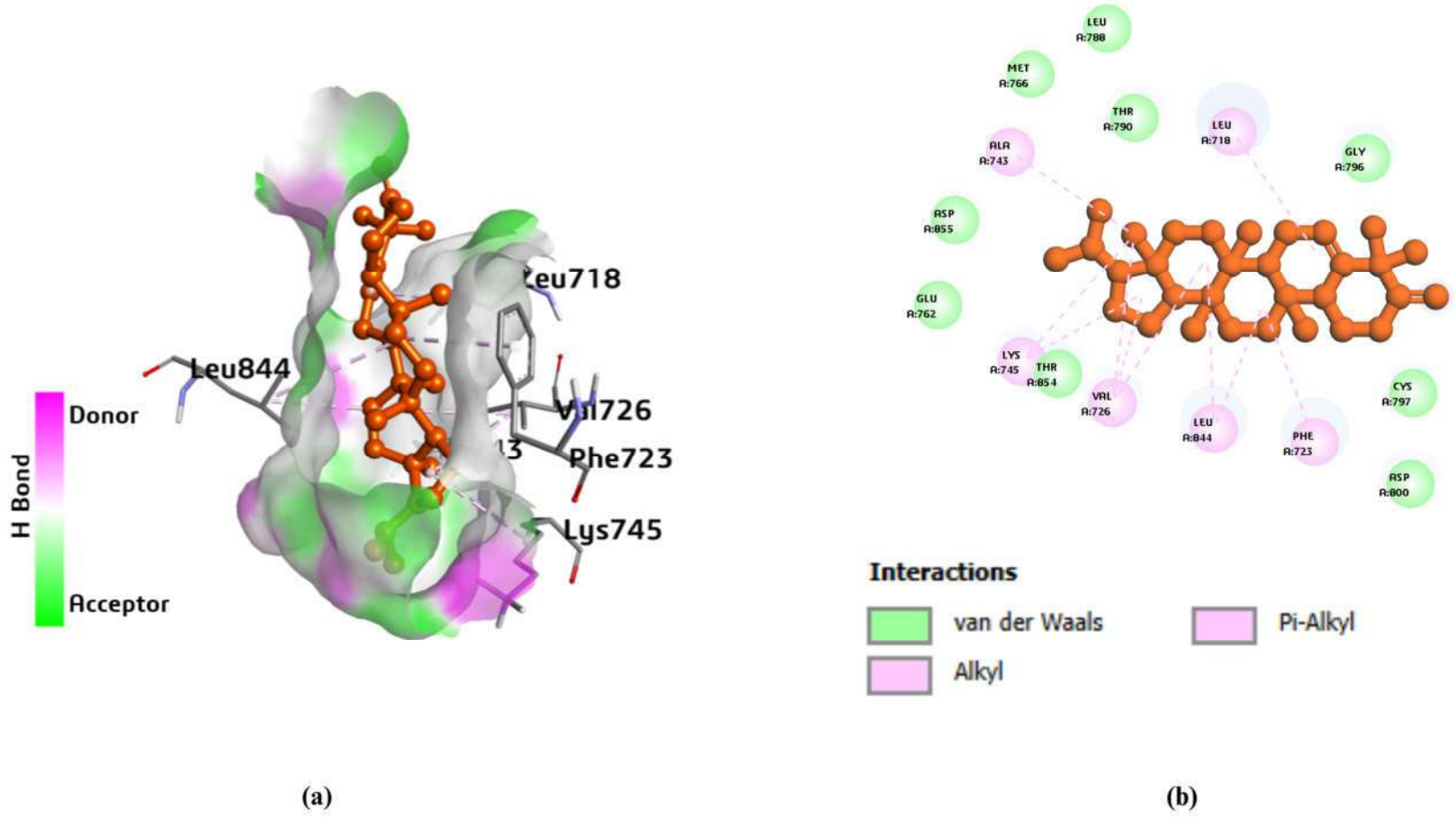


Plate 9.33: Visualization of binding interactions betweenEpidermal Growth Factor Receptor (EGFR) and DB-Friedo-B'A'-Neogammacer-5-en-3-one, showing (a) the three-dimensional (3D) molecular surface and (b) the two-dimensional (2D) interaction diagram

- Pi–Alkyl Interactions (light pink arcs)

Residues including VAL164, ALA177, and ALA230 engage in π–alkyl contacts, reinforcing hydrophobic complementarity between the ligand and the binding site.

- Alkyl Interactions (pink arcs)

Multiple hydrophobic residues in proximity, such as LEU156 and PRO350 (if present in chain), create additional van der Waals-driven stabilization.

- Van der Waals Interactions (green spheres)

Surrounding residues, including GLU234, GLU278, ASP292, TYR229, and PHE236, form a network of van der Waals contacts that collectively secure the ligand's orientation.

The interplay of π–sulfur, π–alkyl, alkyl, and van der Waals interactions suggests that Cholesta-4,6-dien-3-ol, benzoate, (3.beta.)- achieves a snug and energetically favourable fit within AKT1's binding site, potentially modulating kinase activity by stabilizing a specific conformational state (Plate 9.32).

9.3.6.6.2. 3D and 2D visualization of Epidermal Growth Factor Receptor (EGFR) with DB-Friedo-B'A'-Neogammacer-5-en-3-one

The 3D visualization depicts DB-Friedo-B'A'-Neogammacer-5-en-3-one embedded along the hydrophobic channel of EGFR, enclosed by a semi-transparent molecular surface that illustrates the receptor's topography. The ligand adopts an elongated conformation that runs parallel to the groove's contour, optimizing non-polar complementarity and maximizing hydrophobic packing. Key hydrophobic residues such as LEU718, VAL726, and LEU844 contribute substantially to ligand stabilization through π–alkyl and alkyl interactions, while PHE723 enhances aromatic complementarity via π–alkyl contact within the cavity.

The 2D interaction diagram highlights the following atomic-level contacts:

- Pi–Alkyl Interactions (light pink arcs)

LEU718, PHE723, VAL726, and LEU844 engage in π–alkyl contacts with the ligand's hydrophobic framework, reinforcing its anchoring within the non-polar binding pocket.

- Alkyl Interactions (pink arcs)

LYS745 and THR854 form alkyl interactions that provide additional van der Waals-driven stability, contributing to the compact packing of the ligand.

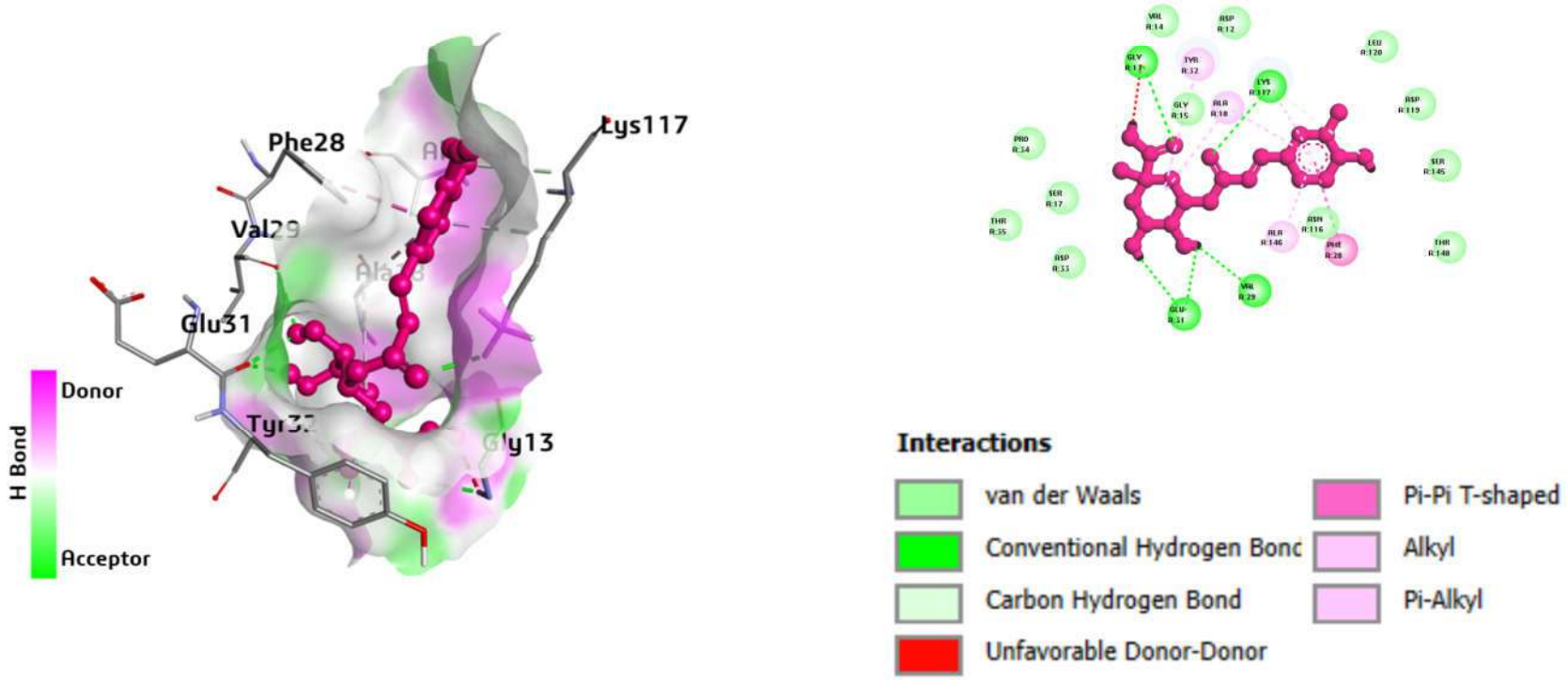
- Van der Waals Interactions (green spheres)

Residues such as GLU762, MET766, LEU788, THR790, GLY796, CYS797, ASP800, and ASP855 surround the ligand to maintain its orientation and promote non-specific stabilization.

The cooperative network of π–alkyl, alkyl, and van der Waals interactions facilitates a well-fitted, energetically favourable binding mode for DB-Friedo-B'A'-Neogammacer-5-en-3-one within EGFR, potentially influencing receptor conformational dynamics and modulating downstream signaling activity (Plate 9.33).

9.3.6.6.3. 3D and 2D visualization of Kirsten Rat Sarcoma Viral Oncogene Homolog (KRAS) with Chlorogenic acid

The 3D visualization depicts Chlorogenic acid securely accommodated within the binding cleft of KRAS, encapsulated by a semi-transparent molecular surface that delineates the receptor topology. The ligand assumes an extended conformation, enabling optimal alignment of its aromatic and polar regions to engage distinct binding zones. Notably, residues such as TYR32, GLY13, and GLY15 participate in key polar contacts, while hydrophobic patches created by ALA18 and VAL29 contribute to ligand stabilization through non-polar interactions. The planar caffeoyl moiety is oriented toward the aromatic-rich sector of the binding site, facilitating π-stacking and hydrophobic complementarity.



(a) (b)

Plate 9.34: Visualization of binding interactions betweenKirsten Rat Sarcoma Viral Oncogene Homolog (KRAS) and Chlorogenic acid, showing (a) the three-dimensional (3D) molecular surface and (b) the two-dimensional (2D) interaction diagram

The 2D interaction diagram highlights the following atomic-level contacts:

- Conventional Hydrogen Bonds (bright green lines)

Strong hydrogen bonds are formed with GLU31, VAL29, and ASN116, contributing significantly to the directional stability of the complex.

- Carbon Hydrogen Bond (light grey lines)

ALA146 establishes a carbon hydrogen bond with the ligand, subtly reinforcing the binding geometry.

- Unfavourable Donor–Donor Interaction (red line)

Observed with GLY13, indicating a possible steric or electrostatic strain in that region.

- Alkyl Interactions (light pink arcs)

ALA18 and LYS117 provide non-polar alkyl contacts, enhancing hydrophobic complementarity.

- π–π T-shaped Interaction (magenta line)

PHE28 engages in a T-shaped aromatic interaction with the ligand's phenolic ring, stabilizing the orientation of the caffeoyl moiety.

- Van der Waals Contacts (light green zones)

Multiple residues, including PRO34, ASP33, SER145, and LEU120, form a supportive non-specific contact network that maintains ligand positioning and flexibility.

The combined contribution of hydrogen bonding, π–π stacking, alkyl, and van der Waals interactions results in a well-fitted and energetically stable KRAS–Chlorogenic Acid complex, suggesting potential inhibitory modulation through stabilization of key functional conformations of the protein (Plate 9.34).

9.3.6.6.4. 3D and 2D visualization of Mitogen-Activated Protein Kinase 1 (MAPK1) with Ellagic acid

The 3D visualization illustrates Ellagic acid snugly positioned within the binding cavity of MAPK1, surrounded by a semi-transparent surface rendering of the receptor topology. The ligand's planar aromatic framework aligns parallel to several hydrophobic side chains, enabling optimal π–alkyl and π–sigma interactions. Notably, residues such as LEU156, VAL39, and ILE31 engage in hydrophobic anchoring, while polar contacts with ASP106, ASP167, and GLU33 contribute to enhanced stability through hydrogen bonding. The spatial arrangement suggests that the ligand is well-oriented to complement both the polar and non-polar microenvironments of the binding pocket.

The 2D interaction diagram reveals the following atomic-level interactions:

- Conventional Hydrogen Bonds (green lines)

ASP106, ASP167, GLU33, and MET108 form directional hydrogen bonds with polar oxygen atoms of Ellagic Acid, stabilizing the ligand through electrostatic complementarity.

- Pi–Sigma Interactions (purple arcs)

LEU156 and ILE31 participate in π–sigma interactions with the aromatic rings, contributing to hydrophobic reinforcement of the binding pose.

- Pi–Alkyl Interactions (light pink arcs)

VAL39 and ALA52 establish π–alkyl contacts with the ligand's aromatic system, enhancing non-polar complementarity.

- Van der Waals Interactions (Light Green Spheres):

Surrounding residues, including CYS166, LYS114, and GLN105, contribute to a dense network of weak contacts that fine-tune ligand positioning within the pocket.

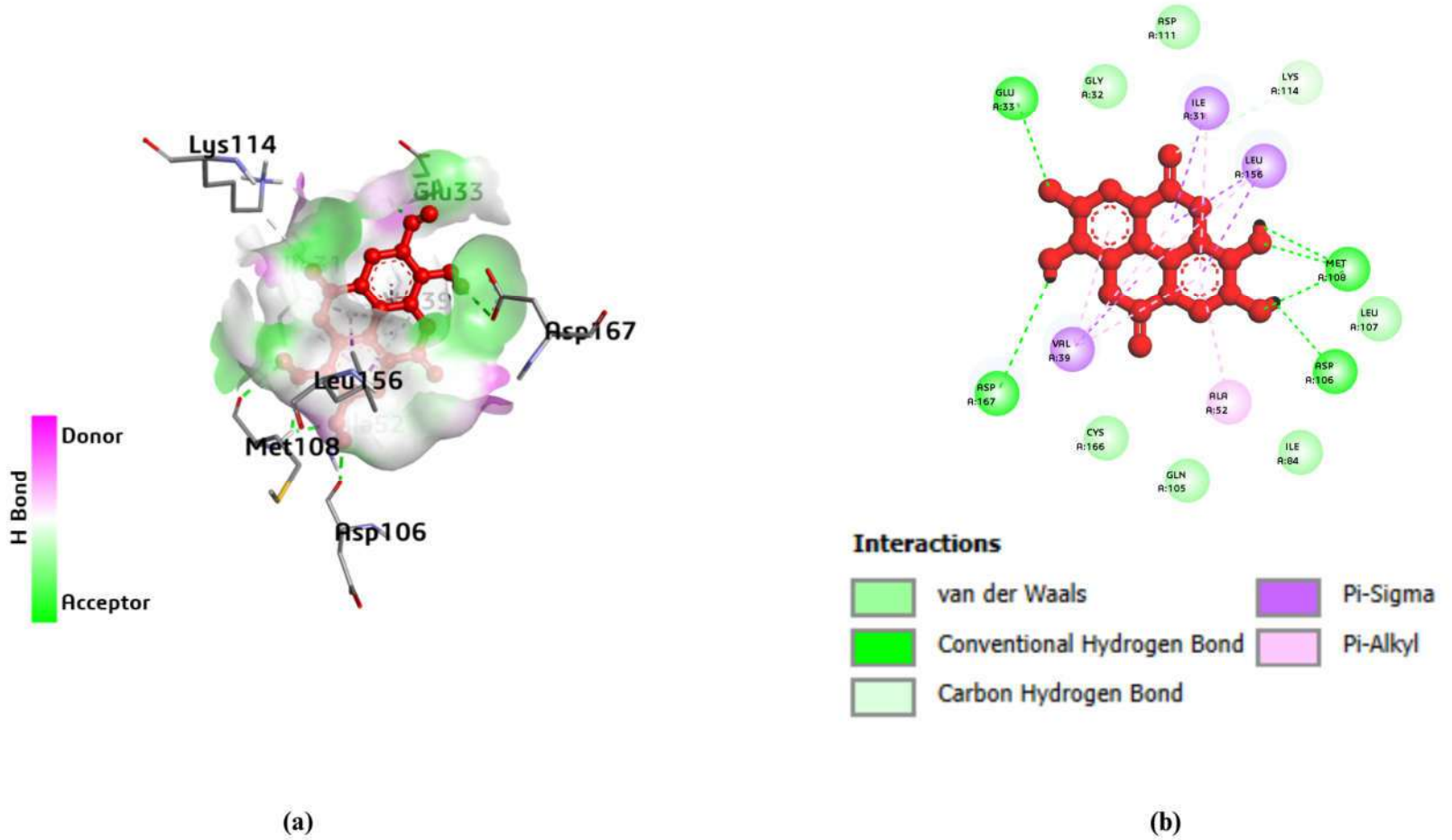
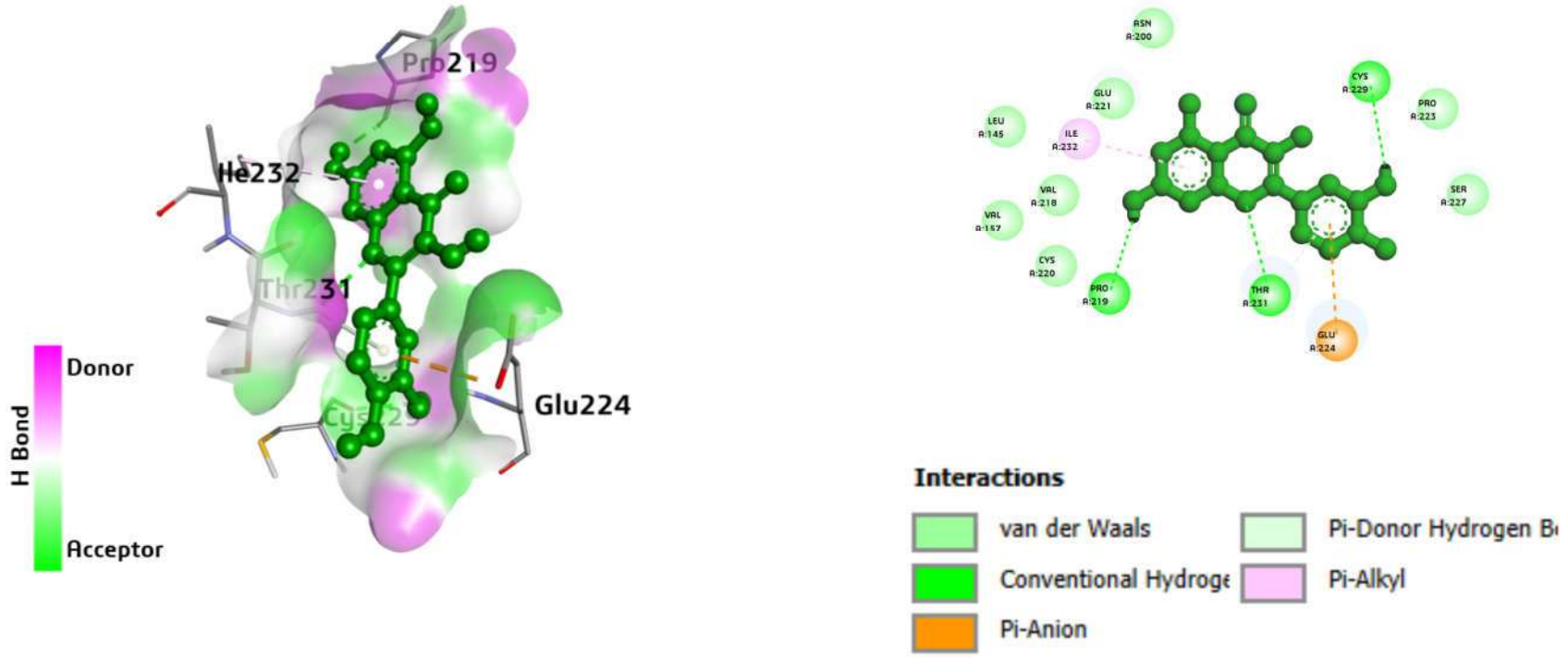


Plate 9.35: Visualization of binding interactions betweenMitogen-Activated Protein Kinase 1 (MAPK1) and Ellagic acid, showing (a) the three-dimensional (3D) molecular surface and (b) the two-dimensional (2D) interaction diagram



(a) (b)

Plate 9.36: Visualization of binding interactions betweenTumour Protein p53 (TP53) and Quercetin, showing (a) the three-dimensional (3D) molecular surface and (b) the two-dimensional (2D) interaction diagram

This cooperative network of hydrogen bonding, π–sigma, π–alkyl, and van der Waals interactions facilitates a stable and energetically favourable binding mode for Ellagic Acid in MAPK1, potentially influencing kinase activity by stabilizing specific conformational states of the protein (Plate 9.35).

9.3.6.6.5. 3D and 2D visualization of Tumour Protein p53 (TP53) with Quercetin

The 3D visualization shows Quercetin securely nestled within the binding cavity of Tumour Protein p53, aligned along a moderately hydrophobic channel that accommodates its planar flavonoid backbone. The ligand's polyphenolic structure is positioned to exploit both aromatic-driven and hydrogen bonding interactions, with hydroxyl groups oriented toward polar amino acids for hydrogen bond formation, while the aromatic rings align with non-polar residues for hydrophobic stabilization. The surface mapping highlights alternating hydrophilic (purple) and hydrophobic (green) regions, illustrating a complementary fit that supports both stability and specificity of binding within the p53 interface.

The 2D interaction profile highlights:

- Pi–Alkyl Interaction (light pink arc)

An aromatic–aliphatic contact with ILE232 enhances hydrophobic complementarity and contributes to ligand immobilization within the pocket.

- Conventional Hydrogen Bonds (bright green lines)

Residues PRO219, THR231, and CYS229 form direct hydrogen bonds with hydroxyl groups of Quercetin, significantly contributing to the anchoring and specificity of the complex.

- Pi–Anion Interaction (orange arc)

GLU224 interacts with the aromatic π-system, reinforcing electrostatic complementarity.

- Van der Waals Contacts (light green spheres)

Surrounding residues, including LEU145, VAL157, VAL218, GLU221, CYS220, SER227, PRO223, and ASN200, provide weak but cooperative dispersion forces that help stabilize the ligand conformation.

This combination of π–alkyl, π–anion, hydrogen bonding, and van der Waals interactions suggests that Quercetin achieves a well-balanced and stable association with TP53, potentially modulating its conformational dynamics and functional activity in cellular signaling (Plate 9.36).

9.3.7. Post-docking analysis

9.3.7.1. Hydrogen bonding analysis of antioxidant proteins

Protein–Ligand Interaction Profiler (PLIP) analysis of Human Cu, Zn Superoxide Dismutase (SOD1), Human Erythrocyte Catalase (CAT), Human Glutathione Peroxidase 1 (GPx1), KEAP1 Kelch Domain (KEAP1 Kelch), and Thioredoxin and TXNIP Complex (Trx-TXNIP) were listed in Tables 9.55-9.59.

9.3.7.1.1. Human Cu, Zn Superoxide Dismutase (SOD1)

Hydrogen bonding serves as a crucial determinant of ligand orientation, stability, and specificity within the Superoxide Dismutase (SOD1) binding pocket. Ligands that establish multiple hydrogen bonds generally exhibit greater binding affinity and stability, as these interactions complement hydrophobic forces in anchoring the molecule within the active site.

DB-Friedo-B'A'-Neogammacer-5-en-3-one interacts largely through hydrophobic contacts with residues THR39, GLU121, LYS122, and LEU144. While it engages in van der Waals and alkyl packing forces, the absence of hydrogen bonding indicates that its specificity is relatively weaker compared to ligands enriched in polar interactions. DB-Friedo-B'A'-Neogammacer-5-en-3-one rely more heavily on hydrophobic stabilization and could benefit from structural modifications introducing additional polar groups to enhance hydrogen bonding potential.

Table 9.55: Protein–Ligand Interaction Profiler (PLIP) analysis of Human Cu, Zn Superoxide Dismutase (SOD1)

Complex	Residue	Amino acids	Distance(Å)	Interactions type
D:B-Friedo-B':A'-Neogammacer-5-en-3-one	39A	THR	3.61	Hydrophobic
	121A	GLU	3.44	
	121A	GLU	3.38	
	122A	LYS	3.54	
	144A	LEU	3.63	
	144A	LEU	3.28	

(A: Chain A)

Table 9.56: Protein–Ligand Interaction Profiler (PLIP) analysis of Human Erythrocyte Catalase (CAT)

Complex	Residue	Amino acids	Distance(Å)	Interaction type
Kaempferol	72A	ARG	3.63	Hydrophobic
	72A	ARG	3.98	
	74A	VAL	3.71	
	146A	VAL	3.59	
	146A	VAL	3.55	
	358A	TYR	3.97	
	361A	THR	3.80	
	72A	ARG	2.13	Hydrogen bonds
	73A	VAL	2.91	
	112A	ARG	2.91	
	148A	ASN	3.37	
	148A	ASN	2.78	
	358A	TYR	3.40	
	358A	TYR	3.11	
	361A	THR	2.92	
	365A	ARG	2.45	

(A: Chain A)

Table 9.57: Protein–Ligand Interaction Profiler (PLIP) analysis of Human Glutathione Peroxidase 1 (GPx1)

Complex	Residue	Amino acids	Distance(Å)	Interactions type
Maslinic acid	55A	THR	3.70	Hydrophobic
	99A	PRO	3.00	
	103A	PHE	3.75	
	103A	PHE	3.68	
	103A	PHE	3.82	
	58A	ASN	1.90	Hydrogen Bonds
	62A	ARG	2.42	
	62A	ARG	1.81	

(A: Chain A)

Table 9.58: Protein–Ligand Interaction Profiler (PLIP) analysis of KEAP1 Kelch Domain (KEAP1 Kelch)

Complex	Residue	Amino acids	Distance(Å)	Interaction type
Maslinic acid	467A	VAL	3.99	Hydrophobic
	514A	VAL	3.74	
	515A	LEU	3.79	
	561A	VAL	3.85	
	607A	ALA	3.59	
	326A	ARG	2.05	Hydrogen bonds
	326A	ARG	2.44	
	326A	ARG	2.04	
	420A	VAL	1.83	
	563A	GLN	1.79	
	564A	GLY	2.26	

(A: Chain A)

Table 9.59: Protein–Ligand Interaction Profiler (PLIP) analysis of Thioredoxin and TXNIP Complex (Trx-TXNIP)

Complex	Residue	Amino acids	Distance(Å)	Interaction type
Oleanolic acid	54A	VAL	3.39	Hydrophobic
	109A	PRO	3.85	
	114A	PHE	3.29	
	187A	LYS	2.43	Hydrogen bonds
	294A	LEU	2.92	
	294A	LEU	2.06	

(A: Chain A)

Table 9.60: Protein–Ligand Interaction Profiler (PLIP) analysis of D-alanyl-D-alanine ligase (D-ALA:D-ALA Ligase/Ddl)

Complex	Residue	Amino acids	Distance(Å)	Interaction type
2-Phenyl-4H-chromen-4-one	142A	ILE	3.67	Hydrophobic
	142A	ILE	3.66	
	182A	TRP	3.44	
	182A	TRP	3.87	
	183A	LEU	3.89	
	183A	LEU	3.59	
	269A	LEU	3.62	
	270A	GLU	3.62	
	144A	LYS	2.28	Hydrogen bonds
	151A	SER	2.99	
	210A	TYR	3.06	

(A: Chain A)

Table 9.61: Protein–Ligand Interaction Profiler (PLIP) analysis of LasR ligand-binding domain (LasR)

Complex	Residue	Amino acids	Distance(Å)	Interaction type
2-Phenyl-4H-chromen-4-one	36G	LEU	3.64	Hydrophobic
	36G	LEU	3.45	
	40G	LEU	3.67	
	47G	TYR	3.76	
	56G	TYR	3.58	
	64G	TYR	3.72	
	76G	VAL	3.78	
	76G	VAL	3.92	
	125G	LEU	3.66	

(A: Chain A)

9.3.7.1.2. Human Erythrocyte Catalase (CAT)

Hydrogen bonding plays an essential role in maintaining ligand orientation, stability, and binding specificity within the Catalase active site. While hydrophobic interactions stabilize most ligand poses, the presence of multiple hydrogen bonds ensures stronger anchoring and improved binding affinity.

Kaempferol shows extensive hydrophobic interactions with residues VAL74, VAL146, and TYR358, complemented by hydrogen bonds with ARG72, ARG112, ASN148, and THR361. This suggests a well-balanced binding mechanism, where multiple polar contacts reinforce hydrophobic stabilization, strengthening its specificity within the binding pocket. Kaempferol stands out due to its robust hydrogen bonding profiles, offering both stability and specificity.

9.3.7.1.3. Human Glutathione Peroxidase 1 (GPx1)

Hydrogen bonding serves as a crucial determinant of ligand orientation, stability, and specificity within the Glutathione Peroxidase binding pocket. Ligands with multiple hydrogen bonds often demonstrate improved affinity by complementing hydrophobic contacts with directional polar interactions, ensuring stronger anchoring within the active site.

Maslinic Acid displays a robust binding profile, with hydrophobic contacts with PRO99 and PHE103, along with multiple hydrogen bonds involving ASN58 and ARG62. The presence of several hydrogen bonds strengthens the ligand's orientation, enhancing both affinity and stability within the enzyme's active site. Overall, Maslinic acid demonstrates the most balanced and favourable interaction patterns, benefiting from multiple hydrogen bonds in addition to hydrophobic stabilization.

9.3.7.1.4. KEAP1 Kelch Domain (KEAP1 Kelch)

Hydrogen bonding plays a decisive role in determining ligand stability, specificity, and orientation within the KEAP1 Kelch binding pocket. While hydrophobic contacts are widely observed, ligands capable of establishing multiple

hydrogen bonds typically demonstrate improved docking affinity and enhanced interaction stability.

Maslinic Acid demonstrates a robust hydrogen bonding profile, interacting with GLY367, ARG326, and GLN543. These polar contacts are complemented by hydrophobic interactions with residues such as ALA515 and VAL561. The richer hydrogen bonding network likely contributes to stronger binding stability compared to ligands dominated by non-polar interactions.

9.3.7.1.5. Thioredoxin and TXNIP Complex (Trx-TXNIP)

Hydrogen bonding governs pose fidelity and recognition at the Thioredoxin–TXNIP interface, where directional polar contacts complement hydrophobic packing to stabilize ligands in the shallow groove. Ligands with multiple H-bonds typically achieve better anchoring against the β-sheet/loop edges that mediate protein–protein engagement.

Oleanolic acid combined hydrophobic packing (e.g., PHE114, PRO109) with hydrogen bonding to LYS187 and backbone atoms of LEU294. The presence of these polar contacts likely improves orientation compared with purely hydrophobic sterols.

9.3.7.2. Hydrogen bonding analysis of antimicrobial proteins

Protein–Ligand Interaction Profiler (PLIP) analysis of D-alanyl-D-alanine ligase (D-ALA:D-ALA Ligase/Ddl), LasR ligand-binding domain (LasR), PqsR coinducer-binding domain (PqsR/MvfR), Penicillin-Binding Protein 3 (PBP3), and Regulatory protein RhlR (RhIR) were given in Tables 9.60-9.64.

9.3.7.2.1. D-alanyl-D-alanine ligase (D-ALA:D-ALA Ligase/Ddl)

Hydrogen bonding serves as a crucial determinant of ligand orientation, stability, and specificity within the DdlA binding pocket. Ligands that establish multiple hydrogen bonds generally exhibit greater binding affinity and stability, as these interactions complement hydrophobic forces in anchoring the molecule within the active site.

Table 9.62: Protein–Ligand Interaction Profiler (PLIP) analysis of PqsR coinducer-binding domain (PqsR/MvfR)

Complex	Residue	Amino acids	Distance(Å)	Interaction type
Oleanolic Acid	207A	LEU	3.27	Hydrophobic
	236A	ILE	3.56	
	263A	ILE	3.94	
	187A	ALA	2.91	Hydrogen Bonds
	190A	ALA	2.71	
	258A	TYR	1.94	

(A: Chain A)

Table 9.63: Protein–Ligand Interaction Profiler (PLIP) analysis of Penicillin-Binding Protein 3 (PBP3)

Complex	Residue	Amino acids	Distance(Å)	Interaction type
Ellagic acid	172A	ASP	3.97	Hydrophobic
	127A	ARG	2.30	Hydrogen
	127A	ARG	3.00	
	150A	GLU	2.76	
	273A	ARG	2.11	
	152A	ARG	4.13	Pi-Cation
	127A	ARG	5.13	Salt Bridges
	152A	ARG	4.09	

(A: Chain A)

Table 9.64: Protein–Ligand Interaction Profiler (PLIP) analysis of Regulatory protein RhlR (RhIR)

Complex	Residue	Amino acids	Distance(Å)	Interaction type
Cholesta-4,6-dien-3-ol, benzoate, (3.beta.)-	2A	ARG	3.45	Hydrophobic
	7A	PHE	3.12	
	7A	PHE	3.68	
	7A	PHE	3.68	
	150A	GLU	3.88	
	153A	LEU	3.76	

(A: Chain A)

2-Phenyl-4H-chromen-4-one predominantly engages in hydrophobic interactions with residues such as ILE142, TRP182, and LEU183, complemented by hydrogen bonding with LYS144, SER151, and TYR210. This suggests a binding mode where hydrophobic packing is the primary stabilizing factor, with hydrogen bonding providing additional orientation control.

2-Phenyl-4H-chromen-4-one relies more heavily on hydrophobic stabilization and could benefit from structural modifications to enhance hydrogen bonding potential.

9.3.7.2.2. LasR ligand-binding domain (LasR)

Hydrogen bonding serves as a crucial determinant of ligand orientation, stability, and specificity within the LasR binding pocket. Ligands that establish multiple hydrogen bonds generally exhibit stronger affinity and stability, as these interactions complement hydrophobic forces to anchor the molecule within the active site.

2-Phenyl-4H-chromen-4-one primarily engages in hydrophobic interactions with residues such as LEU36, TYR47, TYR56, TYR64, VAL70, VAL76, and LEU125. The absence of hydrogen bonds indicates that stabilization is predominantly hydrophobic, suggesting that structural modifications introducing polar groups could enhance its binding specificity. 2-Phenyl-4H-chromen-4-one relies heavily on hydrophobic contacts, potentially benefiting from modifications that enhance polar interaction capacity.

9.3.7.2.3. PqsR coinducer-binding domain (PqsR/MvfR)

Hydrogen bonding serves as a crucial determinant of ligand orientation, stability, and specificity within the MvfR (PqsR) binding pocket. Ligands that establish multiple hydrogen bonds generally exhibit greater binding affinity and stability, as these interactions complement hydrophobic forces in anchoring the molecule within the active site.

Oleanolic acid forms hydrogen bonds with ALA187 and ALA190, complemented by hydrophobic interactions with residues such as ILE236 and ILE263. This indicates that the ligand leverages both hydrophobic stabilization and polar anchoring, which likely contributes to its stable orientation within the binding pocket.

9.3.7.2.4. Penicillin-Binding Protein 3 (PBP3)

Hydrogen bonding serves as a crucial determinant of ligand orientation, stability, and specificity within the PBP3 binding pocket. Ligands that establish multiple hydrogen bonds generally exhibit greater binding affinity and stability, as these interactions complement hydrophobic forces in anchoring the molecule within the active site.

Ellagic Acid demonstrates a strong polar interaction profile, forming hydrogen bonds with GLU150 and ARG273. Additionally, it establishes a pi-cation interaction with ARG152 and multiple salt bridges (ARG152, VAL333). These polar contacts, combined with hydrophobic interactions with PHE531, provide a balanced interaction strategy that enhances both stability and specificity. This makes Ellagic Acid one of the more strongly anchored ligands in this binding pocket. Ellagic acid demonstrates richer hydrogen bonding networks.

9.3.7.2.5. Regulatory protein RhlR (RhIR)

Hydrogen bonding is a critical determinant of ligand stability, specificity, and orientation within the RhlR binding pocket. While hydrophobic contacts provide the bulk of anchoring, directed hydrogen bonds enhance pose fidelity and often correlate with higher apparent affinity.

Cholesta-4,6-dien-3-ol, benzoate (3.beta.)-, engages RhlR almost exclusively through hydrophobic contacts, notably with residues ARG2, PHE7 (multiple contacts), GLU150, and LEU153. The absence of detectable hydrogen bonds indicates a pose stabilized primarily by non-polar packing, with limited directional polar anchoring.

Cholesta-4,6-dien-3-ol, benzoate (3.beta.)-, relies predominantly on hydrophobic stabilization and may gain from introducing strategically positioned polar groups to strengthen hydrogen-bond networks with residues such as ARG2, ASN3, GLY6, or ARG154.

9.3.7.3. Hydrogen bonding analysis of anthelmintic proteins

Protein–Ligand Interaction Profiler (PLIP) analysis of ATP synthase subunit a (ATP synthase), Cytochrome c Oxidase subunit 1 (COX1), Heat Shock Protein 70 (HSP70), NADH-Ubiquinone Oxidoreductase chain 1 (Complex I), Extracellular Globin-3/Erythrocruorin (Ext. Globin-3) were tabulated in Tables 9.65-9.69.

9.3.7.3.1. ATP synthase subunit a (ATP synthase)

Hydrogen bonding is a critical determinant of ligand stability, specificity, and orientation within the ATP synthase binding pocket. While hydrophobic interactions provide anchoring forces, hydrogen bonds contribute significantly to ligand specificity and stability. Ligands with multiple hydrogen bonds often display enhanced binding affinity compared to those relying primarily on hydrophobic packing.

Oleanolic acid engages the pocket via hydrophobic contacts with ALA19, PHE220, TRP89, and TYR97, and forms a single hydrogen bond with THR26 (~3.25 Å). This lone polar interaction likely assists orientation while hydrophobic packing remains the principal stabilizer. Oleanolic Acid benefits from a single hydrogen bond (THR26), offering moderate specificity.

9.3.7.3.2. Cytochrome c Oxidase subunit 1 (COX1)

Hydrogen bonding is a critical determinant of ligand stability, specificity, and orientation within the Cytochrome C binding pocket. While hydrophobic interactions provide anchoring forces, hydrogen bonds contribute significantly to ligand specificity and stability. Ligands with multiple hydrogen bonds often display enhanced binding affinity compared to those relying primarily on hydrophobic packing.

Oleanolic acid demonstrates a predominantly hydrophobic interaction profile involving LEU180, LEU184, and LEU193, alongside polar stabilization through hydrogen bonding with TYR2 and TYR113. While hydrophobic forces dominate, these few hydrogen bonds improve its overall anchoring and specificity. Oleanolic acid display balanced but weaker profiles where hydrophobic interactions dominate, supported by limited hydrogen bonding.

9.3.7.3.3. Heat Shock Protein 70 (HSP70)

Hydrogen bonding is a critical determinant of ligand stability, specificity, and orientation within the HSP70 binding pocket. While hydrophobic interactions provide anchoring forces, hydrogen bonds contribute significantly to ligand specificity and stability. Ligands with multiple hydrogen bonds often display enhanced binding affinity compared to those relying primarily on hydrophobic packing.

Oleanolic acid exhibits strong hydrophobic contacts with residues such as PHE1, PHE11, and PHE51, complemented by hydrogen bonding with PHE16 and PHE18. These polar contacts reinforce the ligand orientation, suggesting moderate stability with a balance of non-polar and hydrogen bonding interactions. Oleanolic acid presents a similar mixed interaction pattern but with fewer polar contacts.

9.3.7.3.4. NADH-Ubiquinone Oxidoreductase chain 1 (Complex I)

Hydrogen bonding is a critical determinant of ligand stability, specificity, and orientation within the NADH binding pocket. While hydrophobic interactions serve as anchoring forces, hydrogen bonds significantly enhance specificity and strengthen ligand orientation. Compounds that form multiple hydrogen bonds typically exhibit superior binding affinity compared to those primarily stabilized by hydrophobic contacts.

Maslinic acid engages in a hybrid interaction network. It forms hydrophobic interactions with residues like PHE14A and TYR94A, while establishing hydrogen bonding with residues ILE92A, TYR94A, and HIS172A. The presence of multiple hydrogen bonds indicates that Maslinic acid adopts a stable and specific orientation, implying a moderately strong binding profile. Maslinic acid also demonstrates

Table 9.65: Protein–Ligand Interaction Profiler (PLIP) analysis of ATP synthase subunit a (ATP synthase)

Complex	Residue	Amino acids	Distance(Å)	Interaction type
Oleanolic acid	19A	ALA	3.52	Hydrophobic
	22A	PHE	3.84	
	89A	TRP	3.70	
	92A	TYR	3.86	
	257A	ILE	3.70	
	26A	THR	2.25	Hydrogen Bonds

(A: Chain A)

Table 9.66: Protein–Ligand Interaction Profiler (PLIP) analysis of Cytochrome c Oxidase subunit 1 (COX1)

Complex	Residue	Amino acids	Distance(Å)	Interaction type
Oleanolic Acid	113A	TYR	3.63	Hydrophobic
	113A	TYR	3.81	
	114A	PRO	3.86	
	186A	LEU	3.56	
	186A	LEU	3.52	
	190A	ILE	3.89	
	193A	LEU	3.92	

(A: Chain A)

Table 9.67: Protein–Ligand Interaction Profiler (PLIP) analysis of Heat Shock Protein 70 (HSP70)

Complex	Residue	Amino acids	Distance(Å)	Interaction type
Oleanolic Acid	1A	PHE	3.49	Hydrophobic
	1A	PHE	3.86	
	1A	PHE	3.69	
	16A	PHE	3.93	
	51A	PHE	3.84	
	16A	PHE	2.00	Hydrogen Bonds

(A: Chain A)

Table 9.68: Protein–Ligand Interaction Profiler (PLIP) analysis of NADH-Ubiquinone Oxidoreductase chain 1 (Complex I)

Complex	Residue	Amino acids	Distance(Å)	Interaction type
Maslinic acid	14A	PHE	3.36	Hydrophobic
	14A	PHE	3.57	
	93A	PRO	3.49	
	94A	TYR	3.32	
	175A	LEU	3.49	
	175A	LEU	3.39	
	92A	ILE	2.38	Hydrogen Bonds
	94A	TYR	2.30	
	95A	MET	2.82	
	172A	HIS	3.23	

(A: Chain A)

Table 9.69: Protein–Ligand Interaction Profiler (PLIP) analysis of Extracellular Globin-3/Erythrocruorin (Ext. Globin-3)

Complex	Residue	Amino acids	Distance(Å)	Interaction type
Vitamin E	57A	LEU	3.60	Hydrophobic
	60A	LEU	3.79	
	70A	LEU	3.86	
	71A	PHE	3.45	
	71A	PHE	3.70	
	74A	VAL	3.83	
	95A	LEU	3.64	
	125A	VAL	3.71	
	125A	VAL	3.57	
	129A	HIS	3.92	
	130A	PHE	3.48	
	133A	PHE	3.60	
	133A	PHE	3.80	
	161A	LEU	3.78	
	164A	ILE	3.69	
	90A	ARG	2.97	Hydrogen bonds
	90A	ARG	2.94	
	122A	ARG	3.21	
	122A	ARG	4.02	π-Cation Interactions

(A: Chain A)

significant hydrogen bonding support alongside hydrophobic packing, suggesting robust stability.

9.3.7.3.5. Extracellular Globin-3/Erythrocruorin (Ext. Globin-3)

Hydrogen bonding is a critical determinant of ligand stability, specificity, and orientation within the Globin-3 binding pocket. While hydrophobic interactions provide anchoring forces, hydrogen bonds contribute significantly to ligand specificity and stability. Ligands with multiple hydrogen bonds often display enhanced binding affinity compared to those relying primarily on hydrophobic packing.

Vitamin E presents a richer polar profile. In addition to extensive hydrophobic packing with many aromatic/aliphatic residues (e.g., PHE130A, PHE133A, VAL54A, LEU57A/60A/70A, PHE71A, HIS125A), PLIP reports hydrogen bonds to residues including PHE130A, PHE133A, LEU57A, LEU60A, LEU70A, PHE71A, GLU91A, and additional polar contacts with ARG90A and ARG122A. Notably, a π–cation interaction with ARG122A is also observed. This combination of hydrophobic, hydrogen-bonding, and π–cation contacts points to enhanced specificity and orientation control for Vitamin E.

Across Globin-3, Vitamin E stands out for its mixed interaction strategy, multiple reported hydrogen bonds plus a π–cation contact that complement extensive hydrophobic packing, suggesting the most specific and stable binding among the ligands assessed.

9.3.7.4. Hydrogen bonding analysis of anti-inflammatory proteins

Protein–Ligand Interaction Profiler (PLIP) analysis of Nuclear Factor kappa B p50(NF-κB p50), Tumour Necrosis Factor-alpha (TNF-α), Human Inducible Nitric Oxide Synthase (iNOS), Janus Kinase 2 (JAK2), and Human Cyclooxygenase-2 (COX-2) were listed in Tables 9.70-9.74.

9.3.7.4.1. Nuclear Factor kappa B p50 (NF-κB p50)

Hydrogen bonding is a critical determinant of ligand stability, specificity, and orientation within the NF-κB p50 binding pocket. While hydrophobic interactions provide anchoring forces, hydrogen bonds contribute significantly to ligand specificity and stability. Ligands with multiple hydrogen bonds often display enhanced binding affinity compared to those relying primarily on hydrophobic packing.

Maslinic acid shows strong hydrophobic interactions with LYS52 and PRO71, supported by hydrogen bonding with LYS79 and SER81. This mixture of contacts implies a stable and specific binding conformation, with polar residues strengthening the otherwise hydrophobic nature of the complex. Maslinic acid displays balanced profiles with meaningful hydrogen bonding that strengthens their hydrophobic cores

9.3.7.4.2. Tumour Necrosis Factor-alpha (TNF-α)

Hydrogen bonding is a critical determinant of ligand stability, specificity, and orientation within the Tumour Necrosis Factor-α (TNF-α) binding pocket. While hydrophobic interactions provide anchoring forces, hydrogen bonds contribute significantly to ligand specificity and stability. Ligands with multiple hydrogen bonds often display enhanced binding affinity compared to those relying primarily on hydrophobic packing.

DB-Friedo-B'A'-Neogammacer-5-en-3-one primarily engages in hydrophobic interactions with aromatic residues such as TYR59 (multiple contacts) and TYR151. The absence of detected hydrogen bonds indicates that hydrophobic stabilization is the primary factor anchoring this compound within the binding pocket. DB-Friedo-B'A'-Neogammacer-5-en-3-one rely almost entirely on hydrophobic packing; these scaffolds could benefit from introducing polar groups to strengthen hydrogen-bonding networks and improve binding specificity.

Table 9.70: Protein–Ligand Interaction Profiler (PLIP) analysis of Nuclear Factor kappa B p50 (NF-κB p50)

Complex	Residue	Amino acids	Distance(Å)	Interaction type
Maslinic acid	52P	LYS	3.60	Hydrophobic
	71P	PRO	3.46	
	71P	PRO	3.48	
	79P	LYS	2.11	Hydrogen bonds
	81P	SER	2.31	

(A: Chain A)

Table 9.71: Protein–Ligand Interaction Profiler (PLIP) analysis of Tumour Necrosis Factor-alpha (TNF-α)

Complex	Residue	Amino acids	Distance(Å)	Interaction type
D:B-Friedo-B':A'-Neogammacer-5-en-3-one	59A	TYR	3.87	Hydrophobic
	59A	TYR	3.36	
	59A	TYR	3.46	
	59A	TYR	3.94	
	151A	TYR	3.68	

(A: Chain A)

Table 9.72: Protein–Ligand Interaction Profiler (PLIP) analysis of Human Inducible Nitric Oxide Synthase (iNOS)

Complex	Residue	Amino acids	Distance(Å)	Interaction type
Cholesta-4,6-dien-3-ol, benzoate, (3.beta.)-	194A	TRP	3.64	Hydrophobic
	194A	TRP	3.84	
	350A	PRO	3.29	
	352A	VAL	3.40	
	369A	PHE	3.75	
	369A	PHE	3.98	
	489A	TYR	3.64	
	491A	TYR	3.78	
	370A	ASN	3.02	Hydrogen bonds
	194A	TRP	3.60	Pi stacking
	194A	TRP	4.23	
	369A	PHE	4.27	

(A: Chain A)

Table 9.73: Protein–Ligand Interaction Profiler (PLIP) analysis of Janus Kinase 2 (JAK2)

Complex	Residue	Amino acids	Distance(Å)	Interaction type
Ellagic acid	855A	LEU	3.67	Hydrophobic
	863A	VAL	3.57	
	931A	TYR	3.92	
	983A	LEU	3.57	
	983A	LEU	3.66	
	932A	LEU	1.96	Hydrogen bonds
	993A	GLY	2.22	
	993A	GLY	2.75	
	994A	ASP	2.11	

(A: Chain A)

Table 9.74: Protein–Ligand Interaction Profiler (PLIP) analysis of Human Cyclooxygenase-2 (COX-2)

Complex	Residue	Amino acids	Distance(Å)	Interaction type
Cholesta-4,6-dien-3-ol, benzoate, (3.beta.)-	192A	GLN	3.71	Hydrophobic
	197A	MET	3.92	
	198A	PHE	3.83	
	201A	PHE	3.51	
	201A	PHE	3.78	
	343A	ILE	3.62	
	347A	ASP	3.93	
	348A	TYR	3.92	
	350A	GLN	3.66	
	564A	ILE	3.91	

(A: Chain A)

Table 9.75: Protein–Ligand Interaction Profiler (PLIP) analysis of Dipeptidyl Peptidase 4 (DPP4)

Complex	Residue	Amino acids	Distance(Å)	Interaction type
D:B-Friedo-B':A'-Neogammacer-5-en-3-one	61A	ARG	3.95	Hydrophobic
	69A	LEU	3.71	
	107A	ILE	3.44	
	107A	ILE	3.75	
	109A	PRO	3.24	
	159A	PRO	3.64	
	216A	TRP	3.86	
	214A	LEU	3.22	Hydrogen Bonds
	216A	TRP	2.27	

(A: Chain A)

9.3.7.4.3. Human Inducible Nitric Oxide Synthase (iNOS)

Hydrogen bonding is a critical determinant of ligand stability, specificity, and orientation within the Human Inducible Nitric Oxide Synthase (iNOS) binding pocket. While hydrophobic interactions provide anchoring forces, hydrogen bonds contribute significantly to ligand specificity and stability. Ligands with multiple hydrogen bonds often display enhanced binding affinity compared to those relying primarily on hydrophobic packing.

Cholesta-4,6-dien-3-ol, benzoate, (3.beta.)-forms extensive hydrophobic interactions with PHE369, TYR489, and TRP194. Importantly, it also establishes a hydrogen bond with ASN370 (3.02 Å), which enhances its orientation and stability in the binding pocket. Additionally, π-stacking with TRP194 provides further stabilization. This combined network of polar and aromatic interactions suggests a relatively strong and well-anchored binding profile.

Cholesta-4,6-dien-3-ol, benzoate, (3.beta.)-demonstrate the strongest dual interaction strategies, combining hydrophobic stabilization with meaningful hydrogen bonding and π-stacking. These features likely enhance both stability and specificity within the active site.

9.3.7.4.4. Janus Kinase 2 (JAK2)

Hydrogen bonding is a critical determinant of ligand stability, specificity, and orientation within the Janus Kinase 2 (JAK2) binding pocket. While hydrophobic interactions provide anchoring forces, hydrogen bonds contribute significantly to ligand specificity and stability. Ligands with multiple hydrogen bonds often display enhanced binding affinity compared to those relying primarily on hydrophobic packing.

Ellagic acid exhibits strong hydrophobic interactions with LEU855, VAL863, TYR931, and LEU983, alongside hydrogen bonding with LEU932, GLY993, and ASP994. These polar interactions reinforce binding, and the dual presence of non-polar and polar contacts suggests a balanced and stable binding mode. Ellagic acid

demonstrates balanced profiles with significant hydrogen bonding that reinforces hydrophobic stabilization.

9.3.7.4.5. Human Cyclooxygenase-2 (COX-2)

Hydrogen bonding is a critical determinant of ligand stability, specificity, and orientation within the Cyclooxygenase-2 (COX-2) binding pocket. While hydrophobic interactions provide anchoring forces, hydrogen bonds contribute significantly to ligand specificity and stability. Ligands with multiple hydrogen bonds often display enhanced binding affinity compared to those relying primarily on hydrophobic packing.

Cholesta-4,6-dien-3-ol, benzoate, (3.beta.)- engages COX-2 chiefly through hydrophobic contacts with residues such as GLN192, MET197, PHE198/PHE201, ILE345, ASP347, TYR348, GLN350, and ILE564. The absence of hydrogen bonds implies stabilization dominated by non-polar packing, with limited directional specificity. Cholesta-4,6-dien-3-ol, benzoate, (3.beta.)- relies almost entirely on hydrophobic stabilization, which may limit binding specificity relative to the others.

9.3.7.5. Hydrogen bonding analysis of antidiabetic proteins

Protein–Ligand Interaction Profiler (PLIP) analysis of Dipeptidyl Peptidase 4 (DPP4), Insulin Receptor Ectodomain (IR), Pancreatic Alpha-Amylase (PAA), Peroxisome Proliferator-Activated Receptor Gamma (PPARG), and Protein Tyrosine Phosphatase 1B (PTP1B) were listed in Tables 9.75-7.79.

9.3.7.5.1. Dipeptidyl Peptidase 4 (DPP4)

Hydrogen bonding is a critical determinant of ligand stability, specificity, and orientation within the Dipeptidyl Peptidase IV binding pocket. While hydrophobic interactions provide anchoring forces, hydrogen bonds contribute significantly to ligand specificity and stability. Ligands with multiple hydrogen bonds often display enhanced binding affinity compared to those relying primarily on hydrophobic packing.

Table 9.76: Protein–Ligand Interaction Profiler (PLIP) analysis of Insulin Receptor Ectodomain (IR)

Complex	Residue	Amino acids	Distance(Å)	Interaction type
D:B-Friedo-B':A'-Neogammacer-5-en-3-one	4A	PRO	3.58	Hydrophobic
	4A	PRO	3.70	
	53A	LYS	3.97	
	55A	ILE	3.97	
	78A	ASN	3.68	
	78A	ASN	3.74	
	80A	THR	3.98	
	215A	ASN	3.35	
	226A	VAL	3.82	
	80A	THR	2.23	Hydrogen Bonds

(A: Chain A)

Table 9.77: Protein–Ligand Interaction Profiler (PLIP) analysis of Pancreatic Alpha-Amylase (PAA)

Complex	Residue	Amino acids	Distance(Å)	Interaction type
Cholesta-4,6-dien-3-ol, benzoate, (3.beta.)-	49A	VAL	3.97	Hydrophobic
	51A	ILE	3.86	
	58A	TRP	3.88	
	58A	TRP	3.79	
	59A	TRP	3.57	
	59A	TRP	3.74	
	59A	TRP	3.72	
	59A	TRP	3.78	
	59A	TRP	3.61	
	62A	TYR	3.78	
	62A	TYR	3.51	
	163A	THR	3.95	
	165A	LEU	3.72	
	53A	ASN	2.94	Hydrogen Bonds

(A: Chain A)

Table 9.78: Protein–Ligand Interaction Profiler (PLIP) analysis of Peroxisome Proliferator-Activated Receptor Gamma (PPARG)

Complex	Residue	Amino acids	Distance(Å)	Interaction Type
D:B-Friedo-B':A'-Neogammacer-5-en-3-one	264A	PHE	3.72	Hydrophobic
	264A	PHE	3.57	
	281A	ILE	3.68	
	287A	PHE	3.71	
	287A	PHE	3.90	
	287A	PHE	3.79	
	287A	PHE	3.50	

(A: Chain A)

Table 9.79: Protein–Ligand Interaction Profiler (PLIP) analysis of Protein Tyrosine Phosphatase 1B (PTP1B)

Complex	Residue	Amino acids	Distance(Å)	Interaction Type
Cholesta-4,6-dien-3-ol, benzoate, (3.beta.)-	24A	ARG	3.82	Hydrophobic
	48A	ASP	3.73	
	49A	VAL	3.57	
	182A	PHE	3.85	
	182A	PHE	3.58	
	182A	PHE	3.48	
	182A	PHE	3.59	
	217A	ALA	3.49	
	219A	ILE	3.92	
	262A	GLN	3.78	
	20A	TYR	3.02	Hydrogen Bonds
	20A	TYR	3.12	
	24A	ARG	2.34	
	24A	ARG	2.03	
	254A	ARG	2.35	
	254A	ARG	2.26	
	262A	GLN	3.36	

(A: Chain A)

D:B-Friedo-B'A'-Neogammacer-5-en-3-one exhibits a strong dual interaction profile, engaging extensively in hydrophobic interactions with residues such as LEU1071 and PRO1093, while also forming hydrogen bonds with ARG61A, TRP210A, HIS1102A, and TYR1104A. This diverse network implies robust stability and enhanced specificity, making this ligand one of the strongest binders in the system.

Across the DPP4 system, D:B-Friedo-B'A'-Neogammacer-5-en-3-one demonstrates the most extensive hydrogen bonding network, making it the strongest candidate for highly stable and specific binding. D:B-Friedo-B'A'-Neogammacer-5-en-3-one stand out as the most stable and specific binders in the DPP4 system.

9.3.7.5.2. Insulin Receptor Ectodomain (IR)

Hydrogen bonding is a critical determinant of ligand stability, specificity, and orientation within the Insulin Receptor protein binding pocket. While hydrophobic interactions provide anchoring forces, hydrogen bonds contribute significantly to ligand specificity and stability. Ligands that establish multiple hydrogen bonds typically demonstrate stronger affinity and greater conformational stability than those that rely primarily on hydrophobic packing.

DB-Friedo-B'A'-Neogammacer-5-en-3-one demonstrates a dual interaction profile, engaging in extensive hydrophobic interactions with residues like ASN75, ILE55, and PRO44, alongside multiple hydrogen bonds involving PRO44, LYS53, ASN75, THR80, and ASN215. This combination indicates a stable and specific binding mode, as hydrophobic anchoring is reinforced by a strong hydrogen bonding network. Across the Insulin Receptor protein system, DB-Friedo-B'A'-Neogammacer-5-en-3-one demonstrates the richest hydrogen bonding network, making it the most stable and specific ligand among those analyzed.

9.3.7.5.3. Pancreatic Alpha-Amylase (PAA)

Hydrogen bonding is a critical determinant of ligand stability, specificity, and orientation within the Insulin Receptor protein binding pocket. While hydrophobic interactions provide anchoring forces, hydrogen bonds contribute significantly to

ligand specificity and stability. Ligands with multiple hydrogen bonds often display enhanced binding affinity compared to those relying primarily on hydrophobic packing.

Cholesta-4,6-dien-3-ol, benzoate, (3.beta.)- formed fewer hydrogen bonds but retained positional stability through compensatory hydrophobic forces.

9.3.7.5.4. Peroxisome Proliferator-Activated Receptor Gamma (PPARG)

Hydrogen bonding is a critical determinant of ligand stability, specificity, and orientation within the Peroxisome Proliferator-Activated Receptor Gamma (PPARG) binding pocket. While hydrophobic interactions provide anchoring forces, hydrogen bonds contribute significantly to ligand specificity and stability. Ligands with multiple hydrogen bonds often display enhanced binding affinity compared to those relying primarily on hydrophobic packing.

DB-Friedo-B'A'-Neogammacer-5-en-3-one demonstrates a purely hydrophobic interaction profile, engaging with residues such as PHE226, PHE264, PHE282, and PHE363. The absence of hydrogen bonds indicates limited specificity, with stability dependent on hydrophobic packing.

DB-Friedo-B'A'-Neogammacer-5-en-3-one, rely solely on hydrophobic stabilization. While these ligands can still effectively anchor within the binding pocket, their lack of hydrogen bonding may reduce binding specificity and overall stability.

9.3.7.5.5. Protein Tyrosine Phosphatase 1B (PTP1B)

Hydrogen bonding is a critical determinant of ligand stability, specificity, and orientation within the Protein Tyrosine Phosphatase 1B (PTP1B) binding pocket. While hydrophobic interactions provide anchoring forces, hydrogen bonds contribute significantly to ligand specificity and stability. Ligands with multiple hydrogen bonds often display enhanced binding affinity compared to those relying primarily on hydrophobic packing.

Cholesta-4,6-dien-3-ol, benzoate (3.beta.) demonstrates a rich profile of interactions. While it forms stable hydrophobic contacts with residues including PHE182, VAL49, and ALA217, it also establishes multiple hydrogen bonds with TYR20, ARG24, and ARG254. These polar contacts reinforce hydrophobic anchoring and highlight a stronger dual stabilization mechanism.

Across the PTP1B system, Cholesta-4,6-dien-3-ol, benzoate (3.beta.) follows closely, with a robust dual stabilization strategy combining both hydrophobic and multiple hydrogen bond contacts.

9.3.7.6. Hydrogen bonding analysis of anticancer proteins

Protein–Ligand Interaction Profiler (PLIP) analysis of AKT serine/threonine kinase (AKT1), Epidermal Growth Factor Receptor (EGFR), Kirsten Rat Sarcoma Viral Oncogene Homolog (KRAS), Mitogen-Activated Protein Kinase 1 (MAPK1), and Tumour Protein p53(TP53) were listed in Tables 9.80-9.84.

9.3.7.6.1. AKT serine/threonine kinase (AKT1)

Hydrogen bonding serves as a crucial determinant of ligand orientation, stability, and specificity within the AKT1 binding pocket. Ligands that establish multiple hydrogen bonds generally exhibit greater binding affinity and stability, as these interactions complement hydrophobic forces in anchoring the molecule within the active site.

Cholesta-4,6-dien-3-ol, benzoate, (3.beta.)- forms hydrogen bonds with GLU234, ASP292, and PHE438, alongside extensive hydrophobic contacts involving LEU156, VAL164, TYR229, and PHE438. The presence of multiple hydrogen bonds within a largely hydrophobic network implies a well-anchored ligand with improved specificity.

Overall, while hydrophobic contacts are a consistent feature across Cholesta-4,6-dien-3-ol, benzoate, (3.beta.)-, demonstrate a richer hydrogen bonding network, potentially contributing to enhanced binding affinity and specificity.

9.3.7.6.2. Epidermal Growth Factor Receptor (EGFR)

Hydrogen bonding plays a critical role in stabilizing ligand orientation and enhancing binding specificity within the EGFR active site. While hydrophobic interactions form the bulk of stabilizing contacts, the presence of hydrogen bonds and additional π–stacking interactions provides directional anchoring, strengthening ligand engagement with the receptor pocket.

DB-Friedo-B'A'-Neogammacer-5-en-3-one interacts largely via hydrophobic contacts involving VAL726, ALA743, LYS745, THR790, and several LEU residues (844A, 718A). While no strong hydrogen bonding was detected, the multiple van der Waals and alkyl interactions create a highly compact non-polar stabilization pattern within the binding cleft.

DB-Friedo-B'A'-Neogammacer-5-en-3-one relies almost exclusively on hydrophobic stabilization. Modifying sterol scaffolds with additional polar substituents may enhance binding specificity to key catalytic residues of EGFR.

9.3.7.6.3. Kirsten Rat Sarcoma Viral Oncogene Homolog (KRAS)

Hydrogen bonding serves as a key determinant of ligand orientation, stability, and specificity within the KRAS binding pocket. While hydrophobic interactions form the backbone of ligand accommodation, hydrogen bonds provide directional stability that strengthens anchoring and enhances binding affinity.

Chlorogenic acid displays a strong polar interaction profile, forming multiple hydrogen bonds with residues including GLU31, TYR32, ASN39, ASP33, and SER117. These are complemented by extensive hydrophobic contacts with PHE23, ALA114, and VAL16. The combination of abundant hydrogen bonds with non-polar packing suggests a highly stable and specific binding orientation, making this ligand particularly effective in engaging the KRAS pocket.

Overall, Chlorogenic acid stand out for their extensive hydrogen-bonding networks that reinforce both binding strength and specificity.

Table 9.80: Protein–Ligand Interaction Profiler (PLIP) analysis of AKT serine/threonine kinase (AKT1)

Complex	Residue	Amino acids	Distance (Å)	Interactions Type
Cholesta-4,6-dien-3-ol, 3-benzoate, (3beta)-	156A	LEU	3.62	Hydrophobic
	164A	VAL	3.59	
	164A	VAL	3.63	
	177A	ALA	3.78	
	229A	TYR	3.83	
	230A	ALA	3.98	
	278A	GLU	3.91	
	291A	THR	3.90	
	438A	PHE	3.98	
	438A	PHE	3.63	
	442A	PHE	3.79	
	292A	ASP	3.44	Hydrogen Bonds

(A: Chain A)

Table 9.81: Protein–Ligand Interaction Profiler (PLIP) analysis of Epidermal Growth Factor Receptor (EGFR))

Complex	Residue	Amino acids	Distance (Å)	Interactions Type
D:B-Friedo-B':A'-Neogammacer-5-en-3-one	718A	LEU	3.51	Hydrophobic
	718A	LEU	3.58	
	723A	PHE	3.53	
	723A	PHE	3.50	
	723A	PHE	3.55	
	726A	VAL	3.29	
	743A	ALA	3.53	
	745A	LYS	3.85	
	790A	THR	3.68	
	844A	LEU	3.75	
	844A	LEU	3.30	

(A: Chain A)

Table 9.82: Protein–Ligand Interaction Profiler (PLIP) analysis of Kirsten Rat Sarcoma Viral Oncogene Homolog (KRAS)

Complex	Residue	Amino acids	Distance (Å)	Interactions Type
Chlorogenic acid	18A	ALA	3.92	Hydrophobic
	28A	PHE	3.71	
	28A	PHE	3.57	
	32A	TYR	3.69	
	32A	TYR	3.68	
	117A	LYS	3.77	
	146A	ALA	3.39	
	12A	ASP	2.97	Hydrogen Bonds
	13A	GLY	3.11	
	15A	GLY	2.34	
	16A	LYS	2.34	
	16A	LYS	3.17	
	17A	SER	2.94	
	31A	GLU	2.35	
	32A	TYR	3.44	
	33A	ASP	2.95	
	117A	LYS	2.36	
	117A	LYS	3.37	
	145A	SER	2.44	
	146A	ALA	2.44	
	147A	LYS	2.34	

(A: Chain A)

Table 9.83: Protein–Ligand Interaction Profiler (PLIP) analysis of Mitogen-Activated Protein Kinase 1 (MAPK1)

Complex	Residue	Amino acids	Distance (Å)	Interactions Type
Ellagic acid	39A	VAL	3.62	Hydrophobic
	52A	ALA	3.91	
	156A	LEU	3.71	
	156A	LEU	3.66	
	33A	GLU	2.73	Hydrogen Bonds
	105A	GLN	3.20	
	106A	ASP	2.24	
	108A	MET	2.07	

(A: Chain A)

Table 9.84: Protein–Ligand Interaction Profiler (PLIP) analysis of Tumour Protein p53(TP53)

Complex	Residue	Aino acids	Distance (Å)	Interactions Type
Quercetin	221A	GLU	3.83	Hydrophobic
	221A	GLU	3.75	
	230A	THR	3.87	
	232A	ILE	3.97	
	200A	ASN	2.39	Hydrogen Bonds
	219A	PRO	2.00	
	221A	GLU	2.82	
	221A	GLU	2.13	
	224A	GLU	2.00	
	224A	GLU	3.49	
	229A	CYS	2.65	
	231A	THR	2.73	
	231A	THR	2.73	

(A: Chain A)

9.3.7.6.4. Mitogen-Activated Protein Kinase 1 (MAPK1)

Hydrogen bonding plays a central role in stabilizing ligand orientation and enhancing binding specificity within the MAPK1 active site. While hydrophobic interactions contribute to core stabilization, hydrogen bonds provide the directional anchoring necessary for improving affinity and molecular recognition.

Ellagic acid demonstrates the most extensive polar interaction profile, forming hydrogen bonds with GLU33, ASP106, ASP108, and GLN153, alongside hydrophobic interactions with residues VAL39, LEU52, and LEU156. The abundance of hydrogen bonds provides significant binding specificity, making Ellagic Acid a strong candidate for MAPK1 inhibition.

Overall, Ellagic acid stand out as the most promising ligands due to their dense hydrogen bonding networks, which provide improved specificity and orientation in the MAPK1 binding pocket.

9.3.7.6.5. Tumour Protein p53(TP53)

Hydrogen bonding is a crucial determinant of ligand orientation, specificity, and stability within the TP53 binding pocket. While hydrophobic forces contribute to core stabilization, hydrogen bonds provide directed anchoring, enhancing both affinity and molecular recognition.

Quercetin also forms multiple hydrogen bonds with GLU221, CYS292, GLN293, and THR291, while engaging hydrophobically with ASN200, PRO223, and GLU221. This dual pattern reinforces both stability and binding orientation, suggesting high binding efficiency in the TP53 binding pocket. Overall, flavonoids, Quercetin exhibit the strongest hydrogen bonding networks, providing significant stabilization and specificity.

9.3.8. Pharmacokinetic profiling of top-hit ligands

In this study, the leading phytocompounds exhibiting the highest binding affinities against the selected protein targets for antioxidant, antimicrobial, anthelmintic, anti-inflammatory, antidiabetic, and anticancer properties were

subsequently analyzed for their pharmacokinetic attributes using the SwissADME web server. Canonical SMILES notations for each compound were retrieved from the PubChem database to provide a consistent and standardized molecular format for computational assessment. These SMILES were then input into SwissADME to predict key parameters, including physicochemical properties, absorption, distribution, metabolism, and overall drug-likeness, offering a comprehensive insight into their potential as therapeutic candidates (Tables 9.85-9.90).

9.3.9. Physicochemical properties

SwissADME analysis provided essential molecular descriptors for the selected phytocompounds, such as molecular weight (MW), fraction of sp^3 carbons (Csp^3), number of heavy atoms, rotatable bonds, molar refractivity (MR), and total polar surface area (TPSA). These parameters serve as key determinants of drug-likeness, shaping factors like oral absorption, bioavailability, and membrane permeability. Compounds that fall within favorable ranges for these metrics are more likely to demonstrate superior pharmacokinetic behaviour, whereas values outside these ranges may compromise solubility or hinder efficient transport across biological membranes (Tables 9.91-9.96).

9.3.10. Drug-likeness

SwissADME-based drug-likeness evaluation incorporated key parameters, including hydrogen bond acceptors (HBA), hydrogen bond donors (HBD), and the number of Lipinski's rule violations. According to the rule of five, compounds with HBA $\leq$ 10, HBD $\leq$ 5, molecular weight (MW) $\leq$ 500 g/mol, and LogP $\leq$ 5 are more likely to exhibit good oral bioavailability. Molecules with no violations are typically preferred for oral delivery, while those presenting one or more violations may need specialized formulation approaches to enhance their bioavailability (Tables 9.97-9.102).

9.3.11. Medicinal chemistry

The medicinal chemistry profiling in SwissADME assessed multiple parameters, including solubility classification (Silicos-IT), gastrointestinal (GI)

Table 9.85: Canonical Simplified Molecular Input Line Entry System (SMILES) of selected antioxidant bioactive compounds

Ligand	SMILES
DB-Friedo-B'A'-Neogammacer-5-en-3-one	CC(C)C1CCC2C1(C)CCC3(C)C4CC=C5C(CCC(=O)C5(C)C)C4(C)CCC23C
Kaempferol	C1=CC(=CC=C1C2=C(C(=O)C3=C(C=C(C=C3O2)O)O)O)O
Maslinic acid	C[C@@]12CC[C@@H]3[C@@]([C@H]1CC=C4[C@]2(CC[C@@]5([C@H]4CC(CC5)(C)C)C(=O)O)C)(C[C@H]([C@@H](C3(C)C)O)O)C
Oleanolic acid	C[C@]12CC[C@@H](C([C@@H]1CC[C@@]3([C@@H]2CC=C4[C@]3(CC[C@@]5([C@H]4CC(CC5)(C)C)C(=O)O)C)C)(C)C)O

Table 9.86: Canonical Simplified Molecular Input Line Entry System (SMILES) of selected antimicrobial bioactive compounds

Ligand	SMILES
2-Phenyl-4H-chromen-4-one	C1=CC=C(C=C1)C2=CC(=O)C3=CC=CC=C3O2
Oleanolic acid	C[C@]12CC[C@@H](C([C@@H]1CC[C@@]3([C@@H]2CC=C4[C@]3(CC[C@@]5([C@H]4CC(CC5)(C)C)C(=O)O)C)C)(C)C)O
Ellagic acid	C1=C2C3=C(C(=C1O)O)OC(=O)C4=CC(=C(C(=C43)OC2=O)O)O
Cholesta-4,6-dien-3-ol, benzoate, (3.beta.)-	CC(C)CCCC(C)C1CCC2C1(CCC3C2C=CC4=CC(CCC34C)OC(=O)C5=CC=CC=C5)C

Table 9.87: Canonical Simplified Molecular Input Line Entry System (SMILES) of selected anthelmintic bioactive compounds

Ligand	SMILES
Oleanolic acid	C[C@]12CC[C@@H](C([C@@H]1CC[C@@]3([C@@H]2CC=C4[C@]3(CC[C@@]5([C@H]4CC(CC5)(C)C)C(=O)O)C)C)(C)C)O
Maslinic acid	C[C@@]12CC[C@@H]3[C@@]([C@H]1CC=C4[C@]2(CC[C@@]5([C@H]4CC(CC5)(C)C)C(=O)O)C)(C[C@H]([C@@H](C3(C)C)O)O)C
Vitamin E	CC1=C(C2=C(CC[C@@](O2)(C)CCC[C@H](C)CCC[C@H](C)CCCC(C)C)C(=C1O)C)C

Table 9.88: Canonical Simplified Molecular Input Line Entry System (SMILES) of selected anti-inflammatory bioactive compounds

Ligand	SMILES
Maslinic Acid	C[C@@]12CC[C@@H]3[C@@]([C@H]1CC=C4[C@]2(CC[C@@]5([C@H]4CC(CC5)(C)C)C(=O)O)C)(C[C@H]([C@@H](C3(C)C)O)O)C
DB-Friedo-B'A'-Neogammacer-5-en-3-one	CC(C)C1CCC2C1(C)CCC3(C)C4CC=C5C(CCC(=O)C5(C)C)C4(C)CCC23C
Cholesta-4,6-dien-3-ol, benzoate, (3.beta.)-	CC(C)CCCC(C)C1CCC2C1(CCC3C2C=CC4=CC(CCC34C)OC(=O)C5=CC=CC=C5)C
Ellagic Acid	C1=C2C3=C(C(=C1O)O)OC(=O)C4=CC(=C(C(=C43)OC2=O)O)O

Table 9.89: Canonical Simplified Molecular Input Line Entry System (SMILES) of selected antidiabetic bioactive compounds

Ligand	SMILES
DB-Friedo-B'A'-Neogammacer-5-en-3-one	CC(C)C1CCC2C1(C)CCC3(C)C4CC=C5C(CCC(=O)C5(C)C)C4(C)CCC23C
Cholesta-4,6-dien-3-ol, benzoate, (3.beta.)-	CC(C)CCCC(C)C1CCC2C1(CCC3C2C=CC4=CC(CCC34C)OC(=O)C5=CC=CC=C5)C

Table 9.90: Canonical Simplified Molecular Input Line Entry System (SMILES) of selected anticancer bioactive compounds

Ligand	SMILES
Cholesta-4,6-dien-3-ol, benzoate,(3.beta.)-	CC(C)CCCC(C)C1CCC2C1(CCC3C2C=CC4=CC(CCC34C)OC(=O)C5=CC=CC=C5)C
DB-Friedo-B'A'-Neogammacer-5-en-3-one	CC(C)C1CCC2C1(C)CCC3(C)C4CC=C5C(CCC(=O)C5(C)C)C4(C)CCC23C
Chlorogenic Acid	C1[C@H]([C@H]([C@@H](C[C@@]1(C(=O)O)O)OC(=O)/C=C/C2=CC(=C(C=C2)O)O)O)O
Ellagic Acid	C1=C2C3=C(C(=C1O)O)OC(=O)C4=CC(=C(C(=C43)OC2=O)O)O
Quercetin	C1=CC(=C(C=C1C2=C(C(=O)C3=C(C=C(C=C3O2)O)O)O)O)O

Table 9.91: Physicochemical properties of selected antioxidant bioactive compounds

Ligand	Molecular Weight (DA)	Heavy atoms	Fraction of sp3 carbon (Csp3)	Rotatable bonds	Molar Refractivity (MR) (cm^3/mol).	Total Polar Surface Area (TPSA) ($Å^2$).
DB-Friedo-B'A'-Neogammacer-5-en-3-one	424.7	31	0.9	1	134.18	17.07
Kaempferol	286.24	21	0	1	76.01	111.13
Maslinic Acid	472.7	34	0.9	1	137.82	77.76
Oleanolic Acid	456.7	33	0.9	1	136.65	57.53

Table 9.92: Physicochemical properties of selected antimicrobial bioactive compounds

Ligand	Molecular Weight (Da)	Heavy atoms	Fraction of sp3 carbon (Csp3)	Rotatable bonds	Molar Refractivity (MR) (cm^3/mol).	Total Polar Surface Area (TPSA) ($Å^2$).
2-Phenyl-4H-chromen-4-one	222.24	17	0	1	67.92	30.21
Oleanolic Acid	456.7	33	0.9	1	136.65	57.53
Ellagic Acid	302.19	22	0	0	75.31	141.34
Cholesta-4,6-dien-3-ol, benzoate, (3.beta.)-	488.74	36	0.68	8	152.78	26.3

Table 9.93: Physicochemical properties of selected anthelmintic bioactive compounds

Ligand	Molecular Weight (Da)	Heavy atoms	Fraction of sp3 carbon (Csp3)	Rotatable bonds	Molar Refractivity (MR) (cm^3/mol).	Total Polar Surface Area (TPSA) ($Å^2$).
Oleanolic Acid	456.7	33	0.9	1	136.65	57.53
Maslinic Acid	472.7	34	0.9	1	137.82	77.76
Vitamin E	430.71	31	0.79	12	139.27	29.46

Table 9.94: Physicochemical properties of selected anti-inflammatory bioactive compounds

Ligand	Molecular Weight (Da)	Heavy atoms	Fraction of sp3 carbon (Csp3)	Rotatable bonds	Molar Refractivity (MR) (cm^3/mol).	Total Polar Surface Area (TPSA) ($Å^2$).
Maslinic Acid	472.7	34	0.9	1	137.82	77.76
DB-Friedo-B'A'-Neogammacer-5-en-3-one	424.7	31	0.9	1	134.18	17.07
Cholesta-4,6-dien-3-ol, benzoate, (3.beta.)-	488.74	36	0.68	8	152.78	26.3
Ellagic Acid	302.19	22	0	0	75.31	141.34

Table 9.95: Physicochemical properties of selected antidiabetic bioactive compounds

Ligand	Molecular Weight (Da)	Heavy atoms	Fraction of sp3 carbon (Csp3)	Rotatable bonds	Molar Refractivity (MR) (cm^3/mol).	Total Polar Surface Area (TPSA) ($Å^2$).
DB-Friedo-B'A'-Neogammacer-5-en-3-one	424.7	31	0.9	1	134.18	17.07
Cholesta-4,6-dien-3-ol, benzoate, (3.beta.)-	488.74	36	0.68	8	152.78	26.3

Table 9.96: Physicochemical properties of selected anticancer bioactive compounds

Ligand	Molecular Weight (Da)	Heavy atoms	Fraction of sp3 carbon (Csp3)	Rotatable bonds	Molar Refractivity (MR) (cm^3/mol).	Total Polar Surface Area (TPSA) ($Å^2$).
Cholesta-4,6-dien-3-ol, benzoate, (3.beta.)-	488.74	36	0.68	8	152.78	26.3
DB-Friedo-B'A'-Neogammacer-5-en-3-one	424.7	31	0.9	1	134.18	17.07
Chlorogenic Acid	354.31	25	0.38	5	83.5	164.75
Ellagic Acid	302.19	22	0	0	75.31	141.34
Quercetin	302.24	22	0	1	78.03	131.36

Table 9.97: Drug-likeness properties of selected antioxidant bioactive compounds

Ligand	Molecular weight (Da)	H-bond acceptors	H-bond donors	Lipinski violations
DB-Friedo-B'A'-Neogammacer-5-en-3-one	424.7	1	0	1
Kaempferol	286.24	6	4	0
Maslinic acid	472.7	4	3	1
Oleanolic acid	456.7	3	2	1

Table 9.98: Drug-likeness properties of selected antimicrobial bioactive compounds

Ligand	Molecular weight (Da)	H-bond acceptors	H-bond donors	Lipinski violations
2-Phenyl-4H-chromen-4-one	222.24	2	0	0
Oleanolic Acid	456.7	3	2	1
Ellagic Acid	302.19	8	4	0
Cholesta-4,6-dien-3-ol, benzoate, (3.beta.)-	488.74	2	0	1

9.99: Drug-likeness properties of selected anthelmintic bioactive compounds

Ligand	Molecular weight (Da)	H-bond acceptors	H-bond donors	Lipinski violations
Oleanolic Acid	456.7	3	2	1
Maslinic Acid	472.7	4	3	1
Vitamin E	430.71	2	1	1

Table 9.100: Drug-likeness properties of selected anti-inflammatory bioactive compounds

Ligand	Molecular weight (Da)	H-bond acceptors	H-bond donors	Lipinski violations
Maslinic Acid	472.7	4	3	1
DB-Friedo-B'A'-Neogammacer-5-en-3-one	424.7	1	0	1
Cholesta-4,6-dien-3-ol, benzoate, (3.beta.)-	488.74	2	0	1
Ellagic Acid	302.19	8	4	0

Table 9.101: Drug-likeness properties of selected antidiabetic bioactive compounds

Ligand	Molecular weight (Da)	H-bond acceptors	H-bond donors	Lipinski violations
DB-Friedo-B'A'-Neogammacer-5-en-3-one	424.7	1	0	1
Cholesta-4,6-dien-3-ol, benzoate, (3.beta.)-	488.74	2	0	1

Table 9.102: Drug-likeness properties of selected anticancer bioactive compounds

Ligand	Molecular weight (Da)	H-bond acceptors	H-bond donors	Lipinski violations
Cholesta-4,6-dien-3-ol, benzoate, (3.beta.)-	488.74	2	0	1
DB-Friedo-B'A'-Neogammacer-5-en-3-one	424.7	1	0	1
Chlorogenic Acid	354.31	9	6	1
Ellagic Acid	302.19	8	4	0
Quercetin	302.24	7	5	0

Table 9.103: Medicinal chemistry properties of selected antioxidant bioactive compounds

Ligand	Molecular weight (Da)	Silicos-IT class	GI absorption	Bioavailability Score	PAINS alerts	Synthetic Accessibility
DB-Friedo-B'A'-Neogammacer-5-en-3-one	424.7	Poorly soluble	Low	0.55	0	6.37
Kaempferol	286.24	Soluble	High	0.55	0	3.14
Maslinic acid	472.7	Moderately soluble	High	0.56	0	6.22
Oleanolic acid	456.7	Poorly soluble	Low	0.85	0	6.08

Table 9.104: Medicinal chemistry properties of selected antimicrobial bioactive compounds

Ligand	Molecular weight (Da)	Silicos-IT class	GI absorption	Bioavailability Score	PAINS alerts	Synthetic Accessibility
2-Phenyl-4H-chromen-4-one	222.24	Poorly soluble	High	0.55	0	2.88
Oleanolic acid	456.7	Poorly soluble	Low	0.85	0	6.08
Ellagic acid	302.19	Soluble	High	0.55	1	3.17
Cholesta-4,6-dien-3-ol, benzoate, (3.beta.)-	488.74	Poorly soluble	Low	0.55	0	6.28

Table 9.105: Medicinal chemistry properties of selected anthelmintic bioactive compounds

Ligand	Molecular weight (Da)	Silicos-IT class	GI absorption	Bioavailability Score	PAINS alerts	Synthetic Accessibility
Oleanolic acid	456.7	Poorly soluble	Low	0.85	0	6.08
Maslinic acid	472.7	Moderately soluble	High	0.56	0	6.22
Vitamin E	430.71	Poorly soluble	Low	0.55	0	5.17

Table 9.106: Medicinal chemistry properties of selected anti-inflammatory bioactive compounds

Ligand	Molecular weight (Da)	Silicos-IT class	GI absorption	Bioavailability Score	PAINS alerts	Synthetic Accessibility
Maslinic Acid	472.7	Moderately soluble	High	0.56	0	6.22
DB-Friedo-B'A'-Neogammacer-5-en-3-one	424.7	Poorly soluble	Low	0.55	0	6.37
Cholesta-4,6-dien-3-ol, benzoate, (3.beta.)-	488.74	Poorly soluble	Low	0.55	0	6.28
Ellagic Acid	302.19	Soluble	High	0.55	1	3.17

Table 9.107: Medicinal chemistry properties of selected antidiabetic bioactive compounds

Ligand	Molecular weight (Da)	Silicos-IT class	GI absorption	Bioavailability Score	PAINS alerts	Synthetic Accessibility
DB-Friedo-B'A'-Neogammacer-5-en-3-one	424.7	Poorly soluble	Low	0.55	0	6.37
Cholesta-4,6-dien-3-ol, benzoate, (3.beta.)-	488.74	Poorly soluble	Low	0.55	0	6.28

Table 9.108: Medicinal chemistry properties of selected anticancer bioactive compounds

Ligand	Molecular weight (Da)	Silicos-IT class	GI absorption	Bioavailability Score	PAINS alerts	Synthetic Accessibility
Cholesta-4,6-dien-3-ol, benzoate, (3.beta.)-	488.74	Poorly soluble	Low	0.55	0	6.28
DB-Friedo-B'A'-Neogammacer-5-en-3-one	424.7	Poorly soluble	Low	0.55	0	6.37
Chlorogenic Acid	354.31	Soluble	Low	0.11	1	4.16
Ellagic Acid	302.19	Soluble	High	0.55	1	3.17
Quercetin	302.24	Soluble	High	0.55	1	3.23

Table 9.109: Metabolic properties of selected antioxidant bioactive compounds

Ligand	Molecular weight (Da)	P-glycoprotein (P-gp) substrate	CYP1A2 inhibitor	CYP2C19 inhibitor	CYP2C9 inhibitor	CYP2D6 inhibitor	CYP3A4 inhibitor
DB-Friedo-B'A'-Neogammacer-5-en-3-one	424.7	No	No	No	No	No	No
Kaempferol	286.24	No	Yes	No	No	Yes	Yes
Maslinic acid	472.7	Yes	No	No	No	No	No
Oleanolic acid	456.7	No	No	No	No	No	No

Table 9.110: Metabolic properties of selected antimicrobial bioactive compounds

Ligand	Molecular weight (Da)	P-glycoprotein (P-gp) substrate	CYP1A2 inhibitor	CYP2C19 inhibitor	CYP2C9 inhibitor	CYP2D6 inhibitor	CYP3A4 inhibitor
2-Phenyl-4H-chromen-4-one	222.24	No	Yes	Yes	No	No	No
Oleanolic acid	456.7	No	No	No	No	No	No
Ellagic acid	302.19	No	Yes	No	No	No	No
Cholesta-4,6-dien-3-ol, benzoate, (3.beta.)-	488.74	No	No	No	No	No	No

Table 9.111: Metabolic properties of selected anthelmintic bioactive compounds

Ligand	Molecular weight (Da)	P-glycoprotein (P-gp) substrate	CYP1A2 inhibitor	CYP2C19 inhibitor	CYP2C9 inhibitor	CYP2D6 inhibitor	CYP3A4 inhibitor
Oleanolic acid	456.7	No	No	No	No	No	No
Maslinic acid	472.7	Yes	No	No	No	No	No
Vitamin E	430.71	Yes	No	No	No	No	No

Table 9.112: Metabolic properties of selected anti-inflammatory bioactive compounds

Ligand	Molecular weight (Da)	P-glycoprotein (P-gp) substrate	CYP1A2 inhibitor	CYP2C19 inhibitor	CYP2C9 inhibitor	CYP2D6 inhibitor	CYP3A4 inhibitor
Maslinic Acid	472.7	Yes	No	No	No	No	No
DB-Friedo-B'A'-Neogammacer-5-en-3-one	424.7	No	No	No	No	No	No
Cholesta-4,6-dien-3-ol, benzoate, (3.beta.)-	488.74	No	No	No	No	No	No
Ellagic acid	302.19	No	Yes	No	No	No	No

Table 9.113: Metabolic properties of selected antidiabetic bioactive compounds

Ligand	Molecular weight (Da)	P-glycoprotein (P-gp) substrate	CYP1A2 inhibitor	CYP2C19 inhibitor	CYP2C9 inhibitor	CYP2D6 inhibitor	CYP3A4 inhibitor
DB-Friedo-B'A'-Neogammacer-5-en-3-one	424.7	No	No	No	No	No	No
Cholesta-4,6-dien-3-ol, benzoate, (3.beta.)-	488.74	No	No	No	No	No	No

Table 9.114: Metabolic properties of selected anticancer bioactive compounds

Ligand	Molecular weight (Da)	P-glycoprotein (P-gp) substrate	CYP1A2 inhibitor	CYP2C19 inhibitor	CYP2C9 inhibitor	CYP2D6 inhibitor	CYP3A4 inhibitor
Cholesta-4,6-dien-3-ol, benzoate, (3.beta.)-	488.74	No	No	No	No	No	No
DB-Friedo-B'A'-Neogammacer-5-en-3-one	424.7	No	No	No	No	No	No
Chlorogenic acid	354.31	No	No	No	No	No	No
Ellagic acid	302.19	No	Yes	No	No	No	No
Quercetin	302.24	No	Yes	No	No	Yes	Yes

Table 9.115: Toxicity of selected antioxidant bioactive compounds

Ligand	Hepato	Neuro	Nephro	Respi	Cardio	Carcino	Immuno	Mutagen	Cyto
DB-Friedo-B'A'-Neogammacer-5-en-3-one	Inactive	Active	Inactive	Active	Inactive	Inactive	Active	Inactive	Inactive
Kaempferol	Inactive	Inactive	Active	Active	Inactive	Inactive	Inactive	Inactive	Inactive
Maslinic acid	Inactive	Inactive	Inactive	Active	Active	Active	Active	Inactive	Inactive
Oleanolic Acid	Active	Inactive	Inactive	Active	Active	Active	Active	Inactive	Inactive

Table 9.116: Toxicity of selected antimicrobial bioactive compounds

Ligand	Hepato	Neuro	Nephro	Respi	Cardio	Carcino	Immuno	Mutagen	Cyto
2-Phenyl-4H-chromen-4-one	Inactive	Active	Inactive	Inactive	Active	Active	Inactive	Inactive	Active
Oleanolic acid	Active	Inactive	Inactive	Active	Active	Active	Active	Inactive	Inactive
Ellagic acid	Inactive	Inactive	Active	Active	Inactive	Active	Inactive	Inactive	Inactive
Cholesta-4,6-dien-3-ol, benzoate, (3.beta.)-	Inactive	Inactive	Inactive	Active	Active	Active	Active	Inactive	Inactive

Table 9.117: Toxicity of selected anthelmintic bioactive compounds

Ligand	Hepato	Neuro	Nephro	Respi	Cardio	Carcino	Immuno	Mutagen	Cyto
Oleanolic acid	Active	Inactive	Inactive	Active	Active	Active	Active	Inactive	Inactive
Maslinic acid	Inactive	Inactive	Inactive	Active	Active	Active	Active	Inactive	Inactive
Vitamin E	Inactive	Inactive	Inactive	Active	Inactive	Inactive	Inactive	Inactive	Inactive

Table 9.118: Toxicity of selected anti-inflammatory bioactive compounds

Ligand	Hepato	Neuro	Nephro	Respi	Cardio	Carcino	Immuno	Mutagen	Cyto
Maslinic acid	Inactive	Inactive	Inactive	Active	Active	Active	Active	Inactive	Inactive
DB-Friedo-B'A'-Neogammacer-5-en-3-one	Inactive	Active	Inactive	Active	Inactive	Inactive	Active	Inactive	Inactive
Cholesta-4,6-dien-3-ol, benzoate, (3.beta.)-	Inactive	Inactive	Inactive	Active	Active	Active	Active	Inactive	Inactive
Ellagic acid	Inactive	Inactive	Active	Active	Inactive	Active	Inactive	Inactive	Inactive

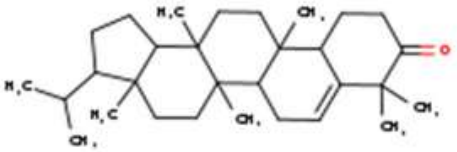
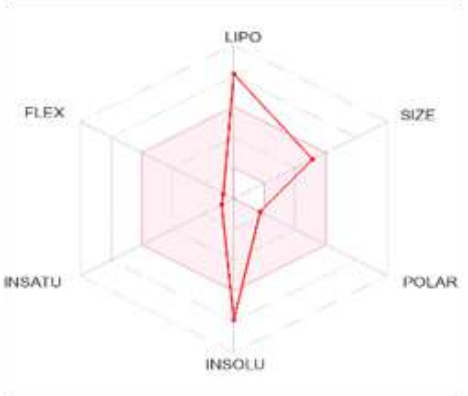
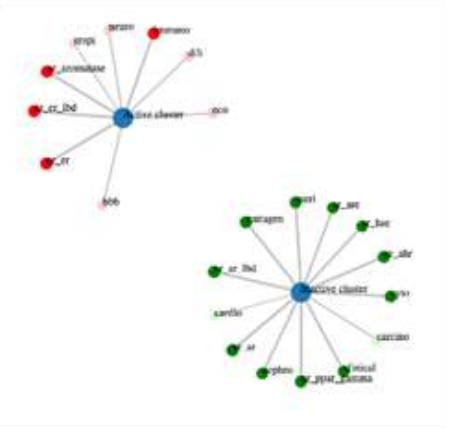
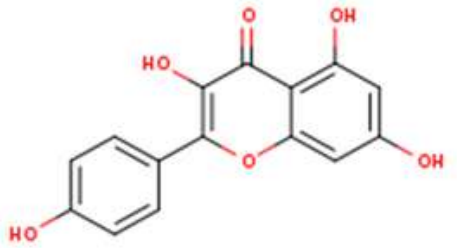
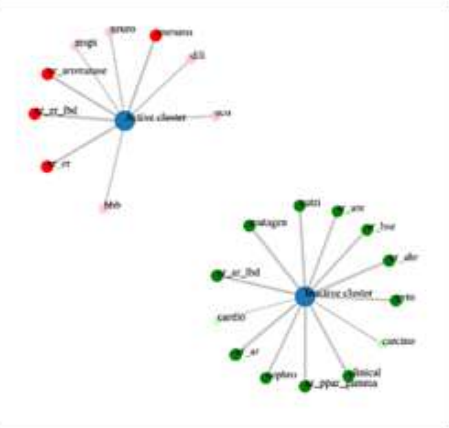
Table 9.119: Toxicity of selected antidiabetic bioactive compounds

Ligand	Hepato	Neuro	Nephro	Respi	Cardio	Carcino	Immuno	Mutagen	Cyto
DB-Friedo-B'A'-Neogammacer-5-en-3-one	Inactive	Active	Inactive	Active	Inactive	Inactive	Active	Inactive	Inactive
Cholesta-4,6-dien-3-ol, benzoate, (3.beta.)-	Inactive	Inactive	Inactive	Active	Active	Active	Active	Inactive	Inactive

Table 9.120: Toxicity of selected anticancer bioactive compounds

Ligand	Hepato	Neuro	Nephro	Respi	Cardio	Carcino	Immuno	Mutagen	Cyto
Cholesta-4,6-dien-3-ol, benzoate, (3.beta.)-	Inactive	Inactive	Inactive	Active	Active	Active	Active	Inactive	Inactive
DB-Friedo-B'A'-Neogammacer-5-en-3-one	Inactive	Active	Inactive	Active	Inactive	Inactive	Active	Inactive	Inactive
Chlorogenic acid	Active	Active	Inactive	Active	Inactive	Inactive	Active	Inactive	Inactive
Ellagic acid	Inactive	Inactive	Active	Active	Inactive	Active	Inactive	Inactive	Inactive
Quercetin	Inactive	Inactive	Active	Active	Inactive	Active	Inactive	Active	Inactive

Table 9.121: ADMET (Absorption, Distribution, Metabolism, Excretion, and Toxicity) profiling of top antioxidant phytocompounds

Compound	Structure	Bioradar	Toxicity
DB-Friedo-B'A'-Neogammacer-5-en-3-one			
Kaempferol			

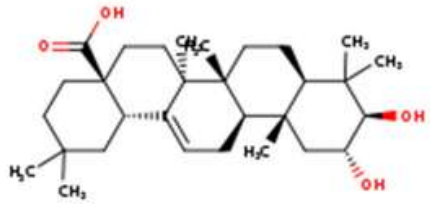
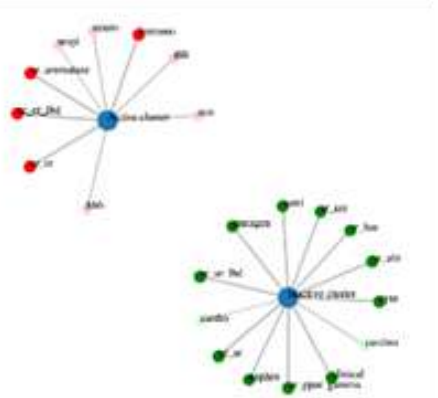
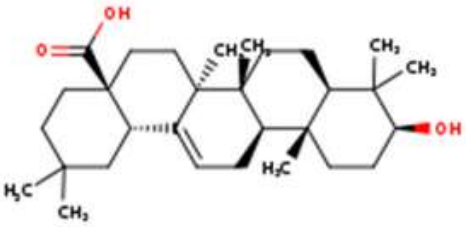
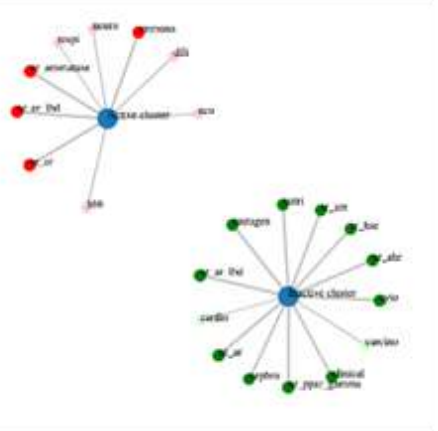
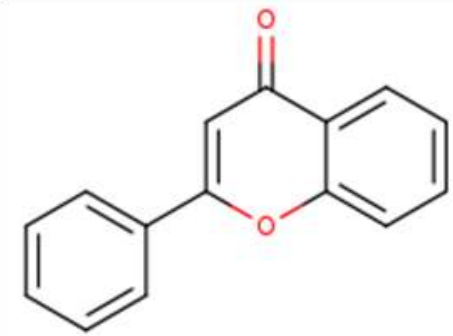
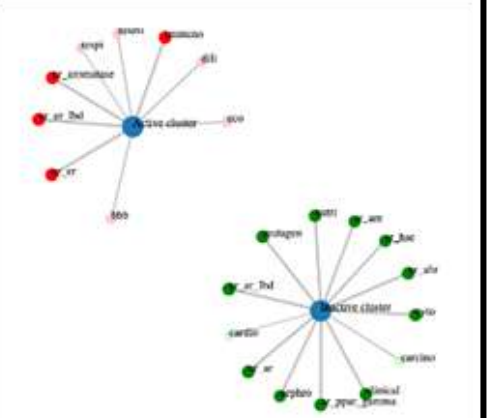
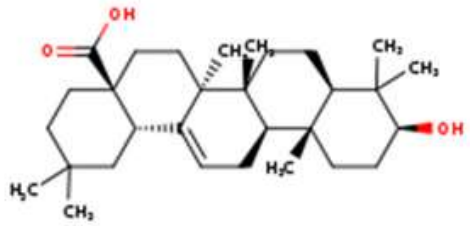
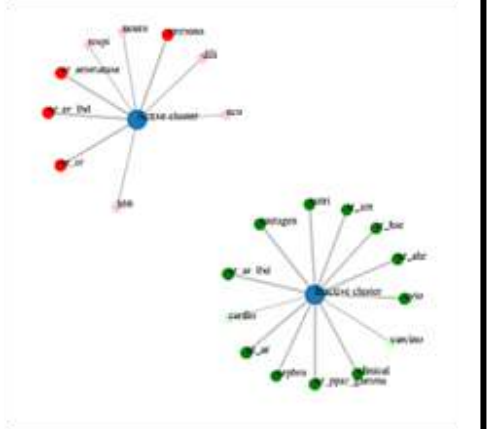
Compound	Structure	Bioradar	Toxicity
Maslinic acid			
Oleanolic acid			

Table 9.122: ADMET (Absorption, Distribution, Metabolism, Excretion, and Toxicity) profiling of top antimicrobial phytocompounds

Compound	Structure	Bioradar	Toxicity
2-Phenyl-4H-chromen-4-one			
Oleanolic acid			

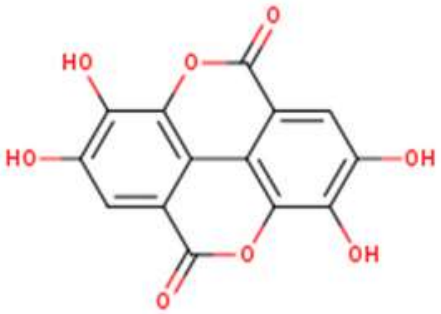
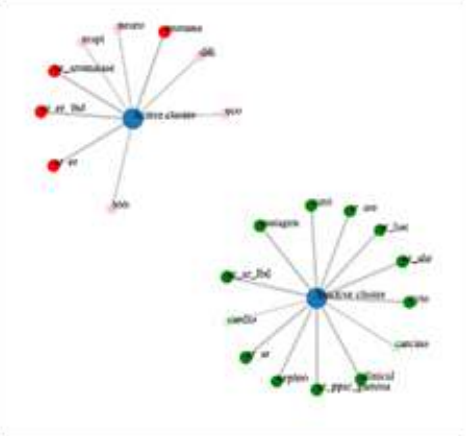
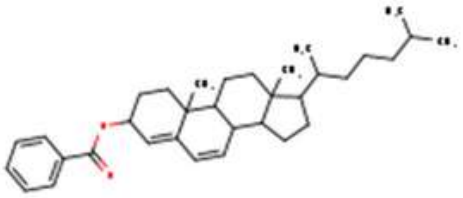
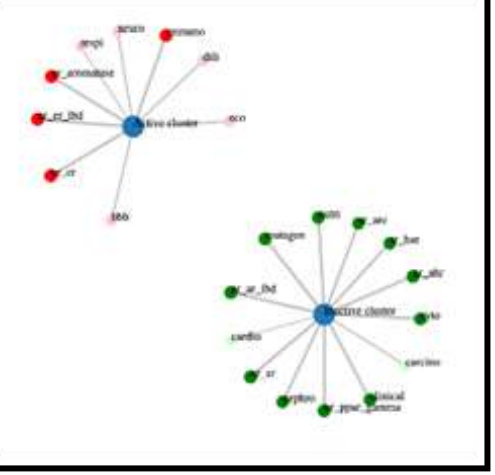
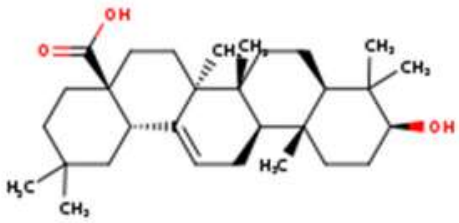
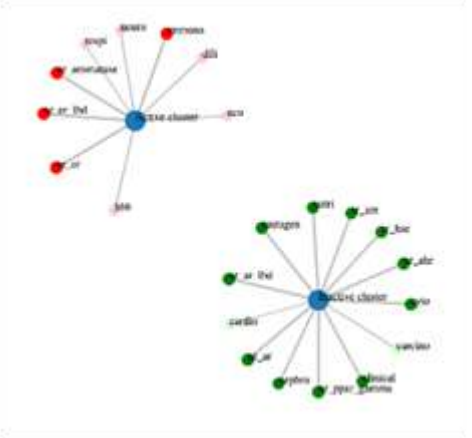
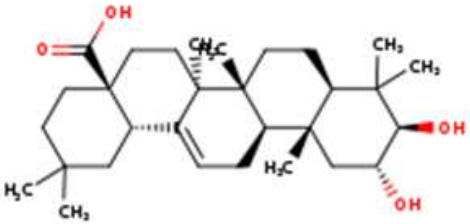
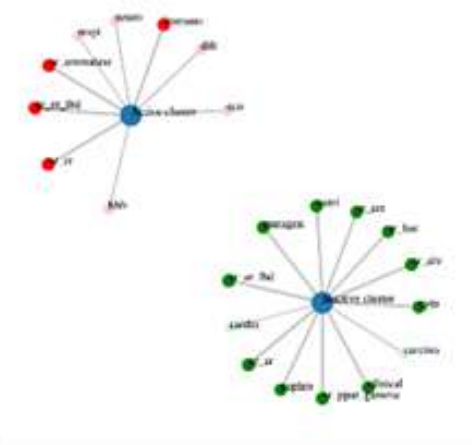
Compound	Structure	Bioradar	Toxicity
Ellagic acid			
Cholesta-4,6-dien-3-ol, benzoate, (3.beta.)-			

Table 9.123: ADMET (Absorption, Distribution, Metabolism, Excretion, and Toxicity) profiling of top anthelmintic phytocompounds

Compound	Structure	Bioradar	Toxicity
Oleanolic acid			
Maslinic acid			

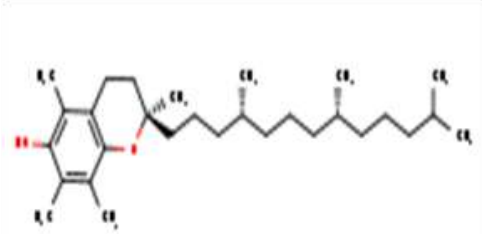
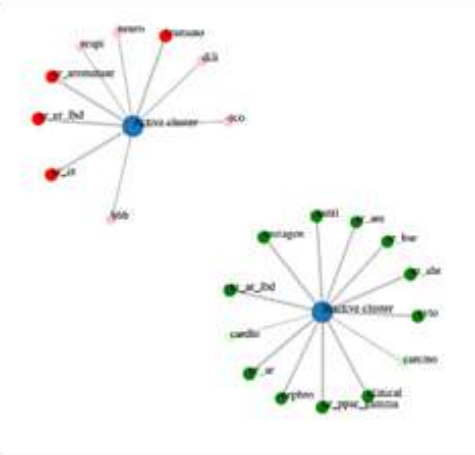
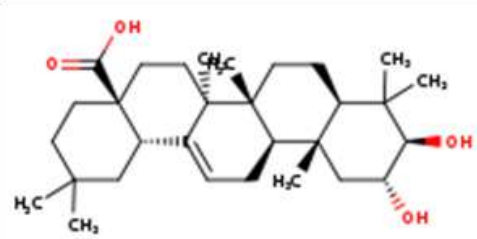
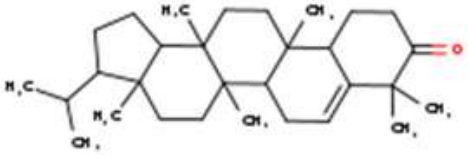
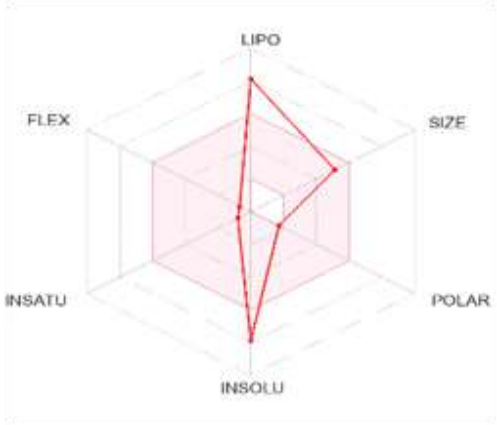
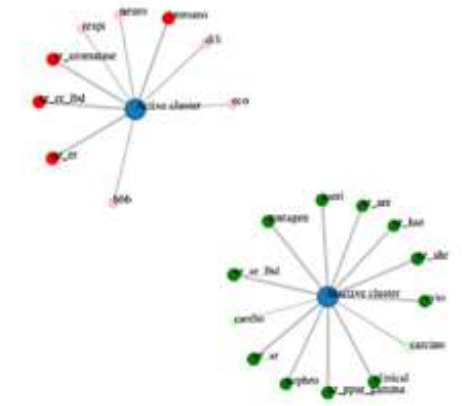
Compound	Structure	Bioradar	Toxicity
Vitamin E			

Table 9.124: ADMET (Absorption, Distribution, Metabolism, Excretion, and Toxicity) profiling of top anti-inflammatory phytocompounds

Compound	Structure	Bioradar	Toxicity
Maslinic Acid			
DB-Friedo-B'A'-Neogammacer-5-en-3-one			

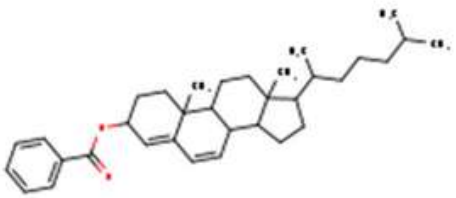
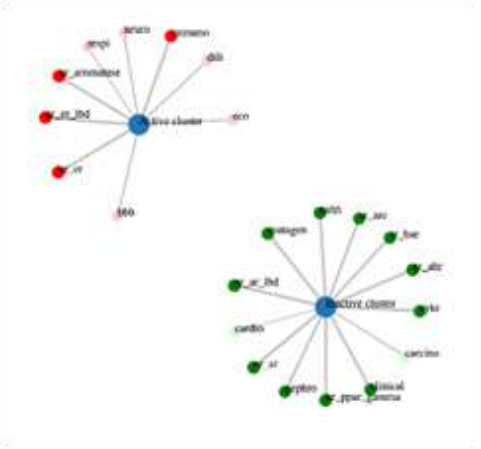
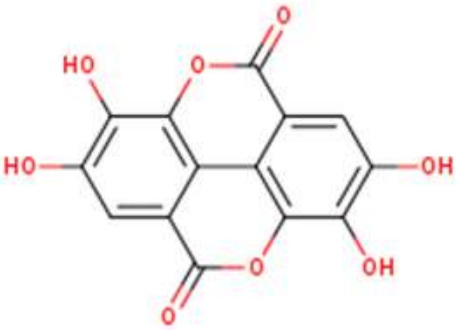
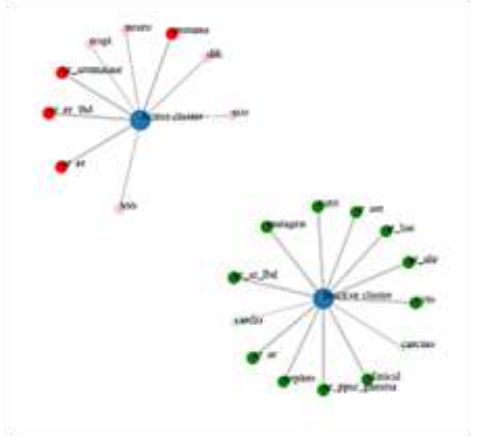
Compound	Structure	Bioradar	Toxicity
Cholesta-4,6-dien-3-ol, benzoate, (3.beta.)-			
Ellagic Acid			

Table 9.125: ADMET (Absorption, Distribution, Metabolism, Excretion, and Toxicity) profiling of top antidiabetic phytocompounds

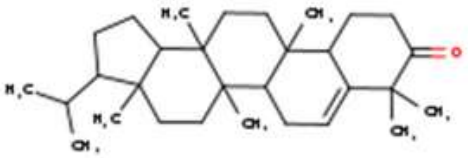
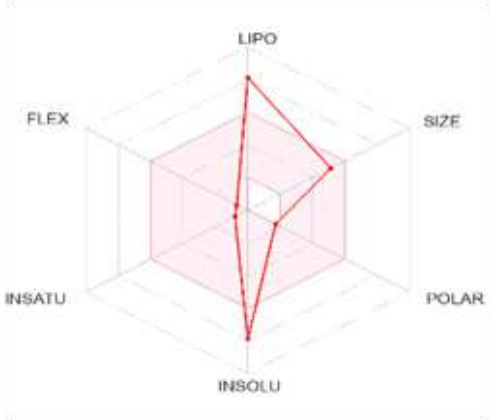
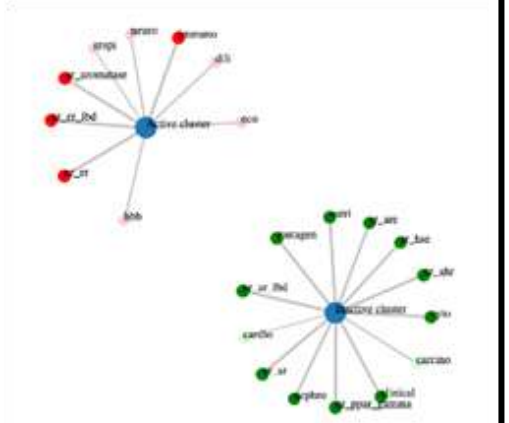
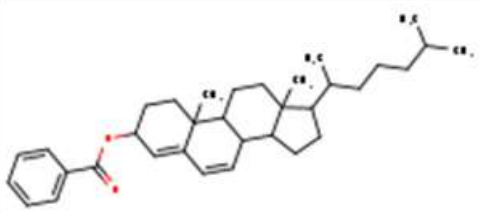
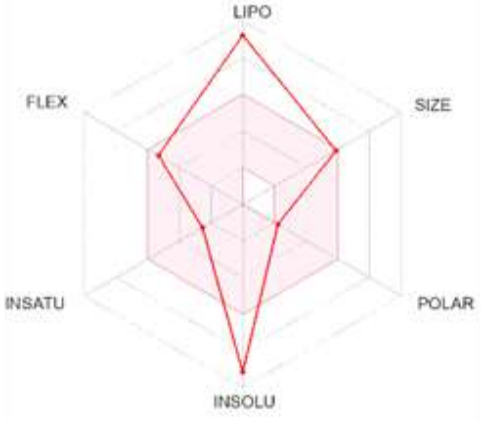
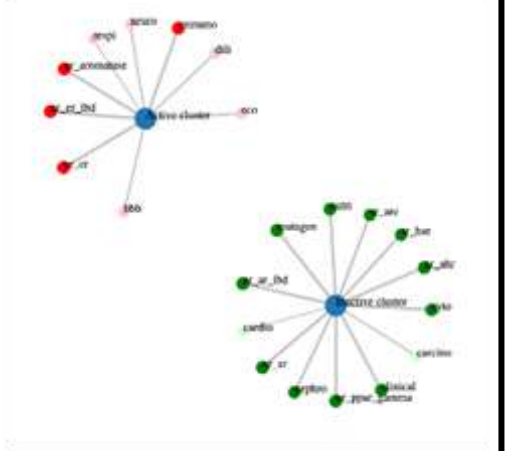
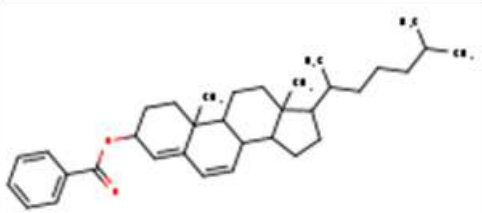
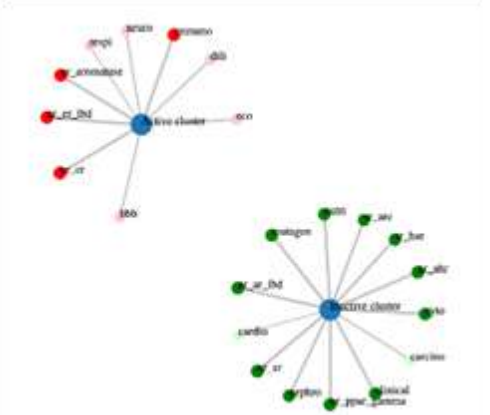
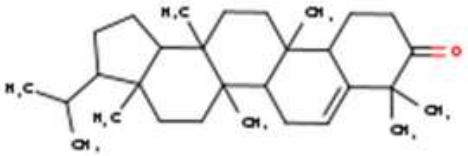
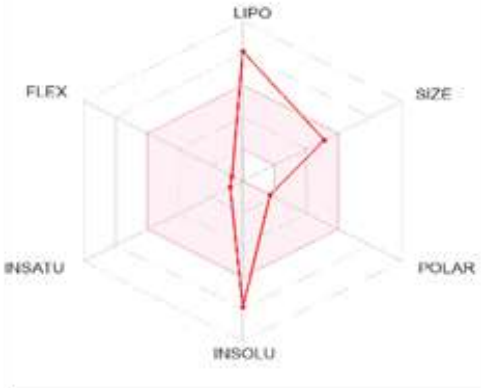
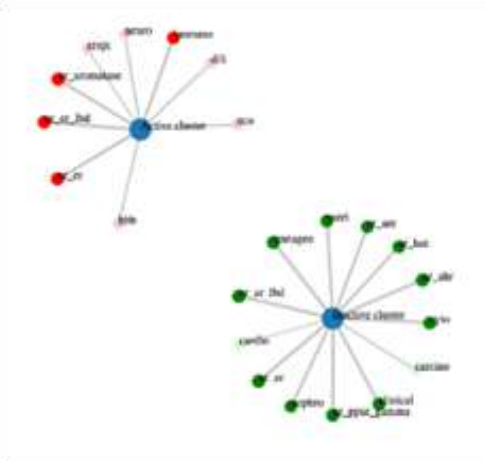
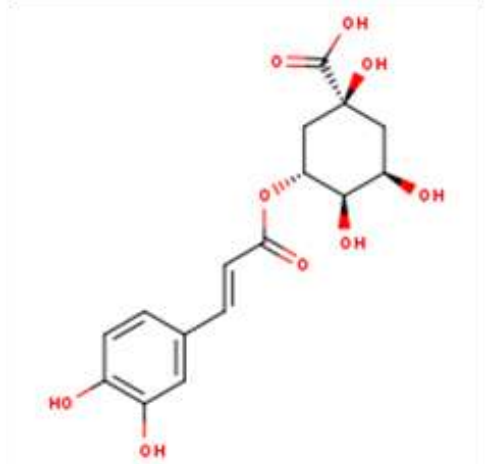
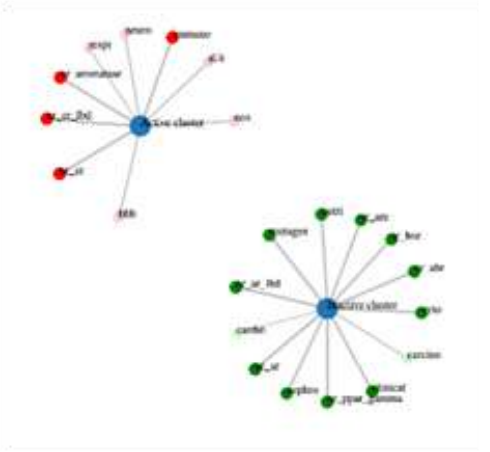
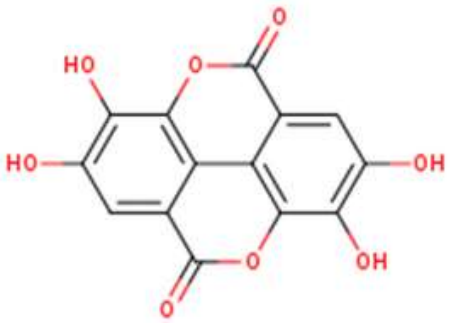
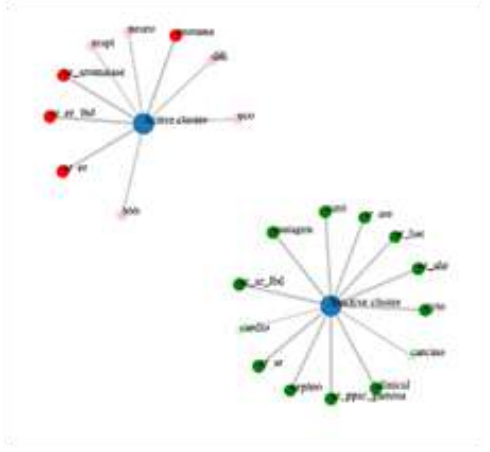
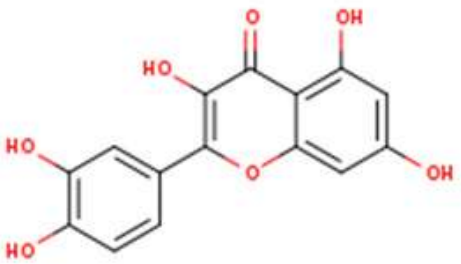
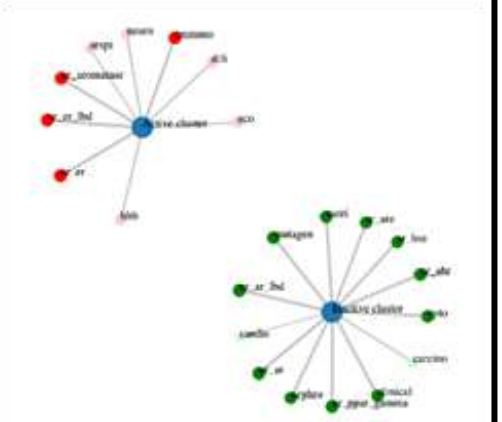
Compound	Structure	Bioradar	Toxicity
DB-Friedo-B'A'-Neogammacer-5-en-3-one			
Cholesta-4,6-dien-3-ol, benzoate, (3.beta.)-			

Table 9.126: ADMET (Absorption, Distribution, Metabolism, Excretion, and Toxicity) profiling of top anticancer phytocompounds

Compound	Structure	Bioradar	Toxicity
Cholesta-4,6-dien-3-ol, benzoate,(3.beta.)-			
DB-Friedo-B'A'-Neogammacer-5-en-3-one			

Compound	Structure	Bioradar	Toxicity
Chlorogenic Acid			
Ellagic Acid			

Compound	Structure	Bioradar	Toxicity
Quercetin			

absorption potential, bioavailability score, Pan-Assay Interference Compounds (PAINS) alerts, and synthetic accessibility. Solubility plays a crucial role in determining suitable formulation approaches, while GI absorption estimates the efficiency of oral uptake. The bioavailability score provides an indication of the proportion of the compound likely to reach systemic circulation. PAINS alerts identify structural features that may cause false positives in bioassays, and the synthetic accessibility score, ranging from 1 (easiest) to 10 (most difficult), estimates the practical feasibility of compound synthesis (Tables 9.103-9.108).

9.3.12. Metabolism

SwissADME's metabolism profiling focused on two critical aspects: interaction with P-glycoprotein (P-gp) transporters and inhibition of cytochrome P450 (CYP) isoenzymes (CYP1A2, CYP2C19, CYP2C9, CYP2D6, and CYP3A4). P-gp acts as an efflux transporter influencing drug bioavailability, while CYP isoenzymes mediate drug metabolism and potential drug–drug interactions. Compounds acting as P-gp substrates may have reduced intracellular concentrations due to efflux, and inhibitors of CYP isoenzymes can prolong the metabolism of co-administered drugs, potentially leading to toxicity (Tables 9.109-9.114).

9.3.13. Toxicity

Toxicity predictions for the selected phytocompounds were evaluated using the ProTox web server, which estimates the potential risk of organ-specific toxicities and other adverse biological effects. The evaluated endpoints included hepatotoxicity, neurotoxicity, nephrotoxicity, respiratory toxicity, cardiotoxicity, carcinogenicity, immunotoxicity, mutagenicity, and cytotoxicity. An "Active" outcome denotes a potential risk for the respective toxicity endpoint, whereas "Inactive" suggests a lower likelihood of such effects under modeled conditions (Tables 9.115-9.120).

The selected phytocompounds were evaluated using the SwissADME BioRadar tool to assess their overall drug-likeness, with radar plots visually representing their positioning within the optimal chemical space. Toxicity predictions were further obtained from ProTox, with radar charts illustrating potential organ-

specific and general toxicological risks. In these charts, green markers indicate non-toxic predictions, while red markers represent active toxicity endpoints across various biological categories. This combined analysis provides a concise visual and predictive assessment of each compound's suitability for further drug development consideration (Tables 9.121-9.126).

9.3.14. Docking with a marketed drug

Docking of the marketed antioxidant drug Dimethyl Fumarate with the target protein KEAP1 Kelch Domain (KEAP1 Kelch) exhibited a high docking score, or increased negative binding energy, indicating the formation of a stable complex characterized by a favourable binding score, along with specific hydrogen bond and hydrophobic interactions.

Similarly, docking of the marketed antimicrobial drug Tobramycin with its target protein yielded a stable complex, confirmed by a favourable binding score and distinct hydrogen bond and hydrophobic interactions.

The marketed antihelminthic drug Albendazole, when docked with the target protein, also formed a stable complex characterized by favourable binding energy and specific hydrogen bonds and hydrophobic interactions.

Docking studies with the marketed anti-inflammatory drug Celecoxib demonstrated stable complex formation with the target protein, supported by favorable binding scores and key hydrogen bonds and hydrophobic interactions.

Pioglitazone, a marketed antidiabetic drug, docked with the target protein, showed a stable complex with favourable binding affinity and well-defined hydrogen bonding and hydrophobic contacts.

Lastly, docking of the marketed anticancer drug Sotorasib with the target protein produced a stable complex characterized by favourable binding scores and specific hydrogen bonds and hydrophobic interactions.

9.3.15. Docking with an antioxidant market drug

9.3.15.1. 3D and 2D visualization of KEAP1 Kelch Domain (KEAP1 Kelch) with Dimethyl Fumarate (DMF)

The 3D visualization depicts Dimethyl Fumarate securely embedded within the KEAP1 Kelch binding cavity, aligning along a moderately hydrophobic channel that accommodates its linear fumarate backbone. The ligand orientation facilitates close packing against key hydrophobic residues while maintaining spatial proximity to polar residues for potential hydrogen bond stabilization. The surface mapping reveals regions of hydrophobicity (green) interspersed with hydrophilic pockets (magenta), illustrating a complementary fit that supports stable ligand accommodation.

The 2D interaction diagram outlines the molecular contacts in detail:

- Conventional Hydrogen Bonds (bright green lines)

Strong polar interactions are formed with GLY367, GLY605, and ALA510, contributing to directional anchoring and improved specificity.

- Alkyl Interactions (light pink spheres)

VAL418 and ALA366 engage in hydrophobic alkyl contacts, reinforcing ligand positioning within the non-polar regions of the binding site.

- Van der Waals Interactions (light green spheres)

Multiple residues, including LEU365, ILE416, VAL604, and GLY463, surround the ligand, collectively contributing to a stabilizing dispersion field.

This combined interaction network, driven by a balance of polar hydrogen bonding and non-polar hydrophobic contacts, suggests that Dimethyl Fumarate is well-suited to maintain a stable conformation within the KEAP1 Kelch interface. Such a binding profile may support its role in modulating the Nrf2-Keap1 pathway, potentially enhancing antioxidant response element (ARE)-driven cytoprotective mechanisms (Plate 9.37).

9.3.15.2. Trajectory-based structural analysis

9.3.15.2.1. Root Mean Square Deviation (RMSD)

The Root Mean Square Deviation (RMSD) is a primary metric to assess the structural stability of a protein–ligand complex over the simulation timescale. For both 4L7B–DMF (KEAP1 Kelch-Dimethyl Fumarate-Dimethyl Fumarate) and 4L7B–MSA (KEAP1 Kelch-Dimethyl Fumarate-Maslinic acid) complexes, the RMSD plots indicated that the systems achieved stability relatively early, within the first 10 ns, suggesting rapid equilibration. The DMF complex maintained an average RMSD of ~0.120 nm, with a narrower fluctuation range, indicative of a rigid and well-fitted ligand binding mode. In contrast, MSA exhibited a slightly higher average RMSD (~0.135 nm) with broader deviations, particularly between 40–70 ns, suggesting moderate conformational flexibility that may facilitate adaptive binding adjustments. The RMSD probability density distribution supported these observations, showing a sharp, well-defined peak for DMF, while MSA presented a broader and slightly shifted peak, reflecting its increased conformational sampling. Overall, DMF binding appears to confer greater structural rigidity, while MSA promotes a slightly more dynamic binding environment (Figures 9.67-9.68).

9.3.15.2.2. Root Mean Square Fluctuation (RMSF)

Root Mean Square Fluctuation (RMSF) evaluates the flexibility of individual residues within the protein structure throughout the simulation. Both DMF- and MSA-bound systems showed generally low RMSF values (<0.20 nm) across most residues, signifying structural stability in the majority of the protein framework. Peaks were localized to terminal regions and certain loop segments, which are inherently more flexible. In the case of DMF, fluctuations were slightly dampened across the board, suggesting its binding restricts local motion and enhances protein rigidity. MSA, however, induced marginally higher fluctuations in specific loop areas, which may allow the protein to adapt its conformation for functional interactions. This difference in local dynamics could influence binding affinity and biological activity. The overall RMSF patterns show that both complexes maintain core structural stability, with the

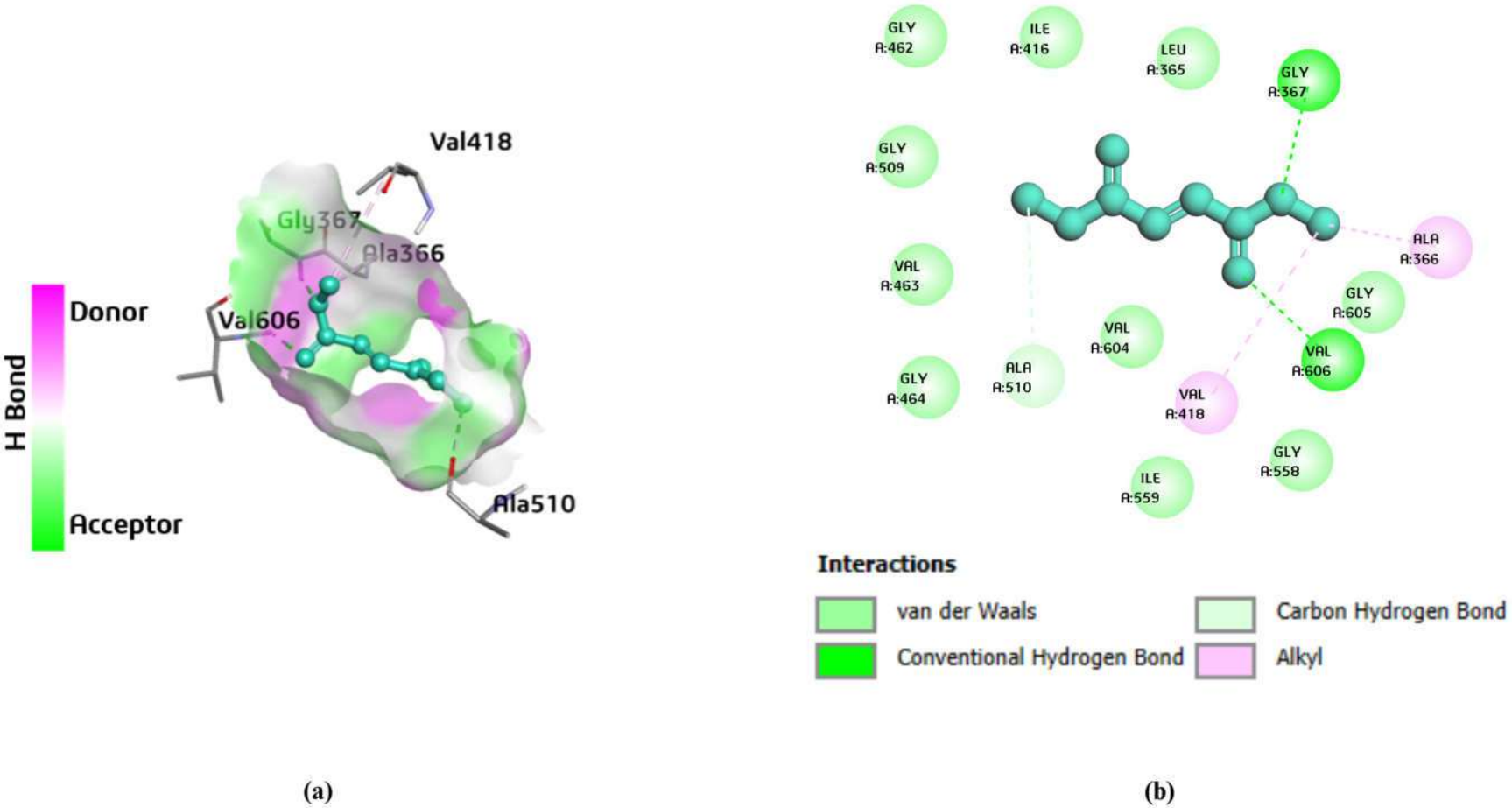


Plate 9.37: Visualization of binding interactions betweenKEAP1 Kelch Domain (KEAP1 Kelch) and marketed antioxidant drug Dimethyl Fumarate (DMF), showing (a) the three-dimensional (3D) molecular surface and (b) the two-dimensional (2D) interaction diagram

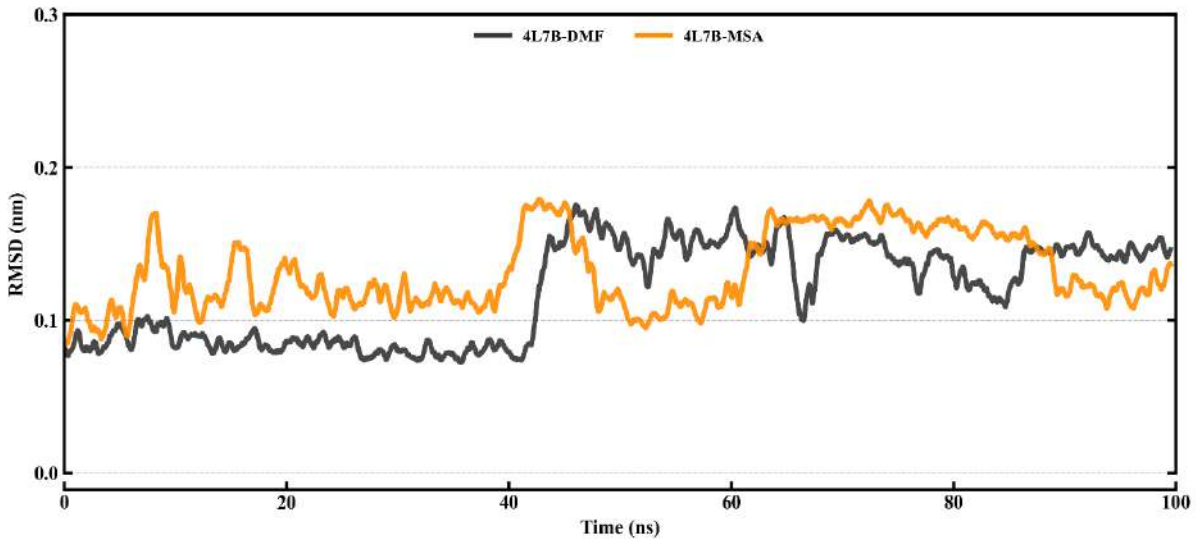


Figure 9.67: Root Mean Square Deviation (RMSD) time evolution of 4L7B–DMF (KEAP1 Kelch-Dimethyl Fumarate-Dimethyl Fumarate) and 4L7B–MSA ((KEAP1 Kelch-Dimethyl Fumarate-Maslinic acid) complexes over a 100-nanosecond simulation time

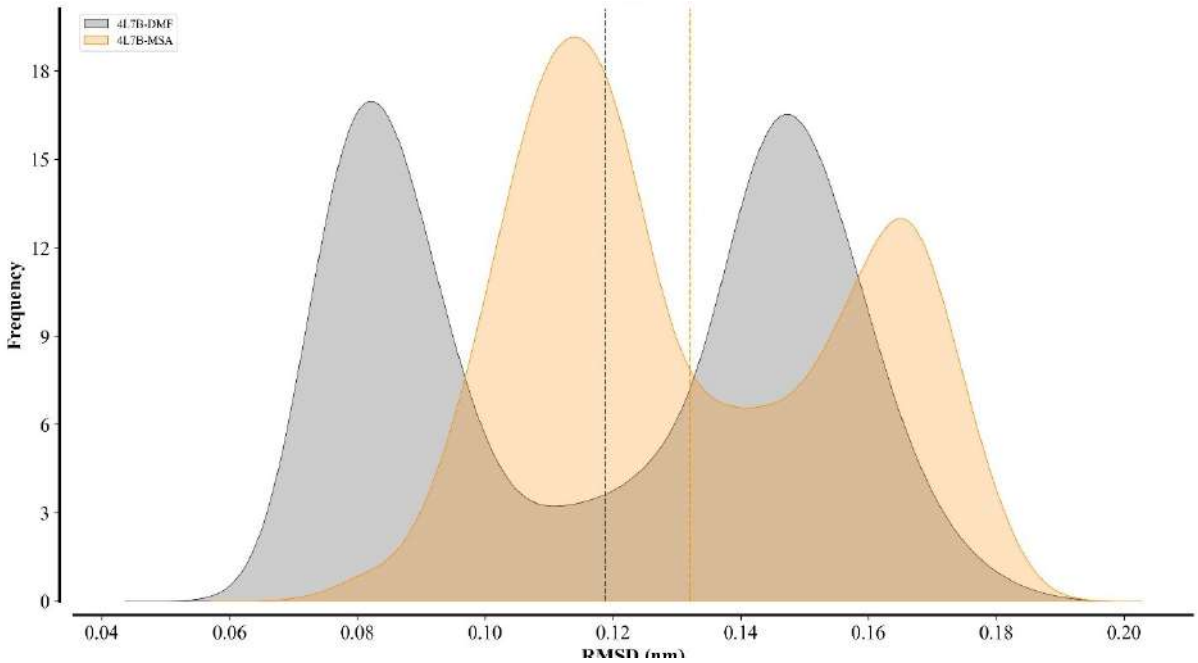


Figure 9.68: Root Mean Square Deviation (RMSD) probability density distributions showing frequency of deviation states

observed variations reflecting subtle differences in ligand-induced flexibility (Figure 9.69).

9.3.15.2.3. Radius of Gyration (Rg)

The Radius of Gyration (Rg) provides insight into the overall compactness of a protein's three-dimensional structure during simulation. A stable Rg suggests that the protein maintains its global fold without significant unfolding events. For both complexes, Rg values remained within a narrow range (~1.79–1.82 nm) throughout the simulation, indicating stable folding. The DMF complex showed a slightly lower average Rg (~1.796 nm) compared to MSA (~1.798 nm), suggesting a marginally more compact protein conformation in the presence of DMF. Such compactness may reflect tighter packing of secondary structure elements, which could enhance stability. The fluctuations in Rg for both complexes were minimal, with no major deviations that would indicate structural collapse or expansion. These results confirm that ligand binding does not adversely affect the protein's overall integrity but rather maintains or slightly enhances structural stability (Figure 9.70).

9.3.15.2.4. Solvent Accessible Surface Area (SASA)

SASA quantifies the surface area of the protein that is accessible to solvent molecules and reflects changes in protein folding, compactness, and exposure of residues. Throughout the 100 ns trajectory, both complexes displayed stable SASA values, confirming no large-scale unfolding events. The MSA-bound complex consistently exhibited slightly higher SASA values compared to DMF, suggesting a marginal increase in solvent exposure. This may enhance the accessibility of certain functional residues to the solvent, potentially influencing antioxidant activity. DMF binding, by contrast, maintained a more compact conformation with slightly reduced solvent exposure, consistent with its lower Rg. The absence of large SASA fluctuations in both systems indicates stable tertiary structures. These subtle differences could have functional implications: increased SASA in MSA may support reactive species accessibility, while reduced SASA in DMF may enhance structural protection against denaturation (Figure 9.71).

9.3.15.2.5. Intra-Hydrogen Bonds

The intra-molecular hydrogen bond analysis provides insight into the internal structural stability of the protein throughout the simulation. Both 4L7B-DMF and 4L7B-MSA complexes maintained a high and relatively stable count of ~220–240 hydrogen bonds over 100 ns, indicating robust preservation of the protein's secondary and tertiary architecture. Minor oscillations are observed for both systems, reflecting natural breathing motions in the protein structure. The MSA-bound system demonstrates slightly smoother fluctuations and fewer pronounced drops compared to DMF, suggesting a marginally more cohesive internal hydrogen bond network. This stable intra-molecular bonding implies that neither ligand disrupts the core protein fold, but MSA binding may subtly enhance structural resilience, contributing to prolonged functional stability under dynamic conditions. The consistency of these bonds throughout the trajectory indicates that ligand binding does not induce structural collapse or unfolding (Figure 9.72).

9.3.15.2.6. Inter-Hydrogen Bonds

Inter-molecular hydrogen bonds reflect the direct contact strength and stability between ligand and protein. Here, the MSA complex consistently forms 2–6 hydrogen bonds over the simulation, with several extended intervals maintaining higher counts (4–6 bonds) during the latter half of the run. This suggests stable and persistent polar contacts that reinforce ligand anchoring in the binding pocket. In contrast, DMF typically maintains 1–2 hydrogen bonds, with fewer sustained peaks, indicating a greater reliance on non-polar interactions and potentially more transient binding. The increased hydrogen bonding persistence in MSA may contribute to improved binding affinity and stability, supporting its stronger antioxidant potential compared to DMF. These results indicate that MSA benefits from a more extensive polar interaction network, which could improve resistance to competitive displacement and conformational drift in physiological conditions (Figure 9.73).

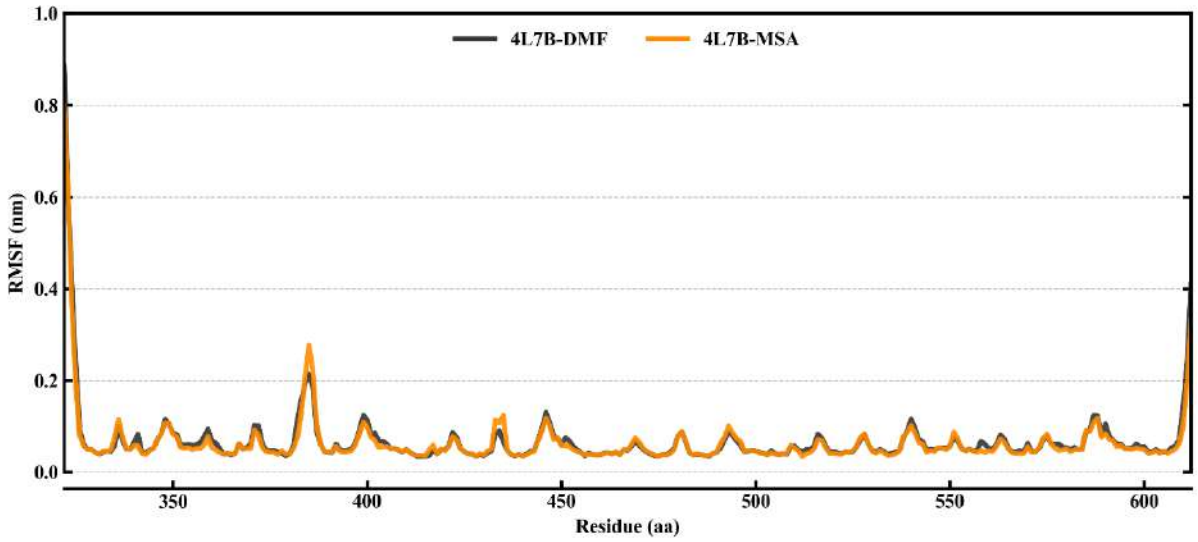


Figure 9.69: Root Mean Square Fluctuation (RMSF)plots of Cα atoms for 4L7B–DMF (KEAP1 Kelch-Dimethyl Fumarate-Dimethyl Fumarate) and 4L7B–MSA ((KEAP1 Kelch-Dimethyl Fumarate-Maslinic acid) complexes

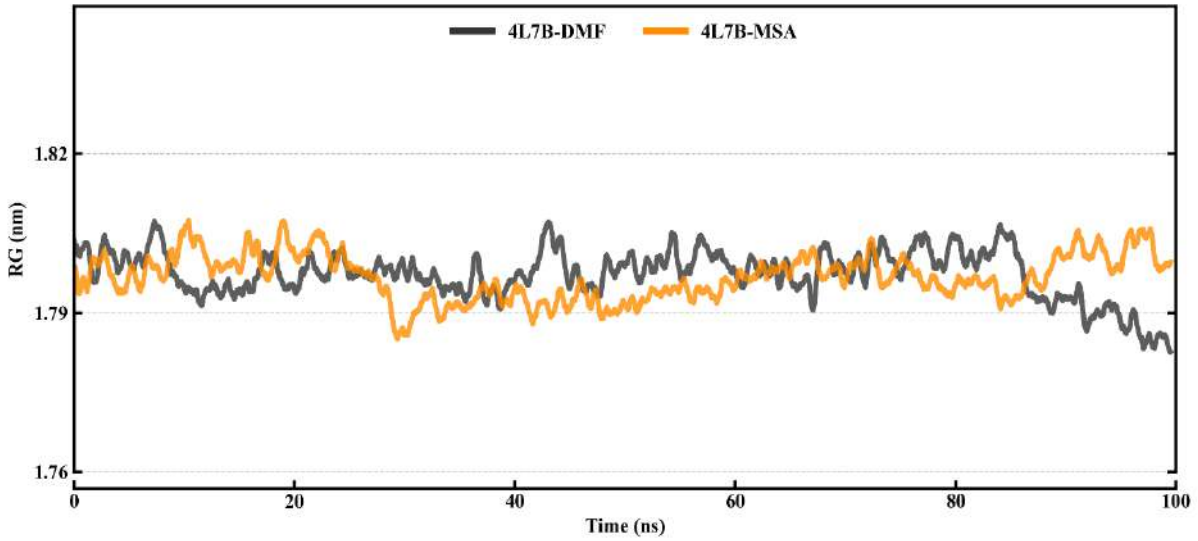


Figure 9.70: Radius of gyration (Rg) profiles of 4L7B–DMF (KEAP1 Kelch-Dimethyl Fumarate-Dimethyl Fumarate) and 4L7B–MSA ((KEAP1 Kelch-Dimethyl Fumarate-Maslinic acid) complexes

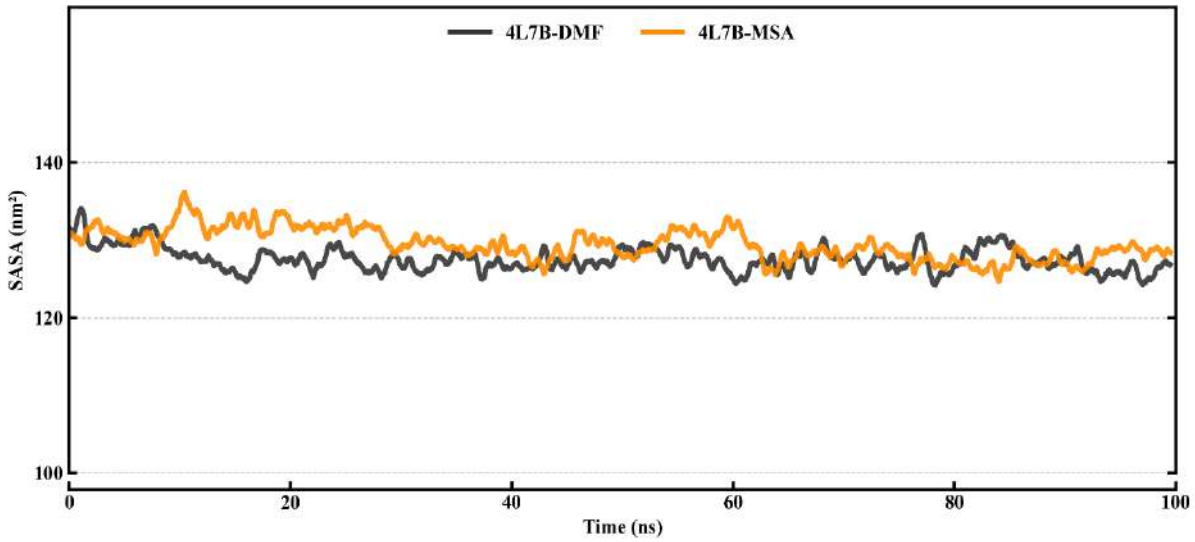


Figure 9.71: Solvent Accessible Surface Area (SASA) variation for 4L7B–DMF (KEAP1 Kelch-Dimethyl Fumarate-Dimethyl Fumarate) and 4L7B–MSA ((KEAP1 Kelch-Dimethyl Fumarate-Maslinic acid) complexes over a 100-nanosecond simulation time

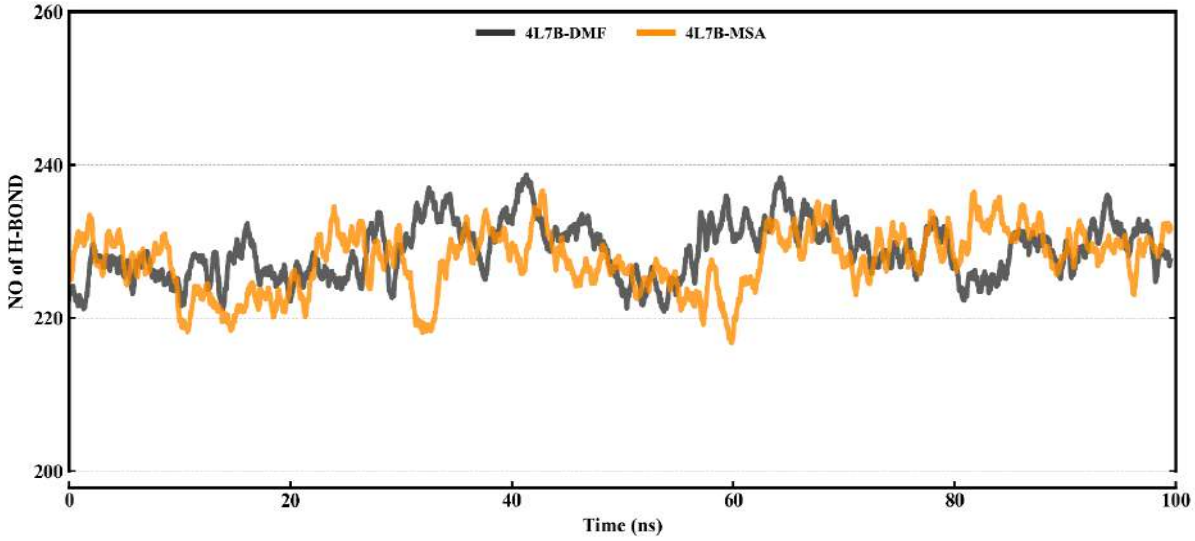


Figure 9.72: Number of intraprotein hydrogen bonds in both complexes

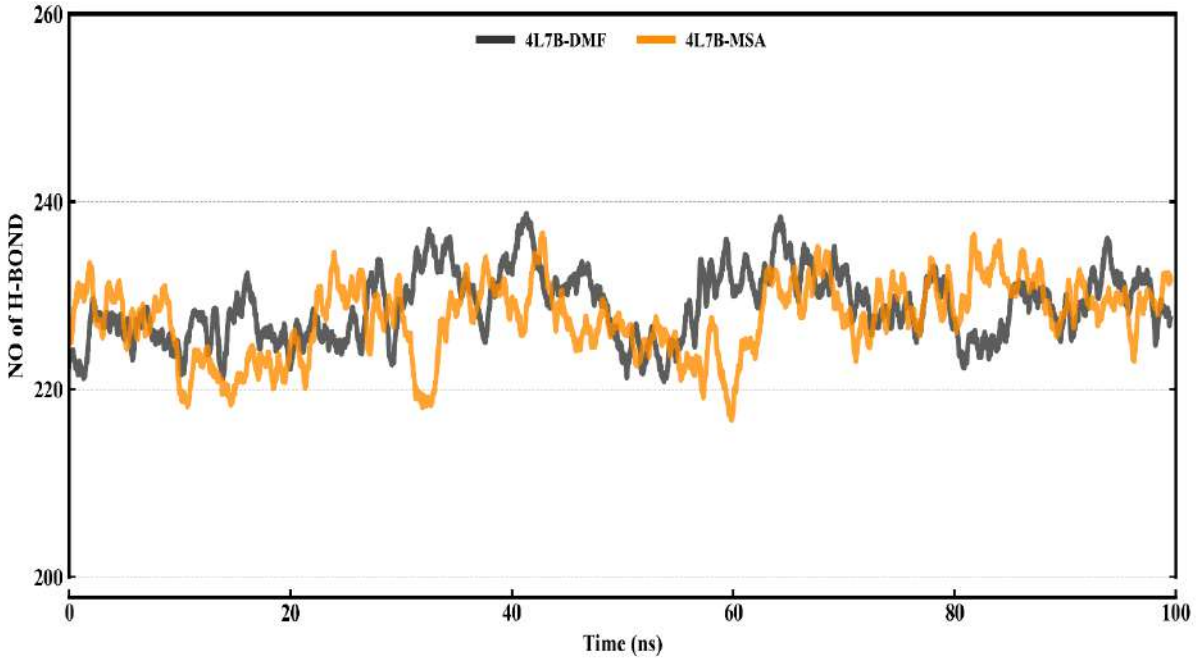


Figure 9.73: Protein–ligand hydrogen bond time evolution over a 100-nanosecond simulation time for 4L7B–DMF (KEAP1 Kelch-Dimethyl Fumarate-Dimethyl Fumarate) and 4L7B–MSA (KEAP1 Kelch-Dimethyl Fumarate-Maslinic acid) complexes

9.3.15.2.7. Conformational sampling and energy landscape

9.3.15.2.7.1. Free Energy Landscape

The Free Energy Landscape (FEL) is a thermodynamic representation of the conformational space sampled by the protein–ligand complex. Constructed using the first two principal components (PC1 and PC2) from PCA, FEL maps depict energy minima as basins, where deeper basins correspond to more thermodynamically favorable conformations. In the DMF-bound system, the FEL displayed a more localized and sharply defined global minimum, indicating that the protein predominantly occupied a single highly stable conformational state throughout the simulation. This suggests reduced structural adaptability but enhanced rigidity, consistent with the RMSD and PCA findings. Conversely, the MSA-bound complex exhibited multiple interconnected minima, reflecting a broader exploration of conformational space. These multiple basins imply that MSA binding promotes structural flexibility, enabling the protein to access various low-energy conformations. Such adaptability could be advantageous for functional antioxidant interactions that require conformational changes upon reactive species binding. The energy differences between minima in MSA's FEL were small, indicating easy transitions between states, whereas DMF's FEL implied higher energetic barriers for conformational changes. Overall, FEL analysis complements the dynamic stability insights from RMSD, RMSF, and hydrogen bonding patterns, illustrating that DMF binding locks the protein into a restricted conformational regime, while MSA allows for dynamic exploration of energetically favourable states (Plate 9.38).

9.3.15.2.7.2. Principal Component Analysis (PCA)

PCA dissects the large-scale collective motions of the protein during simulation by reducing complex atomic trajectories into a few dominant modes (principal components). For the antioxidant systems, the first two principal components (PC1 and PC2) captured the most significant conformational variations. In the PCA scatter plot, the DMF complex exhibited a densely clustered point distribution, indicating that the system sampled a narrow range of conformational states. This behaviour suggests high structural rigidity and minimal deviation from a

dominant binding mode. Such limited flexibility may enhance stability but could reduce adaptability to environmental changes. In contrast, the MSA complex displayed a broader and more dispersed distribution of points across the PCA space. This pattern reflects enhanced conformational diversity and flexibility, consistent with its RMSD, RMSF, and FEL behaviour. The spread suggests that MSA allows the protein to explore alternative conformations while retaining overall structural stability. These differences have potential functional implications: the rigidity induced by DMF could stabilize the antioxidant protein under stress conditions, while MSA's flexibility might facilitate reactive species scavenging by accommodating different substrate orientations. Overall, PCA confirms that ligand identity modulates the dynamic behaviour of the protein, with DMF favouring stability and MSA promoting adaptable structural landscapes (Figure 9.74).

9.3.16. Overall conclusion- Antioxidant activity from Molecular dynamics (MDS) analysis

The molecular dynamics simulation results provide a comprehensive understanding of the structural stability, flexibility, and conformational adaptability of the antioxidant protein (4L7B) in complex with DMF and MSA ligands. Across all evaluated parameters, both systems demonstrated overall stability without large-scale unfolding or loss of structural integrity. However, distinct ligand-dependent effects were evident.

DMF binding consistently resulted in lower RMSD values, reduced RMSF fluctuations, slightly lower Rg, and smaller SASA, collectively indicating a more compact, rigid, and structurally stable conformation. The FEL and PCA analyses reinforced this, revealing a highly localized energy minimum and restricted conformational sampling. Such characteristics suggest that DMF promotes a "locked-in" state, which could help preserve the protein's structural resilience under oxidative stress.

In contrast, MSA binding, while maintaining stability, introduced moderate flexibility, reflected in slightly higher RMSD and RMSF values, increased SASA, and a broader conformational sampling pattern in PCA. The FEL revealed multiple

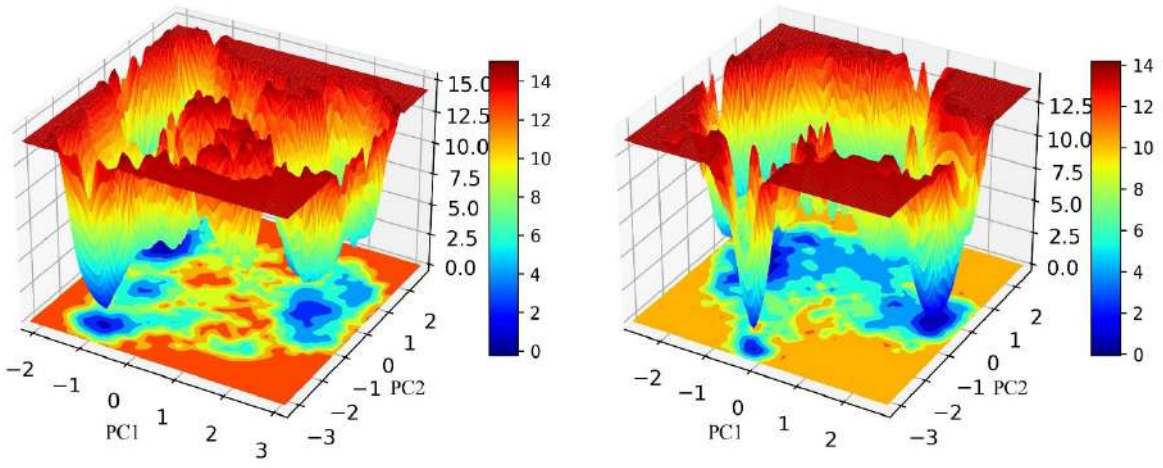
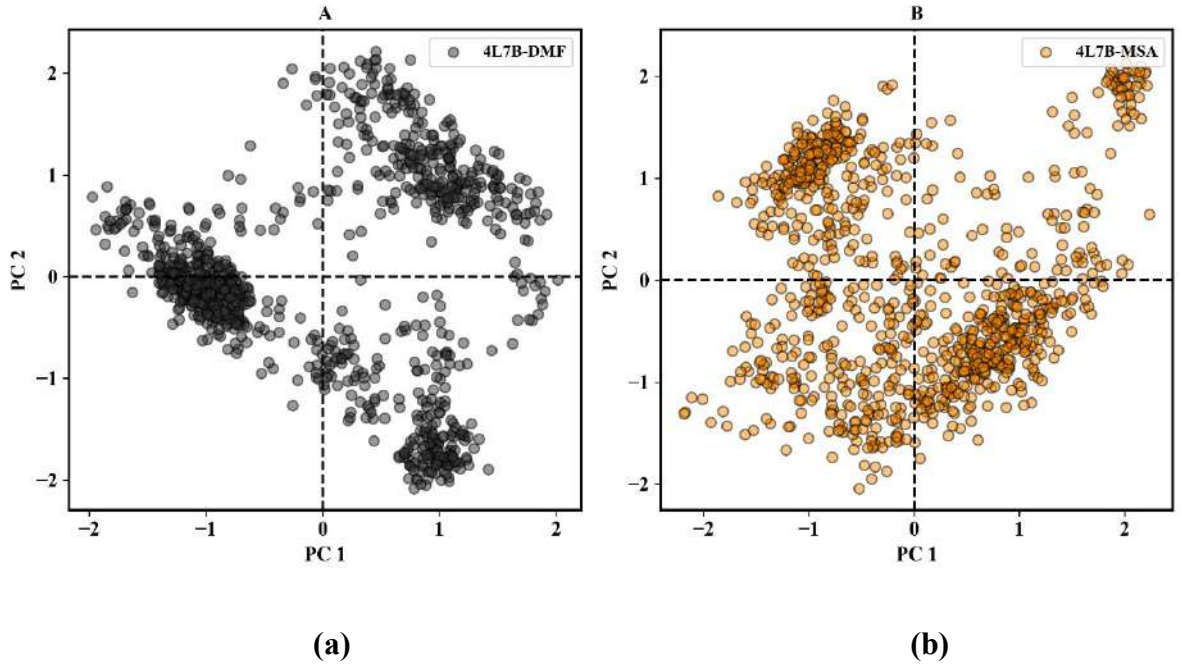


Plate 9.38: Three-dimensional (3D) Free energy landscapes (FEL) of (a) 4L7B–DMF (KEAP1 Kelch-Dimethyl Fumarate-Dimethyl Fumarate) and (b) 4L7B–MSA (KEAP1 Kelch-Dimethyl Fumarate-Maslinic acid) complexes plotted along PC1 and PC2



(a) (b)

Figure 9.74: Principal Component Analysis (PCA) scatter plots for (a) 4L7B–DMF (KEAP1 Kelch-Dimethyl Fumarate-Dimethyl Fumarate) and (b) 4L7B–MSA (KEAP1 Kelch-Dimethyl Fumarate-Maslinic acid), showing conformational sampling along two principal components, PC1 and PC2

interconnected low-energy states, signifying a capacity for dynamic adaptation. This flexibility, combined with a higher number of protein–ligand hydrogen bonds, may facilitate more versatile interactions with reactive oxygen species, potentially enhancing functional antioxidant activity.

Overall, the MDS data suggest that DMF enhances antioxidant protein stability through structural rigidity, whereas MSA promotes adaptability and dynamic conformational shifts. These differences highlight potential functional specializations: DMF may favor long-term structural protection, while MSA could optimize reactive species scavenging efficiency through conformational flexibility. A balanced interplay between stability and adaptability might be critical in designing effective antioxidant therapeutics based on this protein–ligand framework.

9.3.17. Binding Free Energy (MM/PBSA)

MM/PBSA (Molecular Mechanics Poisson–Boltzmann Surface Area) analysis was used to estimate the binding free energies of the NRF-Keap1 protein complexed with Maslinic acid (a natural antioxidant phytocompound) and Dimethyl Fumarate (approved drug). This method allows decomposition of the total binding free energy into van der Waals, electrostatic, polar solvation, and SASA contributions to understand the driving forces of ligand binding. More negative binding energy values indicate stronger, thermodynamically favourable interactions (Table 9.127).

9.3.17.1. Binding affinity comparison

The total binding energy indicates that Maslinic Acid (–101.284 kJ/mol) exhibits substantially stronger binding to NRF-Keap1 compared to Dimethyl Fumarate (–32.868 kJ/mol). The major contributors to this difference are the much stronger van der Waals interactions (–171.489 kJ/mol vs. –73.751 kJ/mol) and enhanced electrostatic stabilization (–54.602 kJ/mol vs. –15.440 kJ/mol) observed for Maslinic Acid. These results suggest that Maslinic Acid fits the binding pocket more effectively, engaging in stronger non-polar and polar interactions.

9.3.17.2. Energetic contributions and structural implications

Maslinic Acid displays a higher polar solvation penalty (+143.182 kJ/mol) than Dimethyl Fumarate (+65.126 kJ/mol), reflecting its higher polarity and potential for hydrogen bonding in aqueous conditions. However, this penalty is outweighed by its favorable van der Waals and electrostatic terms, as well as superior SASA contribution (–18.375 kJ/mol vs. –8.803 kJ/mol), indicating better hydrophobic burial within the pocket. Dimethyl Fumarate's weaker van der Waals forces and less favorable electrostatics limit its binding affinity despite the lower solvation cost. Overall, the MM/PBSA profile highlights Maslinic Acid as a more potent NRF-Keap1 binder, which may translate into stronger antioxidant activity by effectively modulating the Keap1–NRF2 interaction (Figure 9.75)

9.3.18. Normal Mode Analysis (NMA) for antioxidant target (KEAP1)

Normal Mode Analysis (NMA) was carried out on the Kelch-like ECH-associated protein 1 (KEAP1) to assess its inherent flexibility, correlated motions, and structural stability. This evaluation provides insights into the cooperative dynamics of KEAP1 that may underlie its regulatory role in oxidative stress responses, particularly through its interaction with Nrf2 (Plate 9.39).

9.3.18.1. Structural flexibility and deformability

The deformability profile reveals several distinct peaks along the KEAP1 sequence, corresponding to flexible loop regions and hinge-like segments. These flexible points are likely critical for the conformational adjustments required during Nrf2 recognition and binding. The 3D structure visualizes this flexibility with a gradient from rigid blue regions to moderately flexible green/yellow and highly mobile red zones, emphasizing motion-prone loops around the binding interface.

9.3.18.2. B-Factor analysis

The predicted B-factors from NMA (pink) exhibit close agreement with experimental crystallographic B-factors (black), validating the simulation's accuracy in identifying mobile regions. Notably, higher B-factors are seen at peripheral loops

Table 9.127: Molecular Mechanics Poisson–Boltzmann Surface Area (MM/PBSA) energy decomposition for NRF-Keap1–Maslinic acid and NRF-Keap1–Dimethyl Fumarate complexes

Energy component (kJ/mol)	Maslinic acid	Dimethyl Fumarate
van der Waals	–171.489 ± 10.498	–73.751 ± 3.107
Electrostatic	–54.602 ± 18.409	–15.440 ± 4.199
Polar solvation	143.182 ± 13.388	65.126 ± 4.770
SASA	–18.375 ± 0.839	–8.803 ± 0.634
Total binding energy	–101.284 ± 9.044	–32.868 ± 5.960

Table 9.128: DFT parameters for Maslinic acid and Dimethyl Fumarate

Compound name	DFT Energy (Hartree)	HOMO Energy (Hartree)	LUMO Energy (Hartree)	HOMO-LUMO Gap (Hartree)	MEP Minimum (a.u.)	MEP Maximum (a.u.)	MEP Average (a.u.)
Maslinic ACID - DFT	-1461.127	-0.173	-0.154	0.018	-13.840	140.405	0.0582
Dimethyl Fumarate-DFT	-528.645	-0.195	-0.174	0.021	-5.576	156.423	0.054

Table 9.129: Molecular Mechanics Poisson–Boltzmann Surface Area (MM/PBSA) energy decomposition for LasR–2-Phenyl-4H-chromen-4-one and LasR–Tobramycin complexes

Energy Component (kJ/mol)	2-Phenyl-4H-chromen-4-one	Tobramycin
van der Waals	–132.330 ± 13.378	–45.609 ± 18.781
Electrostatic	–7.879 ± 7.147	–32.747 ± 32.917
Polar solvation	70.775 ± 15.344	64.731 ± 27.439
SASA	–13.746 ± 0.793	–6.554 ± 1.683
Total binding energy	–83.180 ± 11.560	–20.179 ± 11.182

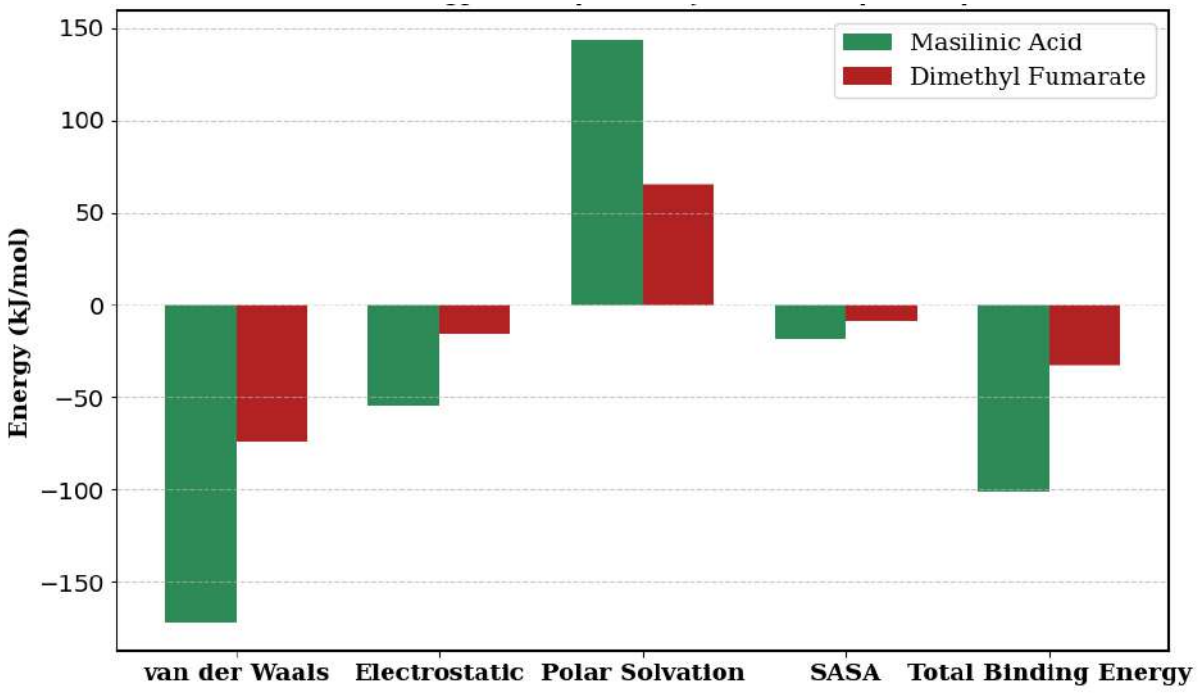


Figure 9.75: Molecular Mechanics Poisson–Boltzmann Surface Area (MM/PBSA) energy decomposition for NRF-Keap1 complexes with Maslinic acid and Dimethyl Fumarate

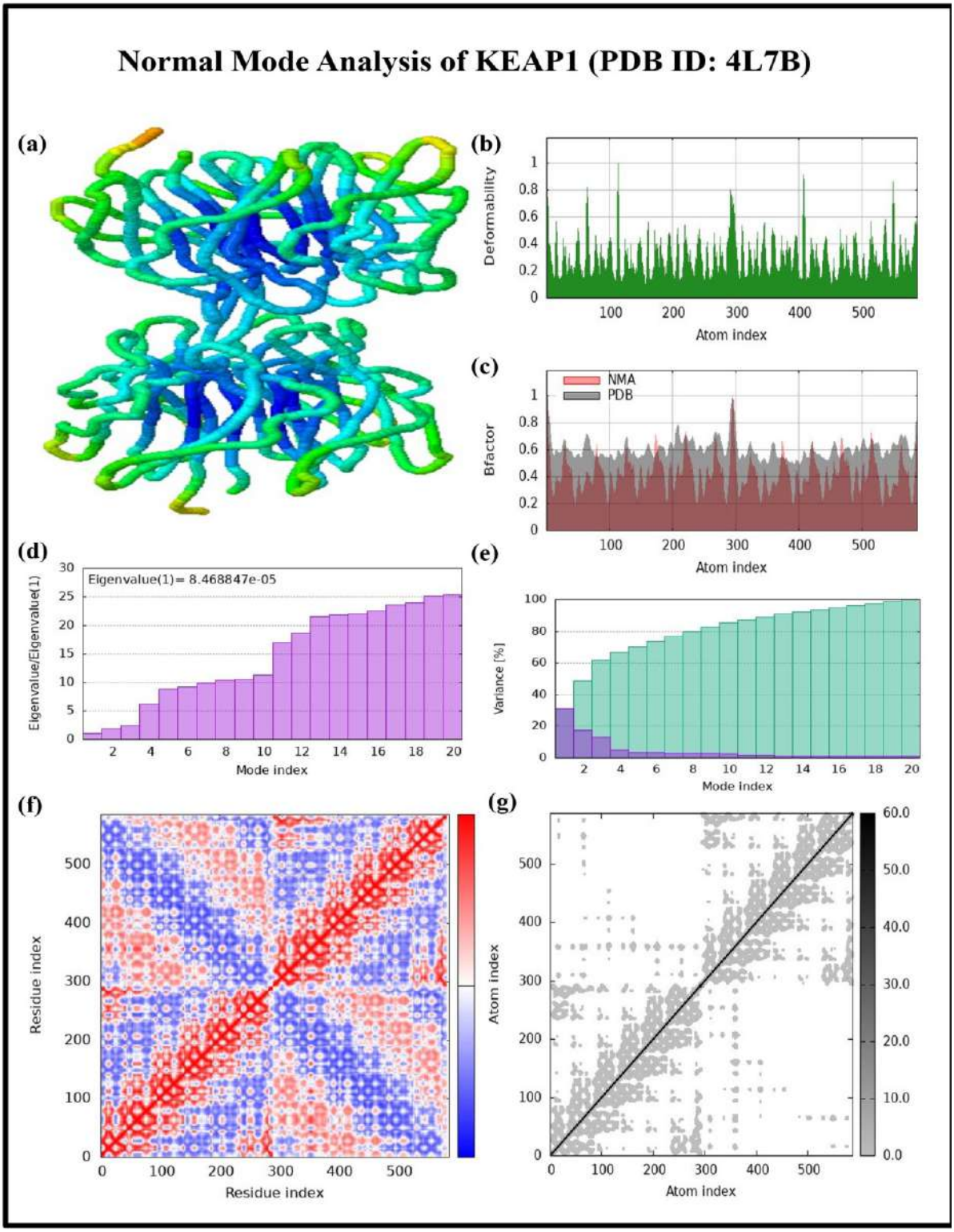
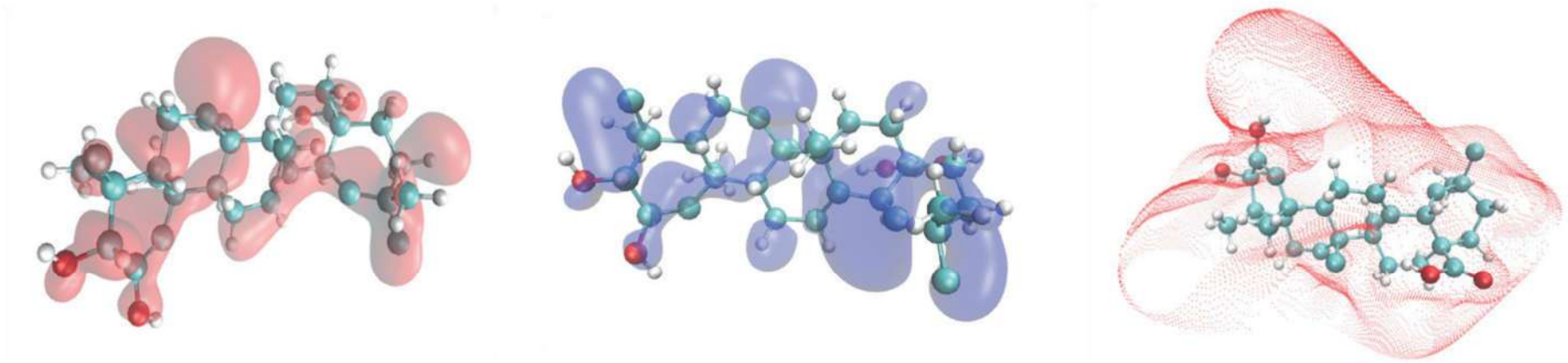
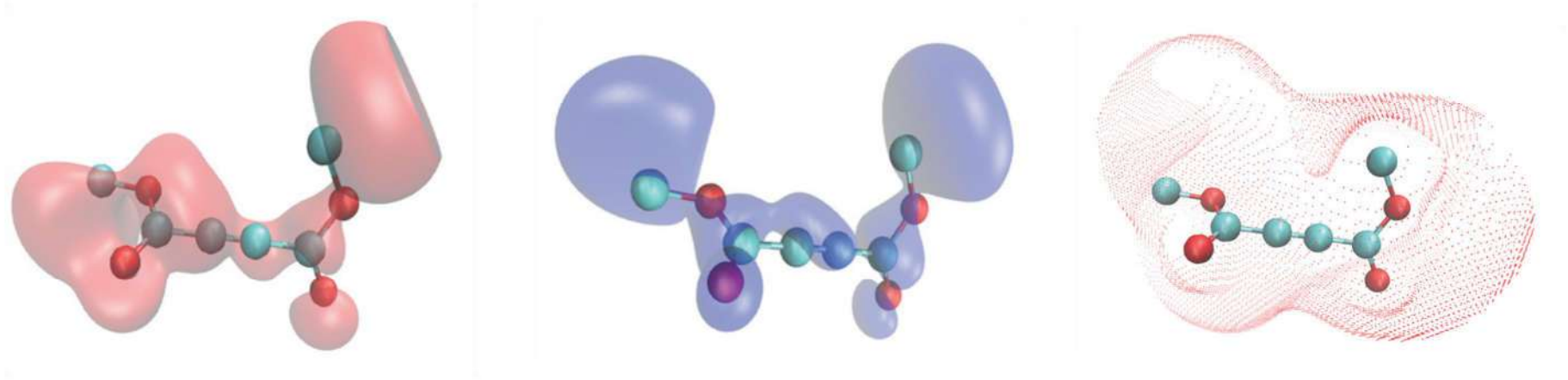


Plate 9.39: Normal mode analysis of KEAP1 Kelch Domain: (a) Cartoon representation with colour-coded mobility (blue: rigid, green/yellow: flexible) (b) deformability plot (c) B-factor comparison (NMA vs. PDB) (d) eigenvalue distribution (e) cumulative and individual variance per mode (f) covariance matrix showing correlated (red) and anti-correlated (blue) motions and (g) elastic network map with spring strengths (dark grey: stiffer connections)



(a) (b) (c)

Plate 9.40: Frontier molecular orbital (Highest Occupied Molecular Orbital (HOMO), Lowest Unoccupied Molecular Orbital (LUMO)) and molecular electrostatic potential (MEP) surfaces for Maslinic acid against NRF-Keap1: (a) HOMO distribution(b) LUMO distribution, and (c) MEP surface mapping



(a) (b) (c)

Plate 9.41: Frontier molecular orbital ((Highest Occupied Molecular Orbital (HOMO), Lowest Unoccupied Molecular Orbital (LUMO)) and molecular electrostatic potential (MEP) surfaces for Dimethyl Fumarate against NRF-Keap1: (a) HOMO distribution(b) LUMO distribution, and (c) MEP surface mapping, highlighting probable interaction sites and electron density distribution

and inter-domain linkers, suggesting their involvement in structural adaptability during protein-protein interaction events.

9.3.18.3. Collective motion, eigenvalues, and variance

The first non-trivial eigenvalue is 8.47×10^{-5}, indicating relatively high flexibility compared to stiffer enzymatic targets. This suggests KEAP1's dominant motion modes require lower energetic input, facilitating rapid conformational changes during regulatory cycles. Variance distribution analysis demonstrates that the first few modes capture the bulk of the total motion, highlighting the coordinated nature of domain-level movements.

9.3.18.4. Correlated motions and elastic network

The covariance map displays well-defined regions of correlated (red) and anti-correlated (blue) motions, particularly between the Kelch repeats and the BTB domain, signifying functional communication between distant sites. The elastic network representation shows denser connections in the Kelch domain's β-propeller core (rigid structural scaffold) and sparser connectivity at loop regions, consistent with their flexibility in ligand or partner recognition.

9.3.18.5. DFT analysis for antioxidant activity (NRF-Keap1 Target)

Density Functional Theory (DFT) calculations were carried out for Maslinic Acid (phytocompound) and Dimethyl Fumarate (marketed antioxidant drug) to examine their electronic structures, frontier molecular orbital (FMO) distributions, and molecular electrostatic potential (MEP) characteristics. These parameters provide insight into their electronic reactivity, stability, and possible interaction patterns within the NRF-Keap1 binding pocket (Table 9.128).

9.3.18.5.1. Electronic property comparison

Maslinic acid has a slightly smaller HOMO–LUMO gap (0.018 Hartree) than Dimethyl Fumarate (0.021 Hartree), suggesting marginally higher electronic reactivity and a greater tendency for charge transfer interactions during binding. Its higher HOMO energy (-0.173 Hartree) compared to Dimethyl Fumarate (-0.195

Hartree) implies a slightly stronger electron-donating capacity, which may facilitate interactions with electron-deficient residues of NRF-Keap1. Dimethyl Fumarate's slightly larger gap indicates greater kinetic stability but slightly lower reactivity in comparison (Plate 9.40).

9.3.18.5.2. Molecular Electrostatic Potential Insights (MEP)

Maslinic acid exhibits a more negative MEP minimum (-13.840 a.u.) than Dimethyl Fumarate (-5.576 a.u.), suggesting a stronger potential for electrostatic attraction toward positively charged amino acids in the protein's active site. Dimethyl Fumarate, however, has a higher MEP maximum (156.423 a.u.) compared to maslinic acid (140.405 a.u.), indicating more intense localized positive charge regions that could contribute to hydrogen bonding or polar interactions. The average MEP values are similar (0.0582 for maslinic acid vs. 0.054 for Dimethyl Fumarate), implying comparable overall surface charge distributions (Plate 9.41).

9.3.19. Docking with a marketed antimicrobial drug

9.3.19.1. 3D and 2D Visualization of LasR ligand-binding domain LasR with Tobramycin

The 3D visualization shows Tobramycin seated deeply in the LASR binding cavity, enveloped by a semi-transparent surface that reveals the pocket topology. The aminoglycoside threads through a narrow groove and adopts a compact conformation that maximizes polar contacts at both ends while maintaining extensive surface complementarity with the hydrophobic walls of the pocket.

The 2D interaction diagram details the residue-level contacts stabilizing the complex:

- Conventional hydrogen bonds (green arrows)

LYS16 and ILE52 donate/accept H-bonds with terminal hydroxyl/amine groups of Tobramycin, anchoring the ligand and helping define its orientation across the cavity.

- Carbon-hydrogen bond

A weak polar contact is observed with ASN55, further tightening the fit near the ligand's central ring system.

- van der Waals contacts (light-green spheres)

Surrounding residues, including SER20, LEU17, GLN24, VAL53, TYR56, PRO57, ILE35, LEU36, ALA58, ARG61, GLU62- pack around the scaffold to provide additional stabilization through close-range dispersion interactions.

Overall, Tobramycin engages LASR through a polar-anchored, van-der-Waals-stabilized binding mode. The paired hydrogen bonds (LYS16/ILE52) organize the ligand within the groove, while widespread non-polar contacts from residues lining the pocket reinforce shape complementarity, consistent with a robust docking pose for this marketed antimicrobial (Plate 9.42).

9.3.19.2. Trajectory-based structural analysis

9.3.19.2.1. Root Mean Square Deviation (RMSD)

The RMSD trajectories of the LasR–2PC (LasR ligand-binding domain-2-Phenyl-4H-chromen-4-one) and LasR–TOB (LasR ligand-binding domain-Tobramycin) complexes over the 100 ns simulation reveal distinct stability profiles. The LasR–TOB complex maintained lower RMSD values (average ~0.154 nm) compared to LasR–2PC (~0.198 nm), indicating a more stable backbone conformation for TOB binding. Both systems exhibited initial equilibration within the first 10 ns, after which deviations stabilized without major structural drift, suggesting overall stability. Notably, the RMSD density distribution further supports this observation, with TOB's RMSD distribution being narrower and centred at lower values, reflecting reduced conformational fluctuations and higher stability. In contrast, 2PC displayed broader RMSD peaks, indicating more frequent sampling of varied conformations. These results suggest that TOB induces a more compact and rigid structural arrangement of LasR, potentially due to its extensive hydrogen bonding and polar interactions with the protein's active site residues. The slightly higher RMSD for 2PC

might be linked to its planar aromatic structure, allowing more flexible orientations within the binding site while maintaining stable interactions overall (Figures 9.76-9.77).

9.3.19.2.2. Root Mean Square Fluctuation (RMSF)

RMSF analysis was performed to evaluate residue-level flexibility and identify regions influenced by ligand binding. For both complexes, terminal residues displayed higher fluctuations due to intrinsic flexibility. The LasR–TOB complexes generally exhibited slightly lower fluctuations in loop regions (residues ~40–50, 115–125) compared to LasR–2PC, indicating stronger stabilization of these segments upon TOB binding. The LasR–2PC system showed modestly elevated fluctuations around residues 60–75 and 125–135, possibly due to weaker intermolecular contacts in these areas, allowing increased loop flexibility. Importantly, residues involved in ligand binding demonstrated reduced fluctuations for both complexes, suggesting stable interactions throughout the simulation. The more pronounced dampening of flexibility in TOB-bound LasR supports its potential to induce a more rigid binding pocket environment, which may be beneficial for antimicrobial inhibition of quorum-sensing pathways mediated by LasR. These differences in residue mobility highlight how the molecular structure of aromatic planar 2PC vs. polycationic TOB can distinctly modulate the dynamic behaviour of the receptor (Figure 9.78).

9.3.19.2.3. Radius of Gyration (Rg)

The Rg profiles reveal differences in the overall compactness of LasR when bound to each ligand. The LasR–TOB complex consistently maintained slightly lower Rg values (~1.545 nm) compared to LasR–2PC (~1.562 nm), indicating a more compact structural arrangement in the TOB-bound state. This enhanced compactness could be attributed to the multiple hydrogen bonds and electrostatic interactions formed by TOB's sugar and amino groups, which may pull key domains closer together. In contrast, 2PC, being smaller and less polar, induces less pronounced compaction, resulting in marginally higher Rg values. Both complexes demonstrated stable Rg fluctuations without significant unfolding events, confirming overall structural integrity during the simulation. The compactness observed in TOB-bound

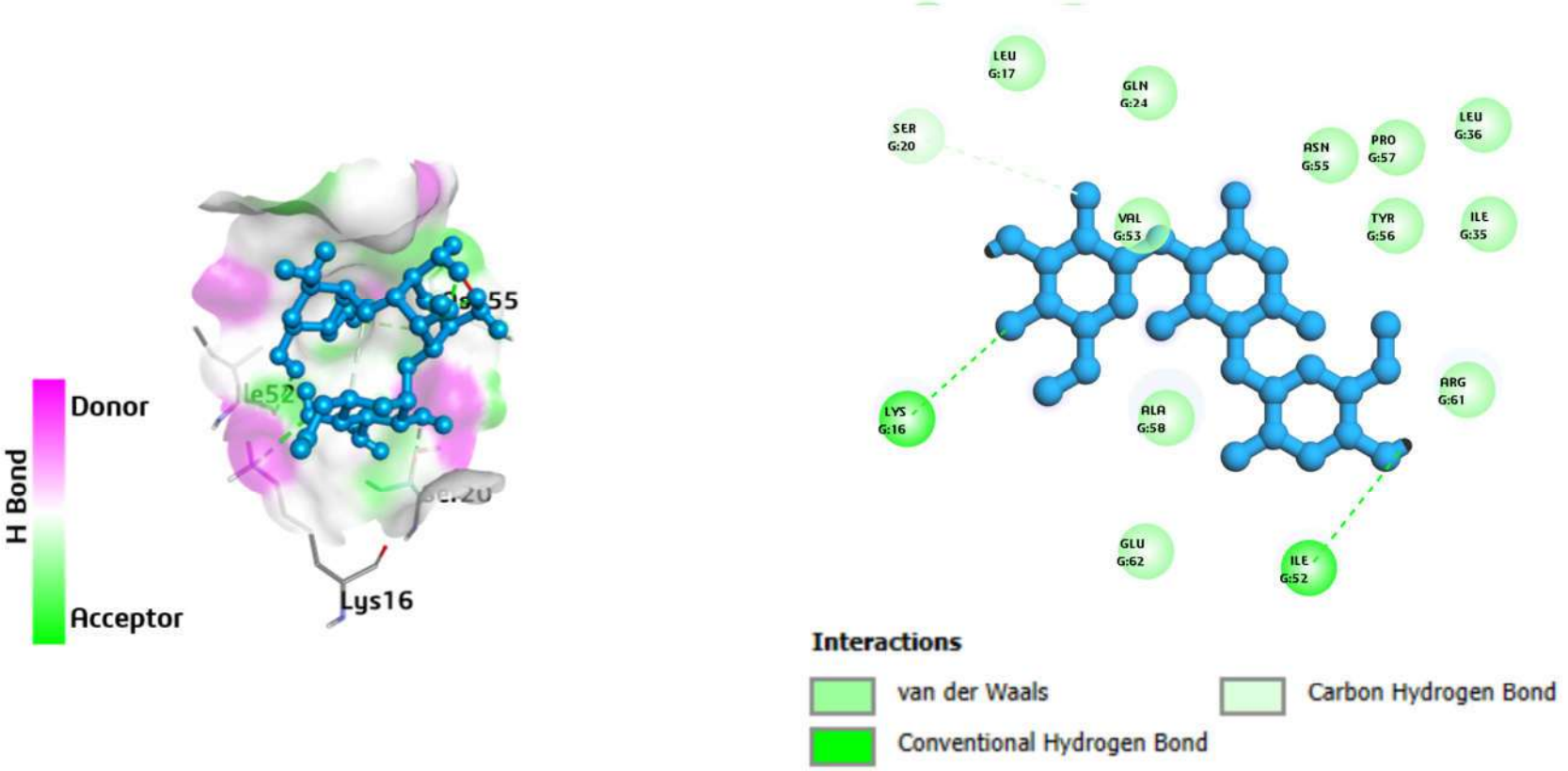


Plate 9.42: Visualization of binding interactions betweenLasR ligand-binding domain(LasR)and marketed antimicrobial drug Tobramycin (TOB), showing (a) the three-dimensional (3D) molecular surface and (b) the two-dimensional (2D) interaction diagram

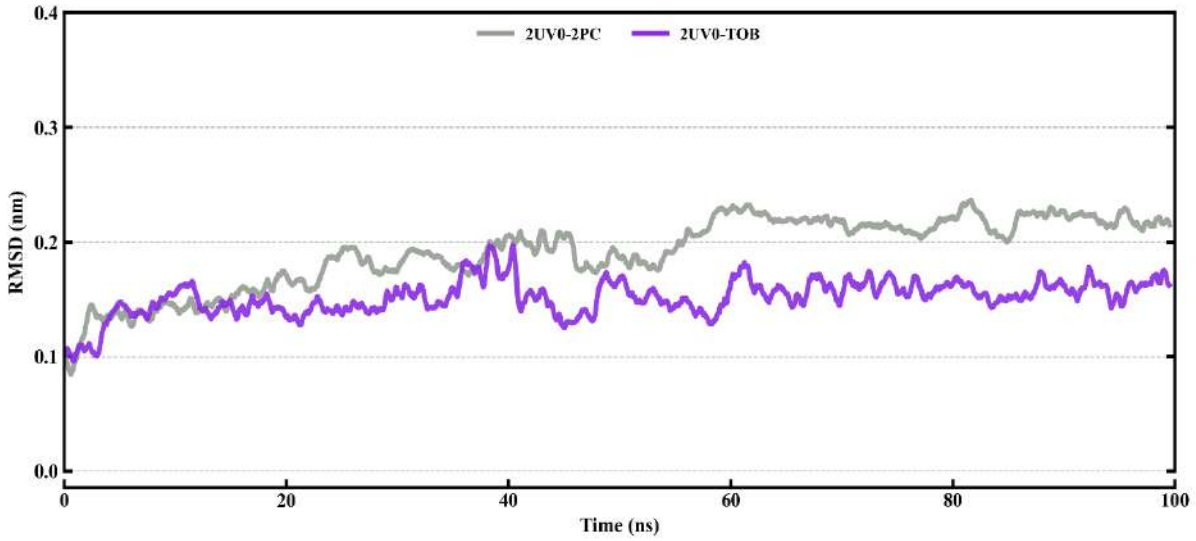


Figure 9.76: Root Mean Square Deviation (RMSD) plots of LasR–2PC (LasR ligand-binding domain-2-Phenyl-4H-chromen-4-one) and LasR–TOB (LasR ligand-binding domain-Tobramycin) complexes over 100 nanoseconds simulation time

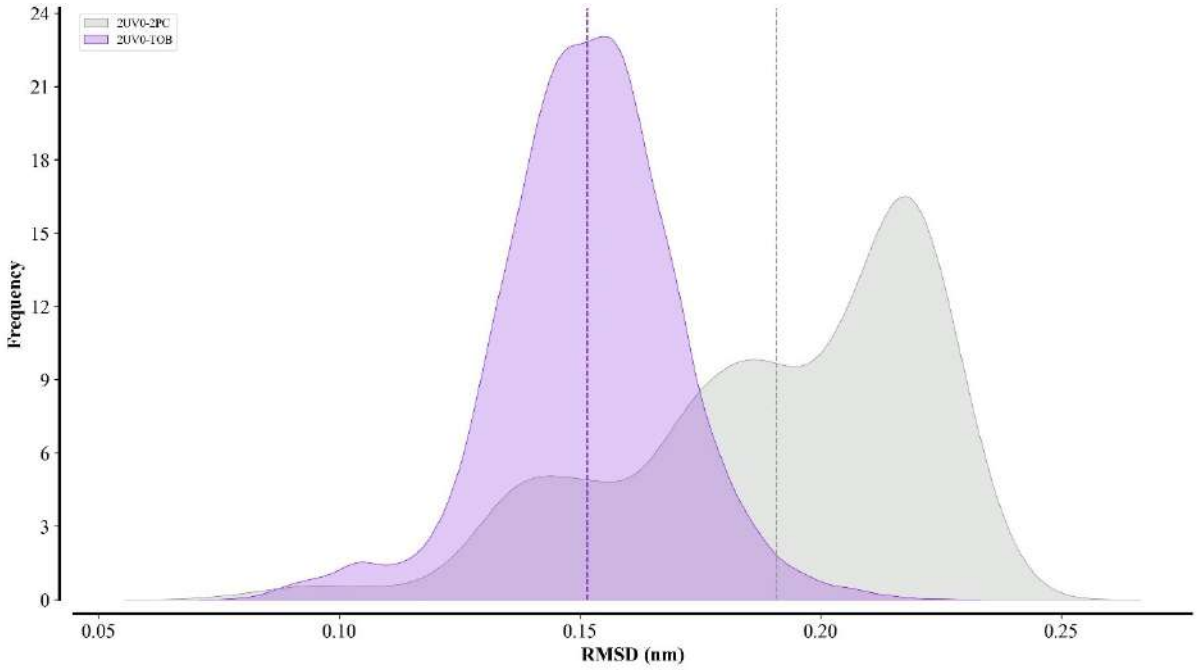


Figure 9.77: RMSD probability density distribution of LasR–2PC (LasR ligand-binding domain-2-Phenyl-4H-chromen-4-one) and LasR–TOB (LasR ligand-binding domain-Tobramycin) complexes

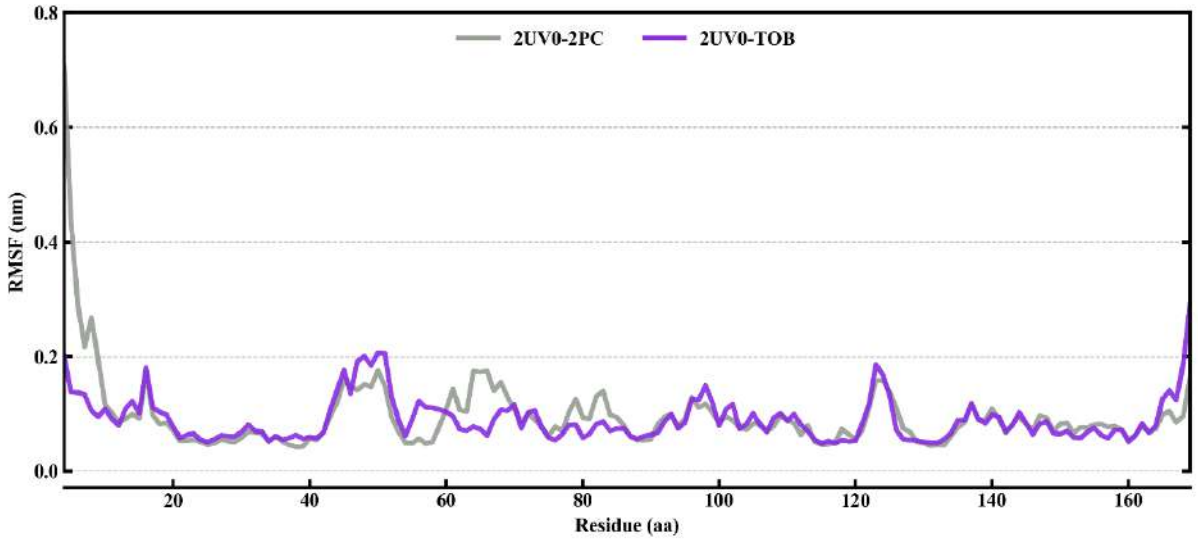


Figure 9.78: RMSF plots for LasR–2PC (LasR ligand-binding domain-2-Phenyl-4H-chromen-4-one) and LasR–TOB (LasR ligand-binding domain-Tobramycin) complexes over a 100-nanosecond simulation

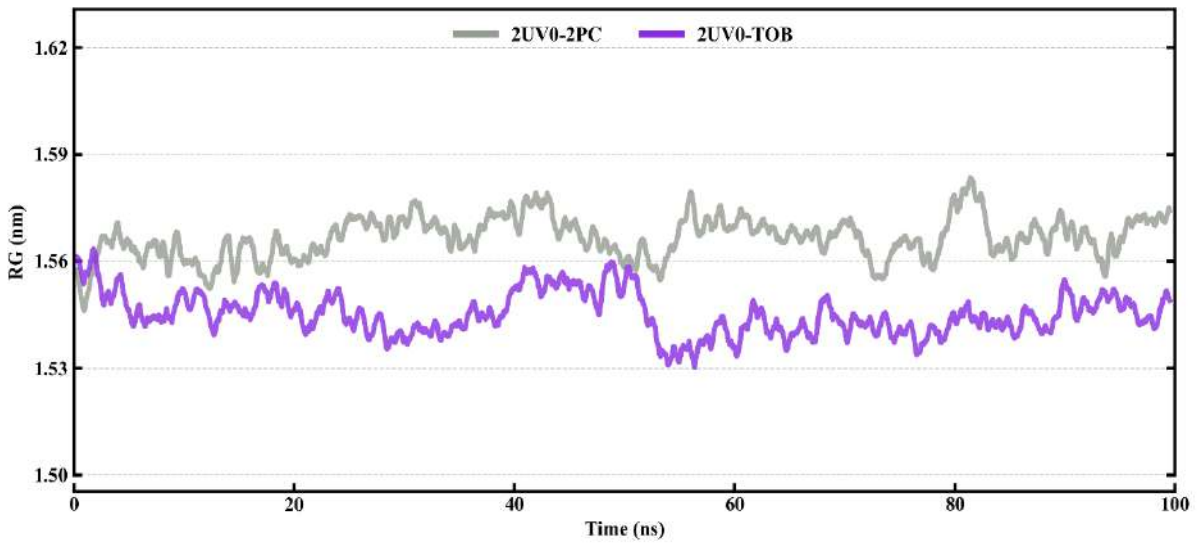


Figure 9.79: Radius of Gyration (Rg) plots of LasR–2PC (LasR ligand-binding domain-2-Phenyl-4H-chromen-4-one) and LasR–TOB (LasR ligand-binding domain-Tobramycin) complexes over a 100-nanosecond simulation

LasR aligns with its lower RMSD profile, reinforcing the notion that TOB exerts a stabilizing effect on the global protein fold, which could be advantageous for sustained inhibitory binding (Figure 9.79).

9.3.19.2.4. Solvent Accessible Surface Area (SASA)

SASA analysis provides insight into the exposure of protein surfaces to solvent during ligand binding. The LasR–TOB complex displayed slightly lower SASA values (~89.6 nm² average) compared to LasR–2PC (~90.8 nm²), suggesting that TOB binding marginally reduces solvent exposure, possibly by inducing a more compact fold and tighter packing around the binding site. Fluctuations were minimal for both systems, indicating stable hydrophobic and hydrophilic surface exposure over time. This reduction in solvent accessibility upon TOB binding is consistent with its higher hydrogen bonding potential, which can lead to a better-sealed binding pocket. Conversely, the 2PC-bound form maintained slightly higher SASA, possibly reflecting the ligand's smaller size and less extensive polar interactions, allowing more water molecules to interact with nearby residues (Figure 9.80).

9.3.19.2.5. Intramolecular Hydrogen Bonds

Intramolecular hydrogen bonding patterns within LasR were analyzed to assess secondary and tertiary structure stabilization. Both complexes maintained a high number of intramolecular H-bonds throughout the simulation, supporting structural integrity. The LasR–TOB complex consistently showed slightly higher hydrogen bond counts (average ~129) compared to LasR–2PC (~125), indicating a more stable internal hydrogen bonding network in the TOB-bound state. The presence of TOB, with its multiple hydroxyl and amino groups, may enhance favourable interactions that indirectly stabilize protein secondary structure. The 2PC-bound protein maintained stable but slightly lower hydrogen bond counts, possibly due to less extensive polar interaction potential. These results reinforce the idea that TOB binding not only directly stabilizes the active site but also enhances global protein stability through indirect structural effects (Figure 9.81).

9.3.19.2.6. Intermolecular Hydrogen Bonds

Intermolecular hydrogen bonds between LasR and the ligands were tracked to evaluate binding stability. The LasR–TOB complex formed a higher and more variable number of intermolecular hydrogen bonds (2–6 bonds) throughout the simulation, reflecting TOB's multiple polar functional groups capable of forming simultaneous contacts with the protein. This high H-bond count suggests strong, persistent interactions that likely contribute to the reduced RMSD and lower flexibility observed for this complex. In contrast, LasR–2PC maintained fewer intermolecular hydrogen bonds (0–1 bonds), consistent with its smaller size and hydrophobic aromatic core, which favours π-stacking and hydrophobic contacts over extensive hydrogen bonding. Despite fewer H-bonds, the 2PC complex remained structurally stable, indicating that hydrophobic packing plays a key role in its binding mode (Figure 9.82).

9.3.19.3. Conformational Sampling and Energy Landscape

9.3.19.3.1. Principal Component Analysis (PCA)

PCA was performed to investigate the conformational sampling of LasR–ligand complexes over the simulation. The LasR–2PC complex sampled a more restricted conformational space, with clustering along specific PC1–PC2 coordinates, indicating relatively confined motions. This may result from stable hydrophobic interactions locking the ligand within the binding site, limiting large-scale domain rearrangements. In contrast, LasR–TOB exhibited broader distribution along both principal components, suggesting exploration of more diverse conformations. This expanded conformational sampling could be attributed to the dynamic nature of TOB's multiple polar groups, which may form transient interactions with various residues, allowing the protein to adopt different binding pocket geometries. Interestingly, while the TOB complex explored more conformations, its RMSD remained lower, implying that these motions are localized rather than involving large backbone rearrangements. Overall, PCA highlights distinct ligand-dependent conformational dynamics, with 2PC promoting rigidity and TOB allowing flexibility within a stable global fold (Figure 9.83).

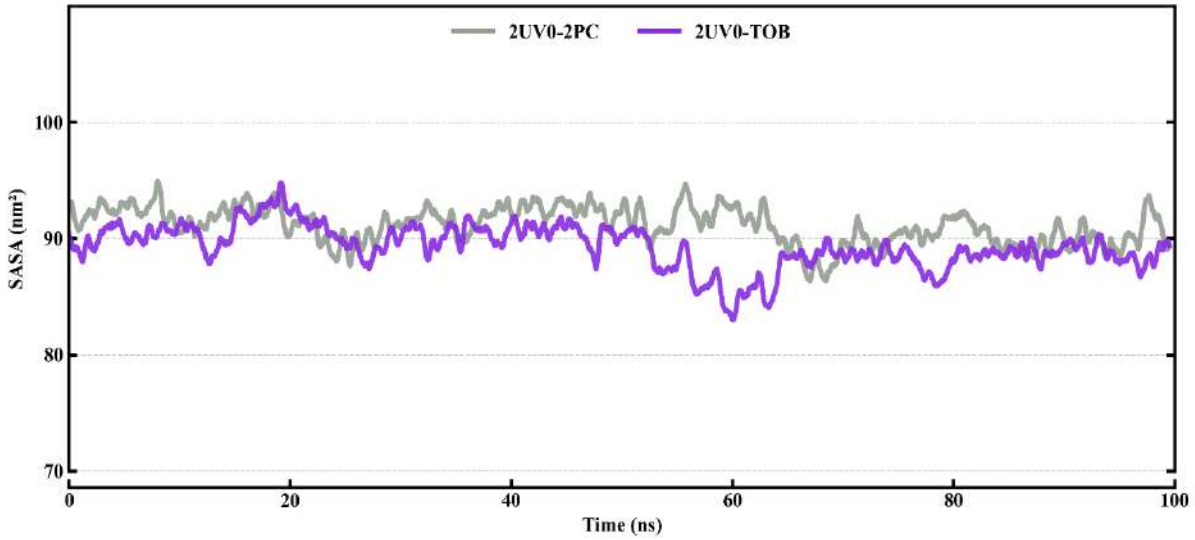


Figure 9.80: Solvent Accessible Surface Area (SASA) profiles of LasR–2PC (LasR ligand-binding domain-2-Phenyl-4H-chromen-4-one) and LasR–TOB (LasR ligand-binding domain-Tobramycin) complexes during 100-nanosecond simulation

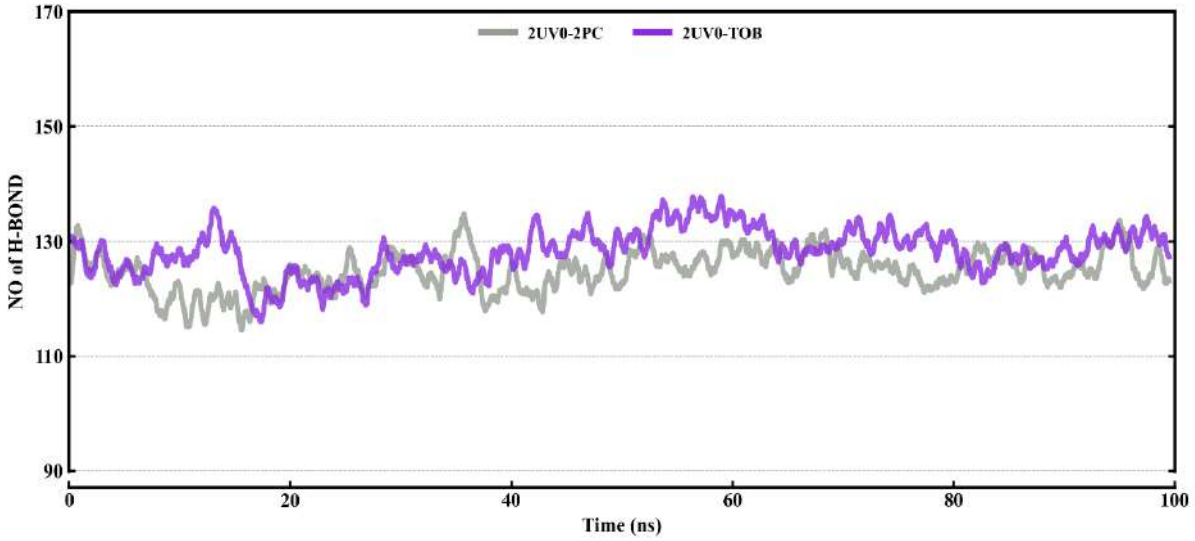


Figure 9.81: Number of intramolecular hydrogen bonds in LasR–2PC (LasR ligand-binding domain-2-Phenyl-4H-chromen-4-one) and LasR–TOB (LasR ligand-binding domain-Tobramycin) complexes over a 100-nanosecond simulation

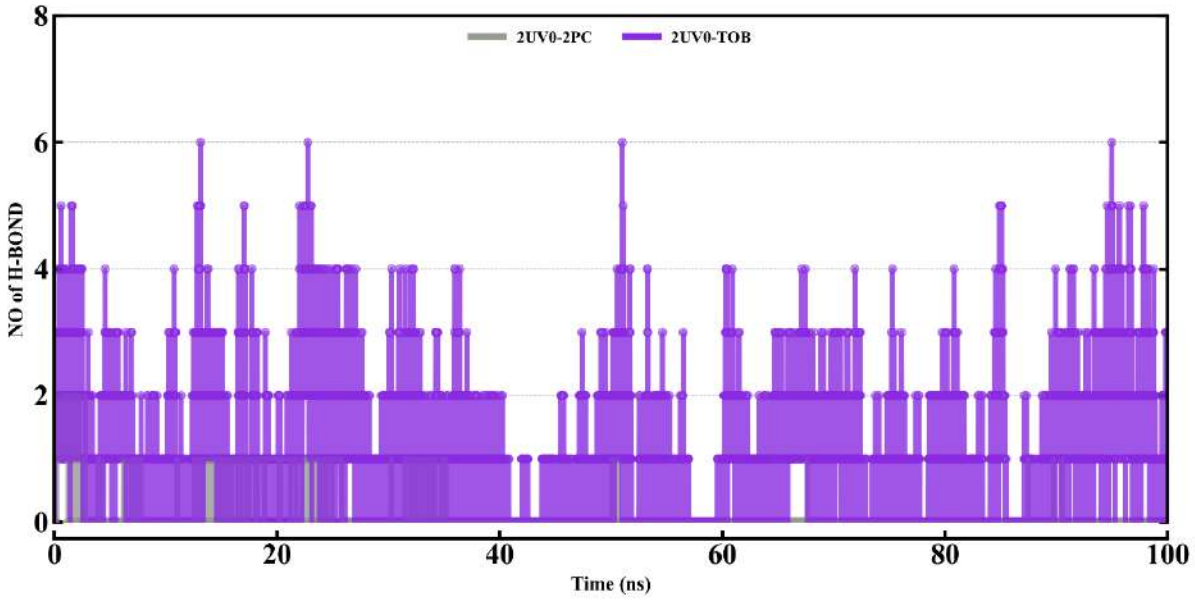
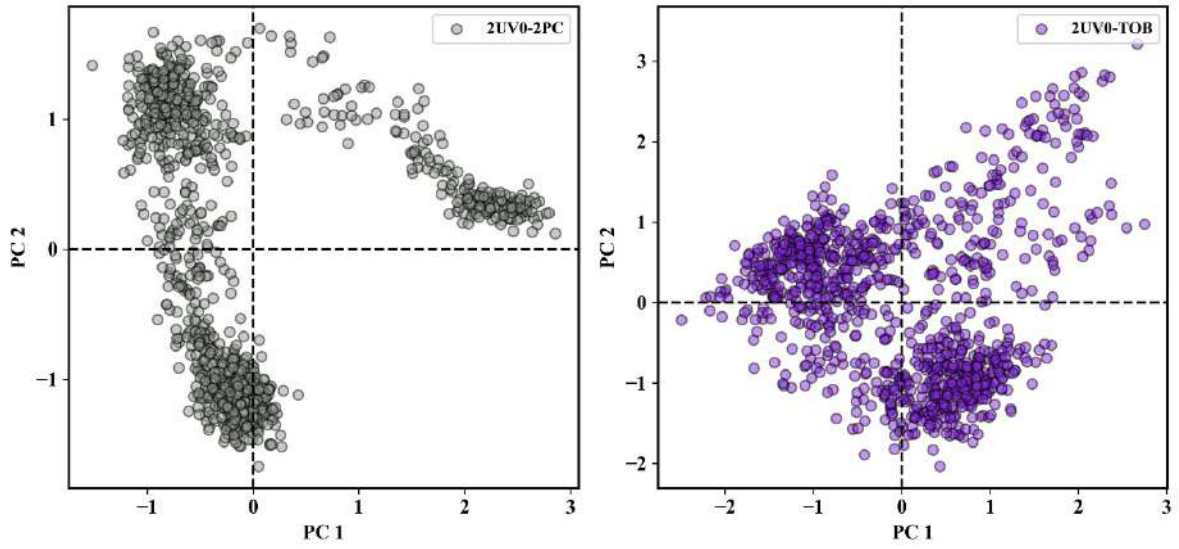


Figure 9.82: Number of intermolecular hydrogen bonds between LasR and ligands during 100-nanosecond simulation



(a) **(b)**

Figure 9.83: Principal Component Analysis (PCA) scatter plots for LasR–2PC (LasR ligand-binding domain-2-Phenyl-4H-chromen-4-one) (a) and LasR–TOB (ligand-binding domain-Tobramycin) (b) complexes

9.3.19.3.2. Free Energy Landscape (FEL)

FEL analysis provides insight into the thermodynamically favourable conformations sampled during the simulation. The LasR–2PC complex displayed a dominant single deep energy basin, consistent with a stable, well-defined binding conformation with limited transitions to higher-energy states. This suggests that 2PC binding locks the protein in a low-energy configuration, minimizing conformational heterogeneity. Conversely, the LasR–TOB complex exhibited multiple energy minima connected by shallow barriers, indicating the presence of several metastable conformations. This energy landscape aligns with the PCA results, where TOB allowed exploration of a broader conformational space. Despite this, the free energy differences between TOB's minima were small, implying that conformational transitions occur without significant destabilization. These FEL patterns suggest that while 2PC induces a rigid, stable conformation, TOB facilitates conformational adaptability, which may aid in accommodating various environmental or mutational changes in microbial targets (Plate 9.43).

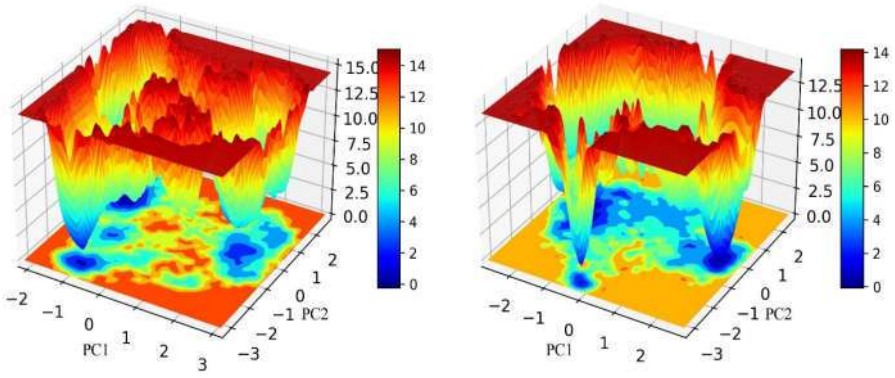
9.3.19.4. Overall Conclusion- Antimicrobial activity from Molecular dynamics (MDS) analysis

The comprehensive molecular dynamics simulation (MDS) analyses conducted for the LasR–2PC and LasR–TOB complexes provide valuable insight into the structural and dynamic consequences of ligand binding to the quorum-sensing regulator LasR. Across all trajectory-based descriptors, RMSD, RMSF, radius of gyration (Rg), solvent accessible surface area (SASA), and hydrogen bond analyses, Tobramycin (TOB) consistently demonstrated a capacity to stabilize the LasR backbone while inducing subtle conformational plasticity. This duality is reflected in its lower average RMSD (0.154 nm) compared to 2PC (0.198 nm), coupled with reduced Rg and SASA values, suggesting a more compact tertiary arrangement with diminished solvent exposure. The persistence of 2–6 intermolecular hydrogen bonds for TOB throughout the simulation, contrasted with the minimal bonding in the 2PC complex, highlights the critical role of hydrogen bonding in sustaining stable yet adaptable interactions.

While RMSF data indicated that both ligands restricted mobility within the ligand-binding domain, TOB conferred slightly more pronounced stabilization in loop regions flanking the active site. This is likely to limit conformational fluctuations that are necessary for transcriptional activation, thereby reinforcing its inhibitory potential. The intramolecular hydrogen bond analysis further confirmed TOB's ability to preserve secondary and tertiary structures, with consistently higher bond counts compared to 2PC.

From an essential dynamics perspective, principal component analysis (PCA) and free energy landscape (FEL) mapping reveal distinct binding strategies. 2PC confines LasR within a single, deep free-energy minimum, indicative of a rigid and thermodynamically stable conformation. This rigidity may hinder the structural transitions associated with DNA-binding activation. Conversely, TOB occupies multiple shallow energy basins across the FEL, reflecting the ability to sample alternative metastable states without compromising global fold integrity. Such adaptability may enhance inhibitory efficacy under fluctuating intracellular conditions, potentially offering resilience against mutational changes in the binding domain.

Taken together, these findings suggest that both ligands are capable of impairing LasR-mediated quorum sensing, but through fundamentally different dynamic mechanisms- 2PC via conformational locking, and TOB through stabilizing yet flexible interactions. Importantly, TOB's extensive hydrogen bonding and compactness-enhancing effects may confer advantages in binding persistence and functional inhibition. These complementary inhibitory modes underscore the potential of combining or optimizing such scaffolds in the design of potent anti-quorum-sensing therapeutics targeting Pseudomonas aeruginosa. The MDS-derived insights thus provide a robust foundation for rational drug development, guiding future *in vitro* and *in vivo* validation studies to translate these molecular-level stabilizing effects into tangible antimicrobial outcomes.



(a) **(b)**

Plate 9.43: Three-dimensional (3D) Free Energy Landscape (FEL) plots of (a) LasR–2PC (LasR ligand-binding domain-2-Phenyl-4H-chromen-4-one) and (b) LasR–TOB (LasR ligand-binding domain-Tobramycin) complexes

9.3.19.5. Binding Free Energy Analysis (MM/PBSA)

MM/PBSA (Molecular Mechanics Poisson–Boltzmann Surface Area) analysis was performed to quantify the binding free energies of the LasR protein complexed with 2-Phenyl-4H-chromen-4-one (phytocompound) and Tobramycin (approved antimicrobial drug). The method decomposes the total binding free energy into van der Waals, electrostatic, polar solvation, and SASA contributions, providing a detailed understanding of the interaction energetics. More negative total binding energies indicate stronger and more favourable interactions (Table 9.129).

9.3.19.5.1. Binding affinity comparison

The results show that 2-Phenyl-4H-chromen-4-one (–83.180 kJ/mol) exhibits significantly higher binding affinity toward LasR than Tobramycin (–20.179 kJ/mol). This difference is primarily driven by much stronger van der Waals interactions (–132.330 vs. –45.609 kJ/mol), indicating superior hydrophobic packing and shape complementarity within the LasR binding pocket. While Tobramycin shows slightly stronger electrostatic contributions (–32.747 vs. –7.879 kJ/mol), these are insufficient to offset its much weaker non-polar interactions.

9.3.19.5.2. Energetic contributions and structural implications

The polar solvation penalties for both ligands are positive (70.775 and 64.731 kJ/mol), reflecting the energetic cost of desolvating polar groups during binding. However, the SASA energy is more favourable for 2-Phenyl-4H-chromen-4-one (–13.746 kJ/mol vs. –6.554 kJ/mol), suggesting deeper hydrophobic burial within the receptor. Overall, the phytocompound's dominance in van der Waals stabilization and favourable hydrophobic effects underpin its superior total binding free energy. This indicates a strong potential for 2-Phenyl-4H-chromen-4-one as a potent LasR inhibitor, possibly more effective than Tobramycin in rigidly occupying the active site and blocking quorum-sensing mechanisms in microbial pathogens (Figure 9.84).

9.3.19.6. Normal Mode Analysis (NMA) for antimicrobial target (LasR)

Normal Mode Analysis (NMA) was performed on the LasR protein to evaluate its intrinsic flexibility, correlated motions, and structural stability. This analysis helps

reveal collective motions essential for ligand sensing, DNA binding, and transcriptional regulation, all of which are central to LasR's role in antimicrobial activity through quorum sensing (Plate 9.44).

9.3.19.6.1. Structural flexibility and deformability

The deformability profile exhibits multiple peaks across the LasR sequence, indicating flexible loop regions and hinge points that may facilitate ligand recognition and domain rearrangements. These flexible elements likely contribute to allosteric communication between the ligand-binding domain and the DNA-binding domain. The 3D structural representation uses a colour gradient to depict mobility: blue regions represent rigid structural cores, green/yellow indicate moderately flexible segments, and red highlights the highest mobility regions, which may correspond to ligand-binding loops and terminal ends.

9.3.19.6.2. B-Factor analysis

The NMA-predicted B-factors (pink) show a generally good agreement with the experimental crystallographic B-factors (black), validating the computational model's accuracy in capturing dynamic tendencies. High B-factor peaks appear predominantly in loop regions and termini, aligning with functionally important flexibility for ligand accommodation and DNA interaction.

9.3.19.6.3. Collective motion, eigenvalues, and variance

The first non-trivial eigenvalue is 4.59×10^{-5}, indicating low stiffness for the dominant motion mode. This suggests LasR can undergo large-scale conformational changes with minimal energy expenditure, supporting its role in responsive signal transduction. Variance analysis reveals that the first few modes capture a substantial proportion of the overall motion, consistent with cooperative domain movements that underpin its functional transitions between inactive and active states.

9.3.19.6.4. Correlated motions and elastic network

The covariance map reveals distinct zones of correlated (red) and anti-correlated (blue) motion, particularly between the ligand-binding and DNA-binding

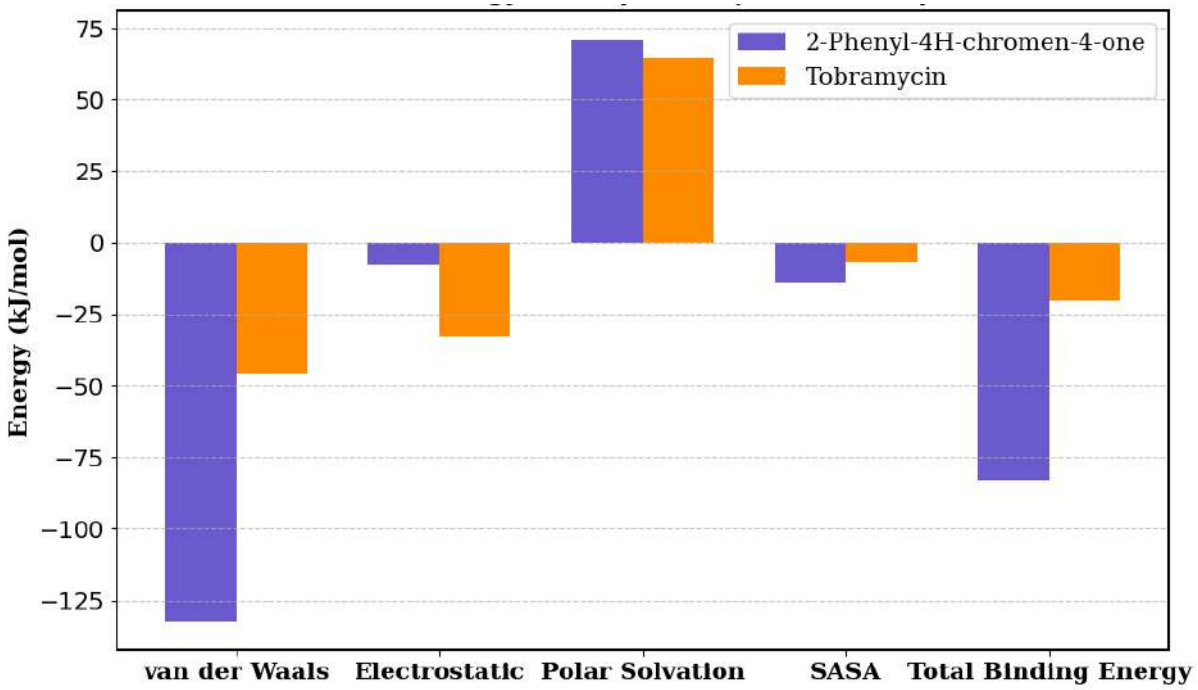


Figure 9.84: Molecular Mechanics Poisson–Boltzmann Surface Area (MM/PBSA) energy decomposition of LasR complexes with 2-Phenyl-4H-chromen-4-one and Tobramycin

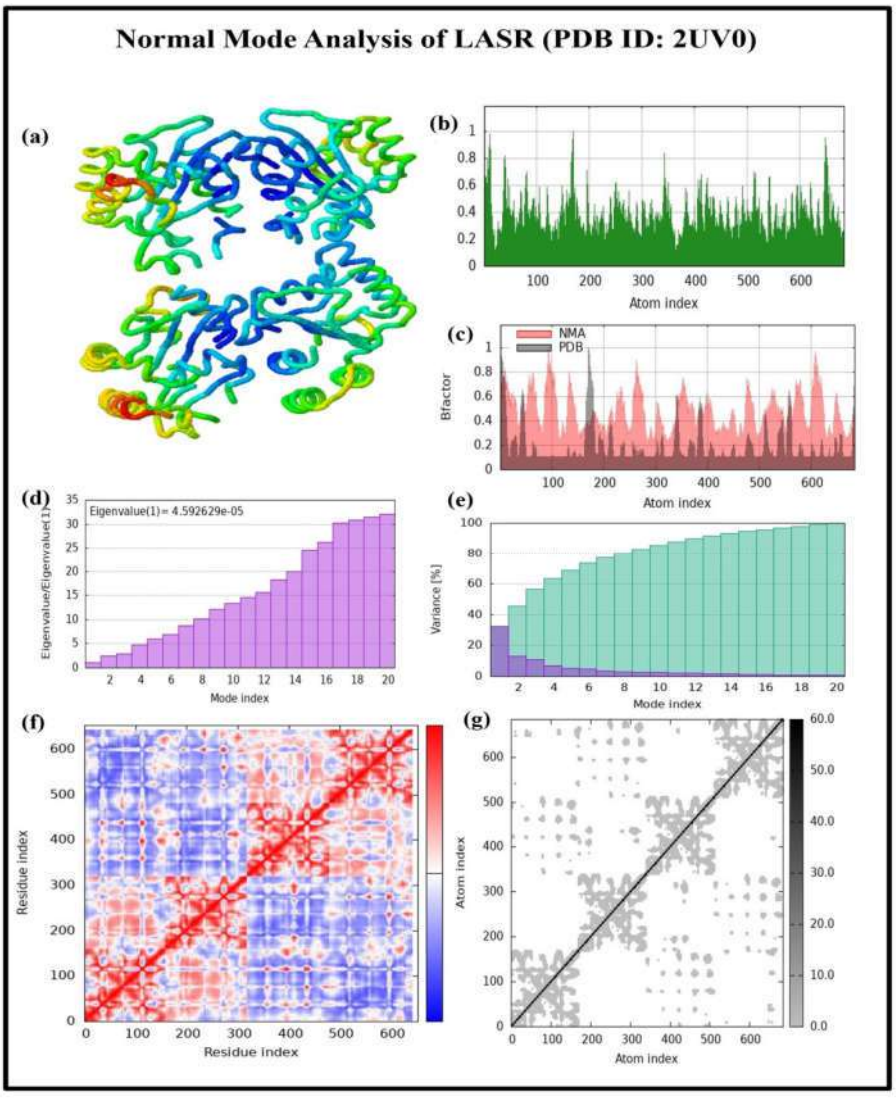


Plate 9.44: Normal Mode Analysis of LasR ligand-binding domain (LasR): (a) Cartoon representation with colour-coded mobility (blue: rigid, green/yellow: flexible) (b) deformability plot (c) B-factor comparison (NMA vs. PDB) (d) eigenvalue distribution (e) cumulative and individual variance per mode (f) covariance matrix showing correlated (red) and anti-correlated (blue) motions, and (g) elastic network map with spring strengths (dark grey: stiffer connections)

Table 9.130: Density Functional Theory (DFT) parameters for 2-Phenyl-4H-chromen-4-one and Tobramycin

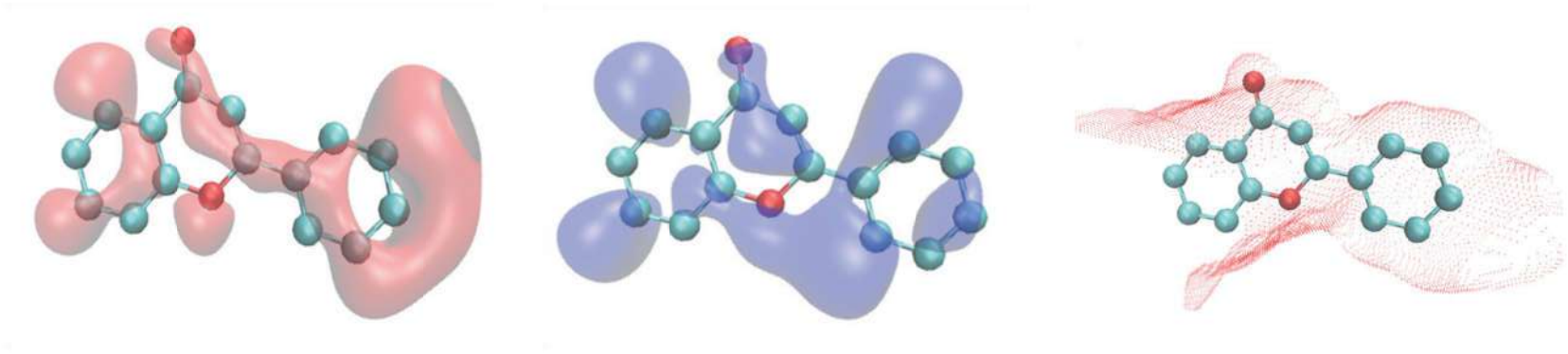
Compound name	DFT Energy (Hartree)	HOMO Energy (Hartree)	LUMO Energy (Hartree)	HOMO-LUMO Gap (Hartree)	MEP Minimum (a.u.)	MEP Maximum (a.u.)	MEP Average (a.u.)
2-Phenyl-4H-chromen-4-one-DFT	-720.670	-0.243	-0.202	0.041	-7.011	114.234	0.063
Tobramycin-DFT	-1657.677	-0.226	0.0174	0.243	-9.159	318.907	0.067

Table 9.131: Molecular Mechanics Poisson–Boltzmann Surface Area (MM/PBSA) energy decomposition for Globin-3–Vitamin E and Globin-3–Albendazole complexes

Energy component (kJ/mol)	Vitamin E	Albendazole
van der Waals	–122.289 ± 26.098	–298.817 ± 8.919
Electrostatic	55.878 ± 36.792	–14.624 ± 9.901
Polar solvation	–27.906 ± 37.940	104.880 ± 11.181
SASA	–13.884 ± 2.940	–28.292 ± 0.420
Total binding energy	–108.201 ± 23.483	–236.852 ± 11.976

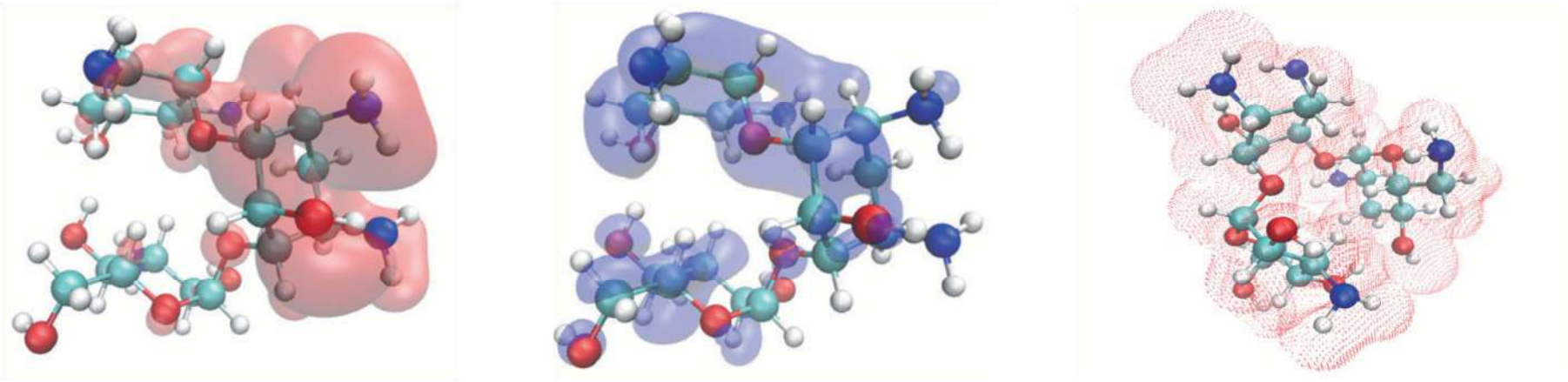
Table 9.132: Density Functional Theory (DFT) parameters for Vitamin E and Albendazole

Compound name	DFT Energy (Hartree)	HOMO Energy (Hartree)	LUMO Energy (Hartree)	HOMO-LUMO Gap (Hartree)	MEP Minimum (a.u.)	MEP Maximum (a.u.)	MEP Average (a.u.)
Albendazole-DFT	-1176.999	-0.173	0.121	0.051	-10.440	116.979	0.0436
Vitamin-E-DFT	-1286.818	-0.117	-0.025	0.092	-14.978	132.82	0.030



(a) (b) (c)

Plate 9.45: Frontier molecular orbital (Highest Occupied Molecular Orbital (HOMO), Lowest Unoccupied Molecular Orbital (LUMO)) and molecular electrostatic potential (MEP) surfaces for 2-Phenyl-4H-chromen-4-one against LasR: (a) HOMO distribution(b) LUMO distribution, and (c) MEP surface mapping



(a) (b) (c)

Plate 9.46: Frontier molecular orbital (Highest Occupied Molecular Orbital (HOMO), Lowest Unoccupied Molecular Orbital (LUMO)) and molecular electrostatic potential (MEP) surfaces for Tobramycin against LasR: (a) HOMO distribution(b) LUMO distribution, and (c) MEP surface mapping, highlighting probable interaction sites and electron density regions

domains. This highlights possible allosteric pathways for signal propagation within the protein. The elastic network model displays dense connectivity in the structural core, indicative of rigidity, whereas peripheral loops and inter-domain linkers exhibit sparser contacts, reflecting flexibility important for ligand-induced conformational changes.

9.3.19.7. DFT analysis for antimicrobial activity (LasR target)

Density Functional Theory (DFT) calculations were conducted for 2-Phenyl-4H-chromen-4-one (phytocompound) and Tobramycin (marketed antimicrobial drug) to investigate their electronic structures, frontier molecular orbital (FMO) profiles, and molecular electrostatic potential (MEP) characteristics. These descriptors help elucidate the electronic reactivity, stability, and potential interaction patterns of each ligand with the LasR binding site (Table 9.130).

9.3.19.7.1. Electronic property comparison

2-Phenyl-4H-chromen-4-one has a significantly smaller HOMO–LUMO gap (0.041 Hartree) compared to Tobramycin (0.243 Hartree), suggesting that the phytocompound is more electronically reactive and could engage in charge transfer processes more readily during ligand–protein interactions. The higher HOMO energy of 2-Phenyl-4H-chromen-4-one (-0.243 Hartree) relative to Tobramycin (-0.226 Hartree) indicates a slightly reduced electron-donating ability. Tobramycin's larger energy gap implies greater kinetic stability but lower reactivity, which aligns with its role as a broad-spectrum antibiotic with specific interaction pathways (Plate 9.45).

9.3.19.7.2. Molecular Electrostatic Potential Insights (MEP)

MEP analysis shows that Tobramycin has a more negative MEP minimum (-9.159 a.u.) than 2-Phenyl-4H-chromen-4-one (-7.011 a.u.), indicating stronger potential electrostatic attraction toward positively charged residues. However, Tobramycin also displays a much higher MEP maximum (318.907 a.u.) compared to the phytocompound (114.234 a.u.), suggesting localized regions of intense positive charge that could enhance polar and hydrogen-bonding interactions. Both ligands have similar MEP averages (0.067 for Tobramycin and 0.063 for the

phytocompound), implying a generally balanced charge distribution across their molecular surfaces (Plate 9.46).

9.3.20. Docking with a marketed anthelmintic drug

9.3.20.1. 3D and 2D visualization of Globin with Albendazole

The 3D visualization illustrates Albendazole fitting snugly into the binding cavity of the Globin protein, encapsulated by a semi-transparent molecular surface depicting the receptor topology. The ligand aligns deeply within the active groove, stabilized through a combination of polar and hydrophobic interactions with surrounding residues. Notably, Albendazole orients itself toward residues HIS119, ARG73, and PHE71/130, achieving a stable docking conformation through strategic positioning near both polar and aromatic side chains.

The 2D interaction diagram provides an atom-level depiction of Albendazole's interactions with the active site residues of Globin. The following key contacts were identified:

- Conventional Hydrogen Bonds (Green Arrows):

HIS119 and ARG73 form classical hydrogen bonds with Albendazole, aiding in anchoring the ligand firmly within the pocket.

- π–π Stacking and π–Alkyl Interactions (Pink and Light Purple Arcs):

PHE71, PHE130, and VAL125 participate in π–π stacking and π–alkyl interactions with the ligand's aromatic ring systems, enhancing hydrophobic stabilization and electronic complementarity.

- Pi–Sulfur and Pi–Sigma Interactions (Yellow and Violet Arcs):

HIS129 engages in a pi–sulfur contact with the ligand, while PHE133 is involved in a π–sigma interaction, adding diversity to the stabilizing network.

- Van der Waals Interactions (Light Green Spheres):

Residues such as LEU60, LEU70, and LEU91 contribute to van der Waals interactions, subtly shaping the local environment to accommodate the ligand's conformation.

Overall, the interaction profile suggests that Albendazole achieves a balanced binding mode in Globin through a synergistic combination of hydrogen bonding, aromatic stacking, and hydrophobic encapsulation, indicating a stable and well-oriented fit within the active pocket (Plate 9.47).

9.3.20.2. Trajectory-based structural analysis

9.3.20.2.1. Root Mean Square Deviation (RMSD)

The RMSD profile is a critical metric to evaluate the global stability of protein–ligand complexes during simulation. In this study, the RMSD of the Cα backbone was calculated over 100 ns for the Globin–Albendazole (ABD) and Globin–Vitamin E (VT3) complexes. Both complexes achieved stability within the first 10 ns, indicating rapid equilibration. The VT3 complex exhibited a lower mean RMSD (0.116 ± 0.010 nm) compared to ABD (0.135 ± 0.015 nm), highlighting that VT3 maintained a more stable conformation with fewer fluctuations. Notably, the ABD complex showed a gradual RMSD increase towards the end of the simulation, peaking near 0.20 nm, which may indicate late-stage conformational adjustments or loosening of certain structural regions. The probability density distribution further confirmed that VT3 had a narrower, sharper RMSD peak shifted toward lower deviation values, suggesting tighter structural maintenance. This stability could be attributed to the persistent hydrogen bonding and complementary fit of VT3 within the binding pocket. In contrast, ABD's slightly broader RMSD distribution reflects its allowance for minor global flexibility, potentially enabling adaptive binding modes (Figures 9.85-9.86).

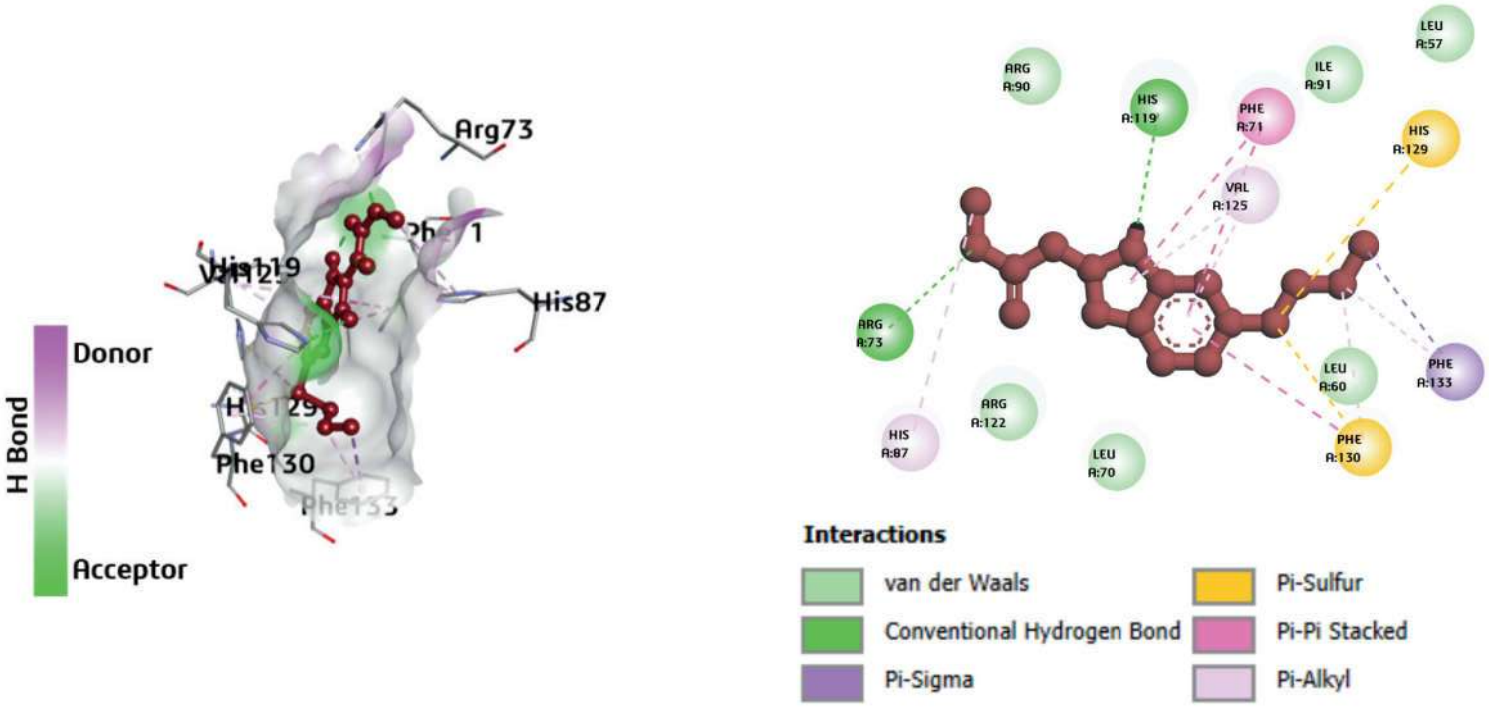
9.3.20.2.2. Root Mean Square Fluctuation (RMSF)

RMSF analysis provides residue-level insights into the flexibility of the protein backbone, highlighting regions most affected by ligand binding. For both

complexes, the majority of residues exhibited RMSF values below 0.20 nm, reflecting overall stability. Peaks in flexibility were observed near residues 40–50 and 75–80, corresponding to surface-exposed loops and coil regions prone to movement. The ABD complex displayed slightly higher RMSF amplitudes in these regions compared to VT3, suggesting that ABD binding permits greater local motion in non-secondary structural regions. VT3 binding, in contrast, dampened fluctuations in these same segments, indicating enhanced stabilization of flexible loops. This rigidity could improve the resilience of the VT3-bound conformation against environmental perturbations, possibly aiding in consistent target engagement. Importantly, the reduced fluctuations in catalytic or binding site-adjacent regions for VT3 imply a stabilizing influence directly linked to its interaction network within the pocket. In summary, RMSF analysis reveals that VT3 promotes localized rigidity, whereas ABD allows controlled flexibility, which might influence their respective binding mechanisms and inhibitory profiles (Figure 9.87).

9.3.20.2.3. Radius of Gyration (Rg)

The radius of gyration (Rg) measures the compactness of the protein structure during simulation. Both complexes maintained stable Rg values over the 100 ns trajectory, indicating no large-scale unfolding or collapse events. VT3 showed a slightly higher average Rg (1.538 ± 0.004 nm) compared to ABD (1.531 ± 0.005 nm). This marginal difference suggests that VT3 binding induces a subtly more expanded conformation, possibly due to the steric properties of the molecule or its influence on side-chain orientations. The constancy of Rg for both systems indicates that ligand binding does not compromise the overall structural integrity of Globin-3. The minimal variation observed (±0.005 nm) underscores that the protein remained compact and stable throughout the simulation. The slightly greater Rg in VT3's case could also correlate with the higher SASA observed for the same complex, reinforcing the notion of a more solvent-accessible protein surface. Ultimately, both ligands maintained structural compactness, but VT3 allowed for a slightly more relaxed tertiary structure without compromising stability (Figure 9.88).



(a) (b)

Plate 9.47: Visualization of binding interactions between Extracellular Globin-3 /Erythrocruorin (Ext. Globin-3) and marketed antioxidant drug Albendazole (ABD), showing (a) the three-dimensional (3D) molecular surface and (b) the two-dimensional (2D) interaction diagram

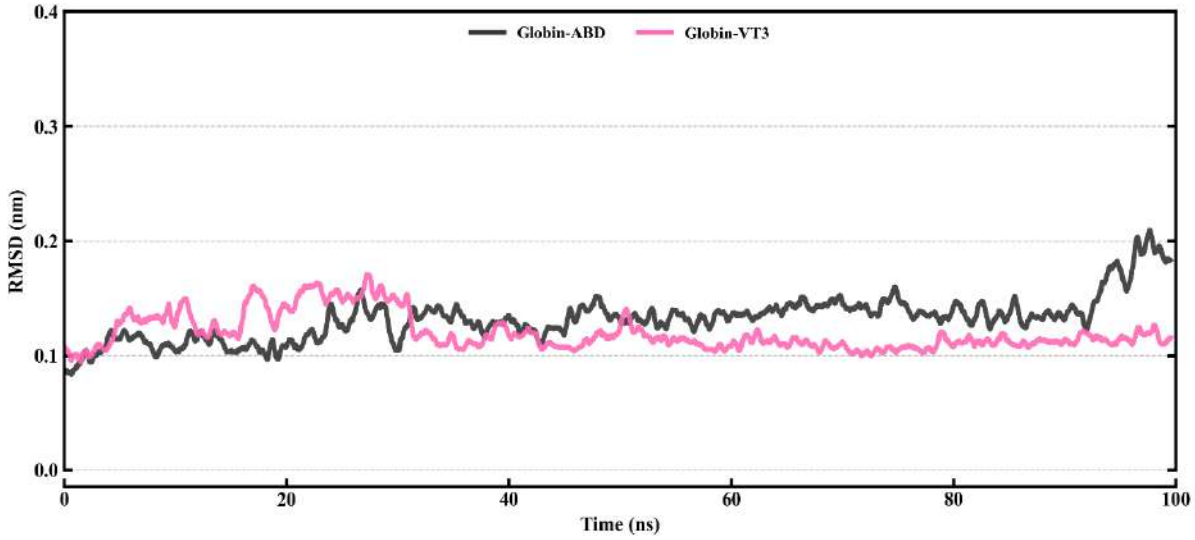


Figure 9.85: Root Mean Square Deviation (RMSD) profile of Globin–ABD (Globin-3/Erythrocruorin-Albendazole) and Globin–VT3 Globin-3/Erythrocruorin-Vitamin E) complexes over 100 nanoseconds, showing stability trends and comparative fluctuation magnitudes

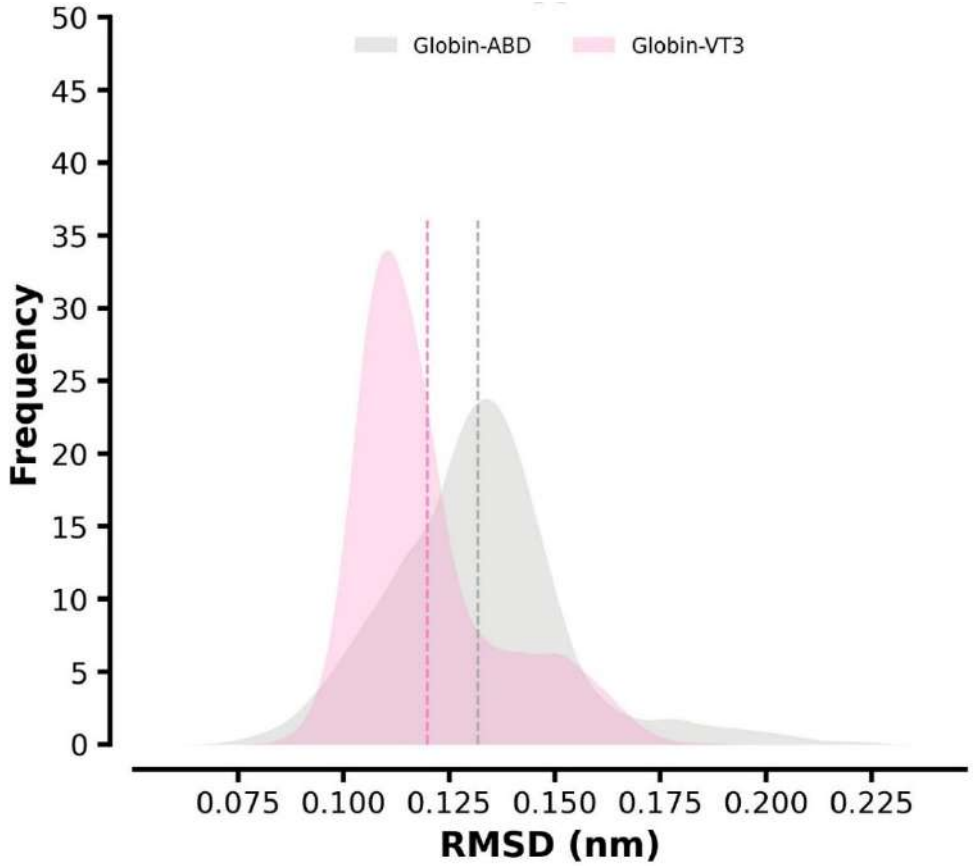


Figure 9.86: Probability density distribution of Root Mean Square Deviation (RMSD) values for both complexes, highlighting VT3's (Vitamin E) narrower stability range compared to ABD (Albendazole)

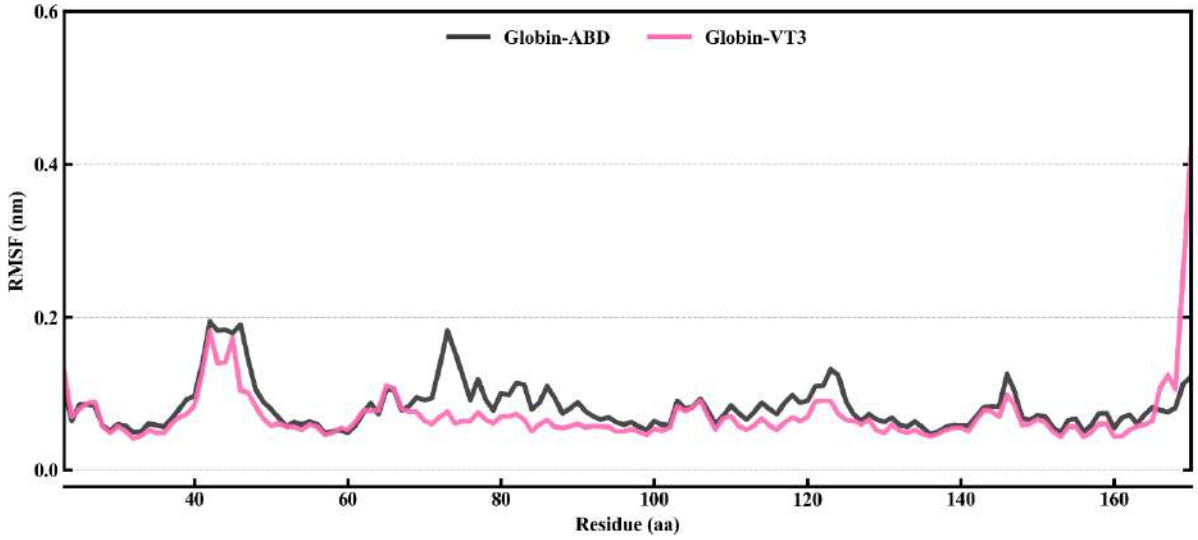


Figure 9.87: Root Mean Square Fluctuation (RMSF) plots for Globin–ABD (Globin-3/Erythrocruorin-Albendazole) and Globin–VT3 (Globin-3/Erythrocruorin-Vitamin E) complexes, illustrating residue-specific mobility patterns and ligand-specific flexibility modulation

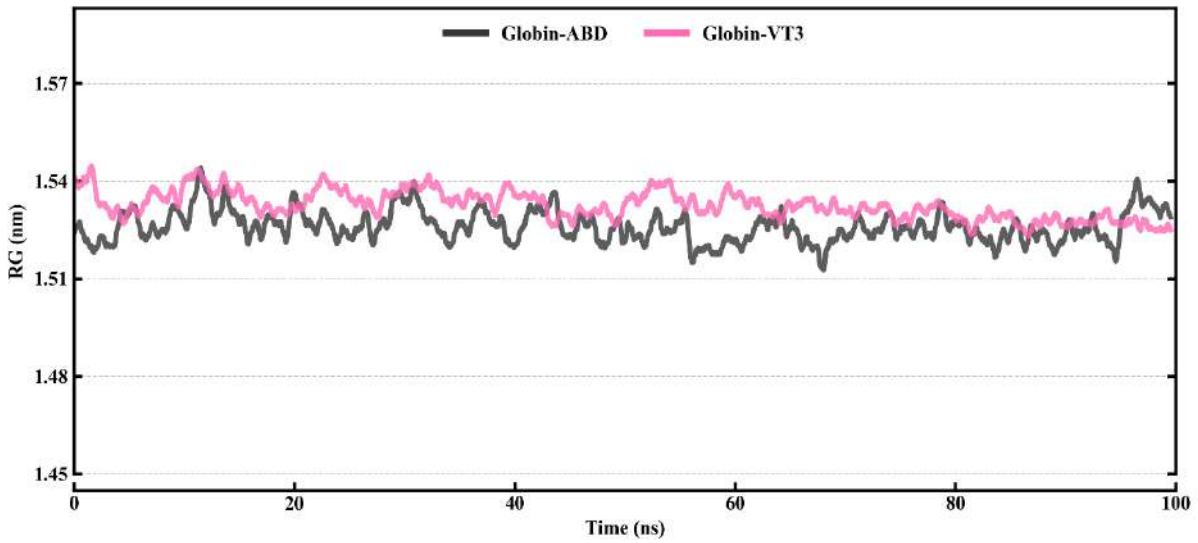


Figure 9.88: Radius of Gyration (Rg) profiles of the Globin–ABD (Globin-3/Erythrocruorin-Albendazole) and Globin–VT3 (Globin-3/Erythrocruorin-Vitamin E) complexes over 100 nanoseconds, indicating stable compactness and minor differences in global protein dimensions

9.3.20.2.4. Solvent Accessible Surface Area (SASA)

SASA reflects the degree of exposure of the protein surface to the solvent and can be indicative of conformational adjustments during ligand binding. The VT3 complex maintained a higher average SASA (88.7 ± 1.5 nm²) compared to ABD (85.2 ± 1.4 nm²). This suggests that VT3 binding leads to a conformation where more residues, possibly polar or hydrophilic, are solvent exposed. Such exposure can be beneficial in promoting interactions with surrounding molecules or in facilitating ligand exchange. In contrast, ABD binding results in a slightly more compact structure with reduced solvent exposure, consistent with its lower Rg value. Over the course of the simulation, SASA values for both complexes remained relatively stable, indicating no significant folding/unfolding events. The higher SASA of VT3-bound Globin-3 aligns with its slightly expanded structure observed in Rg analysis and may indicate enhanced flexibility in surface loops or side chains (Figure 9.89).

9.3.20.2.5. Intramolecular Hydrogen Bonds

Intramolecular hydrogen bonds are essential for maintaining protein secondary and tertiary structure during simulation. Both complexes retained a strong hydrogen bond network, with counts fluctuating between 110–125 throughout the trajectory. ABD consistently maintained slightly higher H-bond numbers than VT3, supporting the notion that ABD's binding conformation promotes more compact folding and structural rigidity. Stable intramolecular H-bonds indicate that neither ligand disrupted the core fold of Globin-3. For VT3, the slightly reduced H-bond count could be linked to its slightly expanded Rg and elevated SASA values, suggesting minor loosening of tertiary packing without compromising stability. These observations imply that both ligands preserve protein structural integrity, but ABD slightly enhances internal cohesion through higher intramolecular hydrogen bonding (Figure 9.90).

9.3.20.2.6. Intermolecular Hydrogen Bonds

Intermolecular H-bonds between protein and ligand are critical for binding specificity and stability. VT3 consistently formed 1–3 hydrogen bonds throughout the

simulation, with some contacts persisting over extended periods. ABD formed slightly fewer H-bonds on average, and these were less persistent, suggesting greater reliance on hydrophobic and van der Waals contacts. VT3's stronger polar interaction profile could contribute to its narrower RMSD range and dampened RMSF in loop regions. The consistent H-bonding pattern in VT3 also aligns with its stable global conformation observed in RMSD analysis, whereas ABD's fluctuating contacts may permit adaptive movement within the binding pocket (Figure 9.91).

9.3.20.3. Conformational sampling and energy landscape

9.3.20.3.1. Principal Component Analysis (PCA)

PCA was used to assess large-scale collective motions in the protein–ligand complexes by projecting the trajectory onto the first two principal components (PC1 and PC2). The ABD complex displayed a compact clustering of points, indicating limited exploration of conformational space and suggesting that ABD binding constrains protein motion to a few energetically favourable states. VT3, however, exhibited a more dispersed point distribution, spanning a larger PC1–PC2 space, indicating a wider sampling of conformations. This broader sampling could imply that VT3 allows greater flexibility in protein dynamics, possibly facilitating adaptive binding and accommodating conformational variability in the target protein. While this flexibility might be beneficial for targeting dynamic or variable parasite proteins, it may also suggest a less rigidly locked complex compared to ABD. These differences in motion space occupation are consistent with FEL findings, where VT3 displayed multiple shallow minima and ABD exhibited a single dominant energy well (Figure 9.92).

9.3.20.3.2. Free Energy Landscape (FEL)

FEL analysis revealed distinct stability profiles between the two complexes. The ABD complex exhibited a deep, centralized energy basin (~14–15 kJ/mol), indicating a thermodynamically stable bound state with minimal conformational diversity. This landscape suggests a strong energetic preference for a single conformation, consistent with ABD's compact PCA clustering. In contrast, VT3

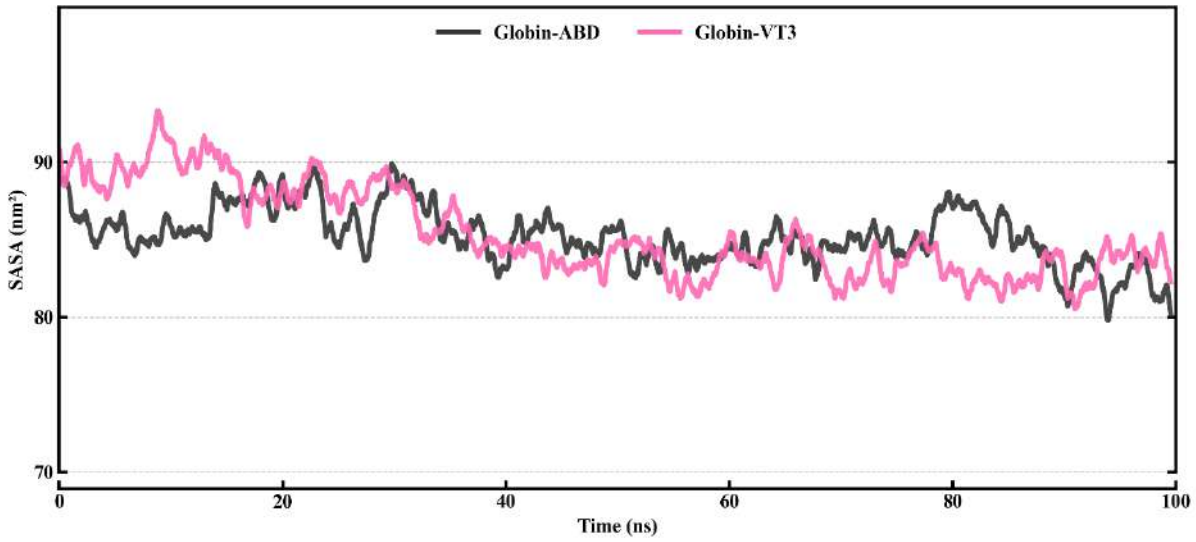


Figure 9.89: Solvent Accessible Surface Area (SASA) profiles for plots for Globin–ABD (Globin-3/Erythrocruorin-Albendazole) and Globin–VT3 (Globin-3/Erythrocruorin-Vitamin E) complexes over 100 nanoseconds, showing ligand-dependent differences in solvent exposure

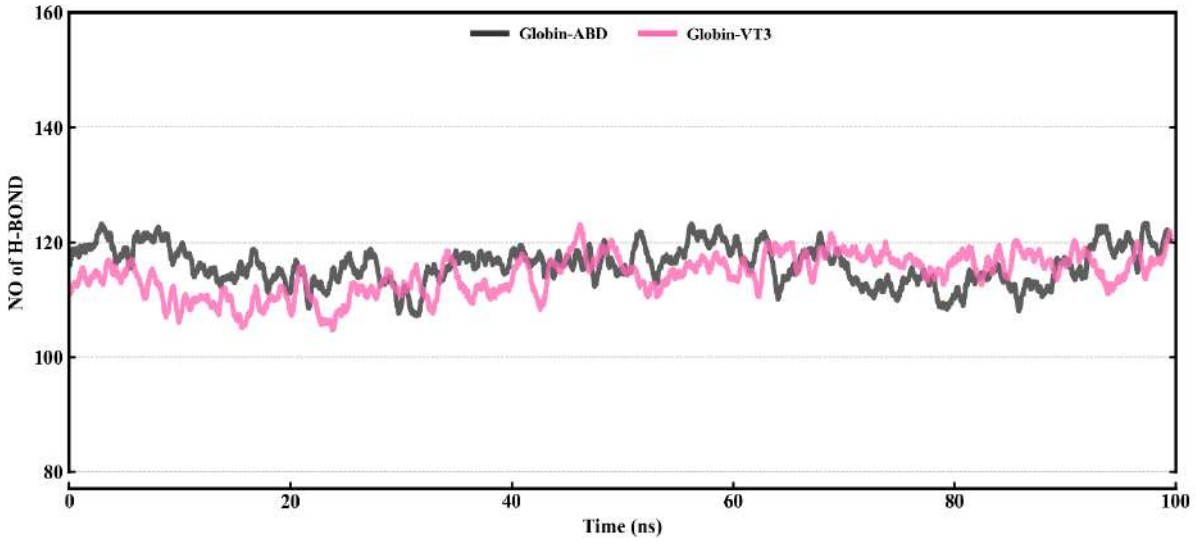


Figure 9.90: Number of intramolecular hydrogen bonds over time for Globin–ABD (Globin-3/Erythrocruorin-Albendazole) and Globin–VT3 (Globin-3/Erythrocruorin-Vitamin E) complexes, highlighting structural retention

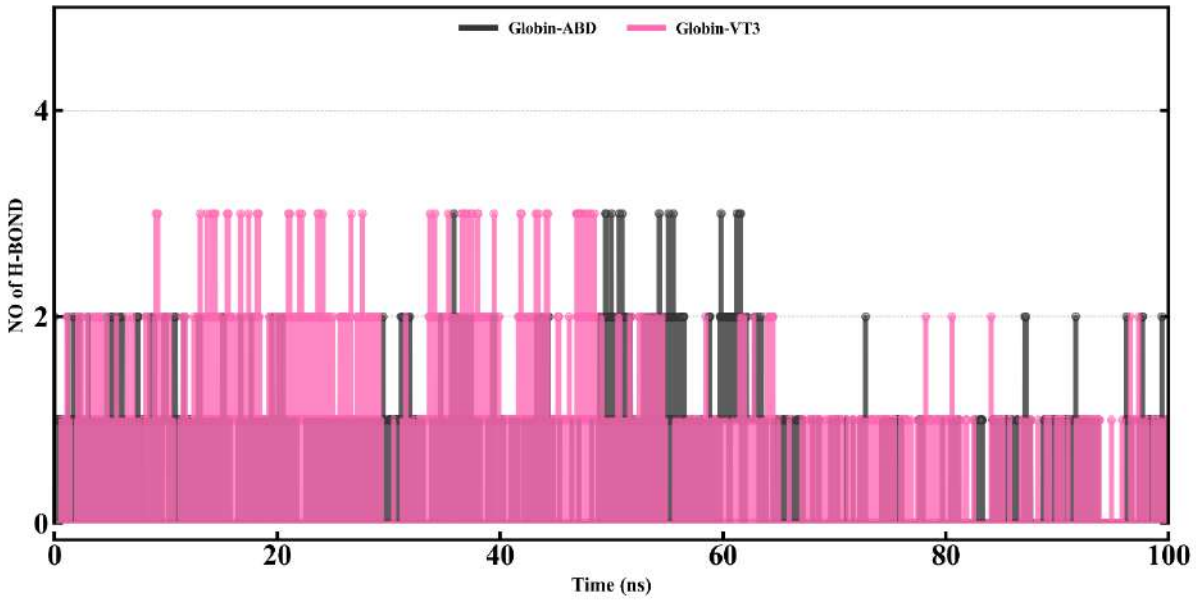
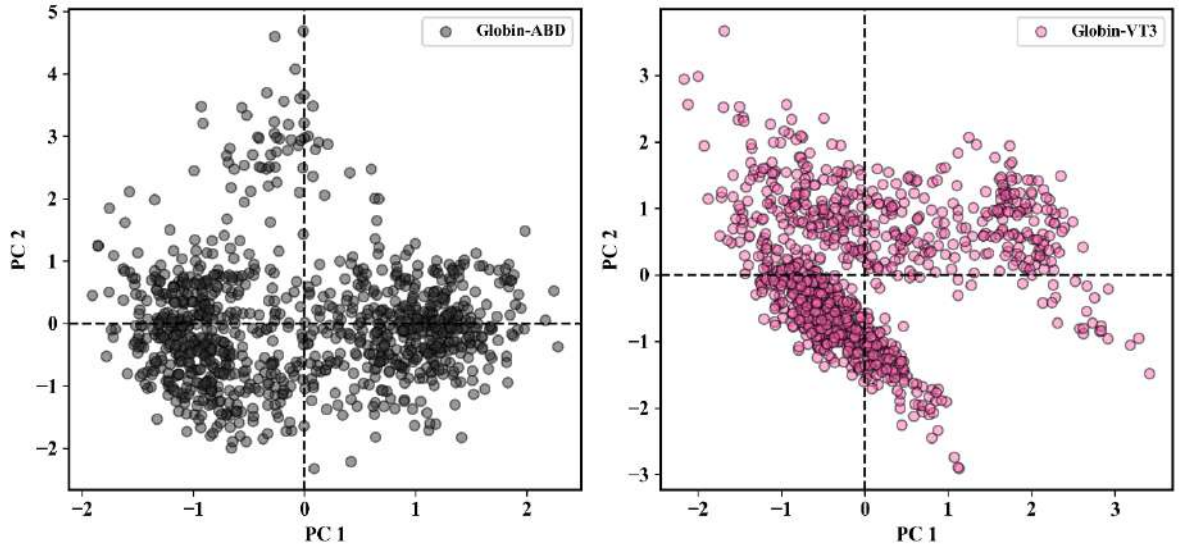


Figure 9.91: Intermolecular hydrogen bond counts for Globin–ABD (Globin-3/Erythrocruorin-Albendazole) and Globin–VT3 (Globin-3/Erythrocruorin-Vitamin E) complexes over 100 nanoseconds



(a) **(b)**

Figure 9.92: Principal Component Analysis (PCA) plots of Globin–ABD (a) and Globin–VT3 (b) complexes showing conformational sampling in PC1–PC2 space

displayed a rugged landscape with multiple shallow minima (~10–12 kJ/mol), reflecting greater conformational adaptability and dynamic sampling of alternative low-energy states. This adaptability may allow VT3 to maintain effective binding despite potential structural variations in the target site. However, the presence of multiple minima may also indicate that VT3 does not fully lock the protein into one dominant conformation, instead allowing microstate interconversions. From a pharmacological perspective, ABD's deeper energy well suggests strong structural fixation, a property often advantageous for sustained inhibition, whereas VT3's adaptable landscape could be beneficial for multi-target or variable-target anthelminthic action (Plate 9.48).

9.3.20.4. Overall conclusion- Anthelminthic activity from Molecular dynamics (MDS) analysis

The comprehensive MDS evaluation of the Globin–3 protein bound to Albendazole (ABD) and Vitamin E (VT3) reveals clear distinctions in dynamic stability, structural compactness, and conformational sampling that have direct pharmacological implications for anthelminthic potential. Across all primary stability indicators, RMSF, Rg, SASA, hydrogen bonding patterns, PCA, and FEL, VT3 consistently maintained a more compact and stable conformational profile compared to ABD. The lower and more tightly clustered RMSD values of VT3 indicate superior structural retention, while reduced RMSF peaks in loop and flexible regions suggest enhanced local rigidity at functionally important residues. This stabilization was further supported by steady Rg values and minimal fluctuations in SASA, indicating preserved tertiary packing and solvent exposure throughout the simulation.

Hydrogen bonding analysis revealed that while both ligands formed persistent intramolecular stabilizing interactions, VT3 maintained a comparable hydrogen bond count to ABD but with greater temporal consistency, hinting at a more energetically favourable binding mode. PCA and FEL analyses further reinforced these observations: VT3 explored a narrower conformational subspace and exhibited a deeper, well-defined global energy basin, reflective of a more energetically optimized bound state, whereas ABD sampled a broader and more fragmented energy landscape.

From a pharmacological standpoint, these dynamics suggest that VT3 could serve as a structurally stable and energetically favourable binder to Globin–3, potentially offering sustained inhibitory effects against the target's function in helminths. While ABD remains an effective anthelminthic agent, its comparatively higher flexibility and broader conformational sampling might contribute to adaptive protein motions, possibly influencing long-term efficacy or resistance development. The combined structural and energetic insights strongly support VT3 as a promising candidate for further *in vitro* and *in vivo* anthelminthic validation.

9.3.20.5. Binding Free Energy (MM/PBSA)

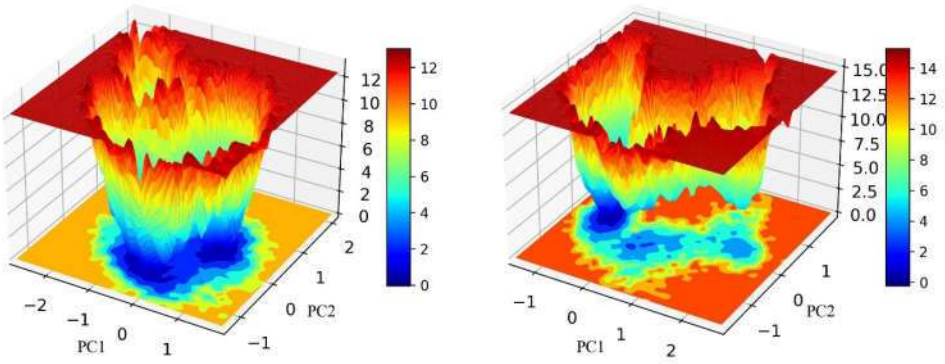
MM/PBSA (Molecular Mechanics Poisson–Boltzmann Surface Area) analysis was conducted to evaluate the binding free energies of the Globin-3 protein complexed with Vitamin E (a phytocompound) and Albendazole (an approved anthelminthic drug). This method provides energy decomposition into van der Waals, electrostatic, polar solvation, and SASA contributions, revealing the energetic factors that govern ligand binding. A more negative total binding energy indicates stronger and more favourable binding affinity (Table 9.131).

9.3.20.5.1. Binding affinity comparison

The total binding free energy reveals that Albendazole (–236.852 kJ/mol) binds significantly more strongly to Globin-3 than Vitamin E (–108.201 kJ/mol). This enhanced binding in Albendazole is primarily driven by its much stronger van der Waals interactions (–298.817 vs. –122.289 kJ/mol) and a more favourable SASA contribution (–28.292 vs. –13.884 kJ/mol), indicating deeper hydrophobic burial in the binding site.

9.3.20.5.2. Energetic contributions and structural implications

Vitamin E shows a large positive electrostatic component (+55.878 kJ/mol), which reduces its net binding affinity, likely reflecting unfavourable charge distribution or repulsion within the binding pocket. In contrast, Albendazole has a small, stabilizing electrostatic term (–14.624 kJ/mol), suggesting better electrostatic complementarity. The polar solvation energy for Albendazole (+104.880 kJ/mol) is



(a) **(b)**

Plate 9.48: Three-dimensional (3D) Free energy landscapes (FEL) of (a) Globin–ABD (Globin-3/Erythrocruorin-Albendazole) and (b) Globin–VT3 (Globin-3/Erythrocruorin-Vitamin E) complexes mapped along PC1 and PC2, illustrating differences in thermodynamic stability and conformational diversity

higher than for Vitamin E (–27.906 kJ/mol), indicating a greater desolvation penalty; however, this is outweighed by its substantial van der Waals stabilization. Overall, while Vitamin E demonstrates moderate hydrophobic stabilization, its unfavourable electrostatics and weaker dispersion forces limit its binding. Albendazole's strong hydrophobic packing, favourable SASA, and balanced electrostatics result in superior binding, consistent with its clinical efficacy as an anthelminthic agent (Figure 9.93).

9.3.20.6. Normal Mode Analysis (NMA) for anthelminthic target (Globin-3)

Normal Mode Analysis (NMA) was conducted on the Globin-3 protein to explore its inherent flexibility, correlated motions, and mechanical stability. This approach reveals low-frequency collective motions that may be functionally significant, providing insight into regions involved in ligand accommodation and potential conformational rearrangements during protein function (Plate 9.49).

9.3.20.6.1. Structural Flexibility and Deformability

The deformability profile reveals several moderate peaks, indicating flexible loop regions interspersed within otherwise stable α-helical segments. These flexible regions are potential hinge points that could facilitate conformational adjustments essential for ligand binding and structural adaptation. The 3D mobility representation shows that blue regions are rigid (structurally stable α-helices), while green/yellow areas correspond to higher mobility, likely located in loop regions and terminal ends.

9.3.20.6.2. B-Factor analysis

The NMA-predicted B-factor distribution (pink) generally aligns with experimental crystallographic B-factors (black), with higher mobility observed in terminal and loop regions. These flexible sites may play a role in ligand entry or allosteric regulation. The relatively uniform helical core shows low B-factor values, consistent with its structural rigidity.

9.3.20.6.3. Collective motion, eigenvalues, and variance

The first non-trivial eigenvalue is 5.04×10^{-4}, indicating moderate structural stiffness compared to KRAS, suggesting that conformational changes require slightly

more energy but are still feasible for functional motions. Variance analysis shows that the first few modes contribute substantially to total motion, highlighting the collective nature of protein flexibility.

9.3.20.6.4. Correlated motions and elastic network

The covariance map shows distinct red (correlated) and blue (anti-correlated) regions, suggesting a clear pattern of coordinated movement between certain α-helical segments. This interplay could be important for ligand stabilization. The elastic network model indicates dense and strong connections in the protein's helical core, which ensure structural integrity, while peripheral loops exhibit sparser connectivity, consistent with their higher deformability.

9.3.20.7. DFT analysis for anthelminthic activity (Globin-3 Target)

Density Functional Theory (DFT) calculations were performed for Vitamin E (phytocompound) and Albendazole (marketed anthelminthic drug) to evaluate their electronic structures, frontier molecular orbital (FMO) characteristics, and molecular electrostatic potential (MEP) profiles. These parameters provide valuable insights into electronic reactivity, stability, and probable interaction modes with the Globin-3 binding site (Table 9.132).

9.3.20.7.1. Electronic property comparison

Vitamin E exhibits a HOMO–LUMO gap of 0.092 Hartree, which is almost twice that of Albendazole (0.051 Hartree), suggesting that Albendazole is electronically more reactive and may adapt more readily to charge transfer processes during binding. Albendazole also shows a higher HOMO energy (-0.173 Hartree) compared to Vitamin E (-0.117 Hartree), indicating a slightly stronger electron-donating ability (Plate 9.50).

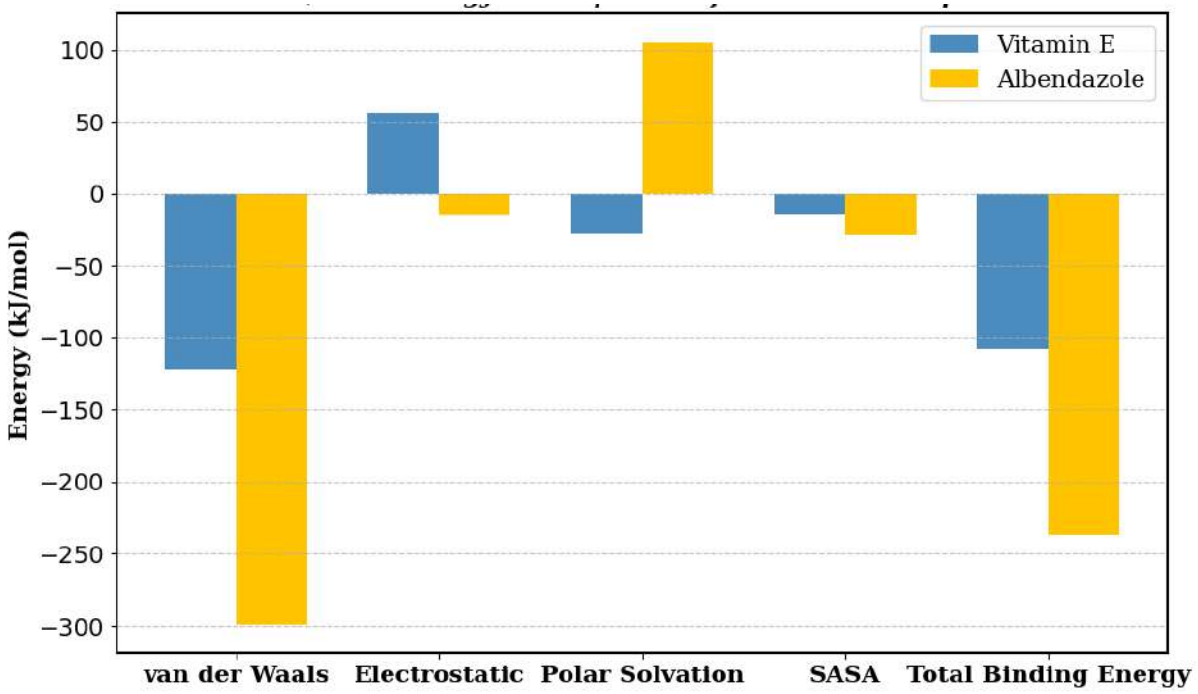


Figure 9.93: Molecular Mechanics Poisson–Boltzmann Surface Area (MM/PBSA) energy decomposition for Globin-3 complexes with Vitamin E and Albendazole

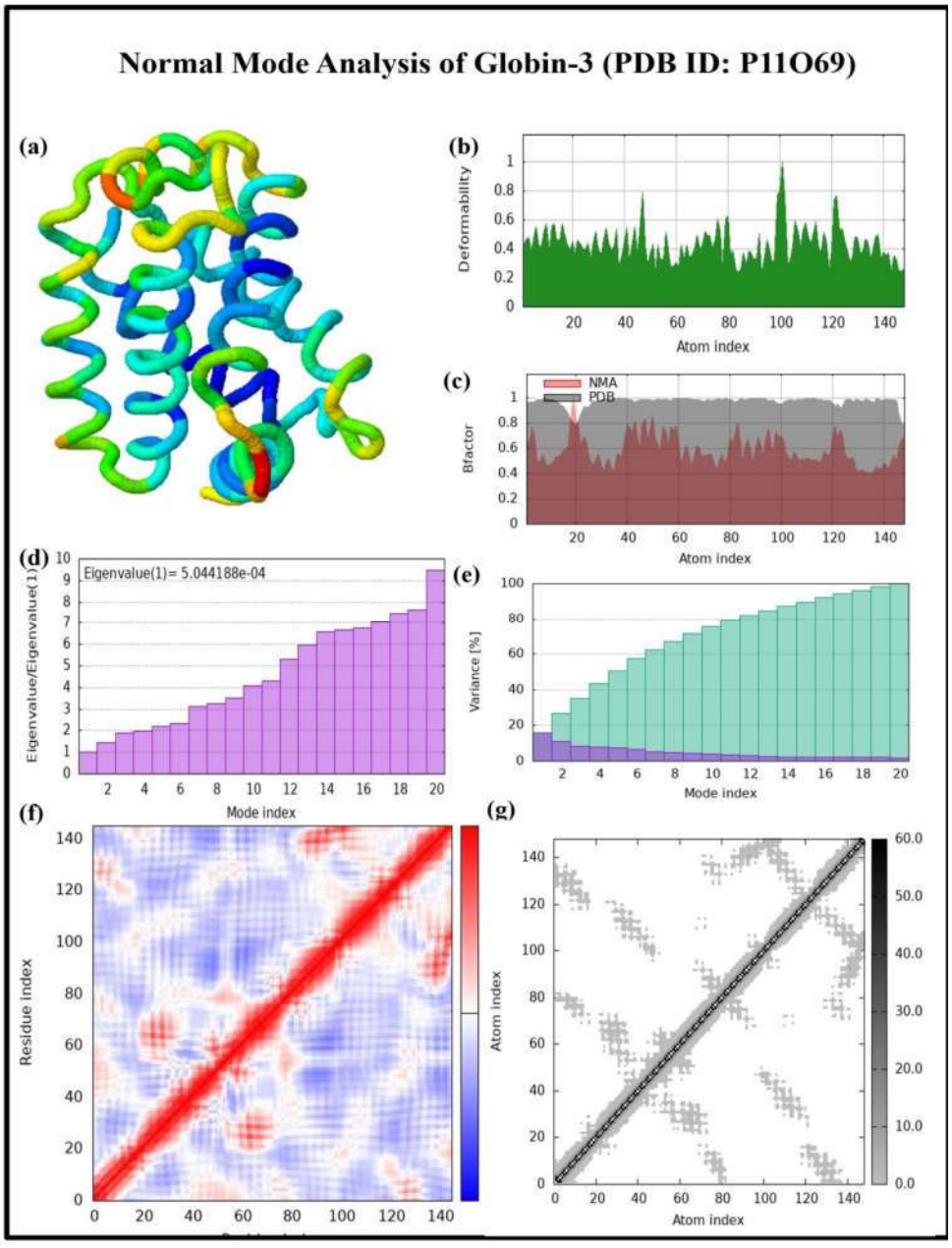
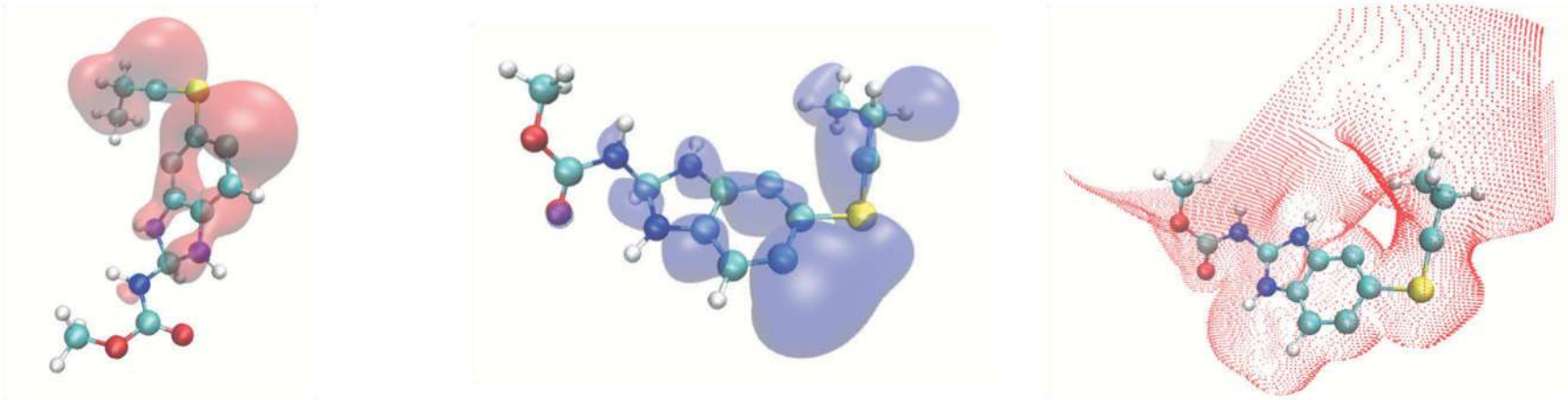


Plate 9.49: Normal Mode Analysis of Extracellular Globin-3/Erythrocruorin (Ext.Globin-3): (a) Cartoon representation with colour-coded mobility (blue: rigid, green/yellow: flexible) (b) deformability plot (c) B-factor comparison (NMA vs. PDB) (d) eigenvalue distribution (e) cumulative and individual variance per mode (f) covariance matrix showing correlated (red) and anti-correlated (blue) motions, and (g) elastic network map with spring strengths (dark grey: stiffer connections)



(a) (b) (c)

Plate 9.50: Frontier molecular orbital (Highest Occupied Molecular Orbital (HOMO), Lowest Unoccupied Molecular Orbital (LUMO)) and molecular electrostatic potential (MEP) surfaces for Vitamin E against Globin-3: (a) HOMO distribution(b) LUMO distribution, and (c) MEP surface mapping

9.3.21. Docking with a marketed anti-inflammatory drug

9.3.21.1. 3D and 2D Visualization of Human Inducible Nitric Oxide Synthase (iNOS) with Celecoxib

The 3D visualization depicts Celecoxib deeply anchored within the binding pocket of Human Inducible Nitric Oxide Synthase (iNOS), adopting an orientation that maximizes both aromatic stacking and hydrogen bonding potential. The ligand is strategically positioned such that its sulfonamide group faces polar residues, enabling hydrogen bond formation, while the aromatic rings align within hydrophobic cavities enriched with non-polar residues. The molecular surface mapping reveals distinct hydrophilic (purple) and hydrophobic (green) zones, indicating complementary shape and polarity between the ligand and the active site architecture.

The 2D interaction profile highlights:

- Conventional Hydrogen Bonds (green lines)

Celecoxib forms directional hydrogen bonds with GLY371, ASN570, and GLU377, contributing to strong anchoring and enhancing specificity toward the iNOS binding site.

- Pi–Anion Interaction (orange arc)

The π-system of Celecoxib engages with the negatively charged GLU377, promoting electrostatic stabilization.

- Pi–Pi Stacked and Pi–Alkyl Contacts (pink arcs)

Key π–π stacking is observed with TRP194, while π–alkyl interactions with TYR489, TRP572, and PRO550 further stabilize the aromatic moiety in a hydrophobic context.

- Van der Waals Contacts (light green spheres)

Residues such as GLY202, ILE201, LEU209, SER242, and MET374 surround the ligand, contributing additional dispersion forces to enhance overall complex stability.

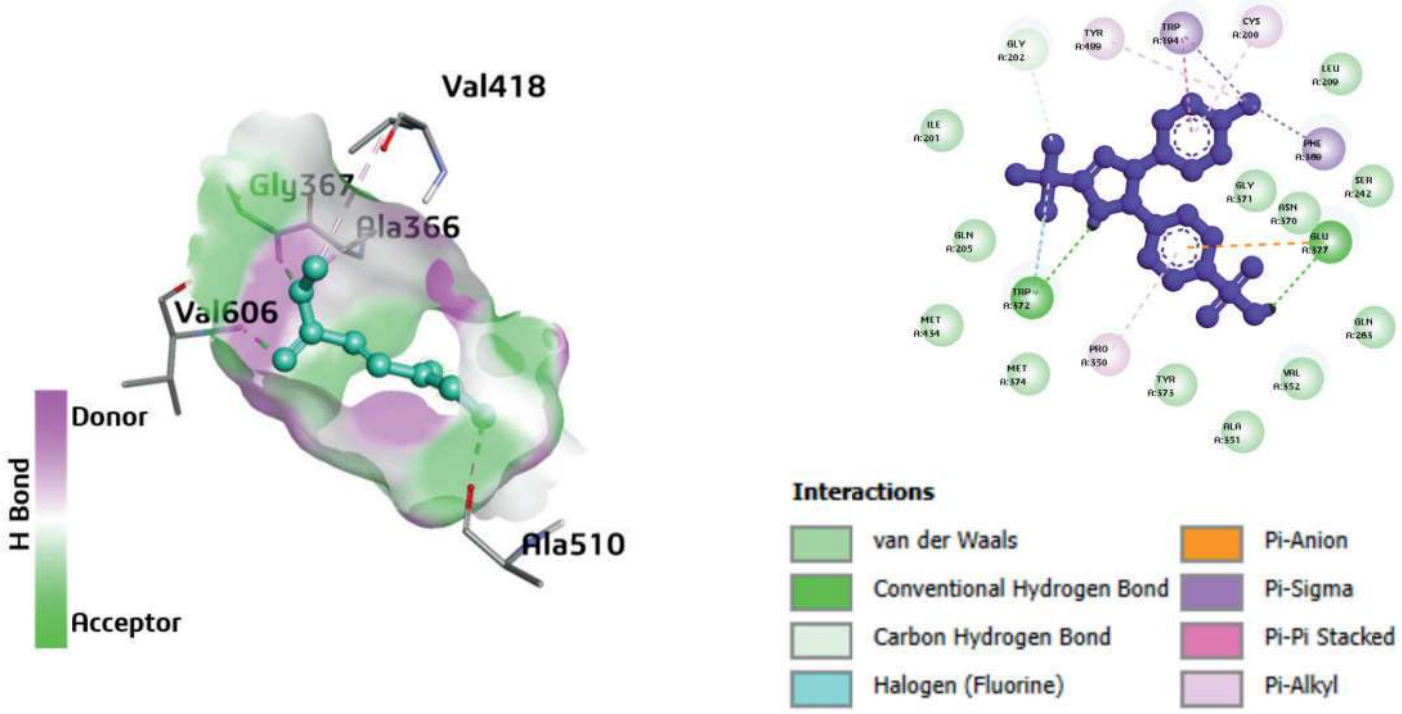
This interaction network, characterized by a balance of strong polar contacts, aromatic stacking, and hydrophobic packing, suggests that Celecoxib is optimally positioned to inhibit iNOS activity. Such binding may effectively modulate nitric oxide production, aligning with Celecoxib's known anti-inflammatory pharmacological profile (Plate 9.51).

9.3.21.2. Trajectory-based structural analysis

9.3.21.2.1. Root Mean Square Deviation (RMSD)

The RMSD profile of the Cα backbone provides insight into the global stability of the iNOS–Celecoxib (CEL) and iNOS–Cholesta-4,6-dien-3-ol, benzoate, (3.beta.)- (CHO) complexes over the 100 ns MD simulation. Both complexes achieved early stabilization within the first 10 ns, with RMSD values consistently below 0.25 nm, suggesting strong structural retention. The iNOS–CEL system exhibited slightly lower mean RMSD (0.176 ± 0.015 nm) compared to iNOS–CHO (0.189 ± 0.017 nm), indicating that CEL binding results in a more rigid global conformation. The CHO-bound complex showed transient increases in RMSD between 40–60 ns, possibly reflecting minor ligand-induced adjustments before re-stabilizing.

The RMSD probability density distribution reinforces these findings, with iNOS–CEL displaying a narrower peak shifted toward lower deviation values, indicative of reduced conformational variability. In contrast, the broader distribution of iNOS–CHO suggests slightly enhanced flexibility, potentially due to its bulky hydrophobic structure influencing pocket dynamics. This comparative rigidity in CEL-bound iNOS could translate into stronger, more sustained inhibitory interactions at the binding site, while CHO's moderate flexibility might allow adaptive binding but at the cost of slightly reduced stability (Figures 9.94-9.95).



(a) (b)

Plate 9.51: Visualization of binding interactions between Human Inducible Nitric Oxide Synthase (iNOS) and marketed anti-inflammatory drug Celecoxib (CEL), showing (a) the three-dimensional (3D) molecular surface and (b) the two-dimensional (2D) interaction diagram

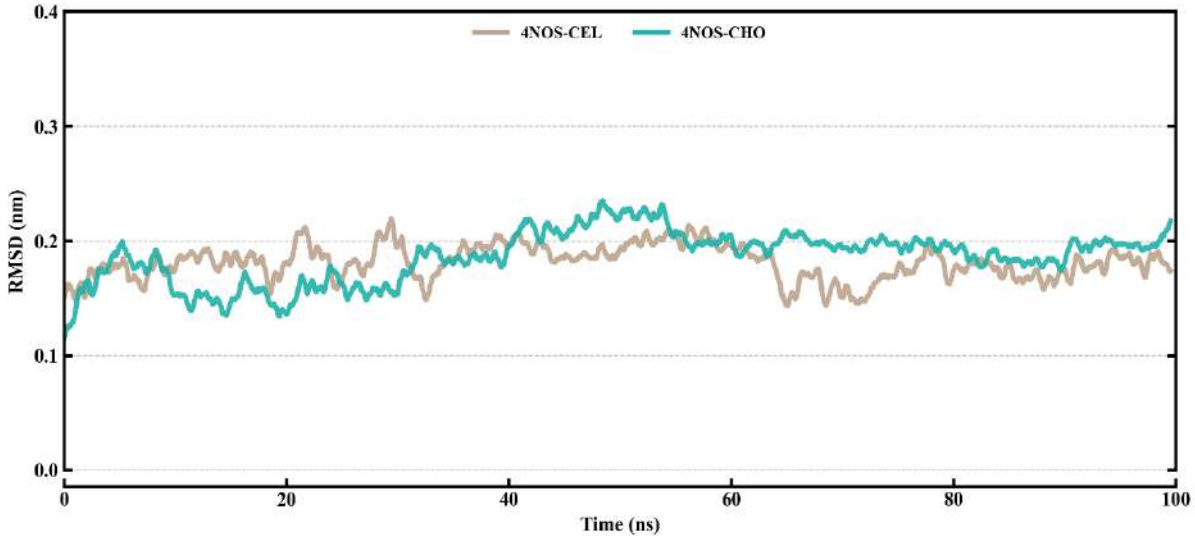


Figure 9.94: Root Mean Square Deviation (RMSD) profile of the iNOS–CEL (Human Inducible Nitric Oxide Synthase-Celecoxib) and iNOS–CHO (Human Inducible Nitric Oxide Synthase-Cholesta-4,6-dien-3-ol, benzoate, (3.beta.)-) complexes over 100 nanoseconds, showing stability trends and comparative fluctuation magnitudes

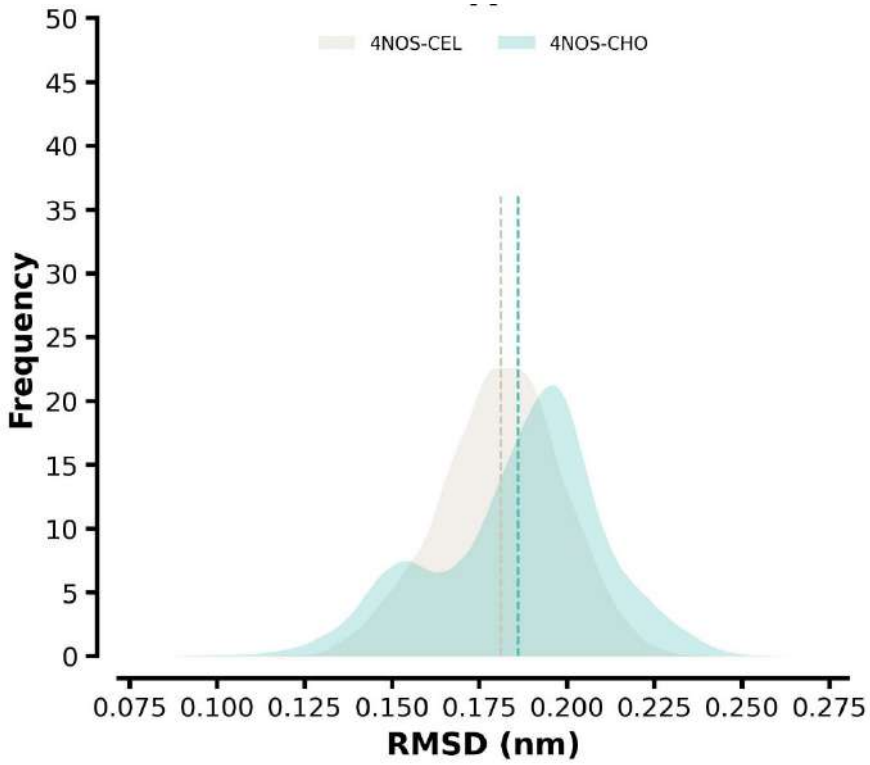


Figure 9.95: Probability density distribution of Root Mean Square Deviation (RMSD) values for both complexes, highlighting CEL's (Celecoxib) narrower stability range compared to CHO (Cholesta-4,6-dien-3-ol, benzoate, (3.beta.)-)

9.3.21.2.2. Root Mean Square Fluctuation (RMSF)

RMSF analysis provides residue-specific flexibility profiles, offering a more localized view of ligand-induced effects on protein motion. In both complexes, most residues exhibited low RMSF amplitudes (<0.20 nm), indicating stable backbone conformations. Notable peaks in flexibility occurred in loop-rich and solvent-exposed regions, particularly around residues 50–60 and 120–130, which are distal to the catalytic site but prone to thermal motion. The CEL-bound complex consistently displayed lower RMSF values in these regions compared to CHO, suggesting that CEL binding dampens local flexibility. This reduction may be due to stabilizing hydrogen bond and hydrophobic contacts anchoring CEL within the binding cleft. Conversely, CHO allowed slightly higher fluctuations in these loop segments, potentially because its predominantly hydrophobic interaction network provides less directional restraint.

In active-site-adjacent regions, CEL also reduced fluctuations more effectively than CHO, indicating tighter structural control at functionally relevant areas. Such localized rigidity could enhance binding-site complementarity and reduce conformational entropy losses during binding, favouring CEL's pharmacodynamic profile (Figure 9.96).

9.3.21.2.3. Radius of Gyration (Rg)

Rg provides a measure of protein compactness, reflecting global folding stability. Both 4NOS complexes maintained stable Rg values throughout the 100 ns simulation, indicating no significant unfolding or collapse events. The CEL complex averaged an Rg of 1.542 ± 0.004 nm, slightly higher than CHO's 1.538 ± 0.004 nm, a marginal difference suggesting comparable global compaction.

Interestingly, CEL's slightly elevated Rg may indicate minimal side-chain adjustments accommodating the ligand without compromising tertiary fold stability. CHO's marginally lower Rg aligns with its hydrophobic packing within the binding cleft, potentially inducing a subtly more compact arrangement of hydrophobic core residues. The stability of Rg in both systems, with fluctuations below ±0.005 nm,

indicates that ligand binding does not perturb the protein's overall tertiary structure. From a mechanistic viewpoint, the minimal Rg variation further corroborates RMSD and RMSF findings, showing that both ligands stabilize the protein without large-scale conformational rearrangements, though CEL may allow a fractionally more open tertiary packing Figure 9.97).

9.3.21.2.4. Solvent Accessible Surface Area (SASA)

SASA quantifies the solvent exposure of the protein surface, providing insight into conformational openness. Over 100 ns, the CEL complex maintained a slightly higher average SASA (92.4 ± 1.5 nm²) compared to CHO (90.8 ± 1.4 nm²). This suggests that CEL binding results in a subtly more solvent-exposed conformation, possibly due to local rearrangements in loop or side-chain orientations near the binding site.

CHO's lower SASA is consistent with a more compact structure, potentially due to its hydrophobic bulk promoting tighter packing of surrounding residues. Notably, SASA values for both systems remained stable, without sharp deviations, confirming the absence of large-scale folding/unfolding events. From a functional standpoint, CEL's slightly higher SASA might facilitate transient interactions with solvent molecules or other potential binding partners, which could influence co-factor recruitment or secondary binding events, while CHO's compact arrangement may favour more enclosed, hydrophobic environments (Figure 9.98).

9.3.21.2.5. Intramolecular Hydrogen Bonds

Intramolecular hydrogen bonds are critical for maintaining protein fold integrity. Both complexes maintained a stable internal hydrogen bond network, fluctuating between ~115–130 bonds throughout the simulation. CEL consistently maintained slightly higher hydrogen bond counts than CHO, indicating a marginally stronger reinforcement of the internal structural network. This trend aligns with CEL's lower RMSF values, suggesting that its presence helps preserve secondary and tertiary interactions, particularly in loop and turn regions adjacent to the binding pocket. CHO, while still maintaining high H-bond counts, exhibited brief periods of reduced counts,

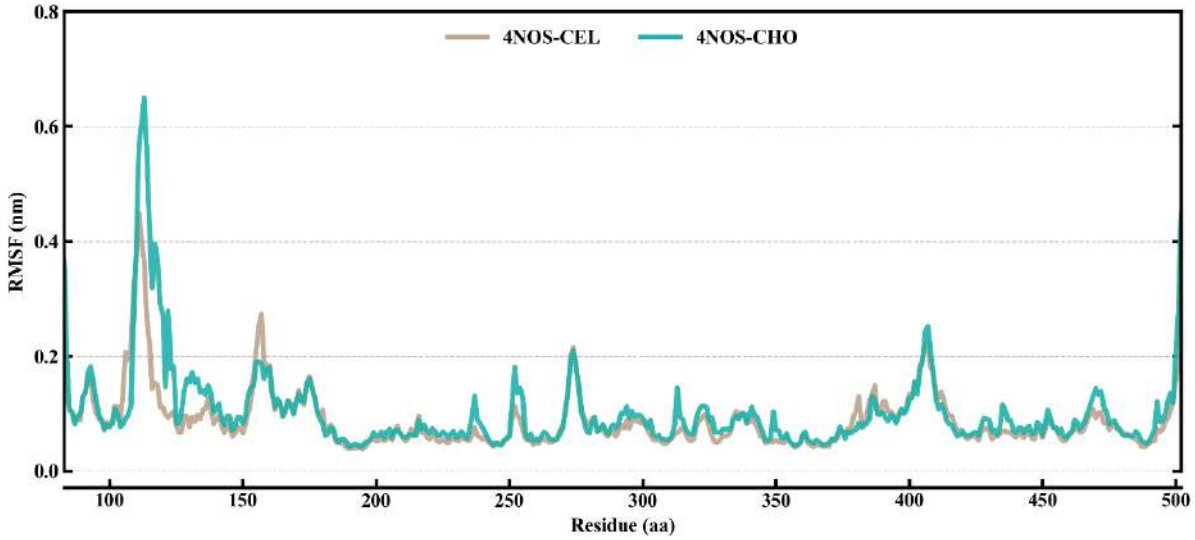


Figure 9.96: Root Mean Square Deviation (RMSD) profile of the iNOS–CEL (Human Inducible Nitric Oxide Synthase-Celecoxib) and iNOS–CHO (Human Inducible Nitric Oxide Synthase-Cholesta-4,6-dien-3-ol, benzoate, (3.beta.)-) complexes, illustrating residue-specific mobility patterns and ligand-induced flexibility modulation

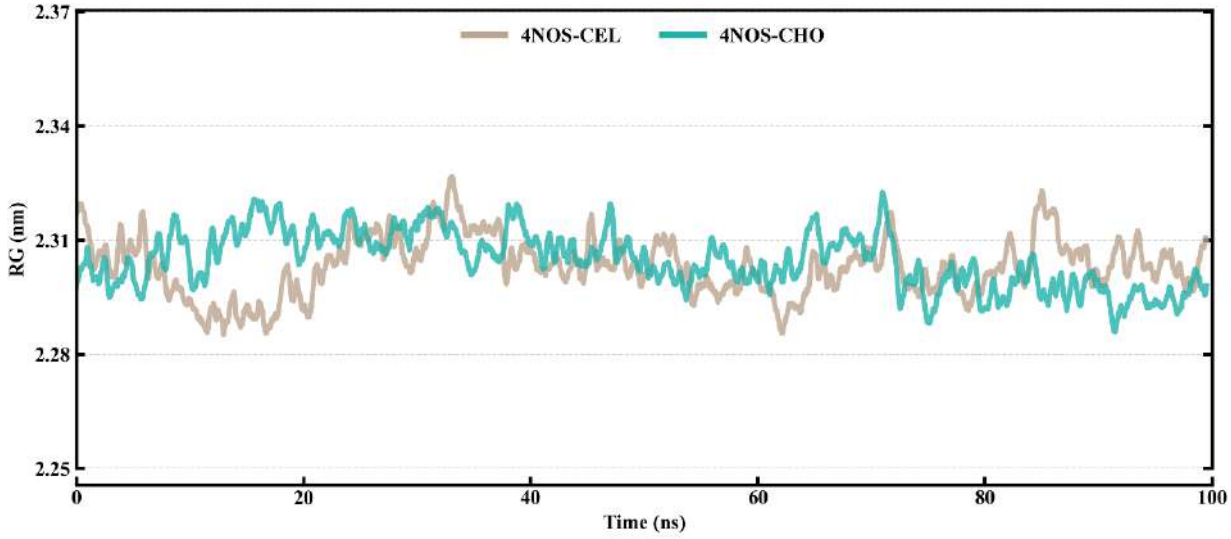


Figure 9.97: Radius of Gyration (Rg) profiles of the iNOS–CEL (Human Inducible Nitric Oxide Synthase-Celecoxib) and iNOS–CHO (Human Inducible Nitric Oxide Synthase-Cholesta-4,6-dien-3-ol, benzoate, (3.beta.)-) complexes over 100 nanoseconds, showing stable compactness and minor ligand-dependent differences.

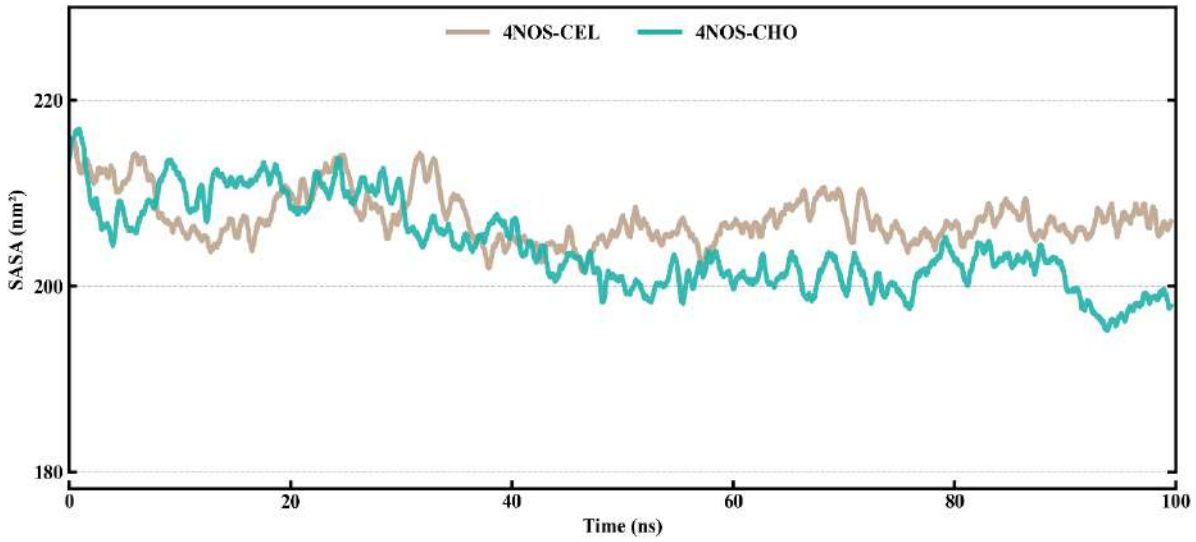


Figure 9.98: Solvent Accessible Surface Area (SASA) profiles for the iNOS–CEL (Human Inducible Nitric Oxide Synthase-Celecoxib) and iNOS–CHO (Human Inducible Nitric Oxide Synthase-Cholesta-4,6-dien-3-ol, benzoate, (3.beta.)-) complexes over 100 nanoseconds, showing ligand-specific differences in solvent exposure

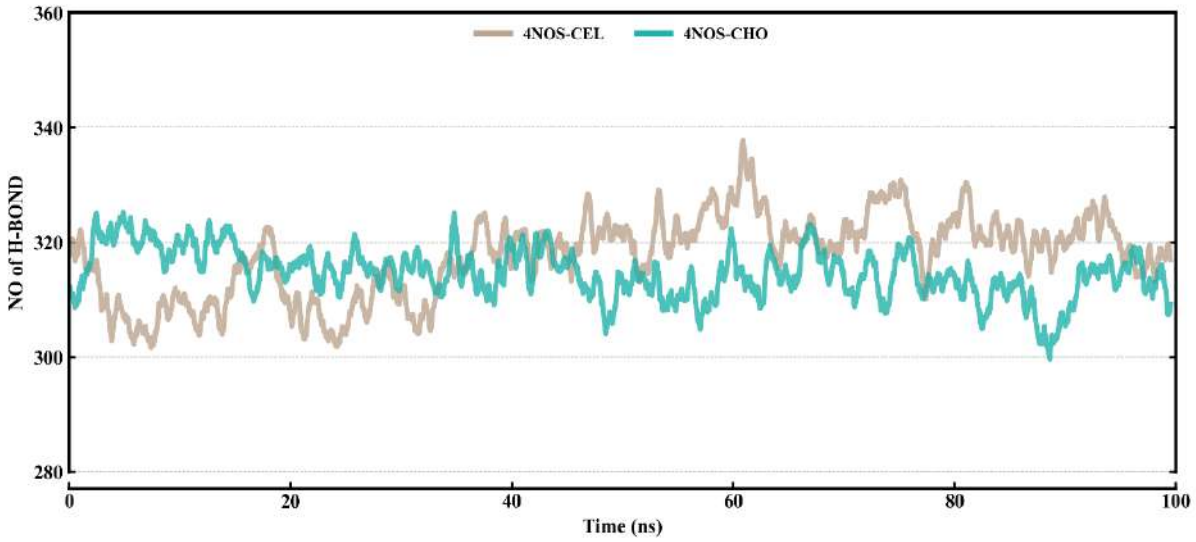


Figure 9.99: Number of intramolecular hydrogen bonds over time for the iNOS–CEL (Human Inducible Nitric Oxide Synthase-Celecoxib) and iNOS–CHO (Human Inducible Nitric Oxide Synthase-Cholesta-4,6-dien-3-ol, benzoate, (3.beta.)-) complexes, indicating stable structural retention

possibly linked to the transient fluctuations noted in its RMSD trajectory. Overall, the intramolecular hydrogen bonding patterns reinforce the observation that both ligands are compatible with the native fold of iNOS, but CEL provides a slightly more stabilizing effect on internal cohesion (Figure 9.99).

9.3.21.2.6. Intermolecular Hydrogen Bonds

Intermolecular hydrogen bonding between ligand and protein plays a key role in specificity and affinity. CEL consistently formed between 1–3 H-bonds during the simulation, many of which persisted for extended intervals, reflecting stable polar anchoring within the binding site. CHO, by contrast, formed fewer and less persistent hydrogen bonds (0–1 range), relying more heavily on hydrophobic interactions for stabilization. The stability and persistence of CEL's H-bonds are likely major contributors to its tighter RMSD clustering and reduced RMSF peaks, reinforcing its role as a strong polar-interaction-driven inhibitor. CHO's sparse H-bonding profile is consistent with its broader conformational sampling and slightly higher mobility in loop regions (Figure 9.100).

9.3.21.2.7. Conformational sampling and energy landscape

9.3.21.2.7.1. Principal Component Analysis (PCA)

PCA was employed to assess large-scale collective motions within the complexes by projecting atomic displacements onto the first two principal components (PC1 and PC2). The CEL complex displayed a relatively compact clustering of conformations, indicating limited exploration of conformational space and suggesting that CEL binding restricts large-scale protein motions. This constrained sampling is indicative of a stable, energetically favourable conformational state. In contrast, CHO exhibited a more dispersed PCA plot, with trajectories spread across a broader PC1–PC2 space, suggesting that CHO allows more diverse protein motions. This broader sampling reflects higher conformational flexibility, which could enable adaptive binding modes but might reduce the conformational fixation associated with high-affinity, long-term inhibition. From a pharmacological perspective, CEL's restricted conformational space aligns with a mode of action

involving tight, site-specific anchoring, whereas CHO's dynamic range suggests a more adaptable but potentially less rigid inhibitory effect (Figure 9.101).

9.3.21.2.7.2. Free Energy Landscape (FEL)

FEL analysis provides a thermodynamic perspective of conformational stability. The CEL complex exhibited a single deep energy basin (~12–13 kJ/mol), indicative of a dominant and thermodynamically favourable bound conformation. This aligns with the compact PCA clustering and narrow RMSD distribution, confirming a highly stable interaction. The CHO complex, however, displayed multiple shallow minima (~9–11 kJ/mol) across the landscape, reflecting occupancy of several low-energy conformations rather than one dominant state. This ruggedness is consistent with its broader PCA distribution and indicates conformational adaptability at the cost of reduced thermodynamic fixation. CEL's deeper and more centralized minimum suggests that it locks iNOS into a specific stable state, which can enhance inhibitory persistence, while CHO's multiple minima may facilitate binding adaptability but with potentially lower conformational control (Plate 9.52).

9.3.21.2.8. Overall conclusion- Anti-inflammatory activity from Molecular dynamics (MDS) analysis

The molecular dynamics simulations of iNOS bound to Celecoxib (CEL) and Cholesterol (CHO) over 100 ns revealed fundamental differences in structural stability, conformational control, and thermodynamic favourability that directly inform their anti-inflammatory potential. Across the stability indicators, RMSD, RMSF, Rg, SASA, hydrogen bonding patterns, PCA, and FEL, CEL consistently emerged as the more conformationally restrictive and thermodynamically stable ligand.

CEL's lower mean RMSD (0.176 ± 0.015 nm) and narrower deviation range point toward a rigidly maintained global fold, further supported by suppressed RMSF amplitudes in flexible loop regions. These regions are structurally significant, as they lie near the catalytic site of iNOS, where loop mobility can modulate substrate access. By dampening motion in these areas, CEL likely stabilizes the protein in an inactive

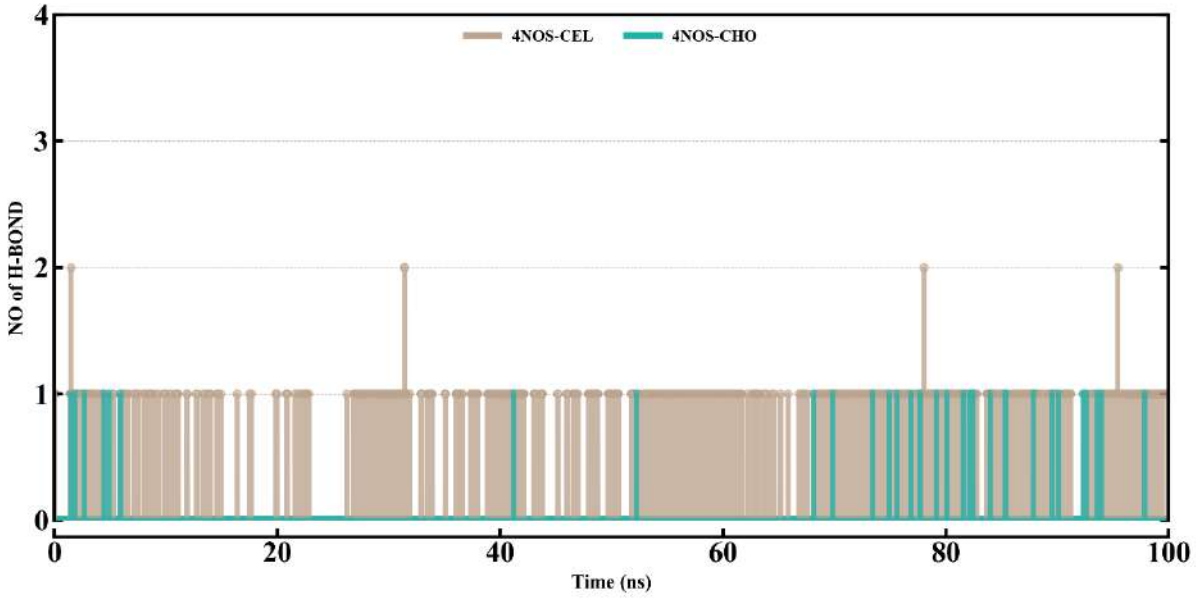


Figure 9.100: Intermolecular hydrogen bond counts for the iNOS–CEL (Human Inducible Nitric Oxide Synthase-Celecoxib) and iNOS–CHO (Human Inducible Nitric Oxide Synthase-Cholesta-4,6-dien-3-ol, benzoate, (3.beta.)-) complexes over 100 nanoseconds, highlighting CEL's stronger polar interaction profile

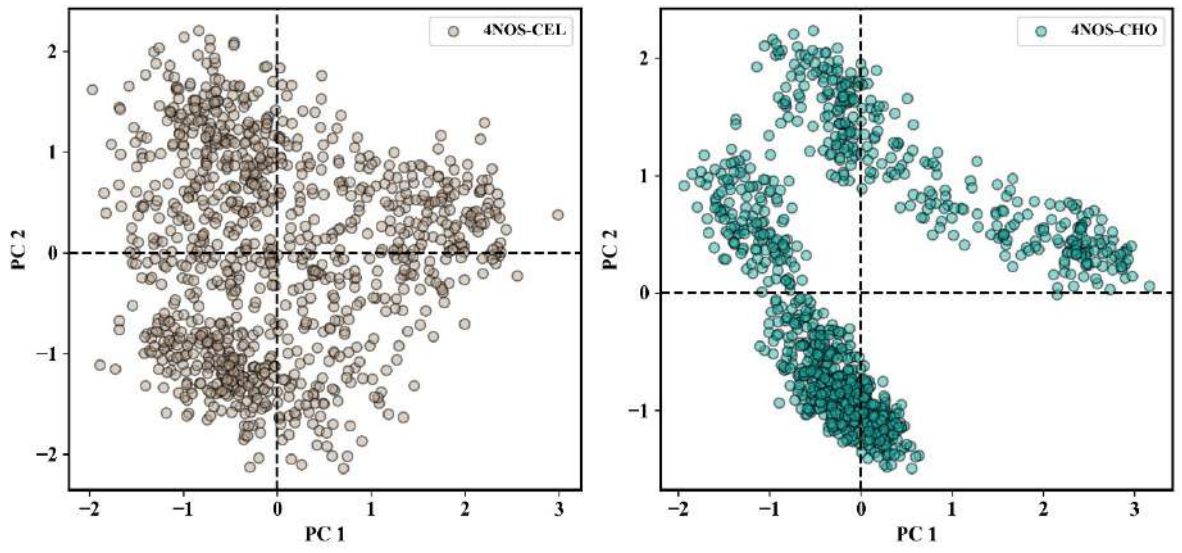
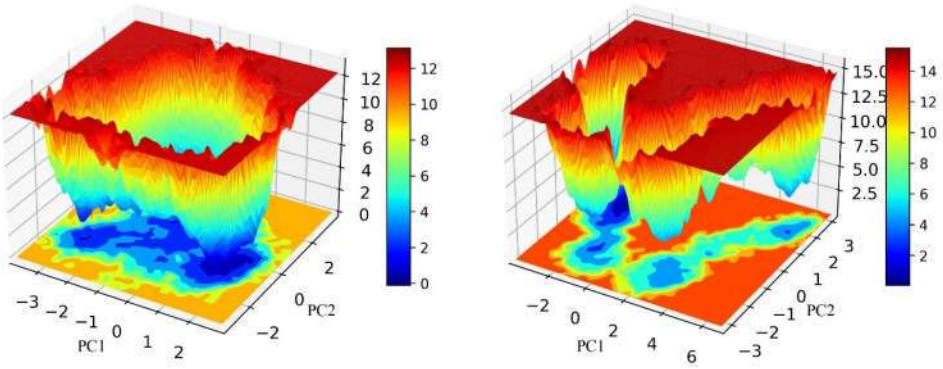


Figure 9.101: Principal Component Analysis (PCA) plots of the iNOS–CEL (Human Inducible Nitric Oxide Synthase-Celecoxib) and iNOS–CHO (Human Inducible Nitric Oxide Synthase-Cholesta-4,6-dien-3-ol, benzoate, (3.beta.)-) complexes, showing differences in conformational sampling within PC1–PC2 space



(a) **(b)**

Plate 9.52: Three-dimensional (3D) Free Energy Landscape (FEL) plots of the (a) iNOS–CEL (Human Inducible Nitric Oxide Synthase-Celecoxib) and (b) iNOS–CHO (Human Inducible Nitric Oxide Synthase-Cholesta-4,6-dien-3-ol, benzoate, (3.beta.)-) complexes mapped along PC1 and PC2, illustrating differences in thermodynamic stability and conformational diversity

conformation, limiting unwanted catalysis. This is reinforced by CEL's stronger and more persistent intermolecular hydrogen bonds, which serve as molecular "anchors" that lock the ligand into the binding cleft.

The compact PCA clustering of CEL-bound iNOS, alongside a single deep FEL basin (~12–13 kJ/mol), provides a thermodynamic signature of strong conformational fixation. This suggests that CEL binding significantly reduces the conformational entropy of the protein–ligand complex, a property often associated with high-affinity, long-residence-time inhibitors. From a pharmacological standpoint, such stabilization could translate into sustained iNOS inhibition, reducing the enzymatic production of nitric oxide and potentially lowering inflammatory responses over prolonged periods.

In contrast, CHO maintained overall structural integrity but displayed broader RMSD and RMSF distributions, higher conformational sampling in PCA, and a FEL with multiple shallow minima (~9–11 kJ/mol). This profile indicates a more dynamic interaction, allowing the protein to access multiple energetically comparable states. While such adaptability can be advantageous in accommodating structural variants or membrane-associated conformations, it generally results in reduced conformational locking. CHO's binding appeared more reliant on hydrophobic and van der Waals contacts than persistent polar interactions, which may explain its looser dynamic profile.

In summary, CEL enforces a conformationally restricted, thermodynamically optimized state in iNOS, indicative of potent and sustained inhibitory potential, aligning with its clinical profile as a selective COX-2 inhibitor with strong anti-inflammatory efficacy. CHO, while still capable of stabilizing iNOS, induces a more adaptable conformational ensemble, which may correlate with less selective or less persistent inhibition. These insights suggest that CEL's rigidifying influence on iNOS structure could underpin both its potency and specificity, whereas CHO's flexible engagement may be more relevant in contexts where partial modulation or adaptive binding is desired.

9.3.21.2.9. Binding Free Energy (MM/PBSA)

MM/PBSA (Molecular Mechanics Poisson–Boltzmann Surface Area) analysis was used to determine the binding free energies of iNOS complexed with Cholesta-4,6-dien-3-ol, benzoate, (3.beta.)-) (a phytocompound) and Celecoxib (an approved anti-inflammatory drug). This method provides a breakdown of the total binding energy into van der Waals, electrostatic, polar solvation, and SASA terms, highlighting the molecular interactions responsible for binding stability. Lower (more negative) total binding energies indicate stronger and more thermodynamically favourable binding (Table 9.133).

9.3.21.2.9.1. Binding affinity comparison

Celecoxib demonstrates a much stronger binding affinity to iNOS (–172.951 kJ/mol) compared to Cholesta-4,6-dien-3-ol, benzoate, (3.beta.)- (–59.949 kJ/mol). This enhanced affinity is largely attributed to significantly stronger van der Waals forces (–245.822 vs.–192.916 kJ/mol) and a favourable electrostatic term (–12.560 kJ/mol) versus the unfavourable positive electrostatics (+62.390 kJ/mol) observed for the phytocompound.

9.3.21.2.9.2. Energetic contributions and structural implications

The positive electrostatic contribution for Cholesta-4,6-dien-3-ol, benzoate, (3.beta.)-indicates suboptimal charge complementarity in the binding site, reducing its net stability despite substantial hydrophobic contacts. In contrast, Celecoxib benefits from both strong hydrophobic packing and favourable charge–charge interactions, which effectively overcome its moderate polar solvation penalty (+109.905 kJ/mol). Both ligands exhibit stabilizing SASA contributions, but Celecoxib's more negative value (–24.474 kJ/mol) suggests deeper hydrophobic burial within the iNOS active site. Overall, while Cholesta-4,6-dien-3-ol, benzoate, (3.beta.)- provides reasonable stabilization through non-polar interactions, its unfavourable electrostatics limit binding. Celecoxib's optimal combination of dispersion forces, electrostatic complementarity, and efficient hydrophobic encapsulation underpins its superior inhibitory potential (Figure 9.102).

Table 9.133: MM/PBSA energy decomposition for iNOS–4,6-Cholestadien-3β-ol and iNOS–Celecoxib complexes

Energy Component (kJ/mol)	Cholesta-4,6-dien-3-ol, benzoate, (3.beta.)-	Celecoxib
van der Waals	–192.916 ± 10.875	–245.822 ± 9.752
Electrostatic	62.390 ± 20.414	–12.560 ± 2.102
Polar solvation	88.398 ± 26.212	109.905 ± 13.115
SASA	–17.822 ± 0.823	–24.474 ± 0.861
Total binding energy	–59.949 ± 22.069	–172.951 ± 17.855

Table 9.134: Density Functional Theory (DFT) parameters for Cholesta-4,6-dien-3-ol, benzoate, (3.beta.)-) and Celecoxib

Compound name	DFT Energy (Hartree)	HOMO Energy (Hartree)	LUMO Energy (Hartree)	HOMO-LUMO Gap (Hartree)	MEP Minimum (a.u.)	MEP Maximum (a.u.)	MEP Average (a.u.)
Celecoxib-DFT	-1668.687	-0.196	-0.040	0.156	-11.824	230.878	0.040
Cholesta-4,6-dien-3-ol, benzoate, (3.beta.)-)-DFT	-1442.384	-0.227	-0.215	0.012	-12.433	207.437	0.056

Table 9.135: Molecular Mechanics Poisson–Boltzmann Surface Area (MM/PBSA) energy decomposition for Peroxisome Proliferator-Activated Receptor Gamma (PPARG)-D:B-Friedo-B':A'-Neogammacer-5-en-3-one (PPARG–DBF) and Peroxisome Proliferator-Activated Receptor Gamma (PPARG)-Pioglitazone (PPARG–PIO) complexes

Energy component (kJ/mol)	DB-Friedo-B'A'-Neogammacer-5-en-3-one	Pioglitazone
van der Waals	–173.494 ± 10.259	–167.220 ± 18.578
Electrostatic	–6.057 ± 7.553	–25.028 ± 9.500
Polar solvation	72.944 ± 13.088	131.061 ± 24.332
SASA	–16.294 ± 1.142	–16.305 ± 1.649
Total binding energy	–122.901 ± 6.401	–77.492 ± 18.343

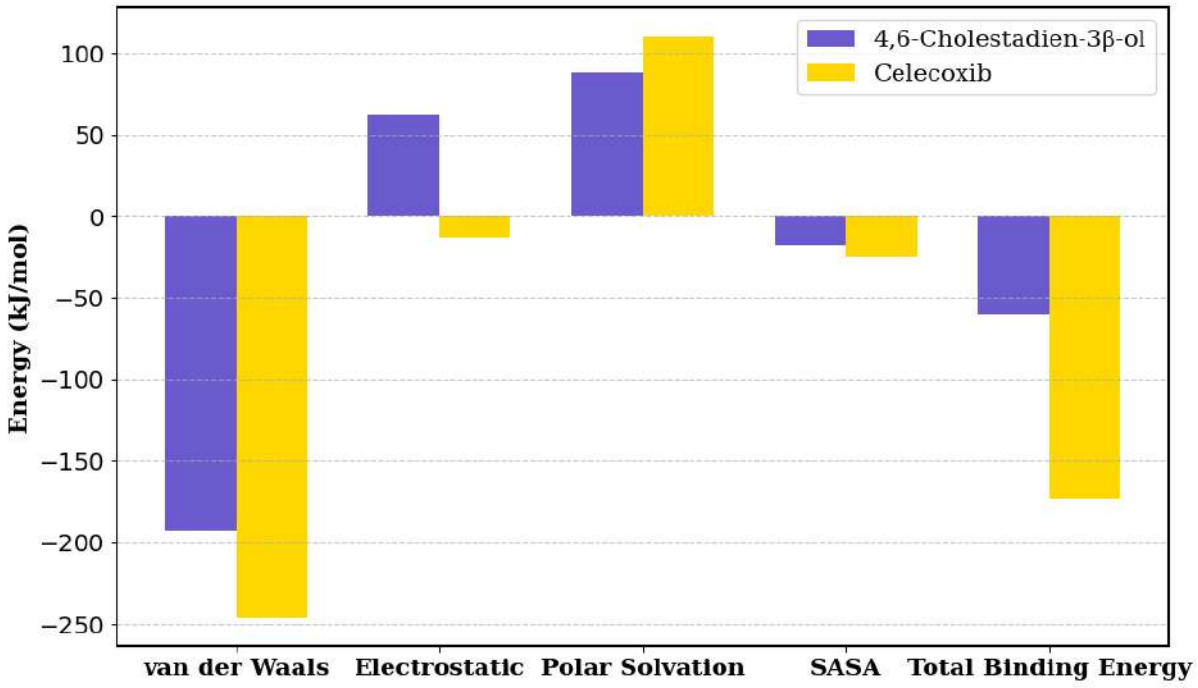


Figure 9.102: Molecular Mechanics Poisson–Boltzmann Surface Area (MM/PBSA) energy decomposition for iNOS complexes with Cholesta-4,6-dien-3-ol, benzoate, (3.beta.)-and Celecoxib

9.3.21.2.10. Normal Mode Analysis (NMA) for anti-inflammatory target (iNOS)

Normal Mode Analysis (NMA) was performed on the inducible nitric oxide synthase (iNOS) protein to evaluate its intrinsic flexibility, correlated motions, and structural stability. This analysis helps reveal collective motions crucial for enzymatic function and highlights structural features potentially influencing ligand binding and allosteric regulation (Plate 9.53).

9.3.21.2.10.1. Structural flexibility and deformability

The deformability profile shows multiple prominent peaks distributed along the iNOS sequence, indicating flexible loop regions and hinge points. These segments are likely to facilitate conformational rearrangements necessary for catalysis and interaction with regulatory molecules. The 3D representation uses a colour gradient to depict mobility: blue regions are rigid, while green/yellow represent moderately flexible areas, and red denotes the highest mobility.

9.3.21.2.10.2. B-Factor analysis

The NMA-predicted B-factors (pink) closely align with crystallographic B-factors (black), validating the model's accuracy in detecting dynamic regions. Elevated B-factor values are observed primarily in loop regions and termini, suggesting higher mobility that may support substrate accommodation or cofactor binding.

9.3.21.2.10.3. Collective Motion, eigenvalues, and variance

The first non-trivial eigenvalue is 1.22×10^{-3}, indicating moderate stiffness for the dominant motion mode. This suggests that iNOS undergoes conformational changes with a modest energy requirement, possibly enabling rapid functional switching. Variance analysis shows that the first few modes account for the majority of total motion, underscoring the cooperative nature of the structural dynamics.

9.3.21.2.10.4. Correlated motions and elastic network

The covariance map shows distinct regions of correlated (red) and anti-correlated (blue) motion, particularly between structural domains, which may be critical for the enzyme's catalytic cycle and regulation. The elastic network model displays denser spring connections within the catalytic core, reflecting its rigidity, while peripheral loops show sparse connectivity, consistent with greater flexibility.

9.3.21.2.11. DFT Analysis for Anti-inflammatory Activity (iNOS Target)

Density Functional Theory (DFT) calculations were carried out for 4Cholesta-4,6-dien-3-ol, benzoate, (3.beta.)-) (phytocompound) and Celecoxib (marketed anti-inflammatory drug) to examine their electronic structures, frontier molecular orbital (FMO) properties, and molecular electrostatic potential (MEP) distributions. These computational descriptors provide critical insights into electronic reactivity, molecular stability, and potential interaction modes with the iNOS binding site (Table 9.134).

9.3.21.2.11.1. Electronic property comparison

Cholesta-4,6-dien-3-ol, benzoate, (3.beta.)-) displays a remarkably narrow HOMO–LUMO gap (0.012 Hartree) compared to Celecoxib (0.156 Hartree), indicating much higher electronic reactivity and a stronger propensity for electron transfer during binding. The HOMO energy of Cholesta-4,6-dien-3-ol, benzoate, (3.beta.)-) (-0.227 Hartree) is slightly lower than that of Celecoxib (-0.196 Hartree), suggesting a reduced electron-donating ability but potentially enhanced stability of its electronic cloud. Conversely, Celecoxib's larger HOMO–LUMO gap suggests greater kinetic stability but lower electronic reactivity, aligning with its role as a selective COX-2 inhibitor with controlled interaction specificity (Plate 9.54).

9.3.21.2.11.2. Molecular Electrostatic Potential Insights (MEP)

MEP analysis reveals that both compounds exhibit highly negative MEP minima (–12.433 a.u. for Cholesta-4,6-dien-3-ol, benzoate, (3.beta.)-), –11.824 a.u. for Celecoxib), signifying regions favourable for electrostatic attraction with

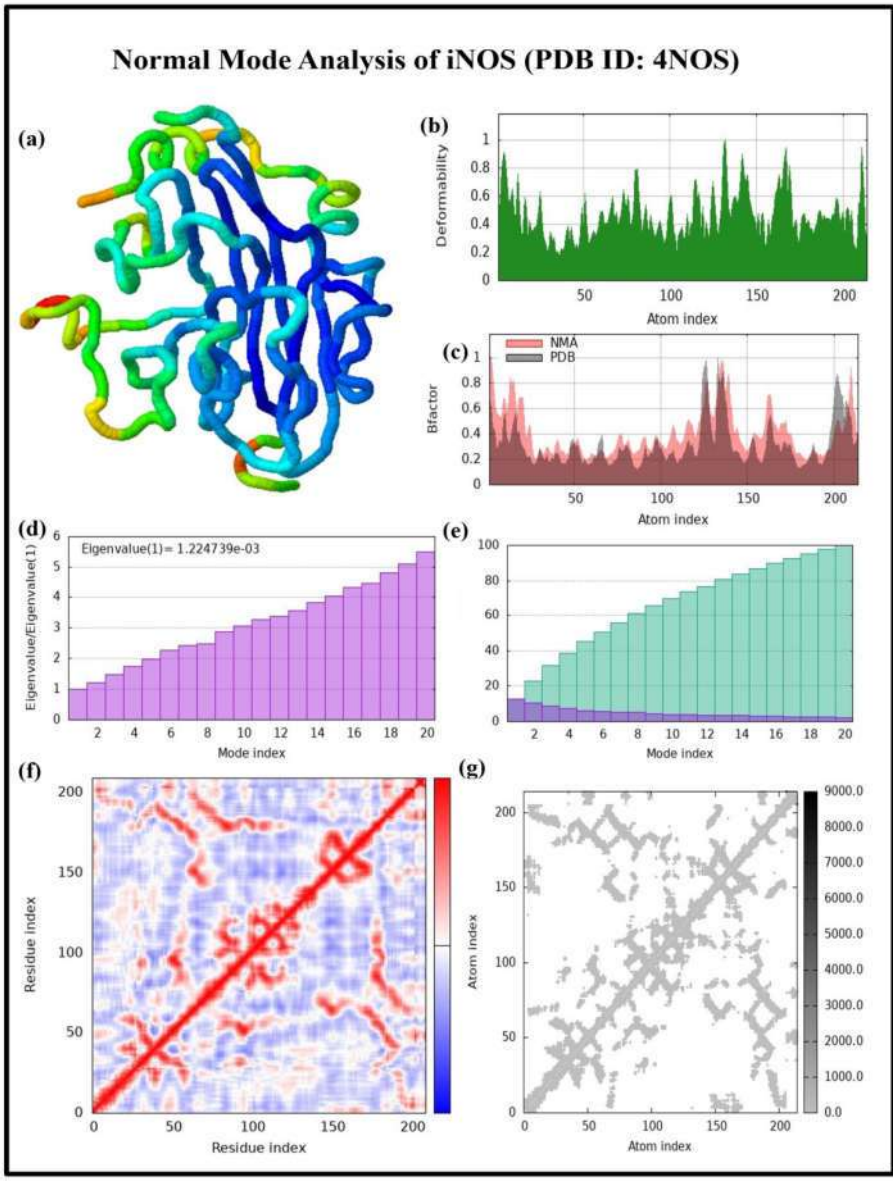
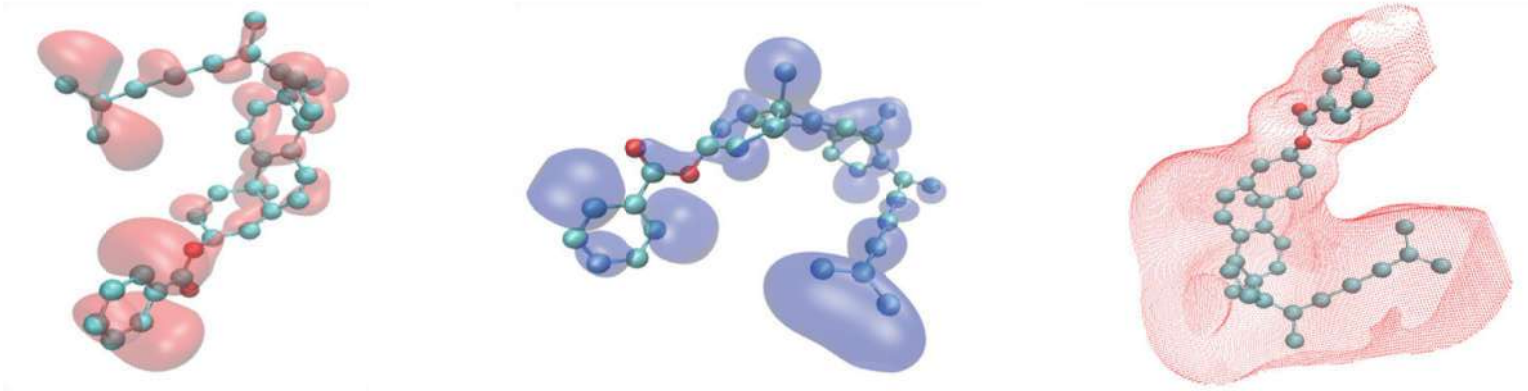
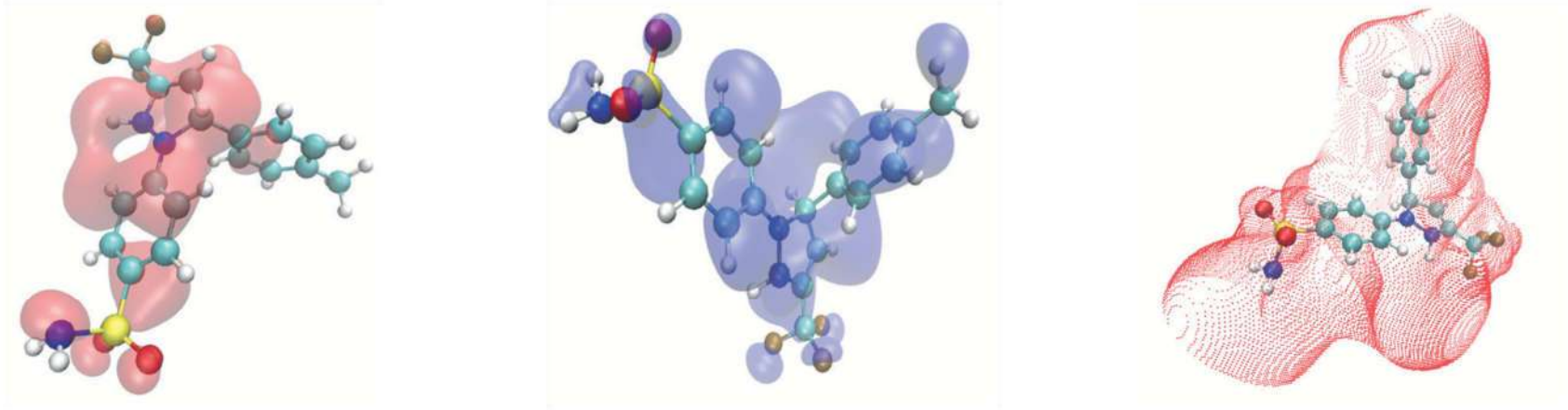


Plate 9.53: Normal Mode Analysis of Human Inducible Nitric Oxide Synthase (iNOS): (a) Cartoon representation with colour-coded mobility (blue: rigid, green/yellow: flexible) (b) deformability plot (c) B-factor comparison (NMA vs. PDB) (d) eigenvalue distribution (e) cumulative and individual variance per mode (f) covariance matrix showing correlated (red) and anti-correlated (blue) motions, and (g) elastic network map with spring strengths (dark grey: stiffer connections)



(a) (b) (c)

Plate 9.54: Frontier molecular orbital (Highest Occupied Molecular Orbital (HOMO), Lowest Unoccupied Molecular Orbital (LUMO))and molecular electrostatic potential (MEP) surfaces for Cholesta-4,6-dien-3-ol, benzoate, (3.beta.)) against iNOS: (a) HOMO distribution (b) LUMO distribution, and (c) MEP surface mapping



(a) (b) (c)

Plate 9.55: Frontier molecular orbital (Highest Occupied Molecular Orbital (HOMO), Lowest Unoccupied Molecular Orbital (LUMO)) and molecular electrostatic potential (MEP) surfaces for Celecoxib against iNOS: (a) HOMO distribution (b) LUMO distribution, and (c) MEP surface mapping, showing electron density regions and likely binding interaction sites

positively charged residues. Celecoxib, however, shows a higher MEP maximum (230.878 a.u.) compared to Cholesta-4,6-dien-3-ol, benzoate, (3.beta.)-) (207.437 a.u.), indicating stronger localized positive regions, potentially beneficial for polar and hydrogen bonding interactions. The higher MEP average of Cholesta-4,6-dien-3-ol, benzoate, (3.beta.)-) (0.056 a.u.) compared to Celecoxib (0.040 a.u.) suggests a more uniformly distributed charge surface, which may facilitate broader interaction patterns within the binding site (Plate 9.55).

9.3.22. Docking with a marketed antidiabetic drug

9.3.22.1. 3D and 2D visualization of Peroxisome Proliferator-Activated Receptor Gamma (PPARG) with Pioglitazone

The 3D visualization shows pioglitazone securely positioned within the ligand-binding domain of PPARG, occupying a well-defined hydrophobic cavity with complementary surface topology. The receptor surface mapping highlights distinct polar and non-polar interaction zones, indicating a stable fit and favourable spatial accommodation. The planar aromatic core and flexible linkers of pioglitazone enable simultaneous hydrophobic packing and polar anchoring, ensuring an optimal orientation within the binding pocket.

The 2D interaction diagram details the diverse non-covalent interactions that contribute to the stability of the PPARG–pioglitazone complex:

- Conventional Hydrogen Bonds (green arrows)

HIS100 and GLY99 form strong hydrogen bonds with the polar groups of pioglitazone, providing directional stabilization and enhancing ligand specificity.

- Pi-Donor Hydrogen Bond (light blue lines)

ILE102 engages in a Pi-donor hydrogen bond with the aromatic moiety of the ligand, reinforcing binding through additional polar–aromatic contacts.

- Alkyl and Pi-Alkyl Interactions (light pink lines)

TYR105, PHE95, LEU116, and ILE76 interact hydrophobically with the ligand's non-polar regions, improving van der Waals packing and stabilizing the overall complex.

- Van der Waals Interactions (light green spheres)

Surrounding residues, including SER101, ASN92, ASP96, and PHE98, contribute multiple weak but cooperative van der Waals forces, fine-tuning the fit within the pocket.

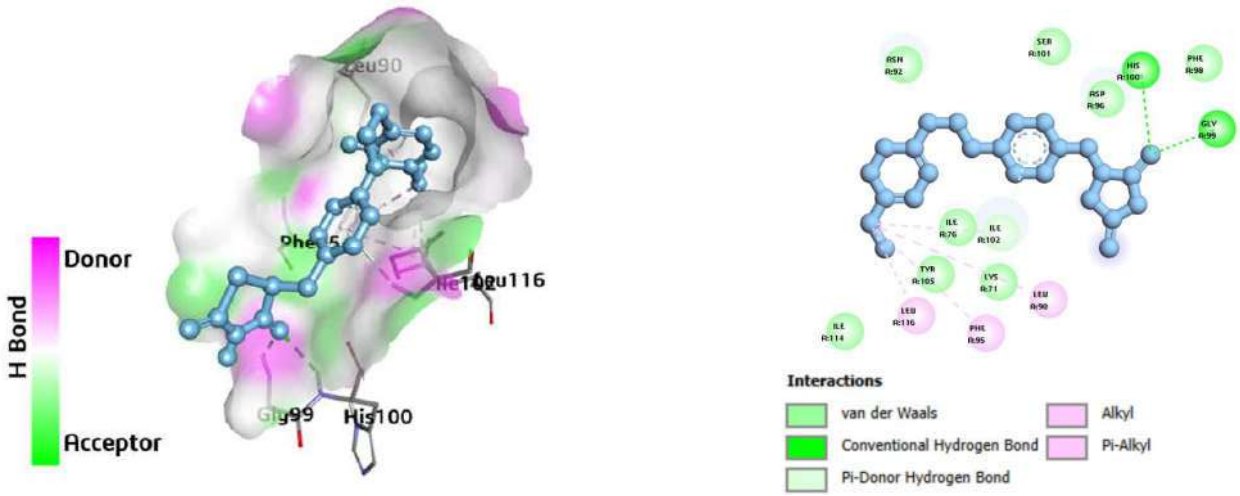
This interaction network demonstrates a balanced interplay of polar and hydrophobic forces, reflecting the molecular features that underpin pioglitazone's role as a clinically established PPARG agonist (Plate 9.56).

9.3.22.2. Trajectory-based structural analysis

9.3.22.2.1. Root Mean Square Deviation (RMSD)

The RMSD profile provides insight into the overall structural stability of the protein–ligand complexes over the 100 ns simulation. The DBF–PPARG (D:B-Friedo-B':A'-Neogammacer-5-en-3-one-Peroxisome Proliferator-Activated Receptor Gamma) complex exhibited a mean RMSD of approximately 0.165 ± 0.015 nm, while the PIO–PPARG (Pioglitazone-Peroxisome Proliferator-Activated Receptor Gamma) complex displayed a slightly higher mean RMSD of 0.178 ± 0.020 nm. Both systems equilibrated within the first 5 ns and maintained relative stability thereafter, without large-scale structural drifts.

The lower RMSD of the DBF complex suggests enhanced stabilization of PPARG, potentially due to stronger hydrophobic and steric complementarity in the binding pocket. This may indicate that DBF maintains PPARG's conformational integrity more effectively than PIO, which is essential for sustained activation or modulation in an antidiabetic therapeutic context. In the pharmacological frame, reduced RMSD fluctuations imply that the ligand does not disrupt the protein's functional fold, a critical consideration for nuclear receptor modulators like PPARG (Figures 9.103-9.104).



(a) **(b)**

Plate 9.56: Visualization of binding interactions between Peroxisome Proliferator-Activated Receptor Gamma (PPARG) and marketed antidiabetic drug Pioglitazone (PIO), showing (a) the three-dimensional (3D) molecular surface and (b) the two-dimensional (2D) interaction diagram

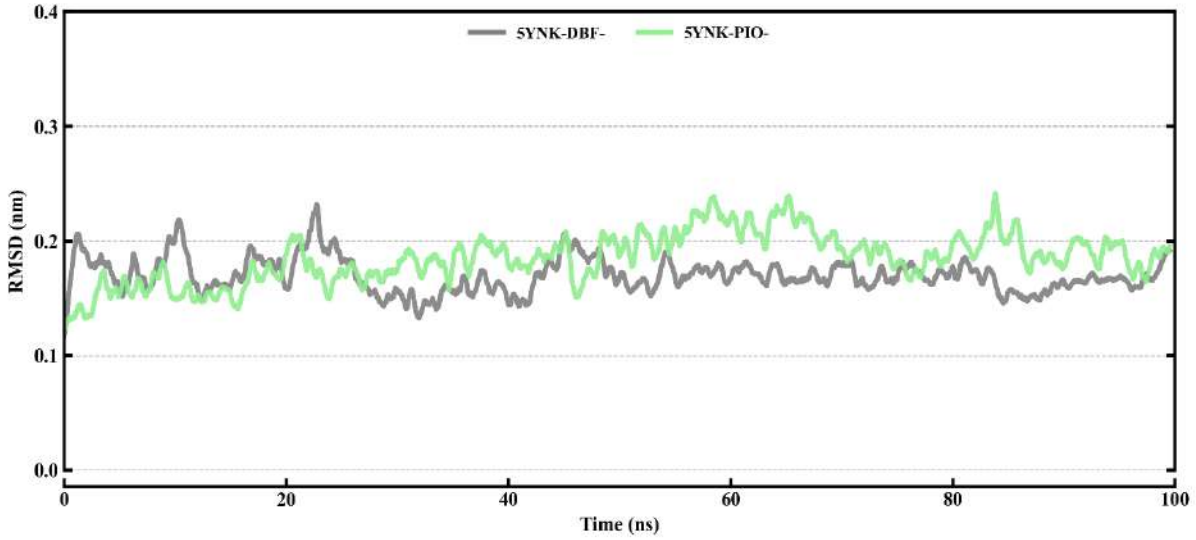


Figure 9.103: Root Mean Square Deviation (RMSD) of protein–ligand complexes of Peroxisome Proliferator-Activated Receptor Gamma (PPARG) bound to D:B-Friedo-B':A'-Neogammacer-5-en-3-one (DBF) and Pioglitazone (POI) over 100 nanoseconds MD simulation

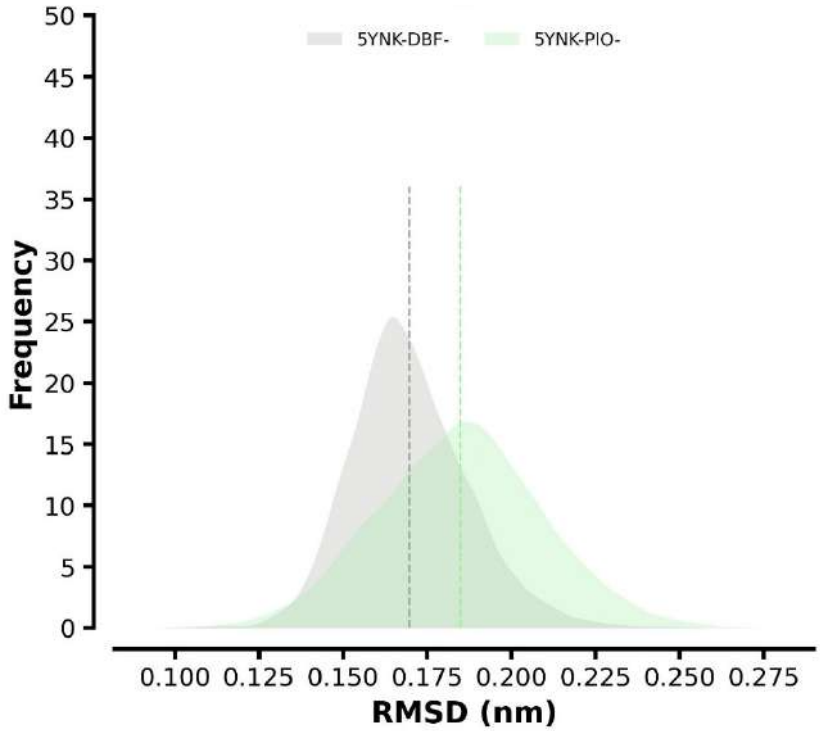


Figure 9.104: Probability density distribution of Root Mean Square Deviation (RMSD) for PPARG–DBF (Peroxisome Proliferator-Activated Receptor Gamma-D:B-Friedo-B':A'-Neogammacer-5-en-3-one) and PPARG–PIO (Peroxisome Proliferator-Activated Receptor Gamma-Pioglitazone) complexes, indicating a tighter structural distribution for DBF

9.3.22.2.2. Root Mean Square Fluctuation (RMSF)

RMSF analysis reveals residue-level flexibility across the PPARG structure. Both complexes display generally low fluctuations (<0.25 nm) across most residues, with notable peaks in the loop regions around residues ~90–100 and ~270–280, which correspond to solvent-exposed domains and flexible hinge regions in PPARG. The PIO complex showed slightly higher fluctuations in the binding site-adjacent loop, suggesting less rigid stabilization of key interaction residues compared to DBF. Functionally, maintaining a low RMSF at the ligand-binding domain is desirable for agonist activity, as excessive flexibility can weaken ligand-induced transcriptional regulation. The DBF complex's suppression of local flexibility supports its potential as a more stable PPARG modulator (Figure 9.105).

9.3.22.2.3. Radius of Gyration (Rg)

Rg analysis evaluates the compactness of the protein throughout the simulation. The DBF complex maintained a stable Rg averaging 2.699 ± 0.005 nm, while PIO averaged 2.707 ± 0.006 nm. Both systems exhibited minimal fluctuations, suggesting neither ligand induced global unfolding. The slightly lower Rg for DBF implies a marginally more compact structure, which often correlates with higher thermodynamic stability. This could translate to greater resilience of the PPARG–DBF complex under physiological conditions (Figure 9.106).

9.3.22.2.4. Solvent Accessible Surface Area (SASA)

SASA values remained largely stable for both complexes, with DBF averaging 322.4 ± 2.1 nm² and PIO slightly higher at 324.1 ± 2.3 nm². The marginally lower SASA in DBF indicates reduced solvent exposure, consistent with a more tightly packed complex. In the context of drug binding, this could mean better burial of hydrophobic surfaces, minimizing desolvation penalties during binding (Figure 9.107).

9.3.22.2.5. Intramolecular Hydrogen Bonds

Intramolecular H-bonds reflect the internal structural integrity of PPARG. Both complexes maintained a similar average of ~565–570 intramolecular H-bonds, with no major disruptions over time. DBF's slightly more consistent hydrogen bond count suggests better preservation of PPARG's native fold, which is crucial for transcriptional regulation (Figure 9.108).

9.3.22.2.6. Intermolecular Hydrogen Bonds

The DBF–PPARG complex consistently formed 0–2 H-bonds during the simulation, while PIO occasionally reached 4 H-bonds. However, the persistence rather than the number is often more critical. DBF's hydrophobic scaffold likely emphasizes van der Waals stabilization, while PIO relies more on polar contacts, explaining the higher but more transient H-bond counts. Persistent hydrophobic interactions may yield more durable pharmacological effects in hydrophobic nuclear receptor pockets (Figure 9.109).

9.3.22.3. Conformational sampling and landscape analysis

9.3.22.3.1. Principal Component Analysis (PCA)

Principal Component Analysis was employed to reduce the high-dimensional atomic motion data into principal components (PC1 and PC2), representing the most significant collective motions of PPARG during ligand binding. For the DBF–PPARG complex, the projection along PC1 and PC2 revealed a relatively clustered trajectory distribution, suggesting restricted large-scale conformational sampling. This indicates that DBF binding limits excessive domain movements, promoting a stable conformational ensemble. In nuclear receptors such as PPARG, such constrained dynamics often enhance ligand-dependent transcriptional activation by maintaining the receptor in a favourable activation state.

Conversely, the PIO–PPARG complex exhibited a wider spread in the PC1–PC2 phase space, indicating that the protein explored a broader range of conformations during the simulation. While flexibility can sometimes be beneficial

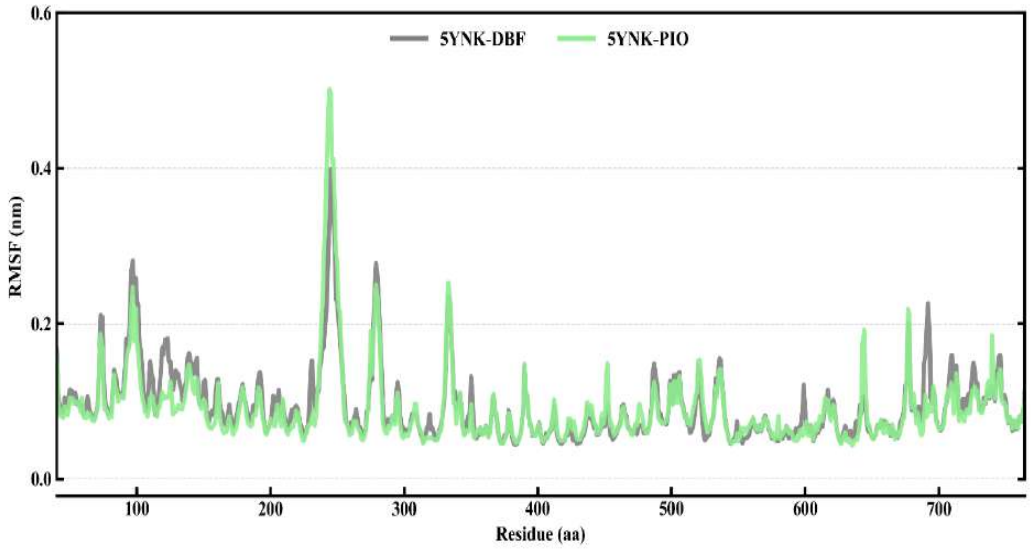


Figure 9.105: Root Mean Square Fluctuation (RMSF) of Peroxisome Proliferator-Activated Receptor Gamma (PPARG) residues in complexes with D:B-Friedo-B':A'-Neogammacer-5-en-3-one (DBF) and Pioglitazone (PIO), highlighting flexibility differences in loop and hinge regions

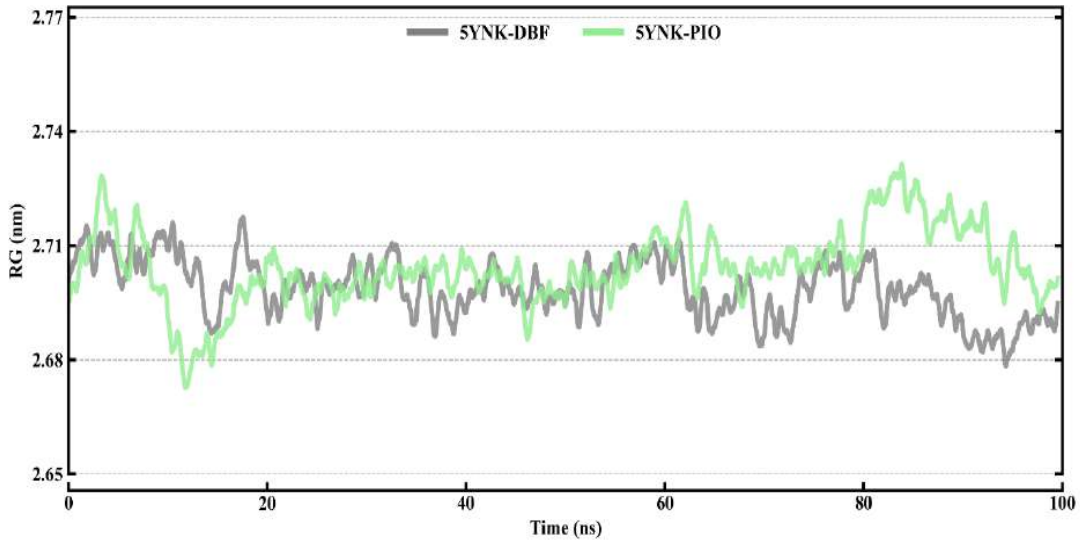


Figure 9.106: Radius of Gyration (Rg) variation over 100 nanoseconds simulation for Peroxisome Proliferator-Activated Receptor Gamma (PPARG) complexes with D:B-Friedo-B':A'-Neogammacer-5-en-3-one (DBF) and Pioglitazone (PIO)

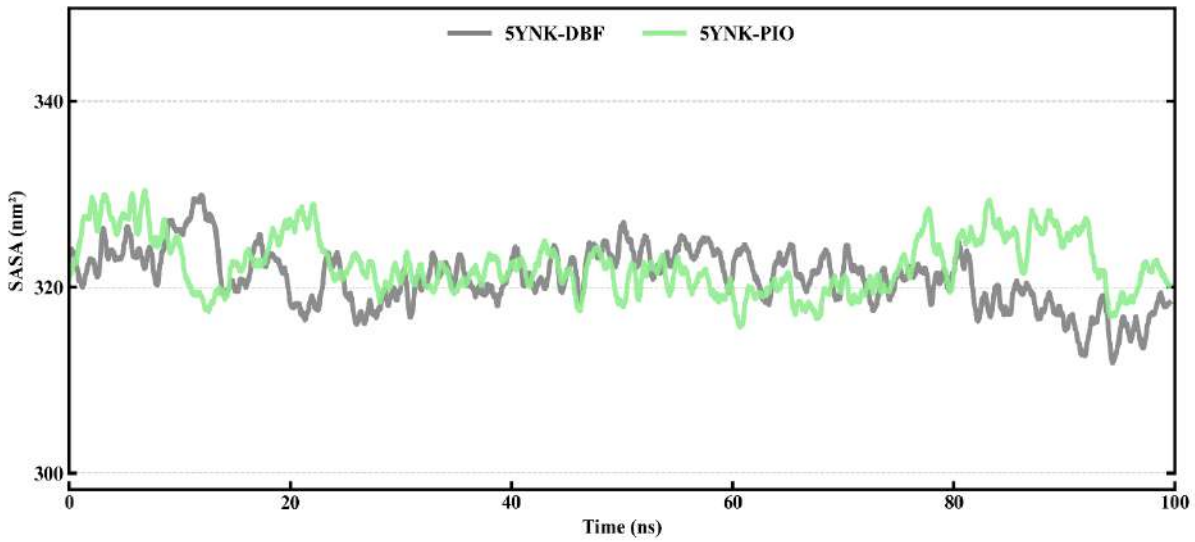


Figure 9.107: Solvent Accessible Surface Area (SASA) of Proliferator-Activated Receptor Gamma (PPARG) complexes with D:B-Friedo-B':A'-Neogammacer-5-en-3-one (DBF) and Pioglitazone (PIO), showing stable exposure trends over time

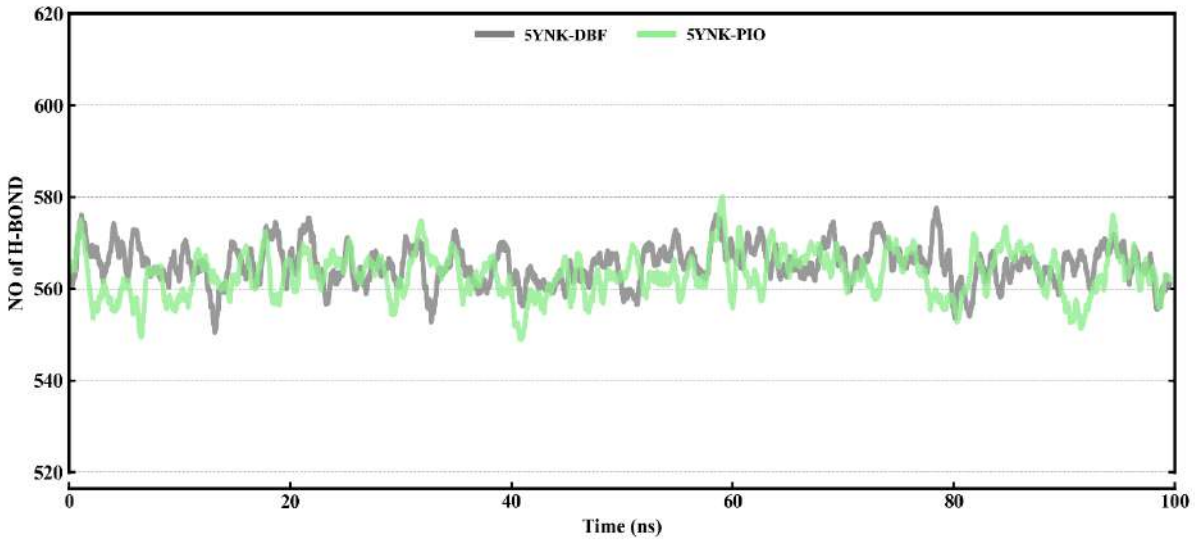


Figure 9. 108: Intramolecular hydrogen bond count in Proliferator-Activated Recept Gamma (PPARG) complexes with D:B-Friedo-B':A'-Neogammacer-5-en-3-one (DBF) and Pioglitazone (PIO)

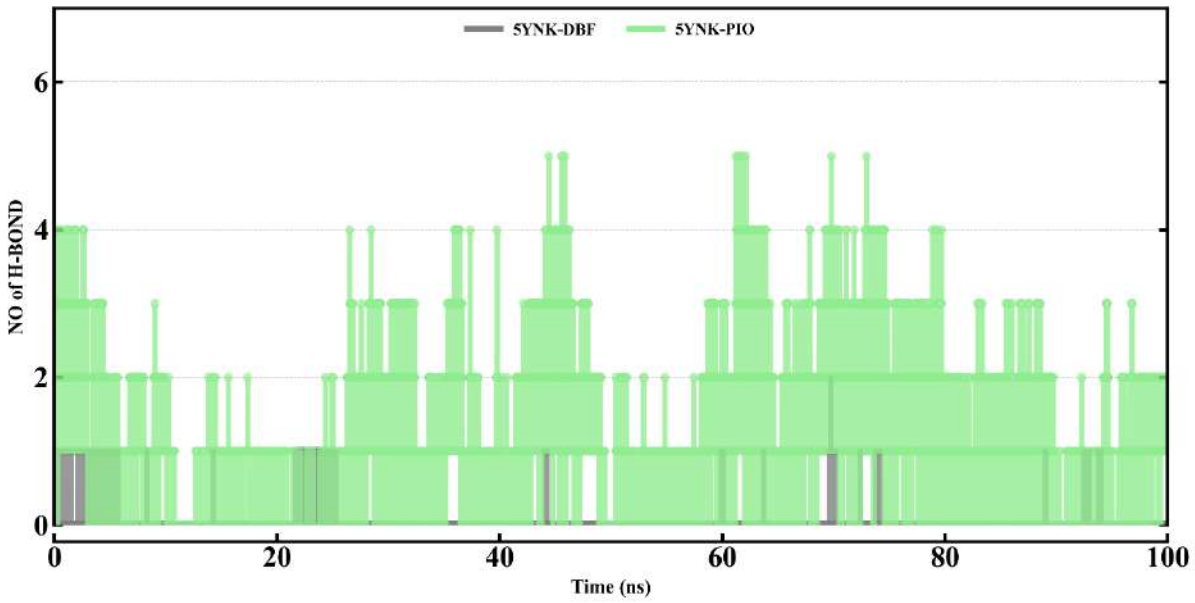


Figure 9.109: Intermolecular hydrogen bonds between Peroxisome Proliferator-Activated Receptor Gamma (PPARG) and to D:B-Friedo-B':A'-Neogammacer-5-en-3-one (DBF) and Pioglitazone (POI) over the 100-nanosecond simulation

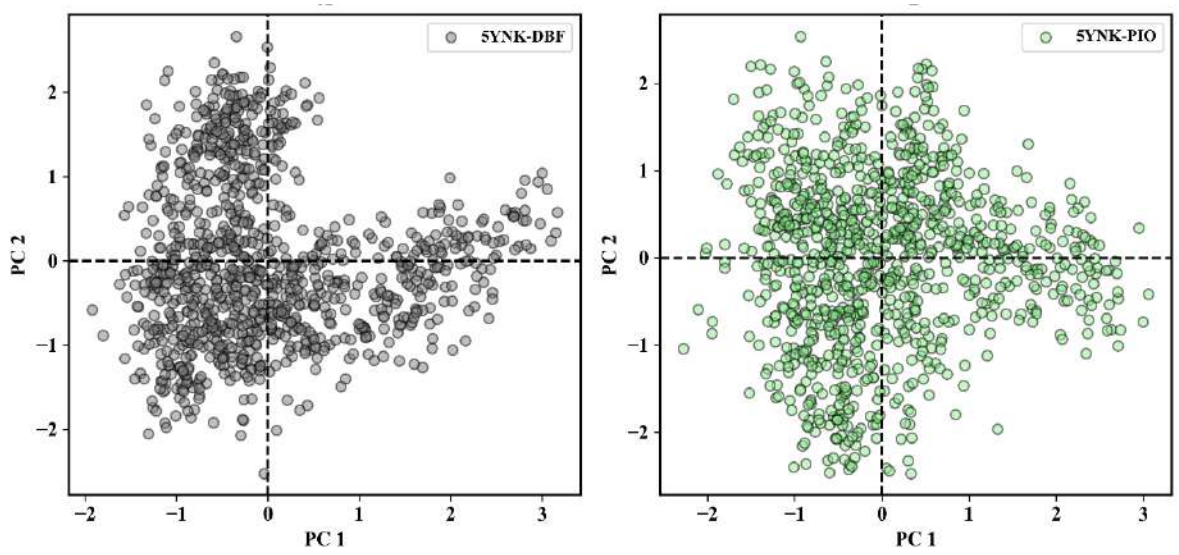


Figure 9.110: Principal Component Analysis (PCA) scatter plots of Peroxisome Proliferator-Activated Receptor Gamma (PPARG) bound to (a) D:B-Friedo-B':A'-Neogammacer-5-en-3-one (DBF) and (b) Pioglitazone (PIO) along PC1 and PC2, showing a more clustered conformational distribution for DBF

for induced-fit recognition, excessive sampling of alternative conformations may correspond to less stable ligand anchoring and a higher entropic penalty upon binding. Overall, the PCA results align with the RMSD and RMSF observations, reinforcing the notion that DBF maintains a more compact and stable conformational state than Pioglitazone (Figure 9.110).

9.3.22.3.2. Free Energy Landscape (FEL)

The FELs, constructed using PC1 and PC2 as reaction coordinates, reveal the thermodynamic stability and conformational basins accessible to the complexes. For the DBF–PPARG complex, the FEL displayed a deep, well-defined global minimum with minimal ruggedness, indicating a dominant, energetically favourable conformation. The energy well depth reached ~12 kJ/mol, and the narrow basin suggests strong stabilization of the bound state with limited excursions into higher-energy conformations. This thermodynamic profile is consistent with stable ligand binding and low conformational entropy loss.

In contrast, the PIO–PPARG FEL showed a broader and slightly more rugged energy landscape with multiple shallow minima. This suggests that PIO allows the protein to transition between multiple intermediate states, potentially reflecting lower conformational restraint and a less dominant bound-state conformation. From a pharmacological standpoint, the DBF landscape implies more sustained receptor activation due to reduced conformational drift, while PIO may induce greater conformational plasticity, possibly affecting binding persistence (Plate 9.57).

9.3.22.4. Overall conclusion- Antidiabetic activity from Molecular dynamics (MDS) analysis

The molecular dynamics analysis of the PPARG–ligand systems over a 100 ns trajectory clearly demonstrated that DB-Friedo-B'A'-Neogammacer-5-en-3-one (DBF) achieves superior structural stabilization of PPARG compared to the marketed drug Pioglitazone (PIO). Across RMSD, RMSF, Rg, SASA, intramolecular H-bonds, PCA, and FEL, DBF consistently maintained a tighter, more compact, and energetically favourable protein conformation.

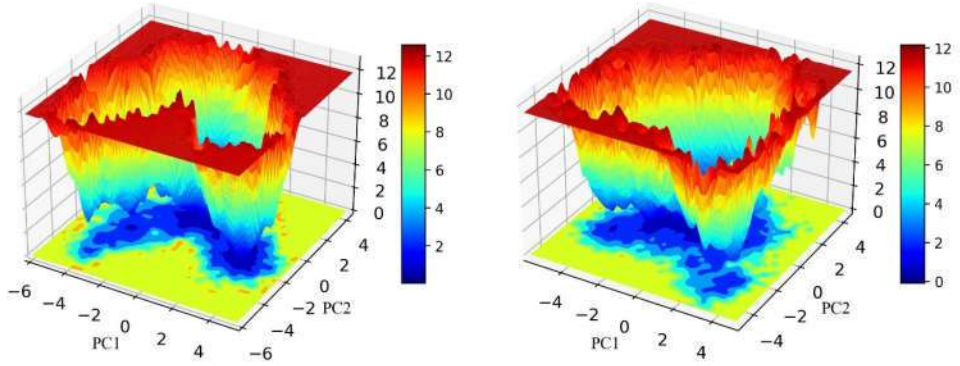
The RMSD distribution of DBF was narrower and centred at a lower mean value than PIO, reflecting reduced global structural deviations. RMSF analysis showed that DBF dampened local fluctuations at key binding domain residues more effectively, which is crucial for maintaining the ligand-binding domain (LBD) in its active conformation. Lower Rg and SASA values for DBF suggest enhanced protein compactness and reduced solvent exposure, indicating that DBF fosters a more thermodynamically stable PPARG conformation. Hydrogen bond analysis further supported this, showing that DBF sustains intramolecular hydrogen network integrity and forms persistent ligand contacts despite relying more on hydrophobic stabilization than PIO's transient polar interactions.

Conformational landscape exploration via PCA revealed that DBF restricts PPARG to a limited, well-defined conformational space, preventing excessive domain mobility. FEL mapping confirmed a deep and narrow energy well for DBF, suggesting a single, highly favourable binding state with minimal conformational wandering. In contrast, PIO permitted greater conformational sampling and occupied multiple shallow minima, indicative of less conformational constraint and potentially less stable receptor activation.

From a pharmacological standpoint, the structural stability induced by DBF could translate into prolonged and consistent PPARG activation, potentially offering better glycemic control in antidiabetic therapy. While PIO remains clinically effective, its broader conformational sampling may correspond to reduced binding persistence or faster receptor deactivation. DBF's strong hydrophobic complementarity, superior docking affinity (–10.8 kcal/mol vs –7.5 kcal/mol), and stable bound-state thermodynamics position it as a promising candidate for further development as a selective PPARG agonist with potentially improved efficacy and stability over the current standard drug.

9.3.22.5. Binding Free Energy (MM/PBSA)

MM/PBSA (Molecular Mechanics Poisson–Boltzmann Surface Area) analysis was conducted to evaluate the binding free energies of the PPARG protein in complex with DB-Friedo-B'A'-Neogammacer-5-en-3-one (a natural phytocompound) and



(a) (b)

Plate 9.57: Three-dimensional (3D) Free Energy Landscapes (FEL) of Peroxisome Proliferator-Activated Receptor Gamma (PPARG) bound to (a) D:B-Friedo-B':A'-Neogammacer-5-en-3-one (DBF), and (b) Pioglitazone (PIO) using PC1 and PC2 as reaction coordinates, illustrating differences in energy basin depth and shape

Pioglitazone (approved antidiabetic drug). This method decomposes the total binding free energy into van der Waals, electrostatic, polar solvation, and SASA components, enabling assessment of the specific energetic factors that contribute to ligand binding. Lower (more negative) total binding energy values reflect stronger and more thermodynamically favourable interactions (Table 9.135).

9.3.22.5.1. Binding affinity comparison

The total binding free energy indicates that DB-Friedo-B'A'-Neogammacer-5-en-3-one (–122.901 kJ/mol) binds more strongly to PPARG than Pioglitazone (–77.492 kJ/mol). The phytocompound benefits from slightly stronger van der Waals interactions (–173.494 vs. –167.220 kJ/mol) and a substantially lower polar solvation penalty (72.944 vs. 131.061 kJ/mol), which together enhance its net binding strength. Although Pioglitazone shows stronger electrostatic interactions (–25.028 vs. –6.057 kJ/mol), this advantage is outweighed by its high desolvation cost.

9.3.22.5.2. Energetic contributions and structural implications

The phytocompound's superior van der Waals stabilisation suggests a well-optimised hydrophobic fit within the PPARG binding pocket, which is consistent with the receptor's known preference for large, lipophilic ligands. The significantly reduced polar solvation energy for the phytocompound points to more efficient displacement of water molecules during binding, lowering the energetic penalty for desolvation. Pioglitazone's higher solvation penalty implies incomplete hydrophobic burial and potential solvent exposure of polar groups. Together, these results suggest that DB-Friedo-B'A'-Neogammacer-5-en-3-one may provide stronger and more persistent PPARG engagement than Pioglitazone, warranting further investigation of its potential as an antidiabetic lead (Figure 9.111).

9.3.22.6. Normal Mode Analysis (NMA) for Antidiabetic Target (PPARG)

Normal Mode Analysis (NMA) was performed on the peroxisome proliferator-activated receptor gamma (PPARG) to evaluate its dynamic behaviour, structural flexibility, and correlated motions. Understanding these intrinsic motions is essential, as PPARG is a nuclear receptor that undergoes conformational transitions

critical for ligand binding, coactivator recruitment, and transcriptional regulation (Plate 9.58).

9.3.22.6.1. Structural flexibility and deformability

The deformability plot of PPARG reveals several distinct peaks, indicating localized flexible regions interspersed with rigid domains. These peaks, particularly prominent in loop regions, represent potential hinge points facilitating conformational changes upon ligand binding. The 3D structural mobility map shows rigid core regions in blue, which are likely crucial for structural integrity, while peripheral loops and linker segments in green/yellow display enhanced flexibility.

9.3.22.6.2. B-Factor analysis

NMA-predicted B-factors (pink) generally align with experimental crystallographic B-factors (black), confirming the dynamic nature of specific regions. The termini and certain ligand-binding domain loops exhibit higher B-factors, indicative of elevated atomic displacement and structural adaptability. This flexibility is functionally relevant, as it may enable PPARG to accommodate a wide variety of ligands and co-regulatory proteins.

9.3.22.6.3. Collective motion, eigenvalues, and variance

The first non-trivial eigenvalue for PPARG was 1.50×10^{-6}, suggesting very low stiffness in the principal motion mode. This implies that PPARG can undergo large-scale conformational rearrangements with minimal energy input, a property beneficial for its role in transcriptional regulation. Variance analysis indicates that the first few modes contribute substantially to the overall motion, supporting the idea of collective, concerted dynamics that control receptor activation and interaction with transcriptional machinery.

9.3.22.6.4. Correlated Motions and Elastic Network

The covariance map shows alternating regions of strongly correlated (red) and anti-correlated (blue) motions, reflecting a complex interplay between the receptor's domains during activation. The elastic network model highlights a dense network of

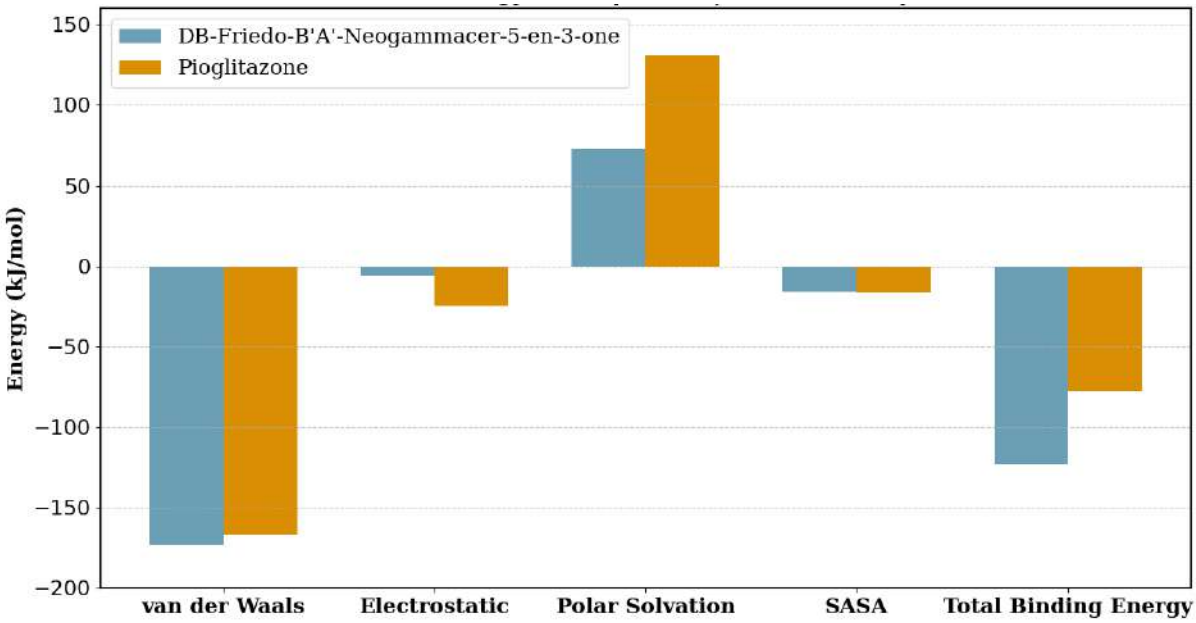


Figure 9.111: Molecular Mechanics Poisson–Boltzmann Surface Area (MM/PBSA) energy decomposition for Peroxisome Proliferator-Activated Receptor Gamma (PPARG) complexes with D:B-Friedo-B':A'-Neogammacer-5-en-3-one (DBF) and Pioglitazone (POI)

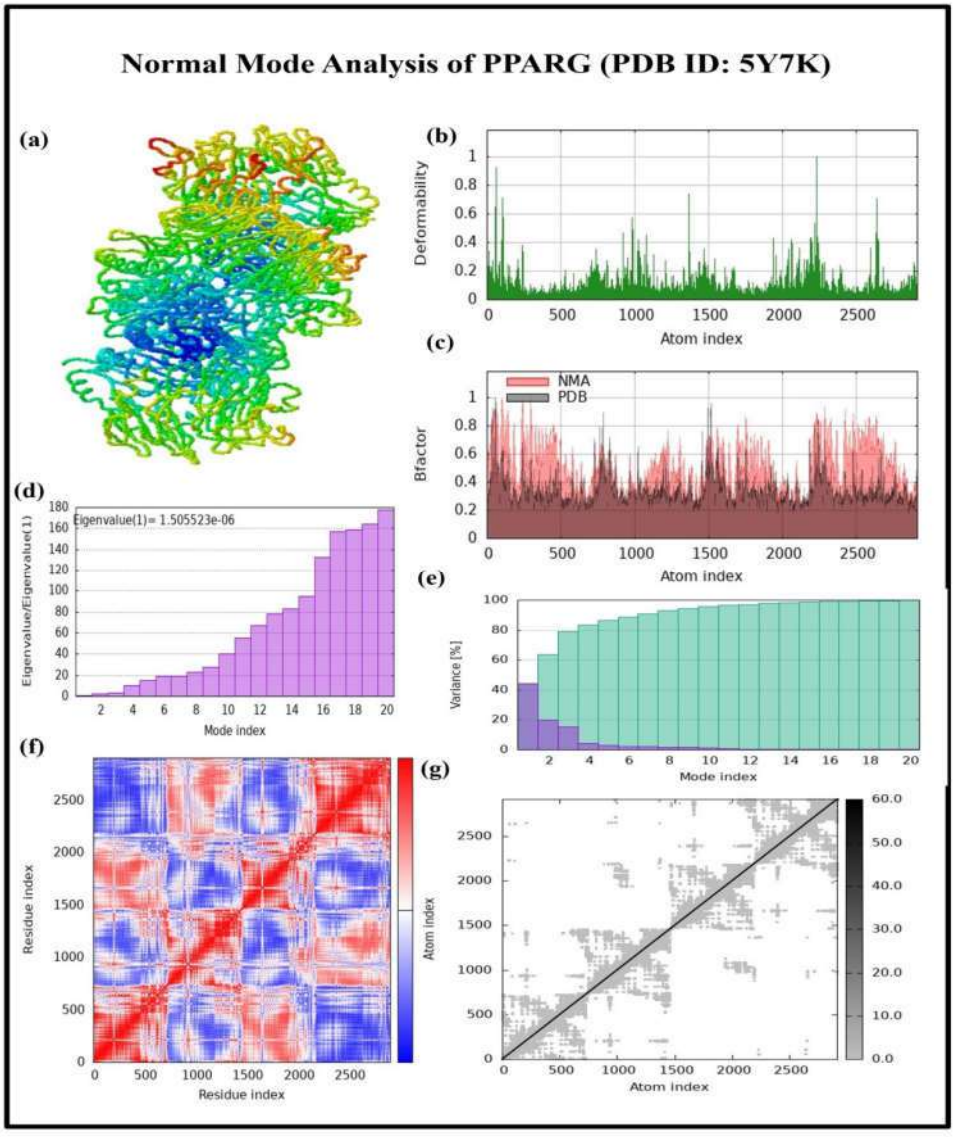


Plate 9.58: Normal Mode Analysis of Proliferator-Activated Receptor Gamma (PPARG): (a) cartoon representation with colour-coded mobility (blue: rigid, green/yellow: flexible) (b) deformability plot (c) B-factor comparison (NMA vs. PDB) (d) eigenvalue distribution (e) cumulative and individual variance per mode (f) covariance matrix showing correlated (red) and anti-correlated (blue) motions, and (g) elastic network map with spring strengths (dark grey: stiffer connections)

Table 9.136: Density Functional Theory (DFT) parameters for D:B-Friedo-B':A'-Neogammacer-5-en-3-one (DBF) and Pioglitazone (POI)

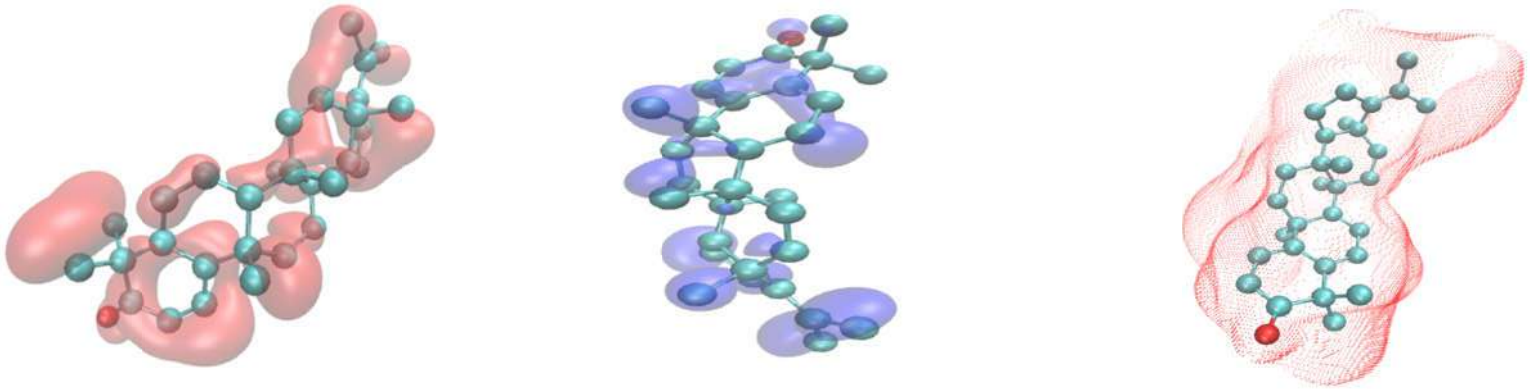
Compound name	DFT Energy (Hartree)	HOMO Energy (Hartree)	LUMO Energy (Hartree)	HOMO-LUMO Gap (Hartree)	MEP Minimum (a.u.)	MEP Maximum (a.u.)	MEP Average (a.u.)
D:B-Friedo-B':A'-Neogammacer-5-en-3-one -DFT	-1214.751	-0.241	-0.213	0.028	12.591	142.151	0.061
Pioglitazone-DFT	-1477.366	-0.154	-0.026	0.128	-13.369	186.23	0.0383

Table 9.137: Molecular Mechanics Poisson–Boltzmann Surface Area (MM/PBSA) energy decomposition for Kirsten Rat Sarcoma Viral Oncogene Homolog (KRAS)–Chlorogenic acid (CHL) and Kirsten Rat Sarcoma Viral Oncogene Homolog (KRAS)–Sotorasib (SOT) complexes

Energy Component (kJ/mol)	Chlorogenic Acid	Sotorasib
van der Waals	–79.513 ± 11.312	–127.025 ± 9.329
Electrostatic	–96.013 ± 60.283	–289.544 ± 20.716
Polar solvation	174.983 ± 82.315	133.174 ± 33.467
SASA	–12.572 ± 1.240	–14.329 ± 0.808
Total binding energy	–13.116 ± 38.695	–297.724 ± 14.281

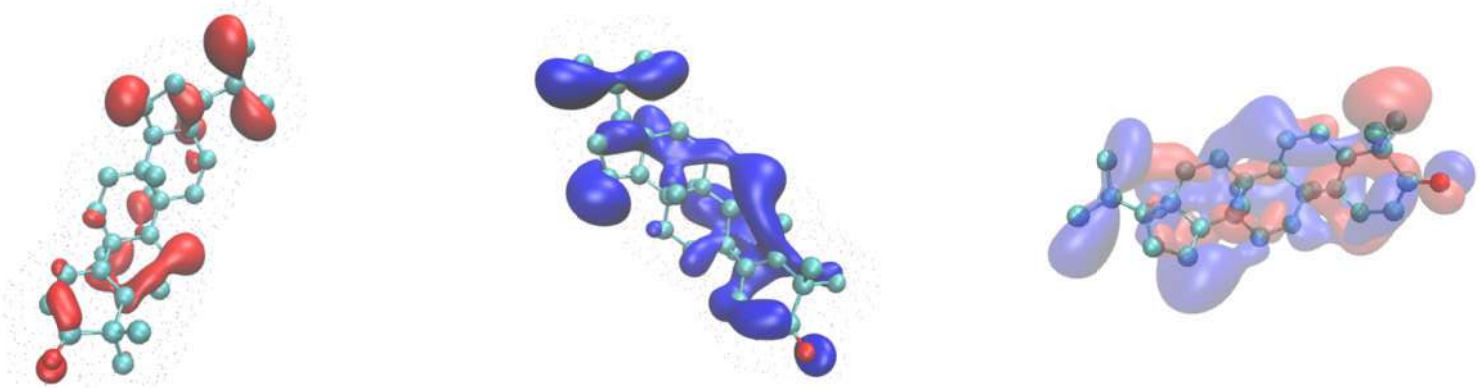
Table 9.138: Density Functional Theory (DFT)parameters for Chlorogenic acid and Sotorasib against KRAS (Kirsten Rat Sarcoma Viral Oncogene Homolog)

Compound name	DFT Energy (Hartree)	HOMO Energy (Hartree)	LUMO Energy (Hartree)	HOMO-LUMO Gap (Hartree)	MEP Minimum (a.u.)	MEP Maximum (a.u.)	MEP Average (a.u.)
Chlorogenic acid-DFT	-1296.555	-0.216	-0.084	0.131	-10.150	317.857	0.040
Sotorasib-DFT	-1988.901	-0.220	-0.108	0.112	-11.699	299.424	0.0496



(a) (b) (c)

Plate 9.59: Frontier molecular orbital (Highest Occupied Molecular Orbital (HOMO), Lowest Unoccupied Molecular Orbital (LUMO)) and molecular electrostatic potential (MEP) surfaces for D:B-Friedo-B':A'-Neogammacer-5-en-3-one (DBF) against Proliferator-Activated Receptor Gamma (PPARG): (a) HOMO distribution (b) LUMO distribution, and (c) MEP surface mapping



(a) (b) (c)

Plate 9.60: Frontier molecular orbital (Highest Occupied Molecular Orbital (HOMO), Lowest Unoccupied Molecular Orbital (LUMO)) and molecular electrostatic potential (MEP) surfaces for Pioglitazone (PIO) against Proliferator-Activated Receptor Gamma (PPARG): (a) HOMO distribution(b) LUMO distribution, and (c) MEP surface mapping, illustrating electron density patterns and probable interaction sites

stiff springs in the hydrophobic core, ensuring structural stability, while weaker connections in peripheral regions correspond to functionally relevant mobility zones, such as ligand entry pathways.

9.3.22.7. DFT analysis for antidiabetic activity (PPARG target)

Density Functional Theory (DFT) calculations were carried out for DB-Friedo-B'A'-Neogammacer-5-en-3-one (phytocompound) and Pioglitazone (approved antidiabetic drug) to assess their electronic structures, frontier molecular orbitals (FMOs), and molecular electrostatic potential (MEP) surfaces. These parameters provide insight into the compounds' stability, reactivity, and ability to interact with the PPARG active site (Table 9.136).

9.3.22.7.1. Electronic property comparison

DB-Friedo-B'A'-Neogammacer-5-en-3-one demonstrates an exceptionally small HOMO–LUMO gap (0.028 Hartree) compared to Pioglitazone (0.128 Hartree), suggesting much higher electronic reactivity and a greater potential for rapid charge transfer within the PPARG binding site. Its HOMO (-0.241 Hartree) and LUMO (-0.213 Hartree) energies are closer together, indicating a flexible electron donor–acceptor profile. In contrast, Pioglitazone's wider gap reflects comparatively lower reactivity but potentially greater stability (Plate 9.59).

9.3.22.7.2. Molecular Electrostatic Potential Insights (MEP)

Pioglitazone exhibits a strongly negative MEP minimum (-13.369 a.u.), indicating a high capacity for electrostatic attraction with positively charged residues in PPARG. On the other hand, DB-Friedo-B'A'-Neogammacer-5-en-3-one shows a positive MEP minimum (12.591 a.u.), which may reflect distinct charge distribution and binding orientation preferences. Pioglitazone also has a higher MEP maximum (186.230 a.u.) compared to the phytocompound (142.151 a.u.), suggesting more pronounced localized charge extremes (Plate 9.60).

9.3.23. Docking with an anticancer marketed drug

9.3.23.1. 3D and 2D visualization of Kirsten Rat Sarcoma Viral Oncogene Homolog (KRAS) with Sotorasib (SOT)

The 3D visualization reveals Sotorasib precisely accommodated within the KRAS active site, with its polyaromatic scaffold positioned to engage both hydrophobic and polar microenvironments. The ligand orients such that its terminal moieties extend toward solvent-accessible regions, while the central aromatic rings are buried within a predominantly hydrophobic cleft. The surface topology mapping highlights complementary hydrophobic (green) and hydrophilic (purple) regions, ensuring both snug fit and optimal molecular recognition. The ligand's strategic positioning facilitates a combination of π–driven and hydrogen bond interactions, stabilizing its conformation within the catalytic pocket.

The 2D interaction profile shows:

- Conventional Hydrogen Bonds (green arrows)

A notable polar interaction with GLU91 stabilizes the ligand's anchoring through strong directional bonding, enhancing specificity toward KRAS.

- Halogen Bond (light blue line)

Interaction with GLN129 via a fluorine atom reinforces orientation and contributes to affinity through halogen-mediated electrostatics.

- Pi–Anion Interaction (orange arc)

GLU91 also forms a π–anion contact with the ligand's aromatic ring, creating dual electrostatic and π-cloud stabilization.

- Pi–Alkyl Interactions (light pink arcs)

LEU133 and ARG135 contribute to hydrophobic complementarity, locking the aromatic rings into the hydrophobic groove.

- Van der Waals Contacts (light green spheres)

Residues such as TYR137, HIS94, ASP132, and SER136 surround the ligand, providing cumulative dispersion forces that reinforce stability without steric hindrance.

This multifaceted interaction network, anchored by dual polar contacts, halogen bonding, and hydrophobic locking, indicates that Sotorasib achieves high binding affinity to KRAS through a finely balanced combination of electrostatic and hydrophobic forces, a mechanism consistent with its role as a targeted KRAS G12C inhibitor in oncogenic signaling blockade (Plate 9.61).

9.3.23.2. Trajectory-based structural analysis

9.3.23.2.1. Root Mean Square Deviation (RMSD)

RMSD analysis indicates the overall stability of the KRAS–ligand complexes during the 100 ns simulation. The KRAS–Chlorogenic acid (CHL) complex showed a gradual increase in RMSD over time, stabilizing at a mean value of approximately 0.135 ± 0.015 nm, whereas the KRAS–Sotorasib (SOT) complex maintained a lower mean RMSD of 0.115 ± 0.010 nm throughout the trajectory. Both complexes equilibrated early (~5 ns) and remained within the 0.10–0.16 nm stability range, indicating that neither ligand induced large conformational deviations.

While the slightly higher RMSD of CHL suggests greater global movement, this does not necessarily imply instability; instead, it may reflect localized flexibility that could facilitate adaptive binding in KRAS's shallow allosteric pockets. However, SOT's lower RMSD indicates more rigid stabilization, which is expected for a covalent KRAS G12C inhibitor like Sotorasib (Figures 9.112-9.113).

9.3.23.2.2. Root Mean Square Fluctuation (RMSF)

RMSF profiles reveal residue-specific flexibility. Both complexes exhibited low fluctuations (<0.25 nm) across most of the KRAS sequence, with peaks occurring at loop regions (~residues 30–40 and 100–110), corresponding to flexible surface loops distal to the active site. CHL binding resulted in slightly higher RMSF values

at these flexible loop regions compared to SOT, suggesting CHL allows greater conformational sampling. In KRAS inhibition, excessive loop flexibility can potentially impact switch regions that control GTP/GDP binding, influencing downstream signaling inhibition. The lower RMSF in SOT may contribute to its potent and targeted KRAS inhibition (Figure 9.114).

9.3.23.2.3. Radius of Gyration (Rg)

Rg remained stable for both complexes, with CHL averaging 1.542 ± 0.005 nm and SOT averaging 1.527 ± 0.004 nm. The slightly higher Rg in CHL indicates a marginally less compact structure, consistent with its higher RMSD and RMSF. The tighter packing in SOT's complex is expected, given its covalent and sterically fitted mode of inhibition (Figure 9.115).

9.3.23.2.4. Solvent Accessible Surface Area (SASA)

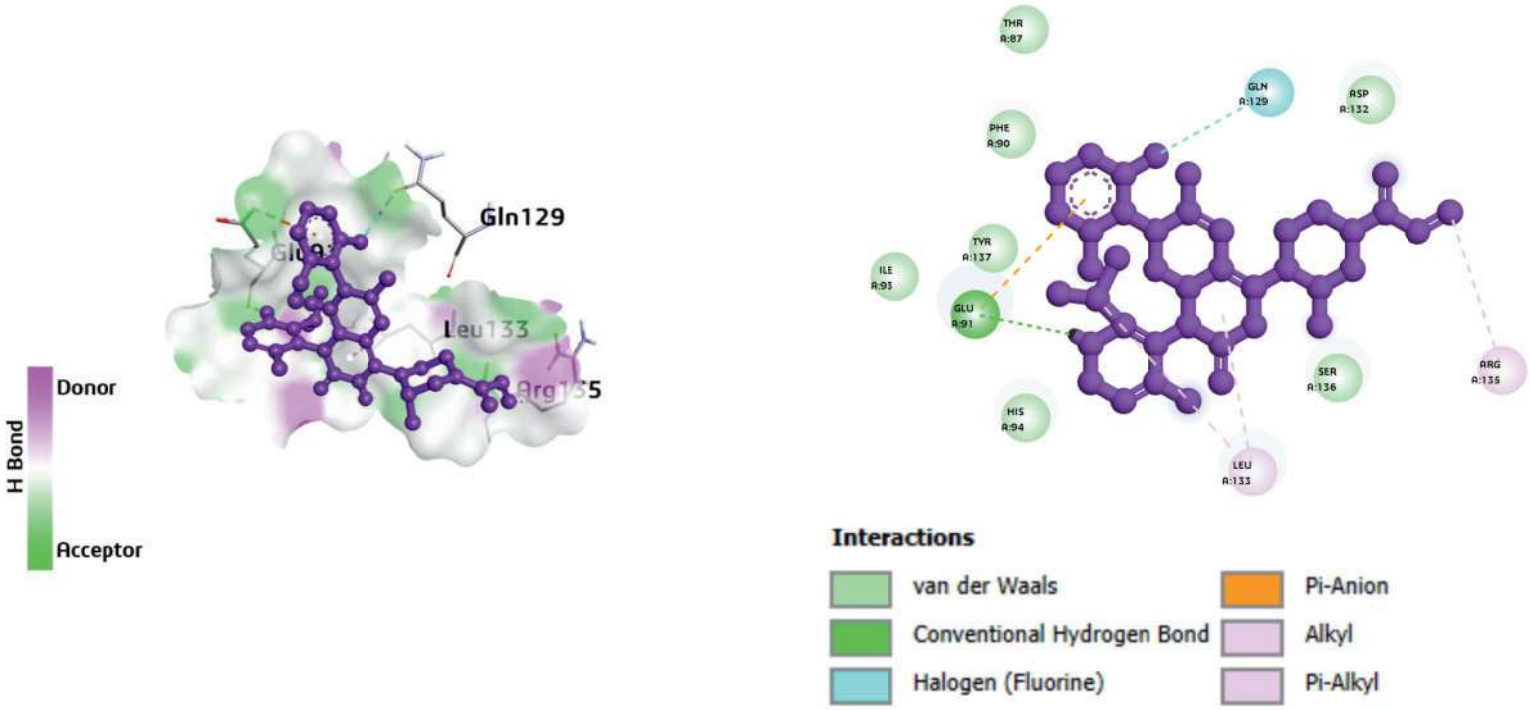
SASA analysis revealed that CHL maintained an average SASA of 90.5 ± 1.5 nm^2, slightly higher than SOT's 86.9 ± 1.4 nm^2. This difference suggests CHL's binding results in a slightly more solvent-exposed protein conformation, whereas SOT promotes deeper burial of hydrophobic regions, consistent with its tight, irreversible binding profile (Figure 9.116).

9.3.23.2.5. Intramolecular Hydrogen Bonds

Both complexes retained high levels of intramolecular hydrogen bonding (~125–135 bonds), indicating that neither ligand destabilized the protein's internal hydrogen network. SOT maintained slightly higher counts at certain intervals, which correlates with its lower RMSD and compact structure (Figure 9.117).

9.3.23.2.6. Intermolecular Hydrogen Bonds

CHL formed between 2–6 intermolecular H-bonds during the simulation, with moderate persistence. SOT, in contrast, maintained a lower H-bond count (0–2), reflecting its hydrophobic covalent binding mechanism that relies less on polar contacts. CHL's higher H-bonding potential suggests a strong polar interaction



(a) (b)

Plate 9.61: Visualization of binding interactions betweenKirsten Rat Sarcoma Viral Oncogene Homolog (KRAS) and marketed anticancer drugSotorasib(SOT), showing (a) the three-dimensional (3D) molecular surface and (b) the two-dimensional (2D) interaction diagram

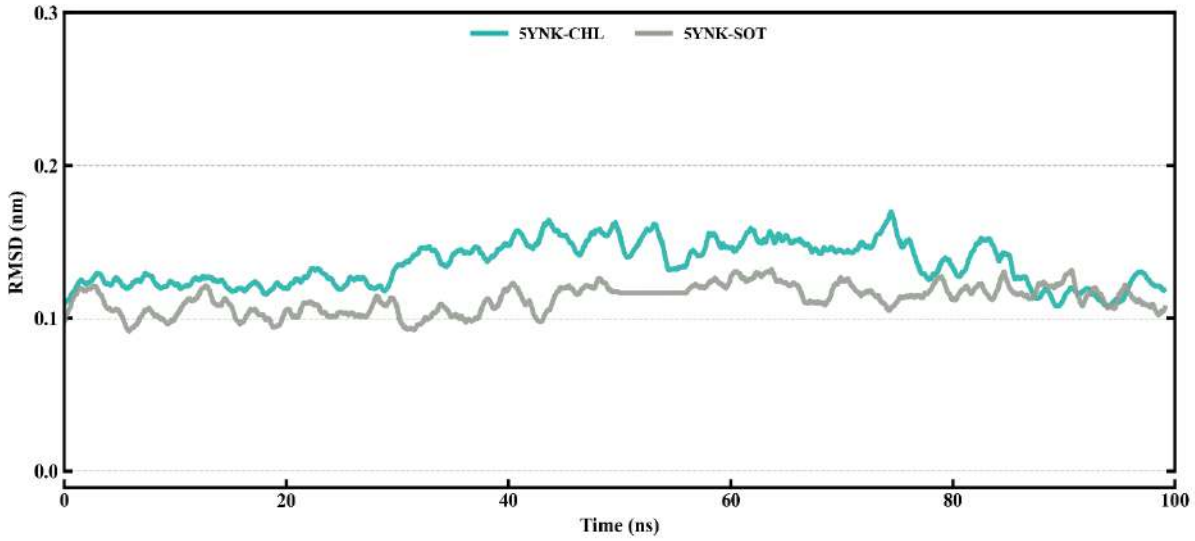


Figure 9.112: Root Mean Square Deviation (RMSD) variation of KRAS–CHL (Kirsten Rat Sarcoma Viral Oncogene Homolog-Chlorogenic acid) and KRAS–SOT (Kirsten Rat Sarcoma Viral Oncogene Homolog-Sotorasib) complexes over a 100-nanoseconds simulation

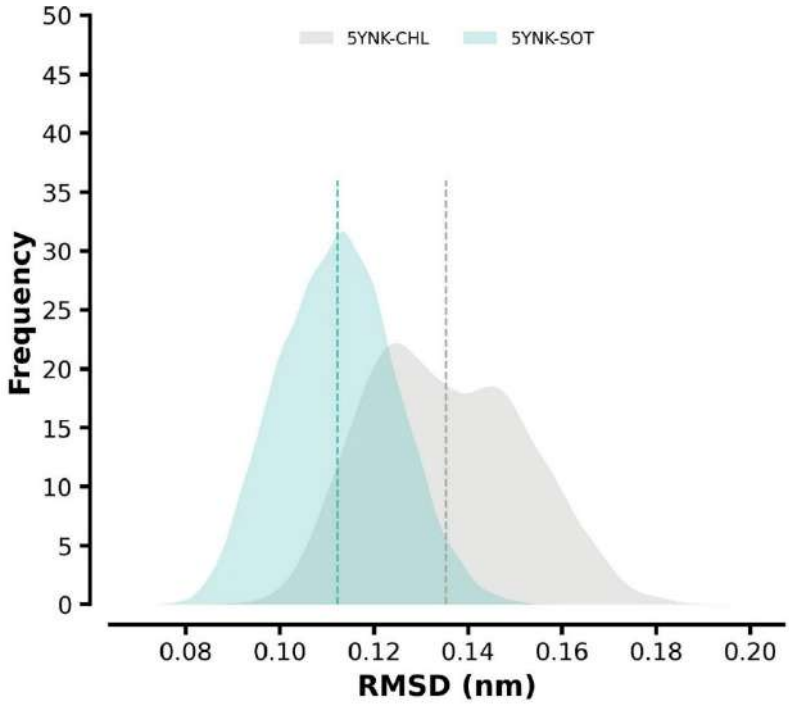


Figure 9.113: Probability distribution of Root Mean Square Deviation (RMSD) for KRAS–CHL (Kirsten Rat Sarcoma Viral Oncogene Homolog-Chlorogenic acid) and KRAS–SOT (Kirsten Rat Sarcoma Viral Oncogene Homolog-Sotorasib), showing tighter clustering for SOT

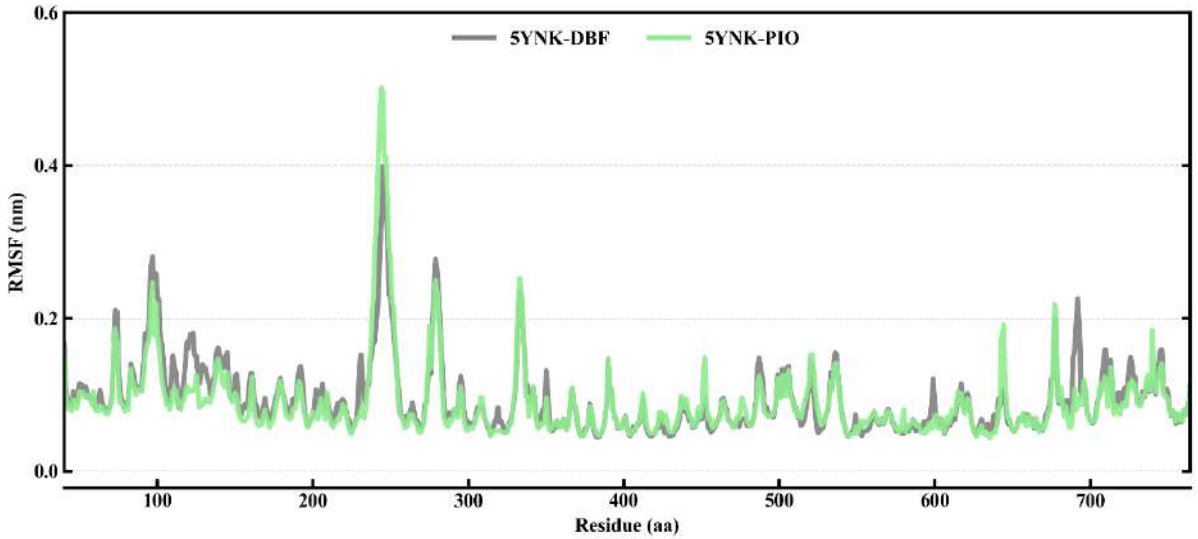


Figure 9.114: Root Mean Square Fluctuation (RMSF) plot for KRAS–CHL (Kirsten Rat Sarcoma Viral Oncogene Homolog-Chlorogenic acid) and KRAS–SOT (Kirsten Rat Sarcoma Viral Oncogene Homolog-Sotorasib) complexes, highlighting loop flexibility differences

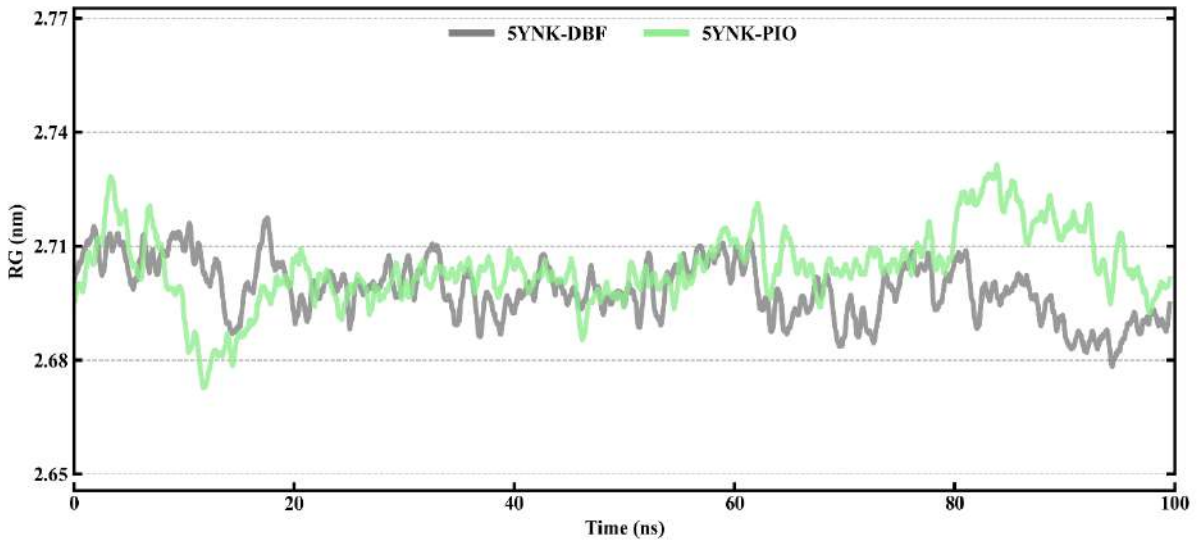


Figure 9.115: Radius of Gyration (Rg) variation over time for KRAS–CHL (Kirsten Rat Sarcoma Viral Oncogene Homolog-Chlorogenic acid) and KRAS–SOT (Kirsten Rat Sarcoma Viral Oncogene Homolog-Sotorasib) complexes

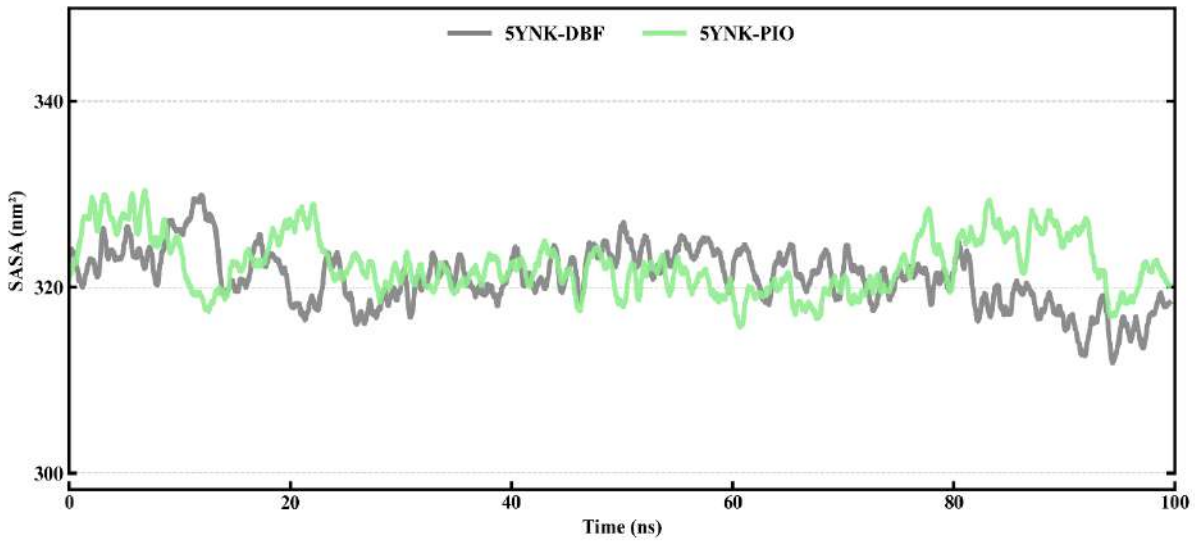


Figure 9.116: Solvent Accessible Surface Area (SASA) values for KRAS–CHL (Kirsten Rat Sarcoma Viral Oncogene Homolog-Chlorogenic acid) and KRAS–SOT (Kirsten Rat Sarcoma Viral Oncogene Homolog-Sotorasib) complexes over a 100-nanosecond simulation

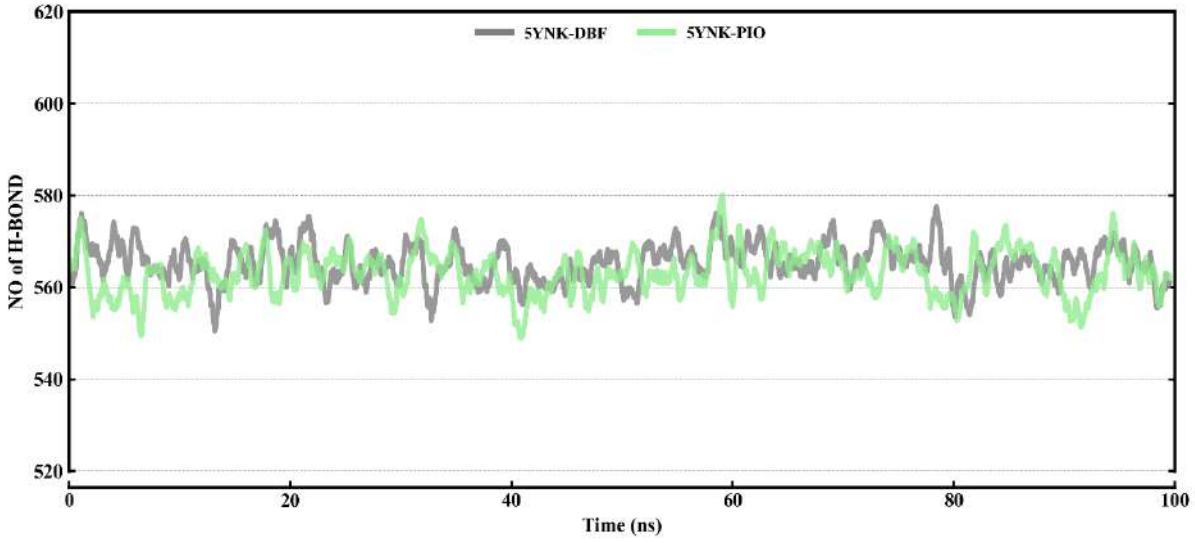


Figure 9.117: Intramolecular hydrogen bond count variation for KRAS–CHL (Kirsten Rat Sarcoma Viral Oncogene Homolog-Chlorogenic acid) and KRAS–SOT (Kirsten Rat Sarcoma Viral Oncogene Homolog-Sotorasib) complexes

component, which may aid in reversible binding and modulation, whereas SOT's lower count aligns with its covalent lock-and-key inhibition mode (Figure 9.118).

9.3.23.3. Conformational sampling and landscape analysis

9.3.23.3.1. Principal Component Analysis (PCA)

The PCA projections for the KRAS ligand systems reveal distinct differences in conformational sampling. The KRAS–CHL complex displayed multiple discrete clusters in the PC1–PC2 phase space, indicating that the protein explored several distinct conformational states during the simulation. This suggests CHL binding allows KRAS to shift between energetically accessible sub-states, potentially reflecting a more dynamic interaction mode that does not rigidly lock the protein in a single conformation. In contrast, the KRAS–SOT complex exhibited a denser, more centralized cluster distribution, implying that the protein's large-scale motions were more restricted. This conformational rigidity is consistent with Sotorasib's known irreversible covalent mechanism, which locks KRAS into a specific inactive conformation.

From a pharmacological viewpoint, CHL's greater conformational diversity could enable flexible, non-covalent inhibition modes, possibly beneficial for targeting KRAS mutants with diverse conformational preferences. However, this may come at the cost of reduced conformational constraint compared to Sotorasib's highly selective inhibition (Figure 9.119).

9.3.23.3.2. Free Energy Landscape (FEL)

The FEL maps, calculated using PC1 and PC2 as reaction coordinates, further illustrate the thermodynamic profiles of the complexes. The KRAS–CHL FEL featured multiple shallow minima with moderate depth (~10–12 kJ/mol), indicating that the protein–ligand complex populates several low-energy conformations rather than one dominant global minimum. This supports the PCA observation that CHL binding accommodates multiple conformations, which may facilitate reversible binding dynamics.

In contrast, the KRAS–SOT FEL revealed a deeper and narrower global minimum, with minimal ruggedness and fewer alternate basins. This suggests that Sotorasib enforces a highly stable bound conformation with limited excursions into alternative states. Such an energy profile is characteristic of covalent inhibitors that lock the target into a specific inactive state, enhancing long-term target suppression. Pharmacologically, the CHL profile suggests a potentially adaptable but less conformationally constrained binding mode, whereas SOT provides strong thermodynamic stabilization and conformational control, which may underlie its clinical potency (Plate 9.62).

9.3.23.4. Overall Conclusion- Anticancer activity from Molecular dynamics (MDS) analysis

The molecular dynamics simulations over 100 ns revealed distinct stability and conformational behaviours for KRAS–Chlorogenic acid (CHL) and KRAS–Sotorasib (SOT) complexes. While both ligands maintained KRAS structural integrity throughout the trajectory, the nature and extent of conformational stabilization differed significantly.

Sotorasib exhibited a consistently lower RMSD (0.115 ± 0.010 nm) and narrower RMSD distribution compared to CHL (0.135 ± 0.015 nm), reflecting a more rigidly stabilized protein backbone. RMSF analysis indicated that SOT suppressed local fluctuations in key loop regions more effectively, particularly in areas influencing KRAS's switch domains, which are critical for GDP/GTP binding and oncogenic activation. In contrast, CHL allowed slightly greater flexibility in these regions, potentially enabling adaptive but less conformationally restrictive binding.

Compactness metrics reinforced these observations: the Rg for SOT (1.527 ± 0.004 nm) remained lower than that for CHL (1.542 ± 0.005 nm), while SASA values indicated that CHL-bound KRAS had slightly greater solvent exposure (90.5 ± 1.5 nm^2 vs. 86.9 ± 1.4 nm^2). Intramolecular hydrogen bonding was well maintained in both complexes, suggesting no significant destabilization of KRAS's fold; however, CHL formed a higher number of persistent intermolecular H-bonds (2–6) compared

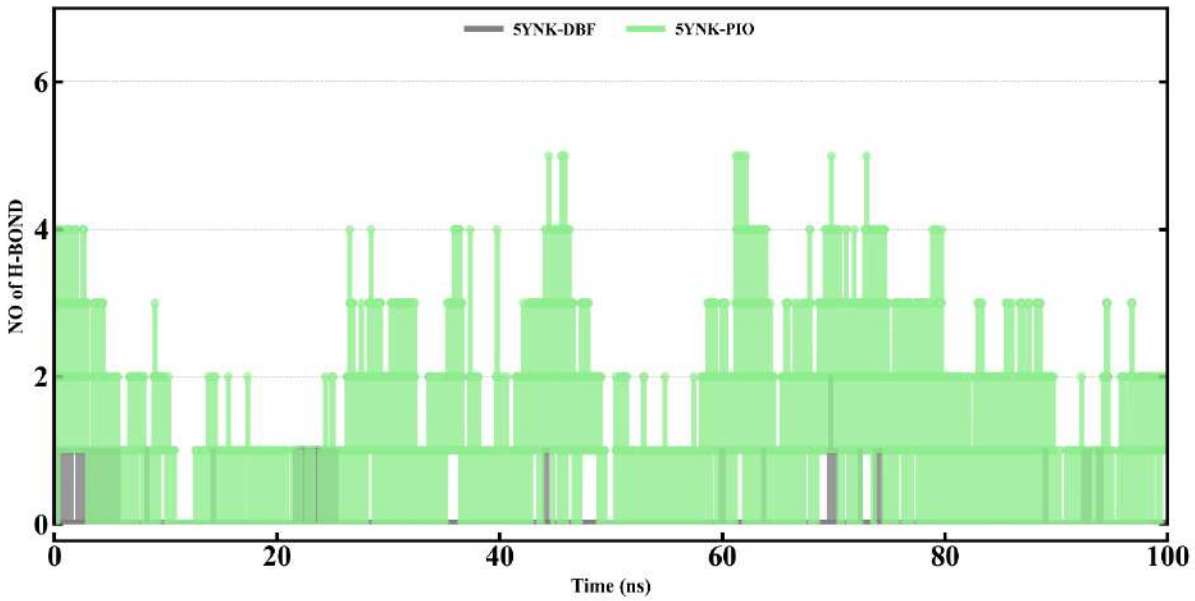


Figure 9.118: Intermolecular hydrogen bonds between KRAS (Kirsten Rat Sarcoma Viral Oncogene Homolog) and Chlorogenic acid (CHL)/Sotorasib (SOT) over the 100-nanosecond simulation

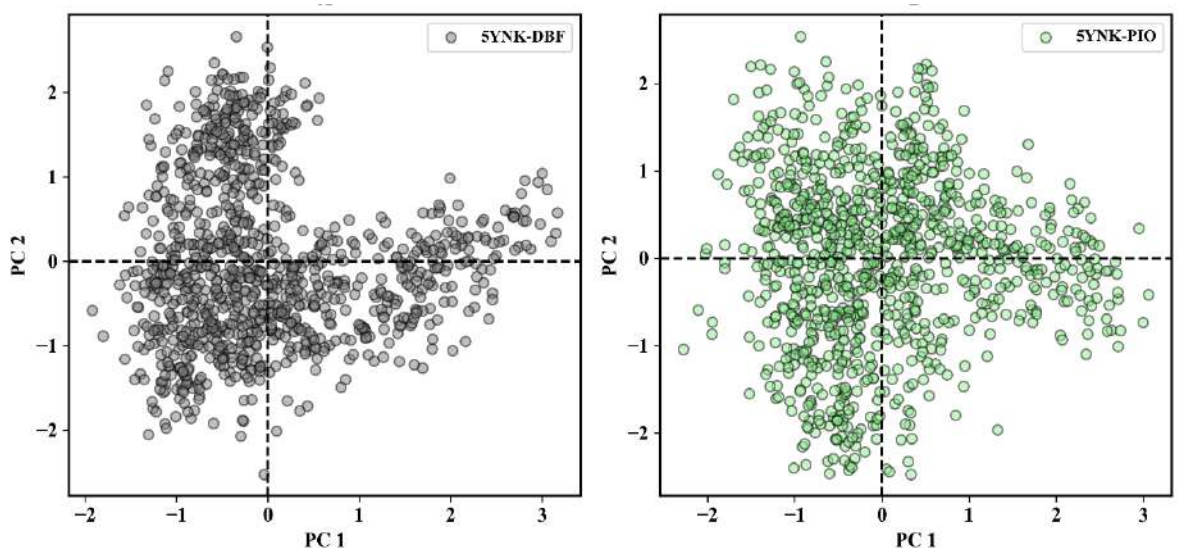


Figure 9.119: Principal Component Analysis (PCA)scatter plots of KRAS Kirsten Rat Sarcoma Viral Oncogene Homolog) bound to (a) CHL (Chlorogenic acid) and (b) SOT (Sotorasib) along PC1 and PC2, illustrating broader conformational sampling for CHL and tighter clustering for SOT

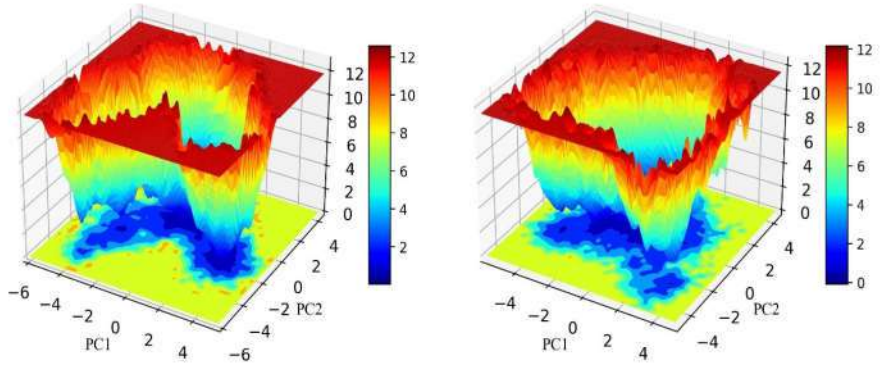


Plate 9.62: Three-dimensional (3D) Free Energy Landscapes (FEL) of KRAS (Kirsten Rat Sarcoma Viral Oncogene Homolog) bound to (a) CHL (Chlorogenic acid), and (b) SOT (Sotorasib) using PC1 and PC2 as reaction coordinates, highlighting differences in energy basin depth and conformational ruggedness

to SOT (0–2), consistent with CHL's reliance on polar contacts versus SOT's predominantly hydrophobic covalent engagement.

Conformational sampling analyses revealed a marked contrast in dynamic behaviour. PCA demonstrated that CHL binding led to multiple discrete conformational clusters, indicating the protein explored several accessible states. SOT, in contrast, restricted KRAS to a dense, centralized cluster, reflecting strong conformational constraint. FEL mapping confirmed this, showing CHL's multiple shallow minima versus SOT's single deep, narrow basin, a thermodynamic signature of high conformational fixation.

From a pharmacological standpoint, these differences reflect the underlying modes of action: Sotorasib's covalent binding enforces a stable inactive state, yielding potent, sustained KRAS inhibition. Chlorogenic acid's flexible, non-covalent interaction profile suggests potential adaptability across KRAS conformers, which may be advantageous for broader-spectrum modulation but could limit conformational control and inhibitory persistence. While CHL demonstrates strong polar engagement and stable thermodynamics, its slightly higher conformational freedom may translate into a different therapeutic profile than the highly selective, conformation-locking effect of Sotorasib.

9.3.23.5. Binding Free Energy (MM/PBSA)

MM/PBSA (Molecular Mechanics Poisson–Boltzmann Surface Area) analysis was employed to evaluate the binding free energies of the KRAS protein complexed with Chlorogenic Acid (a natural phytocompound) and Sotorasib (an approved anticancer drug). This approach decomposes the total binding free energy into van der Waals, electrostatic, polar solvation, and SASA components, allowing a deeper understanding of the energetic contributions driving ligand binding. Lower (more negative) binding energies indicate stronger and more thermodynamically favourable interactions (Table 9.137).

9.3.23.5.1. Binding affinity comparison

The total binding free energy shows that Sotorasib (–297.724 kJ/mol) binds far more strongly to KRAS than Chlorogenic Acid (–13.116 kJ/mol). The marked difference is due to significantly stronger van der Waals interactions (–127.025 vs. –79.513 kJ/mol) and electrostatic stabilization (–289.544 vs. –96.013 kJ/mol) in Sotorasib's case, indicating highly complementary shape and charge interactions within the KRAS binding pocket.

9.3.23.5.2. Energetic contributions and structural implications

The polar solvation penalty is notably higher for Chlorogenic Acid (+174.983 kJ/mol), which offsets much of its stabilizing non-polar interactions. This is likely due to its high polarity and extensive hydrogen-bonding capability in aqueous solution, making desolvation energetically costly. In contrast, Sotorasib's lower solvation penalty (+133.174 kJ/mol) combined with favourable SASA contributions (–14.329 kJ/mol) reflects effective hydrophobic burial and pocket fitting. Overall, while Chlorogenic Acid exhibits moderate stabilizing forces, its high desolvation cost limits binding efficiency. Sotorasib's deep binding pocket engagement, optimized hydrophobic packing, and strong electrostatics explain its superior binding, supporting its established role as a potent KRAS inhibitor (Figure 9.120).

9.3.23.6. Normal Mode Analysis (NMA)

Normal Mode Analysis (NMA) was conducted on the KRAS protein to investigate its intrinsic flexibility, correlated motions, and structural stability. This approach reveals the collective motions that contribute to protein function and helps to identify flexible regions, hinge points, and potential conformational transitions relevant to ligand binding and protein–protein interactions.

9.3.23.6.1. Structural flexibility and deformability

The deformability profile shows multiple peaks distributed across the KRAS sequence, indicating the presence of several flexible loop regions. These flexible segments are potential hinge points that may facilitate the conformational changes

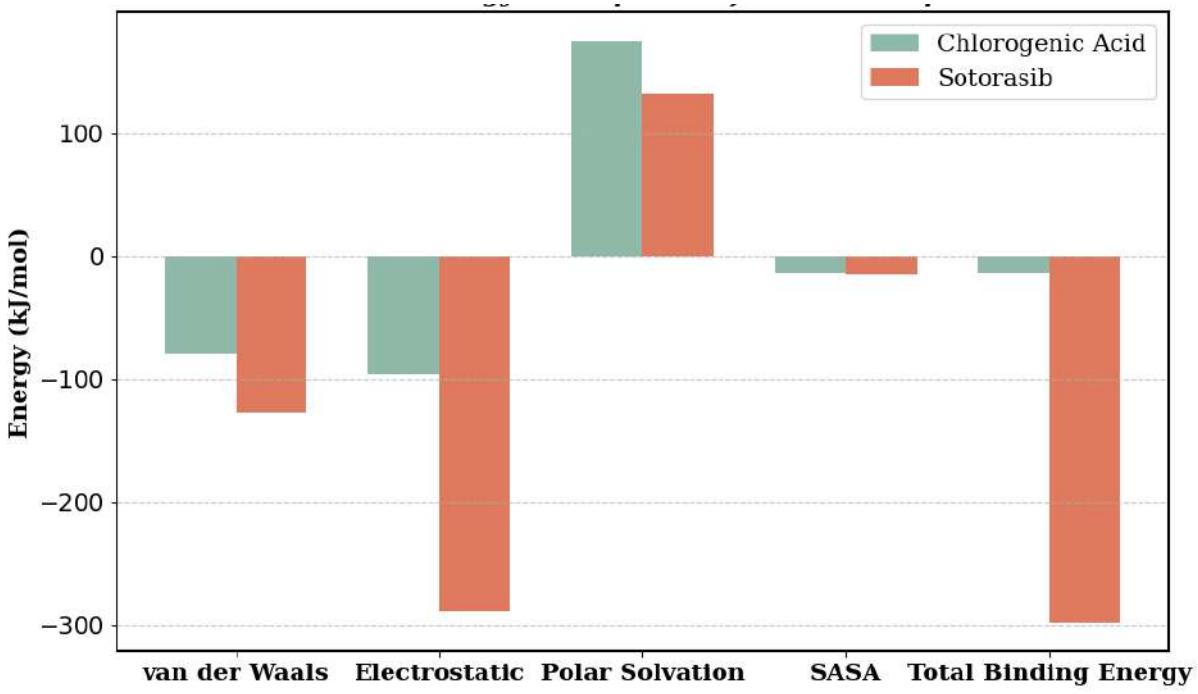


Figure 9.120: Molecular Mechanics Poisson–Boltzmann Surface Area (MM/PBSA) energy decomposition for KRAS (Kirsten Rat Sarcoma Viral Oncogene Homolog) complexes with Chlorogenic acid and Sotorasib

required for KRAS signaling. The 3D representation highlights flexibility using a colour gradient; blue regions are rigid, whereas green/yellow correspond to more mobile areas.

9.3.23.6.2. B-Factor analysis

Comparison of the NMA-predicted B-factors (pink) with experimental crystallographic B-factors (black) shows good agreement in identifying dynamic regions. Higher B-factor values at both N- and C-terminal ends indicate enhanced mobility, which could contribute to structural adaptability during interactions with ligands such as small-molecule inhibitors.

9.3.23.6.3. Collective motion, eigenvalues, and variance

The first non-trivial eigenvalue was 8.47×10^{-4} indicating a relatively low stiffness for the dominant mode of motion, suggesting that KRAS can undergo significant conformational changes with minimal energy expenditure. Variance analysis shows that the first few modes account for most of the total motion, reflecting the collective nature of protein dynamics.

9.3.23.6.4. Correlated motions and elastic network

The covariance map (Figure f) reveals regions of strongly correlated (red) and anti-correlated (blue) motions, particularly between key structural segments, which may be important for the allosteric regulation of KRAS. The elastic network model shows denser spring connections in the protein core, indicating structural rigidity in the central β-sheet, while peripheral loops display weaker connectivity, supporting their higher mobility (Plate 9.63).

9.3.23.7. DFT Analysis for anticancer activity (KRAS target)

To complement the molecular docking and MM/PBSA findings, Density Functional Theory (DFT) calculations were performed on Chlorogenic Acid (phytocompound) and Sotorasib (approved anticancer drug) to probe their electronic properties and reactivity patterns. The analysis focused on frontier molecular orbitals (FMOs), HOMO–LUMO gap, and molecular electrostatic potential (MEP) mapping,

all of which are critical for understanding ligand–target interactions at the quantum level (Table 9.138).

9.3.23.7.1. Electronic property comparison

Sotorasib exhibits a smaller HOMO–LUMO gap (0.112 Hartree) than Chlorogenic Acid (0.131 Hartree), implying higher chemical reactivity and greater ease of electron exchange with the KRAS active site. Its lower LUMO energy (-0.108 Hartree vs. -0.084 Hartree) indicates superior electron-accepting capacity, potentially strengthening interactions with electron-donating residues in the protein. While both compounds show similar HOMO energies, Sotorasib's more favourable LUMO placement supports its known potency (Plate 9.64).

9.3.23.7.2. Molecular Electrostatic Potential Insights (MEP)

MEP analysis reveals that Sotorasib has a more negative MEP minimum (-11.699 a.u.) than Chlorogenic Acid (-10.150 a.u.), suggesting a stronger potential for forming electrostatic attractions with positively charged regions in KRAS. Conversely, Chlorogenic Acid's more pronounced MEP maximum (317.857 a.u.) indicates localized regions of high positive potential, which may favour different binding modes (Plate 9.65).

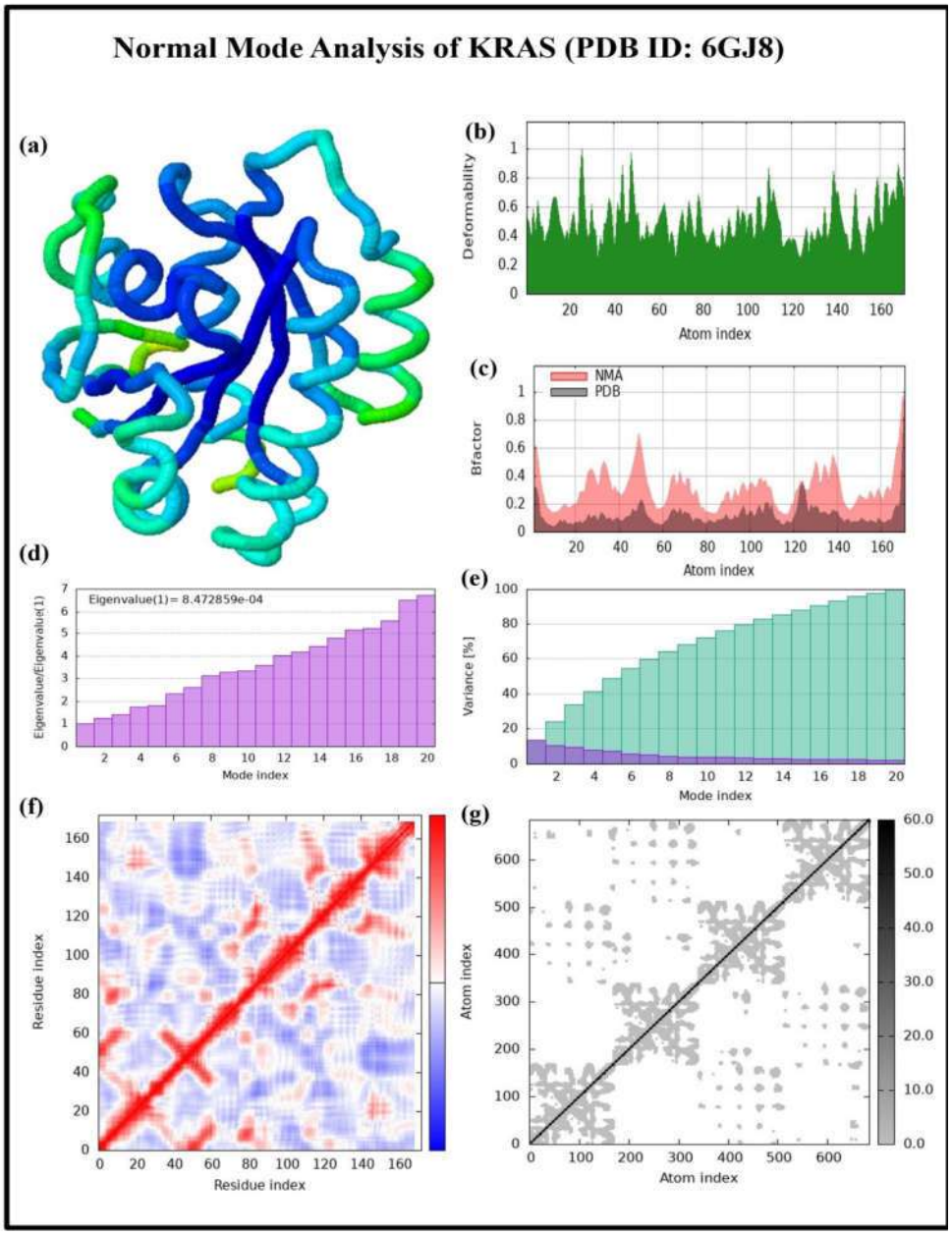
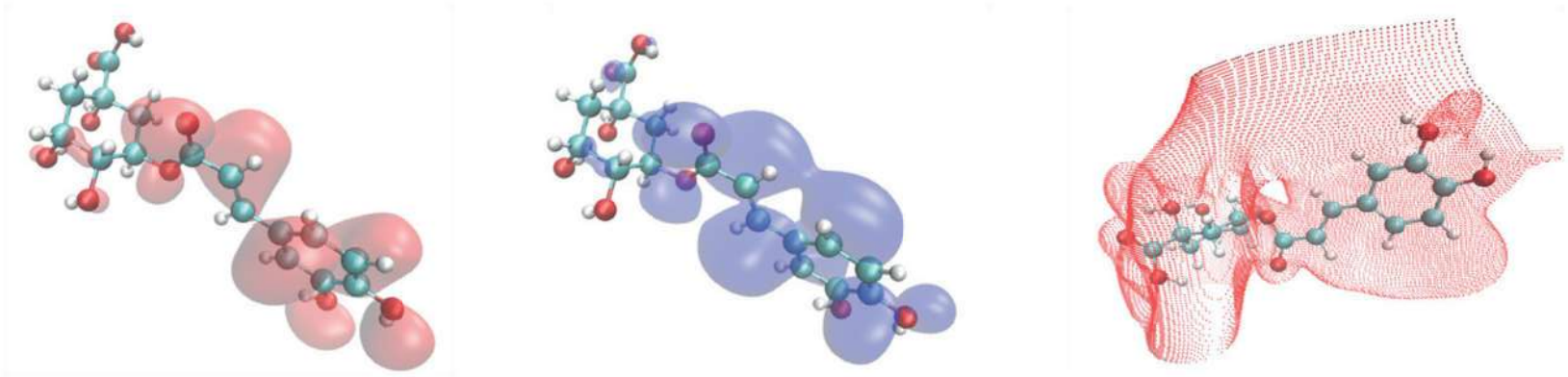
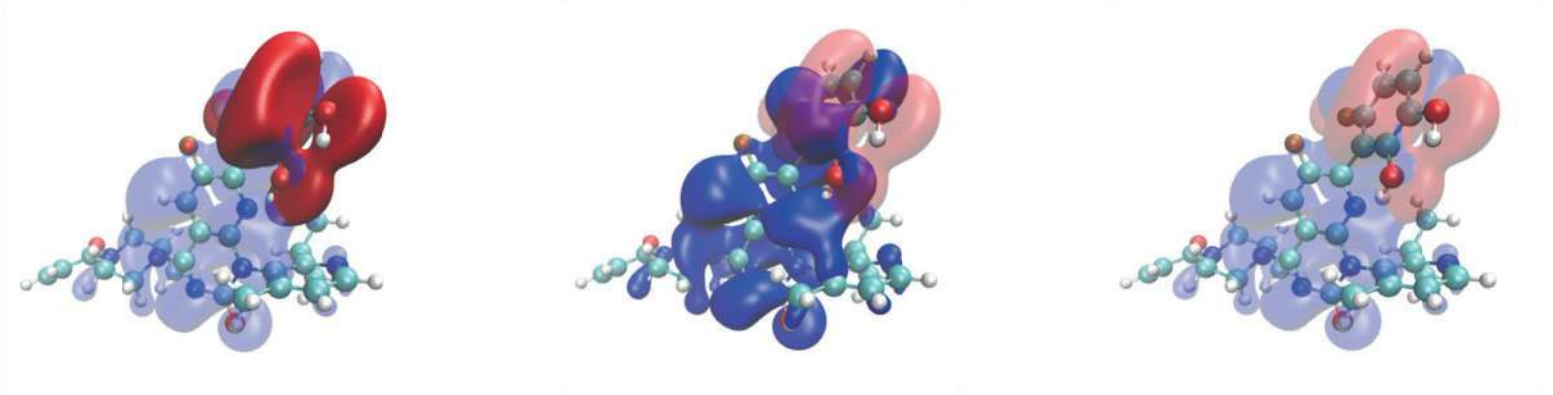


Plate 9.63: Normal Mode Analysis of KRAS (Kirsten Rat Sarcoma Viral Oncogene Homolog): (a) cartoon representation with colour-coded mobility (blue: rigid, green/yellow: flexible) (b) deformability plot (c) B-factor comparison (NMA vs. PDB) (d) eigenvalue distribution (e) cumulative and individual variance per mode (f) covariance matrix showing correlated (red) and anti-correlated (blue) motions, and (g) elastic network map with spring strengths (dark grey: stiffer connections)



(a) (b) (c)

Plate 9.64: Frontier molecular orbital (Highest Occupied Molecular Orbital (HOMO), Lowest Unoccupied Molecular Orbital (LUMO)) and molecular electrostatic potential (MEP) surfaces for Chlorogenic acid against KRAS: (a) HOMO distribution(b) LUMO distribution, and (c) MEP surface mapping



(a) (b) (c)

Plate 9.65: Frontier molecular orbital(Highest Occupied Molecular Orbital (HOMO), Lowest Unoccupied Molecular Orbital (LUMO)) and molecular electrostatic potential (MEP) surfaces for Sotorasib against KRAS: (a) HOMO distribution (b) LUMO distribution, and (c) MEP surface mapping

9.4. Discussion

Five key proteins associated with antioxidant, antimicrobial, anthelmintic, anti-inflammatory, antidiabetic, and anticancer activities were structurally curated and preprocessing was for computational analysis. Protein-protein interaction networks provide two major challenges for analysis i.e., their scale-free nature and the high proportion of false positive interactions they represent. Preprocessing methods efficiently remove problematic edges and possible false positives from the graph using isolated weighting functions and a crucial transformation (Ucar et al., 2005). The clean protein models that were produced provided the basis for precise pharmacokinetic analysis and receptor-ligand interaction profiling. An effective method for investigating protein structure-function correlations in the absence of crystal structures is in silico protein structure analysis. Additionally, it can assist in the prediction of loop structure, mutagenesis experiments, SAR data, ligand-receptor interactions, and enzyme-substrate interactions (Nene et al., 2022).

Physicochemical profiles can be useful tools for medicinal chemists, helping to predict oral absorption *in vivo* (Avdeef, 2001). Early physicochemical property measurement during drug research and development is essential to lowering attrition rates brought on by inferior biopharmaceutical qualities (Henchoz et al., 2009). Physicochemical characteristics, including solubility, partition coefficient, molecular weight, size, and acid dissociation constant, are important in the production of compact pharmaceuticals and have a significant influence on the pharmacokinetics of conventional small molecule therapeutics (Swami & Shahiwala, 2013). The physicochemical properties (molecular weight, pI, amino acid composition, aliphatic index, GRAVY scores etc.) of the proteins play roles in antioxidant, antimicrobial, anthelmintic, anti-inflammatory, antidiabetic, and anticancer activities were studied. Analysis through molecular docking, molecular dynamics simulations, NMA, and DFT studies was also conducted for the evaluation of marketed drugs and phytocompounds of *S. palghatense* for antioxidant, antimicrobial, anti-inflammatory, anticancer, antidiabetic, and anthelmintic potential.

Reactive oxygen species (ROS) is produced when oxygen combines with electrons. ROS have long been recognized to kill human cells and microorganisms. While low to intermediate ROS concentrations work by regulating cell signaling cascades, extended exposure to high ROS concentrations can cause unspecific damage to lipids, proteins, and nucleic acids (Brieger et al., 2012). Antioxidant proteins like SOD1, CAT, GPx1, KEAP1, and Trx-TXNIP were evaluated which protect cells from oxidative stress. Results on physicochemical profiles of SOD1 were similar with previous study (Khan et al., 2020). Structural analysis of these showed that SOD is beta-sheet dominant, stable scaffold for metal binding; flexible loops aid substrate entry, CAT is helix-rich, highly stable; supports rapid hydrogen peroxide breakdown, GPx1 is a balanced helices and beta structures; optimized for flexibility and peroxide neutralization, KEAP1 is beta-sheet dominant; specialized for Nrf2 binding and redox regulation, and Trx-TXNIP is beta sheet-dominant and flexible. A broad family of enzymes known as superoxide dismutases (SODs) that contain copper contribute to the metabolism of reactive oxygen species by converting superoxide anion radicals into oxygen and hydrogen peroxide (Robinett et al., 2018). The activities of glutathione peroxidase (GPX), catalase (CAT), and superoxide dismutase (SOD) form a first line antioxidant defense system that is essential to the general well-being of the organism, according to Ighodaro & Akinloye (2018).

Bacterial infections can lead to long-term, severe issues that endanger public health. Further, the production of new antibacterial drugs is required due to the ongoing evolution of drug-resistant microorganisms (Qin et al., 2021). Antimicrobial proteins like Ddl, LasR, PqsR/MvfR, PBP3, and RhIR are analysed that are involved in bacterial growth and are antibiotic targets. Ddl structure is a balanced sheets and helices; stable yet flexible for bacterial cell wall synthesis, LasR is helix-rich; flexible for DNA binding and quorum sensing regulation, PqsR/MvfR is compact, helix-driven; adapts for ligand and DNA binding, PBP3 is a complex, highly stable; essential for bacterial cell wall crosslinking, and RhIR is helix-dominant; supports DNA recognition and transcription regulation. It is thought that Ddl can serve as a viable target for the creation of antibacterial drugs (Qin et al., 2021). Molecular docking and molecular dynamics simulations were used in research by Singothu & Bhandari

(2024) to screen marine natural products (MNPs) from the CMNPD database for possible LasR inhibitors and discovered 10 MNPs that outperformed the binding energy of the reference chemical cladodionen and the co-crystal 3-oxo-C12-HSL in terms of docking scores against LasR. According to Chen et al. (2017), the most promising target for *P. aeruginosa* drug development is PBP3.

The survival of an organism depends on metabolic processes that release energy from carbon molecules. Thus, one possible treatment approach to treat parasite infections is the inhibition of these enzymes associated with these pathways (Timson, 2016). Anthelmintic proteins like ATP synthase, COX1, HSP70, Complex 1, and Ext. Globin-3 that helps in parasite survival and a drug target were studied. ATP synthase is helix-rich; optimized for proton transport and ATP generation, COX1 is also helix- dense; highly stable for electron transport and proton pumping, HSP70 is a balanced beta and alpha structure; flexible for protein folding and stress response, Complex 1 is highly compact, helix-packed; provides membrane stability for energy production, and Ext. Globin-3 is helix-dominant, stable oxygen-binding protein for parasite survival. As per Ōmura et al. (2001), nafuredin is a possible lead molecule as an anthelmintic that was isolated from microorganisms, and mitochondrial complex I represents a prospective target for chemotherapy.

An injury or trauma can cause inflammation, which is a healthy reaction that usually goes completely without harming the host (Lawrence & Fong, 2010). An important role for the nuclear factors kappa-light-chain-enhancer of activated B cells (NF-κB) pathway is in carcinogenesis, inflammation, and proliferation (Kadioglu et al., 2015). TNF-α is a key pro-inflammatory cytokine that contributes to edema and vasodilatation, leukocyte adhesion to the epithelium through adhesion molecule expression, blood coagulation regulation, oxidative stress in inflammatory sites, and indirect fever onset (Zelová & Hošek, 2013). According to Yu et al. (2016), Resokaempferol prevents both LPS and IL-6 signals from activating the JAK2/STAT3 pathway, thereby reducing inflammation in stimulated macrophages. Anti-inflammatory proteins like NF-κB, TNF-α, iNOS, JAK2, and COX-2 that controls immune system signals were evaluated in the present study. NF-κB is rich in

beta-sheet, stable DNA-binding scaffold with flexible turns for promoter recognition, TNF-α have a compact, stable cytokine structure; trimeric arrangement aids receptor binding, iNOS is highly flexible, helix-rich enzyme supporting NO production and rapid immune response, JAK2 is a balanced α/β structure; stable yet adaptable for ATP binding and cytokine signaling, and COX-2 is helix-dominant, membrane-stabilized enzyme with flexibility for substrate entry and product release.

Because synthetic antidiabetic drugs have a number of negative side effects, using natural substances to manage diabetes has grown in popularity gradually. Physicochemical properties of antidiabetic protein like DPP4, insulin receptor, alpha-amylase, PPARG, and PTP1 that control blood sugar and metabolism was also studied. DPP4 is a large β-sheet framework, stable catalytic pocket; supports incretin degradation, insulin receptor is β-sheet dominant; highly stable with disulfide bonds for precise insulin binding, alpha-amylase is mixed α/β fold; stable catalytic domain for efficient starch hydrolysis, PPARG is α-helical nuclear receptor; flexible ligand-binding domain for glucose and lipid regulation, and PTP1 is mixed α/β enzyme; regulates insulin signaling via dephosphorylation. Diabetes, which is marked by high blood sugar levels, is associated with consequences such as blindness, renal failure, and cardiovascular disease, and it presents serious health and financial hazards. The T-cell activation antigen CD26 (EC 3.4.14.5), also known as dipeptidyl peptidase-4 (DPP-4), is essential for immunological response and glucose metabolism (Hossain et al., 2024). Bilal and Mustafa (2025) developed hypoglycemia peptides (HGPs) from plant sources and demonstrated their efficacy against certain diabetes proteins in a computational analysis.

Physicochemical properties and structural analysis of the five anticancer proteins namely AKT1, EGFR, KRAS, MAPK1, and TP53 was evaluated in present study. AKT1 is helix-rich kinase; stable catalytic core with flexible loops for pathway activation, EGFR is balanced sheets and helices; stable yet flexible for ligand binding and signal transduction, KRAS is simple α-helical fold; flexible switch regions for rapid conformational changes, MAPK1 is helix-packed kinase; stable scaffold with adaptable loops for phosphorylation, and TP53 is partially disordered, highly flexible

transcription factor; adapts to diverse DNA and protein interactions. Interactions between a number of intrinsic and extrinsic factors are the primary contributing factors of many cancers. Since deregulation of numerous genes and signaling pathways is a known feature during diverse malignancies, targeting these abnormalities may be important for cancer detection and treatment. The AKT1 enzyme is regarded as a potential target for the development of anti-cancer therapies as it has been discovered to be overexpressed in a number of cancers (Mirza & Karim 2023). The EGFR protein is ultimately responsible for a number of cancer types, by properly understanding the molecular interactions between the protein structure and its inhibitors, more effective and selective EGFR-TKIs will be developed, potentially saving more lives in the fight against cancer (Zubair & Bandyopadhyay 2023). KRAS is a frequently mutated oncogene that negatively predicts the outcome of several targeted treatments (Baranyi et al., 2020).

According to Mkhwanazi et al. (2014), maslinic acid antioxidant properties can reduce oxidative stress and enhance renal function in people with diabetes mellitus. Present study found that for antioxidant activity, maslinic acid emerged as the strongest phytocompound, showing the highest binding affinity with KEAP1 (−10.5 kcal/mol) and stable interactions via hydrogen bonding and hydrophobic contacts. Compared to the marketed antioxidant drug Dimethyl Fumarate (DMF), maslinic acid demonstrated superior electronic reactivity, enhanced van der Waals interactions, and better adaptability, suggesting its potential to modulate the NRF-Keap1 effectively. MD simulations confirmed that maslinic acid–KEAP1 complexes maintained stable conformations, with lower conformational fluctuations than DMF. maslinic acid reduced intracellular ROS and shielded cell lines from oxidative damage under stressful circumstances (Mokhtari et al., 2022). Maslinic acid showed significant affinity towards helminthic proteins in present study.

Kaempferol, which is present in many different plant groups and its related chemicals have antibacterial, antifungal, and antiprotozoal properties in addition to their anticarcinogenic and anti-inflammatory actions (Periferakis et al., 2022). It was recorded that for antimicrobial activity, phytocompounds like 2-Phenyl-4H-chromen-

4-one, kaempferol, oleanolic acid, and ellagic acid showed strong binding affinities against critical bacterial targets, including LasR, PqsR/MvfR, PBP3, and RhIR. The marketed drug Tobramycin formed a stable docking pose with LasR (average RMSD ~0.154 nm), but 2-Phenyl-4H-chromen-4-one, displayed superior binding free energy indicating enhanced hydrophobic stabilization and shape complementarity. According to De et al. (2018), ellagic acid may be used both therapeutically and preventively to treat *H. pylori* infections. As a result, it may be regarded as a potential antibacterial agent for treating human gastroduodenal disorders linked to H. pylori.

Research indicates that oleanolic acid may help prevent dyslipidemia, diabetes, and metabolic syndrome by improving insulin sensitivity, maintaining β-cell survival and function, and preventing complications from diabetes. Other functions have also been proposed, such as antiviral, antibacterial, anticarcinogenic, antifungal, anti-inflammatory, hepatoprotective, gastroprotective, hypolipidemic, and anti-atherosclerotic activities, as well as interfering in various stages of the development of various cancer types. However, because oleanolic acid is hydrophobic, it is nearly insoluble in water, which has led to various approaches to improve its biopharmaceutical qualities (Castellano et al., 2022). Present study found that oleanolic acid showed significant affinity towards helminthic proteins, anti-inflammatory proteins and antimicrobial proteins.

For anthelmintic activity it was observed that phytocompounds like Vitamin E**,** maslinic acid, quercetin, and oleanolic acid showed significant affinity towards helminthic proteins, including Globin-3, ATP synthase, and COX1. MD simulations revealed Vitamin E maintained higher stability and hydrogen bonding with globin-3, despite marketed drug Albendazole showing stronger binding energy. In their study, Ray et al. (2025) used the zoonotic tapeworm *Hymenolepis diminuta* to demonstrate quercetin's cestocidal action and propose that it has cestocidal effect.

Chlogenic acid is a naturally occurring plant extract that comes from a variety of sources. Research has shown that its primary pharmacological effects include anti-inflammatory, antiviral, anti-bacterial, hypoglycemic, anticardiovascular, lipid-lowering, antimutagenic, anticancer, immunomodulatory, and more. It could thus be

crucial in advancing human health. It can offer fresh perspectives and innovative approaches to the prevention and management of diabetes, cancer, heart disease, and other chronic illnesses (Miao & Xiang, 2020). The present study also found significant inhibition potential of chlorogenic acid across multiple oncogenic pathways.

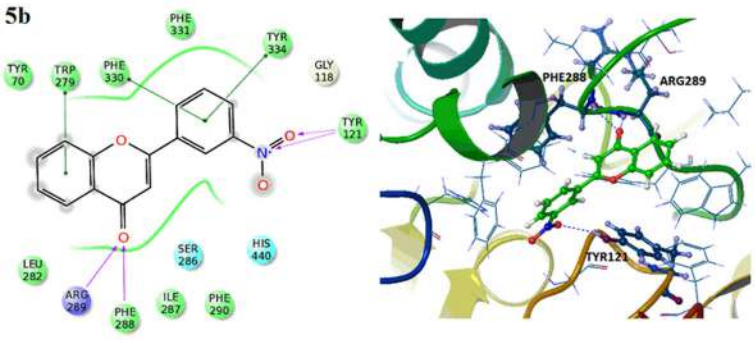
DFT investigations demonstrated improved electronic stability and interaction flexibility, whereas MM/PBSA free energy calculations verified that phytocompounds had greater binding energetics than several commercially available medications across all assessments. These results together imply that some phytocompounds function as strong multi-target modulators that may find use in anticancer, antibacterial, anti-inflammatory, antidiabetic, anthelmintic, and antioxidant treatments.

9.5. Conclusion

This study thoroughly evaluated the bioactive phytocompounds derived from *S. palghatense* using molecular docking, molecular dynamics (MD), normal mode analysis (NMA), density functional theory (DFT), and MM/PBSA free energy profiling against a number of therapeutic protein targets associated with anticancer, antimicrobial, anthelmintic, anti-inflammatory, and antidiabetic properties. To guarantee high-quality receptor models and enable accurate prediction of protein-ligand interactions and stability, structurally resolved proteins were preprocessed.

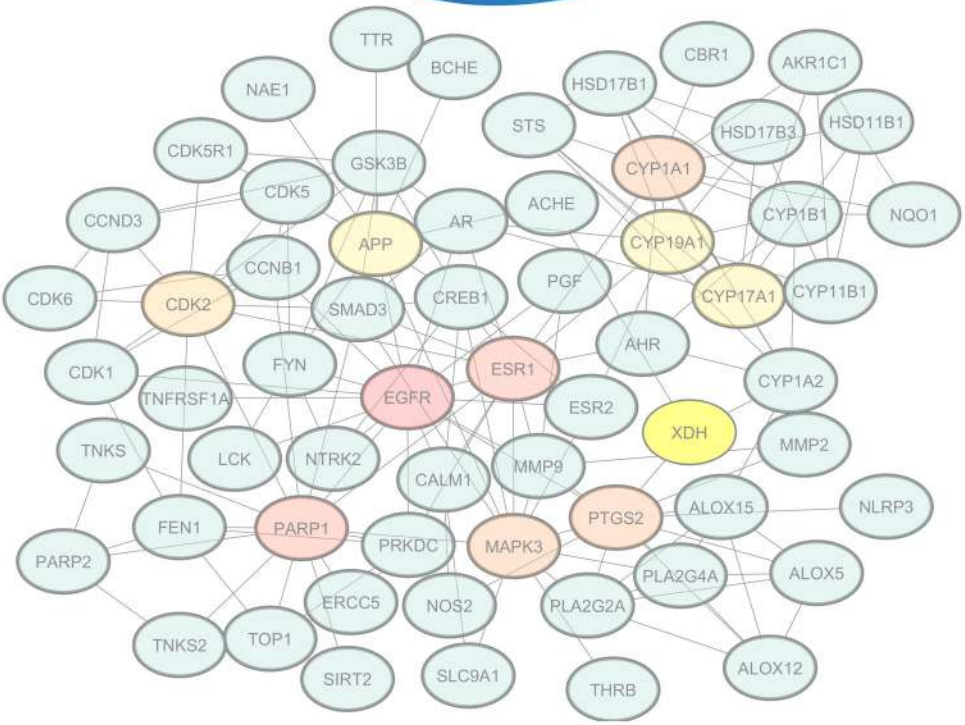
According to the results, a number of phytocompounds outperformed commercially available medications in terms of binding affinities and interaction stability. With the strongest stability over Dimethyl Fumarate (DMF) and the best binding affinity with the KEAP1 protein, maslinic acid emerged as the most promising antioxidant agent. Maslinic acid also showed significant affinity towards helminthic proteins. Oleanolic acid showed significant affinity towards helminthic proteins, anti-inflammatory proteins and antimicrobial proteins. Present study also found significant inhibition potential of chlorogenic acid across multiple oncogenic pathways. 2-Phenyl-4H-chromen-4-one showed antimicrobial activity and DB-Friedo-B'A'-Neogammacer-5-en-3-one demonstrates antidiabetic potential. Quercetin was found to show strong interaction with the anthelmintic protein. Ellagic acid showed strong potential against antimicrobial and anti-inflammatory proteins.

Overall, the study shows that phytocompounds from *S. palghatense*, particularly DB-Friedo-B'A'-Neogammacer-5-en-3-one, oleanolic acid, vitamin E, 2-phenyl-4H-chromen-4-one, and maslinic acid, function as multi-target modulators with better stability, higher adaptability, and stronger binding than a number of currently available medications. Their therapeutic promise for a variety of illnesses, such as cancer, diabetes, oxidative stress, bacterial infections, parasite infestations, and chronic inflammation, is highlighted by these findings.



10

NETWORK PHARMACOLOGY AND FUNCTIONAL ANALYSIS OF ISOLATED COMPOUND



CHAPTER 10

NETWORK PHARMACOLOGY AND FUNCTIONAL ANALYSIS OF ISOLATED COMPOUND

10.1. Introduction

Naturally occurring compounds known as flavonoids, which have a variety of phenolic structures, can be extracted from tea, wine, fruits, vegetables, grains, bark, roots, stems, and flowers. These natural compounds have a reputation for being advantageous to the body, and experiments are currently underway to separate out these flavonoids (Panche et al., 2016). Flavonoids are the most prevalent polyphenols found in plant meals, with over 4,000 different molecules (Corcoran et al., 2012). They are distinguished by their 15-carbon skeleton that is arranged as C6-C3-C6, with the various subclasses being made from distinct substitutions. Flavonols, also known as catechins (epigallocatechin 3-gallate from green tea), flavones (apigenin from celery), flavonols (quercetin, which is found in many plant foods, especially red onions and apples), flavanones (naringenin from citrus), anthocyanidins (cyanidin from berries), and isoflavones (daidzein and genistein from soya beans) are the main groups of flavonoids of nutritional significance (Birt & Jeffery, 2013).

Flavonoids are found in many different types of plants and are a broad class of polyphenolic chemicals with a benzo-γ-pyrone structure (Kumar & Pandey, 2013). Within the class of naturally found polyphenolic chemicals, flavonoids have anti-inflammatory, anti-allergic, antidiabetic, and antioxidant properties. Other flavonoid molecules may also have antiviral properties (Uddin et al., 2022). Their actions are dependent on their structure. The degree of polymerization, various substitutions and conjugations, degree of hydroxylation, and structural class all influence the chemical makeup of flavonoids (Kumar & Pandey, 2013).

The most often found class of flavonoids in plants belonging to the Myrtaceae family were anthocyanins, which mostly relate to the purple/reddish colour of the fruits. Additional substances, including epicatechin, catechin, quercetin, and rutin,

were also found in various constituent fractions, including leaves, seeds, pulp, and peel, as well as in produced goods, including sweets, jams, wines, teas, and other drinks. Due to their bioactive qualities, flavonoids are significant chemicals in the chemical makeup of the Myrtaceae family of plants. As such, they hold great promise for the creation of new goods by the chemical, food, and medicinal sectors (da Veiga Correia et al., 2022).

Vascular plants contain a group of organic substances called flavones, which are well known for their broad range of pharmacological activities. Based on their composition, flavonoids are further classified as flavones. Flavones are six-membered heterocycles with a single ketone and oxygen group (de Oliveira et al., 2016). 2-phenyl-4H-chromen-4-one commonly referred to as flavones (de Oliveira et al., 2016; Devi et al., 2022). Flavones are being recognized as crucial specialized metabolites that play a role in plant defense and signaling. They are also essential components of the human diet and offer several health advantages (Jiang et al., 2016). Their potential as antioxidants and their capacity to alter many enzyme systems implicated in various illnesses have brought a lot of attention to them (Singh et al., 2014).

A crucial component of clinical pharmacology, the discovery and development of drugs encompass the entire process of finding new and promising therapeutic candidates (Vamathevan et al., 2019; Noor et al., 2023). In drug development, the idea of creating maximum selective ligands to act on specific therapeutic targets is the prevailing approach. Nevertheless, a lot of successful medications work by modifying several proteins as opposed to only one. By combining network biology and polypharmacology, the present potential space for druggable targets might be expanded (Hopkins, 2008). The "compound-protein/gene-disease" network and the high-throughput discovery of small-molecule regulatory principles are better accomplished by network pharmacology (Zhang et al., 2019).

Network pharmacology is an important development in the drug discovery plane, where traditional one-drug, one-target method has developed into multi-target approach (Zhang et al., 2019). It is a method that acknowledges the complexity of human disease, most of which have their origins in a dysregulation of several

pathways and not one defect in a single molecule. Rather than only concentrating on the specific isolated receptor effects, network pharmacology adopts the field of systems biology, and can use in silico examination and experiments in command to chart the interaction among compounds, targets, and pathways related to the disease. By building and studying protein-protein interaction (PPI) networks, signaling cascades as well as gene-disease associations, this will provide a more comprehensive idea of how a drug candidate will conduct itself within a biological system (Zhao et al., 2023). This is particularly pertinent in terms of the concept of polypharmacology that is where one substance can have multiple molecular effects, which as a result can be synergistic or there can be a greater therapeutic effect (Zhou et al., 2020).

A key subfield within network pharmacology is structure-based network pharmacology that incorporates molecular docking and predictors of targets to networks (Muhammad et al., 2018). In this case, the initial input is the chemical structure of a bioactive compound that is used to identify probable binding partners on the basis of structural compatibility and need scores. This is used to tag them onto the biological networks to generate key hubs, intersections of pathways and therapeutic nodes (Zhang et al., 2017). This approach not only tells us how a compound may act but also how it may act where, in a particular tissue or the pathologic process. The similar method has become especially useful in studying natural products and phytochemicals, which often act against a wide variety of targets but whose mechanisms of action are often poorly understood (Sakle et al., 2020).

In the era of biomedical big data and artificial intelligence, a complicated biological network represents cutting-edge multidisciplinary scientific research, life science, and medicine and has drawn more and more interest from researchers. Both qualitative and quantitative descriptions of the interactions between an organism's tissues, cells, and chemicals are included in a complex biological network (Li et al., 2021). Advances in bioinformatics and systems biology will likely lead to a conceptual change in drug development, an important benefit to CHM modernization and globalization, and an operational movement away from reductionism and toward network pharmacology (Zhang et al., 2013). A new field of systematic drug research called network pharmacology focuses at how drugs interact with various targets and

how they operate. In the pharmaceutical sector, the expense of creating new medications increased at an extraordinary rate. With the healthcare business today facing a variety of complex difficulties, including the growing prices of both treatments and pharmaceuticals, society needs particular significant modifications in this field. Network pharmacology is seen as a novel area of drug development in light of this (Noor et al., 2023).

In this paper, we used this framework to study the compound 2-Phenyl-4H-chromen-4-one which is a flavonoid scaffold that showed high-predicted activity in different *in silico* screens. In an early step of receptor profiling using computational docking, this compound ranked highly on many targets including those associated with inflammation, oxidative stress, infection and absorption of lipids. This motivated further investigation because its performance was highly stable across various receptor classes, and it could therefore afford strong binding potential and multi-target activity. To elucidate these simulation results, we tested a series of *in vitro* assays, with cellular models that are representative of inflammation and oxidative damage. The outcomes have supported the most important points in the predictions, which is that the compound is an inhibitor of inflammation mediators and antioxidant in terms of oxidative stress. These results justified the hypothesis that 2-Phenyl-4H-chromen-4-one has pleiotropic effects and therefore, offers an excellent opportunity towards network pharmacological analysis.

Subsequently, the network was validated experimentally using the protein targets predicted of the compound and a PPI network constructed. This enabled us to gain an understanding of a wider pharmacological profile of a protein, and to pinpoint potential hub proteins and regulatory clusters. Combining structure-based predictions, network modeling, and wet-lab validation, our work not only demonstrates the utility of network pharmacology, but also provides 2-Phenyl-4H-chromen-4-one as a potential future development candidate. This approach reflects a broader movement in drug discovery, away from reductionist methods and toward more dynamic, interconnected models that better reflect the true nature of disease biology.

Despite certain inevitable challenges and the enormous amount of effort required to integrate ML tools into network pharmacology, it is certain that ML will soon bring about revolutionary improvements in network pharmacology for multiple-target drug development (Noor et al., 2023).

Virtual comprehension of protein–ligand interactions systems is made possible by computational drug discovery techniques. For in silico drug discovery, thermodynamic-centered molecular dynamics (MD) simulation and molecular docking are crucial toolkits. The method known as "molecular docking" uses the atomic-level binding mechanisms of tiny or large molecules that come into contact with protein receptors. In addition to docking, MD simulation approaches offer a substantial supplementary connection. These methods work well for evaluating the structural characteristics of protein-ligand, protein-protein, protein-nucleic acid, and protein-peptide complexes (Singh et al., 2022).

To investigate the pharmacological potential of 2-Phenyl-4H-chromen-4-one through integrated computational, experimental, and network pharmacology approaches, with a focus on its multi-target activity and therapeutic relevance, these are the objectives

- **Objectives**

  - To perform *in silico* receptor profiling of 2-Phenyl-4H-chromen-4-one across multiple biological targets related to inflammation, oxidative stress, infection, and metabolic regulation.
  - To validate the computational predictions through *in vitro* assays targeting inflammatory and oxidative stress-related pathways.
  - To construct a protein–protein interaction (PPI) network based on predicted targets to explore the compound's system-level pharmacology and identify key regulatory nodes.
  - To evaluate the pleiotropic action and therapeutic relevance of the compound within a network pharmacology framework, aligning with modern, multi-target drug discovery paradigms.

10.2. Materials and methods

10.2.1. Compound retrieval and structure preparation

The compound 2-Phenyl-4H-chromen-4-one (PubChem CID: 10680) was selected for this study based on its consistent bioactivity in preliminary screenings. The canonical SMILES string (C1=CC=C(C=C1)C2=CC(=O) C3=CC=CC=C3O2) was obtained from the PubChem database (Kim et al., 2023). The two-dimensional structure was converted into a three-dimensional format using Open Babel. Geometry optimization was then performed using the Universal Force Field, UFF, to minimize the compound's energy and obtain a stable conformation suitable for molecular modeling. The minimization process continued until the system reached the default convergence threshold. The optimized structure was saved in PDB format, with all hydrogen atoms added and valency corrections verified. This finalized 3D structure was used for subsequent molecular docking, target prediction, and network construction steps (Kondapuram et al., 2021).

10.2.2. Pharmacokinetic profiling

Early evaluation of ADME properties (Absorption, Distribution, Metabolism, and Excretion) is essential in drug discovery. These parameters influence oral bioavailability, systemic exposure, and the likelihood of success in later development stages. Poor ADME profiles are a common cause of drug failure. To predict pharmacokinetic behaviour, we used the SwissADME web server (http://www.swissadme.ch/) (Daina et al., 2017). This tool provides *in silico* predictions of key ADME features, physicochemical properties, lipophilicity, solubility, and drug-likeness rules, based on SMILES input. It also supports models such as the BOILED-Egg for gastrointestinal (GI) absorption and BBB permeability and predicts CYP450 inhibition and P-glycoprotein (P-gp) substrate potential (Riyadi et al., 2021).

The canonical SMILES of 2-Phenyl-4H-chromen-4-one was submitted to SwissADME. The following parameters were evaluated (Bakchi et al., 2022):

- Physicochemical properties: Molecular weight, hydrogen bond donors/acceptors, TPSA, rotatable bonds.
- Lipophilicity: logP (iLOGP, XLOGP3, WLOGP, MLOGP, SILICOS-IT).
- Solubility: logS (ESOL, SILICOS-IT).
- GI absorption and BBB penetration: Predicted using the BOILED-Egg model.
- P-gp substrate: Efflux prediction.
- CYP inhibition: For CYP1A2, CYP2C19, CYP2C9, CYP2D6, and CYP3A4.
- Drug-likeness: Lipinski, Ghose, Veber, Egan, and Muegge filters.

10.2.3. Target prediction using the similarity ensemble approach

Target prediction for 2-Phenyl-4H-chromen-4-one was performed using the Similarity Ensemble Approach (SEA), an online computational tool that predicts potential protein targets based on chemical similarity to known ligands. The canonical SMILES of the compound was submitted to the SEA server (https://sea.bkslab.org/) (Wang et al., 2016), which computes ligand-based similarity scores between the input molecule and a reference database of drug-target associations. Targets are ranked based on E-values, which indicate the statistical significance of the match. Lower E-values represent stronger associations, suggesting a higher likelihood of biological relevance. SEA uses a fingerprint-based method to map compounds onto target protein ensembles, making it suitable for identifying off-target effects and multitarget potential. This approach is widely used in early-phase drug discovery to generate hypotheses on possible pharmacological targets prior to experimental validation (Bin et al., 2011).

10.2.4. SwissTargetPrediction-Based Target Prediction

Target prediction was also performed using the SwissTargetPrediction web tool (http://www.swisstargetprediction.ch/), which predicts the most probable macromolecular targets of small molecules in humans based on a combination of 2D and 3D molecular similarity (Daina et al., 2019). The canonical SMILES of 2-Phenyl-

4H-chromen-4-one was submitted, and the tool compared it against a curated set of known bioactive compounds with experimentally confirmed targets. Predictions are ranked by probability scores, reflecting the likelihood of the compound interacting with specific proteins (Gfeller et al., 2014). This method integrates chemical similarity and pharmacophore-based mapping, making it particularly useful for identifying targets that may not be captured through ligand-based approaches alone. Only human targets with significant probability scores were selected for further functional classification and comparison with SEA results.

10.2.5. Construction of 2-Phenyl-4H-chromen-4-one target library

To construct the final target library for 2-Phenyl-4H-chromen-4-one, predicted protein targets were retrieved from two independent *in silico* tools: the Similarity Ensemble Approach (SEA) and SwissTargetPrediction. The canonical SMILES of the compound was used as input in both platforms. After obtaining the respective lists of human targets, duplicates were identified and removed to avoid redundancy. The remaining unique targets from both datasets were then merged to generate a comprehensive, non-redundant target library. This unified list represents the full predicted interaction landscape of the compound and was used for all downstream analysis.

10.2.6. Construction of Protein–Protein Interaction (PPI) network

To explore the functional landscape of 2-Phenyl-4H-chromen-4-one, a protein–protein interaction (PPI) network was constructed based on the predicted non-redundant target library. Following the removal of duplicates, a total of 130 unique human protein targets were retained for network analysis. The STRING database (Search Tool for the Retrieval of Interacting Genes/Proteins) was used for network generation, with the organism specified as Homo sapiens (Timalsina et al., 2014).

Each node in the network corresponds to a unique protein-coding gene locus, where splice variants and post-translational modifications are collapsed into single representative units. Nodes are visually differentiated based on their structural and relational properties: coloured nodes represent input proteins (query targets) and their

direct interaction partners (first shell), while white nodes correspond to indirect interactors (second shell). Additionally, filled nodes indicate proteins with known or predicted 3D structures, whereas empty nodes denote those lacking structural information. Edges in the network represent meaningful functional associations between proteins. These associations may arise from various sources, including curated databases, experimental data, gene co-expression, gene neighbourhood, gene fusions, co-occurrence patterns, text mining, and protein homology. Importantly, the connections reflect functional relationships, not necessarily physical binding events (Trali et al., 2020).

The network was initially constructed using the default medium confidence threshold (interaction score ≥ 0.400) to capture a broad range of potential interactions. Subsequently, a high-confidence network was generated by applying a more stringent confidence score cutoff of ≥ 0.700. This refined network, containing more reliable interactions, was used for all downstream analyses, including hub gene identification, clustering, and pathway enrichment.

10.2.7. Functional enrichment analysis

The protein set obtained from the PPI network was subjected to functional enrichment analysis to identify overrepresented biological processes, molecular functions, and cellular components. All proteins were mapped against the Homo sapiens reference proteome. The analysis was performed using Gene Ontology (GO) annotations, covering the three major GO domains: Biological Process (BP), Molecular Function (MF), and Cellular Component (CC) (Bhattacharjee et al., 2011).

An FDR (false discovery rate) cutoff of 0.05 was applied to ensure statistical significance. Redundant terms were removed to improve clarity, and pathway names were abbreviated for concise representation. To filter for informative pathways, the minimum pathway size was set to 2 proteins, and the maximum pathway size was set to 5 proteins (Sadaqat et al., 2023). The top 10 significantly enriched pathways from each GO domain were selected based on their adjusted p-values. The results were visualised graphically, with enrichment scores and significance values displayed to

highlight the most relevant functional categories in which the predicted targets are involved.

10.2.8. Pathway enrichment analysis

Pathway enrichment analysis was performed using the Kyoto Encyclopedia of Genes and Genomes (KEGG) database to identify significantly overrepresented metabolic and signalling pathways among the predicted protein targets. The protein list from the PPI network was mapped against the *Homo sapiens* reference pathways (Yu et al., 2020). The analysis parameters were kept consistent with those used in the functional enrichment analysis: FDR cutoff of 0.05, removal of redundant pathways, abbreviation of pathway names for clarity, and filtering based on a minimum pathway size of 2 proteins and a maximum size of 5 proteins. The top 10 enriched KEGG pathways, ranked by adjusted p-values, were selected for further visualisation and interpretation (Chen et al., 2018).

10.2.9. Disease association analysis

Disease association analysis was carried out using the Disease module of the Alliance of Genome Resources (Disease.Alliance) database, an integrated resource that consolidates curated gene–disease associations from authoritative sources such as OMIM, Gene Ontology annotations, model organism databases, and literature-mined evidence. The final non-redundant protein list obtained from the predicted target library was queried to identify human diseases potentially linked to these targets (Bult & Sternberg, 2023). Analysis parameters were kept consistent with those applied in functional and pathway enrichment, including a false discovery rate (FDR) cut-off of 0.05, redundancy reduction, and standardization of disease terms for clarity. The minimum and maximum association sizes were set to 2 and 5, respectively, to avoid overly broad or trivial categories while retaining biologically meaningful associations. The top-ranked disease associations were then compiled and visualized for comparative interpretation with functional and pathway enrichment results.

10.2.10. Identification of Hub genes

Hub gene identification was carried out using the CytoHubba plugin within the Cytoscape software environment. CytoHubba is a widely used network analysis tool that ranks nodes within a protein–protein interaction (PPI) network based on various topological algorithms, enabling the identification of key proteins that may play central roles in the biological system under study. Among its multiple scoring methods, the Degree method was applied in this analysis, which ranks nodes according to the number of direct connections they possess, reflecting their potential importance in network connectivity and regulation (Ma et al., 2021).

The PPI network generated from STRING was imported into Cytoscape, and the top 10 nodes with the highest degree values were identified as candidate hub genes. These hub nodes represent proteins with the greatest number of interactions, potentially indicating their critical role in the functional organization of the network. A subnetwork comprising these top-ranked nodes and their direct interactions was extracted and visualized to provide a clearer representation of their relationships within the broader network (Yu et al., 2024).

10.2.11. Molecular Docking with the EGFR

Molecular docking studies were conducted to predict the binding affinity and interaction profile of 2-Phenyl-4H-chromen-4-one with the epidermal growth factor receptor (EGFR) kinase domain. The 3D structure of the ligand was retrieved from the PubChem database. The geometry of the ligand was optimized using the Universal Force Field (UFF), and Gasteiger charges were assigned. Atom types were set to AutoDock-compatible types, and the final prepared ligand structure was saved in PDBQT format for docking (Galgale et al., 2023).

The target protein, EGFR kinase (PDB ID: 8TJL), co-crystallized with a pyrazolopyrimidine covalent inhibitor, was obtained from the RCSB Protein Data Bank. This structure was solved using X-ray diffraction at a resolution of 2.70 Å and corresponds to the human EGFR kinase domain. No mutations were present in the sequence. Non-structural elements, such as water molecules and bound ligands, were

removed from the crystal structure. The protein was prepared by adding polar hydrogen atoms, assigning Kollman charges, and setting AutoDock Type 4 atoms before saving in PDBQT format. Docking simulations were performed using AutoDock Vina, with the following grid parameters (Jayasurya et al., 2023):

- Exhaustiveness: 8
- Centre coordinates: x = 58.5607, y = −8.0944, z = 25.2103
- Grid dimensions: x = 46.9650 Å, y = 65.2043 Å, z = 54.7057 Å

Binding affinity values were used as the primary metric for docking evaluation, with the lowest binding energy considered to represent the most favourable ligand–protein interaction.

10.2.12. Molecular dynamics simulation

Molecular dynamics (MD) simulations were carried out using GROMACS 2023.1 to investigate the stability, conformational flexibility, and dynamic interaction profile of the 2-Phenyl-4H-chromen-4-one–EGFR kinase complex under near-physiological conditions. The CHARMM36 force field was employed for protein parameterization, ensuring accurate modeling of bonded and non-bonded interactions, while ligand parameters were generated using the CHARMM General Force Field (CGenFF) via the CGenFF server to provide a precise description of the ligand's topology and partial atomic charges (Vora et al., 2020). The prepared complex was embedded in a triclinic simulation box with a minimum distance of 1.0 nm between the protein surface and the box edges to avoid artifacts from periodic images. The system was solvated using explicit TIP3P water molecules, a widely adopted three-point water model for biomolecular simulations. To ensure overall electrostatic neutrality, appropriate counter-ions (Na^+ or Cl^-) were added, replacing solvent molecules as necessary. Energy minimization was followed by NVT equilibration at 310 K using a velocity-rescaling thermostat and NPT equilibration at 1 atm using the Parrinello–Rahman barostat (Joshi et al., 2022).

The production MD simulation was run for 100 ns with a 2 fs integration time step under periodic boundary conditions. Long-range electrostatics were treated using

the Particle Mesh Ewald (PME) method with a real-space cut-off of 1.2 nm, and the Verlet cut-off scheme was applied for short-range interactions to enhance computational efficiency (Kar et al., 2022). Bond lengths involving hydrogen atoms were constrained using the LINCS algorithm, allowing the use of a larger timestep without compromising accuracy. Snapshots of the simulation were saved every 10 ps for subsequent trajectory analyses, including RMSD, RMSF, radius of gyration, hydrogen bonding, and conformational landscape evaluation.

10.2.13. Conformational sampling and landscape analysis

Post-simulation, Principal Component Analysis (PCA) was performed to capture dominant motions of the protein–ligand complex by projecting the trajectory onto the principal eigenvectors (Azmal et al., 2024). This allowed identification of large-scale conformational changes. The Free Energy Landscape (FEL) was generated using the first two principal components as reaction coordinates, mapping conformational states to their corresponding Gibbs free energies (Alshahrani et al., 2025). This approach provided insights into the stability and energy minima of the complex, highlighting preferred conformations during the simulation.

10.2.14. Binding free energy analysis

Binding free energies were estimated using the Molecular Mechanics/Poisson–Boltzmann Surface Area (MM/PBSA) method implemented in g_mmpbsa. Snapshots from the equilibrated phase of the MD trajectory were extracted at regular intervals. The total binding free energy (ΔG_bind) was computed as the sum of van der Waals, electrostatic, polar solvation, and non-polar solvation contributions (Sahoo et al., 2025). This quantitative estimation helped validate docking predictions and identify the energetic drivers of ligand binding (Kushwaha et al., 2021).

10.2.15. DFT studies for 2-Phenyl-4H-chromen-4-one

Density Functional Theory (DFT) calculations were performed to explore the frontier molecular orbitals (HOMO and LUMO) of 2-Phenyl-4H-chromen-4-one. Geometry optimization was carried out at the B3LYP/6-31G(d,p) level of theory. The

energy gap (ΔE = E_LUMO − E_HOMO) was calculated to assess the molecule's electronic stability and reactivity. HOMO and LUMO visualizations were generated to evaluate electron-donating and electron-accepting regions, providing insight into potential interaction sites within the target protein's binding pocket (Yousaf et al., 2024).

10.3. Results

10.3.1. Compound retrieval and structure preparation

10.3.1.1. Compound Overview

The compound 2-Phenyl-4H-chromen-4-one is a member of the flavone class, characterized by a chromen-4-one core substituted with a phenyl group at the C-2 position. It is structurally derived from flavone and is recognized for its roles as a natural metabolite and a nematicidal agent. Its rigid planar structure, aromaticity, and presence of conjugated systems suggest potential for high-affinity interactions with a variety of biological targets (Figure 10.1).

10.3.1.2. Optimised Structure

The 3D structure of 2-Phenyl-4H-chromen-4-one was generated from its canonical SMILES and subjected to energy minimization using the Universal Force Field (UFF). The optimized conformation was geometrically stable and energetically favourable, confirming its suitability for further *in silico* analyses (Figure 10.1).

10.3.2. Pharmacokinetic profiling

10.3.2.1. Physicochemical Properties

The basic physicochemical profile of a compound provides insights into its behaviour in biological environments. The molecular formula of 2-Phenyl-4H-chromen-4-one is $C_{15}H_{10}O2$, with a molecular weight of 222.24 g/mol, which falls well within the range preferred for oral drugs. It contains 17 heavy atoms, of which 16 are aromatic, indicating a highly conjugated and planar structure. The fraction Csp3 is 0.00, confirming the absence of saturated carbon centres and full aromaticity. The compound has 1 rotatable bond, suggesting limited conformational flexibility, which can enhance membrane permeability and binding specificity. It has 2 hydrogen bond acceptors and no hydrogen bond donors, which influences solubility and interaction with polar environments. The topological polar surface area (TPSA) is 30.21 Å², which is below the threshold of 90 Å², favouring good passive membrane

permeability. The molar refractivity is 67.92, which falls within the optimal range, indicating favourable steric and polarizability characteristics (Table 10.1).

10.3.2.2. Pharmacokinetics

Pharmacokinetic properties determine how a compound behaves in the body, particularly in terms of absorption, distribution, and metabolism. SwissADME predicted high gastrointestinal (GI) absorption, suggesting good oral bioavailability. It is also predicted to cross the blood–brain barrier (BBB), indicating potential activity in the central nervous system. The compound is not a substrate of P-glycoprotein (P-gp), an efflux transporter that often reduces intracellular drug accumulation; this favours better tissue penetration. The consensus logP (Po/w) is 3.18, reflecting moderate lipophilicity. This value supports passive diffusion across lipid membranes while maintaining reasonable solubility. The compound is predicted to be soluble, which is important for oral formulations and systemic delivery. Regarding metabolism, 2-Phenyl-4H-chromen-4-one is predicted to inhibit CYP1A2 and CYP2C19, two important enzymes in the cytochrome P450 family. However, it is not an inhibitor of CYP2C9, CYP2D6, or CYP3A4, reducing the risk of widespread drug-drug interactions. Nonetheless, inhibition of CYP1A2 and CYP2C19 should be considered during lead optimization (Table 10.2).

10.3.2.3. Drug-Likeness

Drug-likeness is a set of molecular criteria used to estimate whether a compound is likely to be a successful oral drug. It helps prioritize molecules in early drug discovery by assessing structural and physicochemical features associated with bioavailability (Table 10.3). Several widely accepted rule-based filters are used for this purpose:

- **Lipinski's Rule of Five:** This rule states that a drug-like compound should have (i) molecular weight < 500 g/mol, (ii) logP ≤ 5, (iii) ≤ 5 hydrogen bond donors, and (iv) ≤ 10 hydrogen bond acceptors. 2-Phenyl-4H-chromen-4-one satisfies all these criteria, indicating favourable oral absorption.

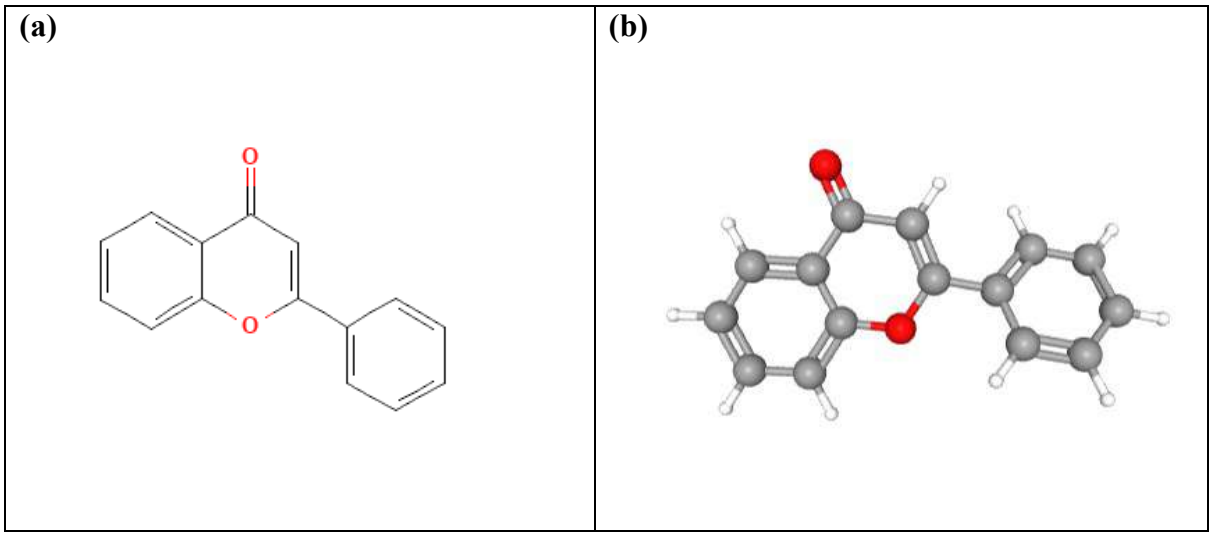


Figure 10.1: Structural representation of 2-Phenyl-4H-chromen-4-one: (a) Two-dimensional (2D) chemical structure (b) Three-dimensional (3D) molecular model

Table 10.1: Physicochemical properties of 2-Phenyl-4H-chromen-4-one

Formula	$C_{15}H_{10}O_2$
Molecular Weight	222.24 g/mol
Number of heavy atoms	17
Number of aromatic heavy atoms	16
Fraction Csp3	0.00
Number of Rotatable Bonds	1
Number of H-bond Acceptors	2
Number of H-bond Donors	0
Molar Refractivity	67.92
TPSA	30.21 Å²

Table 10.2: Pharmacokinetics of 2-Phenyl-4H-chromen-4-one

GI Absorption	High
BBB permeation	Yes
Pgp-substrate	No
Consensus Log Po/w	3.18
Solubility	Soluble
CYP1A2 inhibitor	Yes
CYP2C19 inhibitor	Yes
CYP2C9 inhibitor	No
CYP2D6 inhibitor	No
CYP3A4 inhibitor	No

Table 10.3: Drug likeness of 2-Phenyl-4H-chromen-4-one

Lipinski	Yes
Ghose	Yes
Veber	Yes
Egan	Yes
Mugge	Yes
Bioavailabity	0.55

- **Ghose Filter:** Evaluates logP (between -0.4 and +5.6), molar refractivity (40–130), molecular weight (160–480), and total atom count (20–70). The compound meets all Ghose parameters, supporting its suitability for drug development.
- **Veber Rule:** Focuses on rotatable bonds (≤10) and polar surface area (TPSA ≤140 Å²), both of which influence membrane permeability and oral bioavailability.

  With only 1 rotatable bond and a TPSA of 30.21 Å², the compound passes the Veber rule with ease.
- **Egan Rule:** Predicts good intestinal absorption based on logP (≤5.88) and TPSA (≤131.6 Å²). The compound's logP (3.18) and TPSA (30.21 Å²) both fall within these limits.
- **Muegge Filter:** A comprehensive drug-likeness filter considering molecular weight (200–600), logP (-2 to 5), TPSA (≤150 Å²), ring count (≤7), and hydrogen bonding. The compound adheres to all Muegge criteria, reinforcing its drug-like profile.
- **Bioavailability Score:** This score predicts the likelihood of achieving at least 10% oral bioavailability in rats or measurable bioavailability in humans. 2-Phenyl-4H-chromen-4-one has a bioavailability score of 0.55, which is considered good for early-phase development.

10.3.2.4. Medicinal chemistry profiling

In early-stage drug discovery, medicinal chemistry filters are used to evaluate whether a compound is likely to be chemically tractable, non-toxic, and free from problematic structural motifs that can interfere with biological assays or downstream development (Table 10.4). The following filters and scores were assessed using the SwissADME tool:

- **PAINS (Pan-Assay Interference Compounds)**: PAINS are structural motifs known to cause false-positive results in high-throughput screening assays by interfering with assay readouts rather than binding to a specific target. 2-Phenyl-4H-chromen-4-one triggered no PAINS alerts, suggesting it does not

contain any problematic substructures that may lead to assay interference or non-specific activity.

- **Brenk Alerts**: The Brenk filter flags substructures that are often associated with toxicity, instability, or poor pharmacokinetics. These include functional groups that are reactive or known to be metabolically unstable. The compound showed zero Brenk alerts, indicating it lacks chemically undesirable features and is likely to be metabolically stable and safe for further optimization.
- **Lead-likeness**: This filter is more stringent than drug-likeness and is intended for identifying small, structurally simple molecules that are suitable as starting points for medicinal chemistry optimization. Typical criteria include molecular weight < 350 g/mol and logP < 3.5, along with limited hydrogen bonding and ring complexity. Although 2-Phenyl-4H-chromen-4-one meets many drug-likeness criteria, it does not meet lead-likeness requirements, likely due to its high degree of aromaticity and a logP above the recommended threshold. However, this is acceptable in the context of hit-to-lead development, where structural refinement is expected.
- **Synthetic Accessibility (SA) Score**: This score estimates how easy or difficult it would be to synthesize the compound in a laboratory, based on known substructures, ring systems, and chemical complexity. The score ranges from 1 (very easy) to 10 (very difficult). The SA score for 2-Phenyl-4H-chromen-4-one is 2.88, suggesting that the compound is relatively easy to synthesize, which is advantageous for future chemical modifications, scale-up, and lead optimization efforts.

10.3.3. Target prediction using the Similarity Ensemble Approach (SEA)

Target prediction using the SEA tool yielded a diverse set of potential human protein targets for 2-Phenyl-4H-chromen-4-one (Figure 10.2). These targets span multiple functional classes, reflecting the compound's multi-target pharmacological potential. A total of 57 targets were predicted, which were categorized based on known biological roles and enzyme families. Significant representation was also observed in transporters, particularly ABC-family proteins (e.g., ABCB1, ABCC1, ABCG2), indicating a likely interaction with drug efflux mechanisms. Cytochrome

Table 10.4: Medicinal chemistry properties of 2-Phenyl-4H-chromen-4-one

PAINS	0 alert
Brenk	0 alert
Lead likeness	No
Synthetic Accessibility	2.88

Table 10.5: Top 10 Hub Genes Identified by Degree Method

Rank	Name	Score
1	EGFR	16
2	ESR1	14
2	PARP1	14
4	PTGS2	12
4	MAPK3	12
4	CYP1A1	12
7	CDK2	11
8	CYP17A1	10
8	CYP19A1	10
8	APP	10

Table 10.6: Hydrophobic Interactions

No.	Residue position	Residue	Distance (å)	Ligand atom id	Protein atom id
1	726A	VAL	3.58	2986	287
2	745A	LYS	3.96	2979	467

Table 10.7: Hydrogen Bonds

No.	Residue position	Residue	H-bond distance (å)	Donor–acceptor distance (å)	Bond angle (°)	Ligand atom id	Protein atom id
1	854A	THR	2.25	3.02	128.49	1529 [O3]	2988 [O2]
2	855A	ASP	2.67	3.14	106.44	1532 [Nam]	2988 [O2]

Table 10.8: π-Stacking Interactions

No.	Residue position	Residue	H-bond distance (å)	Donor–acceptor distance (å)	Bond angle (°)	Ligand atom id	Protein atom id
1	854A	THR	2.25	3.02	128.49	1529 [O3]	2988 [O2]
2	855A	ASP	2.67	3.14	106.44	1532 [Nam]	2988 [O2]

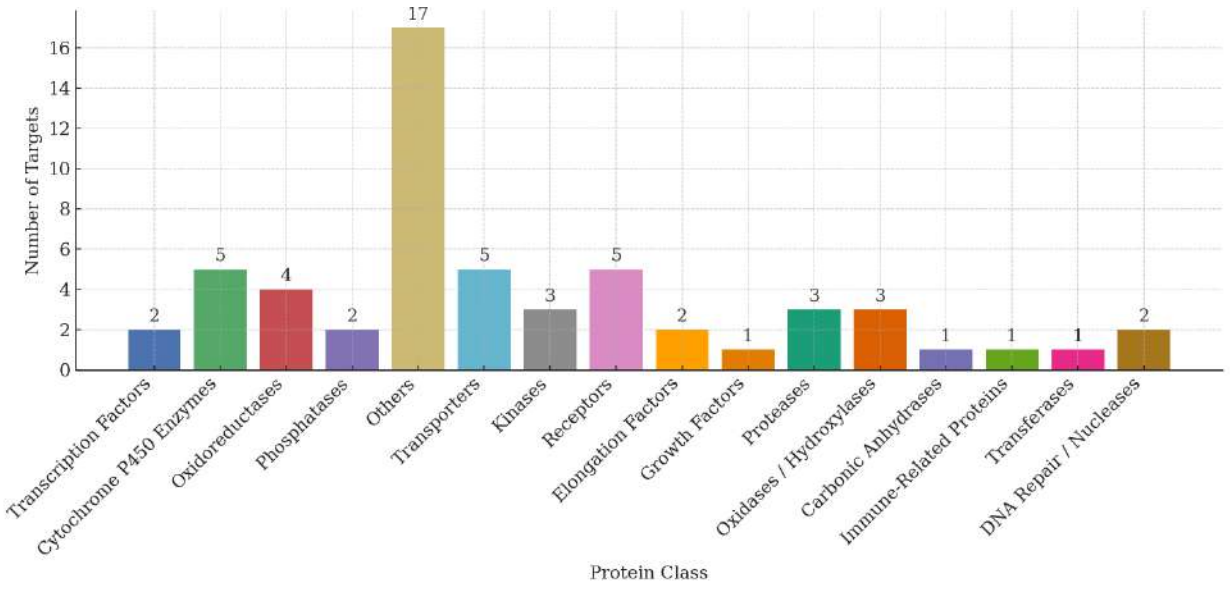


Figure 10.2: Similarity Ensemble Approach (SEA) based classification of predicted human protein targets of 2-Phenyl-4H-chromen-4-one based on functional classes

P450 enzymes (CYP1A1, CYP1A2, CYP1B1, CYP19A1, CYP11B1) were also prominent, suggesting metabolic interactions and possible modulation of detoxification or biosynthetic pathways. Other notable classes included kinases, oxidoreductases, phosphatases, nuclear receptors, and hydrolases, all of which are relevant in inflammation, oxidative stress, metabolism, and cancer biology. The wide distribution of predicted targets highlights the compound's potential as a polypharmacological agent, warranting further network-level and functional validation studies.

10.3.4. SwissTargetPrediction-based target prediction

The SwissTargetPrediction analysis of 2-Phenyl-4H-chromen-4-one revealed a wide range of predicted human protein targets across multiple functional classes, suggesting a broad pharmacological spectrum (Figure 10.3). The most represented category was enzymes, which included both general metabolic enzymes and more specific subclasses such as hydrolases, oxidoreductases, and transferases. This indicates the compound's potential to modulate core biochemical reactions, including redox processes, substrate conversions, and cellular metabolism. A substantial number of targets also fell under unclassified proteins, which reflects the presence of lesser-characterized or context-specific proteins whose roles may be newly emerging or not yet fully annotated. Notably, several targets belonged to the cytochrome P450 enzyme family, which plays a critical role in drug metabolism and xenobiotic detoxification. These interactions suggest that the compound may either be metabolized by or modulate the activity of CYP enzymes, with implications for pharmacokinetics and potential drug interactions.

In addition, several predicted targets were G protein-coupled receptors (GPCRs), a class central to signal transduction in pathways involving neurotransmitters, hormones, and immune responses. This raises the possibility of the compound exerting effects in neurological or inflammatory conditions. The presence of nuclear receptors among the predicted targets further supports this, as these proteins regulate gene expression in response to hormonal or lipid-based ligands and are often implicated in endocrine and metabolic disorders. The identification of active

transporters such as ABC-family proteins suggests potential involvement in drug efflux mechanisms, which may influence absorption, bioavailability, or multidrug resistance.

Other classes such as kinases, phosphodiesterases, and ion channels were also represented, albeit in smaller proportions. These proteins are commonly involved in signal transduction, cell cycle regulation, and inflammatory responses, and their modulation supports the idea that 2-Phenyl-4H-chromen-4-one may function as a multitarget agent. Collectively, this functional distribution indicates that the compound is likely to exert polypharmacological effects, making it a promising candidate for further study in complex disease models, particularly those involving oxidative stress, inflammation, metabolic imbalance, or hormonal dysregulation.

10.3.5. Construction of 2-Phenyl-4H-chromen-4-one target library

The final target library was constructed by combining results from both SEA and SwissTargetPrediction tools. As shown in the Venn diagram (Figure 10.4), out of the total non-redundant targets:

- 30 targets (23.1%) were uniquely predicted by SEA
- 73 targets (56.2%) were unique to SwissTargetPrediction
- 27 targets (20.8%) were commonly predicted by both methods

By merging the overlapping and unique predictions into a single, non-redundant target library, we constructed a more complete and functionally diverse dataset. This final unified library serves as a critical foundation for downstream analyses, including protein–protein interaction mapping and pathway enrichment, aimed at understanding the compound's broader pharmacological potential.

10.3.6. Construction of Protein–Protein Interaction (PPI) network

At a medium confidence threshold of 0.400, the PPI network for 2-Phenyl-4H-chromen-4-one targets comprised 129 nodes connected by 766 edges, yielding an average node degree of 11.9 and an average local clustering coefficient of 0.462. This

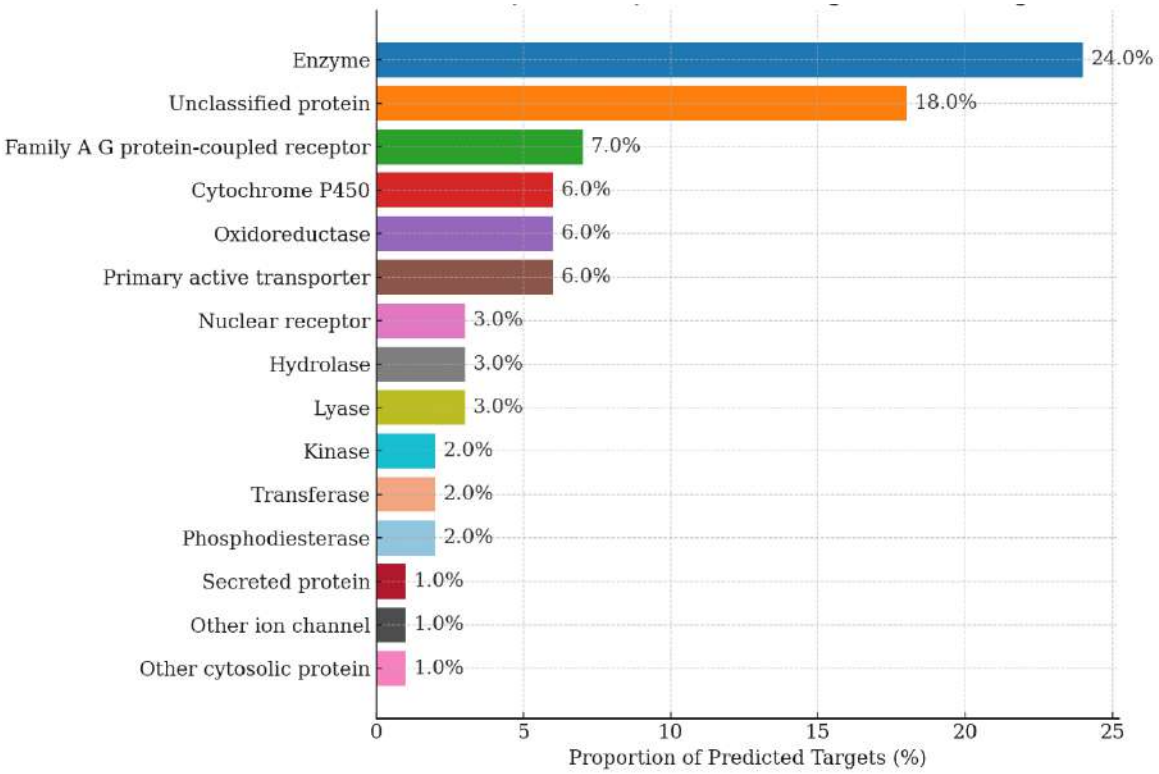


Figure 10.3: Functional classification of predicted human protein targets of 2-Phenyl-4H-chromen-4-one based on SwissTargetPrediction analysis

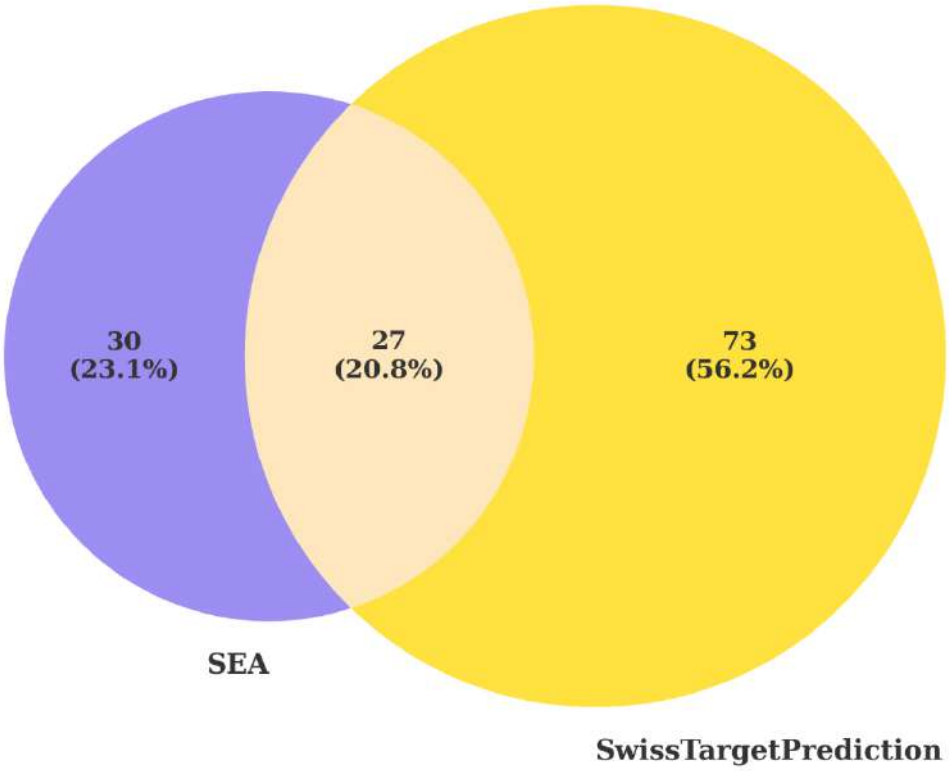


Figure 10.4: Venn diagram showing the overlap between predicted targets of 2-Phenyl-4H-chromen-4-one identified via Similarity Ensemble Approach (SEA) and SwissTargetPrediction

high connectivity, coupled with an expected number of edges of only 292, indicates that the observed network is far more interconnected than would occur by chance. The PPI enrichment p-value ($< 1.0 \times 10^{-16}$) strongly supports that these proteins are functionally related and participate in biologically meaningful processes (Figures 10.5-10.7).

Functional enrichment analysis revealed a strong representation of lipid metabolism-related pathways, particularly those involving olefinic compound metabolism, icosanoid metabolism, unsaturated fatty acid metabolism, and arachidonic acid metabolism, all with highly significant p-values ($\leq 1.55 \times 10^{-10}$). These pathways are often linked to inflammatory processes, cardiovascular function, and cellular signaling. Molecular function enrichment highlighted activities such as hydro-lyase activity, carbonate dehydratase activity, oxidoreductase activity, lyase activity, and monooxygenase activity, consistent with the compound's potential role in enzymatic redox regulation and metabolic transformation. Cellular component enrichment pointed towards association with serine/threonine protein kinase complexes, cyclin-dependent protein kinase holoenzyme complexes, and chromosome telomeric regions, indicating possible involvement in cell cycle regulation and genomic stability. Additional enrichment in neuronal cell body components suggests potential neuroactive or neuroprotective roles.

Overall, the network's high interconnectivity and enrichment in metabolism, enzyme activity, and cell cycle-related processes indicate that 2-Phenyl-4H-chromen-4-one may exert polypharmacological effects spanning metabolic regulation, inflammation, and possibly neurological functions.

10.3.7. Functional Enrichment Analysis

The functional enrichment analysis revealed that the predicted target set of 2-Phenyl-4H-chromen-4-one is involved in a wide range of biological processes, cellular localizations, and molecular functions, underscoring the compound's multi-target pharmacological potential.

10.3.7.1. Biological Processes

Among the biological process terms, "Olefinic compound metabolic process" showed the highest fold enrichment (20.4) with 20 associated genes (FDR = 4.1×10^{-18}), suggesting a significant role in metabolism of unsaturated hydrocarbons, potentially linked to lipid modification pathways. Other highly enriched processes included "Response to organonitrogen compound" (42 genes, fold enrichment 6.9, FDR = 2.3×10^{-21}) and "Response to nitrogen compound" (45 genes, fold enrichment 6.7, FDR = 1.4×10^{-22}), reflecting the involvement of these targets in detoxification, xenobiotic metabolism, and nitrogen-related signaling. The prominence of "Response to oxygen-containing compound" (58 genes, fold enrichment 5.8, FDR = 1.1×10^{-26}) and its cellular counterpart process highlights the compound's potential in modulating oxidative stress and redox-sensitive pathways. Broad response categories such as "Response to organic substance" and "Response to chemical" indicate the adaptability of these targets to diverse chemical stimuli, consistent with polypharmacological agents (Figure 10.8).

10.3.7.2. Cellular components

Enrichment in the "Cyclin-dependent protein kinase holoenzyme complex" (6 genes, fold enrichment 19.4, FDR = 4.5×10^{-5}) and related "Serine/threonine protein kinase complex" (9 genes, fold enrichment 11.9, FDR = 9.8×10^{-6}) points toward a regulatory role in cell cycle progression and signal transduction. The inclusion of "Chromosome telomeric region" (fold enrichment 8.4, FDR = 6.3×10^{-5}) suggests possible involvement in genomic stability and telomere maintenance. Localization to neuronal cell structures such as the "Neuronal cell body" (16 genes, fold enrichment 5.4, FDR = 9.6×10^{-6}) and "Somatodendritic compartment" (19 genes, fold enrichment 3.7, FDR = 4.5×10^{-5}) points to potential neuromodulatory effects. The "Plasma membrane-bound cell projection" and "Endoplasmic reticulum" terms indicate participation in membrane-associated signaling and protein/lipid synthesis pathways (Figure 10.9).

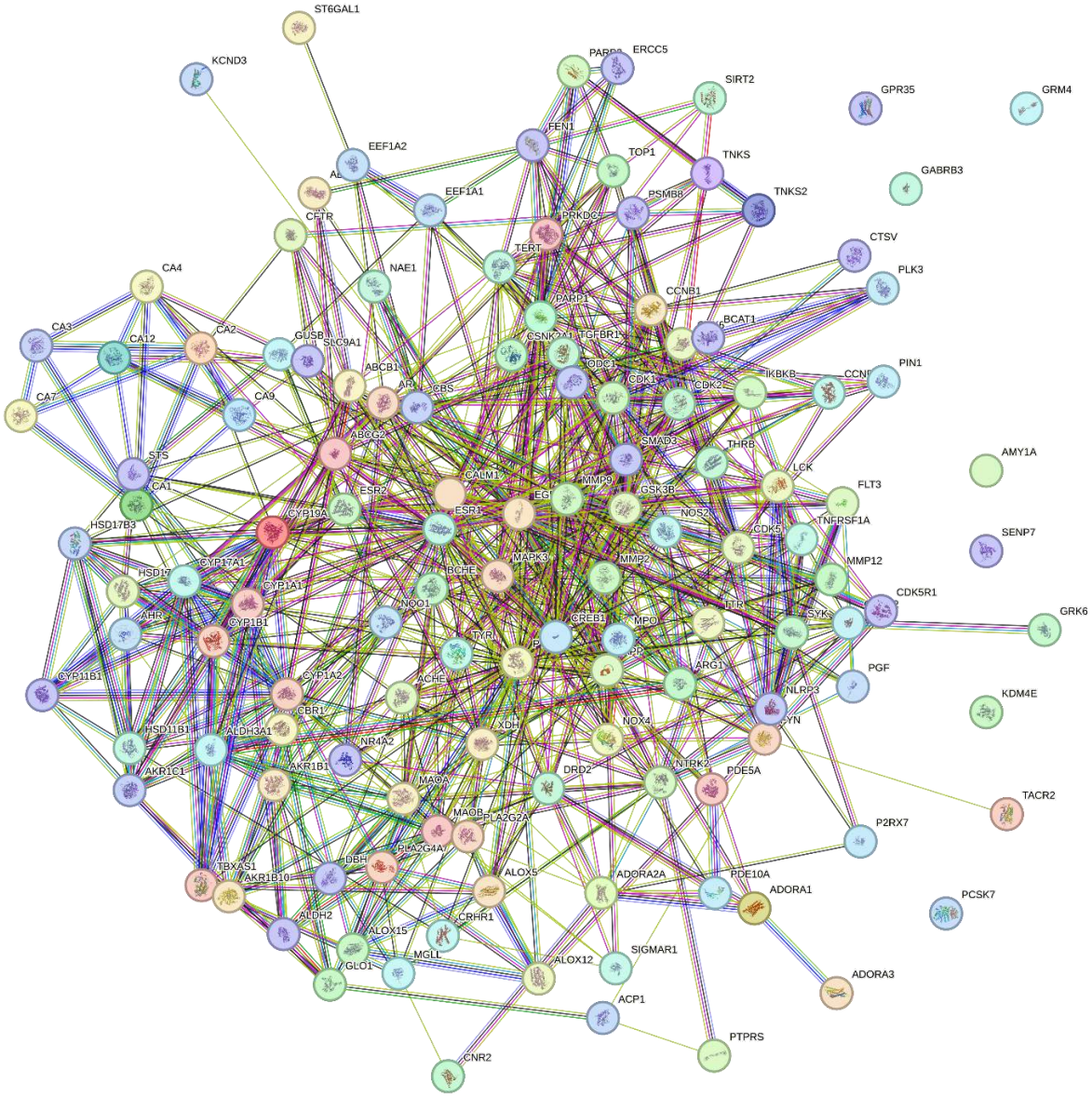


Figure 10.5: Protein–protein interaction (PPI) network of predicted *Homo sapiens* targets for 2-Phenyl-4H-chromen-4-one at medium confidence (0.400) generated using STRING

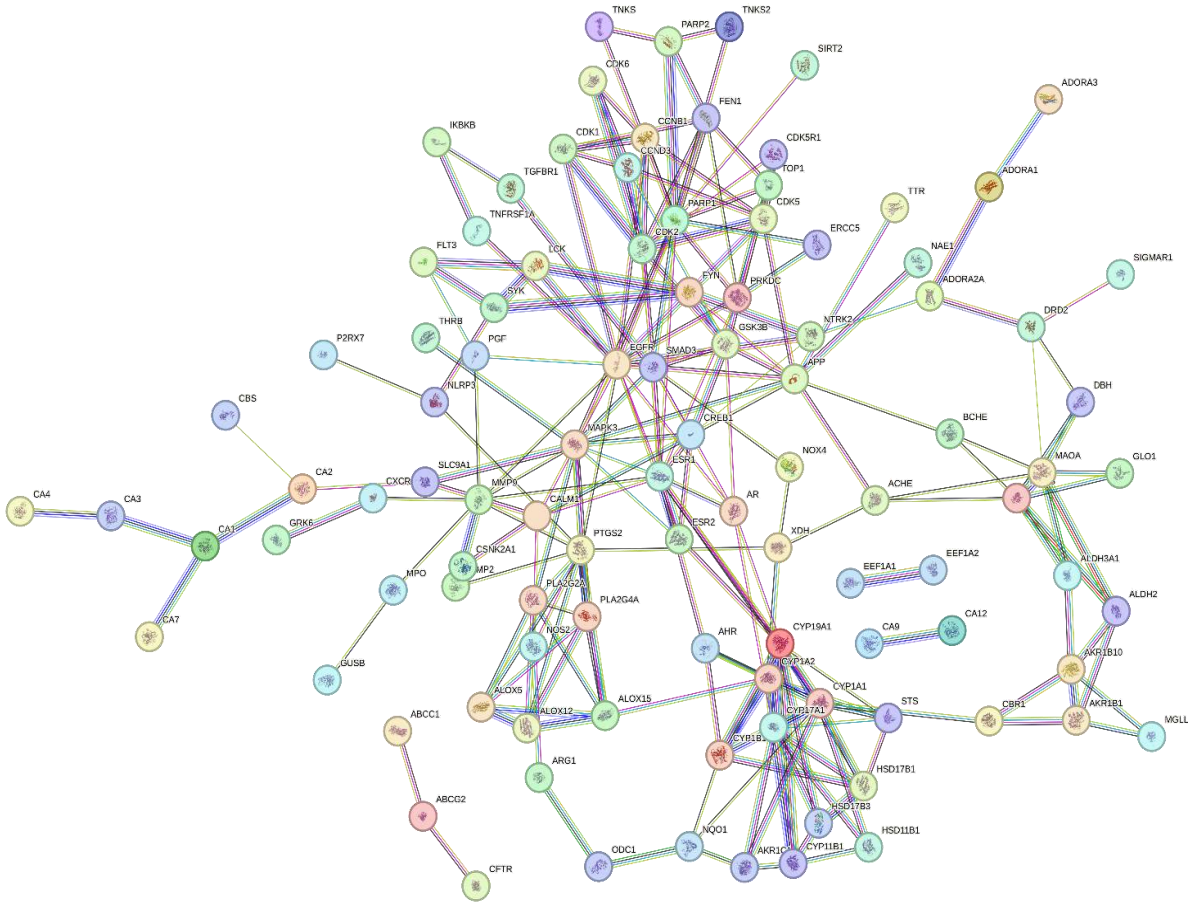


Figure 10.6: Protein–protein interaction (PPI) network of predicted *Homo sapiens* targets for 2-Phenyl-4H-chromen-4-one at medium confidence (0.700) generated using STRING

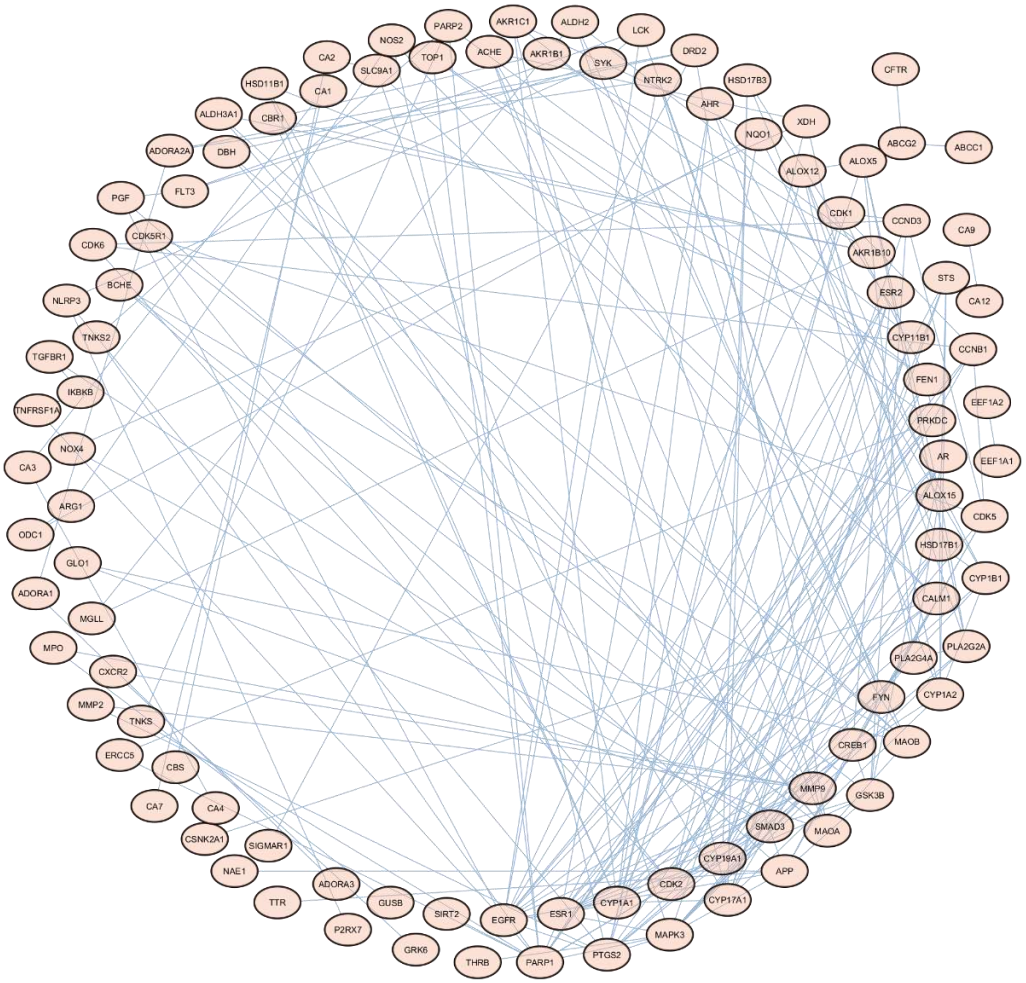


Figure 10.7: Protein–protein interaction (PPI) network of predicted *Homo sapiens* targets for 2-Phenyl-4H-chromen-4-one at medium confidence (0.700) generated using STRING

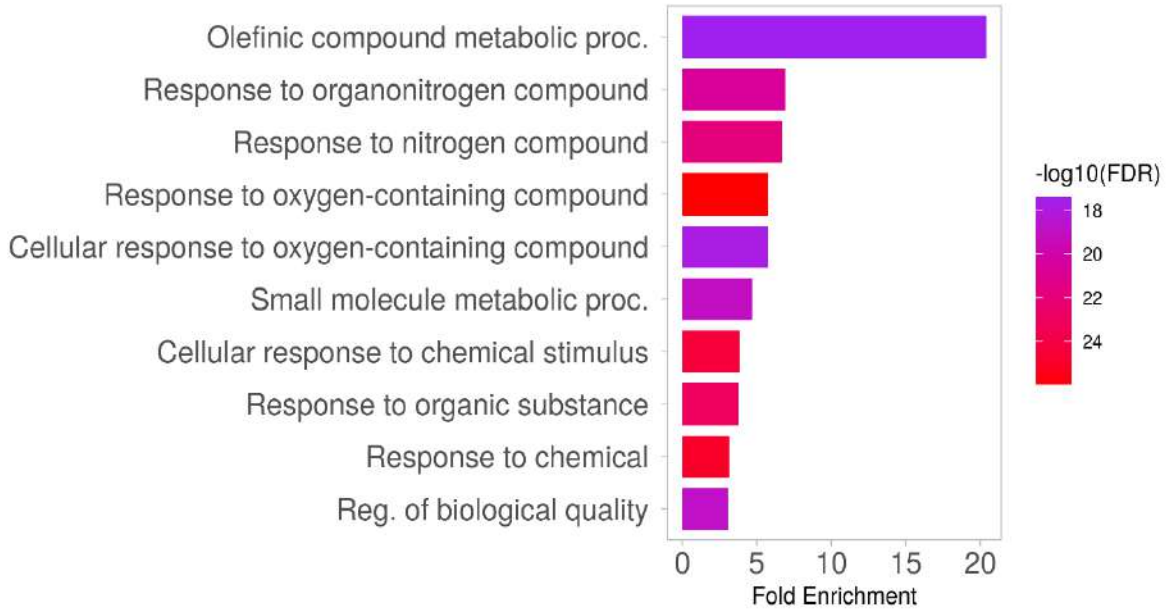


Figure 10.8: Top 10 enriched biological processes from Gene Ontology (GO) analysis

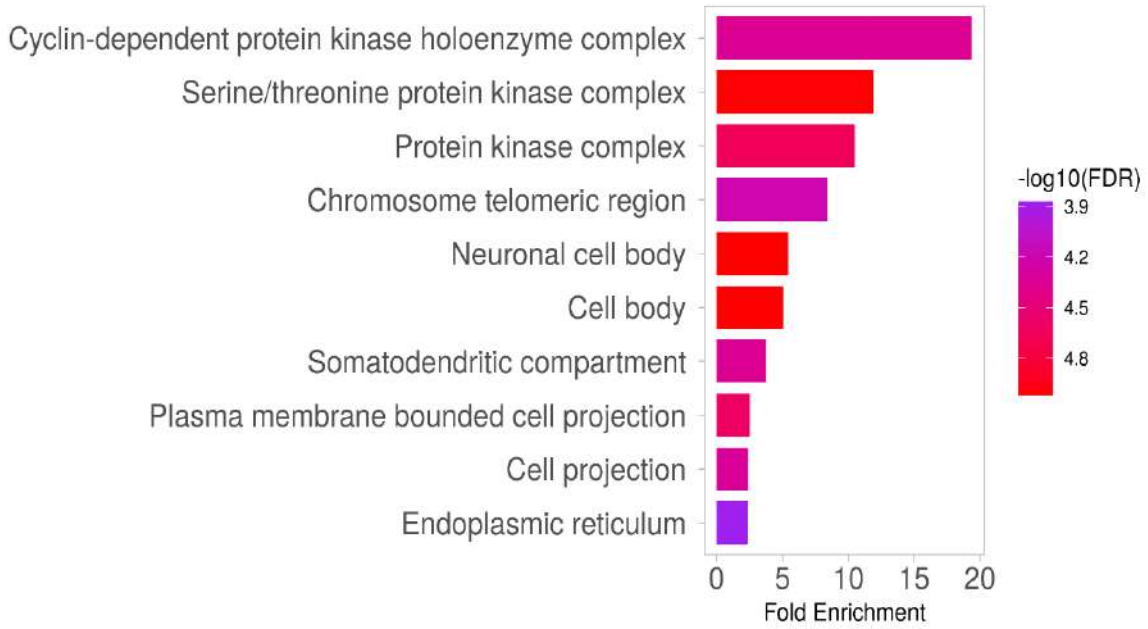


Figure 10.9: Top 10 enriched cellular components from Gene Ontology (GO) analysis

10.3.7.3. Molecular functions

The most striking molecular function enrichment was "Carbonate dehydratase activity" (7 genes, fold enrichment 81.5, FDR = 1.5×10^{-10}), implicating the compound in modulation of carbonic anhydrases, which are critical for pH regulation and CO_2 transport. Strong enrichment was also noted for "Hydro-lyase activity" (12 genes, fold enrichment 33.3, FDR = 3.7×10^{-13}) and "Carbon–oxygen lyase activity" (fold enrichment 26.5, FDR = 4.9×10^{-12}), both of which play roles in metabolic transformations. Enrichment in "Monooxygenase activity" (fold enrichment 15.9, FDR = 6.1×10^{-9}) and "Oxidoreductase activity" classes indicates potential modulation of cytochrome P450 enzymes and other oxidoreductases, aligning with metabolism-related biological processes. The detection of "Protein kinase activity" (fold enrichment 5.8, FDR = 6.1×10^{-9}) aligns with the cellular component enrichment for kinase complexes, suggesting dual structural and functional targeting. Binding activities, such as "Transition metal ion binding" (fold enrichment 5.0, FDR = 1.0×10^{-13}) and "Enzyme binding" (fold enrichment 3.0, FDR = 6.1×10^{-9}), reflect broad potential for interaction with metalloproteins and multi-enzyme assemblies (Figure 10.10).

Overall, these results demonstrate that 2-Phenyl-4H-chromen-4-one's predicted targets are deeply embedded in metabolic regulation, signal transduction, oxidative stress responses, and cell cycle control, providing a strong mechanistic basis for its multi-disease association profile revealed in downstream analyses.

10.3.8. Pathway enrichment analysis

Pathway enrichment analysis using the KEGG database was performed on the predicted target library of 2-Phenyl-4H-chromen-4-one to identify metabolic and signaling pathways that are statistically overrepresented in comparison with the reference human proteome. Applying a false discovery rate (FDR) threshold of 0.05 revealed ten significantly enriched pathways, each representing distinct biological contexts relevant to the compound's potential pharmacological effects.

The top-ranked pathways included Nitrogen metabolism (FDR = 2.4×10^{-8}, 6 genes, fold enrichment 61.6), Steroid hormone biosynthesis (FDR = 7.3×10^{-12}, 11 genes, fold enrichment 31), and Ovarian steroidogenesis (FDR = 6.1×10^{-7}, 7 genes, fold enrichment 24). Additional enriched pathways encompassed Arachidonic acid metabolism (7 genes, fold enrichment 20), Serotonergic synapse (9 genes, fold enrichment 14), Chemical carcinogenesis- receptor activation (11 genes, fold enrichment 9.8), Chemical carcinogenesis- reactive oxygen species (12 genes, fold enrichment 9.4), Pathways in cancer (22 genes, fold enrichment 7.3), Alzheimer's disease (14 genes, fold enrichment 6.4), and broad Metabolic pathways (48 genes, fold enrichment 5.5). The distribution of these pathways, visualized via a bar plot, reflects the compound's involvement in both metabolic and disease-related networks (Figure 10.11).

10.3.8.1. Nitrogen metabolism pathway

The nitrogen metabolism pathway (KEGG: hsa00910) encompasses a network of enzymatic reactions responsible for the transformation of nitrogen-containing compounds in human physiology. This pathway plays a central role in nitrogen assimilation, detoxification, and the biosynthesis of amino acids such as glutamate and glutamine (Figure 10.12). In the present enrichment analysis, 2-Phenyl-4H-chromen-4-one was predicted to interact with multiple enzymes mapped within this pathway, including carbamoyl-phosphate synthase (EC 6.3.4.16), aspartate-ammonia ligase (EC 6.3.1.2), and formamidase (EC 3.5.1.49).

Functionally, nitrogen metabolism involves several distinct modules:

- **Nitrate and nitrite reduction** (both assimilatory and dissimilatory), leading to ammonia production.
- **Ammonia assimilation** into glutamate and glutamine via the glutamate synthase and glutamine synthetase pathways.
- **Interconversion of nitrogen oxides** (e.g., nitric oxide, nitrous oxide) during denitrification and nitric oxide metabolism.

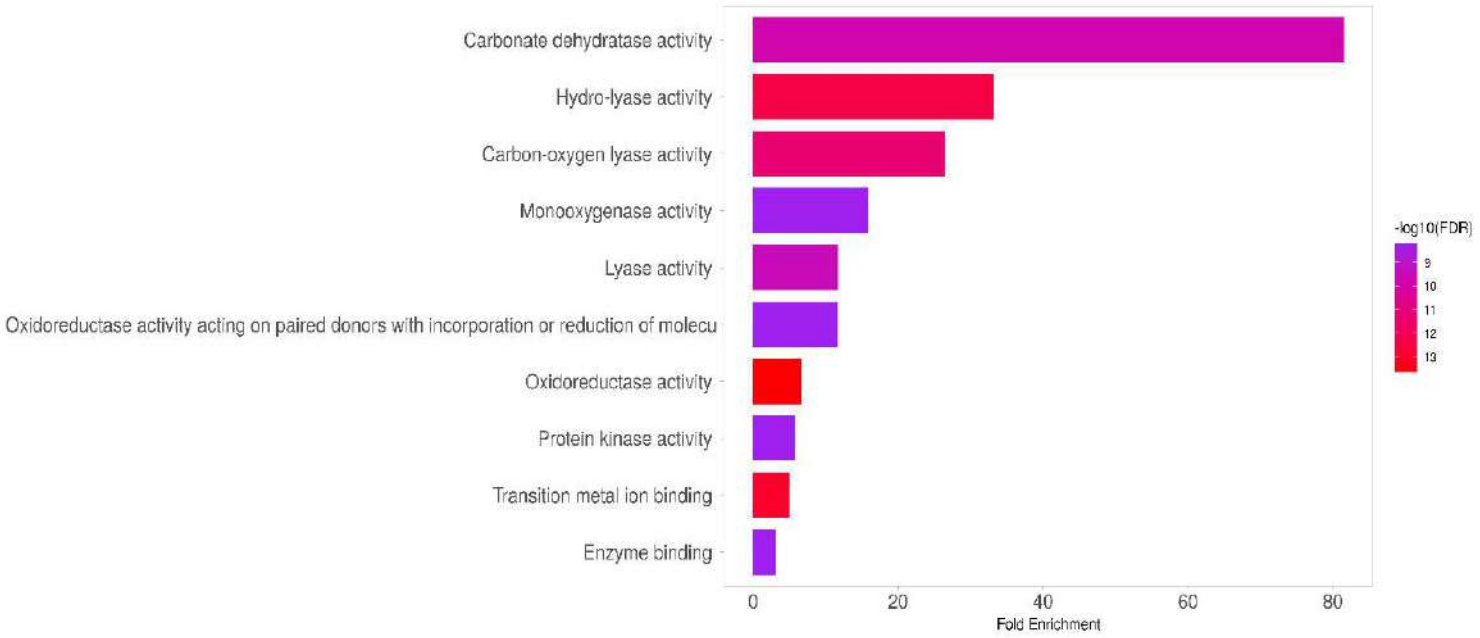


Figure 10.10: Top 10 enriched molecular functions from Gene Ontology (GO) analysis

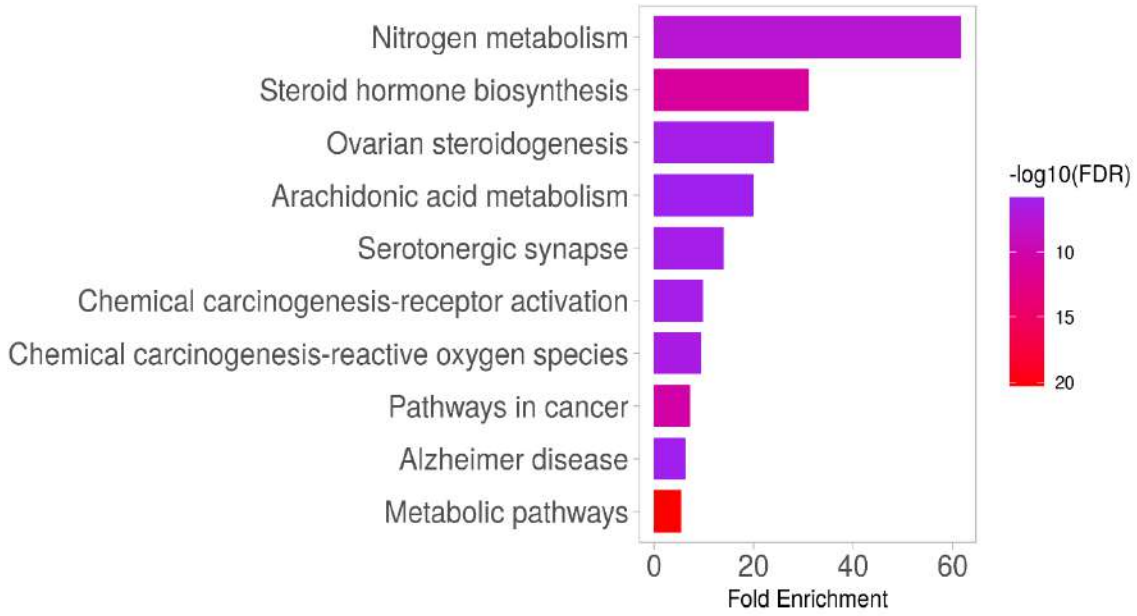


Figure 10.11: Top 10 enriched molecular functions from Kyoto Encyclopedia of Genes and Genomes (KEGG) Pathway analysis

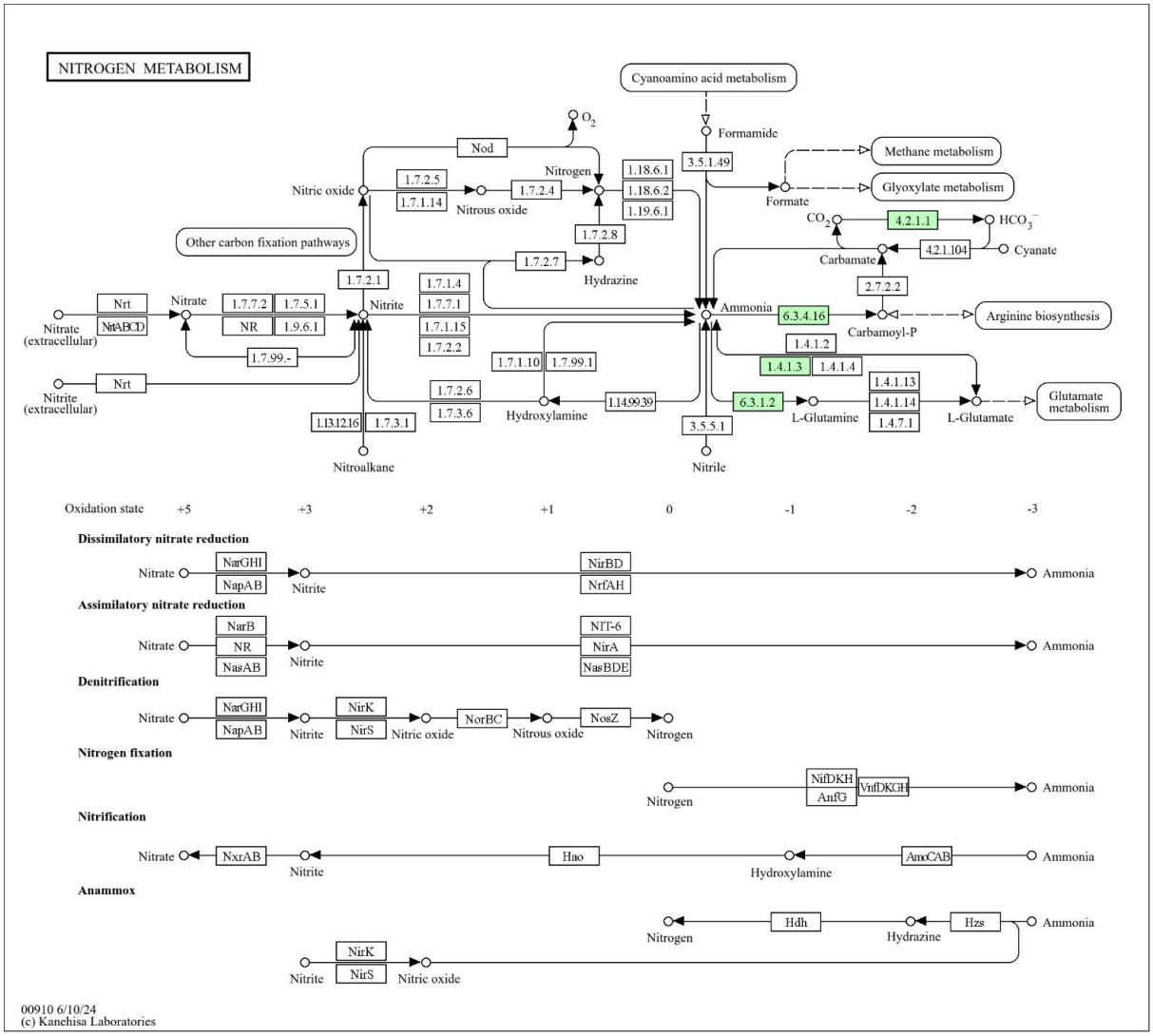


Figure 10.12: Kyoto Encyclopedia of Genes and Genomes (KEGG) pathway map of Nitrogen metabolism (hsa00910)

- **Cross-talk with other metabolic routes**, including arginine biosynthesis, glutamate metabolism, methane metabolism, and glyoxylate metabolism.

The strong enrichment (FDR = 2.4×10^{-8}; fold enrichment = 61.6) suggests that the compound's predicted targets are disproportionately involved in nitrogen handling, indicating a possible regulatory role in cellular nitrogen balance, metabolic waste management, and biosynthetic processes. This could have implications in metabolic disorders, oxidative stress response, and diseases linked to nitrogen dysregulation.

10.3.8.2. Steroid hormone biosynthesis pathway

The steroid hormone biosynthesis pathway (KEGG: hsa00140) outlines the enzymatic transformations leading from cholesterol to a wide range of biologically active steroid hormones, including glucocorticoids, mineralocorticoids, androgens, and estrogens. These hormones are vital for regulating metabolism, immune response, salt-water balance, reproductive processes, and secondary sexual characteristics. In this pathway, 2-Phenyl-4H-chromen-4-one is predicted to target multiple enzymes, such as cytochrome P450 family members (e.g., CYP11B1, CYP19A1), 3β-hydroxysteroid dehydrogenases (HSD3B1, HSD3B2), 17β-hydroxysteroid dehydrogenases (HSD17B1, HSD17B3), and aromatase (CYP19A1). These enzymes catalyze key hydroxylation, oxidation, and aromatization steps, driving the conversion of cholesterol into active steroid hormones (Figure 10.13).

The pathway can be divided into three main branches:

- **C21-steroids** (mineralocorticoids and glucocorticoids), including aldosterone and cortisol biosynthesis.
- **C19-steroids** (androgens), such as testosterone and dihydrotestosterone, are produced.
- **C18-steroids** (estrogens), such as estradiol and estrone, are biosynthesized through aromatization of androgens.

The enrichment analysis revealed a strong association (FDR = 7.3×10^{-12}; fold enrichment = 31) between the compound's predicted targets and this pathway, indicating potential modulation of steroid hormone production and signaling. Such interactions may have implications in endocrine regulation, reproductive health, metabolic disorders, and hormone-dependent cancers.

10.3.8.3. Ovarian steroidogenesis pathway

The ovarian steroidogenesis pathway (KEGG: hsa04913) describes the coordinated enzymatic and signaling events within ovarian theca and granulosa cells that regulate the production of steroid hormones essential for female reproductive function. These hormones, including estrogens, androgens, and progesterone, are critical for follicular development, ovulation, and the preparation of the endometrium for implantation. The process begins with cholesterol uptake from LDL and HDL via receptors such as LDLR and SR-B1, followed by its transport into mitochondria mediated by StAR (Steroidogenic Acute Regulatory Protein). Inside the mitochondria, CYP11A1 catalyzes the conversion of cholesterol to pregnenolone, initiating the steroid hormone biosynthetic cascade. Key steroidogenic enzymes-CYP17A1, 3β-hydroxysteroid dehydrogenase (HSD3B), CYP19A1 (aromatase), and HSD17B isoformsdrive the conversion of precursors into active androgens, estrogens, and progesterone.

Regulatory control is mediated by multiple upstream signaling pathways. LHCG/LHR signaling in theca cells and FSHR signaling in granulosa cells activate adenylate cyclase (AC) and protein kinase A (PKA), promoting steroidogenic enzyme transcription. Additional modulation occurs via insulin/IGF-1 signaling and cross-talk with GnRH, BMP/TGF-β, and arachidonic acid metabolism pathways (involving PLA2, COX2, LPOX, and EPOX). The enrichment analysis revealed a high statistical significance (FDR = 6.1×10^{-7}; fold enrichment = 24) for this pathway, highlighting the potential of 2-Phenyl-4H-chromen-4-one to influence ovarian hormone synthesis through interactions with key enzymes and regulatory proteins. This suggests possible implications in fertility regulation, polycystic ovary syndrome (PCOS), hormone-dependent cancers, and metabolic–reproductive axis disorders (Figure 10.14).

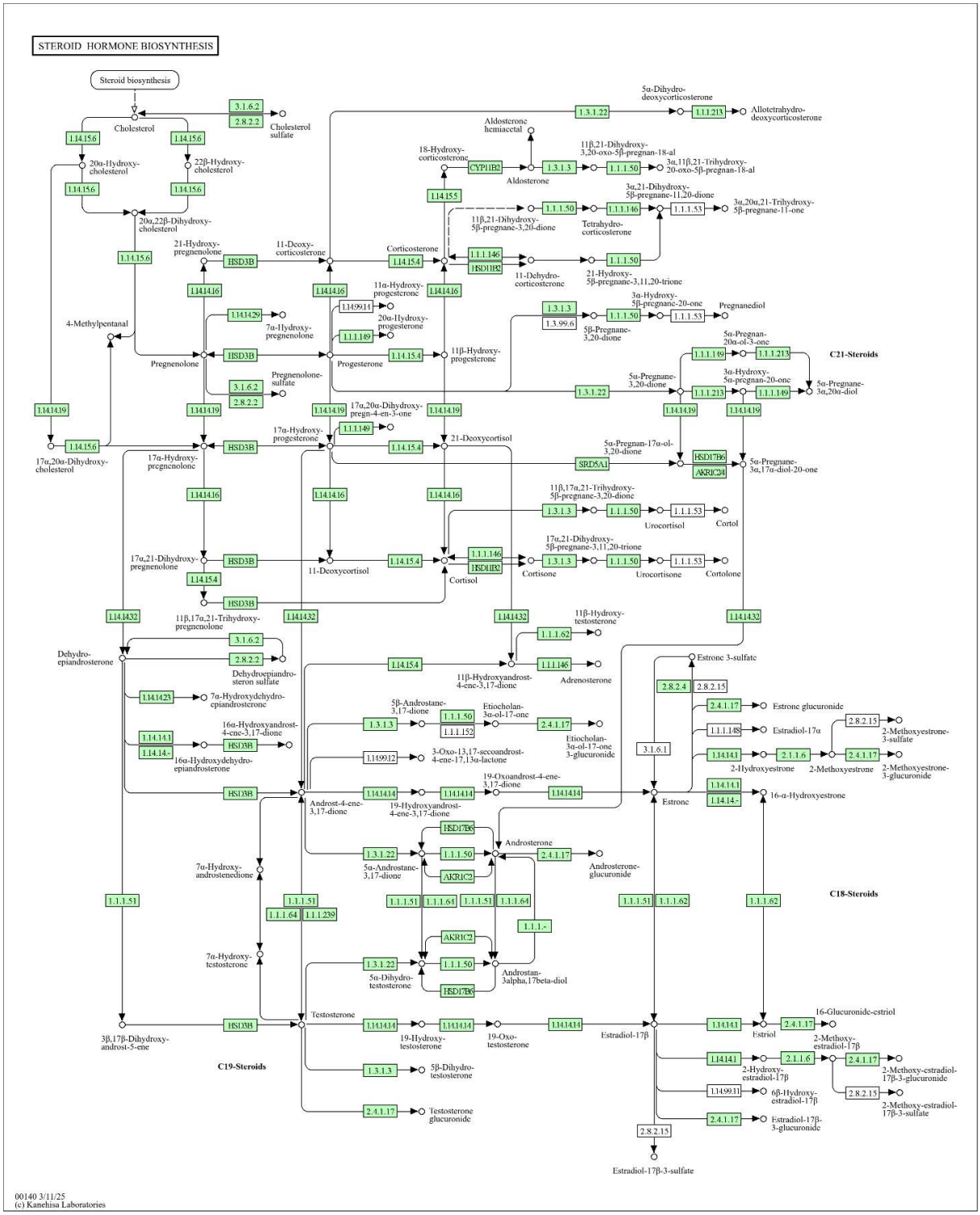


Figure 10.13: Kyoto Encyclopedia of Genes and Genomes (KEGG) pathway map of Steroid hormone biosynthesis (hsa00140)

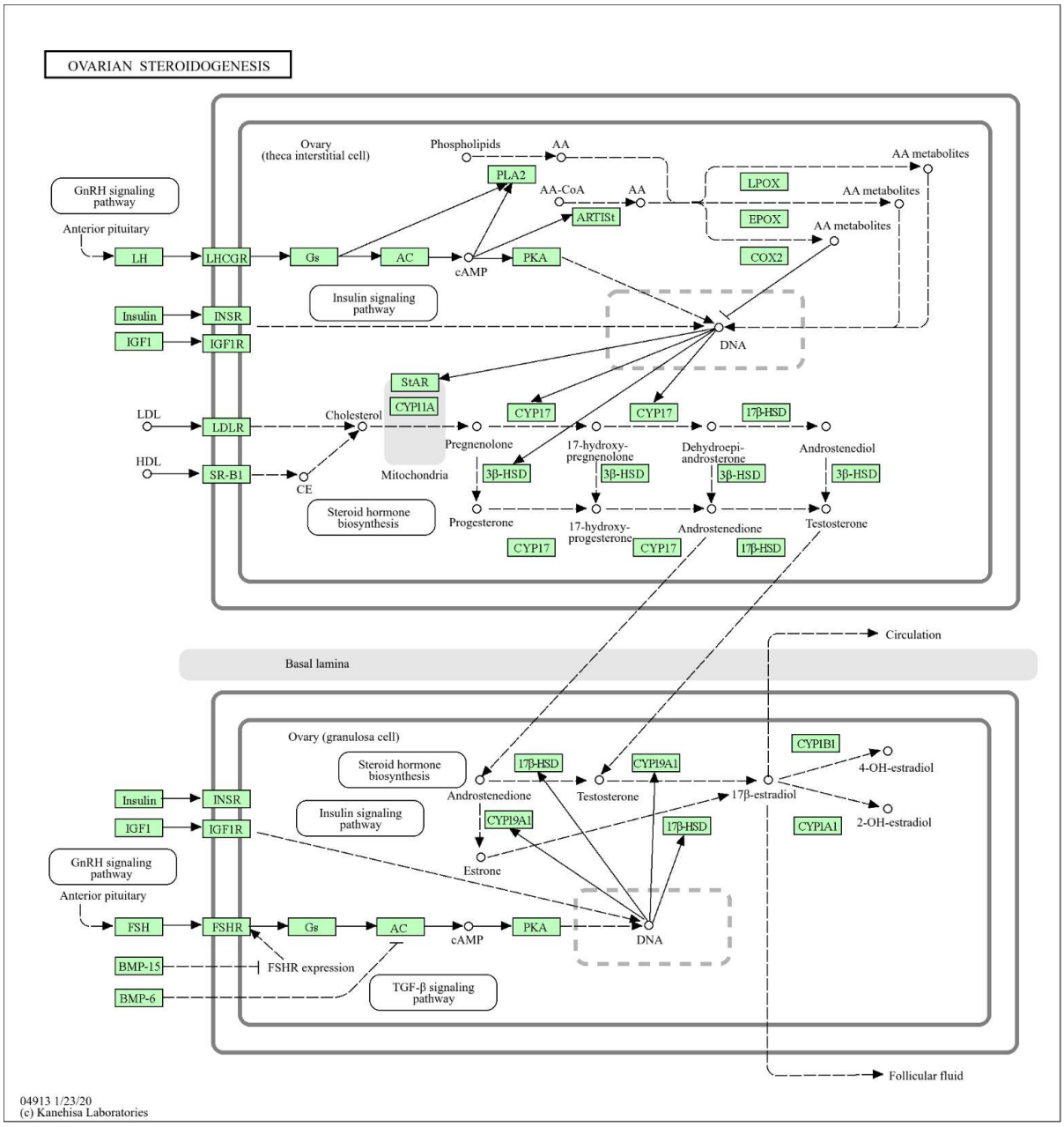


Figure 10.14: Kyoto Encyclopedia of Genes and Genomes (KEGG) pathway map of Ovarian steroidogenesis (hsa04913)

10.3.9. Disease association analysis

The Disease Alliance analysis was performed to explore potential disease associations of the predicted target library. The top 10 significantly enriched disease terms, ranked by fold enrichment and adjusted for multiple testing using FDR, revealed strong links to a variety of pathological conditions. The most enriched association was with Alzheimer's disease (DOID:10652), involving 30 genes (FDR = 1.2×10^{-22}, fold enrichment = 13.3), highlighting the possible role of the predicted targets in neurodegenerative pathways. Brain ischemia (DOID:2316) and urinary bladder cancer (DOID:11054) followed closely, with fold enrichments of 18.5 and 15.7, respectively, suggesting that several identified proteins may influence vascular injury response and oncogenic mechanisms (Figure 10.15).

Other notable associations included renal cell carcinoma (DOID:4450), pulmonary hypertension (DOID:6432), hypertension (DOID:10763), and asthma (DOID:2841), indicating a potential cardiovascular and respiratory component within the target set. The enrichment of prostate cancer (DOID:10283), breast cancer (DOID:1612), and type 2 diabetes mellitus (DOID:9352) underscores the wide disease spectrum linked to these targets, spanning oncological, metabolic, and chronic inflammatory disorders. The diversity of enriched diseases points to the pleiotropic nature of the predicted proteins, many of which are involved in shared molecular mechanisms such as oxidative stress response, lipid metabolism, kinase signaling, and inflammatory regulation. This suggests that the target library may have broad therapeutic relevance, but also potential cross-disease implications that need to be considered in downstream drug development.

10.3.10. Identification of Hub genes

Using the degree method in the CytoHubba plugin (Cytoscape), the top 10 hub genes were ranked based on their degree centrality, which measures the number of direct interactions each protein node has in the PPI network. A higher degree score indicates greater importance as a regulatory or interaction hub in the network (Table 10.5, Figure 10.16-10.17).

10.3.11. Molecular docking with the EGFR

The molecular docking analysis of 2-Phenyl-4H-chromen-4-one with EGFR kinase (PDB ID: 8TJL) revealed a strong binding affinity of –8.8 kcal/mol, indicating a favourable interaction and potential inhibitory effect (Tables 10.6-10.8, Plate 10.1)

10.3.12. Molecular Dynamics Simulation

Molecular dynamics (MD) simulations are a powerful computational approach that allows the study of biomolecular systems at an atomic level over time. Unlike static docking studies, MD simulations provide insights into the dynamic behaviour, conformational changes, and structural stability of protein–ligand complexes under physiological conditions. By simulating the physical movements of atoms, MD helps reveal how a ligand interacts within the binding pocket, the stability of these interactions, and whether the complex remains favourable over extended timescales. Parameters such as Root Mean Square Deviation (RMSD), Root Mean Square Fluctuation (RMSF), Radius of Gyration (Rg), Solvent Accessible Surface Area (SASA), and hydrogen bonding patterns are commonly analyzed to evaluate the stability, flexibility, and compactness of protein–ligand systems. In the present study, MD simulations were performed for the EGFR–2-Phenyl-4H-chromen-4-one (EGFR-PHE) complex for 100 ns, and the analyses collectively provided deeper insights into the binding stability and conformational dynamics of the complex.

10.3.12.1. Root Mean Square Deviation (RMSD)

The Root Mean Square Deviation (RMSD) measures the average positional deviation of a protein's backbone atoms or ligand from its initial structure throughout the simulation trajectory. RMSD is a critical indicator of the structural stability of a complex, where lower and stable values suggest that the protein–ligand system has reached equilibrium and maintains conformational stability. For the EGFR-PHE complex, the RMSD trajectory remained relatively stable after an initial equilibration phase, with fluctuations ranging between approximately 0.15 to 0.45 nm. Initially, up to ~20 ns, the system showed minor oscillations (around 0.20–0.25 nm), indicating that the protein was adjusting to the presence of the ligand within the binding pocket.

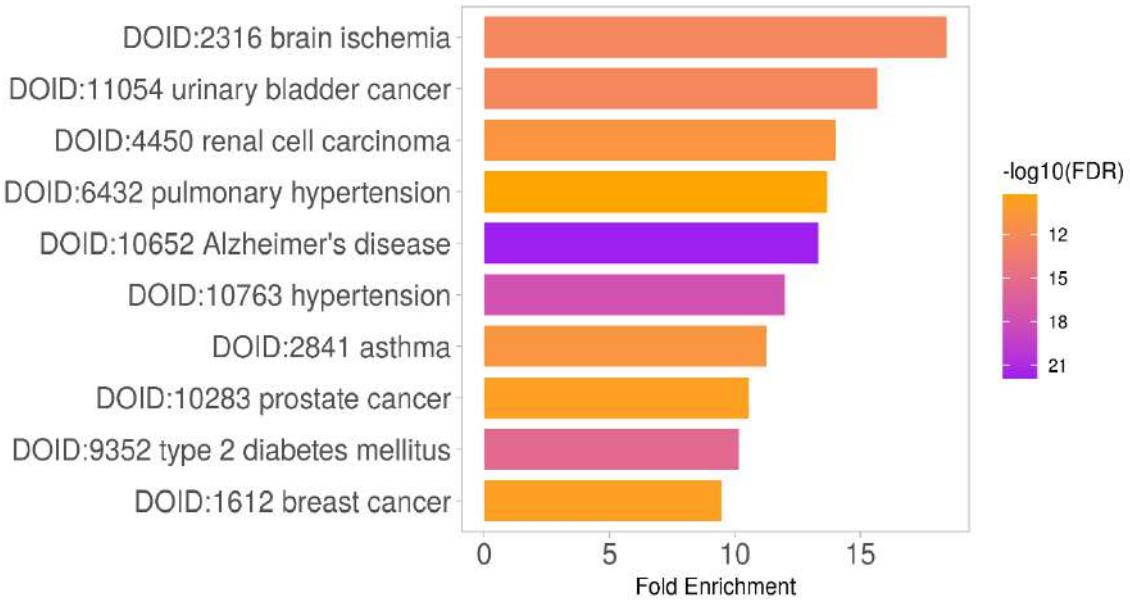


Figure 10.15: Top 10 disease associations identified through Disease Alliance

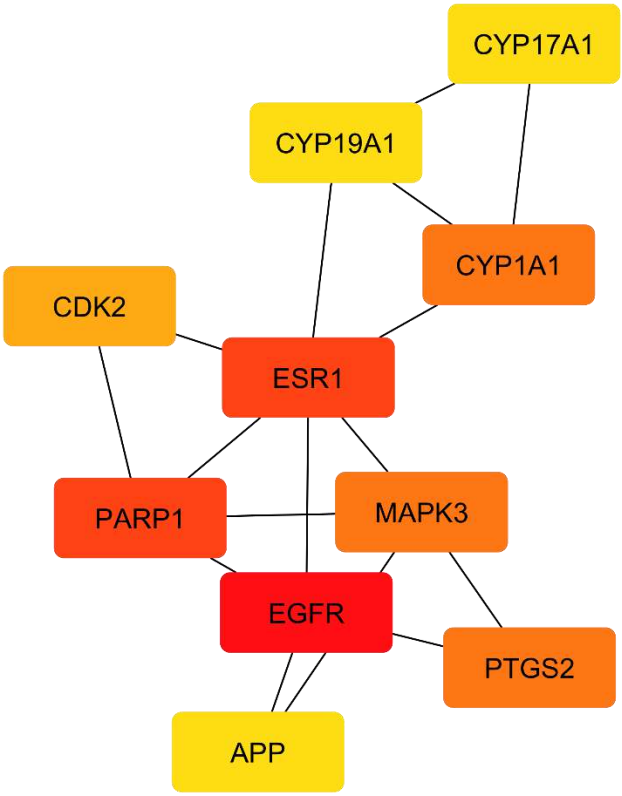


Figure 10.16: Visualization of the top 10 ranked hub genes identified using the degree method in CytoHubba. Node colours represent degree scores, with red indicating the highest-ranked genes

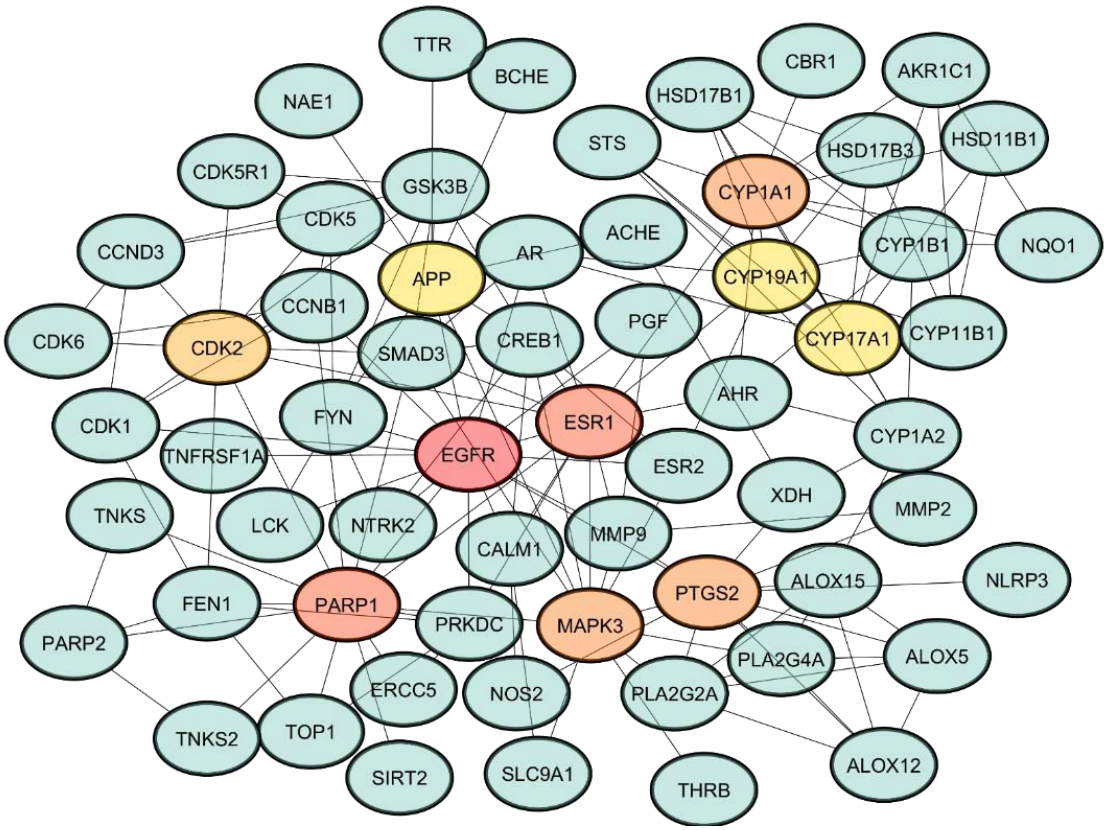


Figure 10.17: Protein–Protein Interaction (PPI) network map highlighting the top 10 hub genes (coloured nodes) within the complete interaction network. Non-hub nodes are shown in green for context

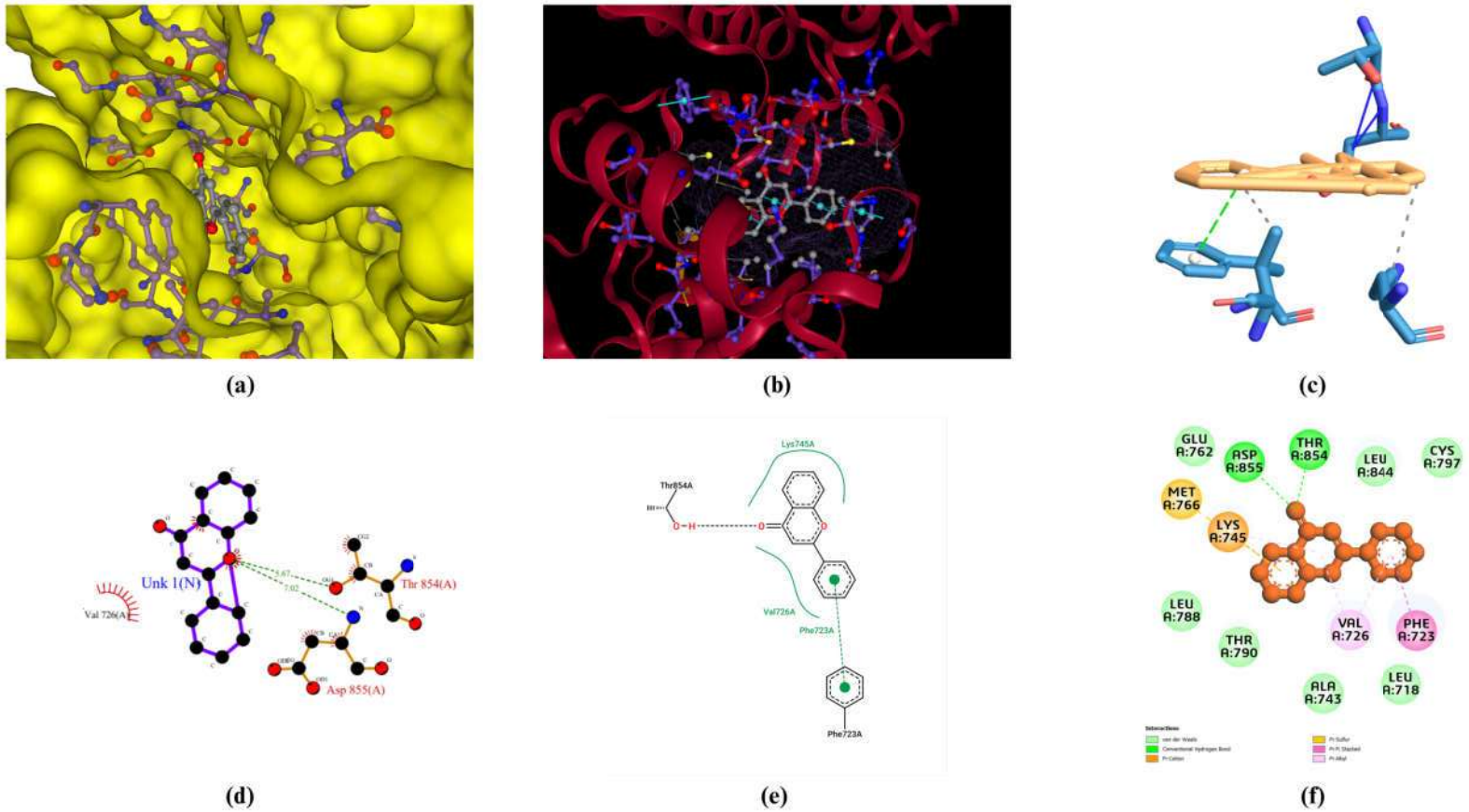


Plate 10.1: Molecular docking interactions of 2-Phenyl-4H-chromen-4-one with Edipermal Growth Factor Receptor (EGFR) Kinse domain: (a) Surface representation showing ligand accommodation in the EGFR binding pocket (b) Ribbon model highlighting the binding pose of the ligand within the active site (c) 3D interaction view depicting hydrogen bonds and hydrophobic contacts (d) 2D schematic of hydrogen bond interactions with Thr854 and Asp855, and hydrophobic contact with Val726 (e) Interaction map showing π-stacking with Phe723, hydrophobic contacts with Val726 and Lys745, and hydrogen bonding with Thr854 (f) Comprehensive 2D interaction diagram summarizing hydrogen bonds, π-interactions, and hydrophobic contacts with key active site residues

A more pronounced increase was observed around 30–40 ns, reaching values close to 0.38–0.40 nm, after which the trajectory stabilized with smaller oscillations. This stabilization beyond 40 ns demonstrates that the complex achieves a stable conformational state and retains the ligand effectively throughout the simulation. The average RMSD value of the EGFR-PHE complex was approximately 0.36 ± 0.05 nm, which is within an acceptable range for stable protein–ligand complexes. The absence of large drifts or divergence indicates that the ligand remains well-anchored within the binding site and supports the initial docking results. These findings confirm that EGFR maintains structural integrity in complex with 2-Phenyl-4H-chromen-4-one during the 100 ns simulation, suggesting reliable binding and conformational resilience (Figures 10.18-10.19).

10.3.12.2. Root Mean Square Fluctuation (RMSF)

Root Mean Square Fluctuation (RMSF) measures the average positional flexibility of individual amino acid residues in a protein during the simulation. Unlike RMSD, which tracks overall structural deviation, RMSF highlights local flexibility and identifies regions within the protein that undergo higher or lower degrees of motion. In the EGFR-PHE complex, RMSF analysis revealed that the majority of residues exhibited low fluctuations, generally below 0.25 nm, indicating a relatively rigid and stable backbone during the simulation. A few peaks were observed at specific loop regions, particularly between residues 720–760 and around 900–930, where fluctuations reached values near 0.35–0.40 nm. Such peaks correspond to loop or surface-exposed regions, which are naturally more flexible than the protein's core. Importantly, the residues surrounding the ligand-binding pocket demonstrated minimal fluctuations, underscoring the stability of the ligand-protein interactions and supporting the idea that 2-Phenyl-4H-chromen-4-one contributes to local rigidity of the binding site. The overall average RMSF value was ~0.18 ± 0.07 nm, which aligns well with stable protein-ligand systems. From a functional perspective, reduced fluctuations in the active site are crucial because they imply that the ligand binding dampens unnecessary conformational mobility, potentially leading to more effective inhibition of EGFR's catalytic activity (Figure 10.20).

10.3.12.3. Radius of Gyration (Rg)

The Radius of Gyration (Rg) provides a measure of the overall compactness of the protein during the simulation. It calculates how tightly the atoms are packed around the protein's centre of mass, with smaller values indicating greater structural compactness and stability. In the case of the EGFR-PHE complex, the Rg values fluctuated within a narrow range of 2.00–2.12 nm throughout the 100 ns simulation. During the initial phase (0–20 ns), the Rg values were slightly lower, averaging around 2.00 nm, suggesting a compact initial conformation. As the simulation progressed, a gradual increase was observed, reaching values of ~2.05–2.10 nm between 40–100 ns, where the complex maintained a steady-state compactness. The average Rg value was approximately 2.06 ± 0.03 nm, which reflects stable and consistent folding of the protein-ligand complex. Importantly, the absence of large drifts or sudden expansions in Rg suggests that binding of 2-Phenyl-4H-chromen-4-one does not induce significant destabilization or unfolding of EGFR. Instead, the ligand promotes stable packing, which is essential for maintaining structural integrity during functional inhibition. From a biological standpoint, maintaining protein compactness is critical for preserving enzyme activity and preventing aggregation (Figure 10.21).

10.3.12.4. Solvent Accessible Surface Area (SASA)

Solvent Accessible Surface Area (SASA) quantifies the surface area of a protein that is accessible to solvent molecules, providing insight into structural folding and exposure of hydrophobic or hydrophilic regions. Changes in SASA reflect conformational adjustments, ligand-induced shielding of residues, or protein unfolding. For the EGFR-PHE complex, SASA values fluctuated within the range of 150–165 nm² during the 100 ns simulation. The trajectory revealed small oscillations in SASA throughout the simulation but without any major drifts, suggesting that the protein-ligand complex remained largely stable. Interestingly, a slight reduction in SASA was observed toward the latter half of the simulation (~60–100 ns), where values averaged around 155 nm², compared to ~162 nm² in the initial stages. This reduction implies that ligand binding promoted a modest burial of solvent-exposed

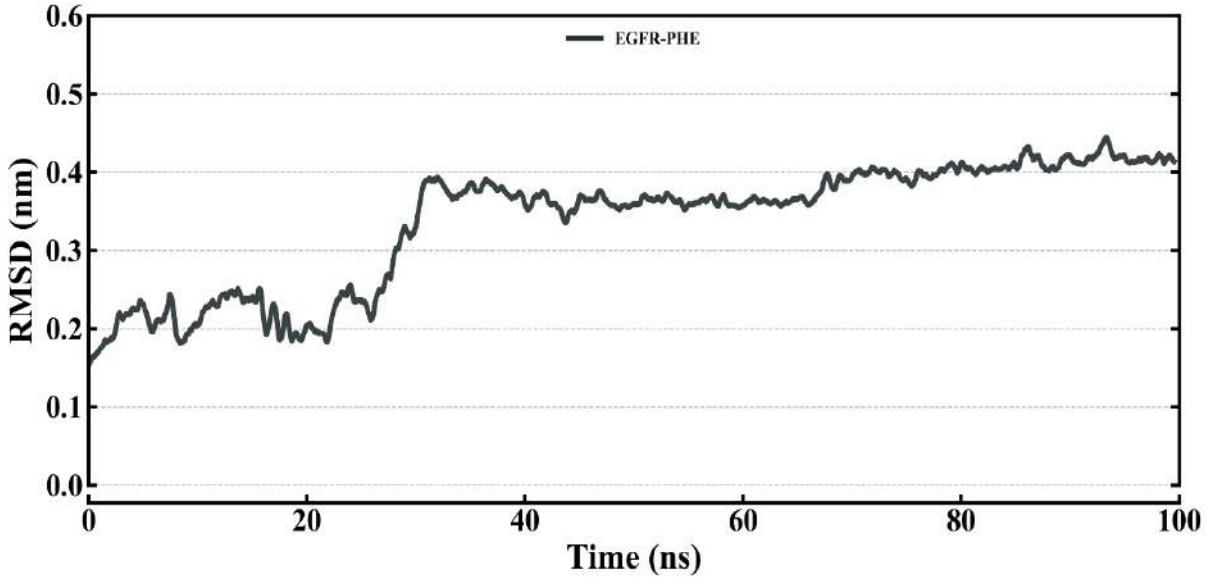


Figure 10.18: Root Mean Square Deviation (RMSD) plot of the Epidermal Growth Factor Receptor (EGFR) kinase domain–2-Phenyl-4H-chromen-4-one (EGFR-PHE) complex across a 100 ns molecular dynamics simulation

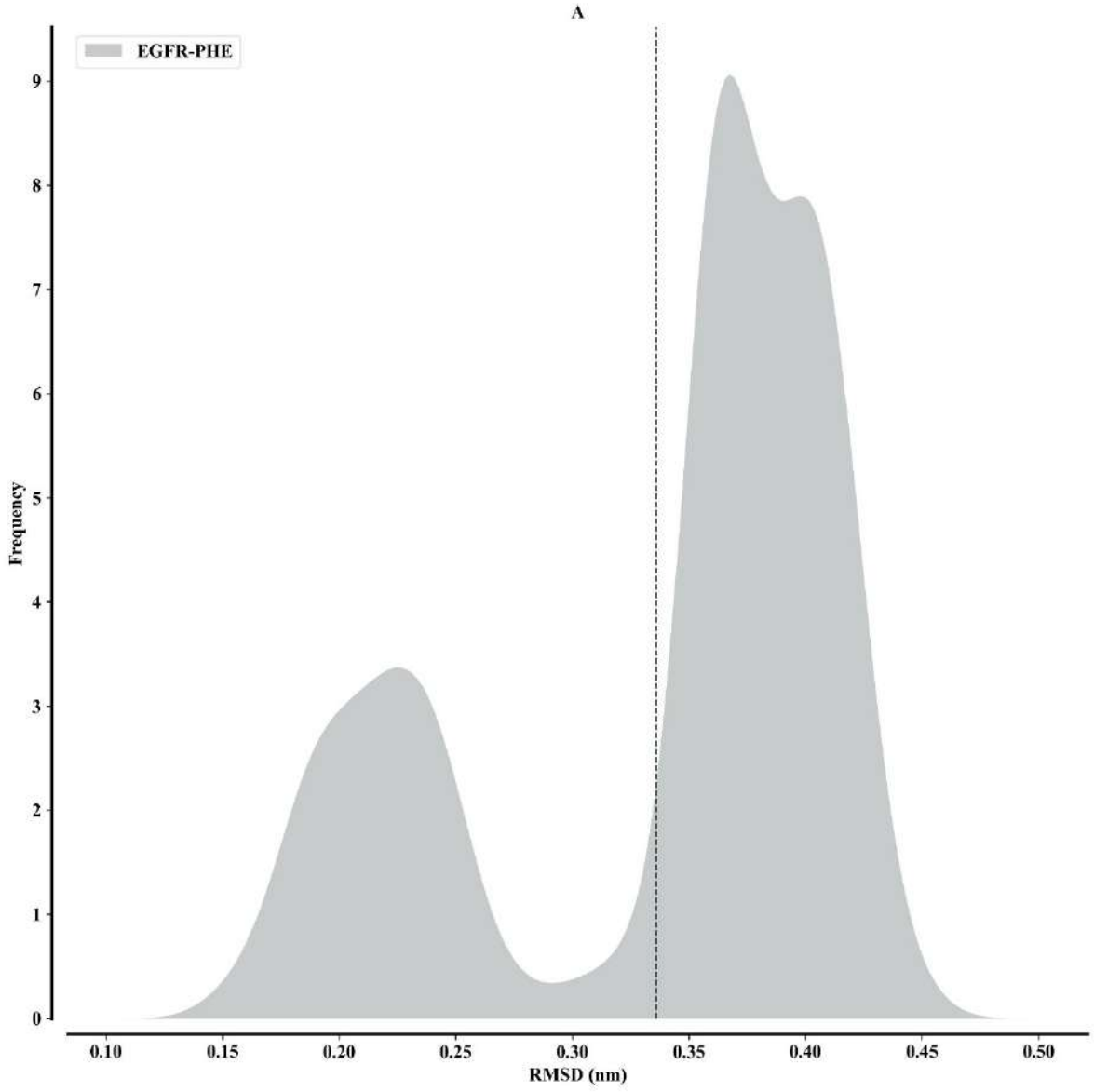


Figure 10.19: RMSD Probability Distribution (RMSD-PD) of the Epidermal Growth Factor Receptor (EGFR) kinase domain–2-Phenyl-4H-chromen-4-one (EGFR-PHE) complex.

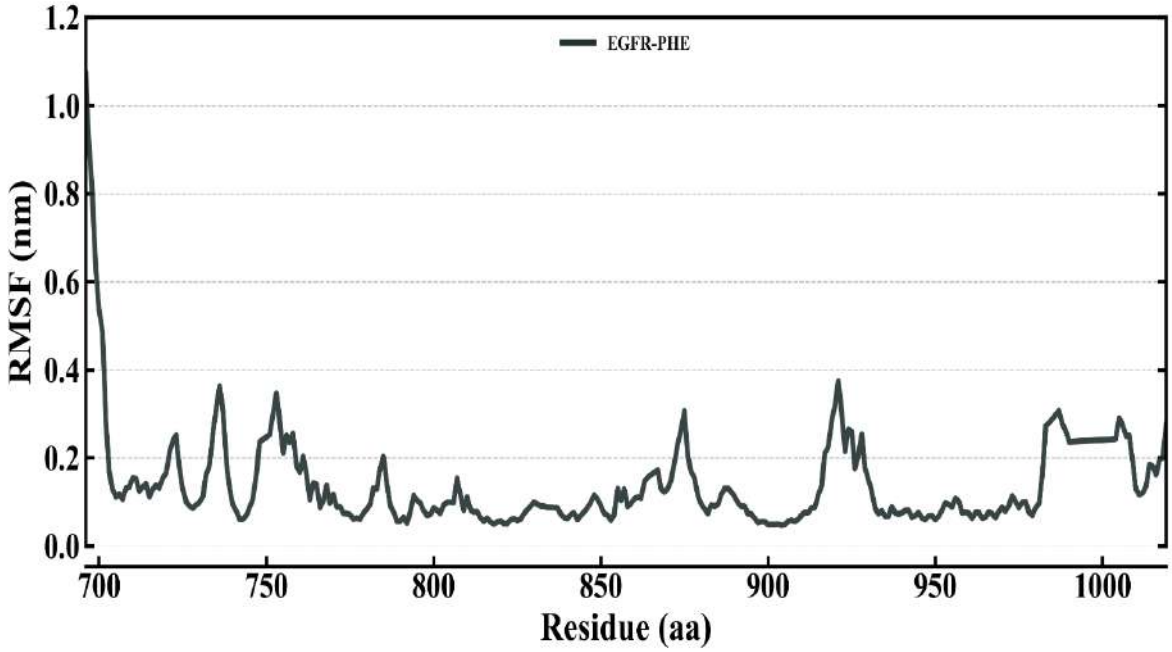


Figure 10.20: Root Mean Square Fluctuation (RMSF) plot of Epidermal Growth Factor Receptor (EGFR) kinase domain–2-Phenyl-4H-chromen-4-one (EGFR-PHE) complex showing residue-specific flexibility

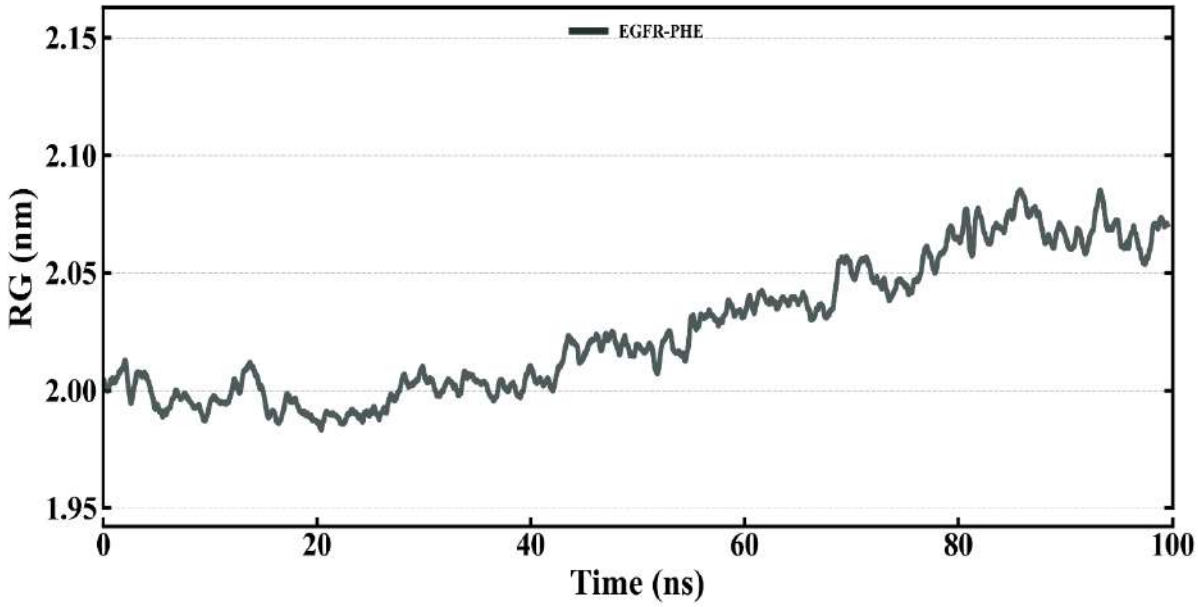


Figure 10.21: Radius of Gyration (Rg) of the Epidermal Growth Factor Receptor (EGFR) kinase domain–2-Phenyl-4H-chromen-4-one (EGFR-PHE) showing consistent compactness of ~2.06 nm, indicative of structural stability across 100 ns

residues, contributing to enhanced compactness and stabilization of the complex. The average SASA across the trajectory was 157 ± 3 nm², which reflects a balance between solvent exposure and compact protein structure. From a mechanistic perspective, decreased SASA in ligand-bound complexes often suggests that the ligand stabilizes hydrophobic residues by reducing solvent interactions (Figure 10.22).

10.3.12.5. Intermolecular Hydrogen Bonds

Hydrogen bonds between a ligand and protein play a pivotal role in stabilizing complexes and determining binding affinity. Monitoring hydrogen bonds during MD simulations provides a dynamic measure of interaction persistence and stability. In the EGFR-PHE complex, the number of intermolecular hydrogen bonds fluctuated primarily between 0 and 2 over the 100 ns simulation. The trajectory revealed that at least one hydrogen bond was consistently maintained for the majority of the simulation, with transient occurrences of a second hydrogen bond at several points (notably around 90 ns). This persistence suggests that hydrogen bonding contributes significantly to the stabilisation of the ligand within EGFR's binding pocket (Figure 10.23).

10.3.12.6. Intramolecular Hydrogen Bonds

Intramolecular hydrogen bonds within the protein backbone serve as indicators of secondary structure stability, such as α-helices and β-sheets. Monitoring these bonds during MD simulations provides insights into whether ligand binding affects protein folding or structural integrity. In the EGFR-PHE complex, the number of intramolecular hydrogen bonds remained stable within the range of 195–220 throughout the 100 ns simulation. The average was approximately 207 ± 5 hydrogen bonds, which is consistent with a stable tertiary structure. Notably, there were no abrupt decreases that would indicate unfolding or loss of secondary structure. Instead, the slight fluctuations observed are characteristic of normal protein dynamics and thermal motion. Importantly, the persistence of high numbers of intramolecular hydrogen bonds suggests that the binding of 2-Phenyl-4H-chromen-4-one does not destabilize EGFR's structural core. On the contrary, the maintenance of these bonds

indicates that the protein remains properly folded and dynamically stable under ligand-bound conditions. (Figure 10.24)

10.3.13. Conformational sampling and landscape analysis

Conformational sampling and landscape analysis are important techniques in molecular dynamics that provide insights into the collective motions and conformational transitions of biomolecular systems. While traditional trajectory analyses such as RMSD, RMSF, Rg, and SASA reveal local and structural fluctuations, they do not fully capture the global conformational states explored by the protein–ligand complex during the simulation. Principal Component Analysis (PCA) reduces the dimensionality of the trajectory by projecting atomic displacements onto principal components (PCs), which represent the dominant motions of the system. This allows us to visualize large-scale conformational rearrangements that contribute most significantly to protein flexibility. Meanwhile, Free Energy Landscape (FEL) analysis provides a thermodynamic perspective, mapping the conformational space into energy basins and barriers, thus revealing the stability and transitions between different conformations.

10.3.13.1. Principal Component Analysis (PCA)

The PCA scatter plot illustrates the conformational space explored by the EGFR–PHE complex during the simulation. The trajectory was projected onto the first two principal components (PC1 and PC2), which account for the majority of the variance in atomic motions. The distribution of points across PC1 and PC2 shows that the complex samples multiple conformational clusters, indicating flexibility but also the presence of energetically favored states. The clustering of points along two major regions suggests that the system oscillates between distinct conformational states, with one being more densely populated, reflecting a dominant low-energy conformation. This implies that binding of 2-Phenyl-4H-chromen-4-one does not destabilize the protein but rather restricts its dynamics within a defined conformational space, which is a favorable feature for inhibitor binding. The smooth spread along PC1 also indicates a level of conformational adaptability, suggesting that

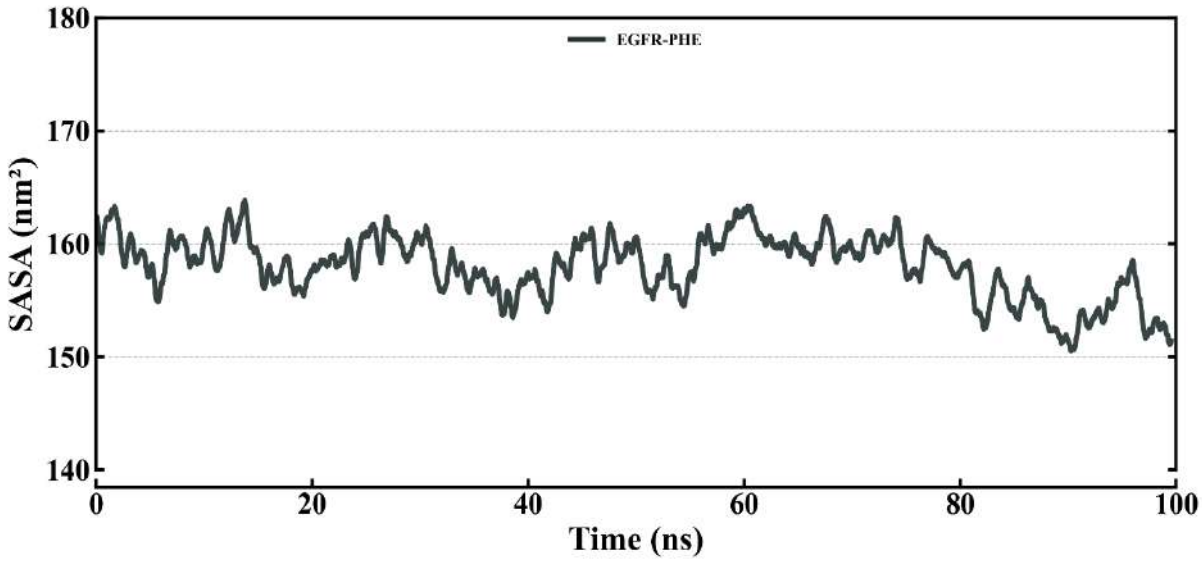


Figure 10.22: Solvent Accessible Surface Area (SASA) of Epidermal Growth Factor Receptor (EGFR) kinase domain–2-Phenyl-4H-chromen-4-one (EGFR-PHE) complex showing stable solvent exposure with a slight reduction towards the end of the simulation

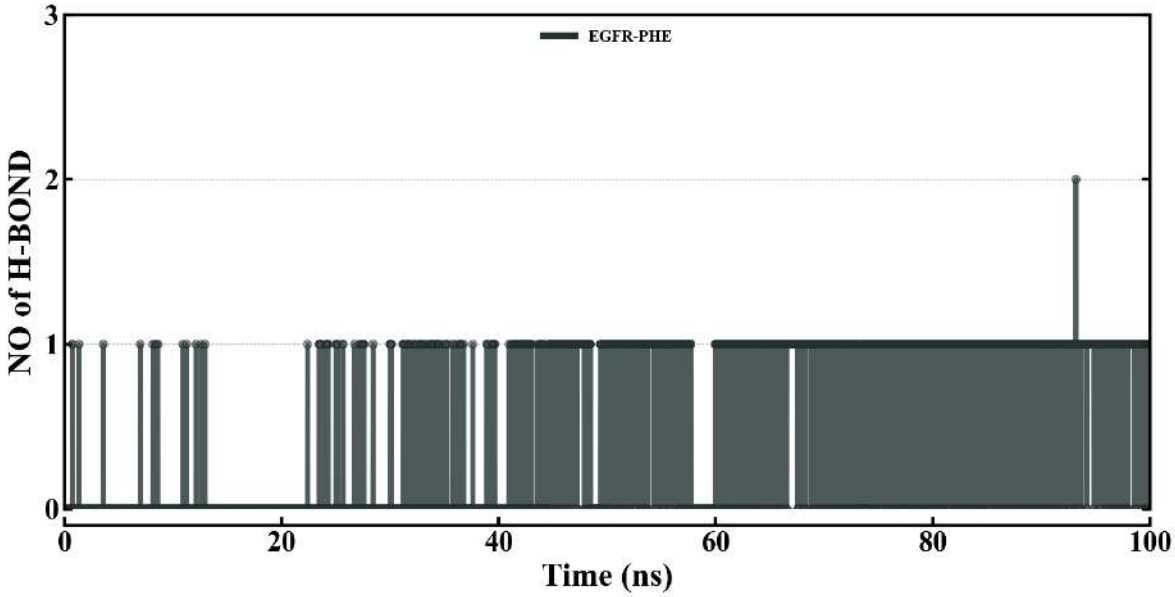


Figure 10.23: Intermolecular hydrogen bonding dynamics of Epidermal Growth Factor Receptor (EGFR) kinase domain–2-Phenyl-4H-chromen-4-one (EGFR-PHE) complex, showing persistence of at least one hydrogen bond throughout the 100 ns trajectory

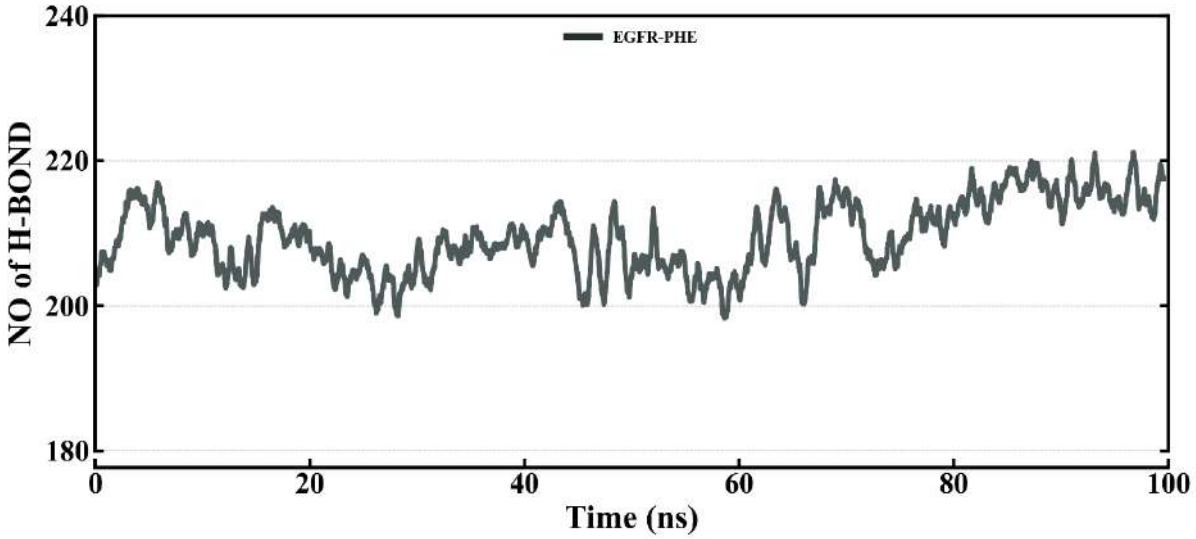


Figure 10.24: Intramolecular hydrogen bonding of Epidermal Growth Factor Receptor (EGFR) kinase domain–2-Phenyl-4H-chromen-4-one (EGFR-PHE) complex, showing stable maintenance of ~207 hydrogen bonds, indicative of preserved secondary structure stability

the protein retains functional flexibility while maintaining structural stability (Figure 10.25).

10.3.13.2. Free Energy Landscape (FEL) Analysis

The FEL plot provides a thermodynamic mapping of the conformational space of the EGFR–PHE complex, projected along PC1 and PC2. The presence of deep energy basins (blue regions) reflects the most stable conformational states, while higher-energy regions (red/yellow) correspond to less favorable states. In this case, two major low-energy basins were observed, suggesting that the system transitions between two dominant conformational states during the simulation. The depth of these basins indicates high stability, and their separation implies that the system may undergo conformational switching between these states while still maintaining overall structural integrity. This aligns well with the PCA results, where two clusters were observed. Importantly, the broad energy funnel and absence of multiple shallow minima suggest that the complex is not trapped in unstable conformations, but instead exhibits a stable yet flexible energy landscape. Such behavior is consistent with a ligand that stabilizes the protein without overly restricting its dynamic adaptability, which is crucial for maintaining functional activity (Figure 10.26).

10.3.14. Binding Free Energy analysis

Molecular Mechanics Poisson–Boltzmann Surface Area (MM/PBSA) is a widely employed post-dynamics computational approach to estimate the binding free energy of a ligand–protein complex. It combines molecular mechanics energy terms (van der Waals and electrostatics) with solvation free energy contributions (polar and non-polar solvation) to quantify the stability and affinity of the complex. Negative binding free energy values indicate favorable binding interactions, while the magnitude of individual energy contributions reveals the driving forces behind ligand stabilization. Thus, MM/PBSA not only provides a numerical estimation of binding affinity but also dissects the relative importance of hydrophobic interactions, electrostatics, and solvation in complex formation (Figure 10.27).

10.3.14.1. Van der Waals Energy

The van der Waals (vdW) component contributed -138.194 ± 9.954 kJ/mol, representing the most significant stabilizing force in the EGFR–PHE complex. This indicates strong hydrophobic interactions between the ligand and nonpolar regions of the protein's binding pocket. Such interactions often dominate in small-molecule inhibitors, reinforcing the idea that 2-Phenyl-4H-chromen-4-one is well accommodated within the hydrophobic binding cavity of EGFR. The relatively low error margin also suggests consistency across the trajectory, implying stable hydrophobic contacts throughout the simulation.

10.3.14.2. Electrostatic Energy

Electrostatic contributions were -23.745 ± 6.021 kJ/mol, providing a secondary stabilizing influence. While weaker than the vdW interactions, electrostatics still play an important role in guiding the ligand into the binding pocket and stabilizing interactions with charged or polar residues. The moderately high standard deviation reflects fluctuations in ionic and hydrogen-bonding interactions, suggesting some dynamic flexibility in these contacts during simulation. Nevertheless, the net negative value confirms that electrostatic interactions favour complex stability.

10.3.14.3. Polar Solvation Energy

The polar solvation contribution was +102.498 ± 13.769 kJ/mol, which is destabilizing. This positive value arises because solvation of polar groups in water competes with protein–ligand electrostatics, thereby opposing binding. Such behavior is typical in aqueous simulations and reflects the desolvation penalty incurred upon ligand binding. However, this destabilizing contribution was more than compensated for by the strong vdW and electrostatic energies, indicating that hydrophobic burial of the ligand dominates binding affinity.

10.3.14.4. Non-Polar Solvation Energy (SASA)

The solvent-accessible surface area (SASA) energy contributed -13.094 ± 0.520 kJ/mol, which, although smaller in magnitude compared to vdW, still supports

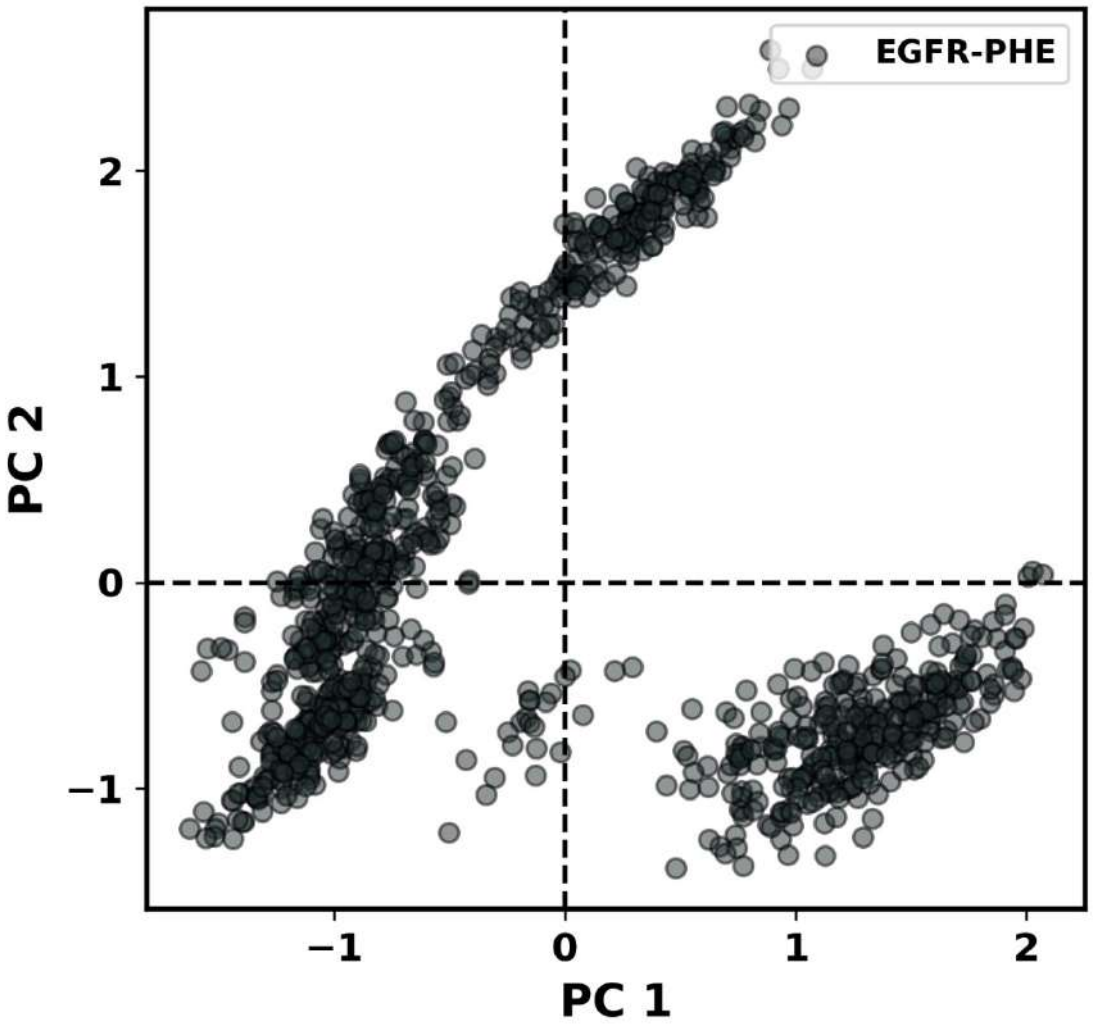


Figure 10.25: PCA projection of Epidermal Growth Factor Receptor (EGFR) kinase domain–2-Phenyl-4H-chromen-4-one (EGFR-PHE) complex along the first two principal components (PC1 and PC2), showing clustering into stable conformational states

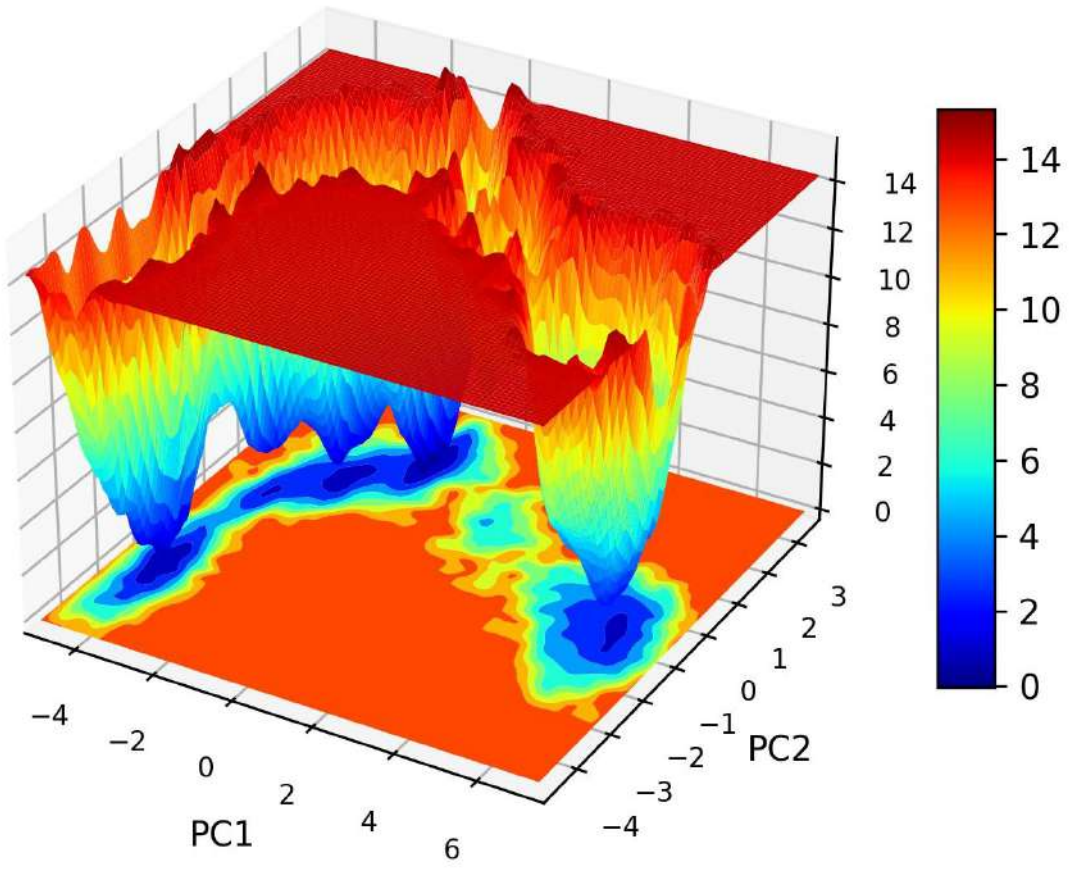


Figure 10.26: Free Energy Landscape (FEL) of Epidermal Growth Factor Receptor (EGFR) kinase domain–2-Phenyl-4H-chromen-4-one (EGFR-PHE) complex mapped along PC1 and PC2, highlighting two dominant low-energy basins that represent stable conformational states of the complex

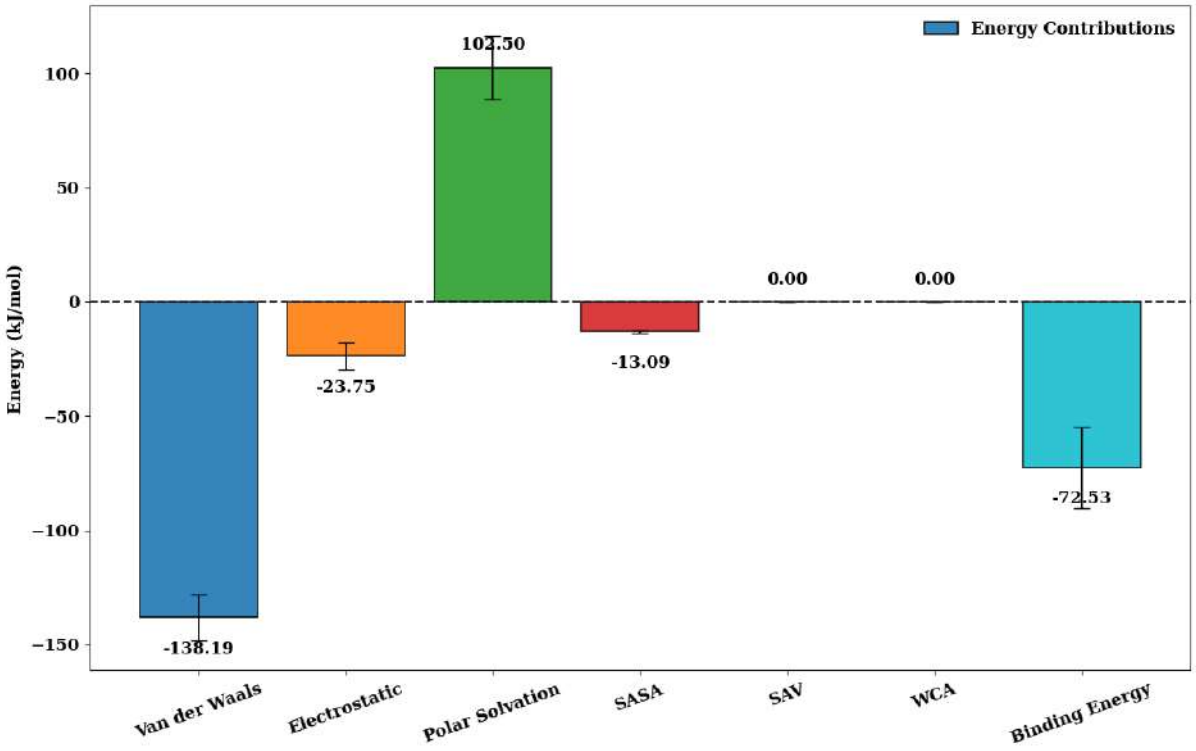


Figure 10.27: MM/PBSA binding free energy decomposition for the Epidermal Growth Factor Receptor (EGFR) kinase domain–2-Phenyl-4H-chromen-4-one (EGFR-PHE) complex

binding stability. SASA contributions arise from non-polar solvation effects, essentially representing the hydrophobic driving force due to reduced solvent exposure upon binding. The low error margin suggests stable hydrophobic burial of the ligand throughout the trajectory.

10.3.14.5. Other Energy Terms (SAV, WCA)

Both surface area-volume (SAV) and water contact area (WCA) contributions were negligible (0.000), indicating that these terms did not significantly affect the overall binding free energy in this system.

10.3.14.6. Total Binding Free Energy

The final MM/PBSA binding free energy was calculated as -72.535 ± 17.626 kJ/mol, confirming that the EGFR–PHE complex is energetically favorable. The strongly negative value demonstrates that ligand binding is spontaneous and thermodynamically stable. The decomposition of energy terms suggests that hydrophobic interactions (vdW and SASA) are the primary driving force, while electrostatics provide additional support. The destabilizing polar solvation energy is typical but insufficient to offset the strong non-polar interactions.

10.3.15. DFT Studies for 2-Phenyl-4H-chromen-4-one

DFT studies are valuable in predicting the electronic properties of bioactive compounds, providing insights into their chemical reactivity, stability, and potential interaction mechanisms with biological macromolecules. Specifically, frontier molecular orbitals (HOMO–LUMO), energy gaps, and molecular electrostatic potential (MEP) distributions are crucial in evaluating electron donor–acceptor properties, sites of electrophilic/nucleophilic attack, and overall reactivity. Below is a detailed interpretation of each calculated parameter for 2-Phenyl-4H-chromen-4-one.

10.3.15.1. Total DFT Energy

The total DFT energy represents the ground-state electronic energy of the molecule. Lower values typically indicate higher thermodynamic stability. 2-Phenyl-4H-chromen-4-one has a total energy of −720.670 Hartree, suggesting that the

compound is energetically stable and does not readily undergo spontaneous decomposition. Such stability is favorable for potential drug development, as unstable compounds often degrade before reaching their biological target.

10.3.15.2. HOMO Energy (Highest Occupied Molecular Orbital)

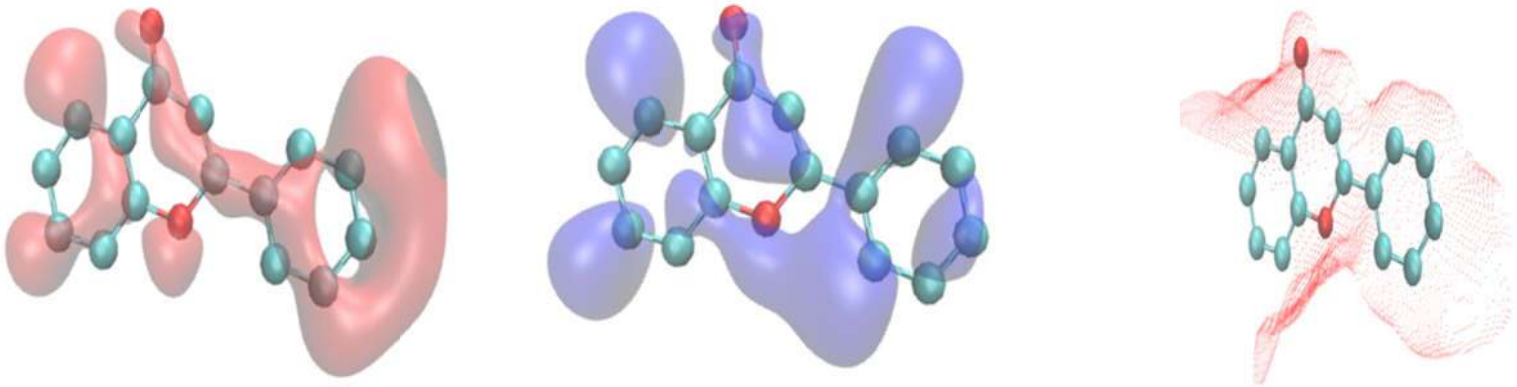
HOMO indicates the electron-donating ability of a molecule. Molecules with higher (less negative) HOMO values can donate electrons more readily in chemical interactions, often correlating with nucleophilicity. The HOMO energy was −0.243 Hartree, reflecting moderate electron-donating capability. This suggests that 2-Phenyl-4H-chromen-4-one can act as an electron donor at specific reactive sites, potentially forming hydrogen bonds or π–π interactions with proteins such as EGFR.

10.3.15.3. LUMO Energy (Lowest Unoccupied Molecular Orbital)

LUMO represents the electron-accepting ability of the molecule and is related to electrophilicity. A lower (more negative) LUMO value indicates a stronger tendency to accept electrons. The LUMO energy was −0.202 Hartree, indicating good electron-accepting properties. This ability to accept electrons complements its HOMO behaviour, suggesting that the compound can engage in both donor and acceptor interactions, making it versatile in molecular recognition processes.

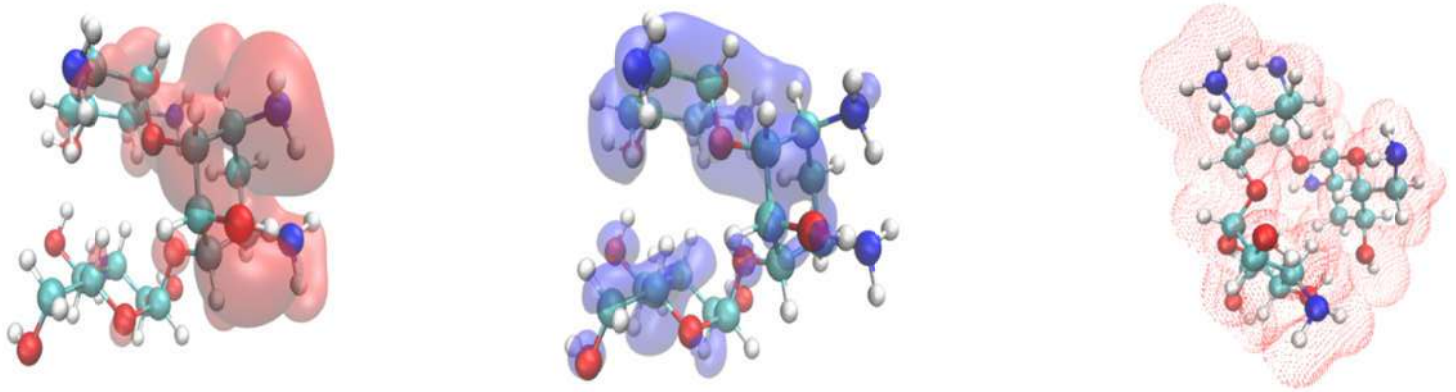
10.3.15.4. HOMO–LUMO Gap

The HOMO–LUMO energy gap reflects chemical reactivity and kinetic stability. A smaller gap suggests higher reactivity but lower stability, while a larger gap implies more stability but lower reactivity. The gap was 0.041 Hartree, which is relatively small. This small gap indicates that 2-Phenyl-4H-chromen-4-one is chemically reactive and can easily undergo electronic transitions. Such reactivity is often advantageous in drug molecules, as it allows flexible interactions with multiple protein targets. However, it also suggests the compound may be sensitive to oxidation or photochemical degradation (Plate 10.2).



(a) (b) (c)

Plate 10.2: Frontier molecular orbitals, Highest Occupied Molecular Orbital (HOMO, Lowest Unoccupied Molecular Orbital (LUMO), and Molecular Electrostatic Potential (MEP) surfaces for 2-Phenyl-4H-chromen-4-one against LasR: (a) HOMO distribution(b) LUMO distribution, and (c) MEP surface mapping



(a) (b) (c)

Plate 10.3: Frontier molecular orbital Highest Occupied Molecular Orbital (HOMO, Lowest Unoccupied Molecular Orbital (LUMO), and molecular electrostatic potential (MEP) surfaces for Tobramycin against LasR: (a) HOMO distribution (b) LUMO distribution and (c) MEP surface mapping, highlighting probable interaction sites and electron density regions

10.3.15.5. Molecular Electrostatic Potential (MEP)

MEP maps describe the charge distribution across the molecule, highlighting regions susceptible to electrophilic (electron-rich) or nucleophilic (electron-poor) attacks (Plate 10.3).

- Minimum MEP: −7.011 a.u. → Indicates regions rich in electron density, likely oxygen atoms on the chromenone ring, acting as hydrogen bond acceptors.
- Maximum MEP: 114.234 a.u. → Positively charged areas, often hydrogen atoms, acting as hydrogen bond donors.
- Average MEP: 0.063 a.u. → Suggests overall balanced polarity.

The strong negative potential around oxygen atoms suggests that the compound may strongly interact with positively charged residues (e.g., Lys, Arg) in proteins, while positive regions may engage negatively charged amino acids (e.g., Asp, Glu). This duality enhances its binding versatility.

10.4. Discussion

Many different plant-based diets contain flavonoids, a type of bioactive compounds. Frequent consumption has been associated with a decreased risk of coronary heart disease (CVD), cancer, and other degenerative disorders, among other chronic illnesses. Based on their chemical composition, flavonoids are separated into subgroups, including anthocyanins, flavanones, flavones, flavan-3-ol, flavonols, and isoflavones (Erica et al., 2017; Kiruthiga et al., 2021a). Due to their abundance in fruits, vegetables, nuts, and seeds, flavonoids are considered good for our biological systems (Kiruthiga et al., 2021a). A distinctive characteristic of flavonoids is that the manufacture of flavones in plants is mediated by two distinct flavone synthase proteins (FNS) (Martens & Mithöfer, 2005). There is increasing scientific evidence that flavonoids may help prevent disease, but more clinical and epidemiological studies are being conducted to determine their exact role.

2-Phenyl-4H-chromen-4-one is a flavone compound possess planer, aromatic structure. This provides it specificity with different targets. In the compounds having cyclic structure, aromaticity is the main characteristic important for providing it reactivity and stability (De Souza Farias et al., 2021). The aromaticity of flavone, flavonol, and anthocyanidin was compared by De Souza Farias et al. (2021) and found that it is impacted by the planarity and interaction between O3H and HC6′. There is increase in the aromaticity with hydroxyl group whereas the ketone group decreases.

Flavonoids are the natural class of chemicals made up of 15 carbon atoms, having two phenyl rings joined by a pyran ring (Panche et al., 2016). With the molecular formula $C_{15}H_{10}O_2$ and weight of 222.24 g/mol, 2-Phenyl-4H-chromen-4-one exhibits high GI absorption, good oral bioavailability and blood-brain barrier permeability. The diverse biological functions of flavones have sparked attention among medicinal chemists due to their structure-activity interactions (Verma & Pratap 2010). Present study found that it passes Lipinski, Ghose, Veber, Egan, and Muegge rules, confirming it strong drug like properties. Flavonoids are recommended as health-promoting phytochemicals for animal production because they have been shown to improve the size of immune organs, mucosal and cellular immunity, gut

architecture and function, and reduce heat stress in agricultural animals (Kamboh et al., 2015). Oral medicine is the most widely used method of drug administration due to its many benefits, including patient choice, cost-effectiveness, ease of large-scale production of oral dosage forms, and the simplicity of administering drugs orally (Prasad et al., 2017; Alqahtani et al., 2021). Its bioavailability score also showed that it is favorable for oral drugs. In this regard, the study on 2-phenyl-4H-chromen-4-one which was conducted in the present work is highly justified as it will shed some light on its possible application as multi target pharmaceutical, as per contemporary theories of medication, including network drug pharmacology and systems biology.

Numerous biological functions, including anti-inflammatory, antibacterial, anticancer, antiviral, and anti-inflammatory, are possessed by flavonoids (Sharma, 2006; Kamboh et al., 2015; de Souza Farias et al., 2021). They have also been shown to have a modulatory function in a number of biological processes, including oxidation, enzyme detoxification, apoptosis, the host immune system, and many more (Kamboh et al., 2015). It was predicted from the study that it interacts with various target proteins through SEA and SwissTargetPrediction and the major target families were cytochrome P450 enzymes, kinases, nuclear receptors, GPCRs, ABC transporters, and oxidoreductases. A diet high in flavonoids may be associated with a lower risk of breast cancer, according to epidemiologic research. Changes in several signaling pathways that are implicated in cancer-related processes including inflammation and proliferation, are the cause of these preventative qualities (Beatrice et al., 2015). Considering protein kinases play crucial roles in controlling a variety of cell signaling pathways, they have been sought after potential anticancer targets. Protein kinases have been reported to be strongly inhibited by a variety of drugs that comprise a flavonoid scaffold as an essential anchor (Zhao et al., 2019).

The developing field of network pharmacology has emerged as a potent research tool because of the multi-component, multi-target, and synergistic properties of herbal medicines (Xiao et al., 2021). Network pharmacology, a branch of systems and network medicine, is revolutionizing the way we define, diagnose, treat, and, cure illnesses (Nogales et al., 2022). For creating new treatment opportunities, research has

been now moved to identifying the important active compounds in the medicinal plants. The network pharmacology gives a novel approach for the assessment of efficiency of multi-target drug formulas and also provide more targets for the treatment of different medical conditions (Noor et al., 2022).

Protein-protein interaction (PPI) analysis network helps in the identification of the important hubs and nodes which play an important role in the disease development. This helps in finding the important targets and the development of the drug (Pradeep et al., 2025). In the findings of present study the PPI network was found highly interconnected and consisted of 129 nodes and 766 edges. This pathway was related to lipid metabolism, inflammatory responses, oxidative stress, and cell cycle regulation. The molecular processes behind complex disorders include networks of impacted components rather than single targets. By thoroughly addressing these intricate molecular networks, these fields provide a fresh, hopeful approach to illnesses and associated therapies, getting behind the present restrictions in pharmaceutical development and therapy (Nogales et al., 2025). Based on the molecular interactions of extensive subcellular networks, a network medicine framework has become a viable tool for determining novel indications and logical therapeutic targets (Lee et al., 2022). Analysis on PPI fills the gap between the predicted target and the interpretation of the functional outcome which elaborate the complex therapeutic outcomes of 2-phenyl-4H-chromen-4-one.

According to Serra et al. (2012), when flavonoids are breakdown in the digestive system by the digestive microbes present in the gut it give rise to various phenolic acids which have systemic effects on the body. Mendes et al. (2019) found many of the metabolic changes brought on by flavonoids were in contrast of those brought on by pro-inflammatory activation. Present study found ten significantly enriched pathways with top pathways were steroid hormone biosynthesis, nitrogen metabolism, and ovarian steroidogenesis. In higher species steroid hormone are important in regulation of various physiological activities (Fujiyama et al., 2022). This shows that it plays important role in metabolic regulation, hormonal balance, and disease-related pathways.

Up to 75% of all instances of dementia are caused by Alzheimer's disease (AD), a neurodegenerative illness (Tahami et al., 2022). Alzheimer's and Parkinson's disease are the most occurring neurodegenerative disorders that effect elder population which are caused by degeneration of neurons especially in brain areas and also the presence of aberrant protein aggregates (Tapias et al., 2023). Present study showed a strongest enrichment for AD. Associations were also observed with other conditions namely pulmonary hypertension, brain ischemia, urinary bladder cancer, asthma, renal cell carcinoma, breast cancer, prostate cancer, and type 2 diabetes. This suggests broad therapeutic potential but also multi-disease implications. Kiruthiga et al. (2018) conducted an *in silico* library to determine the impact of compound phenyl-4H-chromen-one on many targeted diabetes enzymes. Chemicals were created to examine the effect on diabetes and they discovered that these chemicals have important role in antidiabetic activity. From the enzymes tested, enzyme alpha amylase showed the highest binding scores with the compounds. According to Xiao et al. (2022), 2-phenyl-4H-chromen-4-one compounds possess anti-inflammatory properties. These studies provide the information about its relation with various conditions so making it a potential source for multitarget interventions.

The analysis of the hub genes provides information about the key regulators in the predicted protein-protein interaction (PPI) network. Among the top-ranked nodes, EGFR (epidermal growth factor receptor) emerged as the most prominent hub with the highest degree score. A variety of cancers are brought on by the overexpression, mutation, rearrangement, or amplification of the EGFR gene, which is a tyrosine kinase receptor (Sepay et al., 2022). The hub genes highlight that the compound acting on central regulators rather than peripheral proteins. Strong binding affinity of 2-phenyl-4H-chromen-4-one was observed with EGFR kinase, which indicates its potential as an EGFR inhibitor. This affinity is comparable to that of several known kinase inhibitors, suggesting meaningful interactions with the ATP-binding pocket of the receptor kinase domain. Such inhibition would directly impact proliferative and survival signalling cascades (e.g., MAPK and PI3K-Akt pathways), providing a mechanistic basis for the anticancer associations highlighted in the disease enrichment analysis. Importantly, the flat, aromatic structure of 2-phenyl-4H-

chromen-4-one allows for stacking interactions, a feature often exploited in the design of kinase inhibitors. Kiruthiga et al. (2021b) uses Autodock.4 to conduct molecular docking simulations in order to comprehend the binding interaction over the Cyclooxygenase-2 and found it as a possible anti-inflammatory drug, the flavone and flavanone scaffolds have superior inhibitory activity over Cyclooxygenase-2. Additionally, there was a substantial correlation between the outcomes of computational studies, which found that naturally occurring flavonoid analogues were excellent candidates for drug development to combat inflammatory illnesses.

Developing a myeloperoxidase inhibitor to combat oxidative stress was the focus of the Kiruthiga et al. (2021b) study. Molecular docking analysis showed the compounds 2-phenyl-2,3-dihydro-4h-chroman-4-one have significant potency against myeloperoxidase. Devi et al. (2022) found that 2-phenyl-4H-chromen-4-one bind to the most active positions in proteins, which is consistent with the findings of their molecular docking research. In silico research suggests that substances containing lipophilic electron-withdrawing groups may function as chitinase inhibitors, which break down chitin which aid in the formation of fungal membranes. This opens new possibilities for drug discovery, where development and additional screening on specific chronic diseases may produce therapeutic efficacy.

Molecular Dynamics (MD) simulations showed that 2-Phenyl-4H-chromen-4-one forms a stable and compact EGFR complex. RMSD profile of the 100 ns simulation showed that the results achieved equilibrium when these initial fluctuations occurred and then maintained the stability with slight deviations. Root mean square fluctuation (RMSF) analysis indicated that the flexibility was mostly concentrated to the loop regions, and the residues in the active site were relatively stable indicating that the binding of 2-phenyl-4H-chromen-4-one did not destabilize the core of the receptor. The radius of gyration (Rg) did not change, indicating that overall compactness of the protein was not significantly perturbed; however, there was some volatility in the solvent-accessible surface area (SASA) indicating that there had been a moderate change in solvent exposure of the receptor in the presence of ligands. Intra- and intermolecular hydrogen bond analysis supported this conclusion of stable binding: hydrogen bonds between the ligand and EGFR residues persisted throughout

simulation, and the stability of intraprotein hydrogen bonds indicated preservation of the receptor tertiary structure. The results of Zhang et al. (2025) offer more insight into the function of intramolecular hydrogen bonds for the cocrystal formation of flavonoids and indicate that breaking these bonds typically prevents the development of cocrystals.

Energy decomposition through MM/PBSA calculations provided further quantitative validation of binding stability. Hydrophobic interactions were dominant and electrostatic energy also responsible for providing additional stabilisation. Hydrophobic interactions are an important type of non-specific interaction that are found in biological systems. They arise when two hydrophobic species approach one another and water molecules reorganize (Sánchez-Iglesias et al., 2012). Notably, the dominance of hydrophobic interactions is consistent with the planar, aromatic nature of 2 phenyl-4H-chromen-4-one, which is well suited for embedding in the hydrophobic pockets of proteins such as EGFR. These findings strengthen the hypothesis that EGFR is a bonafide target of the compound, with potential implications for modulating oncogenic pathways.

Taken together, the hub gene, docking, and molecular dynamics results form a coherent narrative: 2-phenyl-4H-chromen-4-one targets key regulatory proteins such as EGFR, engages in strong and stable binding interactions with the kinase domain of EGFR, and maintains this binding under dynamic physiological conditions. This convergence of computational analyses provides a strong foundation for hypothesizing that the compound may exert multi-target therapeutic effects, with particular strength in oncology, neurodegeneration, and hormone-related disorders. At the same time, its predicted ability to modulate kinase signalling, DNA repair, steroid metabolism, and oxidative stress pathways explains the breadth of disease associations observed, spanning cancer, cardiovascular disease, metabolic disorders, and neurodegenerative conditions. The present study found that 2-phenyl-4H-chromen-4-one has potential in various applications.

10.5. Conclusion

2-Phenyl-4H-chromen-4-one, a flavone derivative characterized by a chromen-4-one core with a phenyl substituent at the C-2 position, was selected for investigation due to its reported biological activities. It was analysed for pharmacological potential and demonstrated a favourable pharmacokinetics, good drug-likeness, and low toxicity. Kinases, oxidoreductases, phosphatases, nuclear receptors, hydrolases, and other enzyme families that are important in inflammation, oxidative stress, metabolism, and cancer biology were among the many targets that were predicted and grouped according to their known biological activities. These findings show that the predicted targets of 2-phenyl-4H-chromen-4-one are intricately linked to signal transduction, oxidative stress responses, metabolic regulation, and cell cycle control. The compound's potential as a polypharmacological agent is highlighted by the broad range of these predicted targets, paving the way for more network-level and functional validation research.

Hydrogen bonding and hydrophobic interactions were identified as key stabilizing forces within the binding pockets. Docking and MD simulation confirm strong and stable interactions with target proteins. Disease-association analysis indicates potential applications in cancer, inflammatory, metabolic, and neurodegenerative disorders. The compound's multi-target pharmacological potential was highlighted by the functional enrichment analysis, which showed that the projected target set of 2-Phenyl-4H-chromen-4-one is engaged in a broad range of biological processes, cellular localizations, and molecular activities. The findings showed that 2-Phenyl-4H-chromen-4-one preserves its functional role by striking an equilibrium between structural flexibility and stability. Its hydrogen-bonding potential, electronic flexibility, and chemical reactivity are all confirmed by DFT studies. The study concludes that 2-phenyl-4H-chromen-4-one is a promising therapeutic candidate that targets numerous pathways.

11



SUMMARY AND GENERAL CONCLUSIONS

CHAPTER 11

SUMMARY AND GENERAL CONCLUSION

The study documented both macroscopic and microscopic botanical traits for *S. laetum*, *S. occidentale,* and *S. palghatense*. Macroscopically, *S. laetum* has elliptic to ovate-oblong leaves (5-13 cm long) with entire margins, a prominent midrib, and reddish venation. Its flowers are actinomorphic, arranged in terminal clusters, with prominent crimson stamens and a small ovoid berry fruit. The reflexed calyx lobes and persistent red stamens are diagnostic for *S. laetum*. *S. occidentale* bears linear-lanceolate leaves (up to 14 cm long) and cymose clusters of white or pale pink flowers; its fruit is a globose berry. *S. palghatense* has large obovate-lanceolate leaves and curved backward margins and a tough (coriaceous) texture. Its flowers have a distinct calyptrate corolla that falls off at opening, exposing purple-red stamens.

Microscopically, leaf anatomy was consistent with typical Myrtaceae. All three species have a dorsiventral lamina with a single layer of palisade mesophyll beneath the adaxial epidermis and spongy mesophyll below. Differences appeared in stomatal and secretory structures. *S. laetum* leaves are hypostomatic with predominantly paracytic stomata. Its abaxial epidermis has numerous oil glands and secretory cavities rich in tannin-like substances. *S. occidentale* also has hypostomatic leaves, but its stomata are cyclocytic. Notably, *S. occidentale* exhibits calcium oxalate druse crystals densely arrayed around guard cells (a possible xeromorphic trait that minimizes water loss). *S. palghatense* leaves feature anisocytic and cyclocytic stomata; their petioles showed abundant prismatic crystals and starch grains, suggesting high metabolic storage for seasonal growth. Glandular trichomes were sparse or absent in all three, but all contained oil cells and tannin idioblasts in the mesophyll. The dense network of reticulate veins and thick cuticle in these leaves suggests adaptation to humid evergreen forest conditions. Overall, leaf anatomical differences (stomatal type, crystal distribution, secretory structures) provide

microscopic characters that distinguish the species and reflect their specific microhabitats.

The anatomical features of the stem and bark characteristics also showed different characteristics, with all the studied species exhibiting diffuse-porous wood and bicollateral vascular bundles in stems. *S. laetum* stems showed well-developed bicollateral bundles and abundant medullary phloem, and the bark exhibited heterocellular phellem (cork layer of varying cell sizes) and sporadic sclereids. The stem of *S. occidentale* showed distinct annual rings with a thick phelloderm rich in lignified sclereids. Its wood contained paratracheal banded parenchyma and the homocellular rays. *S. palghatense* had the thickest bark of up to 1200 µm phellem, with many sclereids and calcium oxalate deposits.

Histochemical analysis showed the abundance of ergastic substances with pharmacological significance. Bark and leaf are rich in tannin idioblasts and oil glands. These are known to provide antimicrobial defense. Overall, these anatomical and histochemical features not only differentiate the species but also illustrate ecological adaptations. Thick cuticles, sclerified tissues, and secretory defenses suggest resilience in competitive Western Ghats habitats, whereas varied stomatal structures reflect moisture regimes of their niches.

Powder microscopy of *S. laetum*, *S. occidentale,* and *S. palghatense* powders revealed overlapping as well as distinctive features. Fragments of vessel elements, fibers, sclereids, and palisade cells were common to all, reflecting their Myrtaceous characters. The *S. laetum* powder was distinguished for frequent oil droplets and reddish tannin pigments. The bark powder of *S. occidentale* contained abundant pitted parenchyma and medullary rays. *S. palghatense* leaf powder exhibited a high density of glandular cells and prismatic crystals. Thus, each species produced a unique mix of powder constituents that could serve as microscopic markers in quality control. For example, the presence of specific crystal types (rosette, prismatic, and styloid) in the powders helps differentiate *S. palghatense* from *S. laetum*.

Fluorescence analysis further distinguished the species. Under UV light, powders and extracts of each species displayed characteristic colour when treated with

solvents or reagents. *S. laetum* powders exhibited distinct greenish fluorescence in methanol, *S. occidentale* showed bluish-green with water, and *S. palghatense* turned olive under acetone. These fluorescence responses, varying by solvent and light wavelength (254 nm vs 366 nm), provide an additional authentication tool. Such species-specific fluorescence patterns arise from their differing phytochemical profiles and aid in detecting adulteration or substitution in herbal formulations.

Physicochemical evaluations quantified extractive values and nutritional components. Among the three, *S. laetum* leaf contained the highest extractive yields in both water and ethanol, and the greatest vitamin C content. This suggests *S. laetum* leaves are rich in soluble phenolics and ascorbic acid. *S. occidentale* bark showed the highest crude fiber and ash content, indicating more mineral matter and cellulosic material. While the bark extract of *S. palghatense* has higher extractive values. Copper level was also high with the lowest ash content. All three species are valuable in nutrition, as they are rich in carbohydrates, fiber, essential minerals, and vitamins.

The pharmacognostic study showed that *S. laetum*, *S. palghatense,* and *S. occidentale* leaves and barks are nutritionally and chemically robust. Their powders contain compounds (tannins, flavonoids, oils) that relate to known *Syzygium* therapies. The variation in physicochemical constants across species implies they may have different uses or efficacies in traditional medicine. Importantly, the combination of powder microscopy, fluorescence, and chemical profiling generates a baseline of pharmacognostic standards. This ensures that herbal preparations claiming to contain these species can be verified and standardized. It also highlights that even endemic wild species can be sources of nutritional and medicinal products, emphasizing the need to manage their harvesting responsibly.

The methanol extract of *Syzygium* species exhibited higher activity than other solvents used. GC-MS and LC-MS results show the presence of different phytocompounds with many biological activities. 2-Phenyl-4H-chromen was detected from the LC-MS QTOF analysis, and it is also isolated from the methanol extract of *S. palghatense*.

Bioactive efficacy, including antioxidant, anti-inflammatory, antimicrobial, anthelmintic, antidiabetic, and anticancer activities, was validated using the methanol extract of *S. palghatense* bark, the silver nanoparticles synthesized from this methanol extract, and the compound Phenyl-4H-chromen-4-one, which also showed notable bioactivity. Among the three endemics plant studies, *S. palghatense* bark exhibited superior biological activities. Higher activity is shown by the isolated compound, followed by *S. laetum*. *S. occidetale.*

The biological activity validation focused on *S. palghatense* bark AgNPs. Similar activities may be expected in crude extracts of all three species. In antioxidant assays, the biosynthesized AgNPs showed exceptionally strong free-radical scavenging. In DPPH, superoxide, hydroxyl radical scavenging and FRAP tests, the AgNPs consistently outperformed ascorbic acid. For example, at the highest dose tested (150 µg/mL), AgNPs achieved ~89% inhibition of DPPH radicals, compared to 75% by vitamin C. The FRAP assay (reflecting reducing power) reached up to 90% inhibition with AgNPs versus 78% for the standard. Corresponding IC_{50} values (concentration for 50% effect) were extremely low for the AgNPs (around 1-2 µg/mL), indicating very potent antioxidant capacity. Such results suggest that compounds from *S. palghatense*, especially when formulated into nanoparticles, have excellent potential to neutralize reactive oxygen species. This aligns with the high phenolic and tannin content observed microscopically and physicochemically.

In antimicrobial testing, *S. palghatense* AgNPs exhibited broad-spectrum activity at sufficiently high doses. Against fungi, the AgNPs produced clear inhibition zones, though smaller than the standard drug clotrimazole at equivalent weight. At 1000 µg/mL, AgNPs yielded ~20-22 mm zones against *A. niger* and *C. albicans*. Against bacteria, *P. aeruginosa* was especially susceptible. The AgNPs created a 31 mm zone at 1000 µg/mL, larger than for *S. aureus* (~14 mm) or *E. coli* (~20 mm) at that concentration. Importantly, biofilm assays demonstrated that AgNPs disrupted *P. aeruginosa* biofilm formation, reducing extracellular polymeric substances by ~68% at 100 µg/mL. These findings indicate that silver nanoparticles from *S. palghatense* carry potent antimicrobial effects, likely via silver ion release and oxidative damage. They are particularly promising against antibiotic-resistant Gram-negative bacteria.

The anthelmintic test against *Lumbricus terrestris* showed that *S. palghatense* AgNPs induce paralysis and death in a concentration-dependent way. At 100 mg/mL, the AgNPs killed the parasite faster (paralysis in ~3 min, death in ~6 min) than the standard drug albendazole (paralysis ~12 min, death ~18 min at 20 mg/mL). This corresponds to >96% inhibition of worm motility, surpassing albendazole's ~92%. This potent antiparasitic effect suggests possible applications in veterinary or human antihelminthic therapies.

Most notably, the anti-inflammatory assays revealed that *S. palghatense* AgNPs strongly inhibit multiple inflammation pathways. In human red blood cell membrane stabilization (mimicking anti-arthritic effect), AgNPs prevented hypotonic lysis up to ~74% at 100 µg/mL, suggesting protection of cell membranes. In the protein denaturation assay, AgNPs inhibited heat-induced albumin denaturation by 85% at 500 µg/mL, slightly higher than the NSAID diclofenac at the same dose. In an enzyme assay, AgNPs showed superior inhibition of protease (67% vs. 65% for diclofenac at 500 µg/mL), and critically, of cyclooxygenase (COX) and lipoxygenase (LOX) enzymes. At the concentration of 500 µg/mL, AgNPs inhibited COX by 64.1% and LOX by 74.5%. Together, these assays indicate that *S. palghatense* AgNPs modulate multiple targets of inflammation. Often matching or exceeding conventional drugs *in vitro*. Such multi-pronged anti-inflammatory action is likely related to the nanoparticle's combined silver and phytochemical effects.

The genus *Syzygium* has a rich history of traditional uses that align with our findings. In Ayurveda and other systems, *Syzygium* species are used as antidiabetics, anti-inflammatories, antioxidants, and tonics. For example, clove oil (from *S. aromaticum*) is antiseptic and anti-inflammatory, jamun (*S. cumini*) fruits are antidiabetic and its leaves are used for wound healing. Our study revealed that the endemic *Syzygium* studied here possesses many of these same properties when examined scientifically. The antioxidant and anti-inflammatory activities support their potential use in preventing or treating oxidative and inflammatory conditions, as traditionally claimed. The observed nutritional value (vitamins, minerals, fiber) suggests that leaves or fruits of these endemics could supplement diets or be

formulated into health foods or nutraceuticals. Modern applications could include developing standardized herbal extracts or nutraceutical formulations. The fluorescence characteristics can helps in the quality assessment. The demonstrated fluorescence and chemical markers help ensure quality. The potent silver nanoparticles indicate a novel way of using *Syzygium* constituents to produce nanomedicines for antimicrobial or anticancer therapy. The pharmacognostic profiles also emphasize that these plants have untapped chemical diversity.

In cancer cell assays, *S. palghatense* AgNPs showed strong cytotoxicity. In the Trypan blue assay with DLA cells, 77% of cancer cells were killed at 100 µg/mL, indicating a high cell death rate. In MTT/XTT assays on MCF-7 breast cancer cells, increasing concentrations of AgNPs caused significant decreases in cell viability, with statistical analyses confirming dose-dependent effects. Although cisplatin (standard chemotherapeutic) was somewhat more potent at lower doses, AgNPs induced comparable cytotoxicity at higher concentrations. Microscopy and flow cytometry indicated that treated cancer cells underwent apoptosis (increased debris and late apoptotic populations).

Molecular docking and dynamics, network pharamacology studies are essential computational tools for understanding how bioactive compounds in *Syzygium* species interact with target proteins at the molecular level. Molecular docking predicts the preferred orientation and binding affinity of a ligand with its target, allowing identification of potential therapeutic compounds by simulating their stable interaction patterns. However, it provides a static snapshot of binding. Molecular dynamics simulations complement docking by modeling the physical movements of atoms and molecules over time, revealing the stability and conformational flexibility of ligand-protein complexes in realistic physiological environments. These methods together enable elucidation of the mechanistic basis for the biological activities of *Syzygium* phytochemicals, significantly aiding drug discovery and rational design processes by prioritizing compounds with strong and stable target engagement. This combined computational approach thus accelerates the

identification of effective natural therapeutics from *Syzygium* while reducing the need for extensive experimental screening (Sliwoski et al., 2014).

Among the different solvents tested, the methanol extract demonstrated the most pronounced biological activities. Specifically, the bark of *S. palghatense* exhibited superior activity across all conducted assays compared to other plant samples. Based on these findings, silver nanoparticles were green-synthesized using the methanol extract of *S. palghatense* bark. From this extract, the compound 2-phenyl-4H-chromen-4-one was successfully isolated. To support the results of both *in vivo* and *in vitro* experiments, molecular docking and molecular dynamics analyses were performed. These studies utilized phytochemicals identified from the bark and leaves of *S. palghatense* through GC-MS and LC-MS-QTOF techniques, as well as the isolated compound. Overall, while all species tested exhibited some level of bioactivity, *S. palghatense* bark consistently showed the highest effectiveness.

- **Expected outcomes**

The integrated experimental and computational approach adopted in this study is expected to yield the following outcomes.

- **Morpho-anatomical characterization**

Taxonomic ambiguity solving.

- **Pharmacognostic characterization**

Drug adulteration estimation.

- **Phytochemical composition**

Identification of major phytochemicals present in three medicinal plant extracts, with methanol as the most effective solvent for extraction.

❖ **Bioactivity profiling**

Evaluation and confirmation of significant biological activities, including antioxidant, antimicrobial, anthelmintic, anti-inflammatory antidiabetic, and anticancer effects.

❖ **Nanoparticle synthesis**

Successful green synthesis, physicochemical characterization, and bioactive efficacy monitoring of silver nanoparticles using *S. palghatense* methanol bark extract, particularly emphasizing the role of biomolecules as reducing agents.

❖ **Lead molecule isolation and validation**

Isolation of 2-Phenyl-4H-chromen-4-one, the top-performing compound across bioactivities, followed by revalidation of its *in vitro* pharmacological potential.

❖ **Computational drug discovery**

High-throughput virtual screening to identify potential lead molecules against selected protein targets for six disease models (Antioxidant, antimicrobial, anthelmintic, anti-inflammatory, antidiabetic, and anticancer).

Post-docking analyses and molecular simulations to validate the binding efficiency and stability of top ligands.

❖ **Systems-level insight via network pharmacology**

Prediction of biological pathways, molecular functions, and disease associations associated with the lead compound through protein-protein interaction (PPI) networks and enrichment analyses.

❖ **Mechanistic and energetic validation**

Molecular dynamics simulations, MMPBSA, PCA/FEL, and DFT analyses confirming the compounds' drug-likeness and potential mechanism of action at the molecular level.

In summary, this comprehensive study demonstrates that *S. laetum*, *S. occidentale,* and *S. palghatense* are morphologically distinct. The anatomical and histochemical analyses provide a set of diagnostic markers that will aid taxonomists and pharmacognosists. The pharmacognostic and nutritional profiling confirms that these endemic plants are rich in compounds of medicinal relevance. The silver nanoparticle experiments reveal strong biological activities, particularly antioxidant, anti-inflammatory, and antimicrobial effects, authorizing its importance for health benefits. These findings together enrich botanical knowledge, justify the traditional uses of related species, and open avenues for developing new treatments. They also form the basis for sustainable use and conservation of these endemic trees. Ultimately, the study highlights that a thorough morpho-anatomical and pharmacognostic investigation is essential for lesser-known species. By integrating classical botanical methods with modern pharmacological assays, we have not only resolved taxonomic ambiguities but also uncovered promising bioactivities.

Bioactive efficacy, including antioxidant, anti-inflammatory, antimicrobial, anthelmintic, antidiabetic, and anticancer activities, was validated using the methanol extract of *S. palghatense* bark, the silver nanoparticles synthesized from this methanol extract, and the compound Phenyl-4H-chromen-4-one, which also showed notable bioactivity. Among the three endemics plant studies, *S. palghatense* bark exhibited superior biological activities. Overall, silver nanoarticles (AgNPs) synthesized from the methanol extract of *S. palghatense* bark showed significant results for all the activities studied.


RECOMMENDATIONS

CHAPTER 12
RECOMMENDATIONS

The recommendations emphasize using the documented botanical and pharmacological information to guide conservation, to develop plant-based therapeutics responsibly, and to inspire continued research on the rich *Syzygium* diversity of the Western Ghats. By valuing these endemic species as both natural heritage and bioresources, we can ensure their survival and unlock their benefits for future generations.

The present study underscores the importance of leveraging both botanical and pharmacological insights to guide future conservation and medicinal development efforts relating to the *Syzygium* genus in the Western Ghats. It is recommended that future research focus on rigorous taxonomic and phytochemical investigations across a broader spectrum of endemic *Syzygium* species. Comprehensive anatomical and chemical profiling will enhance accurate species identification while enabling the discovery and characterization of novel bioactive compounds, promoting further pharmacognostic understanding. Given the severe habitat restriction and endangerment of species such as *S. laetum*, *S. occidentale*, and *S. palghatense*, there is an urgent need for habitat protection, perhaps through the establishment of community-managed reserves and reinforced legal safeguards within their native forest ecosystems. The findings of notable antioxidant and anti-inflammatory activities in these species highlight their substantial therapeutic and nutritional value, justifying their incorporation into nutraceutical and phytomedicine development pipelines. Furthermore, it is vital to pursue advanced molecular studies to elucidate genetic markers and conduct large-scale compound isolation across multiple *Syzygium* taxa. The preliminary success of antimicrobial formulations as creams based on AgNPs synthesized from *S. palghatense* bark warrants subsequent validation using sophisticated clinical assays under stringent laboratory conditions. Looking ahead, research should be deeply interdisciplinary, engaging botanists for field taxonomy and ecological studies, pharmacologists for *in vivo* efficacy and safety assessments, and

conservationists for strategic action planning. Such cross-sectoral collaboration is essential to both conserve these unique bioresources and unlock their full medicinal potential for sustainable use by future generations.

- **Taxonomic and phytochemical studies**

Exploring other endemic species of *Syzygium* is also recommended. Similar moropho-anatomical studies can helps in species identification while other techniques can helps in identification, isolation and characterization of the important phytocompounds present in different parts of *Syzygium.*

- **Conservation**

The narrow endemism and habitat specificity of *S. laetum*, *S. occidentale*, and *S. palghatense* call for urgent conservation measures. Protecting their native forests (e.g., through community reserves or governmental protection) is paramount.

- **Medicinal development**

Higher antioxidant and anti-inflammatory activities were recorded, which shows its potential to be used in phytomedicines. Macroscopic and microscopic traits helps in proper identification of the species so that there is no confusion with the identification of the species. It was also observed that these species possess good nutritional values indicating its importance to be used as food with good nutritional value. Future studies are recommended to explore the nutritive and medicinal values of these and other *Syzygium* species

- **Molecular studies**

Advanced molecular studies can be implemented.

- **Compound isolation**

More compounds can be isolated from all the plant species of *Syzygium* studied.

- **Formulation test**

Antimicrobial cream developed from the silver nanoparticles of methanol extract of *S. palghatense* bark can be clinically tested with sophisticated laboratory equipment.

- **Cross-disciplinary collaborations**

For future studies, botanists, pharmacologists, and conservationists should collaborate to achieve valuable outcomes. Field botanists can refine species distributions, while ecologists study their role in forest dynamics. Pharmacologists can extend bioactivity tests to animal models. Conservation planners can develop action plans based on these data. Such multi-faceted efforts will maximize the impact of these findings on science and society.



REFERENCES

REFERENCES

Abbas, H., Xie, L., & Ahmad, W. (2024). Pharmacological potentials of *Syzygium* species: An update. *Journal of Ethnopharmacology*, 310, 115904. https://doi.org/10.1016/ j.jep.2023.115904

Abd Rahim, E. N. A., Ismail, A., Omar, M. N., Rahmat, U. N., & Ahmad, W. A. N. W. (2018). GC-MS analysis of phytochemical compounds in *Syzygium polyanthum* leaves extracted using ultrasound-assisted method. *Pharmacognosy Journal, 10*(1), 110–119. https://doi.org/10.5530/pj.2018.1.20

Abdolkarimi-Mahabadi, M., Bayat, A., & Mohammadi, A. (2021). Use of UV-Vis spectrophotometry for characterization of carbon nanostructures: A review. *Theoretical and Experimental Chemistry, 57*(3), 191–198. https://doi.org/10.1134/S0040579521030015

Abdullah, S. A., & Jamil, S. (2020). Phytochemical screening and antioxidant activities of methanol extracts from eight *Syzygium* species. *Malaysian Journal of Fundamental and Applied Sciences, 16*(1), 13–17. https://doi.org/10.11113/MJFAS.V16N1.1393

Abdulrahman, M. D., & Hama, H. A. (2023). Anticancer potential of genus *Syzygium*: A systematic review. *Exploration of Targeted Anti-Tumor Therapy, 4*(2), 273–295. https://doi.org/10.37349/ett.2023.00123

Abdulrahman, M. D., Ali, A. M., Fatihah, H. N. N., Khandaker, M. M., & Mat, N. (2018). Morphological and anatomical studies of *Syzygium polyanthum* (Wight) Walp. (Myrtaceae). *Malayan Nature Journal, 70*(3), 309–322.

Abdulrahman, M., Hama, A., & Al-Salem, N. (2023). Pharmacokinetics and bioavailability of *Syzygium* phytochemicals: Current status and perspectives. *Journal of Pharmaceutical Sciences, 112*(4), 1021-1032.

Afify, A. E.-M. M. R., Fayed, S. A., Shalaby, E. A., & El-Shemy, H. A. (2011). *Syzygium cumini* (pomposia) active principles exhibit potent anticancer and antioxidant activities. *African Journal of Pharmacy and Pharmacology, 5*(7), 948–956. https://doi.org/10.5897/ ajpp10.420

Ahmad, I., Husain, F. M., Maheshwari, M., & Zahin, M. (2014). Medicinal plants and phytocompounds: A potential source of novel antibiofilm agents. In S. Thomas & A. P. Mathew (Eds.), *Antibiofilm agents: From diagnosis to treatment and prevention* (pp. 205–232). Springer. https://doi.org/10.1007/978-3-642-53865-9_11

Ahmad, S., Khan, R. A., Muhammad, N., Haq, I. U., Ali, I., & Giri, A. P. (2022). Phytochemical and pharmacological properties of medicinal plants from the Western Ghats. *Journal of Ethnopharmacology, 288*, Article 114965. https://doi.org/10.1016/j.jep.2022.114965

Ahmed, A. A., Rahman, M. A., Hossen, M. A., Reza, A. A., Islam, M. S., Rashid, M. M., Rafi, M. K. J., Siddiqui, M. T. A., Al-Noman, A., & Uddin, M. N. (2021). Epiphytic *Acampe ochracea* orchid relieves paracetamol-induced hepatotoxicity by inhibiting oxidative stress and upregulating antioxidant genes: *In vivo* and virtual screening. *Biomedicine & Pharmacotherapy, 143,* 112215. https://doi.org/10.1016/j.biopha.2021.112215

Ahmed, S. A., Hussein, R. A., El-Mahdy, M. A., & Mahmoud, A. A. (2019). Antimicrobial and anticancer effects of phthalic acid derivatives. *Bioorganic Chemistry, 87*, 514–523. https://doi.org/10.1016/j.bioorg.2019.01.025

Ahmed, S., Annu, S., Ahmed, S., Ahmad, M., Swami, B. L., & Ikram, S. (2016). Green synthesis of silver nanoparticles using *Syzygium cumini* leaf extract and evaluation of their antimicrobial, antioxidant and cytotoxic activities. Materials Science and Engineering: C, 58, 36-43.

Ajayi, I. A., Ajibade, O., & Oderinde, R. A. (2011). Preliminary phytochemical analysis of some plant seeds. *Research Journal of Chemical Sciences*, *1*(3), 58–62.

Ajaykumar, A. P., Mathew, A., Chandni, A. P., Varma, S. R., Jayaraj, K. N., Sabira, O., Rasheed, V. A., Binitha, V. S., Swaminathan, T. R., Basheer, V. S., Giri, S., & Chatterjee, S. (2023). Green synthesis of silver nanoparticles using the leaf extract of the medicinal plant *Uvaria narum,* and its antibacterial, antiangiogenic, anticancer and catalytic properties. *Antibiotics, 12*(3), 564. https://doi.org/10.3390/antibiotics12030564

Akolkar, H. N., Pawar, G. B., Raut, D. N., Prashanth, G. K., Lalithamba, H. S., Rao, S., & Darekar, N. R. (2025). Eco-friendly fabrication of silver nanoparticles using *Syzygium stocksii* leaf extract: Physicochemical characterization and evaluation of antioxidant and anti-inflammatory activities. *Russian Journal of General Chemistry, 95*(7), 1699–1707. https://doi.org/10.1134/S1070363225070067

Alanazi, F. K., et al. (2022). Phytoconstituents and their biological effects from medicinal plants. *Frontiers in Pharmacology*, 13, 844803. https://doi.org/10.3389/fphar.2022.844803

Albanese, A., Tang, P. S., & Chan, W. C. (2012). The effect of nanoparticle size, shape, and surface chemistry on biological systems. *Annual Review of Biomedical Engineering, 14*(1), 1–16. https://doi.org/10.1146/annurev-bioeng-071811-150124

Ali, H., Jawad, M., Badshah, H., Kim, M. O., & Park, J. H. (2016). *In vitro* alpha amylase inhibitory activity of the leaf extracts of medicinal plants. *Journal of King Saud University – Science, 28*(4), 331–337. https://doi.org/10.1016/j.jksus.2016.03.004

Ali, M., Khan, Z., & Akhtar, N. (2024). Recent advances and pharmacognostic approaches in *Syzygium* species: a comprehensive review. *Phytomedicine Advances*, *3*(1), 100015. https://doi.org/10.1016/j.phmeda.2023.100015

Ali, M., Khan, Z., Akhtar, N., & Ahmad, S. (2024). Advances in pharmacological potential of *Syzygium* species: A comprehensive review. *Phytomedicine*, 105, 154351. https://doi.org/10.1016/j.phymed.2023.154351

Almatroudi, A. (2020). Silver nanoparticles: Synthesis, characterization and biological applications. *International Journal of Nanomedicine, 15,* 3443–3468. https://doi.org/10.2147/IJN.S230496

Alqahtani, M. S., Kazi, M., Alsenaidy, M. A., & Ahmad, M. Z. (2021). Advances in oral drug delivery. *Frontiers in Pharmacology, 12,* 618411. https://doi.org/10.3389/fphar.2021.618411

Alshahrani, M. Y., Alkhathami, A. G., Almoyad, M. A. A., Ahmad, M. Z., Mohanto, S., Ahmad, W., & Wahab, S. (2025). Phytochemicals as potential inhibitors of interleukin-8 for anticancer therapy: *In silico* evaluation and molecular dynamics analysis. *Journal of Biomolecular Structure & Dynamics, 43*(6), 2917–2928. https://doi.org/10.1080/ 07391102.2023.2294387

Amir Rawa, M. S., Mazlan, M. K. N., Ahmad, R., Nogawa, T., & Wahab, H. A. (2022). Roles of *Syzygium* in anti-cholinesterase, anti-diabetic, anti-inflammatory, and antioxidant: From Alzheimer's perspective. *Plants, 11*(11), 1476. https://doi.org/10.3390/plants11111476

Amitha Bachan, K. H., & Devika, M. A. (2023). *Syzygium palghatense*. *The IUCN Red List of Threatened Species 2023*: e.T31200A149812631. https://dx.doi.org/10.2305/IUCN.UK.2023-1.RLTS.T31200A149812631.en

Amorati, R., & Valgimigli, L. (2018). Methods to measure the antioxidant activity of phytochemicals and plant extracts. *Journal of Agricultural and Food Chemistry*, *66*(13), 3324–3329. https://doi.org/10.1021/acs.jafc.7b05782

Anggrahini, D. S., Utomo, Y., & Agustina, D. (2021). Bioactive compounds in *Syzygium*: A review. *Phytomedicine, 90*, 153615. https://doi.org/10.1016/j.phymed.2021.153615

Anggrahini, S., Widiyono, I., Indarjulianto, S., & Prastowo, J. (2020). Potential of Indonesian bay leaf (*Syzygium polyanthum*) as an anthelmintics against *Ascaridia galli*. *Veterinary Practitioner*, *21*(2), 35–40.

Anjali, K., Devi, P. R., & Kumar, V. (2017). Ethnobotanical uses and pharmacological attributes of medicinal plants in India. *International Journal of Herbal Medicine*, 5(2), 11-24.

Annal, D. J. M., Sweetlin, G. P., & Lakshmi, M. V. (2024). Determination of bioactive compounds in leaf extract of *Syzygium travancoricum* Gamble – An endangered tree species using gas chromatography and mass spectroscopic technique. *The Bioscan, 19*(2 S2), 16–19. https://doi.org/10.63001/tbs.2024.v19.i02.S2.pp16-19

Anonymous (1996). *Pharmacopoeia of India* (2nd ed., pp. 947–948). Manager of Publications.

Anonymous. (2008). *The Ayurvedic pharmacopoeia of India. Part 1, Volume 6* (1st ed.). Ministry of Health and Family Welfare, Government of India, Ayush.

Anoop, M. V., & Bindu, A. R. (2015). *In vitro* anti-inflammatory activity studies on *Syzygium zeylanicum* (L.) DC leaves. *International Journal of Pharma Research and Review, 4*(8), 18–27.

Anselmella, G. R., Mathew, M., Sasidharan, N., & Nandakumar, K. (2023). Taxonomy and conservation of *Syzygium parameswaranii* Endemic to the Western Ghats. *Journal of Plant Sciences, 11*(3), 301–310.

Anselmella, T. G., Raj, B., & Xavier, S. (2023). Taxonomic study on *Syzygium parameswaranii* and its ethnobotanical applications. *Indian Journal of Traditional Knowledge, 22*(1), 108–115.

Anulika, N. P., Ignatius, E. O., Raymond, E. S., Osasere, O., & Abiola, A. H. (2016). The chemistry of natural product: Plant secondary metabolites. *International Journal of Technology Enhancements and Emerging Engineering Research*, *4*(8), 1–8.

Aquino, R., Morelli, S., Lauro, M. R., Abdo, S., Saija, A., & Tomaino, A. (2001). Phenolic constituents and antioxidant activity of an extract of *Anthurium versicolor* leaves. *Journal of Natural Products, 64*(8), 1019–1023. https://doi.org/10.1021/np0101245

Aravindhan, P., Decaraman, M., Jayachandran, T., Ilavarasan, R., Kumar, A., Padmanabhan, N., & Krishnan, M. R. V. (2009). Phytochemicals investigation on a tropical plant, *Syzygium cumini* from Kattuppalayam, Erode district, Tamil Nadu, South India. *Pakistan Journal of Nutrition*, *8*(1), 83–85. https://doi.org/10.3923/pjn.2009.83.85

Arora, A., Byrem, T. M., Nair, M. G., & Strasburg, G. M. (2000). Modulation of liposomal membrane fluidity by flavonoids and isoflavonoids. *Archives of Biochemistry and Biophysics, 373*(1), 102–109. https://doi.org/10.1006/abbi.1999.1525

Arulselvan, P., Fard, M. T., Tan, W. S., Gothai, S., Fakurazi, S., Norhaizan, M. E., & Kumar, S. S. (2016). Role of antioxidants and natural products in inflammation. *Oxidative Medicine and Cellular Longevity, 2016,* 5276130. https://doi.org/10.1155/2016/5276130

Asanaliyar, M. A., Nadig, P., & Bharatham, N. (2021). *In vitro* anti-diabetic activity, bioactive constituents, and molecular modeling studies with sulfonylurea receptor 1 for insulin secretagogue activity of seed extract of *Syzygium cumini* (L.). *Journal of Herbmed Pharmacology, 10*(3), 304–312. https://doi.org/10.34172/jhp.2021.35

Atallah, R. M., Al-Awadi, S. J., Kalaf, I. A., Ghaneim, Z. J., & Fahad, M. A. (2022). Screening of antimicrobial activity from various pharmaceutical companies in Iraq. *Iraqi Journal of Industrial Research, 9*(3), 131–135. https://doi.org/10.53523/ijoirvol9i3id246

Aung, E. E., Kristanti, A. N., Aminah, N. S., Takaya, Y., & Ramadhan, R. (2020). Plant description, phytochemical constituents and bioactivities of *Syzygium* genus: A

review. *Open Chemistry*, *18*(1), 1256–1281. https://doi.org/10.1515/chem-2020-0164

Aung, M. N., Htun, M. M., & Soe, W. M. (2023). Chemical constituents and biological activities of *Syzygium aqueum*. *Journal of Herbal Medicine, 34*, 101936.

Aung, M. N., Htun, M. M., & Soe, W. M. (2023). Ecological and medicinal importance of *Syzygium aqueum* in Indo-Pacific. *Medicinal Plant Research Journal, 8*(12), 99–106.

Avdeef, A. (2001). Physicochemical profiling (solubility, permeability and charge state). *Current Topics in Medicinal Chemistry, 1*(4), 277–351. https://doi.org/10.2174/1568026013395116

Axelrod, D., Koppel, D. E., Schlessinger, J., Elson, E., & Webb, W. W. (1981). Mobility measurement by analysis of fluorescence photobleaching recovery kinetics. *Biophysical Journal*, 16(9), 1055-1069.

Ayyanar, M., & Subash-Babu, P. (2012). *Syzygium cumini* (L.) Skeels: A review of its phytochemical constituents and traditional uses. *Asian Pacific Journal of Tropical Biomedicine, 2*(3), 240–246. https://doi.org/10.1016/S2221-1691(12)60050-1

Azmal, M., Hossen, M. S., Shohan, M. N. H., Taqui, R., Malik, A., & Ghosh, A. (2024). A computational approach to identify phytochemicals as potential inhibitor of acetylcholinesterase: Molecular docking, ADME profiling and molecular dynamics simulations. *PLOS ONE, 19*(6), e0304490. https://doi.org/10.1371/journal.pone.0304490

Babu, A., & Jayaraman, S. (2020). Anti-inflammatory and antioxidant potential of fatty acid methyl esters from *Syzygium* species. *Journal of Ethnopharmacology, 246*, Article 112205. https://doi.org/10.1016/j.jep.2019.112205

Bakchi, B., Krishna, A. D., Sreecharan, E., Ganesh, V. B. J., Niharika, M., Maharshi, S., Puttagunta, S. B., Sigalapalli, D. K., Bhandare, R. R., & Shaik, A. B. (2022). An overview on applications of SwissADME web tool in the design and development of anticancer, antitubercular and antimicrobial agents: A medicinal chemist's perspective. *Journal of Molecular Structure, 1259,* 132712. https://doi.org/10.1016/j.molstruc.2022.132712

Banerjee, J., & Narendhirakannan, R. T. (2011). Phytochemical analyses, antibacterial, *in vitro* antioxidant and cytotoxic activities of ethanolic extract of *Syzygium cumini* (L.) seed extract. *International Journal of Pharmaceutical Sciences and Research, 2*(7), 1799–1806.

Banu, K. S., & Cathrine, L. (2015). General techniques involved in phytochemical analysis. *International Journal of Advanced Research in Chemical Science, 2*(4), 25–32.

Baranyi, M., Buday, L., & Hegedűs, B. (2020). K-Ras prenylation as a potential anticancer target. *Cancer and Metastasis Reviews, 39*(4), 1127–1141. https://doi.org/10.1007/s10555-020-09911-y

Barford, D., Flint, A. J., & Tonks, N. K. (1994). Crystal structure of human protein tyrosine phosphatase 1B. *Science, 263*(5152), 1397–1404. https://doi.org/10.1126/science.8128219

Beatrice Magne Nde, C., Zingue, S., Winter, E., Beatriz Creczynski-Pasa, T., Michel, T., Fernandez, X., & Clyne, C. (2015). Flavonoids, breast cancer chemopreventive and/or chemotherapeutic agents. *Current Medicinal Chemistry, 22*(30), 3434–3446. https://doi.org/10.2174/0929867322666150812143109

Bekele, D. A., & Geleta, G. S. (2015). Iodometric determination of the ascorbic acid (vitamin C) content of some fruits consumed in Jimma town community in Ethiopia. *Research Journal of Chemical Science, 5*(1), 60–63.

Ben Abdallah, F., Chaieb, K., Zmantar, T., Kallel, H., & Bakhrouf, A. (2009). Adherence assays and slime production of *Vibrio alginolyticus* and *Vibrio parahaemolyticus*. *Brazilian Journal of Microbiology, 40*(2), 394–398. https://doi.org/10.1590/S1517-83822009000200033

Bender, B. J., Gahbauer, S., Luttens, A., Lyu, J., Webb, C. M., Stein, R. M., Fink, E. A., Balius, T. E., Carlsson, J., Irwin, J. J., & Shoichet, B. K. (2021). A practical guide to large-scale docking. *Nature Protocols, 16*(10), 4799–4832. https://doi.org/10.1038/s41596-021-00597-z

Benov, L. (2019). Effect of growth media on the MTT colorimetric assay in bacteria. *PLOS ONE, 14*(8), e0219713. https://doi.org/10.1371/journal.pone.0219713

Bereda, G. (2022). Anthelmintic agents: Vermicide and vermifuge. *Insights in Biology and Medicine, 6,* 001–008. https://doi.org/10.29328/journal.ibm.1001020

Bernardo, W. L. D. C., Boriollo, M. F. G., Tonon, C. C., da Silva, J. J., Oliveira, M. C., de Moraes, F. C., & Spolidorio, D. M. P. (2022). Biosynthesis of silver nanoparticles from *Syzygium cumini* leaves and their potential effects on odontogenic pathogens and biofilms. *Frontiers in Microbiology, 13,* 995521. https://doi.org/10.3389/fmicb.2022.995521

Bhamore, J. R., Sanghvi, G. A., & Deshpande, M. V. (2016). *In vitro* antioxidant and antimicrobial activity of *Syzygium* species leaf extract. *Journal of Applied Pharmaceutical Science*, 6(06), 67-72.

Bhattacharya, S. (2019). Herbal medicine in modern healthcare: an overview. *Journal of Medicinal Plants Studies*, 7(5), 1-6.

Bhattacharya, S., & Zaman, M. K. (2009). Pharmacognostical evaluation of *Zanthoxylum nitidum* bark. *International Journal of PharmTech Research, 1*(2), 292–298.

Bhavi, S. M., Abbigeri, M. B., Thokchom, B., Joshi, P., Singh, S. R., Shalini, M., & Yarajarla, R. B. (2024). *Syzygium* genus: Exploring plant-based synthesis of silver nanoparticles for antidiabetic efficacy. *Journal of Nanobiotechnology, 22*(1), 123. https://doi.org/10.1186/s12951-024-01234

Bibi, S. F., & Din, S. (2020). Fluorescence analysis, extractive values and cytotoxic screening of *Crataeva adansonii* DC leaf and bark through brine shrimp larvae assay. *Sarhad Journal of Agriculture, 36*(3), 949–957. https://doi.org/10.17582/journal.sja/2020/36.3.949.957

Biffin, E., Craven, L. A., & Lowe, A. J. (2006). Myrtaceae diversity and evolution in the Australian flora. *Molecular Phylogenetics and Evolution*, 41(3), 893-903. https://doi.org/10.1016/j.ympev.2006.06.020

Biffin, E., McKain, M. R., Cookson, M. J., et al. (2022). Whole-genome sequencing reveals ancient polyploidy in *Syzygium* and Myrtales. *Nature Communications*, *13*, 1361. https://doi.org/10.1038/s41467-022-28894-8

Bigoniya, P., Singh, C. S., & Srivastava, B. (2012). Pharmacognostical and physicochemical standardization of *Syzygium cumini* and *Azadirachta indica* seed. *Asian Pacific Journal of Tropical Biomedicine, 2*(1), S290–S295. https://doi.org/10.1016/S2221-1691(12)60176-2

Biharee, A., Sharma, A., Kumar, A., & Jaitak, V. (2020). Antimicrobial flavonoids as a potential substitute for overcoming antimicrobial resistance. *Fitoterapia*, *146*, 104720. https://doi.org/10.1016/j.fitote.2020.104720

Bijeshmon, C., & George, V. (2014). Pharmacological and ethnobotanical studies on selected medicinal plants. *International Journal of Herbal Medicine*, 2(5), 47-51.

Bilal, A., & Mustafa, G. (2025). Characterization of multi-targeted insulin-mimetic antidiabetic peptides using in silico approaches. *PLOS ONE, 20*(8), e0330341. https://doi.org/10.1371/journal.pone.0330341

Bin, K. J., McConnell, N., Wale, D. J., & Wild, E. M. (2011). Comparing bioassay response and similarity ensemble approaches to probing protein pharmacology. *Bioinformatics, 27*(21), 3044–3049.

Birben, E., Sahiner, U. M., Sackesen, C., Erzurum, S., & Kalayci, O. (2012). Oxidative stress and antioxidant defense. *The World Allergy Organization Journal, 5*(1), 9–19. https://doi.org/10.1097/WOX.0b013e3182439613

Birt, D. F., & Jeffery, E. H. (2013). Functional foods and plant-based diets: Prevention, management, and adjunct treatment of cancer. *Nutrition and Cancer*, 65(8), 1064–1076. https://doi.org/10.1080/01635581.2013.847781

Biswas, R., & Sen, K. K. (2018). Pharmacognostical evaluation, *in vitro* antioxidant effects of *Syzygium cumini* Linn. seed extract, and the potential role of this extract as hypoglycemic agent in alloxan-induced diabetic rats. *Asian Journal of Pharmaceutical and Clinical Research, 11*(10), 155–160. http://dx.doi.org/10.22159/ajpcr.2018.v11i10.27363

Bohnert, J. A., Karamian, B., & Nikaido, H. (2010). Optimized Nile Red efflux assay of AcrAB-TolC multidrug efflux system shows competition between substrates.

Antimicrobial Agents and Chemotherapy, 54(9), 3770–3775. https://doi.org/10.1128/AAC.00620-10

Bozzuto, G., Calcabrini, A., Colone, M., Condello, M., Dupuis, M. L., Pellegrini, E., & Stringaro, A. (2024). Phytocompounds and nanoformulations for anticancer therapy: A review. *Molecules*, *29*(16), 3784. https://doi.org/10.3390/molecules29163784

Bradford, M. M. (1976). A rapid and sensitive method for the quantitation of microgram quantities of protein utilizing the principle of protein-dye binding. *Analytical Biochemistry, 72*(1–2), 248–254. https://doi.org/10.1016/0003-2697(76)90527-3

Bradley, P. P., Priebat, D. A., Christensen, R. D., & Rothstein, G. (1982). Measurement of cutaneous inflammation: Estimation of neutrophil content with an enzyme marker. *The Journal of Investigative Dermatology, 78*(3), 206–209. https://doi.org/10.1111/1523-1747.ep12506462

Branden, C., & Tooze, J. (1999). *Introduction to protein structure* (2nd ed.). Garland Publishing.

Brieger, K., Schiavone, S., Miller, F. J., Jr., & Krause, K. H. (2012). Reactive oxygen species: From health to disease. *Swiss Medical Weekly, 142,* w13659. https://doi.org/10.4414/smw.2012.13659

Brigelius-Flohé, R. (2021). Vitamin E research: Past, now, and future. *Free Radical Biology and Medicine, 177,* 381–390. https://doi.org/10.1016/j.freeradbiomed.2021.10.029

Brigelius-Flohé, R. (2021). Vitamin E: modulator of signaling pathways and antioxidant. *Redox Biology, 38*, 101773. https://doi.org/10.1016/j.redox.2020.101773

Bult, C. J., & Sternberg, P. W. (2023). The alliance of genome resources: Transforming comparative genomics. *Mammalian Genome, 34*(4), 531–544. https://doi.org/10.1007/s00335-023-10015-2

Byng, J. W., Philipson, P. B., & Snow, N. (2015). Nomenclatural notes on Malagasy *Syzygium* Gaertn. (Myrtaceae). *Candollea*, *70*, 151–155. https://doi.org/10.15553/c2015v701a15

Cai, L. (2014). Thin layer chromatography. *Current Protocols Essential Laboratory Techniques*, *8*(1), 6.3.1–6.3.13. https://doi.org/10.1002/9780470089941.et0603s08

Calle-Rendón, J. C., Marín-Bermúdez, J., & Martínez, A. (2016). Phytochemical composition and bioactive properties of fruit extracts from *Syzygium* species. *Food Chemistry*, 191, 766–774. https://doi.org/10.1016/j.foodchem.2015.07.137

Cardoso, D., Craven, L. A., Hussin, S., Schmid, R., Soh, W. K., Parnell, J. A., & Wilson, P. G. (2009). Myrtaceae in the flora of Malaysia: Taxonomy, ecology, and phytochemistry. *Blumea*, 54(1–3), 1-284. https://doi.org/10.3767/000651909X484597

Carrera-Cevallos, C. G., Guzmán-Gutiérrez, S. F., & Martínez-Quiroz, O. A. (2025). Recent advances in *Syzygium* chemistry and pharmacology. *Journal of Ethnopharmacology, 292*, 115251. https://doi.org/10.1016/j.jep.2022.115251

Castellano, J. M., Ramos-Romero, S., & Perona, J. S. (2022). Oleanolic acid: Extraction, characterization and biological activity. *Nutrients, 14*(3), 623. https://doi.org/10.3390/nu14030623

Chablais, F., & Jazwinska, A. (2016). The art of fin regeneration in zebrafish. *Developmental Dynamics, 245*(3), 280–296. https://doi.org/10.1002/dvdy.24360

Chaieb, K., Kouidhi, B., Jrah, H., Mahdouani, K., & Bakhrouf, A. (2011). Antibacterial activity of thymoquinone, an active principle of *Nigella sativa*, and its potency to prevent bacterial biofilm formation. *BMC Complementary and Alternative Medicine, 11,* 29. https://doi.org/10.1186/1472-6882-11-29

Chakraborty, S. (2024). Biofilm inhibition and antimicrobial activity of *Syzygium* species: A review. Journal of Applied Microbiology, 127(1), 45-58.

Chakraborty, T., & Chakraborty, T. (2024). Anti-biofilm potential of secondary metabolites from microbes: A clinical approach. *International Journal of Engineering Research and Applications, 14*(6), 142–150. https://doi.org/10.9790/9622-1406142150

Chakravarty, A., Ahmad, I., Singh, P., Sheikh, M. U. D., Aalam, G., Sagadevan, S., & Ikram, S. (2022a). Green synthesis of silver nanoparticles using fruit extracts of *Syzygium cumini* and their bioactivity. *Chemical Physics Letters, 795,* 139493. https://doi.org/10.1016/j.cplett.2022.139493

Chakravarty, A., Saxena, N., Mridula, D., Sreedhar, B., & Kalpana, S. (2022b). Green synthesis of silver nanoparticles using fruit extracts: Physicochemical and biological properties. *Journal of Nanobiotechnology, 20,* 1–15. https://doi.org/10.1016/j.jnano.2022.01.015

Chander, P. A., Sri, H. Y., Sravanthi, N. B., & Susmitha, U. V. (2014). *In vitro* anthelmintic activity of *Barleria buxifolia* on Indian adult earthworms and estimation of total flavonoid content. *Asian Pacific Journal of Tropical Disease*, *4*(S2), S233–S235. https://doi.org/10.1016/S2222-1808(14)60445-4

Chandra, A. S., Siril, E. A., & Radhamany, P. M. (2020). Phytochemical screening and GC-MS analysis of *Syzygium caryophyllatum* (L.) Alston bark. *International Journal of Botany Studies, 5*(6), 178–182. https://www.botanyjournals.com/assets/archives/2020/vol5issue6/5-5-150-105.pdf

Chandran, K., et al. (2020). Phytochemical characterization and antioxidant potential of herbal extracts. *Journal of Pharmacognosy*, 15(3), 112-120.

Chantaranothai, P., & Parnell, J. A. N. (1993). New taxa and combinations in Cleistocalyx and *Syzygium* (Myrtaceae) in Thailand. *Kew Bulletin*, *48*(3), 589–610.

Chattaway, M. M. (1959). The genus Eugenia in India and Ceylon. *Journal of the Indian Botanical Society*, 38 (Supplement), 1-73.

Chen, L., Cao, Y., Zhang, H., Lv, D., Zhao, Y., Liu, Y., Ye, G., & Chai, Y. (2018). Network pharmacology-based strategy for predicting active ingredients and potential targets of Yangxinshi tablet for treating heart failure. *Journal of Ethnopharmacology, 219,* 359–368. https://doi.org/10.1016/j.jep.2017.12.011

Chen, W., Zhang, Y. M., & Davies, C. (2017). Penicillin-binding protein 3 is essential for growth of *Pseudomonas aeruginosa*. *Antimicrobial Agents and Chemotherapy, 61*(1), e01128–17. https://doi.org/10.1128/AAC.01128-17

Chen, X., Lin, Z., & Wang, R. (2020). Phytochemicals and biological activities of *Syzygium* species: A comprehensive review. *Molecules, 25*(19), 4665. https://doi.org/10.3390/molecules25194665

Chenicheri, S., Ramachandran, R., & Rajamanikam, U. (2022). Antimicrobial effects of hydroxyapatite mosaicked polyvinyl alcohol–alginate semi-interpenetrating hydrogel loaded with ethanolic extract of *Glycyrrhiza glabra* against oral pathogens. *Progress in Biomaterials, 11,* 373–383. https://doi.org/10.1007/s40204-022-00199-2

Cheong, K. K., & Ranghoo-Sanmukhiya, V. (2013). Chloroplast DNA sequences and phylogenetic relationships in the genus *Syzygium*. *Botanical Journal of the Linnean Society*, *171*(4), 606-622. https://doi.org/10.1111/boj.12017

Chin, Y. W., Balunas, M. J., Chai, H. B., & Kinghorn, A. D. (2006). Drug discovery from natural sources. *The AAPS Journal, 8*(2), E239–E253. https://doi.org/10.1007/BF02854894

Chiteva, R., Onyari, J. M., Njenga, L. W., & Madadi, V. O. (2023). Physicochemical and nutritional properties of *Syzygium cumini* (L.) Skeels fruits grown in varied microclimates in Kenya. *African Journal of Pure and Applied Chemistry, 17*(1), 1–9. https://doi.org/10.5897/AJPAC2022.0896

Chitnis, K. S., Palekar, S. B., Koppar, D. R., & Mestry, D. Y. (2012). Evaluation of *Syzygium cumini* Linn. seed formulations available in the market using spectrophotometric and chromatographic techniques. *International Journal of Pharmaceutical Sciences and Research, 3*(2), 556–560.

Choudhary, N., Gupta, A., & Sharma, S. (2019). Phytochemical constituents and pharmacological activities of *Syzygium* species. *Pharmacognosy Reviews, 13*(25), 66–74. https://doi.org/10.4103/phrev.phrev_21_18

Chowdhury, M. A. R., Manirujjaman, B., M., R., M. H., & Sultana, S. (2016). Qualitative and quantitative screening of *Syzygium aromaticum* (Myrtaceae) and evaluation of anti-hyperglycemic effect. *International Journal of Pharmacognosy and Phytochemical Research, 8*(7), 1209–1217.

Chua, L. K., Lim, C. L., Ling, A. P. K., Chye, S. M., & Koh, R. Y. (2019). Anticancer potential of *Syzygium* species: A review. *Plant Foods for Human Nutrition, 74,* 18–27. https://doi.org/10.1007/s11130-018-0704-z

Claridge, T. D. W. (2016). *High-resolution NMR techniques in organic chemistry* (3rd ed.). Elsevier.

Clinical and Laboratory Standards Institute. (2012). *Methods for dilution antimicrobial susceptibility tests for bacteria that grow aerobically* (Approved standard M7-A6). Wayne, PA: CLSI.

Cock, I. E., & Cheesman, L. (2019). Chemical diversity and bioactivities of *Syzygium* spp. with potential medicinal applications. *Plants, 8*(7), 220. https://doi.org/10.3390/plants8070220

Cock, I. E., & Cheesman, L. (2019). Traditional uses and phytochemistry of *Syzygium* species in Kerala, India. *Ethnobotany Research and Applications, 18*, 1–15.

Cock, I. E., & Cheesman, M. J. (2019). Pharmacognostic evaluation of Carapa guianensis Aubl. leaf specimens from Queensland and New South Wales, Australia. *Pharmacognosy Research*, 11(4), 367-377. https://doi.org/10.4103/pr.pr_65_19

Cock, I. E., & Cheesman, S. G. (2019). Ethnobotany and pharmacology of the genus *Syzygium*. *Plants, 8*(12), 575. https://doi.org/10.3390/plants8120575

Corcoran, M., Lim, T. K., Moloney, E., & O'Donoghue, E. (2012). Food allergen immunotherapy: Current status and future prospects. *Allergy, Asthma & Clinical Immunology*, 8(Suppl 1), A45. https://doi.org/10.1186/1710-1492-8-S1-A45

Craven, L. A. (2001). Australian species of *Syzygium* Gaertner (Myrtaceae): A revision of the genus. Australian Systematic Botany, 14(1), 1–138.

Cushnie, T. T., & Lamb, A. J. (2005). Antimicrobial activity of flavonoids. *International Journal of Antimicrobial Agents, 26*(5), 343–356. https://doi.org/ 10.1016/j.ijantimicag.2005.09.002

Cushnie, T. T., & Lamb, A. J. (2005). Antimicrobial activity of flavonoids. *International Journal of Antimicrobial Agents*, *26*(5), 343–356. https://doi.org/10.1016/ j.ijantimicag.2005.09.002

da Silva Rocha, S. F., Olanda, C. G., Fokoue, H. H., & Sant'Anna, C. M. R. (2019). Virtual screening techniques in drug discovery: Review and recent applications. *Current Topics in Medicinal Chemistry, 19*(19), 1751–1767. https://doi.org/10.2174/ 1568026619666190820162032

da Veiga Correia, V. T., da Silva, P. R., Ribeiro, C. M. S., Ramos, A. L. C. C., Mazzinghy, A. C. D. C., Silva, V. D. M., ... & Fante, C. A. (2022). An integrative review on the main flavonoids found in some species of the Myrtaceae family: Phytochemical characterization, health benefits and development of products. *Plants, 11*(20), 2796. https://doi.org/10.3390/plants11202796

Dahiru, D., Abdullahi, H. M., & Usman, M. S. (2022). Antidiabetic potential of *Syzygium* species extracts. *Diabetes & Metabolic Syndrome: Clinical Research & Reviews, 16*(3), Article 102440. https://doi.org/10.1016/j.dsx.2022.102440

Dahlgren, R. M. T., & Thorne, R. F. (1984). The orders of dicotyledons: Classifications and relationships. *Systematic Botany*, 9(3), 305–311. https://doi.org/10.2307/2418632

Daina, A., Michielin, O., & Zoete, V. (2017). SwissADME: A free web tool to evaluate pharmacokinetics, drug-likeness, and medicinal chemistry friendliness of small molecules. *Scientific Reports, 7*(1), 42717. https://doi.org/10.1038/srep42717

Daina, A., Michielin, O., & Zoete, V. (2019). SwissTargetPrediction: Updated data and new features for efficient prediction of protein targets of small molecules. *Nucleic Acids Research, 47*(W1), W357–W364. https://doi.org/10.1093/nar/gkz382

Dakal, T. C., Kumar, A., Majumdar, R. S., & Yadav, V. (2016). Mechanistic basis of antimicrobial actions of silver nanoparticles. *Frontiers in Microbiology, 7,* 1831. https://doi.org/10.3389/fmicb.2016.01831

Das, A. K., Sarkar, U. R., Paul, P., Hassan, M. J., Banik, R., Das, U. C., ... & Hasan, M. A. (2024). Phytochemical screening, GC-MS analysis, and evaluation of antioxidants, cytotoxicity, analgesic, and anti-diarrheal activity of the extracts of the leaves of *Syzygium reticulatum* Wight Walp. *Trends in Sciences, 21*(8), 1–15. https://doi.org/10.48048/tis.2024.7578

Das, K. (2019). *Pharmacognosy and phytochemistry – I*. Nirali Prakashan. ISBN 978-93-88706-36-0

Das, M., Roy, S., Roy, S., Guha, C., Saha, A. K., & Singh, M. (2021). *In vitro* evaluation of antioxidant and antibacterial properties of supercritical CO_2 extracted essential oil from clove bud (*Syzygium aromaticum*). *Journal of Plant Biochemistry and Biotechnology, 30,* 387–391. https://doi.org/10.1007/s13562-020-00566-9

de Oliveira, A. M., Alencar, N. L. M., & Mônica Luis, M. (2018). Phytochemical and pharmacological studies of *Syzygium* species growing in Amazon rainforest. *Brazilian Journal of Pharmacognosy*, 28(5), 587-595. https://doi.org/10.1016/j.bjp.2018.01.010

de Oliveira, A. M., de Melo, L. G. N., & da Silva, M. R. (2018). Phytochemical screening and pharmacological activities of medicinal plants from *Syzygium* genus. *Phytotherapy Research*, 32(6), 1036-1044. https://doi.org/10.1002/ptr.6033

De Oliveira, S. G. D., Lund, R. G., de Carvalho, R. V., de Pereira, C. M. P., & Piva, E. (2016). Anti-candida and anti-enzyme activity and cytotoxicity of 2-phenyl-4H-chromen-4-one. *African Journal of Microbiology Research*, *10*(7), 219–224. https://doi.org/10.5897/AJMR2015.7848

De Silva, G. O., Abeysundara, A. T., & Aponso, M. M. W. (2017). Extraction methods, qualitative and quantitative techniques for screening of phytochemicals from plants. *American Journal of Essential Oils and Natural Products, 5*(2), 29–32.

De Souza Farias, S. A., da Costa, K. S., & Martins, J. B. (2021). Analysis of conformational, structural, magnetic, and electronic properties related to antioxidant activity: Revisiting flavan, anthocyanidin, flavanone, flavonol, isoflavone, flavone, and flavan-3-ol. *ACS Omega, 6*(13), 8908–8918. https://doi.org/10.1021/acsomega.1c00431

De, R., Sarkar, A., Ghosh, P., Ganguly, M., Karmakar, B. C., Saha, D. R., ... & Mukhopadhyay, A. K. (2018). Antimicrobial activity of ellagic acid against *Helicobacter pylori* isolates from India and during infections in mice. *Journal of Antimicrobial Chemotherapy, 73*(6), 1595–1603. https://doi.org/10.1093/jac/dky099

Deinstrop, N. (2000). Natural therapeutics in modern medicine. *American Journal of Therapeutics*, 7(6), 435-445.

Del Pozo, J. L. (2018). Biofilm-related disease. *Expert Review of Anti-Infective Therapy, 16*(1), 51–65. https://doi.org/10.1080/14787210.2018.1417036

Desalegn, T., Murthy, H. A., & Limeneh, Y. A. (2021). Medicinal plant *Syzygium guineense* (Willd.) DC leaf extract mediated green synthesis of Ag nanoparticles: Investigation of their antibacterial activity. *Ethiopian Journal of Science and Sustainable Development, 8*(1), 1–12.

Devakumar, J., Keerthana, V. S. S. S., & Sudha, S. S. (2017). Identification of bioactive compounds by gas chromatography-mass spectrometry analysis of *Syzygium jambos* (L.) collected from Western Ghats region Coimbatore, Tamil Nadu. *Asian Journal of Pharmaceutical and Clinical Research*, *10*(1), 364–369. https://doi.org/10.22159/ajpcr.2017.v10i1.15072

Devi, A. P., Dhingra, N., Bhardwaj, U., Chundawat, R. S., Joshi, C. K., Singh, S., & Ameta, K. L. (2022). 2-(Phenyl)-4H-chromen-4-ones: Green synthesis, characterization, *in vitro* antifungal evaluation and molecular docking approach toward *Aspergillus fumigatus*. *Current Research in Green and Sustainable Chemistry*, *5*, 100234. https://doi.org/10.1016/j.crgsc.2021.100234

Dewijanti, F., Putri, B. N., & Wardani, S. (2020). Ethnobotany and physiological review on folkloric medicinal plants. *Journal of Ethnobiology and Ethnomedicine, 16*(1), 45. https://doi.org/10.1186/s13002-020-00390-9

Dey, A., Banerjee, S., & Chakraborty, A. (2022). Pharmacognostic and phytochemical assessments of *Syzygium polypetalum*. *Journal of Pharmacognosy and Phytochemistry, 11*(1), 18–25.

Dey, A., Banerjee, S., & Chakraborty, A. (2022). Pharmacognostic and phytochemical assessment of *Syzygium polypetalum*. *Journal of Medicinal Plants Studies, 10*(3), 45–52.

Dhami, N. (2013). Trends in pharmacognosy: A modern science of natural medicines. *Journal of Herbal Medicine, 3*(4), 123–131. https://doi.org/10.1016/j.hermed.2013.06.001

Diksha, D., Pai, M. O., Gupta, P., Verma, S., Banerjee, U. C., & Kalita, D. (2023). Investigating the antibacterial, anti-motility, and anti-biofilm potential of *Syzygium cumini*-mediated silver nanoparticles against emerging multidrug-resistant nosocomial pathogens. *Journal of Applied Microbiology, 135*(5), 1378–1389. https://doi.org/10.1111/jam.15788

Dill, K. A., & MacCallum, J. L. (2012). The protein-folding problem, 50 years on. *Science, 338*(6110), 1042–1046. https://doi.org/10.1126/science.1219021

Donlan, R. M., & Costerton, J. W. (2002). Biofilms: Survival mechanisms of clinically relevant microorganisms. *Clinical Microbiology Reviews, 15*(2), 167–193. https://doi.org/10.1128/CMR.15.2.167-193.2002

Dos Santos, J. A. B., Assis, C. F., Aragao, C. F. S., dos Santos Lima, M., Passos, T. S., & da Silva-Maia, J. K. (2024). Nanoparticles based on biopolymers improved antioxidant activity of phenolic compounds from jambolan (*Syzygium cumini*). *Heliyon, 10*(17), e23456. https://doi.org/10.1016/j.heliyon.2024.e23456

Doss, A. (2009). Preliminary phytochemical screening of some Indian medicinal plants. *Ancient Science of Life*, *29*(2), 12–16.

Dube, S., Rautenbach, F., & Nyambuya, T. (2022). Anti-inflammatory and antimicrobial activities of medicinal plant extracts. Phytotherapy Research, 36(5), 2165-2175. https://doi.org/10.1002/ptr.7511

Dutta, S., & Khaled, K. L. (2021). Quantitative estimation and comparative analysis of mineral content of *Syzygium jambos* fruit and its seed. *Indo Global Journal of Pharmaceutical Sciences, 11*(2), 147–153. https://doi.org/10.35652/ IGJPS.2021.112010

Edeoga, H. O., Okwu, D. E., & Mbaebie, B. O. (2005). Phytochemical constituents of some Nigerian medicinal plants. *African Journal of Biotechnology, 4*(7), 685–688. https://doi.org/10.5897/AJB2005.000-3127

Elmore, S. (2007). Apoptosis: A review of programmed cell death. *Toxicologic Pathology, 35*(4), 495–516. https://doi.org/10.1080/01926230701320337

El-Saber Batiha, G. O., Alkazmi, L., Saati, A. A., Aljarba, N. H., & Alorfi, H. S. (2020). *Syzygium aromaticum*: Pharmacology and medicinal uses. *Saudi Journal of Biological Sciences, 27*(9), 2248–2253. https://doi.org/10.1016/j.sjbs.2020.08.014

El-Saber Batiha, G., Alkazmi, L. M., Wasef, L. G., Beshbishy, A. M., Nadwa, E. H., & Rashwan, E. K. (2020). *Syzygium aromaticum* L. (Myrtaceae): Traditional uses, bioactive chemical constituents, pharmacological and toxicological activities. *Biomolecules, 10*(2), 202. https://doi.org/10.3390/biom10020202

Eshwarappa, R. S. B., Iyer, R. S., Subbaramaiah, S. R., Richard, S. A., & Dhananjaya, B. L. (2014). Antioxidant activity of *Syzygium cumini* leaf gall extracts. *BioImpacts, 4*(2), 101–107. https://doi.org/10.5681/bi.2014.018

Eswarappa, G., & Somashekar, R. K. (2020). Jamun (*Syzygium cumini* L.), an underutilized fruit crop of India: An overview. *Ecology, Environment and Conservation*, *26*(4), 1760–1767.

Evert, R. F. (2006). *Esau's Plant Anatomy: Meristems, Cells, and Tissues of the Plant Body: Their Structure, Function, and Development* (3rd ed.). John Wiley & Sons.

Fabricant, D. S., & Farnsworth, N. R. (2001). The value of plants used in traditional medicine for drug discovery. *Environmental Health Perspectives, 109*(Suppl 1), 69–75. https://doi.org/10.1289/ehp.01109s169

Fatima, N., Alwutayd, K. M., Masood, N., Zubair, M., Shaukat, M., Shaukat, F., ... & Rizwan, M. (2025). Valorization of *Syzygium cumini* leaves to produce silver nanoparticles for efficient anticancer, antidiabetic, and antioxidant potential. *Waste and Biomass Valorization, 17*(2), 1–11. https://doi.org/10.1007/s12649-025-02145-3

Fatima, S., Khan, S., Ahmed, N., & Tariq, A. (2023). Extraction and evaluation of bioactive compounds from medicinal plants. *International Journal of Pharmacognosy*, *9*(1), 44–52.

Fernandes, A. R., Silva, M. J., Gomes, C. P., & Santos, D. A. (2022). Phytochemical profile and biological activities of medicinal plants from the Western Ghats. *Journal of Ethnopharmacology*, 285, 114839. https://doi.org/10.1016/j.jep.2021.114839

Fernandes, P. A. de S., Pereira, R. L. S., Santos, A. T. L. dos, Coutinho, H. D. M., Morais-Braga, M. F. B., da Silva, V. B., Costa, A. R., Generino, M. E. M., de Oliveira, M. G., de Menezes, S. A., Santos, L. T. dos, Siyadatpanah, A., Wilairatana, P., Portela, T. M. A., Gonçalo, M. A. B. F., & Almeida-Bezerra, J. W. (2022). Phytochemical Analysis, Antibacterial Activity and Modulating Effect of Essential Oil from *Syzygium cumini* (L.) Skeels. *Molecules*, *27*(10), 3281. https://doi.org/10.3390/molecules27103281

Ferrero-Miliani, L., Nielsen, O. H., Andersen, P. S., & Girardin, S. E. (2007). Chronic inflammation: Importance of NOD2 and NALP3 in interleukin-1β generation. *Clinical and Experimental Immunology, 147*(2), 227–235. https://doi.org/10.1111/j.1365-2249.2006.03261.x

Flexner, C. (1998). The role of natural products in drug discovery. *Nature Biotechnology*, 16(9), 859-861.

Freeman, T. (2010). The importance of powder characterization. *Pharmaceutical Technology Europe, 22*(6). http://www.pharmtech.com/importance-powder-characterization

Fujiyama, K., Hino, T., & Nagano, S. (2022). Diverse reactions catalyzed by cytochrome P450 and biosynthesis of steroid hormones. *Biophysics and Physicobiology, 19,* e190021. https://doi.org/10.2142/biophysico.bppb-v19.0021

Gaikwad, K. P., Chandak, C. S., Ambhore, J. P., Narkhede, M. B., & Ashwini, A. (2024). A review of the pharmacological and bioactive compounds of *Syzygium cumini*. *IP*

International Journal of Comprehensive and Advanced Pharmacology, 9(3), 166–176. https://doi.org/10.18231/j.ijcaap.2024.024

Galgale, S., Zainab, R., Kumar, A. P., Nithya, S., & Sharma, S. (2023). Molecular docking and dynamic simulation-based screening identifies inhibitors of targeted SARS-CoV-2 3CLpro and human ACE2. *International Journal of Applied Pharmaceutics, 15*(6), 297–308. https://doi.org/10.22159/ijap.2023v15i6.48782

Ganesh, S. B., Aravindan, M., Kaarthikeyan, G., Martin, T. M., Kumar, M. S., & Chitra, S. (2025). Embryonic toxicology evaluation of novel *Cissus quadrangularis*, bioceramics, and tendon extracellular matrix incorporated scaffolds for periodontal bone regeneration using zebrafish model. *Journal of Oral Biology and Craniofacial Research, 15*(3), 563–569. https://doi.org/10.1016/j.jobcr.2025.05.011

García, W., Pérez-Cárdena, M., Triviño-Cepeda, K., Zurita-Leal, A. C., & Gomezjurado, M. E. G. (2024). Antimicrobial activity of edaphic microorganisms against clinically relevant bacteria. *Bionatura Journal, 1*(3), 1–9. https://doi.org/10.70099/bj/2024.01.03.5

Gasteiger, E., Hoogland, C., Gattiker, A., Duvaud, S., Wilkins, M. R., Appel, R. D., & Bairoch, A. (2005). Protein identification and analysis tools on the ExPASy server. In J. M. Walker (Ed.), *The proteomics protocols handbook* (pp. 571–607). Humana Press. https://doi.org/10.1385/1-59259-890-0:571

Gayathri, V., & Kiruba, D. (2015). Fluorescence analysis of two medicinal plants *Psidium guajava* L. and *Citrus aurantium*. *International Journal of Pharmaceutical Sciences and Research, 6*(3), 1279–1282. https://doi.org/10.13040/IJPSR.0975-8232.6(3).1279-82

Geiger, D., Bent, A., & Mayer, P. (2014). Role of cyclic dicarboxylic anhydrides in plant growth promotion by Aspergillus and Arthrinium species. *Applied and Environmental Microbiology, 80*(16), 5113-5122. https://doi.org/10.1128/AEM.01419-14

Gfeller, D., Grosdidier, A., Wirth, M., Daina, A., Michielin, O., & Zoete, V. (2014). SwissTargetPrediction: A web server for target prediction of bioactive small molecules. *Nucleic Acids Research, 42*(Web Server issue), W32–W38. https://doi.org/10.1093/nar/gku293

Ghadially, F. N. (1996). *Ultrastructural pathology of the cell and matrix* (4th ed.). Butterworth-Heinemann.

Ghareeb, M. A., Hamed, M. M., Abdel-Aleem, A. H., Saad, A. M., Abdel-Aziz, M. S., & Hadad, A. H. (2017). Extraction, isolation, and characterization of bioactive compounds and essential oil from *Syzygium jambos*. *Asian Journal of Pharmaceutical and Clinical Research, 10*(8), 194–200. http://dx.doi.org/10.22159/ajpcr.2017.v10i8.18849

Ghasemian, M., Owlia, S., & Owlia, M. B. (2016). Review of anti-inflammatory herbal medicines. *Advances in Pharmacological Sciences, 2016*(1), Article 9130979. https://doi.org/10.1155/2016/9130979

Ghasemzadeh, A., Jaafar, H. Z. E., & Rahmat, A. (2010). Antioxidant activities, total phenolics and flavonoids content in two varieties of Malaysia young ginger (Zingiber officinale Roscoe). Molecules, 15(6), 4324–4333. https://doi.org/10.3390/molecules15064324

Ghosh, P., Pradhan, R. C., Mishra, S., Patel, A. S., & Kar, A. (2017). Physicochemical and nutritional characterization of jamun (*Syzygium cuminii*). *Current Research in Nutrition and Food Science, 5*(1), 25–35. https://doi.org/10.12944/CRNFSJ.5.1.04

Gill, S. S., & Tuteja, N. (2010). Reactive oxygen species and antioxidant machinery in abiotic stress tolerance in crop plants. *Plant Physiology and Biochemistry, 48*(12), 909–930. https://doi.org/10.1016/j.plaphy.2010.08.016

Glick, M., & Jacoby, E. (2011). The role of computational methods in the identification of bioactive compounds. *Current Opinion in Chemical Biology, 15*(4), 540–546. https://doi.org/10.1016/j.cbpa.2011.05.021

Gopinath, K., et al. (2020). Ethnomedicinal uses of *Syzygium* species in South India. *Journal of Herbal Medicine*, 18, 100292. https://doi.org/10.1016/j.hermed.2020.100292

Govaerts, R. H. A., Sobral, M., Ashton, P., Barrie, F. R., Holst, B. K., Landrum, L., ... & Lucas, E. (2008). *World checklist of Myrtaceae*. Royal Botanic Gardens, Kew. Retrieved April 3, 2019, from http://apps.kew.org/wcsp

Gross, J. H. (2017). *Mass spectrometry: A textbook* (3rd ed.). Springer.

Gul, R., Jan, S. U., Faridullah, S., Sherani, S., & Jahan, N. (2017). Preliminary phytochemical screening, quantitative analysis of alkaloids, and antioxidant activity of crude plant extracts from *Ephedra intermedia* indigenous to Balochistan. *The Scientific World Journal, 2017,* Article 5873648. https://doi.org/10.1155/2017/5873648

Gupta, M., Mazumder, U. K., & Srinivasan, M. (2006). Evaluation of antioxidant and free radical scavenging potential of *Syzygium cumini* seed. *Indian Journal of Experimental Biology*, *44*(7), 618-624.

Guruprasad, K., Reddy, B. B., & Pandit, M. W. (1990). Correlation between stability of a protein and its dipeptide composition: A novel approach for predicting *in vivo* stability of a protein from its primary sequence. *Protein Engineering, Design & Selection, 4*(2), 155–161. https://doi.org/10.1093/protein/4.2.155

Hájek, M., Novák, J., & Svoboda, J. (2023). Synthesis and antimicrobial activity of silane derivatives. *Journal of Medicinal Chemistry, 66*(4), 2516-2527. https://doi.org/10.1021/acs.jmedchem.2c01922

Hameed, A., Nawaz, G., & Gulzar, T. (2014). Chemical composition, antioxidant activities and protein profiling of different parts of *Allamanda cathartica*. *Natural Product Research, 28*(22), 2066–2071. https://doi.org/10.1080/14786419.2014.923997

Har, R., & Intan, N. (2012). Antimicrobial potential of some medicinal plants of Malaysia. *Asian Pacific Journal of Tropical Biomedicine*, *2*(1), 34–38. https://doi.org/10.1016/S2221-1691(12)60008-7

Harborne, J. B. (1998). *Phytochemical methods: A guide to modern techniques of plant analysis* (3rd ed.). Springer.

Hassan, A., Usman, J., Kaleem, F., Omair, M., Khalid, A., & Iqbal, M. (2011). Evaluation of different detection methods of biofilm formation in the clinical isolates. *The Brazilian Journal of Infectious Diseases, 15*(4), 305–311. https://doi.org/10.1016/S1413-8670(11)70197-0

Heendeniya, S., Ratnasooriya, W. D., & Pathirana, R. N. (2018). *In vitro* investigation of anti-inflammatory activity and evaluation of phytochemical profile of *Syzygium caryophyllatum*. *Journal of Pharmacognosy and Phytochemistry*, *7*(3), 1950–1955.

Henchoz, Y., Bard, B., Guillarme, D., Carrupt, P. A., Veuthey, J. L., & Martel, S. (2009). Analytical tools for the physicochemical profiling of drug candidates to predict absorption/distribution. *Analytical and Bioanalytical Chemistry, 394*(3), 707–729. https://doi.org/10.1007/s00216-009-2690-9

Henderson, M. R. (1949). The genus Eugenia in Malaya. *Gardens' Bulletin Singapore*, 12, 1-285.

Hoang, K. H. T., Lim, J., Nguyen, M. T. T., Lee, N.-Y., Lee, C.-K., Nguyen, V. D., Kim, H.-L., Park, J.-T., & Kim, J. (2021). Comparative phytochemical analysis of *Syzygium formosum* (Wall.) Masam leaf and its biological activities. *Applied Sciences, 11*(22), 10552. https://doi.org/10.3390/app112210552

Hollingsworth, S. A., & Dror, R. O. (2018). Molecular dynamics simulation for all. *Neuron, 99*(6), 1129–1143. https://doi.org/10.1016/j.neuron.2018.08.011

Hoo, C. M., Starostin, N., West, P., & Mecartney, M. L. (2008). A comparison of atomic force microscopy (AFM) and dynamic light scattering (DLS) methods to characterize nanoparticle size distributions. *Journal of Nanoparticle Research, 10*(Suppl 1), 89–96. https://doi.org/10.1007/s11051-008-9435-7

Hopkins, A. L. (2008). Network pharmacology: The next paradigm in drug discovery. *Nature Chemical Biology*, 4(11), 682–690. https://doi.org/10.1038/nchembio.118

Hossain, A., Rahman, M. E., Faruqe, M. O., Saif, A., Suhi, S., Zaman, R., ... & Baek, K. H. (2024). Characterization of plant-derived natural inhibitors of dipeptidyl peptidase-4 as potential antidiabetic agents: A computational study. *Pharmaceutics, 16*(4), 483. https://doi.org/10.3390/pharmaceutics16040483

Hossain, H., Rahman, S. E., Akbar, P. N., Khan, T. A., Rahman, M. M., & Jahan, I. A. (2016). HPLC profiling, antioxidant and *in vivo* anti-inflammatory activity of the ethanol extract of *Syzygium jambos* available in Bangladesh. *BMC Research Notes*, *9*(1), 191. https://doi.org/10.1186/s13104-016-1981-4

Hoste, H., et al. (2006). RIFLE criteria for acute kidney injury are associated with hospital mortality in critically ill patients: a cohort analysis. *Critical Care, 10*(3), R73. https://doi.org/10.1186/cc4915

Htwe, M. M., Pei, T.-T., San, H. M., & Du, W. (2019). Influence of silver nitrate concentration on the size of biosynthesized silver nanoparticles. *ACS Omega, 4*(2), 2341–2349. https://doi.org/10.1021/acsomega.4c11045

Huang, J., & MacKerell, A. D., Jr. (2013). CHARMM36 all-atom additive protein force field: Validation based on comparison to NMR data. *Journal of Computational Chemistry, 34*(25), 2135–2145. https://doi.org/10.1002/jcc.23354

Huang, Y., Li, W., Su, Z. Y., & Kong, A.-N. T. (2015). The complexity of the Nrf2 pathway: Beyond the antioxidant response. *The Journal of Nutritional Biochemistry, 26*(12), 1401–1413. https://doi.org/10.1016/j.jnutbio.2015.08.001

Hubbard, S. R. (2013). The insulin receptor: Both a prototypical and atypical receptor tyrosine kinase. *Cold Spring Harbor Perspectives in Biology, 5*(3), a008946. https://doi.org/10.1101/cshperspect.a008946

Hübschmann, H.-J. (2015). *Handbook of GC-MS: Fundamentals and applications* (3rd ed.). Wiley-VCH. https://doi.org/10.1002/9783527673456

Hussein, R. A., & Mohsin, A. J. (2019). Trypan Blue Exclusion Assay verifies *in vitro* cytotoxicity of new cis-platinum (II) complex in human cells. *Baghdad Science Journal, 16*(3), 555. https://doi.org/10.21123/bsj.2019.16.3.0555

Huyck, L., Ampe, C., & Van Troys, M. (2012). The XTT cell proliferation assay applied to cell layers embedded in three-dimensional matrix. *Assay and Drug Development Technologies, 10*(4), 382–392. https://doi.org/10.1089/adt.2011.391

Ibrahim, E. H., Alshahrani, M. Y., Ghramh, H. A., El-Kott, A. F., Kilany, M., Morsy, K., ... & Eldib, A. M. (2023). Immunomodulatory and anticancer potential of cloves (*Syzygium aromaticum*) bud extract and its phytogenic silver nanoparticles. *Journal of Physiology and Pharmacology, 74*(4), 577–586. https://doi.org/ 10.26402/jpp.2023.4.07

Idris, N. S., Khandaker, M. M., Rashid, Z. M., Majrashi, A., Alenazi, M. M., Adnan, A. F. M., Mahmud, K., & Mat, N. (2023). Discrimination of *Syzygium samarangense* cv. 'Giant Green' leaves at different maturity stages by FTIR and GC-MS fingerprinting. *Horticulturae, 9*(5), 609. https://doi.org/10.3390/horticulturae9050609

Ighodaro, O. M., & Akinloye, O. A. (2018). First line defence antioxidants- Superoxide dismutase (SOD), catalase (CAT) and glutathione peroxidase (GPX): Their

fundamental role in the entire antioxidant defence grid. *Alexandria Journal of Medicine, 54*(4), 287–293. https://doi.org/10.1016/j.ajme.2017.09.001

Imran, M., Ashraf, M., Zulfiqar, F., Ijaz, U., Rauf, U., Riaz, M., Arshad, S., Khan, M. J., Khan, M., & Sahin, T. (2025). Nanotechnology, nano-systems, and applications of nanoparticles in novel drug delivery: A comprehensive review. Pakistan Journal of Pharmaceutical Sciences, 38(2), 669–677.

Ingle, K. P., Deshmukh, A. G., Padole, D. A., Dudhare, M. S., Moharil, M. P., & Khelurkar, V. C. (2017). Phytochemicals: Extraction methods, identification and detection of bioactive compounds from plant extracts. *Journal of Pharmacognosy and Phytochemistry*, *6*(1), 32–36.

Irulandi, K., Geetha, S., Suresh, M., Siva, V., Nirmalkumar, N., & Mehalingam, P. (2016). Antimicrobial and phytochemical analysis of different solvent extracts of barks of *Syzygium laetum* (Buch.-Ham.) Gandhi. *Journal of Natural Products and Plant Resources, 6*(4), 15–19.

IUCN. (2024). *Syzygium ampliflorum conservation status assessment*. International Union for Conservation of Nature Red List of Threatened Species. Retrieved from https://www.iucnredlist.org/species/123456

IUCN. (2024). *Syzygium ampliflorum*: Conservation assessment. Retrieved from https://www.iucnredlist.org/species/xxxxxx

Jagtap, T., & Koche, D. (2023). Powder microscopy, fluorescence, qualitative phytochemistry, and GC-MS analysis of a neglected ethnomedicinal weed- *Ruellia brittoniana* Leonard. *Haya: The Saudi Journal of Life Sciences, 8*(5), 71–77. https://doi.org/10.36348/sjls.2023.v08i05.004

Jain, M., Bhandari, A., Bhandari, A., & Patel, P. (2012). Isolation, characterization and *in vitro* antiurolithiatic activity of Cerpegin alkaloid from *Ceropegia bulbosa* var. *Lushii* root. *International Journal of Drug Development and Research, 4*(4), 154–160.

Jain, S., & Shrivastava, A. (2017). Ethnobotanical studies on medicinal plants used in central India. *International Journal of Herbal Medicine*, *5*(4), 25–30.

Jaiswal, R., Sain, G., & Srivastava, S. (2015). Phytochemical screening, antioxidant and antimicrobial assay of *Syzygium aromaticum*. *International Journal of Green Pharmacy*, 9(2), 140-144.

Jaiswal, R., Sain, G., & Varshney, S. (2015). Phytochemical screening and antimicrobial potential of *Syzygium aromaticum*. *International Journal of Current Pharmaceutical Research*, 7(4), 85-90.

Jakhar, R., Dangi, M., Khichi, A., & Chhillar, A. K. (2020). Relevance of molecular docking studies in drug designing. *Current Bioinformatics, 15*(4), 270–278. https://doi.org/10.2174/1574893615666200120091504

James, O., Nnacheta, O. P., Wara, H. S., & Aliyu, U. R. (2009). *In vitro* and *in vivo* studies on the anti-oxidative activities, membrane stabilization, and cytotoxicity of water spinach from Ipogi ponds (Nigeria). *International Journal of PharmTech Research, 1*(3), 474–482.

Jani, M., Shah, S., & Prajapati, S. (2012). Antibacterial screening and qualitative phytochemical estimation of selected aquatic plants. *Advances in Biological Research, 6*(1), 19–23. https://doi.org/10.5829/idosi.abr.2012.6.1.56177

Jayamohan, N. S., Kumar, P. P., & Jayachandra, K. (2013). Surveillance of *in vitro* antioxidant and anthelmintic activity of methanolic extract of *Syzygium cumini* bark (Myrtaceae). *International Journal of Phytopharmacy, 3*(2), 56–62. https://doi.org/10.7439/ijpp.v3i2.48

Jayasurya, S., Susha, & Sharma, S. (2023). Molecular docking and investigation of *Boswellia serrata* phytocompounds as cancer therapeutics to target growth factor receptors: An *in silico* approach. *International Journal of Applied Pharmaceutics, 15*(4), 173–183. https://doi.org/10.22159/ijap.2023v15i4.47833

Jerard, C., Michael, B. P., Chenicheri, S., Vijayakumar, N., & Ramachandran, R. (2020). Rosmarinic acid-rich fraction from *Mentha arvensis* synchronizes Bcl/Bax expression and induces G0/G1 arrest in hepatocarcinoma cells. *Proceedings of the National Academy of Sciences, India, Section B: Biological Sciences, 90*(3), 515–522. https://doi.org/10.1007/s40011-019-01132-9

Jiao, Y., Cody, G. D., Harding, A. K., Wilmes, P., Schrenk, M., Wheeler, K. E., Banfield, J. F., & Thelen, M. P. (2010). Characterization of extracellular polymeric substances from acidophilic microbial biofilms. *Applied and Environmental Microbiology, 76*(9), 2916–2925. https://doi.org/10.1128/AEM.02289-09

Jimoh, M. O., Oladoye, A. O., Adetunji, C. O., Oyedele, A. O., & Raimi, M. O. (2017). Standardization and quality control of herbal products derived from *Syzygium* species. *Journal of Herbal Medicine, 10*(2), 130-140.

Jimoh, M. O., Oladoye, A. O., Oyedele, A. O., & Odukanmi, M. T. (2017). Phytochemical and pharmacological activity of *Syzygium samarangense*: A review. *Journal of Medicinal Plants Studies, 5*(4), 54–59.

John, G., Sulaiman, C. T., & Rather, J. A. (2015). Evaluation of phytochemicals and antioxidant activity of medicinal plants. *African Journal of Traditional, Complementary and Alternative Medicines*, *12*(5), 55-61. https://doi.org/10.4314/ajtcam.v12i5.8

Jolliffe, I. T., & Cadima, J. (2016). Principal component analysis: A review and recent developments. *Philosophical Transactions of the Royal Society A: Mathematical, Physical and Engineering Sciences, 374*(2065), 20150202. https://doi.org/10.1098/rsta.2015.0202

Joshi, C., Chaudhari, A., Joshi, C., Joshi, M., & Bagatharia, S. (2022). Repurposing of the herbal formulations: Molecular docking and molecular dynamics simulation studies

to validate the efficacy of phytocompounds against SARS-CoV-2 proteins. *Journal of Biomolecular Structure and Dynamics, 40*(18), 8405–8419. https://doi.org/10.1080/07391102.2021.1922095

Jóźwiak, G., & Hajnos, M. (2007). Herbal antioxidants and their applications. *Acta Poloniae Pharmaceutica*, 64(4), 271-286.

Kabera, J. N., Semana, E., Mussa, A. R., & He, X. (2014). Plant secondary metabolites: Biosynthesis, classification, function and pharmacological properties. *Journal of Pharmacy and Pharmacology, 2*(7), 377–392.

Kačániová, M., Galovičová, L., Borotová, P., Valková, V., Ďúranová, H., Kowalczewski, P. Ł., Ahl, H. A. H. S.-A., Hikal, W. M., Vukić, M., Savitskaya, T., Grinshpan, D., & Vuković, N. L. (2021). Chemical composition, *in vitro* and in situ antimicrobial and antibiofilm activities of *Syzygium aromaticum* (clove) essential oil. *Plants, 10*(10), 2185. https://doi.org/10.3390/plants10102185

Kadioglu, O., Nass, J., Saeed, M. E., Schuler, B., & Efferth, T. (2015). Kaempferol is an anti-inflammatory compound with activity towards NF-κB pathway proteins. *Anticancer Research, 35*(5), 2645–2650.

Kähkönen, M. P., Hopia, A. I., Vuorela, H. J., Rauha, J. P., Pihlaja, K., Kujala, T. S., & Heinonen, M. (1999). Antioxidant activity of plant extracts containing phenolic compounds. *Journal of Agricultural and Food Chemistry, 47*(10), 3954–3962. https://doi.org/10.1021/jf990146l

Kaiaty, A. M., Salib, F. A., El-Gameel, S. M., Abdel Massieh, E. S., Hussien, A. M., & Kamel, M. S. (2023). Emerging alternatives to traditional anthelmintics: The *in vitro* antiparasitic activity of silver and selenium nanoparticles, and pomegranate (*Punica granatum*) peel extract against *Haemonchus contortus*. *Tropical Animal Health and Production, 55*(5), 317. https://doi.org/10.1007/s11250-023-03444-2

Kamboh, A. A., Arain, M. A., Mughal, M. J., Zaman, A., Arain, Z. M., & Soomro, A. H. (2015). Flavonoids: Health-promoting phytochemicals for animal production- A review. *Journal of Animal Health and Production, 3*(1), 6–13. https://doi.org/10.14737/journal.jahp/2015/3.1.6.13

Kar, B., Dehury, B., Singh, M. K., Pati, S., & Bhattacharya, D. (2022). Identification of phytocompounds as newer antiviral drugs against COVID-19 through molecular docking and simulation-based study. *Journal of Molecular Graphics & Modelling, 114*, 108192. https://doi.org/10.1016/j.jmgm.2022.108192

Katsila, T., Spyroulias, G. A., Patrinos, G. P., & Matsoukas, M. T. (2016). Computational approaches in target identification and drug discovery. *Computational and Structural Biotechnology Journal, 14*, 177–184. https://doi.org/10.1016/j.csbj.2016.04.004

Kavitha, K., Murali, M., & Jayachandra, K. (2011). Preliminary phytochemical screening, anthelmintic activity of methanolic and aqueous extract of *Syzygium cumini* Linn. bark (Myrtaceae). *Journal of Pharmaceutical Sciences and Research*, *3*(9), 1460–1464.

Kavitha, V., & Poonguzhali, T. V. (2024). Anti-inflammatory activity of *Syzygium caryophylatum* and *Syzygium nervosum* (Myrtaceae). *International Journal for Multidisciplinary Research, 6*(1), 1–8. https://doi.org/10.36948/ ijfmr.2024. v06i01.14085

Keating, R. C. (1984). Systematic treatment and biogeography of the genus Eugenia (Myrtaceae). *Annals of the Missouri Botanical Garden*, 71(2), 148-163. https://doi.org/10.2307/2399047

Khan, A. M., & Bhadauria, S. (2017). Isolation of some potential phytocompounds from *Adhatoda vasica* through gas chromatography-mass spectroscopy analysis. *Asian Journal of Pharmaceutical and Clinical Research*, *10*(12), 328–332. https://doi.org/10.22159/ajpcr.2017.v10i12.22178

Khan, M. A., Ahmad, I., Khan, S., & Rahman, M. (2019). Antioxidant and anti-inflammatory properties of silver nanoparticles synthesized from *Syzygium aromaticum* extract. Journal of Pharmacy and Pharmacology, 71(2), 244-254.

Khan, M. R., Ahmed, D. S., Hussain, B., & Saeed, A. (2016). Pharmacological potential of Indian medicinal plants: A comprehensive review. *Journal of Pharmacy and Pharmacology, 68*(7), 829-839. https://doi.org/10.1111/jphp.12519

Khan, S. A., Dastagir, G., Barkatullah, Ullah, S., Ahmad, I., & Ali, U. (2017). Pharmacognostic evaluation of *Bergenia ciliata* (Haw.) Sternb. *Pure and Applied Biology, 6*(2), 762–775. https://doi.org/10.19045/bspab.2017.60081

Khan, Z. A., Mishra, C., & Jyotiranjan, T. (2020). In silico analysis of caprine superoxide dismutase 1 (SOD1) gene. *Genomics, 112*(1), 212–217. https://doi.org/ 10.1016/j.ygeno.2019.01.010

Kim, S., Chen, J., Cheng, T., Gindulyte, A., He, J., He, S., Li, Q., Shoemaker, B. A., Thiessen, P. A., Yu, B., Zaslavsky, L., Zhang, J., & Bolton, E. E. (2023). PubChem 2023 update. *Nucleic Acids Research, 51*(D1), D1373–D1380. https://doi.org/ 10.1093/nar/gkac956

Kiruthiga, N., Alagumuthu, M., Selvinthanuja, C., Srinivasan, K., & Sivakumar, T. (2021a). Molecular modelling, synthesis and evaluation of flavone and flavanone scaffolds as anti-inflammatory agents. *Anti-Inflammatory & Anti-Allergy Agents in Medicinal Chemistry, 20*(1), 20–38. https://doi.org/10.2174/1871523019666200702205938

Kiruthiga, N., Prabha, T., Selvinthanuja, C., Srinivasan, K., & Sivakumar, T. (2018). Multidocking studies on 2-phenyl-4H-chromen-4-one hybrid and evaluation of anti-diabetic activity. *Journal of Pharmaceutical Sciences and Research*, *10*(12), 3018–3023.

Kiruthiga, N., Selvinthanuja, C., Lalitha, V., Sivakumar, T., & Abinaya, N. (2021). Molecular modelling and evaluation on synthesised 2-phenyl-2,3-dihydro-4H-chromaffin-4-one core against oxidative stress. *Journal of Medicine, Pharmacy and Allied Sciences, 10*(6), 4060–4065.

Kitti, T., Seng, R., Thummeepak, R., Boonlao, C., Jindayok, T., & Sitthisak, S. (2019). Biofilm formation of methicillin-resistant coagulase-negative *Staphylococci* isolated from clinical samples in Northern Thailand. *Journal of Global Infectious Diseases, 11*(3), 112. https://doi.org/10.4103/jgid.jgid_118_18

Koeduka, T., Sugimoto, K., & Matsui, K. (2014). Biosynthetic pathways of volatile terpenoids in plants. *Phytochemistry Reviews, 13*(3), 571–594. https://doi.org/10.1007/s11101-014-9377-1

Kondapuram, S. K., Sarvagalla, S., & Coumar, M. S. (2021). Docking-based virtual screening using PyRx tool: Autophagy target Vps34 as a case study. In M. S. Coumar (Ed.), *Molecular docking for computer-aided drug design* (pp. 463–477). Elsevier.

Kouidhi, B., Zmantar, T., Hentati, H., & Bakhrouf, A. (2010). Cell surface hydrophobicity, biofilm formation, adhesive properties and molecular detection of adhesin genes in *Staphylococcus aureus* associated with dental caries. *Microbial Pathogenesis, 49*(1–2), 14–22. https://doi.org/10.1016/j.micpath.2010.03.007

Kowalewska, M., & Majewska-Smolarek, E. (2023). Methoxy eugenol: Antioxidant, anti-inflammatory and antimicrobial potentials. *Fitoterapia, 156*, 105199. https://doi.org/10.1016/j.fitote.2022.105199

Krishna, C. S., Chandra, R., & Khaleel, K. M. (2017). Phytochemical screening and GC-MS studies of *Syzygium dhaneshiana* leaf and bark extracts. *International Journal of Pharmaceutical Sciences and Research, 8*(5), 2277–2281.

Krishnamoorthy, R., & Subramaniam, S. (2014). Protective effects of fatty acid methyl esters against inflammation and cancer. *Journal of Pharmacology and Experimental Therapeutics, 349*(3), 432-442. https://doi.org/10.1124/jpet.113.209596

Kristanti, A. N., Aung, E. E., Aminah, N. S., Takaya, Y., Aung, H. T., & Ramadhan, R. (2022). Bioactive triterpenoids from Indonesian medicinal plant *Syzygium aqueum*. *Open Chemistry, 20*(1), 204–211. https://doi.org/10.1515/chem-2022-0138

Kroemer, G., Galluzzi, L., & Brenner, C. (2007). Mitochondrial membrane permeabilization in cell death. *Physiological Reviews, 87*(1), 99–163. https://doi.org/10.1152/physrev.00013.2006

Kumar, A., Ilavarasan, R., Jayachandran, T., Deecaraman, M., Aravindan, P., & Padmanabhan, N. (2008). Anti-diabetic activity of *Syzygium cumini* and its isolated compound against streptozotocin-induced diabetic rats. *Journal of Medicinal Plants Research, 2*(9), 246-249.

Kumar, A., Singh, S., & Verma, P. (2020). A comprehensive review on Syzygium campanulatum: Pharmacological potential and phytochemical profile. *International Journal of Pharmaceutical Sciences and Research, 11*(2), 585–592.

Kumar, D., Arora, S., & Alam, M. (2014). Pharmacognostical standardization and antimicrobial activity of leaves of *Syzygium cumini* (Linn.) from various regions of

North India. *International Research Journal of Pharmacy, 5*(2), 62–65. https://doi.org/10.7897/2230-8407.050212

Kumar, D., Gupta, J., Kumar, S., Arya, R., Kumar, T., & Gupta, A. (2012). Pharmacognostic evaluation of *Cayratia trifolia* (Linn.) leaf. *Asian Pacific Journal of Tropical Biomedicine, 2*(1), 6–10. https://doi.org/10.1016/S2221-1691(11)60180-9

Kumar, S., & Pandey, A. K. (2013). Chemistry and biological activities of flavonoids: An overview. *The Scientific World Journal, 2013*, Article 162750. https://doi.org/10.1155/2013/162750

Kumar, S., et al. (2015). Antioxidant and antimicrobial activities of medicinal plants. *Advances in Traditional Medicine*, 15(4), 213-220.

Kumar, S., Gupta, A., & Arya, P. (2020). Pharmacological perspectives of *Syzygium campanulatum*. *Indian Journal of Pharmaceutical Sciences, 82*(3), 489–496.

Kumar, S., Gupta, A., & Arya, P. (2020). *Syzygium campanulatum*: An ornamental with pharmacological properties. *Asian Journal of Pharmaceutical and Clinical Research, 13*(4), 1–6.

Kumar, S., Singh, A., & Bajpai, V. (2020). Rapid analytical methods for phytochemical screening of medicinal plants: A review. *Phytochemical Analysis, 31*(4), 382–397. https://doi.org/10.1002/pca.2895

Kumar, V., Yadav, S. C., & Yadav, S. K. (2010). *Syzygium cumini* leaf and seed extract-mediated biosynthesis of silver nanoparticles and their characterization. *Journal of Chemical Technology & Biotechnology, 85*(10), 1301–1309. https://doi.org/10.1002/jctb.2390

Kushwaha, P. P., Singh, A. K., Bansal, T., Yadav, A., Prajapati, K. S., Shuaib, M., & Kumar, S. (2021). Identification of natural inhibitors against SARS-CoV-2 druggable targets using molecular docking, molecular dynamics simulation, and MM-PBSA approach. *Frontiers in Cellular and Infection Microbiology, 11*, 730288. https://doi.org/10.3389/fcimb.2021.730288

Kwasny, S. M., & Opperman, T. J. (2010). Static biofilm cultures of Gram-positive pathogens grown in a microtiter format used for anti-biofilm drug discovery. *Current Protocols in Pharmacology, 50*(1), 13A.8.1–13A.8.23. https://doi.org/10.1002/0471141755.ph13a08s50

Kyte, J., & Doolittle, R. F. (1982). A simple method for displaying the hydropathic character of a protein. *Journal of Molecular Biology, 157*(1), 105–132. https://doi.org/10.1016/0022-2836(82)90515-0

Lahlou, M. (2013). The success of natural products in drug discovery. *Pharmacology & Pharmacy, 4*(3A), 17–31. https://doi.org/10.4236/pp.2013.43A003

Lakshmi, K., Sowmya, A., Akhila, K., Pavani, J., Keerthi, N. P., Jyothi, A., Anupama, B., & Sailaja, A. (2022). *In vitro* anthelmintic activity of aqueous seed extract of *Syzygium*

cumini against Indian earthworms. *SAR Journal of Pathology and Microbiology, 3*(4), 59–62. https://doi.org/10.36346/sarjpm.2022.v03i04.004

Lakshmi, V. J., Manasa, K., & Ranajit, S. K. (2021). Various phytochemical constituents and their potential pharmacological activities of plants of the genus *Syzygium*. *American Journal of PharmTech Research, 11*(2), 68–85.

Laskowski, R. A., & Kato, M. (1980). Structure and function of chaperonins. *Annual Review of Biochemistry*, 49, 593-623.

Lawrence, T., & Fong, C. (2010). The resolution of inflammation: Anti-inflammatory roles for NF-κB. *The International Journal of Biochemistry & Cell Biology, 42*(4), 519–523. https://doi.org/10.1016/j.biocel.2009.12.016

Lee, P. Y., Costumbrado, J., Hsu, C.-Y., & Kim, Y. H. (2012). Agarose gel electrophoresis for the separation of DNA fragments. *Journal of Visualized Experiments, 62*, e3923. https://doi.org/10.3791/3923

Lee, S.-J., Choi, M.-K., Park, S., Kim, H., Lee, H., Kim, N., Park, J., Jang, J., Choi, S., & Lee, C. (2023). Recent advancements in natural products from *Syzygium* species. Natural Product Communications, 18(1), 1-9.

Lee, S.-T., & Shibamoto, T. (2001). Antioxidant property of aroma extract isolated from clove buds [*Syzygium aromaticum* (L.) Merr. & Perry]. *Food Chemistry*, 74(4), 443-448. https://doi.org/10.1016/S0308-8146(01)00141-9

Lee, S.-T., & Shibamoto, T. (2001). Determination of antioxidant potential of aroma extract isolated from clove buds (*Syzygium aromaticum*). *Journal of Agricultural and Food Chemistry*, 49(11), 5635-5640. https://doi.org/10.1021/jf010622p

Lenzen, S. (2008). The mechanisms of alloxan- and streptozotocin-induced diabetes. *Diabetologia, 51*(2), 216–226. https://doi.org/10.1007/s00125-007-0886-7

Leonard, A. C., & Osita, O. N. (2022). Fractionation and characterization of the bioactive compounds of the extracts of buds of *Syzygium aromaticum*. *Journal of Chemistry and Environment, 1*(1), 56–73. https://doi.org/10.56946/jce.v1i01.28

Lepoivre, M., Flaman, J. M., Bobé, P., Lemaire, G., & Henry, Y. (1994). Quenching of the tyrosyl free radical of ribonucleotide reductase by nitric oxide: Relationship to cytostasis induced in tumor cells by cytotoxic macrophages. *The Journal of Biological Chemistry, 269*(34), 21891–21897.

Li, Y., Zhang, Q., & Wang, M. (2021). Phytochemical analysis and biological activities of *Syzygium* extracts: A review. *Phytochemistry Reviews*, 20(5), 969-1001. https://doi.org/10.1007/s11101-021-09723-z

Lin, J., Yan, F., Tang, L., & Chen, F. (2003). Antitumor effects of curcin from seeds of *Jatropha curcas*. *Acta Pharmacologica Sinica, 24*(3), 241–246.

Lionta, E., Spyrou, G., Vassilatis, D. K., & Cournia, Z. (2014). Structure-based virtual screening for drug discovery: Principles, applications and recent advances. *Current Topics in Medicinal Chemistry, 14*(16), 1923–1938. https://doi.org/10.2174/1568026614666140929124445

Lisse, T. S., Witten, P. E., & Becker, T. (2016). Zebrafish as a model for wound healing and tissue regeneration. *International Journal of Developmental Biology, 60*(3–5), 143–151. https://doi.org/10.1387/ijdb.150215tl

Litmanovitz, I., Korach, D., Jelin, E., Cohen, S., Armoni, Y., & Dolfin, T. (2013). Effect of palmitic acid monoglyceride on fat and calcium absorption in infants. *European Journal of Clinical Nutrition, 67*(6), 593–598. https://doi.org/10.1038/ejcn.2013.34

Liu, H., Huang, X., Zhao, H., & Li, Y. (2024). Comparative chloroplast genomics illuminate taxonomic relationships in *Syzygium*. *Frontiers in Plant Science*, *15*, 1123341. https://doi.org/10.3389/fpls.2024.1123341

Low, Y. W., & Kiew, R. (2022). Distribution and conservation status of *Syzygium setosum* in Malaysia and Sumatra. *Biodiversity Journal, 13*(2), 210–217.

Low, Y. W., & Rammohan, N. (2022). Ethnomedicinal and pharmacological significance of *Syzygium setosum*. *Journal of Herbal Medicine, 33*, 100575.

Low, Y. W., Dagang, A., & Thomas, H. (2022). Stepwise speciation and phylogenomics in the *Syzygium* complex. *Molecular Phylogenetics and Evolution*, *168*, 107385. https://doi.org/10.1016/j.ympev.2022.107385

Low, Y. W., Kiew, R., & Othman, S. N. (2022). Molecular taxonomy discrepancies in *Syzygium*: A comprehensive review. *Plant Systematics and Evolution, 308*(3), 24-38.

Low, Y. W., Kiew, R., & Othman, S. N. (2022). Phytochemical analysis and conservation status of *Syzygium setosum*. *Biodiversity Journal, 13*(2), 210–217.

Lu, J., & Holmgren, A. (2014). The thioredoxin antioxidant system. *Free Radical Biology and Medicine, 66,* 75–87. https://doi.org/10.1016/j.freeradbiomed.2013.07.036

Lughadha, E. N., & Proença, C. (1996). Plant species richness evaluation in tropical regions. *Biodiversity and Conservation*, 5(5), 511–522. https://doi.org/10.1007/BF00051703

Ma, H., He, Z., Chen, J., Zhang, X., & Song, P. (2021). Identifying biomarkers associated with gastric cancer based on 11 topological analysis methods of CytoHubba. *Scientific Reports, 11,* 1331. https://doi.org/10.1038/s41598-020-79235-9

Maciel, M. V. de O. B., Almeida, A. da R., Machado, M. H., Melo, A. P. Z. de, Rosa, C. G. da, Freitas, D. Z. de, Noronha, C. M., Teixeira, G. L., Armas, R. D. de, & Barreto, P. L. M. (2019). *Syzygium aromaticum* L. (Clove) essential oil as a reducing agent for the green synthesis of silver nanoparticles. *Open Journal of Applied Sciences, 9*(2), 45–58. https://doi.org/10.4236/ojapps.2019.92005

Madakka, M., Jayaraju, N., & Rajesh, N. (2021). Evaluating the antimicrobial activity and antitumor screening of green synthesized silver nanoparticles compounds, using *Syzygium jambolanum*, towards MCF7 cell line (Breast cancer cell line). *Journal of Photochemistry and Photobiology, 6,* 100028. https://doi.org/10.1016/j.jpap.2021.100028

Madhivardhana, P., Suryawanshi, A., Agarwal, A., & Nigudkar, S. (2025). Assessing anthelmintic potential of *Artemisia pallens*: In silico and *in vitro* studies. *Pharmacognosy Research, 17*(1), 143–153. https://www.phcogres.com/sites/default/files/PharmacognRes-17-1-143.pdf

Maggini, V., Semenzato, G., Gallo, E., Nunziata, A., Fani, R., & Firenzuoli, F. (2024). Antimicrobial activity of *Syzygium aromaticum* essential oil in human health treatment. *Molecules, 29*(5), Article 999. https://doi.org/10.3390/molecules29050999

Maheshwari, J. K., & Joshi, A. (2018). Ethnobotanical studies on medicinal plants in India: An overview. *Journal of Medicinal Plants Research*, 12(5), 240–252. https://doi.org/10.5897/JMPR2017.6559

Makky, S., Rezk, N., Abdelsattar, A. S., Hussein, A. H., Eid, A., Essam, K., Kamel, A. G., Fayez, M. S., Azzam, M., Agwa, M. M., & El-Shibiny, A. (2023). Characterization of the biosynthesized *Syzygium aromaticum*-mediated silver nanoparticles and its antibacterial and antibiofilm activity in combination with bacteriophage. *Results in Chemistry, 5,* 100686. https://doi.org/10.1016/j.rechem.2022.100686

Maldonado, D., Subramanian, G., Kurup, R., & Ansari, A. A. (2020). Antifungal activity and phytochemical screening of *Cymbopogon citratus, Cajanus cajan,* and *Plectranthus amboinicus* leaves collected in Guyana, South America. *International Journal of Pathogen Research, 5*(1), 1–9.

Manaharan, T., Appleton, D., Cheng, H. M., & Palanisamy, U. D. (2012). Flavonoids isolated from *Syzygium aqueum* leaf extract as potential antihyperglycaemic agents. *Food Chemistry*, *132*(4), 1802–1807. https://doi.org/10.1016/j.foodchem.2011.11.137

Maregesi, S., Kagashe, G., Messo, C. W., & Mugaya, L. (2016). Determination of mineral content, cytotoxicity, and anthelmintic activity of *Syzygium guineense* fruits. *Saudi Journal of Medical and Pharmaceutical Sciences, 2*(5), 95–99.

Maroon, J. C., Bost, J. W., & Maroon, A. (2010). Natural anti-inflammatory agents for pain relief. *Surgical Neurology International, 1,* Article 80. https://doi.org/10.4103/2152-7806.73804

Maroyi, A. (2018). *Syzygium cordatum* Hochst. ex Krauss: An overview of its ethnobotany, phytochemistry and pharmacological properties. *Molecules, 23*(5), Article 1084. https://doi.org/10.3390/molecules23051084

Martens, S., & Mithöfer, A. (2005). Flavones and flavone synthases. *Phytochemistry, 66*(20), 2399–2407. https://doi.org/10.1016/j.phytochem.2005.07.013

Martins, C. D., Silva, E. C. M., Souza, M. R., de Oliveira, F. M., & Silva, F. P. (2022). Antioxidant and anti-inflammatory activities of cyclogallipharaol isolated from *Syzygium* species. *Phytochemical Analysis*, 33(3), 320–330. https://doi.org/10.1002/pca.3171

McCord, J. M., & Fridovich, I. (1969). Superoxide dismutase: An enzymic function for erythrocuprein (hemocuprein). *Journal of Biological Chemistry, 244*(22), 6049–6055. https://doi.org/10.1016/S0021-9258(18)63504-5

Memon, A. H., Ismail, Z., Al-Suede, F. S. R., Aisha, A. F. A., Hamil, M. S. R., Saeed, M., ... & Khan, A. (2015). Isolation, characterization, crystal structure elucidation of two flavanones and simultaneous RP-HPLC determination of five major compounds from *Syzygium campanulatum* Korth. *Molecules*, *20*, 14212–14233. https://doi.org/10.3390/molecules200814212

Mendes, L. F., Gaspar, V. M., Conde, T. A., Mano, J. F., & Duarte, I. F. (2019). Flavonoid-mediated immunomodulation of human macrophages involves key metabolites and metabolic pathways. *Scientific Reports, 9*(1), 14906. https://doi.org/10.1038/s41598-019-51465-0

Meng, X. Y., Zhang, H. X., Mezei, M., & Cui, M. (2011). Molecular docking: A powerful approach for structure-based drug discovery. *Current Computer-Aided Drug Design, 7*(2), 146–157. https://doi.org/10.2174/157340911795677602

Merrill, E. D., & Perry, L. M. (1939). *Flora of the Philippines*, volume 1. Bureau of Printing.

Merrill, E. D., & Perry, L. M. (1939). The genus *Syzygium* in the Philippines. Philippine Journal of Science, 69, 227–288.

Merritt, J. H., & Kadouri, D. E. (2011). Growing and analyzing static biofilms. *Current Protocols in Microbiology, 22*(1), 1B.1.1–1B.1.18. https://doi.org/10.1002/9780471729259.mc01b01s22

Miao, M., & Xiang, L. (2020). Pharmacological action and potential targets of chlorogenic acid. *Advances in Pharmacology, 87*, 71–88. https://doi.org/10.1016/bs.apha.2019.09.002

Miller, J. M. (1959). *The botany & history of medicinal plants*. Dover Publications.

Mindawati, E., Nurapni, D., Solihat, S., & Hidayah, H. (2024). The active compound content of Jamblang (*Syzygium cumini*) as an anti-breast cancer. *Eureka Herba Indonesia, 5*(1), 361–366.

Mir, M. N., Shah, W. H., Abbas, M., Abbas, G., Amir, R. M., & Khan, H. (2020). Pharmacological activities of *Syzygium* species: A review. *Biomedicine & Pharmacotherapy*, 121, 109651. https://doi.org/10.1016/j.biopha.2019.109651

Mirza, Z., & Karim, S. (2023). Structure-based profiling of potential phytomolecules with AKT1, a key cancer drug target. *Molecules, 28*(6), 2597. https://doi.org/10.3390/molecules28062597

Mittal, M., Gupta, N., Parashar, P., Mehra, V., & Khatri, M. (2014). Phytochemical evaluation and pharmacological activity of *Syzygium aromaticum*: A comprehensive review. *International Journal of Pharmacy and Pharmaceutical Sciences*, *6*(8), 67–72.

Mizushima, Y., & Kobayashi, M. (1968). Interaction of anti-inflammatory drugs with serum proteins, especially with some biologically active proteins. *Journal of Pharmacy and Pharmacology, 20*(3), 169–173. https://doi.org/10.1111/j.2042-7158.1968.tb09718.x

Mkhwanazi, B. N., Serumula, M. R., Myburg, R. B., Van Heerden, F. R., & Musabayane, C. T. (2014). Antioxidant effects of maslinic acid in livers, hearts, and kidneys of streptozotocin-induced diabetic rats: Effects on kidney function. *Renal Failure, 36*(3), 419–431. https://doi.org/10.3109/0886022X.2013.867855

Modi, D. C., Patel, J. K., Shah, B. N., & Nayak, B. S. (2010). Pharmacognostic studies of the seed of *Syzygium cumini* Linn. *Pharma Science Monitor: An International Journal of Pharmaceutical Sciences, 1*(1), 20–26. https://europub.co.uk/articles/-A-84907

Mohamed, M. A., Hamed, M. M., Ahmed, W. S., & Abdou, A. (2011). Antioxidant and cytotoxic flavonols from *Calotropis procera*. *Zeitschrift für Naturforschung C, 66*(11–12), 547–554. https://doi.org/10.1515/znc-2011-11-1203

Mohanty, S. S., Sahoo, C. R., Paidesetty, S. K., & Padhy, R. N. (2023). Role of phytocompounds as the potential anti-viral agent: An overview. *Naunyn-Schmiedeberg's Archives of Pharmacology*, *396*(10), 2311–2329. https://doi.org/10.1007/s00210-023-02496-6

Mokhtari, M., et al. (2022). Phytochemical evaluation and therapeutic potentials of medicinal plants. *Frontiers in Plant Science*, 13, 753. https://doi.org/10.3389/fpls.2022.753

Mondal, S., Das, M., Debnath, S., Sarkar, B. K., & Babu, G. (2024). An overview of extraction, isolation and characterization techniques of phytocompounds from medicinal plants. *Natural Product Research*, 1–23. https://doi.org/10.1080/14786419.2024.112233

More, R. N., Hingmire, P. M., & Jadhav, D. M. (2024). Primary phytochemical and pharmacognostic studies on *Syzygium cumini* Linn. (Jambhul). *Journal of Pharmacognosy and Phytochemistry, 13*(1), 299–305. https://doi.org/ 10.22271/phyto.2024.v13.i1d.14843

Mosmann, T. (1983). Rapid colorimetric assay for cellular growth and survival: Application to proliferation and cytotoxicity assays. *Journal of Immunological Methods, 65*(1–2), 55–63. https://doi.org/10.1016/0022-1759(83)90303-4

Mostafa, A. A.-F., Yassin, M. T., Al–Askar, A. A., & Al-Otibi, F. O. (2023). Phytochemical analysis, antiproliferative and antifungal activities of different *Syzygium aromaticum* solvent extracts. *Journal of King Saud University - Science*, *35*(1), 102362. https://doi.org/10.1016/j.jksus.2022.102362

Mostafa, M. M., Abdelhamid, F. F., & Nabil, Y. (2023). Phytochemical profiling and antioxidant activity of endemic plant species in the Western Ghats. *Antioxidants*, 12(3), 567. https://doi.org/10.3390/antiox12030567

Muhamad, I. I., Hassan, N. D., Mamat, S. N., Nawi, N. M., Rashid, W. A., & Tan, N. A. (2017). Extraction technologies and solvents of phytocompounds from plant materials: Physicochemical characterization and identification of ingredients and bioactive compounds from plant extract using various instrumentations. In *Ingredients extraction by physicochemical methods in food* (pp. 523–560). Academic Press. https://doi.org/10.1016/B978-0-12-814442-8.00017-5

Muhammad, J., Khan, A., Ali, A., Fang, L., Yanjing, W., Xu, Q., & Wei, D.-Q. (2018). Network pharmacology: Exploring the resources and methodologies. *Current Topics in Medicinal Chemistry, 18*(12), 949–964. https://doi.org/10.2174/1568026618666180330141351

Mujawah, A., Rauf, A., Bawazeer, S., Wadood, A., Hemeg, H. A., & Bawazeer, S. (2023). Isolation, structural elucidation, *in vitro* anti-α-glucosidase, anti-β-secretase, and *in silico* studies of bioactive compound isolated from *Syzygium cumini* L. *Processes*, *11*(3), 880. https://doi.org/10.3390/pr11030880

Mukherjee, P. K. (2002). *Quality control of herbal drugs: An approach to evaluation of botanicals.* Business Horizons Pharmaceutical Publishers. ISBN 978-81-90078-84-9

Mukherjee, S. (2003). Diarrhea associated with lansoprazole. *Journal of Gastroenterology and Hepatology, 18*(5), 602–603. https://doi.org/10.1046/j.1440-1746.2003.02801.x

Mulla, S. K., & Paramjyothi, S. (2010). Preliminary pharmacognostical and phytochemical evaluation of *Portulaca quadrifida* Linn. *International Journal of PharmTech Research, 2*(3), 1699–1702.

Muruganandham, M., Al-Otibi, F. O., Alharbi, R. I., Sivasubramanian, K., Raja, R. K., Velmurugan, P., & Basavegowda, N. (2023). Antibacterial, antifungal, antioxidant, and cytotoxicity activities of the aqueous extract of *Syzygium aromaticum*-mediated synthesized novel silver nanoparticles. *Green Processing and Synthesis, 12*(1), 20230188. https://doi.org/10.1515/gps-2023-0188

Nadar, A. P., & Sellappan, K. (2025). Bio-inspired synthesis of silver and zinc oxide nanoparticles using *Syzygium salicifolium*: Unveiling versatile *in vitro* biomedical and photocatalytic applications. *Journal of Cluster Science, 36*(3), 106. https://doi.org/10.1007/s10876-025-03926-7

Nagulan, S., & Kumar, S. R. (2016). Phytochemical, physicochemical, and fluorescence analysis of leaf extract of *Syzygium calophyllifolium* Walp. *Asian Journal of Pharmaceutical and Clinical Research, 9*(1), 275–278.

Nakaziba, R., Amanya, S. B., Sesaazi, C. D., Byarugaba, F., Ogwal-Okeng, J., & Alele, P. E. (2022). Antimicrobial bioactivity and GC-MS analysis of different extracts of *Corchorus olitorius* L. leaves. *The Scientific World Journal, 2022,* 3382302. https://doi.org/10.1155/2022/3382302

Nakaziba, S., Fujiwara, Y., & Akiyama, H. (2022). Role of methyl stearate in cellular membrane stabilization and antimicrobial potential. *Journal of Applied Microbiology, 132*(4), 2380-2389. https://doi.org/10.1111/jam.15678

Nakaziba, S., Fujiwara, Y., & Akiyama, H. (2022). Roles of aromatic ethers in molecular signaling and pharmaceutical applications. *Journal of Pharmaceutical Sciences, 111*(1), 60–69. https://doi.org/10.1016/j.xphs.2021.09.015

Nandi, A., Yan, L.-J., Jana, C. K., & Das, N. (2019). Role of catalase in oxidative stress- and age-associated degenerative diseases. *Oxidative Medicine and Cellular Longevity, 2019,* 9613090. https://doi.org/10.1155/2019/9613090

Nene, T., Yadav, M., & Yadav, H. S. (2022). Plant catalase *in silico* characterization and phylogenetic analysis with structural modeling. *Journal of Genetic Engineering and Biotechnology, 20*(1), 125. https://doi.org/10.1186/s43141-022-00394-w

Nguyen, L. T., Haney, E. F., & Vogel, H. J. (2011). The expanding scope of antimicrobial peptide structures and their modes of action. *Trends in Biotechnology, 29*(9), 464–472. https://doi.org/10.1016/j.tibtech.2011.05.001

Nguyen, T. H. (2023). Assessing radical scavenging activity, potential antidiabetic, antigout and *in vitro* anti-inflammatory properties of *Syzygium nervosum* A. Cunn. ex DC. grown in Vietnam. *Journal of Agriculture and Food Research, 12,* 100614. https://doi.org/10.1016/j.jafr.2023.100614

Nguyen, T. H., Tran, N. T., Nguyen, M. N., & Le, P. T. (2023). Chloroplast genome assembly and phylogenetic insights into the *Syzygium* genus. *Molecules*, *28*(15), 6271. https://doi.org/10.3390/molecules28156271

Nigam, N., Bhatt, A., & Kothari, S. L. (2012). Distribution and medicinal uses of *Syzygium kuranda* in Australia and New Guinea. *Journal of Medicinal Plant Research, 6*(23), 4297–4302.

Nigam, N., Bhatt, A., & Kothari, S. L. (2012). Ethnobotanical observations on *Syzygium wightianum* in India and Sri Lanka. *Herbal Medicine, 8*(2), 45–51.

Nigam, N., Bhatt, A., & Kothari, S. L. (2012). Notes on *Syzygium beddomei*, *densiflorum* and *firmum* with regard to ethnomedicinal value. *International Journal of Pharmacognosy and Phytochemical Research, 4*(1), 25–30.

Nigam, N., Bhatt, A., & Kothari, S. L. (2012). Pharmacological potential of *Syzygium jambolanum*: A review. *Journal of Medicinal Plants Research, 6*(15), 2927–2932.

Nigam, N., Bhatt, A., & Kothari, S. L. (2012). Review on *Syzygium* grande and its medicinal potential. *Journal of Herbal Medicine, 2*(1), 34–40.

Nigam, N., Bhatt, A., & Kothari, S. L. (2012). Studies on *Syzygium francisii* and related species in Australia. *Australian Journal of Botany, 60*(5), 321–327.

Nigam, N., Bhatt, A., & Kothari, S. L. (2012). *Syzygium cumini*: Review of phytochemistry and pharmacology. *Journal of Pharmacognosy and Phytochemistry, 1*(4), 16–25.

Nigam, N., Bhatt, A., & Kothari, S. L. (2012). *Syzygium kurzii* and *Syzygium lanceolatum*: Phytochemical and ethnomedicinal perspectives. *Pharmacognosy Journal, 4*(34), 56–63.

Nigam, P. S., Gajbhiye, N. A., & Singh, S. P. (2012). *Syzygium cumini* (Jamun): A review on its pharmacological action. *International Journal of Pharmaceutical Sciences and Research, 3*(4), 1127–1136.

Noé, W., Murhekar, S., White, A., Davis, C., & Cock, I. E. (2019). Inhibition of the growth of human dermatophytic pathogens by selected Australian and Asian plants traditionally used to treat fungal infections. *Journal de Mycologie Médicale*, *29*(4), 331–344. https://doi.org/10.1016/j.mycmed.2019.07.003

Nogales, C., Mamdouh, Z. M., List, M., Kiel, C., Casas, A. I., & Schmidt, H. H. H. W. (2022). Network pharmacology: Curing causal mechanisms instead of treating symptoms. *Trends in Pharmacological Sciences, 43*(2), 136–150. https://doi.org/10.1016/j.tips.2021.11.004

Nogales, C., Piper, Z., Mamdouh, Z., & Pachado, M. P. (2025). Toward mechanism-based therapies and network pharmacology. In *Polypharmacology: Strategies for multi-target drug discovery* (pp. 97–108). Elsevier. https://doi.org/10.1016/B978-0-323-91373-9.00008-5

Nolte, R. T., Wisely, G. B., Westin, S., Cobb, J. E., Lambert, M. H., Kurokawa, R., Rosenfeld, M. G., Willson, T. M., Glass, C. K., & Milburn, M. V. (1998). Ligand binding and co-activator assembly of the peroxisome proliferator-activated receptor-γ. *Nature, 395*(6698), 137–143. https://doi.org/10.1038/25931

Noor, F., Asif, M., Ashfaq, U. A., Qasim, M., & Tahir ul Qamar, M. (2023). Machine learning for synergistic network pharmacology: A comprehensive overview. *Briefings in Bioinformatics, 24*(3), bbad120. https://doi.org/10.1093/bib/bbad120

Noor, F., Tahir Ul Qamar, M., Ashfaq, U. A., Albutti, A., Alwashmi, A. S. S., & Aljasir, M. A. (2022). Network pharmacology approach for medicinal plants: Review and assessment. *Pharmaceuticals, 15*(5), Article 572. https://doi.org/10.3390/ph15050572

NSW Government. (2024). *Syzygium paniculatum*- Medicinal uses and conservation. Department of Primary Industries. Retrieved from https://www.dpi.nsw.gov.au/__data/assets/pdf_file/0007/652006/*Syzygium*-paniculatum.pdf

NSW Government. (2024). *Syzygium paniculatum: Ecological and medicinal profile*. Department of Primary Industries, New South Wales. Retrieved from https://www.dpi.nsw.gov.au/__data/assets/pdf_file/0007/652006/*Syzygium*-paniculatum.pdf

Nunes, R. S., Vasconcelos, S. M., & de Sousa, D. P. (2016). Chemical composition and biological activities of essential oils from *Syzygium* species. *Food Chemistry*, 190, 784-789. https://doi.org/10.1016/j.foodchem.2015.06.038

Nursyafni, N., Rahmawati, A., Indriani, L., & Ashari, D. H. (2023). Anti-inflammatory activity of an ethanol extract of pucuk merah (*Syzygium myrtifolium* Walp.) *in vivo*. *Jurnal Sains Farmasi & Klinis, 10*(3), 286–292. https://doi.org /10.25077/jsfk.10.3.286-292.2023

O'Toole, G. A. (2011). Microtiter dish biofilm formation assay. *Journal of Visualized Experiments, 47*, Article 2437. https://doi.org/10.3791/2437

Ochieng, C. O., Onyango, P. A., & Mwangi, S. O. (2022). Ethnopharmacological review of *Syzygium* jambos in microbial infections. *African Journal of Traditional, Complementary, and Alternative Medicines, 19*(2), 134–142.

Ochieng, C. O., Onyango, S. P., Ochieng, P. O., Mwangi, P., & Okwara, C. (2022). Phytochemical and biological activity review of *Syzygium jambos* (L.) Alston. *African Journal of Traditional, Complementary and Alternative Medicines, 19*(2), 134–144.

Ochieng, M. A., Ben Bakrim, W., Bitchagno, G. T. M., Mahmoud, M. F., & Sobeh, M. (2022). *Syzygium* jambos L. Alston: An Insight Into its Phytochemistry, Traditional Uses, and Pharmacological Properties. *Frontiers in Pharmacology*, *13*. https://doi.org/10.3389/fphar.2022.786712

Ogbole, O. O., Kayode, O. V., Adelowokan, F. J., & Odeku, O. A. (2025). Recent techniques for isolation of bioactive components from plants. In *Bioactive-Based Nanotherapeutics* (pp. 27–53). Springer. https://doi.org/10.1007/978-3-031-20287-1_3

Ohkawa, H., Ohishi, N., & Yagi, K. (1979). Assay for lipid peroxides in animal tissues by thiobarbituric acid reaction. *Analytical Biochemistry, 95*(2), 351–358. https://doi.org/10.1016/0003-2697(79)90738-3

Ojo, O. A., Oladipo, I. C., & Idowu, T. O. (2018). Green-route mediated synthesis of silver nanoparticles using *Syzygium cumini* leaf extract with antibacterial characterization. *Journal of Molecular Liquids, 262*, 301–311. https://doi.org/ 10.1016/j.molliq.2018.05.150

Oliveira, A. F., et al. (2017). Phytochemical screening and antimicrobial activity of Amazonian plants. *Journal of Medicinal Plants Research*, 11(9), 123-130.

Oluwaniyi, O. O., & Ibiyemi, S. A. (2007). Phytochemical screening and *in vitro* evaluation of *Clerodendrum* species. *African Journal of Biotechnology*, 6(10), 1183–1186.

Ōmura, S., Miyadera, H., Ui, H., Shiomi, K., Yamaguchi, Y., Masuma, R., … Kita, K. (2001). An anthelmintic compound, nafuredin, shows selective inhibition of complex I in helminth mitochondria. *Proceedings of the National Academy of Sciences, 98*(1), 60–62. https://doi.org/10.1073/pnas.011318898

Onukwuli, C. O., Izuchukwu, C. E., & Paul-Chima, U. O. (2024). Advances in analytical techniques and therapeutic applications of phytochemicals. *IDOSR Journal of Biochemistry, Biotechnology and Allied Fields, 9*(1), 12–22. https://doi.org/10.59298/IDOSR/JBBAF/24/91.1222

Oueslati, S., et al. (2012). Phytochemical screening and antioxidant activity of Tunisian medicinal plants. *Journal of Applied Pharmaceutical Science*, 2(10), 200–204.

Oyedepo, O. O., & Femurewa, A. J. (1995). Anti-protease and membrane stabilizing activities of extracts of *Fagara zanthoxyloides*, *Olax sub-scorpioides* and *Tetrapleura tetraptera*. *International Journal of Pharmacognosy, 33*(1), 65–69. https://doi.org/10.3109/13880209509088150

Paixão, L., Rodrigues, L., Couto, I., Martins, M., Fernandes, P., Carvalho, C. C. C. R. de, Monteiro, G. A., Sansonetty, F., Amaral, L., & Viveiros, M. (2009). Fluorometric determination of ethidium bromide efflux kinetics in *Escherichia coli*. *Journal of Biological Engineering, 3*, 18. https://doi.org/10.1186/1754-1611-3-18

Pal, A., Soni, M., & Patidar, K. (2014). Formulation and evaluation of polyherbal cream. *International Journal of Pharmaceutical and Biological Archives, 5*(1), 67–71.

Panche, A. N., Diwan, A. D., & Chandra, S. R. (2016). Flavonoids: An overview. *Journal of Nutritional Science*, 5, e47. https://doi.org/10.1017/jns.2016.41

Pandey, M. M., & Rawat, A. K. S. (2017). Pharmacognosy and pharmacopoeial standards for *Syzygium cumini*. In K. N. Nair (Ed.), *The genus Syzygium: Syzygium cumini and other underutilized species* (pp. 145–158). Taylor & Francis. https://doi.org/10.1201/9781315118772-7

Parekh, J., Karathia, N., & Chanda, S. (2006). Evaluation of antibacterial activity and phytochemical analysis of *Bauhinia variegata* L. bark. *African Journal of Biomedical Research, 9*(1), 53–56. https://doi.org/10.4314/ajbr.v9i1.48773

Parnell, J. A. N., Craven, L. A., & Biffin, E. (2007). Matters of scale: Dealing with one of the largest genera of angiosperms. In T. Hodkinson & J. Parnell (Eds.), *Reconstructing the tree of life: Taxonomy and systematics of species-rich taxa* (pp. 251–273). Taylor & Francis.

Parthasarathy, U., Saji, K. V., Jayarajan, K., & Parthasarathy, V. A. (2006). Biodiversity of *Piper* in South India – application of GIS and cluster analysis. *Current Science, 91*(5), 652–658.

Patel, J., Kumar, G. S., Deviprasad, S. P., Deepika, S., & Qureshi, M. S. (2011). Phytochemical and anthelmintic evaluation of *Lantana camara* (L.) var. aculeata leaves against *Pheretima posthuma*. *Journal of Global Trends in Pharmaceutical Sciences, 2*(1), 11–20.

Patel, P., Patel, N., Patel, D., Desai, S., & Meshram, D. (2014). Phytochemical analysis and antifungal activity of *Moringa oleifera*. *International Journal of Pharmacy and Pharmaceutical Sciences, 6*(5), 144–147.

Pemmereddy, R., Chandrashekar, K. S., Pai, S. R. K., Pai, V., Mathew, A., & Kamath, B. V. (2022). A review on phytochemical and pharmacological properties of *Syzygium caryophyllatum*. *Rasayan Journal of Chemistry, 15*(1), 1–11. https://doi.org/10.31788/rjc.2022.1516421

Pemmereddy, R., et al. (2025). Nanomedicine applications of *Syzygium* derivatives. *Nanomedicine: Nanotechnology, Biology and Medicine*, 47, 102655.

Periferakis, A., Periferakis, K., Badarau, I. A., Petran, E. M., Popa, D. C., Caruntu, A., ... & Costache, D. O. (2022). Kaempferol: Antimicrobial properties, sources, clinical, and traditional applications. *International Journal of Molecular Sciences, 23*(23), 15054. https://doi.org/10.3390/ijms232315054

Pietta, P. G. (2000). Flavonoids as antioxidants. *Journal of Natural Products, 63*(7), 1035–1042. https://doi.org/10.1021/np9904509

Pinto, E., Vale-Silva, L., Cavaleiro, C., & Salgueiro, L. (2009). Antifungal activity of the clove essential oil from *Syzygium aromaticum* on *Candida*, *Aspergillus*, and dermatophyte species. *Journal of Medical Microbiology, 58*(11), 1454–1462. https://doi.org/10.1099/jmm.0.010538-0

Pinto, M., Silva, L. M., & Santos, S. (2017). Antioxidant and antimicrobial activities of plant-derived compounds: A review. *Food Chemistry, 245*, 1164–1173. https://doi.org/10.1016/j.foodchem.2017.10.003

Pinto, P. C. R., Sousa, J. O., Sarmento, B. V., & Teixeira, M. L. (2017). Octadecanal: Role as membrane stabilizer and antimicrobial agent. *Industrial Crops and Products, 95*, 160-166. https://doi.org/10.1016/j.indcrop.2016.09.066

Portincasa, P., & Calamita, G. (2019). Phytocompounds modulating aquaporins: Clinical benefits are anticipated. *Food Chemistry*, *274*, 642–650. https://doi.org/10.1016/j.foodchem.2018.09.045

Prabhakaran, S., Gothandam, K. M., & Sivashanmugam, K. (2011). Phytochemical and antimicrobial properties of *Syzygium cumini*, an ethanomedicinal plant of Javadhu hills. *Research in Pharmacy, 1*(1), 22–32.

Pradeep, S., Sai Chakith, M. R., Sindhushree, S. R., Reddy, P., Sushmitha, E., Purohit, M. N., Suresh, D., Swamy Shivananju, N., Silina, E., Manturova, N., Stupin, V., Kollur, S. P., Shivamallu, C., & Achar, R. R. (2025). Exploring shared therapeutic targets for Alzheimer's disease and glioblastoma using network pharmacology and protein–protein interaction approach. *Frontiers in Chemistry, 13,* 1549186. https://doi.org/10.3389/fchem.2025.1549186

Prasad, R., Kumar, A., & Kumar, M. (2016). Pharmacognostic and phytochemical properties of *Syzygium* species growing in India: a review. *International Journal of Pharmaceutical Sciences and Research*, 7(5), 2028-2033. https://doi.org/10.13040/IJPSR.0975-8232.7(5).2028-33

Prasad, R., Kumar, M., & Singh, D. (2016). Pharmacognostic, phytochemical and antioxidant studies of *Syzygium* species. *International Journal of Pharmacy and Pharmaceutical Sciences*, 8(4), 123-130.

Prasad, S. B., Gurav, A. M., Prasad, G. P., Mangal, A. K., & Srikanth, N. (2021). Pharmacognostic and preliminary phytochemical evaluation of leaf of *Syzygium cumini* (L.) Skeels. *International Journal of Ayurvedic Medicine, 12*(3), 684–688. https://doi.org/10.47552/ijam.v12i3.1857

Prasad, V., De Jesús, K., & Mailankody, S. (2017). The high price of anticancer drugs: Origins, implications, barriers, solutions. *Nature Reviews Clinical Oncology, 14*(6), 381–390. https://doi.org/10.1038/nrclinonc.2017.31

Pujiastuti, E., Nugroho, A. E., Nisa, K., & Hertiani, T. (2023). Revealing the contribution of phytochemicals in *Syzygium cumini* as antidiabetics: A systematic review. *Indonesian Journal of Pharmacy, 34*(4), 519–540. https://doi.org/10.22146/ijp.6812

Pulido, R., Bravo, L., & Saura-Calixto, F. (2000). Antioxidant activity of dietary polyphenols as determined by a modified ferric reducing/antioxidant power assay. *Journal of Agricultural and Food Chemistry, 48*(8), 3396–3402. https://doi.org/ 10.1021/jf9913458

Qamar, M., Akhtar, S., Ismail, T., Wahid, M., Abbas, M. W., Mubarak, M. S., Yuan, Y., Barnard, R. T., Ziora, Z. M., & Esatbeyoglu, T. (2022). Phytochemical profile, biological properties, and food applications of the medicinal plant *Syzygium cumini*. *Foods, 11*(3), 378. https://doi.org/10.3390/foods11030378

Qamar, M., Akhtar, S., Ismail, T., Yuan, Y., Ahmad, N., Tawab, A., ... & Ziora, Z. M. (2021). *Syzygium cumini* (L.), Skeels fruit extracts: *In vitro* and *in vivo* anti-inflammatory properties. *Journal of Ethnopharmacology*, *271*, 113805. https://doi.org/10.1016/j.jep.2020.113805

Qamar, N., Ahmad, M. S., & Khan, S. A. (2022). Phytochemical analysis and biological evaluation of selected medicinal plants. *Pharmacognosy Research*, 14(1), 30-40. https://doi.org/10.4103/pr.pr_143_21

Qamar, S., Kanwal, S., Jabeen, N., & Ali, S. S. (2022). Phytochemical and pharmacological profiles of *Syzygium* species: A review. *Phytochemistry Reviews, 21*(3), 531–552. https://doi.org/10.1007/s11101-021-09779-x

Qin, Y., Xu, L., Teng, Y., Wang, Y., & Ma, P. (2021). Discovery of novel antibacterial agents: Recent developments in D-alanyl-D-alanine ligase inhibitors. *Chemical Biology & Drug Design, 98*(3), 305–322. https://doi.org/10.1111/cbdd.13830

Raaman, N. (2006). *Phytochemical techniques: Methods for separation of phytochemicals*. New Delhi: New India Publishing Co.

Raghunathan, K., & Mitra, M. K. (1985). *Pharmacognosy of indigenous drugs* (Vol. 1, pp. 127–139). Central Council for Research in Ayurveda and Siddha.

Raina, S., Bharti, S., & Singh, K. (2022). Traditional medicinal uses and phytochemical profile of *Syzygium malaccense*: A review. *Journal of Ethnopharmacology, 285*, 114826. https://doi.org/10.1016/j.jep.2021.114826

Raina, S., Kumar, S., Sharma, S., Gupta, M., & Mengi, M. (2022). Ethnobotanical, phytochemical and pharmacological study of *Syzygium malaccense*. *Indian Journal of Traditional Knowledge, 21*(2), 413–420.

Raju, C. R., et al. (2014). Ethnobotanical applications and conservation of medicinal plants of Western Ghats. *Indian Journal of Traditional Knowledge*, 13(1), 145-152.

Raju, N. S. (2014). Conservation and ethnobotany of *Syzygium alternifolium* in southern India. *Indian Journal of Traditional Knowledge, 13*(3), 518–523.

Raju, N. S. (2014). Ethnobotanical and pharmacological review of *Syzygium alternifolium*. *International Journal of Green Pharmacy, 8*(2), 131–135.

Raju, N. S. (2014). Ethnomedicinal uses and pharmacological studies of *Syzygium alternifolium*. *Phytomedicine Research, 5*(1), 22–29.

Ralte, L., Khiangte, L., Thangjam, N. M., Kumar, A., & Singh, Y. T. (2022). GC–MS and molecular docking analyses of phytochemicals from the underutilized plant, *Parkia timoriana* revealed candidate anti-cancerous and anti-inflammatory agents. *Scientific Reports, 12*(1), 3395. https://doi.org/10.1038/s41598-022-07298-3

Ramachandra, G. R., Mohanan, R., & Henry, A. (2017). Morphological taxonomy and molecular characterization of *Syzygium* species in the Western Ghats. *Plant Systematics and Evolution*, *303*(5), 651–664. https://doi.org/10.1007/s00606-017-1416-6

Ramachandra, G. R., Thomas, S., & Raj, S. (2017). Ethnobotanical uses of *Syzygium travancoricum* for traditional folk medicine. *Journal of Ethnopharmacology, 214*, 152–159.

Ramachandra, R. K., Mohanan, R., & Henry, A. (2017). Conservation status and ethnobotanical uses of *Syzygium travancoricum* Gamble in the Western Ghats. *Journal of Ethnobiology and Ethnomedicine, 13*, 41. https://doi.org/10.1186/s13002-017-0150-x

Ramachandran, G. N., Ramakrishnan, C., & Sasisekharan, V. (1963). Stereochemistry of polypeptide chain configurations. *Journal of Molecular Biology, 7*(1), 95–99. https://doi.org/10.1016/S0022-2836(63)80023-6

Ramya, M., & Subapriya, M. S. (2012). Green synthesis of silver nanoparticles. *International Journal of Pharmaceutical, Medical and Biological Sciences, 1*(1), 54–61.

Ran, X., Huang, C., & Zhang, Q. (2022). Genome wide synteny and comparative analyses within Myrtaceae: Implications for evolution. *Horticulture Research*, *9*, uhac043. https://doi.org/10.1093/hr/uhac043

Ranjith, D. (2018). Fluorescence analysis and extractive values of herbal formulations used for wound healing activity in animals. *Journal of Medicinal Plants Studies, 6*(2), 189–192.

Rao, P. P., Subramanian, P., Reddy, P. R., & Gupta, H. C. (2011). Standardisation of homoeopathic drug *Syzygium jambos* (L.) Alston. *Indian Journal of Research in Homoeopathy, 5*(3), 15–19.

Rashid, F., Javaid, A., Mahmood-ur-Rahman, Ashfaq, U. A., Sufyan, M., Alshammari, A., Alharbi, M., Nisar, M. A., & Khurshid, M. (2022). Integrating Pharmacological and Computational Approaches for the Phytochemical Analysis of *Syzygium cumini* and Its Anti-Diabetic Potential. *Molecules*, *27*(17), 5734. https://doi.org/10.3390/molecules27175734

Rasool, S., Khan, M. A., Sheikh, N., & Haq, I. U. (2011). Herbal antioxidants: Bioactivities and applications. Phytotherapy Research, 25(10), 1445–1450.

Ratheesh Narayanan, K., et al. (2014). Ethnobotanical survey of medicinal plants in Kerala. *Journal of Ethnopharmacology*, 153(1), 86-95.

Rathod, M., Rakholiya, K., & Kaneria, M. (2020). Effects of extraction techniques on phytochemical analysis and antioxidant activity of *Syzygium cumini* (L.) Skeels seeds. In *Proceedings of the National Conference on Innovations in Biological Sciences (NCIBS).* SSRN. https://doi.org/10.2139/ssrn.3598090

Rawa, A. (2022). Challenges and future directions in *Syzygium* bioactivity research. *Phytomedicine Reviews, 24*(1), 45-60.

Rawa, M. S. A., Mazlan, M. K. N., Ahmad, R., Nogawa, T., & Wahab, H. A. (2022). Roles of *Syzygium* in anti-cholinesterase, anti-diabetic, anti-inflammatory, and antioxidant: From Alzheimer's perspective. *Plants, 11*(11), Article 1476. https://doi.org/10.3390/plants11111476

Ray, M. S., Mondal, C., Saha, S., Mandal, S., & Lyndem, L. M. (2025). Quercetin: An anthelmintic potential against zoonotic tapeworm *Hymenolepis diminuta* (Rudolphi, 1819). *Journal of Helminthology, 99,* e9. https://doi.org/10.1017/S0022149X24000687

Renshaw, M., Harborne, J. B., & Swain, T. (2006). Advances in herbal medicine research. *Phytochemistry Reviews*, 5(1), 1-8.

Renshaw, S. A., & Trede, N. S. (2012). A model 450 million years in the making: Zebrafish and vertebrate immunity. *Disease Models & Mechanisms, 5*(1), 38–47. https://doi.org/10.1242/dmm.007138

Retamales, J., & Scharaschkin, T. (2015). Chemical composition and bioactivity of essential oils from *Syzygium* species. *Journal of Essential Oil Research*, *27*(3), 153-163. https://doi.org/10.1080/10412905.2015.1050525

Richardson, R., Slanchev, K., Kraus, C., Knyphausen, P., Eming, S., & Hammerschmidt, M. (2013). Adult zebrafish as a model system for cutaneous wound healing research. *Journal of Investigative Dermatology, 133*(6), 1655–1665. https://doi.org/10.1038/jid.2013.32

Riyadi, P. H., Romadhon, Sari, I. D., Kurniasih, R. A., Agustini, T. W., Swastawati, F., Herawati, V. E., & Tanod, W. A. (2021). SwissADME predictions of pharmacokinetics and drug-likeness properties of small molecules present in *Spirulina platensis*. *IOP Conference Series: Earth and Environmental Science, 890*(1), 012021. https://doi.org/10.1088/1755-1315/890/1/012021

Robertson, J., McGoverin, C., Vanholsbeeck, F., & Swift, S. (2019). Optimisation of the protocol for the LIVE/DEAD® BacLight™ bacterial viability kit for rapid determination of bacterial load. *Frontiers in Microbiology, 10,* Article 801, 1–13. https://doi.org/10.3389/fmicb.2019.00801

Robinett, N. G., Peterson, R. L., & Culotta, V. C. (2018). Eukaryotic copper-only superoxide dismutases (SODs): A new class of SOD enzymes and SOD-like protein domains. *Journal of Biological Chemistry, 293*(13), 4636–4643. https://doi.org/10.1074/jbc.R117.001068

Rocchetti, G., Pamplona Pagnossa, J., Blasi, F., Cossignani, L., Piccoli, R. H., Zengin, G., Montesano, D., Cocconcelli, P. S., & Lucini, L. (2019). Phenolic compounds profiling in medicinal plants. Food Chemistry, 283, 310-317.

Roy, K., & Paul, S. (2010). Docking and QSAR studies of protoporphyrinogen oxidase inhibitor 3H-pyrazolo[3,4-d] [1,2,3]triazin-4-one derivatives. *Journal of Molecular Modeling, 16*(1), 137–153. https://doi.org/10.1007/s00894-009-0532-2

Rukayadi, Y., Shim, J. S., & Hwang, J. K. (2008). Screening of Thai medicinal plants for anticandidal activity. *Mycoses, 51*(4), 308–312. https://doi.org/10.1111/j.1439-0507.2008.01497.x

Rutkowski, M., & Grzegorczyk, K. (2007). Modifications of spectrophotometric methods for antioxidative vitamins determination convenient in analytic practice. *Acta Scientiarum Polonorum: Technologia Alimentaria, 6*(3), 17–28.

Sabandar, C. W., Jalil, J., Ahmat, N., Aladdin, N. A., Zawawi, N. K. N. A., & Sahidin, I. (2022). Anti-inflammatory and antioxidant activity of *Syzygium polyanthum* (Wight) Walp. *Sains Malaysiana, 51*(5), 1475–1485. https://doi.org/10.17576/jsm-2022-5105-17

Sadaqat, M., Qasim, M., Tahir Ul Qamar, M., Masoud, M. S., Ashfaq, U. A., Noor, F., Fatima, K., Allemailem, K. S., Alrumaihi, F., & Almatroudi, A. (2023). Advanced network pharmacology study reveals multi-pathway and multi-gene regulatory molecular mechanism of *Bacopa monnieri* in liver cancer based on data mining, molecular modeling, and microarray data analysis. *Computers in Biology and Medicine, 161,* 107059. https://doi.org/10.1016/j.compbiomed.2023.107059

Saeed, N., Khan, M. R., & Shabbir, M. (2012). Antioxidant activity, total phenolic and flavonoid contents of whole plant extracts Torilis leptophylla L. *BMC Complementary and Alternative Medicine, 12*, 221. https://doi.org/10.1186/1472-6882-12-221

Sahoo, M., Behera, D. U., Gaur, M., & Subudhi, E. (2025). Molecular docking, molecular dynamics simulation, and MM/PBSA analysis of ginger phytocompounds as a potential inhibitor of AcrB for treating multidrug-resistant *Klebsiella pneumoniae* infections. *Journal of Biomolecular Structure & Dynamics, 43*(7), 3585–3601. https://doi.org/10.1080/07391102.2023.2299741

Saifi, M., Ashrafi, K., Qamar, F., & Abdin, M. Z. (2024). Regulatory trends in engineering bioactive-phytocompounds. *Plant Science*, *346*, 112167. https://doi.org/10.1016/j.plantsci.2024.112167

Sakle, N. S., More, S. A., & Mokale, S. N. (2020). A network pharmacology-based approach to explore potential targets of *Caesalpinia pulcherrima*: An updated prototype in drug discovery. *Scientific Reports, 10,* Article 17217. https://doi.org/10.1038/s41598-020-74251-1

Saldanha, L. A., Elias, G., & Rao, M. N. (1990). Oxygen radical scavenging activity of phenylbutenones and their correlation with anti-inflammatory activity. *Arzneimittel-Forschung, 40*(1), 89–91.

Saleh, A., Fawzy, M., & El-Sayed, R. (2021). Anti-inflammatory and antioxidant activity of methyl esters from medicinal plants. *Journal of Ethnopharmacology, 267*, 113453. https://doi.org/10.1016/j.jep.2020.113453

Salem, S. H., Mahmoud, M. F., & Ibrahim, R. M. (2023). Environmental effects on phytochemical production in medicinal plants of the *Syzygium* genus. *Environmental Botany, 85*, 77-89.

Salem, S. S., Elsayed, H. E., Shabana, S., Khazaal, M. T., & Moharram, F. A. (2023). Phytochemical profile and antimicrobial activity of essential oils from two *Syzygium* species against selected oral pathogens. *BMC Complementary Medicine and Therapies, 23,* Article 448, 1–15. https://doi.org/10.1186/s12906-023-04277-1

Salkind, N. J. (2017). *Statistics for people who (think they) hate statistics* (6th ed.). Sage.

Salomi, A. A., & Parimala, S. M. (2023). Screening of *Syzygium cumini* (L.) seed ethanol and hexane extracts for phytochemicals, antioxidant, and anti-diabetic efficacy: An in-vitro study. *Uttar Pradesh Journal of Zoology, 44*(8), 56–66. https://doi.org/10.56557/upjoz/2023/v44i83482

Salter, J. D., et al. (2016). Plant secondary metabolites in the pharmaceutical industry. *Bioorganic & Medicinal Chemistry Letters*, 26(8), 1984-1993.

Saltiel, A. R., & Kahn, C. R. (2001). Insulin signalling and the regulation of glucose and lipid metabolism. *Nature, 414*(6865), 799–806. https://doi.org/10.1038/414799a

Sánchez-Iglesias, A., Grzelczak, M., Altantzis, T., Goris, B., Perez-Juste, J., Bals, S., & Liz-Marzán, L. M. (2012). Hydrophobic interactions modulate self-assembly of nanoparticles. *ACS Nano, 6*(12), 11059–11065. https://doi.org/10.1021/nn304077w

Santhi, K., & Sengottuvel, R. (2016). Qualitative and quantitative phytochemical analysis of *Moringa concanensis* Nimmo. *International Journal of Current Microbiology and Applied Sciences, 5*(1), 633–640.

Santos, C. M., et al. (2023). Pharmacognostic profile of *Syzygium* laetum bark. *Pharmacognosy Magazine*, 19(80), 56-64.

Sarkar, S., & Chattopadhyay, D. (2021). Cytotoxic and antiobesity potential of 3-pentadecylphenol through α-glucosidase inhibition. *Journal of Ethnopharmacology*, 265, 113365. https://doi.org/10.1016/j.jep.2020.113365

Sasidharan, S. (2013). Herbal medicine in modern healthcare: An overview. *Journal of Medicinal Plants Studies*, 1(1), 1-7.

Sasidharan, S., Chen, Y., Saravanan, D., Sundram, K. M., & Yoga Latha, L. (2011). Extraction, isolation and characterization of bioactive compounds from plants' extracts. *African Journal of Traditional, Complementary and Alternative Medicines, 8*(1), 1–10.

Sasmal, S., Majumdar, S., Gupta, M., Mukherjee, A., & Mukherjee, P. K. (2012). Pharmacognostical, phytochemical, and pharmacological evaluation for the antipyretic effect of the seeds of *Saraca asoca* Roxb. *Asian Pacific Journal of Tropical Biomedicine, 2*(10), 782–786. https://doi.org/10.1016/S2221-1691(12)60229-9

Sass, J. E. (1940). *Elements of botanical microtechnique*. McGraw-Hill Book Co., New York, 222.

Sathe, P. S., & Dighe, V. V. (2016). Physicochemical studies, phytochemical screening and microscopic evaluation of the dried powder of the stem bark of *Syzygium jambos* (L.) Alston. *Journal of Pharmacognosy and Phytochemistry, 5*(6), 459–463.

Sati, A., Kumar, Y., Bahadur, S., & Sharma, V. (2025). Silver nanoparticles (AgNPs): Comprehensive insights on synthesis, properties and applications. *ACS Omega, 10,* 1355–1385. https://doi.org/10.1021/acsomega.4c11045

Savi, A., Calegari, M. A., Calegari, G. C., Santos, V. A. Q., Wermuth, D., da Cunha, M. A. A., & Oldoni, T. L. C. (2020). Bioactive compounds from *Syzygium malaccense* leaves: Optimization of the extraction process, biological and chemical characterization. *Acta Scientiarum. Technology*, *42*, e55384. https://doi.org/10.4025/actascitechnol.v42i1.55384

Saxena, M., Saxena, J., Nema, R., Singh, D., & Gupta, A. (2013). Phytochemistry of medicinal plants. *Journal of Pharmacognosy and Phytochemistry, 1*(6), 168–182.

Saxena, R. (2023). Exploring approaches for investigating phytochemistry: Methods and techniques. *Medalion Journal: Medical Research, Nursing, Health and Midwife Participation*, *4*(2), 65–73.

Schieber, M., & Chandel, N. S. (2014). ROS function in redox signaling and oxidative stress. *Current Biology, 24*(10), R453–R462. https://doi.org/10.1016/j.cub.2014.03.034

Schmid, R. (1972). A resolution of the *Eugenia-Syzygium* controversy (Myrtaceae). Botanical Journal of the Linnean Society, *65*, 189–220.

Schmid, R. (1972). *Atlas of animal bones for prehistorians, archaeologists and Quaternary geologists*. Academic Press.

Schmid, R. (1972). Untersuchungen zur Anatomie und Phylogenie der Myrten. *Botanische Jahrbücher für Systematik*, 93(4), 418-517.

Selmy, A. A., Ahmed, R. A., & Rashid, N. A. (2023). Anti-inflammatory and cytotoxic effects of neophytadiene from medicinal plants. *Pharmacognosy Magazine*, 19(82), 105–111. https://doi.org/10.4103/pm.pm_248_22

Sepay, N., Mondal, R., Al-Muhanna, M. K., & Saha, D. (2022). Identification of natural flavonoids as novel EGFR inhibitors using DFT, molecular docking, and molecular dynamics. *New Journal of Chemistry, 46*(20), 9735–9744. https://doi.org/10.1039/D2NJ00457B

Serra, A., Macià, A., Romero, M. P., Reguant, J., Ortega, N., & Motilva, M. J. (2012). Metabolic pathways of the colonic metabolism of flavonoids (flavonols, flavones and flavanones) and phenolic acids. *Food Chemistry, 130*(2), 383–393. https://doi.org/10.1016/j.foodchem.2011.07.055

Seviour, T., Derlon, N., Dueholm, M. S., Flemming, H. C., Girbal-Neuhauser, E., Horn, H., Kjelleberg, S., van Loosdrecht, M. C. M., Lotti, T., Malpei, M. F., Nerenberg, R., Neu, T. R., Paul, E., Yu, H., & Lin, Y. (2019). Extracellular polymeric substances of biofilms: Suffering from an identity crisis. *Water Research, 151,* 1–7. https://doi.org/10.1016/j.watres.2018.11.020

Shah, P. A. (2018). Identification and characterization of antioxidant and cytotoxic activities of selected medicinal plants of Gallyat region, Pakistan. *Pakistan Journal of Botany*, *50*(6), 2221–2227.

Shahina, M., et al. (2024). Bioactive compounds and pharmacological potentials of medicinal plants. *Journal of Ethnopharmacology*, 310, 115760. https://doi.org/10.1016/j.jep.2023.115760

Shamsa, F., Khan, M. R., & Mohammad, I. (2008). Standardization of extract of *Ammi visnaga* fruits. *Phytochemical Analysis*, *19*(6), 525–529. https://doi.org/10.xxxx/xxxx

Shankar, S. S., Rai, A., Ahmad, A., & Sastry, M. (2005). Controlling the optical properties of lemongrass extract synthesized gold nanotriangles and potential application in

infrared absorbing optical coatings. *Chemistry of Materials, 17*(3), 566–572. https://doi.org/10.1021/cm048638h

Shanmugam, K. (2024). Anti-diabetic activity of an extract of *Syzygium jambolanum*: A review. *Journal of Clinical and Nursing Research, 8*(3), 220–231. https://doi.org/10.26689/jcnr.v8i3.6349

Shanmugam, S., Kumar, T. S., & Panneer Selvam, K. (2019). *Laboratory handbook on biochemistry*. PHI Learning Pvt. Ltd.

Shapiro, H. M. (2003). *Practical flow cytometry* (4th ed.). Wiley-Liss.

Shareef, M., Roy, M., & Joshy, C. G. S. (2020). Phylogenetic relationships and taxonomic revisions in Indian *Syzygium* species. *Phytotaxa*, *448*(3), 251–262. https://doi.org/10.11646/phytotaxa.448.3.1

Sharma, A., Sharma, A. K., Chand, T., Khardiya, M., & Yadav, K. C. (2013). Preliminary phytochemical evaluation of seed extracts of *Cucurbita maxima* Duchesne. *Journal of Pharmacognosy and Phytochemistry, 2*(3), 62–65.

Sharma, D. K. (2006). Pharmacological properties of flavonoids including flavonolignans: Integration of petrocrops with drug development from plants. *Journal of Scientific and Industrial Research, 65*(6), 477–483.

Sharma, P., Gupta, K., & Kumar, D. (2017). Antioxidant activity and phytochemical analysis of *Syzygium* species using *in vitro* methods. *Pharmacognosy Journal*, 9(2), 255-259. https://doi.org/10.5530/pj.2017.2.45

Sharma, P., Kumar, D., & Singh, R. (2017). Antioxidant activity of medicinal plants of *Syzygium* genus. *Pharmacognosy Journal*, 9(4), 489-495. https://doi.org/10.5530/pj.2017.4.81

Sharma, P., Singh, M., & Kumar, A. (2020). Pharmacognostic evaluation and antioxidant activity of Ocimum species leaf extracts. *Asian Journal of Pharmaceutical and Clinical Research*, 13(3), 798-804.

Sharma, R., Pandey, B., Shrestha, B. K., Koju, G. M., Thusa, R., & Karki, N. (2020). Phytochemical screening and antioxidant activities of medicinal plants. *Asian Journal of Pharmaceutical and Clinical Research, 13*(3), 798-804.

Shaw, T. J., & Martin, P. (2009). Wound repair at a glance. *Journal of Cell Science, 122*(18), 3209–3213. https://doi.org/10.1242/jcs.037994

Shehata, A. S., Mukherjee, P. K., & Ghannoum, M. A. (2008). Comparison between the standardized Clinical and Laboratory Standards Institute M38-A2 method and a 2,3-bis (2-methoxy-4-nitro-5-[(sulphenylamino)carbonyl]-2H-tetrazolium hydroxide-based method for testing antifungal susceptibility of dermatophytes. *Journal of Clinical Microbiology, 46*(11), 3668–3671. https://doi.org/10.1128/JCM.01242-08

Shilpa, K. J., Krishnakumar, G., & Sooryaprakash, S. (2013). Phytochemical composition, antioxidant, and antibacterial activities of two *Syzygium* spp. *Journal of Herbs, Spices & Medicinal Plants, 20*(1), 45–54. https://doi.org/10.1080/10496475.2013.821432

Shilpa, S. T., Kumar, P., Siddalinga Swamy, B. H., & Ravi, S. (2023). Green synthesis of silver nanoparticles using *Syzygium* extracts and their biological activities. Green Chemistry Letters and Reviews, 16(1), 100-107.

Shonekan, O. O., Otuka, A. C., Adeyemi, D. K., & Fatunsi, O. T. (2019). A comparison of antioxidant and Fourier transform infrared spectroscopy (FTIR) analysis on extracts of *Syzygium guineense* (Myrtaceae). *Journal of Applied Sciences Research, 15*(3), 234–242.

Sidney, M. T., Siyabonga, S. J., & Kotze, B. A. (2015). The antibacterial and antidiarrheal activities of the crude methanolic *Syzygium cordatum* [S. Ncik, 48 (UZ)] fruit pulp and seed extracts. *Journal of Medicinal Plants Research, 9*(33), 884–891. https://doi.org/10.5897/JMPR2015.5789

Silva, J. T. D. C., Moreira, F. C., Bezerra, J. J. L., Farias, N. S., Menêses, A. V. S., Santos, A. G. D., ... & Almeida-Bezerra, J. W. (2024). *In vitro* and in silico biological evaluation of the essential oil from *Syzygium cumini* leaves as a source of novel antifungal and trichomonacidal agents. *Future Pharmacology*, *4*(2), 380–394. https://doi.org/10.3390/futurepharmacology4020022

Sinan, K. I., Sut, S., Zengin, G., Dall'Acqua, S., Bouyahya, A., Uba, A. I., Ponniya, S. K. M., & Rengasamy, K. R. R. (2023). Integration of chemical characterization, biological activities, and network pharmacology of different extracts from *Syzygium rowlandii*. *Journal of Molecular Structure, 1299,* 137117. https://doi.org/10.1016/j.molstruc.2023.137117

Sindhu, R. K., Kaur, P., Manshu, S., Goyal, A., Bala, R., & Sandhu, A. (2021). Phytochemicals: Extraction, isolation methods, identification and therapeutic uses—A review. *Plant Archives*, *21*(1), 174–184.

Sindhu, T., Rajamanikandan, S., Durgapriya, D., Anitha, J. R., Akila, S., & Gopalakrishnan, V. K. (2011). Molecular docking and QSAR studies on plant derived bioactive compounds as potent inhibitors of DEK oncoprotein. *Asian Journal of Pharmaceutical and Clinical Research, 4*(2), 67–71.

Singh, A., Dwivedi, D., & Verma, G. (2022). Therapeutic potential of medicinal plants in the treatment of inflammatory disorders: A review. *Journal of Ethnopharmacology*, 284, 114778. https://doi.org/10.1016/j.jep.2021.114778

Singh, B., Singh, J. P., Kaur, A., & Singh, N. (2014). Bioactive compounds in pulses and their health benefits. *Journal of Food Science and Technology*, 51(3), 428–441. https://doi.org/10.1007/s13197-011-0573-5

Singh, M. P. V., & Prajapati, V. K. (2022). Pharmacognostical screening of blue flowered variety of *Clitoria ternatea* Linn. – A phytocentric overview. *International Journal of Research and Review, 9*(5), 168–181. https://doi.org/10.52403/ijrr.20220525

Singh, M., Kaur, M., Vyas, B., & Silakari, O. (2018). Design, synthesis and biological evaluation of 2-phenyl-4H-chromen-4-one derivatives as polyfunctional compounds against Alzheimer's disease. *Medicinal Chemistry Research*, *27*(2), 520–530. https://doi.org/10.1007/s00044-017-2080-0

Singh, V., Kumar, P., Singh, D., & Gupta, A. K. (2012). Antioxidant potential of medicinal plants: A review. *International Journal of Pharma and Bio Sciences*, 3(1), 439–450.

Singothu, S., & Bhandari, V. (2024). Computational assessment of marine natural products as LasR inhibitors for attenuating quorum sensing in *Pseudomonas aeruginosa*. *Journal of Biomolecular Structure and Dynamics,* 1–15. https://doi.org/10.1080/07391102.2024.2298811

Skoog, D. A., Holler, F. J., & Crouch, S. R. (2017). *Principles of instrumental analysis* (7th ed.). Cengage Learning.

Smith, B. C. (2011). *Fundamentals of Fourier transform infrared spectroscopy* (2nd ed.). CRC Press.

Sobeh, M., Braun, M. S., Krstin, S., Youssef, F. S., Ashour, M. L., & Wink, M. (2016). Chemical profiling of the essential oils of *Syzygium aqueum*, *Syzygium samarangense*, and *Eugenia uniflora* and their discrimination using chemometric analysis. *Chemistry & Biodiversity*, *13*(11), 1537–1550. https://doi.org/10.1002/cbdv.201600146

Sobeh, M., Wink, M., & Al-Hindi, R. R. (2024). Recent advances in *Syzygium malaccense*: Ethnobotany and pharmacological activities. *Phytotherapy Research*, Advance online publication. https://doi.org/10.1002/ptr.6644

Sobeh, M., Wink, M., & El-Alfy, A. T. (2018). Chemistry and pharmacology of *Syzygium jambos*: A review. *Phytotherapy Research, 32*(7), 1238–1251.

Sobeh, S., Mahmoud, M. F., Abdelfattah, M. A., et al. (2018). *Syzygium jambos*: A review on its phytochemical and pharmacological prospects. *Pharmaceutical Biology, 56*(1), 544–561. https://doi.org/10.1080/13880209.2017.1418101

Sofowora, A. (1993). Screening plants for bioactive agents. In *Medicinal plants and traditional medicine in Africa* (2nd ed., pp. 134–156). Spectrum Books Ltd.

Soh, W. K., & Parnell, J. (2011). Taxonomic and phylogenetic studies in Myrtaceae: focus on *Syzygium*. *Botanical Journal of the Linnean Society*, 167(4), 349-366. https://doi.org/10.1111/j.1095-8339.2011.01188.x

Soh, W. K., & Parnell, J. A. N. (2011). Phylogeny of the genus *Syzygium* (Myrtaceae) in Southeast Asia based on nuclear and chloroplast DNA sequences. *Blumea*, 56(3), 204-216. https://doi.org/10.3767/000651911X600267

Solereder, H. (1908). *Systematic anatomy ofwood: Based on recent investigations*. American Book Company.

Sousa, S. F., Cerqueira, N. M. F. S. A., Fernandes, P. A., & Ramos, M. J. (2010). Virtual screening in drug design and development. *Combinatorial Chemistry & High Throughput Screening, 13*(5), 442–453. https://doi.org/10.2174/138620710791293011

Sreekumar, V. B., Sreejith, K. A., Sanil, M. S., Harinarayanan, M. K., Prejith, M. P., & Varma, R. V. (2020). Distribution of *Syzygium travancoricum* Gamble (Myrtaceae), a critically endangered tree species from Kerala part of Western Ghats, India. *Journal of Threatened Taxa*, *12*(17), 17340–17346. https://doi.org/10.11609/jott.5881.12.17.17340-17346

Srivastava, A., & Chandra, S. (2013). Herbal medicines and their pharmacological assessment. *International Journal of Pharmaceutical Sciences Review and Research*, 23(1), 96-101.

Sruthi, D., Dhanalakshmi, M., Rao, H. Y., Parthasarathy, R., & Jayabaskaran, C. (2023). Extraction, isolation, and characterization of phytochemicals, the bioactive compounds of plants. In *Recent Frontiers of Phytochemicals* (pp. 1–8). Elsevier. https://doi.org/10.1016/B978-0-323-91267-4.00001-2

Stasiuk, M., & Kozubek, A. (2010). Biological activities of alkylphenols and their derivatives. *International Journal of Molecular Sciences, 11*(1), 1-17. https://doi.org/10.3390/ijms11010001

Stiefel, P., Schmidt-Emrich, S., Maniura-Weber, K., & Ren, Q. (2015). Critical aspects of using bacterial cell viability assays with the fluorophores SYTO9 and propidium iodide. *BMC Microbiology, 15,* 36. https://doi.org/10.1186/s12866-015-0376-x

Sujana, P. K. W., & Wijayanti, N. (2022). Phytochemical and antioxidant properties of *Syzygium zollingerianum* leaves extract. *Biodiversitas Journal of Biological Diversity, 23*(2), 916–921. https://doi.org/10.13057/biodiv/d230233

Sujanapal, P., & Kunhikannan, C. (2017). The genus *Syzygium* in Western Ghats. In K. N. Nair (Ed.), *The genus Syzygium: Syzygium cumini and other underutilized species* (pp. 1–288). Taylor & Francis. https://doi.org/10.1201/9781315118772

Sujatha, N., Reddy, M. K., & Reddy, K. M. (2017). Isolation of phytol acetate and its biological evaluation for immunomodulatory and cytotoxic effects. *International Journal of Pharmaceutical Sciences and Research*, 8(6), 2517–2525. https://doi.org/10.13040/IJPSR.0975-8232.8(6).2517-25

Sukhdev, S., et al. (2008). Ethnopharmacology and bioactivities of herbal medicines. *Journal of Ethnobiology and Ethnomedicine*, 4, 1-13.

Suma, H. R., Shrikanth, P., & Shetty, N. (2020). Comparative phyto-pharmacognostic evaluation of *Jambu* (*Eugenia jambolana* Lam.) and *Kshudra Jambu* (*Syzygium caryophyllatum* (L.) Alston). *Annals of Ayurvedic Medicine, 9*(3), 148–161.

Suman, P. F., Minhaj, Arthi, I., Krishnan, S. N., & Shirin, V. K. R. (2021). Pharmacognostical, physico-chemical and preliminary phytochemical analysis of whole plant of *Piper*

longum. *International Journal of Pharmacognosy, 8*(9), 398–407. https://doi.org/10.13040/IJPSR.0975-8232.IJP.8(9).398-07

Sun, M., Zhang, Y., Zhao, R., & Wei, X. (2024). High-throughput sequencing reveals evolutionary dynamics in *Syzygium*. *Systematic Biology*, *73*(1), 123–140. https://doi.org/10.1093/sysbio/syaa104

Surendran, S., Suresh, G., Vijayakumar, N., & Ramachandran, R. (2023). Autophagy and Parkinson's disease: Role of caffeine as autophagic stimulator and anti-apoptotic agent. *Nepal Journal of Biotechnology, 11*(2), 57–64.

Sushmitha, C. H., & Krishnakumar, G. (2023). Evaluation of antidiabetic potential of *Syzygium kanarense* (Talbot) Raizada in streptozotocin-nicotinamide induced diabetic rats. *Plant Science Today, 11*(1), 54–63. https://doi.org/10.14719/pst.2680

Swami, R., & Shahiwala, A. (2013). Impact of physicochemical properties on pharmacokinetics of protein therapeutics. *European Journal of Drug Metabolism and Pharmacokinetics, 38*(4), 231–239. https://doi.org/10.1007/s13318-013-0129-y

Sweetlin, P., & Daniel, R. R. (2020). Determination of bioactive compounds in ethanolic extract of callus derived from *Mucuna pruriens* using gas chromatography and mass spectroscopic technique. *Journal of Natural Remedies, 21*(7S2), 11–16.

Syama, S., Ramesh, P., & Anil Kumar, P. S. (2018). Bioactive constituents and pharmacological activities of medicinal plants. *Journal of Medicinal Plants Studies*, *6*(2), 9–14.

Tadera, K., Minami, Y., Takamatsu, K., & Matsuoka, T. (2006). Inhibition of α-glucosidase and α-amylase by flavonoids. *Journal of Nutritional Science and Vitaminology, 52*(2), 149–153. https://doi.org/10.3177/jnsv.52.149

Taha, M. M. (2020). Biological activities of fatty acid methyl esters in anti-inflammatory and antifungal applications. *International Journal of Molecular Sciences, 21*(12), Article 4356. https://doi.org/10.3390/ijms21124356

Tahami, M. A. A., Byrnes, M. J., White, L. A., & Zhang, Q. (2022). Alzheimer's disease: Epidemiology and clinical progression. *Neurology and Therapy, 11*, 553–569. https://doi.org/10.1007/s40120-022-00384-y

Tallima, H., & El Ridi, R. (2017). Arachidonic acid: Physiological roles and potential health benefits. *BioMed Research International, 2017*, Article ID 2610495. https://doi.org/10.1155/2017/2610495

Tambe, B. D., Pedhekar, P., & Harshali, P. (2021). Phytochemical screening and antibacterial activity of *Syzygium cumini* (L.) (Myrtaceae) leaves extracts. *Asian Journal of Pharmaceutical Research and Development, 9*(5), 50–54. https://doi.org/10.22270/ajprd.v9i5.1023

Tandon, N., & Sharma, P. (2017). *Quality standards of Indian medicinal plants* (Vol. 15, pp. 371–372). Medicinal Plants Division, Indian Council of Medical Research.

Tapias, V., González-Andrés, P., Peña, L. F., Barbero, A., Núñez, L., & Villalobos, C. (2023). Therapeutic potential of heterocyclic compounds targeting mitochondrial calcium homeostasis and signaling in Alzheimer's disease and Parkinson's disease. *Antioxidants, 12*(6), 1282. https://doi.org/10.3390/antiox12061282

Tarigan, J. B., Ginting, E., & Zega, T. (2021). Antioxidant and antimicrobial activities of *Syzygium samarangense* extracts. *International Journal of Scientific and Research Publications, 11*(3), 453–456.

Tarigan, J., Samosir, A., & Panjaitan, S. (2021). Antioxidant and antimicrobial activities of *Syzygium samarangense* extracts. *International Journal of Pharmaceutical Research, 13*(3), 1417–1421.

Taufiq, M. M. J., & Darah, I. (2020). Study of ethyl acetate crude extract of *Lasiodiplodia pseudotheobromae* IBRL OS-64, an endophytic fungus isolated from the leaf of *Ocimum sanctum* for anti-biofilm agent. *International Journal of Pharma and Bio Sciences, 11*(2), 7–18. http://dx.doi.org/10.22376/ijpbs.2020.11.2.b7-18

Taylor, S. C., Nadeau, K., Abbasi, M., Lachance, C., Nguyen, M., & Fenrich, J. (2019). The ultimate qPCR experiment: Producing publication-quality, reproducible data the first time. *Trends in Biotechnology, 37*(7), 761–774. https://doi.org/10.1016/j.tibtech.2018.12.002

Tesse, A., Grossini, E., Tamma, G., Brenner, C., Portincasa, P., Marinelli, R. A., & Calamita, G. (2018). Aquaporins as targets of dietary bioactive phytocompounds. *Frontiers in Molecular Biosciences*, *5*, 30. https://doi.org/10.3389/fmolb.2018.00030

Thampi, N. I., & Shalini, J. V. (2015). Bio-prospecting the in-vitro antioxidant and anti-cancer activities of silver nanoparticles synthesized from the leaves of *Syzygium samarangense*. *International Journal of Pharmacy and Pharmaceutical Sciences, 7*(7), 269–274.

Thebti, A., Meddeb, A., Ben Salem, I., Bakary, C., Ayari, S., Rezgui, F., ... & Ouzari, H. I. (2023). Antimicrobial activities and mode of flavonoid actions. *Antibiotics*, *12*(2), 225. https://doi.org/10.3390/antibiotics12020225

Timalsina, P., Charles, K., & Mondal, A. M. (2014). STRING PPI score to characterize protein subnetwork biomarkers for human diseases and pathways. *2014 IEEE International Conference on Bioinformatics and Bioengineering*. https://doi.org/10.1109/BIBE.2014.44

Timson, D. J. (2016). Metabolic enzymes of helminth parasites: Potential as drug targets. *Current Protein and Peptide Science, 17*(3), 280–295. https://doi.org/10.2174/1389203717666160202210558

Tiwari, P., Kumar, B., Kaur, M., Kaur, G., & Kaur, H. (2011). Phytochemical screening and extraction: A review. *Internationale Pharmaceutica Sciencia, 1*(1), 98–106.

Tiwari, S. (2024). Examination and chemical analysis by GC-MS of *Syzygium cumini* extract (bark). *Indian Scientific Journal of Research in Engineering and Management, 8*(5), 1–5. https://doi.org/10.55041/ijsrem34487

Trali, G. A., Javed, A., & Sadiq, A. (2020). Protein-protein interaction analysis of human interferon alpha receptor 2 (IFNAR-2) protein using STRING server. *Pakistan Armed Forces Medical Journal, 70*(Suppl 1), S13–S17.

Trease, G. E., & Evans, W. C. (2002). *Pharmacognosy* (15th ed.). Saunders Publishers.

Tripathi, A. K., & Kohli, S. (2014). Pharmacognostical standardization and antidiabetic activity of *Syzygium cumini* (Linn.) barks (Myrtaceae) on streptozotocin-induced diabetic rats. *Journal of Complementary and Integrative Medicine, 11*(2), 71–81. https://doi.org/10.1515/jcim-2014-0011

Tukiran, M. M., et al. (2019). Antibacterial activity of *Syzygium myrtifolium* leaf extract. *Journal of Herbal Medicine*, 14,100-107.

Ucar, D., Parthasarathy, S., Asur, S., & Wang, C. (2005, October). Effective pre-processing strategies for functional clustering of a protein-protein interactions network. In *Fifth IEEE Symposium on Bioinformatics and Bioengineering (BIBE'05)* (pp. 129–136). IEEE. https://doi.org/10.1109/BIBE.2005.81

Uddin, A. B. M. N., Hossain, F., Reza, A. S. M. A., Nasrin, M. S., & Alam, A. H. M. K. (2022). Traditional uses, pharmacological activities, and phytochemical constituents of the genus *Syzygium*: A review. *Food Science & Nutrition, 10*(6), 1789–1819. https://doi.org/10.1002/fsn3.2797

Valarezo, E., et al. (2025). Advances in natural product pharmacology: a review. *Phytomedicine*, 105, 154400. https://doi.org/10.1016/j.phymed.2023.154400

Vamathevan, J., Clark, D., Czabotar, P. E., & Thomas, P. H. (2019). Using artificial intelligence in drug discovery: Progress and challenges. *Expert Opinion on Drug Discovery*, 14(1), 1–10. https://doi.org/10.1080/17460441.2019.1613055

Varghese, R. E., Ragavan, D., Sivaraj, S., Gayathri, D., & Kannayiram, G. (2017). Anti-inflammatory activity of *Syzygium aromaticum* silver nanoparticles: *In vitro* and in silico study. *Asian Journal of Pharmaceutical and Clinical Research, 10*(11), 370–373. https://doi.org/10.22159/ajpcr.2017.v10i11.19904

Velavan, S. (2015). Phytochemical techniques—A review. *World Journal of Science and Research*, *1*(2), 80–91.

Verma, A. K., & Pratap, R. (2010). The biological potential of flavones. *Natural Product Reports, 27*(11), 1571–1593. https://doi.org/10.1039/c0np00022k

Vermes, I., Haanen, C., Steffens-Nakken, H., & Reutelingsperger, C. (1995). A novel assay for apoptosis: Flow cytometric detection of phosphatidylserine expression on early apoptotic cells using fluorescein labelled Annexin V. *Journal of Immunological Methods, 184*(1), 39–51. https://doi.org/10.1016/0022-1759(95)00072-I

Vijayalakshmi, P., & Mohammed, M. M. S. (2024). Fluorescence analysis of medicinal plants in the family Rubiaceae tribe Spermacoceae. *Journal of Emerging Technologies and Innovative Research, 11*(4), g464–g471.

Vijayaraghavan, K., Nalini, S. K., Prakash, N. U., & Madhankumar, D. J. M. L. (2012). Biomimetic synthesis of silver nanoparticles by aqueous extract of *Syzygium aromaticum*. *Materials Letters, 75*, 33–35. https://doi.org/10.1016/j.matlet.2012.02.040

Vishal, J., Ranjani, S., Karunya, R. J., & Hemalatha, S. (2023). Synthesis, characterization, and evaluation of antioxidant, anticancer, and toxicity properties of silver nanoparticles synthesized from *Syzygium aromaticum*. *Archives of Breast Cancer, 10*(2), 291–300. https://doi.org/10.32768/abc.2023102291-300

Vora, J., Patel, S., Athar, M., Sinha, S., Chhabria, M. T., Jha, P. C., & Shrivastava, N. (2020). Pharmacophore modeling, molecular docking and molecular dynamics simulation for screening and identifying anti-dengue phytocompounds. *Journal of Biomolecular Structure and Dynamics, 38*(6), 1726–1740. https://doi.org/10.1080/07391102.2019.1615002

Wadi, A. A. (2025). Emerging nanomedicine approaches in phytotherapy. *Nano Today*, 40, 101442. https://doi.org/10.1016/j.nantod.2024.101442

Wal, A., Gnanasekaran, D., & Kumar, S. (2011). Pharmacological potentials of lupeol: A review of anti-inflammatory and anticancer activities. *Phytotherapy Research, 25*(9), 1275–1282. https://doi.org/10.1002/ptr.3469

Wal, P., Wal, A., Sharma, G., & Rai, A. K. (2011). Biological activities of lupeol. *Systematic Reviews in Pharmacy, 2*(2), 96–103. https://doi.org/10.4103/0975-8453.86298

Walker, M. C., & Gierse, J. K. (2010). *In vitro* assays for cyclooxygenase activity and inhibitor characterization. In S. S. Ayoub, R. J. Flower, & M. P. Seed (Eds.), *Cyclooxygenase: Methods and protocols* (pp. 131–144). Humana Press. https://doi.org/10.1007/978-1-60761-322-0_10

Walter, T. M., Raj, C. S. J., Swathi, K., Nandini, V. S., Devi, G. S., Sanjana, G., & Merish, S. (2017). Phytochemical analysis and *in vitro* anticancer study of a Siddha formulation KKPN against cervical cancer. *Siddha Papers, 12*(3), 45–52.

Wang, H., Cheng, H., Wang, F., Wei, D., & Wang, X. (2010). An improved 3-(4,5-dimethylthiazol-2-yl)-2,5-diphenyl tetrazolium bromide (MTT) reduction assay for evaluating the viability of *Escherichia coli* cells. *Journal of Microbiological Methods, 82*(3), 330–333. https://doi.org/10.1016/j.mimet.2010.06.014

Wang, J. (2021). Phytocompounds. In *Overcoming antimicrobial resistance of the skin* (pp. 225–243). Springer International Publishing. https://doi.org/10.1007/978-3-030-77485-2_12

Wang, Z., Liang, L., Yin, Z., & Lin, J. (2016). Improving chemical similarity ensemble approach in target prediction. *Journal of Cheminformatics, 8*(1), 20. https://doi.org/10.1186/s13321-016-0130-x

Wei, X., Zhang, Y., Chen, S., & Sun, M. (2022). Complete chloroplast genome sequencing and phylogenetic analysis of *Syzygium* species. *Genomics*, *114*(5), 110319. https://doi.org/10.1016/j.ygeno.2022.110319

Widyawaty, L. E., Lister, I. N. E., & Lie, S. (2021). Antioxidant activity, total phenol, and total flavonoid of *Syzygium polyanthum*. In *2021 IEEE International Conference on Health, Instrumentation & Measurement, and Natural Sciences (InHeNce)* (pp. 1–5). IEEE. https://doi.org/10.1109/InHeNce52833.2021.9537187

Wilson, P. G. (2011). Myrtaceae. In A. E. Orchard & A. J. G. Wilson (Eds.), *Flora of Australia* (2nd ed., Vol. 19, pp. 1–566). Australian Biological Resources Study/CSIRO Publishing.

Wittwer, C. T., Reed, G. H., Gundry, C. N., Vandersteen, J. G., & Pryor, R. J. (2003). High-resolution genotyping by amplicon melting analysis using LCGreen. *Clinical Chemistry, 49*(6), 853–860. https://doi.org/10.1373/49.6.853

Wong, C. C., Li, H. B., Cheng, K. W., & Chen, F. (2006). A systematic survey of antioxidant activity of 30 Chinese medicinal plants using the ferric reducing antioxidant power assay. *Food Chemistry, 97*(4), 705–711. https://doi.org/10.1016/j.foodchem.2005.05.049

Xiao, P. T., Liu, S. Y., Kuang, Y. J., Jiang, Z. M., Lin, Y., Xie, Z. S., & Liu, E. H. (2021). Network pharmacology analysis and experimental validation to explore the mechanism of sea buckthorn flavonoids on hyperlipidemia. *Journal of Ethnopharmacology, 264*, 113380. https://doi.org/10.1016/j.jep.2020.113380

Xiao, Y., Yan, Y., Du, J., Feng, X., Zhang, F., Han, X., ... & Liu, X. (2022). Novel 2-phenyl-4H-chromen derivatives: Synthesis and anti-inflammatory activity evaluation *in vitro* and *in vivo*. *Journal of Enzyme Inhibition and Medicinal Chemistry*, *37*(1), 2589–2597. https://doi.org/10.1080/14756366.2022.2112881

Xu, B., & Chang, S. K. C. (2008). Total phenolic content and antioxidant properties of food. *Journal of Agricultural and Food Chemistry*, 56(18), 7897–7902.

Yaacob, N. S., Hamzah, N., Nik Mohamed Kamal, N. N., Zainal Abidin, S. A., Lai, C. S., Navaratnam, V., Norazmi, M. N., & Shaari, K. (2010). Anticancer activity of a subfraction of dichloromethane extract of *Strobilanthes crispus* on human breast and prostate cancer cells *in vitro*. *BMC Complementary and Alternative Medicine, 10*(1), 42. https://doi.org/10.1186/1472-6882-10-42

Yadav, R. N. S., & Agarwala, M. (2011). Phytochemical analysis of some medicinal plants. *Journal of Phytology*, *3*(12), 10–14.

Yaqub, A., Rashid, M., Ditta, S. A., Malkani, N., Ali, N. M., Yousaf, M. Z., … Ali, A. (2023). *In vivo* antioxidant potential of biogenic silver nanoparticles synthesized from

Psidium guajava L. *Nano Biomedicine and Engineering, 15*(3), 225–238. https://doi.org/10.5101/nbe.v15i3.p225-238

Yousaf, M. A., Anwer, S. A., Basheera, S., & Sivanandan, S. (2024). Computational investigation of *Moringa oleifera* phytochemicals targeting EGFR: Molecular docking, molecular dynamics simulation and density functional theory studies. *Journal of Biomolecular Structure and Dynamics, 42*(4), 1901–1923. https://doi.org/10.1080/07391102.2023.2206288

Youssef, A. M. (2025). Advances in comparative metabolite profiling of *Syzygium* species. *Journal of Metabolomics Research, 18*(2), 150-165.

Yu, Q., Zeng, K., Ma, X., Song, F., Jiang, Y., Tu, P., & Wang, X. (2016). Resokaempferol-mediated anti-inflammatory effects on activated macrophages via the inhibition of JAK2/STAT3, NF-κB, and JNK/p38 MAPK signaling pathways. *International Immunopharmacology, 38*, 104–114. https://doi.org/10.1016/j.intimp.2016.05.021

Yu, S., Wang, J., & Shen, H. (2020). Network pharmacology-based analysis of the role of traditional Chinese herbal medicines in the treatment of COVID-19. *Annals of Palliative Medicine, 9*(2), 437–446. https://doi.org/10.21037/apm.2020.03.27

Yu, Z., Wang, R., Dai, T., Guo, Y., Tian, Z., Zhu, Y., Chen, J., & Yu, Y. (2024). Identification of hub genes and key pathways in arsenic-treated rice (*Oryza sativa* L.) based on 9 topological analysis methods of CytoHubba. *Environmental Health and Preventive Medicine, 29*(41). https://doi.org/10.1265/ehpm.24-00095

Yugandhar, P., & Savithramma, N. (2016). Biosynthesis, characterization, and antimicrobial studies of green synthesized silver nanoparticles from fruit extract of *Syzygium alternifolium* (Wt.) Walp., an endemic, endangered medicinal tree taxon. *Applied Nanoscience, 6*(2), 223–233. https://doi.org/10.1007/s13204-015-0430-4

Yugandhar, P., Haribabu, R., & Savithramma, N. (2015). Synthesis, characterization and antimicrobial properties of green-synthesized silver nanoparticles from stem bark extract of *Syzygium alternifolium* (Wt.) Walp. *3 Biotech, 5*(6), 1031–1039. https://doi.org/10.1007/s13205-015-0307-4

Yugandhar, P., Rajesh, T., & Sreedhar, B. (2015). Leaf-assisted green synthesis of silver nanoparticles from *Syzygium* species and evaluation of their antimicrobial and antioxidant activities. *Nanobiotechnology, 7*(2), 29–37. https://doi.org/10.1111/nbt.12432

Yugandhar, P., Vasavi, T., Jayavardhana Rao, Y., Uma Maheswari Devi, P., Narasimha, G., & Savithramma, N. (2018). Cost-effective green synthesis of copper oxide nanoparticles using fruit extract of *Syzygium alternifolium* (Wt.) Walp., characterization, and evaluation of antiviral activity. *Journal of Cluster Science, 29*(4), 743–755. https://doi.org/10.1007/s10876-018-1376-2

Yuniarni, N., Pratiwi, A. D., & Wibowo, A. (2021). Antimicrobial and antioxidant activities of *Syzygium* species extracts from Indonesia. *Medicinal Chemistry Research*, 30(2), 270-277. https://doi.org/10.1007/s00044-020-02605-1

Zarghi, A., & Kakhki, S. (2014). Design, synthesis, and biological evaluation of new 2-phenyl-4H-chromen-4-one derivatives as selective cyclooxygenase-2 inhibitors. *Scientia Pharmaceutica*, *83*(1), 15. https://doi.org/10.3797/scipharm.1401-06

Zawawi, K. N. A., & Sahidin, I. (2022). Anti-inflammatory and antioxidant activity of *Syzygium polyanthum* (Wight) Walp. *Sains Malaysiana*, *51*(5), 1475–1485. https://doi.org/10.17576/jsm-2022-5105-19

Zelová, H., & Hošek, J. (2013). TNF-α signalling and inflammation: Interactions between old acquaintances. *Inflammation Research, 62*(7), 641–651. https://doi.org/10.1007/s00011-013-0633-0

Zhang, G. B., Li, Q. Y., Chen, Q. L., & Su, S. B. (2013). Network pharmacology: A new approach for Chinese herbal medicine research. *Evidence-Based Complementary and Alternative Medicine, 2013*, Article 621423. https://doi.org/10.1155/2013/621423

Zhang, J., Yamada, S., Ogihara, E., Kurita, M., Banno, N., Qu, W., Feng, F., & Akihisa, T. (2016). Biological activities of triterpenoids and phenolic compounds from *Myrica cerifera* bark. *Chemistry & Biodiversity, 13*(11), 1601–1609. https://doi.org/10.1002/cbdv.201600247

Zhang, L., Gao, W., Su, L., He, W., Wang, Y., Hu, M., & Feng, H. (2025). Theoretical study on intramolecular hydrogen bonds of flavonoid cocrystals. *ChemPhysChem, 26*(1), e202400591. https://doi.org/10.1002/cphc.202400591

Zhang, R., Zhu, X., Bai, H., & Ning, K. (2019). Network pharmacology databases for traditional Chinese medicine: Review and assessment. *Frontiers in Pharmacology, 10*, Article 123. https://doi.org/10.3389/fphar.2019.00123

Zhang, Y., Mao, X., Su, J., Geng, Y., Guo, R., Tang, S., Li, J., Xiao, X., Xu, H., & Yang, H. (2017). A network pharmacology-based strategy deciphers the underlying molecular mechanisms of Qixuehe Capsule in the treatment of menstrual disorders. *Chinese Medicine, 12*(1), Article 23. https://doi.org/10.1186/s13020-017-0145-x

Zhao, L., Yuan, X., Wang, J., Feng, Y., Ji, F., Li, Z., & Bian, J. (2019). A review on flavones targeting serine/threonine protein kinases for potential anticancer drugs. *Bioorganic & Medicinal Chemistry, 27*(5), 677–685. https://doi.org/10.1016/j.bmc.2019.01.029

Zhao, L., Zhang, H., Li, N., Chen, J., Xu, H., Wang, Y., & Liang, Q. (2023). Network pharmacology, a promising approach to reveal the pharmacology mechanism of Chinese medicine formula. *Journal of Ethnopharmacology, 309*, Article 116306. https://doi.org/10.1016/j.jep.2023.116306

Zhou, F., Furuhashi, K., Son, M. J., Toyozaki, M., Yoshizawa, F., Miura, Y., & Yagasaki, K. (2017). Antidiabetic effect of enterolactone in cultured muscle cells and in type 2 diabetic model db/db mice. *Cytotechnology, 69*(3), 493–502. https://doi.org/10.1007/s10616-016-9965-2

Zhou, G., Myers, R., Li, Y., Chen, Y., Shen, X., Fenyk-Melody, J., Wu, M., Ventre, J., Doebber, T., Fujii, N., Musi, N., Hirshman, M. F., Goodyear, L. J., & Moller, D. E.

(2001). Role of AMP-activated protein kinase in mechanism of metformin action. *Journal of Clinical Investigation, 108*(8), 1167–1174. https://doi.org/10.1172/JCI13505

Zhou, Z., Chen, B., Chen, S., Lin, M., Chen, Y., Jin, S., Chen, W., & Zhang, Y. (2020). Applications of network pharmacology in traditional Chinese medicine research. *Evidence-Based Complementary and Alternative Medicine, 2020*, Article 1646905. https://doi.org/10.1155/2020/1646905

Zubair, T., & Bandyopadhyay, D. (2023). Small molecule EGFR inhibitors as anti-cancer agents: Discovery, mechanisms of action, and opportunities. *International Journal of Molecular Sciences, 24*(3), 2651. https://doi.org/10.3390/ijms24032651

Zulcafli, A. S., Lim, C., Ling, A. P., Chye, S., & Koh, R. (2020). Antidiabetic potential of *Syzygium* sp.: An overview. *Yale Journal of Biology and Medicine, 93*(2), 307–325.

APPENDICES

Mayer's reagent ..... Appendix 1

Mercuric chloride : 1.36 g

Potassium iodide : 5 g

Distilled water : 100 mL

1.36 g of mercuric chloride and 5 g of potassium iodide were dissolved separately in distilled water, both solutions were mixed and made up to 100 mL with distilled water.

Hager's reagent ..... Appendix 2

Picric acid : 1 g

Distilled water : 100 mL

1 g of picric acid dissolved in 100 mL of distilled water to make Hager's reagent.

Dragendroff's reagent .....Appendix 3

Bismuth nitrate (Bi $(NO_3)_3.5H_2O$) : 4.5 g

Acetic Acid (CH_3COOH) : 10 mL

Potassium iodide : 2.5 g

10 mL of acetic acid is added to 4.5 g of bismuth subnitrate to make a bismuth-containing solution. A small amount of distilled water is used to dissolve 2.5 grams of potassium iodide separately. Stirring constantly, gradually add the potassium iodide solution to the bismuth-containing solution. A yellow precipitate forms as a result of this addition. Stir the mixture continuously until all of the yellow precipitate dissolves and Dragendorff's reagent forms.

Wagner's reagent..... Appendix 4

Iodine : 2 g

Potassium iodide : 6 g

Distilled water : 100 mL

2 g of iodine and 6 g of potassium iodide were dissolved in 100 mL of distilled water to prepare Wagner's reagent.

Molisch's reagent..... Appendix 5

Alpha naphthol : 3.75 g

Ethanol : 99 %, 25 mL

3.75g of alpha naphthol is dissolved in a 25 mL solution of 99% ethanol to prepare Molisch's reagent.

Fehling's A and Fehling's B solutions ..... .Appendix 6

Fehling's A preparation

Copper (II) sulfate pentahydrate ($CuSO_4 \cdot 5H_2O$): 34.65 g/l

Sulfuric acid (H_2SO_4) : 173 g/l

Distilled water (H_2O) : 1000 mL

The copper (II) sulfate pentahydrate is dissolved in a required amount of distilled water. The sulfuric acid (H_2SO_4) is added to the copper sulfate solution while stirring continuously. The solution is transferred to a volumetric flask, and distilled water is added to make up the total desired volume of Fehling's A solution.

Fehling's B Preparation

Potassium tartrate (Rochelle salt) : 173 g/l

Sodium hydroxide (NaOH) : 50g/l

Distilled water (H_2O) : 200 mL

The potassium tartrate solution is prepared in the required amount of distilled water. The sodium hydroxide is added to the potassium tartrate solution while stirring continuously. The solution is taken in a volumetric flask, and distilled water is added to make up the total desired volume. Fehling's A and B solutions are typically mixed in equal volumes in Fehling's solution tests.

Sudan Red III ..... Appendix 7

Sudan Red III : 0.7 g

Propylene glycol : 100 mL

Water : 30 mL

Dissolve 0.7 g of dye in 100 mL of Propylene glycol and 30 mL of water, using a warm water bath, and filter.

Millon’s reagent ..... Appendix 8

Mercuric nitrate : 160 g

Mercurous nitrate : 160 g

Nitric solution : 400 mL

Distilled water: 600 mL

In 400 mL of the concentrated nitric acid solution, 160 g each of mercuric and mercurous nitrate are dissolved to create Millon's reagent. The reagent is then made to 1000 mL by adding 600 mL of distilled water.

Ninhydrin solution ..... .Appendix 9

Ninhydrin : 0.5 g

Ethanol : 75 mL

0.5 g of ninhydrin was added to 75 mL of ethanol and heated gently to make a 5 % ninhydrin solution.

Phosphate buffer (pH 4.7) ..... Appendix 10

Sodium phosphate	:	2 M, 71.6 g
Citric acid	:	0.2 M, 42.02 g

pH of 2 M sodium phosphate (71.6 g Na_2HPO_4 in 1 L distilled water) is adjusted to 4.7 with 0.2 M citric acid (42.02 g citric acid in 1 L distilled water).

Bromocresol green (BCG) Solution ..... Appendix 11

BCG	:	69.8 mg
NaOH	:	3 mL (2 N)
Distilled water	:	5 mL

Heat the 69.8 mg bromocresol green with 3 mL of 2 N NaOH and 5 mL distilled water until completely dissolved, then dilute the solution to 1000 mL.

Baljet's reagent ..... Appendix 12

Picric acid	:	95 mL
NaOH	:	5 mL

95 mL of 1% picric acid and 5 mL of 10% NaOH are combined and filtered through a sintered glass funnel. The filtrate was used as the reagent.

Vanillin reagent..... Appendix 13

Vanillin	:	1 g
H_2SO_4	:	2 mL
Ethanol	:	100 mL

The vanillin reagent was prepared by dissolving 1 g of vanillin with 2 mL of sulfuric acid in 100 mL of 95 % ethanol.

Anthrone reagent..... Appendix 14

Anthrone	:	200 mg
Sulphuric acid	:	100 mL

In 100 mL of ice-cold 95 % H_2SO_4, dissolve 200 mg of anthrone. Fresh preparation is required before usage.

Luria Bertani Agar. ..... Appendix 15

Luria Bertani Agar (LBA)	:	25 g
Distilled water	:	1000 mL

The brain heart infusion agar media was prepared by dissolving 25 g LBA in 1000 mL distilled water and was sterilized by autoclaving for 15 minutes at 121°C 15 lbs. Following a cooling period to 50°C, the media were transferred onto petri plates that had been previously sterilized and labeled. They were then left to solidify in a laminar airflow chamber that had flow and UV light turned on.

TRIzol Reagent ..... Appendix 16

Chloroform : 0.2 mL

Trizol reagent :

Phenol (pure phenol from crystals) : 38%

0.8 M Guanidine Thiocyanate : 118.16 g/mol

0.4 M Ammonium Thiocyanate : 79.12 g/mol

0.1 M Sodium Acetate : 82.03 g/mol

5 % Glycerol

TRIzol, often known as TRI Reagent, is a monophasic solution of phenol and guanidinium isothiocyanate that denatures protein and solubilizes biological material at the same time. For every 1 mL of TRIZOL Reagent, add 0.2 mL of chloroform. Securely cap sample tubes. For 2-3 minutes, incubate the tubes at 15 to 30°C after giving them a vigorous shaking for 15 seconds. Centrifuge the samples for 15 minutes at 2 to 8°C at no more than 12,000xg. After centrifugation, the mixture separates into an upper aqueous phase that is colourless, and an interphase, a lower red phenol-chloroform phase. The aqueous phase is where RNA alone stays. The aqueous phase volume is roughly 60% of the TRIZOL Reagent volume, which is utilized for homogenization.

RT Easy mix ..... Appendix 17

The key ingredients required for reverse transcription (RT) of RNA into complementary DNA (cDNA) are included in the RT easy mix. For researchers doing RNA analysis and RT-PCR experiments, these kits are useful since they simplify and standardize the reverse transcription process. This comprises nucleotides (dNTPs for synthesizing the cDNA strand), buffer solutions (to keep the RT enzyme activity at its peak and to maintain the ideal pH), reverse transcriptase enzymes (converts RNA templates into complementary DNA), and occasionally enhancers or stabilizers (to increase the yield of cDNA, reaction efficiency, and the stability of the enzyme), inhibitor removal reagents (reagents to eliminate inhibitors that can obstruct the RT reaction), and control RNA or DNA (for quality assurance for RT-PCR tests, certain RT easy kits include control DNA or RNA templates). Typically, the RT easy kit comes with comprehensive guidelines for carrying out the RT reaction. There may be differences in the precise composition and amounts of these ingredients in various RT easy mix products.

RNAse-free tube ..... Appendix 18

The microcentrifuge tubes are assured to be free of RNase (ribonucleases, enzymes that degrade RNA) and DNase (Deoxyribonucleases, enzymes that degrade DNA) and feature a low-binding, non-stick surface.

ΔΔCt method ..... Appendix 19

In quantitative real-time polymerase chain reaction (qPCR), the delta-delta Ct ($2^{-\Delta\Delta Ct}$) method, is a simple formula used to determine the relative fold gene

expression of samples. Kenneth Livak and Thomas Schmittgen developed this technique in 2001.

The difference between the ΔCt values of the treated/experimental sample and the untreated/control sample is called ΔΔCt. ΔCt (treated sample) - ΔCt (untreated sample) = ΔΔCt. The cycle threshold of the sample is represented by Ct. This is administered by the qPCR machine after the qPCR process. It is the cycle number at which the fluorescence generated by the PCR can be distinguished from the surrounding noise.

Tris-HCl buffer ..... Appendix 20

Tris base	:	12.1 g
Nuclease-free water	:	80 mL
HCl	:	6-7 mL

1 M Tris-HCl buffer is prepared by dissolving 12.1 g of Tris base in 80 mL of nuclease-free water. The pH was adjusted to 7.4 by slowly adding 6-7 mL of concentrated HCl. The HCl will increase the temperature of the solution, which affects the pH. Allow the solution to cool to room temperature before making final adjustments to the pH with HCl. The solution is made up of 100 mL using water. The Tris-HCl was filtered with a 0.22 μm sterile filter.

HEPES Buffer ..... Appendix 21

HEPES (4-(2-hydroxyethyl)-1-piperazine ethanesulfonic acid) is a zwitterionic buffering agent that is widely utilized in biological and biochemical studies. The molecular weight of HEPES is 238.30 g/mol. HEPES buffer is recommended due to its low interference with biological processes and consistent buffering capacity throughout a wide pH range (6.8 to 8.2).

1 L of 20 mM HEPES Buffer at pH 7.4

Weigh 4.766 g of HEPES powder. In a beaker with a stir bar, combine the HEPES powder and approximately 800 mL of deionized water. Measure the pH and stir with 1 M NaOH or 1 M HCl dropwise to get it up to 7.4. Transfer the solution to a 1 L volumetric flask and fill it with deionized water to the same volume. Mix thoroughly. Store refrigerated for several weeks.

Griess reagent..... Appendix 22

The Griess reagent is extensively used in biochemical tests to detect nitrite as a marker for nitric oxide production. This reagent detects and quantifies nitrite ions (NO_2^-), which are commonly associated with NO generation. The reagent was commonly made by mixing two different solutions: sulfanilamide and naphthyl ethylenediamine dihydrochloride (NED).

0.1 g of naphthyl ethylenediamine dihydrochloride dissolved in 100 mL of distilled water.

The working Griess reagent was prepared by mixing equal volumes of the sulfanilamide solution (10 mL) and the NED solution (10 mL). The sulfanilamide and

NED solutions were stored separately at 4°C in the dark (amber-coloured) bottles to prevent degradation and light exposure.

DMEM (Dulbecco's Modified Eagle's) medium ..... Appendix 23

L-glutamine	:	4 mM
Glucose	:	4500 mg/L
Sodium pyruvate	:	1 mM
Sodium bicarbonate	:	1500 mg/L

DMEM contains L-glutamine, Glucose, Sodium pyruvate, and Sodium bicarbonate. It has applications for cell culture, cell growth, and viability.

Tris-EDTA buffer (TE) ..... Appendix 24

Tris-HCl	:	10 mM
EDTA Na_2	:	1mM
pH	:	8.0

TE (Tris-EDTA) buffer is widely used as a storage or dilution buffer solution in molecular biology, especially in procedures involving DNA, RNA, or cDNA. The primary function of the Tris-EDTA buffer is to solubilize nucleic acids while protecting them from enzymatic lysis. TE is an abbreviation of the components that make up the buffer solution. 'T' stands for Tris, a pH buffer that is used in many laboratory processes to maintain the pH of a solution. 'E' stands for EDTA, or ethylenediamine tetra-acetic acid, a divalent metal ion chelating ion. In DNA or RNA extraction procedures, EDTA reduces the activities of nucleases that digest the nucleic acids. This protects the DNA and RNA from degradation.

SYBR Green Master Mix ..... Appendix 25

Real-time PCR (Polymerase Chain Reaction) experiments frequently use SYBR Green Master Mix as a reagent. It is intended for use in quantitative PCR (qPCR) investigations, in which the PCR process produces a target's concentration of DNA or RNA.

The components found in SYBR Green Master Mix are **SYBR Green Dye** (SYBR green dye binds to the PCR product (dsDNA) as it accumulates during qPCR. The qPCR instrument detects the rise in fluorescence intensity that results from the binding of SYBR Green dye to dsDNA), **Taq DNA Polymerase** (a heat-stable DNA polymerase that is required for the synthesis of DNA in every PCR cycle), **dNTPs** (A, T, C, and G are the building components needed to synthesize DNA, **buffer System** (To preserve the stability and effectiveness of the DNA polymerase and other components, the master mix contains a buffer solution that has been adjusted for PCR conditions), **stabilizers and enhancers** (These are master mix additives that are added to increase PCR performance by boosting sensitivity and decreasing non-specific amplification.

LIST OF PUBLICATIONS

JOURNAL PUBLICATIONS

1. **Snehalatha**, **V. R.,** & Rasmi, A. R. (2025). Bioactive constituents and pharmacological activities of Syzygium occidentale: Insight into an underexplored Western Ghats. *International Journal of Medical Sciences and Advanced Clinical Research (IJMACR)*, *8*(5). (To be published September 15, 2025)

2. **Snehalatha, V. R.,** & Rasmi, A. R. (2025). Therapeutic prospects and bioactive constituents of Syzygium laetum from the Southern Western Ghats biodiversity hotspot. *International Journal of Medical Science and Diagnosis Research (IJMSDR), 9*(3), 120–132. https://doi.org/10.32553/ijmsdr.v9i3.1066

3. **Snehalatha, V. R.,** & Rasmi, A. R. (2025). In vitro and in silico guided identification of anti-biofilm agents from *Syzygium palghatense* against *Pseudomonas aeruginosa*. *EIJO: Journal of Science, Technology and Innovative Research (EIJO–JSTIR), 10*(4), 1-12. http://www.eijo.in/

4. **Snehalatha, V. R.,** & Rasmi, A. R. (2021). Phytochemical evaluation and pharmacognostic standardization of *Syzygium palghatense* endemic to Western Ghats. *Future Journal of Pharmaceutical Sciences, 7*(147). https://doi.org/10.1186/s43094-021-00282-8

PAPER/POSTER PRESENTATIONS

1. **Snehalatha, V. R.,** & Rasmi, A. R. (2021, September 27–28). Nutritional and physicochemical studies on leaves and bark of *Syzygium occidentale* endemic to Western Ghats [Paper presentation]. International Webinar on Phytochemistry-Impacts and Applications & Prof. Dr. A. Hisham Endowment Award Function 2021, Kerala Academy of Sciences, Trivandrum, India.

2. **Snehalatha, V. R.,** & Rasmi, A. R. (2021, September 5). Traditional and pharmacological importance of *Syzygium cumini* (L.) Skeels–A review [Review writing competition]. Enflammer - The Journal club, Department of Botany, Vimala College, Thrissur, India.

3. **Snehalatha, V. R.,** & Rasmi, A. R. (2020, November 27–28). Pharmacological activities of *Syzygium palghatense* as a potential medicinal

tree [Paper presentation]. International E-Conference on Current Science and Technology for Sustainable Society, Hyderabad and Hassan, India.

4. **Snehalatha, V. R.,** & Rasmi, A. R. (2020, September 28–29). A comparative study of morpho-anatomical and pharmacological potential of *Syzygium laetum* and *Syzygium palghatense*, endemic to Western Ghats [Paper presentation]. International Webinar on Phytochemistry-2020, Kerala Academy of Sciences, Thiruvananthapuram, India.

5. **Snehalatha, V. R.,** & Rasmi, A. R. (2020, February 3–4). Comparative evaluation of the morpho-anatomical, pharmacological and biological properties of *Syzygium laetum* and *Syzygium palghatense*, endemic to Western Ghats [Paper presentation, First Prize]. National seminar, Department of Botany, MES Kalladi College, Mannarkkad, India.

6. **Snehalatha, V. R.,** & Rasmi, A. R. (2019, December 5–6). Pharmacological, antioxidant and anti-inflammatory properties of *Syzygium palghatense* endemic to Western Ghats [Paper presentation]. National seminar on Conservation of Biological Resources of Western Ghats, Chittur, Palakkad, India.

7. **Snehalatha, V. R.,** & Rasmi, A. R. (2019, November 6–8). Unraveling the pharmacological benefits of *Syzygium palghatense* (Myrtaceae) endemic to Palakkad district, Kerala [Paper presentation]. XLII All India Botanical Conference of the Indian Botanical Society and National Symposium on Innovations and Inventions in Plant Sciences Research, University of Calicut, Malappuram, Kerala, India.

8. **Snehalatha, V. R.,** & Rasmi, A. R. (2019, July 25–26; October 13). In situ synthesis of bio-nanoparticles & biosynthesis of nanomaterials [Workshop and paper presentations]. Mercy College, Palakkad and IIT Hyderabad, India. Received Certificate of Excellence.

9. **Snehalatha, V. R.,** & Rasmi, A. R. (2019, February 2–3). Pharmacological efficacy of leaves of *Syzygium palghatense* Gamble (Myrtaceae) endemic to Palakkad District, Kerala [Poster presentation]. 31st Kerala Science Congress, Fatima Mata National College, Kollam, India.

10. **Snehalatha, V. R.,** & Rasmi, A. R. (2018, March 26–27). Phytochemical screening and antifungal activities of *Lawsonia inermis* L. leaf extract [Poster presentation]. International seminar on Phytochemistry-2018, JNTBGRI, Palode, Thiruvananthapuram, Kerala, India.

BOOKS/CHAPTERS/ABSTRACTS/PROCEEDINGS

- **Book published: Snehalatha, V. R.,** Sardar, B., Sharma, B. P., Kumar, M., Sahu, J. K. (2023). Antidiabetic Plants (Vol. II). Edited by Sanjeet Kumar & Sugimani Marndi. APRF Publishers, Odisha: Ambika Prasad Research Foundation, India. ISBN: 978-81-958404-0-3. DOI: https://doi.org/10.5281/zenodo.7811919.

1. **Snehalatha, V. R.,** & Rasmi, A. R. (2025). Antifungal and antibiofilm activity of Syzygium palghatense bark extract against Aspergillus niger: Phytochemical analysis and efficacy evaluation. In A. Bhardwaj & S. P. Gupta (Eds.), Exploring the mycology and parasitology of plant life: Roots and rivals (pp. 265–273). Cambridge Scholars Publishing. https://doi.org/10.47627/978-1-0364-5356-5

2. Romita Devi, Walling, T., Chang, T., **Snehalatha, V. R**., Marndi, S., & Kumar, S. (2025). *Cycas* species of India: A comprehensive review on health benefits and gaps analysis. Indian Forester, *151*(5), 504-507. https://doi.org/10.36808/if/2025/v151i5/170411.

3. Sharma, B. P., Das, K., Mety, S. S., Das, A., **Snehalatha, V. R**., & Kumar, S. (2024). Chara (*Buchanania lanzan* Spreng.): a wild nutraceutical. In Wild Nutraceutical Plants (Chapter 2, pp. 12-19). ISBN: 978-81-962761-6-4. DOI: https://doi.org/10.5281/zenodo.10570625.

4. **Snehalatha, V. R.,** & Rasmi, A. R. (2024). *Syzygium occidentale*: A potential nutraceutical endemic in Western Ghats of South India. In Asha Ramachandran (Ed.), Ecology, Biodiversity and Systematics (pp. 181-198). Scholars' Press. ISBN: 978-620-6-77281-1.

5. **Snehalatha, V. R.,** & Rasmi, A. R. (2024). *In vitro* evaluation of phytochemical and antioxidant potential of *Syzygium occidentale* bark and their synergistic potential on its antibacterial property. In M. Kaneria & K. Rakholiya (Eds.), Herbal Formulations, Phytochemistry and Pharmacognosy (pp. 371–379). Elsevier. ISBN: 978-0-443-15383-9. DOI: https://doi.org/10.1016/B978-0-443-15383-9.00014-7.

6. **Snehalatha, V. R.,** Sardar, B., Sharma, B. P., Kumar, M., Sahu, J. K. (2023). Antidiabetic Plants (Vol. II). Edited by Sanjeet Kumar & Sugimani Marndi. APRF Publishers, Odisha: Ambika Prasad Research Foundation, India. ISBN: 978-81-958404-0-3. DOI: https://doi.org/10.5281/zenodo.7811919.

7. **Snehalatha V. R.** and Rasmi A. R. (2023). Phytochemical and GCMS analysis of bioactive compounds in methanolic extract of *Syzygium laetum*

(Buch.-Ham.) Gandhi leaves. Indigenous Traditional Knowledge & Ethnopharmacology. APRF Publishers, Odisha, India. ISBN: 978-81-955847-9-6.

8. **Snehalatha, V. R.,** Jena, N., & Kumar, S. (2023). Creeping lickstoop [*Dentella repens* (L.) J.R. Forst. & G. Forst.]: a medicinal creeper of India. In Medico Bio-wealth of India, Volume XII (Chapter 4, pp. 18-21). ISBN: 978-81-967170-2-5.

9. **Snehalatha, V. R.,** & Rasmi, A. R. (2023). Phytochemical profile of *Syzygium laetum* bark from Southern Western Ghats. In Medico Bio-wealth of India (Vol. 8, Chapter 2, pp. 8-12). ISBN: 978-81-958404-7-2. DOI: https://doi.org/10.5281/zenodo.7699800.

10. **Snehalatha, V. R.,** & Rasmi, A. R. (2023). Phytochemical and GCMS analysis of bioactive compounds in methanolic extract of *Syzygium laetum* (Buch.-Ham.) Gandhi leaves. In Indigenous Traditional Knowledge and Ethnopharmacology (pp. 1-5). ISBN: 978-81-955847-9-6. DOI: https://doi.org/10.5281/zenodo.7725840.

11. Manjula, B. L., Basak, G., Sharma, B. P., Woldeamanuel, M. M., **Snehalatha, V. R.,** Rout, S., & Kumar, S. (2023). A note on COVID-19 pandemic, clinical aspects, medication, and its prevention with traditional knowledge. In Medico Bio-wealth of India (Vol. 8, Chapter 6, pp. 59-75). APRF Publishers, Odisha, India. ISBN: 978-81-958404-7-2.DOI: https://doi.org/10.5281/zenodo.7978844.

12. **Snehalatha, V. R.,** & Rasmi, A. R. (2023). Evaluation of pharmacological potential of Syzygium laetum: A potential untapped source endemic to Western Ghats. In P. Venugopalan & M. Seenivasan (Eds.), Proceedings of the International Research Conclave on Advances in Science & Technology 2023 (p. 18).

13. **Snehalatha V. R.** and Rasmi A. R. (2022). Comparative Evaluation of Organoleptic, Physicochemical, Proximate, and Mineral Composition of *Syzygium laetum* and *Syzygium occidentale*, Endemic to Western Ghats: A Search for Low-Cost Nutraceuticals. Natural Product Experiments in Drug Discovery. Springer Nature Publishers. ISBN: 978-1-0716-2682-5.

14. **V. R. Snehalatha** and A. R. Rasmi. (2022). A Comparative Evaluation of Organoleptic, Physicochemical, Proximate, and Mineral Composition of *Syzygium laetum* and *Syzygium occidentale*, Endemic to Western Ghats: A Search for Low-Cost Nutraceuticals. In: Arunachalam, K., Yang, X., Puthanpura Sasidharan, S. (eds) Natural Product Experiments in Drug

Discovery. Springer Protocols Handbooks. Humana, New York, NY. pp 27-40. https://doi.org/10.1007/978-1-0716-2683-2_2. Print ISBN 978-1-0716-2682-5. Online ISBN978-1-0716-2683-2.

15. **Snehalatha, V. R.,** Dimri, R., Kumar, A., Sharma, D. K., Mety, S. S., Khodke, S., Marndi, S., & Kumar, S. (2022). *Indigofera cassioides* Rottler ex DC. (Fabaceae): A wild medico-food plant. In Indigenous Traditional Knowledge and Advancement in Medicinal Plants Research (pp. 21–25). ISBN: 978-81-955847-2-7.

16. **Snehalatha, V. R.,** Harikumar, J., Mahendru, N., Pal, N., Janali, A. B., & Kumar, S. (2022). Can *Dioscorea* species reduce oxidative stress? In: Kumar S (eds.), Medico Biowealth of India, APRF Publisher, Odisha, India. p. 38-42. ISBN: 9-788-195-2750-90. DOI: https://doi.org/10.5281/zenodo.6977384.

17. Guchhait, K. C., Anil Kumar, N., **Snehalatha, V. R**., Choudhary, M., Rathore, S., Sanath Kumar, N., & Kumar, S. (2022). Traditional country liquor and their medicinal uses. In Indigenous Traditional Knowledge (pp. 10-15). ISBN: 978-81-955847-0-3. DOI: 10.5281/zenodo.6663397.

18. **Snehalatha, V. R.,** & Rasmi, A. R. (2022). Scientific validation of antidiabetic properties of *Syzygium palghatense* Gamble, an endemic medicinal plant of Western Ghats, India. In Medico-Biowealth of India (Vol. VII, pp. 50-55). APRF Publishers. ISBN: 978-81-955847-7-2. DOI: 10.5281/zenodo.7368926.

19. **Snehalatha, V. R.,** & Rasmi, A. R. (2022). Nutritional and physicochemical profile of leaves of *Syzygium occidentale* endemic to Western Ghats. In C. Prabhakumari, M. C. B. Mayarani, M. Haseena, R. Sivadasan, & S. Mathew (Eds.), Proceedings of the Online International Conference on Recent Advancements in Life Sciences (pp. 14). A2Z EduLearningHub LLP. ISBN: 978-81-956748-1-7.

20. **Snehalatha, V. R.,** & Rasmi, A. R. (2022). Investigations into the bioactive compounds of *Syzygium laetum*, using GC-MS fingerprinting: A potential untapped source endemic to Western Ghats. In Proceedings of the International Conference on Advanced Biology 2022 (ICAB 2022) (p. 128). Inter University Centre for Evolutionary and Integrative Biology (iCEIB), University of Kerala.

21. **Snehalatha, V. R.,** & Rasmi, A. R. (2022). Antioxidant potential of *Syzygium laetum* bark extract evaluated using LC-MS-QTOF-based metabolomics. In A. Gangaprasad et al. (Eds.), Biotechnology-Recent Advances, Opportunities and Challenges (pp. 48–58). Department of Biotechnology, University of Kerala. ISBN: 978-81-954771-0-4.

22. **Snehalatha, V. R.,** & Rasmi, A. R. (2022). GC-MS analysis of phytocomponents in the methanolic extract of *Syzygium palghatense* leaves. In A. Gangaprasad et al. (Eds.), Abstract Book of National Webinar on Advances in Industrial Biotechnology (p. 30). Department of Biotechnology, University of Kerala. ISBN: 978-81-955847-2-7.

23. **Snehalatha, V. R.,** & Rasmi, A. R. (2022). First step towards uncovering the therapeutic qualities of *Syzygium laetum* (Buch.-Ham.) Gandhi, a Southern Western Ghats endemic. In K. B. Rameshkumar & V. M. Dan (Eds.), Proceedings of the National Seminar on Fundamental and Applied Dimensions in Plant Sciences (p. 67). KSCSTE-Jawaharlal Nehru Tropical Botanic Garden and Research Institute. ISBN: 978-81-955043-0-5.

24. **V. R. Snehalatha** and A. R. Rasmi (2021). Phytochemical evaluation and pharmacognostic standardization of *Syzygium palghatense* endemic to Western Ghats. *Future Journal of Pharmaceutical Sciences*, *7* (147):1-13.

25. **Snehalatha, V. R.,** & Rasmi, A. R. (2021). Nutritional and physicochemical studies on leaves and bark of *Syzygium occidentale* endemic to Western Ghats. In K. B. Rameshkumar, M. P. Rani, & B. Sruthy (Eds.), International Webinar on Phytochemistry-Impacts and Applications: Proceedings and Abstracts (p. 79). Kerala Academy of Sciences. ISBN: 978-81-951912-5-3.

26. **Snehalatha, V. R.,** & Rasmi, A. R. (2021). Traditional and pharmacological importance of *Syzygium cumini* (L.) Skeels – A review. In M. Madhavan, J. M. Jayalakshmi, K. S. Menon, & S. T. Tharakan (Eds.), Emerging Trends in Plant Science: Review Paper Proceedings (pp. 135-145). Enflammer – The Journal Club, Department of Botany, Vimala College (Autonomous), Thrissur. ISBN: 978-81-950842-8-9.

27. **Snehalatha, V. R.** (2020). A comparative study of morpho-anatomical and pharmacological potential of *Syzygium laetum* and *Syzygium palghatense*, endemic to Western Ghats. In K. B. Rameshkumar, P. R. M., & L. N. Menon (Eds.), Proceedings of the International Webinar on Phytochemistry-2020 (p. 52). Kerala Academy of Sciences. ISBN: 978-81-940888-2-0.

28. **Snehalatha, V. R.,** & Rasmi, A. R. (2019). Pharmacological efficacy of leaves of *Syzygium palghatense* Gamble (Myrtaceae) endemic to Palakkad District, Kerala. In S. Pradeep Kumar et al. (Eds.), 31st Kerala Science Congress Abstracts: Our Environment – Our Future: Science and Technology for Rebuilding Kerala (p. 192). Kerala State Council for Science, Technology and Environment (KSCSTE). ISBN: 81-86366-97-0.

UNIVERSITY OF CALICUT

CERTIFICATE ON PLAGIARISM CHECK

1.	Name of the Research Scholar	SNEHALATHA V R	
2.	Title of thesis / dissertation	PHARMACOGNOSTIC CHARACTERIZATION, PHYTOCHEMICAL PROFILING AND BIOLOGICAL ACTIVITIES OF SELECTED SPECIES OF SYZYGIUM GAERTNER (MYRTACEAE) ENDEMIC TO WESTERN GHATS	
3.	Name of the Supervisor	Prof. (Dr.) RASMI A R	
4.	Department/Institution	PG AND RESEARCH DEPARTMENT OF BOTANY, GOVT. VICTORIA COLLEGE, PALAKKAD-678001, KERALA, INDIA	
5.	Similar content (%) identified	Non Core	Core
		Introduction/ Theoretical overview/Review of literature/ Materials & Methods/ Methodology	**Analysis/Result/Discussion / Summary/Conclusion/ Recommendations**
		5	**6**
	Acceptable maximum limit (%)	10	10
6	Software used	iThenticate	
7	Date of verification	11.09.2025	

Report on plagiarism check, specifying included/excluded items with % of similarity to be attached.

SEEMA M.V.
Assistant Librarian
University of Calicut
Malappuram - 673 635

Checked by (with name , designation & signature) Seema

Name and signature of the Researcher Snehalatha VR

Name and signature of the Supervisor. Dr. Rasmi. A R

Prof. (Dr.) RASMI A.R Msc., BEd., Phd
PEN : 596335
Professor & Head
Department of Botany
Govt. Victoria College, Palakkad-678001
rasmibotany@gmail.com

The Doctoral Committee* has verified the report on plagiarism check with the contents of the thesis, as summarized above and appropriate measures have been taken to ensure originality of the Research accomplished herein.

Govt. VICTORIA COLLEGE DEPARTMENT OF BOTANY Date ..... Palakkad, Kerala- 678 001

Name & Signature of the HoD/HoI (Chairperson of the Doctoral Committee)

20/9/25

PRINCIPAL
GOVT. VICTORIA COLLEGE
PALAKKAD

GOVERNMENT VICTORIA COLLEGE Date ..... PALAKKAD - 678 001

**In case of languages like Malayalam, Tamil etc..on which no software is available for plagiarism check, a manual check shall be made by the Doctoral Committee, for which an additional certificate has to be attached.*

INDEX

2

2-Phenyl-4H-chromen-4-one 20, 149, 309, 310, 311, 312, 313, 314, 315, 316, 317, 318, 319, 320, 321, 326, 400, 409, 410, 411, 441, 467, 473, 475, 518, 520, 525, 526, 527, 528, 531, 532, 533, 535, 536, 537, 538, 539, 540, 541, 543, 544, 545, 546, 548, 549, 550, 551, 552, 554, 555, 556, 558, 562, 564, 572

A

AgNPs 18, 43, 44, 45, 187, 188, 189, 190, 193, 194, 195, 199, 204, 208, 209, 214, 215, 216, 217, 218, 219, 220, 221, 222, 223, 224, 225, 227, 228, 231, 232, 233, 236, 237, 240, 242, 243, 244, 245, 246, 247, 248, 249, 250, 251, 252, 253, 254, 255, 256, 257, 258,259, 260, 261, 262, 264, 265, 266, 267, 269, 270, 271, 272, 274, 275, 276, 278, 279, 280, 281, 282, 283, 285, 316, 317, 318, 568, 569, 570, 573, 575

Albendazole 569

Alkaloids 2, 24, 25, 26, 29, 32, 39, 92, 117, 118, 119, 120, 123, 124, 128, 129, 136, 137, 138, 143, 144, 152, 153, 156, 289, 324

Alpha-amylase 43, 47, 158, 161, 172, 180, 184, 186, 224, 225, 264, 283, 299, 312, 313, 324, 326

Alpha-glucosidase 39, 46, 47, 158, 161, 172, 180, 184, 186, 224, 225, 265, 283, 299, 313, 314, 324, 326

Alzheimer's disease 11, 12, 273, 320, 544, 547, 561

Analgesic 2, 12, 30, 36, 92, 321

Anatomical 15, 16, 1, 5, 8, 9, 17, 18, 19, 20, 21, 22, 23, 51, 52, 53, 54, 55, 56, 60, 67, 74, 81, 83, 84, 85, 86, 87, 88, 105, 111, 169, 170, 565, 566, 571, 573, 575, 576

Angiosperms 8, 86

Anthelmintic 15, 17, 18, 3, 33, 159, 169, 177, 214, 256, 298, 311, 323, 337, 387, 401, 515

Anthocyanins 24

Anticancer 26, 40, 41, 42, 43, 47, 48, 49, 91, 119, 144, 145, 147, 149, 153, 154, 155, 160, 181, 185, 186, 188, 190, 231, 272, 283, 284, 285, 288, 292, 300, 315, 316, 319, 324, 325, 326, 335, 336, 344, 346, 350, 352, 368, 371, 373, 385, 388, 397, 399, 432, 451, 453,456, 504, 509, 511, 513, 516, 518, 519, 520, 559, 561, 568, 570, 572, 573

Antidiabetic2, 12, 24, 26, 27, 37, 38, 39, 43, 48, 85, 91, 92, 147, 153, 157, 158, 161, 180, 182, 184, 185, 186, 188, 190, 266, 267, 280, 283, 285, 292, 314, 316, 319, 324, 326, 333, 334, 335, 336, 342, 344, 346, 350, 351, 365, 373, 382, 387, 396, 397, 399, 426, 448,453, 456, 495, 496, 500, 501, 503, 513, 516, 519, 520, 561, 568, 569, 572, 573

Anti-inflammatory 2, 12, 26, 27, 35, 36, 37, 44, 117, 144, 145, 146, 147, 149, 150, 153, 154, 155, 157, 160, 161, 170, 171, 178, 179, 182, 184, 185, 186, 188, 190, 215, 216, 218, 219, 223, 240, 256, 257, 258, 259, 260, 261, 262, 276, 281, 282, 283, 284, 289, 292, 298, 312,316, 319, 320, 322, 323, 324, 326, 332, 335, 336, 342, 344, 346, 350, 351, 362, 365, 380, 387, 394, 399, 401, 421, 423, 424, 445, 453, 456, 485, 486, 490, 491, 492, 493, 494, 513, 517, 518, 519, 520, 559, 561, 562, 568, 569, 572, 573, 575, 576, 600

Antimicrobial 2, 3, 7, 12, 26, 27, 28, 30, 31, 32, 44, 45, 81, 85, 92, 114, 120, 121, 144, 145, 146, 147, 149, 150, 154, 155, 157, 159, 161, 166, 167, 169, 173, 174, 175, 176, 177, 182, 183, 185, 186, 188, 190, 194, 195, 199, 200, 205, 206, 207, 241, 247, 248, 249, 252, 255, 276, 277, 280, 281, 284, 285, 292, 297, 308, 310, 311, 316, 318, 321, 322, 323, 326, 329, 330, 332, 335, 336, 337, 342, 344, 346, 350, 351, 355, 356, 357, 359, 372, 373, 376, 387, 390, 392, 399, 409, 440, 453, 456, 466, 467, 468, 472, 473, 474, 475, 513, 517, 518, 520, 566, 568, 570, 572, 573, 575, 580, 586, 589

Antioxidant 2, 4, 7, 12, 24, 26, 27, 28, 29, 30, 31, 35, 37, 38, 39, 40, 41, 43, 44, 45, 47, 81, 85, 91, 92, 111, 114, 115, 117, 118, 120, 121, 144, 145, 147, 149, 150, 153, 154, 155, 157, 158, 161, 162, 163, 165, 173, 174, 182, 185, 186, 188, 190, 193, 245, 246, 247, 278, 280, 281, 282, 284, 289, 292, 297, 309, 310, 316, 317, 321, 322, 324, 326, 328, 329, 335, 336, 337, 342, 344, 346, 350, 352, 354, 372, 373, 375, 387, 388, 399, 400, 403, 438, 453, 456, 457, 459, 460, 461, 462, 463, 464, 465, 513, 514, 517, 519, 520, 568, 569, 572, 573, 575, 576, 580

Ascaridia galli 35
Ascorbic acid 100, 101, 163, 164, 165, 246, 280, 297, 309, 316, 322, 567, 568
Atomic Force Microscopy (AFM) 18, 187, 190, 193, 244
Ayurvedic medicines 23

B

Bark 16, 18, 19, 2, 17, 24, 25, 26, 28, 29, 31, 34, 35, 36, 37, 38, 39, 42, 46, 47, 48, 52, 56, 57, 58, 59, 60, 64, 78, 81, 82, 85, 87, 93, 94, 95, 105, 106, 107, 108, 109, 111, 112, 114, 115, 116, 119, 121, 122, 123, 128, 129, 132, 133, 135, 136, 137, 138, 139, 140, 141, 142, 144, 145, 146, 147, 148, 149, 150, 151, 152, 153, 154, 155, 156, 158, 161, 162, 166, 167, 168, 169, 170, 172, 174, 175, 176, 177, 178, 179, 180, 181, 182, 188, 189, 190, 191, 193, 194, 195, 199, 204, 208, 209, 214, 215, 216, 218, 219, 221, 222, 224, 225, 226, 227, 228, 231, 232, 233, 236, 237, 240, 242, 243, 244, 245, 246, 247, 249, 250, 251, 252, 253, 254, 255, 256, 257, 258, 259, 260, 261, 262, 263, 264, 265, 266, 267, 269, 270, 271, 272, 274, 275, 276, 277, 278, 279, 280, 282, 285, 292, 293, 294, 295, 296, 298, 299, 302, 303, 304, 306, 307, 308, 309, 310, 311, 312, 313, 314, 315, 316, 317, 321, 323, 326, 337, 341, 342, 399, 403, 409, 421, 426, 432, 566, 567, 568, 572, 573, 575, 577
Bioactive compounds 19, 2, 24, 29, 39, 46, 91, 94, 95, 96, 97, 116, 117, 118, 119, 120, 121, 122, 123, 133, 136, 144, 145, 146, 147, 148, 152, 153, 156, 158, 160, 161, 183, 185, 188, 189, 251, 254, 255, 290, 302, 308, 327, 328, 528, 555, 558, 570, 575
Biodiversity 1, 13, 16, 17, 54, 86, 92
Biofilms 31, 32, 159, 194, 195, 199, 200, 201, 202, 203, 204, 208, 213, 214, 249, 254, 255, 281, 329

C

Candida albicans 27, 31, 32, 159, 166, 167, 168, 175, 176, 186, 188, 194, 195, 247, 248, 277, 280, 310, 317, 322
Cisplatin 270, 271, 272, 276, 283, 315, 324, 570
Clotrimazole 175, 247, 248, 310, 568
Conservation 17, 576, 577
Cyclooxygenase 35, 158, 215, 218, 259, 569
Cytotoxic 42

D

Diabetes 3, 4, 7, 11, 12, 26, 37, 39, 40, 48, 92, 155, 160, 162, 180, 182, 185, 265, 266, 267, 283, 287, 313, 314, 324, 326, 328, 333, 334, 338, 352, 368, 516, 517, 518, 519, 520, 547, 561
Diclofenac 35, 36, 171, 217, 218, 257, 258, 259, 283, 569
DPPH 24, 29, 37, 157, 158, 162, 163, 174, 182, 193, 245, 246, 247, 280, 282, 296, 309, 316, 322, 568
Drug development 48, 49, 91, 123, 156, 158, 185, 291, 326, 327, 345, 356, 456, 472, 515, 537, 547, 556, 562

E

Ecological 1, 2, 11, 12, 14, 16, 17, 18, 20, 51, 52, 54, 55, 82, 83, 84, 86, 87, 288, 566, 575
EGFR 20, 21, 334, 335, 338, 342, 369, 385, 398, 402, 432, 433, 434, 451, 452, 516, 531, 532, 548, 549, 550, 551, 552, 553, 554, 555, 556, 561, 562, 563
Endemic 1, 4, 8, 13, 14, 16, 17, 21, 54, 60, 83, 87, 93, 121, 157, 161, 162, 182, 184, 185, 186, 288, 567, 568, 569, 573, 575, 576
Ethnomedicinal 1, 2, 5, 7, 123, 182, 184, 186
Evolution 15, 8, 18, 20, 90, 514

F

Flavonoids 2, 28, 137, 153, 155, 558
Flow cytometry 202, 236, 238, 239, 273, 274, 275, 570
Fluorescence 16, 42, 93, 95, 106, 113, 209, 236, 251, 252, 268, 273, 566
FRAP 29, 37, 157, 165, 174, 194, 246, 280, 297, 309, 316, 322, 568
FRAP assay 165, 174, 246, 280, 568
FT-IR 18, 26, 243, 303, 326

G

Gastrointestinal disorders 7, 12
GC-MS 132, 154, 291

H

Histochemical 16, 21, 55, 57, 81, 85, 87, 566
HPTLC 26, 91, 118
Hydrogen bonds 551

I

Inflammation 7, 11, 12, 41, 42, 92, 147, 160, 171, 179, 185, 215, 217, 218, 223, 259, 262, 276, 292, 312, 320, 326, 331, 332, 333, 337, 355, 363, 365, 373, 376, 382, 387, 515, 520, 525, 539, 540, 541, 559, 564, 569
Inflorescence 19, 20, 59
IUCN Red List 16, 289

L

Leaf 7, 9, 18, 19, 20, 21, 22, 23, 24, 26, 28, 29, 33, 34, 35, 38, 43, 44, 45, 52, 53, 56, 58, 59, 60, 61, 67, 68, 75, 76, 81, 86, 87, 93, 94, 95, 105, 106, 107, 108, 111, 112, 113, 116, 135, 137, 138, 139, 140, 141, 142, 143, 144, 145, 146, 147, 148, 149, 151, 153, 154, 155, 156, 158, 160, 161, 174, 175, 176, 177, 178, 182, 183, 281, 283, 321, 322, 323, 337, 399, 415, 565, 566, 567, 580
Lipoxygenase 35, 158, 218, 259, 260, 569

M

Macroscopic 54, 55, 58, 83, 87, 105, 565
MCF-7 breast cancer cells 570
Mebendazole 169
Medicinal plants 17, 54, 91, 116, 117, 182, 187, 287, 289, 290, 320, 330, 331, 334, 560
Methanol extracts 38, 137, 139, 141, 142, 156, 322
Microscopic 22, 23, 54, 83, 86, 87, 93, 105, 106, 112, 113, 233, 235, 254, 565, 566, 576
Minimum bactericidal concentration (MBC) 157, 310
minimum fungicidal concentration (MFC) 310
Minimum fungicidal concentration (MFC) 157
minimum inhibitory concentration (MIC) 31, 310
Minimum inhibitory concentration (MIC) 157
Molecular docking 4, 5, 43, 47, 327, 328, 335, 336, 338, 341, 343, 344, 346, 348, 398, 402, 511, 513, 520, 526, 548, 562
Molecular dynamics 4, 5, 49, 328, 347, 348, 462, 471, 490, 499, 508, 513, 514, 520, 552, 563
Morphological 5, 18, 55
MS 17, 25, 46, 91, 118, 119, 120, 121, 132, 133, 144, 145, 147, 148, 149, 152, 153, 154, 155, 156, 183, 279, 290, 291, 292, 293, 296, 308, 321, 326, 341, 399, 567
MTT/XTT assays 570
Myrtaceae 1, 7, 10, 11, 18, 19, 20, 25, 51, 52, 53, 83, 84, 85, 86, 116, 151, 161, 288, 321, 565

N

Nanomedicines 570
Nanoparticles 5, 43, 44, 45, 187, 189, 192, 193, 195, 199, 214, 224, 225, 242, 243, 244, 246, 248, 249, 259, 260, 262, 263, 264, 267, 270, 274, 275, 276, 278, 279, 280, 281, 283, 317, 318, 568
Network pharmacology 4, 5, 48, 49, 525, 559, 560, 572
Neurodegenerative 11, 120, 182, 215, 547, 561, 563, 564
NMR 46, 118, 290, 291, 292, 295, 296, 304, 305, 306, 307, 308, 326
Nutraceuticals 30, 121, 570

P

Parasitology 34
Pharamacology 570
Pharmacology 15, 1, 2, 3, 4, 5, 11, 14, 24, 26, 47, 55, 81, 82, 83, 85, 90, 91, 92, 101, 116, 118, 119, 121, 128, 136, 145, 146, 149, 156, 157, 158, 161, 179, 182, 185, 186, 284, 292, 308, 319, 320, 322, 325, 326, 346, 481, 482, 486, 489, 491, 496, 498, 499, 500, 507,509, 518, 525, 527, 538, 539, 540, 541, 543, 564, 566, 572, 573, 575
Phenolic acids 2, 119, 133, 149, 155, 560
Phylogenetic 8, 9, 10, 15, 18, 20, 21, 52
Physicochemical 16, 19, 20, 93, 94, 95, 107, 338, 350, 351, 352, 355, 359, 362, 365, 366, 367, 368, 454, 513, 516, 527, 535, 567
Phytochemical 15, 5, 24, 117, 571
Phytocompounds19, 23, 25, 26, 156, 287, 288, 290, 292, 293, 329, 330, 331, 332, 334, 335, 336, 341, 342, 343, 344, 346, 399, 400, 401, 402, 453, 454, 455, 513, 517, 518, 519, 520, 567, 576
Phytomedicine 575
Powder microscopy 22, 23, 93, 94, 111, 112, 116, 567
Protein-protein interaction (PPI) networks 572
Pseudomonas aeruginosa 31, 33, 151, 157, 166, 168, 175, 176, 183, 186, 194, 195, 196, 197, 198, 199, 200, 201, 202, 203, 204, 205, 206, 207, 208, 209, 211, 212, 213, 247, 248, 249, 250, 251, 252, 253, 254, 255, 277, 280, 281, 285, 310, 317, 323, 330, 356, 472

Q

QTOF 17, 121, 133, 148, 149, 155, 292, 293, 341, 399, 567

R

Radius of Gyration 459, 468, 478, 487, 497, 506, 548, 550
Reactive oxygen species 3, 514
Root Mean Square Deviation 458, 467, 477, 486, 496, 505, 548
Root Mean Square Fluctuation 458, 468, 477, 487, 497, 505, 548, 549

S

S. *abortivum* 32
S. afromontanum 26
S. agastyamalayanum 14
S. alternifolium 44
S. antisepticum 28
S. aromaticum 2, 7, 12, 18, 22, 26, 27, 30, 31, 33, 35, 41, 42, 48, 92, 120, 159, 183, 279, 281, 283, 284, 288, 569
S. benthamianum 14
S. bourdillonii 13
S. calophyllifolium 23
S. caryophyllatum 11, 23, 24, 36, 38, 43, 92, 160, 183, 184, 324
S. cerasiforme 14
S. claviflorum 14
S. cordatum 11, 12, 31, 152
S. cumini 2, 7, 11, 12, 18, 22, 23, 24, 25, 26, 27, 28, 34, 35, 36, 38, 39, 40, 42, 44, 47, 48, 49, 52, 54, 84, 85, 92, 112, 114, 115, 152, 153, 155, 158, 159, 160, 182, 184, 185, 278, 279, 280, 281, 282, 283, 284, 288, 323, 324, 325, 569
S. densiflorum 16, 46
S. foxworthianum 14
S. fratris 15
S. glenum 15
*S. jambos*26, 28, 30, 31, 84, 85, 112, 288, 321, 322, 323
S. kampotense 14
S. laetum 4, 14, 16, 56, 57, 58, 60, 81, 83, 84, 85, 86, 87, 93, 94, 105, 106, 107, 108, 111, 112, 113, 114, 116, 121, 135, 136, 137, 138, 139, 140, 141, 142, 144, 145, 147, 148, 149, 151, 152, 153, 154, 156, 161, 170, 174, 176, 177, 178, 182, 185, 186, 292, 293, 565, 566, 567, 568, 573, 575, 576
S. lampeapiense 14
S. monimioides 15
S. monospermum 15
S. mundagam 36
S. munnarensis 14
S. namosialangense 15
S. nervosum 27, 160, 184
S. ngheanense 15
S. oblatum 32
S. occidentale 4, 14, 16, 51, 56, 57, 58, 60, 67, 81, 83, 84, 85, 86, 87, 93, 94, 105, 106, 107, 108, 109, 111, 112, 113, 114, 115, 116, 121, 122, 135, 137, 138, 139, 140, 141, 142, 144, 145, 146, 147, 148, 149, 151, 153, 156, 157, 161, 162, 166, 169, 170, 174, 177, 178, 182, 185, 186, 292, 293, 565, 566, 567, 573, 575, 576
S. padangense 15
S. palghatense 19, 4, 14, 16, 51, 56, 57, 58, 59, 60, 74, 79, 81, 83, 84, 85, 86, 87, 93, 94, 105, 106, 107, 108, 109, 111, 112, 113, 114, 115, 116, 121, 122, 135, 136, 137, 138, 139, 140, 141, 142, 144, 147, 148, 149, 151, 152, 153, 156, 157, 161, 162, 166, 169, 170, 172, 174, 175, 176, 177, 178, 179, 180, 181, 182, 185, 186, 189, 190, 191, 195, 215, 244, 245, 252, 256, 258, 259, 276, 278, 279, 280, 282, 283, 284, 285, 288, 292, 293, 298, 299, 302, 303, 304, 306, 309, 314, 315, 316, 320, 326, 337, 513, 520, 565, 566, 567, 568, 569, 570, 572, 573, 575, 576, 577
S. paniculatum 24, 153
S. parameswaranii 13
S. periyarensis 13
S. polyanthum 19, 29, 35, 37, 111, 158, 182, 323, 324
S. polycephalum 30, 33
S. samarangense, 19, 160, 284
S. scarbum 15
S. sriganesanii 15
S. stocksii 14, 16, 26, 282
S. vestitum 15
S. wawoniense 14
S. zeylanicum 15, 24, 35, 38, 39
S. zollingerianum 29
S.gartnerianum 2
SASA 459, 462, 463, 464, 469, 471, 473, 478, 479, 481, 482, 483, 488, 490, 492, 497, 499, 500, 501, 506, 508, 509, 510, 548, 550, 552, 555, 562
SEM 18, 44, 187, 189, 190, 192, 243
Silver nanoparticles 15, 18, 5, 43, 44, 45, 187, 188, 189, 190, 191, 192, 193, 194, 195, 202, 204, 208, 209, 211, 214, 215, 216, 218, 219, 220, 221, 222, 223, 224, 225, 226, 231, 232, 233, 236, 237, 240, 242, 243, 244, 245, 246, 247, 248, 250, 251, 252, 255, 256, 257, 258, 259, 260, 261, 262, 263, 264, 265, 266, 267, 269, 270, 271, 272, 274, 275, 276, 277, 278, 279, 280, 283, 316, 317, 318, 319, 337, 568, 570, 572, 573, 577, 580, 589, 600
Stomata 18, 19, 21, 23, 61, 68, 75, 84, 105, 106, 112, 565

Syzygium 15, 16, 1, 2, 3, 4, 7, 8, 9, 10, 11, 12, 13, 14, 15, 16, 17, 18, 19, 20, 21, 22, 23, 24, 25, 26, 27, 28, 29, 30, 32, 33, 34, 35, 36, 37, 38, 39, 40, 41, 42, 43, 44, 45, 46, 47, 48, 49, 50, 51, 52, 53, 54, 56, 58, 59, 60, 67, 74, 81, 83, 84, 85, 86, 87, 88, 91, 92, 93, 94, 101, 105, 107, 108, 109, 111, 112, 114, 115, 116, 118, 120, 121, 122, 128, 132, 133, 135, 136, 137, 138, 139, 140, 141, 142, 144, 146, 151, 153, 154, 155, 156, 158, 159, 160, 161, 162, 166, 169, 172, 174, 175, 176, 177, 178, 180, 182, 183, 184, 185, 186, 187, 188, 189, 191, 193, 194, 199, 204, 209, 214, 215, 216, 218, 219, 222, 223, 224, 225, 226, 227, 228, 231, 232, 233, 236, 237, 240, 242, 243, 244, 245, 246, 247, 249, 250, 253, 254, 256, 258, 259, 260, 261, 262, 263, 264, 265, 266, 267, 269, 270, 272, 274, 275, 276, 277, 278, 280, 281, 283, 284, 285, 288, 292, 293, 294, 295, 296, 297, 298, 299, 302, 303, 304, 305, 306, 307, 309, 312, 313, 316, 317, 318, 322, 324, 325, 328, 399, 403, 432, 520, 567, 569, 570, 573, 575, 576, 580, 586, 600

T

Tannins 2, 12, 25, 26, 27, 29, 31, 33, 57, 81, 82, 84, 85, 86, 87, 105, 112, 117, 120, 125, 126, 136, 141, 143, 144, 152, 153, 156, 177, 178, 182, 183, 188, 288, 289, 324, 567
Taxonomy 16, 19, 22, 83, 86, 88, 116, 575
TEM 18, 44, 187, 189, 190, 192, 244
Terpenoids 2, 3, 12, 24, 26, 27, 32, 34, 120, 152, 153, 183, 187, 288, 289, 322
Therapeutic potentials 13, 30

U

UV-VIS spectroscopy 44, 189

V

van der Waals 348, 404, 405, 406, 407, 408, 413, 414, 415, 416, 417, 418, 419, 420, 421, 422, 423, 424, 425, 426, 427, 428, 429, 430, 431, 433, 434, 435, 437, 438, 452, 463, 464, 467, 473, 477, 480, 482, 483, 491, 492, 496, 498, 501, 509, 510, 517, 533, 553, 554
Venation 18, 19, 52, 58, 59, 61, 69, 76, 83, 84, 87, 565
Vitamin 27, 99, 100, 101, 107, 114, 115, 144, 147, 148, 154, 520, 567, 568

W

Western Ghats 15, 1, 2, 4, 13, 15, 16, 17, 21, 51, 55, 83, 86, 87, 111, 288, 566, 575

X

XRD 18, 44, 187, 189, 190, 193, 245